Introduction to Geophysical Fluid Dynamics

Physical and Numerical Aspects

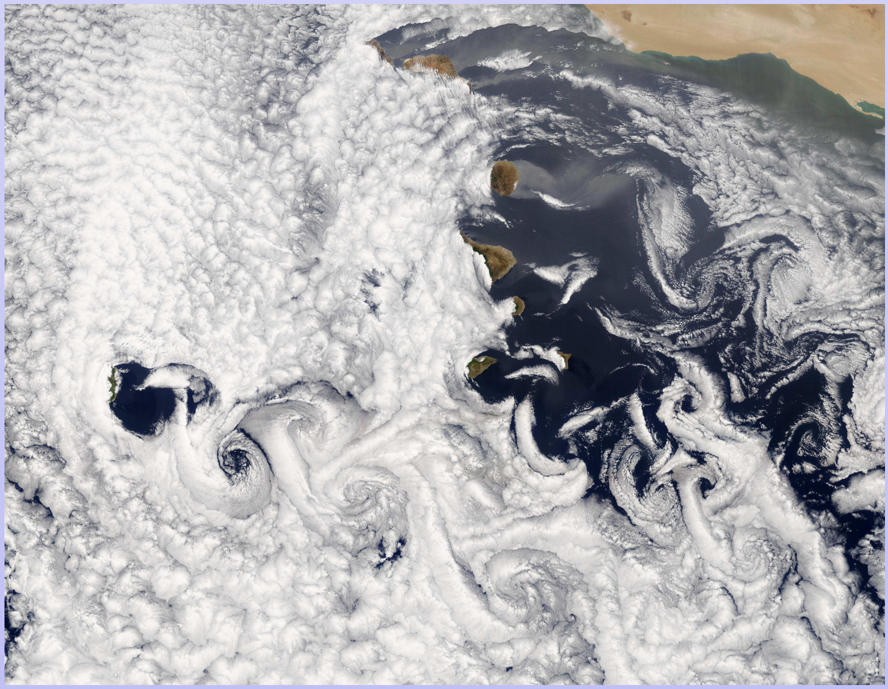

Benoit Cushman-Roisin and Jean-Marie Beckers

Under contract with ACADEMIC PRESS

October 18, 2006

INTRODUCTION TO GEOPHYSICAL FLUID DYNAMICS

Physical and Numerical Aspects

Benoit Cushman-Roisin
Thayer School of Engineering
Dartmouth College
Hanover, New Hampshire 03755
USA

Jean-Marie Beckers
Département d'Astrophysique, Géophysique et Océanographie
Université de Liège
B-4000 Liège
Belgium

March 2006

Under contract with

ACADEMIC PRESS

Cover photograph: Vortex street near Canary Islands as seen from the Terra satellite (*Image courtesy of MODIS Rapid Response Project at NASA/GSFC.*)

Library of Congress Cataloging-in-Publication Data:

Introduction to Geophysical Fluid Dynamics /
Benoit Cushman-Roisin and Jean-Marie Beckers
p. cm.
Includes bibliographical references and index.
ISBN 0-
1. Fluid Mechanics 2. Meteorology 3. Oceanography 4. Numerical Analysis I. Title

Contents

FOREWORD

This Foreword is to be written by an eminent scientist to be determined at a later stage of production

(Space for an eventual second page of the Foreword)

PREFACE

The intent of *Introduction to Geophysical Fluid Dynamics - Physical and Numerical Aspects* is to introduce its readers to the principles governing air and water flows on large terrestrial scales and to the methods by which these flows can be simulated on the computer. First and foremost the book is directed to students and scientists in dynamical meteorology and physical oceanography. In addition, the environmental concerns raised by the possible impact of industrial activities on climate and the accompanying variability of the atmosphere and oceans create a strong desire on the part of atmospheric chemists, biologists, engineers and many others to understand the basic concepts of atmospheric and oceanic dynamics. It is hoped that those will find here a readable reference text that will provide them with the necessary fundamentals.

The present volume is a significantly enlarged and updated revision of *Introduction to Geophysical Fluid Dynamics* published by Prentice-Hall in 1994, but the objective has not changed, namely to provide an introductory textbook and an approachable reference book. Simplicity and clarity have therefore remained the guiding principles in writing the text. Whenever possible, the physical principles are illustrated with the aid of the simplest existing models, and the computer methods are shown in juxtaposition with the equations to which they apply. The terminology and notation have also been selected to alleviate to a maximum the intellectual effort necessary to extract the meaning from the text. For example, the expressions planetary wave and stratification frequency are preferred to Rossby wave and Brunt-Väisälä frequency, respectively.

The book is divided in five parts. Following a presentation of the fundamentals in Part I, the effects of rotation and of stratification are explored separately in Parts II and III. Then, Part IV investigates the combined effects of rotation and stratification, which are at the core of geophysical fluid dynamics. The book closes with Part V, which gathers a group of more applied topics of contemporary interest. Each part is divided into short, relatively well contained chapters to provide flexibility of coverage to the professor and ease of access to the researcher. Physical principles and numerical topics are interspersed in order to show the relation of the latter to the former, but a clear division in sections and subsections makes it possible to separate the two if necessary.

Used as a textbook, the present volume should meet the needs of two courses, which are almost always taught sequentially in oceanography and meteorology curricula, namely Geophysical Fluid Dynamics and Numerical Modeling of Geophysical Flows. The integration of both subjects here under a single cover makes it possible to teach both courses with a unified notation and clearer connection of one part to the other than the traditional use of two textbooks, one for each subject. To facilitate the use as a textbook, a number of exercises are offered at the end of every chapter, some more theoretical to reinforce the understanding of the physical principles and others requiring access to a computer to apply the numerical methods. An accompanying CD-ROM contains an assortment of data sets and MATLAB™ codes that permit instructors to ask students to perform realistic and challenging exercises. At the end of every chapter, the reader will also find short biographies, which together form a history of the intellectual developments of the subject matter and should inspire students to achieve similar levels of distinction.

A general remark about notation is appropriate. Because mathematical physics in general and this discipline in particular involve an array of symbols to represent a multitude of variables and constants, with and without dimensions, some conventions are desirable in order to maximize clarity and minimize ambiguity. To this end, a systematic effort has been made to reserve classes of symbols for certain types of variables: Dimensional variables are denoted by lowercase Roman letters (such as u, v and w for the three velocity components), dimensional constants and parameters use uppercase Roman letters (such as H for domain height and L for length scale), and dimensionless quantities are assigned lowercase Greek letters (such as α for an angle and ϵ for a small dimensionless ratio). In keeping with a well established convention in fluid mechanics, dimensionless numbers credited to particular scientists are denoted by the first two letters of their name (*e.g.*,, Ro for the Rossby number and Ek for the Ekman number). Numerical notation is borrowed from Patrick J. Roache, and numerical variables are represented by tildas ($\tilde{}$). Of course, rules breed exceptions (*e.g.*,, g for the gravitational acceleration, ω for frequency and ψ for streamfunction).

We the authors wish to acknowledge the assistance from numerous colleagues across the globe, too many to permit an exhaustive list here. There is one person, however, who deserves a very special note of recognition. Prof. Eric Deleersnijder of the Université catholique de Louvain, Belgium, suggested that the numerical aspects be intertwined with the physics of Geophysical Fluid Dynamics. He also provided significant assistance during the writing of these numerical topics. An additional debt of gratitude goes to our students, who provided us not only with a testing ground for the teaching of this material but also with numerous and valuable comments. The following people are acknowledged for their pertinent remarks and suggestions made on earlier versions of the text, and which have improved both the clarity and accuracy of the presentation: *(Hans Burchard, Charles Troupin, Evan Mason, Anders Omstedt, Alexander Barth, list of names here, to be finalized in later stages of production)*.

Benoit Cushman-Roisin
Jean-Marie Beckers
March 2006

PREFACE OF THE FIRST EDITION

The intent of *Introduction to Geophysical Fluid Dynamics* is to introduce readers to this developing field. In the late 1950s, this discipline emerged as a few scientists, building on a miscellaneous heritage of fluid mechanics, meteorology, and oceanography, began to model complex atmospheric and oceanic flows by relatively simple mathematical analysis, thereby unifying atmospheric and oceanic physics. Turning from art to science, the discipline then matured during the 1970s. Appropriately, a first treatise titled *Geophysical Fluid Dynamics* by Joseph Pedlosky (Springer-Verlag) was published in 1979. Since then, several other authoritative textbooks have become available, all aimed at graduate students and researchers dedicated to the physics of the atmosphere and oceans. It is my opinion that the teaching of geophysical fluid dynamics is now making its way into science graduate curricula outside of meteorology and oceanography (*e.g.*,, physics and engineering). Simultaneously and in view of today's concerns regarding global change, acid precipitations, sea-level rise, and so forth, there is also a growing desire on the part of biologists, atmospheric chemists and engineers to understand the rudiments of climate and ocean dynamics. In this perspective, I believe that the time has come for an introductory text aimed at upper-level undergraduate students, graduate students, and researchers in environmental fluid dynamics.

In the hope of fulfilling this need, simplicity and clarity have been the guiding principles in preparing this book. Whenever possible, the physical principles are illustrated with the aid of the simplest existing models, and the terminology and notation have been selected to maximize the physical interpretation of the concepts and equations. For example, the expression *planetary wave* is preferred to *Rossby wave*,and subscripts are avoided whenever not strictly indispensable.

The book is divided in five parts. After the fundamentals have been established in Part I, the effects of rotation and stratification are explored separately in the following two parts. Then, Part IV analyzes the combined effects of rotation and stratification, and the book closes with Part V, on miscellaneous topics of contemporary interest. Each part is divided into short, relatively well contained chapters to provide flexibility in the choice of materials to be covered, according to the needs of the curriculum or the reader's interests. Each chapter corresponds to one or two lectures, occasionally three, and the length is deemed suitable for a one-semester course (45 lectures). Although it is also an inevitable reflection of my personal choices, the selection of materials has been guided by the desire to emphasize the physical principles at work behind observed phenomena. Such emphasis is also much in keeping with the traditional teaching of geophysical fluid dynamics. The scientist interested in the description of atmospheric and oceanic phenomena will find available an abundance of introductory texts in meteorology and oceanography.

Unlike existing texts in geophysical fluid dynamics, this book offers a number of exercises at the end of every chapter. There, the reader/teacher will also find short biographies and suggestions for laboratory demonstrations. Finally, the text ends with an appendix on wave kinematics, for it is my experience that not all students are familiar with the concepts of wave number, dispersion relation, and group velocity, whereas these are central to the understanding of geophysical wave phenomena.

A general remark on the notation is appropriate. Because mathematical physics in general and this discipline in particular involve symbols representing variables and constants, with and without dimensions, I believe that clarity is brought to the mathematical description of the subject when certain classes of symbols are reserved for certain types of terms. In that spirit, a systematic effort has been placed to assign the notation according to the following rules: Dimensional variables are denoted by lowercase Roman letters (such as u, v, and w for the velocity components), dimensional constants and parameters use uppercase Roman letters (such as H for the domain depth, L for length scale), and dimensionless quantities are assigned lowercase Greek letters (such as θ for an angle). In keeping with a well-established convention of fluid mechanics, dimensionless numbers credited to particular scientists are denoted by the first two letters of those scientists' names (*e.g.*,, Ro for the Rossby number). Of course, conventions breed exceptions (*e.g.*,, g for the constant gravitational acceleration, ω for frequency, and ψ for streamfunction).

In closing, I wish to acknowledge inspiration from numerous colleagues from across the globe, too many to permit an exhaustive list here. I am also particularly indebted to my students at Dartmouth College; their thirst for knowledge prompted the present text. Don L. Boyer, Arizona State University, Pijush K. Kundu, Nova University, Peter D. Killworth, Robert Hooke Institute, Fred Lutgens, Central Illinois College, Joseph Pedlosky, Woods Hole Oceanographic Institution, and George Veronis, Yale University, made many detailed and invaluable suggestions, which have improved both the clarity and accuracy of the presentation. Finally, deep gratitude goes to Lori Terino for her expertise and patience in typing the text.

Benoit Cushman-Roisin
1993

Part I

Fundamentals

Chapter 1

Introduction

(October 18, 2006) **SUMMARY**: This opening chapter defines the discipline known as Geophysical Fluid Dynamics, stresses its importance, and highlights its most distinctive attributes. A brief history of numerical simulations in meteorology and oceanography is also presented. Scale analysis and their relationship with finite differences are introduced to show how discrete numerical grids depend on the scales under investigation and how finite differences allow to approximate derivatives at those scales. The problem of unresolved scales is introduced as an aliasing problem in discretization.

1.1 Objective

The object of geophysical fluid dynamics is the study of naturally occurring, large-scale flows on Earth and elsewhere, but mostly on Earth. Although the discipline encompasses the motions of both fluid phases – liquids (waters in the ocean, molten rock in the outer core) and gases (air in our atmosphere, atmospheres of other planets, ionized gases in stars) – a restriction is placed on the *scale* of these motions. Only the larger-scale motions fall within the scope of geophysical fluid dynamics. For example, problems related to river flow, microturbulence in the upper ocean, and convection in clouds are traditionally viewed as topics specific to hydrology, oceanography, and meteorology, respectively. Geophysical fluid dynamics deals exclusively with those motions observed in various systems and under different guises but nonetheless governed by similar dynamics. For example, large anticyclones of our weather are dynamically germane to vortices spun off by the Gulf Stream and to Jupiter's Great Red Spot. Most of these problems, it turns out, are at the large-scale end, where either the ambient rotation (of Earth, planet or star) or density differences (warm and cold air masses, fresh and saline waters) or both assume some importance. In this respect, geophysical fluid dynamics comprises rotating-stratified fluid dynamics.

Typical problems in geophysical fluid dynamics concern the variability of the atmosphere (weather and climate dynamics), of the ocean (waves, vortices and currents) and, to a lesser extent, the motions in the earth's interior responsible for the dynamo effect, vortices on other planets (such as Jupiter's Great Red Spot, and Neptune's Great Dark Spot), and convection in stars (the sun, in particular).

1.2 Importance of geophysical fluid dynamics

Without its atmosphere and oceans, it is certain that our planet would not sustain life. The natural fluid motions occurring in these systems are therefore of vital importance to us, and their understanding extends beyond intellectual curiosity – it is a necessity. Historically, weather vagaries have baffled scientists and laypersons alike since times immemorial. Likewise, conditions at sea have long influenced a wide range of human activities, from exploration to commerce, tourism, fisheries, and even wars.

Thanks in large part to advances in geophysical fluid dynamics, the ability to predict with some confidence the paths of hurricanes (Figures 1-1 and 1-2) has led to the establishment of a warning system that, no doubt, has saved numerous lives at sea and in coastal areas (Abbott, 2004). Warning systems, however, are only useful if sufficiently dense observing systems are implemented, fast prediction capabilities are available and efficient flow of information is ensured. A dreadful example of a situation in which a warning system was not yet adequate to save lives was the earthquake off Indonesia's Sumatra Island on 26 December 2004. The tsunami generated by the earthquake was not detected, its consequences not assessed and authorities not alerted within the two hours needed for the wave to reach beaches in the region. On a larger scale, the passage every 3 to 5 years of an anomalously warm water mass along the tropical Pacific Ocean and the western coast of South America, known as the El-Niño event, has long been blamed for serious ecological damage and disastrous economical consequences in some countries (O'Brien, 1978; Glantz, 2001). Now, thanks to increased understanding of long oceanic waves, atmospheric convection, and natural oscillations in air-sea interactions (Philander, 1990; D'Aleo, 2002), scientists have successfully removed the veil of mystery on this complex event, and numerical models (*e.g.*, Chen *et al.*, 2004) offer reliable predictions with at least one year of *lead time*, *i.e.*, there is a year between the moment the prediction is made and the time to which it applies.

Having acknowledged that our industrial society is placing a tremendous burden on the planetary atmosphere and consequently on all of us, scientists, engineers, and the public are becoming increasingly concerned about the fate of pollutants and greenhouse gases dispersed in the environment and especially about their cumulative effect. Will the accumulation of greenhouse gases in the atmosphere lead to global climatic changes that, in turn, will affect our lives and societies? What are the various roles played by the oceans in maintaining our present climate? Is it possible to reverse the trend toward depletion of the ozone in the upper atmosphere? Is it safe to deposit hazardous wastes on the ocean floor? Such pressing questions cannot find answers without, first, an in-depth understanding of atmospheric and oceanic dynamics and, second, the development of predictive models. In this twin endeavor, geophysical fluid dynamics assumes an essential role, and the numerical aspects should not be underestimated in view of the required predictive tools.

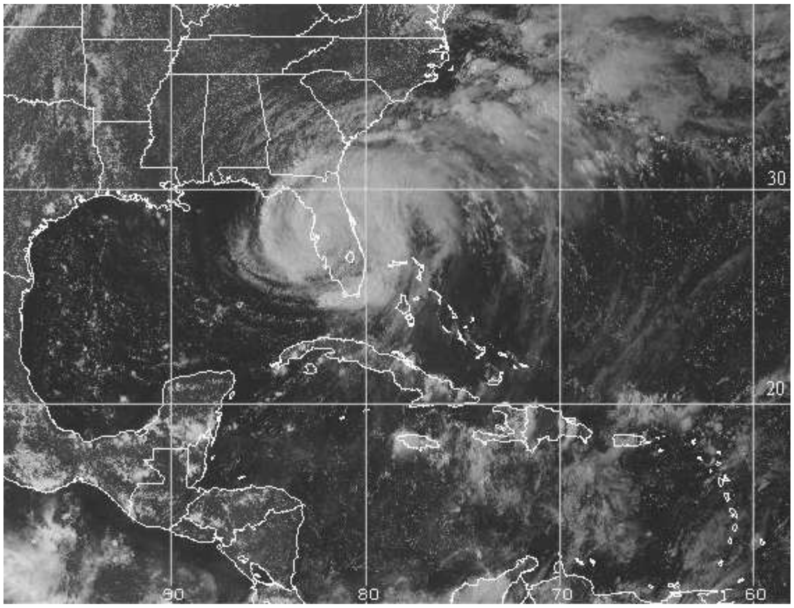

Figure 1-1 Hurricane Frances during her passage over Florida on 5 September 2004. The diameter of the storm is about 830 km and its top wind speed approaches 200 km per hour. (Courtesy of NOAA, Department of Commerce, Washington, D.C.)

1.3 Distinguishing attributes of geophysical flows

Two main ingredients distinguish the discipline from traditional fluid mechanics: the effects of rotation and those of stratification. The controlling influence of one, the other, or both leads to peculiarities exhibited only by geophysical flows. In a nutshell, the present book can be viewed as an account of these peculiarities.

The presence of an ambient rotation, such as that due to the earth's spin about its axis, introduces in the equations of motion two acceleration terms that, in the rotating framework, can be interpreted as forces. They are the Coriolis force and the centrifugal force (for a detailed explanation, see Stommel and Moore, 1989). Although the latter is the more palpable of the two, it plays no role in geophysical flows, however surprising this may be. The former and less intuitive of the two turns out to be a crucial factor in geophysical motions.

In anticipation of the following chapters, it can be mentioned here (without explanation) that a major effect of the Coriolis force is to impart a certain vertical rigidity to the fluid. In rapidly rotating, homogeneous fluids, this effect can be so strong that the flow displays strict columnar motions; that is, all particles along the same vertical evolve in concert, thus retaining their vertical alignment over long periods of time. The discovery of this property is attributed to Geoffrey I. Taylor, a British physicist famous for his varied contributions to fluid dynamics. (See the short biography at the end of Chapter 7.) It is said that Taylor first arrived at the rigidity property with mathematical arguments alone. Not believing that this could be correct, he then performed laboratory experiments that revealed, much to his amazement, that

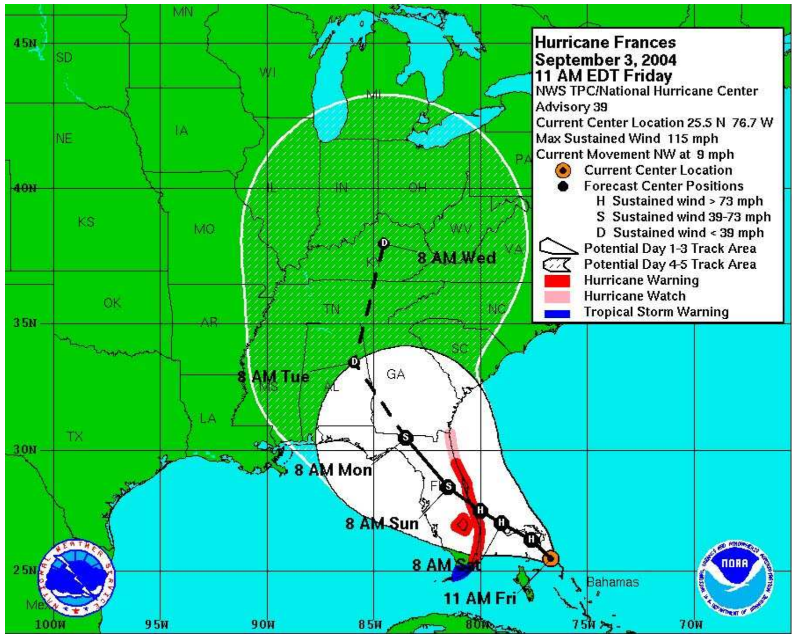

Figure 1-2 Computer prediction of the path of Hurricane Frances. The calculations were performed on Friday 3 September 2004 to predict the hurricane path and characteristics over the next 5 days (until Wednesday 8 September). The outline surrounding the trajectory indicates the level of uncertainty. Compare the position predicted for Sunday 5 September with the actual position shown on Figure 1-1. (Courtesy of NOAA, Department of Commerce, Washington, D.C.)

the theoretical prediction was indeed correct. Drops of dye released in such rapidly rotating, homogeneous fluids form vertical streaks, which, within a few rotations, shear laterally to form spiral sheets of dyed fluid (Figure 1-3). The vertical coherence of these sheets is truly fascinating!

In large-scale atmospheric and oceanic flows, such state of perfect vertical rigidity is not realized, chiefly because the rotation rate is not sufficiently fast and the density is not sufficiently uniform to mask other, ongoing processes. Nonetheless, motions in the atmosphere, in the oceans, and on other planets manifest a tendency toward columnar behavior. For example, currents in the western North Atlantic have been observed to extend vertically over 4000 m without significant change in amplitude and direction (Schmitz, 1980).

Stratification, the other distinguishing attribute of geophysical fluid dynamics, arises because naturally occurring flows typically involve fluids of different densities (*e.g.*, warm and cold air masses, fresh and saline waters). Here, the gravitational force is of great importance, for it tends to lower the heaviest fluid and to raise the lightest. Under equilibrium conditions, the fluid is stably stratified, consisting of vertically stacked horizontal layers. Fluid motions, however, disturb this equilibrium, which gravity systematically strives to restore. Small perturbations generate internal waves, the three-dimensional analogue of surface waves, with which we are all familiar. Large perturbations, especially those maintained over time, may

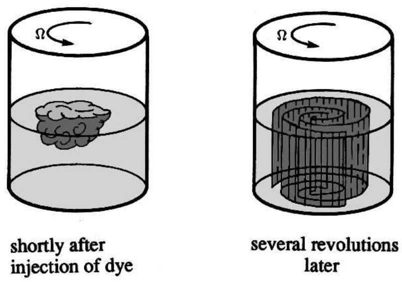

Figure 1-3 Experimental evidence of the rigidity of a rapidly rotating, homogeneous fluid. In a spinning vessel filled with clear water, an initially amorphous cloud of aqueous dye is transformed in the course of several rotations into perfectly vertical sheets, known as *Taylor curtains*.

cause mixing and convection. For example, the prevailing winds in our atmosphere are manifestations of the planetary convection driven by the pole-to-equator temperature difference.

It is worth mentioning the perplexing situation in which a boat may experience strong resistance to forward motion while sailing under apparently calm conditions. This phenomenon, called *dead waters* by mariners, was first documented by the Norwegian oceanographer Fridtjof Nansen, famous for his epic expedition on the *Fram* through the Arctic Ocean, begun in 1893. Nansen reported the problem to his Swedish colleague Vagn Walfrid Ekman who, after performing laboratory simulations (Ekman, 1904), affirmed that internal waves were to blame. The scenario is as follows: During times of dead waters , Nansen must have been sailing in a layer of relatively fresh water capping the more saline oceanic waters and of thickness, coincidently, comparable to the ship draft; the ship created a wake of internal waves along the interface (Figure 1-4), unseen at the surface but radiating considerable energy and causing the noted resistance to the forward motion of the ship.

1.4 Scales of motions

To discern whether a physical process is dynamically important in any particular situation, geophysical fluid dynamicists introduce *scales of motion*. These are dimensional quantities expressing the overall magnitude of the variables under consideration. They are estimates rather than precisely defined quantities and are understood solely as *orders of magnitude* of physical variables. In most situations, the key scales are those for time, length and velocity. For example, in the dead-water situation investigated by Ekman (Figure 1-4), fluid motions comprise a series of waves whose dominant wavelength is about the length of the submerged ship hull; this length is the natural choice for the length scale L of the problem; likewise, the ship speed provides a reference velocity that can be taken as the velocity scale U; finally, the time taken for the ship to travel the distance L at its speed U is the natural choice of time scale: $T = L/U$.

As a second example, consider Hurricane Frances during her course over the southeastern United States in early September 2004 (Figure 1-1). The satellite picture reveals a nearly circular feature spanning approximately 7.5° of latitude (830 km). Sustained surface wind speeds of a category-4 hurricane such as Frances range from 59 to 69 m/s. In general, hurricane tracks display appreciable change in direction and speed of propagation over 2-day

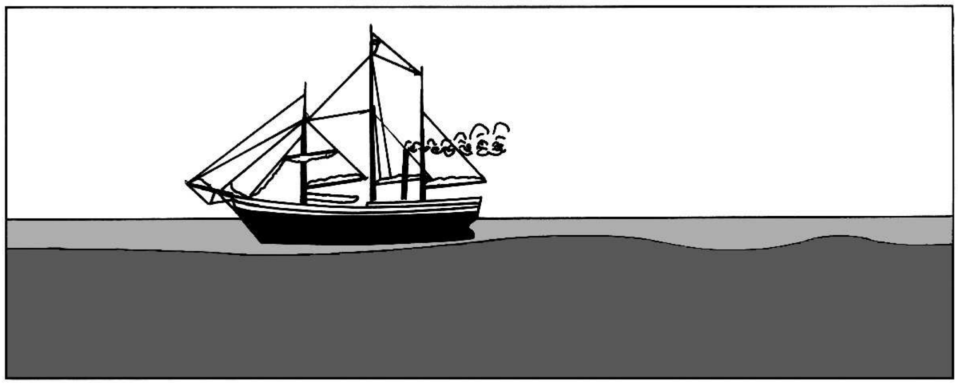

Figure 1-4 A laboratory experiment by V. W. Ekman (1904) showing internal waves generated by a model ship in a tank filled with two fluids of different densities. The heavier fluid at the bottom has been colored to make the interface visible. The model ship (the superstructure of which was drawn onto the original picture to depict Fridtjof Nansen's *Fram*) is towed from right to left, causing a wake of waves on the interface. The energy consumed by the generation of these waves produces a drag that, for a real ship, would translate into a resistance to forward motion. The absence of any significant surface wave has prompted sailors to call such situations *dead waters*. (From Ekman, 1904, and adapted by Gill, 1982)

intervals. Altogether, these elements suggest the following choice of scales for a hurricane: L = 800 km, U = 60 m/s and $T = 2 \times 10^5$ s (= 55.6 h).

As a third example, consider the famous Great Red Spot in Jupiter's atmosphere (Figure 1-5), which is known to have existed at least several hundred years. The structure is an elliptical vortex centered at 22°S and spanning approximately 12° in latitude and 25° in longitude; its highest wind speeds exceed 110 m/s, and the entire feature slowly drifts zonally at a speed of 3 m/s (Ingersoll *et al.*, 1979; Dowling and Ingersoll, 1988). Knowing that the planet's equatorial radius is 71,400 km, we determine the vortex semi-major and semi-minor axes (14,400 km and 7,500 km, respectively) and deem L = 10,000 km to be an appropriate length scale. A natural velocity scale for the fluid is U = 100 m/s. The selection of a time scale is somewhat problematic in view of the nearly steady state of the vortex; one choice is the time taken by a fluid particle to cover the distance L at the speed U ($T = L/U = 10^5$ s), whereas another is the time taken by the vortex to drift zonally over a distance equal to its longitudinal extent ($T = 10^7$ s). Additional information on the physics of the problem is clearly needed before selecting a time scale. Such ambiguity is not uncommon because many natural phenomena vary on different temporal scales (*e.g.*, the terrestrial atmosphere exhibits daily weather variation as well as decadal climatic variations, among others). The selection of a time scale then reflects the particular choice of physical processes being investigated in the system.

There are three additional scales that play important roles in analyzing geophysical fluid problems. As we mentioned earlier, geophysical fluids generally exhibit a certain degree of density heterogeneity, called stratification. The important parameters are then the average

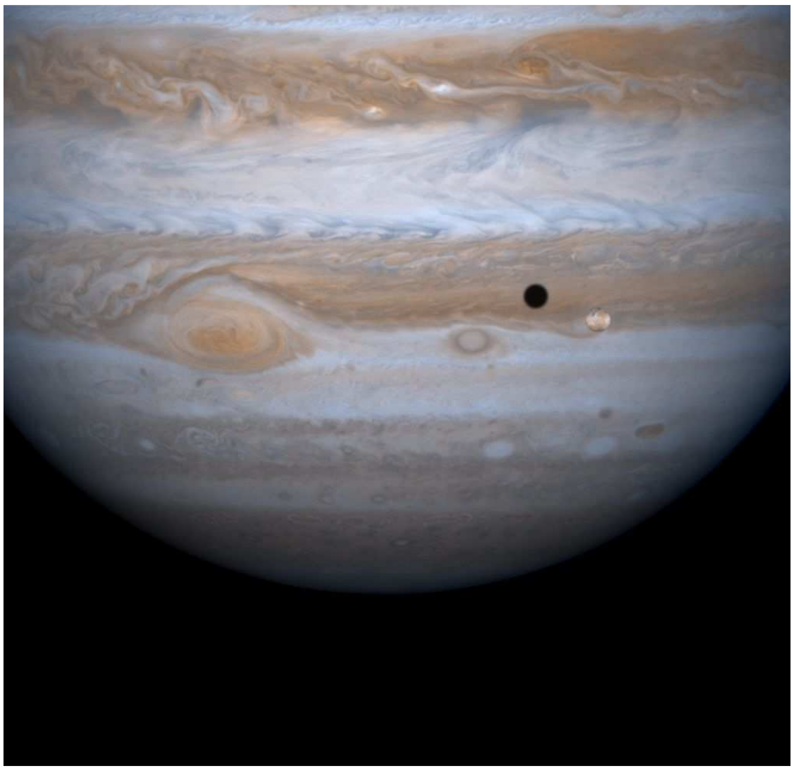

Figure 1-5 Southern Hemisphere of Jupiter as seen by the spacecraft *Cassini* in 2000. The Jupiter moon Io, of size comparable to our moon, projects its shadow onto the zonal jets between which the Great Red Spot of Jupiter is located (on the left). For further images visit `http://photojournal.jpl.nasa.gov/target/Jupiter`. (Image courtesy of NASA/JPL/University of Arizona)

density ρ_0, the range of density variations $\Delta\rho$, and the height H over which such density variations occur. In the ocean, the weak compressibility of water under changes of pressure, temperature, and salinity translates into values of $\Delta\rho$ always much less than ρ_0, whereas the compressibility of air renders the selection of $\Delta\rho$ in atmospheric flows somewhat delicate. Since geophysical flows are generally bounded in the vertical direction, the total depth of the fluid may be substituted for the height scale H. Usually, the smaller of the two height scales is selected.

As an example, the density and height scales in the dead-water problem (Figure 1-4) can be chosen as follows: ρ_0 = 1025 kg/m^3, the density of either fluid layer (almost the same); $\Delta\rho$ = 1 kg/m^3, the density difference between lower and upper layers (much smaller than ρ_0); and H = 5 m, the depth of the upper layer.

As the person new to geophysical fluid dynamics has already realized, the selection of scales for any given problem is more an art than a science. Choices are rather subjective. The trick is to choose quantities that are relevant to the problem, yet simple to establish. There is freedom. Fortunately, small inaccuracies are inconsequential because the scales are meant only to guide in the clarification of the problem, whereas grossly inappropriate scales will usually lead to flagrant contradictions. Practice, which forms intuition, is necessary to build confidence.

1.5 Importance of rotation

Naturally, we may wonder at which scales the ambient rotation becomes an important factor in controlling the fluid motions. To answer this question, we must first know the ambient rotation rate, which we denote by Ω and define as:

$$\Omega = \frac{2\pi \text{ radians}}{\text{time of one revolution}} . \tag{1.1}$$

Since our planet Earth actually rotates in two ways simultaneously, once per day about itself and once a year around the sun, the terrestrial value of Ω consists of two terms, 2π/24 hours + 2π/365.24 days = 2π/1 sidereal day = 7.2921 $\times$ 10^{-5} s^{-1}. The *sidereal day*, equal to 23 hours 56 minutes and 4.1 seconds, is the period of time spanning the moment when a fixed (distant) star is seen one day and the moment on the next day when it is seen at the same angle from the same point on Earth. It is slightly shorter than the 24–hour solar day, the time elapsed between the sun reaching its highest point in the sky two consecutive times, because the earth's orbital motion about the sun makes the earth rotate slightly more than one full turn with respect to distant stars before reaching the same Earth-Sun orientation.

If fluid motions evolve on a time scale comparable to or longer than the time of one rotation, we anticipate that the fluid does feel the effect of the ambient rotation. We thus define the dimensionless quantity

$$\omega = \frac{\text{time of one revolution}}{\text{motion time scale}} = \frac{2\pi/\Omega}{T} = \frac{2\pi}{\Omega T} , \tag{1.2}$$

where T is used to denote the time scale of the flow. Our criterion is as follows: If ω is on the order of or less than unity ($\omega \lesssim 1$), rotation effects should be considered. On Earth, this

Table 1.1 LENGTH AND VELOCITY SCALES OF MOTIONS IN WHICH ROTATION EFFECTS ARE IMPORTANT

L = 1 m	$U \leq$ 0.012 mm/s
L = 10 m	$U \leq$ 0.12 mm/s
L = 100 m	$U \leq$ 1.2 mm/s
L = 1 km	$U \leq$ 1.2 cm/s
L = 10 km	$U \leq$ 12 cm/s
L = 100 km	$U \leq$ 1.2 m/s
L = 1000 km	$U \leq$ 12 m/s
L = Earth radius = 6371 km	$U \leq$ 74 m/s

occurs when T exceeds 24 hours.

A second and usually more useful criterion results from considering the velocity and length scales of the motion. Let us denote these by U and L, respectively. Naturally, if a particle traveling at the speed U covers the distance L in a time longer than or comparable to a rotation period, we expect the trajectory to be influenced by the ambient rotation, and so we write

$$\begin{aligned} \epsilon &= \frac{\text{time of one revolution}}{\text{time taken by particle to cover distance } L \text{ at speed } U} \\ &= \frac{2\pi/\Omega}{L/U} = \frac{2\pi U}{\Omega L}. \end{aligned} \tag{1.3}$$

If ϵ is on the order of or less than unity ($\epsilon \lesssim 1$), we conclude that rotation is important.

Let us now consider a variety of possible length scales, using the value Ω for Earth. The corresponding velocity criteria are listed in Table 1.1.

Obviously, in most engineering applications, such as the flow of water at a speed of 5 m/s in a turbine 1 m in diameter ($\epsilon \sim 4 \times 10^5$) or the air flow past a 5-m wing on an airplane flying at 100 m/s ($\epsilon \sim 2 \times 10^6$), the inequality is not met, and the effects of rotation can be ignored. Likewise, the common task of emptying a bathtub (horizontal scale of 1 m, draining speed on the order of 0.01 m/s and a lapse of about 1000 s, giving $\omega \sim 90$ and $\epsilon \sim 900$) does not fall under the scope of Geophysical Fluid Dynamics. On the contrary, geophysical flows (such as an ocean current flowing at 10 cm/s and meandering over a distance of 10 km or a wind blowing at 10 m/s in a 1000-km-wide anticyclonic formation) do meet the inequality. This demonstrates that rotation is usually important in geophysical flows.

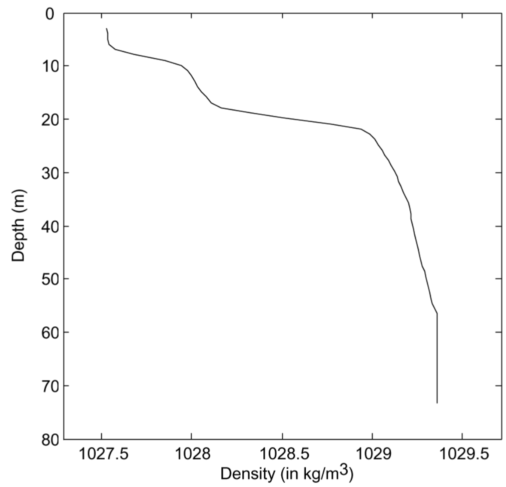

Figure 1-6 Vertical profile of density in the northern Adriatic Sea (43°32′N, 14°03′E) on 27 May 2003. Density increases downward by leaps and bounds, revealing the presence of different water masses stacked on top of one another in such a way that lighter waters float above denser waters. A region where the density increases significantly faster than above and below, marking the transition from one water mass to the next, is called a *pycnocline*. (Data courtesy of Drs. Hartmut Peters and Mirko Orlić)

1.6 Importance of stratification

The next question concerns the condition under which stratification effects are expected to play an important dynamical role. Geophysical fluids typically consist of fluid masses of different densities, which under gravitational action tend to arrange themselves in vertical stacks (Figure 1-6), corresponding to a state of minimal potential energy. But, motions continuously disturb this equilibrium, tending to raise dense fluid and lower light fluid. The corresponding increase of potential energy is at the expense of kinetic energy, thereby slowing the flow. On occasions, the opposite happens: Previously disturbed stratification returns toward equilibrium, potential energy converts into kinetic energy, and the flow gains momentum. In sum, the dynamical importance of stratification can be evaluated by comparing potential and kinetic energies.

If $\Delta\rho$ is the scale of density variations in the fluid and H is its height scale, a prototypical perturbation to the stratification consists in raising a fluid element of density $\rho_0 + \Delta\rho$ over the height H and, in order to conserve volume, lowering a lighter fluid element of density ρ_0 over the same height. The corresponding change in potential energy , per unit volume, is $(\rho_0+\Delta\rho)\, gH - \rho_0 gH = \Delta\rho gH$. With a typical fluid velocity U, the kinetic energy available per unit volume is $\frac{1}{2}\rho_0 U^2$. Accordingly, we construct the comparative energy ratio

$$\sigma = \frac{\frac{1}{2}\rho_0 U^2}{\Delta\rho g H}\,, \tag{1.4}$$

to which we can give the following interpretation. If σ is on the order of unity ($\sigma \sim 1$), a typical potential-energy increase necessary to perturb the stratification consumes a sizable portion of the available kinetic energy, thereby modifying the flow field substantially. Stratification is then important. If σ is much less than unity ($\sigma \ll 1$), there is insufficient kinetic energy to perturb significantly the stratification, and the latter greatly constrains the flow. Finally, if σ is much greater than unity ($\sigma \gg 1$), potential-energy modifications occur at very little cost to the kinetic energy, and stratification hardly affects the flow. In conclusion, stratification effects cannot be ignored in the first two cases – that is, when the dimensionless ratio defined in (1.4) is on the order of or much less than unity ($\sigma \lesssim 1$). In other words, σ is to stratification what the number ϵ, defined in (1.3), is to rotation.

A most interesting situation arises in geophysical fluids when rotation and stratification effects are simultaneously important, yet neither dominates over the other. Mathematically, this occurs when $\epsilon \sim 1$ and $\sigma \sim 1$ and yields the following relations among the various scales:

$$L \sim \frac{U}{\Omega} \quad \text{and} \quad U \sim \sqrt{\frac{\Delta\rho}{\rho_0} gH} \, . \tag{1.5}$$

(The factors 2π and $\frac{1}{2}$ have been omitted because they are secondary in a scale analysis.) Elimination of the velocity U yields a fundamental length scale:

$$L \sim \frac{1}{\Omega} \sqrt{\frac{\Delta\rho}{\rho_0} gH} \, . \tag{1.6}$$

In a given fluid, of mean density ρ_0 and density variation $\Delta\rho$, occupying a height H on a planet rotating at rate Ω and exerting a gravitational acceleration g, the scale L arises as a preferential length over which motions take place. On Earth (Ω = 7.29 $\times$ 10^{-5} s^{-1} and g = 9.81 m/s^2), typical conditions in the atmosphere (ρ_0 = 1.2 kg/m^3, $\Delta\rho$ = 0.03 kg/m^3, H = 5000 m) and in the ocean (ρ_0 = 1028 kg/m^3, $\Delta\rho$ = 2 kg/m^3, H = 1000 m) yield the following natural length and velocity scales:

$$\begin{array}{llll} L_{\text{atmosphere}} \sim 500\ \text{km} & & U_{\text{atmosphere}} \sim 30\ \text{m/s} \\ L_{\text{ocean}} \sim 60\ \text{km} & & U_{\text{ocean}} \sim 4\ \text{m/s} \end{array}$$

Although these estimates are relatively crude, we can easily recognize here the typical size and wind speed of weather patterns in the lower atmosphere and the typical width and speed of major currents in the upper ocean.

1.7 Distinction between the atmosphere and oceans

Generally, motions of the air in our atmosphere and of seawater in the oceans that fall under the scope of geophysical fluid dynamics occur on scales of several kilometers up to the size of the earth. Atmospheric phenomena comprise the coastal sea breeze, local to regional processes associated with topography, the cyclones, anticyclones, and fronts that form our daily weather, the general atmospheric circulation, and climatic variations. Oceanic phenomena of interest include estuarine flow, coastal upwelling and other processes associated with the presence of a coast, large eddies and fronts, major ocean currents such as the Gulf Stream, and the large-scale circulation. Table 1.2 lists the typical velocity, length and time scales of these motions, while Figure 1-7 ranks a sample of atmospheric and oceanic processes according to their spatial and temporal scales. As we can readily see, the general rule is that oceanic motions are slower and slightly more confined than their atmospheric counterparts. Also, the ocean tends to evolve more slowly than the atmosphere.

Table 1.2 LENGTH, VELOCITY AND TIME SCALES IN THE EARTH'S ATMOSPHERE AND OCEANS

Phenomenon	Length Scale L	Velocity Scale U	Time Scale T
Atmosphere:			
Microturbulence	10–100 cm	5–50 cm/s	few seconds
Thunderstorms	few km	1–10 m/s	few hours
Sea breeze	5–50 km	1–10 m/s	6 hours
Tornado	10–500 m	30–100 m/s	10–60 minutes
Hurricane	300–500 km	30–60 m/s	Days to weeks
Mountain waves	10–100 km	1–20 m/s	Days
Weather patterns	100–5000 km	1–50 m/s	Days to weeks
Prevailing winds	Global	5–50 m/s	Seasons to years
Climatic variations	Global	1–50 m/s	Decades and beyond
Ocean:			
Microturbulence	1–100 cm	1–10 cm/s	10–100 s
Internal waves	1–20 km	0.05–0.5 m/s	Minutes to hours
Tides	Basin scale	1–100 m/s	Hours
Coastal upwelling	1–10 km	0.1–1 m/s	Several days
Fronts	1–20 km	0.5–5 m/s	Few days
Eddies	5–100 km	0.1–1 m/s	Days to weeks
Major currents	50–500 km	0.5–2 m/s	Weeks to seasons
Large-scale gyres	Basin scale	0.01–0.1 m/s	Decades and beyond

Besides notable scale disparities, the atmosphere and oceans also have their own peculiarities. For example, a number of oceanic processes are caused by the presence of lateral boundaries (continents, islands), a constraint practically non-existent in the atmosphere. On the other hand, atmospheric motions are sometimes strongly dependent on the moisture content of the air (clouds, precipitation), a characteristic without oceanic counterpart.

Flow patterns in the atmosphere and oceans are generated by vastly different mechanisms. By and large, the atmosphere is thermodynamically driven, that is, its primary source of energy is the solar radiation. Briefly, this shortwave solar radiation traverses the air layer to be partially absorbed by the continents and oceans, which in turn re-emit a radiation at longer wavelengths. This second-hand radiation effectively heats the atmosphere from below, and the resulting convection drives the winds.

In contrast, the oceans are forced by a variety of mechanisms. In addition to the periodic gravitational forces of the moon and sun that generate the tides, the ocean surface is subjected to a wind stress that drives most ocean currents. Finally, local differences between air and sea temperatures generate heat fluxes, evaporation, and precipitation, which in turn act as thermodynamical forcings capable of modifying the wind-driven currents or of producing additional currents.

In passing, while we are contrasting the atmosphere with the oceans, it is appropriate to mention an enduring difference in terminology. Because meteorologists and laypeople alike are generally interested in knowing from where the winds are blowing, it is common in meteorology to refer to air velocities by their direction of origin, such as easterly (from

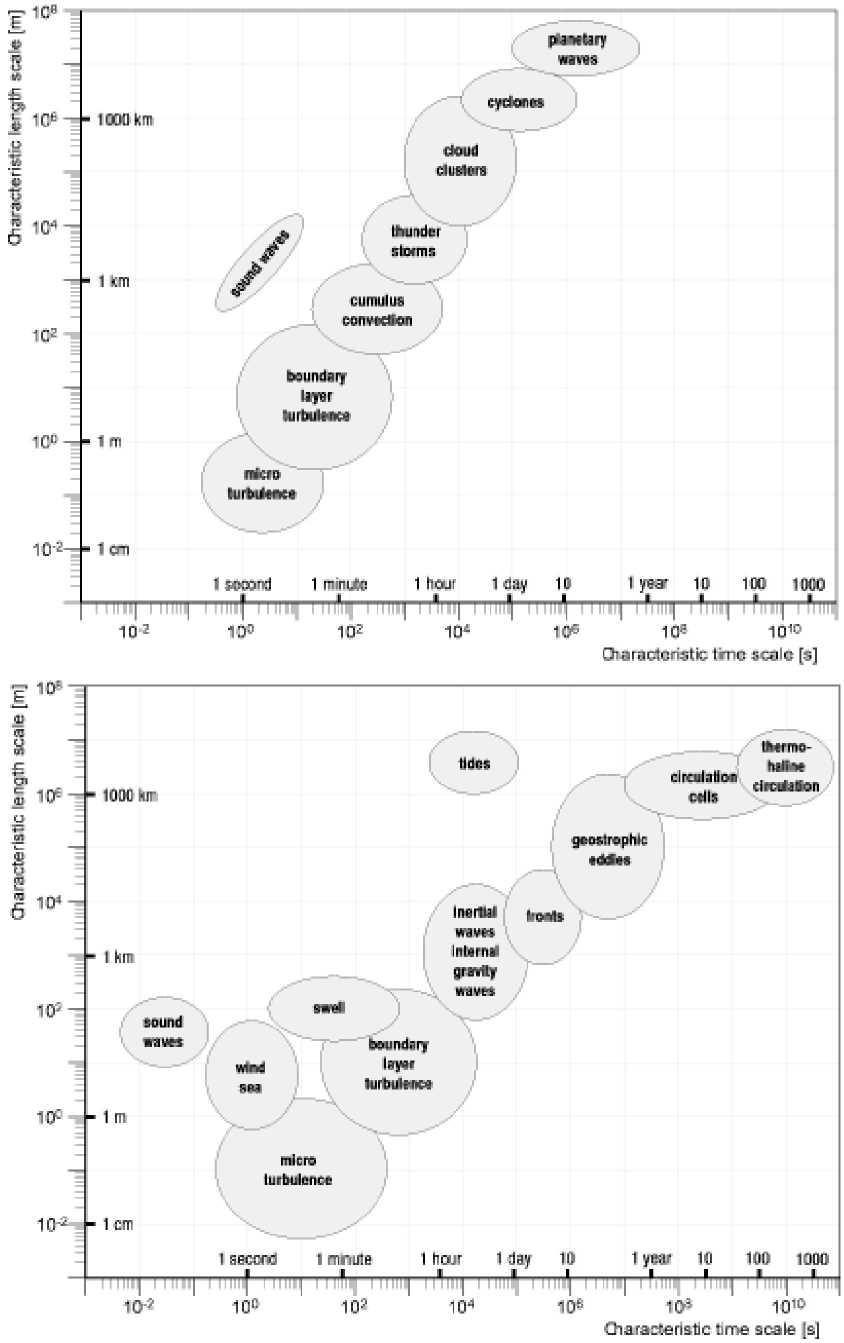

Figure 1-7 Various types of processes and structures in the atmosphere (top panel) and oceans (bottom panel), ranked according to their respective length and time scales. (Diagram courtesy of Hans von Storch)

the east – that is, toward the west). On the contrary, sailors and navigators are interested in knowing where ocean currents may take them. Hence, oceanographers designate currents by their downstream direction, such as westward (from the east or to the west). Meteorologists and oceanographers agree, however, on the terminology for vertical motions: upward or downward.

1.8 Data acquisition

Because geophysical fluid dynamics deals exclusively with naturally occurring flows and, moreover, those of rather sizable proportions, full-scale experimentation must be ruled out. Indeed, how could one conceive of changing the weather, even locally, for the sake of a scientific inquiry? Also, the Gulf Stream determines its own fancy path, irrespective of what oceanographers wish to study about it. In that respect, the situation is somewhat analogous to that of the economist who may not ask the government to prompt a disastrous recession for the sake of determining some parameters of the national economy. The inability to control the system under study is greatly alleviated by simulations. In geophysical fluid dynamics, these investigations are conducted via laboratory experiments and numerical models.

As well as being reduced to noting the whims of nature, observers of geophysical flows also face length and time scales that can be impractically large. A typical challenge is the survey of an oceanic feature several hundred kilometers wide. With a single ship (which is already quite expensive, especially if the feature is far away from the home shore), a typical survey can take several weeks, a time interval during which the feature might translate, distort, or otherwise evolve substantially. A faster survey might not reveal details with a sufficiently fine horizontal representation. Advances in satellite imagery and other methods of remote sensing (Conway *et al.*, 1997; Marzano and Visconti, 2002) do provide synoptic (*i.e.*, quasi-instantaneous) fields, but those are usually restricted to specific levels in the vertical (*e.g.*, cloud tops and ocean surface) or provide vertically integrated quantities. Also, some quantities simply defy measurement, such as the heat flux and vorticity. Those quantities can only be derived by an analysis on sets of proxy observations.

Finally, there are processes for which the time scale is well beyond the span of human life, if not the age of civilization. For example, climate studies require a certain understanding of glaciation cycles. Our only recourse here is to be clever and to identify today some traces of past glaciation events, such as geological records. Such an indirect approach usually requires a number of assumptions, some of which may never be adequately tested. Finally, exploration of other planets and of the sun is even more arduous.

At this point one may ask: What can we actually measure in the atmosphere and oceans with a reasonable degree of confidence? First and foremost, a number of scalar properties can be measured directly and with conventional instruments. For both the atmosphere and ocean, it is generally not difficult to measure the pressure and temperature. In fact, in the ocean the pressure can be measured so much more accurately than depth that, typically, depth is calculated from measured pressure on instruments that are gradually lowered into the sea. In the atmosphere, one can also accurately measure the water vapor, rainfall and some radiative heat fluxes (Rao *et al.*, 1990; Marzano and Visconti, 2002). Similarly, the salinity of seawater can be either determined directly or inferred from electrical conductivity (Pickard and

Emery, 1990). Also, the sea level can be monitored at shore stations. The typical problem, however, is that the measured quantities are not necessarily those preferred from a physical perspective. For example, one would prefer direct measurements of the Bernoulli function, diffusion coefficients, and turbulent correlation quantities.

Vectorial quantities are usually more difficult to obtain than scalars. Horizontal winds and currents can now be determined routinely by anemometers and currentmeters of various types, including some without rotating components (Lutgens and Tarbuck, 1986; Pickard and Emery, 1990), although usually not with the desired degree of spatial resolution. Fixed instruments, such as anemometers atop buildings and oceanic currentmeters at specific depths along a mooring line, offer fine temporal coverage, but adequate spatial coverage typically requires a prohibitive number of such instruments. To remedy the situation, instruments on drifting platforms (*e.g.*, balloons in the atmosphere and drifters or floats in the ocean) are routinely deployed. However, these instruments provide information that is mixed in time and space, and thus is not ideally suited to most purposes. A persistent problem is the measurements of the vertical velocity. Although vertical speeds can be measured with acoustic Doppler current profilers, the meaningful signal is often buried below the level of ambient turbulence and of instrumental error (position and sensitivity). Measuring the vector vorticity, so dear to theoreticians, is out of the question, as is the three-dimensional heat flux.

Also, some uncertainty resides in the interpretation of the measured quantities. For example, can the wind measured in the vicinity of a building be taken as representative of the prevailing wind over the city and so be used in weather forecasting, or is it more representative of a small-scale flow pattern resulting from the obstruction of the wind by the building?

Finally, sampling frequencies might not always permit the unambiguous identification of a process. Measuring quantities at a given location every week might well lead to a data set that includes also residual information on faster processes than weekly variations or a slower signal that we would like to capture with our measurements. For example, if we measure temperature on Monday at 3 o'clock in the afternoon one week and Monday at 7 o'clock in the morning the next week, the measurement will include a diurnal heating component superimposed on the weekly variations. The measurements are thus not necessarily representative of the process of interest.

1.9 The emergence of numerical simulations

Given the complexity of weather patterns and ocean currents, one can easily anticipate that the equations governing geophysical fluid motions, which we are going to establish in this book, are formidable and not amenable to analytical solution except in rare instances and after much simplification. Thus, one faces the tall challenge of having to solve the apparently unsolvable. The advent of the electronic computer has come to the rescue, but at a definite cost. Indeed, computers cannot solve differential equations but can only perform the most basic arithmetic operations. The partial differential equations (PDEs) of Geophysical Fluid Dynamics (GFD) need therefore to be transformed into a sequence of arithmetic operations. This process requires careful transformations and attention to details.

The purpose of numerical simulations of GFD flows is not limited to weather prediction, operational ocean forecasting and climate studies. There are situations when one desires to gain insight and understanding of a specific process, such as a particular form of instability or the role of friction under particular conditions. Computer simulations are our only way to experiment with the planet. Also, there is the occasional need to experiment with a novel numerical technique in order to assess its speed and accuracy. Finally, simulations can be a retracing of the past (*hindcasting*) or a smart interpolation of scattered data (*nowcasting*), as well as the prediction of future states (*forecasting*).

Models of GFD flows in meteorology, oceanography and climate studies come in all types and sizes, depending on the geographical domain of interest (local, regional, continental, basinwide or global) and the desired level of physical realism. Regional models are far too numerous to list here, and we only mention the existence of Atmospheric General Circulations Models (AGCMs), Oceanic General Circulation Models (OGCMs) and coupled General Circulation Models (GCMs). A truly comprehensive model does not exist, because the coupling of air, sea, ice and land physics over the entire planet is always open to the inclusion of yet one more process heretofore excluded from the model. In developing a numerical model of some GFD system, the question immediately arises as to what actually needs to be simulated. The answer largely dictates the level of details necessary and, therefore also, the level of physical approximation and the degree of numerical resolution.

Geophysical flows are governed by a set of coupled, nonlinear equations in four-dimensional space–time and exhibit a high sensitivity to small details. In mathematical terms, it is said that the system possesses chaotic properties, and the consequence is that geophysical flows are inherently unpredictable, as Lorenz demonstrated for the atmosphere several decades ago (Lorenz, 1969). The physical reality is that geophysical fluid systems are replete with instabilities, which amplify in a finite time minor details into significant structures (the butterfly-causing-a-tempest syndrome). The cyclones and anticyclones anticyclones of mid-latitude weather and the meandering of the coastal currents are but a couple of examples among many. Needless to say, the simulation of atmospheric and oceanographic fluid motions is a most highly challenging task.

The initial impetus for simulations of geophysical fluid simulations was, not surprisingly, weather prediction, an aspiration as old as mankind. More recently, climate studies have become another leading force in model development, because of their need for extremely large and complex models.

The first decisive step in the quest for weather prediction was made by Vilhelm Bjerknes (1904) in a paper titled *The Problem of Weather Prediction Considered from the Point of View of Mechanics and Physics*. He was the first to pose the problem as a set of time-dependent equations derived from physics and to be solved from a given, and hopefully complete, set of initial conditions. Bjerknes immediately faced the daunting task of integrating complicated partial differential equations, and, because this was well before electronic computers, resorted to graphical methods of solution. Unfortunately, these had little practical value and never surpassed the art of subjective forecasting by a trained person pouring over weather charts.

Taking a different tack, Lewis Fry Richardson (see biography at end of Chapter 14) decided that it would be better to reduce the differential equations to a set of arithmetic operations (additions, subtractions, multiplications and divisions exclusively) so that a step-by-step method of solution may be followed and performed by people not necessarily trained in meteorology. Such reduction could be accomplished, he reasoned, by seeking the solution at only selected points in the domain and by approximating spatial derivatives of the unknown variables by finite differences across those points. Likewise, time could be divided into finite

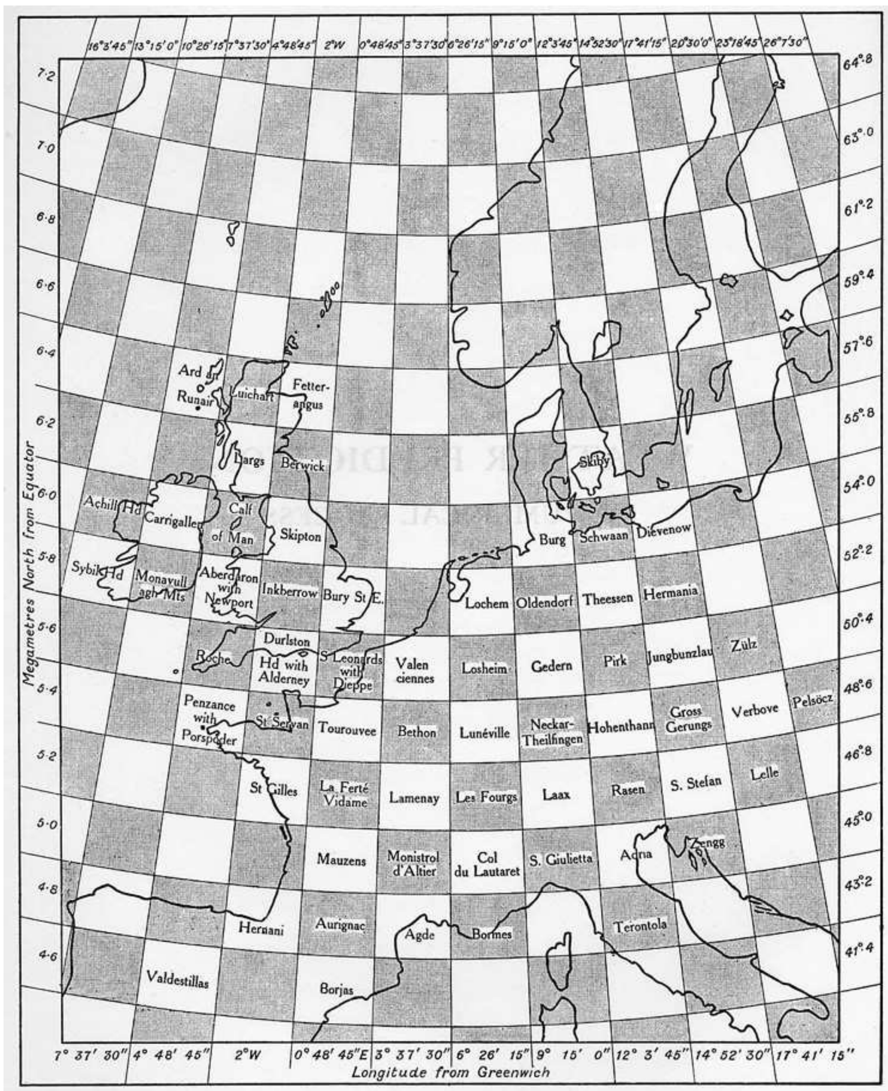

Figure 1-8 Model grid used by Lewis Fry Richardson as reported in his 1922 book *Weather Prediction by Numerical Process*. The grid was designed to optimize the fit between cells and existing meteorological stations, with observed surface pressures being used at the center of every shaded cell and winds at the center of every white cell.

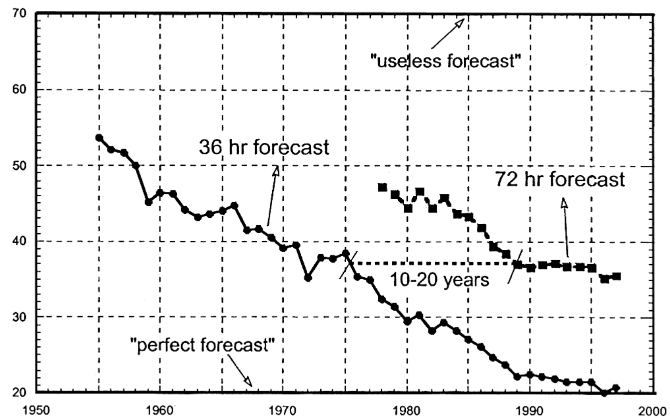

Figure 1-9 Historical improvement of weather forecasting skill over North America. The S1 score shown here is a measure of the relative error in the pressure gradient predictions at mid-height in the troposphere. (From Kalnay *et al.*, 1998, reproduction with the kind permission of the *American Meteorological Society*)

intervals and temporal derivatives approximated as differences across those time intervals. And thus was born numerical analysis. Richardson's work culminated in his 1922 book entitled *Weather Prediction by Numerical Process*. His first grid, to forecast weather over western Europe, is reproduced here as Figure 1-8. After the equations of motion had been dissected into a sequence of individual arithmetic operations, the first algorithm before the word existed, computations were performed by a large group of people, called *computers*, sitting around an auditorium equipped with slide rules and passing their results to their neighbors. Synchronization was accomplished by a leader in the pit of the auditorium as a conductor leads an orchestra. Needless to say, the work was tedious and slow, requiring an impractically large number of people to conduct the calculations quickly enough so that a 24-hour forecast could be obtained in less than 24 hours.

Despite an enormous effort on Richardson's part, the enterprise was a failure, with predicted pressure variations rapidly drifting away from meteorologically acceptable values. In retrospective, we now know that Richardson's model was improperly initiated for lack of upper-level data and that its six-hour time step was exceeding the limit required by numerical stability, of which, of course, he was not aware. The concept of numerical stability was not known until 1928 when it was elucidated by Richard Courant, Karl Friedrichs and Hans Lewy.

The work of Richardson was abandoned and relegated to the status of a curiosity or, as he put it himself, "a dream", only to be picked up again seriously at the advent of electronic computers. In the 1940s, the mathematician John von Neumann (see biography at end of Chapter 5) became interested in hydrodynamics and was seeking mathematical aids to solve nonlinear differential equations. Contact with Alan Turing, the inventor of the electronic computer, gave him the idea to build an automated electronic machine that could perform sequential calculations at a speed greatly surpassing that of humans. He collaborated with

Howard Aiken at Harvard University, who built the first electronic calculator, named the ASCC (Automatic Sequence Controlled Calculator). In 1943, von Neumann helped build the ENIAC (Electronic Numerical Integrator and Computer) at the University of Pennsylvania and, in 1945, the EDVAC (Electronic Discrete Variable Calculator) at Princeton University. Primarily because of the war-time need for improved weather forecasts and also out of personal challenge, von Neumann paired with Jule Charney (see biography at end of Chapter 16) and selected weather forecasting as the scientific challenge. But, unlike Richardson before them, von Neumann and Charney started humbly with a much reduced set of dynamics, a single equation to predict the pressure at mid-level in the troposphere. The results (Charney, 1950) exceeded expectations.

Success with a much reduced set of dynamics only encouraged further development. Phillips (1956) developed a two-layer quasi-geostrophic[1] model over a hemispheric domain. The results did not predict actual weather but did behave like weather, with realistic cyclones generated at the wrong places and times. This was nonetheless quite encouraging. A major limitation of the quasi-geostrophic simplification is that it fails near the Equator, and the only remedy was a return to the full equations (called *primitive equations*), back to where Lewis Richardson started. The main problem, it was found by then, is that primitive equations retain fast-moving gravity waves and, although these hold only a small amount of energy, their resolution demands both a much shorter time step of integration and a far better set of initial conditions than were available at the time.

From then on, the major intellectual challenges were overcome, and steady progress (Figure 1-9) has been achieved thanks to ever faster and larger computers (Figure 1-10) and to the gathering of an ever denser array of data around the globe. The reader interested in the historical developments of weather forecasting will find an excellent book-length account in Nebeker (1995).

1.10 Scales analysis and finite differences

In the preceding section, we saw that computers are used to solve numerically equations otherwise difficult to apprehend. Yet, even with the latest supercomputers and unchanged physical laws, scientists are requesting more computer power than ever, and we may rightfully ask what is the root cause of this unquenchable demand. To answer, we introduce a simple numerical technique (*finite differences*) that shows the strong relationship between scale analysis and numerical requirement. It is a prototypical example foreshowing a characteristic of more elaborate numerical methods that will be introduced in later chapters for more realistic problems.

When performing a time-scale analysis, we assume that a physical variable u changes significantly over a time scale T by a typical value U (Figure 1-11). With this definition of scales, the time derivative is on the order of

$$\frac{du}{dt} \sim \frac{U}{T}. \tag{1.7}$$

[1]Quasi-geostrophic dynamics are fully described in Chapter 16. It suffices here to say that the formalism eliminates the velocity components under the assumption that rotational effects are very strong. The result is a drastic reduction in the number of equations.

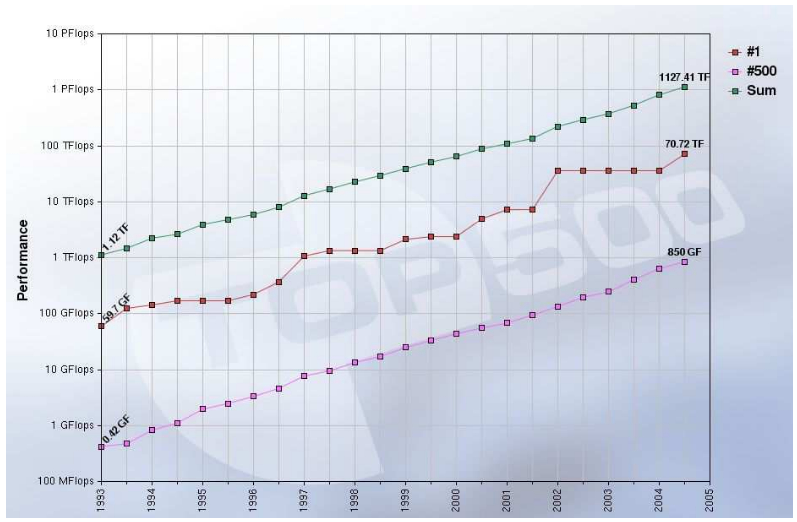

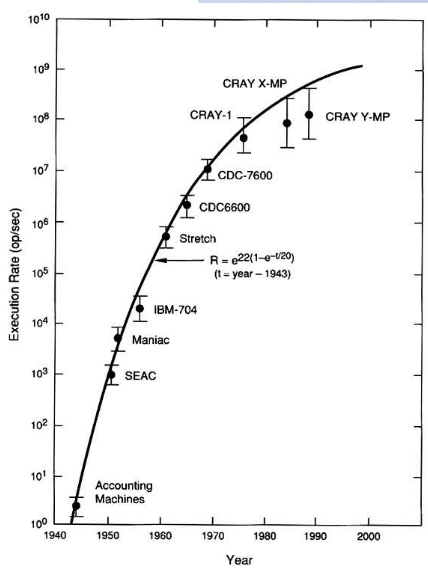

Figure 1-10 Historical increase of computational speed, as measured by the number of operations performed per second. (Adapted and supplemented from Hack (1992), who gives credit to a 1987 personal communication with Worlton and with recent data from `http://www.top500.org`)

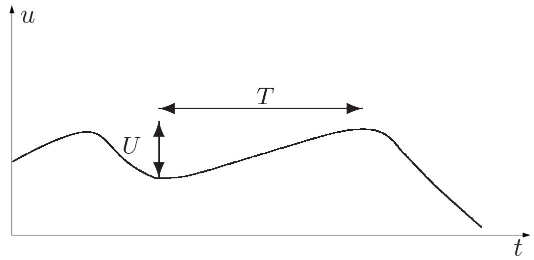

Figure 1-11 Time-scale analysis of a variable u. The time scale T is the time interval over which the variable u exhibits variations comparable to its standard deviation U.

If we then assume that the time scale over which the function u changes is also the one over which its derivative changes (in other words, we assume the time scale T to be representative of all type of variabilities, including derived fields), we can also estimate the order of magnitude of variations of the second derivative

$$\frac{d^2u}{dt^2} = \frac{d}{dt}\left(\frac{du}{dt}\right) \sim \frac{U/T}{T} = \frac{U}{T^2}\,, \tag{1.8}$$

and so on for higher-order derivatives. This approach is the basis for estimating the relative importance of different terms in time-marching equations, an exercise we will repeat several times in the next chapters.

We now turn our attention to the question of estimating derivatives with more accuracy than by a mere order of magnitude. Typically, this problem arises upon discretizing equations, a process by which all derivatives are replaced by algebraic approximations based on a few discrete values of the function u (Figure 1-12). Such *discretization* is necessary because computers possess a finite memory and are incapable of manipulating derivatives. We then face the following problem: Having stored only a few values of the function, how can we retrieve the value of the function's derivatives that appear in the equations?

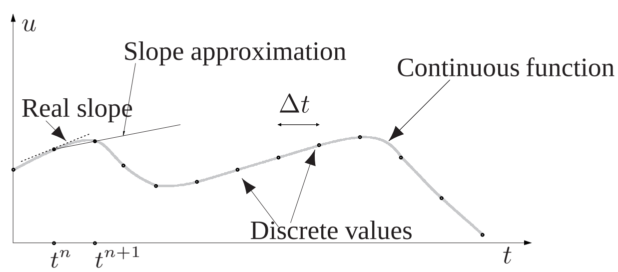

Figure 1-12 Representation of a function by a finite number of sampled values and approximation of a first derivative by a finite difference over Δt.

First, it is necessary to discretize the independent variable time t, since the first dynamical equations that we shall solve numerically are time-evolving equations. For simplicity, we shall suppose that the discrete time moments t^n, at which the function values are to be known, are uniformly distributed with a constant *time step* Δt

$$t^n = t^0 + n\,\Delta t, \quad n = 1, 2, ... \tag{1.9}$$

where the superscript index (not an exponent) n identifies the discrete time. Then, we note by u^n the value of u at time t^n, *i.e.*, $u^n = u(t^n)$. We now would like to determine the value of the derivative du/dt at time t^n knowing only the discrete values u^n. From the definition of a derivative

$$\frac{du}{dt} = \lim_{\Delta t \to 0} \frac{u(t+\Delta t) - u(t)}{\Delta t}, \tag{1.10}$$

we could directly deduce an approximation by allowing Δt to remain the finite time step

$$\frac{du}{dt} \simeq \frac{u(t+\Delta t) - u(t)}{\Delta t} \rightarrow \left.\frac{du}{dt}\right|_{t^n} \simeq \frac{u^{n+1} - u^n}{\Delta t}. \tag{1.11}$$

The accuracy of this approximation can be determined with the help of a Taylor series:

$$u(t+\Delta t) = u(t) + \Delta t \left.\frac{du}{dt}\right|_t + \underbrace{\frac{\Delta t^2}{2} \left.\frac{d^2u}{dt^2}\right|_t}_{\Delta t^2 \frac{U}{T^2}} + \underbrace{\frac{\Delta t^3}{6} \left.\frac{d^3u}{dt^3}\right|_t}_{\Delta t^3 \frac{U}{T^3}} + \underbrace{\mathcal{O}(\Delta t^4)}_{\Delta t^4 \frac{U}{T^4}}. \tag{1.12}$$

To the leading order for small Δt, we obtain the following estimate

$$\frac{du}{dt} = \frac{u(t+\Delta t) - u(t)}{\Delta t} + \mathcal{O}\left(\frac{\Delta t}{T}\frac{U}{T}\right). \tag{1.13}$$

The *relative* error on the derivative (the difference between the finite-difference approximation and the actual derivative, divided by the scale U/T) is therefore of the order $\Delta t/T$. For the approximation to be acceptable, this relative error should be much smaller than one, which demands that the time step Δt be sufficiently short compared to the time-scale at hand:

$$\Delta t \ll T. \tag{1.14}$$

This condition can be visualized graphically by considering the effect of various values of Δt on the resulting estimation of the time derivative (Figure 1-13). In the following we write the formal approximation as

$$\left.\frac{du}{dt}\right|_{t^n} = \frac{u^{n+1} - u^n}{\Delta t} + \mathcal{O}(\Delta t), \tag{1.15}$$

where it is understood that the measure of whether or not Δt is "small enough" must be based on the time-scale T of the variability of the variable u. Since in the simple finite difference (1.15), the error, called *truncation error* , is proportional to Δt, the approximation is said to be of first order. For an error proportional to Δt^2, the approximation is said of second order and so on.

For spatial derivatives, the preceding analysis is easily applicable, and we obtain a condition on the horizontal grid size Δx relatively to the horizontal length scale L, while the vertical grid space Δz is constrained by the vertical length scale H of the variable under investigation:

$$\Delta x \ll L, \quad \Delta z \ll H. \tag{1.16}$$

With these constraints on time-steps and grid sizes, we can begin to understand the need for significant computer resources in GFD simulations: The number of grid points M in a 3D domain of surface S and height H is

$$M = \frac{H}{\Delta z}\frac{S}{\Delta x^2}\ , \tag{1.17}$$

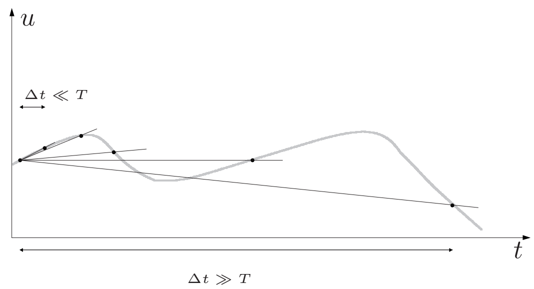

Figure 1-13 Finite differencing with various Δt values. Only when the time step is sufficiently short compared to the time scale, $\Delta t \ll T$, is the finite-difference slope close to the derivative, *i.e.*, the true slope.

while the total number of time steps N needed to cover a time period P is

$$N = \frac{P}{\Delta t}. \tag{1.18}$$

For a model covering the Atlantic Ocean ($S \sim 10^{14}\,\mathrm{m}^2$), resolving geostrophic eddies (see Figure 1-7: $\Delta x \sim \Delta y \leq 10^4$ m) and stratified water masses ($H/\Delta z \sim 50$) the number of grid points is about $M \sim 5 \times 10^7$. Then, at each of these points, several variables need to be stored and calculated (three-dimensional velocity, pressure, temperature *etc.*). Since each variable takes 4 or 8 bytes of memory depending on the desired number of significant digits, 2 Gigabytes of RAM is required. The number of floating point operations to be executed to simulate a single year can be estimated by taking a time-step resolving the rotational period of Earth $\Delta t \sim 10^3$ s, leading to $N \sim 30000$ time steps. The total number of operations to simulate a full year can then be estimated by observing that for every grid point and time step, a series of calculations must be performed (typically several hundreds), so that the total number of calculations amounts to $10^{14} - 10^{15}$. Therefore, on a contemporary supercomputer (one of the top 500 machines) with 1 Teraflops = 10^{12} floating operations per second exclusively dedicated to the simulation, less than half an hour would pass before the response is available, while on a high-end PC (1-2 Gigaflops), we would need to wait several days before getting our results. And yet, even with such a large model, we can only resolve the largest scales of motion (see Figure 1-7), while motions on shorter spatial and temporal scales simply cannot be simulated with this level of grid resolution. This does not mean, however, that those shorter-scale motions may altogether be neglected and, as we will see (*e.g.*, Chapter 14), one of the problems of large-scale oceanic and atmospheric models is the need for appropriate *parameterization* of shorter-scale motions so that they may properly bear their effects onto the larger-scale motions.

Should we dream to avoid such a parameterization by explicitly calculating all scales, we would need about $M \sim 10^{24}$ grid points demanding 5×10^{16} Gigabytes of computer memory, and $N \sim 3 \times 10^7$ time steps, for a total number of operations on the order of 10^{34}. Willing to wait only for 10^6 seconds before obtaining the results, we would need a computer delivering 10^{28} flops . This is a factor $10^{16} = 2^{53}$ higher than the present capabilities, both for speed and memory requirements. Using Moore's Law, the celebrated rule that forecasts a factor 2 in gain every 18 months, we would have to wait 53 times 18 months, *i.e.*, for about 80 years before computers could handle such a task.

Increasing resolution will therefore continue to call for the most powerful computers available, and models will need to include parameterization of turbulence or other unresolved motions for quite some time. Grid spacing will thus remain a crucial aspect of all GFD models, simply because of the large domain sizes and broad range of scales.

1.11 Higher-order methods

Rather than to increase resolution to better represent structures, we may wonder whether using other approximations for derivatives than our simple finite difference (1.11) would allow larger time-steps or higher quality approximations and improved model results. Based on a Taylor series

$$u^{n+1} = u^n + \Delta t \left.\frac{du}{dt}\right|_{t^n} + \frac{\Delta t^2}{2} \left.\frac{d^2u}{dt^2}\right|_{t^n} + \frac{\Delta t^3}{6} \left.\frac{d^3u}{dt^3}\right|_{t^n} + \mathcal{O}(\Delta t^4) \quad (1.19)$$

$$u^{n-1} = u^n - \Delta t \left.\frac{du}{dt}\right|_{t^n} + \frac{\Delta t^2}{2} \left.\frac{d^2u}{dt^2}\right|_{t^n} - \frac{\Delta t^3}{6} \left.\frac{d^3u}{dt^3}\right|_{t^n} + \mathcal{O}(\Delta t^4), \quad (1.20)$$

we can imagine that instead of using a *forward difference* approximation of the time derivative (1.11) we try a backward Taylor series (1.20) to design a *backward difference* approximation. This approximation is obviously still of first order because of its truncation error:

$$\left.\frac{du}{dt}\right|_{t^n} = \frac{u^n - u^{n-1}}{\Delta t} + \mathcal{O}(\Delta t). \quad (1.21)$$

Comparing (1.19) with (1.20), we observe that the truncation errors of the first-order forward and backward finite differences are the same but have opposite signs, so that by averaging both, we obtain a second-order truncation error (you can verify this statement by taking the difference between (1.19) and (1.20)):

$$\left.\frac{du}{dt}\right|_{t^n} = \frac{u^{n+1} - u^{n-1}}{2\Delta t} + \mathcal{O}(\Delta t^2). \quad (1.22)$$

Before considering higher-order approximations, let us first check whether the increase in order of approximation actually leads to improved approximations of the derivatives. To do so, consider the sinusoidal function of period T (and associated frequency ω)

$$u = U \sin\left(2\pi \frac{t}{T}\right) = U \sin(\omega t), \quad \omega = \frac{2\pi}{T}. \quad (1.23)$$

Knowing that the exact derivative is $\omega U \cos(\omega t)$, we can calculate the errors made by the various finite-difference approximations (Figure 1-14). Both the forward and backward finite differences converge towards the exact value for $\omega \Delta t \to 0$, with errors decreasing proportionally to Δt. As expected, the second-order approximation (1.22) exhibits a second-order convergence (the slope is 2 in a log-log graph).

The convergence rate obeys our theoretical estimate for $\omega \Delta t \ll 1$. However, when the time-step is relatively large (Figure 1-15), the error associated with the finite-difference approximations can be as large as the derivative itself. For coarse resolution, $\omega \Delta t \sim \mathcal{O}(1)$, the relative error is of order one, so that we expect a 100% error on the finite-difference approximation. Obviously, even with a second-order finite difference, we need at least $\omega \Delta t \leq$

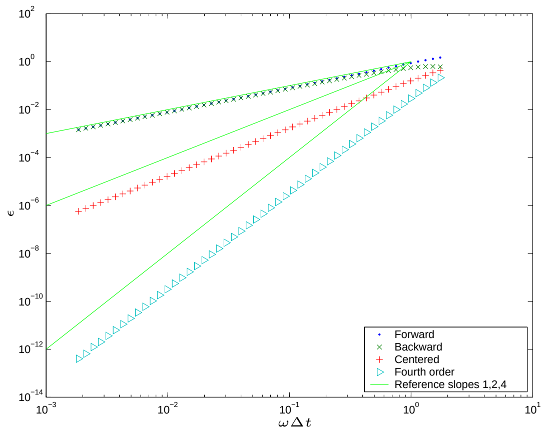

Figure 1-14 Relative error ϵ of various finite-difference approximations of the first derivative of the sinusoidal function as function of $\omega\Delta t$ when $\omega t = 1$. Scales are logarithmic and continuous lines of slope 1, 2 and 4 are added. First-order methods have a slope of 1, and the second-order method a slope of 2. The error behaves as expected for decreasing Δt.

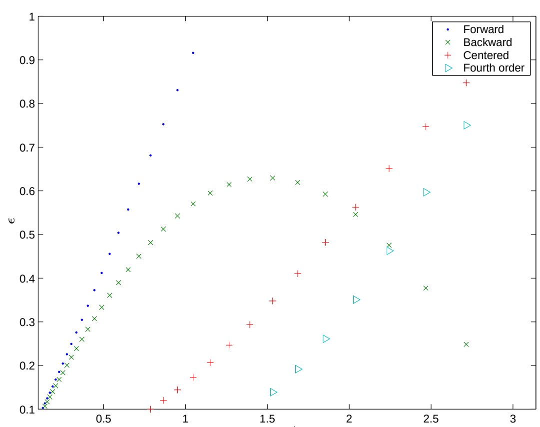

Figure 1-15 Relative error ϵ of various finite-difference approximations of the first derivative of the sinusoidal function as function of $\omega\Delta t$ when $\omega t = 1$. For coarse resolution $\omega\Delta t \sim \mathcal{O}(1)$, the relative error is of order one, so that we expect a 100% error on the finite-difference approximation.

0.8 to keep the relative error below 10%. In terms of the period of the signal $T = (2\pi)/\omega$, we need a time-step not larger than $\Delta t \lesssim T/8$, which implies that 8 points are needed along one period to resolve its derivatives within a 10% error level. Even a fourth-order method (to be shown shortly) cannot reconstruct derivatives correctly from a function sampled with fewer than several points per period.

The design of the second-order difference was accomplished simply by inspection of a Taylor series, a technique which cannot be extended to obtain higher-order approximations. An alternate method exists to obtain in a systematic way finite-difference approximations to any desired order, and it can be illustrated with the design of a fourth-order centered finite-difference approximation of the first derivative. Expecting that higher-order approximations need more information about a function in order to estimate its derivative at time t^n, we will combine values over a longer time interval, including $t^{n-2}, t^{n-1}, t^n, t^{n+1}$ and t^{n+2}:

$$\left.\frac{du}{dt}\right|_{t^n} \simeq a_{-2}u^{n-2} + a_{-1}u^{n-1} + a_0u^n + a_1u^{n+1} + a_2u^{n+2}. \tag{1.24}$$

Expanding u^{n+2} and the other values around t^n, we can write

$$\begin{aligned}\left.\frac{du}{dt}\right|_{t^n} &= (a_{-2} + a_{-1} + a_0 + a_1 + a_2)\; u^n \\ &+ (-2a_{-2} - a_{-1} + a_1 + 2a_2)\,\Delta t\; \left.\frac{du}{dt}\right|_{t^n} \\ &+ (4a_{-2} + a_{-1} + a_1 + 4a_2)\,\frac{\Delta t^2}{2}\; \left.\frac{d^2u}{dt^2}\right|_{t^n} \\ &+ (-8a_{-2} - a_{-1} + a_1 + 8a_2)\,\frac{\Delta t^3}{6}\; \left.\frac{d^3u}{dt^3}\right|_{t^n} \\ &+ (16a_{-2} + a_{-1} + a_1 + 16a_2)\,\frac{\Delta t^4}{24}\; \left.\frac{d^4u}{dt^4}\right|_{t^n} \\ &+ (-32a_{-2} - a_{-1} + a_1 + 32a_2)\,\frac{\Delta t^5}{120}\; \left.\frac{d^5u}{dt^5}\right|_{t^n} \\ &+\mathcal{O}(\Delta t^6).\end{aligned} \tag{1.25}$$

There are 5 coefficients, a_{-2} to a_2, to be determined. Two conditions must be satisfied to obtain an approximation that tends to the first derivative as $\Delta t \to 0$

$$\begin{aligned}a_{-2} + a_{-1} + a_0 + a_1 + a_2 = 0, \\ (-2a_{-2} - a_{-1} + a_1 + 2a_2)\,\Delta t = 1.\end{aligned}$$

After satisfying these two necessary conditions, we have three parameters that can be freely chosen so as to obtain the highest possible level of accuracy. This is achieved by imposing that the coefficients of the next three truncation errors be zero:

$$\begin{aligned}4a_{-2} + a_{-1} + a_1 + 4a_2 &= 0 \\ -8a_{-2} - a_{-1} + a_1 + 8a_2 &= 0 \\ 16a_{-2} + a_{-1} + a_1 + 16a_2 &= 0.\end{aligned}$$

Equipped with 5 equations for 5 unknowns, we can proceed with the solution:

$$-a_{-1} = a_1 = \frac{8}{12\Delta t}\ ,\ a_0 = 0,\ \ -a_{-2} = a_2 = -\frac{1}{12\Delta t}\ ,$$

so that the fourth-order finite-difference approximation of the first derivative is:

$$\left.\frac{du}{dt}\right|_{t^n} \simeq \frac{4}{3}\left(\frac{u^{n+1}-u^{n-1}}{2\Delta t}\right) - \frac{1}{3}\left(\frac{u^{n+2}-u^{n-2}}{4\Delta t}\right). \tag{1.26}$$

This formula can be interpreted as a linear combination of two centered differences, one across $2\Delta t$ and the other across $4\Delta t$. The truncation error can be assessed by looking at the next term in the series (1.25)

$$(-32a_{-2} - a_{-1} + a_1 + 32a_2)\,\frac{\Delta t^5}{120}\ \left.\frac{d^5u}{dt^5}\right|_{t^n} = -\frac{\Delta t^4}{30}\ \left.\frac{d^5u}{dt^5}\right|_{t^n}, \tag{1.27}$$

which shows that the approximation is indeed of fourth order.

The method can be generalized to approximate a derivative of any order p at time t^n using the current value u^n, m points in the past (before t^n) and m points in the future (after t^n):

$$\left.\frac{d^pu}{dt^p}\right|_{t_n} = a_{-m}u^{n-m} + ... + a_{-1}u^{n-1} + a_0u^n + a_1u^{n+1} + ... + a_mu^{n+m}. \tag{1.28}$$

The discrete points $n-m$ to $n+m$ involved in the approximation define the so-called *numerical stencil* of the operator.
Using a Taylor expansion for each term

$$u^{n+q} = u^n + q\Delta t\ \left.\frac{du}{dt}\right|_{t^n} + q^2\frac{\Delta t^2}{2}\ \left.\frac{d^2u}{dt^2}\right|_{t^n} + ... + q^p\frac{\Delta t^p}{p!}\ \left.\frac{d^pu}{dt^p}\right|_{t^n} + \mathcal{O}(\Delta t^{p+1}) \tag{1.29}$$

and injecting (1.29) for $q = -m, ..., m$ into the approximation (1.28), we have on the left-hand side the derivative we want to approximate and on the right a sum of derivatives. We impose that the sum of coefficients multiplying a derivative lower than order p be zero whereas the sum of the coefficients multiplying the p-th derivative be one. This forms a set of $p+1$ equations for the $2m+1$ unknown coefficients a_q ($q = -m, ..., m$). All constraints can be satisfied simultaneously only if we use a number $2m+1$ of points equal to or greater than $p+1$, *i.e.*, $2m \geq p$. When there are more points than necessary, we can take advantage of the remaining degrees of freedom to cancel the next few terms in the truncation errors. With $2m+1$ points we can then obtain a finite difference of order $2m-p+1$. For example, with $m=1$ and $p=1$, we obtained (1.22), a second-order approximation of the first derivative, and with $m=2$ and $p=1$, (1.26), a fourth-order approximation.

Let us now turn to the second derivative, a very common occurence, at least when considering spatial derivatives. With $p=2$, m must be at least 1, *i.e.*, 3 values of the function are required as a minimum: 1 old, 1 current and 1 future values. Applying the preceding method, we immediately obtain

$$\left.\frac{d^2u}{dt^2}\right|_{t_n} \simeq \left(\frac{u^{n-1}-2u^n+u^{n+1}}{\Delta t^2}\right), \tag{1.30}$$

a result we could also have obtained by direct inspection of (1.19) and (1.20).

Appendix C recapitulates a variety of discretization schemes for different orders of derivatives and various levels of accuracy. It also includes skewed schemes, which are not symmetric between past and future values but can be constructed in a way similar to the fourth-order finite-difference approximation of the first derivative.

1.12 Aliasing

We learned that the accuracy of a finite difference approximation of the first derivative degrades rapidly when the time step Δt is not kept much lower than the time scale T of the variable, and we might wonder what would happen if Δt should by some misfortune be larger than T. To answer this question, we return to a physical signal u of period T

$$u = U \sin(\omega t + \phi), \quad \omega = \frac{2\pi}{T} \tag{1.31}$$

sampled on a uniform grid of time step Δt

$$u^n = U \sin(n\, \omega \Delta t + \phi) \tag{1.32}$$

and assume that there exists another signal v of higher frequency $\tilde{\omega}$ given by

$$v = U \sin(\tilde{\omega} t + \phi), \quad \tilde{\omega} = \omega + \frac{2\pi}{\Delta t}. \tag{1.33}$$

The sampling of this other function at the same time intervals yields a discrete set of values

$$v^n = U \sin(n\, \tilde{\omega} \Delta t + \phi) = U \sin(n\, \omega \Delta t + 2n\pi + \phi) = u^n, \tag{1.34}$$

which cannot be distinguished from the discrete values u^n of the first signal, although the two signals are clearly not equal to each other. Thus, frequencies ω and $\omega + 2\pi/\Delta t$ cannot be separated in a sampling with time interval Δt because the higher-frequency signal masquerades as the lower-frequency signal. This unavoidable consequence of sampling is called *aliasing* .

Since signals of frequency $\omega + 2\pi/\Delta t$ and ω cannot be distinguished from each other, it appears that only frequencies within the following range

$$-\frac{\pi}{\Delta t} \;\le\; \omega \;\le\; \frac{\pi}{\Delta t} \tag{1.35}$$

can be recognized with a sampling interval Δt, and all other frequencies should preferably be absent, lest they contaminate the sampling process.

Since a negative frequency corresponds to a 180° phase shift, because $\sin(-\omega t + \phi) = \sin(\omega t - \phi + \pi)$, the useful range is actually $0 \;\le\; \omega \;\le\; \pi/\Delta t$, and to sample a wave of frequency ω the time step Δt may not exceed $\Delta t_{\max} = \pi/\omega = T/2$, which implies that at least two samples of the signal must be taken per period. This minimum required sampling frequency is called the *Nyquist frequency*. Looking at the problem in a different way, with

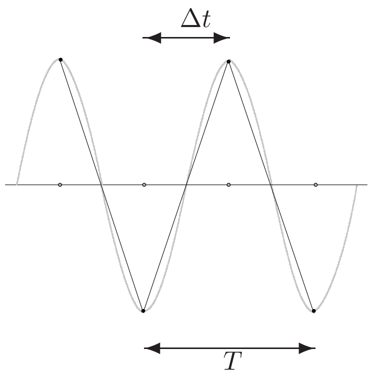

Figure 1-16 Shortest wave (at *cut-off frequency* $\pi/\Delta t$ or period $2\Delta t$) resolved by uniform grid in time.

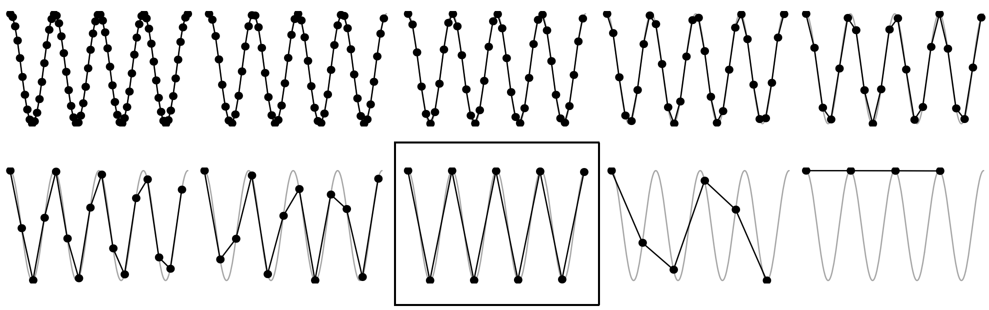

Figure 1-17 Aliasing illustrated by sampling a given signal (gray sinusoidal curve) with an increasing time interval. A high sampling rate (top row of images) resolves the signal properly. The boxed image on the bottom row corresponds to the cut-off frequency, and the sampled signal appears as a seesaw. The last two images correspond to excessively long time intervals that alias the signal, making it appear as if it had a longer period than it actually has.

a given sampling interval Δt (rather than a given frequency), we recognize that the highest resolved frequency is $\pi/\Delta t$, called the *cutoff frequency* (Figure 1-16).

Should higher frequencies be present and sampled, aliasing inevitably occurs, as illustrated by a sinusoidal function sampled with increasingly fewer points per period (Figure 1-17). The reader is also invited to experiment with MATLAB™ script `aliasanim.m`. Up to $\Delta t = T/2$, the signal is recognizable, but, beyond, lines connecting consecutive sampled values appear to tunnel through crests and troughs, giving the impression of a signal with longer period.

Aliasing is a major concern, and the danger it poses is often underestimated. This is because we do not know whether the signal being represented by the discretization scheme contains frequencies higher than the cut-off frequency, precisely because variability at those frequencies is not retained and computed. In geophysical situations, the time step and grid spacing is most often set not by the physics of the problem but by computer-hardware limits. This forces the modeler to discard variability at unresolved frequencies and wavelengths, and creates aliasing. Methods to overcome the undesired effects of aliasing will be presented in subsequent chapters.

Physical Problems

1-1. Name three naturally occurring flows in the atmosphere.

1-2. How did geophysical flows contribute to Christopher Columbus' discovery of the New World and to the subsequent exploration of the eastern shore of North America? (Think of both large-scale winds and major ocean currents.)

1-3. The sea breeze is a light wind blowing from the sea as the result of a temperature difference between land and sea. As this temperature difference reverses from day to night, the daytime sea breeze turns into a nighttime land breeze. If you were to construct a numerical model of the sea-land breeze, should you include the effects of the planetary rotation?

1-4. The Great Red Spot of Jupiter, centered at 22°S and spanning 12° in latitude and 25° in longitude, exhibits wind speeds of about 100 m/s. The planet's equatorial radius and rotation rates are, respectively, 71,400 km and 1.763 x 10^{-4} s^{-1}. Is the Great Red Spot influenced by planetary rotation?

1-5. Can you think of a technique for measuring wind speeds and ocean velocities with an instrument that has no rotating component? (*Hint*: Think of measurable quantities whose values are affected by translation.)

Numerical Exercises

1-1. Using the temperature measurements of Nansen (Figure 1-18 left), estimate typical vertical temperature gradient values and typical temperature values. Compare those values to the estimates based on a Mediterranean profile (Figure 1-18 right). Which temperature scale do you need for the estimation of gradients in each case?

1-2. Perform a numerical derivation of $e^{-\omega(t+|t|)}$ using $\omega\Delta t = 0.1,\ 0.01,\ 0.001$. Compare the first-order forward, first-order backward and second-order centered schemes at $t = 1/\omega$. Then, repeat the derivation and comparison for $t = 0$. What do you conclude?

1-3. Apply forward, backward, second-order, and fourth-order discretizations to $\sinh(kx)$ at $x = 1/k$ for values of $k\Delta x$ covering the range $[10^{-4}, 1]$. Plot errors on a logarithmic scale and verify the convergence rates. Repeat the exercise for $x = 0$. What strange effect do you observe and why?

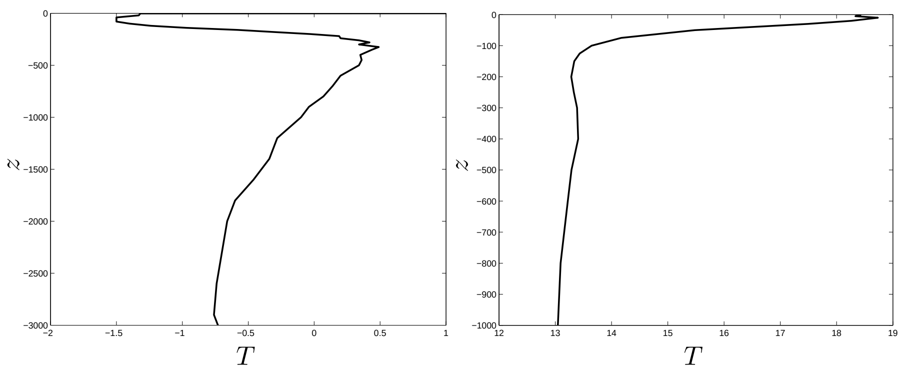

Figure 1-18 Temperature values measured by Nansen during his 1894 North Pole expedition (left) and a typical temperature profile in the Mediterranean Sea (from `Medar`© data base, right).

1-4. Establish a purely forward, finite-difference approximation of a first derivative that is of second or higher order in accuracy. How many sampling points are required as a function of the order of accuracy?

1-5. Suppose you need to evaluate $\partial u/\partial x$ not at grid node i, but at mid-distance between nodes $x_i = i\Delta x$ and $x_{i+1} = (i+1)\Delta x$. Establish second-order and fourth-order finite difference approximations to do so and compare the truncation errors to the corresponding discretizations centered on the nodal point i. What does this analysis suggest?

1-6. Assume that a spatial two-dimensional domain is covered by a uniform grid with spacing Δx in the x-direction and Δy in the y-direction. How can you discretize $\partial^2 u/\partial x \partial y$ to second order? Does the approximation satisfy a similar property as its mathematical counterpart $\partial^2 u/\partial x \partial y = \partial^2 u/\partial y \partial x$?

1-7. Determine how a wave of wavelength $\frac{4}{3}\Delta x$ and period $\frac{5}{3}\Delta t$ is interpreted in a uniform grid of mesh Δx and time step Δt. How does the computed propagation speed resulting from the discrete sampling compare to the true speed?

1-8. Suppose you use numerical finite differencing to estimate derivatives of a function that was sampled with some noise. Assuming the noise is uncorrelated (*i.e.*, purely randomly distributed, independently of the sampling interval), what do you expect would happen during the finite differencing of first-order derivatives, second derivatives *etc.*? Devise a numerical program that verifies your assertion, by adding a random noise of intensity $A/10$ to the function $A\sin(\omega t)$, where the frequency ω is well resolved by the numerical sampling ($\omega\Delta t = 0.05$). Did you correctly guess what would happen? Now plot the convergence as a function of $\omega\Delta t$ for increasing levels of noise.

Walsh Cottage , Woods Hole, Massachusetts
1962 – present

Every summer since 1962, this unassuming building of the Woods Hole Oceanographic Institution (Falmouth, Massachusetts, USA) has been home to the Geophysical Fluid Dynamic Summer Program, which has gathered oceanographers, meteorologists, physicists and mathematicians from around the world. This program (begun in 1959) has single-handedly been responsible for many of the developments of geophysical fluid dynamics, from its humble beginnings to its present status as a recognized discipline in physical sciences. (*Drawing by Ryuji Kimura, reproduced with permission*)

UK Meteorological Office, Exeter, England
1854-present

The Meteorological Office in the United Kingdom was established in 1854 to provide meteorological information and sea currents by telegraph to people at sea and, within a few years, began also to issue storm warnings to seaports and weather forecasts to the press. In 1920, separate meteorological military services established during World War I were merged with the civilian office under the Air Ministry. World War II led to another large increase in both personnel and resources, including the use of balloons. The “Met Office” has an outstanding record of capitalizing on new technologies, beginning broadcasts on radio (in 1922) and then on television (in 1936 by means of simple captions, and live broadcasts in 1954). The first electronic computer was installed in 1962, and satellite imagery was incorporated in 1964.

As weather forecasts began to depend less on trained meteorologists drawing weather maps and more on computational models, the need for the latest and best performing computer platform became a driving force, leading to the acquisition of a Cyber supercomputer in 1981, and a series of ever faster Cray supercomputers in the 1990s.

The impact of the Met Office can hardly be underestimated: Its numerical activities have contributed enormously not only to the field of meteorology but also to the development of computational fluid dynamics and physical oceanography, while the scope of its data analyses and forecasts has spread well beyond tomorrow’s weather to other areas such as the impact of the weather on the environment and human health. (*For additional information see* `http://www.met-office.gov.uk`)

Chapter 2

The Coriolis Force

(October 18, 2006) **SUMMARY**: The object of this chapter is to examine the Coriolis force, a fictitious force arising from the choice of a rotating framework of reference. Some physical considerations are offered to provide insight on this non-intuitive but essential element of geophysical flows. The numerical section of this chapter treats time stepping introduced in the particular case of inertial oscillations and generalized afterwards.

2.1 Rotating framework of reference

From a theoretical point of view, all equations governing geophysical fluid processes could be stated with respect to an inertial framework of reference, fixed with respect to distant stars. But, we people on Earth observe fluid motions with respect to this rotating system. Also, mountains and ocean boundaries are stationary with respect to Earth. Common sense therefore dictates that we write the governing equations in a reference framework rotating with our planet. (The same can be said for other planets and stars.) The trouble arising from the additional terms in the equations of motion is less than that which would arise from having to reckon with moving boundaries and the need to subtract systematically the ambient rotation from the results.

To facilitate the mathematical developments, let us first investigate the two-dimensional case (Figure 2-1). Let the X– and Y–axes form the inertial framework of reference and the x– and y–axes be those of a framework with the same origin but rotating at the angular rate Ω (defined as positive in the trigonometric sense). The corresponding unit vectors are denoted ($\mathbf{I}$, $\mathbf{J}$) and ($\mathbf{i}$, $\mathbf{j}$). At any time t, the rotating x–axis makes an angle Ωt with the fixed X–axis. It follows that

$$\mathbf{i} = +\mathbf{I}\cos\Omega t + \mathbf{J}\sin\Omega t \quad (2.1a) \qquad \mathbf{I} = +\mathbf{i}\cos\Omega t - \mathbf{j}\sin\Omega t \quad (2.2a)$$
$$\mathbf{j} = -\mathbf{I}\sin\Omega t + \mathbf{J}\cos\Omega t \quad (2.1b) \qquad \mathbf{J} = +\mathbf{i}\sin\Omega t + \mathbf{j}\cos\Omega t, \quad (2.2b)$$

and that the coordinates of the position vector $\mathbf{r} = X\mathbf{I} + Y\mathbf{J} = x\mathbf{i} + y\mathbf{j}$ of any point in the

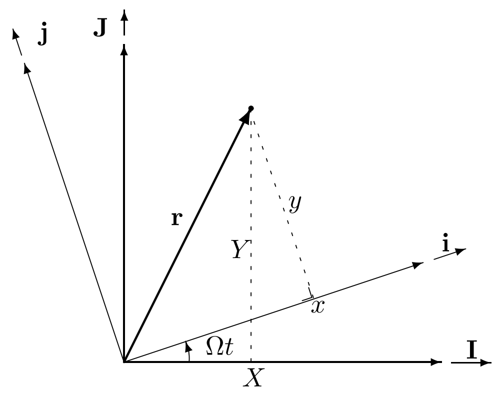

Figure 2-1 Fixed (X, Y) and rotating (x, y) frameworks of reference.

plane are related by

$$x = +X \cos\Omega t + Y \sin\Omega t \tag{2.3a}$$
$$y = -X \sin\Omega t + Y \cos\Omega t. \tag{2.3b}$$

The first time derivative of the preceding expressions yields

$$\frac{dx}{dt} = +\frac{dX}{dt}\cos\Omega t + \frac{dY}{dt}\sin\Omega t \overbrace{-\Omega X \sin\Omega t + \Omega Y \cos\Omega t}^{+\Omega y} \tag{2.4a}$$
$$\frac{dy}{dt} = -\frac{dX}{dt}\sin\Omega t + \frac{dY}{dt}\cos\Omega t \underbrace{-\Omega X \cos\Omega t - \Omega Y \sin\Omega t}_{-\Omega x}. \tag{2.4b}$$

The quantities dx/dt and dy/dt give the rates of change of the coordinates relative to the moving frame as time evolves. They are thus the components of the relative velocity:

$$\mathbf{u} = \frac{dx}{dt}\,\mathbf{i} + \frac{dy}{dt}\,\mathbf{j} = u\mathbf{i} + v\mathbf{j}. \tag{2.5}$$

Similarly, dX/dt and dY/dt give the rates of change of the absolute coordinates and form the absolute velocity:

$$\mathbf{U} = \frac{dX}{dt}\,\mathbf{I} + \frac{dY}{dt}\,\mathbf{J}.$$

Writing the absolute velocity in terms of the rotating unit vectors, we obtain [using (2.2)]

$$\begin{aligned}\mathbf{U} &= \left(\frac{dX}{dt}\cos\Omega t + \frac{dY}{dt}\sin\Omega t\right)\mathbf{i} + \left(-\frac{dX}{dt}\sin\Omega t + \frac{dY}{dt}\cos\Omega t\right)\mathbf{j} \\ &= U\mathbf{i} + V\mathbf{j}.\end{aligned} \tag{2.6}$$

Thus, dX/dt and dY/dt are the components of the absolute velocity $\mathbf{U}$ in the inertial frame, whereas U and V are the components of the same vector in the rotating frame. Use of (2.4) and (2.3) in the preceding expression yields the following relations between absolute and relative velocities:

$$U \;=\; u \;-\; \Omega y, \qquad V \;=\; v \;+\; \Omega x. \tag{2.7}$$

These equalities simply state that the absolute velocity is the relative velocity plus the entraining velocity due to the rotation of the reference framework.

A second derivative with respect to time provides in a similar manner:

$$\begin{aligned} \frac{d^2x}{dt^2} \;&=\; \left(\frac{d^2X}{dt^2} \cos\Omega t + \frac{d^2Y}{dt^2} \sin\Omega t \right) \;+\; 2\Omega \underbrace{\left(- \frac{dX}{dt} \sin\Omega t + \frac{dY}{dt} \cos\Omega t \right)}_{V} \\ &\quad -\; \Omega^2 \underbrace{\left(X \;\cos\Omega t \;+\; Y \;\sin\Omega t \right)}_{x} \qquad\qquad (2.8a) \\ \frac{d^2y}{dt^2} \;&=\; \left(- \frac{d^2X}{dt^2} \sin\Omega t + \frac{d^2Y}{dt^2} \cos\Omega t \right) \;-\; 2\Omega \underbrace{\left(\frac{dX}{dt} \cos\Omega t + \frac{dY}{dt} \sin\Omega t \right)}_{U} \\ &\quad -\; \Omega^2 \underbrace{\left(- X \;\sin\Omega t \;+\; Y \;\cos\Omega t \right)}_{y}. \qquad\qquad (2.8b) \end{aligned}$$

Expressed in terms of the relative and absolute accelerations

$$\begin{aligned} \mathbf{a} \;&=\; \frac{d^2x}{dt^2}\,\mathbf{i} \;+\; \frac{d^2y}{dt^2}\,\mathbf{j} \;=\; \frac{du}{dt}\,\mathbf{i} \;+\; \frac{dv}{dt}\,\mathbf{j} \;=\; a\mathbf{i} \;+\; b\mathbf{j} \\ \mathbf{A} \;&=\; \frac{d^2X}{dt^2}\,\mathbf{I} \;+\; \frac{d^2Y}{dt^2}\,\mathbf{J} \\ &=\; \left(\frac{d^2X}{dt^2} \cos\Omega t + \frac{d^2Y}{dt^2} \sin\Omega t \right) \mathbf{i} + \left(\frac{d^2Y}{dt^2} \cos\Omega t - \frac{d^2X}{dt^2} \sin\Omega t \right) \mathbf{j} \;=\; A\mathbf{i} \;+\; B\mathbf{j}, \end{aligned}$$

expressions (2.8) condense to

$$a \;=\; A \;+\; 2\Omega V \;-\; \Omega^2 x, \qquad b \;=\; B \;-\; 2\Omega U \;-\; \Omega^2 y.$$

In analogy with the absolute velocity vector, d^2X/dt^2 and d^2Y/dt^2 are the components of the absolute acceleration $\mathbf{A}$ in the inertial frame, whereas A and B are the components of the same vector in the rotating frame. The absolute acceleration components, necessary later to formulate Newton's law, are obtained by solving for A and B and using (2.7):

$$A \;=\; a \;-\; 2\Omega v \;-\; \Omega^2 x, \qquad B \;=\; b \;+\; 2\Omega u \;-\; \Omega^2 y. \tag{2.9}$$

We now see that the difference between absolute and relative acceleration consists of two contributions. The first, proportional to Ω and to the relative velocity, is called the Coriolis acceleration; the other, proportional to Ω^2 and to the coordinates, is called the centrifugal acceleration. When placed on the other side of the equality in Newton's law, these terms can be assimilated to forces (per unit mass). The centrifugal force acts as an outward pull, whereas the Coriolis force depends on the direction and magnitude of the relative velocity.

Formally, the preceding results could have been derived in a vector form. Defining the vector rotation

$$\mathbf{\Omega} \;=\; \Omega \mathbf{k},$$

where $\mathbf{k}$ is the unit vector in the third dimension (which is common to both systems of reference), we can write (2.7) and (2.9) as

$$\begin{aligned} \mathbf{U} &= \mathbf{u} + \mathbf{\Omega} \times \mathbf{r} \\ \mathbf{A} &= \mathbf{a} + 2\mathbf{\Omega} \times \mathbf{u} + \mathbf{\Omega} \times (\mathbf{\Omega} \times \mathbf{r}), \end{aligned} \tag{2.10}$$

where $\times$ indicates the vectorial product. This implies that taking a time derivative of a vector with respect to the inertial framework is equivalent to applying the operator

$$\frac{d}{dt} \;+\; \mathbf{\Omega} \times$$

in the rotating framework of reference.

A very detailed exposition of the Coriolis and centrifugal accelerations can be found in the book by Stommel and Moore (1989). In addition, the reader will find a historical perspective in Ripa (1994).

2.2 Unimportance of the centrifugal force

Unlike the Coriolis force, which is proportional to the velocity, the centrifugal force depends solely on the rotation rate and the distance of the particle to the rotation axis. Even at rest with respect to the rotating planet, particles experience an outward pull. Yet, on the earth as on other celestial bodies, no matter goes flying out to space. How is that possible? Obviously, gravity keeps everything together.

In the absence of rotation, gravitational forces keep the matter together to form a spherical body (with the denser materials at the center and the lighter ones on the periphery). The outward pull caused by the centrifugal force distorts this spherical equilibrium, and the planet assumes a slightly flattened shape. The degree of flattening is precisely that necessary to keep the planet in equilibrium for its rotation rate.

The situation is depicted on Figure 2-2. By its nature, the centrifugal force is directed outward, perpendicular to the axis of rotation, whereas the gravitational force points toward the planet's center. The resulting force assumes an intermediate direction, and this direction is precisely the direction of the local vertical. Indeed, under this condition a loose particle would have no tendency of its own to fly away from the planet. In other words, every particle at rest on the surface will remain at rest unless it is subjected to additional forces.

The flattening of the earth, as well as that of other celestial bodies in rotation, is important to neutralize the centrifugal force. But, this is not to say that it greatly distorts the geometry. On the earth, for example, the distortion is very slight, because gravity by far exceeds the

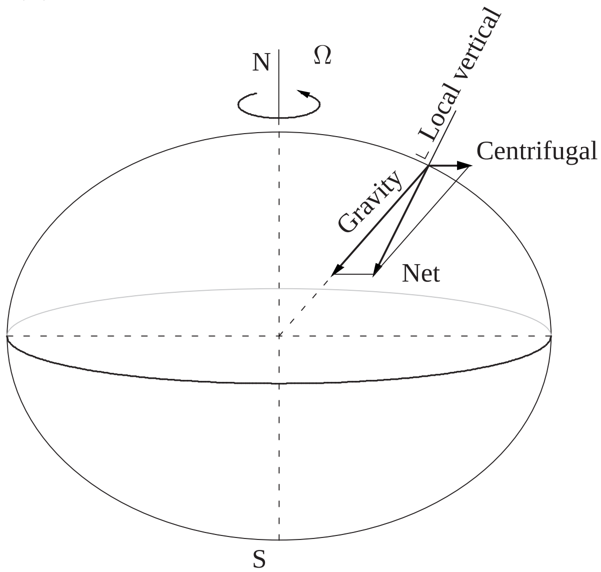

Figure 2-2 How the flattening of the rotating earth (grossly exaggerated in this drawing) causes the gravitational and centrifugal forces to combine into a net force aligned with the local vertical, so that equilibrium is reached.

centrifugal force; the terrestrial equatorial radius is 6378 km, slightly greater than its polar radius of 6357 km. The shape of the rotating oblate earth is treated in detail by Stommel and Moore (1989) and by Ripa (1994).

For the sake of simplicity in all that follows, we will call the gravitational force the resultant force, aligned with the vertical and equal to the sum of the true gravitational force and the centrifugal force. Due to inhomogeneous distributions of rocks and magma on earth, the true gravitational force is not directed towards the center of the earth. For the same reason as the centrifugal force has rendered the earth surface oblate, this inhomogeneous true gravity has deformed the earth surface until the total (apparent) gravitational force is perpendicular to it. The surface so obtained is called a *geoid* and can be interpreted as the surface of an ocean at rest (with a continuous extension on land). This virtual continuous surface is perpendicular at every point to the direction of gravity (including the centrifugal force) and forms an *equipotential* surface, meaning that a particle moving on that surface undergoes no change in potential energy. This surface will be the reference surface from which land elevations, (dynamic) sea surface elevations and ocean depth will be defined. For more on the geoid, the reader is referred to Robinson (2004), Chapter 11.

In a rotating laboratory tank, the situation is similar but not identical. The rotation causes a displacement of the fluid toward the periphery. This proceeds until the resulting inward pressure gradient prevents any further displacement. Equilibrium then requires that at any point on the surface, the downward gravitational force and the outward centrifugal force combine into a resultant force normal to the surface (Figure 2-3), so that the surface becomes an equipotential surface. Although the surface curvature is crucial in neutralizing the centrifugal force, the vertical displacements are rather small. In a tank rotating at the rate of one revolution every two seconds (30 rpm) and 40 cm in diameter, the difference in fluid height between the rim and the center is a modest 2 cm.

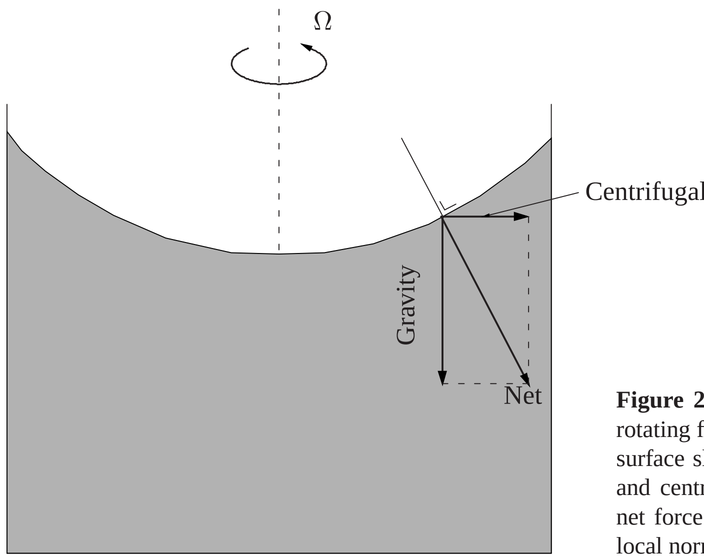

Figure 2-3 Equilibrium surface of a rotating fluid in an open container. The surface slope is such that gravitational and centrifugal forces combine into a net force everywhere aligned with the local normal to the surface.

2.3 Free motion on a rotating plane

The preceding argument allows us to combine the centrifugal force with the gravitational force, but the Coriolis force remains. To have an idea of what this force can cause, let us examine the motion of a free particle (that is, a particle not subject to any external force) on a plane attached to the North pole of the rotating earth.

If the particle is free of any force, its acceleration in the inertial frame is nil, by Newton's law. According to (2.9), with the centrifugal-acceleration terms no longer present, the equations governing the velocity components of the particle are

$$\frac{du}{dt} - 2\Omega v = 0, \quad \frac{dv}{dt} + 2\Omega u = 0. \tag{2.11}$$

The general solution to this system of linear equations is

$$u = V \sin(ft + \phi), \quad v = V \cos(ft + \phi), \tag{2.12}$$

where $f = 2\Omega$, called the Coriolis parameter, has been introduced for convenience, and V and ϕ are two arbitrary constants of integration. Without loss of generality, V can always be chosen as nonnegative. (Do not confuse this constant V with the y–component of the absolute velocity introduced in Section 2.1.) A first result is that the particle speed $(u^2+v^2)^{1/2}$ remains unchanged in time. It is equal to V, a constant determined by the initial conditions.

Although the speed remains unchanged, the components u and v do depend on time, implying a change in direction. To document this curving effect, it is most instructive to derive the trajectory of the particle. The coordinates of the particle position change, by definition of the vector velocity, according to $dx/dt = u$ and $dy/dt = v$, and a second time integration provides

$$x = x_0 - \frac{V}{f}\cos(ft + \phi) \tag{2.13a}$$

$$y = y_0 + \frac{V}{f}\sin(ft + \phi), \tag{2.13b}$$

where x_0 and y_0 are additional constants of integration to be determined from the initial coordinates of the particle. From the last relations, it follows directly that

$$(x - x_0)^2 + (y - y_0)^2 = \left(\frac{V}{f}\right)^2. \tag{2.14}$$

This implies that the trajectory is a circle centered at (x_0, y_0) and of radius $V/|f|$. The situation is depicted on Figure 2-4.

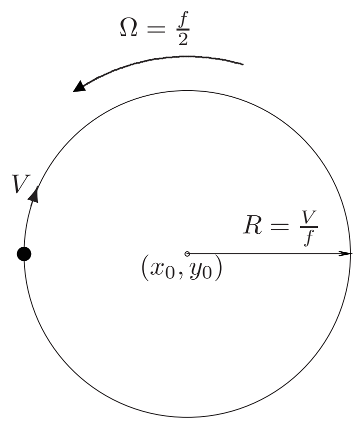

Figure 2-4 Inertial oscillation of a free particle on a rotating plane. The orbital period is exactly half of the ambient revolution period. This figure has been drawn with a positive Coriolis parameter, f, representative of the Northern Hemisphere. If f were negative (as in the Southern Hemisphere), the particle would veer to the left.

In the absence of rotation ($f = 0$), this radius is infinite, and the particle follows a straight path, as we could have anticipated. But, in the presence of rotation ($f \neq 0$), the particle turns constantly. A quick examination of (2.13) reveals that the particle turns to the right (clockwise) if f is positive or to the left (counterclockwise) if $f$is negative. In sum, the rule is that the particle turns in the sense opposite to that of the ambient rotation.

At this point, we may wonder whether this particle rotation is none other than the negative of the ambient rotation, in such a way as to keep the particle at rest in the absolute frame of reference. But, there are at least two reasons why this is not so. The first is that the coordinates of the center of the particle's circular path are arbitrary and are therefore not required to coincide with those of the axis of rotation. The second and most compelling reason is that the two frequencies of rotation are simply not the same: the ambient rotating plane completes one revolution in a time equal to $T_a = 2\pi/\Omega$, whereas the particle covers a full circle in a time equal to $T_p = 2\pi/f = \pi/\Omega$, called *inertial period*. Thus, the particle goes around its orbit twice as the plane accomplishes a single revolution.

The spontaneous circling of a free particle endowed with an initial velocity in a rotating environment bears the name of *inertial oscillation*. Note that, since the particle speed can

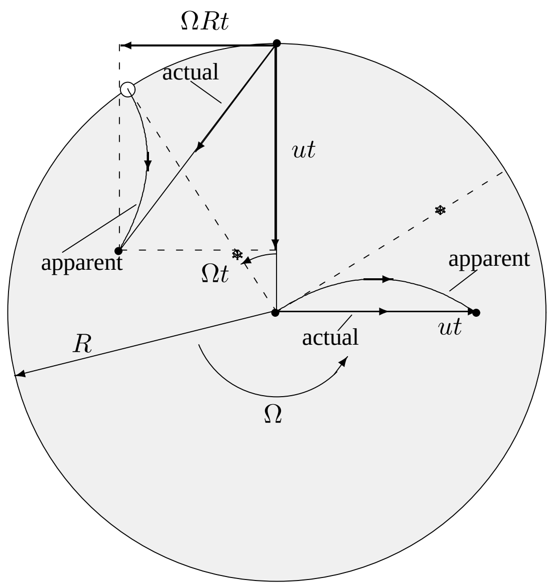

Figure 2-5 Geometrical interpretation of the apparent veering of a particle trajectory viewed in a rotating framework. The veering is to the right when the ambient rotation is counterclockwise, as shown here for two particular trajectories, one originating from the rim, the other from the axis of rotation.

vary, so can the inertial radius, $V/|f|$, whereas the frequency , $|f| = 2|\Omega|$, is a property of the rotating environment and is independent of the initial conditions.

The preceding exercise may appear rather mathematical and devoid of any physical interpretation. There exists, however, a geometric argument and a physical analogy. Let us first discuss the geometric argument. Consider a rotating table and, on it, a particle initially (t = 0) at a distance R from the axis of rotation, approaching the latter at a speed u (Figure 2-5). At some later time t, the particle has approached the axis of rotation by a distance ut and has covered the distance ΩRt laterally. It now lies at the position indicated by a solid dot. During the lapse t, the table has rotated by an angle Ωt, and, to an observer rotating with the table, the particle seems to have originated from the point on the rim indicated by the open circle. The construction shows that, although the actual trajectory is perfectly straight, the apparent path as noted by the observer rotating with the table curves to the right. A similar conclusion holds for a particle radially pushed away from the center with a speed u. In absolute axes, the trajectory is a straight line again arriving at a distance ut from the center. During the lapse t, the table has rotated and for an observer on the rotating platform, the particle, instead of arriving in the location of the asterisk, apparently veered to the right.

The problem with this argument is that to construct the absolute trajectory, we chose a straight path, that is, we implicitly considered the total absolute acceleration, which in the rotating framework includes the centrifugal acceleration. The latter, however, should not have been retained for consistency with the case of terrestrial rotation, but because it is a radial force, it does not account for the transverse displacement. Therefore, the apparent veering is, at least for a short interval of time, entirely due to the Coriolis effect.

2.4 Analogies and physical interpretations

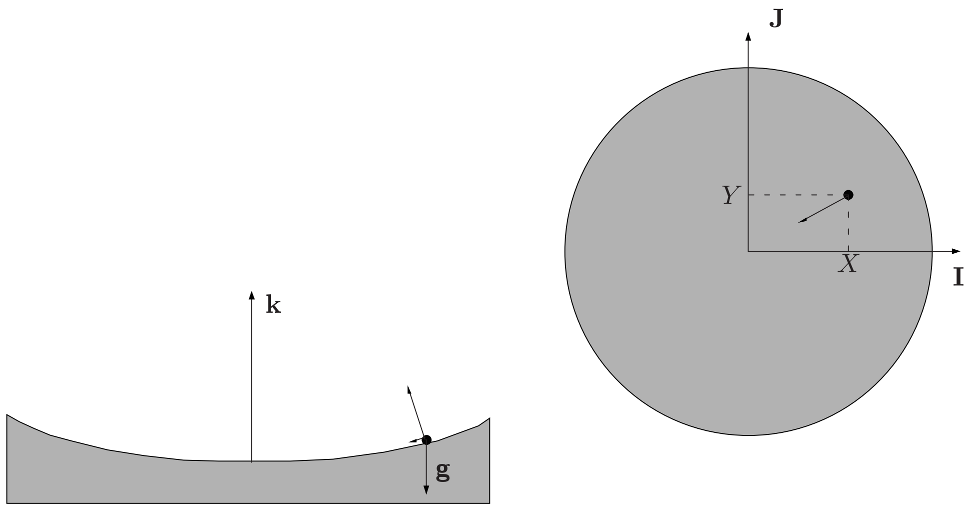

Figure 2-6 Side view (a) and top view (b) of a mass on a paraboloid surface.

Consider[1] a particle of mass M in a gravitational field g on a paraboloid surface (Figure 2-6) of elevation Z given by

$$Z = \frac{\Omega^2}{2g}\left(X^2 + Y^2\right). \tag{2.15}$$

Provided that the paraboloid is sufficiently flat compared to its radius R ($\Omega^2 R/2g \ll 1$), the equations of motions of the mass are easily derived

$$\frac{d^2X}{dt^2} = -g\,\frac{\partial Z}{\partial X} = -\,\Omega^2 X, \quad \frac{d^2Y}{dt^2} = -g\,\frac{\partial Z}{\partial Y} = -\,\Omega^2 Y, \tag{2.16}$$

and describe a pendulum motion.

The frequency Ω measures the curvature of the surface and is the pendulum's natural frequency of oscillation. Note how the gravitational restoring force takes on the form of a negative centrifugal force. Without loss of generality, we can choose the initial position of the particle as $X = X_0$, $Y = 0$. In that location, we launch the particle with an initial velocity of $dX/dt = U_0$ and $dY/dt = V_0$ in absolute axes. The trajectory in absolute axes is easily found as the solution of (2.16)

$$X = X_0 \cos\Omega t + \frac{U_0}{\Omega}\sin\Omega t \tag{2.17a}$$

$$Y = \frac{V_0}{\Omega}\sin\Omega t. \tag{2.17b}$$

[1] A similar analogy was suggested to the authors by Prof. Satoshi Sakai at Kyoto University.

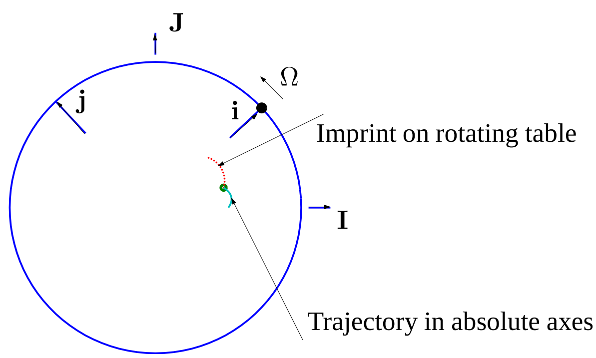

Figure 2-7 Oscillation of the paraboloid pendulum viewed in absolute axes. Dots represent the imprint of the mass on the paraboloid which rotates with the rotation rate Ω.

Two particular solutions are noteworthy. If the initial condition is a pure radial displacement ($V_0 = 0$), the particle forever oscillates in the vertical plane $Y = 0$. The oscillation, of period $2\pi/\Omega$, takes it to the center twice per period, that is, every π/Ω time interval. At the other extreme, the particle can be imparted an initial azimuthal velocity of magnitude such that the outward centrifugal force of the ensuing circling motion exactly cancels the inward gravitational pull at that radial distance:

$$U_0 = 0, \; V_0 = \pm \Omega X_0, \tag{2.18}$$

in which case the particle remains at a fixed distance from the center ($X^2 + Y^2 = X_0^2$) and circles at a constant angular rate Ω, counterclockwise or clockwise, depending on the direction of the initial azimuthal velocity.

Outside of these two extreme behaviors, the particle describes an elliptical trajectory of size, eccentricity, and phase related to the initial condition. The orbit does not take it through the center but brings it, twice per period, to a distance of closest approach (*perigee*) and, twice, to a distance of largest excursion (*apogee*).

At this point, the reader may rightfully wonder: Where is the analogy with the motion of a particle subject to the Coriolis force? To show this analogy, let us now view the particle motion in a rotating frame, but, of course, not any rotating frame: Let us select the angular rotation rate Ω equal to the particle's frequency of oscillation. This choice is made so that, in the rotating frame of reference, the outward centrifugal force, is everywhere and at all times exactly canceled by the inward gravitational pull experienced on the parabolic surface. Thus, the equations of motion expressed in the rotating frame include only the relative acceleration and the Coriolis force, that is, they are none other than (2.11).

Let us now consider the oscillations as seen by an observer in the rotating frame (Figure 2-8). When the particle oscillates strictly back and forth, the rotating observer sees a curved trajectory. Because the particle passes by the origin twice per oscillation, the orbit seen by the rotating observer also passes by the origin twice per period. When the particle reaches its extreme displacement on one side, it reaches an apogee on its orbit as viewed in the rotating frame; then, by the time it reaches its maximum displacement on the opposite side, π/Ω later, the rotating framework has rotated exactly by half a turn, so that this second apogee of the orbit coincides with the first. Therefore, the reader can readily be convinced that the orbit in the rotating frame is drawn twice per period of oscillation. Algebraic or geometric developments reveal that the orbit in the rotating framework is circular (Figure 2-8a).

In the other extreme situation, when the particle circles at a constant distance from the origin, two cases must be distinguished, depending on whether it circles in the direction of or opposite to the observer's rotating frame. If the direction is the same [positive sign in (2.18)], the observer simply chases the particle, which then appears stationary, and the orbit reduces to a single point (Figure 2-8b). This case corresponds to the state of rest of a particle in a rotating environment [V = 0 in (2.12) through (2.13)]. If the sense of rotation is opposite [minus sign in (2.18)], the reference frame rotates at the rate Ω in one direction, whereas the particle circles at the same rate in the opposite direction. To the observer, the particle appears to rotate at the rate 2Ω. The orbit is obviously a circle centered at the origin and of radius equal to the particle's radial displacement; it is covered twice per revolution of the rotating frame (Figure 2-8c). Finally, for arbitrary oscillations, the orbit in the rotating frame is a circle of finite radius that is not centered at the origin, does not pass by the origin, and may or may not include the origin (Figure 2-8d). The reader may experiment with MATLAB™ code `parabolic.m` for further explorations of trajectories.

2.5 Acceleration on a three-dimensional rotating planet

For all practical purposes, except as outlined earlier when the centrifugal force was discussed (Section 2.2), the earth can be taken as a perfect sphere. This sphere rotates about its North Pole – South Pole axis. At any given latitude φ, the north–south direction departs from the local vertical, and the Coriolis force assumes a form different from that established in the preceding section.

Figure 2-9 depicts the traditional choice for a local Cartesian framework of reference: the x–axis is oriented eastward, the y–axis, northward and the z–axis, upward. In this framework, the earth's Rotation vector is expressed as

$$\mathbf{\Omega} \;=\; \Omega\,\cos\varphi\,\mathbf{j} \;+\; \Omega\,\sin\varphi\,\mathbf{k}. \tag{2.19}$$

The absolute acceleration minus the centrifugal component,

$$\frac{d\mathbf{u}}{dt} \;+\; 2\,\mathbf{\Omega}\;\times\;\mathbf{u},$$

has the following three components

$$x: \quad \frac{du}{dt} \quad + \quad 2\Omega\,\cos\varphi\,w \;-\; 2\Omega\,\sin\varphi\,v \tag{2.20a}$$

$$y: \quad \frac{dv}{dt} \quad + \quad 2\Omega\,\sin\varphi\,u \tag{2.20b}$$

$$z: \quad \frac{dw}{dt} \quad - \quad 2\Omega\,\cos\varphi\,u. \tag{2.20c}$$

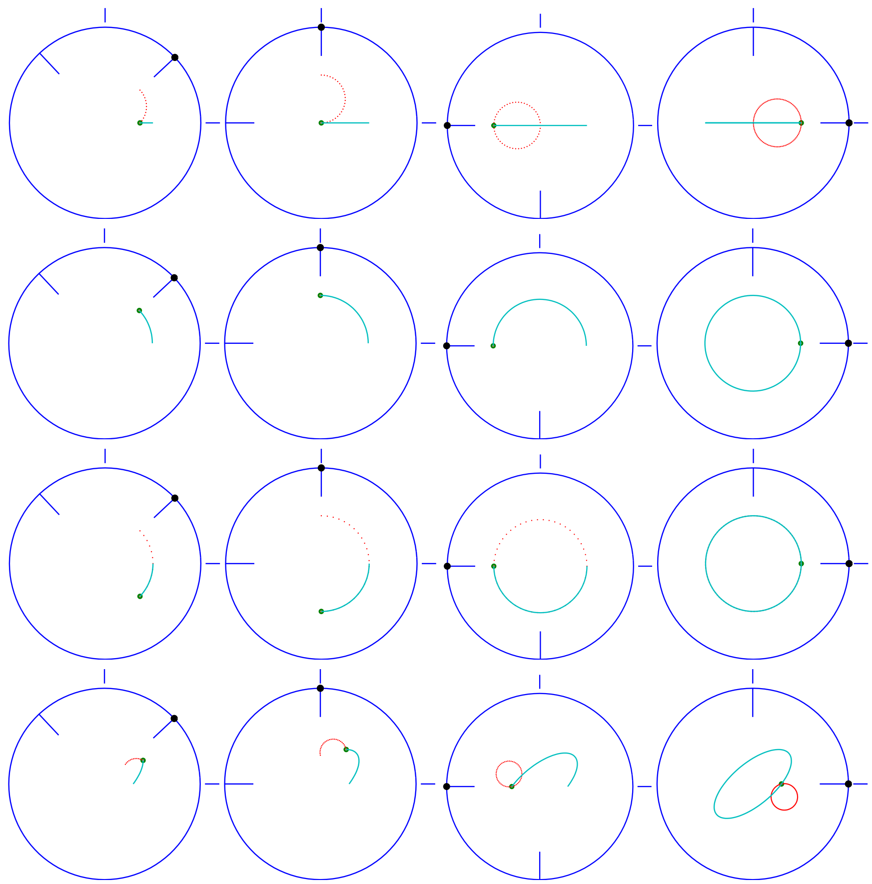

Figure 2-8 Orbits (full line) in absolute axes with imprint of trajectories (dots) on rotating framework (apparent trajectory). Each row shows the situation for a different initial condition and after 1/8, 1/4, 1/2 and a full period $2\pi\Omega^{-1}$. Orbits differ according to the initial velocity: the first row (a) shows oscillations obtained without initial velocity, the second row (b) was created with initial velocity $U_0 = 0,\ V_0 = X_0\Omega$, the third row (c) corresponds to the opposite initial velocity $U_0 = 0,\ V_0 = -X_0\Omega$, and the last row (d) corresponds to an arbitrary initial velocity.

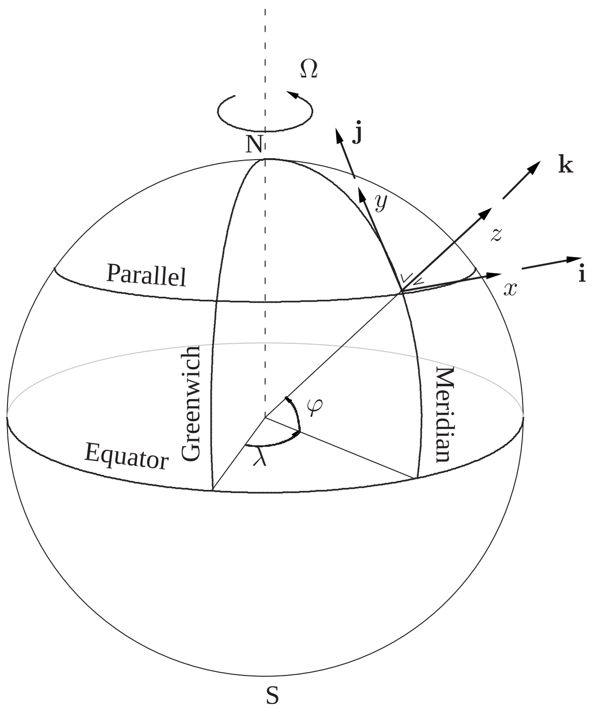

Figure 2-9 Definition of a local Cartesian framework of reference on a spherical earth. The coordinate x is directed eastward, y northward, and z upward.

With x, y, and z everywhere aligned with the local eastward, northward, and vertical directions, the coordinate system is curvilinear, and additional terms arise in the components of the relative acceleration. These terms will be introduced in Section 3.2, only to be quickly dismissed because of their relatively small size in most instances.

For convenience, we define the quantities

$$f = 2\Omega \sin\varphi \quad (2.21)$$

$$f_* = 2\Omega \cos\varphi. \quad (2.22)$$

The coefficient f is called the *Coriolis parameter*, whereas f_* has no traditional name and will be called here the *reciprocal Coriolis parameter*. In the Northern Hemisphere, f is positive; it is zero at the equator and negative in the Southern Hemisphere. In contrast, f_* is positive in both hemispheres and vanishes at the poles. An examination of the relative importance of the various terms (Section 4.3) will reveal that, generally, the f–terms are important, whereas the f_*–terms may be neglected.

Horizontal, unforced motions are described by

$$\frac{du}{dt} - fv = 0 \quad (2.23a)$$

$$\frac{dv}{dt} + fu = 0 \quad (2.23b)$$

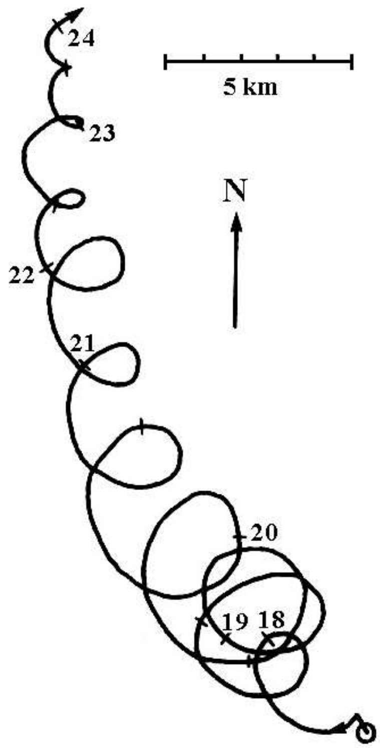

Figure 2-10 Evidence of inertial oscillations in the Baltic Sea, as reported by Gustafson and Kullenberg (1936). The plot is a progressive–vector diagram constructed by the successive addition of velocity measurements at a fixed location. For weak or uniform velocities, such a curve approximates the trajectory that a particle starting at the point of observation would have followed during the period of observation. Numbers indicate days of the month. Note the persistent veering to the right, at a period of about 14 hours, which is the value of $2\pi/f$ at that latitude (57.8°N). [From Gustafson and Kullenberg, 1936, as adapted by Gill, 1982]

and are still characterized by solution (2.12). The difference resides in the value of f, now given by (2.21). Thus, inertial oscillations on Earth have periodicities equal to $2\pi/f = \pi/\Omega\sin\varphi$, ranging from 12 h at the poles to infinity along the equator. Pure inertial oscillations are, however, quite rare because of the usual presence of pressure gradients and other forces. Nonetheless, inertial oscillations are not uncommonly found to contribute to observations of oceanic currents. An example of such an occurrence, where the inertial oscillations made up almost the entire signal, was reported by Gustafson and Kullenberg (1936). Current measurements in the Baltic Sea showed periodic oscillations about a mean value. When added to one another to form a so-called progressive vector diagram (Figure 2-10), the currents distinctly showed a mean drift, on which were superimposed quite regular clockwise oscillations. The theory of inertial oscillation predicts clockwise rotation in the Northern Hemisphere with period of $2\pi/f = \pi/\Omega\sin\varphi$, or 14 h at the latitude of observations, thus confirming the interpretation of the observations as inertial oscillations.

2.6 Numerical approach to oscillatory motions

The equations of free motion on a rotating plane (2.11) have been considered in some detail in Section 2.3, and it is now appropriate to consider their discretization, as the corresponding terms are part of all numerical models of geophysical flows. Upon introducing the time increment Δt, an approximation to the components of the velocity will be determined at the discrete instants $t^n = n\Delta t$ with $n = 1, 2, 3, ...$, which are denoted $\tilde{u}^n = \tilde{u}(t_n)$ and $\tilde{v}^n = \tilde{v}(t_n)$, with tildes used to distinguish the discrete solution from the exact one. The so-called *Euler method* based on first-order forward differencing yields the simplest discretization of equations (2.11):

$$\begin{aligned}
\frac{du}{dt} - fv = 0 \quad &\longrightarrow \quad \frac{\tilde{u}^{n+1} - \tilde{u}^n}{\Delta t} - f\tilde{v}^n = 0 \\
\frac{dv}{dt} + fu = 0 \quad &\longrightarrow \quad \frac{\tilde{v}^{n+1} - \tilde{v}^n}{\Delta t} + f\tilde{u}^n = 0.
\end{aligned}$$

The latter pair can be cast into a recursive form as follows:

$$\tilde{u}^{n+1} = \tilde{u}^n + f\Delta t\, \tilde{v}^n \tag{2.24a}$$
$$\tilde{v}^{n+1} = \tilde{v}^n - f\Delta t\, \tilde{u}^n. \tag{2.24b}$$

Thus, given initial values $\tilde{u}^0$ and $\tilde{v}^0$ at t^0, the solution can be computed easily at time t^1

$$\tilde{u}^1 = \tilde{u}^0 + f\Delta t\, \tilde{v}^0 \tag{2.25}$$
$$\tilde{v}^1 = \tilde{v}^0 - f\Delta t\, \tilde{u}^0. \tag{2.26}$$

Then, by means of the same algorithm, the solution can be obtained iteratively at times t^2, t^3 and so on (do not confuse the temporal index with an exponent here and in the following). Clearly, the main advantage of the preceding scheme is its simplicity, but it is not sufficient to render it acceptable, as we shall soon learn.

To explore the numerical error generated by the Euler method, we carry out Taylor expansions of the type

$$\tilde{u}^{n+1} = \tilde{u}^n + \Delta t \left[\frac{d\tilde{u}}{dt}\right]_{t=t^n} + \frac{\Delta t^2}{2}\left[\frac{d^2\tilde{u}}{dt^2}\right]_{t=t^n} + \mathcal{O}(\Delta t^3)$$

and similarly for $\tilde{v}$ to obtain the following expressions from (2.24)

$$\left[\frac{d\tilde{u}}{dt} - f\tilde{v}\right]_{t=t^n} = -\left[\frac{d^2\tilde{u}}{dt^2}\right]_{t=t^n}\frac{\Delta t}{2} + \mathcal{O}(\Delta t^2) \tag{2.27a}$$
$$\left[\frac{d\tilde{v}}{dt} + f\tilde{u}\right]_{t=t^n} = -\left[\frac{d^2\tilde{v}}{dt^2}\right]_{t=t^n}\frac{\Delta t}{2} + \mathcal{O}(\Delta t^2). \tag{2.27b}$$

Derivation of (2.27a) with respect to time and use of (2.27b) allow to recast (2.27a) into a simpler form, and similarly for (2.27b):

$$\frac{d\tilde{u}^n}{dt} - f\tilde{v}^n = \frac{f^2\Delta t}{2}\,\tilde{u}^n + \mathcal{O}(\Delta t^2) \tag{2.28a}$$

$$\frac{d\tilde{v}^n}{dt} + f\tilde{u}^n = \frac{f^2\Delta t}{2}\,\tilde{v}^n + \mathcal{O}(\Delta t^2). \tag{2.28b}$$

Obviously, the numerical scheme mirrors the original equations, except that an additional term appears in each right-hand side. This additional term takes the form of anti-friction (friction would have a minus sign instead) and will therefore increase the discrete velocity over time.

The *truncation error* of the Euler scheme – the right-hand side of the preceding expressions – tends to zero as Δt vanishes, which is why the scheme is said to be *consistent*. The truncation is on the order of Δt at the first power and the scheme is therefore said to be *first-order accurate*, which is the lowest possible level of accuracy. Nonetheless, this is not the chief weakness of the present scheme, since we must expect that the introduction of anti-friction will create an unphysical acceleratation. Indeed, elementary manipulations of the time-stepping algorithm (2.24) lead to $(\tilde{u}^{n+1})^2 + (\tilde{v}^{n+1})^2 = (1+f^2\Delta t^2)\left\{(\tilde{u}^n)^2 + (\tilde{v}^n)^2\right\}$ so that by recursion

$$\|\,\tilde{\mathbf{u}}\,\|^2 = (\tilde{u}^n)^2 + (\tilde{v}^n)^2 = (1+f^2\Delta t^2)^n\ \left\{(\tilde{u}^0)^2 + (\tilde{v}^0)^2\right\}. \tag{2.29}$$

So, although the kinetic energy (directly proportional to the squared norm $\|\tilde{\mathbf{u}}\|^2$) of the inertial oscillation must remain constant, as was seen in Section 2.3, the kinetic energy of the discrete solution increases without bound[2] even if the time step Δt is taken much smaller than the characteristic time $1/f$. Algorithm (2.24) is *unstable*. Because such a behavior is not acceptable, we need to formulate an alternative type of discretization.

In our first scheme, the time derivative was taken by going forward from time level t^n to t^{n+1} and the other terms at t^n, and the scheme became a recursive algorithm to calculate the next values from the current values. Such a discretization is called an *explicit scheme*. By contrast, in an *implicit scheme*, the terms other than the time derivatives are taken at the new time t^{n+1} (which is similar to taking a backward difference for the time derivative):

$$\frac{\tilde{u}^{n+1} - \tilde{u}^n}{\Delta t} - f\tilde{v}^{n+1} = 0 \tag{2.30a}$$

$$\frac{\tilde{v}^{n+1} - \tilde{v}^n}{\Delta t} + f\tilde{u}^{n+1} = 0. \tag{2.30b}$$

In this case, the norm of the discrete solution decreases monotonically toward zero, according to

$$(\tilde{u}^n)^2 + (\tilde{v}^n)^2 = (1+f^2\Delta t^2)^{-n}\ \left\{(\tilde{u}^0)^2 + (\tilde{v}^0)^2\right\}. \tag{2.31}$$

This scheme can be regarded as *stable*, but as the kinetic energy should neither decrease or increase, it may rather be considered as *overly stable*.

Of interest is the family of algorithms based on a weighted average between explicit and implicit schemes:

[2] ¿From the context it should be clear that ^{n} in $(1+f^2\Delta t^2)^n$ is an exponent, whereas in $\tilde{u}^n$ it is the time index. In the following text, we will not point out this distinction again, leaving it to the reader to verify the context.

$$\frac{\tilde{u}^{n+1} - \tilde{u}^n}{\Delta t} \;-\; f[(1-\alpha)v^n \;+\; \alpha\tilde{v}^{n+1}] \;=\; 0 \tag{2.32a}$$

$$\frac{\tilde{v}^{n+1} - \tilde{v}^n}{\Delta t} \;+\; f[(1-\alpha)u^n \;+\; \alpha\tilde{u}^{n+1}] \;=\; 0, \tag{2.32b}$$

with $0 \le \alpha \le 1$. The numerical scheme is explicit when $\alpha = 0$ and implicit when $\alpha = 1$. Hence, the coefficient α may be regarded as the degree of implicitness in the scheme. It has a crucial impact on the time evolution of the kinetic energy:

$$(\tilde{u}^n)^2 + (\tilde{v}^n)^2 \;=\; \left[\frac{1 + (1-\alpha)^2 f^2 \Delta t^2}{1 + \alpha^2 f^2 \Delta t^2}\right]^n \; \left\{(\tilde{u}^0)^2 + (\tilde{v}^0)^2\right\} \;. \tag{2.33}$$

According to whether α is less than, equal to or greater than $1/2$, the kinetic energy increases, remains constant or decreases over time. It seems therefore appropriate to select the scheme with $\alpha = 1/2$, which is usually said to be *semi-implicit*.

It is now instructive to compare the semi-implicit approximate solution with the exact solution (2.12). For this to be relevant, the same initial conditions are prescribed, *i.e.*, $\tilde{u}^0 = V \sin\phi$ and $\tilde{u}^0 = V\cos\phi$. Then, at any time t^n, the discrete velocity may be shown to be

$$\begin{aligned} \tilde{u}^n &= V\sin(\tilde{f}t^n + \phi) \\ \tilde{v}^n &= V\cos(\tilde{f}t^n + \phi), \end{aligned}$$

with the angular frequency $\tilde{f}$ given by

$$\tilde{f} \;=\; \frac{1}{\Delta t}\;\arctan\left(\frac{f\Delta t}{1 - f^2\Delta t^2/4}\right) \;. \tag{2.34}$$

Although the amplitude of the oscillation (V) is correct, the numerical angular frequency, $\tilde{f}$, differs from the true value f. However, the smaller the dimensionless product $f\Delta t$, the smaller the error:

$$\tilde{f} \;\to\; f\left(1 \;-\; \frac{f^2\Delta t^2}{12}\right) \quad \text{as} \quad f\Delta t \;\to\; 0.$$

In other words, selecting a time increment Δt much shorter than $1/f$, the time scale of inertial oscillations, leads to a frequency that is close to the exact one.

2.7 Numerical convergence and stability

When carrying out a Taylor-series expansion on the discrete equations of the inertial oscillations, we showed that the truncation error vanishes as Δt tends to zero. However, we are not so much interested in knowing that the limit of the discretized equation for increasing resolution is the exact equation (*consistency*) as we are in making sure that the *solution* of the discretized equation tends to the *solution* of the differential equations (*i.e.*, the exact solution). If the difference between the exact and discrete solutions tends to zero as Δt vanishes, then the discretization is said to *converge*.

Unfortunately proving convergence is not a trivial task, especially as we generally do not know the exact solution, in which case the use of numerical discretizations would be superfluous. Even the exact solution of the discrete equation can most often not be written in a closed form, the discretization only providing a method, an *algorithm*, to advance the solution in time.

Without knowing precisely the solutions of either the continuous problem or its discrete version, direct proofs of convergence involve mathematics well beyond the scope of the present book and will be not pursued further. We will, however, rely on a famous theorem called the *Lax-Richtmyer equivalence theorem* [lax and Richtmyer, 1956], which states that

> A consistent finite-difference scheme for a linear partial differential equation for which the initial value problem is well posed is convergent if and only if it is stable.

So, while proof of convergence is a mathematical exercise for researchers well versed in functional analysis, we will restrict ourselves here and in every other instance across the book to verify consistency and stability and will then invoke the theorem to ascertain convergence. This is a particularly interesting approach, not only because checking stability and consistency is much easier than proving directly convergence, but also because stability analysis provides further insight in propagation properties of the numerical scheme (see section 5.4). There remains, however, to define stability and to design efficient methods to verify the stability of numerical schemes. Our analysis of the explicit Euler scheme (2.24) for the discretization of inertial oscillations led us to conclude that it is unstable because the velocity norm, and hence the energy of the system, gradually increases with every time step.

The adjective *unstable* seems quite natural in this context but lacks precision, and an exact definition is yet to be given. Imagine for example the use of an implicit Euler scheme (generally taken as the archetype of a stable scheme) on a standard linear differential equation:

$$\frac{\partial u}{\partial t} = \gamma u \quad \rightarrow \quad \frac{\tilde{u}^{n+1} - \tilde{u}^n}{\Delta t} = \gamma\, \tilde{u}^{n+1}. \tag{2.35}$$

We readily see that for $0 < \gamma \Delta t < 1$, the norm of $\tilde{u}$ increases:

$$\tilde{u}^n = \left(\frac{1}{1-\gamma\Delta t}\right)^n \tilde{u}^0. \tag{2.36}$$

We would however hardly disqualify the scheme as unstable, since the numerical solution increases its norm simply because the exact solution $u = u^0 e^{\gamma t}$ does so. In the present case we can even show that the numerical solution actually converges to the exact solution:

$$\lim_{\Delta t \to 0} \tilde{u}^n = \tilde{u}^0 \lim_{\Delta t \to 0} \left(\frac{1}{1-\gamma\Delta t}\right)^n = \tilde{u}^0 \lim_{\Delta t \to 0} \left(\frac{1}{1-\gamma\Delta t}\right)^{t/\Delta t} = \tilde{u}^0 e^{\gamma t}. \tag{2.37}$$

with $t = n\Delta t$.

Stability is thus a concept that should not only be related to the behavior of the discrete solution, but also to the behavior of the exact solution. Loosely speaking, we will qualify a numerical scheme as unstable if its solution grows much faster than the exact solution and, likewise, overstable if its solution decreases much faster than the exact solution.

2.7.1 Formal stability definition

A mathematical definition of stability, one which allows the discrete solution to grow but only to a certain extent, is as follows. If the discrete state variable is represented by an array $\mathbf{x}$ (collecting into a single vector the values of all variables at all spatial grid points), which is stepped in time by an algorithm based on the selected discretization, the corresponding numerical scheme is said to be stable over a fixed time interval T if there exists a constant C such that

$$\| \mathbf{x}^n \| \ \leq \ C \, \| \mathbf{x}^0 \| \tag{2.38}$$

for all $n\Delta t \leq T$. A scheme is thus stable if regardless of Δt ($\leq T$), the numerical solution remains bounded for $t \leq T$.

This definition of stability leaves the numerical solution quite some room for growth, very often well beyond what a modeler is willing to tolerate. This definition of stability is, however, the necessary and sufficient stability used in the lax-Richtmyer equivalence theorem and thus allows us to verify convergence. If we permit a slower rate of growth in the numerical solution, we will not destroy convergence. In particular, we could decide to use the so-called strict stability condition.

2.7.2 Strict stability

For a system conserving one or several integral norms (such as total energy or wave action), we may naturally impose that the corresponding norm of the numerical solution not grow at all over time:

$$\| \mathbf{x}^n \| \ \leq \ \| \mathbf{x}^0 \| \, . \tag{2.39}$$

Obviously, a scheme that is stable in the sense of (2.39) is also stable in the sense of (2.38), while the inverse is not necessarily true. The more stringent definition (2.39) will be called *strict stability condition* and refers to the condition that the norm of the numerical solution is not allowed to increase at all.

2.7.3 Choice of a stability criterion

The choice of stability criterion will depend largely on the mathematical and physical problem at hand. For a wave-propagation problem, for example, strict stability will be the natural choice (assuming some norm is conserved in the physical process), while for physically unbounded problems, the less stringent numerical stability definition (2.38) may be used.

We can now examine two previous discretization schemes in the light of these two stability definitions. For the explicit Euler discretization (2.24) of inertial oscillation, the scheme is unstable in the sense of (2.39) (and deserves this label in view of the required energy conservation), although it is technically stable in the sense of (2.38), as we will proceed to show. Since the norm of the velocity is, according to (2.29),

$$\parallel \tilde{\mathbf{u}}^n \parallel = \left(1 + f^2 \Delta t^2\right)^{n/2} \parallel \tilde{\mathbf{u}}^0 \parallel, \tag{2.40}$$

we simply need to demonstrate[3] that the amplification is limited by a constant independent of n and Δt:

$$\left(1 + f^2 \Delta t^2\right)^{n/2} \leq \left(1 + f^2 \Delta t^2\right)^{T/(2\Delta t)} \leq e^{\frac{f^2 \Delta t T}{2}} \leq e^{\frac{f^2 T^2}{2}}. \tag{2.42}$$

The scheme is thus stable in the sense of (2.38) and even if growth of the norm can be quite important, according to the lax-Richtmyer equivalence theorem, the solution will converge as the time step is reduced. This is indeed what is observed (Figure 2-11) and can be proved explicitly (see numerical exercise 2.5). In practice, however, the time step is never allowed to be very small for obvious computer constraints. Also, the time window T over which simulations take place can be very large and any increase of the velocity norm is unacceptable even if the solution is guaranteed to converge for smaller time steps. For this reason, the strict stability condition (2.39) is preferred, and the semi-implicit Euler discretization chosen.

In the second example, that of the implicit Euler scheme applied to the growth equation, the scheme (2.35) is stable in the sense of (2.38) (since it converges), but allows growth in the numerical solution as does the mathematical solution.

Recapitulating the different concepts encountered in the numerical discretization, we now have a recipe to construct a convergent method: Design a discretization for which consistency (an equation-related property) can be verified by straightforward Taylor-series expansion, then check stability of the numerical scheme (some practical methods will be provided later) and finally invoke the lax-Richtmyer equivalence theorem to prove convergence (a solution-related property). But, as the equivalence theorem is strictly valid only for linear equations, surprises may arise in nonlinear systems. We also have to mention that establishing convergence by this indirect method demands that initial and boundary conditions, too, converge to those of the continuous differential system. Finally, convergence is assured only for well posed initial-value problems. This, however, is not a concern here, since all geophysical fluid models are physically well posed.

2.8 Predictor-corrector methods

Up to now, we have illustrated numerical discretizations on the linear equations describing inertial oscillations. The methods can be easily generalized to equations with a nonlinear source term Q in the equation governing the variable u, as

[3] For the demonstration we use the inequality

$$(1+a)^b \leq e^{ab} \text{ for } a, b \geq 0 \tag{2.41}$$

which can be easily be proved by observing that $(1+a)^b = e^{b\ln(1+a)}$ and that $\ln(1+a) \leq a$ when $a \geq 0$.

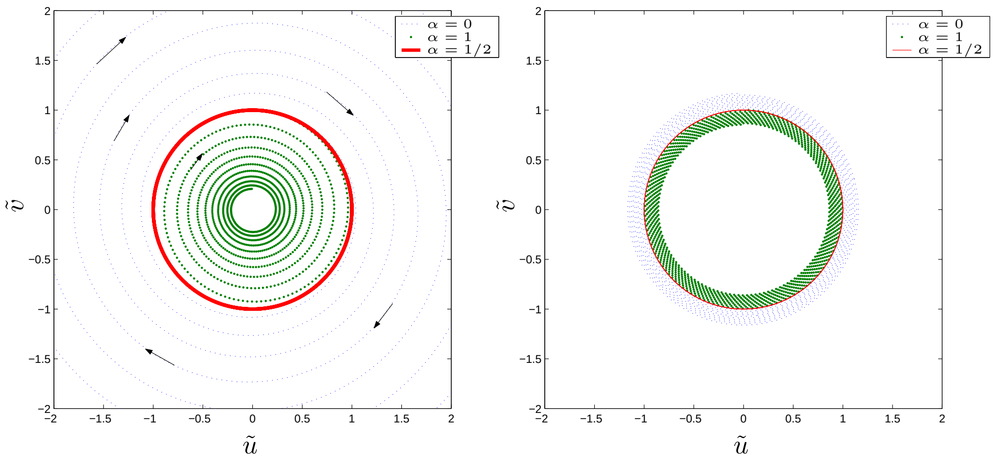

Figure 2-11 Representation (called a hodograph) of the numerical solution $(\tilde{u}, \tilde{v})$ (2.32a)–(2.32b) of the explicit discretization of the inertial oscillation ($\alpha = 0$), the implicit version ($\alpha = 1$) and the semi-implicit scheme ($\alpha = 1/2$). The hodograph on the left was obtained with $f\Delta t = 0.05$ and the one on the right panel with $f\Delta t = 0.005$. The inertial oscillation (Figure 2-4) is clearly visible, but the explicit scheme induces spiralling out and the implicit scheme spiralling in. When the time step is reduced (moving from left panel to right panel), the solution approaches the exact solution. In both cases, 10 inertial periods were simulated.

$$\frac{du}{dt} = Q(t, u). \tag{2.43}$$

For simplicity, we consider here a scalar variable u, but extension to a state vector $\mathbf{x}$, such as $\mathbf{x} = (u, v)$, is straightforward.

The previous methods can be recapitulated as follows:

- The explicit Euler method (*forward scheme*):

$$\tilde{u}^{n+1} = \tilde{u}^n + \Delta t\, Q^n \tag{2.44}$$

- The implicit Euler method (*backward scheme*):

$$\tilde{u}^{n+1} = \tilde{u}^n + \Delta t\, Q^{n+1} \tag{2.45}$$

- The semi-implicit Euler scheme (*trapezoidal scheme*):

$$\tilde{u}^{n+1} = \tilde{u}^n + \frac{\Delta t}{2}\left(Q^n + Q^{n+1}\right) \tag{2.46}$$

- A general two-points scheme (with $0 \le \alpha \le 1$):

$$\tilde{u}^{n+1} = \tilde{u}^n + \Delta t\left[(1-\alpha)Q^n + \alpha Q^{n+1}\right]. \tag{2.47}$$

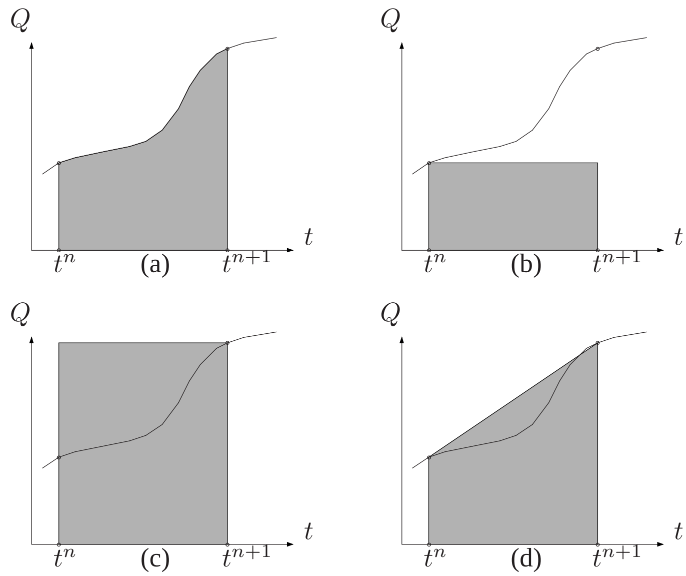

Figure 2-12 Time integration of the source term Q between t^n and t^{n+1}: (a) exact integration, (b) explicit scheme, (c) implicit scheme, and (d) semi-implicit, trapezoidal scheme.

Note that these schemes may be interpreted either as finite-difference approximations of the time derivative or finite-difference approximations of the time integration of the source term. Indeed,

$$u(t^{n+1}) = u(t^n) + \int_{t^n}^{t^{n+1}} Q \, dt, \tag{2.48}$$

and the various schemes can be viewed as different ways of approximating the integral, as depicted in Figure 2-12. All discretization schemes based on the exclusive use of Q^n and Q^{n+1} to evaluate the integral between t^n and t^{n+1}, which are called *two-point methods*, are inevitably first-order methods, except the semi-implicit (or trapezoidal) scheme, which is of second order. Second order is thus the highest order achievable with a two-point method. To achieve an order higher than two, denser sampling of the Q term must be used to approximate the time integration.

Before considering this, however, a serious handicap should be noted: The source term Q depends on the unknown variable $\tilde{u}$, and we face the problem of not being able to calculate Q^{n+1} *before* we know $\tilde{u}^{n+1}$, which is to be calculated from the value of Q^{n+1}. There is a vicious circle here! In the original case of inertial oscillations, the circular dependence was overcome by an algebraic manipulation of the equations prior to solution (gathering all $n+1$ terms on the left), but when the source term is nonlinear, as is often the case, such preliminary manipulation is generally not possible and we need to circumvent the exact calculation by searching for a good approximation.

Such an approximation may proceed by using a first guess $\tilde{u}^\star$ in the Q term:

$$Q^{n+1} \simeq Q(t^{n+1}, \tilde{u}^\star), \tag{2.49}$$

as long as $\tilde{u}^\star$ is a sufficiently good estimate of $\tilde{u}^{n+1}$. The closer $\tilde{u}^\star$ is to $\tilde{u}^{n+1}$, the more faithful is the scheme to the ideal the implicit value. If this estimate $\tilde{u}^\star$ is provided by a preliminary explicit (forward) step, according to:

$$\tilde{u}^\star = \tilde{u}^n + \Delta t \, Q(t^n, \tilde{u}^n) \tag{2.50a}$$

$$\tilde{u}^{n+1} = \tilde{u}^n + \frac{\Delta t}{2} \left(Q(t^n, \tilde{u}^n) + Q(t^{n+1}, \tilde{u}^\star) \right) \tag{2.50b}$$

we obtain a two-step algorithm, called the *Heun method*. It can be shown to be second-order accurate.

This second-order method is actually a particular member of a family of so-called *predictor-corrector methods*, in which a first guess $\tilde{u}^\star$ is used as a proxy of $\tilde{u}^{n+1}$ in the computation of complicated terms.

2.9 Higher-order schemes

If we want to go beyond second-order methods, we need to take into account a greater number of values of the Q term than those at t^n and t^{n+1}. We have two basic possibilities: either to include intermediate points between t^n and t^{n+1}, or to use Q values at previous steps $n-1, n-2, \ldots$. The first approach leads to the so-called family of *Runge-Kutta methods* (or *multi-stage methods*), while the second generates the so-called *multi-step methods*.

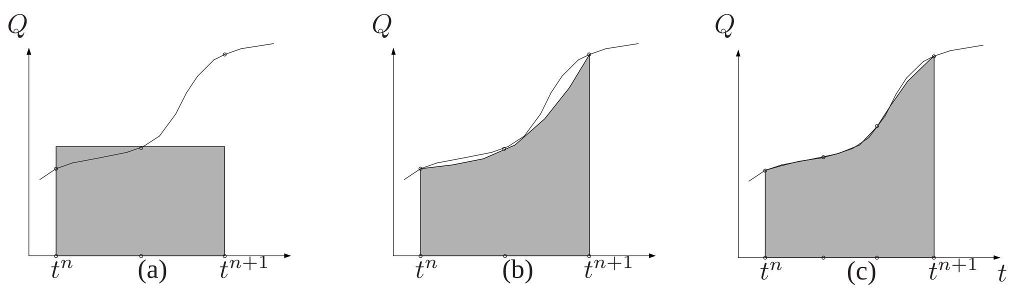

Figure 2-13 Runge-Kutta schemes of increasing complexity: (a) mid-point integration, (b) integration with parabolic interpolation, (c) with cubic interpolation.

The simplest method, using a single intermediate point, is the so-called *mid-point method*. In this case (Figure 2-13), the integration is achieved by first calculating the value $\tilde{u}^{n+1/2}$ (playing the role of $\tilde{u}^\star$) at an intermediate stage $t^{n+1/2}$ and then integrating for the whole step based on this mid-point estimate:

$$\tilde{u}^{n+1/2} = \tilde{u}^n + \frac{\Delta t}{2}\, Q(t^n, \tilde{u}^n) \tag{2.51a}$$

$$\tilde{u}^{n+1} = \tilde{u}^n + \Delta t\, Q(t^{n+1/2}, \tilde{u}^{n+1/2}). \tag{2.51b}$$

This method, however, is only second-order accurate and offers no improvement over the earlier Heun method (2.50).

A popular fourth-order method can be constructed by using a parabolic interpolation between the values of Q with two successive estimates at the central point before proceeding with the full step:

$$\tilde{u}_a^{n+1/2} = \tilde{u}^n + \frac{\Delta t}{2}\, Q(t^n, \tilde{u}^n) \tag{2.52a}$$

$$\tilde{u}_b^{n+1/2} = \tilde{u}^n + \frac{\Delta t}{2}\, Q(t^{n+1/2}, \tilde{u}_a^{n+1/2}) \tag{2.52b}$$

$$\tilde{u}^{\star} = \tilde{u}^n + \Delta t\, Q(t^{n+1/2}, \tilde{u}_b^{n+1/2}) \tag{2.52c}$$

$$\tilde{u}^{n+1} = \tilde{u}^n + \Delta t \left(\frac{1}{6} Q(t^n, \tilde{u}^n) + \frac{2}{6} Q(t^{n+1/2}, \tilde{u}_a^{n+1/2}) + \frac{2}{6} Q(t^{n+1/2}, \tilde{u}_b^{n+1/2}) + \frac{1}{6} Q(t^{n+1}, \tilde{u}^{\star}) \right). \tag{2.52d}$$

We can increase the order to any desired level by using higher-polynomial interpolations (Figure 2-13).

As mentioned earlier, instead of using intermediate points to increase the order of accuracy, we can exploit already available evaluations of Q from previous steps (Figure 2-14). The most popular method in GFD models is the *leapfrog method*, which simply reuses the value at time step $n-1$ to "jump over" the Q term at t^n in a $2\Delta t$ step:

$$\tilde{u}^{n+1} = \tilde{u}^{n-1} + 2\Delta t\, Q^n. \tag{2.53}$$

This algorithm offers second-order accuracy while being fully explicit.

An alternative second-order method using the value at $n-1$ is the so-called *Adams-Bashforth method*:

$$\tilde{u}^{n+1} = \tilde{u}^n + \Delta t \frac{\left(3Q^n - Q^{n-1}\right)}{2}, \tag{2.54}$$

which can be interpreted in the light of Figure 2-14 (bottom panel). Higher-order methods can be constructed by recalling more points from the past ($n-2, n-3, ...$), but we will not pursue this approach further for the following two reasons. Firstly, using anterior points creates a problem at the start of the calculation from the initial condition. The first step must be different in order avoid using one or several points that do not exist, and an explicit Euler scheme is usually performed. One such step is sufficient to initiate the leapfrog and Adams-Bashforth schemes, but methods that use earlier values (at $n-2, n-3, ...$) require more cumbersome care, which can amount to considerable effort in a GFD code. Secondly, the use of several points in the past demands a proportional increase in computer storage, because

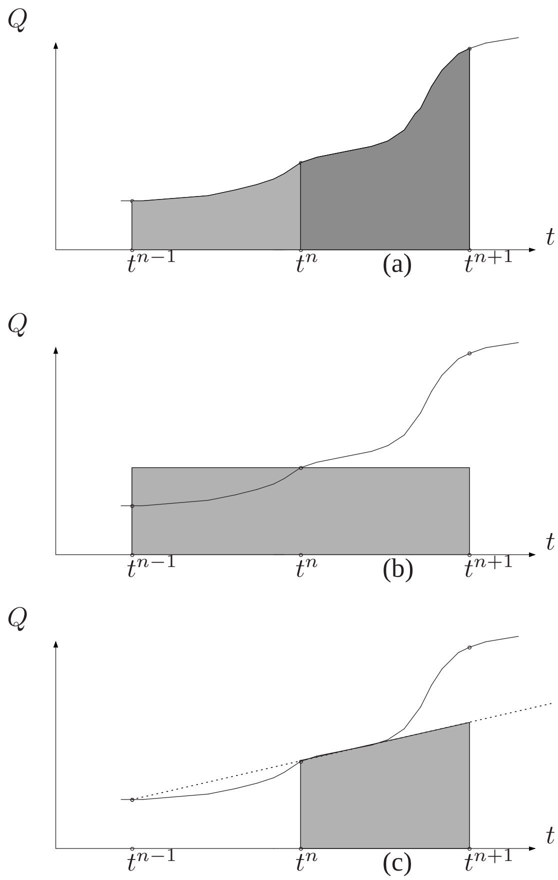

Figure 2-14 (a) Exact integration from t^{n-1} or t^n towards t^{n+1}, (b) leapfrog integration starts from t^{n-1} to reach t^{n+1}, whereas (c) Adams-Bashforth integration starts from t^n to reach t^{n+1}, using previous values to extrapolate Q over the integration interval t^n, t^{n+1}.

values cannot be discarded as quickly before making room for newer values. Again, for a single equation, this is not much of a trouble, but in actual applications, size matters and only a few past values can be stored in the central memory of the machine. A similar problem arises also with multi-stage methods, although these do not need any particular starting mechanism.

We can conclude the section by remarking that higher-order methods can always be designed but at the price of more frequent evaluations of the right-hand side of the equation (potentially a very complicated term) and/or greater storage of numerical values at different time steps. Since higher-order methods create more burden on the computation, we ought to ask whether they at least provide better numerical solutions than lower-order methods. We have therefore to address the question of accuracy of these methods, which will be considered in Section 4.8.

A fundamental difference between analytical solutions and numerical approximations emerges. For some equations, properties of the solution can be derived without actually solving the equations. It is easy to prove, for example, that the velocity magnitude remains constant during an inertial oscillation. The numerical solution on the other hand is generally not guaranteed to satisfy the same property as its analytical counterpart (the explicit Euler

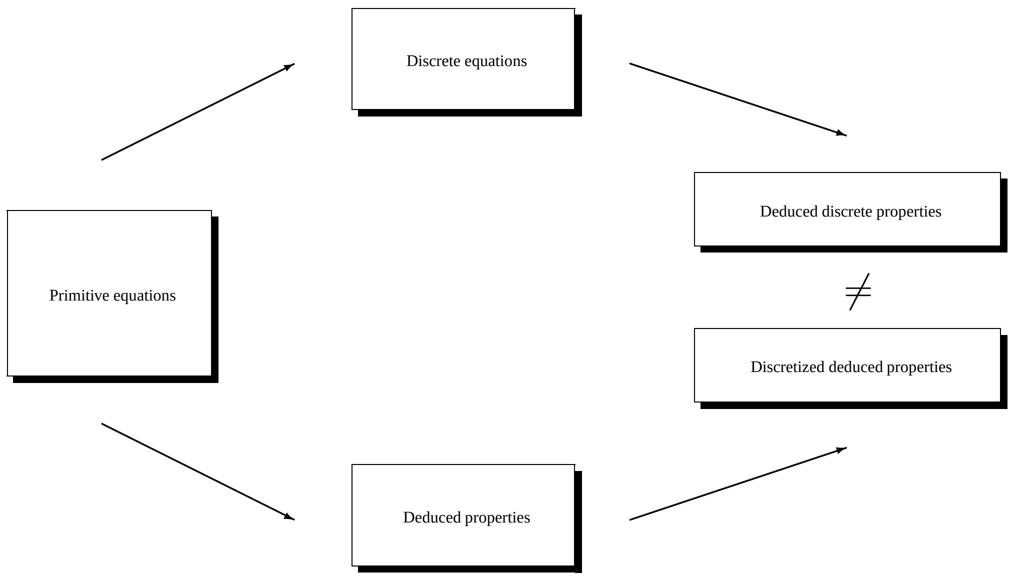

Figure 2-15 Schematic representation of discretization properties and mathematical properties interplay.

discretization did not conserve the velocity norm). Therefore, we cannot be sure that mathematical properties of the analytical solutions will also be present in the numerical solution. This might appear as a strong drawback of numerical methods but can actually be used to assess the quality of numerical schemes. Also, for numerical schemes with adjustable parameters (as the implicit factor), those parameters can be chosen so that the numercial solution respects as best as possible the exact properties.

We can summarize by recognizing the fact that numerical solutions generally do not inherit the mathematical properties of the exact solution (Figure 2-15), a handicap particularly easy to understand in the case of inertial oscillation and its discretization by an explicit scheme (Figure 2-16). Later we will encounter other properties (energy conservation, potential-vorticity conservation, positiveness of concentrations, etc.) that can be used to guide the choice of parameter values in numerical schemes.

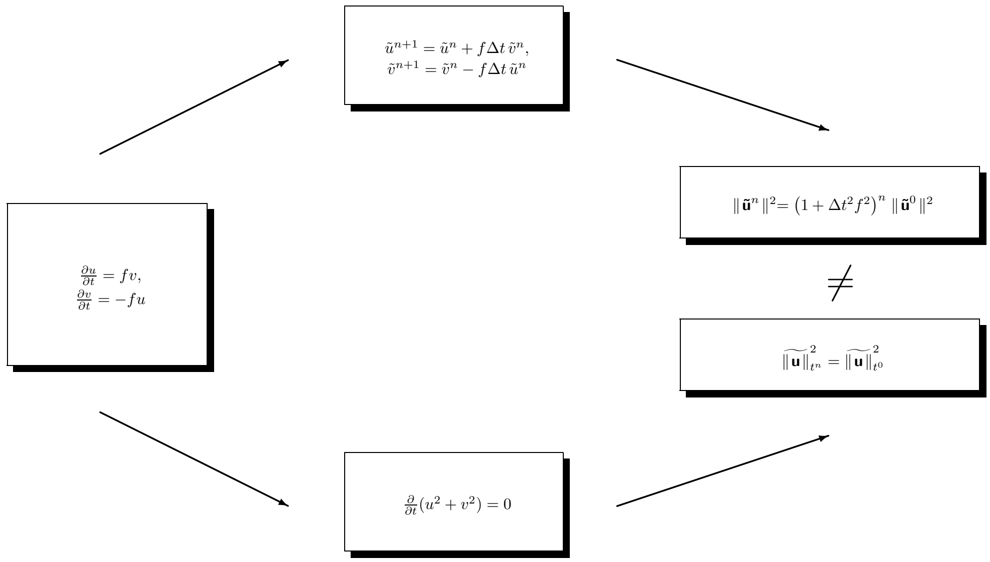

Figure 2-16 Schematic representation of discretization properties and mathematical properties interplay exemplified in the case of inertial oscillation.

Analytical Problems

2-1. On Jupiter, a day lasts 9.9 Earth hours and the equatorial circumference is 448,600 km. Knowing that the measured gravitational acceleration at the equator is 26.4 m/s^2, deduce the true gravitational acceleration and the centrifugal acceleration.

2-2. The Japanese Shinkansen train (bullet train) zips from Tokyo to Ozaka (both at approximately 35°N) at a speed of 185 km/h. In the design of the train and tracks, do you think that engineers had to worry about the earth's rotation? (*Hint*: The Coriolis effect induces an oblique force, the lateral component of which could produce a tendency of the train to lean sideways.)

2-3. Determine the lateral deflection of a cannonball that is shot in London (51°31′N) and flies for 25 s at an average horizontal speed of 120 m/s. What would be the lateral deflection in Murmansk (68°52′N) and Nairobi (1°18′S)?

2-4. On a perfectly smooth and frictionless hockey field at Dartmouth College (43°38′N), how slowly should a puck be driven to perform an inertial circle of diameter equal to the field width (26 m)?

2-5. A stone is dropped from a 300-m-high bridge at 35°N. In which cardinal direction is it deflected under the effect of the earth's rotation? How far from the vertical does the stone land? (Neglect air drag.)

2-6. At 43°N, raindrops fall from a cloud 2500 m above ground through a perfectly still atmosphere (no wind). In falling, each raindrop experiences gravity, a linear drag force with coefficient C = 1.3 s^{-1} (*i.e.*, the drag force in the x, y and z directions is respectively $-Cu$, $-Cv$ and $-Cw$ per unit mass) and is also subjected to the three-dimensional Coriolis force. What is the trajectory of one raindrop? How far eastward and northward has the Coriolis force deflected the raindrop by the time it hits the ground? (*Hint*: It can be shown that the terminal velocity is reached very quickly relatively to the total falling time.)

2-7. A set of two identical solid particles of mass M attached to each other by a weightless rigid rod of length L are moving on a horizontal rotating plane in the absence of external forces (Figure 2-17). As in geophysical fluid dynamics, ignore the centrifugal force caused by the ambient rotation. Establish the equations governing the motion of the set of particles, derive the most general solution, and discuss its physical implications.

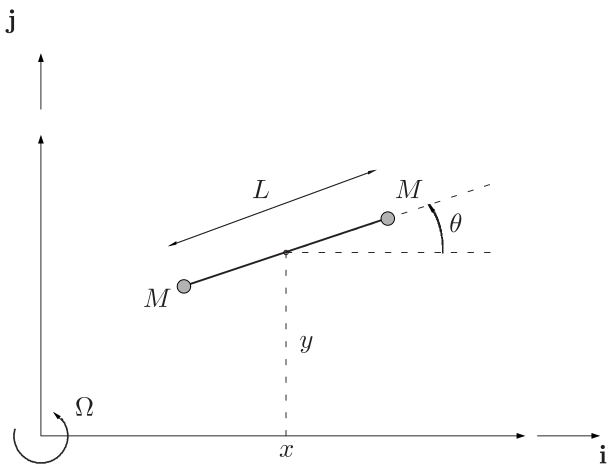

Figure 2-17 Two linked masses on a rotating plane (Problem 2-7).

2-8. At $t = 0$, two particles of equal mass m but opposite electrical charges q are released from rest at a distance L from each other on a rotating plane (constant rotation rate $\Omega = f/2$). Assuming as in GFD that the centrifugal force is externally balanced, write the equations of motion of the two particles and the accompanying initial conditions. Then, show that the center of mass (the mid-point between the particles) is not moving, and write a differential equation governing the evolution of the distance $r(t)$ between the two particles. Is it possible that, as on a non-rotating plane, the electrical attraction between the two particles will make them collide ($r = 0$)?

2-9. Study the trajectory of a free particle of mass M released from a state of rest on a rotating, sloping, rigid plane (Figure 2-18). The angular rotation rate is Ω, and the angle formed by the plane with the horizontal is α. Friction and the centrifugal force are negligible. What is the maximum speed acquired by the particle, and what is its maximum downhill displacement?

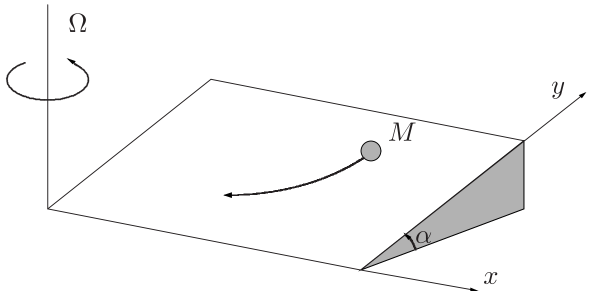

Figure 2-18 A free particle on a rotating, frictionless slope (Problem 2-9).

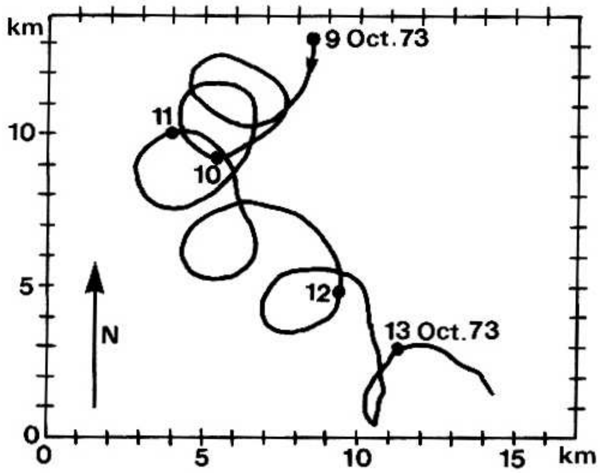

Figure 2-19 Progressive vector diagram constructed from current-meter observation in the Mediterranean Sea taken in October 1973 (Problem 2-10). [Courtesy of Martin Mork, University of Bergen, Norway]

2-10. The curve reproduced in Figure 2-19 is a progressive vector diagram constructed from current-meter observations at latitude 43°09′N in the Mediterranean Sea . Under the assumption of a uniform but time-dependent flow field in the vicinity of the mooring, the curve can be interpreted as the trajectory of a water parcel. Using the marks counting the days along the curve, show that this set of observations reveals the presence of inertial oscillations. What is the average orbital velocity in these oscillations?

Numerical Exercises

2-1. When using the semi-implicit scheme (2.32a) – (2.32b) with α = 1/2, how many time steps are required per complete cycle (period of $2\pi/f$) to guarantee a relative error on f not exceeding 1%?

2-2. Develop an Euler scheme to calculate the position coordinates x and y of a particle undergoing inertial oscillations from its velocity components u and v, themselves calculated with an Euler scheme. Graph the trajectory $[\tilde{x}^n,\ \tilde{y}^n]$ for $n = 1, 2, 3, ...$ of the particle. What do you notice?

2-3. For the semi-implicit discretization of the inertial oscillation, calculate the number of complete cycles it takes before the exact solution and its numerical approximation are in phase opposition (180° phase shift). Show this number of cycles as a function of the parameter $f\Delta t$. What can you conclude for a scheme for which $f\Delta t = 0.1$ in terms of time windows that can be analyzed before the solution is out of phase?

2-4. Devise a leapfrog scheme for inertial oscillations and analyze its stability and angular frequency properties by searching for a numerical solution of the following form[4]:

$$\tilde{u}^n = V\varrho^n \sin(\tilde{f}n\Delta t + \phi),\ \ \tilde{v}^n = V\varrho^n \cos(\tilde{f}n\Delta t + \phi).$$

2-5. Calculate the discrete solution of the explicit Euler-scheme applied to inertial oscillations by searching for a solution of the same form as in Problem 2-4 where ϱ and $\tilde{f}$ are again parameters to be determined. Show that the discrete solution converges to the exact solution (2.12).

2-6. Prove the assertion that scheme (2.51) is of second order.

2-7. Adapt `coriolisdis.m` for a discretization of inertial oscillation with a frictional term

$$\frac{du}{dt} = fv - c\,u \tag{2.55}$$

$$\frac{dv}{dt} = -fu - c\,v, \tag{2.56}$$

where $c = f\,k$. Run the explicit discretization with increasing values of k in $[0, 1]$. For which value of k does the explicit Euler discretization give you a solution with constant norm? Can you interpret this result in view of the modified equation?

2-8. Try several time discretization methods on the following set of equations:

$$\frac{du}{dt} = fv \tag{2.57}$$

$$\frac{dv}{dt} = -fu + fk\,(1-u^2)v, \tag{2.58}$$

with initial condition $u = 2$, $v = 0$ at $t = 0$. Use two values for the parameter k: first $k = 0.1$ and then $k = 1$. Finally try $k = 5$. What do you notice?

[4]For ϱ^n, n is an exponent, not an index.

Pierre Simon Marquis de Laplace
1749 – 1827

¿From humble roots in rural France, Pierre Simon Laplace distinguished himself early by his abilities and went on to Paris. There, at the Académie des Sciences, Jean D'Alembert recognized the talents of the young Laplace and secured for him a position in the military school. Set with this appointment, Laplace began a study of planetary motions, which led him to make advances in integral calculus and differential equations. Skillful at changing his political views during the turbulent years of the French Revolution, Laplace managed to survive and continued his research almost without interruption. In 1799, he published the first volume of a substantial memoir titled *Mécanique Céleste*, which later grew into a five-volume treatise and has since been regarded as a cornerstone of classical physics. Some have said that this work is Isaac Newton's *Principia* (of 1687) translated in the language of differential calculus with the clarification of many important points that had remained puzzling to Newton. One such aspect is the theory of ocean tides, which Laplace was the first to establish on firm mathematical grounds.

The name Laplace is attached today to a differential operator (the sum of second derivatives), which arises in countless problems of physics, including geophysical fluid dynamics (see Chapter 16). (*Photo from* `http://occawlonline.pearsoned.com` *– Pearson Education.*)

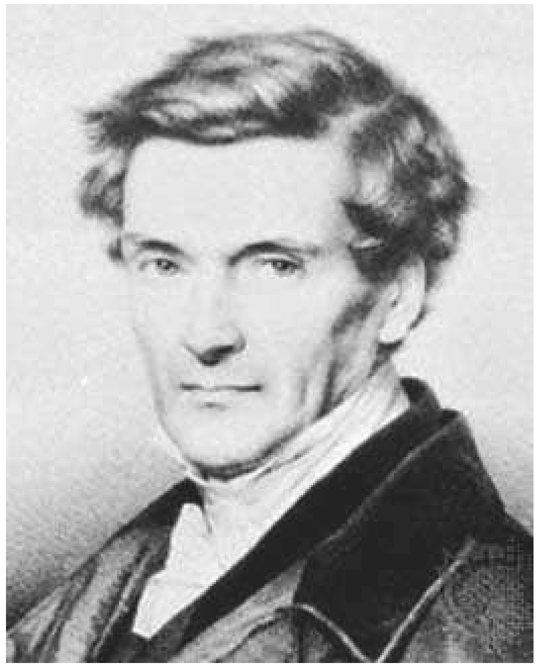

Gaspard Gustave de Coriolis
1792 – 1843

Born in France and trained as an engineer, Gaspard Gustave de Coriolis began a career in teaching and research at age 24. Fascinated by problems related to rotating machinery, he was led to derive the equations of motion in a rotating framework of reference. The result of these studies was presented to the Académie des Sciences in the summer of 1831. In 1838, Coriolis stopped teaching to become director of studies at the Ecole Polytechnique, but his health declined quickly and he died a few short years later.

The world's largest experimental rotating table, at the Institut de Mécanique in Grenoble, France, is named after him and has been used in countless simulations of geophysical fluid phenomena. (*Photo from the archives of the Académie des Sciences, Paris.*)

Chapter 3

Equations of Fluid Motion

(October 18, 2006) **SUMMARY**: The object of this chapter is to establish the equations governing the movement of a stratified fluid in a rotating environment. These equations are then simplified somewhat by taking advantage of the so-called Boussinesq approximation. The chapter concludes by introducing finite-volume discretizations and showing their relation to the budget calculations used to establish the mathematical equations of motion.

3.1 Mass budget

A necessary statement in fluid mechanics is that mass be conserved. That is, any imbalance between convergence and divergence in the three spatial directions must create a local compression or expansion of the fluid. Mathematically, the statement takes the form:

$$\frac{\partial \rho}{\partial t} + \frac{\partial}{\partial x}(\rho u) + \frac{\partial}{\partial y}(\rho v) + \frac{\partial}{\partial z}(\rho w) = 0, \tag{3.1}$$

where ρ is the density of the fluid (in kg/m^3), and (u, v, w) are the three components of velocity (in m/s). All four variables generally vary in the three spatial directions, x and y in the horizontal, z in the vertical, as well as time t.

This equation, often called the *continuity equation*, is classical in traditional fluid mechanics. Sturm (2001, page 4) reports that Leonardo da Vinci (1452–1519) had derived a simplified form of the statement of mass conservation for a stream with narrowing width. However, the three-dimensional differential form provided here was most likely written much later and credit ought probably to go to Leonhard Euler (1707–1783). For a detailed derivation, the reader is referred to Batchelor (1967), Fox and McDonald (1992), or Appendix A of the present text.

Note that spherical geometry introduces additional curvature terms, which we neglect to be consistent with our previous restriction to length scales substantially shorter than the global scale.

3.2 Momentum budget

For a fluid, Isaac Newton's second law "*mass times acceleration equals the sum of forces*" is better stated per unit volume with density replacing mass and, in the absence of rotation ($\Omega = 0$), the resulting equations are called the Navier-Stokes equations. For geophysical flows, rotation is important and acceleration terms must be augmented as done in (2.20):

$$x: \quad \rho \left(\frac{du}{dt} + f_* w - f v \right) = - \frac{\partial p}{\partial x} + \frac{\partial \tau^{xx}}{\partial x} + \frac{\partial \tau^{xy}}{\partial y} + \frac{\partial \tau^{xz}}{\partial z} \tag{3.2}$$

$$y: \quad \rho \left(\frac{dv}{dt} + f u \right) = - \frac{\partial p}{\partial y} + \frac{\partial \tau^{xy}}{\partial x} + \frac{\partial \tau^{yy}}{\partial y} + \frac{\partial \tau^{yz}}{\partial z} \tag{3.3}$$

$$z: \quad \rho \left(\frac{dw}{dt} - f_* u \right) = - \frac{\partial p}{\partial z} - \rho g + \frac{\partial \tau^{xz}}{\partial x} + \frac{\partial \tau^{yz}}{\partial y} + \frac{\partial \tau^{zz}}{\partial z}, \tag{3.4}$$

where the x–, y– and z–axes are directed eastward, northward and upward, respectively, $f = 2\Omega \sin\varphi$ is the Coriolis parameter, $f_* = 2\Omega\cos\varphi$ the reciprocal Coriolis parameter, ρ density, p pressure, g the gravitational acceleration, and the τ terms represent the normal and shear stresses due to friction.

That the pressure force is equal and opposite to the pressure gradient and that the viscous force involves the derivatives of a stress tensor should be familiar to the student who has had an introductory course in fluid mechanics. Appendix A retraces the formulation of those terms for the student new to fluid mechanics.

The effective gravitational force (sum of true gravitational force and the centrifugal force; see Section 2.2) is ρg per unit volume and is directed vertically downward. So, the corresponding term occurs only in the third equation, for the vertical direction.

Because the acceleration in a fluid is not counted as the rate of change in velocity at a fixed location but as the change in velocity of a fluid particle as it moves along with the flow, the time derivatives in the acceleration components, du/dt, dv/dt and dw/dt, consist of both the local time rate of change and the so-called advective terms:

$$\frac{d}{dt} = \frac{\partial}{\partial t} + u\,\frac{\partial}{\partial x} + v\,\frac{\partial}{\partial y} + w\,\frac{\partial}{\partial z}. \tag{3.5}$$

This derivative is called the *material derivative*.

The preceding equations assume a Cartesian system of coordinates and thus hold only if the dimension of the domain under consideration is much shorter than the earth's radius. On Earth, a length scale not exceeding 1000 km is usually acceptable. The neglect of the curvature terms is in some ways analogous to the distortion introduced by mapping the curved earth's surface onto a plane.

Should the dimensions of the domain under consideration be comparable to the size of the planet, the x–, y– and z–axes need to be replaced by spherical coordinates, and curvature terms enter all equations. See Appendix A for those equations. For simplicity in the exposition of the basic principles of geophysical fluid dynamics, we shall neglect throughout this book the extraneous curvature terms and use Cartesian coordinates exclusively.

Equations (3.2) through (3.4) can be viewed as three equations providing the three velocity components, u, v and w. They implicate, however, two additional quantities, namely, the pressure p and the density ρ. An equation for ρ is provided by the conservation of mass (3.1), and one additional equation is still required.

3.3 Equation of state

The description of the fluid system is not complete until we also provide a relation between density and pressure. This relation is called the *equation of state* and tells us about the nature of the fluid. To go further, we need to distinguish between air and water.

For an incompressible fluid such as pure water at ordinary pressures and temperatures, the statement can be as simple as ρ = constant. In this case, the preceding set of equations is complete. In the ocean, however, water density is a complicated function of pressure, temperature and salinity. Details can be found in Gill (1982 – Appendix 3), but for most applications, it can be assumed that the density of seawater is independent of pressure (Incompressibility) and linearly dependent upon both temperature (warmer waters are lighter) and salinity (saltier waters are denser), according to:

$$\rho \;=\; \rho_0 \, [1 \;-\; \alpha(T - T_0) \;+\; \beta(S - S_0)], \tag{3.6}$$

where T is the temperature (in degrees Celsius or Kelvin) and S the salinity (defined in the past as grams of salt per kilogram of seawater, *i.e.*, in parts per thousand, denoted by ‰, and more recently by the so-called practical salinity unit "psu", derived from measurements of conductivity and having no units). The constants ρ_0, T_0, and S_0 are reference values of density, temperature, and salinity, respectively, whereas α is the coefficient of thermal expansion and β is called, by analogy, the coefficient of saline contraction[1]. Typical seawater values are ρ_0 = 1028 kg/m^3, T_0 = 10°C = 283 K, S_0 = 35, α = 1.7 × 10^{-4} K^{-1}, and β = 7.6 × 10^{-4}.

For air, which is compressible, the situation is quite different. Dry air in the atmosphere behaves approximately as an ideal gas, and so we write:

$$\rho \;=\; \frac{p}{RT} \,, \tag{3.7}$$

where R is a constant, equal to 287 m^2/(s^2 K) at ordinary temperatures and pressures. In the preceding equation, T is the absolute temperature (temperature in degrees Celsius + 273.15).

Air in the atmosphere most often contains water vapor. For moist air, the preceding equation is generalized by introducing a factor that varies with the *specific humidity* q:

$$\rho \;=\; \frac{p}{RT(1 + 0.608q)} \,. \tag{3.8}$$

The specific humidity q is defined as

$$q \;=\; \frac{\text{mass of water vapor}}{\text{mass of air}} \;=\; \frac{\text{mass of water vapor}}{\text{mass of dry air + mass of water vapor}} \,. \tag{3.9}$$

[1]The latter expression is a misnomer, since salinity increases density not by contraction of the water but by the added mass of dissolved salt.

For details, the reader is referred to Curry and Webster (1999).

Unfortunately, our set of governing equations is not yet complete. Although we have added one equation, by so doing we have also introduced additional variables, namely temperature and, depending on the nature of the fluid, either salinity or specific humidity. Additional equations are clearly necessary.

3.4 Energy budget

The equation governing temperature arises from conservation of energy. The principle of energy conservation, also known as the first law of thermodynamics, states that the internal energy gained by a parcel of matter is equal to the heat it receives minus the mechanical work it performs. Per unit mass and unit time, we have

$$\frac{de}{dt} \;=\; Q \;-\; W, \tag{3.10}$$

where d/dt is the material derivative introduced in (3.5), e is the internal energy, Q the rate of heat gain, and W the rate of work done by the pressure force onto the surrounding fluid, all per unit mass. The internal energy, a measure of the thermal agitation of the molecules inside the fluid parcel, is proportional to the temperature:

$$e \;=\; C_v T$$

temperature
where C_v is the heat capacity at constant volume, and T the absolute temperature. For air at sea-level pressure and ambient temperatures, C_v = 718 J/(kg K), while for seawater C_v = 3990 J/(kg K).

In the ocean, there is no internal heat source[2], whereas in the atmosphere release of latent heat by water-vapor condensation or, conversely, uptake of latent heat by evaporation constitute internal sources. Leaving such complication for more advanced textbooks in dynamical and physical meteorology (Curry and Webster, 1999), the Q term in (3.10) includes only the heat gained by a parcel through its contact with its neighbors via the process of diffusion. Using the Fourier law of heat conduction, we write

$$Q = \frac{k_T}{\rho}\, \nabla^2 T,$$

where k_T is the thermal conductivity of the fluid and the Laplace operator ∇^2 is defined as the sum of double derivatives:

$$\nabla^2 \;=\; \frac{\partial^2}{\partial x^2} \;+\; \frac{\partial^2}{\partial y^2} \;+\; \frac{\partial^2}{\partial z^2}\;.$$

[2]In most cases, the absorption of solar radiation in the first meters of the upper ocean is treated as a surface flux, though occasionally it must be taken into account as a radiative absorption.

The work done by the fluid is the pressure force (= pressure $\times$ area) multiplied by the displacement in the direction of the force. Counting area times displacement as volume, the work is pressure multiplied by the change in volume, and on a per–mass and per–time basis:

$$W = p\frac{d\mathfrak{v}}{dt},$$

where $\mathfrak{v}$ is the volume per mass, *i.e.*, $\mathfrak{v} = 1/\rho$.

With its pieces assembled, Equation (3.10) becomes

$$\begin{aligned} C_v \frac{dT}{dt} &= \frac{k_T}{\rho} \nabla^2 T - p \frac{d\mathfrak{v}}{dt} \\ &= \frac{k_T}{\rho} \nabla^2 T + \frac{p}{\rho^2} \frac{d\rho}{dt}. \end{aligned} \tag{3.11}$$

Elimination of $d\rho/dt$ with the continuity equation (3.1) leads to:

$$\rho C_v \frac{dT}{dt} + p \left(\frac{\partial u}{\partial x} + \frac{\partial v}{\partial y} + \frac{\partial w}{\partial z} \right) = k_T \nabla^2 T. \tag{3.12}$$

This is the energy equation, which governs the evolution of temperature.

For water, which is nearly incompressible, the divergence term $(\partial u/\partial x + \partial v/\partial y + \partial w/\partial z)$ can be neglected (to be shown later), while for air, one may introduce the *potential temperature* θ defined as

$$\theta = T \left(\frac{\rho_0}{\rho} \right)^{R/C_v}, \tag{3.13}$$

for which the physical interpretation will be given later (Section 11.3). Taking its material derivative, and using (3.11), lead successively to

$$\begin{aligned} C_v \frac{d\theta}{dt} &= \left(\frac{\rho_0}{\rho} \right)^{R/C_v} \left(C_v \frac{dT}{dt} - \frac{RT}{\rho} \frac{d\rho}{dt} \right) \\ C_v \frac{d\theta}{dt} &= \frac{\theta}{T} \left(C_v \frac{dT}{dt} - \frac{p}{\rho^2} \frac{d\rho}{dt} \right) \\ \rho C_v \frac{d\theta}{dt} &= k_T \frac{\theta}{T} \nabla^2 T. \end{aligned} \tag{3.14}$$

The net effect of this transformation of variables is the elimination of the divergence term.

When k_T is zero or negligible, the right-hand side of the equation vanishes, leaving only

$$\frac{d\theta}{dt} = 0. \tag{3.15}$$

Unlike the actual temperature T, which is subject to the compressibility effect (through the divergence term), the potential temperature θ of an air parcel is conserved in the absence of heat diffusion.

3.5 Salt and moisture budgets

The set of equations is not yet complete because there is a remaining variable for which a last equation is required: salinity in the ocean and specific humidity in the atmosphere.

For seawater, density varies with salinity as stated in (3.6). Its evolution is governed by the salt budget:

$$\frac{dS}{dt} = \kappa_S \nabla^2 S, \tag{3.16}$$

which simply states that a seawater parcel conserves its salt content, except for redistribution by diffusion. The coefficient κ_S is the coefficient of salt diffusion, which plays a role analogous to the heat diffusivity k_T.

For air, the remaining variable is specific humidity and, because of the possibility of evaporation and condensation, its budget is complicated. Leaving this matter for more advanced texts in meteorology, we simply write an equation similar to that of salinity:

$$\frac{dq}{dt} = \kappa_q \nabla^2 q, \tag{3.17}$$

which states that specific humidity is redistributed by contact with neighboring parcels of different moisture content, and in which the diffusion coefficient κ_q is the analogue of κ_T and κ_S.

3.6 Summary of governing equations

Our set of governing equations is now complete. For air (or any ideal gas), there are seven variables (u, v, w, p, ρ, T and q), for which we have a continuity equation (3.1), three momentum equations (3.2) through (3.4), an equation of state (3.7), an energy equation (3.12), and a humidity equation (3.17). conduction (see biography at the end of this chapter) is credited for having been the first to recognize that atmospheric physics can, in theory, be fully described by a set of equations governing the evolution of the seven aforementioned variables (Bjerknes, 1904; see also Nebeker, 1995, chapter 5).

For seawater, the situation is similar. There are again seven variables (u, v, w, p, ρ, T and S) for which we have the same continuity, momentum and energy equations, the equation of state (3.6), and the salt equation (3.16). No particular person is credited with this set of equations.

3.7 Boussinesq approximation

Although the equations established in the previous sections already contain numerous simplifying approximations, they are still too complicated for the purpose of geophysical fluid dynamics. Additional simplifications can be obtained by the so-called *Boussinesq approximation* without appreciable loss of accuracy.

In most geophysical systems, the fluid density varies, but not greatly, around a mean value. For example, the average temperature and salinity in the ocean are $T = 4°$C and S = 34.7, to which corresponds a density ρ = 1028 kg/m^3 at surface pressure. Variations in density within one ocean basin rarely exceed 3 kg/m^3. Even in estuaries where fresh river waters (S = 0) ultimately turn into salty seawaters (S = 34.7), the relative density difference is less than 2%.

By contrast, the air of the atmosphere becomes gradually more rarefied with altitude, and its density varies from a maximum at ground level to nearly zero at great heights, thus covering a 100% range of variations. Most of the density changes, however, can be attributed to hydrostatic pressure effects, leaving only a moderate variability caused by other factors. Furthermore, weather patterns are confined to the lowest layer, the troposphere (approximately 10 km thick), within which the density variations responsible for the winds are usually no more than 5%.

As it appears justifiable in most instances[3] to assume that the fluid density, ρ, does not depart much from a mean reference value, ρ_0, we take the liberty to write:

$$\rho \;=\; \rho_0 \;+\; \rho'(x,\; y,\; z,\; t) \quad \text{with} \quad |\rho'| \ll \rho_0, \tag{3.18}$$

where the variation ρ' caused by the existing stratification and/or fluid motions is small compared to the reference value ρ_0. Armed with this assumption, we proceed to simplify the governing equations.

The continuity equation, (3.1), can be expanded as follows:

$$\rho_0 \left(\frac{\partial u}{\partial x} + \frac{\partial v}{\partial y} + \frac{\partial w}{\partial z}\right) \;+\; \rho' \left(\frac{\partial u}{\partial x} + \frac{\partial v}{\partial y} + \frac{\partial w}{\partial z}\right) \;+\; \left(\frac{\partial \rho'}{\partial t} + u\frac{\partial \rho'}{\partial x} + v\frac{\partial \rho'}{\partial y} + w\frac{\partial \rho'}{\partial z}\right) \;=\; 0.$$

Geophysical flows indicate that relative variations of density in time and space are not larger than – and usually much less than – the relative variations of the velocity field. This implies that the terms in the third group are on the same order as – if not much less than – those in the second. But, terms in this second group are always much less than those in the first because $|\rho'| \ll \rho_0$. Therefore, only that first group of terms needs to be retained, and we write

$$\frac{\partial u}{\partial x} + \frac{\partial v}{\partial y} + \frac{\partial w}{\partial z} \;=\; 0. \tag{3.19}$$

Physically, this statement means that conservation of mass has become conservation of volume. The reduction is to be expected because volume is a good proxy for mass when mass per volume (= density) is nearly constant. A hidden implication of this simplification is the elimination of sound waves, which rely on compressibility for their propagation.

The x– and y–momentum equations (3.2) and (3.3), being similar to each other, can be treated simultaneously. There, ρ occurs as a factor only in front of the left-hand side. So, wherever ρ' occurs, ρ_0 is there to dominate. It is thus safe to neglect ρ' next to ρ_0 in that pair of equations. Further, the assumption of a Newtonian fluid (viscous stresses proportional

[3] The situation is obviously somewhat uncertain on other planets that are known to possess a fluid layer (Jupiter and Neptune, for example), and on the sun.

to velocity gradients), with the use of the reduced continuity equation, (3.19), permits us to write the components of the stress tensor as

$$
\begin{aligned}
\tau^{xx} &= \mu\left(\frac{\partial u}{\partial x} + \frac{\partial u}{\partial x}\right), \quad \tau^{xy} = \mu\left(\frac{\partial u}{\partial y} + \frac{\partial v}{\partial x}\right), \quad \tau^{xz} = \mu\left(\frac{\partial u}{\partial z} + \frac{\partial w}{\partial x}\right) \\
\tau^{yy} &= \mu\left(\frac{\partial v}{\partial y} + \frac{\partial v}{\partial y}\right), \quad \tau^{yz} = \mu\left(\frac{\partial v}{\partial z} + \frac{\partial w}{\partial y}\right) \\
\tau^{zz} &= \mu\left(\frac{\partial w}{\partial z} + \frac{\partial w}{\partial z}\right), \qquad (3.20)
\end{aligned}
$$

where μ is called the coefficient of dynamic viscosity. A subsequent division by ρ_0 and the introduction of the *kinematic viscosity* $\nu = \mu/\rho_0$ yield

$$\frac{du}{dt} + f_* w - f v = -\frac{1}{\rho_0}\frac{\partial p}{\partial x} + \nu \nabla^2 u \qquad (3.21)$$

$$\frac{dv}{dt} + f u = -\frac{1}{\rho_0}\frac{\partial p}{\partial y} + \nu \nabla^2 v. \qquad (3.22)$$

The next candidate for simplification is the z–momentum equation, (3.4). There, ρ appears as a factor not only in front of the left-hand side, but also in a product with g on the right. On the left, it is safe to neglect ρ' in front of ρ_0 for the same reason as previously, but on the right it is not. Indeed, the term ρg accounts for the weight of the fluid, which, as we know, causes an increase of pressure with depth (or, a decrease of pressure with height, depending on whether we think of the ocean or atmosphere). With the ρ_0 part of the density goes a hydrostatic pressure p_0, which is a function of z only:

$$p = p_0(z) + p'(x, y, z, t) \quad \text{with} \quad p_0(z) = P_0 - \rho_0 g z, \qquad (3.23)$$

so that $dp_0/dz = -\rho_0 g$, and the vertical-momentum equation at this stage reduces to

$$\frac{dw}{dt} - f_* u = -\frac{1}{\rho_0}\frac{\partial p'}{\partial z} - \frac{\rho' g}{\rho_0} + \nu \nabla^2 w, \qquad (3.24)$$

after a division by ρ_0 for convenience. No further simplification is possible because the remaining ρ' term no longer falls in the shadow of a neighboring term proportional to ρ_0. Actually, as we will see later, the term $\rho' g$ is the one responsible for the buoyancy forces that are such a crucial ingredient of geophysical fluid dynamics.

Note that the hydrostatic pressure $p_0(z)$ can be subtracted from p in the reduced momentum equations, (3.21) and (3.22), because it has no derivatives with respect to x and y, and is dynamically inactive.

For water, the treatment of the energy equation, (3.10), is straightforward. First, continuity of volume, (3.19), eliminates the middle term, leaving

$$\rho C_v \frac{dT}{dt} = k_T \nabla^2 T.$$

Next, the factor ρ in front of the first term can be replaced once again by ρ_0, for the same reason as it was done in the momentum equations. Defining the heat kinematic diffusivity $\kappa_T = k_T/\rho_0 C_v$, we then obtain

$$\frac{dT}{dt} = \kappa_T \nabla^2 T, \tag{3.25}$$

which is isomorphic to the salt equation, (3.16).

For seawater, the pair of equations (3.16) for salinity and (3.25) for temperature combine to determine the evolution of density. A simplification results if it may be assumed that the salt and heat diffusivities, κ_S and κ_T, can be taken as equal. If diffusion is primarily governed by molecular processes, this assumption is invalid. In fact, a substantial difference between the rates of salt and heat diffusion is responsible for peculiar small-scale features, such as salt fingers, which are studied in the discipline called *double diffusion* (Turner, 1973, Chapter 8). However, molecular diffusion generally affects only small-scale processes, up to a meter or so, whereas turbulence regulates diffusion on larger scales. In turbulence, efficient diffusion is accomplished by eddies, which mix salt and heat at equal rates. The values of diffusivity coefficients in most geophysical applications may not be taken as those of molecular diffusion; instead, they should be taken much larger and equal to each other. The corresponding turbulent diffusion coefficient, also called *eddy diffusivity*, is typically expressed as the product of a turbulent eddy velocity with a mixing length (Tennekes and Lumley, 1972; Pope, 2000) and, although there exists no single value applicable to all situations, the value $\kappa_S = \kappa_T = 10^{-2}$ m^2/s is frequently adopted. Noting $\kappa = \kappa_S = \kappa_T$ and combining equations (3.16) and (3.25) with the equation of state (3.6), we obtain

$$\frac{d\rho'}{dt} = \kappa \nabla^2 \rho', \tag{3.26}$$

where $\rho' = \rho - \rho_0$ is the density variation. In sum, the energy and salt-conservation equations have been merged into a density equation, which is not to be confused with mass conservation (3.1).

For air, the treatment of the energy equation (3.12) is more subtle, and the reader interested in a rigorous discussion is referred to the article by Spiegel and Veronis (1960). Here, for the sake of simplicity, we limit ourselves to suggestive arguments. First, the change of variable (3.13) from actual temperature to potential temperature eliminates the divergence term in (3.12) and takes care of the compressibility effect. Then, for weak departures from a reference state, the relation between actual and potential temperatures and the equation of state can both be linearized. Finally, assuming that heat and moisture are diffused by turbulent motions at the same rate, we can combine their respective budget into a single equation, (3.26).

In summary, the Boussinesq approximation, rooted in the assumption that the density does not depart much from a mean value, has allowed the replacement of the actual density ρ by its reference value ρ_0 everywhere, except in front of the gravitational acceleration and in the energy equation, which has become an equation governing density variations.

At this point, since the original variables ρ and p no longer appear in the equations, it is customary to drop the primes from ρ' and p' without risk of ambiguity. So, from here on, the variables ρ and p will be used exclusively to denote the perturbation density and perturbation pressure. This perturbation pressure is sometimes called the *dynamic pressure*, because it is usually a main contributor to the flow field. The only place where total pressure comes into play is then the equation of state.

3.8 Flux formulation and conservative form

The preceding equations form a complete set of equations and there is no need to invoke further physical laws. Nevertheless we can manipulate the equations to write them in another form, which, though mathematically equivalent, has some practical advantages. Consider for example the equation for temperature (3.25), which was deduced from the energy equation using the Boussinesq approximation. Under the same Boussinesq approximation, mass conservation was reduced to volume conservation (3.19) and we can write the temperature equation by first expanding the material derivative (3.5)

$$\frac{\partial T}{\partial t} + u\,\frac{\partial T}{\partial x} + v\,\frac{\partial T}{\partial y} + w\,\frac{\partial T}{\partial z} = \kappa_T\,\nabla^2 T, \tag{3.27}$$

and then using volume conservation (3.19) to obtain

$$\begin{aligned} &\frac{\partial T}{\partial t} + \frac{\partial}{\partial x}(uT) + \frac{\partial}{\partial y}(vT) + \frac{\partial}{\partial z}(wT) \\ &- \frac{\partial}{\partial x}\left(\kappa_T \frac{\partial T}{\partial x}\right) - \frac{\partial}{\partial y}\left(\kappa_T \frac{\partial T}{\partial y}\right) - \frac{\partial}{\partial z}\left(\kappa_T \frac{\partial T}{\partial z}\right) = 0. \end{aligned} \tag{3.28}$$

The latter form is called a *conservative formulation*, the reason for which will become clear upon applying the divergence theorem. This theorem, also known as Gauss's Theorem, states that for any vector (q_x, q_y, q_z) the volume integral of its divergence is equal to the integral of the flux over the enclosing surface:

$$\int_{\mathcal{V}} \left(\frac{\partial q_x}{\partial x} + \frac{\partial q_y}{\partial y} + \frac{\partial q_z}{\partial z}\right) dx\,dy\,dz = \int_{\mathcal{S}} (q_x n_x + q_y n_y + q_z n_z)\,d\mathcal{S} \tag{3.29}$$

where the vector (n_x, n_y, n_z) is the outward unit vector normal to the surface $\mathcal{S}$ delimiting the volume $\mathcal{V}$ (Figure 3-1). Integrating the conservative form (3.28) over a fixed volume is then particularly simple and leads to an expression for the evolution of the heat content in the volume as a function of the fluxes entering and leaving the volume:

$$\frac{d}{dt}\int_{\mathcal{V}} T\,dt + \int_{\mathcal{S}} q\cdot\mathbf{n}\,d\mathcal{S} = 0. \tag{3.30}$$

The flux q of temperature is composed of an advective flux (uT, vT, wT) due to flow across the surface and a diffusive (conductive) flux $-\kappa_T(\partial T/\partial x, \partial T/\partial y, \partial T/\partial z)$. If the value of each flux is known on a closed surface, the evolution of the average temperature inside the volume can be calculated without knowing the detailed distribution of temperature. This property will be used now for the development of a particular discretization method.

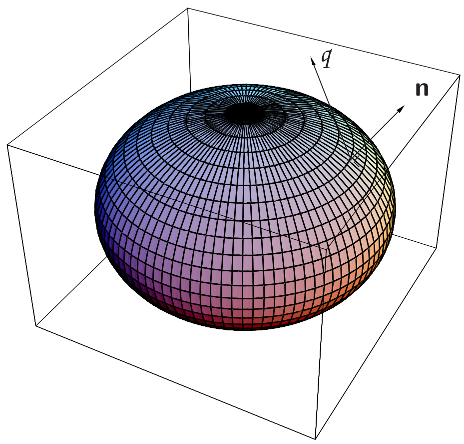

Figure 3-1 The divergence theorem allows the replacement of the integral over the volume $\mathcal{V}$ of the divergence $\partial q_x/\partial x + \partial q_y/\partial y + \partial q_z/\partial z$ of a flux vector $q = (q_x, q_y, q_z)$ by the integral, over the surface $\mathcal{S}$ containing the volume, of the scalar product of the flux vector and the normal vector **n** to this surface.

3.9 Finite-volume discretization

The conservative form (3.28) naturally leads to a numerical method with a clear physical interpretation, the so-called *finite-volume* approach. To illustrate the concept, we consider the equation for temperature in a one-dimensional (*1D*) case

$$\frac{\partial T}{\partial t} + \frac{\partial q}{\partial x} = 0, \tag{3.31}$$

in which the flux q for temperature $T = T(x,t)$ includes both advection uT and diffusion $-\kappa_T \partial T/\partial x$

$$q = uT - \kappa_T \frac{\partial T}{\partial x}. \tag{3.32}$$

We can integrate (3.31) over a given interval (labeled by index i) whose boundaries are noted by indices $i-1/2$ and $i+1/2$, so that we integrate over x in the range $x_{i-1/2} < x < x_{i+1/2}$. Though the interval of integration is of finite size $\Delta x_i = x_{i+1/2} - x_{i-1/2}$ (Figure 3-2), the integration is performed exactly:

$$\frac{d}{dt}\int_{x_{i-1/2}}^{x_{i+1/2}} T\,dx + q_{i+1/2} - q_{i-1/2} = 0. \tag{3.33}$$

By defining the cell-average temperature $\bar{T}_i$ for cell i as

$$\bar{T}_i \;=\; \frac{1}{\Delta x_i}\int_{x_{i-1/2}}^{x_{i+1/2}} T\,dx, \tag{3.34}$$

we obtain the evolution equation of the discrete field $\bar{T}_i$:

$$\frac{d\bar{T}_i}{dt} \;+\; \frac{q_{i+1/2} - q_{i-1/2}}{\Delta x_i} \;=\; 0. \tag{3.35}$$

Although we seem to have fallen back on a *discretization* of the spatial derivative, of q in this instance, the equation we just obtained is *exact*. This seems to be paradoxical compared to our previous discussions on inevitable errors associated with discretization. At first sight it appears that we found a discretization method without errors, but we must realize that (3.35) is still incomplete in the sense that two different variables appear in a single equation, the discretized average $\bar{T}_i$ and the discretized flux, $q_{i-1/2}$ and $q_{i+1/2}$. These two, however, are related to the *local* value of the continuous temperature field [the advective flux at $x_{i\pm 1/2}$ is $uT(x_{i\pm 1/2}, t)$], whereas the integrated equation is written for the *average* value of temperature. The averaging of the equation prevents us from retrieving information at the local level, and only average values (over the spatial scale Δx_i) can be determined. Therefore, we have to find an approximate way of assessing the local value of fluxes based solely on average temperature values. We also observe that with the grid size Δx_i we only retain information at scales longer than Δx_i, a property we have already mentioned in the context of aliasing (Section 1.12). The shorter spatial scales have simply been eliminated by the spatial averaging (Figure 3-2).

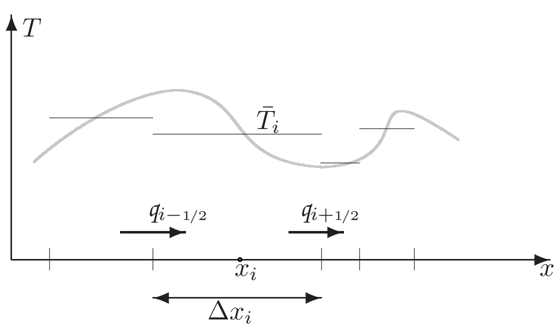

Figure 3-2 Replacement of the continuous function T by its cell-averaged discrete values $\bar{T}_i$. The evolution of the finite-volume averaged temperature is given by the difference of the flux q between the surrounding interfaces at $x_{i-1/2}$ and $x_{i+1/2}$.

A further exact time-integration of (3.35) yields

$$\bar{T}_i^{n+1} - \bar{T}_i^{n} \;+\; \frac{\int_{t^n}^{t^{n+1}} q_{i+1/2}\,dt - \int_{t^n}^{t^{n+1}} q_{i-1/2}\,dt}{\Delta x_i} \;=\; 0,$$

expressing that the difference in average temperature (*i.e.*, heat content) is given by the net flux entering the finite cell during the given time interval. Again, to this stage, no approximation is needed, and the equation is *exact* and can be formulated in terms of time-averaged fluxes $\hat{q}$

$$\hat{q} \;=\; \frac{1}{\Delta t_n} \int_{t^n}^{t^{n+1}} q \, dt \tag{3.36}$$

to yield an equation for discrete averaged quantities:

$$\frac{\bar{T}_i^{n+1} - \bar{T}_i^n}{\Delta t_n} \;+\; \frac{\hat{q}_{i+1/2} - \hat{q}_{i-1/2}}{\Delta x_i} \;=\; 0. \tag{3.37}$$

This equation is still *exact* but to be useful needs to be supplemented with a scheme to calculate the average fluxes $\hat{q}$ as functions of average temperatures $\bar{T}$. Only at that point are discretization approximations required, and discretization errors introduced.

It is noteworthy also to realize how easy the introduction of non-uniform grid spacing and time-stepping has been up to this point. Though we reference the interfaces by index $i \pm 1/2$, the position of an interface does not need to lie at mid-distance between consecutive grid nodes x_i. Only their logical, topological position must be ordered in the sense that grid nodes and interfaces must be interleaved.

Without further investigation of the way average fluxes can be computed, we interpret different discretization methods in relation to the mathematical budget formulation used to establish the governing equations (Figure 3-3). From brute-force replacement of differential operators by finite differences to the establishment of equations for finite volumes and subsequent discretization of fluxes, all methods aim at replacing the continuous problem by a finite set of discrete equations.

One of the main advantages of the finite-volume approach presented here is its conservation property. Consider the set of integrated equations for consecutive cells:

$$\begin{aligned}
\Delta x_1 \bar{T}_1^{n+1} &= \Delta x_1 \bar{T}_1^n \;+\; \Delta t_n \hat{q}_{1/2} - \Delta t_n \hat{q}_{1+1/2} \\
&\dots \\
\Delta x_{i-1} \bar{T}_{i-1}^{n+1} &= \Delta x_{i-1} \bar{T}_{i-1}^n \;+\; \Delta t_n \hat{q}_{i-1-1/2} - \Delta t_n \hat{q}_{i-1/2} \\
\Delta x_i \bar{T}_i^{n+1} &= \Delta x_i \bar{T}_i^n \;+\; \Delta t_n \hat{q}_{i-1/2} - \Delta t_n \hat{q}_{i+1/2} \\
\Delta x_{i+1} \bar{T}_{i+1}^{n+1} &= \Delta x_{i+1} \bar{T}_{i+1}^n \;+\; \Delta t_n \hat{q}_{i+1/2} - \Delta t_n \hat{q}_{i+1+1/2} \\
&\dots \\
\Delta x_m \bar{T}_m^{n+1} &= \Delta x_m \bar{T}_m^n \;+\; \Delta t_n \hat{q}_{m-1/2} - \Delta t_n \hat{q}_{m+1/2}.
\end{aligned}$$

Since every flux appears in two consecutive equations with opposite sign, the flux leaving a cell enters its neighbor and there is no loss or gain of the quantity being transported across cells (heat in the case of temperature). This is an expression of *local conservation* between grid cells.

Furthermore, summation of all equations leads to complete cancellation of the fluxes except for the very first and last ones. What we obtain is none other than the exact expression for evolution of the total quantity. In the case of temperature, this is a global heat budget:

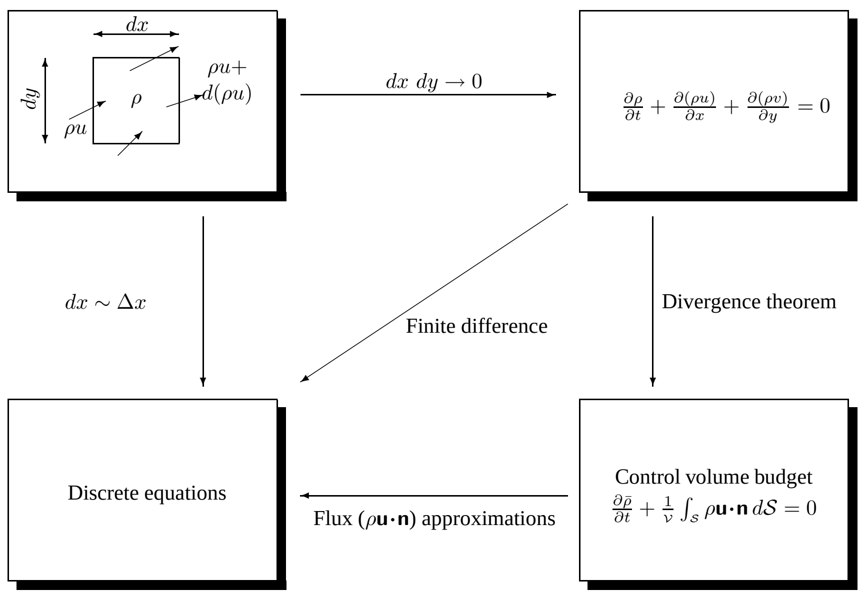

Figure 3-3 Schematic representation of several discretization methods. ¿From the budget calculations (upper-left box), the limit to infinitesimal values of dx, dy leads to the continuous equations (upper-right box), whereas keeping differentials formally at finite values leads to crude finite differencing (downward path from upper left to bottom left). If the operators in the continuous equations are discretized using Taylor expansions, higher-quality finite-difference methods are obtained (diagonal path from upper right to lower left). Finally, by preliminary integration of the continuous equations over a finite volume and then discretization of fluxes (path from upper right to lower right and then to lower left), discrete equations satisfying conservation properties can be designed.

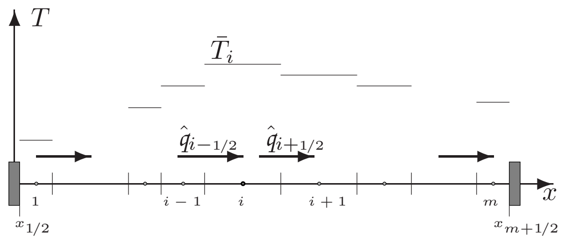

Figure 3-4 Within a domain covered by m finite volumes, fluxes at the interface ensure conservation of the relevant property (heat in the case of temperature) between finite volumes, since the fluxes are uniquely defined at interfaces. Fluxes therefore redistribute the property from cell to cell across the domain, without actually changing their total content, except for import and export at the end points. The finite-volume approach easily ensures both local and global conservation.

$$\frac{d}{dt}\int_{x_{1/2}}^{x_{m+1/2}} T\,dx \;=\; q_{1/2} - q_{m+1/2} \tag{3.38}$$

which states that the total heat content of the system increases or decreases over time according to the import or export of heat at the extremities of the domain. In particular, if the domain is insulated ($q = 0$ at both boundaries), the total heat content is conserved in the numerical scheme as well as in the original mathematical model. Moreover, this holds irrespectively of the way by which the fluxes are evaluated from the cell-averaged temperatures, provided that they are uniquely defined at every cell interface $x_{i+1/2}$. Therefore, the finite-volume approach also ensures *global conservation*.

We will show later how advective and diffusive fluxes can be approximated using the cell-averaged discrete values $\bar{T}_i$, but will have to remember then that the conservative character of the finite-volume approach is ensured simply by using a unique flux estimate at each volume interface.

Analytical Problems

3-1. Derive the energy equation (3.12) from equations (3.1) and (3.11).

3-2. Derive the continuity equation (3.19) from first principles by invoking conservation of volume. (*Hint*: State that the volume in a cube of dimensions $\Delta x \Delta y \Delta z$ is unchanged as fluid is imported and exported through all six sides.)

3-3. A laboratory tank consists of a cylindrical container 30 cm in diameter, filled whilst at rest with 20 cm of fresh water and then spun at 30 rpm. After a state of solid-body rotation is achieved, what is the difference in water level between the rim and the center? How does this difference compare to the minimum depth at the center?

3-4. Consider the Mediterranean Sea of surface $\mathcal{S} = 2.5 \times 10^{12}$ m^2 over which an average heat loss of 7 W/m^2 is observed. Due to an average surface water loss of 0.9 m/year (evaporation being more important than rain and river runoff combined), salinity would increase, water level drop and temperature decrease, if it were not for a compensation by exchange with the Atlantic Ocean through the Strait of Gibraltar. Assuming that water, salt and heat contents of the Mediterranean do not change over time and that exchange across Gibraltar is accomplished by a two-layer process (Figure 3-5), establish sea-wide budgets of water, salt and heat. Given that the Atlantic inflow is characterized by T_a = 15.5°C, S_a = 36.2 and a volume flow of 1.4 Sv (1 Sv= 10^6 m^3/s), what are the outflow characteristics? Is the outflow at the surface or at the bottom?

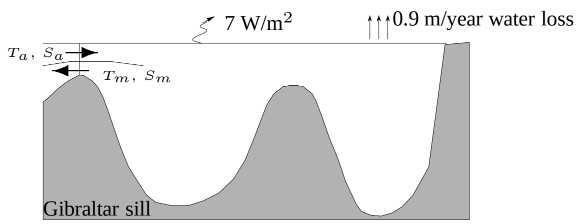

Figure 3-5 Schematic representation of the Mediterranean basin and its exchanges across the Strait of Gibraltar in order to perform budget calculations, relating Atlantic Water characteristics T_a, S_a, and losses over the basin, to Mediterranean outflow characteristics T_m, S_m.

3-5. Within the Boussinesq approximation and for negligible diffusion in (3.26), show that for an ocean at rest, density can only be a function of depth: $\rho = \rho(z)$. (*Hint*: The situation at rest is characterized by the absence of movement and temporal variations.)

3-6. Neglecting atmospheric pressure, calculate the pressure $p_0(z) = -\rho_0 g z$ at 500 m depth in the ocean. Compare it with the dynamic pressure of an ocean at rest of density $\rho = \rho_0 - \rho' e^{z/h}$, where ρ' = 5 kg/m^3 and h = 30 m. What do you conclude? Do you think measurements of absolute pressure could be useful in determining the depth of observation?

3-7. In a dry atmosphere where the potential temperature is constant over the vertical, the density $\rho(z)$ can be expressed in terms of the actual temperature $T(z)$ as

$$\rho(z) \;=\; \rho_0 \left(\frac{T(z)}{\theta}\right)^{C_v/R} \tag{3.39}$$

according to (3.13). This allows the equation of state (3.7) to be expressed in terms of only pressure $p(z)$ and temperature. By taking the vertical derivative of this expression and using the hydrostatic balance ($dp/dz = -\rho g$), show that the vertical temperature gradient dT/dz is constant. Of what sign is this constant?

Numerical Exercises

3-1. Compare values of density obtained with the full equation of state for seawater found in MATLAB™ file `iew80.m` with values obtained from the linearized version (3.6), for various trial values of T and S. Then compare density differences between two different water masses, calculated again with both state equations. Finally, using numerical derivatives of the full equation of state with the help of MATLAB™ file `iew80.m`, can you provide a numerical estimate for the expansion coefficients α and β introduced in (3.6) for a Mediterranean water mass of T_0 = 12.8°C, S_0 = 38.4?

3-2. Generalize the finite-volume method to a two-dimensional system. In particular, what kind of fluxes do you have to define and how do you interpret them? Is local and global conservation still ensured?

3-3. Derive a conservative form of the momentum equations without friction in spherical coordinates and design a finite-volume discretization. (*Hint*: Use volume conservation expressed in spherical coordinates and volume integrals in spherical coordinates according to $\int_{\mathcal{V}} u \, d\mathcal{V} = \int_r \int_\lambda \int_\varphi u \, r^2 \cos\varphi \, d\varphi \, d\lambda \, dr$.)

3-4. Using the finite-volume approach of the one-dimensional temperature evolution assuming that only advection is present, with a flow directed towards increasing x ($u > 0$), discretize the average fluxes. What kind of hypothesis do you need to make to obtain an algorithm allowing you to calculate $\bar{T}_i^{n+1}$ knowing the values of $\bar{T}$ at the preceding time-step? Does your approximation remain valid when $u < 0$?

Joseph Valentin Boussinesq
1842 – 1929

Perhaps not as well known as he deserves, Joseph Boussinesq was a French physicist who made significant contributions to the theory of hydrodynamics, vibration, light and heat. One possible reason for this relative obscurity is the ponderous style of his writings. Among his subjects of study was hydraulics, which led to his research on turbulent flow. In 1896, the work of Osborne Reynolds (see biography at the end of the following chapter) was barely a year old when it was picked up by Boussinesq, who applied the partitioning between average and fluctuating quantities to observations of pipe and river flows. This led him to identify correctly that the cause of turbulence in those instances is friction against boundaries. This paved the way for Ludwig Prandtl's theory of boundary layers (see biography at end of Chapter 8).

It can almost be claimed that the word *turbulence* itself is owed in large part to Boussinesq. Indeed, while Osborne Reynolds spoke of "sinuous motion", Boussinesq used the more expressive phrase "écoulement tourbillonnant et tumultueux", which was reduced by one of his followers to "régime turbulent", hence turbulence. (*Photo from Ambassade de France au Canada*)

Vilhelm Frimann Koren Bjerknes
1862 – 1951

Early in his career, Bjerknes became interested in applying the then-recent work of Lord Kelvin and Hermann von Helmholtz on energy and vorticity dynamics to motions in the atmosphere and ocean. He argued that the dynamics of air and water flows on geophysical scales could be framed as a problem of physics and that, given a particular state of the atmosphere, one should be able to compute its future states. In other words, weather forecasting is reducible to seeking the solution of a mathematical problem. This statement, self-evident today, was quite revolutionary at the time (1904).

When in 1917, he was offered a professorship at the University of Bergen in Norway, Bjerknes founded the Bergen Geophysical Institute and began systematic efforts at developing a self-contained mathematical model for the evolution of weather based on measurable quantities. Faced by the complexity of these equations, he gradually shifted his efforts toward more qualitative aspects of weather description, and out of this work came the now familiar concepts of air masses, cyclones and fronts.

Throughout his work, Bjerknes projected enthusiasm for his ideas and was able to attract and stimulate young scientists to follow in his footsteps, including his son Jacob Bjerknes. (*Photo courtesy of the Bergen Geophysical Institute*)

Chapter 4

Equations Governing Geophysical Flows

(October 18, 2006) **SUMMARY**: This chapter continues the development of the equations that form the basis of dynamical meteorology and physical oceanography. Averaging is performed over turbulent fluctuations and further simplifications are justified based on a scale analysis. In the process, some important dimensionless numbers are introduced. The need for an appropriate set of initial and boundary conditions is also explored from mathematical, physical and numerical points of view.

4.1 Reynolds-averaged equations

Geophysical flows are typically in a state of turbulence, and most often we are only interested in the statistically averaged flow, leaving aside all turbulent fluctuations. To this effect and following Reynolds (1894), we decompose each variable into a mean, denoted with a set of brackets, and a fluctuation, denoted by a prime:

$$u \;=\; \langle u \rangle \;+\; u', \tag{4.1}$$

such that $\langle u' \rangle = 0$ by definition.

There are several ways to define the averaging process, some more rigorous than others, but we shall not be concerned here with those issues, prefering to think of the mean as a temporal average over rapid turbulent fluctuations, on a time interval long enough to obtain a statistically significant mean, yet short enough to retain the slower evolution of the flow under consideration. Our hypothesis is that such an intermediate time interval exists.

Quadratic expressions such as the product uv of two velocity components have the following property:

$$\begin{aligned}\langle uv\rangle &= \langle\langle u\rangle\langle v\rangle\rangle + \langle\langle u\rangle \cancelto{=0}{v'}\rangle + \langle\langle v\rangle \cancelto{=0}{u'}\rangle + \langle u'v'\rangle \\ &= \langle u\rangle\langle v\rangle + \langle u'v'\rangle \end{aligned} \tag{4.2}$$

and similarly for $\langle uu\rangle$, $\langle wu\rangle$, $\langle u\rho\rangle$ *etc.* We recognize here that the average of a product is not equal to the product of the averages. This is a double-edged sword: On one hand, it generates mathematical complications but, on the other hand, it also creates interesting situations.

Our objective is to establish equations governing the mean quantities, $\langle u\rangle$, $\langle v\rangle$, $\langle w\rangle$, $\langle p\rangle$ and $\langle\rho\rangle$. Starting with the average of the $x-$momentum equation (3.21), we have:

$$\frac{\partial\langle u\rangle}{\partial t} + \frac{\partial\langle uu\rangle}{\partial x} + \frac{\partial\langle vu\rangle}{\partial y} + \frac{\partial\langle wu\rangle}{\partial z} + f_*\langle w\rangle - f\langle v\rangle = -\frac{1}{\rho_0}\frac{\partial\langle p\rangle}{\partial x} + \nu\nabla^2\langle u\rangle \tag{4.3}$$

which becomes

$$\begin{aligned}\frac{\partial\langle u\rangle}{\partial t} + \frac{\partial(\langle u\rangle\langle u\rangle)}{\partial x} + \frac{\partial(\langle u\rangle\langle v\rangle)}{\partial y} + \frac{\partial(\langle u\rangle\langle w\rangle)}{\partial z} + f_*\langle w\rangle - f\langle v\rangle = \\ -\frac{1}{\rho_0}\frac{\partial\langle p\rangle}{\partial x} + \nu\nabla^2\langle u\rangle - \frac{\partial\langle u'u'\rangle}{\partial x} - \frac{\partial\langle u'v'\rangle}{\partial y} - \frac{\partial\langle u'w'\rangle}{\partial z}\,.\end{aligned} \tag{4.4}$$

We note that this last equation for the mean field looks identical to the original equation, except for the presence of three new terms at the end of the right-hand side. These terms represent the effects of the turbulent fluctuations on the mean flow. Combining these terms with corresponding frictional terms

$$\frac{\partial}{\partial x}\left(\nu\frac{\partial\langle u\rangle}{\partial x} - \langle u'u'\rangle\right)\ ,\ \frac{\partial}{\partial y}\left(\nu\frac{\partial\langle u\rangle}{\partial y} - \langle u'v'\rangle\right)\ ,\ \frac{\partial}{\partial z}\left(\nu\frac{\partial\langle u\rangle}{\partial z} - \langle u'w'\rangle\right)$$

indicates that the averages of velocity fluctuations add to the viscous stresses (for example, $-\langle u'w'\rangle$ adds to $\nu\partial\langle u\rangle/\partial z$) and can therefore be considered as frictional stresses caused by turbulence. To give credit to Osborne Reynolds who first decomposed the flow into mean and fluctuating components, the expressions $-\langle u'u'\rangle$, $-\langle u'v'\rangle$ and $-\langle u'w'\rangle$ are called *Reynolds stresses*. Since they do not have the same form as the viscous stresses ($\nu\partial\langle u\rangle/\partial x$ *etc.*), it can be said that the mean turbulent flow behaves as a fluid governed by a frictional law other than that of viscosity. In other words, turbulent flow behaves as a non-Newtonian fluid.

Similar averages of the y- and z-momentum equations (3.22)–(3.24) over the turbulent fluctuations yield

$$\begin{aligned}\frac{\partial\langle v\rangle}{\partial t} + \frac{\partial(\langle u\rangle\langle v\rangle)}{\partial x} + \frac{\partial(\langle v\rangle\langle v\rangle)}{\partial y} + \frac{\partial(\langle v\rangle\langle w\rangle)}{\partial z} + f\langle u\rangle - \frac{1}{\rho_0}\frac{\partial\langle p\rangle}{\partial y} = \\ \frac{\partial}{\partial x}\left(\nu\frac{\partial\langle v\rangle}{\partial x} - \langle u'v'\rangle\right) + \frac{\partial}{\partial y}\left(\nu\frac{\partial\langle v\rangle}{\partial y} - \langle v'v'\rangle\right) + \frac{\partial}{\partial z}\left(\nu\frac{\partial\langle v\rangle}{\partial z} - \langle v'w'\rangle\right)\end{aligned} \tag{4.5}$$

$$\frac{\partial \langle w\rangle}{\partial t} + \frac{\partial(\langle u\rangle \langle w\rangle)}{\partial x} + \frac{\partial(\langle v\rangle \langle w\rangle)}{\partial y} + \frac{\partial(\langle w\rangle \langle w\rangle)}{\partial z} - f_* \langle u\rangle - \frac{1}{\rho_0}\frac{\partial \langle p\rangle}{\partial z} = -g\langle \rho\rangle$$
$$\frac{\partial}{\partial x}\left(\nu\frac{\partial \langle w\rangle}{\partial x} - \langle u'w'\rangle\right) + \frac{\partial}{\partial y}\left(\nu\frac{\partial \langle w\rangle}{\partial y} - \langle v'w'\rangle\right) + \frac{\partial}{\partial z}\left(\nu\frac{\partial \langle w\rangle}{\partial z} - \langle w'w'\rangle\right). \quad (4.6)$$

4.2 Eddy coefficients

Computer models of geophysical fluid systems are limited in their spatial resolution. They are therefore incapable of resolving all but the largest turbulent fluctuations, and all motions of lengths shorter than the mesh size. In one way or another, we must state something about these unresolved turbulent and sub-grid scale motions in order to incorporate their aggregate effect on the larger, resolved flow. This process is called *sub-grid scale parameterization*. Here, we present the simplest of all schemes. More sophisticated parameterizations will follow in later sections of the book, particularly Chapter 14.

The primary effect of fluid turbulence and of motions at sub-grid scales (small eddies and billows) is dissipation. It is therefore tempting to represent both the Reynolds stresses and the effect of unresolved motions as some form of super viscosity. This is done summarily by replacing the molecular viscosity ν of the fluid by a much larger *eddy viscosity* to be defined in terms of turbulence and grid properties. This rather crude approach was first proposed by Boussinesq.

The parameterization, however, recognizes one essential property: the anisotropy of the flow field and of its modeling grid. Horizontal and vertical directions are treated differently by assigning two distinct eddy viscosities, $\mathcal{A}$ in the horizontal and ν_E in the vertical. Because turbulent motions and mesh size cover longer distances in the horizontal than in the vertical, $\mathcal{A}$ covers a much larger span of unresolved motions and needs to be significantly larger than ν_E. Furthermore, as they ought to depend in some elementary way on flow properties and grid dimensions, each of which may vary from place to place, eddy viscosities should be expected to exhibit some spatial variations. Returning to the basic manner by which the momentum budget was established, with stress differentials among forces on the right-hand sides, we are led to retain these eddy coefficients inside the first derivatives, as follows:

$$\frac{\partial u}{\partial t} + u\frac{\partial u}{\partial x} + v\frac{\partial u}{\partial y} + w\frac{\partial u}{\partial z} + f_* w - fv =$$
$$-\frac{1}{\rho_0}\frac{\partial p}{\partial x} + \frac{\partial}{\partial x}\left(\mathcal{A}\frac{\partial u}{\partial x}\right) + \frac{\partial}{\partial y}\left(\mathcal{A}\frac{\partial u}{\partial y}\right) + \frac{\partial}{\partial z}\left(\nu_E\frac{\partial u}{\partial z}\right), \quad (4.7a)$$

$$\frac{\partial v}{\partial t} + u\frac{\partial v}{\partial x} + v\frac{\partial v}{\partial y} + w\frac{\partial v}{\partial z} + fu =$$
$$-\frac{1}{\rho_0}\frac{\partial p}{\partial y} + \frac{\partial}{\partial x}\left(\mathcal{A}\frac{\partial v}{\partial x}\right) + \frac{\partial}{\partial y}\left(\mathcal{A}\frac{\partial v}{\partial y}\right) + \frac{\partial}{\partial z}\left(\nu_E\frac{\partial v}{\partial z}\right), \quad (4.7b)$$

$$\frac{\partial w}{\partial t} + u\frac{\partial w}{\partial x} + v\frac{\partial w}{\partial y} + w\frac{\partial w}{\partial z} - f_* u =$$
$$-\frac{1}{\rho_0}\frac{\partial p}{\partial z} - -\frac{g\rho}{\rho_0} + \frac{\partial}{\partial x}\left(\mathcal{A}\frac{\partial w}{\partial x}\right) + \frac{\partial}{\partial y}\left(\mathcal{A}\frac{\partial w}{\partial y}\right) + \frac{\partial}{\partial z}\left(\nu_E\frac{\partial w}{\partial z}\right), \qquad (4.7c)$$

Since we will work exclusively with averaged equations in the rest of the book (unless otherwise specified), there is no longer any need to denote averaged quantities with brackets. Consequently, $\langle u \rangle$ has been replaced by u and similarly for all other variables.

In the energy (density) equation, heat and salt molecular diffusion needs likewise to be superseded by the dispersing effect of unresolved turbulent motions and sub-grid scale processes. Using the same horizontal eddy viscosity $\mathcal{A}$ for energy as for momentum is generally adequate, because the larger turbulent motions and subgrid processes act to disperse heat and salt as effectively as momentum. In the vertical, however, the practice is usually to distinguish dispersion of energy from that of momentum by introducing a vertical *eddy diffusivity* κ_E that differs from the vertical eddy viscosity ν_E. The energy (density) equation then becomes:

$$\frac{\partial \rho}{\partial t} + u\frac{\partial \rho}{\partial x} + v\frac{\partial \rho}{\partial y} + w\frac{\partial \rho}{\partial z} =$$
$$\frac{\partial}{\partial x}\left(\mathcal{A}\frac{\partial \rho}{\partial x}\right) + \frac{\partial}{\partial y}\left(\mathcal{A}\frac{\partial \rho}{\partial y}\right) + \frac{\partial}{\partial z}\left(\kappa_E\frac{\partial \rho}{\partial z}\right), \qquad (4.8)$$

The linear continuity equation is not subjected to any such adaptation and remains unchanged:

$$\frac{\partial u}{\partial x} + \frac{\partial v}{\partial y} + \frac{\partial w}{\partial z} = 0 \qquad (4.9)$$

For more details on eddy viscosity and diffusivity and some schemes to make those depend on flow properties, the reader is referred to textbooks on turbulence, such as Tennekes and Lumley (1972) or Pope (2000). A widely used method to incorporate sub-grid scale processes in the horizontal eddy viscosity is that proposed by Smagorinsky (1964):

$$\mathcal{A} = \Delta x\, \Delta y \sqrt{\left(\frac{\partial u}{\partial x}\right)^2 + \left(\frac{\partial v}{\partial y}\right)^2 + \frac{1}{2}\left(\frac{\partial u}{\partial y} + \frac{\partial v}{\partial x}\right)^2}, \qquad (4.10)$$

in which Δx and Δy are the local grid dimensions. Because such sub-grid scale parameterization is meant to represent physical processes, it ought to obey certain symmetry properties, notably invariance with respect to rotation of the coordinate system in the horizontal plane. An appropriate formulation for $\mathcal{A}$ ought therefore to be expressed solely in terms of the rotational invariants of the tensor formed by the velocity derivatives. One should note that the preceding formulation unfortunately does not satisfy this condition. Nonetheless it is often used in numerical models.

Table 4.1 TYPICAL SCALES OF ATMOSPHERIC AND OCEANIC FLOWS

Variable	Scale	Unit	Atmospheric value	Oceanic value
x	L	m	100 km = 10^5 m	10 km = 10^4 m
y	L			
z	H	m	1 km = 10^3 m	100 m = 10^2 m
t	T	s	$\geq \frac{1}{2}$ day $\simeq 4 \times 10^4$ s	≥ 1 day $\simeq 9 \times 10^4$ s
u	U	m/s	10 m/s	0.1 m/s
v	U			
w	W	m/s		
p	P	kg/m·s^2		
ρ	$\Delta\rho$	kg/m^3		

4.3 Scales of motion

Simplifications of the equations established in the preceding section are possible beyond the Boussinesq approximation and averaging over turbulent fluctuations. However, these require a preliminary discussion of orders of magnitude. Accordingly, let us introduce a scale for every variable, as we already did in a limited way in 1.10. By *scale*, we mean a dimensional constant of dimensions identical to that of the variable and having a numerical value representative of the values of that same variable. Table 4.1 provides illustrative scales for the variables of interest in geophysical fluid flow. Obviously, scale values do vary with every application, and the values listed in Table 4.1 are only suggestive. Even so, the conclusions drawn from the use of these particular values stand in the vast majority of cases. If doubt arises in a specific situation, the following scale analysis can always be redone.

In the construction of Table 4.1, we were careful to satisfy the criteria of geophysical fluid dynamics outlined in Sections 1.5 and 1.6,

$$T \gtrsim \frac{1}{\Omega}, \tag{4.11}$$

for the time scale and

$$\frac{U}{L} \lesssim \Omega, \tag{4.12}$$

for the velocity and length scales. It is generally not required to discriminate between the two horizontal directions, and we assign the same length scale L to both coordinates and the same velocity scale U to both velocity components. The same, however, cannot be said of the vertical direction. Geophysical flows are typically confined to domains that are much wider than they are thick, and the *aspect ratio* H/L is small. The atmospheric layer that determines our weather is only about 10 km thick, yet cyclones and anticyclones spread over thousands of kilometers. Similarly, ocean currents are generally confined to the upper hundred meters of the water column but extend over tens of kilometers or more, up to the width of the ocean basin. It follows that for large-scale motions

$$H \ll L, \tag{4.13}$$

and we expect W to be vastly different from U.

The continuity equation in its reduced form (4.9) contains three terms, of respective orders of magnitude:

$$\frac{U}{L}\,,\quad \frac{U}{L}\,,\quad \frac{W}{H}\quad .$$

We ought to examine three cases: W/H is much less than, on the order of, or much greater than U/L. The third case must be ruled out. Indeed, if $W/H \gg U/L$, the equation reduces in first approximation to $\partial w/\partial z$ = 0, which implies that w is constant in the vertical; because of a bottom somewhere, that flow must be supplied by lateral convergence (see later section 4.6.1), and we deduce that the terms $\partial u/\partial x$ and/or $\partial v/\partial y$ may not be both neglected at the same time. In sum, w must be much smaller than initially thought.

In the first case, the leading balance is two-dimensional, $\partial u/\partial x + \partial v/\partial y = 0$, which implies that convergence in one horizontal direction must be compensated by divergence in the other horizontal direction. This is very possible. The intermediate case, with W/H on the order of U/L, implies a three-way balance, which is also acceptable. In summary, the vertical-velocity scale must be constrained by

$$W \lesssim \frac{H}{L}\,U \tag{4.14}$$

and, by virtue of (4.13),

$$W \ll U. \tag{4.15}$$

In other words, large-scale geophysical flows are shallow ($H \ll L$) and nearly two-dimensional ($W \ll U$).

Let us now consider the x–momentum equation in its Boussinesq and turbulence-averaged form (4.7a). Its various terms scale sequentially as

$$\frac{U}{T}\,,\quad \frac{U^2}{L}\,,\quad \frac{U^2}{L}\,,\quad \frac{WU}{H}\,,\quad \Omega W\,,\quad \Omega U\,,\quad \frac{P}{\rho_0 L}\,,\quad \frac{\mathcal{A}U}{L^2}\,,\quad \frac{\mathcal{A}U}{L^2}\,,\quad \frac{\nu_E U}{H^2}\,.$$

The previous remark immediately shows that the fifth term (ΩW) is always much smaller than the sixth (ΩU) and can be safely neglected[1].

Because of the fundamental importance of the rotation terms in geophysical fluid dynamics, we can anticipate that the pressure-gradient term will scale as the Coriolis terms, *i.e.*,

$$\frac{P}{\rho_0 L} = \Omega U \quad \rightarrow \quad P = \rho_0 \Omega L U. \tag{4.16}$$

[1]Note, however, that near the Equator, where f goes to zero while f_* reaches its maximum, the simplification may be invalidated. If this is the case, a re-examination of the scales is warranted. The fifth term is likely to remain much smaller than some other terms, such as the pressure gradient, but there may be instances when the f_* term must be retained. Because such a situation is exceptional, we will dispense with the f_* term here.

For typical geophysical flows, this dynamic pressure is much smaller than the basic hydrostatic pressure due to the weight of the fluid.

Although horizontal and vertical dissipation due to turbulent and sub-grid scale processes is retained in the equation (its last three terms), it cannot dominate the Coriolis force in geophysical flows, which ought to remain among the dominant terms. This implies

$$\frac{\mathcal{A}U}{L^2} \text{ and } \frac{\nu_E U}{H^2} \lesssim \Omega U. \tag{4.17}$$

Similar considerations apply to the y–momentum equation (4.7b). But, the vertical momentum equation (4.7c) may be subjected to additional simplifications. Its various terms scale sequentially as

$$\frac{W}{T}\,,\quad \frac{UW}{L}\,,\quad \frac{UW}{L}\,,\quad \frac{W^2}{H}\,,\quad \Omega U\,,\quad \frac{P}{\rho_0 H}\,,\quad \frac{g\Delta\rho}{\rho_0}\,,\quad \frac{\mathcal{A}W}{L^2}\,,\quad \frac{\mathcal{A}W}{L^2}\,,\quad \frac{\nu_E W}{H^2}\,.$$

The first term (W/T) cannot exceed ΩW, which is itself much less than ΩU, by virtue of (4.11) and (4.15). The next three terms are also much smaller than ΩU, this time because of (4.12), (4.14) and (4.15). Thus, the first four terms may all be neglected compared to the fifth. But, this fifth term is itself quite small. Its ratio to the first term on the right-hand side is

$$\frac{\rho_0 \Omega H U}{P} \sim \frac{H}{L}\,,$$

which, according to (4.16) and (4.13) is much less than one.

Finally, the last three terms are small. When W is substituted for U in (4.17), we have

$$\frac{\mathcal{A}W}{L^2} \text{ and } \frac{\nu_E W}{H^2} \lesssim \Omega W \ll \Omega U. \tag{4.18}$$

Thus, the last three terms on the right-hand side of the equation are much less than the fifth term on the left, which was already found to be very small. In summary, only two terms remain, and the vertical-momentum balance reduces to the simple *hydrostatic balance*

$$0 = -\frac{1}{\rho_0}\frac{\partial p}{\partial z} - \frac{g\rho}{\rho_0}\,. \tag{4.19}$$

In the absence of stratification (density perturbation ρ nil), the next term in line that should be considered as a possible balance to the pressure gradient $(1/\rho_0)(\partial p/\partial z)$ is $f_* u$. However, under such balance, the vertical variation of the pressure p would be given by the vertical integration of $\rho_0 f_* u$ and its scale be $\rho_0 \Omega H U$. Since this is much less than the already established pressure scale (4.16), it is negligible, and we conclude that the vertical variation of p is very weak. In other words, p is nearly z–independent in the absence of stratification:

$$0 = -\frac{1}{\rho_0}\frac{\partial p}{\partial z}\,. \tag{4.20}$$

So, the hydrostatic balance (4.19) continues to hold in the limit $\rho \to 0$.

Since the pressure p is already a small perturbation to a much larger pressure, itself in hydrostatic balance, we conclude that geophysical flows tend to be fully hydrostatic even in the presence of substantial motions[2]. Looking back, we note that the main reason behind this reduction is the strong geometric disparity of geophysical flows ($H \ll L$).

In rare instances when this disparity between horizontal and vertical scales does not exist, such as in convection plumes and short internal waves, the hydrostatic approximation ceases to hold and the vertical-momentum balance includes a three-way balance between vertical acceleration, pressure gradient and buoyancy.

4.4 Recapitulation of equations governing geophysical flows

The Boussinesq approximation performed in the previous chapter and the preceding developments have greatly simplified the equations. We recapitulate them here.

$$x-\text{momentum:} \quad \frac{\partial u}{\partial t} + u\,\frac{\partial u}{\partial x} + v\,\frac{\partial u}{\partial y} + w\,\frac{\partial u}{\partial z} - fv = -\frac{1}{\rho_0}\,\frac{\partial p}{\partial x} + \frac{\partial}{\partial x}\left(\mathcal{A}\frac{\partial u}{\partial x}\right) + \frac{\partial}{\partial y}\left(\mathcal{A}\frac{\partial u}{\partial y}\right) + \frac{\partial}{\partial z}\left(\nu_E\frac{\partial u}{\partial z}\right) \tag{4.21a}$$

$$y-\text{momentum:} \quad \frac{\partial v}{\partial t} + u\,\frac{\partial v}{\partial x} + v\,\frac{\partial v}{\partial y} + w\,\frac{\partial v}{\partial z} + fu = -\frac{1}{\rho_0}\,\frac{\partial p}{\partial y} + \frac{\partial}{\partial x}\left(\mathcal{A}\frac{\partial v}{\partial x}\right) + \frac{\partial}{\partial y}\left(\mathcal{A}\frac{\partial v}{\partial y}\right) + \frac{\partial}{\partial z}\left(\nu_E\frac{\partial v}{\partial z}\right) \tag{4.21b}$$

$$z-\text{momentum:} \quad 0 = -\frac{\partial p}{\partial z} - \rho g \tag{4.21c}$$

$$\text{continuity:} \quad \frac{\partial u}{\partial x} + \frac{\partial v}{\partial y} + \frac{\partial w}{\partial z} = 0 \tag{4.21d}$$

$$\text{energy:} \quad \frac{\partial \rho}{\partial t} + u\,\frac{\partial \rho}{\partial x} + v\,\frac{\partial \rho}{\partial y} + w\,\frac{\partial \rho}{\partial z} = \frac{\partial}{\partial x}\left(\mathcal{A}\frac{\partial \rho}{\partial x}\right) + \frac{\partial}{\partial y}\left(\mathcal{A}\frac{\partial \rho}{\partial y}\right) + \frac{\partial}{\partial z}\left(\kappa_E\frac{\partial \rho}{\partial z}\right), \tag{4.21e}$$

where the reference density ρ_0 and the gravitational acceleration g are constant coefficients, the Coriolis parameter $f = 2\Omega\sin\varphi$ is dependent on latitude or taken as a constant, and the eddy viscosity and diffusivity coefficients $\mathcal{A}$, ν_E and κ_E may taken as constants or functions of flow variables and grid parameters. These five equations for the five variables u, v, w, p and ρ form a closed set of equations, the cornerstone of geophysical fluid dynamics, sometimes called *primitive equations*.

Using the continuity equation (4.21d), the horizontal-momentum and density equations

[2] According to Nebeker (1995, page 51), the scientist deserving credit for the hydrostatic balance in geophysical flows is Alexis Clairaut (1713–1765).

can be written in *conservative form*:

$$\frac{\partial u}{\partial t} + \frac{\partial (uu)}{\partial x} + \frac{\partial (vu)}{\partial y} + \frac{\partial (wu)}{\partial z} - fv =$$

$$-\frac{1}{\rho_0} \frac{\partial p}{\partial x} + \frac{\partial}{\partial x}\left(\mathcal{A}\frac{\partial u}{\partial x}\right) + \frac{\partial}{\partial y}\left(\mathcal{A}\frac{\partial u}{\partial y}\right) + \frac{\partial}{\partial z}\left(\nu_E \frac{\partial u}{\partial z}\right) \tag{4.22a}$$

$$\frac{\partial v}{\partial t} + \frac{\partial (uv)}{\partial x} + \frac{\partial (vv)}{\partial y} + \frac{\partial (wv)}{\partial z} + fu =$$

$$-\frac{1}{\rho_0} \frac{\partial p}{\partial y} + \frac{\partial}{\partial x}\left(\mathcal{A}\frac{\partial v}{\partial x}\right) + \frac{\partial}{\partial y}\left(\mathcal{A}\frac{\partial v}{\partial y}\right) + \frac{\partial}{\partial z}\left(\nu_E \frac{\partial v}{\partial z}\right) \tag{4.22b}$$

$$\frac{\partial \rho}{\partial t} + \frac{\partial (u\rho)}{\partial x} + \frac{\partial (v\rho)}{\partial y} + \frac{\partial (w\rho)}{\partial z} =$$

$$\frac{\partial}{\partial x}\left(\mathcal{A}\frac{\partial \rho}{\partial x}\right) + \frac{\partial}{\partial y}\left(\mathcal{A}\frac{\partial \rho}{\partial y}\right) + \frac{\partial}{\partial z}\left(\kappa_E \frac{\partial \rho}{\partial z}\right) , \tag{4.22c}$$

These will be found useful in numerical discretization.

4.5 Important dimensionless numbers

The scaling analysis of Section 4.3 was developed to justify the neglect of some small terms. But this does not necessarily imply that the remaining terms are equally large. We now wish to estimate the relative sizes of those terms that have been retained.

The terms of the horizontal momentum equations in their last form (4.21a) and (4.21b) scale sequentially as

$$\frac{U}{T}, \quad \frac{U^2}{L}, \quad \frac{U^2}{L}, \quad \frac{WU}{H}, \quad \Omega U, \quad \frac{P}{\rho_0 L}, \quad \frac{\mathcal{A}U}{L^2}, \quad \frac{\nu_E U}{H^2}.$$

By definition, geophysical fluid dynamics treats those motions in which rotation is an important factor. Thus, the term ΩU is central to the preceding sequence. A division by ΩU, to measure the importance of all other terms relative to the Coriolis term, yields the following sequence of dimensionless ratios:

$$\frac{1}{\Omega T}, \quad \frac{U}{\Omega L}, \quad \frac{U}{\Omega L}, \quad \frac{WL}{UH} \cdot \frac{U}{\Omega L}, \quad 1, \quad \frac{P}{\rho_0 \Omega L U}, \quad \frac{\mathcal{A}}{\Omega L^2}, \quad \frac{\nu_E}{\Omega H^2}.$$

The first ratio,

$$Ro_T = \frac{1}{\Omega T}, \tag{4.23}$$

is called the *temporal Rossby number*. It compares the local time rate of change of the velocity to the Coriolis force and is on the order of unity or less, as has been repeatedly stated [see (4.11)]. The next number,

$$Ro = \frac{U}{\Omega L} , \tag{4.24}$$

which compares advection to Coriolis force, is called the *Rossby number*[3] and is fundamental in geophysical fluid dynamics. Like its temporal analogue Ro_T, it is at most on the order of unity by virtue of (4.12). As a general rule, the characteristics of geophysical flows vary greatly with the values of the Rossby numbers.

The next number is the product of the Rossby number by WL/UH, which is on the order of one or less by virtue of (4.14). It will be shown in Section 11.5 that the ratio WL/UH is generally on the order of the Rossby number itself. The next ratio, $P/\rho_0 \Omega LU$, is on the order of unity by virtue of (4.16).

The last two ratios measure the relative importance of horizontal and vertical friction. Of the two, only the latter bears a name:

$$Ek = \frac{\nu_E}{\Omega H^2} , \tag{4.25}$$

is called the *Ekman number*. For geophysical flows, this number is small. For example, with an eddy viscosity ν_E as large as 10^{-2} m^2/s, Ω = 7.3 $\times$ 10^{-5} s^{-1} and H = 100 m, Ek = 1.4 $\times$ 10^{-2}. The Ekman number is even smaller in laboratory experiments where the viscosity reverts to its molecular value and the height scale H is much more modest. [Typical experimental values are Ω = 4 s^{-1}, H = 20 cm, and ν(water) = 10^{-6} m$^2/$s, yielding Ek = 6 $\times$ 10^{-6}.] Although the Ekman number is small, indicating that the dissipative terms in the momentum equation may be negligible, these need to be retained. The reason will become clear in Chapter 8, when it is shown that vertical friction creates a very important boundary layer.

In nonrotating fluid dynamics, it is customary to compare inertial and frictional forces by defining the *Reynolds number*, Re. In the preceding scaling, inertial and frictional forces were not compared to each other but each was instead compared to the Coriolis force, yielding the Rossby and Ekman numbers, respectively. There exists a simple relationship between the three numbers and the aspect ratio H/L:

$$Re = \frac{UL}{\nu_E} = \frac{U}{\Omega L} \cdot \frac{\Omega H^2}{\nu_E} \cdot \frac{L^2}{H^2} = \frac{Ro}{Ek} \left(\frac{L}{H}\right)^2 . \tag{4.26}$$

Since the Rossby number is on the order of unity or slightly less, but the Ekman number and the aspect ratio H/L are both much smaller than unity, the Reynolds number of geophysical flows is extremely large, even after the molecular viscosity has been replaced by a much larger eddy viscosity.

With (4.16), the two terms in the hydrostatic equation (4.21c) scale respectively as

$$\frac{P}{H} , \quad g\Delta\rho$$

and the ratio of the latter over the former is

$$\frac{gH\Delta\rho}{P} = \frac{gH\Delta\rho}{\rho_0 \Omega LU} = \frac{U}{\Omega L} \cdot \frac{gH\Delta\rho}{\rho_0 U^2} = Ro \cdot \frac{gH\Delta\rho}{\rho_0 U^2} .$$

[3] See biographic note at the end of this chapter.

This leads to the additional dimensionless ratio

$$Ri = \frac{gH\Delta\rho}{\rho_0 U^2}, \tag{4.27}$$

which we already encountered in Section 1.6. It is called the *Richardson number*[4]. For geophysical flows, this number may be much less than, on the order of, or much greater than unity, depending on whether stratification effects are negligible, important or dominant.

4.6 Boundary conditions

The equations of section 4.4 governing geophysical flows form a closed set of equations, with the number of unknown functions being equal to the number of available independent equations. However, the solution of those equations is uniquely defined only when additional specifications are provided. Those auxiliary conditions concern information on the initial state and geographical boundaries of the system (Figure 4-1).

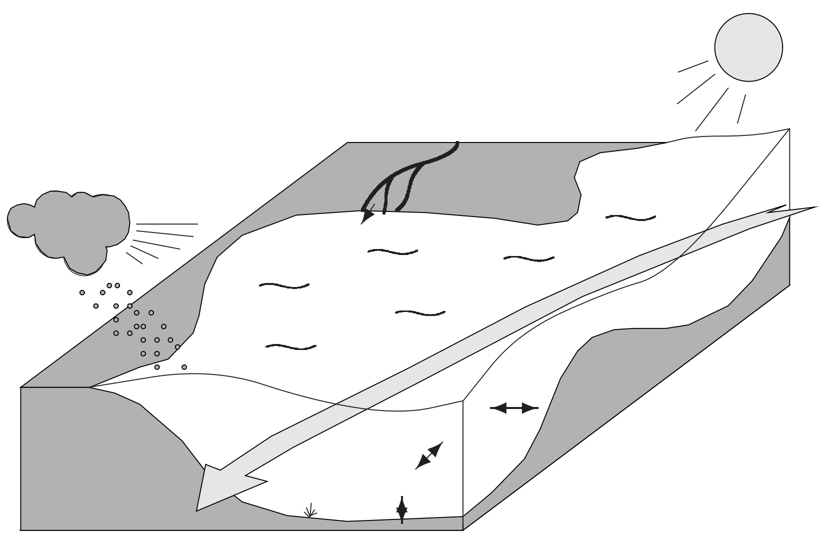

Figure 4-1 Schematic representation of possible exchanges between the system under investigation and the surrounding environment. Boundary conditions must specify the influence of this outside world on the evolution within the domain. Exchanges may take place at the air-sea interface, in bottom layers, along coasts and/or at any other boundary of the domain.

Because the governing equations (4.21) contain first-order time derivatives of u, v and ρ, *initial conditions* are required, one for each of these three-dimensional fields. Because the respective equations, (4.21a), (4.21b) and (4.21e), provide *tendencies* for these variables in order to calculate future *values*, it is necessary to specify from where to start. The variables

[4]See biography at the end of Chapter 14

for which such initial conditions are required are called *state variables*. The remaining variables w and p, which have no time derivative in the equations, are called *diagnostic* variables, *i.e.*, they are variables that can be determined at any moment from the knowledge of the other variables at the same moment. Note that, if a non-hydrostatic formalism is retained, the time derivative of the vertical velocity arises [see (4.7c)], and w passes from being a diagnostic variable to a state variable, and an initial condition becomes necessary for it, too.

The determination of pressure needs special care depending on whether the hydrostatic approximation is applied and on the manner in which sea surface height is modeled. Since the pressure gradient is a major force in geophysical flows, the handling of pressure is a central question in the development of GFD models. This point deserves a detailed analysis, which we postpone to section 7.6.

The conditions to impose at *spatial* boundaries of the domain are more difficult to ascertain than initial conditions. The mathematical theory of partial differential equations teaches us that the number and type of required boundary conditions depend on the nature of the partial differential equations. Standard classification (*e.g.*, Durran 1999) of second-order partial differential equations makes the distinction between *hyperbolic*, *parabolic* and *elliptic* equations. This classification is based on the concept of *characteristics*, which are lines along which information propagates. The geometry of these lines constrains where information is propagated from the boundary into the domain or from the domain outward across the boundary and therefore prescribes along which portion of the domain's boundary information needs to be specified in order to define uniquely the solution within the domain.

A major problem with the GFD governing equations is that their classification cannot be established once and for all. Firstly, the coupled set of equations (4.21) is more complicated than a single second-order equation for which standard classification can be performed and, secondly, the equation type can change with the solution itself. Indeed, propagation of information is mostly accomplished by a combination of flow advection and wave propagation, and these may at various times leave and enter through the same boundary segment. Thus, the number and type of required boundary conditions is susceptible to change over time with the solution of the problem, which is obviously not known *a priori*. It is far from a trivial task to establish the mathematically correct set of boundary conditions, and the reader is referred to specialized literature for further information (*e.g.*, Blayo and Debreu, 2000; Durran, 1999). The imposition of boundary conditions during analytical studies in the present book will be guided by purely physical arguments, and the well behaved nature of the subsequent solution will serve as *a posteriori* verification.

For the many situations when no analytical solution is available, not only is *a posteriori* verification out of the question, but the problem is further complicated by the fact that numerical discretization solves modified equations with truncation errors, rather than the original equations. The equations may demand fewer or more boundary and initial conditions. If the numerical scheme asks for more conditions than those provided by the original equations, these conditions must be related to the truncation error in such a way that they disappear when the grid size (or time step) vanishes: We demand that all boundary and initial conditions be consistent.

Let us for example revisit the initialization problem of the leapfrog scheme from this point of view. As we have seen (Section 2.9), the leapfrog discretization $\partial u/\partial t = Q \rightarrow \tilde{u}^{n+1} = \tilde{u}^{n-1} + 2\Delta t Q^n$ needs two values, $\tilde{u}^0$ and $\tilde{u}^1$, to start the time-stepping. The original problem, however, indicates that only one initial condition, $\tilde{u}^0$, may be imposed, the value of which is dictated by the physics of the problem. The second condition, $\tilde{u}^1$, must then be such that its influence disappears in the limit $\Delta t \to 0$. This will be the case with the explicit Euler scheme $\tilde{u}^1 = \tilde{u}^0 + \Delta t Q$ [where $Q(t^0, \tilde{u}^0)$ stands for the other terms in the equation at time t^0]. Indeed, $\tilde{u}^1$ tends to the actual initial value $\tilde{u}^0$ and the first leapfrog step yields $\tilde{u}^2 = \tilde{u}^0 + 2\Delta t Q(t^1, \tilde{u}^0 + \mathcal{O}(\Delta t))$ which is consistent with a finite difference over a $2\Delta t$ time step.

Leaving for later sections the complexity of the additional conditions that may be required by virtue of the discretization schemes, the following sections present the boundary conditions that are most commonly encountered in GFD problems. They stem from basic physical requirements.

4.6.1 Kinematic conditions

A most important condition, independent of any physical property or sub-grid scale parameterization, is that air and water flows do not penetrate land[5]. To translate this impermeability requirement into a mathematical boundary condition, we simply express that the velocity must be tangent to the land boundary, that is, the normal vector to the boundary surface and the velocity vector are orthogonal to each other.

Consider the solid bottom of the domain. With this boundary defined as $z - b(x, y) = 0$, the normal vector is given by $[\partial(z-b)/\partial x, \partial(z-b)/\partial y, \partial(z-b)/\partial z] = [-\partial b/\partial x, -\partial b/\partial y, 1]$, the boundary condition is

$$w = u \frac{\partial b}{\partial x} + v \frac{\partial b}{\partial y} \quad \text{at the bottom.} \tag{4.28}$$

We can interpret this condition in terms of a fluid budget at the bottom (Figure 4-2) or alternatively as the condition that the bottom is a material surface of the fluid, not crossed by the flow and immobile. Expressing that the bottom is a material surface indeed demands

$$\frac{d}{dt}(z - b) = 0, \tag{4.29}$$

which is equivalent to (4.28) since $dz/dt = w$ and $\partial b/\partial t = 0$.

At a *free surface*, the situation is similar to the bottom except for the fact that the boundary is moving with the fluid. If we exclude overturning waves, the position of the surface is uniquely defined at every horizontal point by its vertical position η (Figure 4-3), and $z-\eta = 0$ is the equation of the boundary. We then express that it is a material surface[6]:

$$\frac{d}{dt}(z - \eta) = 0 \quad \text{at the free surface} \tag{4.30}$$

and obtain the surface boundary condition

$$w = \frac{\partial \eta}{\partial t} + u \frac{\partial \eta}{\partial x} + v \frac{\partial \eta}{\partial y} \quad \text{at} \quad z = \eta. \tag{4.31}$$

[5] There is no appreciable penetration of land by water and air at geophysical scales.

[6] Exceptions are evaporation and precipitation at the air-sea interface. When important, these may be accommodated in a straightforward manner.

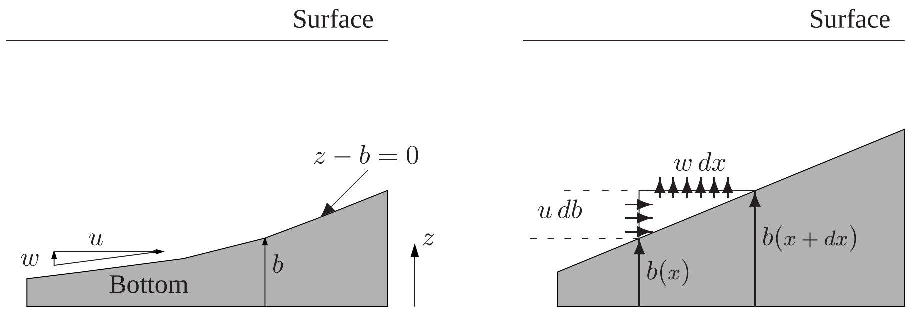

Figure 4-2 Notation and two physical interpretations of the bottom boundary condition illustrated here in a (x, z) plane for a topography independent of y. The impermeability of the bottom imposes that the velocity be tangent to the bottom defined by $z - b = 0$. In terms of the fluid budget, which can be extended to a finite volume approach, expressing that the horizontal inflow matches the vertical outflow requires $u\,(b(x+dx) - b(x)) = w\,dx$, which for $dx \to 0$ leads to (4.28). Note that the velocity ratio w/u is equal to the topographic slope db/dx, which scales like the ratio of vertical to horizontal length scales, *i.e.*, the *aspect ratio*.

Particularly simple cases are those of a flat bottom and of a free surface of which the vertical displacements are neglected (such as small water waves on the surface of the deep sea) — called the *rigid-lid* approximation, which will be scrutinized in Section 7.6. In such cases, the vertical velocity is simply zero at the corresponding boundary.

A difficulty with the free surface boundary arises because the boundary condition is imposed at $z = \eta$, *i.e.*, at a location changing over time, depending on the flow itself. Such a problem is called a *moving boundary problem*, a topic which is a discipline unto itself in Computational Fluid Dynamics (CFD) (*e.g.*, Crank 1987).

In oceanic models, lateral walls are introduced in addition to bottom and top boundaries so that the water depth remains non-zero all the way to the edge (Figure 4-4). This is because watering and dewatering of land that would otherwise occur at the outcrop of the ocean floor is difficult to model with a fixed grid. At a vertical wall, impermeability demands that the normal component of the horizontal velocity be zero.

4.6.2 Dynamic condition

The previous impermeability conditions are purely kinematic, involving only velocity components. Dynamical conditions, implicating forces, are sometimes also necessary, for example when requiring continuity of pressure at the air-sea interface.

Ignoring the effect of surface tension, which is important only for very short water waves (*capillary* waves, with wavelengths no longer than a few centimeters), the pressure $p_{\rm atm}$ exerted by the atmosphere on the sea must equal the pressure $p_{\rm sea}$ exerted by the ocean onto the atmosphere:

$$p_{\rm atm} = p_{\rm sea} \quad \text{at air-sea interface.} \tag{4.32}$$

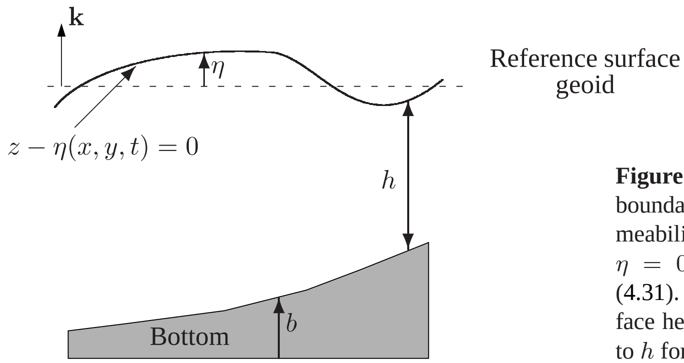

Figure 4-3 Notation for the surface boundary condition. Expressing impermeability of the moving surface $z - \eta = 0$ results in boundary condition (4.31). (The elevation of the sea surface height η is exaggerated compared to h for the purpose of illustration.)

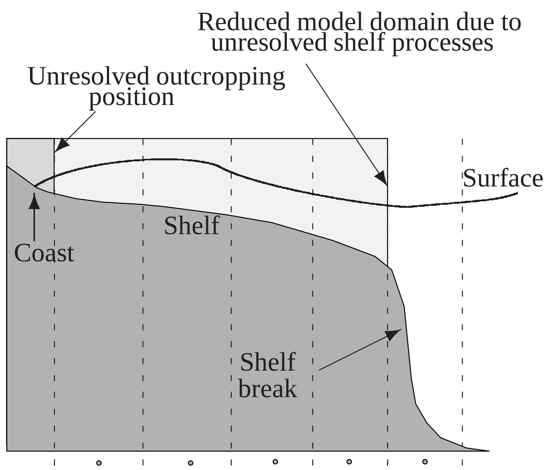

Figure 4-4 Vertical section across an oceanic domain reaching the coast. Besides surface and bottom boundaries, the coast introduces an additional *lateral* boundary. Introducing an artificial vertical wall is necessary because a fixed numerical grid cannot describe well the exact position of the water's edge. Occasionally, a vertical wall is assumed at the shelf break, removing the entire shelf area from the domain, because the reduced physics of the model are incapable of representing some processes on the shelf.

If the sea surface elevation is η and pressure is hydrostatic below, it follows that continuity of pressure at the actual surface $z = \eta$ implies

$$p_{\text{sea}}(z = 0) \;=\; p_{\text{atm at sea level}} + \rho_0 g \eta \tag{4.33}$$

at the more convenient reference sea level $z = 0$.

Another dynamical boundary condition depends on whether the fluid is considered inviscid or viscous. In reality all fluids are subject to internal friction, so that, in principle, a fluid particle next to fixed boundary must adhere to that boundary and its velocity be zero. However, the distance over which the velocity falls to zero near a boundary is usually short because viscosity is weak. This short distance restricts the influence of friction to a narrow band of fluid along the boundary, called a *boundary layer*. If the extent of this boundary layer is negligible compared to the length scale of interest, and generally it is, it is permissible to neglect friction altogether in the momentum equations. In this case, slip between the fluid and the boundary must be allowed, and the only boundary condition to be applied is the impermeability condition.

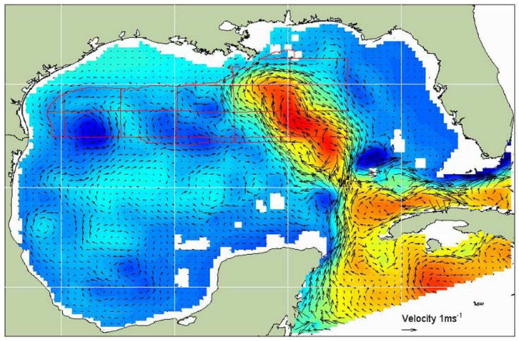

Figure 4-5 Open boundaries are common in regional modeling. Conditions at open boundaries are generally difficult to impose. In particular the nature of the condition depends on whether the flow enters the domain (carrying unknown information from the exterior) or leaves it (exporting known information). (*Courtesy of the HYCOM Consortium on Data-Assimilative Modeling*)

If viscosity is taken into account, however, zero velocity must be imposed at a fixed boundary, whereas along a moving boundary between two fluids, continuity of both velocity and tangential stress is required. From the oceanic point of view this requires

$$\rho_0 \nu_E \left(\frac{\partial u}{\partial z}\right)\bigg|_{\text{at surface}} = \tau^x, \quad \rho_0 \nu_E \left(\frac{\partial v}{\partial z}\right)\bigg|_{\text{at surface}} = \tau^y \tag{4.34}$$

where τ^x and τ^y are the components of the wind stress exerted by the atmosphere onto the sea. These are usually taken as quadratic functions of the wind velocity $\mathbf{u}_{10}$ 10 meters above the sea and parameterized using a drag coefficient:

$$\tau^x = C_d \, \rho_{\text{air}} \, U_{10} u_{10}, \quad \tau^y = C_d \, \rho_{\text{air}} \, U_{10} v_{10}, \tag{4.35}$$

where u_{10} and v_{10} are the x and y components of the wind vector $\mathbf{u}_{10}$, $U_{10} = \sqrt{u_{10}^2 + v_{10}^2}$ is the wind speed, and C_d is a drag coefficient with approximate value of 0.0015 for wind over the sea.

Lastly, an edge of the model may be an *open boundary*, by which we mean that the model domain is terminated at some location that cuts across a broader natural domain. Such a situation arises because computer resources or data availability restrict the attention to a portion of a broader system. Examples are regional meteorological models and coastal ocean models (Figure 4-5). Ideally, the influence of the outside system onto the system of interest should be specified along the open boundary, but this is most often impossible in practice, for the obvious reason that the un-modeled part of the system is not known. Certain conditions, however, can be applied. For example, waves may be allowed to exit but not enter through the open boundary, or flow properties may be specified where the flow enters the domain but not where it leaves the domain. In oceanic tidal models, the sea surface may be imposed as a periodic function of time.

With increased computer power over the last decade, it has become common nowadays to *nest* models into one another, that is, the regionally limited model of interest is embedded in another model of lower spatial resolution but larger size, which itself may be embedded in a yet larger model of yet lower resolution, all the way to a model that has no open boundary (entire ocean basin or globe for the atmosphere). A good example is regional weather forecasting over a particular country: A grid covering this country and a few surrounding areas is nested into a grid that covers the continent, which itself is nested inside a grid that covers the entire globe.

4.6.3 Heat, salt and tracer boundary conditions

For equations similar to those governing the evolution of temperature, salt or density, *i.e.*, including advection and diffusion terms, we have the choice of imposing the value of the variable, its gradient, or a mixture of both. Prescribing the value of the variable (*Dirichlet condition*) is natural in situations where it is known from observations (sea surface temperature from satellite data, for example). Setting the gradient (*Neumann condition*) is done to impose the diffusive flux of the quantity (*e.g.*, heat flux) and is therefore often associated with the prescription of turbulent air-sea exchanges. A mixed condition (*Cauchy condition*, *Robin condition*) is typically used to prescribe a total, advective plus diffusive, flux. For a 1D heat flux, for example, one sets the value of $uT - \kappa_T \partial T/\partial x$ at the boundary. For an insulating boundary this flux is simply zero.

To choose the value of the variable or its gradient at the boundary, either observations are invoked or exchange laws prescribed. The most complex exchange laws are those for the air-sea interface, which involve calculation of fluxes depending on the sea surface water temperature $T_{\rm sea}$ (often called SST), air temperature $T_{\rm air}$, wind speed $\mathbf{u}_{10}$ at 10 meters above the sea, cloudiness, moisture *etc.* Formally,

$$-\,\kappa_T \left.\frac{\partial T}{\partial z}\right|_{z=\eta} = F(T_{\rm sea}, T_{\rm air}, \mathbf{u}_{10}, \text{cloudiness}, \text{moisture}, ...). \tag{4.36}$$

For heat fluxes, imposing the condition at $z = 0$ rather than at the actual position $z = \eta$ of the sea surface introduces an error much below the error in the heat flux estimate itself and is a welcomed simplification.

If the density equation is used as a combination of both salinity and temperature equations by invoking the linearized state equation, $\rho = -\alpha T + \beta S$, and if it can be reasonably assumed that all are dispersed with the turbulent diffusivity, the boundary condition on density can be formulated as a weighted sum of prescribed temperature and salt fluxes:

$$\nu_E \frac{\partial \rho}{\partial z} = -\,\alpha \nu_E \frac{\partial T}{\partial z} + \beta \nu_E \frac{\partial S}{\partial z}\,. \tag{4.37}$$

For any tracer (a quantity advected and dispersed by the flow), a condition similar to those on temperature and salinity can be imposed and, in particular, a zero total flux is common when there is no tracer input at the boundary.

4.7 Numerical implementation of boundary conditions

Once mathematical boundary conditions are specified and values assigned at the boundaries, we can tackle the task of implementing the boundary condition numerically. We illustrate the process again with temperature as the example.

In addition to nodes forming the grid covering the domain being modeled, other nodes are placed exactly at or slightly beyond the boundaries (Figure 4-6). These additional nodes are introduced to facilitate the implementation of the boundary condition. If the condition is to specify the value T_b of the numerical variable $\tilde{T}$, it is most natural to place a node at the boundary (Figure 4-6 right side) so that

$$\tilde{T}_m \;=\; T_b, \tag{4.38}$$

requires no interpolation and forms an exact implementation.

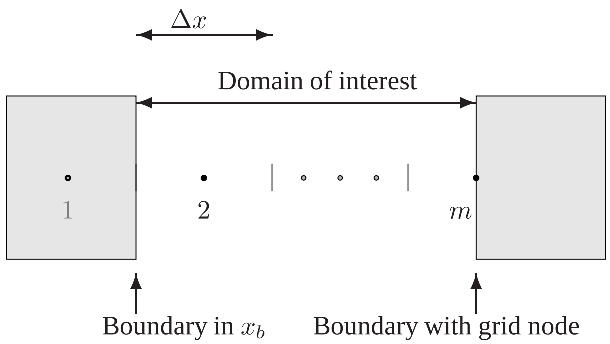

Figure 4-6 Grid nodes cover the interior of the domain of interest. Additional nodes may be placed *beyond* a boundary as illustrated on the left side or placed *on* the boundary as illustrated on the right. The numerical implementation of the boundary condition depends on the arrangement selected.

If instead the boundary condition is in the form of a flux, it is more practical to have two grid nodes straddling the boundary, with one slightly outside the domain and the other slightly inside (Figure 4-6 left side). In this manner, the derivative of the variable is more precisely formulated at the location of the boundary. With the index notation of Figure 4-6,

$$\frac{\tilde{T}_2 - \tilde{T}_1}{\Delta x} \simeq \left.\frac{\partial T}{\partial x}\right|_{x_b} \;+\; \frac{\Delta x^2}{24}\left.\frac{\partial^3 T}{\partial x^3}\right|_{x_b} \tag{4.39}$$

yields a second-order approximation, and the flux boundary condition $-\kappa_T(\partial T/\partial x) \;=\; q_b$ turns into

$$\tilde{T}_1 \;=\; \tilde{T}_2 \;+\; \Delta x\,\frac{q_b}{\kappa_T}\,. \tag{4.40}$$

There are cases, however, when the situation is less ideal. This occurs when a total, advective plus diffusive, flux boundary condition is specified ($uT - \kappa_T(\partial T/\partial x) \;=\; q_b$). Either the ending node is *at* the boundary, complicating the discretization of the derivative, or it is placed *beyond* the boundary and the value of T must be extrapolated. In the latter case, extrapolation is performed with second-order accuracy,

$$\frac{\tilde{T}_1 + \tilde{T}_2}{2} \;\simeq\; T(x_b) \;+\; \frac{\Delta x^2}{8}\left.\frac{\partial^2 T}{\partial x^2}\right|_{x_b}, \tag{4.41}$$

and the total flux condition becomes

$$u_b\,\frac{\tilde{T}_1 + \tilde{T}_2}{2} \;-\; \kappa_T\,\frac{\tilde{T}_2 - \tilde{T}_1}{\Delta x} \;=\; q_b \tag{4.42}$$

yielding the following condition on the end value $\tilde{T}_1$:

$$\tilde{T}_1 = \frac{2q_b \Delta x + (2\kappa_b - u_b \Delta x)\tilde{T}_2}{2\kappa_T + u_b \Delta x} . \tag{4.43}$$

In the former case, when the ending grid node lies exactly at the boundary, the straight-foward difference

$$\frac{\partial T}{\partial x} \simeq \frac{\tilde{T}_m - \tilde{T}_{m-1}}{\Delta x} \tag{4.44}$$

provides only first-order accuracy at point x_m, and to recover second-order accuracy with this node placement we need a numerical stencil that extends further into the domain (see Exercise 4-8). Therefore, to implement a flux condition, the preferred placement of the ending node is half a grid step beyond the boundary. With this configuration the accuracy is greater than with the ending point placed at the boundary itself. The same conclusion is reached for the finite-volume approach, since imposing a flux condition consists of replacing the flux calculation at the boundary by the imposed value. We immediately realize that in this case the natural placement of the boundary is at the interface between grid points, because it is the location where fluxes are calculated in the finite-volume approach.

The question that comes to mind at this point is whether or not the level of truncation error in the boundary-condition implementation is adequate. To answer the question, we have to compare this truncation error to other errors, particularly the truncation error within the domain. Since there is no advantage in having a more accurate method at the relatively few boundary points than at the many interior points, the sensible choice is to use the same truncation order at the boundary as within the domain. The model then possesses a uniform level of approximation. Sometimes, however, a lower order near the boundary may be tolerated because there are many fewer boundary points than interior points, and a locally higher error level should not penalize the overall accuracy of the solution. In the limit of $\Delta x \to 0$, the ratio of boundary points to the total number of grid points tends to zero, and the effect of less accurate approximations at the boundaries disappears.

In (4.43), we used the boundary condition to calculate a value at a point outside of the domain so that when applying the numerical scheme at the first interior point, the boundary condition is automatically satisfied. The same approach can also be used to implement the artificial boundary conditions that are sometimes required by the numerical scheme. Consider for example the fourth-order discretization (1.26) now applied to spatial derivatives in the domain interior coupled with the need to impose a single boundary condition at x_m of Dirichlet type. The discrete operator in the interior

$$\left.\frac{\partial T}{\partial x}\right|_{x_i} \simeq \frac{4}{3}\left(\frac{\tilde{T}_{i+1} - \tilde{T}_{i-1}}{2\Delta x}\right) - \frac{1}{3}\left(\frac{\tilde{T}_{i+2} - \tilde{T}_{i-2}}{4\Delta x}\right) \tag{4.45}$$

can be applied up to $i = m - 2$. At $i = m - 1$, the formula can no longer be applied, unless we provide a value at a virtual point $\tilde{T}_{m+1}$ (Figure 4-7). This can be accomplished by requiring that a skewed fourth-order discretization near the boundary have the same effect as the centered version using the virtual value.

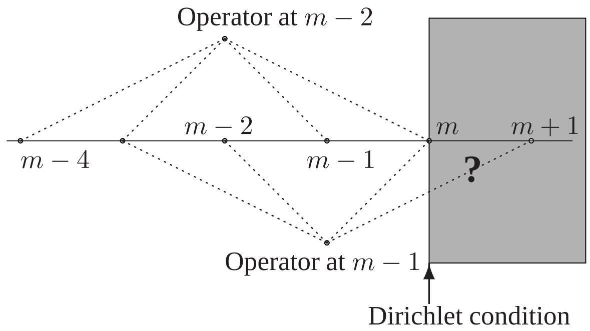

Figure 4-7 An operator spanning 2 points on each side of the calculation point can be applied only up to $m-2$ if a single Dirichlet condition is prescribed. When applying the same operator at $m-1$ we face the problem that the value at $m+1$ does not exist.

4.8 Accuracy and errors

Errors in a numerical model can be of several types. Following Ferziger and Perić (1999) we classify them according to their origin.

- *Modeling errors*: This error is caused by the imperfections of the mathematical model in representing the physical system. It is thus the difference between the evolution of the real system and that of the exact solution of its mathematical representation. Earlier in this chapter we introduced simplifications to the equations and added parameterizations of unresolved processes, which all introduce errors of representation. Furthermore, even if the model formulation had been ideal, coefficients remain imperfecly known. Uncertainties in the accompanying boundary conditions also contribute to modeling errors.

- *Discretization errors*: This error is introduced when the original equations are approximated to transform them into a computer code. It is thus the difference between the exact solution of the continuous problem and the exact numerical solution of the discretized equations. Examples are the replacement of derivatives by finite differences and the use of guesses in predictor-corrector schemes.

- *Iteration errors*: This error originates with the use of iterative methods to perform intermediate steps in the algorithm and is thus measured as the difference between the exact solution of the discrete equations and the numerical solution actually obtained. An example is the use of the so-called Jacobi method to invert a matrix at some stage of the calculations: for the sake of time, the iterative process is interrupted before full convergence is reached.

- *Rounding errors*: These errors are due to the fact that only a finite number of digits are used in the computer to represent real numbers.

A well constructed model should ensure that

$$\text{rounding errors} \ll \text{iteration errors} \ll \text{discretization errors} \ll \text{modeling errors.}$$

The order of these inequalities is easily understood: If the discretization error were larger than the modeling error, there would be no way to tell whether the mathematical model is an adequate approximation of the physical system we are trying to describe. If the iteration error were larger than the discretization error, the claim could not be made that the algorithm generates a numerical solution that satisfies the discretized equations, etc.

In the following, we will deal neither with rounding errors (generally controlled by appropriate compiler options, loop arrangements and double precision instructions), nor with iteration errors (generally controlled by sensitivity analysis or *a priori* knowledge of acceptable error levels for the convergence of the iterations). Modeling errors are discussed when performing scale analysis and additional modeling hypotheses or simplifications (see for example the Boussinesq and hydrostatic approximations), so that we may restrict our attention here to the discretization error associated with the transformation of a continuous mathematical model into a discrete numerical scheme.

The concepts of consistence, convergence and stability mentioned in Chapter 1 only provide information on the discretization error behavior when Δt tends to zero. In practice, however, time steps (and spatial steps as well) are never tending towards zero but are kept at fixed values, and the question arises about how accurate is the numerical solution compared to the exact solution. In that case, convergence is only marginally interesting, and even inconsistent schemes, if clever, may be able to provide results that cause lower actual errors than consistent and convergent methods.

By definition, the discretization error ϵ_u on a variable u is the difference between the exact numerical solution $\tilde{u}$ of the discretized equation and the mathematical solution u of the continuous equation:

$$\epsilon_u \;=\; \tilde{u} \;-\; u. \tag{4.46}$$

4.8.1 Discretization error estimates

In the case of explicit discretization (2.24) of inertial oscillations, we can obtain differential equations for the errors by subtracting the modified equations (2.28) from the exact continuous equation (2.23), to the leading order:

$$\frac{d\epsilon_u}{dt} - f\epsilon_v = f^2\frac{\Delta t}{2}\;\tilde{u}\; + \mathcal{O}(\Delta t^2)$$
$$\frac{d\epsilon_v}{dt} + f\epsilon_u = f^2\frac{\Delta t}{2}\;\tilde{v}\; + \mathcal{O}(\Delta t^2).$$

Obviously, we are not going to solve these equations to calculate the error because it would be tantamount to solving the exact problem directly. What we notice, however, is that the error equations have source terms on the order of Δt (which vanish as $\Delta t \to 0$ because the scheme is consistent) and we anticipate that these will give rise to a proportional solution for ϵ_u and ϵ_v. The truncation error of the solution should therefore be of first order:

$$\epsilon_u = \mathcal{O}(\Delta t) \sim \frac{f\Delta t}{2}\;\|\,\tilde{\mathbf{u}}\,\|\;. \tag{4.47}$$

We can verify that the actual error is indeed divided by a factor two when the time step is halved (Figure 4-8).

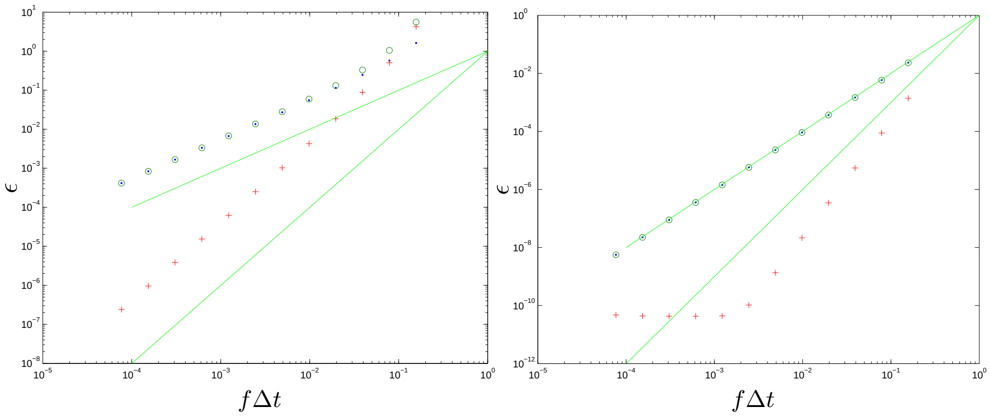

Figure 4-8 Relative discretization error $\epsilon = \epsilon_u / \parallel \tilde{u} \parallel$ as a function of the dimensionless variable $f\Delta t$ in the case of inertial oscillations. The log-log graphs show the real errors (dots) and estimated values of the error (circles) for an explicit scheme (left panel) and semi-explicit scheme (right panel). The slope of the theoretical convergence rates ($m = 1$ on the left panel and $m = 2$ on the right panel) are shown as well as the next order $m + 1$. Actual errors after a Richardson extrapolation (crosses) prove that the order is increased by 1 after extrapolation.

This is to be expected, since the equivalence theorem also states that for a linear problem, the numerical solution and its truncation error share the same order, say m. The difficulty with this approach is that for nonlinear problems, no guarantee can be made that this property continues to hold or that the actual error can be estimated by inspection of the modified equation.

To quantify the discretization error in nonlinear systems, we can resort to a sensitivity analysis. Suppose the leading error of the solution is

$$\epsilon_u = \tilde{u} - u = a\Delta t^m, \tag{4.48}$$

where the coefficient a is unknown and the order m may or may not be known. If m is known, the parameter a can be determined by comparing the solution $\tilde{u}_{2\Delta t}$ obtained with a double step $2\Delta t$ with the solution $\tilde{u}_{\Delta t}$ obtained with the original time step Δt:

$$\tilde{u}_{2\Delta t} - u = a2^m\Delta t^m, \quad \tilde{u}_{\Delta t} - u = a\Delta t^m \tag{4.49}$$

from which[7] falls the value of a:

$$a = \frac{\tilde{u}_{2\Delta t} - \tilde{u}_{\Delta t}}{(2^m - 1)\Delta t^m}\,. \tag{4.50}$$

The error estimate associated with the higher-resolution solution $\tilde{u}_{\Delta t}$ is

$$\epsilon_u = \tilde{u}_{\Delta t} - u = a\Delta t^m = \frac{\tilde{u}_{2\Delta t} - \tilde{u}_{\Delta t}}{(2^m - 1)}, \tag{4.51}$$

[7] Notice that the difference must be done *at the same moment* t, not the same time step n.

with which we can improve our solution by using (4.48)

$$\tilde{u} = \tilde{u}_{\Delta t} - \frac{\tilde{u}_{2\Delta t} - \tilde{u}_{\Delta t}}{(2^m - 1)}. \tag{4.52}$$

This suggests that the two-time-step approach may yield the exact answer because it determines the error. Unfortunately, this cannot be the case because we are working with a discrete representation of a continuous function. The paradox is resolved by realizing that, by using (4.50), we discarded higher-order terms and therefore did not calculate the exact value of a but only an estimate of it. What our manipulation accomplished was the elimination of the leading error term. This procedure is called a *Richardson extrapolation*:

$$u = \tilde{u}_{\Delta t} - \frac{\tilde{u}_{2\Delta t} - \tilde{u}_{\Delta t}}{(2^m - 1)} + \mathcal{O}\left(\Delta t^{m+1}\right). \tag{4.53}$$

Numerical calculations of the real error and error estimates according to (4.51) show good performance of the estimators in the context of inertial oscillations (Figure 4-8). Also, the Richardson extrapolation increases the order by 1, except for the semi-implicit scheme at high resolution, when no gain is achieved because saturation occurs (Figure 4-8, right panel). This asymptote corresponds to the inevitable rounding errors, and we can claim to have solved the discrete equations "exactly".

When considering the error estimate (4.51), we observe that the error estimate of a first-order scheme ($m = 1$), is simply the difference between two solutions obtained with different time steps. This is the basic justification for performing resolution sensitivity analysis on more complicated models: Differences in model results due to a variation in resolution may be taken as estimates of the discretization error. By extension, performing multiple simulations with different model parameter values leads to differences that are indicators of modeling errors.

When the truncation order m is not known, a third evaluation of the numerical solution, with a quadruple time step $4\Delta t$, yields an estimate of both the order m and the coefficient a of the discretization error:

$$\begin{aligned} m &= \frac{1}{\log 2} \log\left(\frac{\tilde{u}_{4\Delta t} - \tilde{u}_{2\Delta t}}{\tilde{u}_{2\Delta t} - \tilde{u}_{\Delta t}}\right) \\ a &= -\frac{\tilde{u}_{2\Delta t} - \tilde{u}_{\Delta t}}{(2^m - 1)\Delta t^m}. \end{aligned} \tag{4.54}$$

As we can see in practice (Figure 4-9), this estimate provides a good estimate of m when resolution is sufficiently fine. This method can thus be used to determine the truncation order of discretizations numerically, which can be useful to assess convergence rates of nonlinear discretized systems or to verify the proper numerical implementation of a discretization (for which the value of m is known). In the latter case, if a method should be of second order but the numerical estimate of m according to (4.54) reveals only first-order convergence on well behaved problems, a programming or implementation error is very likely to blame.

Having access now to an error estimate, we can think of choosing the time step so as to keep discretization errors below a prescribed level. If the time step is prescribed *a priori*, the error estimate allows us to verify that the solution remains within error bounds. The use of

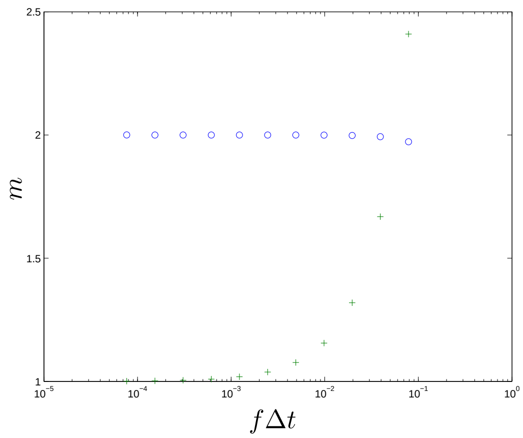

Figure 4-9 Estimator of m for explicit ($+$, tending to 1 for small time steps) and semi-implicit discretization (o, tending to 2) as function of $f\Delta t$.

a fixed time step is common but might not be the most appropriate choice when the process exhibits a mix of slower and faster processes (Figure 4-10). Then, it may be preferable that the time step be adjusted over time so as to follow the time scale of the system. In this case, we speak about *adaptive time stepping*.

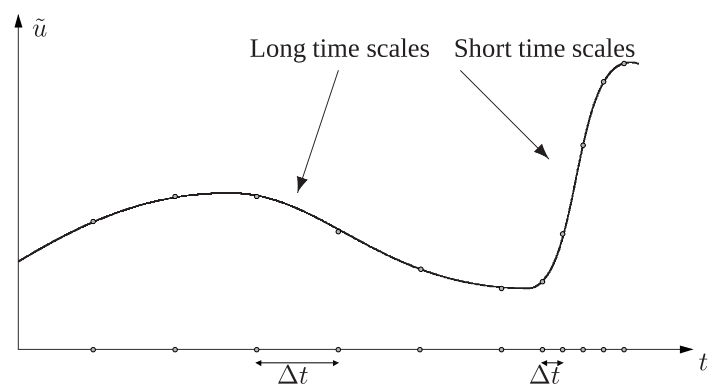

Figure 4-10 Use of different time steps Δt in function of the local error and time scales. The time step is decreased until the local error estimate is smaller than a prescribed value. When estimated errors are much smaller than allowed, the time step is increased.

Adaptive time stepping can be implemented by decreasing the time step whenever the error estimate starts to be excessive. Vice versa, when the error estimate indicates an unnecessarily short time step, it should be allowed to increase again. Adaptive time stepping seems appealing, but the additional work required to track the error estimate (doubling/halving the time step and recomputing the solution) can exceed the gain obtained by maintaining a fixed time step, which is occasionally too short. Also, multi-step methods are not easily generalized to adaptive time steps.

Analytical Problems

4-1. From the weather chart in today's edition of your newspaper, identify the horizontal extent of a major atmospheric feature and find the forecast wind speed. From these numbers, estimate the Rossby number of the weather pattern. What do you conclude about the importance of the Coriolis force? (*Hint*: When converting latitudinal and longitudinal differences in kilometers, use the earth's mean radius, 6371 km.)

4-2. Using the scale given in (4.16), compare the dynamic pressure induced by the Gulf Stream (speed = 1 m/s, width = 40 km, and depth = 500 m) to the main hydrostatic pressure due to the weight of the same water depth. Also, convert the dynamic-pressure scale in equivalent height of hydrostatic pressure (head). What can you infer about the possibility of measuring oceanic dynamic pressures by a pressure gauge?

4-3. Consider a two-dimensional periodic fluctuation of the type ($u' = U\sin(\phi + \alpha_u)$, $v' = V\sin(\phi + \alpha_v)$, $w' = 0$) with $\phi(x, y, t) = k_x x + k_y y - \omega t$ and all other quantities constant. Calculate the Reynolds stresses, such as $-\langle u'v' \rangle$, by taking the average over a 2π-period of the phase ϕ. Show that these stresses are not zero in general (proving that traveling waves may exert a finite stress and therefore accelerate or slow down a background flow on which they are superimposed). Under which relation between α_u and α_v does the shear stress $-\langle u'v' \rangle$ vanish?

4-4. Show that the horizontal eddy viscosity defined in (4.10) vanishes for a vortex flow with velocity components ($u = -\Omega y$, $v = +\Omega x$) with Ω being a constant. Is this a desirable property?

4-5. Why do we need to know the surface pressure distribution when using the hydrostatic approximation?

4-6. Theory tells us that in a pure advection problem for temperature T, a single boundary condition should be imposed at the inflow and none at the outflow, but, when diffusion is present, a boundary condition must be imposed at both ends. What do you expect to happen at the outflow boundary when diffusion is very small? How would you measure the "smallness" of diffusion?

4-7. In forming energy budgets, the momentum equations are multiplied by their respective velocity components (*i.e.*, the $\partial u/\partial t$ equation is multiplied by u and so forth), and the results are added. Show that in this manipulation, the Coriolis terms in f and f_* cancel one another out. What would be your reaction if someone presented you with a model in which the $f_* w$ term were dropped from Equation (4.7a) because w is small compared to u and the term $f_* u$ was retained in Equation (4.7c) for the same reason?

Numerical Exercises

4-1. When air and sea surface temperatures, $T_{\rm air}$ and $T_{\rm sea}$, are close to each other, it is acceptable to use a linearized form to express the heat flux across the air-sea heat interface, such as

$$-\kappa_T \frac{\partial T_{\rm sea}}{\partial z} = \frac{h}{\rho_0 C_v} \left(T_{\rm sea} - T_{\rm air}\right) \tag{4.55}$$

where h is an exchange coefficient in W/(m^2·K). The coefficient multiplying the temperature difference $T_{\rm sea} - T_{\rm air}$ has the units of a velocity and, for this reason, is sometimes called *piston velocity* in the context of gas exchange between air and water. Implement this boundary condition for a finite-volume ocean model. How would you calculate $T_{\rm sea}$ involved in the flux in order to maintain second-order accuracy of the standard second derivative within the ocean domain?

4-2. In some cases, particularly analytical and theoretical studies, the unknown field can be assumed to be periodic in space. How can periodic boundary conditions be implemented in a numerical one-dimensional model, for which the discretization scheme uses one point on each side of every calculation point? How would you adapt the scheme if the interior discretization needs two points on each side instead? Can you imagine what the expression *halo* used in this context refers to?

4-3. How do you generalize periodic boundary conditions (see preceding problem) to two dimensions? Is there an efficient scheme that ensures periodicity without particular treatment of corner points? (*Hint:* Think about a method of copying rows/columns that ensure proper values in corners.)

4-4. Assume you implemented a Dirichlet condition for temperature along a boundary on which a grid node exists but would like to diagnose the heat flux across the boundary. How would you determine the turbulent flux at that point with third-order accuracy?

4-5. Models can be used on parallel machines by distributing work among different processors. One of the possibilities is the so-called *domain decomposition* in which each processor is dedicated to a portion of the total domain. The model of each sub-domain can be interpreted as an open-boundary model. Assuming that the numerical scheme for a single variable uses q points on each side of the local node, how would you subdivide a one-dimensional domain into sub-domains and design data exchange between these subdomains to avoid the introduction of new errors? Can you imagine the problems you are likely to encounter in two dimensions? (*Hint:* Think how periodic boundary conditions were handled in the halo approach of the preceding two problems.)

4-6. Develop a MATLAB™ program to automatically calculate finite-difference weighting coefficients a_i for an arbitrary derivative of order p using l points to the left and m points to the right of the point of interest:

$$\left.\frac{d^p \tilde{u}}{dt^p}\right|_{t_n} \simeq a_{-l}\tilde{u}^{n-l} + ... + a_{-1}\tilde{u}^{n-1} + a_0\tilde{u}^n + a_1\tilde{u}^{n+1} + ... + a_m\tilde{u}^{n+m}. \quad (4.56)$$

The step is taken constant. Test your program on the fourth-order approximation of the first derivative. (*Hint*: Construct the linear system to be solved by observing that Δt should cancel out in all terms except for the relevant derivative so that $\Delta t^p a_i$ can be chosen as the unknowns.)

4-7. Imagine that you perform a series of simulations of the same model with time steps of $8\Delta t$, $4\Delta t$, $2\Delta t$ and Δt. The numerical discretization scheme is of order m. Which combination of the different solutions would best approximate the exact solution, and what truncation order would the combined solution have?

4-8. For a grid node placed on the boundary, show that using the value

$$\tilde{T}_m = \frac{2}{3}\left(-\Delta x \frac{q_b}{\kappa_T} - \frac{1}{2}\tilde{T}_{m-2} + 2\tilde{T}_{m-1}\right). \quad (4.57)$$

allows us to impose a flux condition in m with second-order accuracy.

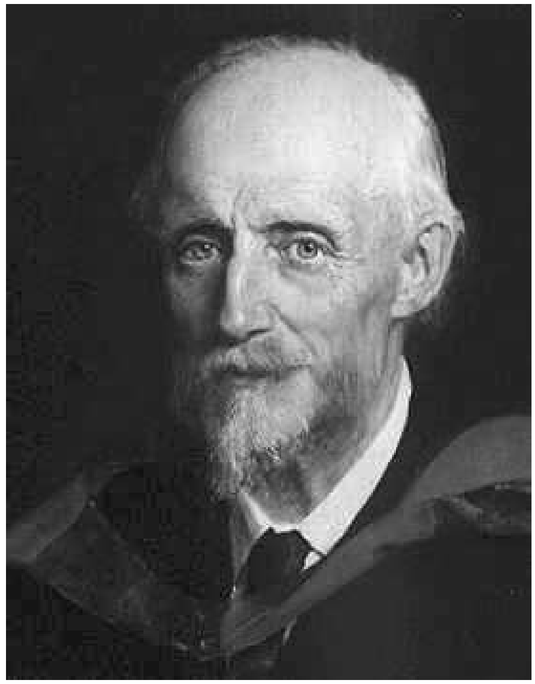

Osborne Reynolds
1842 – 1912

Osborne Reynolds was taught mathematics and mechanics by his father. While a teenager, he worked as an apprentice in the workshop of a mechanical engineer and inventor, where he realized that mathematics was essential for the explanation of certain mechanical phenomena. This motivated him to study mathematics at Cambridge, where he brilliantly graduated in 1867. Later, as a professor of engineering at the University of Manchester, his teaching philosophy was to subject engineering to mathematical description while also stressing the contribution of engineering to human welfare. His best known work is that on fluid turbulence, famous for the idea of separating flow fluctuations from the mean velocity and for his study of the transition from laminar to turbulent flow, leading to the dimensionless ratio that now bears his name. He made other significant contributions to lubrication, friction, heat transfer and hydraulic modeling. Books on fluid mechanics are peppered with the expressions Reynolds number, Reynolds equations, Reynolds stress, and Reynolds analogy. (*Photo courtesy of Manchester School of Engineering*)

Carl-Gustaf Arvid Rossby
1898 – 1957

A Swedish meteorologist, Carl-Gustav Rossby is credited with most of the fundamental principles on which geophysical fluid dynamics rests. Among other contributions, he left us the concepts of radius of deformation (Section 9.2), planetary waves (Section 9.4), and geostrophic adjustment (Section 15.2). However, the dimensionless number that bears his name was first introduced by the Soviet scientist I. A. Kibel' in 1940.

Inspiring to young scientists, whose company he constantly sought, Rossby viewed scientific research as an adventure and a challenge. His accomplishments are marked by a broad scope and what he liked to call the *heuristic approach*, that is, the search for a useful answer without unnecessary complications. During a number of years spent in the United States, he established the meteorology departments at MIT and the University of Chicago. He later returned to his native Sweden to become the director of the Institute of Meteorology in Stockholm. (*Photo courtesy of Harriet Woodcock*)

Chapter 5

Diffusive Processes

(October 18, 2006) **SUMMARY**: All geophysical motions are diffusive because of turbulence. Here, we consider a relatively crude way of representing turbulent diffusion, by means of an eddy diffusivity. Although the theory is straightforward, numerical handling of diffusion terms requires care, and the main objective of this chapter is to treat the related numerical issues, leading to the fundamental concept of numerical stability.

5.1 Isotropic, homogeneous turbulence

It was mentioned in Sections 3.4 and 3.5 that fluid properties such as heat, salt and humidity diffuse, that is, they are exchanged between neighboring particles. In laminar flow, this is accomplished by random (so-called Brownian) motion of the colliding molecules, but in large-scale geophysical systems turbulent eddies accomplish a similar effect far more efficiently. The situation is analoguous to mixing milk in coffee or tea: Left alone, the milk diffuses very slowly through the beverage, but the action of a stirrer generates turbulent eddies that mix the two liquids far more effectively and create a homogeneous mixture in a short time. The difference is that eddying in geophysical fluids is generally not induced by a stirring mechanism but is self-generated by hydrodynamic instabilities.

In Section 4.1, we introduced turbulent fluctuations without saying anything specific about them; we now begin to elucidate some of their properties. At a very basic level, turbulent motion can be interpreted as a population of many eddies (vortices), of different sizes and strengths, embedded within one another and forever changing, giving a random appearance to the flow (Figure 5-1). Two variables then play a fundamental role: d, the characteristic diameter of the eddies, and $\mathring{u}$, their characteristic orbital velocity. Since the turbulent flow consists of many eddies, of varying sizes and speeds, $\mathring{u}$ and d do not each assume a single value but vary within a certain range. In stationary, homogeneous and isotropic turbulence, that is, a turbulent flow that statistically appears unchanging in time, uniform in space and without preferential direction, all eddies of a given size (same d) behave more or less in the same way and can be assumed to share the same characteristic velocity $\mathring{u}$. In other words, we

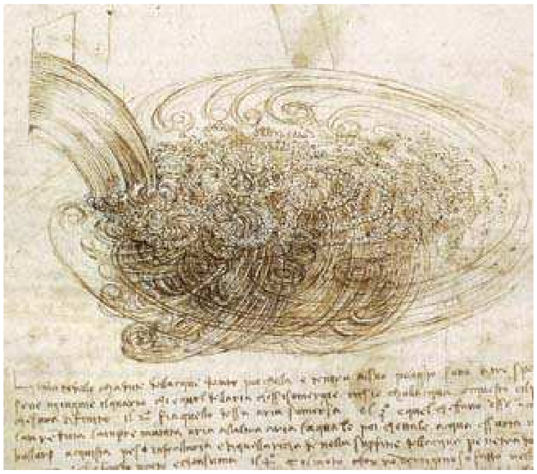

Figure 5-1 Drawing of a turbulent flow by Leonardo da Vinci circa 1507–1509, who recognized that turbulence involves a multitude of eddies at various scales.

make the assumption that $\mathring{u}$ is a function of d (Figure 5-2).

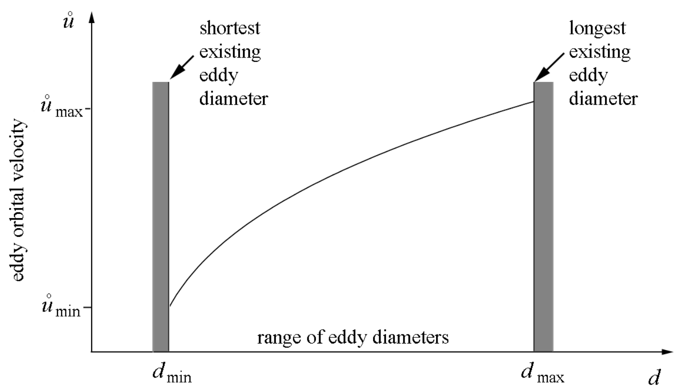

Figure 5-2 Eddy orbital velocity versus eddy length scale in homogeneous and isotropic turbulence. The largest eddies spin the fastest.

5.1.1 Length and velocity scales

In the view of Kolmogorov (1941), turbulent motions span a wide range of scales, from a macroscale at which the energy is supplied, to a microscale at which energy is dissipated by viscosity. The interaction among the eddies of various scales passes energy gradually from the larger eddies to the smaller ones. This process is known as the *turbulent energy cascade* (Figure 5-3).

If the state of turbulence is statistically steady (statistically unchanging turbulence intensity), then the rate of energy transfer from one scale to the next must be the same for all

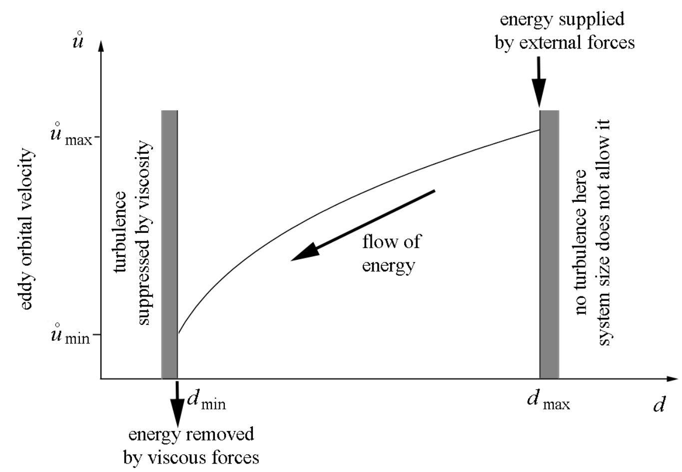

Figure 5-3 The turbulent energy cascade. According to this theory, the energy fed by external forces excites the largest possible eddies and is gradually passed to ever smaller eddies, all the way to a minimum scale where this energy is ultimately dissipated by viscosity.

scales, so that no group of eddies sharing the same scale sees its total energy level increase or decrease over time. It follows that the rate at which energy is supplied at the largest possible scale ($d_{\max}$) is equal to that dissipated at the shortest scale ($d_{\min}$). Let us denote by ϵ this rate of energy supply/dissipation, per unit mass of fluid:

$$\begin{aligned}\epsilon &= \text{energy supplied to fluid per unit mass and time} \\ &= \text{energy cascading from scale to scale, per unit mass and time} \\ &= \text{energy dissipated by viscosity, per unit mass and time.}\end{aligned}$$

The dimensions of ϵ are:

$$[\epsilon] \;=\; \frac{ML^2T^{-2}}{MT} \;=\; L^2T^{-3}. \tag{5.1}$$

With Kolmogorov, we further assume that the characteristics of the turbulent eddies of scale d depend solely on d and on the energy cascade rate ϵ. This is to say that the eddies know how large they are, at what rate energy is supplied to them and at what rate they must supply it to the next smaller eddies in the cascade. Mathematically, $\mathring{u}$ depends only on d and ϵ. Since $[\mathring{u}] = LT^{-1}$, $[d] = L$ and $[\epsilon] = L^2T^{-3}$, the only dimensionally acceptable possibility is:

$$\mathring{u}(d) \;=\; A(\epsilon d)^{1/3}, \tag{5.2}$$

in which A is a dimensionless constant.

Thus, the larger ϵ, the larger $\mathring{u}$. This makes sense, for a greater energy supply to the system generates stronger eddies. Equation (5.2) further tells us that the smaller d, the weaker $\mathring{u}$, and the implication is that the smallest eddies have the lowest speeds, while the largest eddies have the highest speeds and thus contribute most of the kinetic energy.

Typically, the largest possible eddies in the turbulent flow are those that extend across the entire system, from boundary to opposite boundary, and therefore

$$d_{\rm max} \;=\; L, \tag{5.3}$$

where L is the geometrical dimension of the system (such as the width of the domain or the cubic root of its volume). In geophysical flows, there is a noticeable scale disparity between the relatively short vertical extent (depth, height) and the comparatively long horizontal extent (distance, length) of the system. We must therefore clearly distinguish eddies that rotate in the vertical plane (about a horizontal axis) from those that rotate horizontally (about a vertical axis).

The shortest eddy scale is set by viscosity and can be defined as the length scale at which molecular viscosity becomes dominant. Molecular viscosity, denoted by ν, has for dimensions[1]:

$$[\nu] \;=\; L^2 T^{-1}.$$

If we assume that $d_{\rm min}$ depends only on ϵ, the rate at which energy is supplied to that scale, and on ν, because these eddies feel viscosity, then the only dimensionally acceptable relation is:

$$d_{\rm min} \;\sim\; \nu^{3/4} \epsilon^{-1/4}. \tag{5.4}$$

The quantity $\nu^{3/4}\epsilon^{-1/4}$, called the *Kolmogorov scale*, is typically on the order of a few millimeters or shorter.

The span of length scales in a turbulent flow is related to its Reynolds number. Indeed, in terms of the largest velocity scale, which is the orbital velocity of the largest eddies, $U = \mathring{u}(d_{\rm max}) = A(\epsilon L)^{1/3}$, the energy supply/dissipation rate is

$$\epsilon \;=\; \frac{U^3}{A^3 L} \;\sim\; \frac{U^3}{L}\,, \tag{5.5}$$

and the length scale ratio can be expressed as

$$\begin{aligned} \frac{L}{d_{\rm min}} \;&\sim\; \frac{L}{\nu^{3/4}\epsilon^{-1/4}} \\ &\sim\; \frac{L U^{3/4}}{\nu^{3/4} L^{1/4}} \\ &\sim\; Re^{3/4}, \end{aligned} \tag{5.6}$$

where $Re = UL/\nu$ is the Reynolds number of the flow. As we could have expected, a flow with a higher Reynolds number contains a broader range of eddies.

[1]Values for ambient air and water are: $\nu_{\rm air} = 1.51 \times 10^{-5}$ m^2/s and $\nu_{\rm water} = 1.01 \times 10^{-6}$ m^2/s.

5.1.2 Energy spectrum

In turbulence theory, it is customary to consider the so-called *power spectrum*, which is the distribution of kinetic energy per mass across the various length scales. For this, we need to define a wavenumber. Because velocity reverses across the diameter of an eddy, the eddy diameter should properly be considered as half of the wavelength:

$$k \;=\; \frac{2\pi}{\text{wavelength}} \;=\; \frac{\pi}{d}\,. \tag{5.7}$$

The lowest and highest wavenumber values are $k_{\min} = \pi/L$ and $k_{\max} \sim \epsilon^{1/4}\nu^{-3/4}$.

The kinetic energy E per mass of fluid has dimensions $\mathrm{ML^2T^{-2}/M} = \mathrm{L^2T^{-2}}$. The portion dE contained in the eddies with wavenumbers ranging from k to $k + dk$ is defined as

$$dE \;=\; E_k(k)\, dk.$$

It follows that the dimension of E_k is $\mathrm{L^3T^{-2}}$, and dimensional analysis prescribes:

$$E_k(k) \;=\; B\,\epsilon^{2/3}\,k^{-5/3}, \tag{5.8}$$

where B is a second dimensionless constant. It can be related to A of Equation (5.2) because the integration of $E_k(k)$ from $k_{\min} = \pi/L$ to $k_{\max} \sim \infty$ is the total energy per mass in the system, which in good approximation is that contained in the largest eddies, namely $U^2/2$. Thus,

$$\int_{k_{\min}}^{\infty} E_k(k)\, dy \;=\; \frac{U^2}{2}\,, \tag{5.9}$$

from which follows

$$\frac{3}{2\pi^{2/3}}\,B \;=\; \frac{1}{2}\,A^2. \tag{5.10}$$

The value of B has been determined experimentally and found to be about 1.5 (Pope, 2000, page 231). From this, we estimate A to be 1.45.

The $-5/3$ power law of the energy spectrum has been observed to hold well in the *inertial range*, that is, for those intermediate eddy diameters that are remote from both largest and shortest scales. Figure 5-4 shows the superposition of a large number of longitudinal power spectra[2]. The straight line where most data overlap in the range $10^{-4} < k\nu^{3/4}/\epsilon^{1/4} < 10^{-1}$ corresponds to the $-5/3$ decay law predicted by the Kolmogorov turbulent cascade theory. The higher the Reynolds number of the flow, the broader the span of wavenumbers over which the $-5/3$ law holds. Several crosses visible at the top of the plot, which extend from a set of crosses buried in the accumulation of data below, correspond to data in a tidal channel (Grant *et al.*, 1962), for which the Reynolds number was the highest.

There is, however, some controversy over the $-5/3$ power law for E_k. Some investigators (Saffman, 1968; Long, 1997 and 2003) have proposed alternative theories that predict a -2 power law.

[2]The longitudinal power spectrum is the spectrum of the kinetic energy associated with the velocity component in the direction of the wavenumber.

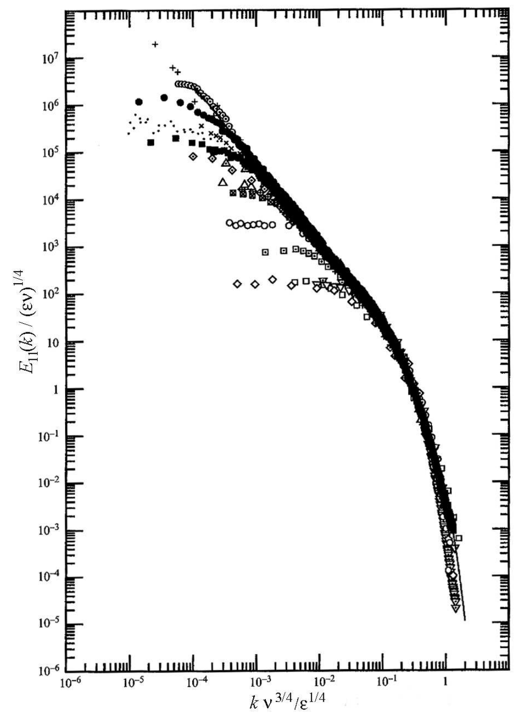

Figure 5-4 Longitudinal power spectrum of turbulence calculated from numerous observations taken outdoors and in the laboratory. [From Saddoughi and Veeravalli, 1994]

5.2 Turbulent diffusion

Our concern here is not to pursue the study of turbulence but to arrive at a heuristic way to represent the dispersive effect of turbulence on those scales too short to be resolved in a numerical model.

Turbulent diffusion or *dispersion* is the process by which a substance is moved from one place to another under the action of random turbulent fluctuations in the flow. Given the complex nature of these fluctuations, it is impossible to describe the dispersion process in an exact manner but some general remarks can be made that lead to a useful parameterization.

Consider the two adjacent cells of Figure 5-5 exchanging fluid between each other. The fluid in the left cell contains a concentration (mass per volume) c_1 of some substance whereas the fluid in the right cell contains a different concentration c_2. Think of c_1 being less than c_2, although this does not necessarily have to be the case. Further assume, in order to focus exclusively on diffusion, that there is no net flow from one cell to the other but that the only exchange velocity is due to a single eddy moving fluid at velocity $\mathring{u}$ on one flank and at velocity $-\mathring{u}$ on its opposite flank. The amount of substance carried per unit area perpendicular to the x–axis and per time, called the *flux*, is equal to the product of the concentration with the velocity, $c_1\mathring{u}$ from left to right and $c_2\mathring{u}$ in the opposite direction. The net flux q in the

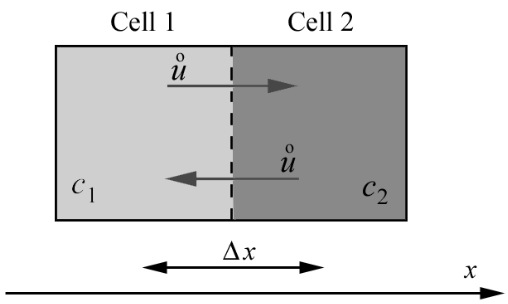

Figure 5-5 Exchange between two adjacent cells illustrating turbulent diffusion. Because of the difference between concentrations, the exchange between cells is uneven. The cell with the least concentration loses less than it receives.

x–direction is the flux from 1 to 2 minus the flux from 2 to 1:

$$\begin{aligned} q &= c_1 \, \mathring{u} \, - \, c_2 \, \mathring{u} \\ &= - \, \mathring{u} \, \Delta c, \end{aligned}$$

where $\Delta c = c_2 - c_1$ is the concentration difference. Multiplying and dividing by the distance Δx between cell centers, we may write:

$$q \; = \; - \; (\mathring{u}\Delta x) \, \frac{\Delta c}{\Delta x} \; .$$

When considering the variation of c over larger scales, those for which the eddy-size Δx appears to be small, we may approximate the previous equation to

$$q \; = \; - \; D \, \frac{dc}{dx} \; , \tag{5.11}$$

where D is equal to the product $\mathring{u}\Delta x$ and is called the turbulent diffusion coefficient or *diffusivity*. Its dimension is $[D] = \mathrm{L}^2\mathrm{T}^{-1}$.

The diffusive flux is proportional to the gradient of the concentration of the substance. In retrospect, this makes sense; if there were no difference in concentrations between cells, the flux from one into the other would be exactly compensated by the flux in the opposite direction. It is the concentration difference (the gradient) that matters.

Diffusion is ‘down-gradient’, that is, the transport is from high to low concentrations, just as heat conduction moves heat from the warmer side to the colder side. (In the preceding example with $c_1 < c_2$, q is negative, and the net flux is from cell 2 to cell 1.) This implies that the concentration increases on the low side and decreases on the high side, and the two concentrations gradually become closer to each other. Once they are equal ($dc/dx = 0$), diffusion stops, although turbulent fluctuations never do. Diffusion acts to homogenize the substance across the system.

The pace at which diffusion proceeds depends critically on the value of the diffusion coefficient D. This coefficient is inherently the product of two quantities, a velocity ($\mathring{u}$) and a length scale (Δx), representing respectively the magnitude of fluctuating motions and their range. Since the numerical model resolves scales down to the grid scale Δx, the turbulent diffusion that remains to represent is that due to the all shorter scales, starting with $d = \Delta x$.

As seen in the previous section, to shorter scales d correspond slower eddy velocities $\mathring{u}$ and thus lower diffusivities. It follows that diffusion is chiefly accomplished by eddies at the largest unresolved scale, Δx, because these generate the greatest value of $\mathring{u}\Delta x$:

$$\begin{aligned} D &= \mathring{u}(\Delta x)\,\Delta x \\ &= A\,\epsilon^{1/3}\,\Delta x^{4/3}. \end{aligned} \tag{5.12}$$

The manner by which the dissipation rate ϵ is related to local flow characteristics, such as a velocity gradient, opens the way to a multitude of possible parameterizations.

The preceding considerations in one dimension were generic in the sense that the direction x could stand for any of the three directions of space, x, y or z. Because of the typical disparity in mesh size between the horizontal and vertical directions in GFD models ($\Delta x \approx \Delta y \gg \Delta z$), care must be taken to use two distinct diffusivities, which we denote $\mathcal{A}$ for the horizontal directions and κ for the vertical direction[3]. While κ must be constructed from the length scale Δz, $\mathcal{A}$ must be formed from a length scale that is hybrid between Δx and Δy. The Smagorinsky formulation presented in (4.10) is a good example.

The components of the three-dimensional flux vector are

$$q_x = -\mathcal{A}\,\frac{\partial c}{\partial x} \tag{5.13a}$$

$$q_y = -\mathcal{A}\,\frac{\partial c}{\partial y} \tag{5.13b}$$

$$q_z = -\kappa\,\frac{\partial c}{\partial z}. \tag{5.13c}$$

And, we are in a position to write a budget for the concentration $c(x, y, z, t)$ of the substance in the flow, by taking an elementary volume of fluid of size dx, dy and dz, as illustrated in Figure 5-6. The net import in the x–direction is the difference in x–fluxes times the area $dy\ dz$ they cross, *i.e.*, $[q_x(x, y, z) - q_x(x + dx, y, z)]\ dy\ dz$, and similarly in the y– and z–directions. The net import from all directions is then

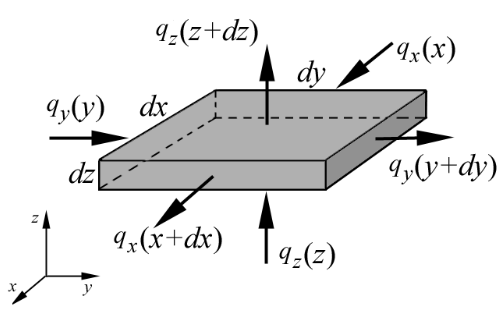

Figure 5-6 An infinitesimal piece of fluid for the local budget of a substance of concentration c in the fluid.

[3] GFD models generally use the same horizontal diffusivity for all variables, including momentum and density – see (4.21) – but distinguish between various diffusivities in the vertical.

$$\begin{aligned}\text{Net import in } dx\, dy\, dz &= [q_x(x,y,z) - q_x(x+dx,y,z)]\, dy\, dz \\ &+ [q_y(x,y,z) - q_y(x,y+dy,z)]\, dx\, dz \\ &+ [q_z(x,y,z) - q_z(x,y,z+dz)]\, dx\, dy,\end{aligned}$$

on a per-time basis. This net import contributes to increasing the amount $c\, dx\, dy\, dz$ inside the volume:

$$\frac{d}{dt}(c\, dx\, dy\, dz) = \text{Net import.}$$

In the limit of an infinitesimal volume (vanishing dx, dy and dz), we have

$$\frac{\partial c}{\partial t} = -\frac{\partial q_x}{\partial x} - \frac{\partial q_y}{\partial y} - \frac{\partial q_z}{\partial z}, \tag{5.14}$$

and, after replacement of the flux components by their expressions (5.13),

$$\frac{\partial c}{\partial t} = \frac{\partial}{\partial x}\left(\mathcal{A}\frac{\partial c}{\partial x}\right) + \frac{\partial}{\partial y}\left(\mathcal{A}\frac{\partial c}{\partial y}\right) + \frac{\partial}{\partial z}\left(\kappa\frac{\partial c}{\partial z}\right), \tag{5.15}$$

where $\mathcal{A}$ and κ are respectively the horizontal and vertical eddy diffusivities. Note the similarity with the dissipation terms in the momentum and energy equations (4.21) of the previous chapter.

For a comprehensive exposition of diffusion and some of its applications, the reader is referred to Ito (1992) and Okubo and Levin (2002).

5.3 One-dimensional numerical scheme

We now illustrate discretization methods for the diffusion equation and begin with a protypical one-dimensional system, representing a horizontally homogeneous piece of ocean or atmosphere, containing a certain substance, such as a pollutant or tracer, which is not exchanged across either bottom or top boundaries. To simplify the analysis further we begin by taking the vertical diffusivity κ as constant until further notice. We then have to solve the following equation

$$\frac{\partial c}{\partial t} = \kappa \frac{\partial^2 c}{\partial z^2}, \tag{5.16}$$

with no-flux boundary conditions at both bottom and top:

$$q_z = -\kappa \frac{\partial c}{\partial z} = 0 \quad \text{at} \quad z = 0 \text{ and } z = h, \tag{5.17}$$

where h is the thickness of the domain.

To complete the problem, we also prescribe an initial condition. Suppose for now that this initial condition is a constant C_0 plus a cosine function of amplitude C_1 ($C_1 \leq C_0$):

$$c(z, t = 0) \;=\; C_0 + C_1 \cos\left(j\pi \frac{z}{h}\right), \tag{5.18}$$

with j being an integer. Then, it is easily verified that

$$c \;=\; C_0 \;+\; C_1\; \cos\left(j\pi \frac{z}{h}\right)\; \exp\left(-j^2\pi^2 \frac{\kappa t}{h^2}\right) \tag{5.19}$$

satisfies the partial differential equation (5.16), both boundary conditions (5.17), and initial condition (5.18). It is thus the exact solution of the problem. As we can expect from the dissipative nature of diffusion, this solution represents a temporal attenuation of the non-constant portion of c, which is more rapid under stronger diffusion (greater κ) and shorter scales (higher j).

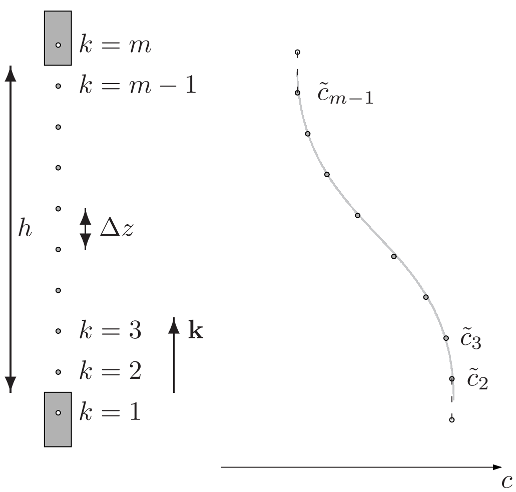

Figure 5-7 Gridding of a vertical interval with m nodes, of which the first and last lie beyond the bottom and top boundaries, respectively. Such points are called *ghost points*. With m nodes and $m - 1$ intervals between nodes among which two are only half long, it follows that $(m-2)$ segments cover the domain and the grid spacing is thus $\Delta z = h/(m-2)$. Neumann conditions (zero derivatives) at both boundaries are implemented by assigning the values $\tilde{c}_1 = \tilde{c}_2$ and $\tilde{c}_m = \tilde{c}_{m-1}$ to the end points, which implies zero derivatives in the middle of the first and last intervals. The calculations using the discretized form of the equation then proceed from $k = 2$ to $k = m - 1$.

Let us now design a numerical method to solve the problem and check its solution against the preceding, exact solution. First, we discretize the spatial derivative by applying a standard finite-difference technique. With a Neumann boundary condition applied at each end, we locate the end grid points not at, but surrounding the boundaries (see Section 4.7) and place the grid nodes at the following locations:

$$z_k \;=\; (k - \tfrac{3}{2})\,\Delta z \quad \text{for} \quad k = 1,\; 2,\; ....,\; m, \tag{5.20}$$

with $\Delta z = h/(m-2)$ so that we use m grid points, among which the first and last are ghost points lying a distance $\Delta z/2$ beyond the boundaries (Figure 5-7).

Discretizing the second spatial derivative with a three-point centered scheme and before performing time discretization, we have

$$\frac{\partial \tilde{c}_k}{\partial t} \;=\; \frac{\kappa}{\Delta z^2}\; (\tilde{c}_{k+1} - 2\tilde{c}_k + \tilde{c}_{k-1}) \quad \text{for} \quad k = 2,\; ...,\; m-1. \tag{5.21}$$

We thus have $m-2$ ordinary, coupled, differential equations for the $m-2$ unknown time dependent functions $\tilde{c}_k$. We can determine the numerical error introduced in this *semi-discrete* set of equations by trying a solution similar to the exact solution:

$$\tilde{c}_k = C_0 + C_1 \cos\left(j\pi \frac{z_k}{h}\right) a(t). \tag{5.22}$$

Trigonometric formulas provide the following equation for the temporal evolution of the amplitude $a(t)$:

$$\frac{da}{dt} = -4a \frac{\kappa}{\Delta z^2} \sin^2\phi \quad \text{with} \quad \phi = j\pi \frac{\Delta z}{2h}, \tag{5.23}$$

of which the solution is

$$a(t) = \exp\left(-4\sin^2\phi \frac{\kappa t}{\Delta z^2}\right). \tag{5.24}$$

With this spatial discretization, we thus obtain an exponential decrease of amplitude a, like in the exact equation (5.19) but with a different damping rate. The ratio τ of the numerical damping rate $4\kappa \sin^2\phi/\Delta z^2$ to the true damping rate $j^2\pi^2\kappa/h^2$ is $\tau = \phi^{-2}\sin^2\phi$. For small Δz compared to the length scale h/j of the c distribution, ϕ is small, and the correct damping is nearly obtained with the semi-discrete numerical scheme. Nothing anomalous is therefore expected from the approach thusfar as long as the discretization of the domain is sufficiently dense to capture adequately the spatial variations in c. Also, the boundary conditions cause no problem because the mathematical requirement of one boundary condition on each side of the domain matches exactly what we need to calculate the discrete values $\tilde{c}_k$ for $k = 2, ..., m-1$. An initial condition is also needed at each node to start the time integration. This is all consistent with the mathematical problem.

We now proceed with the time discretization. First, let us try the simplest of all methods, the explicit Euler scheme:

$$\frac{\tilde{c}_k^{n+1} - \tilde{c}_k^n}{\Delta t} = \frac{\kappa}{\Delta z^2} \left(\tilde{c}_{k+1}^n - 2\tilde{c}_k^n + \tilde{c}_{k-1}^n\right) \quad \text{for} \quad k = 2,\ ...,\ m-1 \tag{5.25}$$

in which $n \geq 1$ stands for the time level. For convenience, we define a dimensionless number that will play a central role in the discretization and solution:

$$\mathsf{D} = \frac{\kappa \Delta t}{\Delta z^2}. \tag{5.26}$$

This definition allows us to write the discretized equation more conveniently as

$$\tilde{c}_k^{n+1} = \tilde{c}_k^n + \mathsf{D} \left(\tilde{c}_{k+1}^n - 2\tilde{c}_k^n + \tilde{c}_{k-1}^n\right) \quad \text{for} \quad k = 2,\ ...,\ m-1. \tag{5.27}$$

The scheme updates the discrete $\tilde{c}_k$ values from their initial values and with the aforementioned boundary conditions (Figure 5-8). Obviously, the algorithm is easily programmed (*e.g.*, `firstdiffusion.m`) and can be tested rapidly.

For simplicity, we start with a gentle profile ($j = 1$, half a wavelength across the domain) and, equipped with our insight in scale analysis, we use a sufficiently small grid spacing

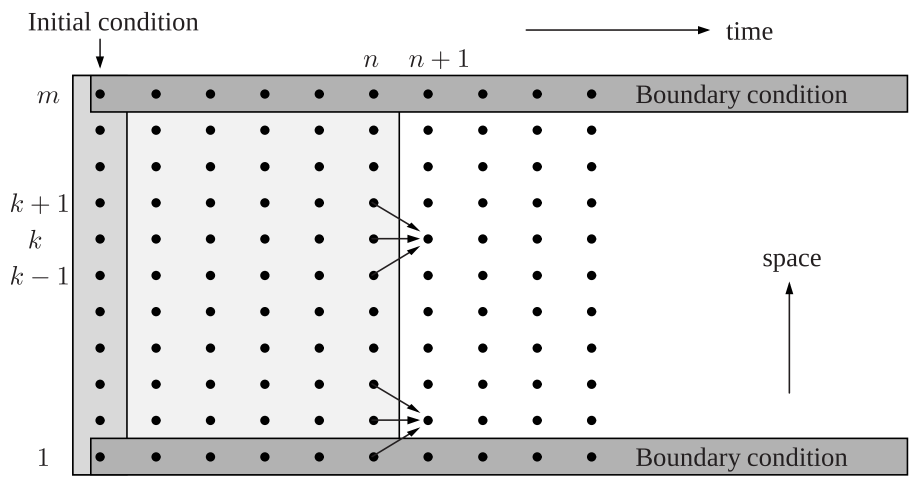

Figure 5-8 Initialized for each grid point, algorithm (5.27) advances the value at node k to the next time step (from n to $n+1$) using the previous values on a stencil spanning points $k-1$, k and $k+1$. A boundary condition is thus needed on each side of the domain, as the original mathematical problem requires. The calculations for the discretized governing equations proceed from $k=2$ to $k=m-1$.

$\Delta z \ll h$ to resolve the cosine function well. To be sure, we take 20 grid points. For the time scale T of the physical process, we use the scale provided by the original equation:

$$\begin{aligned} \frac{\partial c}{\partial t} &= \kappa \, \frac{\partial^2 c}{\partial z^2} \\ \frac{\Delta c}{T} & \quad \kappa \, \frac{\Delta c}{h^2} \end{aligned}$$

to find $T = h^2/\kappa$. Dividing this time scale in 20 steps, we take $\Delta t = T/20 = h^2/20\kappa$ and begin to march algorithm (5.27) forward. Surprisingly, it is not working. After only 20 time steps, the $\tilde{c}_k$ values do not show attenuation but have instead increased by a factor 10^{20}! Furthermore, increasing the spatial resolution to 100 points and reducing the time step proportionally does not help but worsens the situation (Figure 5-9). Yet, there has been no programming error in `firstdiffusion.m`. The problem is more serious: We have stumbled on a crucial aspect of numerical integration, by falling prey to *numerical instability*. The symptoms of numerical instability are explosive behavior and worsening of the problem with increased spatial resolution. At best, the scheme is used outside of a certain domain of validity or, at worst, it is hopeless and in need of replacement by a better, stable scheme. What makes a scheme stable and another unstable is the objective of numerical stability analysis.

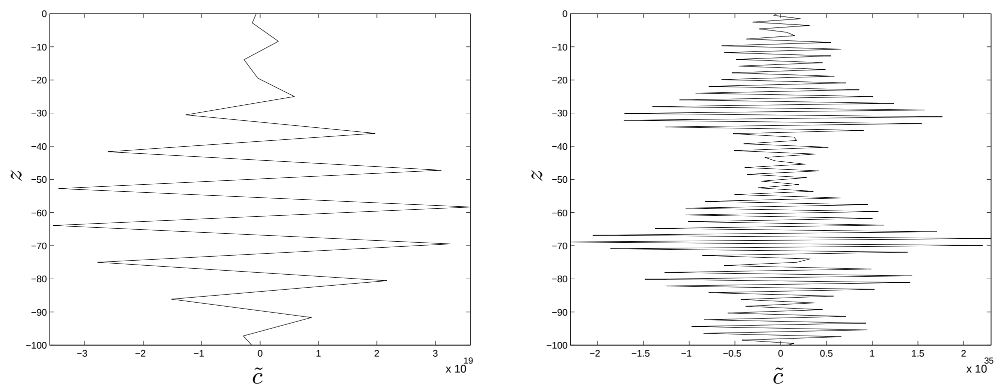

Figure 5-9 Profile of $\tilde{c}$ after 20 time steps of the Euler scheme (5.27). Left panel: 20 grid points and $\Delta t = T/20$. Right panel: 100 grid points and $\Delta t = T/100$. Note the vast difference in values between the two solutions (10^{19} and 10^{35}, respectively), the second solution being much more explosive than the first. Conclusion: Increasing resolution worsens the problem.

5.4 Numerical stability analysis

The most widely used method to investigate the stability of a given numerical scheme is due to John von Neumann[4]. The basic idea of the method is to consider the temporal evolution of simple numerical solutions. As continuous signals and distributions can be expressed as Fourier series of sines and cosines, discrete functions can, too, be decomposed in elementary functions. If one or several of these elementary functions increase without bound over time ('explode'), the reconstructed solution, too, will increase without bound, and the scheme is unstable. Put the other way: A scheme is stable if none among all elementary functions grows without bound over time.

As for Fourier series and simple wave propagation, the elementary functions are periodic. In analogy with the continuous function

$$c(z,t) \;=\; A\, e^{\mathrm{i}\,(k_z z - \omega t)}, \tag{5.28}$$

we use the discrete function $\tilde{c}_k^n$ formed by replacing z by $k\Delta z$ and t by $n\Delta t$:

$$\tilde{c}_k^n \;=\; A\, e^{\mathrm{i}\,(k_z\; k\Delta z - \omega\; n\Delta t)}, \tag{5.29}$$

where k_z is a vertical wavenumber and ω a frequency. To consider periodic behavior in space and possibly explosive behavior in time, k_z is restricted to be real positive whereas $\omega = \omega_r + \mathrm{i}\,\omega_i$ may be complex. Growth without bound occurs if $\omega_i > 0$. (If $\omega_i < 0$, the function decreases exponentially and raises no concern). The origins of z and t do not matter, for they can be adjusted by changing the complex amplitude A.

The range of k_z values is restricted. The lowest value is $k_z = 0$ corresponding to the constant component in (5.22). At the other extreme, the shortest wave is the '$2\Delta x$ *mode*' or 'saw-tooth' ($+1$, -1, $+1$, -1, *etc.*) with $k_z = \pi/\Delta z$. It is most often with this last value

[4]See biography at the end of this chapter.

that trouble occurs, as seen in the rapidly oscillating values generated by the ill-fated Euler scheme (Figure 5-9) and, earlier, aliasing (Section 1.12).

The elementary function, or trial solution, can be recast in the following form to distinguish the temporal growth (or decay) from the propagating part:

$$\tilde{c}_k^n \;=\; A\, e^{+\omega_i \Delta t\; n}\; e^{\mathrm{i}\,(k_z \Delta z\; k - n\omega_r \Delta t\; n)}. \tag{5.30}$$

An alternative way of expressing the elementary function is by introducing a complex number ϱ called the *amplification factor* such that:

$$\tilde{c}_k^n \;=\; A\; \varrho^n\; e^{\mathrm{i}\,(k_z \Delta z)\; k} \tag{5.31a}$$

$$\varrho \;=\; |\varrho|\; e^{\mathrm{i}\;\arg(\varrho)} \tag{5.31b}$$

$$\omega_i \;=\; \frac{1}{\Delta t} \ln |\varrho|, \quad \omega_r \;=\; -\frac{1}{\Delta t} \arg(\varrho). \tag{5.31c}$$

The choice of expression among (5.29), (5.30) and (5.31a) is a matter of ease and convencience.

Stability requires a non-growing numerical solution, with $\omega_i \le 0$ or equivalently $|\varrho| \le 1$. Allowing for *physical* exponential growth – such as the growth of a physically unstable wave – we should entertain the possibility that $c(t)$ may grow as $\exp(\omega_i t)$, in which case $c(t+\Delta t) = c(t)\exp(\omega_i \Delta t) = c(t)\,[1+\mathcal{O}(\Delta t)]$ and $\varrho = 1+\mathcal{O}(\Delta t)$. In other words, instead of $|\varrho| \le 1$, we should adopt the slightly less demanding criterion

$$|\varrho| \le 1 + \mathcal{O}(\Delta t). \tag{5.32}$$

Since there is no exponential growth associated with diffusion, the criterion $|\varrho| \le 1$ applies.

We can now try (5.29) as a solution of the discretized diffusion equation (5.27). After division by the factor $A\varrho^n \exp\left[\mathrm{i}\,(k_z \Delta z)k\right]$ common to all terms, the discretized equation reduces to

$$\varrho \;=\; 1 \;+\; \mathsf{D}\;\left[e^{+\mathrm{i}\,k_z \Delta z} - 2 + e^{-\mathrm{i}\,k_z \Delta z}\right], \tag{5.33}$$

which is satisfied when the amplification factor equals

$$\begin{aligned} \varrho \;&=\; 1 \;-\; 2\mathsf{D}\;\left[1 - \cos(k_z \Delta z)\right] \\ &=\; 1 \;-\; 4\mathsf{D}\sin^2\left(\frac{k_z \Delta z}{2}\right). \end{aligned} \tag{5.34}$$

Since in this case ϱ happens to be real, the stability criterion stipulates $-1 \le \varrho \le 1$, *i.e.*, $4\mathsf{D}\sin^2(k_z \Delta z/2) \le 2$, for all possible k_z values. The most dangerous value is the one that makes $\sin^2(k_z \Delta z/2) = 1$, which is $k_z = \pi/\Delta z$, the wavenumber of the saw-tooth mode. For this mode, ϱ violates $-1 \le \varrho$ unless

$$\mathsf{D} \;=\; \frac{\kappa \Delta t}{\Delta z^2} \;\le\; \frac{1}{2}\,. \tag{5.35}$$

In other words, the Euler scheme is stable only if the time step is shorter than $\Delta z^2/2\kappa$. We are in the presence of a *conditional stability*, and (5.35) is called the *stability condition* of the scheme.

Generally, criterion (5.35) or a similar one in another case is neither necessary nor sufficient since it neglects any effect due to boundary conditions, which can either stabilize an unstable mode or destabilize a stable one. In most situations, however, the criterion obtained by this method turns out to be a necessary condition since it is unlikely that in the middle of the domain boundaries could stabilize an unstable solution, especially the shorter waves that are most prone to instability. On the other hand, boundaries can occasionally destabilize a stable mode in their vicinity. For the preceding scheme applied to the diffusion equation, this is not the case, and (5.35) is both necessary and sufficient.

In addition to stability information, the amplification-factor method also enables a comparison between a numerical property and its physical counterpart. In the case of the diffusion equation, it is the damping rate, but, should the initial equation have described wave propagation, it would have been the dispersion relation. The general solution (5.19) of the exact equation (5.16) leads to the relation

$$\omega_i \ = \ -\,\kappa\, k_z^2, \tag{5.36}$$

which we can compare to the numerical damping rate

$$\begin{aligned} \tilde{\omega}_i &= \frac{1}{\Delta t} \ln |\varrho| \\ &= \frac{1}{\Delta t} \ln \left| 1 - 4\mathsf{D} \sin^2 \left(\frac{k_z \Delta z}{2} \right) \right| . \end{aligned} \tag{5.37}$$

The ratio τ of the numerical damping to the actual damping rate is then given by

$$\tau \ = \ \frac{\tilde{\omega}_i}{\omega_i} \ = \ -\frac{\ln|1 - 4\mathsf{D}\sin^2(k_z\Delta z/2)|}{\mathsf{D}k_z^2\Delta z^2}, \tag{5.38}$$

which for small $k_z \Delta z$, *i.e.*, numerically well resolved modes, behaves as

$$\tau \ = \ 1 \ + \ \left(2\mathsf{D} - \frac{1}{3} \right) \ \left(\frac{k_z \Delta z}{2} \right)^2 \ + \ \mathcal{O}(k_z^4 \Delta z^4). \tag{5.39}$$

For $\mathsf{D} < 1/6$, the numerical scheme dampens less fast than the physical process ($\tau < 1$), while for larger values $1/6 < \mathsf{D} < 1/2$ (*i.e.*, relatively large but still stable time steps), overdamping occurs ($\tau > 1$). In practice, when $\mathsf{D} > 1/4$ (leading to $\varrho < 0$ for the higher k_z values), this overdamping can be unrealistically large and unphysical. The shortest wave resolved by the spatial grid with $k_z \Delta z = \pi$ exhibits not only a saw-tooth pattern in space (as it should) but also a flip-flop behavior in time. This is because, for real negative ϱ, the sequence ϱ^1, ϱ^2, ϱ^3, ... alternates in sign. For $-1 < \varrho < 0$, the solution vanishes not by monotonically decreasing toward zero but instead by oscillating around zero. Though the scheme is stable, the numerical solution behaves unlike the exact solution, and this should be avoided. It is therefore prudent to keep $\mathsf{D} \leq 1/4$ to guarantee a realistic solution.

Let us now give a physical interpretation of the stability condition $2\Delta t \leq \Delta z^2/\kappa$. First, we observe that the instability appears most strongly for the component with the largest wavenumber according to (5.34). Since the length scale of this signal is Δz, the associated diffusion time scale is $\Delta z^2/\kappa$, and the stability criterion expresses the requirement that Δt be set shorter than a fraction of this time scale. It is equivalent to ensuring that the time

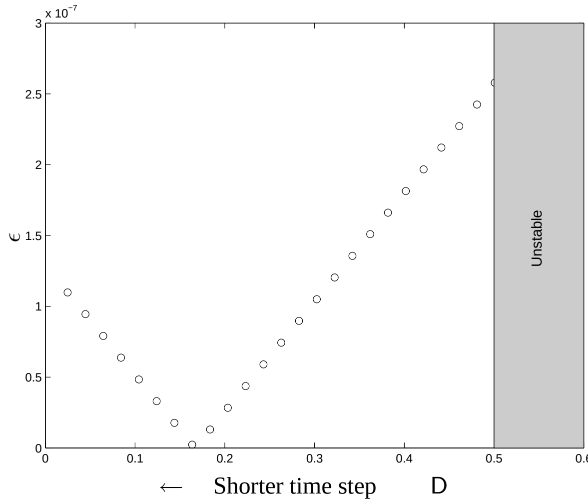

Figure 5-10 Root mean square of error $c - \tilde{c}$ scaled by the initial variation Δc at time $T = h^2/\kappa$ for a fixed space grid ($m = 50$) and decreasing time step (going from right to left). Above $\mathsf{D} = 1/2$, the scheme is unstable and the error extremely large (not plotted). For shorter time steps, the scheme is stable and the error first decreases linearly with D. Below $\mathsf{D} = 1/6 = 0.167$, the error increases again.

step provides an adequate representation of the *shortest* component resolved by the spatial grid. Even when this shortest component is absent from the mathematical solution (in our initial problem only a single length scale, h, was present), it does occur in the numerical solution because of computer round-off errors, and stability is thus conditioned by the *possible* presence of the shortest resolved component. The stability condition ensures that all possible solution components are treated with an adequate time step.

As the preceding simple example shows, the amplification-factor method is easily applied and provides a stability condition as well as other properties of the numerical solution. In practice, however, non-constant coefficients (such as a spatially variable diffusivity κ) or non-uniform spacing of grid points may render its application difficult. Since non-uniform grids may be interpreted as a coordinate transformation, stretching and compressing grid node positions (see also Section 20.7), a non-uniform grid is equivalent to introducing non-constant coefficients into the equation. The procedure is to 'freeze' the coefficients at some value before applying the amplification-factor method and then repeat the analysis with different frozen values within the allotted ranges. Generally, this provides quite accurate estimates of permissible time steps. For nonlinear problems the apprach is to perform a preliminary linearization of the equation, but the quality of the stability condition is not always reliable. Finally, it is important to remember that the amplification-factor method does not deal with boundary conditions. To treat accurately cases with variable coefficients and non-uniform grids and to take boundary conditions into account, the so-called *matrix method* is available (*e.g.*, Kreiss, 1962; Richtmyer and Morton, 1967).

We now have some tools to guarantee stability. Since our diffusion scheme is also consistent, we anticipate convergence by virtue of the Lax-Richtmyer Theorem (see Section 2.7). Let us then verify numerically whether the scheme leads to a linear decrease of the error with decreasing time step. Leaning on the exact solution (5.19) for comparison, we observe (Figure 5-10) that the numerical solution does indeed exhibit a decrease of the error with decreasing time step, but only up to a point (for D decreasing from the stability limit of 0.5 to 1/6). The error increases again for smaller Δt. What happens?

The fact is that two sources of errors (space and time discretization) are simultaneously present and what we are measuring is the *sum* of these errors, not the temporal error in isolation. This can be shown by looking at the modified equation obtained by using a Taylor-series expansion of discrete values $\tilde{c}_{k+1}^n$ *etc.* around $\tilde{c}_k^n$ in the difference equation (5.21). Some algebra leads to

$$\frac{\partial \tilde{c}}{\partial t} = \kappa \, \frac{\partial^2 \tilde{c}}{\partial z^2} + \frac{\kappa \Delta z^2 \, (1 - 6\mathsf{D})}{12} \frac{\partial^4 \tilde{c}}{\partial z^4} + \mathcal{O}(\Delta t^2, \Delta z^4, \Delta t \Delta z^2), \tag{5.40}$$

which shows that the scheme is first order in time (through D) and second order in space. The rebounding error exhibited in Figure 5-10 when Δt is gradually reduced (changing D alone) is readily explained in view of (5.40).

To check on convergence, we should consider the case when both parameters Δt and Δz are reduced simultaneously (Figure 5-11). This is most naturally performed by keeping fixed the stability parameter D, which is a combination of both according to (5.26). The leading error (second term on the right) decreases as Δz^2, except when $\mathsf{D} = 1/6$ in which case the scheme is then of fourth order. It can be shown[5] that in that case the error is on the order of Δz^4. This is consistent with (5.39), where the least error on the damping rate is obtained with $2\mathsf{D} = 1/3$, *i.e.*, $\mathsf{D} = 1/6$, and with Figure 5-10, where the error for fixed Δz is smallest when the time step corresponds to $\mathsf{D} = 1/6$.

5.5 Other one-dimensional schemes

A disadvantage of the simple scheme (5.25) is its fast increase in cost when a higher spatial resolution is sought. For stability reasons Δt decreases as Δz^2, forcing us not only to calculate values at more grid points but also more frequently. For integration over a fixed length of time, the number of calculations grows as m^3. In other words, 1000 more calculations must be performed if the grid size is divided by 10. Because this penalizing increase is rooted in the stability condition, it is imperative to explore other schemes that may have more attractive stability conditions. One such avenue is to consider implicit schemes. With a *fully implicit scheme*, the new values are used in the discretized derivative, and the algorithm is

$$\tilde{c}_k^{n+1} = \tilde{c}_k^n + \mathsf{D} \, \left(\tilde{c}_{k+1}^{n+1} - 2\tilde{c}_k^{n+1} + \tilde{c}_{k-1}^{n+1} \right) \quad k = 2, ..., m-1. \tag{5.41}$$

The application of the stability analysis provides an amplification factor ϱ given implicitely by

$$\varrho \; = \; 1 \; - \; \varrho \, 2\mathsf{D} \; \left[1 - \cos(k_z \Delta z) \right],$$

of which the solution is

$$\varrho \; = \; \frac{1}{1 + 4\mathsf{D} \sin^2(k_z \Delta z/2)} \; \leq \; 1. \tag{5.42}$$

Because this amplification factor is always real and less than unity, there is no stability condition to be met, and the scheme is stable for any time step. This is called *unconditional*

[5]To show this, consider that for $\mathsf{D} = 1/6$, $\Delta t = \Delta z^2/6\kappa$ and all contributions to the error term become proportional to Δz^4.

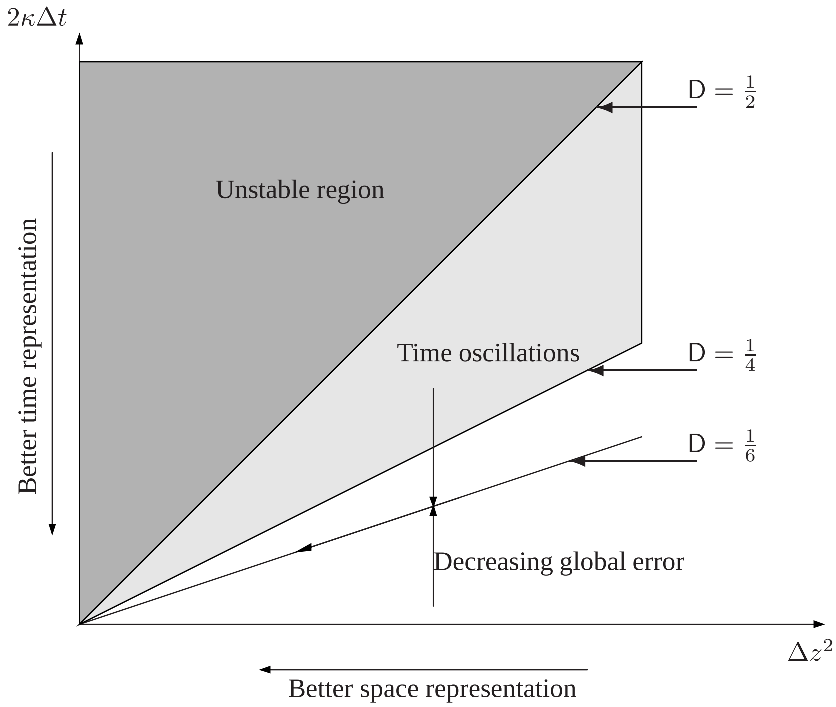

Figure 5-11 Different paths to convergence in the (Δz^2, Δt) plane for the explicit scheme. For excessive values of Δt, $\mathsf{D} \geq 1/2$, the scheme is unstable. Convergence can only be obtained by remaining within the stability region. When Δt alone is reduced (progressing vertically downward in the graph), the error decreases and then increases again. If Δz alone is decreased (progressing horizontally to the left in the graph), the error similarly decreases first and then increases, until the scheme becomes unstable. Reducing both Δt and Δz simultaneously at fixed D within the stability sector leads to monotonic convergence. The convergence rate is highest along the line $\mathsf{D} = 1/6$ because the scheme then happens to be fourth-order accurate.

stability. The implicit scheme therefore allows us in principle to use a time step as large as we wish. We immediately sense, of course, that a large time step cannot be acceptable. Should the time step be too large, the calculated values would not 'explode' but would provide a very inaccurate approximation to the true solution. This is confirmed by comparing the damping of the numerical scheme against its true value:

$$\tau = \frac{\tilde{\omega}_i}{\omega_i} = \frac{\ln|1 + 4\mathsf{D}\,\sin^2(k_z\Delta z/2)|}{4\mathsf{D}\,(k_z\Delta z/2)^2}. \tag{5.43}$$

For small D, the scheme behaves reasonably well, but for larger D, even for scales ten times larger than the grid spacing, the error on the damping rate is similar to the damping rate itself (Figure 5-12).

Setting aside the accuracy restriction, we still have another problem to solve. To calculate the left hand side of (5.41) at grid node k, we have to know the values of the yet-unknowns

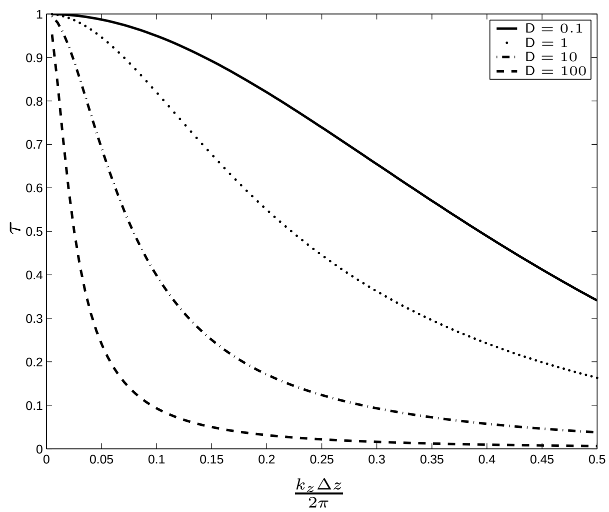

Figure 5-12 Ratio $\tau = \tilde{\omega}_i/\omega_i$ of the numerical damping rate of the implicit scheme to the exact value, as function of $k_z\Delta z/2$ for different values of D. For increasing time steps (increasing value of D), the numerical damping deteriorates rapidly even for relatively well resolved solution components, and it is prudent to use a short time step, if not for stability, at least for accuracy.

$\tilde{c}_{k+1}^{n+1}$ and $\tilde{c}_{k-1}^{n+1}$, which in turn depend on the unknown values at their adjacent nodes. This creates a circular dependency. It is, however, a linear dependency, and all we need to do is to formulate the problem as a set of simultaneous linear equations, *i.e.*, to frame the problem as a matrix to be inverted, once at each time step. Standard numerical techniques are available for such problem, most of them based on the so-called *Gaussian elimination* or *lower-upper decomposition* (*e.g.*, Riley *et al.* 1997). These methods are the most efficient ones for inverting arbitrary matrices of dimension N, and their computational cost increases as N^3. For the one-dimensional[6] case with $N \sim m$, the matrix inversion requires m^3 operations to be performed. Even if we executed only a single time step, the cost would be the same as for the execution of the explicit scheme during the full simulation. We may wonder: Is there some law of conservation of difficulty? Apparently there is, but we can exploit the particular form of the system to reduce the cost.

Since the unknown value at one node depends only the unknown values at the adjacent nodes and not those further away, the matrix of the system is not full but contains many zeroes. All elements are zero except those on the diagonal and those immediately above (corresponding to one neighbor) and immediately below (corresponding to the neighbor on the other side). Such tridiagonal matrix, or *banded matrix*, is quite common, and techniques have been developed for their efficient inversion. The cost of inversion can be reduced to only $5m$ operations[7]. This is comparable to the number of operations for one step of the explicit scheme. And, since the implicit scheme can be run with a longer time step, it can be more efficient than the explicit scheme. A trade off exists, however, between efficiency and accuracy.

An alternative time stepping is the *leapfrog method*, which 'leaps' over the intermediate values, that is, the solution is marched from step $n-1$ to step $n+1$ by using the values

[6]If we anticipate generalization to three dimensions with $N \sim 10^6 - 10^7$ unknowns, a matrix inversion would demand a number of operations proportional to N^3 (at each time step!) and cannot be seriously considered as a viable approach.

[7]See Appendix 22.6 for the formulation of the algorithm called upper-lower decomposition.

at intermediate step n for the terms on the right-hand side of the equation. Applied to the diffusion equation, the leapfrog scheme generates the following algorithm:

$$\tilde{c}_k^{n+1} \;=\; \tilde{c}_k^{n-1} \;+\; 2\mathsf{D}\;\left(\tilde{c}_{k+1}^n - 2\tilde{c}_k^n + \tilde{c}_{k-1}^n\right). \tag{5.44}$$

where $\mathsf{D} = \kappa\Delta t/\Delta z^2$ once again.

Because by the time values at time level $n+1$ are sought all values up to time level n are already known, this algorithm is explicit and does not require any matrix inversion. We can analyze its stability by considering, as before, a single Fourier mode of the type (5.29). The usual substitution into the discrete equation, this time (5.44), application of trigonometric formulas and division by the Fourier mode itself then lead to the following equation for the amplification factor ϱ of the leapfrog scheme:

$$\varrho \;=\; \frac{1}{\varrho} \;-\; 8\mathsf{D}\sin^2\left(\frac{k_z\Delta z}{2}\right). \tag{5.45}$$

This equation is quadratic and has therefore two solutions for ϱ, corresponding to two temporal modes. Only a single mode was expected because the original equation had only a first-order time derivative in time, but, obviously, the scheme has introduced a second, *spurious mode*. With $b = 4\mathsf{D}\sin^2(k_z\Delta z/2)$, the two solutions are

$$\varrho \;=\; -\,b \pm \sqrt{b^2+1}. \tag{5.46}$$

The physical mode is $\varrho = -b + \sqrt{b^2+1}$ because for well resolved components ($k_z\Delta z \ll 1$ and thus $b \ll 1$) it is approximately $\varrho \simeq 1 - b \simeq 1 - \mathsf{D}k_z^2\Delta z^2$, as it should be [see (5.34)]. Its value is always less than one, and the physical mode is numerically stable. The other solution, $\varrho = -b - \sqrt{b^2+1}$ corresponds to the spurious mode and, unfortunately, has a magnitude always larger than one, jeopardizing the overall stability of the scheme. This is an example of *unconditional instability*. Note, however, that although unstable in the diffusion case the leapfrog scheme will be found to be stable when applied to other equations.

The spurious mode causes numerical instability and must therefore be suppressed. One basic method is *filtering* (see Section 10.6). Because numerical instability is manifested by flip-flop in time (due to the negative ϱ value), averaging over two consecutive time steps or taking some kind of running average, called filtering, eliminates the flip-flop mode. Filtering, unfortunately, also alters the physical mode, and, as a rule, it is always prudent not to have a large flip-flop mode in the first place. Its elimination should be done *a priori*, not *a posteriori*. In the case of models using leapfrog for the sake of other terms in the equation, such as advection terms which it handles in a stable manner, the diffusion term is generally discretized at time level $n-1$ rather than n, rendering the scheme as far as the diffusion part is concerned equivalent to the explicit Euler scheme with time step of $2\Delta t$.

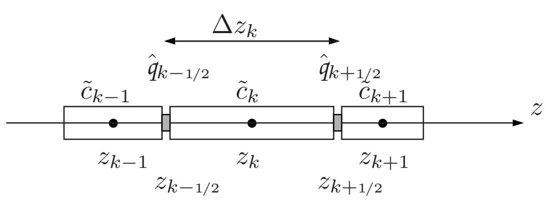

Figure 5-13 Arrangement of cells and interfaces for the finite-volume technique. Concentration values are defined at cell centers whereas flux values are defined between cells. Cell lengths do not have to be uniform.

Finally, we can illustrate the *finite-volume technique* in the more general case of non-uniform diffusion and variable grid spacing. In analogy with (3.37), we integrate the diffusion equation over an interval between two consecutive cell boundaries and over one time step to obtain the grid-cell averages $\bar{c}$ (Figure 5-13)

$$\frac{\bar{c}_k^{n+1} - \bar{c}_k^n}{\Delta t_n} \; + \; \frac{\hat{q}_{k+1/2} - \hat{q}_{k-1/2}}{\Delta z_k} \; = \; 0, \tag{5.47}$$

assuming that the time-averaged flux at the interface between cells

$$\hat{q} \; = \; \frac{1}{\Delta t_n} \int_{t^n}^{t^{n+1}} -\kappa \, \frac{\partial c}{\partial z} \, dt \tag{5.48}$$

is somehow known. Up to this point, the equations are exact. The variable c appearing in the expression of the flux is the actual function, including all its subgrid-scale variations, whereas (5.47) deals only with space-time averages. Discretization enters the formulation as we relate the time-averaged flux to the space-averaged function $\bar{c}$ to close the problem. We can for example estimate the flux using a factor α of implicitness and a gradient approximation:

$$\hat{q}_{k-1/2} \; \simeq \; -(1-\alpha) \, \kappa_{k-1/2} \frac{\tilde{c}_k^n - \tilde{c}_{k-1}^n}{z_k - z_{k-1}} - \alpha \, \kappa_{k-1/2} \frac{\tilde{c}_k^{n+1} - \tilde{c}_{k-1}^{n+1}}{z_k - z_{k-1}}, \tag{5.49}$$

where $\tilde{c}$ is now interpreted as the numerical estimate of the spatial averages. The numerical scheme reads

$$\begin{aligned} \tilde{c}_k^{n+1} = \tilde{c}_k^n \quad &+ \quad (1-\alpha) \frac{\kappa_{k+1/2} \Delta t_n}{\Delta z_k} \frac{\tilde{c}_{k+1}^n - \tilde{c}_k^n}{z_{k+1} - z_k} - (1-\alpha) \frac{\kappa_{k-1/2} \Delta t_n}{\Delta z_k} \frac{\tilde{c}_k^n - \tilde{c}_{k-1}^n}{z_k - z_{k-1}} \\ &+ \quad \alpha \, \frac{\kappa_{k+1/2} \Delta t_n}{\Delta z_k} \frac{\tilde{c}_{k+1}^{n+1} - \tilde{c}_k^{n+1}}{z_{k+1} - z_k} - \alpha \, \frac{\kappa_{k-1/2} \Delta t_n}{\Delta z_k} \frac{\tilde{c}_k^{n+1} - \tilde{c}_{k-1}^{n+1}}{z_k - z_{k-1}}. \end{aligned} \tag{5.50}$$

With uniform grid spacing, κ constant and $\alpha = 0$, we recover (5.25). Since the present finite-volume scheme is by construction conservative (see Section 3.9), we have incidentally proven that (5.25) is conservative in the case of a uniform grid and constant diffusivity, a property that can be verified numerically in `firstdiffusion.m` even in the unstable case.

In practice, it is expedient to program the calculations with the flux values defined and stored alongside the concentration values. The computations then entail two stages in every step: first the computation of the flux values from the concentration values at the same time level and then the update the concentration values from these most recent flux values. In this manner, it is clear how to take into account variable parameters such as the local value of the diffusivity κ (at cell edges rather than cell centers), local cell length, and momentary time step. The approach is also naturally suited for the implementation of flux boundary conditions.

5.6 Multi-dimensional numerical schemes

Explicit schemes are readily generalized to two and three dimensions[8] with indices i, j and k being grid positions in the respective directions x, y and z:

$$\begin{aligned}\tilde{c}^{n+1} = \tilde{c}^{n} &+ \frac{\mathcal{A}\Delta t}{\Delta x^2}\left(\tilde{c}^{n}_{i+1} - 2\tilde{c}^{n} + \tilde{c}^{n}_{i-1}\right)\\ &+ \frac{\mathcal{A}\Delta t}{\Delta y^2}\left(\tilde{c}^{n}_{j+1} - 2\tilde{c}^{n} + \tilde{c}^{n}_{j-1}\right)\\ &+ \frac{\kappa\Delta t}{\Delta z^2}\left(\tilde{c}^{n}_{k+1} - 2\tilde{c}^{n} + \tilde{c}^{n}_{k-1}\right). \end{aligned} \tag{5.51}$$

The stability condition is readily obtained by using the amplification-factor analysis. Substituting the Fourier mode

$$\tilde{c}^{n} = A\varrho^{n}\, e^{\mathrm{i}\,(i\ k_x\Delta x)} e^{\mathrm{i}\,(j\ k_y\Delta y)} e^{\mathrm{i}\,(k\ k_z\Delta z)} \tag{5.52}$$

in the discrete equation, we obtain the following generalization of (5.35):

$$\frac{\mathcal{A}\Delta t}{\Delta x^2} + \frac{\mathcal{A}\Delta t}{\Delta y^2} + \frac{\kappa\Delta t}{\Delta z^2} \leq \frac{1}{2}. \tag{5.53}$$

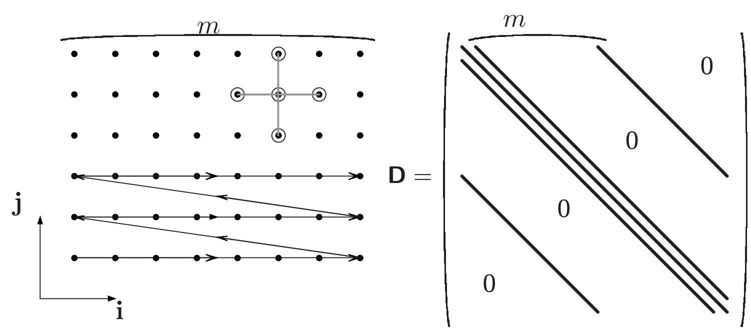

Figure 5-14 If the numerical state vector is constructed row by row in two dimensions, $\tilde{c}_{i,j}$ is the element $(j-1)m+i$ of $\mathbf{x}$. Since the diffusion operator at point i, j involves $\tilde{c}_{i,j}$, $\tilde{c}_{i+1,j}$, $\tilde{c}_{i-1,j}$, $\tilde{c}_{i,j-1}$ and $\tilde{c}_{i,j+1}$, the matrix to be inverted has zero elements everywhere, except on the diagonal (the point itself), the superdiagonal (point $i+1$, j), the subdiagonal (point $i-1$, k) and two lines situated $\pm m$ away from the diagonal (point i, $j \pm 1$).

The implicit version of the scheme is not much more complicated and, again, is unconditionally stable. However, the associated matrix is no longer tridiagonal but has a slightly more complicated structure (Figure 5-14). Unfortunately, there exists no direct solver for which the cost remains proportional to the size of the problem. Several strategies can be developed to keep the method "implicit" with affordable costs.

[8]In order not to overload the notation, indices are written here only if they differ from the local grid point index. Therefore, $\tilde{c}(t^n, x_i, y_j, z_k)$ is written $\tilde{c}^n$ whereas $\tilde{c}^n_{j+1}$ stands for $\tilde{c}(t^n, x_i, y_{j+1}, z_k)$.

In any case, a direct solver is in some way an overkill. It inverts the matrix exactly up to rounding errors, and such precision is not necessary in view of the much larger errors associated with the discretization (see Section 4.8). We can therefore afford to invert the matrix only approximately, and this can be accomplished by the use of iterative methods, which deliver solutions to any degree of approximation depending on the number of iterations performed. A small number of iterations usually yields an acceptable solution because the starting guess values may be taken as the values computed at the preceding time step. Two popular *iterative solvers* of linear systems are the Gauss-Seidel method and the Jacobi method, but there exist many other iterative solvers, more or less optimized for different kinds of problems and computers (*e.g.*, Dongarra *et al.* 1998). In general, most program libraries offer a vast catalogue of methods, and we will only mention a few general approaches, giving more detail on specific methods later when we need to solve a Poisson equation for a pressure or streamfunction (Section 7.6).

Any linear system of simultaneous equations can be cast as

$$\mathsf{A}\mathbf{x} \;=\; \mathsf{b} \tag{5.54}$$

where the matrix A gathers all the coefficients, the vector $\mathbf{x}$ all the unknowns, and the vector b the boundary values and external forcing terms, if any. The objective of an iterative method is to solve this system by generating a sequence of $\mathbf{x}^{(p)}$ that starts from a guess vector $\mathbf{x}^0$ and gradually converges toward the solution. The algorithm is a repeated application of

$$\mathsf{B}\mathbf{x}^{(p+1)} \;=\; \mathsf{C}\mathbf{x}^{(p)} + \mathsf{b} \tag{5.55}$$

where B must be easy to invert, otherwise there is no gain, and is thus typically a diagonal or triangular matrix (non-zero elements only on the diagonal or on the diagonal and one side of it). At convergence, $\mathbf{x}^{(p+1)} = \mathbf{x}^{(p)}$ and we must therefore have $\mathsf{B} - \mathsf{C} = \mathsf{A}$ to have solved (5.54). The closer B is to A, the faster the convergence since at the limit of $\mathsf{B} = \mathsf{A}$ a single iteration would yield the exact answer. Using $\mathsf{C} = \mathsf{B} - \mathsf{A}$, we can rewrite the iterative step as

$$\mathbf{x}^{(p+1)} \;=\; \mathbf{x}^{(p)} \;+\; \mathsf{B}^{-1}\left(\mathsf{b} - \mathsf{A}\mathbf{x}^{(p)}\right) \tag{5.56}$$

which is reminiscent of a time stepping method. Here, B^{-1} denotes the inverse of B. The Jacobi method uses a diagonal matrix B, while the Gauss-Seidel method uses a triangular matrix B. More advanced methods exist that converge faster than these two. Those will be outlined in Section 7.6.

In GFD applications, diffusion is rarely dominant (except for vertical diffusion in strong turbulence), and stability restrictions associated with diffusion are rarely penalizing. Therefore, it is advantageous to make the scheme implicit only in the direction of the strongest diffusion (or largest variability of diffusion), usually the vertical, and to treat the horizontal components explicitly:

$$\begin{aligned}\tilde{c}^{n+1} = \tilde{c}^{n} \quad &+ \quad \frac{\mathcal{A}\Delta t}{\Delta x^2}\left(\tilde{c}^{n}_{i+1} - 2\tilde{c}^{n} + \tilde{c}^{n}_{i-1}\right)\\ &+ \quad \frac{\mathcal{A}\Delta t}{\Delta y^2}\left(\tilde{c}^{n}_{j+1} - 2\tilde{c}^{n} + \tilde{c}^{n}_{j-1}\right)\\ &+ \quad \frac{\kappa\Delta t}{\Delta z^2}\left(\tilde{c}^{n+1}_{k+1} - 2\tilde{c}^{n+1} + \tilde{c}^{n+1}_{k-1}\right).\end{aligned} \tag{5.57}$$

Then, instead of inverting a matrix with multiple bands of non-zero elements, we only need to invert a tridiagonal matrix at each point of the horizontal grid. *Alternating direction implicit* (ADI) methods use the same approach, but change the direction of the implicit sweep through the matrix at every time step. This helps when stability of the horizontal diffusion discretization is a concern.

The biggest challenge associated with diffusion in GFD models is, however, not their numerical stability but rather their physical basis because diffusion is often introduced as a parameterization of unresolved processes. Occasionally, the unphysical behavior of the discretization may create a problem (*e.g.*, Beckers *et al.*, 2000).

Analytical Problems

5-1. What would the energy spectrum $E_k(k)$ be in a turbulent flow where all length scales were contributing equally to dissipation? Is this spectrum realistic?

5-2. Knowing that the average atmospheric pressure on the earth's surface is 1.013 $\times$ 10^5 N/m^2 and that the earth's average radius is 6371 km, deduce the mass of the atmosphere. Then, using this and the fact that the earth receives 1.75 $\times$ 10^{17} W from the sun globally, and assuming that half of the energy received from the sun is being dissipated in the atmosphere, estimate the rate of dissipation ϵ in the atmosphere. Assuming finally that turbulence in the atmosphere obeys the Kolmogorov theory, estimate the smallest eddy scale in the air, its ratio to the largest scale (the earth's radius), and the large-scale wind velocity. Is this velocity scale realistic?

5-3. In a 15-m coastal zone, the water density is 1032 kg/m^3 and the horizontal velocity scale is 0.80 m/s. What are the Reynolds number and the diameter of the shortest eddies? Approximately how many watts are dissipated per square meter of the ocean?

5-4. If you have to simulate the coastal ocean of the previous problem with a numerical model that includes 20 grid points over the vertical, what would be a reasonable value for the vertical eddy diffusivity?

5-5. Estimate the time it takes to reduce by a factor 2 a salinity variation in an ocean of depth $H = 1000$ m in the presence of salt diffusion, with a diffusion coefficient κ. Compare two solutions, one using the molecular diffusion ($\kappa = 10^{-9}$ m^2/s) and the other a turbulent diffusion typical of the deep ocean ($\kappa = 10^{-4}$ m^2/s).

5-6. A deposition at the sea surface of a tracer (normalized and without units) can be modeled by a constant flux $q = -10^{-4}$ m/s. At depth $z = -99$ m a strong current is present and flushes the vertically diffused tracer so that $c = 0$ is maintained at that level. Assuming the diffusion coefficient has the profile of Figure 5-15, calculate the steady solution for the tracer distribution.

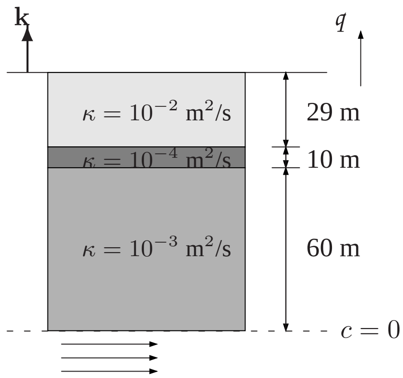

Figure 5-15 Values of a non-uniform eddy diffusion for analytical Problem 5-6. A flux condition is imposed at the surface while $c = 0$ at the base of the domain.

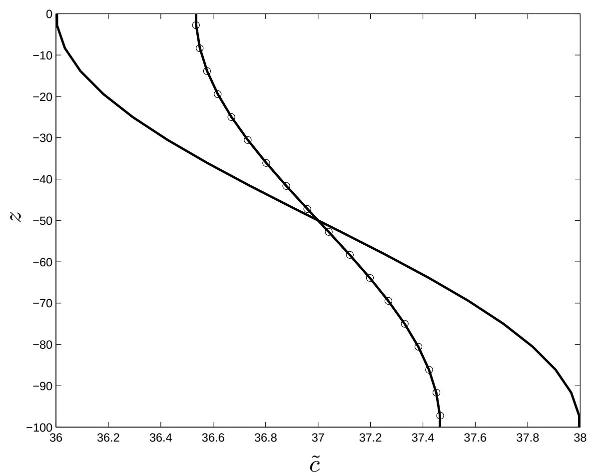

Figure 5-16 With a time step such that $\mathsf{D} = 0.1$, the initial condition (single line) of the 1D diffusion problem has been damped after 500 time steps and the numerical solution of the explicit scheme (open circles) is almost indistinguishable from the exact solution (shown as a line crossing the circles), even with only 30 grid points across the domain.

Numerical Exercises

5-1. Cure the unstable version `firstdiffusion.m` by adapting the time step and verify that below the limit (5.35) the scheme is indeed stable and provides accurate solutions (Figure 5-16).

5-2. For a 1D Euler scheme with implicit factor α, constant grid size and constant diffusion coefficient, prove that the stability condition is $(1 - 2\alpha)\mathsf{D} \leq 1/2$.

5-3. Implement periodic boundary conditions in the 1D diffusion problem (*i.e.*, $c_{\text{top}} = c_{\text{bottom}}$ and $q_{\text{top}} = q_{\text{bottom}}$). Then, search the internet for a tridiagonal matrix inversion algorithm adapted to periodic boundary conditions and implement it.

5-4. Implement the 1D finite-volume method with an implicit factor α and variable diffusion coefficient. Set the problem with the same initial and boundary conditions as in the beginning of Section 5.3. Verify your solution against the exact solution (5.19).

5-5. Apply the code developed in Section 5.6 to the analytical problem 5-6. Start with an arbitrary initial condition and march in time until the solution becomes stationary. Estimate *a priori* the permitted time step and the minimum total number of time steps, depending on the implicit factor. Take $\Delta z = 2$, track convergence during the calculations and compare your final solution with the exact solution for $\Delta z = 2$. Also try to implement the naive discretization

$$\begin{aligned} \frac{\partial}{\partial z}\left(\kappa\,\frac{\partial c}{\partial z}\right)\bigg|_{z_k} &= \kappa\,\frac{\partial^2 c}{\partial z^2}\bigg|_{z_k} + \frac{\partial \kappa}{\partial z}\bigg|_{z_k}\,\frac{\partial c}{\partial z}\bigg|_{z_k} \\ &\sim \frac{\kappa_k\left(\tilde{c}_{k+1} - 2\tilde{c}_k + \tilde{c}_{k-1}\right)}{\Delta z^2} \\ &+ \frac{\left(\kappa_{k+1} - \kappa_{k-1}\right)}{2\Delta z}\frac{\left(\tilde{c}_{k+1} - \tilde{c}_{k-1}\right)}{2\Delta z}. \end{aligned} \tag{5.58}$$

5-6. The Dufort-Frankel scheme approximates the diffusion equation by

$$\tilde{c}_k^{n+1} \;=\; \tilde{c}_k^{n-1} \;+\; 2\mathsf{D}\;\left[\tilde{c}_{k+1}^n - (\tilde{c}_k^{n+1} + \tilde{c}_k^{n-1}) + \tilde{c}_{k-1}^n\right]. \tag{5.59}$$

Verify the consistency of this scheme. What relation must be imposed between Δt and Δz when each approaches zero to ensure consistency? Then, analyze numerical stability using the amplification-factor method.

Andrey Nikolaevich Kolmogorov
1903 – 1987

Andrey Kolmogorov was attracted to mathematics from an early age and, at the time of his studies at Moscow State University, sought the company of the most outstanding mathematicians. While still an undergraduate student, he began research and published several papers of international importance, chiefly on set theory. He had already 18 publications by the time he completed his doctorate in 1929. Kolmogororov's contributions to mathematics spanned a variety of topics, and he is perhaps best known for his work on probability theory and stochastic processes.

Research in stochastic processes led to a study of turbulent flow from a jet engine and, from there, to two famous papers on isotropic turbulence in 1941. It has been remarked that this pair of papers rank among the most important ones since Osborne Reynolds in the long and unfinished history of turbulence theory.

Kolmogorov found much inspiration for his work during nature walks in the outskirts of Moscow accompanied by colleagues and students. The brainstorming that had occurred during the walk often concluded in serious work around the dinner table upon return home. (*Photo from American Mathematical Society*)

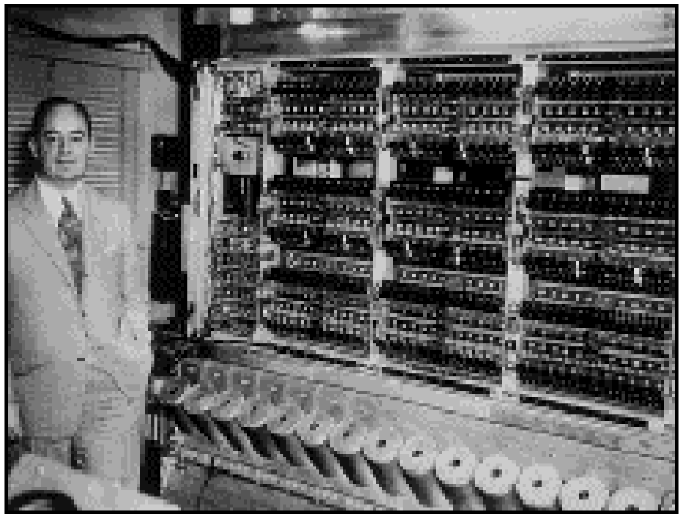

John Louis von Neumann
1903 – 1957

John von Neumann was a child prodigy. At age six, he could mentally divide eight-digit numbers and memorize the entire page of a telephone book in a matter of minutes, to the amazement of his parents' guests at home. Shortly after obtaining his doctorate in 1928, he left his native Hungary to take an appointment at Princeton University (USA). When the Institute for Advanced Studies was founded there in 1933, he was named one of the original Professors of Mathematics.

Besides seminal contributions to ergodic theory, group theory and quantum mechanics, his work included the application of electronic computers to applied mathematics. Together with Jule Charney (see biography at end of Chapter 16) in the 1940s, he selected weather forecasting as the first challenge for the emerging electronic computers, which he helped assemble. Unlike Lewis Richardson before them, von Neumann and Charney started with a single equation, the barotropic vorticity equation. The results exceeded expectations and scientific computing was launched.

A famous quote attributed to von Neumann is: "If people do not believe that mathematics is simple, it is only because they do not realize how complicated life is." (*Photo from Virginia Polytechnic Institute and State University*)

Chapter 6

Transport and Fate

(October 18, 2006) **SUMMARY**: Here, we augment the diffusion equation of the preceding chapter to include the effects of advection (transport by the moving fluid) and fate (diffusion, plus possible source and decay along the way). The numerical section begins with the design of schemes for advection in a fixed (Eulerian) framework and then extends those to include the discretization of diffusion and source/decay terms. Most of the developments are presented in one dimension before generalization to multiple dimensions.

6.1 Combination of advection and diffusion

When considering the heat (3.25), salt (3.16), humidity (3.17) or density (4.8) equations of Geophysical Fluid Dynamics, we note that they each include three types of terms. The first, a time derivative, tells how the variable is changing over time. The second is a group of three terms with velocity components and spatial derivatives, sometimes hidden in the material derivative d/dt. Their effect is to transport the substance with the flow. Collectively, these terms are called *advection*. Finally, the last group of terms, on the right-hand sides, includes an assortment of diffusivities and second-order spatial derivatives. In the light of Chapter 5, we identify these with *diffusion*. Their effect is to spread the substance spatially along and across the flow. Using a generic formulation, we are brought to study an equation of the type

$$\frac{\partial c}{\partial t} + u\,\frac{\partial c}{\partial x} + v\,\frac{\partial c}{\partial y} + w\,\frac{\partial c}{\partial z} = \frac{\partial}{\partial x}\left(\mathcal{A}\frac{\partial c}{\partial x}\right) + \frac{\partial}{\partial y}\left(\mathcal{A}\frac{\partial c}{\partial y}\right) + \frac{\partial}{\partial z}\left(\kappa\frac{\partial c}{\partial z}\right), \quad (6.1)$$

where the variable c may stand for any of the aforementioned variables or represent a substance imbedded in the fluid, such as a pollutant in the atmosphere or in the sea. Note the anisotropy between the horizontal and vertical directions ($\mathcal{A}$ generally $\gg \kappa$).

The examples in the following figures illustrate the combined effects of advection and diffusion. Figure 6-1 shows the fate of the Rhône River waters as they enter the Mediterranean Sea. Advection pulls the plume offshore while diffusion dilutes it. Figure 6-2 is a remarkable

Figure 6-1 Rhône River plume discharging in the Gulf of Lions (circa 43°N) and carrying sediments into the Mediterranean Sea. This satellite picture was taken on 26 February 1999. (*Satellite image provided by the SeaWiFS Project, NASA/Goddard Space Flight Center*)

satellite picture, showing wind advection of sand from the Sahara Desert westward from Africa to Cape Verde (white band across the lower part of the picture) at the same time as, and independently from, marine transport of suspended matter southwestward from the Cape Verde islands (Von Kármán vortices in left of middle of the picture). While sand is being blown quickly and without much diffusion in the air, the sediments follow convoluted paths in the water, pointing to a disparity between the relative effects of advection and diffusion in the atmosphere and ocean.

Often, the substance being carried by the fluid is not simply moved and diffused by the flow. It may also be created or lost along the way. Such is the case of particle matter, which tends to settle at the bottom. Chemical species can be produced by reaction between parent chemicals and be lost by participating in other reactions. An example of this is sulfuric acid (H_2SO_4) in the atmosphere: It is produced by reaction of sulfur dioxide (SO_2) from combustion and lost by precipitation (acid rain or snow). Tritium, a naturally radioactive form of hydrogen enters the ocean by contact with air at the surface and disintegrates along its oceanic journey to become Helium. Dissolved oxygen in the sea is consumed by biological activity and is replenished by contact with air at the surface.

To incorporate these processes, we augment the advection-diffusion equation (6.1) by adding source and sink terms in the right-hand side:

$$\begin{aligned} \frac{\partial c}{\partial t} + u\frac{\partial c}{\partial x} + v\frac{\partial c}{\partial y} + w\frac{\partial c}{\partial z} &= \\ \frac{\partial}{\partial x}\left(\mathcal{A}\frac{\partial c}{\partial x}\right) + \frac{\partial}{\partial y}\left(\mathcal{A}\frac{\partial c}{\partial y}\right) &+ \frac{\partial}{\partial z}\left(\kappa\frac{\partial c}{\partial z}\right) + S - Kc, \end{aligned} \tag{6.2}$$

where the term S stands for the source, the formulation of which depends on the particular process of formation of the substance, and K is a coefficient of decay, which affects how quickly (large K) or slowly (small K) the substance is being lost.

At one-dimension, say in the x–direction, and with constant diffusivity $\mathcal{A}$, the equation

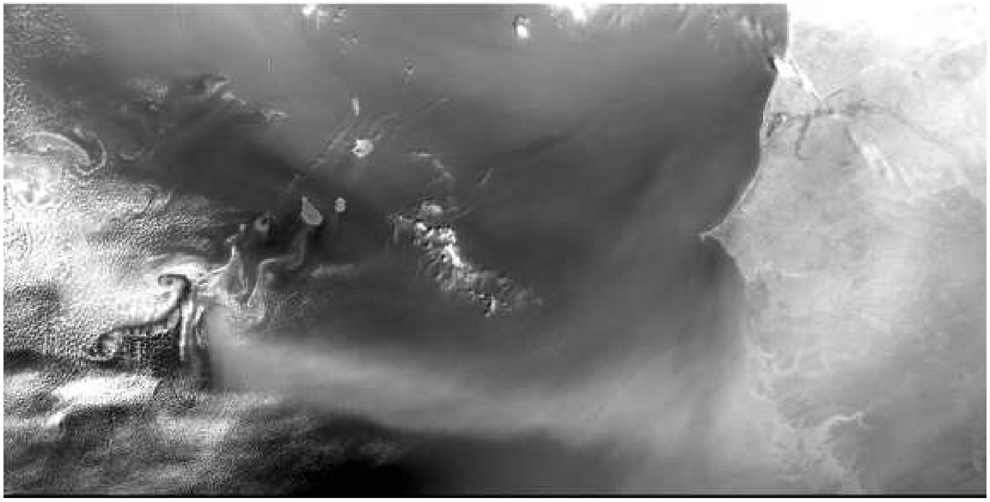

Figure 6-2 Sahara dust blown by the wind from the African continent over the ocean toward Cape Verde islands (15–17°N), while suspended matter in the water is being transported southwestward by a series of Von Kármán vortices in the wake of the islands. Note in passing how these vortices in the water affect the overlying cloud patterns. (*Jacques Descloitres, MODIS Land Science Team*)

reduces to:

$$\frac{\partial c}{\partial t} + u\,\frac{\partial c}{\partial x} = \mathcal{A}\,\frac{\partial^2 c}{\partial x^2} + S - Kc. \tag{6.3}$$

Several properties of the advection-diffusion equation are worth noting because they bear on the numerical procedures that follow: In the absence of source and sink, the total amount of the substance is conserved, and, in the further absence of diffusion, the variance of the concentration distribution, too, is conserved over time.

When we integrate Equation (6.2) over the domain volume $\mathcal{V}$, we can readily integrate the diffusion terms and, if the flux is zero at all boundaries, these vanish, and we obtain:

$$\frac{d}{dt}\int_{\mathcal{V}} c\,d\mathcal{V} = -\int_{\mathcal{V}} \left(u\,\frac{\partial c}{\partial x} + v\,\frac{\partial c}{\partial y} + w\,\frac{\partial c}{\partial z}\right) d\mathcal{V} + \int_{\mathcal{V}} S\,d\mathcal{V} - \int_{\mathcal{V}} Kc\,d\mathcal{V}.$$

After an integration by parts, the first set of terms on the right can be rewritten as

$$\frac{d}{dt}\int_{\mathcal{V}} c\,d\mathcal{V} = +\int_{\mathcal{V}} c\left(\frac{\partial u}{\partial x} + \frac{\partial v}{\partial y} + \frac{\partial w}{\partial z}\right) d\mathcal{V} + \int_{\mathcal{V}} S\,d\mathcal{V} - \int_{\mathcal{V}} Kc\,d\mathcal{V},$$

as long as there is no flux or no advection at all boundaries. Invoking the continuity equation (4.21d) reduces the first term on the right to zero, and we obtain simply:

$$\frac{d}{dt}\int_{\mathcal{V}} c\,d\mathcal{V} = \int_{\mathcal{V}} S\,d\mathcal{V} - \int_{\mathcal{V}} Kc\,d\mathcal{V}. \tag{6.4}$$

Since the concentration c represents the amount of the substance per volume, its integral over the volume is its total amount. Equation (6.4) simply states that this amount remains constant over time when there is no source ($S = 0$) or sink ($K = 0$). Put another way, the substance is moved around but conserved.

Now, if we multiply Equation (6.2) by c and then integrate over the domain, we can integrate the diffusion terms by parts and, if the flux is again zero at all boundaries, we have:

$$\begin{aligned} \frac{1}{2}\frac{d}{dt}\int_{\mathcal{V}} c^2 \, d\mathcal{V} &= -\int_{\mathcal{V}} \left[\mathcal{A}\left(\frac{\partial c}{\partial x}\right)^2 + \mathcal{A}\left(\frac{\partial c}{\partial y}\right)^2 + \kappa\left(\frac{\partial c}{\partial z}\right)^2 \right] d\mathcal{V} \\ &+ \int_{\mathcal{V}} Sc \, d\mathcal{V} - \int_{\mathcal{V}} Kc^2 \, d\mathcal{V}. \end{aligned} \tag{6.5}$$

With no diffusion, source or sink, the right-hand side is zero, and *variance* is conserved in time. Diffusion and decay tend to reduce variance, whereas a source tends to increase it.

This conservation property can be extended, still in the absence of diffusion, source and sink, to any power c^p of c, by multiplying the equation by c^{p-1} before integration. The conservation property even holds for any function $F(c)$. It goes without saying that numerical methods cannot conserve all these quantities, but it is highly desirable that they conserve at least the first two (total amount and variance).

There is one more property worth mentioning, which we will state without demonstration but justify in a few words. Because diffusion acts to smooth the distribution of c, it removes the substance from the areas of higher concentration and brings it into regions of lower concentration. Hence, due to diffusion alone, the maximum of c can only diminish and its minimum can only increase. Advection only redistributes existing values, thus not changing either minimum and maximum. In the absence of source and sink, therefore, no future value of c can fall outside the initial range of values. This is called the *max-min property*. Exceptions are the presence of a source or sink, and the import through one of the boundaries of concentration values outside the initial range.

We call a numerical scheme that maintains the max-min property a *monotonic scheme* or *monotonicity preserving* scheme[1]. Alternatively, the property of *boundedness* is often used to describe a physical solution that does not generate new extrema. If c is initially positive everywhere, as it should be, the absence of new extrema keeps the variable positive at all future times, another property called *positiveness*. A monotonic scheme is thus positive but the reverse is not necessarily true.

6.2 Relative importance of advection: The Peclet number

Since the preceding equations combine the effects of both advection and diffusion, it is important to compare the relative importance of one to the other. In a specific situation, could it be that one dominates over the other or that both impact concentration values to the same extent? To answer this question, we turn once again to scales. Introducing a length scale L, velocity scale U, diffusivity scale D, and a scale Δc to measure concentration differences,

[1] Some computational fluid dynamicists do make a difference between these two labels, but this minor point lies beyond our present text.

we note that advection scales like $U\Delta c/L$ and diffusion like $D\Delta c/L^2$. We can then compare the two processes by forming the ratio of their scales:

$$\frac{\text{advection}}{\text{diffusion}} = \frac{U\Delta c/L}{D\Delta c/L^2} = \frac{UL}{D}.$$

This ratio is by construction dimensionless. It bears the name of Peclet number[2] and is denoted by Pe:

$$Pe = \frac{UL}{D}, \tag{6.6}$$

where the scales U, L and D may stand for the scales of either horizontal (u, v, x, y and $\mathcal{A}$) or vertical (w, z and κ) variables but not a mix of them. The Peclet number leads to an immediate criterion, as follows.

If $Pe \ll 1$ (in practice, if $Pe < 0.1$), the advection term is significantly smaller than the diffusion term. Physically, diffusion dominates and advection is negligible. Diffusive spreading occurs almost symmetrically despite the directional bias of the weak flow. If we wish to simplify the problem, we may drop the advection term [$u\partial c/\partial x$ in (6.3)], as if u were zero. The relative error committed in the solution is expected to be on the order of the Peclet number, and the smaller Pe, the smaller the error. The methods developed in the preceding chapter were based on such simplification and thus apply whenever $Pe \ll 1$.

If $Pe \gg 1$ (in practice, if $Pe > 10$), it is the reverse: the advection term is now significantly larger than the diffusion term. Physically, advection dominates and diffusion is negligible. Spreading is weak, and the patch of substance is mostly moved along, and possibly distorted by, the flow. If we wish to simplify the problem, we may drop the diffusion term [$D\partial^2 c/\partial x^2$ in (6.3)], as if D were zero. The relative error committed in the solution by so doing is expected to be on the order of the inverse of the Peclet number ($1/Pe$), and the larger Pe, the smaller the error.

6.3 Highly advective situations

When a system is highly advective in one direction (high Pe number based on scales U, L and D corresponding to that direction), diffusion is negligible *in that same direction*. This is not to say that it is also negligible in the other directions. For example, high advection in the horizontal does not preclude vertical diffusion, as this is often the case in the lower atmosphere. In such a case, the governing equation is

$$\frac{\partial c}{\partial t} + u\frac{\partial c}{\partial x} + v\frac{\partial c}{\partial y} = \frac{\partial}{\partial z}\left(\kappa\frac{\partial c}{\partial z}\right) + S - Kc. \tag{6.7}$$

Because the diffusion terms are of higher order (second derivatives) than those of advection (first derivatives), the neglect of a diffusion term reduces the order of the equation and, therefore, also reduces the need of boundary conditions by one in the respective direction. The boundary condition at the downstream end of the domain must be dropped: The concentration and flux there are whatever the flow brings to that point. A problem occurs when the

[2]In honor of Jean Claude Eugène Péclet (1793–1857), French physicist who wrote a treatise on heat transfer.

situation is highly advective and the small diffusion term is not dropped. In that case, because the order of the equation is not reduced, a boundary condition is enforced at the downstream end, and a locally high gradient of concentration may occur.

To see this, consider the one-dimensional, steady situation with no source and sink, with constant velocity and diffusivity in the x–direction. The equation is

$$u \frac{dc}{dx} = \mathcal{A} \frac{d^2 c}{dx^2}, \tag{6.8}$$

and its most general solution is

$$c(x) = C_0 + C_1 e^{ux/\mathcal{A}}. \tag{6.9}$$

For $u > 0$, the downstream end is to the right of the domain, and the solution increases exponentially towards the right boundary. Rather, it could be said that the solution decays away from this boundary as x decreases away from it. In other words, a boundary layer exists at the donwstream end. The e-folding length of this boundary layer is $\mathcal{A}/u$, and it can be very short in a highly advective situation (large u and small $\mathcal{A}$). Put another way, the Peclet number is the ratio of the domain length to this boundary-layer thickness, and the larger the Peclet number, the smaller the fraction of the domain occupied by the boundary layer. Why do we need to worry about this? Because in a numerical model it may happen that the boundary-layer thickness falls below the grid size. It is therefore important to check the Peclet number in relation to the spatial resolution. Should the ratio of the grid size to the length scale of the system be comparable to, or larger than, the inverse of the Peclet number, diffusion must be neglected in that direction, or, if it must be retained for some reason, special care must be taken at the downstream boundary.

6.4 Centered and upwind advection schemes

In GFD, advection is generally dominant compared to diffusion, and we therefore begin with the case of pure advection of a tracer concentration $c(x,t)$ along the x–direction. The aim is to solve numerically the following equation:

$$\frac{\partial c}{\partial t} + u \frac{\partial c}{\partial x} = 0. \tag{6.10}$$

For simplicity, we further take the velocity u as constant and positive so that advection carries c in the positive x–direction. The exact solution of this equation is

$$c(x,t) = c_0(x - ut), \tag{6.11}$$

where $c_0(x)$ is the initial concentration distribution (at $t = 0$).

A spatial integration from $x_{i-1/2}$ to $x_{i+1/2}$ across a grid cell (Figure 6-3) leads to the following budget

$$\frac{d\bar{c}_i}{dt} + \frac{q_{i+1/2} - q_{i-1/2}}{\Delta x} = 0, \quad q_{i-1/2} = uc|_{i-1/2}, \tag{6.12}$$

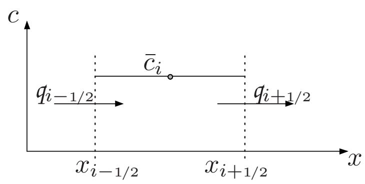

Figure 6-3 One-dimensional finite-volume approach with fluxes at the interfaces between grid cells for a straightforward budget calculation.

which is the basis for the finite-volume technique, as in (3.35). To close the system, we need to relate the local fluxes q to the cell-average concentrations $\bar{c}$. To do so we must introduce an approximation, because we do not know the actual value of c at the interfaces between cells, but only the average value in the cell on each side of it. It appears reasonable to use the following, consistent, numerical interpolation for the flux:

$$\tilde{q}_{i-1/2} \;=\; u \left(\frac{\bar{c}_i + \bar{c}_{i-1}}{2} \right), \tag{6.13}$$

which is tantamount to assuming that the local tracer concentration at the interface is equal to the mean of the surrounding cell averages. Before proceeding with time discretization, we can show that this centered approximation conserves not only the total amount of substance but also its variance, $\sum_i \bar{c}_i$ and $\sum_i (\bar{c}_i)^2$, respectively. Substitution of the flux approximation into (6.12) leads to the following semi-discrete equation for cell-averaged concentrations:

$$\frac{d\bar{c}_i}{dt} \;=\; -\,u\,\frac{\bar{c}_{i+1} - \bar{c}_{i-1}}{2\Delta x}. \tag{6.14}$$

Sum over index i leads to cancellation of terms by pairs on the right, leaving only the first and last $\bar{c}$ values. Then, multiplication of the same equation by c_i followed by the sum over the domain provides the time-evolution equation of the discretized variance:

$$\frac{d}{dt}\left(\sum_i (\bar{c}_i)^2 \right) \;=\; -\,\frac{u}{\Delta x}\,\sum_i \bar{c}_i \bar{c}_{i+1} + \frac{u}{\Delta x}\,\sum_i \bar{c}_i \bar{c}_{i-1},$$

where the sum covers all grid cells. By shifting the index of the last term from i to $i+1$, we note again cancellation of terms by pairs, leaving only contributions from the first and last grid points. Thus, except for possible contributions from the boundaries, the numerical scheme conserves both total amount and variance as the original equation does.

However, the conservation of global variance only holds for the semi-discrete equations. When time discretization is introduced as it must eventually be, conservation properties are often lost. In the literature it is not always clearly stated whether conservation properties hold for the semi-discrete or fully-discretized equations. The distinction, however, is important: The centered-space differencing conserves the variance of the semi-discrete solution, but a simple explicit time discretization renders the scheme unconditionnaly unstable and certainly does not conserve the variance. On the contrary, the latter quantity rapidly increases. Only a scheme that is both stable and consistent leads in the limit of vanishing time step to a solution that satisfies (6.12) and ensures conservation of the variance.

We might wonder why place emphasis on such conservation properties of semi-discrete equations, since by the time the algorithm is keyed into the computer it will always rely on fully-discretized numerical approximations in both space and time. A reason to look at semi-discrete conservation properties is that some special time discretizations maintain the property in the fully-discretized case. We now show that in the case of variance conservation, the trapezoidal time discretization does so. Consider the more general linear equation

$$\frac{d\tilde{c}_i}{dt} + \mathcal{L}(\tilde{c}_i) = 0, \tag{6.15}$$

where $\mathcal{L}$ stands for a linear discretization operator applied to the discrete field $\tilde{c}_i$. For our centered advection, the operator is $\mathcal{L}(\tilde{c}_i) = u(\tilde{c}_{i+1} - \tilde{c}_{i-1})/(2\Delta x)$. Suppose that the operator is designed to satisfy conservation of variance, which demands that at any moment t and for any discrete field $\tilde{c}_i$ the following relation holds:

$$\sum_i \tilde{c}_i \mathcal{L}(\tilde{c}_i) = 0, \tag{6.16}$$

because only then does $\sum_i \tilde{c}_i \; d\tilde{c}_i/dt$ vanish according to (6.15) and (6.16). The trapezoidal time discretization applied to (6.15) leads to

$$\frac{\tilde{c}_i^{n+1} - \tilde{c}_i^n}{\Delta t} \;=\; -\,\frac{\mathcal{L}(\tilde{c}_i^{n+1}) + \mathcal{L}(\tilde{c}_i^n)}{2} \;=\; -\,\frac{1}{2}\,\mathcal{L}(\tilde{c}_i^{n+1} + \tilde{c}_i^n), \tag{6.17}$$

where the last equality follows from the linearity of operator $\mathcal{L}$. Multiplying this equation by $(\tilde{c}_i^{n+1} + \tilde{c}_i^n)$ and summing over the domain then yields

$$\sum_i \frac{(\tilde{c}_i^{n+1})^2 - (\tilde{c}_i^n)^2}{\Delta t} \;=\; -\,\frac{1}{2}\,\sum_i (\tilde{c}_i^{n+1} + \tilde{c}_i^n)\mathcal{L}(\tilde{c}_i^{n+1} + \tilde{c}_i^n). \tag{6.18}$$

The term on the right is zero by virtue of (6.16). Therefore, any spatial discretization scheme that conserves variance continues to conserve variance if the trapezoidal scheme is used for the time discretization. As an additional benefit, the resulting scheme is also unconditionally stable. This does not mean, however, that the scheme is satisfactory, as Numerical Exercise 6-9 shows for the advection of the top-hat signal. Furthermore, there is a price to pay for stability because a system of simultaneous linear equations needs to be solved at each time step if the operator $\mathcal{L}$ uses several neighbors of the local grid point i.

To avoid solving simultaneous equations, alternative methods must be sought for time differencing. Let us explore the leapfrog scheme on the finite-volume approach. Time integration of (6.12) from t^{n-1} to t^{n+1} yields

$$\bar{c}_i^{n+1} \;=\; \bar{c}_i^{n-1} \;-\; 2\,\frac{\Delta t}{\Delta x}\left(\hat{q}_{i+1/2} - \hat{q}_{i-1/2}\right), \tag{6.19}$$

where $\hat{q}_{i-1/2}$ is the time-average advective flux uc across the cell interfaces between cells $i-1$ and i during the time interval from t^{n-1} to t^{n+1}. Using centered operators, this flux can be estimated as

$$\hat{q}_{i-1/2} \;=\; \frac{1}{2\Delta t}\int_{t^{n-1}}^{t^{n+1}} uc|_{i-1/2}\; dt \quad\rightarrow\quad \tilde{q}_{i-1/2} \;=\; u\left(\frac{\tilde{c}_i^n + \tilde{c}_{i-1}^n}{2}\right), \tag{6.20}$$

so that the ultimate scheme is:

$$\tilde{c}_i^{n+1} \;=\; \tilde{c}_i^{n-1} - \mathsf{C}\left(\tilde{c}_{i+1}^n - \tilde{c}_{i-1}^n\right), \tag{6.21}$$

where the coefficient C is defined as

$$\mathsf{C} \;=\; \frac{u\Delta t}{\Delta x}. \tag{6.22}$$

The same discretization could have been obtained by straightforward finite differencing of (6.10).

The parameter C is a dimensionless ratio central to the numerical discretization of advective problems, called the *Courant number* or *CFL parameter* (Courant *et al.*, 1928). It compares the displacement $u\Delta t$ made by the fluid during one time step to the grid size Δx. More generally, the Courant number for a process involving a propagation speed (such as a wave speed) is defined as the ratio of the distance of propagation during one time step to the grid spacing.

To use (6.21), two initial conditions are needed, one of which is physical and the other artificial, The latter must be consistent with the former. As usual, an explicit Euler step may be used to start from the single initial condition $\tilde{c}_i^0$:

$$\tilde{c}_i^1 \;=\; \tilde{c}_i^0 - \frac{\mathsf{C}}{2}\left(\tilde{c}_{i+1}^0 - \tilde{c}_{i-1}^0\right). \tag{6.23}$$

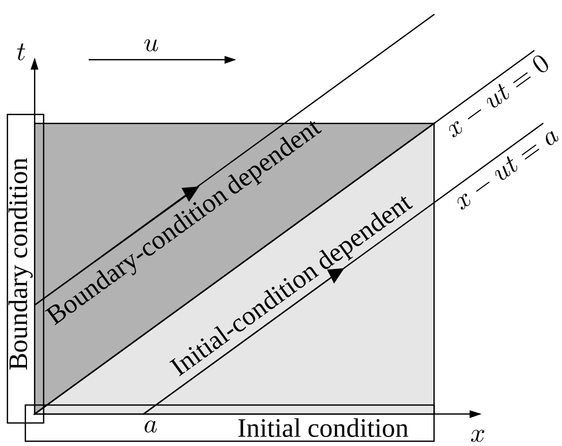

Figure 6-4 The characteristic line $x - ut = a$ propagates information from the initial condition or boundary condition into the domain. If the boundary is located at $x = 0$ and the initial condition given at $t = 0$, the line $x = ut$ divides the space-time frame into two distinct regions: For $x \leq ut$ the boundary condition defines the solution whereas for $x \geq ut$ the initial condition defines the solution.

In considering boundary conditions, we first observe that the exact solution of (6.10) obeys the simple law

$$c(x - ut) \;=\; \text{constant}. \tag{6.24}$$

By virtue of this property, a specified value of c somewhere along the line $x - ut = a$, called a *characteristic*, determines the value of c everywhere along that line. It is then easily seen (Figure 6-4) that, in order to obtain a uniquely defined solution within the domain, a boundary condition must be provided at the upstream boundary but no boundary condition is required at the outflow boundary. The centered space differencing, however, needs a value of $\tilde{c}$ given at each boundary. When discussing artificial boundary conditions (Section 4.7), we argued that these are acceptable as long as they are consistent with the mathematically correct boundary condition. But then, what requirement should the artificial boundary condition at the outflow obey with since there is no physical boundary condition for it to be consistent with? In practice a one-sided space differencing is used at the outflow for the last calculation point $i = m$, so that its value is consistent with the local evolution equation:

$$\tilde{c}_m^{n+1} = \tilde{c}_m^{n-1} - 2\mathsf{C}\left(\tilde{c}_m^n - \tilde{c}_{m-1}^n\right). \tag{6.25}$$

This provides the necessary value at the last grid cell.

For the inflow condition, the physical boundary condition is imposed, and algorithm (6.21) can be used starting from $n = 1$ and marching in time over all points $i = 2, ..., m-1$. Numerically we thus have sufficient information to calculate a solution that will be second-order accurate in both space and time, except near the initial condition and at the outflow boundary. In order to avoid any bad surprise when implementing the method, a stability analysis is advised.

For convenience, we use the Von Neumann method written in Fourier-mode formalism (5.31)

$$\tilde{c}_i^n \;=\; A\, e^{\mathrm{i}\,(k_x\; i\Delta x\; -\; \tilde{\omega}\; n\Delta t)}, \tag{6.26}$$

where the frequency $\tilde{\omega}$ may be complex. Substitution in the difference equation (6.21) provides the numerical dispersion relation

$$\sin(\tilde{\omega}\Delta t) \;=\; \mathsf{C}\sin(k_x\Delta x). \tag{6.27}$$

If $|\mathsf{C}| > 1$ this equation admits complex solutions $\tilde{\omega} = \tilde{\omega}_r + \mathrm{i}\,\tilde{\omega}_i$ for the $4\Delta x$ wave with $\tilde{\omega}_r\Delta t = \pi/2$ and $\tilde{\omega}_i$ such that

$$\sin(\tilde{\omega}_r\Delta t + \mathrm{i}\,\tilde{\omega}_i\Delta t) \;=\; \cosh(\tilde{\omega}_i\Delta t) \;=\; \mathsf{C}, \tag{6.28}$$

which admits two real solutions $\tilde{\omega}_i$ of opposite signs. One of the two solutions, therefore, corresponds to a growing amplitude, and the scheme is unstable.

For $|\mathsf{C}| \leq 1$, dispersion relation (6.27) has two real solutions $\tilde{\omega}$, and the scheme is stable. Therefore, numerical stability requires the condition $|\mathsf{C}| \leq 1$.

In the stable case, the numerical frequency $\tilde{\omega}$ may be compared to the exact value written in terms of discrete parameters

$$\omega \;=\; u\,k_x \quad\rightarrow\quad \omega\Delta t \;=\; \mathsf{C}\,k_x\Delta x. \tag{6.29}$$

Obviously, for $k_x\Delta x \rightarrow 0$ and $\Delta t \rightarrow 0$ the numerical relation (6.27) coincides with the exact relation (6.29). However, when $\tilde{\omega}$ is solution of (6.27) so is also $\pi/\Delta t - \tilde{\omega}$. The numerical solution thus consists of the superposition of the physical mode $\exp[\mathrm{i}\,(k_x\; i\Delta x - \tilde{\omega}\; n\Delta t)]$ and an numerical mode that can be expressed as

$$\tilde{c}_i^n \;=\; A\, e^{\mathrm{i}\,(k_x\; i\Delta x\; +\; \tilde{\omega}\; n\Delta t)}\; e^{\mathrm{i}\,n\pi} \tag{6.30}$$

which, by virtue of $e^{\mathrm{i}\,n\pi} = (-1)^n$, flip-flops in time, irrespectively of how small the time step is or how well the spatial scale is resolved. This second component of the numerical solution, called *spurious mode* or *computational mode*, is traveling upstream, as indicated by the change of sign in front of the frequency. For the linear case discussed here, this spurious mode can be controlled by careful initialization (see Numerical Exercise 6-2), but for nonlinear equations, the mode may still be generated despite careful initialization and boundary conditions. In this case, it might be necessary to use time-filtering (see Section 10.6) to eliminate unwanted signals even if the spurious mode is stable for $|\mathsf{C}| \leq 1$.

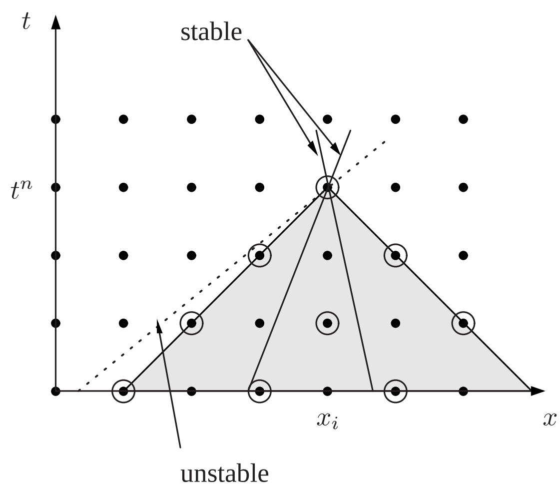

Figure 6-5 Numerical domain of dependence of the leapfrog scheme (in gray) covered by the points (circled dots) that influence the calculation at point i, n. This network of points is constructed recursively by identifying the grid points involved in prior calculations. The physical solution is only influenced by values along the characteristic. If the characteristic falls into the numerical domain of dependence (one of the solid lines for example), this value can be captured by the numerical grid. On the contrary, when the physical characteristic is not included in the numerical domain of dependence (dashed line for example), the numerical scheme uses only information that is physically unrelated to the advection process, and the scheme is unstable. Also note that for the leapfrog scheme the domain of dependence defines a checkerboard pattern and that the grid in (x, t) space includes two numerically independent sets of values (circled and non-circled dots).

The leapfrog scheme is thus conditionally stable. The stability condition $|\mathsf{C}| \leq 1$ was given a clear physical interpretation by Courant, Friedrichs and Lewy in their seminal 1928 paper. It is based on the fact that algorithm (6.21) defines a domain of dependence: Calculation of the value at point i and moment n (at the top of the gray pyramid in Figure 6-5) implicates neighbor points $i \pm 1$ at time n and the cell value i at time $n-1$. Those values in turn depend on their two neighboring and past values, so that a network of points can be constructed that influence the value at grid point i and moment n. This network is the numerical domain of dependence. Physically, however, the solution at point i and time n depends only on the value along the characteristic $x - ut = x_i - ut^n$ according to (6.24). It is clear that, if this line does not fall into the domain of dependence, there is trouble, for an attempt

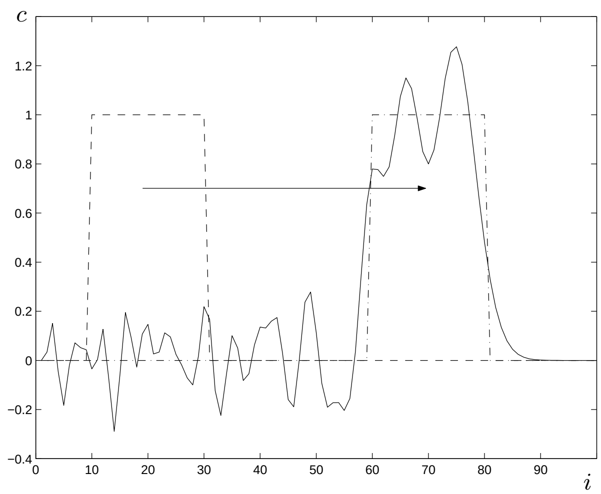

Figure 6-6 Leapfrog scheme applied to the advection of a "top-hat" signal with $\mathsf{C} = 0.5$ for 100 times steps. The exact solution is a mere translation from the initial position (dashed curve on the left) by 50 grid points downstream (dash-dotted curve on the right). The numerical method generates a solution that is roughly similar to the exact solution, with the solution varying around the correct value.

is made to determine a value from an irrelevant set of other values. Numerical instability is the symptom of this unsound approach. It is therefore necessary that the characteristic line passing through (i, n) be included in the numerical domain of dependence.

Except for the undesirable spurious mode, the leapfrog scheme has desirable features, because it is stable for $|\mathsf{C}| \leq 1$, conserves variance for sufficiently small time steps, and leads to the correct dispersion relation for well-resolved spatial scales. But, is it sufficient to ensure a well-behaved solution? A standard test for advection schemes is the translation of a "top-hat" signal. The use of (6.21) leads in this case to the result shown in Figure 6-6, which is somewhat disappointing. The odd behavior can be explained: In terms of Fourier modes, the solution consists of a series of sine/cosine signals of different wavelength, each of which by virtue of the numerical dispersion relation (6.27) travels at its own speed, thus unraveling the signal over time. This also explains the unphysical appearance of both negative values and values in excess of the initial maximum. The scheme does not possess the monotonicity property but creates new extrema.

The cause of the poor performance of the leapfrog scheme is evident: The actual integration should be performed using upstream information exclusively whereas the scheme uses a central average that disregards the origin of the information. In other words, it ignores the physical bias of advection.

To remedy the situation, we now try to take into account the directional information of advection and introduce the so-called *upwind* or *donor cell* scheme. A simple Euler scheme over a single time step Δt is chosen, and fluxes are integrated over this time interval. The essence of this scheme is to calculate the inflow based solely on the average value across the grid cell from where the flow arrives (the donor cell). For positive velocity and a time integration from t^n to t^{n+1}, we obtain

$$\bar{c}_i^{n+1} = \bar{c}_i^n - \frac{\Delta t}{\Delta x}\left(\hat{q}_{i+1/2} - \hat{q}_{i-1/2}\right) \tag{6.31}$$

with

$$\hat{q}_{i-1/2} \;=\; \frac{1}{\Delta t}\int_{t^n}^{t^{n+1}} q_{i-1/2}\,dt \;\simeq\; u\,\tilde{c}_{i-1}^n, \tag{6.32}$$

so that the scheme is

$$\tilde{c}_i^{n+1} \;=\; \tilde{c}_i^n \;-\; \mathsf{C}\,\left(\tilde{c}_i^n - \tilde{c}_{i-1}^n\right). \tag{6.33}$$

Interestingly enough, the scheme can be used without need of artificial boundary conditions or special initialization, as we can see from algorithm (6.33) or the numerical domain of dependence (Figure 6-7). The CFL condition $0 \le \mathsf{C} \le 1$ provides the necessary condition for stability.

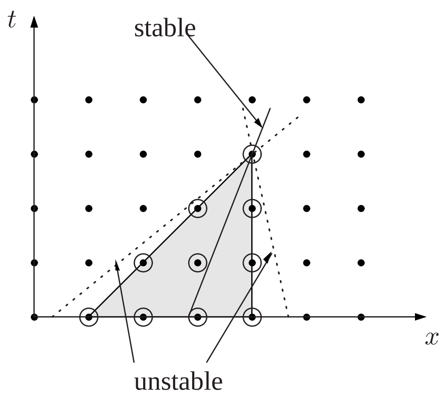

Figure 6-7 Domain of dependence of the upwind scheme. If the characteristic (dashed line) lies outside the numerical domain of dependence, unphysical behavior will be manifested as numerical instability. The necessary CFL stability condition therefore requires $0 \le \mathsf{C} \le 1$ so that the characteristic lies within the numerical domain of dependence (cases of solid lines). One initial condition and one upstream boundary condition are sufficient to determine the numerical solution.

The stability of the scheme could be analyzed with the Von Neumann method, but the simplicity of the scheme permits another approach, the so-called *energy method*. The energy method considers the sum of squares of $\tilde{c}$ and determines whether it remains bounded over time, providing a sufficient condition for stability. We start with (6.33), square it and sum over the domain:

$$\sum_i(\tilde{c}_i^{n+1})^2 = \sum_i(1-\mathsf{C})^2(\tilde{c}_i^n)^2 + \sum_i 2\mathsf{C}(1-\mathsf{C})\tilde{c}_i^n\;\tilde{c}_{i-1}^n + \sum_i \mathsf{C}^2(\tilde{c}_{i-1}^n)^2. \tag{6.34}$$

The first and last terms on the right can be grouped by shifting the index i in the last sum and invoking cyclic boundary conditions so that

$$\sum_i(\tilde{c}_i^{n+1})^2 = \sum_i[(1-\mathsf{C})^2 + \mathsf{C}^2](\tilde{c}_i^n)^2 + \sum_i 2\mathsf{C}(1-\mathsf{C})\tilde{c}_i^n\;\tilde{c}_{i-1}^n. \tag{6.35}$$

We can find an upper bound for the last term by using the following inequality:

$$0 \le \sum_i(\tilde{c}_i^n - \tilde{c}_{i-1}^n)^2 = 2\sum_i(\tilde{c}_i^n)^2 - 2\sum_i \tilde{c}_i^n\;\tilde{c}_{i-1}^n, \tag{6.36}$$

which can be proved by using again the cyclic condition. If $\mathsf{C}(1-\mathsf{C}) > 0$ the last term in (6.35) may be replaced by the upper bound of (6.36) so that

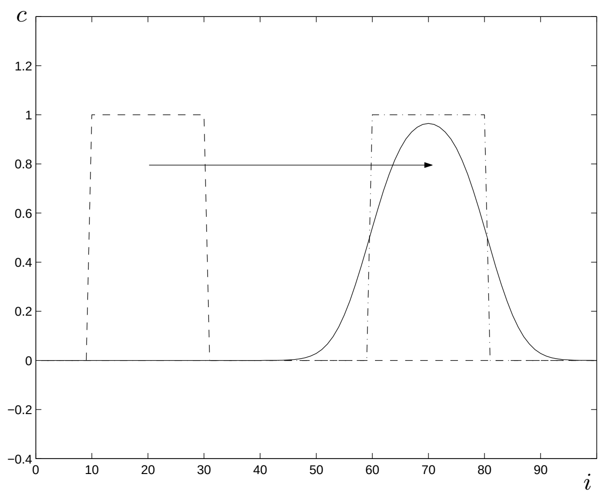

Figure 6-8 Upwind scheme with $\mathsf{C} = 0.5$ applied to the advection of a "top-hat" signal after 100 times steps. Ideally the signal should be translated without change in shape by 50 grid points, but the solution is characterized by a certain diffusion and a reduction in gradient.

$$\sum_i (\tilde{c}_i^{n+1})^2 \leq \sum_i (\tilde{c}_i^n)^2, \tag{6.37}$$

and the scheme is stable because the norm of the solution does not increase in time. Although it is not related to a physical energy, the method derives its the name from its reliance on a quadratic form that bears resemblance with kinetic energy. Methods that prove that a quadratic form is conserved or bounded over time are similar to energy-budget methods used to prove that the energy of a physical system is conserved.

The energy method provides only a sufficient stability condition because the upper bounds used in the demonstration do not need to be reached. But, since in the present case the sufficient stability condition was found to be identical to the necessary CFL condition, the condition $0 \leq \mathsf{C} \leq 1$ is both necessary and sufficient to guarantee the stability of the upwind scheme.

Testing the upwind scheme on the "top-hat" problem (Figure 6-8), we observe that, unlike leapfrog, the scheme does not create new minima or maxima, but somehow diffuses the signal by reducing the gradients. The fact that the scheme is monotonic is readily understood by examining (6.33): The new value at point i is a linear interpolation of previous values found at i and $i-1$, so that no new value can ever fall outside the range of these previous values as long as the condition $0 \leq \mathsf{C} \leq 1$ is satisfied.

The diffusive behavior can be explained by analyzing the modified equation associated with (6.33). A Taylor expansion of the discrete solution around point (i, n) in (6.33) provides the equation that the numerical scheme actually solves:

$$\frac{\partial \tilde{c}}{\partial t} + \frac{\Delta t}{2}\frac{\partial^2 \tilde{c}}{\partial t^2} + \mathcal{O}\left(\Delta t^2\right) + u\,\left(\frac{\partial \tilde{c}}{\partial x} - \frac{\Delta x}{2}\frac{\partial^2 \tilde{c}}{\partial x^2} + \mathcal{O}\left(\Delta x^2\right)\right) = 0. \tag{6.38}$$

The scheme is only of first order as can be expected from the use of a one-sided finite difference. To give a physical interpretation to the equation, the second time derivative should be replaced by a spatial derivative. Taking the derivative of the modified equation with respect to t provides an equation for the second time derivative, which we would like to eliminate, but it involves a cross derivative[3]. This cross derivative can be obtained by differentiating the modified equation with respect to x. Some algebra then provides

$$\frac{\partial^2 \tilde{c}}{\partial t^2} = u^2 \ \frac{\partial^2 \tilde{c}}{\partial x^2} + \mathcal{O}\left(\Delta t, \Delta x^2\right),$$

which can finally be introduced into (6.38) to yield the following equation

$$\frac{\partial \tilde{c}}{\partial t} + u\frac{\partial \tilde{c}}{\partial x} = \frac{u\Delta x}{2}\left(1 - \mathsf{C}\right)\frac{\partial^2 \tilde{c}}{\partial x^2} + \mathcal{O}\left(\Delta t^2, \Delta x^2\right). \tag{6.39}$$

This is the equation that the upwind scheme actually solves.

Up to $\mathcal{O}\left(\Delta t^2, \Delta x^2\right)$, therefore, the numerical scheme solves an advection-diffusion equation instead of the pure advection equation, with diffusivity equal to $(1 - \mathsf{C})\, u\Delta x/2$. For obvious reasons, this is called an artificial diffusion or *numerical diffusion*. The effect is readily seen in Figure 6-8. To decide whether this level of artificial diffusion is acceptable or not, we must compare its size to that of physical diffusion. For a diffusivity coefficient $\mathcal{A}$, the ratio of numerical to physical diffusion is $(1 - \mathsf{C})\, u\Delta x/2\mathcal{A}$. Since it would be an aberration to have numerical diffusion equal or exceed physical diffusion (recall the error analysis of Section 4.8: Discretization errors should not be larger than modeling errors), the *grid Peclet number* $U\Delta x/\mathcal{A}$ may not exceed a value of $\mathcal{O}(1)$ for the upwind scheme to be valid.

When no physical diffusion is present, we must require that the *numerical* diffusion term be small compared to the *physical* advection term, a condition that can be associated with another grid Peclet number:

$$\tilde{Pe} \ = \ 2\,\frac{UL}{U\Delta x\,(1 - \mathsf{C})} \ \sim \ \frac{L}{\Delta x} \ \gg \ 1, \tag{6.40}$$

where L stands for the length scale of any solution component worth resolving. Even for well resolved signals in GFD flows, the Peclet number associated with numerical diffusion is often insufficiently large, and numerical diffusion is a problem that plagues the upwind scheme.

The observation that the scheme introduces artificial diffusion is interesting and annoying, and the question is now to identify its origin in order to reduce it. Compared to the centered scheme, which is symmetric and of second order, the upwind scheme uses exclusively information form the upstream side, the donor cell, and is only of first order. Numerical diffusion must, therefore, be associated with the asymmetry in the flux calculation, and to reduce numerical diffusion we must somehow take into account values of $\tilde{c}$ on both sides of the interface to calculate the flux and thereby seek a scheme that is second-order accurate.

This can be accomplished with the *Lax-Wendroff scheme*, which estimates the flux at the cell interface not by assuming that the function is constant within the cell but varies linearly across it:

[3]Note that using the *original* equations, the physical solution satisfies $\partial^2 c/\partial t^2 = u^2 \partial^2 c/\partial x^2$, which is sometimes used as a shortcut to eliminate the second time derivative from the modified equation. This is, however, incorrect because $\tilde{c}$ does not solve the original equation. In practice, this kind of shortcuts can lead to correct leading truncation errors, but without being sure that no essential term is overlooked.

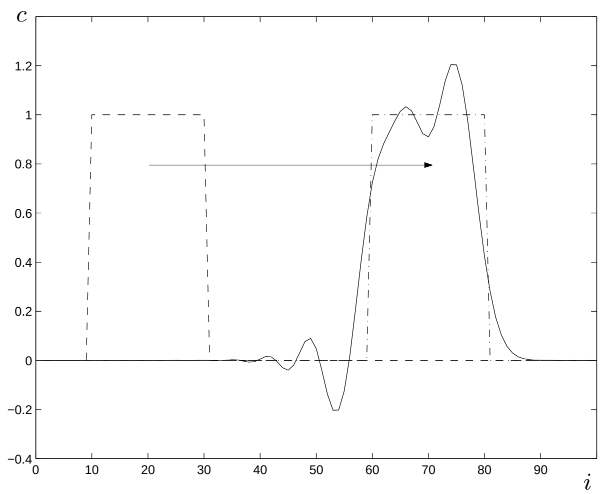

Figure 6-9 Second-order Lax-Wendroff scheme applied to the advection of a "top-hat" signal with $\mathsf{C} = 0.5$ after 100 times steps. Dispersion and non-monotonic behavior are noted.

$$\tilde{q}_{i-1/2} = u \left[\frac{\tilde{c}_i^n + \tilde{c}_{i-1}^n}{2} - \frac{\mathsf{C}}{2}\left(\tilde{c}_i^n - \tilde{c}_{i-1}^n\right)\right]$$
$$= u\,\tilde{c}_{i-1}^n + \underbrace{(1-\mathsf{C})\frac{u\Delta x}{2}\,\frac{\tilde{c}_i^n - \tilde{c}_{i-1}^n}{\Delta x}}_{\simeq(1-\mathsf{C})\frac{u\Delta x}{2}\frac{\partial\tilde{c}}{\partial x}}. \quad (6.41)$$

The last term is in addition to the upwind flux $u\tilde{c}_{i-1}^n$ and serves to negate numerical diffusion by adding an anti-diffusion flux with negative diffusion coefficient $-u\Delta x(1-\mathsf{C})/2$, *i.e.*, the precise opposite of numerical diffusion.

Substitution of this flux into the finite-volume scheme leads to the following scheme:

$$\tilde{c}_i^{n+1} = \tilde{c}_i^n - \mathsf{C}\left(\tilde{c}_i^n - \tilde{c}_{i-1}^n\right) - \frac{\Delta t}{\Delta x^2}(1-\mathsf{C})\frac{u\Delta x}{2}\left(\tilde{c}_{i+1}^n - 2\tilde{c}_i^n + \tilde{c}_{i-1}^n\right) \quad (6.42)$$

which, compared to the upwind scheme, includes an additional anti-diffusion term with coefficient constructed to negate the numerical diffusion of the upwind scheme. The effect of this higher-order approach on the solution of our test case is a reduced overall error but the appearance of dispersion (Figure 6-9). This is due to the fact that we eliminated the truncation error proportional to the second spatial derivative (an even derivative associated with dissipation) and now have a truncation error proportional to the third spatial derivative (an odd derivative associated with dispersion, see theoretical Numerical Exercise 6-8).

The same dispersive behavior is observed with the *Beam-Warming scheme*, in which the anti-diffusion term is shifted upstream so as to anticipate the gradient that will arrive later at the interface:

$$\tilde{q}_{i-1/2} = u\,\tilde{c}_{i-1}^n + (1-\mathsf{C})\,\frac{u}{2}\,(\tilde{c}_{i-1}^n - \tilde{c}_{i-2}^n). \quad (6.43)$$

This scheme is still of second order, since the correction term is only shifted upstream by Δx. The effect of anticipating the incoming gradients enhances stability but does not reduce dispersion (see Numerical Exercise 6-8).

Other methods spanning more grid points can be constructed to obtain higher-order integration of fluxes, implicit methods to increase stability, predictor-corrector methods, or combinations of all these schemes. Here, we only outline some of the approaches and refer the reader to more specialized literature for details (*e.g.*, Durran, 1999; Chung, 2002).

A popular *predictor-corrector method* is the second-order MacCormack scheme: The predictor uses a forward spatial difference (anti-diffusion)

$$\tilde{c}_i^\star = \tilde{c}_i^n - \mathsf{C}\left(\tilde{c}_{i+1}^n - \tilde{c}_i^n\right) \tag{6.44}$$

and the corrector a backward spatial difference on the predicted field (diffusion):

$$\tilde{c}_i^{n+1} = \tilde{c}_i^{n+1/2} - \frac{\mathsf{C}}{2}\left(\tilde{c}_i^\star - \tilde{c}_{i-1}^\star\right) \quad \text{with} \quad \tilde{c}_i^{n+1/2} = \frac{\tilde{c}_i^\star + \tilde{c}_i^n}{2}. \tag{6.45}$$

The elimination of the intermediate value $\tilde{c}_i^{n+1/2}$ from which starts the corrector step provides the expanded corrector step:

$$\tilde{c}_i^{n+1} = \frac{1}{2}\left[\tilde{c}_i^n + \tilde{c}_i^\star - \mathsf{C}\left(\tilde{c}_i^\star - \tilde{c}_{i-1}^\star\right)\right], \tag{6.46}$$

assuming as usual $u > 0$. Substitution of the predictor step into the corrector step shows that the MacCormack scheme is identical to the Lax-Wendroff scheme in the linear case, but differences may arise in nonlinear problems.

An *implicit scheme* can handle centered space differencing and approximates the flux as

$$\tilde{q}_{i-1/2} = \alpha u\, \frac{\tilde{c}_i^{n+1} + \tilde{c}_{i-1}^{n+1}}{2} + (1-\alpha) u\, \frac{\tilde{c}_i^n + \tilde{c}_{i-1}^n}{2}. \tag{6.47}$$

For $\alpha = 1$, the scheme is fully implicit, whereas for $\alpha = 1/2$ it becomes a semi-implicit or trapezoidal scheme (also called *Crank-Nicholson scheme*). The latter has already been shown to be unconditionnaly stable (see variance conservation and the trapezoidal scheme (6.17)). The price to pay for this stability is the need to solve a linear algebraic system at every step. As for the diffusion problem, the system is tridiagonal in the 1D case and more complicated in higher dimensions. The advantage of the implicit approach is a robust scheme when C occasionally happens to exceed unity in a known dimension[4]. It should be noted, however, that for too large a Courant number accuracy degrades.

All of the previous schemes can be mixed in a *linear combination*, as long as the sum of the weights attributed to each scheme is unity for the sake of consistency. An example of combining two schemes consists in averaging the flux calculated with a lower-order scheme $\tilde{q}_{i-1/2}^L$ with that of a higher-order scheme $\tilde{q}_{i-1/2}^H$:

$$\tilde{q}_{i-1/2} = (1-\Phi)\,\tilde{q}_{i-1/2}^L + \Phi\,\tilde{q}_{i-1/2}^H,$$

[4]Typically the vertical Courant number may be so variable that it becomes difficult to ensure that the local vertical C value remains below one. In particular, it is prudent to use an implicit scheme in the vertical when the model has non-uniform grid spacing and when the vertical velocity is weak except on rare occasions.

in which the weight Φ ($0 \leq \Phi \leq 1$) acts as a tradeoff between the undesirable numerical diffusion of the lower-order scheme and numerical dispersion and loss of monotonicity of the higher-order scheme.

All these methods lead to sufficiently accurate solutions, but none except the upwind scheme ensures monotonic behavior. The reason for this disappointing fact can be found in the frustrating theorem by Godunov (1959) regarding the discretized advection equation:

> A consistent linear numerical scheme that is monotonic can at most be first-order accurate.

Therefore, the upwind scheme is the inevitable choice if no over- or under-shoot is permitted. To circumvent the Godunov theorem, state-of-the-art advection schemes relax the linear nature of the discretization and adjust the parameter Φ locally, depending on the behavior of the solution. The function that defines the way Φ is adapted locally is called a *limiter*. Such an approach is able to capture large gradients (fronts). Because of its advanced nature, we delay its presentation until Section 15.7. An example of a nonlinear scheme called TVD, however, is already included in the computer codes provided for the analysis of advection schemes in several dimensions.

6.5 Advection-diffusion with sources and sinks

Having considered separately advection schemes (this chapter), diffusion schemes (Chapter 5) and time discretizations with arbitrary forcing terms (Chapter 2), we can now combine them to tackle the general advection-diffusion equation with sources and sinks. For a linear sink, the 1D equation to be discretized is

$$\frac{\partial c}{\partial t} + u\,\frac{\partial c}{\partial x} = -K\,c + \frac{\partial}{\partial x}\left(\mathcal{A}\frac{\partial c}{\partial x}\right). \tag{6.48}$$

Since we already have a series of discretization possibilities for each individual process, the combination of these provides an even greater number of possible schemes which we cannot describe exhaustively here. We simply show one example to illustrate two important facts that should not be forgotten when combining schemes: The properties of the combined scheme are not simply the sum of the properties of the individual schemes nor is its stability condition the most stringent condition of the separate schemes.

To prove the first statement, we consider (6.48) with zero diffusion ($\mathcal{A} = 0$) and solve by applying the second-order Lax-Wendroff advection scheme with the second-order trapezoidal scheme applied to the decay term. The discretization, after some rearrangement of terms, is:

$$\tilde{c}_i^{n+1} = \tilde{c}_i^n - \frac{\mathsf{B}}{2}\left(\tilde{c}_i^n + \tilde{c}_i^{n+1}\right) - \frac{\mathsf{C}}{2}\left(\tilde{c}_{i+1}^n - \tilde{c}_{i-1}^n\right) + \frac{\mathsf{C}^2}{2}\left(\tilde{c}_{i+1}^n - 2\tilde{c}_i^n + \tilde{c}_{i-1}^n\right), \tag{6.49}$$

where $\mathsf{B} = K\Delta t$ and $\mathsf{C} = u\Delta t/\Delta x$. This scheme actually solves the following modified equation:

$$\begin{aligned}\frac{\partial \tilde{c}}{\partial t} + u\,\frac{\partial \tilde{c}}{\partial x} + K\,\tilde{c} &= -\frac{\Delta t}{2}\,\frac{\partial^2 \tilde{c}}{\partial t^2} - K\frac{\Delta t}{2}\,\frac{\partial \tilde{c}}{\partial t} + \frac{u^2 \Delta t}{2}\,\frac{\partial^2 \tilde{c}}{\partial x^2} + \mathcal{O}(\Delta t^2, \Delta x^2)\\ &= -\frac{uK\Delta t}{2}\,\frac{\partial \tilde{c}}{\partial x} + \mathcal{O}(\Delta t^2, \Delta x^2)\end{aligned} \tag{6.50}$$

where the last equality was obtained by a similar procedure as the one used to find the modified equation (6.39). It is not possible to make the terms on the right-hand side cancel each other unless $K = 0$ or $u = 0$, in which case we recover respectively the second-order Lax-Wendroff or the second-order trapezoidal scheme. In all other cases, the combined scheme is only of first order though the individual schemes are of second order.

For the purpose of illustrating the second statement on stability, we combine the second-order Lax-Wendroff advection scheme (stability condition $|\mathsf{C}| \leq 1$) with the explicit Euler diffusion scheme (stability condition $0 \leq \mathsf{D} \leq 1/2$) and an explicit scheme for the sink term with rate K (stability condition $K\,\Delta t \leq 2$). The discretization, after some rearrangement of the terms, is:

$$\tilde{c}_i^{n+1} = \tilde{c}_i^n - \mathsf{B}\,\tilde{c}_i^n - \frac{\mathsf{C}}{2}\,(\tilde{c}_{i+1}^n - \tilde{c}_{i-1}^n) + \left(\mathsf{D} + \frac{\mathsf{C}^2}{2}\right)\,(\tilde{c}_{i+1}^n - 2\tilde{c}_i^n + \tilde{c}_{i-1}^n), \tag{6.51}$$

where $\mathsf{D} = \mathcal{A}\Delta t/\Delta x^2$. Application of the Von Neumann stability analysis yields the amplification factor

$$\varrho = 1 - \mathsf{B} - 4\left(\mathsf{D} + \frac{\mathsf{C}^2}{2}\right)\sin^2\theta - \mathrm{i}\;2\mathsf{C}\sin\theta\cos\theta, \tag{6.52}$$

where $\theta = k_x \Delta x/2$, so that

$$|\varrho|^2 = \left[1 - \mathsf{B} - 4\left(\mathsf{D} + \frac{\mathsf{C}^2}{2}\right)\xi\right]^2 + 4\mathsf{C}^2\xi(1-\xi), \tag{6.53}$$

where $0 \leq \xi = \sin^2\theta \leq 1$. For $\xi \simeq 0$ (long waves), we obtain the necessary stability condition $\mathsf{B} \leq 2$, corresponding to the stability condition of the sink term alone. For $\xi \simeq 1$ (short waves) we find the more demanding necessary stability condition

$$\mathsf{B} + 2\mathsf{C}^2 + 4\mathsf{D} \;\leq\; 2. \tag{6.54}$$

We can show that the latter condition is also sufficient (Numerical Exercise 6-13), which proves that the stability condition of the combined schemes is more stringent than the most severe stability condition of each individual scheme. Only when two processes are negligible does the stability condition revert to the stability condition of the single remaining process. This seems evident but is not always the case. In some situations, adding even an infinitesimally-small stable process can require a discontinuous reduction in time step (*e.g.*, Beckers and Deleersnijder, 1993). In other situations, adding a process can stabilize an otherwise unconditionally unstable scheme (Numerical Exercise 6-14). Therefore, in theory, the stability of the full scheme should be investigated in every individual case. In practice however, if a complete scheme is too difficult to analyze, sub-schemes (*i.e.*, including only

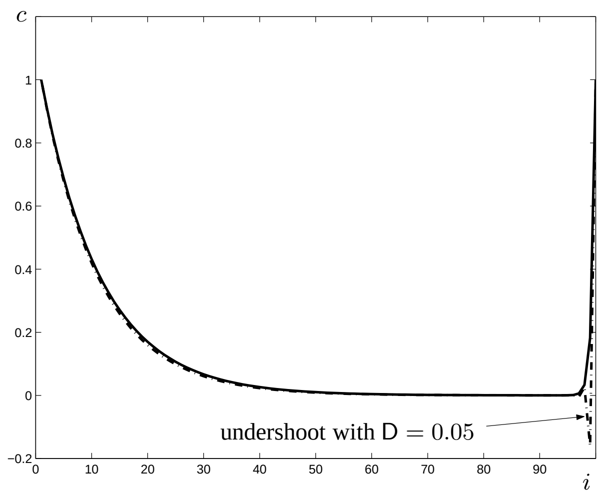

Figure 6-10 Simulation using (6.51) with $\mathsf{B} = 0.05$, $\mathsf{C} = 0.5$ and $\mathsf{D} = 0.25$, after convergence to a stationary solution (solid line). With decreasing diffusion, the scheme eventually fails to resolve adequately the outflow boundary layer, and undershoot appears ($\mathsf{D} = 0.05$, dot-dash line). This corresponds to a situation in which one of the coefficients in the numerical scheme has become negative. The program `advdiffsource.m` can be used to test other combinations of the parameter values.

a few processes) are isolated with the hope that the full scheme does not demand a drastically shorter time step than the one required by the most stringent stability condition of all sub-schemes taken separately.

Stability is an important property of any scheme as is, at least for tracers, monotonic behavior. If we assume the scheme to be explicit, linear and covering a stencil spanning p grid points upstream and q downstream (for a total of $p + q + 1$ points), it can be written in the general form:

$$\tilde{c}_i^{n+1} = a_{-p}\tilde{c}_{i-p}^n + ... + a_{-1}\tilde{c}_{i-1}^n + a_0\tilde{c}_i^n + a_1\tilde{c}_{i+1}^n + ... + a_q\tilde{c}_{i+q}^n. \tag{6.55}$$

To be consistent with (6.48), we need at least to ensure $a_{-p} + ... + a_{-1} + a_0 + a_1 + ... + a_q = 1 - \mathsf{B}$, otherwise, not even a spatially uniform field would be represented correctly.

If there is a negative coefficient a_k, the scheme will not be monotonic, for indeed, if the function is positive at point $i + k$ but zero everywhere else, it will take on a negative value $\tilde{c}_i^{n+1}$. On the other hand, if all coefficients are positive, the sum of the total weights is obviously positive but less than one because it is equal to $(1 - \mathsf{B})$. The scheme thus interpolates while damping, in agreement with physical decay. And, since damping does not create new extrema, we conclude that positive coefficients ensure a monotonic behavior in all situations. For our example (6.51), this demands $\mathsf{B} + \mathsf{C}^2 + 2\mathsf{D} \leq 1$ and $\mathsf{C} \leq \mathsf{C}^2 + 2\mathsf{D}$. The former condition is a slightly more constraining version of the stability condition (6.54), while the latter condition imposes a constraint on the grid Peclet number:

$$Pe_{\Delta x} = \frac{u\Delta x}{\mathcal{A}} = \frac{\mathsf{C}}{\mathsf{D}} \leq \frac{u^2\Delta t}{\mathcal{A}} + 2. \tag{6.56}$$

For short time steps, this imposes a maximum value of 2 on the grid Peclet number. This condition is not a stability condition but a necessary condition for monotonic behavior.

The scheme is now tested on a physical problem. Because of the second derivative, we impose boundary conditions at both upstream *and* downstream, and for simplicity hold $\tilde{c} = 1$ steady at these locations. We then iterate from a zero initial condition until the scheme converges to a stationary solution. This solution (Figure 6-10) exhibits a boundary layer at the downstream end because of weak diffusion, in agreement with the remark made in Section 6.3. For weak diffusion, the grid Peclet number $Pe_{\Delta x}$ is too large and violates (6.56). Undershooting appears, although the solution remains stable. In conclusion, besides the parameters B, C and D that control stability, the grid Peclet number C/D appears as a parameter controlling monotonic behavior.

6.6 Multi-dimensional approach

In addition to the various combinations already encountered in the 1D case, generalization to more dimensions allows further choices and different methods. Here we concentrate on the 2D case because generalizations to 3D do not generally cause more fundamental complications.

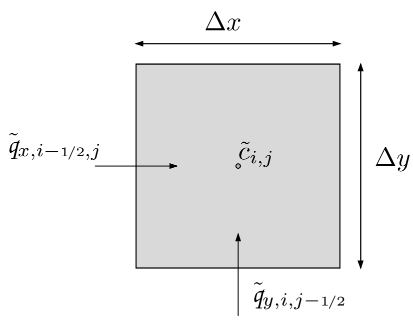

Figure 6-11 Finite volume in 2D with fluxes at the interfaces. The budget involves the total balance of inflowing and outflowing fluxes during one time step.

The finite-volume approach can be easily extended to a 2D grid cell with the normal fluxes defined along the interfaces (Figure 6-11):

$$\frac{\tilde{c}_{i,j}^{n+1} - \tilde{c}_{i,j}^{n}}{\Delta t} + \frac{\tilde{q}_{x,i+1/2,j} - \tilde{q}_{x,i-1/2,j}}{\Delta x} + \frac{\tilde{q}_{y,i,j+1/2} - \tilde{q}_{y,i,j-1/2}}{\Delta y} = 0, \tag{6.57}$$

where $\tilde{q}_{x,i\pm1/2,j}$ and $\tilde{q}_{y,i,j\pm1/2}$ are approximations of the actual fluxes uc and vc, respectively.

For any flux calculation, the least we require is that it be able to represent correctly a uniform tracer field $\mathcal{C}$. All of our 1D flux calculations do so and should do so. When (6.57) is applied to the case of a uniform concentration distribution $\tilde{c} = \mathcal{C}$, we obtain

$$\frac{\tilde{c}_{i,j}^{n+1} - \mathcal{C}}{\Delta t} + \frac{\tilde{u}_{i+1/2,j} - \tilde{u}_{i-1/2,j}}{\Delta x}\,\mathcal{C} + \frac{\tilde{v}_{i,j+1/2} - \tilde{v}_{i,j-1/2}}{\Delta y}\,\mathcal{C} = 0.$$

This can only lead to $\tilde{c}^{n+1} = \mathcal{C}$ at the next time step if the discrete velocity field satisfies the condition

$$\frac{\tilde{u}_{i+1/2,j} - \tilde{u}_{i-1/2,j}}{\Delta x} + \frac{\tilde{v}_{i,j+1/2} - \tilde{v}_{i,j-1/2}}{\Delta y} = 0. \tag{6.58}$$

Since this requirement is an obvious discretization of $\partial u/\partial x + \partial v/\partial y = 0$, the 2D form of the continuity equation (see (4.21d)), it follows that a prerequisite to solving the concentration equation by the finite-volume approach is a non-divergent flow field *in its discretized form*. Ensuring that (6.58) holds is the role of the discretization of the dynamical equations, those governing velocity and pressure.

Here, in order to test numerical advection schemes, we take the flow field as known and obeying (6.58). We can easily generate such a discrete velocity distribution by invoking a discretized *streamfunction* ψ:

$$\tilde{u}_{i-1/2,j} = -\frac{\psi_{i-1/2,j+1/2} - \psi_{i-1/2,j-1/2}}{\Delta y} \tag{6.59}$$

$$\tilde{v}_{i,j-1/2} = \frac{\psi_{i+1/2,j-1/2} - \psi_{i-1/2,j-1/2}}{\Delta x}. \tag{6.60}$$

It is straighforward to show that these $\tilde{u}$ and $\tilde{v}$ values satisfy (6.58) for any set of streamfunction values.

Note that if we had discretized directly the continuous equation

$$\frac{\partial c}{\partial t} + u\,\frac{\partial c}{\partial x} + v\,\frac{\partial c}{\partial y} = 0, \tag{6.61}$$

we would have obtained

$$\frac{\partial \tilde{c}_{i,j}}{\partial t} + u_{i,j}\;\left.\frac{\partial \tilde{c}}{\partial x}\right|_{i,j} + v_{i,j}\;\left.\frac{\partial \tilde{c}}{\partial y}\right|_{i,j} = 0,$$

which guarantees that an initially uniform tracer distribution remains uniform at all later times regardless of the structure of the discretized velocity distribution as long as the discretized form of the spatial derivatives return zeroes for a uniform distribution (a mere requirement of consistency). Such a scheme could appear to offer a distinct advantage, but it is easy to show that it has a major drawback. It looses important conservation properties, including conservation of the quantity of tracer (heat for temperature, salt for salinity, etc.).

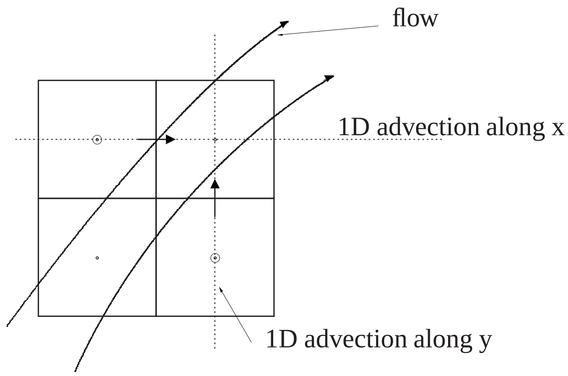

Figure 6-12 Naive 2D generalization using 1D methods along each coordinate line to approximate the advection operator as the sum of $\partial(uc)/\partial x$ and $\partial(vc)/\partial y$.

Assuming the discrete velocity field to be divergence free in the sense of (6.58), the first method that comes to mind to calculate the flux components is to use the discretizations

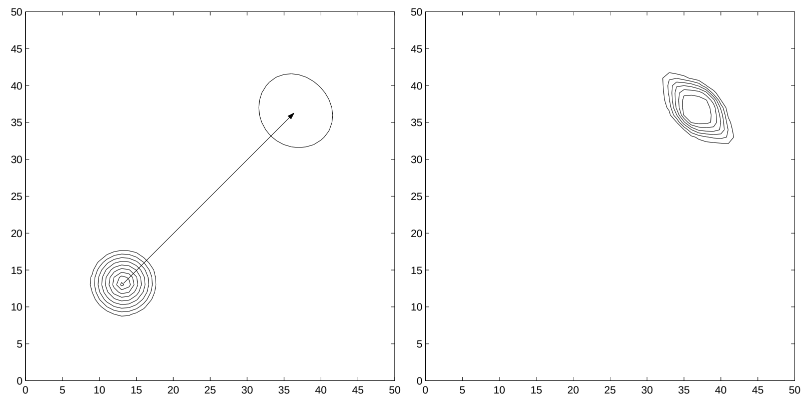

Figure 6-13 Oblique advection of a cone-shaped distribution using the upwind scheme generalized to 2D (left panel) and a TVD scheme (right panel) with $\mathsf{C}_x = \mathsf{C}_y = 0.12$. The upwind scheme severely dampens the signal, to less then 20% of its initial amplitude, while the TVD scheme used as a double 1D problem greatly distorts the solution.

developed in 1D along each coordinate line separately (Figure 6-12). The upwind scheme is then easily generalized as follows:

$$\tilde{q}_{x,i-1/2,j} = \tilde{u}_{i-1/2,j}\, \tilde{c}^n_{i-1,j} \quad \text{if} \quad \tilde{u}_{i-1/2,j} > 0, \qquad \tilde{u}_{i-1/2,j}\, \tilde{c}^n_{i,j} \quad \text{otherwise} \tag{6.62a}$$

$$\tilde{q}_{y,i,j-1/2} = \tilde{v}_{i,j-1/2}\, \tilde{c}^n_{i,j-1} \quad \text{if} \quad \tilde{v}_{i,j-1/2} > 0, \qquad \tilde{v}_{i,j-1/2}\, \tilde{c}^n_{i,j} \quad \text{otherwise.} \tag{6.62b}$$

The other 1D schemes can be generalized similarly. Applying such schemes to the advection of an initially cone-shaped distribution (single peak with same linear drop in all radial directions) embedded in a uniform flow field crossing the domain at 45°, we observe that the upwing scheme is plagued by a very strong numerical diffusion (left panel of Figure 6-13). Using the TVD scheme keeps the signal to a higher amplitude but strongly distorts the distribution (right panel of Figure 6-13).

This distortion is readily understood in terms of the advection process: The information should be carried by the oblique flow, but the flux calculation relies on information strictly along the x or y axes. In the case of a flow oriented at 45° from the x–axis, this ignores that grid point (i, j) is primarily influenced by point $(i-1, j-1)$ whereas points $(i-1, j)$ and $(i, j-1)$ are used in the flux calculations. In conclusion, the double 1D approach is unsatisfactory and rarely used.

The *Corner Transport Upstream* scheme (*CTU*) (*e.g.*, Colella, 1990) takes into account the different contributions of the four grid cells involved in the displacement (Figure 6-14). Assuming uniform positive velocities to illustrate the approach, the following discretization

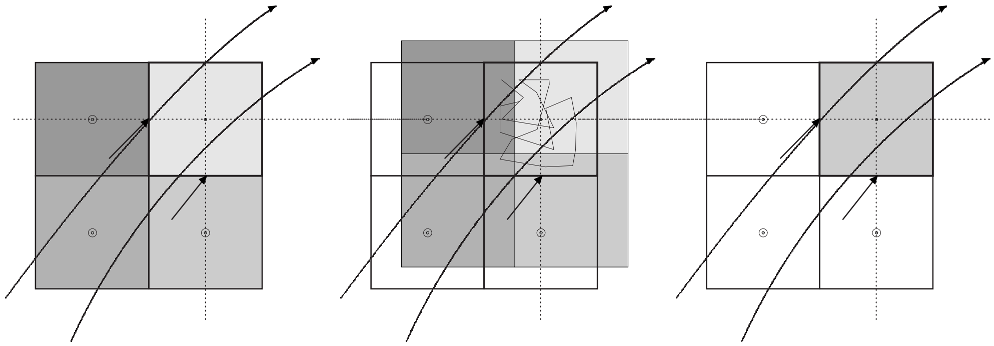

Figure 6-14 2D generalization designed to advect the field obliquely along streamlines. The associated numerical diffusion can then be interpreted as the necessary grid averaging (*i.e.*, mixing) used in the finite-volume technique after displacement of the donor cells. The flux calculations (thick arrows) need to integrate the inflow of c along the flow instead of along the grid lines.

ensures that a diagonal flow brings to the interface a correct mixing of two donor cells:

$$\tilde{q}_{x,i-1/2,j} = \left(1 - \frac{\mathsf{C}_y}{2}\right) \tilde{u}\, \tilde{c}^n_{i-1,j} + \frac{\mathsf{C}_y}{2}\, \tilde{u}\, \tilde{c}^n_{i-1,j-1} \tag{6.63a}$$

$$\tilde{q}_{y,i,j-1/2} = \left(1 - \frac{\mathsf{C}_x}{2}\right) \tilde{v}\, \tilde{c}^n_{i,j-1} + \frac{\mathsf{C}_x}{2}\, \tilde{v}\, \tilde{c}^n_{i-1,j-1}, \tag{6.63b}$$

leading to the expanded scheme

$$\begin{aligned} \tilde{c}^{n+1}_{i,j} = \tilde{c}^n_{i,j} &- \mathsf{C}_x \left(\tilde{c}^n_{i,j} - \tilde{c}^n_{i-1,j}\right) - \mathsf{C}_y \left(\tilde{c}^n_{i,j} - \tilde{c}^n_{i,j-1}\right) \\ &+ \mathsf{C}_x \mathsf{C}_y \left(\tilde{c}^n_{i,j} - \tilde{c}^n_{i-1,j} - \tilde{c}^n_{i,j-1} + \tilde{c}^n_{i-1,j-1}\right), \end{aligned} \tag{6.64}$$

where the last term is an additional term compared to the double 1D approach. Two distinct Courant numbers arise, one for each direction:

$$\mathsf{C}_x = \frac{u \Delta t}{\Delta x}, \qquad \mathsf{C}_y = \frac{v \Delta t}{\Delta y}. \tag{6.65}$$

For $\mathsf{C}_x = \mathsf{C}_y = 1$, the scheme provides $\tilde{c}^{n+1}_{i,j} = \tilde{c}^n_{i-1,j-1}$, with obvious physical interpretation. The scheme may also be written as

$$\begin{aligned} \tilde{c}^{n+1}_{i,j} &= (1 - \mathsf{C}_x)(1 - \mathsf{C}_y)\, \tilde{c}^n_{i,j} \\ &+ (1 - \mathsf{C}_y)\mathsf{C}_x\, \tilde{c}^n_{i-1,j} + (1 - \mathsf{C}_x)\mathsf{C}_y\, \tilde{c}^n_{i,j-1} + \mathsf{C}_x \mathsf{C}_y\, \tilde{c}^n_{i-1,j-1} \end{aligned} \tag{6.66}$$

highligthing the relative weights attached to the four grid points involved in the calculation (Figure 6-14). This expression proves that the method is monotonic for Courant numbers

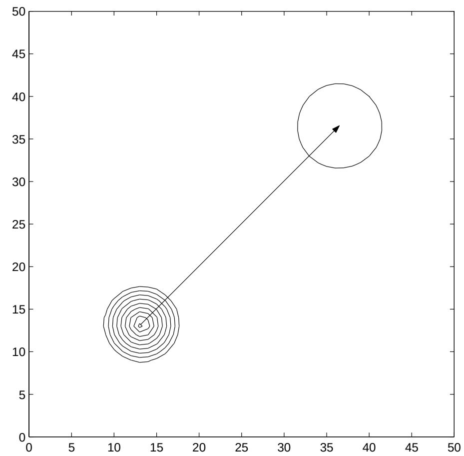

Figure 6-15 2D oblique advection using the CTU scheme (6.66). The solution's asymmetric deformation is reduced, but numerical diffusion still reduces the amplitude significantly.

smaller than one (ensuring that all coefficients on the right-hand side are positive). The method is only of first order according to the Godunov theorem, but it causes less distortion of the solution (Figure 6-15) than the previous approach. It still dampens excessively, however.

Other generalizations of the various 1D schemes to integrate along the current directions are possible but become rapidly complicated. We will therefore introduce a method that is almost as simple as solving a 1D problem but yet takes into account the multidimensional essence of the problem.

The method shown here is a special case of so-called *operator splitting* methods or *fractional steps*. To show the approach, we start from the semi-discrete equation

$$\frac{d\tilde{c}_i}{dt} + \mathcal{L}_1(\tilde{c}_i) + \mathcal{L}_2(\tilde{c}_i) = 0, \tag{6.67}$$

where $\mathcal{L}_1$ and $\mathcal{L}_2$ are two discrete operators, which in the present case are advection operators along x and y. Temporal discretization by time splitting executes:

$$\frac{\tilde{c}_i^\star - \tilde{c}_i^n}{\Delta t} + \mathcal{L}_1(\tilde{c}_i^n) = 0 \tag{6.68a}$$

$$\frac{\tilde{c}_i^{n+1} - \tilde{c}_i^\star}{\Delta t} + \mathcal{L}_2(\tilde{c}_i^\star) = 0, \tag{6.68b}$$

where the second operator is marched forward with a value already updated by the first operator.

In this manner, we solve two sequential one-dimensional problems, which is *a priori* not more complicated than before, but enjoy a major improvement compared to the naive double 1D approach used in (6.62): The initial (predictor) step creates a field that is already advected in the direction of the $\mathcal{L}_1$ operator, and the second (corrector) step advects in the remaining direction the partially displaced field. In this way, point (i, j) is influenced by the upstream value, point $(i-1, j-1)$ in the case of positive velocities (Figure 6-16).

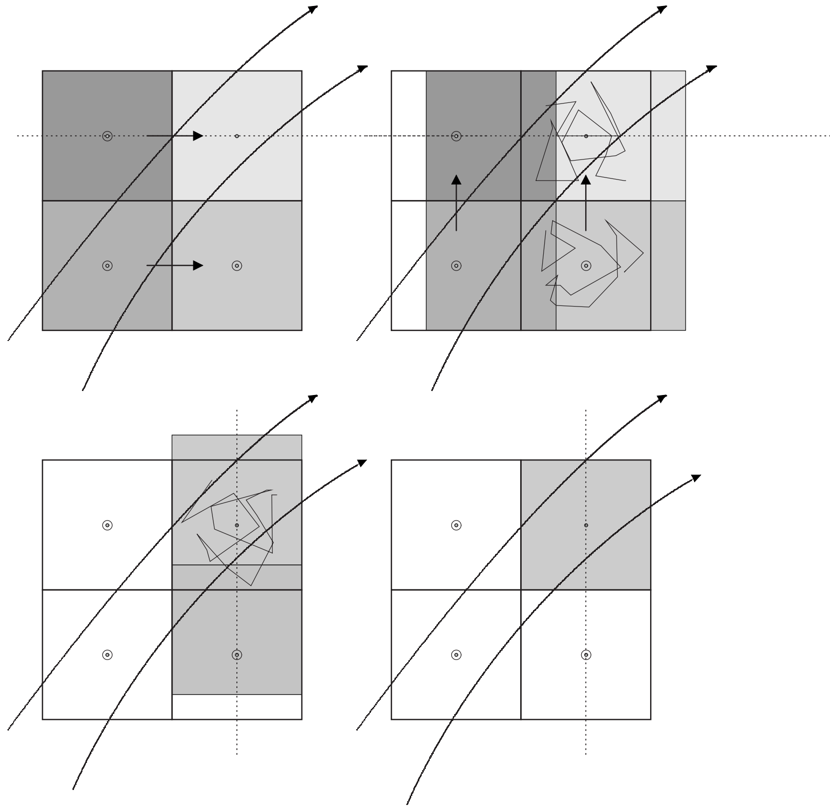

Figure 6-16 The splitting method uses two sequential 1D advection schemes. First the signal is transported along the x-direction and then the intermediate solution is advected along the y-direction. In this way, the information at upstream point $(i-1, j-1)$ is involved in the evolution of the value at (i, j) (case of positive velocity components).

To verify this, we can see how the splitting works with the 1D upwind scheme for positive and uniform velocities:

$$\tilde{c}^{\star}_{i,j} = \tilde{c}^{n}_{i,j} - \mathsf{C}_x(\tilde{c}^{n}_{i,j} - \tilde{c}^{n}_{i-1,j}) \qquad (6.69a)$$

$$\tilde{c}^{n+1}_{i,j} = \tilde{c}^{\star}_{i,j} - \mathsf{C}_y(\tilde{c}^{\star}_{i,j} - \tilde{c}^{\star}_{i,j-1}). \qquad (6.69b)$$

Substitution of the intermediate values $\tilde{c}^{\star}_{i,j}$ into the final step then proves that the scheme is identical to the CTU scheme (6.64) for uniform velocities. Such elimination, however, is not done in practice, and the sequence (6.69) is used. This is particularly convenient because, in the computer program, $\tilde{c}^{\star}$ may be stored during the first step in the future place of $\tilde{c}^{n+1}$ and then moved to the place of $\tilde{c}^{n}$ for the second step; $\tilde{c}^{n+1}$ can then be calculated and stored without need of additional storage.

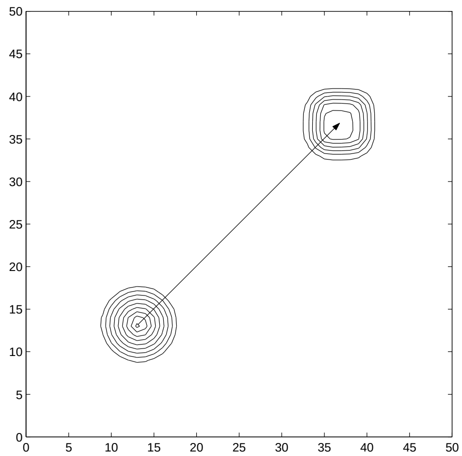

Figure 6-17 Advection at 45° of an initially conical distribution using the splitting method and the TVD scheme.

Using always the same operator with current values and the other with "predicted" values is unsatisfactory because it breaks the symmetry between the two spatial dimensions. Hence, it is recommended to alternate the order in which operators are applied, depending on whether the time step is even or odd. Following a time step using (6.68) we then switch the order of operators by performing

$$\frac{\tilde{c}_i^\star - \tilde{c}_i^{n+1}}{\Delta t} + \mathcal{L}_2(\tilde{c}_i^{n+1}) = 0 \tag{6.70a}$$

$$\frac{\tilde{c}_i^{n+2} - \tilde{c}_i^\star}{\Delta t} + \mathcal{L}_1(\tilde{c}_i^*) = 0. \tag{6.70b}$$

This approach, alternating the order of the directional splitting, is a special case of the more general *Strang splitting* method designed to maintain second-order time accuracy when using time splitting (Strang, 1968).

The splitting approach thus seems attractive. It is not more complicated than applying two successive one-dimensional schemes. In the general case, however, attention must be given to the direction of the local flow so that "upwinding" consistently draws the information from upstream, whatever that direction may be. There is no other complication, and we now proceed with a test of the method with the TVD scheme. As Figure 6-17 reveals, the result is a significant improvement with no increase of computational burden.

A more complicated case of advection can now be tried. For this we choose an initially square distribution of tracer and place it in a narrow sheared flow (Figure 6-18). We expect that the distribution will be distorted by the shear flow. To assess the quality of the advection scheme, we could try to obtain an analytical solution by calculating trajectories from the known velocity field, but a much simpler approach is to flip the sign of the velocity field after some time and continue the integration for an equal amount time. If the scheme were perfect, the patch would return to its original position and shape (without diffusion the system is reversible and trajectories integrated forward and then backward should bring all particles

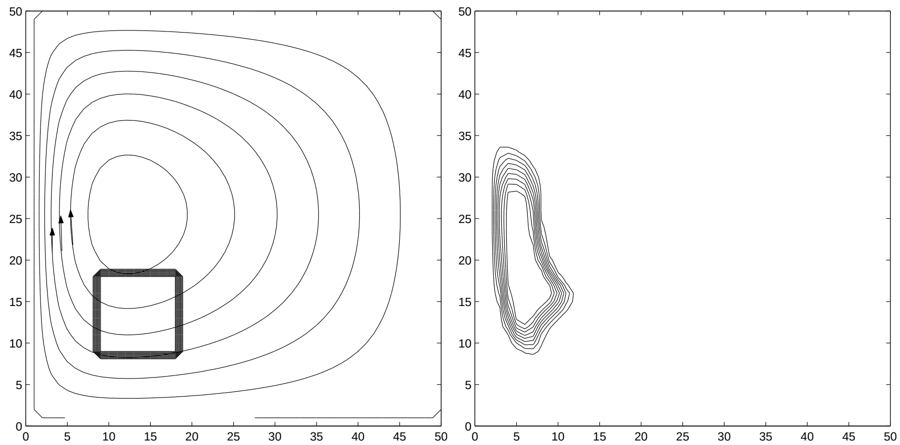

Figure 6-18 Advection of a square signal along a sheared boundary-layer current. *Left panel*: Initial distribution and streamlines. *Right panel*: After some advection. The distortion of the distribution is mostly due to the sheared current, which causes cross-stream squeezing and downstream stretching as the tracer enters the boundary layer.

back to their original position), but this won't be the case and the difference between initial and final states is a measure of the error. Because some of the error generated during the flow in one direction may be negated during the return flow, we also need to consider the result at the moment of current reversal, *i.e.*, the moment of farthest displacement.

For the method developed up to now, some degradation occurs and bizarre results happen, even in regions of almost uniform flow. To discern the cause of this degradation we first have to realize that the oblique advection test case is special in the sense that during a 1D step, the corresponding velocity is uniform. In the present case, the velocity during a sub-step is no longer uniform, and application of the first sub-step on a uniform field $\tilde{c} = \mathcal{C}$ yields

$$\frac{\tilde{c}^{\star}_{i,j} - \mathcal{C}}{\Delta t} + \frac{\tilde{u}_{i+1/2,j} - \tilde{u}_{i-1/2,j}}{\Delta x}\,\mathcal{C} = 0,$$

which provides a value of $\tilde{c}^{\star}_{i,j}$ different from the constant $\mathcal{C}$. The next step is unable to correct this by returning the distribution back to a constant. The problem arises because the sub-step is not characterized by zero divergence of the 1D velocity field, and conservation of the tracer is not met. Conservation in the presence of a converging/diverging velocity in 1D is, however, encountered in another, physical problem: compressible flow. Mimicking this problem, we introduce a *pseudo-compressible approach*, which introduces a density-like variable ρ, to calculate the pseudo-mass conservation written as

$$\frac{\partial}{\partial t}(\rho) + \frac{\partial}{\partial x}(\rho u) + \frac{\partial}{\partial y}(\rho v) = 0 \tag{6.71}$$

and the tracer budget as

$$\frac{\partial}{\partial t}(\rho c) + \frac{\partial}{\partial x}(\rho u c) + \frac{\partial}{\partial y}(\rho v c) = 0. \tag{6.72}$$

The splitting method starts with a constant ρ during the first sub-step yields for the pseudo-mass equation

$$\frac{\rho^\star - \rho}{\Delta t} + \frac{\tilde{u}_{i+1/2,j} - \tilde{u}_{i-1/2,j}}{\Delta x}\, \rho = 0$$

and for the tracer concentration

$$\frac{\rho^\star \tilde{c}_i^\star - \rho \tilde{c}_i^n}{\Delta t} + \rho \mathcal{L}_1(\tilde{c}_i^n) = 0. \tag{6.73}$$

In each calculation the constant ρ is a multiplicative constant and, it can be taken out of the advection operator $\mathcal{L}_1$. The second sub-step follows with

$$\frac{\rho^{n+1} - \rho^\star}{\Delta t} + \frac{\tilde{v}_{i,j+1/2} - \tilde{v}_{i,j-1/2}}{\Delta y}\, \rho = 0,$$

$$\frac{\rho^{n+1} \tilde{c}_i^{n+1} - \rho^\star \tilde{c}_i^\star}{\Delta t} + \rho \mathcal{L}_2(\tilde{c}_i^\star) = 0, \tag{6.74}$$

with the constant ρ used in both spatial operators. Setting the pseudo-density ρ^{n+1} equal to its previous value ρ, so that it disappears from the equations after a full time-step, leads to the constraint that velocity is divergence-free in the sense of (6.58). If this is the case, when $\tilde{c}^n = \mathcal{C}$, it also guarantees $\tilde{c}^{n+1} = \mathcal{C}$.

Other splitting techniques have been devised (*e.g.*, Pietrzak, 1998), but the approach remains essentially the same: pseudo-compression in one direction during the first sub-step, followed by a compensating amount of decompression during the second sub-step in the other direction.

With pseudo-compressibility, the sheared flow advection simulated with a flux limiter indicates that the scheme is quite accurate (Figure 6-19), being both less diffusive than the upwind scheme (Figure 6-20) and less dispersive than the Lax-Wendroff method (Figure 6-21). The Matlab code `tvdadv2D.m` allows the reader to experiment with various strategies, by turning pseudo-compressibility on or off, enabling and disabling time splitting, and using different limiters in sheared and unsheared flow fields (Numerical Exercise 6-15).

Analytical Problems

6-1. Show that

$$c(x,y,t) \;=\; \frac{M}{4\pi \mathcal{A} t}\, e^{-[(x-ut)^2+(y-vt)^2]/4\mathcal{A}t} \tag{6.75}$$

is the solution of the two-dimensional advection-diffusion equation with uniform velocity components u and v. Plot the solution for decreasing values of t and infer the type of physical problem the initial condition is supposed to represent. Provide an interpretation of M. *Hint:* Integrate over the infinite domain.

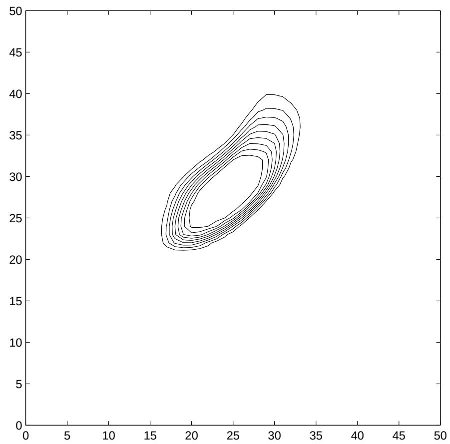

Figure 6-19 Advection with TVD scheme, Strang splitting and pseudo-compressibility. The initial condition is as shown in the left panel of Figure 6-18. *Left panel*: The patch of tracer at its furthest distance from the point of release, at the time of flow reversal. Its deformation is mostly physical and should ideally be undone during the return travel. *Right panel*: End state after return travel. The patch has nearly returned to its original location and shape, indicative of the scheme's good level of performance.

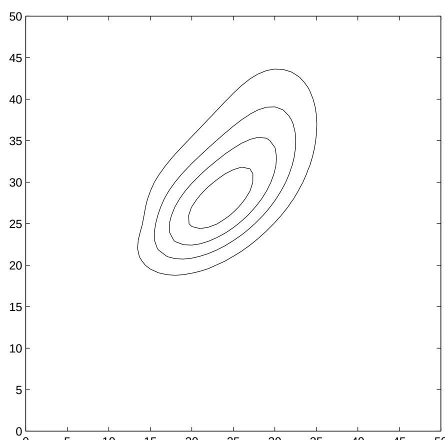

Figure 6-20 Same as Figure 6-19 but with advection by the upwind scheme, using Strang splitting and including pseudo-compressibility. The situation at time of flow reversal (left panel) and after return (right panel) shows that numerical diffusion is clearly stronger than with the TVD scheme. The final distribution is hardly identifiable with the initial condition. The contour values are the same as in Figure 6-19.

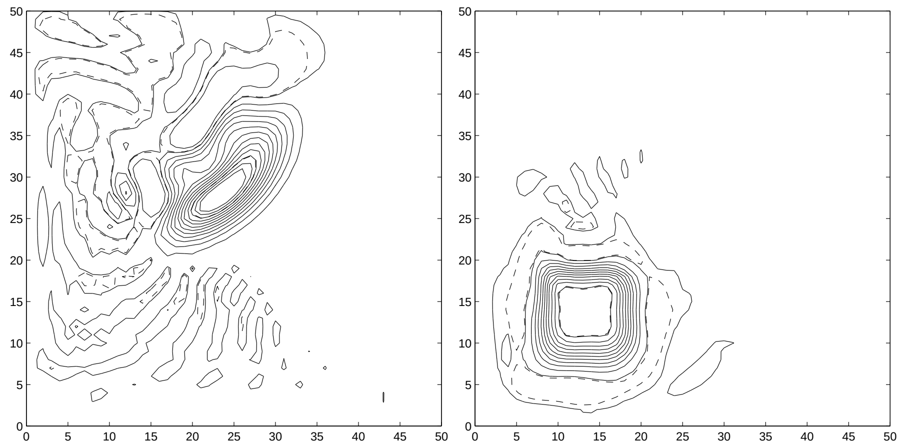

Figure 6-21 Same as Figure 6-19 but with advection by the Lax-Wendroff scheme, using Strang splitting and including pseudo-compressibility. The situation at flow reversal (left panel) shows much dispersion, which is partly undone during the return travel (right panel). At the end, the distribution has been fairly well reconstructed but there is some undershooting around the edges and overshooting in the center. Dashed lines indicate values outside the initial range.

6-2. Extend solution (6.75) to a radioactive tracer with decay constant K. *Hint:* Look for a solution of similar structure but with one more exponential factor.

6-3. Assuming a highly advective situation (high Peclet number), construct the 2D solution corresponding to the continuous release of a substance (S, in mass per time) from a punctual source (located at $x = y = 0$ in the presence of velocity u in the x-direction and diffusion $\mathcal{A}$ in the y-direction.

6-4. An unreported ship accident results in an instantaneous release of a conservative pollutant. This substance floats along the sea surface and disperses for some time until it is eventually detected and measured. The maximum concentration, then equal to $c = 0.1\mu$g/m^3, is found just West of the Azores at 38°30′N 30°00′W. A month later, the maximum concentration has decreased to 0.05μg/m^3 and is located 200 km further South. Assuming a fixed diffusivity $\mathcal{A} = 1000$ m^2/s and uniform steady flow, can you infer the amount of substance that was released from the ship, and the time and location of the accident? Finally, how long will it be before the concentration no longer exceeds 0.01μg/m^3 anywhere?

6-5. Study the dispersion relation of the equation

$$\frac{\partial c}{\partial t} = \kappa \frac{\partial^p c}{\partial x^p} \tag{6.76}$$

where p is a positive integer. Distinguish between even and odd values of p. What should be the sign of the coefficient κ for the solution to be well behaved? Then compare the cases $p = 2$ (standard diffusion) and $p = 4$ (biharmonic diffusion). Show that the latter generates a more scale-selective damping behavior than the former.

6-6. Explain the behavior found in Figure 6-10 by deriving the analytical solution of the corresponding physical problem (6.48).

6-7. In the interior of the Pacific Ocean, a slow upwelling compensating the deep convection of the high latitudes creates an average upward motion of about 5 m/year between depth of 4 km to 1 km. The average background turbulent diffusion in this region is estimated to be of the order of 10^{-4} m^2/s. From the deep region, Radium ^{226}Ra found in the sediments, is brought up, while Tritium ^{3}H of atmospheric origin occurs in surface waters. Radium has a half-life (time for 50% decay) of 1620 years, and Tritium a half-life of 12.43 years. Determine the steady-state solution using a one-dimensional vertical advection-diffusion model, assuming fixed and unit value of Tritium at the surface and zero at 4 km depth. For Radium, assume a unit value at depth of 4 km and zero value at the surface. Compare solutions with and without advection. Which tracer is more influenced by advection? Analyze the relative importance of advective and diffusive fluxes for each tracer at 4 km depth and 1 km depth.

6-8. If you intend to use a numerical scheme with an upwind advection to solve the preceding problem for Carbon-14 ^{14}C (half-life of 5730 years), what vertical resolution would be needed so that the numerical calculation does not introduce an excessively large numerical diffusion?

Numerical Exercises

6-1. Prove the assertion that a forward-in-time, central-in-space approximation to the advection equation is unconditionnaly unstable.

6-2. Use `advleap.m` with different initialization techniques for the first time step of the leapfrog scheme. What happens if an inconsistent approach is used (for example zero values)? Can you eliminate the spurious mode totally by a clever initialization of the auxiliary initial condition c^1 when a pure sinusoidal signal is being advected?

6-3. Use the stability analysis under the form (5.31) using an amplification factor. Verify that the stability condition is $|\mathsf{C}| \leq 1$.

6-4. Verify numerically that the leapfrog scheme conserves variance of the concentration distribution when $\Delta t \rightarrow 0$. Compare with the Lax-Wendroff scheme behavior for the same time steps.

6-5. Analyze the numerical phase speed of the upwind scheme. What happens for $\mathsf{C} = 1/2$? Which particular behavior is observed when $\mathsf{C} = 1$?

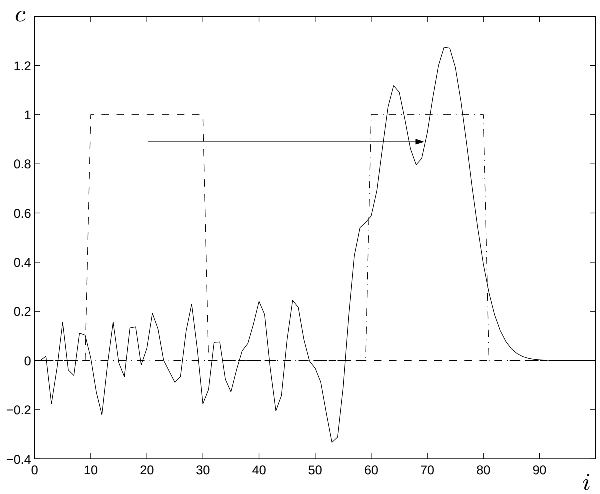

Figure 6-22 Standard test case with the trapezoidal scheme and centered spatial derivatives.

6-6. Design a fourth-order spatial difference and explicit time stepping for the 1D advection problem. What is the CFL condition of this scheme? Compare to the Von Neumann stability condition. Simulate the standard advection test case.

6-7. Design a higher-order finite-volume approach by using higher-order polynomials to calculate the flux integrals. Instead of a linear interpolation as in the Lax-Wendroff scheme, use a parabolic interpolation.

6-8. Show that the Von Neumann stability condition of the Beam-Warming scheme is $0 \leq \mathsf{C} \leq 2$.

6-9. Implement the trapezoidal scheme with centered space difference using the tridiagonal algorithm `thomas.m`. Apply it to the standard problem of the top-hat signal advection and verify that you find the result shown in Figure 6-22. Provide an interpretation of the result in terms of the numerical dispersion relation. Verify numerically that the variance is conserved exactly.

6-10. Show that the higher-order method for flux calculation at an interface using a linear interpolation on a non-uniform grid with spacing Δx_i between interfaces of cell i leads to the following flux, irrespective of the sign of the velocity

$$\tilde{q}_{i-1/2} \;=\; u\,\frac{(\Delta x_{i-1} - u\Delta t)\tilde{c}_i^n \;+\; (\Delta x_i + u\Delta t)\tilde{c}_{i-1}^n}{\Delta x_i + \Delta x_{i-1}}. \tag{6.77}$$

6-11. Use a leapfrog centered scheme for advection with diffusion. Apply it to the standard top-hat for different values of the diffusion parameter and interpret your results.

6-12. Find an explanation for why the $2\Delta x$ mode is stationary in all discretizations of advection. *Hint:* Use a sinusoidal signal of wavelength $2\Delta x$ and zero phase, then sample it. Change the phase (corresponding to a displacement) by different values less than π and resample. What do you observe?

6-13. Prove that (6.54) is the sufficient stability condition of (6.51). *Hint:* Rewrite $|\varrho|^2$ as $(\phi - 2\mathsf{C}^2\xi)^2 + 4\mathsf{C}^2\xi(1-\xi)$ and observe that as a function of ϕ the amplification factor reaches its maxima at the locations of the extrema of ϕ, itself constrained by (6.54).

6-14. Consider the one-dimensional advection-diffusion equation with Euler time discretization. For advection, use a centered difference with implicit factor α, and for diffusion the standard second-order difference with implicit factor β . Show that stability requires $(1-2\alpha)\mathsf{C}^2 \leq 2\mathsf{D}$ and $(1-2\beta)\mathsf{D} \leq 1/2$. Verify that, without diffusion, the explicit centered advection scheme is unstable.

6-15. Use `tvdadv2D.m` with different parameters (splitting or not, pseudo-mass conservation or not) under different conditions (sheared velocity field or solid rotation) and initial conditions (smooth field or strong gradients) with different flux limiters (upwind, Lax-Wendroff, TVD, *etc.*) to get a feeling of the range of different numerical solutions an advection scheme can provide compared to the analytical solution.

Richard Courant
1888 – 1972

Born in Upper Silesia, now in Poland but then part of Germany, Richard Courant was a precocious child and, because of economic difficulties at home, started to support himself by tutoring at an early age. His talents in mathematics led him to study in Göttingen, a magnet of mathematicians at the time, and Courant studied under David Hilbert with whom he eventually published in 1924 a famous treatise on methods of mathematical physics. In the foreword, Courant insists on the need for mathematics to be related to physical problems and warns against the trend of that time to loosen that link.

In 1928, well before the invention of computers, Richard Courant published with Kurt Friedrichs and Hans Lewy a most famous paper on the solution of partial difference equations, in which the now-called CFL stability condition was derived for the first time.

Courant left Germany for the United States, where he was offered a position at New York University. The Courant Institute of Mathematical Sciences at that institution is named after him. (*Photo from the MacTutor History of Mathematics archive at the University of St. Andrews*)

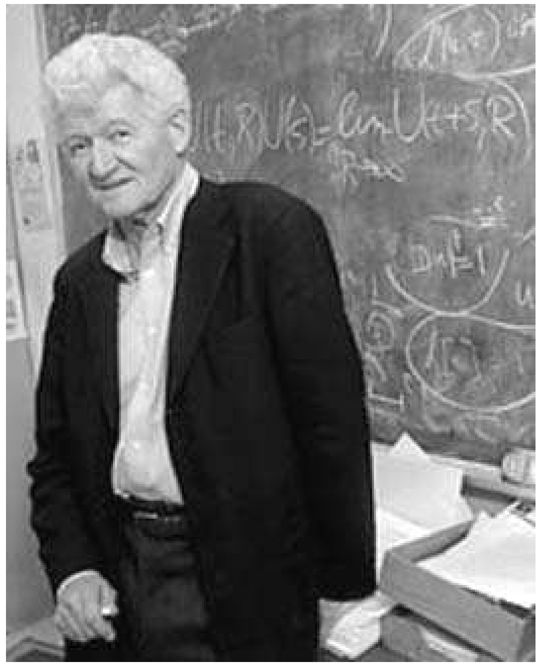

Peter Lax
1926 –

Born in Budapest (Hungary), Peter Lax quickly attracted attention for his mathematical prowess. Almost as soon as his parents and he moved to United States, in November 1941, and while he was still in high school, Peter was visited in his home by John von Neumann (see biography at end of Chapter 5), who had heard about this outstanding Hungarian mathematician. After working on the top-secret Mahattan atomic-bomb project in 1945–46, he completed his first university degree in 1947 and obtained his doctorate in 1949, both at New York University (NYU). In his own words, “these were years of explosive growth in computing”. Lax quickly gained a reputation for his work in numerical analysis.

Lax served as director of Courant Institute at NYU from 1972-1980 and was instrumental in getting the U.S. Government to provide supercomputers for scientific research. (*Photo from the MacTutor History of Mathematics archive at the University of St. Andrews*)

Part II

Rotation Effects

Chapter 7

Geostrophic Flows and Vorticity Dynamics

(October 18, 2006) **SUMMARY**: This chapter treats homogeneous flows with small Rossby and Ekman numbers. It is shown that such flows have a tendency to display vertical rigidity. The concept of potential vorticity is then introduced. The solution of vertically homogeneous flows often involves a Poisson equation for the pressure distribution, and numerical techniques are presented to accomplish this.

7.1 Homogeneous geostrophic flows

Let us consider rapidly rotating fluids by restricting our attention to situations where the Coriolis acceleration strongly dominates the various acceleration terms. Let us further consider homogeneous fluids and ignore frictional effects, by assuming

$$Ro_T \ll 1, \quad Ro \ll 1, \quad Ek \ll 1, \tag{7.1}$$

together with $\rho = 0$ (no density variation). The lowest-order equations governing such homogeneous, frictionless, rapidly rotating fluids are the following simplified forms of equations of motion, (4.21):

$$-fv = -\frac{1}{\rho_0}\frac{\partial p}{\partial x} \tag{7.2}$$

$$+fu = -\frac{1}{\rho_0}\frac{\partial p}{\partial y} \tag{7.3}$$

$$0 = -\frac{1}{\rho_0}\frac{\partial p}{\partial z} \tag{7.4}$$

$$\frac{\partial u}{\partial x} + \frac{\partial v}{\partial y} + \frac{\partial w}{\partial z} = 0, \tag{7.5}$$

where f is the Coriolis parameter.

This reduced set of equations has a number of surprising properties. First, if we take the vertical derivative of the first equation, (7.2), we obtain, successively,

$$-f\,\frac{\partial v}{\partial z} \;=\; -\;\frac{1}{\rho_0}\,\frac{\partial}{\partial z}\left(\frac{\partial p}{\partial x}\right) \;=\; -\;\frac{1}{\rho_0}\,\frac{\partial}{\partial x}\left(\frac{\partial p}{\partial z}\right) \;=\; 0,$$

where the right-hand side vanishes because of (7.4). The other horizontal momentum equation, (7.3), succumbs to the same fate, bringing us to conclude that the vertical derivative of the horizontal velocity must be identically zero:

$$\frac{\partial u}{\partial z} \;=\; \frac{\partial v}{\partial z} \;=\; 0. \tag{7.6}$$

This result is known as the *Taylor–Proudman theorem* (Taylor, 1923; Proudman, 1953). Physically, it means that the horizontal velocity field has no vertical shear and that all particles on the same vertical move in concert. Such vertical rigidity is a fundamental property of rotating homogeneous fluids.

Next, let us solve the momentum equations in terms of the velocity components, a trivial task:

$$u \;=\; \frac{-1}{\rho_0 f}\,\frac{\partial p}{\partial y}, \qquad v \;=\; \frac{+1}{\rho_0 f}\,\frac{\partial p}{\partial x}, \tag{7.7}$$

with the corollary that the vector velocity $(u,\ v)$ is perpendicular to the vector $(\partial p/\partial x,\ \partial p/\partial y)$. Since the latter vector is none other than the pressure gradient, we conclude that the flow is not down-gradient but rather across-gradient. The fluid particles are not cascading from high to low pressures, as they would in a nonrotating viscous flow but, instead, are navigating along lines of constant pressure, called *isobars* (Figure 7-1). The flow is said to be isobaric, and isobars are streamlines. It also implies that no pressure work is performed either on the fluid or by the fluid. Hence, once initiated, the flow can persist without a continuous source of energy.

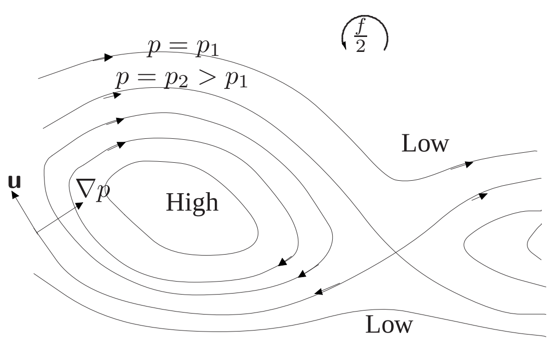

Figure 7-1 Example of geostrophic flow. The velocity vector is everywhere parallel to the lines of equal pressure. Thus, pressure contours act as streamlines. In the Northern Hemisphere (as pictured here), the fluid circulates with the high pressure on its right. The opposite holds for the Southern Hemisphere.

Such a flow field, where a balance is struck between the Coriolis and pressure forces, is called *geostrophic* (from the Greek, $\gamma\eta$ = Earth and $\sigma\tau\rho o\varphi\eta$ = turning). The property is called *geostrophy*. Hence, by definition, all geostrophic flows are isobaric.

A remaining question concerns the direction of flow along pressure lines. A quick examination of the signs in expressions (7.7) reveals that, where f is positive (Northern Hemisphere, counterclockwise ambient rotation), the currents/winds flow with the high pressures on their right. Where f is negative (Southern Hemisphere, clockwise ambient rotation), they flow with the high pressures on their left. Physically, the pressure force is directed from the high pressure toward the low pressure initiating a flow in that direction, but on the rotating planet, this flow is deflected to the right (left) in the Northern (Southern) Hemisphere. Figure 7-2 provides a meteorological example from the Northern Hemisphere.

If the flow field extends over a meridional span that is not too wide, the variation of the Coriolis parameter with latitude is negligible, and f can be taken as a constant. The frame of reference is then called the *f-plane*. In this case, the horizontal divergence of the geostrophic flow vanishes:

$$\frac{\partial u}{\partial x} + \frac{\partial v}{\partial y} = - \frac{\partial}{\partial x}\left(\frac{1}{\rho_0 f}\frac{\partial p}{\partial y}\right) + \frac{\partial}{\partial y}\left(\frac{1}{\rho_0 f}\frac{\partial p}{\partial x}\right) = 0. \tag{7.8}$$

Hence, geostrophic flows are naturally nondivergent on the *f*-plane. This leaves no room for vertical convergence or divergence, as the continuity equation (7.5) implies:

$$\frac{\partial w}{\partial z} = 0. \tag{7.9}$$

A corollary is that the vertical velocity, too, is independent of height. If the fluid is limited in the vertical by a flat bottom (horizontal ground or sea for the atmosphere) or by a flat lid (sea surface for the ocean), this vertical velocity must simply vanish, and the flow is strictly two-dimensional.

7.2 Homogeneous geostrophic flows over an irregular bottom

Let us still consider a rapidly rotating fluid, so that the flow is geostrophic, but now over an irregular bottom. We neglect the possible surface displacements, assuming that they remain modest in comparison with the bottom irregularities (Figure 7-3). An example would be the flow in a shallow sea (homogeneous waters) with depth ranging from 20 to 50 m and under surface waves a few centimeters high.

As shown in the development of kinematic boundary conditions (4.28), if the flow were to climb up or down the bottom, it would undergo a vertical velocity proportional to the slope:

$$w = u\frac{\partial b}{\partial x} + v\frac{\partial b}{\partial y}, \tag{7.10}$$

where b is the bottom elevation above the reference level. The analysis of the previous section implies that the vertical velocity is constant across the entire depth of the fluid. Since it must be zero at the top, it must be so at the bottom as well; that is,

$$u\frac{\partial b}{\partial x} + v\frac{\partial b}{\partial y} = 0, \tag{7.11}$$

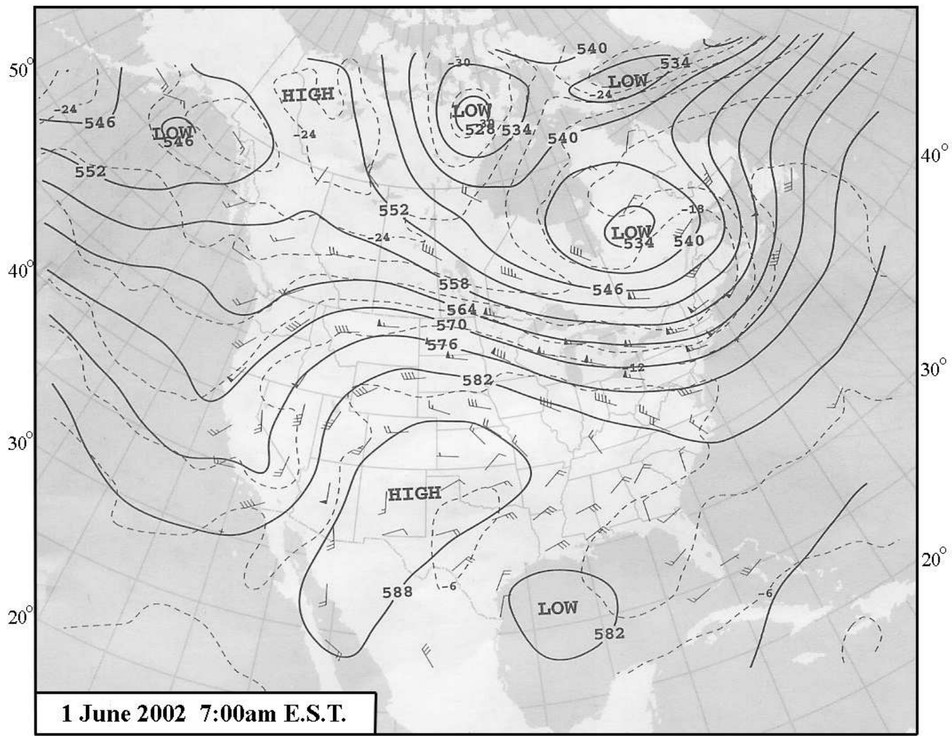

Figure 7-2 A meteorological example showing the high degree of parallelism between wind velocities and pressure contours (isobars), indicative of geostrophic balance. The solid lines are actually height contours of a given pressure (500 mb in this case) and not pressure at a given height. However, because atmospheric pressure variations are large in the vertical and weak in the horizontal, the two sets of contours are nearly identical by virtue of the hydrostatic balance. According to meteorological convention, wind vectors are depicted by arrows with flags and barbs: on each tail, a flag indicates a speed of 50 knots, a barb 10 knots and a half-barb 5 knots (1 knot = 1 nautical mile per hour = 0.5144 m/s). The wind is directed toward the bare end of the arrow, because meteorologists emphasize where the wind comes from, not where it is blowing. The dashed lines are isotherms. (*Chart by the National Weather Service, Department of Commerce, Washington, D.C.*)

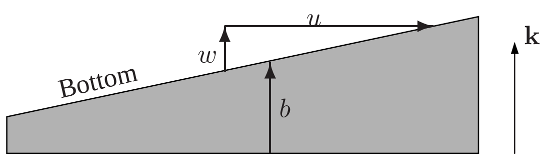

Figure 7-3 Schematic view of a flow over a sloping bottom. A vertical velocity must accompany flow across isobaths.

and the flow is prevented from climbing up or down the bottom slope. This property has profound implications. In particular, if the topography consists of an isolated bump (or dip) in an otherwise flat bottom, the fluid on the flat bottom cannot rise onto the bump, even partially, but must instead go around it. Because of the vertical rigidity of the flow, the fluid parcels at all levels – including levels above the bump elevation – must likewise go around. Similarly, the fluid over the bump cannot leave the bump but must remain there. Such permanent tubes of fluids trapped above bumps or cavities are called *Taylor columns* (Taylor, 1923).

In flat-bottomed regions a geostrophic flow can assume arbitrary patterns, and the actual pattern reflects the initial conditions. But, over a bottom where the slope is non-zero almost everywhere (Figure 7-4), the geostrophic flow has no choice but to follow the depth contours (called *isobaths*). Pressure contours are then aligned with topographic contours, and isobars coincide with isobaths. These lines are sometimes also called *geostrophic contours*. Note that a relation between pressure and fluid thickness exists but cannot be determined without additional information on the flow.

Open isobaths that start and end on a side boundary cannot support any flow, otherwise fluid would be required to enter or leave through lateral boundaries. The flow is simply blocked along the entire length of these lines. In other words, geostrophic flow can occur only along closed isobaths.

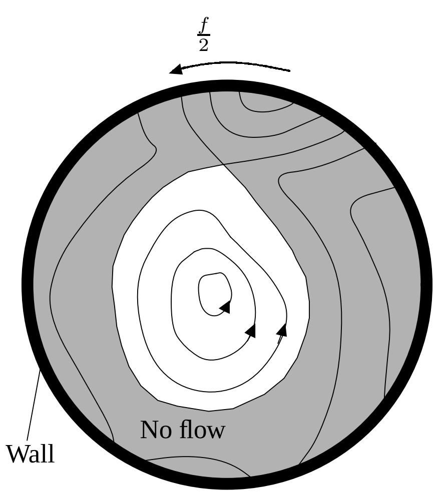

Figure 7-4 Geostrophic flow in a closed domain and over irregular topography. Solid lines are isobaths (contours of equal depth). Flow is permitted only along closed isobaths

The preceding conclusions hold true as long as the upper boundary is horizontal. If this is not the case, it can then be shown that geostrophic flows are constrained to be directed along lines of constant fluid depth. (See Analytical Problem 7-3.) Thus, the fluid is allowed to move up and down, but only as long as it is not being vertically squeezed or stretched. This property is a direct consequence of the inability of geostrophic flows to undergo any two-dimensional divergence.

7.3 Generalization to non-geostrophic flows

Let us now suppose that the fluid is not rotating as rapidly, so that the Coriolis acceleration no longer dwarfs other acceleration terms. We still continue to suppose that the fluid is homogeneous and frictionless. The momentum equations are now augmented to include the relative acceleration terms:

$$\frac{\partial u}{\partial t} + u\frac{\partial u}{\partial x} + v\frac{\partial u}{\partial y} + w\frac{\partial u}{\partial z} - fv = -\frac{1}{\rho_0}\frac{\partial p}{\partial x} \qquad (7.12a)$$

$$\frac{\partial v}{\partial t} + u\frac{\partial v}{\partial x} + v\frac{\partial v}{\partial y} + w\frac{\partial v}{\partial z} + fu = -\frac{1}{\rho_0}\frac{\partial p}{\partial y}. \qquad (7.12b)$$

Pressure still obeys (7.4), and continuity equation (7.5) has not changed.

If the horizontal flow field is initially independent of depth, it will remain so at all future times. Indeed, the nonlinear advection terms and the Coriolis terms are initially z-independent, and the pressure terms are, too, z-independent by virtue of (7.4). Thus, $\partial u/\partial t$ and $\partial v/\partial t$ must be z-independent, which implies that u and v tend not to become depth-varying and thus remain z-independent at all subsequent times. Let us restrict our attention to such flows, which in the jargon of geophysical fluid dynamics are called *barotropic*. Equations (7.12) then reduce to

$$\frac{\partial u}{\partial t} + u\frac{\partial u}{\partial x} + v\frac{\partial u}{\partial y} - fv = -\frac{1}{\rho_0}\frac{\partial p}{\partial x} \qquad (7.13a)$$

$$\frac{\partial v}{\partial t} + u\frac{\partial v}{\partial x} + v\frac{\partial v}{\partial y} + fu = -\frac{1}{\rho_0}\frac{\partial p}{\partial y}. \qquad (7.13b)$$

Although the flow has no vertical structure, the similarity to geostrophic flow ends here. In particular, the flow is not required to be aligned with the isobars, nor is it devoid of vertical velocity. To determine the vertical velocity, we turn to continuity equation (7.5),

$$\frac{\partial u}{\partial x} + \frac{\partial v}{\partial y} + \frac{\partial w}{\partial z} = 0,$$

in which we note that the first two terms are independent of z but do not necessarily add up to zero. A vertical velocity varying linearly with depth can exist, enabling the flow to support two-dimensional divergence and thus allowing a flow across isobaths.

An integration of the preceding equation over the entire fluid depth yields

$$\left(\frac{\partial u}{\partial x} + \frac{\partial v}{\partial y}\right) \int_b^{b+h} dz + [w]_b^{b+h} = 0, \qquad (7.14)$$

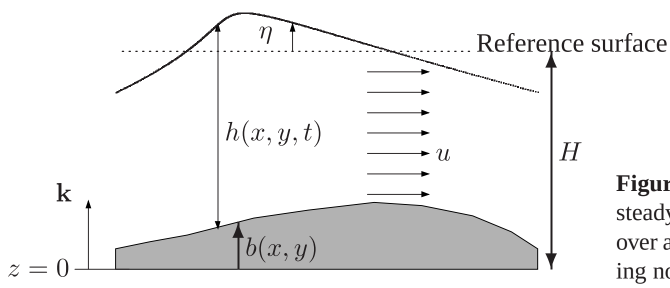

Figure 7-5 Schematic diagram of unsteady flow of a homogeneous fluid over an irregular bottom and the attending notation.

where b is the bottom elevation above a reference level and h is the local and instantaneous fluid layer thickness (Figure 7-5). Because fluid particles on the surface cannot leave the surface and particles on the bottom cannot penetrate through the bottom, the vertical velocities at these levels are given by (4.28) and (4.31)

$$\begin{aligned} w(z=b+h) &= \frac{\partial}{\partial t}(b+h) + u\frac{\partial}{\partial x}(b+h) + v\frac{\partial}{\partial y}(b+h) \qquad (7.15)\\ &= \frac{\partial \eta}{\partial t} + u\frac{\partial \eta}{\partial x} + v\frac{\partial \eta}{\partial y} \\ w(z=b) &= u\frac{\partial b}{\partial x} + v\frac{\partial b}{\partial y}\,. \qquad (7.16)\end{aligned}$$

Equation (7.14) then becomes, using the surface elevation $\eta = b + h - H$:

$$\frac{\partial \eta}{\partial t} + \frac{\partial}{\partial x}(hu) + \frac{\partial}{\partial y}(hv) = 0, \qquad (7.17)$$

which supersedes (7.5) and eliminates the vertical velocity from the formalism.

Finally, since the fluid is homogeneous, the dynamic pressure, p, is independent of depth. In the absence of a pressure variation above the fluid surface (*e.g.*, uniform atmospheric pressure over the ocean), this dynamic pressure is

$$p = \rho_0 g \eta, \qquad (7.18)$$

where g is the gravitational acceleration according to (4.33). With p replaced by the preceding expression, equations (7.13) and (7.17) form a 3-by-3 system for the variables u, v and η. The vertical variable no longer appears, and the independent variables are x, y and t. This system is

$$\frac{\partial u}{\partial t} + u\frac{\partial u}{\partial x} + v\frac{\partial u}{\partial y} - fv = -g\frac{\partial \eta}{\partial x} \qquad (7.19a)$$

$$\frac{\partial v}{\partial t} + u\frac{\partial v}{\partial x} + v\frac{\partial v}{\partial y} + fu = -g\frac{\partial \eta}{\partial y} \qquad (7.19b)$$

$$\frac{\partial \eta}{\partial t} + \frac{\partial}{\partial x}(hu) + \frac{\partial}{\partial y}(hv) = 0. \qquad (7.19c)$$

Although this system of equations is applied as frequently to the atmosphere as to the ocean, it bears the name *shallow-water model*[1]. If the bottom is flat, the equations become

$$\frac{\partial u}{\partial t} + u\,\frac{\partial u}{\partial x} + v\,\frac{\partial u}{\partial y} - fv = -g\,\frac{\partial h}{\partial x} \tag{7.20a}$$

$$\frac{\partial v}{\partial t} + u\,\frac{\partial v}{\partial x} + v\,\frac{\partial v}{\partial y} + fu = -g\,\frac{\partial h}{\partial y} \tag{7.20b}$$

$$\frac{\partial h}{\partial t} + \frac{\partial}{\partial x}(hu) + \frac{\partial}{\partial y}(hv) = 0. \tag{7.20c}$$

This is a formulation that we will encounter in layered models (Chapter 12).

7.4 Vorticity dynamics

In the study of geostrophic flows (Section 7.1), it was noted that the pressure terms cancel in the expression of the two-dimensional divergence. Let us now repeat this operation while keeping the added acceleration terms by subtracting the y-derivative of (7.13a) from the x-derivative of (7.13b). After some manipulations, the result can be cast as follows:

$$\frac{d}{dt}\left(f + \frac{\partial v}{\partial x} - \frac{\partial u}{\partial y}\right) + \left(\frac{\partial u}{\partial x} + \frac{\partial v}{\partial y}\right)\left(f + \frac{\partial v}{\partial x} - \frac{\partial u}{\partial y}\right) = 0, \tag{7.21}$$

where the material time derivative is defined as

$$\frac{d}{dt} = \frac{\partial}{\partial t} + u\frac{\partial}{\partial x} + v\frac{\partial}{\partial y}\,.$$

In the derivation, care was taken to allow for the possibility of a variable Coriolis parameter (which on a sphere varies with latitude and thus with position). The grouping

$$f + \frac{\partial v}{\partial x} - \frac{\partial u}{\partial y} = f + \zeta \tag{7.22}$$

is interpreted as the sum of the ambient vorticity (f) with the relative vorticity ($\zeta = \partial v/\partial x - \partial u/\partial y$). To be precise, the vorticity is a vector, but since the horizontal flow field has no depth-dependence, there is no vertical shear and no eddies with horizontal axes. The vorticity vector is strictly vertical, and the preceding expression merely shows that vertical component.

Similarly, terms in the continuity equation, (7.17), can be regrouped as

$$\frac{d}{dt}h + \left(\frac{\partial u}{\partial x} + \frac{\partial v}{\partial y}\right)h = 0. \tag{7.23}$$

[1] In the absence of rotation, these equations also bear the name of *Saint-Venant equations*, in honor of Jean Claude Saint-Venant (1797–1886) who first derived them in the context of river hydraulics.

If we now consider a narrow fluid column of horizontal cross-section ds, its volume is hds and, by virtue of conservation of volume in an incompressible fluid, the following equation holds:

$$\frac{d}{dt}(h\,ds) \;=\; 0, \tag{7.24}$$

This implies, as intuition suggests, that if the parcel is squeezed vertically (decreasing h), it stretches horizontally (increasing ds), and vice versa (Figure 7-6). Combining (7.23) for h with (7.24) for hds yields an equation for ds:

$$\frac{d}{dt}ds \;=\; \left(\frac{\partial u}{\partial x} \;+\; \frac{\partial v}{\partial y}\right) ds, \tag{7.25}$$

which simply says that horizontal divergence ($\partial u/\partial x + \partial v/\partial y > 0$) causes widening of the cross-sectional area ds, and convergence ($\partial u/\partial x + \partial v/\partial y < 0$) a narrowing of the cross-section. It could have been derived from first principles (see Analytical Problem 7-4).

Now, combining (7.21) and (7.25) yields

$$\frac{d}{dt}\left[(f \;+\; \zeta)\; ds\right] \;=\; 0 \tag{7.26}$$

and implies that the product $(f+\zeta)ds$ is conserved by the fluid parcel. This product can be interpreted as the vorticity flux (vorticity integrated over the cross-section) and is therefore the *circulation* of the parcel. Equation (7.26) is the particular expression for rotating, two-dimensional flows of Kelvin's theorem, which guarantees conservation of circulation in inviscid fluids (Kundu, 1990, pages 124–128).

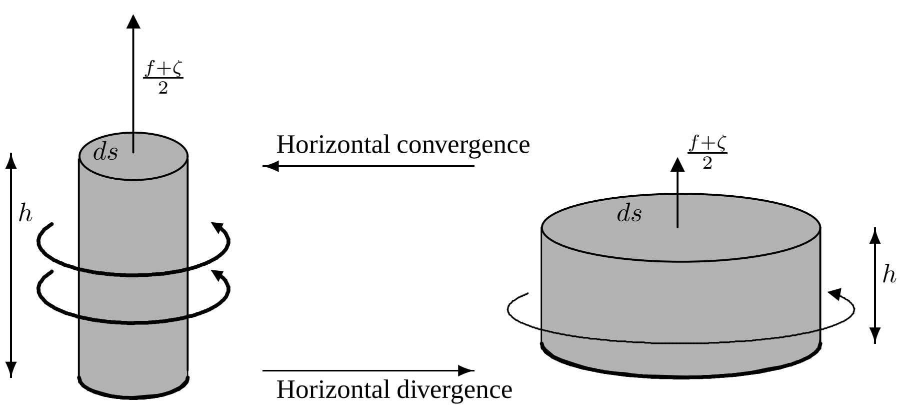

Figure 7-6 Conservation of volume and circulation of a fluid parcel undergoing vertical squeezing or stretching. The products $h\,ds$ and $(f+\zeta)\,ds$ are conserved during the transformation. As a corollary, the ratio $(f+\zeta)/h$, called the potential vorticity, is also conserved.

This conservation principle is akin to that of angular momentum for an isolated system. The best example is that of a ballerina spinning on her toes; with her arms stretched out, she spins slowly, but with her arms brought against her body, she spins more rapidly. Likewise in homogeneous geophysical flows, when a parcel of fluid is squeezed laterally (ds decreasing), its vorticity must increase ($f + \zeta$ increasing) to conserve circulation.

Now, if both circulation and volume are conserved, so is their ratio. This ratio is particularly helpful, for it eliminates the parcel's cross-section and thus depends only on local variables of the flow field:

$$\frac{d}{dt}\left(\frac{f \, + \, \zeta}{h}\right) \; = \; 0, \tag{7.27}$$

where

$$q \; = \; \frac{f + \zeta}{h} \; = \; \frac{f \; + \; \partial v/\partial x \; - \; \partial u/\partial y}{h} \tag{7.28}$$

is called the *potential vorticity*. The preceding analysis interprets potential vorticity as circulation per volume. This quantity, as will be shown on numerous occasions in this book, plays a fundamental role in geophysical flows. Note that equation (7.27) could have been derived directly from (7.21) and (7.23) without recourse to the introduction of the variable ds.

Let us now go full circle and return to rapidly rotating flows, those in which the Coriolis force dominates. In this case, the Rossby number is much less than unity ($Ro = U/\Omega L \ll 1$), which implies that the relative vorticity ($\zeta = \partial v/\partial x - \partial u/\partial y$, scaling as U/L) is negligible in front of the ambient vorticity (f, scaling as Ω). The potential vorticity reduces to

$$q \; = \; \frac{f}{h} \tag{7.29}$$

which, if f is constant – such as in a rotating laboratory tank or for geophysical patterns of modest meridional extent – implies that each fluid column must conserve its height h. In particular, if the upper boundary is horizontal, fluid parcels must follow isobaths, consistent with the existence of Taylor columns (Section 7.2).

Before closing this section, let us derive a germane result, which will be useful later. Consider the dimensionless expression

$$\sigma \; = \; \frac{z - b}{h}, \tag{7.30}$$

which is the fraction of the local height above the bottom to the full depth of the fluid, or, in short, the relative height above bottom ($0 \le \sigma \le 1$). Its material time derivative is

$$\frac{d\sigma}{dt} \; = \; \frac{1}{h}\,\frac{d}{dt}(z - b) \; - \; \frac{z - b}{h^2}\,\frac{dh}{dt}. \tag{7.31}$$

Since $dz/dt = w$ by definition of the vertical velocity and because w varies linearly from db/dt at the bottom ($z = b$) to $d(b + h)/dt$ at the top ($z = b + h$), we have

$$\frac{dz}{dt} \; = \; w \; = \; \frac{db}{dt} \; + \; \frac{z - b}{h}\,\frac{dh}{dt}. \tag{7.32}$$

Use of this last expression to eliminate dz/dt from (7.31) cancels all terms on the right, leaving only:

$$\frac{d\sigma}{dt} = 0. \tag{7.33}$$

Thus, a fluid parcel retains its the relative position within the fluid column.

7.5 Rigid-lid approximation

Except in the case when fast surface waves are of interest (Section 9.1), we can exploit the fact that large-scale motions in the ocean are relatively slow and introduce the so-called *rigid-lid approximation*. Large-scale movements with small Rossby numbers are close to geostrophic equilibrium, and their dynamic pressure thus scales as $p \sim \rho_0 \Omega U L$ (see (4.16)), and, since $p = \rho_0 g \eta$ in a homogeneous fluid, the scale ΔH of surface-height displacements is $\Delta H \sim \Omega U L / g$. Using the latter in the vertically-integrated volume-conservation equation, we can then compare the sizes of the different terms. Assuming that the time scale is not shorter than the inertial time scale $1/\Omega$, we have:

$$\frac{\partial \eta}{\partial t} + \frac{\partial}{\partial x}(hu) + \frac{\partial}{\partial y}(hv) = 0$$

$$\Omega \Delta H \qquad \frac{HU}{L} \qquad \frac{HU}{L},$$

in which $\Omega \Delta H \sim \Omega^2 U L / g$, and the scale ratio of the first term to the other terms is $\Omega^2 L^2 / gH$. In many situations, this ratio is very small,

$$\frac{\Omega^2 L^2}{gH} \ll 1, \tag{7.34}$$

and the time derivative in the volume-conservation equation may be neglected:

$$\frac{\partial}{\partial x}(hu) + \frac{\partial}{\partial y}(hv) = 0. \tag{7.35}$$

This is called the *rigid-lid approximation* (Figure 7-7).

This approximation, however, has a major implication when we solve the equations numerically, because now, instead of using the time-derivative of the continuity equation to march η forward in time and determine the hydrostatic pressure p from it, we somehow need to find a pressure field that ensures that at any moment the *transport* field $(\mathrm{U}, \mathrm{V}) = (hu, hv)$ is nondivergent.

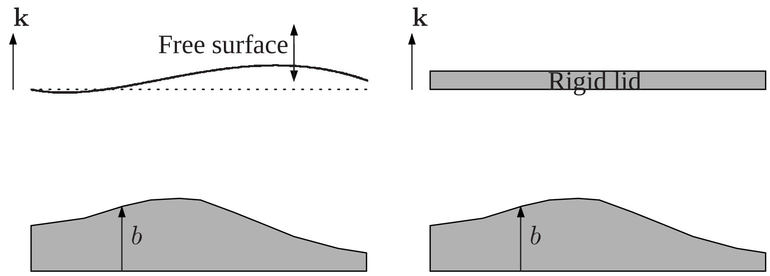

Figure 7-7 A free-surface formulation (left panel) allows the surface to move with the flow, whereas a rigid-lid formulation assumes a fixed surface, under which pressure is not uniform because the "lid" resists any local upward or downward force.

The momentum equations of the shallow-water model can be recast in transport form:

$$\frac{\partial}{\partial t}(hu) = -\frac{h}{\rho_0}\frac{\partial p}{\partial x} + F_x \tag{7.36a}$$
$$\text{with} \quad F_x = -\frac{\partial}{\partial x}(huu) - \frac{\partial}{\partial y}(hvu) + f\,hv$$
$$\frac{\partial}{\partial t}(hv) = -\frac{h}{\rho_0}\frac{\partial p}{\partial y} + F_y \tag{7.36b}$$
$$\text{with} \quad F_y = -\frac{\partial}{\partial x}(huv) - \frac{\partial}{\partial y}(hvv) - f\,hu.$$

Since we have neglected the variation η in surface elevation, we can take in the preceding equations $h = H - b$, a known function of the coordinates x and y. The task ahead of us is to find a way to calculate from the preceding two equations (7.36a) and (7.36b) a pressure field p that leads to satisfaction of constraint (7.35). To do so, we have two approaches at our disposal. The first one is based on a diagnostic equation for pressure (Section 7.6), and the second one on a streamfunction formulation (Section 7.7).

7.6 Numerical solution of the rigid-lid pressure equation

The pressure method uses equations (7.36a) and (7.36b) to construct an equation for pressure while enforcing the no-divergence constraint. This is accomplishes by adding the x-derivative of (7.36a) to the y-derivative of (7.36b) and exploiting (7.35) to eliminate the time derivatives. Placing the pressure terms on the left then yields:

$$\frac{\partial}{\partial x}\left(\frac{h}{\rho_0}\frac{\partial p}{\partial x}\right) + \frac{\partial}{\partial y}\left(\frac{h}{\rho_0}\frac{\partial p}{\partial y}\right) = \frac{\partial F_x}{\partial x} + \frac{\partial F_y}{\partial y} = Q. \tag{7.37}$$

This equation for pressure is the archetype of a so-called *elliptic equation*.

To complement it, appropriate boundary conditions must be provided. These pressure conditions are deduced from the impermeability of solid lateral boundaries or from the inflow/outflow conditions at open boundaries (see Section 4.6). For example, if the boundary is parallel to the y-axis (say $x = x_0$) and is impermeable, we need to impose $hu = 0$ (no normal transport), and the x-momentum equation in transport form reduces there to

$$\frac{h}{\rho_0}\frac{\partial p}{\partial x} = F_x, \tag{7.38}$$

while along an impermeable boundary parallel to the x-axis (say $y = y_0$), we need to impose $hv = 0$ and obtain from the y-momentum equation

$$\frac{h}{\rho_0}\frac{\partial p}{\partial y} = F_y. \tag{7.39}$$

In other words, the normal pressure gradient is given along impermeable boundaries. At inflow/ouflow boundaries, the expression is more complicated but it is still the normal pressure gradient that is imposed. An elliptic equation with the normal derivative prescribed all along the perimeter of the domain is called a Neumann problem[2].

One and only one condition at every point along all boundaries of the domain is necessary and sufficient to determine the solution of the elliptic equation (7.37). Since the pressure appears only through its derivatives in both the elliptic equation (7.37) and the boundary condition (7.38)–(7.39), the solution is only defined within an additional arbitrary constant, the value of which may be chosen freely without affecting the resulting velocity field. There is a natural choice, however, which is to select the constant so that the pressure has a zero average over the domain. By virtue of $p = \rho_0 g\eta$, this corresponds to stating that η has a zero average over the domain.

Numerically, the solution can be sought by discretizing the elliptic equation for pressure across a rectangular box:

$$\begin{aligned}&\frac{1}{\Delta x}\left(h_{i+1/2}\,\frac{\tilde{p}_{i+1,j}-\tilde{p}_{i,j}}{\Delta x} - h_{i-1/2}\,\frac{\tilde{p}_{i,j}-\tilde{p}_{i-1,j}}{\Delta x}\right) + \\ &\frac{1}{\Delta y}\left(h_{j+1/2}\,\frac{\tilde{p}_{i,j+1}-\tilde{p}_{i,j}}{\Delta y} - h_{j-1/2}\,\frac{\tilde{p}_{i,j}-\tilde{p}_{i,j-1}}{\Delta y}\right) = \rho_0 Q_{ij}.\end{aligned} \tag{7.40}$$

This form a set of linear equations for the $\tilde{p}_{i,j}$ values across the grid, connecting five unknowns at each grid point (Figure 7-8), a situation already encountered in the treatment of two-dimensional implicit diffusion (Section 5.6). But there is a circular dependence: The right-hand side $\rho_0 Q_{ij}$ is not known until the velocity components are determined and the determination of these requires the knowledge of the pressure gradient. Because the momentum equations are nonlinear, this is a nonlinear dependence, and the method for constructing and solving a linear system cannot be applied.

[2] If the pressure itself had been imposed all along the perimeter of the domain, the problem would have been called a Dirichlet problem.

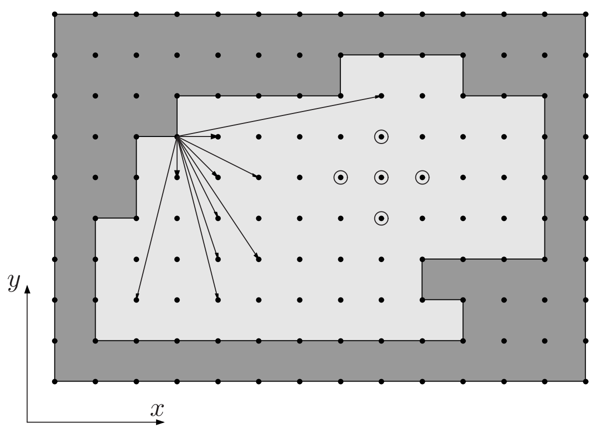

Figure 7-8 Discretization of the two-dimensional elliptic equation. The stencil is a five-point array consisting of the point where the calculation is performed and its four neighbors. These neighboring points are in turn dependent on their respective neighbors, and so on until boundary points are reached. In other words, the value at every point inside the domain is influenced by all other interior and boundary values. Simple accounting indicates that one and only one boundary condition is needed at all boundary points.

The natural way to proceed is to progress incrementally. If we assume that at time level n we have a divergent-free velocity field ($\tilde{u}^n$, $\tilde{v}^n$), we can use (7.40) to calculate the pressure at the same time level n and use its gradient in the momentum equations to update the velocity components for time level $n+1$. But, this offers no guarantee that the updated velocity components will be divergence-free, despite the fact that the pressure distribution corresponds to a divergent-free flow field at the previous time level.

Once again, we face a situation in which discretized equations do not inherit certain mathematical properties of the continuous equations. In this case, we used properties of divergence and gradient operators to build a diagnostic pressure equation from the original equations, but these properties are not transferable to the numerical space unless special care is taken.

The design of adequate discrete equations, however, can be inspired by the mathematical operations used to reach the pressure equation (7.37): We started with the velocity equation and applied the divergence operator to make appear the divergence of the transport that we then set to zero, and we should perform the same operations in the discrete domain to ensure that at any moment the discrete transport field is nondivergent in a finite volume. This is expressed by discrete volume conservation as:

$$\frac{h_{i+1/2}\tilde{u}_{i+1/2} - h_{i-1/2}\tilde{u}_{i-1/2}}{\Delta x} + \frac{h_{j+1/2}\tilde{v}_{j+1/2} - h_{j-1/2}\tilde{u}_{j-1/2}}{\Delta y} = 0. \tag{7.41}$$

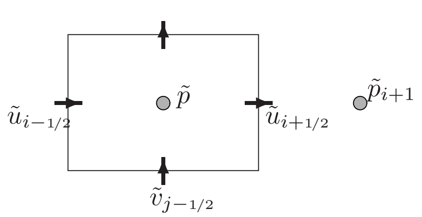

Figure 7-9 Arrangement of numerical unknowns for easy enforcement of numerical volume conservation and pressure-gradient calculations.

Anticipating a *staggered grid* configuration (Figure 7-9), we realize that it would be natural to calculate for each cell the velocity $\tilde{u}$ at the middle of the left and right interfaces $(i \pm 1/2, j)$ and the other velocity component $\tilde{v}$ at the middle of the top and bottom interfaces $(i, j \pm 1/2)$ so that the divergence may be calculated most naturally in (7.41). In contrast, $\tilde{p}$ values are calculated at cell centers. Leapfrog time discretization applied to (7.36a)–(7.36b) then provides:

$$h_{i+1/2}\tilde{u}^{n+1}_{i+1/2} = h_{i+1/2}\tilde{u}^{n-1}_{i+1/2} + 2\Delta t\, F_{x\,i+1/2} - 2\Delta t\, h_{i+1/2}\,\frac{\tilde{p}_{i+1} - \tilde{p}}{\rho_0 \Delta x} \tag{7.42a}$$

$$h_{j+1/2}\tilde{v}^{n+1}_{j+1/2} = h_{j+1/2}\tilde{v}^{n-1}_{j+1/2} + 2\Delta t\, F_{y\,j+1/2} - 2\Delta t\, h_{j+1/2}\,\frac{\tilde{p}_{j+1} - \tilde{p}}{\rho_0 \Delta y}, \tag{7.42b}$$

in which we omitted for clarity the obvious indices i, j and n.

Requesting now that the discretized version (7.41) of the non-divergence constraint hold at time level $n+1$, we can eliminate the velocity values at that time level by combining the equations (7.42) so that these terms cancel out. The result is the sought-after discretized equation for pressure:

$$\begin{aligned}\frac{1}{\Delta x}\left(h_{i+1/2}\frac{\tilde{p}_{i+1} - \tilde{p}}{\Delta x} - h_{i-1/2}\frac{\tilde{p} - \tilde{p}_{i-1}}{\Delta x}\right) + \frac{1}{\Delta y}\left(h_{j+1/2}\frac{\tilde{p}_{j+1} - \tilde{p}}{\Delta y} - h_{j-1/2}\frac{\tilde{p} - \tilde{p}_{j-1}}{\Delta y}\right) \\ = \rho_0\left(\frac{F_{x\,i+1/2} - F_{x\,i-1/2}}{\Delta x} + \frac{F_{y\,j+1/2} - F_{y\,j-1/2}}{\Delta y}\right) \\ + \frac{\rho_0}{2\Delta t}\left(\frac{h_{i+1/2}\tilde{u}^{n-1}_{i+1/2} - h_{i-1/2}\tilde{u}^{n-1}_{i-1/2}}{\Delta x} + \frac{h_{j+1/2}\tilde{v}^{n-1}_{j+1/2} - h_{j-1/2}\tilde{u}^{n-1}_{j-1/2}}{\Delta y}\right),\end{aligned} \tag{7.43}$$

where once again the obvious indices have been omitted.

It is clear that, up to the last term, this equation is a discrete version of (7.37) and resembles (7.40). The difference lies in the last term, which would vanish if the transport field were divergence free at time level $n-1$. We kept that term should the numerical solution of the discrete equation not be exact. Keeping the non-zero discrete divergence at $n-1$ in the equation is a way of applying an automatic correction to the discrete equation in order to insure the non-divergence of the transport at the new time level $n+1$. Neglecting this correction term would result in a gradual accumulation of errors and thus an eventually divergent transport field.

To summarize, the algorithm works as follows: Knowing velocity values at time levels n and $n-1$, we solve (7.43) iteratively for pressure, which is then used to advance velocity in time using (7.42a) and (7.42b). For quickly converging iterations, the pressure calculations can be initialized with the values from the previous time step. This iterative procedure is one of the sources of numerical errors against which the last term of (7.43) is kept as a precaution.

The discretization shown here is relatively simple, but in the more general case of higher-order methods or other grid configurations, the same approach can be used. We must ensure that the divergence operator applied to the transport field is discretized in the same way as the divergence operator is applied to the pressure gradient. Furthermore, the pressure gradient needs be discretized in the same way in both the velocity equation and the elliptic pressure equation. In summary, the derivatives similarly labeled in the equations below must be discretized in identical ways to procure a mathematically coherent scheme:

$$\underbrace{\frac{\partial}{\partial x}}_{(1)}(hu) \quad + \quad \underbrace{\frac{\partial}{\partial y}}_{(2)}(hv) \;=\; 0$$

$$\frac{\partial}{\partial t}(hu) \quad = \quad -\,\frac{h}{\rho_0}\,\underbrace{\frac{\partial p}{\partial x}}_{(3)} \;+\; F_x$$

$$\frac{\partial}{\partial t}(hv) \quad = \quad -\,\frac{h}{\rho_0}\,\underbrace{\frac{\partial p}{\partial y}}_{(4)} \;+\; F_y$$

$$\underbrace{\frac{\partial}{\partial x}}_{(1)}\left(\frac{h}{\rho_0}\underbrace{\frac{\partial p}{\partial x}}_{(3)}\right) \quad + \quad \underbrace{\frac{\partial}{\partial y}}_{(2)}\left(\frac{h}{\rho_0}\underbrace{\frac{\partial p}{\partial y}}_{(4)}\right) \;=\; \underbrace{\frac{\partial}{\partial x}}_{(1)}F_x \;+\; \underbrace{\frac{\partial}{\partial y}}_{(2)}F_y.$$

It also means one can generally not resort to a “black box” elliptic-equation solver to obtain a pressure field that is used in “hand made” discrete velocity equations.

7.7 Numerical solution of the streamfunction equation

Instead of calculating pressure, a second method in use with the rigid-lid approximation is a generalization of the velocity streamfunction ψ to the *volume transport streamfunction* Ψ:

$$hu \;=\; -\frac{\partial(h\psi)}{\partial y} \;=\; -\,\frac{\partial \Psi}{\partial y} \tag{7.45a}$$

$$hv \;=\; +\frac{\partial(h\psi)}{\partial x} \;=\; +\,\frac{\partial \Psi}{\partial x}. \tag{7.45b}$$

The difference between two isolines of Ψ can be interpreted as the volume transport between those lines, directed with the higher Ψ values to its right.

When transport components are calculated according to (7.45), volume conservation (7.35) is automatically satisfied and, as shown in Section 6.6, the numerical counterpart can also be divergence-free. We may therefore discretize the equation governing Ψ without hesitation, sure that its discrete solution will lead to a well behaved discrete velocity field.

To obtain a mathematical equation for the streamfunction, all we have to do is to eliminate the pressure from the momentum equations. This is accomplished by dividing (7.36a) and (7.36b) by h, differentiating the former by y and the latter by x, and finally subtracting one from the other. Replacement of the transport components hu and hv in terms of the streamfunction then yields:

$$\begin{aligned}\frac{\partial}{\partial t}\left[\frac{\partial}{\partial x}\left(\frac{1}{h}\frac{\partial \Psi}{\partial x}\right)+\frac{\partial}{\partial y}\left(\frac{1}{h}\frac{\partial \Psi}{\partial y}\right)\right] &= \frac{\partial}{\partial x}\left(\frac{F_y}{h}\right)-\frac{\partial}{\partial y}\left(\frac{F_x}{h}\right)\\ &= Q.\end{aligned} \tag{7.46}$$

The right-hand side could be further expanded in terms of the streamfunction, but for the sake of the following discussion it is sufficient to lump all its terms into a single "forcing" term Q.

We now consider a leapfrog time discretization or any other time discretization that allows us to write

$$\left[\frac{\partial}{\partial x}\left(\frac{1}{h}\frac{\partial\tilde{\Psi}}{\partial x}\right)^{n+1} + \frac{\partial}{\partial y}\left(\frac{1}{h}\frac{\partial\tilde{\Psi}}{\partial y}\right)^{n+1}\right] = F(\tilde{\Psi}^n, \tilde{\Psi}^{n-1}, ...). \tag{7.47}$$

In the case of a leapfrog discretization the right-hand side is

$$F(\tilde{\Psi}^n, \tilde{\Psi}^{n-1}, ...) = \left[\frac{\partial}{\partial x}\left(\frac{1}{h}\frac{\partial\tilde{\Psi}}{\partial x}\right)^{n-1} + \frac{\partial}{\partial y}\left(\frac{1}{h}\frac{\partial\tilde{\Psi}}{\partial y}\right)^{n-1}\right] + 2\Delta t\, Q^n, \tag{7.48}$$

which can be evaluated numerically knowing $\tilde{\Psi}^n$ and $\tilde{\Psi}^{n-1}$. The problem then amounts to solving (7.47) for $\tilde{\Psi}^{n+1}$. Again, an elliptic equation must be solved, as for the pressure equation in the previous section, and the same method can be applied.

Differences, others than the terms in the right-hand side, are noteworthy. First, instead of h appearing inside the derivatives, $1/h$ is involved, which increases the role played by the streamfunction derivatives in shallow regions ($h \rightarrow 0$, usually near boundaries), possibly amplifying errors on boundary conditions. This is in contrast to the pressure formulation, in which the influence of the vertically integrated pressure gradient decreases in shallow regions. Applications indeed reveal that the solution of the Poisson equation (7.43) is better conditioned and converges better than (7.47).

A second difference is related to the formulation of boundary conditions. While in the pressure approach imposing zero normal velocity leads to a condition on the normal derivative of pressure, a Neumann condition, the streamfunction formulation has the apparent advantage of only demanding that the streamfunction be constant along a solid boundary, a Dirichlet condition. A problem arises for ocean models when islands are present within the domain (Figure 7-10). Knowing that the streamfunction is constant on an impermeable boundary does not tell us what the value of the constant ought to be. This is no small matter because the difference of streamfunction values across a channel defines the volume transport in that channel. Such volume transport should be determined by the dynamics of the flow and not by the modeler's choice.

The streamfunction equation being linear with known right-hand side allows superposition of solutions, and we take one island at a time:

$$\frac{\partial}{\partial x}\left(\frac{1}{h}\frac{\partial\psi_k}{\partial x}\right) + \frac{\partial}{\partial y}\left(\frac{1}{h}\frac{\partial\psi_k}{\partial y}\right) = 0 \tag{7.49}$$

with ψ_k set to zero on all boundaries except $\psi_k = 1$ on the boundary for the k-th island. Each island thus engenders a dimensionless streamfunction $\psi_k(x, y)$ that can be used to construct the overall solution

$$\Psi(x, y, t) = \Psi_f(x, y, t) + \sum_k \Psi_k(t)\psi_k(x, y), \tag{7.50}$$

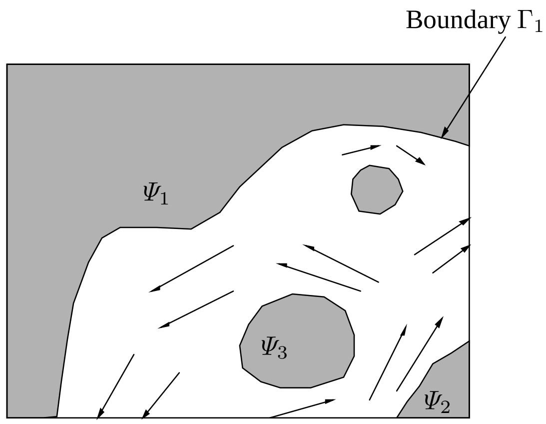

Figure 7-10 Boundary conditions on the streamfunction in an ocean model with islands. The streamfunction value must be prescribed constant along impermeable boundaries. Setting Ψ_1 and Ψ_2 for the outer boundaries is reasonable and amounts to imposing the total flow across the domain, but setting *a priori* the value of Ψ_3 along the perimeter of an island is in principle not permitted, because the flow around the island should depend on the interior solution and its temporal evolution. Clearly, a prognostic equation for the streamfunction value on islands is needed.

where Ψ_f is the particular solution of Equation (7.47) with streamfunction set to zero along all island boundaries and prescribed values along the outer boundaries and wherever the volume flow is known (for example at the inflow boundary as depicted in Figure 7-10). The $\Psi_k(t)$ coefficients are the time-dependent factors by which the island contributions must be multiplied to construct the full solution. What should these factors be is the question.

One possibility is to project the momentum equations onto the direction locally normal to the island boundary, as was done to determine the boundary conditions in the pressure formulation. Invoking Stokes theorem on the closed contour formed by the perimeter of the k-th island then provides an equation for the time derivative $d\Psi_k/dt$. Repeating the procedure for each island leads to a linear set of N equations, where N is the number of islands. These equations can then be integrated in time (*e.g.*, Bryan and Cox, 1972). This approach has become less popular over the years for several reasons, among which is the non-local nature of the equations. Indeed, each island equation involves both area and contour integrals all over the domain, causing serious difficulties when the domain is fragmented for calculation on separate computers working in parallel. Synchronization of the information exchange of different integral pieces across computers can be very challenging. Nevertheless, the streamfunction formulation is still available in most large-scale ocean models.

7.8 Laplacian inversion

Because the inversion of a Poisson-type equation is a recurrent task in numerical models, we now outline some of the methods designed to invert the discrete Poisson equation

$$\frac{\tilde{\psi}_{i+1,j} - 2\tilde{\psi}_{i,j} + \tilde{\psi}_{i-1,j}}{\Delta x^2} + \frac{\tilde{\psi}_{i,j+1} - 2\tilde{\psi}_{i,j} + \tilde{\psi}_{i,j-1}}{\Delta y^2} = \tilde{q}_{i,j} \qquad (7.51)$$

where the right-hand side is given and $\tilde{\psi}$ is the unknown field[3]. Iterative methods outlined in Section 5.6 using pseudo-time iterations were the first methods used to solve a linear system for $\tilde{\psi}_{i,j}$. The Jacobi method with over-relaxation reads

$$\begin{aligned} \tilde{\psi}_{i,j}^{(k+1)} &= \tilde{\psi}_{i,j}^{(k)} + \omega\, \epsilon_{i,j}^{(k)} \\ \left(\frac{2}{\Delta x^2} + \frac{2}{\Delta y^2}\right) \epsilon_{i,j}^{(k)} &= \\ \frac{\tilde{\psi}_{i+1,j}^{(k)} - 2\tilde{\psi}_{i,j}^{(k)} + \tilde{\psi}_{i-1,j}^{(k)}}{\Delta x^2} &+ \frac{\tilde{\psi}_{i,j+1}^{(k)} - 2\tilde{\psi}_{i,j}^{(k)} + \tilde{\psi}_{i,j-1}^{(k)}}{\Delta y^2} - \tilde{q}_{i,j}, \end{aligned} \tag{7.52}$$

in which the residual ϵ is used to correct the previous estimate at iteration (k). Taking the relaxation parameter $\omega > 1$ (*i.e.*, performing over-relaxation) accelerates convergence towards the solution, at the risk of instability. By considering iterations as evolution in pseudo-time, we can assimilate the parameter ω to a pseudo-time step and perform a numerical stability analysis. The outcome is that iterations are stable (*i.e.*, they converge) provided $0 \leq \omega < 2$. In terms of the general iterative solvers of Section 5.6, matrix **B** in (5.56) is diagonal. The algorithm requires at least as many iterations to propagate the information once through the domain as they are grid points across the domain. If M is the total number of grid points in the 2D model, then $\sqrt{M}$ is an estimate of the "width" of the grid, and it takes $\sqrt{M}$ iterations to propagate information once from side to side. Usually, M iterations are needed for convergence, and the cost rapidly becomes prohibitive with increased resolution.

The finite speed at which information is propagated during numerical iterations does not reflect the actual nature of elliptic equation, the interconnectness of which theoretically implies instantaneous adjustment to any change anywhere, and we sense that we should be able to better. Because in practice the iterations are only necessary to arrive at the converged solution, we do not need to mimic the process of a time-dependent equation and can tamper with the pseudo-time.

The Gauss-Seidel method with over-relaxation calculates the residual instead as

$$\begin{aligned} \left(\frac{2}{\Delta x^2} + \frac{2}{\Delta y^2}\right) \epsilon_{i,j}^{(k)} &= \\ \frac{\tilde{\psi}_{i+1,j}^{(k)} - 2\tilde{\psi}_{i,j}^{(k)} + \tilde{\psi}_{i-1,j}^{(k+1)}}{\Delta x^2} &+ \frac{\tilde{\psi}_{i,j+1}^{(k)} - 2\tilde{\psi}_{i,j}^{(k)} + \tilde{\psi}_{i,j-1}^{(k+1)}}{\Delta y^2} - \tilde{q}_{i,j} \end{aligned} \tag{7.53}$$

in which the updated values at the previous neighbors $(i-1, j)$ and $(i, j-1)$ are immediately used (assuming that we loop across the domain with increasing i and j). In other words, the algorithm (7.53) does not delay using the most updated values. With this time saving also comes a saving of storage as old values can be replaced by new values as soon as these are calculated. Matrix **B** of equation (5.56) is triangular, and the Gauss-Seidel loop (7.53) is the matrix inversion performed by backward substitution. The method is called *SOR*, successive over-relaxation.

[3]Generalization to equations with variable coefficients such as h or $1/h$, as encounterd in the preceding two sections for example, is relatively straightforward, and we keep the notation simple here by assuming constant coefficients.

The use of the most recent $\tilde{\psi}$ values during the iterations accelerates convergence but not in a drastic way. Only when the relaxation parameter ω is set at a very particular value can the number of iterations be reduced significantly, from $\mathcal{O}(M)$ down to $\mathcal{O}(\sqrt{M})$ (see Numerical Exercise 7-6). Unfortunately, the optimal value of ω depends on the geometry and type of boundary conditions, and a small departure from the optimal value quickly deteriorates the convergence rate. As a guideline, the optimal value behaves as

$$\omega \sim 2 - \alpha \frac{2\pi}{m} \tag{7.54}$$

for a square and isotropic grid with m grid points in each direction, and with parameter $\alpha = \mathcal{O}(1)$ depending on the nature of the boundary conditions.

Because of its easy implementation, the SOR method was very popular in the early days of numerical modeling, but when vector and, later, parallel computers appeared, some adaptation was required. The recurrence relationships that appear in the loops do not allow to calculate $\tilde{\psi}_{i,j}^{(k+1)}$ before the calculations of $\tilde{\psi}_{i-1,j}^{(k+1)}$ and $\tilde{\psi}_{i,j-1}^{(k+1)}$ are finished, and this prevents independent calculations on parallel processors or vector machines. In response, the so-called *red-black* methods were developed. These perform two Jacobi iterations on two interlaced grids, nicknamed "red" and "black" (Figure 7-11).

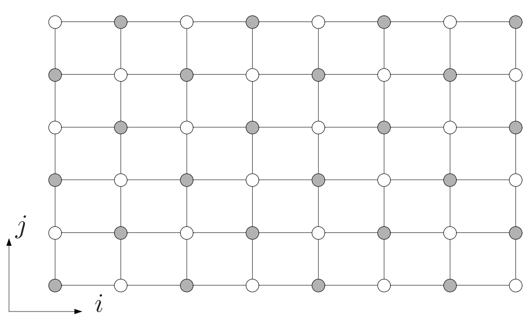

Figure 7-11 To avoid recurrence relationships, the discrete domain is swept by two loops, working on white and gray dots separately. During the loop updating white nodes, only values of the gray nodes are used, so that all white nodes can be updated independently and immediately. The reverse holds for the gray nodes in the second loop, and all calculations may be performed in parallel. Because the original algorithm (*reference here*) used red and black colored nodes, the name red-black is the one given to the two-stage sweep mechanism.

If we want to reduce further the computational burden associated with the inversion of the Poisson equation, we must exploit the very special nature of (7.51) and the resulting linear system to be solved. For the discrete version (7.51) of the Poisson equation, the matrix $\mathbf{A}$ relating the unknowns, now stored in an array $\mathbf{x}$, is symmetric and positive definite (Numerical Exercise 7-10). In this case, the solution of $\mathbf{A}\mathbf{x} = \mathbf{b}$ is equivalent to solving the minimization of

$$J = \frac{1}{2}\mathbf{x}^{\mathsf{T}}\mathbf{A}\mathbf{x} - \mathbf{x}^{\mathsf{T}}\mathbf{b} \tag{7.55}$$

$$\nabla_x J = \mathbf{A}\mathbf{x} - \mathbf{b} \tag{7.56}$$

with respect to $\mathbf{x}$. We then have to search for minima rather than to solve a linear equation and, though apparently more complicated, the task can also be tackled by iterative methods. The minimum of J is reached when the gradient with respect to x is zero: $\nabla_x J = 0$. This is the case when the residual $\mathbf{r} = \mathbf{A}\mathbf{x} - \mathbf{b}$ is zero, *i.e.*, when the linear problem is solved.

The use of a minimization approach (*e.g.*, Golub and van Loan, 1990) instead of a linear-system solver relies on the possibility of using efficient minimization methods. The gradient of J, the residual, is easily calculated and only takes $4M$ operations for the matrix A arising from the discrete Poisson equation. The value of J, if desired, is also readily obtained by calculating two scalar products involving the already available gradient. A standard minimization method used in optimization problems is to minimize the cost function J by following its gradient. In this method, called the *steepest descent* method, a better estimate of $\mathbf{x}$ is sought in the direction in which J decreases fastest. Starting from $\mathbf{x}_0$ and associated residual $\mathbf{r} = \mathbf{A}\mathbf{x}_0 - \mathbf{b}$ a better estimate of $\mathbf{x}$ is sought as

$$\mathbf{x} = \mathbf{x}_0 - \alpha \mathbf{r}, \tag{7.57}$$

which is reminiscent of a relaxation method. The parameter α is then chosen to minimize J. Because the form is quadratic in α, this can be achieved easily (see Numerical Exercise 7-7) by taking

$$\alpha = \frac{\mathbf{r}^\mathsf{T}\mathbf{r}}{\mathbf{r}^\mathsf{T}\,\mathbf{A}\mathbf{r}} \tag{7.58}$$

which, because $\mathbf{A}$ is positive definite, can always be calculated as long as the residual is nonzero. If the residual vanishes, iterations can be stopped because the solution has been found. Otherwise, from the new estimate $\mathbf{x}$, a new residual and gradient are computed, and iterations proceed:

Initialize by first guess $\mathbf{x}^{(0)} = \mathbf{x}_0$

Loop on increasing k until the residual $\mathbf{r}$ is small enough

$\mathbf{r} = \mathbf{A}\mathbf{x}^{(k)} - \mathbf{b}$

$\alpha = \dfrac{\mathbf{r}^\mathsf{T}\mathbf{r}}{\mathbf{r}^\mathsf{T}\,\mathbf{A}\mathbf{r}}$

$\mathbf{x}^{(k+1)} = \mathbf{x}^{(k)} - \alpha \mathbf{r}$

End of loop on k.

where residual and optimal descent parameter α change at each iteration. It is interesting to note that the residuals of two successive iterations are orthogonal to each other (Numerical Exercise 7-7).

Although very natural, the approach does not converge rapidly, and *conjugate gradient* methods have been developed to provide better convergence rates. In these methods, the direction of progress is no longer the direction of the steepest descent but is prescribed from among a set, noted $\mathbf{e}_i$. We then look for the minimum along these possible directions:

$$\mathbf{x} = \mathbf{x}_0 - \alpha_1 \mathbf{e}_1 - \alpha_2 \mathbf{e}_2 - \alpha_3 \mathbf{e}_3 - ... - \alpha_M \mathbf{e}_M. \tag{7.59}$$

If there are M vectors $\mathbf{e}_i$, chosen to be linearly independent, minimization with respect to the M parameters α_i will yield the exact minimum of J. So, instead of searching for the M components of $\mathbf{x}$, we search for the M parameters α_i leading to the optimal state $\mathbf{x}$. This solves the linear system exactly. A simplification in the calculations arises if we choose

$$\mathbf{e}_i^\mathsf{T} \mathbf{A}\, \mathbf{e}_j = 0 \quad \text{when} \quad i \neq j, \tag{7.60}$$

because in this case the quadratic form J takes the form

$$\begin{aligned} J &= \frac{1}{2}\mathbf{x}_0^\mathsf{T}\mathbf{A}\mathbf{x}_0 - \mathbf{x}_0^\mathsf{T}\mathbf{b} \\ &+ \frac{\alpha_1^2}{2}\mathbf{e}_1^\mathsf{T}\mathbf{A}\mathbf{e}_1 - \alpha_1\mathbf{e}_1^\mathsf{T}\left(\mathbf{A}\mathbf{x}_0 - \mathbf{b}\right) \\ &+ \frac{\alpha_2^2}{2}\mathbf{e}_2^\mathsf{T}\mathbf{A}\mathbf{e}_2 - \alpha_2\mathbf{e}_2^\mathsf{T}\left(\mathbf{A}\mathbf{x}_0 - \mathbf{b}\right) \\ &+ \ldots \\ &+ \frac{\alpha_M^2}{2}\mathbf{e}_M^\mathsf{T}\mathbf{A}\mathbf{e}_M - \alpha_M\mathbf{e}_M^\mathsf{T}\left(\mathbf{A}\mathbf{x}_0 - \mathbf{b}\right). \end{aligned} \tag{7.61}$$

This expression is readily minimized with respect to each parameter α_k and yields, with $\mathbf{r}_0 = \mathbf{A}\mathbf{x}_0 - \mathbf{b}$,

$$\alpha_k = \frac{\mathbf{e}_k^\mathsf{T}\mathbf{r}_0}{\mathbf{e}_k^\mathsf{T}\,\mathbf{A}\mathbf{e}_k}, \quad k = 1, ..., M \tag{7.62}$$

In other words, to reach the global minimum and thus the solution of the linear system, we simply have to minimize each term individually. The difficulty, however, is that the construction of the set of directions $\mathbf{e}_k$ is complicated. Hence, the idea is to proceed step-by-step and construct the directions as we iterate, with the plan of stopping iterations when residuals have become small enough. We can start with a first arbitrary direction, typically the steepest descent $\mathbf{e}_1 = \mathbf{A}\mathbf{x}_0 - \mathbf{b}$. Then, once we have a set of k directions that satisfy (7.60), we only minimize along direction $\mathbf{e}_k$ by (7.62):

$$\mathbf{x}^{(k)} = \mathbf{x}^{(k-1)} - \alpha_k\mathbf{e}_k. \tag{7.63}$$

This leads to a new residual $\mathbf{r}_k = \mathbf{A}\mathbf{x}^{(k)} - \mathbf{b}$

$$\begin{aligned} \mathbf{r}_k &= \mathbf{r}_{k-1} - \alpha_k\mathbf{A}\mathbf{e}_k \\ &= \mathbf{r}_0 - \alpha_1\mathbf{A}\mathbf{e}_1 - \alpha_2\mathbf{A}\mathbf{e}_2 - ... - \alpha_k\mathbf{A}\mathbf{e}_k. \end{aligned} \tag{7.64}$$

This shows that, instead of calculating α_k according to (7.62), we can use

$$\alpha_k = \frac{\mathbf{e}_k^\mathsf{T}\mathbf{r}_{k-1}}{\mathbf{e}_k^\mathsf{T}\,\mathbf{A}\mathbf{e}_k}, \tag{7.65}$$

because of property (7.60). We can interpret this result together with (7.64) by showing that the successive residuals are orthogonal to all previous search directions $\mathbf{e}_i$, so that no new search in those directions is needed. Expression (7.65) is also more practical because it requires the storage of only the residual calculated at the previous iteration. The construction of the next direction $\mathbf{e}_{k+1}$ is then performed by a variation of the Gram-Schmidt orthogonalization process of a series of linearly independent vectors. The conjugate gradient method chooses for this set of vectors the residuals already calculated, which can be shown to be orthogonal to one another and hence linearly independent. When applying the Gram-Schmidt orthogonalization in the sense of (7.60), it turns out that the new direction $\mathbf{e}_{k+1}$ is surprisingly easy to calculate in terms of the last residuals and search direction (*e.g.*, Golub and van Loan, 1990):

$$\mathbf{e}_{k+1} = \mathbf{r}_k + \frac{\|\mathbf{r}_k\|^2}{\|\mathbf{r}_{k-1}\|^2}\mathbf{e}_k \tag{7.66}$$

from which we can proceed to the next step. The algorithm is therefore only slightly more complicated than the steepest-descent method, and we note that we no longer need to store all residuals or search directions, not even intermediate values of $\mathbf{x}$. Only the most recent one needs to be stored at any moment for the following algorithm:

`Initialize by first guess`

$\mathbf{x}^{(0)} = \mathbf{x}_0,\ \ \mathbf{r}_0 = \mathbf{A}\mathbf{x}_0 - \mathbf{b},\ \ \mathbf{e}_1 = \mathbf{r}_0,\ \ s_0 = \|\mathbf{r}_0\|^2$

`Loop on increasing` k `until the residual` $\mathbf{r}$ `is small enough`

$\alpha_k = \dfrac{\mathbf{e}_k^{\mathsf{T}}\mathbf{r}_{k-1}}{\mathbf{e}_k^{\mathsf{T}}\,\mathbf{A}\mathbf{e}_k}$

$\mathbf{x}^{(k)} = \mathbf{x}^{(k-1)} - \alpha_k \mathbf{e}_k$

$\mathbf{r}_k = \mathbf{r}_{k-1} - \alpha_k \mathbf{A}\mathbf{e}_k$

$s_k = \|\mathbf{r}_k\|^2$

$\mathbf{e}_{k+1} = \mathbf{r}_k + \dfrac{s_k}{s_{k-1}}\mathbf{e}_k$

`End of loop on` k.

Because we minimize independent terms, we are sure after M steps to be at the minimum, within rounding errors. For the conjugate-gradient method the exact solution is therefore obtained within M iterations, and the overall cost of our special sparse matrix inversion arising from the two-dimensional discrete Poisson equation behaves as M^2. There is, however, no need to find the exact minimum, and, in practice, only a certain number of successive minimizations are necessary, and convergence is generally obtained within $M^{3/2}$ operations. This does not seem an improvement over the optimal over-relaxation, but the conjugate-gradient method is generally robust and has no need of an over-relaxation parameter. If in addition a proper preconditioning is applied, it can lead to spectacular convergence rates.

Preconditioning needs to preserve the symmetry of the problem and is performed by introducing a sparse triangular matrix $\mathbf{L}$ and writing the original problem as

$$\mathbf{L}^{-1}\mathbf{A}\mathbf{L}^{-\mathsf{T}}\mathbf{L}^{\mathsf{T}}\mathbf{x} = \mathbf{L}^{-1}\mathbf{b}, \tag{7.67}$$

so that we now work with the new unknown $\mathbf{L}^\mathsf{T}\mathbf{x}$ and modified matrix $\mathbf{L}^{-1}\mathbf{A}\mathbf{L}^{-\mathsf{T}}$. This matrix is symmetric, and, if $\mathbf{L}$ is chosen correctly, also positive definite if $\mathbf{A}$ is. The resulting algorithm, involving the modified matrix and unknown, is very close to the original conjugate-gradient algorithm after clever rearrangement of the matrix-vector products. The only difference is the appearence of $\mathbf{M}^{-1}\mathbf{r}$, where $\mathbf{M}^{-1} = \mathbf{L}^{-\mathsf{T}}\mathbf{L}^\mathsf{T}$. Because $\mathbf{u} = \mathbf{M}^{-1}\mathbf{r}$ is the solution of $\mathbf{M}\mathbf{u} = \mathbf{r}$, the sparseness and triangular nature of $\mathbf{L}$ allows us to perform this operation quite efficiently. If $\mathbf{L} = \mathbf{C}$ is obtained from a Cholesky decomposition of the symmetric positive-definite matrix $\mathbf{A} = \mathbf{C}\mathbf{C}^\mathsf{T}$, where $\mathbf{C}$ is a triangular matrix, a single step of the conjugate-gradient method would suffice, because the inversion of $\mathbf{A}$ would be directly available. For this reason, $\mathbf{L}$ is often constructed by the Cholesky decomposition but with incomplete and cost-effective calculations, imposing on $\mathbf{L}$ a given sparse pattern. This leads to the incomplete Cholesky preconditioning[4]. This reduces the cost of the Cholesky decomposition itself, but increases the number of iterations needed compared to a situation in which the full Cholesky decomposition is available. On the other hand, it generally reduces the number of iterations compared to the version without preconditioning. An optimum is therefore to be found in the amount of preconditioning, and the particular choice of preconditioning is problem dependent. Stability of the iterations might be an occasional problem.

Most linear-algebra packages contain conjugate-gradient methods including generalizations to solve non-symmetric problems. In this case we can consider the augmented (double) problem

$$\begin{pmatrix} 0 & \mathbf{A} \\ \mathbf{A}^\mathsf{T} & 0 \end{pmatrix} \begin{pmatrix} \mathbf{y} \\ \mathbf{x} \end{pmatrix} = \begin{pmatrix} \mathbf{b} \\ \mathbf{c} \end{pmatrix} \tag{7.68}$$

which is symmetric and possesses the same solution $\mathbf{x}$.

More efficient solution methods for special linear systems, such as our Poisson equation, exist and exhibit a close relationship with Fast Fourier Transforms (FFT, see Appendix C). The cyclic block reduction methods (*e.g.*, Ferziger and Perić, 1999), for example, can be applied when the discretization constants are uniform and boundary conditions simple. But in such a case, we could also use a spectral method coupled with FFT for immediate inversion of the Laplacian operator (see Section 18.4). In these methods, costs can be reduced down to $M \log M$.

Finally, the most efficient methods for very large problems are *multigrid* methods. These start from the observation that the pseudo-evolution approach mimics diffusion, which generally acts more efficiently at smaller scales [see damping rates of discrete diffusion operators (5.34)], leaving larger scales to converge more slowly. But, these larger scales can be made to appear as relatively shorter scales on a grid with wider grid spacing so that their convergence can be accelerated (using, incidentally, a larger pseudo-time step). Thus, introducing a hierarchy of grids as a *multigrid* method does, accelerates convergence by iterating on different grids for different length scales. Typically the method begins with a very coarse grid, on which a few iterations lead to a good estimate of the broad shape of the solution. This solution is then interpolated onto a finer grid on which several more iterations are performed, and so on down to the ultimate resolution of interest. The iterations may also be redone on the coaser grids after some averaging to estimate the broad solution from the finer grid. Multigrid

[4]More generally, an incomplete $\mathbf{LU}$ decomposition approximates any matrix $\mathbf{A}$ by the product of lower and upper sparse triangular matrices.

methods, therefore, iterate and cycle through different grids (*e.g.*, Hackbusch, 1985), and the art is to perform the right number of iterations on each grid and to choose wisely the next grid on which to iterate (the finer or coarser grid). For well chosen strategies, the number of operations required for convergence behaves asymptotically as M, and multigrid methods are therefore the most effective ones for very large problems. Iterations on each of the grids may be of red-black type with over-relaxation or any other method with appropriate convergence properties.

We only scratched here the surface of the problem of solving large and sparse linear algebraic systems to give a flavor of the possible approaches, and the reader should be aware that there is a large number of numerical solvers available for specific problems. Since these are optimized for specific computer hardware, the practical and operational task of large-system inversion of the discrete Poisson equation should be left to libraries provided with the computing system available. Only the choice of when to stop the iterations and the proper preconditioning strategy should be left to the modeler.

Analytical Problems

7-1. A laboratory experiment is conducted in a cylindrical tank 20 cm in diameter, filled with homogeneous water (15 cm deep at the center) and rotating at 30 rpm. A steady flow field with maximum velocity of 1 cm/s is generated by a source-sink device. The water viscosity is 10^{-6} m^2/s. Verify that this flow field meets the conditions of geostrophy.

7-2. (Generalization of the Taylor–Proudman theorem) By reinstating the f_*–terms of equations (3.21) and (3.24) into (7.2) and (7.4), show that motions in fluids rotating rapidly around an axis not parallel to gravity exhibit columnar behavior in the direction of the axis of rotation.

7-3. Demonstrate the assertion made at the end of Section 7.2, namely, that geostrophic flows between irregular bottom and top boundaries are constrained to be directed along lines of constant fluid depth.

7-4. Establish equation (7.25) for the evolution of a parcel's horizontal cross-section from first principles.

7-5. In a fluid of depth H rapidly rotating at the rate $f/2$ (Figure 7-12), there exists a uniform flow U. Along the bottom (fixed), there is an obstacle of height H' ($< H/2$), around which the flow is locally deflected, leaving a quiescent Taylor column. A rigid lid, translating in the direction of the flow at speed $2U$, has a protrusion identical to the bottom obstacle, also locally deflecting the otherwise uniform flow and entraining another quiescent Taylor column. The two obstacles are aligned with the direction of motion so that there will be a time when both are superimposed. Assuming that the fluid is homogeneous and frictionless, what do you think will happen to the Taylor columns?

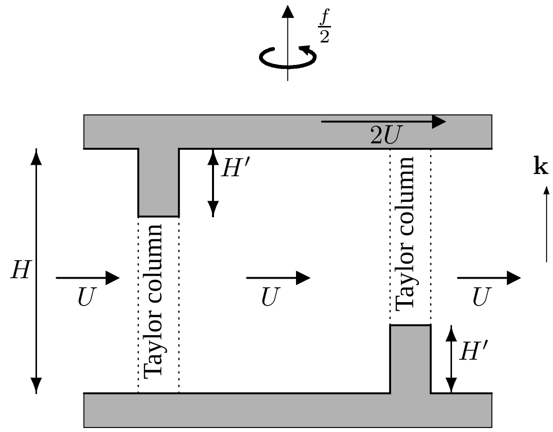

Figure 7-12 Schematic view of a hypothetical system, as described in Problem 7-5.

7-6. As depicted in Figure 7-13, a vertically uniform but laterally sheared coastal current must climb a bottom escarpment. Assuming that the jet velocity still vanishes offshore, determine the velocity profile and the width of the jet downstream of the escarpment using $H_1 = 200$ m, $H_2 = 160$ m, $U_1 = 0.5$ m/s, $L_1 = 10$ km and $f = 10^{-4}$ s^{-1}. What would happen if the downstream depth were only 100 m?

7-7. What are the differences in dynamic pressure across the coastal jet of Problem 7-6 upstream and downstream of the escarpment? Take H_2 = 160 m and ρ_0 = 1022 kg/m^3.

7-8. In Utopia, a narrow 200-m deep channel empties in a broad bay of varying bottom topography (Figure 7-14). Trace the path to the sea and the velocity profile of the channel outflow. Take $f = 10^{-4}$ s^{-1}. (Solve only for straight stretches of the flow and ignore corners.)

7-9. A steady ocean current of uniform potential vorticity $q = 5 \times 10^{-7}$ m^{-1}s^{-1} and volume flux $T = 4 \times 10^6$ m^3/s flows along isobaths of a uniformly sloping bottom (with bottom slope $S = 1$ m/km). Show that the velocity profile across the current is parabolic. What are the width of the current and the depth of the location of maximum velocity? Take $f = 7 \times 10^{-4}$ s^{-1}.

7-10. Show that the rigid-lid approximation can also be obtained by assuming that the vertical velocity at top is much smaller than at the bottom. Establish the necessary scaling conditions that support your assumptions.

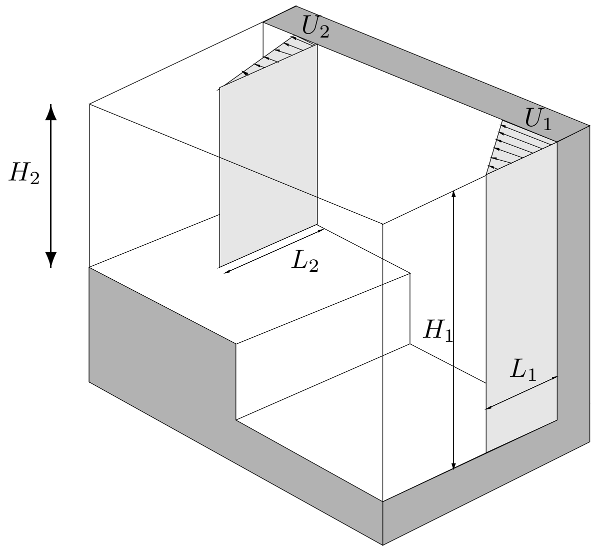

Figure 7-13 A sheared coastal jet negotiating a bottom escarpment (Problem 7-6).

Numerical Exercises

7-1. An atmospheric pressure field p over a flat bottom is given on a rectangular grid according to

$$p_{i,j} = P_H \exp(-r^2/L^2) + p_\epsilon \, \xi_{i,j} \quad r^2 = (x_i - x_c)^2 + (y_j - y_c)^2 \tag{7.69}$$

where ξ is a normal (Gaussian) random variable of zero mean and unit standard deviation. The high pressure anomaly is of $P_H = 40$ hPa and its radius $L = 1000$ km. For the noise level, take $p_\epsilon = 5$ hPa. Use a rectangular grid centered around x_c, y_c with a uniform grid spacing $\Delta x = \Delta y = 50$ km. Calculate and plot the associated geostrophic currents for $f = 10^{-4}$ s^{-1}. To which extent is volume conservation satisfied in your finite-difference scheme? What happens if $p_\epsilon = 10$ hPa or $\Delta x = \Delta y = 25$ km? Can you interpret your finding?

7-2. Use the sea surface height reconstructed from satellite data and stored in file `madt_oer_merged_h_18861.nc` to calculate associated geostrophic ocean currents around the Gulf stream using `topexcirculation.m` to read the data. For conversion from latitude and longitude to local Cartesian coordinates, 1° latitude = 111 km and 1° longitude = 111 km × cos(latitude). (*The altimeter products have been produced by the CLS Space Oceanography Division, see also Ducet et al., 2000*).

7-3. Use the meteorological pressure field at sea level to calculate geostrophic winds over Europe. First use the December 2000 monthly average sea-level pressure. Then look

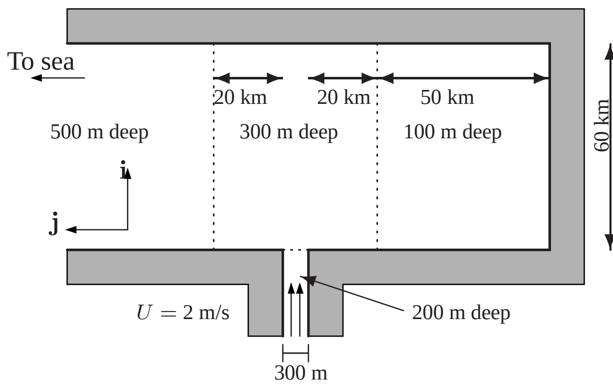

Figure 7-14 Geometry of the idealized bay and channel mentioned in Problem 7-8.

at daily variations. `Era40.m` will help you read the data. Take care of the actual Coriolis parameter value and the distances to be calculated from the longitude-latitude information (see Numerical Exercise 7-2).

What happens if you try to redo your calculations in order to plan your sailing trip in the northern part of Lake Victoria? (*ECMWF ERA-40 data were obtained from the ECMWF data server*).

7-4. Calculate with the red-black approach the numerical solution of (7.51) in the basin depicted in Figure 7-15, with $\tilde{q}_{i,j} = -1$ on the right-hand side of the equation and $\tilde{\psi}_{i,j} = 0$ along all solid boundaries. Implement a stopping criterion based on a relative measure of the residual compared to **b**.

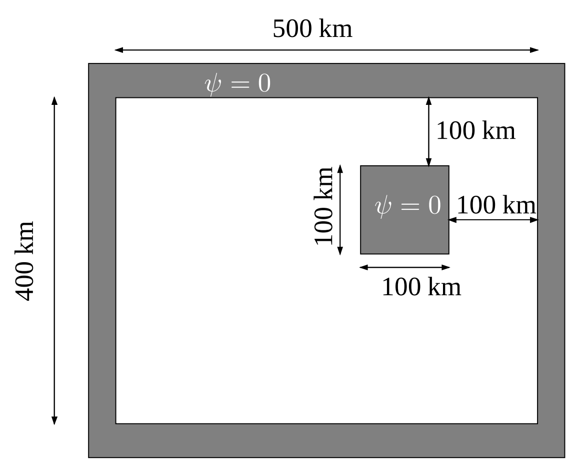

Figure 7-15 Geometry of the idealized basin mentioned in Numerical Exercise 7-4.

7-5. Use the conjugate-gradient implementation called in `test.m` to solve the problem of Numerical Exercise 7-4 with improved convergence.

7-6. Redo Numerical Exercise 7-4 with the Gauss-Seidel approach using over-relaxation and several values of ω between 0.7 and 1.999. For each value of ω, start from zero and converge until reaching a preset threshold for the residual. Plot the required number of iterations until convergence as a function of ω. Design a numerical tool to find the optimal value of ω numerically. Then repeat the problem with other spatial resolutions, taking successively 20, 40, 60, 80 and 100 grid points in each direction. Look at the number of iterations and the optimal value of ω as functions of resolution.

7-7. Prove that the parameter α given by (7.58) leads to a minimum of J defined in (7.55), for a given starting point and fixed gradient $\mathbf{r}$. Also prove that at the next iteration of the steepest-descent method, the new residual is orthogonal to the previous residual. Implement the steepest-descent algorithm. Try to find the minimum of (7.55) with

$$\mathbf{A} = \begin{pmatrix} 3 & 1 \\ 1 & 1 \end{pmatrix}, \quad \mathbf{b} = \begin{pmatrix} 6 \\ 2 \end{pmatrix} \tag{7.70}$$

and observe the successive approximations obtained by the method, starting at the origin of the axes. *Hint:* In the plane defined by the two unknowns, plot isolines of J and plot the line connecting the successive approximations to the solution. Make several zooms near the solution point.

7-8. Implement, as a Matlab function, a general solver for the Poisson equation. Provide for masked grids and variable resolution such that Δx depends on i only and Δy on j only, keeping grid cells rectangular. Also permit variable coefficients in the Laplacian operator, as found in (7.47) and apply to the following situation.

In shallow, wind-driven basins, such as small lakes and lagoons, the flow often strikes a balance between the forces of surface wind, pressure gradient and bottom friction. Upon defining a streamfunction and eliminating the pressure gradient, one obtains for steady flow (Matthieu *et al.*, 2002):

$$\frac{\partial}{\partial x}\left(\frac{2\nu_E}{h^3}\frac{\partial \psi}{\partial x}\right) + \frac{\partial}{\partial y}\left(\frac{2\nu_E}{h^3}\frac{\partial \psi}{\partial y}\right) = \frac{\partial}{\partial y}\left(\frac{\tau^x}{\rho_0 h}\right) - \frac{\partial}{\partial x}\left(\frac{\tau^y}{\rho_0 h}\right), \tag{7.71}$$

where ν_E is the eddy viscosity, $h(x, y)$ is the local bottom depth, and (τ^x, τ^y) the components of the surface wind stress. In the application, take $\nu_E = 10^{-2}$ m^2/s, $\rho_0 = 1000$ kg/m^3, $h(x, y) = 50 - (x^2 + 4y^2/10)$ (in m, with x and y in km), $\tau^x = 0.1$ N/m^2, and $\tau^y = 0$ within an elliptical domain $x^2 + 4y^2 \leq 400$ km^2.

7-9. Use the general tool of Numerical Exercise 7-8 to simulate the stationary flow across the Bering sea, assuming the right-hand side of (7.71) is zero. Use `beringtopo.m` to read the topography of Figure 7-16. To pass from latitude and longitude to Cartesian coordinates, use the rule given in Numerical Exercise 7-2 but with cos(latitude) taken as cos(66.5°N) to obtain a rectangular grid. Compare your solution to the case of constant, average depth instead of the real topography, maintaining the land mask.

7-10. Prove that matrix $\mathbf{A}$ arising from the discretization (7.51) is symmetric and positive definite. Show also that the latter property ensures $\mathbf{z}^\mathsf{T}\mathbf{A}\mathbf{z} > 0$ for any $\mathbf{z} \neq 0$.

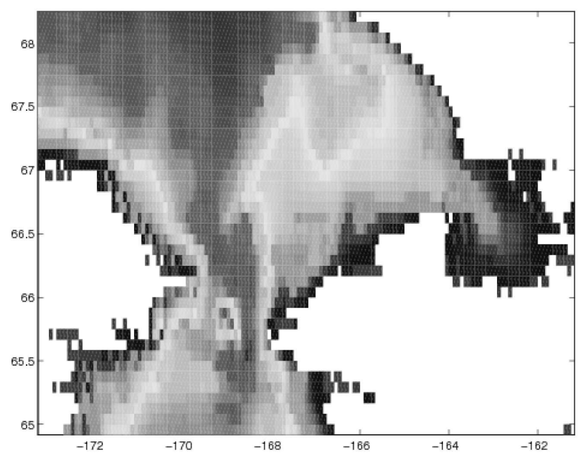

Figure 7-16 Model of the Bering Sea for Numerical Exercise 7-9. For the calculation of the streamfunction, assume that West of -169° longitude all land points have a prescribed streamfunction $\Psi_1 = 0$ and those to the East Ψ_2 = 0.8 Sv (1 Sv = 10^6 m^3/s). For convenience, you may consider closing the western and eastern boundary completely and imposing a zero normal derivative of Ψ along the open boundaries.

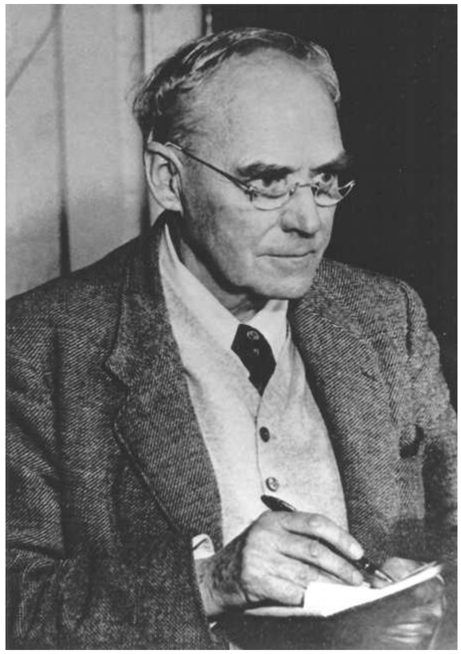

Geoffrey Ingram Taylor
1886 – 1975

Considered one of the great physicists of the 20th century, Sir Geoffrey Taylor contributed enormously to our understanding of fluid dynamics. Although he did not envision the birth and development of geophysical fluid dynamics, his research on rotating fluids laid the foundation for the discipline. His numerous contributions to science also include seminal work on turbulence, aeronautics, and solid mechanics. With a staff consisting of a single assistant-engineer, he maintained a very modest laboratory, constantly preferring to undertake entirely new problems and to work alone. (*Photo courtesy of Cambridge University Press*)

James Cyrus McWilliams
1946 –

A student of George Carrier at Harvard University, James McWilliams is a pioneer in the synthesis of mathematical theory and computational simulation in geophysical fluid dynamics. A central theme of his research is how advection produces the peculiar combinations of global order and local chaos – and vice versa – evident in oceanic currents, as well as analogous phenomena in atmospheric and astrophysical flows. His contributions span a formidable variety of topics across the disciplines of rotating and stratified flows, waves, turbulence, boundary layers, oceanic general circulation, and computational methods.

McWilliams' scientific style is the pursuit of phenomenological discovery in the virtual reality of simulations, leading, on good days, to dynamical understanding and explanation and to confirmation in nature.

(*Photo credit: J. C. McWilliams*)

Chapter 8

The Ekman Layer

(October 18, 2006) **SUMMARY**: Frictional forces, neglected in the previous chapter, are now investigated. Their main effect is to create horizontal boundary layers that support a flow transverse to the main flow of the fluid. The numerical treatment of the velocity profiles dominated by friction is illustrated with a spectral approach.

8.1 Shear turbulence

Because most geophysical fluid systems are much shallower than they are wide, their vertical confinement forces the flow to be primarily horizontal. Unavoidable in such a situation is friction between the main horizontal motion and the bottom boundary. Friction acts to reduce the velocity in the vicinity of the bottom, thus creating a vertical shear. Mathematically, if u is the velocity component in one of the horizontal directions and z the elevation above the bottom, then u is a function of z, at least for small z values. The function $u(z)$ is called the *velocity profile* and its derivative du/dz, the *velocity shear*.

Geophysical flows are invariably turbulent (high Reynolds number) and this greatly complicates the search for the velocity profile. As a consequence, much of what we know is derived from observations of actual flows, either in the laboratory or in nature.

The turbulent nature of the shear flow along a flat or rough surface includes variability at short time and length scales, and the best observational techniques for the detailed measurements of these have been developed for the laboratory rather than outdoor situations. Laboratory measurements of nonrotating turbulent flows along smooth straight surfaces have led to the conclusion that the velocity varies solely with the stress τ_b exerted against the bottom, the fluid molecular viscosity ν, the fluid density ρ and, of course, the distance z above the bottom. Thus,

$$u(z) \;=\; F(\tau_b, \nu, \rho, z).$$

Dimensional analysis permits the elimination of the mass dimension shared by τ_b and ρ but not present in u, ν and z, and we may write more simply:

$$u(z) = F\left(\frac{\tau_b}{\rho}, \nu, z\right).$$

The ratio τ_b/ρ has the same dimension as the square of a velocity, and for this reason it is customary to define

$$u_* = \sqrt{\frac{\tau_b}{\rho}}, \tag{8.1}$$

which is called the *friction velocity* or *turbulent velocity*. Physically, its value is related to the orbital velocity of the vortices that create the cross-flow exchange of particles and the momentum transfer.

The velocity structure thus obeys a relation of the form $u(z) = F(u_*, \nu, z)$ and further use of dimensional analysis reduces it to a function of a single variable:

$$\frac{u(z)}{u_*} = F\left(\frac{u_* z}{\nu}\right). \tag{8.2}$$

In the presence of rotation, the Coriolis parameter enters the formalism and the preceding function depends on two variables:

$$\frac{u(z)}{u_*} = F\left(\frac{u_* z}{\nu}, \frac{fz}{u_*}\right). \tag{8.3}$$

8.1.1 Logarithmic profile

The observational determination of the function F in the absence of rotation has been repeated countless times, yielding the same results every time, and it suffices here to provide a single report (Figure 8-1). When the velocity ratio u/u_* is plotted versus the logarithm of the dimensionless distance $u_* z/\nu$, not only do all the points coalesce onto a single curve, confirming that there is indeed no other variable to be invoked, but the curve also behaves as a straight line over a range of two orders of magnitude (from $u_* z/\nu$ between 10^1 and 10^3).

If the velocity is linearly dependent on the logarithm of the distance, then we can write for this portion of the velocity profile:

$$\frac{u(z)}{u_*} = A \ln \frac{u_* z}{\nu} + B.$$

Numerous experimental determinations of the constants A and B provide $A = 2.44$ and $B = 5.2$ within a 5% error (Pope, 2000). Tradition has it to write the function as:

$$u(z) = \frac{u_*}{\mathcal{K}} \ln \frac{u_* z}{\nu} + 5.2\, u_*, \tag{8.4}$$

where $\mathcal{K} = 1/A = 0.41$ is called the *von Kármán constant*[1]

The portion of the curve closer to the wall, where the logarithmic law fails, may be approximated by the laminar solution. Constant laminar stress $\nu du/dz = \tau_b/\rho = u_*^2$ implies $u(z) = u_*^2 z/\nu$ there. Ignoring the region of transition in which the velocity profile gradually

[1] in honor of Theodore von Kármán (1881–1963), Hungarian-born physicist and engineer who made significant contributions to fluid mechanics while working in Germany and who first introduced this notation.

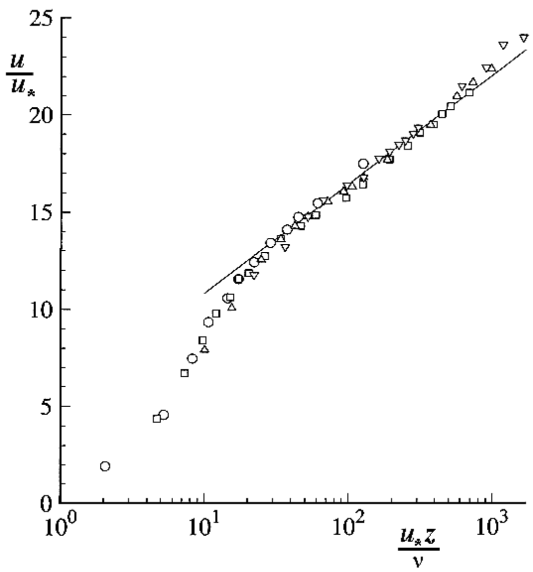

Figure 8-1 Mean velocity profiles in fully developed turbulent channel flow measured by Wei and Willmarth (1989) at various Reynolds numbers: circles Re = 2970, squares Re = 14914, upright triangles Re = 22776, and downright triangles Re = 39582. The straight line on this log-linear plot corresponds to the logarithmic profile of Equation (8.2). (From Pope, 2000)

changes from one solution to the other, we can attempt to connect the two. Doing so yields $u_* z/\nu = 11$. This sets the thickness of the laminar boundary layer δ as the value of z for which $u_* z/\nu = 11$, *i.e.*,

$$\delta \;=\; 11\,\frac{\nu}{u_*}\,. \tag{8.5}$$

Most textbooks (*e.g.*, Kundu, 1990) give $\delta = 5\nu/u_*$, for the region in which the velocity profile is strictly laminar, and label the region between $5\nu/u_*$ and $30\nu/u_*$ as the *buffer layer*, the transition zone between laminar and fully turbulent flow.

For water in ambient conditions, the molecular viscosity ν is equal to 1.0×10^{-6} m^2/s, while the friction velocity in the ocean rarely falls below 1 mm/s. This implies that δ hardly exceeds a centimeter in the ocean and is almost always smaller than the height of the cobbles, ripples and other asperities that typically line the bottom of the ocean basin. Similarly for the atmosphere: the air viscosity at ambient temperature and pressure is about 1.5×10^{-5} m^2/s and u_* rarely falls below 1 cm/s, giving $\delta < 5$ cm, smaller than most irregularities on land and wave heights at sea.

When this is the case, the velocity profile above the bottom asperities no longer depends on the molecular viscosity of the fluid but on the so-called *roughness height* z_0, such that

$$u(z) \;=\; \frac{u_*}{\mathcal{K}}\;\ln\,\frac{z}{z_0}\;, \tag{8.6}$$

as depicted in Figure 8-2. It is important to note that the roughness height is not the average height of bumps on the surface but is a small fraction of it, about one tenth (Garratt, 1992, page 87).

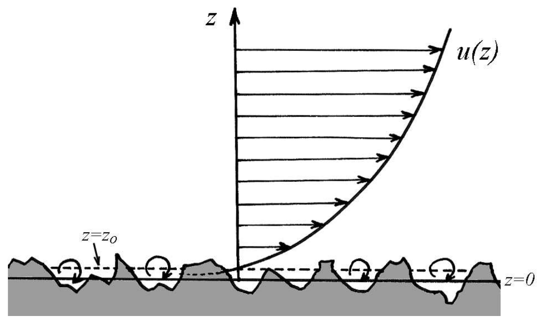

Figure 8-2 Velocity profile in the vicinity of a rough wall. The roughness heigh z_0 is smaller than the averaged height of the surface asperities. So, the velocity u falls to zero somewhere within the asperities, where local flow degenerates into small vortices between the peaks, and the negative values predicted by the logarithmic profile are not physically realized.

8.1.2 Eddy viscosity

We have already mentioned in Section 5.2 what an eddy diffusivity or viscosity is and how it can be formulated in the case of a homogeneous turbulence field, *i.e.*, away from boundaries. Near a boundary, the turbulence ceases to be isotropic and an alternate formulation needs to be developed.

In analogy with Newton's law for viscous fluids, which has the tangential stress τ proportional to the velocity shear du/dz with the coefficient of proportionality being the molecular viscosity ν, we write for turbulent flow:

$$\tau \;=\; \rho_0 \nu_E \,\frac{du}{dz}, \tag{8.7}$$

where the turbulent viscosity ν_E supersedes the molecular viscosity ν. For the logarithmic profile (8.6) of a flow along a rough surface, the velocity shear is $du/dz = u_*/\mathcal{K}z$ and the stress τ is uniform across the flow (at least in the vicinity of the boundary for lack of other significant forces): $\tau = \tau_b = \rho u_*^2$, giving

$$\rho_0 u_*^2 \;=\; \rho_0 \nu_E \,\frac{u_*}{\mathcal{K}z}$$

and thus

$$\nu_E \;=\; \mathcal{K} z u_*. \tag{8.8}$$

Note that unlike the molecular viscosity, the turbulent viscosity is not constant in space, for it is not a property of the fluid but of the flow, including its geometry. From its dimension ($[\nu_E]$ = L^2T^{-1}), we verify that (8.8) is dimensionally correct and note that it can be expressed as the product of a length by the friction velocity

$$\nu_E \;=\; l_m u_*, \tag{8.9}$$

with the *mixing length* l_m defined as

$$l_m \;=\; \mathcal{K} z. \tag{8.10}$$

This parameterization is occasionally used for cases other than boundary layers (see Chapter 14).

The preceding considerations ignored the effect of rotation. When rotation is present, the character of the boundary layer changes dramatically.

8.2 Friction and rotation

After the development of the equations governing geophysical motions (Sections 4.1 to 4.4), a scale analysis was performed to evaluate the relative importance of the various terms (Section 4.5). In the horizontal momentum equations [(4.21a) and (4.21b)], each term was compared to the Coriolis term, and a corresponding dimensionless ratio was defined. For vertical friction, the dimensionless ratio was the *Ekman number*:

$$Ek \;=\; \frac{\nu_E}{\Omega H^2}, \tag{8.11}$$

where ν_E is the eddy viscosity, Ω the ambient rotation rate, and H the height (depth) scale of the motion (the total thickness if the fluid is homogeneous).

Typical geophysical flows, as well as laboratory experiments, are characterized by very small Ekman numbers. For example, in the ocean at midlatitudes ($\Omega \simeq 10^{-4}$ s^{-1}), motions modeled with an eddy-intensified viscosity $\nu_E = 10^{-2}$ m^2/s (much larger than the molecular viscosity of water, equal to 1.0×10^{-6} m^2/s) and extending over a depth of about 1000 m have an Ekman number of about 10^{-4}.

The smallness of the Ekman number indicates that vertical friction plays a very minor role in the balance of forces and may, consequently, be omitted from the equations. This is usually done and with great success. However, something is then lost. The frictional terms happen to be those with the highest order of derivatives among all terms of the momentum equations. Thus, when friction is neglected, the order of the set of differential equations is reduced, and not all boundary conditions can be applied simultaneously. Usually, slipping along the bottom must be accepted.

Since Ludwig Prandtl[2] and his general theory of boundary layers, we know that in such a circumstance the fluid system exhibits two distinct behaviors: At some distance from the boundaries, in what is called the *interior*, friction is usually negligible, whereas, near a boundary (wall) and across a short distance, called the *boundary layer*, friction acts to bring the finite interior velocity to zero at the wall.

The thickness, d, of this thin layer is such that the Ekman number is on the order of one at that scale, allowing friction to be a dominant force:

$$\frac{\nu_E}{\Omega d^2} \;\sim\; 1,$$

which leads to

$$d \;\sim\; \sqrt{\frac{\nu_E}{\Omega}}\,. \tag{8.12}$$

[2] See biography at the end of this chapter.

Obviously, d is much less than H, and the boundary layer occupies a very small portion of the flow domain. For the oceanic values cited above ($\nu_E = 10^{-2}$ m^2/s and $\Omega = 10^{-4}$ s^{-1}), d is about 10 m.

Because of the Coriolis effect, the frictional boundary layer of geophysical flows, called the *Ekman layer*, differs greatly from the boundary layer in nonrotating fluids. Although, the traditional boundary layer has no particular thickness and grows either downstream or with time, the existence of the depth scale d in rotating fluids suggests that the Ekman layer can be characterized by a fixed thickness. [Note that as the rotational effects disappear ($\Omega \to 0$), d tends to infinity, exemplifying this essential difference between rotating and nonrotating fluids.]

8.3 The bottom Ekman layer

Let us consider a uniform, geostrophic flow in a homogeneous fluid over a flat bottom (Figure 8-3). This bottom exerts a frictional stress against the flow, bringing the velocity gradually to zero within a thin layer above the bottom. We now solve for the structure of this layer.

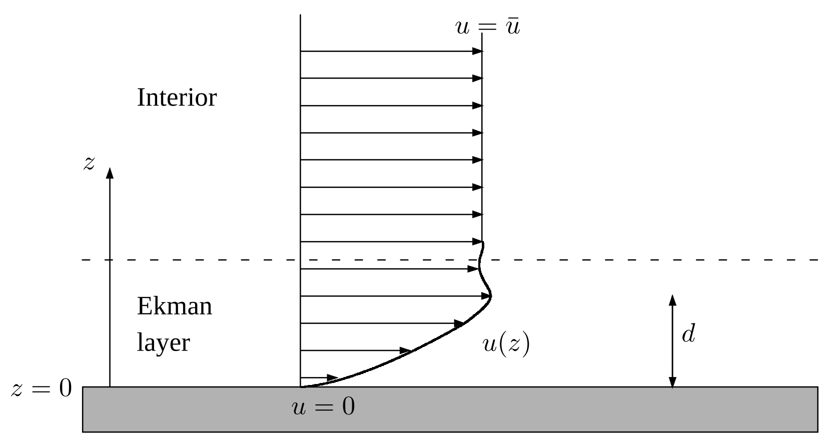

Figure 8-3 Frictional influence of a flat bottom on a uniform flow in a rotating framework.

In the absence of horizontal gradients (the interior flow is said to be uniform) and of temporal variations, continuity equation (4.21d) yields $\partial w/\partial z = 0$ and thus $w = 0$ in the thin layer near the bottom. The remaining equations are the following reduced forms of

(4.21a) through (4.21c):

$$- \; fv \;\; = \;\; - \, \frac{1}{\rho_0} \, \frac{\partial p}{\partial x} \; + \; \nu_E \, \frac{\partial^2 u}{\partial z^2} \tag{8.13a}$$

$$+ \, fu \;\; = \;\; - \, \frac{1}{\rho_0} \, \frac{\partial p}{\partial y} \; + \; \nu_E \, \frac{\partial^2 v}{\partial z^2} \tag{8.13b}$$

$$0 \;\; = \;\; - \, \frac{1}{\rho_0} \, \frac{\partial p}{\partial z} \, , \tag{8.13c}$$

where f is the Coriolis parameter (taken as a constant here), ρ_0 is the fluid density, and ν_E is the eddy viscosity (taken as a constant for simplicity). The horizontal gradient of the pressure p is retained because a uniform flow requires a uniformly varying pressure (Section 7.1). For convenience, we align the x–axis with the direction of the interior flow, which is of velocity $\bar{u}$. The boundary conditions are then

$$\text{Bottom } (z = 0): \qquad u \; = \; 0, \quad v \; = \; 0, \tag{8.14a}$$

$$\text{Toward the interior } (z \gg d): \qquad u \; = \; \bar{u}, \quad v \; = \; 0, \quad p = \bar{p}(x,y). \tag{8.14b}$$

By virtue of equation (8.13c), the dynamic pressure p is the same at all depths; thus, $p = \bar{p}(x,y)$ in the outer flow as well as throughout the boundary layer. In the outer flow ($z \gg d$, mathematically equivalent to $z \to \infty$), equations (8.13a) and (8.13b) relate the velocity to the pressure gradient:

$$0 \;\; = \;\; - \, \frac{1}{\rho_0} \, \frac{\partial \bar{p}}{\partial x},$$

$$f\bar{u} \;\; = \;\; - \, \frac{1}{\rho_0} \, \frac{\partial \bar{p}}{\partial y} \; = \; \text{constant.}$$

Substitution of these derivatives in the same equations, which are now taken at any depth, yields

$$- \; fv \;\; = \;\; \nu_E \, \frac{d^2 u}{dz^2} \tag{8.15a}$$

$$f \, (u \; - \; \bar{u}) \;\; = \;\; \nu_E \, \frac{d^2 v}{dz^2} \, . \tag{8.15b}$$

Seeking a solution of the type $u = \bar{u} + A \exp(\lambda z)$ and $v = B \exp(\lambda z)$, we find that λ obeys $\nu^2 \lambda^4 + f^2 = 0$; that is,

$$\lambda \; = \; \pm \; (1 \; \pm \; \mathrm{i}\,) \frac{1}{d}$$

where the distance d is defined by

$$d \; = \; \sqrt{\frac{2\nu_E}{f}} \; . \tag{8.16}$$

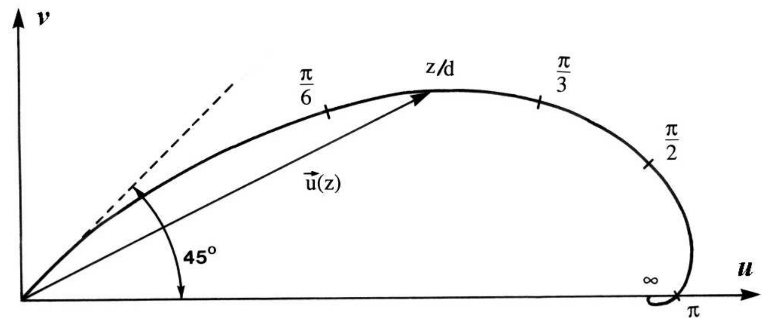

Figure 8-4 The velocity spiral in the bottom Ekman layer. The figure is drawn for the Northern Hemisphere ($f > 0$), and the deflection is to the left of the current above the layer. The reverse holds for the Southern Hemisphere.

Here, we have restricted ourselves to cases with positive f (Northern Hemisphere). Note the similarity to (8.12). Boundary conditions (8.14b) rule out the exponentially growing solutions, leaving

$$u = \bar{u} + e^{-z/d} \left(A \cos \frac{z}{d} + B \sin \frac{z}{d}\right) \quad (8.17a)$$

$$v = e^{-z/d} \left(B \cos \frac{z}{d} - A \sin \frac{z}{d}\right), \quad (8.17b)$$

and the application of the remaining boundary conditions (8.14a) yields $A = -\bar{u}$, $B = 0$, or

$$u = \bar{u} \left(1 - e^{-z/d} \cos \frac{z}{d}\right) \quad (8.18a)$$

$$v = \bar{u}\, e^{-z/d} \sin \frac{z}{d}. \quad (8.18b)$$

This solution has a number of important properties. First and foremost, we notice that the distance over which it approaches the interior solution is on the order of d. Thus, expression (8.16) gives the thickness of the boundary layer. For this reason, d is called the *Ekman depth*. A comparison with (8.12) confirms the earlier argument that the boundary-layer thickness is the one corresponding to a local Ekman number near unity.

The preceding solution also tells us that there is, in the boundary layer, a flow transverse to the interior flow ($v \neq 0$). Very near the bottom ($z \to 0$), this component is equal to the downstream velocity ($u \sim v \sim \bar{u}z/d$), thus implying that the near-bottom velocity is at 45 degrees to the left of the interior velocity (Figure 8-4). (The boundary flow is to the right of the interior flow for $f < 0$.) Further up, where u reaches a first maximum ($z = 3\pi d/4$), the velocity in the direction of the flow is greater than in the interior ($u = 1.07\bar{u}$). (Viscosity can occasionally fool us!)

It is instructive to calculate the net transport of fluid transverse to the main flow:

$$\mathrm{V} = \int_0^{\infty} v\, dz = \frac{\bar{u}d}{2}, \quad (8.19)$$

which is proportional to the interior velocity and the Ekman depth.

8.4 Generalization to non-uniform currents

Let us now consider a more complex interior flow, namely, a spatially nonuniform flow that is varying on a scale sufficiently large to be in geostrophic equilibrium (low Rossby number, as in Section 7.1). Thus,

$$-f\bar{v} = -\frac{1}{\rho_0}\frac{\partial \bar{p}}{\partial x}, \quad f\bar{u} = -\frac{1}{\rho_0}\frac{\partial \bar{p}}{\partial y},$$

where the pressure $\bar{p}(x, y, t)$ is arbitrary. For a constant Coriolis parameter, this flow is non-divergent ($\partial\bar{u}/\partial x + \partial\bar{v}/\partial y = 0$). The boundary-layer equations are now

$$-f(v - \bar{v}) = \nu_E \frac{\partial^2 u}{\partial z^2} \tag{8.20a}$$

$$f(u - \bar{u}) = \nu_E \frac{\partial^2 v}{\partial z^2}, \tag{8.20b}$$

and the solution that satisfies the boundary conditions aloft ($u \to \bar{u}$ and $v \to \bar{v}$ for $z \to \infty$) is

$$u = \bar{u} + e^{-z/d}\left(A \cos\frac{z}{d} + B \sin\frac{z}{d}\right) \tag{8.21}$$

$$v = \bar{v} + e^{-z/d}\left(B \cos\frac{z}{d} - A \sin\frac{z}{d}\right). \tag{8.22}$$

Here, the “constants” of integration A and B are independent of z but, in general, dependent on x and y through $\bar{u}$ and $\bar{v}$. Imposing $u = v = 0$ along the bottom ($z = 0$) sets their values, and the solution is:

$$u = \bar{u}\left(1 - e^{-z/d}\cos\frac{z}{d}\right) - \bar{v}\, e^{-z/d}\sin\frac{z}{d} \tag{8.23a}$$

$$v = \bar{u}\, e^{-z/d}\sin\frac{z}{d} + \bar{v}\left(1 - e^{-z/d}\cos\frac{z}{d}\right). \tag{8.23b}$$

The transport attributed to the boundary-layer structure has components given by

$$\mathrm{U} = \int_0^\infty (u - \bar{u})\, dz = -\frac{d}{2}\,(\bar{u} + \bar{v}) \tag{8.24a}$$

$$\mathrm{V} = \int_0^\infty (v - \bar{v})\, dz = \frac{d}{2}\,(\bar{u} - \bar{v}). \tag{8.24b}$$

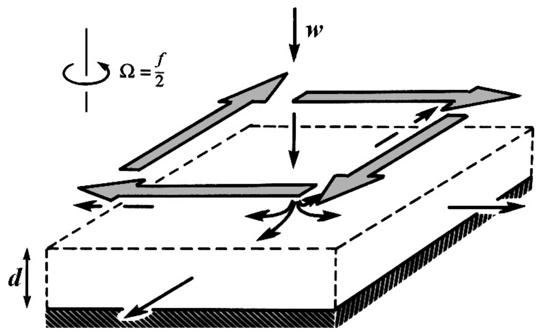

Figure 8-5 Divergence in the bottom Ekman layer and compensating downwelling in the interior. Such a situation arises in the presence of an anticyclonic gyre in the interior, as depicted by the large horizontal arrows. Similarly, interior cyclonic motion causes convergence in the Ekman layer and upwelling in the interior.

Since this transport is not necessarily parallel to the interior flow, it is likely to have a non-zero divergence. Indeed,

$$\begin{aligned} \frac{\partial \mathrm{U}}{\partial x} + \frac{\partial \mathrm{V}}{\partial y} &= \int_0^\infty \left(\frac{\partial u}{\partial x} + \frac{\partial v}{\partial y} \right) dz = -\frac{d}{2} \left(\frac{\partial \bar{v}}{\partial x} - \frac{\partial \bar{u}}{\partial y} \right) \\ &= -\frac{d}{2\rho_0 f} \nabla^2 \bar{p}. \end{aligned} \tag{8.25}$$

The flow in the boundary layer converges or diverges if the interior flow has a relative vorticity. The situation is depicted in Figure 8-5. The question is: From where does the fluid come, or where does it go, to meet this convergence or divergence? Because of the presence of a solid bottom, the only possibility is that it be supplied from the interior by means of a vertical velocity. But, remember (Section 7.1) that geostrophic flows must be characterized by

$$\frac{\partial \bar{w}}{\partial z} = 0, \tag{8.26}$$

that is, the vertical velocity must occur throughout the depth of the fluid. Of course, since the divergence of the flow in the Ekman layer is proportional to the Ekman depth, d, which is very small, this vertical velocity is weak.

The vertical velocity in the interior, called *Ekman pumping*, can be evaluated by a vertical integration of the continuity equation (4.21d), using $w(z=0) = 0$ and $w(z \to \infty) = \bar{w}$:

$$\begin{aligned} \bar{w} &= -\int_0^\infty \left(\frac{\partial u}{\partial x} + \frac{\partial v}{\partial y} \right) dz = \frac{d}{2} \left(\frac{\partial \bar{v}}{\partial x} - \frac{\partial \bar{u}}{\partial y} \right) \\ &= \frac{d}{2\rho_0 f} \nabla^2 \bar{p} = \frac{1}{\rho_0} \sqrt{\frac{\nu_E}{2f^3}} \nabla^2 \bar{p}. \end{aligned} \tag{8.27}$$

So, the greater the vorticity of the mean flow, the greater the upwelling/downwelling. Also, the effect increases toward the equator (decreasing $f = 2\Omega \sin\varphi$ and increasing d). The direction of the vertical velocity is upward in a cyclonic flow (counterclockwise in the Northern Hemisphere) and downward in an anticyclonic flow (clockwise in the Northern Hemisphere).

In the Southern Hemisphere, where $f < 0$, the Ekman layer thickness d must be redefined with the absolute value of f: $d = \sqrt{2\nu_E/|f|}$, but the previous rule remains: the vertical velocity is upward in a cyclonic flow and downward in an anticyclonic flow. The difference is that cyclonic flow is clockwise and anticyclonic flow is counterclockwise.

8.5 The Ekman layer over uneven terrain

It is noteworthy to explore how an irregular topography may affect the structure of the Ekman layer and, in particular, the magnitude of the vertical velocity in the interior. For this, consider a horizontal geostrophic interior flow ($\bar{u}$, $\bar{v}$), not necessarily spatially uniform, over an uneven terrain of elevation $z = b(x,y)$ above a horizontal reference level. To be faithful to our restriction (Section 4.3) to geophysical flows much wider than they are thick, we shall assume that the bottom slope ($\partial b/\partial x$, $\partial b/\partial y$) is everywhere small ($\ll 1$). This is hardly a restriction in most atmospheric and oceanic situations.

Our governing equations are again (8.20), coupled to the continuity equation (4.21d), but the boundary conditions are now

$$\text{Bottom } (z = b): \qquad u = 0, \;\; v = 0, \;\; w = 0, \tag{8.28}$$

$$\text{Toward the interior } (z \gg d): \qquad u = \bar{u}, \;\; v = \bar{v}. \tag{8.29}$$

The solution is the previous solution (8.23) with z replaced by $z - b$:

$$u = \bar{u} - e^{(b-z)/d} \left(\bar{u} \cos\frac{z-b}{d} + \bar{v} \sin\frac{z-b}{d} \right) \tag{8.30a}$$

$$v = \bar{v} + e^{(b-z)/d} \left(\bar{u} \sin\frac{z-b}{d} - \bar{v} \cos\frac{z-b}{d} \right). \tag{8.30b}$$

We note that the vertical thickness of the boundary layer is still measured by $d = \sqrt{2\nu_E/f}$. However, the boundary layer is now oblique, and its true thickness, measured perpendicularly to the bottom, is slightly reduced by the cosine of the small bottom slope.

The vertical velocity is then determined from the continuity equation:

$$
\begin{aligned}
\frac{\partial w}{\partial z} &= -\frac{\partial u}{\partial x} - \frac{\partial v}{\partial y} \\
&= e^{(b-z)/d} \left\{ \left(\frac{\partial \bar{v}}{\partial x} - \frac{\partial \bar{u}}{\partial y} \right) \sin \frac{z-b}{d} \right. \\
&\qquad + \frac{1}{d} \frac{\partial b}{\partial x} \left[(\bar{u} - \bar{v}) \cos \frac{z-b}{d} + (\bar{u} + \bar{v}) \sin \frac{z-b}{d} \right] \\
&\qquad \left. + \frac{1}{d} \frac{\partial b}{\partial y} \left[(\bar{u} + \bar{v}) \cos \frac{z-b}{d} - (\bar{u} - \bar{v}) \sin \frac{z-b}{d} \right] \right\},
\end{aligned}
$$

where use has been made of the fact that the interior geostrophic flow has no divergence ($\partial \bar{u}/\partial x + \partial \bar{v}/\partial y = 0$). A vertical integration from the bottom ($z = b$), where the vertical velocity vanishes ($w = 0$ because u and v are also zero there) into the interior ($z \to +\infty$) where the vertical velocity assumes a vertically uniform value ($w = \bar{w}$), yields

$$
\bar{w} = \left(\bar{u} \frac{\partial b}{\partial x} + \bar{v} \frac{\partial b}{\partial y} \right) + \frac{d}{2} \left(\frac{\partial \bar{v}}{\partial x} - \frac{\partial \bar{u}}{\partial y} \right). \tag{8.31}
$$

The interior vertical velocity thus consists of two parts: a component that ensures no normal flow to the bottom [see (7.10)] and an Ekman-pumping contribution, as if the bottom were horizontally flat [see (8.27)].

The vanishing of the flow component perpendicular to the bottom must be met by the inviscid dynamics of the interior, giving rise to the first contribution to $\bar{w}$. The role of the boundary layer is to bring the tangential velocity to zero at the bottom. This explains the second contribution to $\bar{w}$. Note that the Ekman pumping is not affected by the bottom slope.

The preceding solution can also be applied to the lower portion of the atmospheric boundary layer. This was first done by Akerblom (1908), and matching between the logarithmic layer close to the ground (Section 8.1.1) with the Ekman layer further aloft was performed by Van Dyke (1975). Oftentimes, however, the lower atmosphere is in a stable (stratified) or unstable (convecting) state, and the neutral state during which Ekman dynamics prevail is more the exception than the rule.

8.6 The surface Ekman layer

An Ekman layer occurs not only along bottom surfaces but wherever there is a horizontal frictional stress. This is the case, for example, along the ocean surface, where waters are subject to a wind stress. In fact, this is precisely the situation first examined by Vagn Walfrid Ekman[3]. Fridtjof Nansen[4] had noticed during his cruises to northern latitudes that icebergs drift not downwind but systematically at some angle to the right of the wind. Ekman, his student at the time, reasoned that the cause of this bias was the earth's rotation and subsequently developed the mathematical representation that now bears his name. The solution

[3]See biography at the end of this chapter.

[4]Fridtjof Nansen (1861–1930), Norwegian oceanographer famous for his Arctic expeditions and Nobel Peace Prize laureate (1922).

was originally published in his 1902 doctoral thesis and again, in a more complete article, three years later (Ekman, 1905). In a subsequent article (Ekman, 1906), he mentioned the relevance of his theory to the lower atmosphere, where the wind approaches a geostrophic value with increasing height.

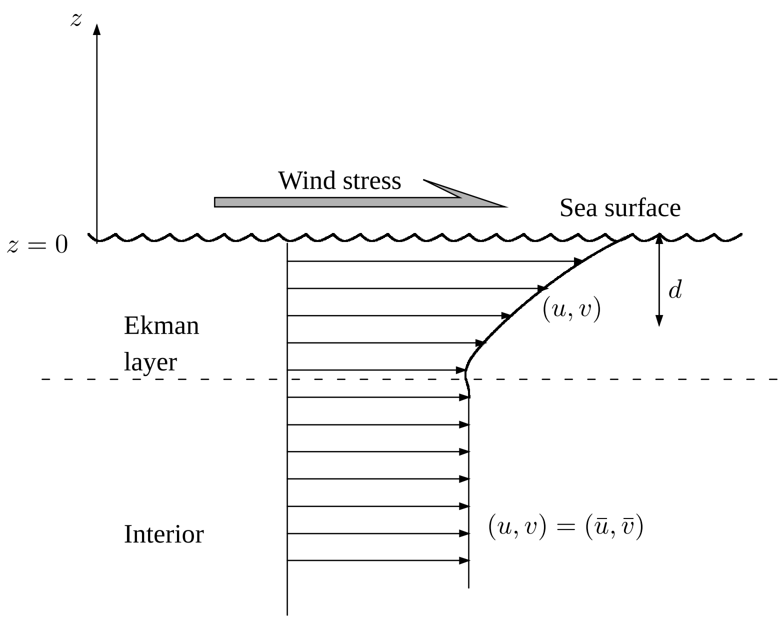

Figure 8-6 The surface Ekman layer generated by a wind stress on the ocean.

Let us consider the situation depicted in Figure 8-6, where an ocean region with interior flow field ($\bar{u}$, $\bar{v}$) is subjected to a wind stress (τ^x, τ^y) along its surface. Again, assuming steady conditions, a homogeneous fluid, and a geostrophic interior, we obtain the following equations and boundary conditions for the flow field (u, v) in the surface Ekman layer:

$$-\ f\,(v-\bar{v}) \;=\; \nu_E\,\frac{\partial^2 u}{\partial z^2} \tag{8.32a}$$

$$+\ f\,(u-\bar{u}) \;=\; \nu_E\,\frac{\partial^2 v}{\partial z^2} \tag{8.32b}$$

$$\text{Surface } (z\ =\ 0): \qquad \rho_0\nu_E\frac{\partial u}{\partial z} \;=\; \tau^x,\quad \rho_0\nu_E\frac{\partial v}{\partial z} \;=\; \tau^y \tag{8.32c}$$

$$\text{Toward interior } (z\ \to\ -\infty): \qquad u \;=\; \bar{u},\quad v \;=\; \bar{v}. \tag{8.32d}$$

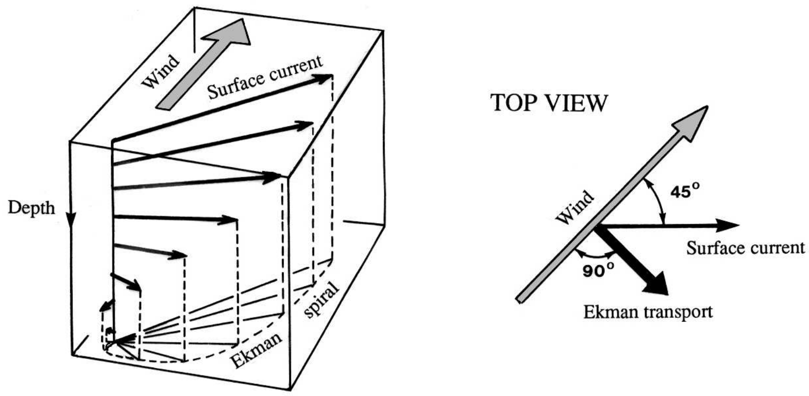

Figure 8-7 Structure of the surface Ekman layer. The figure is drawn for the Northern Hemisphere ($f > 0$), and the deflection is to the right of the surface stress. The reverse holds for the Southern Hemisphere.

The solution to this problem is

$$u = \bar{u} + \frac{\sqrt{2}}{\rho_0 f d}\, e^{z/d} \left[\tau^x \cos\left(\frac{z}{d} - \frac{\pi}{4}\right) - \tau^y \sin\left(\frac{z}{d} - \frac{\pi}{4}\right) \right] \quad (8.33a)$$

$$v = \bar{v} + \frac{\sqrt{2}}{\rho_0 f d}\, e^{z/d} \left[\tau^x \sin\left(\frac{z}{d} - \frac{\pi}{4}\right) + \tau^y \cos\left(\frac{z}{d} - \frac{\pi}{4}\right) \right], \quad (8.33b)$$

in which we note that the departure from the interior flow ($\bar{u}$, $\bar{v}$) is exclusively due to the wind stress. In other words, it does not depend on the interior flow. Moreover, this wind-driven flow component is inversely proportional to the Ekman-layer depth, d, and may be very large. Physically, if the fluid is almost inviscid (small ν, hence short d), a moderate surface stress can generate large drift velocities.

The wind-driven horizontal transport in the surface Ekman layer has components given by

$$\mathrm{U} = \int_{-\infty}^{0} (u - \bar{u})\, dz = \frac{1}{\rho_0 f}\, \tau^y \quad (8.34a)$$

$$\mathrm{V} = \int_{-\infty}^{0} (v - \bar{v})\, dz = \frac{-1}{\rho_0 f}\, \tau^x. \quad (8.34b)$$

Surprisingly, it is oriented perpendicular to the wind stress (Figure 8-7), to the right in the Northern Hemisphere and to the left in the Southern Hemisphere. This fact explains why icebergs, which float mostly underwater, systematically drift to the right of the wind in the North Atlantic, as observed by Fridtjof Nansen.

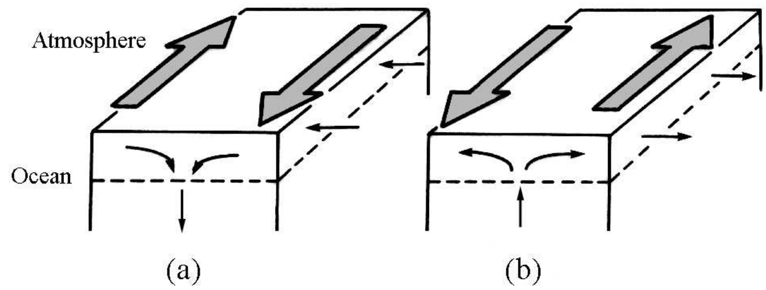

Figure 8-8 Ekman pumping in an ocean subject to sheared winds (case of Northern Hemisphere).

As for the bottom Ekman layer, let us determine the divergence of the flow, integrated over the boundary layer:

$$\int_{-\infty}^{0} \left(\frac{\partial u}{\partial x} + \frac{\partial v}{\partial y}\right) dz = \frac{1}{\rho_0} \left[\frac{\partial}{\partial x}\left(\frac{\tau^y}{f}\right) - \frac{\partial}{\partial y}\left(\frac{\tau^x}{f}\right)\right]. \tag{8.35}$$

At constant f, the contribution is entirely due to the wind stress since the interior geostrophic flow is nondivergent. It is proportional to the wind-stress curl and, most importantly, it is independent of the value of the viscosity. It can be shown furthermore that this property continues to hold even when the turbulent eddy viscosity varies spatially (see Analytical Problem 8-7).

If the wind stress has a non-zero curl, the divergence of the Ekman transport must be provided by a vertical velocity throughout the interior. A vertical integration of the continuity equation, (4.21d), across the Ekman layer with $w(z = 0)$ and $w(z \to -\infty) = \bar{w}$ yields

$$\begin{aligned} \bar{w} &= +\int_{-\infty}^{0} \left(\frac{\partial u}{\partial x} + \frac{\partial v}{\partial y}\right) dz \\ &= \frac{1}{\rho_0} \left[\frac{\partial}{\partial x}\left(\frac{\tau^y}{f}\right) - \frac{\partial}{\partial y}\left(\frac{\tau^x}{f}\right)\right] = w_{\mathrm{Ek}}. \end{aligned} \tag{8.36}$$

This vertical velocity is called *Ekman pumping*. In the Northern Hemisphere ($f > 0$), a clockwise wind pattern (negative curl) generates a downwelling (Figure 8-8a), whereas a counterclockwise wind pattern causes upwelling (Figure 8-8b). The directions are opposite in the Southern Hemisphere. Ekman pumping is a very effective mechanism by which winds drive subsurface ocean currents (Pedlosky, 1996; see also Chapter 20).

8.7 The Ekman layer in real geophysical flows

The preceding models of bottom and surface Ekman layers are highly idealized, and we do not expect their solutions to match actual atmospheric and oceanic observations closely

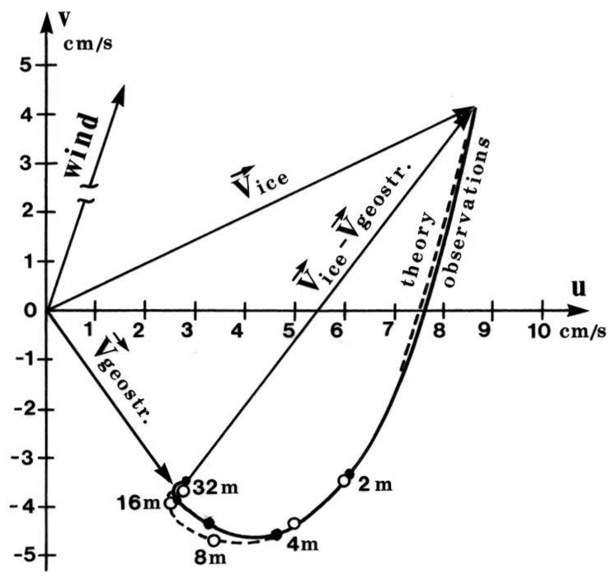

Figure 8-9 Comparison between observed currents below a drifting ice floe at 84.3°N and theoretical predictions based on an eddy viscosity $\nu_E = 2.4 \times 10^{-3}$ m^2/s. (Reprinted from *Deep-Sea Research*, 13, Kenneth Hunkins, Ekman drift currents in the Arctic Ocean, p. 614, ©1966, with kind permission from Pergamon Press Ltd, Headington Hill Hall, Oxford 0X3 0BW, UK)

(except in some cases; see Figure 8-9). Two factors, among others, account for substantial differences: turbulence and stratification.

It was noted at the end of Chapter 4 that geophysical flows have large Reynolds numbers and are therefore in a state of turbulence. Replacing the molecular viscosity of the fluid by a much greater eddy viscosity, as performed in Section 4.2, is a first attempt to recognize the enhanced transfer of momentum in a turbulent flow. However, in a shear flow such as in an Ekman layer, the turbulence is not homogeneous, being more vigorous where the shear is greater and also partially suppressed in the proximity of the boundary where the size of turbulent eddies is restricted. In the absence of an exact theory of turbulence, several schemes have been proposed. At a minimum, the eddy viscosity should be made to vary in the vertical (Madsen, 1977) and should be a function of the bottom stress value (Cushman-Roisin and Malačič, 1997). A number of schemes have been proposed (see Section 4.2), with varying degrees of success. Despite numerous disagreements among models and with field observations, two results nonetheless stand out as quite general. The first is that the angle between the near-boundary velocity and that in the interior or that of the surface stress (depending on the type of Ekman layer) is always substantially less than the theoretical value of 45° and is found to range between 5° and 20° (Figure 8-10). See also Stacey *et al.* (1986).

The second result is a formula for the vertical scale of the Ekman-layer thickness:

$$d \simeq 0.4 \frac{u_*}{f}, \tag{8.37}$$

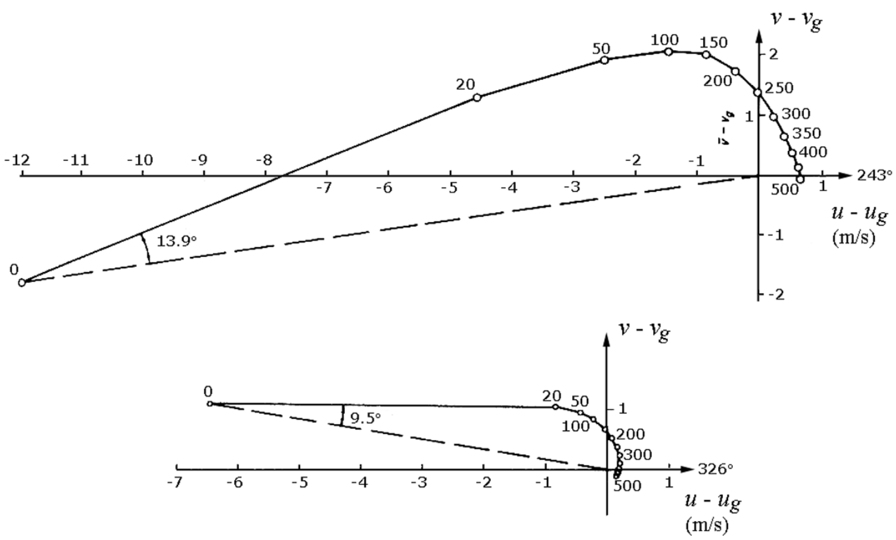

Figure 8-10 Wind vectors minus geostrophic wind as a function of height (in meters) in the maritime friction layer near the Scilly Isles. *Top diagram*: Case of warm air over cold water. *Bottom diagram*: Case of cold air over warm water. (Adapted from Roll, 1965)

where u_* is the turbulent friction velocity defined in (8.1). The numerical factor is derived from observations (Garratt, 1992, Appendix 3). Whereas 0.4 is the most commonly accepted value, there is evidence that certain oceanic conditions call for a somewhat smaller value (Mofjeld and Lavelle, 1984; Stigebrandt, 1985).

Taking u_* as the turbulent velocity and the (unknown) Ekman-layer depth scale, d, as the size of the largest turbulent eddies, we write

$$\nu_E \;\sim\; u_* d. \tag{8.38}$$

Then, using rule 8.12 to determine the boundary-layer thickness, we obtain

$$1 \;\sim\; \frac{\nu_E}{fd^2} \;\sim\; \frac{u_*}{fd}\,,$$

which immediately leads to (8.37).

The other major element missing from the Ekman-layer formulations of the previous sections is the presence of vertical density stratification. Although the effects of stratification are not discussed in detail until Chapter 11, it can be anticipated here that the gradual change of density with height (lighter fluid above heavier fluid) hinders vertical movements, thereby reducing vertical mixing of momentum by turbulence; it also allows the motions at separate levels to act less coherently and to generate internal gravity waves. As a consequence, stratification reduces the thickness of the Ekman layer and increases the veering of the velocity vector with height (Garratt, 1992, Section 6.2). For a study of the oceanic wind-driven Ekman layer in the presence of density stratification, the reader is referred to Price and Sundermeyer (1999).

The surface atmospheric layer during daytime over land and above warm currents at sea is frequently in a state of convection because of heating from below. In such situations, the Ekman dynamics give way to convective motions, and a controlling factor, besides the geostrophic wind aloft, is the intensity of the surface heat flux. An elementary model is presented later (Section 14.7). Because Ekman dynamics then play a secondary role, the layer is simply called the *atmospheric boundary layer*. The interested reader is referred to books on the subject by Stull (1988), Sorbjan (1989), Zilitinkevich (1991) or Garratt (1992).

8.8 Numerical simulation of shallow flows

The theory presented up to now largely relies on the assumption of a constant turbulent viscosity. For real flows, however, turbulence is rarely uniform, and eddy-diffusion profiles must be considered. Such complexity renders the analytical treatment tedious or even impossible, and numerical methods need to be employed.

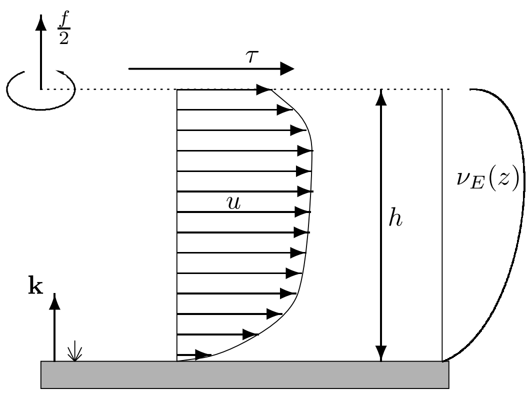

Figure 8-11 A vertically confined fluid flow, with bottom and top Ekman layers bracketing a non-uniform velocity profile. The vertical structure can be calculated by a one-dimensional model spanning the entire fluid column eventhough the turbulent viscosity $\nu_E(z)$ may vary in the vertical.

To illustrate the approach, we reinstate non-stationary terms and assume a vertically varying eddy-viscosity (Figure 8-11) but retain the hydrostatic approximation (8.13c) and continue to consider a fluid of homogeneous density. The governing equations for u and v are

$$\frac{\partial u}{\partial t} - fv = -\frac{1}{\rho_0}\frac{\partial p}{\partial x} + \frac{\partial}{\partial z}\left(\nu_E(z)\frac{\partial u}{\partial z}\right) \tag{8.39a}$$

$$\frac{\partial v}{\partial t} + fu = -\frac{1}{\rho_0}\frac{\partial p}{\partial y} + \frac{\partial}{\partial z}\left(\nu_E(z)\frac{\partial v}{\partial z}\right) \tag{8.39b}$$

$$0 = -\frac{1}{\rho_0}\frac{\partial p}{\partial z}. \tag{8.39c}$$

From the last equation it is clear that the horizontal pressure gradient is independent of z.

A standard finite-volume approach could be applied to the equations, but since we already used the approach several times, its implementation is left as an exercise (see Numerical Problem 8-5). Instead, we introduce here another numerical method, which consists in expanding the solution in terms of preselected functions ϕ_j, called *basis functions*. A finite set of N basis functions is used to construct a *trial solution*:

$$\begin{aligned}\tilde{u}(z,t) &= a_1(t)\phi_1(z) + a_2(t)\phi_2(z) + ... + a_N(t)\phi_N(z) \\ &= \sum_{j=1}^{N} a_j(t)\,\phi_j(z) \end{aligned} \tag{8.40a}$$

$$\begin{aligned}\tilde{v}(z,t) &= b_1(t)\phi_1(z) + b_2(t)\phi_2(z) + ... + b_N(t)\phi_N(z) \\ &= \sum_{j=1}^{N} b_j(t)\,\phi_j(z). \end{aligned} \tag{8.40b}$$

The problem then reduces to finding a way to calculate the unknown coefficients $a_j(t)$ and $b_j(t)$ for $j = 1$ to N such that the trial solution is as close as possible to the exact solution. In other words, we request the residual r_u obtained by substituting the trial solution into the differential x-momentum equation

$$\frac{\partial \tilde{u}}{\partial t} - f\tilde{v} + \frac{1}{\rho_0}\frac{\partial p}{\partial x} - \frac{\partial}{\partial z}\left(\nu_E\,\frac{\partial \tilde{u}}{\partial z}\right) = r_u \tag{8.41}$$

be as small as possible, and similarly with the residual r_v of the y-momentum equation. The residuals r_u and r_v quantify the truncation error of the trial solution, and the objective is to minimize them.

Collocation methods require that the residuals be zero at a finite number of locations z_k across the domain. If each of the two series contains N terms, then taking also N points where the two residual r_u and r_v are forced to vanish provides $2N$ constraints for the $2N$ unknowns a_j and b_j. With a little chance, these constraints will be necessary and sufficient to determine the time evolution of the coefficients $a_j(t)$ and $b_j(t)$. In the present case, the situation is certain because the equations are linear, and the temporal derivatives $da_j(t)/dt$ and $db_j(t)/dt$ appear in linear differential equations, a relatively straightforward problem to be solved numerically, though the matrices involved may have few zeroes. In some cases, however, the equations may be ill conditioned because of inadequate choices of the collocation points z_k (*e.g.*, Gottlieb and Orszag, 1977).

An alternative to requiring zero residuals at selected points is to minimize a global measure of the error. For example, we can multiply the equations by N different weighting functions $\mathsf{w}_i(z)$, and integrate over the domain before requiring that the weighted-average error vanish:

$$\int_0^h \mathsf{w}_i r_u\,dz = 0, \tag{8.42}$$

and similarly for the companion equation. Note that we require that (8.42) holds only for a *finite set* of functions $\mathsf{w}_i,\ \ i = 1, ..., N$. Had we asked instead that the integral be zero for *any* function w, the trial solution would be the exact solution of the equation since r_u and r_v would then be zero everywhere, but this not possible because we have only $2N$ and not an infinity of degrees of freedom at our disposal. The weighted residuals (8.42) must satisfy

$$\int_0^h \mathsf{w}_i \left[\frac{\partial \tilde{u}}{\partial t} - f\tilde{v} + \frac{1}{\rho_0} \frac{\partial p}{\partial x} - \frac{\partial}{\partial z} \left(\nu_E \frac{\partial \tilde{u}}{\partial z} \right) \right] dz = 0, \tag{8.43}$$

for every value of the index i, which leads to

$$\sum_{j=1}^{N} \int_0^h (\mathsf{w}_i \phi_j \, dz) \, \frac{da_j}{dt} - f \sum_{j=1}^{N} \int_0^h (\mathsf{w}_i \phi_j \, dz) \, b_j + \frac{1}{\rho_0} \frac{\partial p}{\partial x} \sum_{i=1}^{N} \int_0^h (\mathsf{w}_i \, dz)$$
$$- \mathsf{w}_i(h) \; \nu_E \frac{\partial u}{\partial z}\bigg|_h + \mathsf{w}_i(0) \; \nu_E \frac{\partial u}{\partial z}\bigg|_0 + \sum_{j=1}^{N} \int_0^h \left(\nu_E \frac{d\mathsf{w}_i}{dz} \frac{d\phi_j}{dz} \, dz \right) a_j = 0, \tag{8.44}$$

and similarly for the y-momentum equation, with the a's replaced by b's, b's by $-a$'s, x by y, and u by v. Note that use was made of the fact that the pressure gradient is independent of z. The top and bottom stresses (first and second terms of the last line) can either be replaced by their value, if known (such as a wind stress on the sea surface), or be expanded in terms of the basis functions, if unknown.

As already mentioned, if Equation (8.44) holds for any weighting function, an exact solution is obtained, but if it only holds for a finite series of weighting functions, an approximate solution is found for which the residual is not zero everywhere but is orthogonal to every weighting function[5]. If N different weights are used and the weighted residuals of each of the 2 equations are required to be zero, we obtain $2N$ ordinary differential equations for the $2N$ unknowns a_j and b_j. To write the sets of equations in compact form, we define square matrices $\mathbf{M}$ and $\mathbf{K}$ and column vector $\mathbf{s}$ by

$$M_{ij} = \int_0^h \mathsf{w}_i \phi_j \, dz, \quad K_{ij} = \int_0^h \nu_E \frac{d\mathsf{w}_i}{dz} \frac{d\phi_j}{dz} \, dz, \quad s_i = \int_0^h \mathsf{w}_i \, dz, \tag{8.45}$$

group coefficients a_j and b_j into column vectors $\mathbf{a}$ and $\mathbf{b}$, and functions $\mathsf{w}_i(z)$ into column vector $\mathbf{w}(z)$. The weighted-residual equations can then be written in matrix notation as

$$\mathbf{M} \frac{d\mathbf{a}}{dt} = +f \, \mathbf{M} \, \mathbf{b} - \mathbf{K} \, \mathbf{a} - \frac{1}{\rho_0} \frac{\partial p}{\partial x} \mathbf{s} + \frac{\tau^x}{\rho_0} \mathbf{w}(h) - \frac{\tau_b^x}{\rho_0} \mathbf{w}(0), \tag{8.46a}$$
$$\mathbf{M} \frac{d\mathbf{b}}{dt} = -f \, \mathbf{M} \, \mathbf{a} - \mathbf{K} \, \mathbf{b} - \frac{1}{\rho_0} \frac{\partial p}{\partial y} \mathbf{s} + \frac{\tau^y}{\rho_0} \mathbf{w}(h) - \frac{\tau_b^y}{\rho_0} \mathbf{w}(0). \tag{8.46b}$$

This set of ordinary differential equations can be solved by any of the time-integration methods of Chapter 2 as long as the temporal evolution of the surface stress, bottom stress and pressure gradient is known.

[5]Orthogonality of two functions is understood here as the property that the product of the two functions integrated over the domain is zero. In the present case, the residual is orthogonal to the weighting functions.

There remains to provide an initial condition on the coefficients a_j and b_j, which must be deduced from the initial condition on the flow profile (see Numerical Exercise 8-1). After solving (8.46), the known values of the coefficients $a_j(t)$ and $b_j(t)$ permit the reconstruction of the solution by means of the expansion (8.40). This method is called the *weighted-residual method*.

A word of caution is necessary with respect to boundary conditions. Top and bottom conditions on the shear stress are automatically taken into account, since the stress appears explicitely in the discrete formulation. A Neumann boundary condition, called a *natural condition*, is thus easily applied. No special demand is placed on the basis functions, and weights are simply required to be different from zero at boundaries where a stress condition is applied. There are situations, however, when the stress on the boundary is not known. This is generally the case at a solid boundary along which a no-slip boundary condition $u = v = 0$ is enforced. The integration method does not make the boundary values of u and v appear, and the basis functions must be chosen carefully to be compatible with the boundary condition. In the case of a no-slip condition, it is required that $\phi_j = 0$ at the concerned boundary, so that the velocity is made to vanish there. This is called an *essential boundary condition*.

Up to now, both basis functions ϕ_j and weights w_i were arbitrary, except for the aforementioned boundary-related constraints, and smart choices can lead to effective methods. The *Galerkin method* makes the rather natural choice of taking the weights equal to the basis functions used in the expansion. The error is then orthogonal to the basis functions. The Galerkin method can also be used with a well chosen set of functions ϕ_j so that an increasing number of functions would eventually lead to the exact solution.

The basis functions ϕ_j do not need to span the entire domain but may be chosen to be zero everywhere, except in finite subdomains. The solution can then be interpreted as the superposition of elementary local solutions. The numerical domain is then divided into subdomains (linear segments in 1D, triangles in 2D, (called *finite elements*)), on each of which only a few basis functions differ from zero. This leads to reduced calculations of the matrices M and K. The finite-element method is one of the most advanced and flexible methods available for the solution of partial differential equations but is also one of the most difficult to implement correctly (see for example Hanert *et al.*, 2003 for the implementation of a 2D ocean model). The interested reader is referred to the specialized literature: Buchanan (1995) and Zienkiewicz and Taylor (2000) for an introduction to general finite-element methods, and Zienkiewicz *et al.* (2005) for the application of finite elements to fluid dynamics.

For the Galerkin method, whether in its finite-element form or using global basis functions, the matrices M and K are symmetric, with components[6]:

$$M_{ij} = \int_0^h \phi_i \phi_j \, dz, \quad K_{ij} = \int_0^h \nu_E \frac{d\phi_i}{dz} \frac{d\phi_j}{dz} \, dz, \quad s_i = \int_0^h \phi_i \, dz. \tag{8.47}$$

For the bottom boundary condition $u = v = 0$, one takes $w_j(0) = \phi_j(0) = 0$, and Equations (8.46) are unchanged, except for the fact that the term including the bottom stress disappears. The method involves matrices coupling all unknowns a_j and b_j, demanding a preliminary matrix inversion (N^3 operations) and then matrix-vector multiplications (N^2 operations) at every time step.

[6]In finite-element jargon, M and K are called, respectively, the mass matrix and stiffness matrix .

For the 1D Ekman layer, the problem can be further simplified (*e.g.*, Heaps, 1987; Davies, 1987) by choosing special basis functions that are designed to obey

$$\frac{\partial}{\partial z}\left(\nu_E(z)\,\frac{\partial \phi_j}{\partial z}\right) \;=\; -\,\varrho_j\,\phi_j(z) \tag{8.48a}$$

$$\phi_i(0) \;=\; 0, \quad \left.\frac{\partial \phi_j}{\partial z}\right|_{z=h} \;=\; 0. \tag{8.48b}$$

In other words, ϕ_j are chosen as the eigenfunctions of the diffusion operator (8.48a), with ϱ_j as the eigenvalues. Multiplication of (8.48a) by ϕ_i and subsequent integration by parts in the left-hand side and use of the boundary conditions (8.48b) yield:

$$\int_0^h \nu_E\,\frac{d\phi_i}{dz}\frac{d\phi_j}{dz}\,dz \;=\; \varrho_i\,\int_0^h \phi_i\phi_j\,dz. \tag{8.49}$$

Note that for $i = j$ this relationship proves the eigenvalues to be positive for positive diffusion coefficients, since all other terms involved are quadratic and thus positive. Switching the indices i and j, we also have

$$\int_0^h \nu_E\,\frac{d\phi_j}{dz}\frac{d\phi_i}{dz}\,dz \;=\; \varrho_j\,\int_0^h \phi_j\phi_i\,dz, \tag{8.50}$$

and subtracting this equation from the preceding one, we obtain

$$(\varrho_i - \varrho_j)\,\int_0^h \phi_i\phi_j\,dz \;=\; 0, \tag{8.51}$$

showing that for non-equal eigenvalues, the basis functions ϕ_i and ϕ_j are orthogonal in the sense that

$$\int_0^h \phi_i(z)\,\phi_j(z)\,dz = 0 \quad \text{if} \quad i \neq j. \tag{8.52}$$

Since the basis functions are defined within an arbitrary multiplicative factor, we may normalize them such that

$$\int_0^h \phi_i(z)\,\phi_j(z)\,dz = \delta_{ij} = \begin{cases} 0 & \text{if} \quad i \neq j \\ 1 & \text{if} \quad i = j \end{cases} \tag{8.53}$$

When eigenfunctions are used as basis functions in the Galerkin method, a so-called *spectral method* is obtained. It is a very elegant method because the equations for the coefficients are greatly reduced. The orthonormality (8.53) of the eigenfunctions yields $\mathbf{M} = \mathbf{I}$, the identity matrix, and (8.49) in matrix form reduces to $\mathbf{K} = \boldsymbol{\varrho}\,\mathbf{M} = \boldsymbol{\varrho}$, where $\boldsymbol{\varrho}$ is a diagonal matrix formed with the eigenvalues ϱ_j. Finally, the equations for components j of $\mathbf{a}$ and $\mathbf{b}$ become:

$$\frac{da_j}{dt} \;=\; +f\,b_j \;-\; \varrho_j\,a_j \;-\; \frac{1}{\rho_0}\frac{\partial p}{\partial x}s_j \;+\; \frac{\tau^x}{\rho_0}\phi_j(h), \tag{8.54a}$$

$$\frac{db_j}{dt} \;=\; -f\,a_j \;-\; \varrho_j\,b_j \;-\; \frac{1}{\rho_0}\frac{\partial p}{\partial y}s_j \;+\; \frac{\tau^y}{\rho_0}\phi_j(h). \tag{8.54b}$$

Note that, since the eigenvalues are positive, the second term on the right corresponds to a damping of the amplitudes a_j and b_j, consistent with physical damping by diffusion.

Because of the decoupling[7] achieved by a set of orthogonal basis functions, we no longer solve a system of $2N$ equations but N systems of 2 equations. This leads to a significant reduction in the number of operations to be performed: The standard Galerkin method requires, at every time step, one inversion of a matrix of size $2N \times 2N$ and a matrix multiplication of cost $4N^2$, while the spectral method demands solving N times a 2×2 system, with cost proportional to N. For a large number of time steps, the computational burden is roughly reduced by a factor N. With typically $10^2 - -10^3$ basis functions retained, the savings are very significant, and the use of a spectral method generates important gains in computing time. It is well worth the preliminary search of eigenfunctions.

In principle, for well behaved $\nu_E(z)$, there exist an infinite but countable number of eigenvalues ϱ_j, and the full set of eigenfunctions ϕ_j allows the decomposition of any function. An approximate solution can thus be obtained by retaining only a finite number of eigenfunctions, and the questions that naturally come to mind are how many functions should be retained and which ones. To know which to retain, we can look at the case of constant viscosity ν_E. Obviously the solution to the eigenproblem is, for $j = 1, 2, ...$:

$$
\begin{aligned}
\phi_j &= \sqrt{\frac{2}{h}}\, \sin\left[(2j-1)\frac{\pi}{2}\frac{z}{h}\right] \\
\varrho_j &= (2j-1)^2\, \frac{\pi^2 \nu}{4h^2} \\
s_j &= \frac{2\sqrt{2h}}{\pi(2j-1)} \\
\phi_j(h) &= (-1)^{(j+1)}\sqrt{\frac{2}{h}}
\end{aligned}
$$

in which the scaling factor $\sqrt{(2/h)}$ was introduced to satisfy normalization requirement (8.53). The name *spectral method* is now readily understood in view of the type of eigenfunctions used in the expansion. The sine functions are indeed nothing else than those used in Fourier series to decompose periodic functions into different wavelengths. The coefficients a_j and b_j are then directly interpretable in terms of modal amplitudes or, in other words, the energy associated with the corresponding Fourier modes. The sets of a_j and b_j then provide an insight into the spectrum of the solution.

We further observe that, the larger the eigenvalue ϱ_j, the more rapidly the function oscillates in space, allowing the capture of finer structures. Thus, a higher resolution is achieved by retaining more eigenfunctions in the expansion, just as adding grid points in finite differencing is done to obtain higher resolution. The number N of functions being retained is a matter of scales to be resolved. For a finite-difference representation with N degrees of freedom, the domain is covered with a uniform grid with spacing $\Delta z = h/N$, and the shortest scale that can be resolved has wavenumber $k_z = \pi/\Delta z$ (see Section 1.12). In the spectral method, the highest mode retained corresponds to wavenumber $k_z = N\pi/h$, which is identical to the one resolved in the finite-difference approach. Both methods are thus able to

[7] Only when equations are linear.

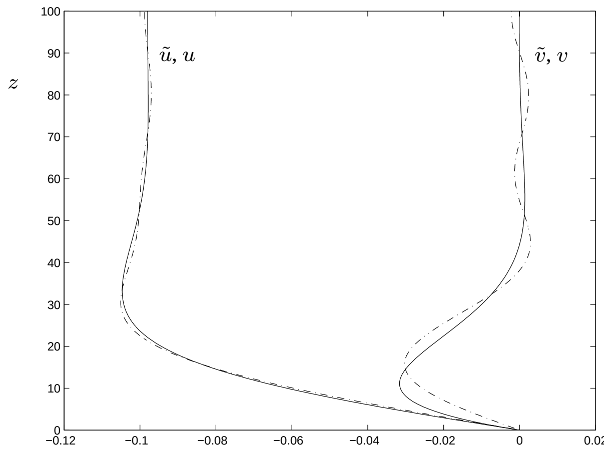

Figure 8-12 Velocity profile forced by a pressure gradient directed along the y–axis above a no-slip bottom and below a stress-free surface. The geostrophic flow aloft has components $u = 0.1$ and $v = 0$. Solid lines represent the exact solution, whereas dash-dotted lines depict the numerical solution obtained by the spectral method with only the first five modes. Note the excellent agreement. Oscillations appearing in the numerical solution give a hint of the sine functions used in expanding the solution.

represent the same spectrum of wavenumbers with an identical number of unknowns. Also, the cost of both methods is directly proportional to the number of unknowns. So, where is the advantage of using a spectral method?

Except for the straightforward interpretation of the coefficients a_j and b_j in terms of Fourier components, the essential advantage of spectral methods resides in their fast convergence for sufficiently gentle solutions and boundary conditions (*e.g.*, Canuto *et al.*, 1988). To illustrate this claim, we calculate the stationary solution of a geostrophic current without surface stress by dropping da_j/dt and db_j/dt from the matrix equations and solve for **a** and **b** before recombining the solution. Even when only 5 basis functions are used (*i.e.*, equivalent to using 5 grid points), the behavior of the solution is well captured (Figure 8-12). Since the equations for different a_j coeffcients are decoupled, increasing the value of N does not modify the values of the previously calculated coefficients and simply adds more terms, each one bringing additional resolution. The amplitude of the new terms is directly proportional to the value of the coefficients a_j and b_j, and their rapid decrease as a function of index j (Figure 8-13 – note the logarithmic scales) explains why fast convergence can be expected.

In order not to miss the most important parts of the solution, it is imperative to use eigenfunctions in their order, that is, without skipping any in the series, up to the preselected number N. In the limit of large N, it can be shown that convergence for a relatively smooth solution is faster than with any finite difference method of any order (*e.g.*, Gottlieb and Orszag 1977). Therefore, the spectral method has a distinctive advantage and is often used in cases when nearly exact numerical solutions are sought.

An alternative to the Galerkin spectral approach is to force the error to vanish at particular grid points, leading to so-called *pseudospectral methods* (*e.g.*, Fornberg, 1998). As for all collocation methods, these do not require evaluation of integrals over the domain.

In concluding the presentation of the function-expansion approach, we insist on the fundamental aspect that the numerical approximation is very different from the point-value sampling used in finite-difference methods. In space, the basis functions ϕ_j are continuous and can therefore be differentiated or manipulated mathematically without approximation. The numerical error arises only due to the fact that a finite number of basis functions are used to

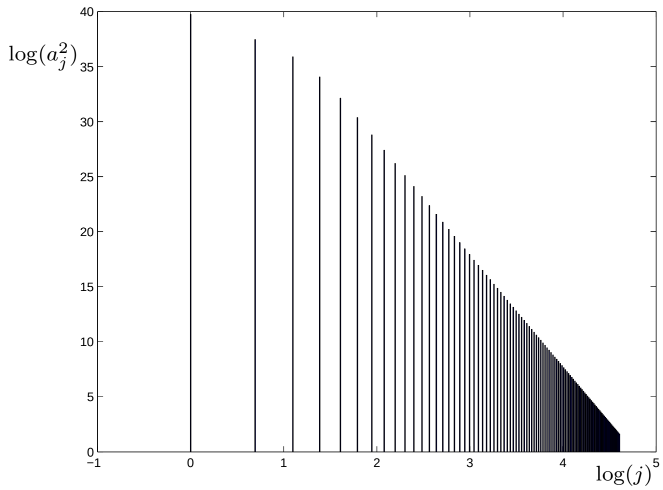

Figure 8-13 The subsequent values of coefficients a_j (scaled by an arbitrary coefficient) obtained with the spectral method applied to the problem of Figure 8-12. Scales are logarithmic, showing the rapid decrease of amplitudes with increasing number of modes in the expansion. Convergence toward the exact solution is fast.

represent the solution.

Analytical Problems

8-1. It is observed that fragments of tea leaves at the bottom of a stirred tea cup conglomerate toward the center. Explain this phenomenon with Ekman-layer dynamics. Also explain why the tea leaves go to the center irrespectively of the direction of stirring (clockwise or counterclockwise).

8-2. Assume that the atmospheric Ekman layer over the earth's surface at latitude 45°N can be modeled with an eddy viscosity ν_E = 10 m^2/s. If the geostrophic velocity above the layer is 10 m/s and uniform, what is the vertically integrated flow across the isobars (pressure contours)? Is there any vertical velocity?

8-3. Meteorological observations above New York (41°N) reveal a neutral atmospheric boundary layer (no convection and no stratification) and a westerly geostrophic wind of 12 m/s at 1000 m above street level. Under neutral conditions, Ekman dynamics apply. Using an eddy viscosity of 10 m^2/s, determine the wind speed and direction atop the Empire State Building, which stands 381 m tall.

8-4. A southerly wind blows at 9 m/s over Taipei (25°N). Assuming neutral atmospheric conditions so that Ekman dynamics apply and taking the eddy viscosity equal to 10 m^2/s, determine the velocity profile from street level to the top of the 509 m tall Taipei Financial Center skyscraper. The wind force per unit height and in the direction of the wind can be taken as $F = 0.93 \rho L V^2$, where ρ = 1.20 kg/m^3 is the standard air density,

L = 25 m is the building width, and $V(z) = (u^2 + v^2)^{1/2}$ is the wind speed at the height considered. With this, determine the total wind force on the southern facade of the Taipei Financial Center.

8-5. Show that although $\bar{w}$ may not be zero in the presence of horizontal gradients, the vertical advection terms $w\partial u/\partial z$ and $w\partial v/\partial z$ of the momentum equations are still negligible, even if the short distance d is taken as the vertical length scale.

8-6. You are working for a company that plans to deposit high-level radioactive wastes on the bottom of the ocean, at a depth of 3000 m. This site (latitude: 33°N) is known to be at the center of a permanent counterclockwise vortex. Locally, the vortex flow can be assimilated to a solid-body rotation with angular speed equal to 10^{-5} s^{-1}. Assuming a homogeneous ocean and a steady, geostrophic flow, estimate the upwelling rate at the vortex center. How many years will it take for the radioactive wastes to arrive at the surface? Take $f = 8 \times 10^{-5}$ s^{-1} and ν = 10^{-2} m^2/s.

8-7. Derive Equation (8.36) more simply not by starting from solution (8.33) as done in the text but by vertical integration of the momentum equations (8.32). Consider also the case of non-uniform eddy viscosity, in which case ν_E must be kept inside the vertical derivative on the right-hand side of the equations, as in the original governing equations (4.21a) and (4.21b).

8-8. Between 15°N and 45°N, the winds over the North Pacific Ocean consist mostly of the easterly trades (15°N to 30°N) and the mid-latitude westerlies (30°N to 45°N). An adequate representation is

$$\tau^x \;=\; \tau_0 \,\sin\left(\frac{\pi y}{2L}\right), \qquad \tau^y \;=\; 0 \quad \text{for} \quad -L \;\leq\; y \;\leq\; L,$$

with τ_0 = 0.15 N/m^2 (maximum wind stress) and L = 1670 km. Taking ρ_0 = 1028 kg/m^3 and the value of the Coriolis parameter corresponding to 30°N, calculate the Ekman pumping. Which way is it directed? Calculate the vertical volume flux over the entire 15°–45°N strip of the North Pacific (width = 8700 km). Express your answer in sverdrup units (1 sverdrup = 1 Sv = 10^6 m^3/s).

8-9. The variation of the Coriolis parameter with latitude can be approximated as $f = f_0 + \beta_0 y$, where y is the northward coordinate (beta-plane approximation, see Section 9.4). Using this, show that the vertical velocity below the surface Ekman layer of the ocean is given by

$$\bar{w}(z) \;=\; \frac{1}{\rho_0}\,\left[\frac{\partial}{\partial x}\,\left(\frac{\tau^y}{f}\right) \;-\; \frac{\partial}{\partial y}\,\left(\frac{\tau^x}{f}\right)\right] \;-\; \frac{\beta_0}{f}\int_z^0 \bar{v}\;dz, \tag{8.55}$$

where τ^x and τ^y are the zonal and meridional wind-stress components, respectively, and $\bar{v}$ is the meridional velocity in the geostrophic interior below the Ekman layer.

8-10. Determine the vertical distribution of horizontal velocity in a 4m deep lagoon subject to a northerly wind stress of 0.2 N/m^2. The density of the brackish water in the lagoon is 1020 kg/m^3. Take $f = 10^{-4}$ s^{-1} and $\nu_E = 10^{-2}$ m^2/s. In which direction is the net transport in this brackish layer?

8-11. Redo Problem 8-10 with $f = 0$ and compare the two solutions. What can you conclude about the role of the Coriolis force in this case?

8-12. Find the stationary solution of (8.13a)–(8.13c) for constant viscosity, a uniform pressure gradient in the y–direction in a domain of finite depth h with no stress at the top and no slip at the bottom. Study the behavior of the solution as h/d varies and compare to the solution in the infinite domain. Then, derive the stationary solution without pressure gradient but with a top stress in the y–direction.

Numerical Exercises

8-1. How can we obtain initial conditions for a_j and b_j in the expansions (8.40) from an initial condition on the physical variables $u = u_0(z)$ and $v = v_0(z)$? *Hint:* Investigate a least-square approach and an approach in which the initial error is forced to vanish in the sense of (8.42). When do the two approaches lead to the same result?

8-2. Use `spectralekman.m` to calculate numerically the stationary solutions of Analytical Problem 8-12. Compare the exact and numerical solutions for $h/d = 4$ and assess the convergence rate as a function of $1/N$, where N is the number of eigenfunctions retained in the trial solution. Compare the convergence rate of both cases (with and without stress at the top) and comment.

8-3. Use `spectralekman.m` to explore how the solution changes as a function of the ratio h/d and how the number N of modes affects your resolution of the boundary layers.

8-4. Modify `spectralekman.m` to allow for time evolution, but maintaining constant wind stress and pressure gradient. Use a trapezoidal method for time integration. Start from rest and observe the temporal evolution. What do you observe?

8-5. Use a finite-volume approach with time splitting for the Coriolis terms and an explicit Euler method to discretize diffusion in (8.39a) and (8.39b). Verify your program in the case of uniform eddy viscosity by comparing with the steady analytical solution. Then use the viscosity profile $\nu_E(z) = \mathcal{K}z(1 - z/h)u_*$. In this case, can you find the eigenfunctions of the diffusion operator and outline the Galerkin method? *Hint:* Look for Legendre polynomials and their properties.

8-6. Assume that your vertical grid spacing in a finite-difference scheme is large compared to the roughness length z_0 and that your first point for velocity calculation is found at the distance $\Delta z/2$ above the bottom. Use the logarithmic profile to deduce the bottom stress as a function of the computed velocity at level $\Delta z/2$. Then use this expression in the finite-volume approach of Numerical Exercise 8-5 to replace the no-slip condition by a stress condition at the lowest level of the grid.

8-7. *Numerical coffee cup?*

Vagn Walfrid Ekman
1874 – 1954

Born in Sweden, Ekman spent his formative years under the tutelage of Vilhelm Bjerknes and Fridtjof Nansen in Norway. One day, Nansen asked Bjerknes to let one of his students make a theoretical study of the influence of the earth's rotation on wind-driven currents, on the basis of Nansen's observations during his polar expedition that ice drifts with ocean currents to the right of the wind. Ekman was chosen and later presented a solution in his doctoral thesis of 1902.

As professor of mechanics and mathematical physics at the University of Lund in Sweden, Ekman became the most famous oceanographer of his generation. The distinguished theoretician also proved to be a skilled experimentalist. He designed a current meter, which bears his name and which has been used extensively. Ekman was also the one who explained the phenomenon of dead water by a celebrated laboratory experiment (see Figure 1-3). (*Photo courtesy of Pierre Welander*)

Ludwig Prandtl
1875 – 1953

A German engineer, Ludwig Prandtl was attracted by fluid phenomena and their mathematical representation. He became professor of mechanics at the University of Hannover in 1901, where he established a world renowned institute for aerodynamics and hydrodynamics. It was while working on wing theory in 1904 and studying friction drag in particular that he developed the concept of boundary layers and the attending mathematical technique. His central idea was to recognize that frictional effects are confined to a thin layer in the vicinity of the boundary, allowing the modeler to treat rest of the flow as inviscid.

Prandtl also made noteworthy advances in the study of elasticity, supersonic flows and turbulence, particularly shear turbulence in the vicinity of a boundary. A mixing length and a dimensionless ratio are named after him.

It has been remarked that Prandtl's keen perception of physical phenomena was balanced by a limited mathematical ability and that this shortcoming prompted him to seek ways of reducing the mathematical description of his objects of study. Thus perhaps, the boundary-layer technique was an invention born out of necessity. (*Photo courtesy of AIP Emilio Segrè Visual Archives, Landé Collection*)

Chapter 9

Barotropic Waves

(October 18, 2006) **SUMMARY**: The aim of this chapter is to describe an assortment of waves that can be supported by an inviscid, homogeneous fluid in rotation and to analyze numerical grid arrangements that facilitate the simulation of wave propagation, in particular for the prediction of tides and storm surges.

9.1 Linear wave dynamics

Chiefly because linear equations are most amenable to methods of solution, it is wise to gain insight into geophysical fluid dynamics by elucidating the possible linear processes and investigating their properties before exploring more intricate, nonlinear dynamics. The governing equations of the previous section are essentially nonlinear; consequently, their linearization can proceed only by imposing restrictions on the flows under consideration.

The Coriolis acceleration terms present in the momentum equations [(4.21a) and (4.21b)] are, by nature, linear and need not be subjected to any approximation. This situation is extremely fortunate because these are the central terms of geophysical fluid dynamics. In contrast, the so-called advective terms (or convective terms) are quadratic and undesirable at this moment. Hence, our considerations will be restricted to low-Rossby-number situations:

$$Ro \;=\; \frac{U}{\Omega L} \;\ll\; 1. \tag{9.1}$$

This is usually accomplished by restricting the attention to relatively weak flows (small U), large scales (large L), or, in the laboratory, fast rotation (large Ω). The terms expressing the local time rate of change of the velocity ($\partial u/\partial t$ and $\partial v/\partial t$) are linear and are retained here in order to permit the investigation of unsteady flows. Thus, the temporal Rossby number is taken as

$$Ro_T \;=\; \frac{1}{\Omega T} \;\sim\; 1. \tag{9.2}$$

Contrasting conditions (9.1) and (9.2), we conclude that we are about to consider slow flow fields that evolve relatively fast. Aren't we asking for the impossible? Not at all, for rapidly moving disturbances do not necessarily require large velocities. In other words, information may travel faster than material particles, and when this is the case, the flow takes the aspect of a wave field. A typical example is the spreading of concentric ripples on the surface of a pond after the throwing of a stone; energy radiates but there is no appreciable water movement across the pond. In keeping with the foregoing quantities, a scale for the wave speed can be defined as the velocity of a signal covering the distance L of the flow during the nominal evolution time T, and, by virtue of restrictions (9.1) and (9.2), it can be compared to the flow velocity:

$$C \;=\; \frac{L}{T} \;\sim\; \Omega L \;\gg\; U. \tag{9.3}$$

Thus, our present objective is to consider wave phenomena.

To shed the best possible light on the mechanisms of the basic wave processes typical in geophysical flows, we further restrict our attention to homogeneous and inviscid flows, for which the shallow-water model (section 7.3) is adequate. With all the preceding restrictions, the horizontal momentum equations (7.12a) and (7.12b) reduce to

$$\frac{\partial u}{\partial t} \;-\; fv \;\;=\;\; -\,g\,\frac{\partial \eta}{\partial x} \tag{9.4a}$$

$$\frac{\partial v}{\partial t} \;+\; fu \;\;=\;\; -\,g\,\frac{\partial \eta}{\partial y}\,, \tag{9.4b}$$

where f is the Coriolis parameter, g the gravitational acceleration, u and v are the velocity components in the x– and y–directions, respectively, and η is the surface displacement (equal to $\eta = h - H$, the total fluid depth h minus the mean fluid thickness H). The independent variables are x, y and t; the vertical coordinate is absent, for the flow is vertically homogeneous (Section 7.3).

In terms of surface height, η, the continuity equation (7.17) can be expanded in several groups of terms:

$$\frac{\partial \eta}{\partial t} \;+\; \left(u\,\frac{\partial \eta}{\partial x} \;+\; v\,\frac{\partial \eta}{\partial y}\right) \;+\; H\,\left(\frac{\partial u}{\partial x} \;+\; \frac{\partial v}{\partial y}\right) \;+\; \eta\,\left(\frac{\partial u}{\partial x} \;+\; \frac{\partial v}{\partial y}\right) \;=\; 0$$

if the mean depth H is constant (flat bottom). Introducing the scale ΔH for the vertical displacement η of the surface, we note that the four groups of terms in the preceding equation are, sequentially, on the order of

$$\frac{\Delta H}{T}\;,\;\; U\frac{\Delta H}{L}\;,\;\; H\frac{U}{L}\;,\;\; \Delta H\frac{U}{L}\;.$$

According to (9.3), L/T is much larger than U, and the second and fourth groups of terms may be neglected compared with the first term, leaving us with the linearized equation

$$\frac{\partial \eta}{\partial t} \;+\; H\left(\frac{\partial u}{\partial x} \;+\; \frac{\partial v}{\partial y}\right) \;=\; 0, \tag{9.5}$$

the balance of which requires $\Delta H/T$ to be on the order of UH/L or, again by virtue of (9.3),

$$\Delta H \ll H. \tag{9.6}$$

We are thus restricted to waves of small amplitudes.

The system of equations (9.4a) through (9.5) governs the linear wave dynamics of inviscid, homogeneous fluids under rotation. For the sake of simple notation, we will perform the mathematical derivations only for positive values of the Coriolis parameter f and then state the conclusions for both positive and negative values of f. The derivations with negative values of f are left as exercises. Before proceeding with the separate studies of geophysical fluid waves, the student or reader not familiar with the concepts of phase speed, wavenumber vector, dispersion relation, and group velocity is directed to Appendix B. A comprehensive account of geophysical waves can be found in the book by LeBlond and Mysak (1978), with additional considerations on nonlinearities in Pedlosky (2003).

9.2 The Kelvin wave

The Kelvin wave is a traveling disturbance that requires the support of a lateral boundary. Therefore, it most often occurs in the ocean where it can travel along coastlines. For convenience, we use oceanic terminology such as coast and offshore.

As a simple model, consider a semi-infinite layer of fluid bounded below by a horizontal bottom, above by a free surface, and on one side (say, the y–axis) by a vertical wall (Figure 9-1). Along this wall ($x = 0$, the coast), the normal velocity must vanish ($u = 0$), but the absence of viscosity allows a non-zero tangential velocity.

As he recounted in his presentation to the Royal Society of Edinburgh in 1879, Sir William Thomson (later to become Lord Kelvin) thought that the vanishing of the velocity component normal to the wall suggested the possibility that it be zero everywhere. So, let us state, in anticipation,

$$u = 0 \tag{9.7}$$

throughout the domain and investigate the consequences. Although Equation (9.4a) contains a remaining derivative with respect to x, Equations (9.4b) and (9.5) contain only derivatives with respect to y and time. Elimination of the surface elevation leads to a single equation for the alongshore velocity:

$$\frac{\partial^2 v}{\partial t^2} = c^2 \frac{\partial^2 v}{\partial y^2}, \tag{9.8}$$

where

$$c = \sqrt{gH} \tag{9.9}$$

is identified as the speed of surface gravity waves in nonrotating shallow waters.

The preceding equation governs the propagation of one-dimensional nondispersive waves and possesses the general solution

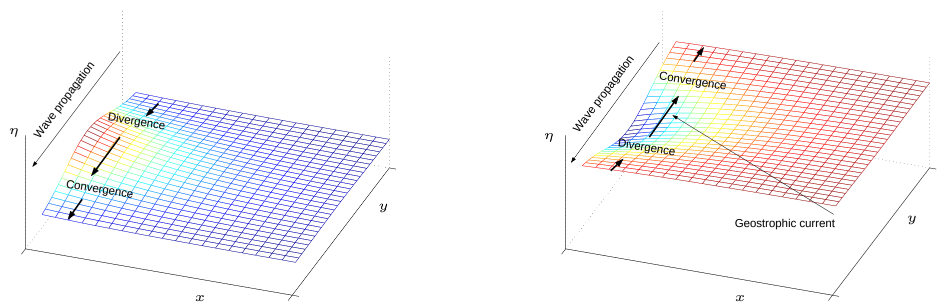

Figure 9-1 Upwelling and downwelling Kelvin waves. In the Northern Hemisphere, both waves travel with the coast on their right, but the accompanying currents differ. Geostrophic equilibrium in the x–momentum equation leads to a velocity v that is maximum at the bulge and directed as the geostrophic equilibrium requires. Because of the different geostrophic velocities at the bulge and further away, convergence and divergence patterns create a lifting or lowering of the surface. The lifting and lowering is such that the wave propagates towards negative y in either case (positive or negative bulge).

$$v \;=\; V_1(x,\; y+ct) \;+\; V_2(x,\; y-ct), \tag{9.10}$$

which consists of two waves, one traveling toward decreasing y and the other in the opposite direction. Returning to either (9.4b) or (9.5) where u is set to zero, we easily determine the surface displacement:

$$\eta \;=\; -\sqrt{\frac{H}{g}}\,V_1(x,\; y+ct) \;+\; \sqrt{\frac{H}{g}}\,V_2(x,\; y-ct). \tag{9.11}$$

(Any additive constant can be eliminated by a proper redefinition of the mean depth H.) The structure of the functions V_1 and V_2 is then determined by the use of the remaining equation, *i.e.*, (9.4a):

$$\frac{\partial V_1}{\partial x} \;=\; -\,\frac{f}{\sqrt{gH}}\,V_1, \qquad \frac{\partial V_2}{\partial x} \;=\; +\,\frac{f}{\sqrt{gH}}\,V_2$$

or

$$V_1 \;=\; V_{10}(y+ct)\,e^{-x/R}\,, \qquad V_2 \;=\; V_{20}(y-ct)\,e^{+x/R},$$

where the length R, defined as

$$R \;=\; \frac{\sqrt{gH}}{f} \;=\; \frac{c}{f}\,, \tag{9.12}$$

combines all three constants of the problem. Within a numerical factor, it is the distance covered by a wave, such as the present one, traveling at the speed c during one inertial period ($2\pi/f$). For reasons that will become apparent later, this quantity is called the *Rossby radius of deformation*, or, more simply, the radius of deformation.

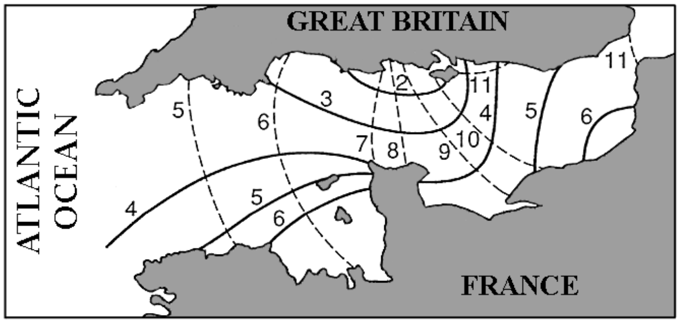

Figure 9-2 Cotidal lines (dashed) with time in lunar hours for the M2 tide in the English Channel showing the eastward progression of the tide from the North Atlantic Ocean. Lines of equal tidal range (solid, with value in meters) reveal larger amplitudes along the French coast, namely to the right of the wave progression in accordance with Kelvin waves. (From Proudman, 1953, as adapted by Gill, 1982.)

Of the two independent solutions, the second increases exponentially with distance from shore and is physically unfit. This leaves the other as the most general solution:

$$u = 0 \tag{9.13a}$$
$$v = \sqrt{gH}\, F(y+ct)\, e^{-x/R} \tag{9.13b}$$
$$\eta = -\,H\, F(y+ct)\, e^{-x/R}, \tag{9.13c}$$

where F is an arbitrary function of its variable.

Because of the exponential decay away from the boundary, the Kelvin wave is said to be trapped. Without the boundary, it is unbounded at large distances and thus cannot exist; the length R is a measure of the trapping distance. In the longshore direction, the wave travels without distortion at the speed of surface gravity waves. In the Northern Hemisphere ($f > 0$, as in the preceding analysis), the wave travels with the coast on its right; in the Southern Hemisphere, with the coast on its left. Note that, although the direction of wave propagation is unique, the sign of the longshore velocity is arbitrary: An upwelling wave (*i.e.*, a surface bulge with $\eta > 0$) has a current flowing in the direction of the wave, whereas a downwelling wave (*i.e.*, a surface trough with $\eta < 0$) is accompanied by a current flowing in the direction opposite to that of the wave (Figure 9-1).

In the limit of no rotation ($f \to 0$), the trapping distance increases without bound and the wave reduces to a simple gravity wave with crests and troughs oriented perpendicularly to the coast.

Surface Kelvin waves (as described previously, and to be distinguished from internal Kelvin waves, which require a stratification, see the end of Chapter 13) are generated by the ocean tides and by local wind effects in coastal areas. For example, a storm off the northeast coast of Great Britain can send a Kelvin wave that follows the shores of the North Sea in a counterclockwise direction and eventually reaches the west coast of Norway. Traveling in approximately 40 m of water and over a distance of 2200 km, it accomplishes its journey in about 31 h.

The decay of the Kelvin-wave amplitude away from the coast is clearly manifested in the English Channel. The North Atlantic tide enters the Channel from the west and travels eastward toward the North Sea (Figure 9-2). Being essentially a surface wave in a rotating fluid bounded by a coast, the tide assumes the character of a Kelvin wave and propagates while leaning against a coast on its right, namely, France. This explains why tides are noticeably higher along the French coast than along the British coast a few tens of kilometers across (Figure 9-2).

9.3 Inertia-gravity waves (Poincaré waves)

Let us now do away with the lateral boundary and relax the stipulation $u = 0$. The system of equations (9.4a) through (9.5) is kept in its entirety. With f constant and in the presence of a flat bottom, all coefficients are constant, and a Fourier-mode solution can be sought. With u, v, and η taken as constant factors times a periodic function

$$\begin{pmatrix} \eta \\ u \\ v \end{pmatrix} = \Re \begin{pmatrix} A \\ U \\ V \end{pmatrix} e^{\mathrm{i}\,(k_x x + k_y y - \omega t)} \tag{9.14}$$

where the symbol $\Re$ indicates the real part of what follows, k_x and k_y are the wavenumbers in the x– and y–directions, respectively, and ω is a frequency, the system of equations becomes algebraic:

$$- \,\mathrm{i}\,\omega U \; - \; fV \;\; = \;\; - \,\mathrm{i}\, g k_x A \tag{9.15a}$$

$$- \,\mathrm{i}\,\omega V \; + \; fU \;\; = \;\; - \,\mathrm{i}\, g k_y A \tag{9.15b}$$

$$- \,\mathrm{i}\,\omega A \; + \; H\,(\mathrm{i}\,k_x U \; + \; \mathrm{i}\,k_y V) \;\; = \;\; 0. \tag{9.15c}$$

This system admits the trivial solution $u = v = \eta = 0$ unless its determinant vanishes. Thus waves occur only when the following condition is met:

$$\omega\,[\omega^2 \; - \; f^2 \; - \; gH\,(k_x^2 \; + \; k_y^2)] \; = \; 0. \tag{9.16}$$

This condition, called the *dispersion relation*, provides the wave frequency in terms of the wavenumber magnitude $k = (k_x^2 + k_y^2)^{1/2}$ and the constants of the problem. The first root, $\omega = 0$, corresponds to a steady geostrophic state. Returning to (9.4a) through (9.5) with the time derivatives set to zero, we recognize the equations governing the geostrophic flow described in Section 7.1. In other words, geostrophic flows can be interpreted as arrested waves of any wavelength. If the bottom were not flat, these “waves” would cease to exist and be replaced by Taylor columns.

The remaining two roots,

$$\omega \; = \; \sqrt{f^2 \; + \; gH\,k^2} \tag{9.17}$$

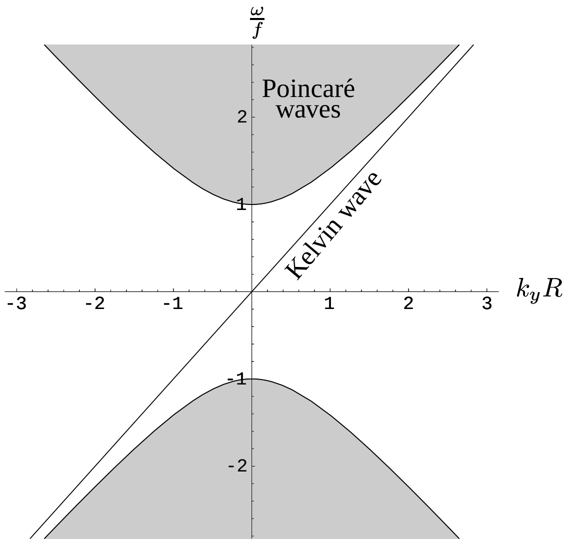

Figure 9-3 Recapitulation of the dispersion relation of Kelvin and Poincaré waves on the f-plane and on a flat bottom. While Poincaré waves (gray shades) can travel in all directions and occupy therefore a continuous spectrum in terms of k_y, the Kelvin wave (diagonal line) propagates only along a boundary.

and its opposite, correspond to bona fide traveling waves, called *Poincaré waves*. In the limit of no rotation ($f = 0$), the frequency is $\omega = k\sqrt{gH}$ and the phase speed is $c = \omega/k = \sqrt{gH}$. The waves become classical shallow-water gravity waves. The same limit also occurs at large wavenumbers [$k^2 \gg f^2/gH$, *i.e.*, wavelengths much shorter than the deformation radius defined in (9.12)]. This is not too surprising, since such waves are too short and too fast to feel the rotation of the earth.

At the opposite extreme of low wavenumbers ($k^2 \ll f^2/gH$, *i.e.*, wavelengths much longer than the deformation radius), the rotation effect dominates, yielding $\omega \simeq f$. At this limit, the flow pattern is virtually laterally uniform, and all fluid particles move in unison, each describing a circular inertial oscillation, as described in Section 2.3. For intermediate wavenumbers, the frequency (Figure 9-3) is always greater than f, and the waves are said to be *superinertial*. Since Poincaré waves exhibit a mixed behavior between gravity waves and inertial oscillations, they are often called *inertia-gravity waves*.

Because the phase speed $c = \omega/k$ depends on the wavenumber, wave components of different wavelengths travel at different speeds, and the wave is said to be *dispersive*. This is in contrast with the nondispersive Kelvin wave, the signal of which travels without distortion, irrespective of its profile. See Appendix B for additional information on these notions.

Seiches, tides and tsunamis are examples of barotropic gravity waves. A *seiche* is a standing wave, formed by the superposition of two waves of equal wavelength and propagating in opposite directions due to reflection on lateral boundaries. Seiches occur in confined water bodies, such as lakes, gulfs and semi-enclosed seas.

A *tsunami* is a wave triggered by an underwater earthquake. With wavelengths ranging from tens to hundreds of kilometers, tsunamis are barotropic waves, but their relatively high frequency (period of a few minutes) makes them only slightly affected by the Coriolis force. What makes tsunamis disastrous is the gradual amplification of their amplitude as they enter shallower waters, so that what may begin as an innocuous 1m wave in the middle of the ocean, which a ship hardly notices, can turn into a catastrophic multi-meter surge on the beach. Disastrous tsunamis occurred in the Pacific Ocean on 22 May 1960 and in the Indian Ocean on 26 December 2004. Tsunamis are relatively easy to forecast with computer models. The key to an effective warning system is the early detection of the originating earthquake, to track the rapid propagation (at speed of $\sqrt{gH}$) of the tsunami from point of origin to the coastline on time to issue a warning before the high wave strikes.

Before concluding this section, a note is in order to warn about the possibility of violating the hydrostatic assumption. Indeed, at short wavelengths (on the order of the fluid depth or shorter), the frequency is high (period much shorter than $2\pi/f$), and the vertical acceleration (equal to $\partial^2\eta/\partial t^2$ at the surface) becomes comparable to the gravitational acceleration g. When this is the case, the hydrostatic approximation breaks down, the assumption of vertical rigidity may no longer be invoked, and the problem becomes three-dimensional. For a study of non-hydrostatic gravity waves, the reader is referred to Section 10 of LeBlond and Mysak (1978) and Lecture 3 of Pedlosky (2003).

9.4 Planetary waves (Rossby waves)

Kelvin and Poincaré waves are relatively fast waves, and we may wonder whether rotating, homogeneous fluids could not support another breed of slower waves. Could it be, for example, that the steady geostrophic flows, those corresponding to the zero frequency solution found in the preceding section, may develop a slow evolution (frequency slightly above zero) when the system is modified somewhat? The answer is yes, and one such class consists of planetary waves, in which the time evolution originates in the weak but important *planetary effect*.

As we may recall from Section 2.5, on a spherical earth (or planet or star, in general), the Coriolis parameter, f, is proportional to the rotation rate, Ω, times the sine of the latitude, φ:

$$f \;=\; 2\Omega \,\sin\, \varphi.$$

Large wave formations such as alternating cyclones and anticyclones contributing to our daily weather and, to a lesser extent, Gulf Stream meanders span several degrees of latitude; for them, it is necessary to consider the meridional change in the Coriolis parameter. If the coordinate y is directed northward and is measured from a reference latitude φ_0 (say, a latitude somewhere in the middle of the wave under consideration), then $\varphi = \varphi_0 + y/a$, where a is the earth's radius (6371 km). Considering y/a as a small perturbation, the Coriolis parameter can be expanded in a Taylor series:

$$f \;=\; 2\Omega\,\sin\varphi_0 \;+\; 2\Omega\,\frac{y}{a}\,\cos\varphi_0 \;+\; ... \tag{9.18}$$

Retaining only the first two terms, we write

$$f \;=\; f_0 \;+\; \beta_0 y, \tag{9.19}$$

where $f_0 = 2\Omega\sin\varphi_0$ is the reference Coriolis parameter and $\beta_0 = 2(\Omega/a)\cos\varphi_0$ is the so-called *beta parameter*. Typical midlatitude values on Earth are $f_0 = 8 \times 10^{-5}$ s^{-1} and $\beta_0 = 2 \times 10^{-11}$ m^{-1}s^{-1}. The Cartesian framework where the beta term is not retained is called the *f-plane*, and that where it is retained is called the *beta plane*. The next step in order of accuracy is to retain the full spherical geometry (which we avoid throughout this book). Rigorous justifications of the beta-plane approximation can be found in Veronis (1963, 1981), Pedlosky (1987), and Verkley (1990).

Note that the beta-plane representation is validated at mid latitudes only if the $\beta_0 y$ term is small compared to the leading f_0 term. For the motion's meridional length scale L, this implies

$$\beta = \frac{\beta_0 L}{f_0} \ll 1, \tag{9.20}$$

where the dimensionless ratio β can be called the *planetary number*.

The governing equations, having become

$$\frac{\partial u}{\partial t} - (f_0 + \beta_0 y)v = -g\frac{\partial \eta}{\partial x} \tag{9.21a}$$

$$\frac{\partial v}{\partial t} + (f_0 + \beta_0 y)u = -g\frac{\partial \eta}{\partial y} \tag{9.21b}$$

$$\frac{\partial \eta}{\partial t} + H\left(\frac{\partial u}{\partial x} + \frac{\partial v}{\partial y}\right) = 0, \tag{9.21c}$$

are now mixtures of small and large terms. The larger ones (f_0, g, and H terms) comprise the otherwise steady, f-plane geostrophic dynamics; the smaller ones (time derivatives and β_0 terms) come as perturbations, which, although small, will govern the wave evolution. In first approximation, the large terms dominate, and thus $u \simeq -(g/f_0)\partial\eta/\partial y$ and $v \simeq +(g/f_0)\partial\eta/\partial x$. Use of this first approximation in the small terms of (9.21a) and (9.21b) yields

$$-\frac{g}{f_0}\frac{\partial^2 \eta}{\partial y \partial t} - f_0 v - \frac{\beta_0 g}{f_0}\, y\, \frac{\partial \eta}{\partial x} = -g\frac{\partial \eta}{\partial x} \tag{9.22}$$

$$+\frac{g}{f_0}\frac{\partial^2 \eta}{\partial x \partial t} + f_0 u - \frac{\beta_0 g}{f_0}\, y\, \frac{\partial \eta}{\partial y} = -g\frac{\partial \eta}{\partial y}\,. \tag{9.23}$$

These equations are trivial to solve with respect to u and v:

$$u = -\frac{g}{f_0}\frac{\partial \eta}{\partial y} - \frac{g}{f_0^2}\frac{\partial^2 \eta}{\partial x \partial t} + \frac{\beta_0 g}{f_0^2}\, y\, \frac{\partial \eta}{\partial y} \tag{9.24}$$

$$v = +\frac{g}{f_0}\frac{\partial \eta}{\partial x} - \frac{g}{f_0^2}\frac{\partial^2 \eta}{\partial y \partial t} - \frac{\beta_0 g}{f_0^2}\, y\, \frac{\partial \eta}{\partial x}\,. \tag{9.25}$$

These last expressions can be interpreted as consisting of the leading and first-correction terms in a regular perturbation series of the velocity field. We identify the first term of each expansion as the geostrophic velocity. By contrast, the next and smaller terms are called *ageostrophic*.

Substitution in continuity equation (9.21c) leads to a single equation for the surface displacement:

$$\frac{\partial \eta}{\partial t} \; - \; R^2 \, \frac{\partial}{\partial t} \; \nabla^2 \, \eta \; - \; \beta_0 R^2 \, \frac{\partial \eta}{\partial x} \; = \; 0, \tag{9.26}$$

where ∇^2 is the two-dimensional Laplace operator and $R = \sqrt{gH}/f_0$ is the deformation radius, defined in (9.12) but now suitably amended to be a constant. Unlike the original set of equations, this last equation has constant coefficients and a solution of the Fourier type, $\cos(k_x x + k_y y - \omega t)$, can be sought. The dispersion relation follows:

$$\omega \; = \; - \; \beta_0 R^2 \, \frac{k_x}{1 \; + \; R^2 \, (k_x^2 \; + \; k_y^2)} \; , \tag{9.27}$$

providing the frequency ω as a function of the wavenumber components k_x and k_y. The waves are called *planetary waves* or *Rossby waves*, in honor of Carl-Gustaf Rossby, who first proposed this wave theory to explain the systematic movement of midlatitude weather patterns. We note immediately that if the beta corrections had not been retained ($\beta_0 = 0$), the frequency would have been nil. This is the $\omega = 0$ solution of Section 9.3, which corresponds to a steady geostrophic flow on the f-plane. The absence of the other two roots is explained by our approximation. Indeed, treating the time derivatives as small terms (*i.e.*,, having in effect assumed a very small temporal Rossby number, $Ro_T \ll 1$), we have retained only the low frequency, the one much less than f_0. In the parlance of wave dynamics, this is called *filtering*.

That the frequency given by (9.27) is indeed small can be verified easily. With L ($\sim 1/k_x \sim 1/k_y$) as a measure of the wavelength, two cases can arise: either $L \lesssim R$ or $L \gtrsim R$; the frequency scale is then given, respectively by

$$\text{Shorter waves :} \qquad L \; \lesssim \; R, \quad \omega \; \sim \; \beta_0 L \tag{9.28}$$

$$\text{Longer waves :} \qquad L \; \gtrsim \; R, \quad \omega \; \sim \; \frac{\beta_0 R^2}{L} \; \lesssim \; \beta_0 L. \tag{9.29}$$

In either case, our premise (9.20) that $\beta_0 L$ is much less than f_0 implies that ω is much smaller than f_0 (subinertial wave), as we anticipated.

Let us now explore other properties of planetary waves. First and foremost, the zonal phase speed

$$c_x \; = \; \frac{\omega}{k_x} \; = \; \frac{-\beta_0 R^2}{1 \; + \; R^2 \, (k_x^2 \; + \; k_y^2)} \tag{9.30}$$

is always negative, implying a phase propagation to the west (Figure 9-4). The sign of the meridional phase speed $c_y = \omega/k_y$ is undetermined, since the wavenumber k_y may have either sign. Thus, planetary waves can propagate only northwestward, westward, or southwestward. Second, very long waves ($1/k_x$ and $1/k_y$ both much larger than R) propagate always westward and at the speed

$$c \; = \; - \; \beta_0 R^2, \tag{9.31}$$

which is the largest wave speed allowed.

Lines of constant frequency ω in the (k_x, k_y) wavenumber space are circles defined by

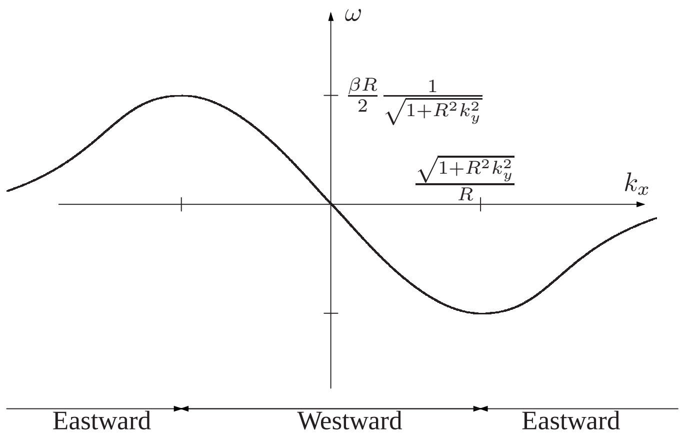

Figure 9-4 Dispersion relation of planetary (Rossby) waves. The frequency ω is plotted against the zonal wavenumber k_x at constant meridional wavenumber k_y. As the slope of the curve reverses, so does the direction of zonal propagation of energy.

$$\left(k_x + \frac{\beta_0}{2\omega}\right)^2 + k_y^2 = \left(\frac{\beta_0^2}{4\omega^2} - \frac{1}{R^2}\right), \tag{9.32}$$

and are illustrated in Figure 9-5. Such circles exist only if their radius is a real number — that is, if $\beta_0^2 > 4\omega^2/R^2$. This implies the existence of a maximum frequency

$$|\omega|_{\max} = \frac{\beta_0 R}{2}, \tag{9.33}$$

beyond which planetary waves do not exist.

The group velocity, at which the energy of a wave packet propagates, defined as the vector $(\partial\omega/\partial k_x, \partial\omega/\partial k_y)$, is the gradient of the function ω in the (k_x, k_y) wavenumber plane (see Appendix B). It is thus perpendicular to the circles of constant ω. A little algebra reveals that the group-velocity vector is directed inward, toward the center of the circle. Therefore, long waves (small k_x and k_y, points near the origin in Figure 9-5) have westward group velocities, whereas energy is carried eastward by the shorter waves (larger k_x and k_y, points on the opposite side of the circle). This dichotomy is also apparent in Figure 9-4, which exhibits reversals in slope ($\partial\omega/\partial k_x$ changing sign).

9.5 Topographic waves

Just as small variations in the Coriolis parameter can turn a steady geostrophic flow into slowly moving planetary waves, so can a weak bottom irregularity. Admittedly, topographic variations can come in a great variety of sizes and shapes, but for the sake of illustrating the wave process in its simplest form, we limit ourselves here to the case of a weak and

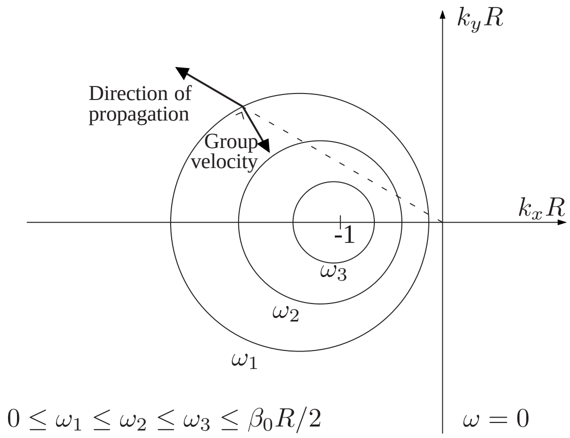

Figure 9-5 Geometric representation of the planetary-wave dispersion relation. Each circle corresponds to a fixed frequency, with frequency increasing with decreasing radius. The group velocity of the (k_x, k_y) wave is a vector perpendicular to the circle at point (k_x, k_y) and directed toward its center.

uniform bottom slope. We also return to the use of a constant Coriolis parameter. This latter choice allows us to choose convenient directions for the reference axes, and, in anticipation of an analogy with planetary waves, we align the y–axis with the direction of the topographic gradient. We thus express the depth of the fluid at rest as:

$$H \;=\; H_0 \;+\; \alpha_0 y, \tag{9.34}$$

where H_0 is a mean reference depth and α_0 is the bottom slope, which is required to be gentle so that

$$\alpha \;=\; \frac{\alpha_0 L}{H_0} \;\ll\; 1, \tag{9.35}$$

where L is the horizontal length scale of the motion. The topographic parameter α plays a role similar to the planetary number, defined in (9.20).

The bottom slope gives rise to new terms in the continuity equation. Starting with the continuity equation (7.17) for shallow water and expressing the instantaneous fluid layer depth as (Figure 9-6)

$$h(x,\, y,\, t) \;=\; H_0 \;+\; \alpha_0 y \;+\; \eta(x,\, y,\, t), \tag{9.36}$$

we obtain

$$\begin{aligned} \frac{\partial \eta}{\partial t} \;+\; \left(u\frac{\partial \eta}{\partial x} \;+\; v\frac{\partial \eta}{\partial y} \right) \;\;+\;\; (H_0 + \alpha_0 y) \left(\frac{\partial u}{\partial x} \;+\; \frac{\partial v}{\partial y} \right) \\ +\; \eta \left(\frac{\partial u}{\partial x} \;+\; \frac{\partial v}{\partial y} \right) \;\;+\;\; \alpha_0 v \;=\; 0. \end{aligned}$$

Once again, we strike out the nonlinear terms by invoking a very small Rossby number (much smaller than the temporal Rossby number) for the sake of linear dynamics. The term $\alpha_0 y$ can

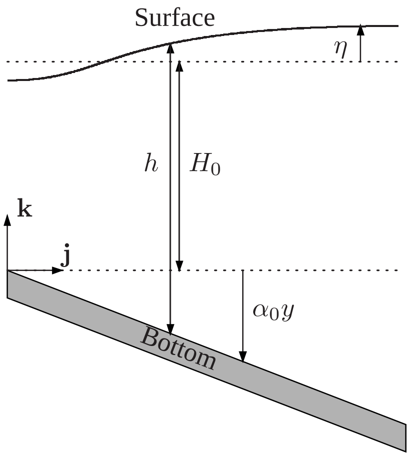

Figure 9-6 A layer of homogeneous fluid over a sloping bottom and the attending notation.

also be dropped next to H_0 by virtue of (9.35). With the momentum equations (9.4a) and (9.4b), our present set of equations is

$$\frac{\partial u}{\partial t} - fv = -g\frac{\partial \eta}{\partial x} \tag{9.37a}$$

$$\frac{\partial v}{\partial t} + fu = -g\frac{\partial \eta}{\partial y} \tag{9.37b}$$

$$\frac{\partial \eta}{\partial t} + H_0\left(\frac{\partial u}{\partial x} + \frac{\partial v}{\partial y}\right) + \alpha_0 v = 0. \tag{9.37c}$$

In analogy with the system of equations governing planetary waves, the preceding set contains both small and large terms. The large ones (terms including f, g, and H_0) comprise the otherwise steady geostrophic dynamics, which correspond to a zero frequency. But, in the presence of the small α_0 term in the last equation, the geostrophic flow cannot remain steady, and the time-derivative terms come into play. We naturally expect them to be small and, compared to the large terms, on the order of α. In other words, the temporal Rossby number, $Ro_T = 1/\Omega T$, is expected to be comparable to α, leading to wave frequencies

$$\omega \sim \frac{1}{T} \sim \alpha\Omega \sim \alpha f \ll f$$

that are very subinertial, just as in the case of planetary waves, for which $\omega \sim \beta f_0$.

Capitalizing on the smallness of the time-derivative terms, we take in first approximation the large geostrophic terms: $u \simeq -(g/f)\partial\eta/\partial y$, $v \simeq +(g/f)\partial\eta/\partial x$. Substitution of these expressions in the small time derivatives yields, to the next degree of approximation:

$$u = -\frac{g}{f}\frac{\partial \eta}{\partial y} - \frac{g}{f^2}\frac{\partial^2 \eta}{\partial x \partial t} \tag{9.38a}$$

$$v = +\frac{g}{f}\frac{\partial \eta}{\partial x} - \frac{g}{f^2}\frac{\partial^2 \eta}{\partial y \partial t}. \tag{9.38b}$$

The relative error is only on the order of α^2. Replacement of the velocity components, u and v, by their last expressions (9.38a) and (9.38b) in the continuity equation (9.37c) provides a single equation for the surface displacement η, which to the leading order is

$$\frac{\partial \eta}{\partial t} \;-\; R^2 \, \frac{\partial}{\partial t} \, \nabla^2 \, \eta \;+\; \frac{\alpha_0 g}{f} \, \frac{\partial \eta}{\partial x} \;=\; 0. \tag{9.39}$$

(The ageostrophic component of v is dropped from the $\alpha_0 v$ term for being on the order of α^2, whereas all other terms are on the order of α.) Note the analogy with equation (9.26) that governs the planetary waves: It is identical, except for the substitution of $\alpha_0 g/f$ for $-\beta_0 R^2$. Here,the deformation radius is defined as

$$R \;=\; \frac{\sqrt{gH_0}}{f} \,, \tag{9.40}$$

that is, the closest constant to the original definition (9.12). A wave solution of the type $\cos(k_x x + k_y y - \omega t)$ immediately provides the dispersion relation:

$$\omega \;=\; \frac{\alpha_0 g}{f} \, \frac{k_x}{1 \;+\; R^2 \; (k_x^2 \;+\; k_y^2)} \,, \tag{9.41}$$

the topographic analogue of (9.27). Again, we note that if the additional ingredient, here the bottom slope α_0, had not been present, the frequency would have been nil, and the flow would have been steady and geostrophic. Because they owe their existence to the bottom slope, these waves are called *topographic waves*.

The discussion of their direction of propagation, phase speed, and maximum possible frequency follows that of planetary waves. The phase speed in the x–direction — that is, along the isobaths — is given by

$$c_x \;=\; \frac{\omega}{k_x} \;=\; \frac{\alpha_0 g}{f} \, \frac{1}{1 \;+\; R^2 \; (k_x^2 \;+\; k_y^2)} \tag{9.42}$$

and has the sign of $\alpha_0 f$. Thus, topographic waves propagate in the Northern Hemisphere with the shallower side on their right. Because planetary waves propagate westward, *i.e.*, with the north to their right, the analogy between the two kinds of waves is "shallow–north" and "deep–south". (In the Southern Hemisphere, topographic waves propagate with the shallower side on their left, and the analogy is "shallow–south", "deep–north".)

The phase speed of topographic waves varies with the wavenumber; they are thus dispersive. The maximum possible wave speed along the isobaths is

$$c \;=\; \frac{\alpha_0 g}{f} \,, \tag{9.43}$$

which is the speed of the very long waves ($k_x^2 + k_y^2 \to 0$). With (9.41) cast in the form

$$\left(k_x \;-\; \frac{\alpha_0 g}{2 f \omega R^2}\right)^2 \;+\; k_y^2 \;=\; \left(\frac{\alpha_0^2 g^2}{4 f^2 R^4 \omega^2} \;-\; \frac{1}{R^2}\right), \tag{9.44}$$

we note that there exists a maximum frequency:

$$|\omega|_{\max} \;=\; \frac{|\alpha_0| g}{2|f| R} \,. \tag{9.45}$$

The implication is that a forcing at a frequency higher than the preceding threshold cannot generate topographic waves. The forcing then generates either a disturbance that is unable to propagate or higher-frequency waves, such as inertia-gravity waves. However, such a situation is rare because, unless the bottom slope is very weak, the maximum frequency given by (9.45) approaches or exceeds the inertial frequency f, and the theory fails before (9.45) can be applied.

As an example, let us take the West Florida Shelf, which is in the eastern Gulf of Mexico. There the ocean depth increases gradually offshore to 200 m over 200 km ($\alpha_0 = 10^{-3}$) and the latitude (27°N) yields $f = 6.6 \times 10^{-5}$ s^{-1}. Using an average depth H_0 = 100 m, we obtain R = 475 km and $\omega_{\max} = 1.6 \times 10^{-4}$ s^{-1}. This maximum frequency, corresponding to a minimum period of 11 min, is larger than f, violates the condition of subinertial motions and is thus meaningless. The wave theory, however, applies to waves whose frequencies are much less than the maximum value. For example, a wavelength of 150 km along the isobaths ($k_x = 4.2 \times 10^{-5}$ m^{-1}, k_y = 0) yields $\omega = 1.6 \times 10^{-5}$ s^{-1} (period of 4.6 days) and a wave speed of c_x = 0.38 m/s.

Where the topographic slope is confined between a coastal wall and a flat-bottom abyss, such as for a continental shelf, topographic waves can be trapped, not unlike the Kelvin wave. Mathematically, the solution is not periodic in the offshore, cross-isobath direction but assumes one of several possible profiles (eigenmodes). Each mode has a corresponding frequency (eigenvalue). Such waves are called *continental shelf waves*. The interested reader can find an exposition of these waves in LeBlond and Mysak (1978) and Gill (1978, pages 408–415).

9.6 Analogy between planetary and topographic waves

We have already discussed some of the mathematical similarities between the two kinds of low-frequency waves. The object of this section is to go to the root of the analogy and to compare the physical processes at work in both kinds of waves.

Let us turn to the quantity called potential vorticity and defined in (7.28). On the beta plane and over a sloping bottom (oriented meridionally for convenience), the expression of the potential vorticity becomes

$$q \;=\; \frac{f_0 \;+\; \beta_0 y \;+\; \partial v/\partial x \;-\; \partial u/\partial y}{H_0 \;+\; \alpha_0 y \;+\; \eta} \;. \tag{9.46}$$

Our assumptions of a small beta effect and a small Rossby number imply that the numerator is dominated by f_0, all other terms being comparatively very small. Likewise, H_0 is the leading term in the denominator because both bottom slope and surface displacements are weak. A Taylor expansion of the fraction yields

$$q \;=\; \frac{1}{H_0}\,\left(f_0 \;+\; \beta_0 y \;-\; \frac{\alpha_0 f_0}{H_0}\, y \;+\; \frac{\partial v}{\partial x} \;-\; \frac{\partial u}{\partial y} \;-\; \frac{f_0}{H_0}\,\eta \right). \tag{9.47}$$

In this form, it is immediately apparent that the planetary and topographic terms (β_0 and α_0 terms, respectively) play identical roles. The analogy between the coefficients β_0 and

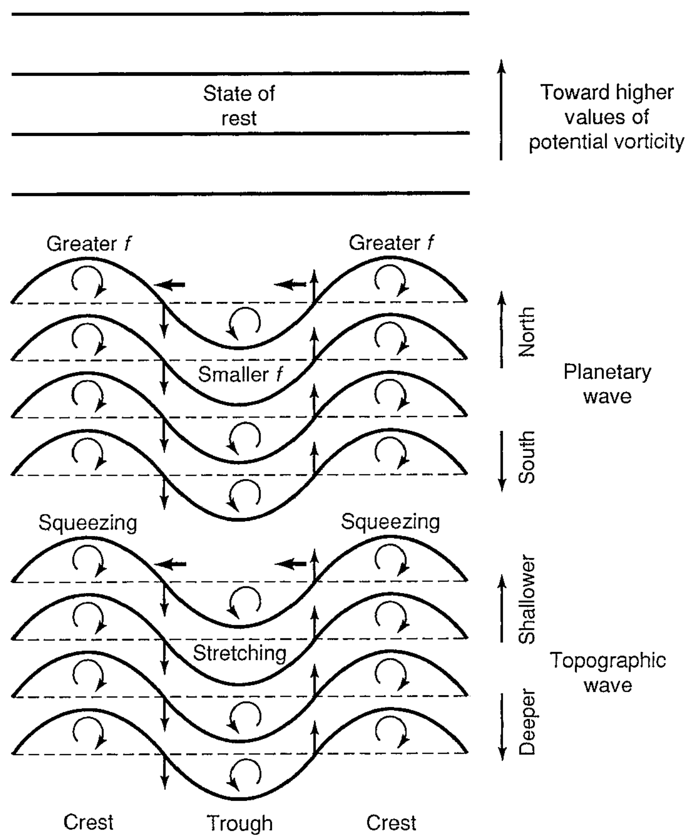

Figure 9-7 Comparison of the physical mechanisms that propel planetary and topographic waves. Displaced fluid parcels react to their new location by developing either clockwise or counterclockwise vorticity. Intermediate parcels are entrained by neighboring vortices, and the wave progresses forward.

$-\alpha_0 f_0/H_0$ is identical to the one noted earlier between $-\beta_0 R^2$ of (9.20) and $\alpha_0 g/f$ of (9.35), since now $R = (gH_0)^{1/2}/f_0$. The physical significance is the following: Just as the planetary effect imposes a potential-vorticity gradient, with higher values toward the north, so the topographic effect, too, imposes a potential-vorticity gradient, with higher values toward the shallower side.

The presence of an ambient gradient of potential vorticity is what provides the *bouncing* effect necessary to the existence of the waves. Indeed, consider Figure 9-7, where the first panel represents a north-hemispheric fluid (seen from the top) at rest in a potential-vorticity gradient, and think of the fluid as consisting of bands tagged by various potential-vorticity values. The next two panels show the same fluid bands after a wavy disturbance has been applied, in the presence of either the planetary or the topographic effect.

Under the planetary effect (middle panel), fluid parcels caught in crests have been displaced northward and have seen their ambient vorticity, $f_0 + \beta_0 y$, increase. To compensate and conserve their initial potential vorticity, they must develop some negative relative vorticity, that is, a clockwise spin. This is indicated by curved arrows. Similarly, fluid parcels in troughs have been displaced southward, and the decrease of their ambient vorticity is met with an increase of relative vorticity, that is, a counterclockwise spin. Focus now on those intermediate parcels that have not been displaced so far. They are sandwiched between two counterrotating vortex patches, and, like an unfortunate finger caught between two gears or the newspaper zipping through the rolling press, they are entrained by the swirling motions and begin to move in the meridional direction. From left to right on the figure, the displacements are southward from crest to trough and northward from trough to crest. Southward displacements set up new troughs whereas northward displacements generate new crests. The net effect is a westward drift of the pattern. This explains why planetary waves propagate westward.

In the third panel of Figure 9-7, the preceding exercise is repeated in the case of an ambient potential-vorticity gradient due to a topographic slope. In a crest, a fluid parcel is moved into a shallower environment. The vertical squeezing causes a widening of the parcel's horizontal cross-section (see Section 7.4), which in turn is accompanied by a decrease in relative vorticity. Similarly, parcels in troughs undergo vertical stretching, a lateral narrowing, and an increase in relative vorticity. From there on, the story is identical to that of planetary waves. The net effect is a propagation of the trough-crest pattern with the shallow side on the right.

The analogy between the planetary and topographic effects has been found to be extremely useful in the design of laboratory experiments. A sloping bottom in rotating tanks can substitute for the beta effect, which would otherwise be impossible to model experimentally. Caution must be exercised, however, for the substitution is acceptable so long as the analogy holds. Three conditions must be met: absence of stratification, gentle slope, and slow motion. If stratification is present, the sloping bottom affects preferentially the fluid motions near the bottom, whereas the true beta effect operates evenly at all levels. And, if the slope is not gentle and the motions are not weak, the expression of potential vorticity cannot be linearized as in (9.47), and the analogy is invalidated.

9.7 Arakawa's grids

The preceding developments had for aim to explain the basic physical mechanisms responsible for shallow-water wave propagation, by simplifying the governing equations down to their simplest, yet meaningful ingredients. Numerical models help us do better in cases where such simplifications are questionable or when it is necessary to calculate wave motions with more accuracy. For the sake of clarity, broadly applicable numerical techniques will be illustrated on simplified cases. The simplest situation arises with inertia-gravity waves, for which the core mechanisms are rotation and gravity (see Section 9.3). In a one-dimensional domain of uniform fluid depth H, the linearized governing equations are

$$\frac{\partial \eta}{\partial t} + H \frac{\partial u}{\partial x} = 0 \tag{9.48a}$$

$$\frac{\partial u}{\partial t} - fv = -g \frac{\partial \eta}{\partial x} \tag{9.48b}$$

$$\frac{\partial v}{\partial t} + fu = 0. \tag{9.48c}$$

A straightforward second-order central differentiation in space yields:

$$\frac{d\tilde{\eta}_i}{dt} + H \frac{\tilde{u}_{i+1} - \tilde{u}_{i-1}}{2\Delta x} = 0 \tag{9.49a}$$

$$\frac{d\tilde{u}_i}{dt} - f\tilde{v}_i = -g \frac{\tilde{\eta}_{i+1} - \tilde{\eta}_{i-1}}{2\Delta x} \tag{9.49b}$$

$$\frac{d\tilde{v}_i}{dt} + f\tilde{u}_i = 0. \tag{9.49c}$$

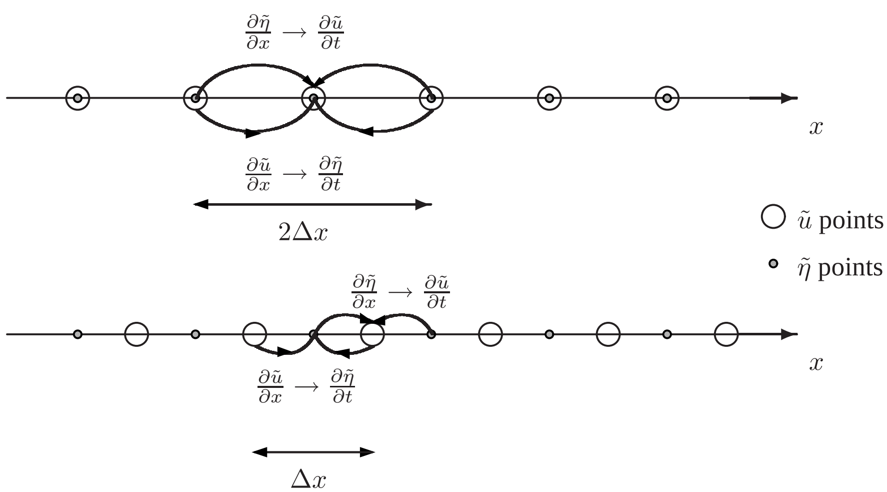

Figure 9-8 For variables $\tilde{\eta}$ and $\tilde{u}$ defined at the same grid points (upper panel), the discretization of inertia-gravity waves demands that approximations of spatial derivatives be made over distances $2\Delta x$, even if the underlying grid has a resolution of Δx. However, if variables $\tilde{\eta}$ and $\tilde{u}$ are defined on two different grids (lower panel), shifted one with respect to the other by $\Delta x/2$, the spatial derivatives can conveniently be discretized over the grid spacing Δx. The origin of each arrow indicates which variable influences the time evolution of the node where the arrow ends.

When analyzing this second-order method (upper part of Figure 9-8), we observe that the effective grid size is $2\Delta x$ in the sense that all derivatives are taken over this distance. This is somehow unsatisfactory because the real grid size, *i.e.*, the distance between adjacent grid nodes is only Δx. To improve the situation, we notice that the spatial derivatives of u are needed to calculate η, while the calculation of u requires the gradients of η. The most natural place to calculate a derivative of η is then at a point mid-way between two grid points of η, since the gradient approximation there is of second order while using a step of only Δx, and the most natural position to calculate the velocity u is therefore at mid-distance between η-grid nodes. Likewise, the most natural place to calculate the time evolution of η is at mid-distance between u nodes. It appears therefore that locating grid nodes for η and u in an interlaced fashion allows a second-order space differencing of *both* fields over a distance Δx (lower part of Figure 9-8). Formally, the discretization on such a *staggered grid* takes the form[1]:

$$\frac{d\tilde{\eta}_i}{dt} + H\,\frac{\tilde{u}_{i+1/2} - \tilde{u}_{i-1/2}}{\Delta x} = 0 \tag{9.50a}$$

$$\frac{d\tilde{u}_{i+1/2}}{dt} - f\tilde{v}_{i+1/2} = -\,g\,\frac{\tilde{\eta}_{i+1} - \tilde{\eta}_i}{\Delta x} \tag{9.50b}$$

$$\frac{d\tilde{v}_{i+1/2}}{dt} + f\tilde{u}_{i+1/2} = 0. \tag{9.50c}$$

Thus, spatial differencing can be performed over a distance Δx instead of $2\Delta x$, as it was done with the original, non-staggered grid arrangement. Since the scheme is centered in space, it is of second order, and its discretization error is reduced by a factor 4 without any additional calculation[2] when using a staggered grid instead of a more naive, collocated grid. This is a prime example of optimization of numerical methods at fixed cost.

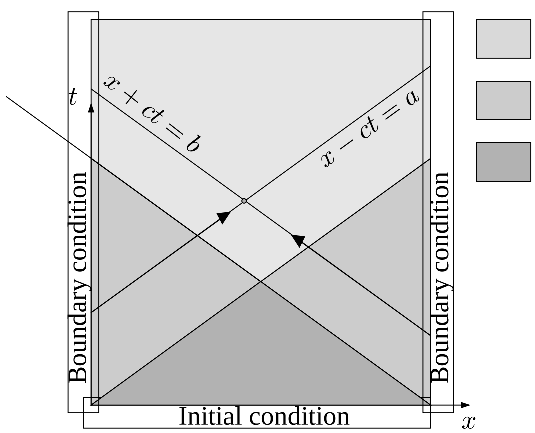

Figure 9-9 Characteristics $x + ct$ and $x - ct$ of wave equation (9.51). Information propagates along these lines from two initial conditions and one boundary condition on each side to set in a unique way the value of the solution at any point (x, t) of the domain.

But, as we will now show, the performance gain is not the sole advantage of the staggered-grid approach. In the case of a negligible Coriolis force ($f \to 0$), elimination of velocity from (9.48) leads to a single wave equation for η:

[1] We arbitrarily choose to place $\tilde{\eta}$ at integer grid indices and $\tilde{u}$ at half indices. We could have chosen the reverse.

[2] Both approaches use the same number of grid points to cover a given domain, and the both schemes demand the same number of operations.

$$\frac{\partial^2 \eta}{\partial t^2} \;=\; c^2\,\frac{\partial^2 \eta}{\partial x^2}, \tag{9.51}$$

where $c^2 = gH$. This equation is the archetype of a hyperbolic equation, which possesses a general solution of the form

$$\eta \;=\; E_1(x+ct) \;+\; E_2(x-ct)\;, \tag{9.52}$$

where the functions E_1 and E_2 are set by initial and boundary conditions. The general solution is therefore the combination of two signals, travelling in opposite directions at speeds $\pm c$ (Figure 9-9). The lines of constant $x+ct$ and $x-ct$ define the characteristics along which the solution is propagated. For $t = 0$, it is then readily seen that two initial conditions are needed, one for η and the other on its time derivative, *i.e.*, the velocity field, before one can determine the two functions E_1 and E_2 at the conclusion of the first step. Later on, when characteristics no longer originate from the initial conditions but have their root in the boundaries, the solution becomes influenced first by the most proximate boundary condition and ultimately by both. If the boundary is impermeable, the condition is $u = 0$, which can be translated into a zero-gradient condition on η. For discretization (9.50), the necessary numerical boundary conditions are consistent with the analytical conditions, whereas the non-staggered version (9.53) needs additional conditions to reach the near-boundary points. We have already learned (Section 4.7) how to deal with artificial conditions.

We now turn our attention to the remaining problem of the non-staggered grid, which is the appearance of spurious, stationary and decoupled modes within the domain. To illustrate the issue, we use a standard leapfrog time discretization with zero Coriolis force so that the non-staggered discretization becomes:

$$\frac{\tilde\eta_i^{n+1}-\tilde\eta_i^{n-1}}{2\Delta t} \;=\; -\,H\,\frac{\tilde u_{i+1}^{n}-\tilde u_{i-1}^{n}}{2\Delta x} \tag{9.53a}$$

$$\frac{\tilde u_i^{n+1}-\tilde u_i^{n-1}}{2\Delta t} \;=\; -\,g\,\frac{\tilde\eta_{i+1}^{n}-\tilde\eta_{i-1}^{n}}{2\Delta x}\;. \tag{9.53b}$$

For the grid-staggered version, we can also introduce a form of time-staggering by using a forward-backward approach in time:

$$\frac{\tilde\eta_i^{n+1}-\tilde\eta_i^{n}}{\Delta t} \;=\; -\,H\,\frac{\tilde u_{i+1/2}^{n}-\tilde u_{i-1/2}^{n}}{\Delta x} \tag{9.54a}$$

$$\frac{\tilde u_{i+1/2}^{n+1}-\tilde u_{i+1/2}^{n}}{\Delta t} \;=\; -\,g\,\frac{\tilde\eta_{i+1}^{n+1}-\tilde\eta_{i}^{n+1}}{\Delta x}\;. \tag{9.54b}$$

While it may first appear that we are dealing with an implicit scheme because of the presence of $\tilde\eta^{n+1}$ on the right of the second equation, it is noted that this quantity has just been calculated when marching the preceding equation one step forward in time. The scheme is thus explicit in the sense that we solve the first equation to get $\tilde\eta^{n+1}$ everywhere in the domain and then use immediately in the second equation to calculate $\tilde u^{n+1}$ without having to invert any matrix.

As for all forms of leap-frogging and staggering, we should be concerned by spurious modes. These can be sought here rather simply by eliminating the discrete field $\tilde{u}$ from each set of equations. This elimination can be performed by taking a finite time difference of the first equation and a finite space difference of the second equation[3]. This is the direct analogue of the mathematical differentiation used in eliminating the velocity between the two governing equations (9.48) to obtain (9.51). For the non-staggered and staggered grids we obtain respectively

$$\tilde{\eta}_i^{n+2} - 2\tilde{\eta}_i^n + \tilde{\eta}_i^{n-2} \;=\; \frac{c^2 \Delta t^2}{\Delta x^2}\;\left(\tilde{\eta}_{i+2}^n - 2\tilde{\eta}_i^n + \tilde{\eta}_{i-2}^n\right) \tag{9.55}$$

$$\tilde{\eta}_i^{n+1} - 2\tilde{\eta}_i^n + \tilde{\eta}_i^{n-1} \;=\; \frac{c^2 \Delta t^2}{\Delta x^2}\;\left(\tilde{\eta}_{i+1}^n - 2\tilde{\eta}_i^n + \tilde{\eta}_{i-1}^n\right). \tag{9.56}$$

These equations are straightforward second-order discretizations of the wave equation (9.51), the first one with spatial and temporal steps twice as large as for the second one. The CFL criterion is $|c|\Delta t/\Delta x \;\leq\; 1$ in each case, since the propagation speeds of the hyperbolic equation are $\pm c$ and the corresponding characteristics must lie in the numerical domain of dependence.

The discretization (9.55) shows that the non-staggered grid is prone to decoupled modes. Indeed, for even values of n and i, all grid indexes involved are even, and the evolution is completely independent of that on points with odd values of n or i, which are nonetheless proximate in both time and space. In fact, there are four different solutions evolving independently, with their only link being through the initial and boundary conditions (left panel of Figure 9-10). Although theoretically acceptable, such decoupled modes typically increase their "distance" from one another in the course of the simulation and induce undesirable space-time oscillations in the solution. In some occasions this can lead to stationary solutions that are simply unphysical (Figure 9-10), such as a solution with zero velocity and $\tilde{\eta}$ alternating in space between two different constants. Solutions of this type are clearly spurious. In contrast, the only stationary solution produced by the staggered equation (9.56) is the physical one. This is a desirable property.

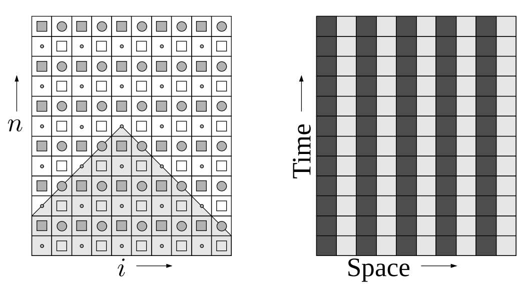

Figure 9-10 Four different solutions, each identified by a different symbol, evolve independently on the non-staggered grid. The numerical domain of dependence is shown as the shaded region (left panel). A spurious stationary mode alternating between two constants (right panel) is incompatible with the original governing equations.

More generally, the spurious stationary solutions of a space discretization can be analyzed in terms of the state-variable vector $\mathbf{x}$, space-discretization operator $\mathbf{D}$, and the semi-discrete equation

[3]For the non-staggered version we make the following formal elimination: Δx [(9.53a)$^{n+1}$ - (9.53a)$^{n-1}$] - $\Delta t H$[(9.53b)$_{i+1}$ - (9.53b)$_{i-1}$]

$$\frac{d\mathbf{x}}{dt} + \mathbf{D}\,\mathbf{x} = 0 \qquad (9.57)$$

so that spurious stationary modes can be found among the non-zero solutions of

$$\mathbf{D}\,\mathbf{x} = 0. \qquad (9.58)$$

In the jargon of matrix calculation (linear algebra), spurious modes lie within the *null-space* of matrix $\mathbf{D}$. In the case of the wave equation, the solution depicted in Figure 9-10 is certainly not a physically valid solution but satisfies (9.58).

All non-zero stationary solutions (members of the null-space), however, do not need to be spurious, and a physically admissible non-zero stationary solution is possible in the presence of Coriolis term, namely the geostrophic equilibrium. In that case, the discretized geostrophic equilibrium solution is also part of the null-space (9.58). It is therefore worthwhile sometimes to analyze the null-space of discretization operators for which the corresponding physical stationary solutions are known.

Having found that staggering has advantages in one-dimension, we can now explore the situation in two dimensions but immediately realize that there is no single way to generalize the approach. Indeed, we have three state variables, u, v and η, which can each be calculated on a different grid. The collocated version, the so-called A–grid model, is readily defined, and discretization[4] of equations (9.4a) through (9.5) with uniform fluid thickness leads to:

$$\frac{d\tilde{\eta}}{dt} = -H\,\frac{\tilde{u}_{i+1}-\tilde{u}_{i-1}}{2\Delta x} - H\,\frac{\tilde{v}_{j+1}-\tilde{v}_{j-1}}{2\Delta y} \qquad (9.59a)$$

$$\frac{d\tilde{u}}{dt} = +f\tilde{v} - g\,\frac{\tilde{\eta}_{i+1}-\tilde{\eta}_{i-1}}{2\Delta x} \qquad (9.59b)$$

$$\frac{d\tilde{v}}{dt} = -f\tilde{u} - g\,\frac{\tilde{\eta}_{j+1}-\tilde{\eta}_{j-1}}{2\Delta y}. \qquad (9.59c)$$

Clearly, a spurious stationnary solution exists, again with zero velocity ($\tilde{u} = \tilde{v} = 0$) and $\tilde{\eta}$ alternating between two constants on the spatial grid (Figure 9-11).

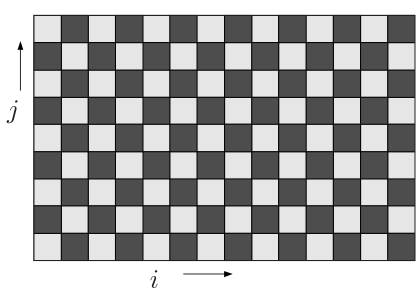

Figure 9-11 A spurious stationary $\tilde{\eta}$ mode alternating between two constants (depicted by two different gray levels) on the A–grid. This mode is called for obvious reasons the *checkerboard mode*.

Starting from the unstaggered grid we can move the variables with respect to the others in different ways and create various staggered grids. These are named Arakawa's grids in

[4]As before, we only write indices that differ from i and j.

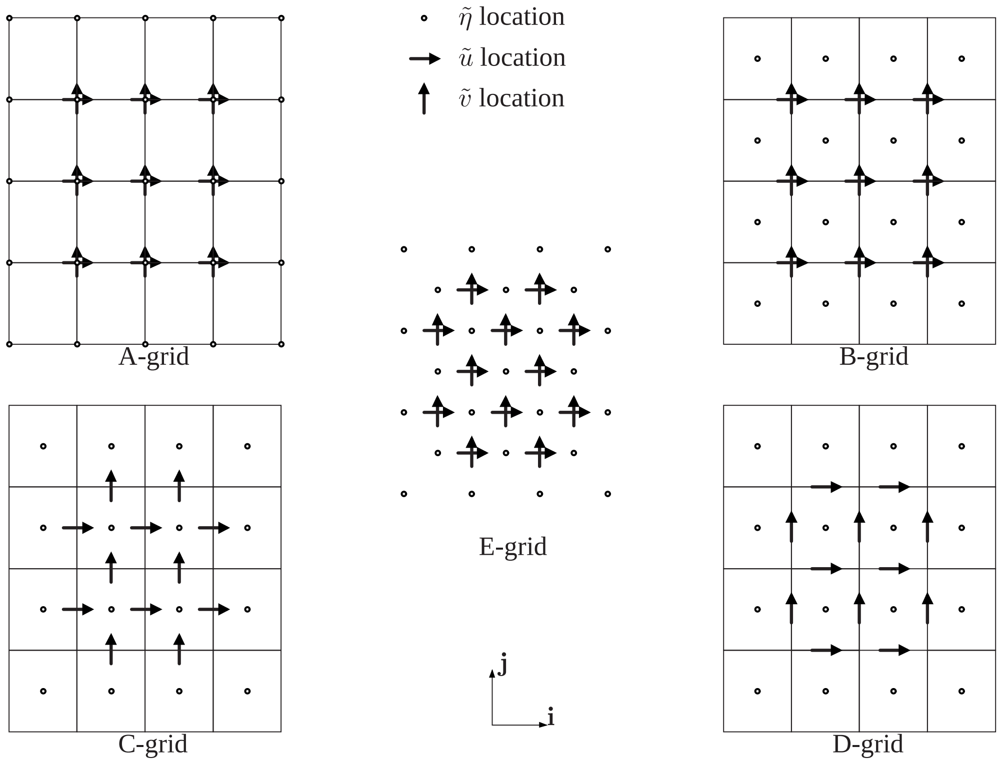

Figure 9-12 The five Arakawa grids. On the A–grid, the variables $\tilde{\eta}$, $\tilde{u}$ and $\tilde{v}$ are collacated, but staggered on other grids, called B–, C–, D– and E–grids. Note that the E–grid (center) has a higher grid point density than the other grids for the same distance between adjacent nodes.

honor of Akio Arakawa[5], and bear the letters A, B, C, D and E depending on where the state variables are located across the mesh (Figure 9-12). For the linear system of equations considered here, it can be shown (*e.g.*, Mesinger and Arakawa, 1976) that the E–Grid a rotated B–grid, so that we do not need to analyze it further.

A two-dimensional staggered grid we already encountered is the so-called C–grid (bottom left of Figure 9-12). For advection [recall Equation (6.58)] and the rigid-lid pressure formulation [recall Equation (7.41)], we tacitly assumed that the velocity u was being calculated halfway between pressure nodes $(i+1, j)$ and (i, j) and v halfway between nodes (i, j) and $(i, j+1)$. In the present wave problem, this approach yields a straightforward and second-order discretization of both divergence term and pressure gradients

$$\left(\frac{\partial u}{\partial x} + \frac{\partial v}{\partial y}\right)_{i,j} \simeq \frac{\tilde{u}_{i+1/2} - \tilde{u}_{i-1/2}}{\Delta x} + \frac{\tilde{v}_{j+1/2} - \tilde{v}_{j-1/2}}{\Delta y} \tag{9.60}$$

5 See biography at the end of this Chapter.

$$\left.\frac{\partial \tilde{\eta}}{\partial x}\right|_{i+1/2,j} \simeq \frac{\tilde{\eta}_{i+1} - \tilde{\eta}}{\Delta x} + \mathcal{O}(\Delta x^2) \tag{9.61a}$$

$$\left.\frac{\partial \tilde{\eta}}{\partial y}\right|_{i,j+1/2} \simeq \frac{\tilde{\eta}_{j+1} - \tilde{\eta}}{\Delta y} + \mathcal{O}(\Delta y^2). \tag{9.61b}$$

exactly as in the advection and surface pressure problems (Figure 9-13). But if we proceed with the discretization of the Coriolis term, a problem arises for the C–grid, because the velocity components are not defined at the same points. The integration of the du/dt equation at the u grid node $(i + 1/2, j)$ requires knowledge of the velocity v, which is only available at node $(i, j \pm 1/2)$. Therefore, an interpolation is necessary. The simplest scheme takes an average of surrounding values:

$$v|_{i+1/2,j} \simeq \frac{\tilde{v}_{j+1/2} + \tilde{v}_{i+1,j+1/2} + \tilde{v}_{j-1/2} + \tilde{v}_{i+1,j-1/2}}{4}\,, \tag{9.62}$$

where the right-hand side can now be calculated from the available values of $\tilde{v}$. Similar averaging to estimate variables at locations where they are not defined can be used to discretize the equations on the other staggered grids. For example, the B–grid is a grid where η is defined on integer grid indices whereas velocity components are defined at corner points $(i \pm 1/2, j \pm 1/2)$. For this grid, the Coriolis term does not require any averaging, since both velocity components are collocated, but the grid arrangement requires the derivative of η in the x–direction at location $(i+1/2, j+1/2)$. We approximate such a term by the appropriate average

$$\left.\frac{\partial \eta}{\partial x}\right|_{i+1/2,j+1/2} \simeq \frac{\frac{\tilde{\eta}_{i+1,j+1}+\tilde{\eta}_{i+1}}{2} - \frac{\tilde{\eta}_{j+1}+\tilde{\eta}}{2}}{\Delta x}\,, \tag{9.63}$$

and similarly for $\partial u/\partial x$, which is needed at (i, j). The full spatial discretization on each grid can be achieved in similar manner, and the derivation is left as an exercice (Numerical Exercise 9-2).

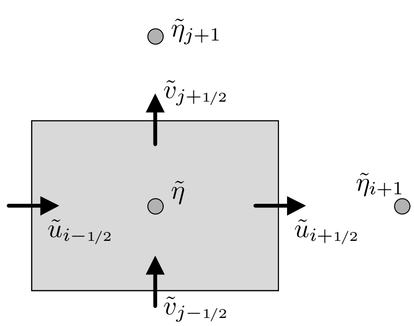

Figure 9-13 Discretization on the C–grid. The divergence operator is discretized most naturally by (9.60) while pressure gradients are calculated with (9.61).

We can then analyze the wave-propagation properties on the different grids by a Fourier analysis, for which we take

$$\begin{pmatrix} \tilde{\eta} \\ \tilde{u} \\ \tilde{v} \end{pmatrix} = \Re \begin{pmatrix} A \\ U \\ V \end{pmatrix} e^{\mathrm{i}\,(ik_x\Delta x + jk_y\Delta y - \tilde{\omega}t)}. \tag{9.64}$$

The insertion of this type of solution in the various finite-difference schemes and then simplification by the common exponential factor provides the following equations

$$-\,\mathrm{i}\,\tilde{\omega}U \;-\; f\alpha V \;=\; -\,\mathrm{i}\,g\alpha_x k_x A \tag{9.65a}$$

$$-\,\mathrm{i}\,\tilde{\omega}V \;+\; f\alpha U \;=\; -\,\mathrm{i}\,g\alpha_y k_y A \tag{9.65b}$$

$$-\,\mathrm{i}\,\tilde{\omega}A \;+\; H\left(\mathrm{i}\,\alpha_x k_x U \;+\; \mathrm{i}\,\alpha_y k_y V\right) \;=\; 0, \tag{9.65c}$$

where the coefficients α, α_x and α_y vary with the type of grid and are given in Table 9.1.

As for the physical solution, a non-zero solution is only possible when the determinant of the system vanishes, and this provides the dispersion relation of the discretized wave physics:

$$\tilde{\omega}\left[\tilde{\omega}^2 - \alpha^2 f^2 - gH\left(\alpha_x^2 k_x^2 + \alpha_y^2 k_y^2\right)\right] \;=\; 0, \tag{9.66}$$

which is the discrete analogue of (9.16).

For small wavenumber values ($k_x\Delta x \ll 1$ and $k_y\Delta y \ll 1$), *i.e.*, long, well resolved waves, we recover the physical dispersion relation because α, α_x and α_y all tend towards unity. For shorter waves, the numerical dispersion relation can be analyzed in detail through the error estimate

$$\frac{\omega^2 - \tilde{\omega}^2}{\omega^2} \;=\; \frac{(1-\alpha^2) + R^2\left[(1-\alpha_x^2)k_x^2 + (1-\alpha_y^2)k_y^2\right]}{1 + R^2\left(k_x^2 + k_y^2\right)} \;\geq\; 0. \tag{9.67}$$

Except for the simple statement $\tilde{\omega}^2 \leq \omega^2$, the analysis of the error is rather complex because it involves five length scales[6] R, $1/k_x$, $1/k_y$, Δx and Δy. For simplicity we take $\Delta x \sim \Delta y$ and $k_x \sim k_y$ to reduce the problem. We then define the length scale $L \sim 1/k_x \sim 1/k_y$ of the wave under consideration. In this case $\alpha_x \sim \alpha_y$, and we can distinguish two situations:

$$\text{Shorter waves :} \qquad L \;\lesssim\; R, \quad \omega^2 \;\sim\; \frac{gH}{L^2} \tag{9.68}$$

$$\text{Longer waves :} \qquad L \;\gtrsim\; R, \quad \omega^2 \;\sim\; f^2. \tag{9.69}$$

The shorter waves are dominated by gravity and the relative error on ω^2 behaves as

$$\frac{\omega^2 - \tilde{\omega}^2}{gH/L^2} \sim 2(1-\alpha_x^2). \tag{9.70}$$

If the wave is well resolved, $\Delta x \ll L$ and the error tends towards zero for all four grids because $\alpha_x \to 1$. For the barely resolved waves, *i.e.*, $\Delta x \sim L$, the errors are largest for the discretizations in which α_x and α_y depart most strongly from unity. In this sense the A–, B– and D–grids have larger errors than the C–grid (see Table 9.1).

[6] Note how the discretization has added two length scales Δx and Δy to the discussion compared to the physical dispersion relation.

Table 9.1 DEFINITION OF THE PARAMETERS INVOLVED IN THE DISCRETE DISPERSION RELATION FOR A, B, C AND D GRIDS WITH $2\theta_x = k_x\Delta x$ AND $2\theta_y = k_y\Delta y$. FOR LONG WAVES, WE CAN VERIFY THAT α, α_x AND α_y ALL TEND TOWARDS UNITY, SO THAT THE METHOD IS CONSISTENT.

Grid	α	$\alpha_x k_x \Delta x$	$\alpha_y k_y \Delta y$
A	1	$\sin 2\theta_x$	$\sin 2\theta_y$
B	1	$2\sin\theta_x \cos\theta_y$	$2\sin\theta_y \cos\theta_x$
C	$\cos\theta_x \cos\theta_y$	$2\sin\theta_x$	$2\sin\theta_y$
D	$\cos\theta_x \cos\theta_y$	$2\cos\theta_x \cos\theta_y \sin\theta_x$	$2\cos\theta_x \cos\theta_y \sin\theta_y$

The longer waves are dominated by rotation, and the relative error on ω^2 behaves as

$$\frac{\omega^2 - \tilde{\omega}^2}{f^2} \sim (1 - \alpha^2). \tag{9.71}$$

Again, α should remain close to unity for all wavenumbers, so that the B–grid outperforms both the C– and D–grids. For details on the errors, an exploration with `abcdgrid.m` in parameter space provides relative errors fields as those depicted in Figure 9-14 for various resolution levels $R/\Delta x$, *etc.* Errors can be further investigated through the analysis of the group velocity behavior (Numerical Exercice 9-5) and in the context of generalized dynamics, including planetary waves, with a clear distinction between zonal and meridional wave behaviors (Dukowicz, 1995; Haidvogel and Beckmann, 1999).

Because the A–grid suffers from spurious modes, and the D–grid is always penalized in terms of accuracy, the B– and C–grids are the most interesting ones among the four types. Since wavelengths up to $\Delta x \sim L$ are to be resolved in a significant way, the C–grid is the better choice as long as $\Delta x \ll R$, whereas for $R \ll \Delta x$ the B–grid should be preferred on the ground that the error in (9.70) and (9.71) is less. This confirms more detailed error analyses of the semi-discrete equations on staggered grids (*e.g.*, Mesinger and Arakawa, 1976; Haidvogel and Beckman, 1999), although additional time discretization or boundary-condition implementation can introduce stability problems (*e.g.*, Beckers and Deleersnijder, 1993; Beckers, 1999). Also, time discretization further complicates the error analysis and may sometimes inverse the error behavior (Beckers, 2002). Nevertheless, the choice of the B–grid for larger grid spacing and the C–grid for finer grid spacing is justified by the fact that for large grid spacing we only capture large-scale movements, which are nearly geostrophic. Since the Coriolis force is dominant in this case, its discretization is crucial. Because the B–grid does not require a spatial average of the velocity components, contrary to the C–grid, its use should be advantageous. The pressure gradient, which is the other dominant force, could arguably be better represented on the C–grid. If the grid is very fine, averaging the large-scale geostrophic equilibrium over four closely spaced nodes does not deteriorate the geostrophic solution, whereas smaller-scale processes such as gravity waves and advection are better captured by the C–grid.

From the preceding interpretation we can establish some general rules for staggering the variables. Starting with the goal of placing variables on the grid so that dominant processes are discretized in the best possible way, we can then afford to represent secondary processes by more crude discrete operators without affecting overall model accuracy. In practice, however, dominant processes may change in time and space so that no single approach can be

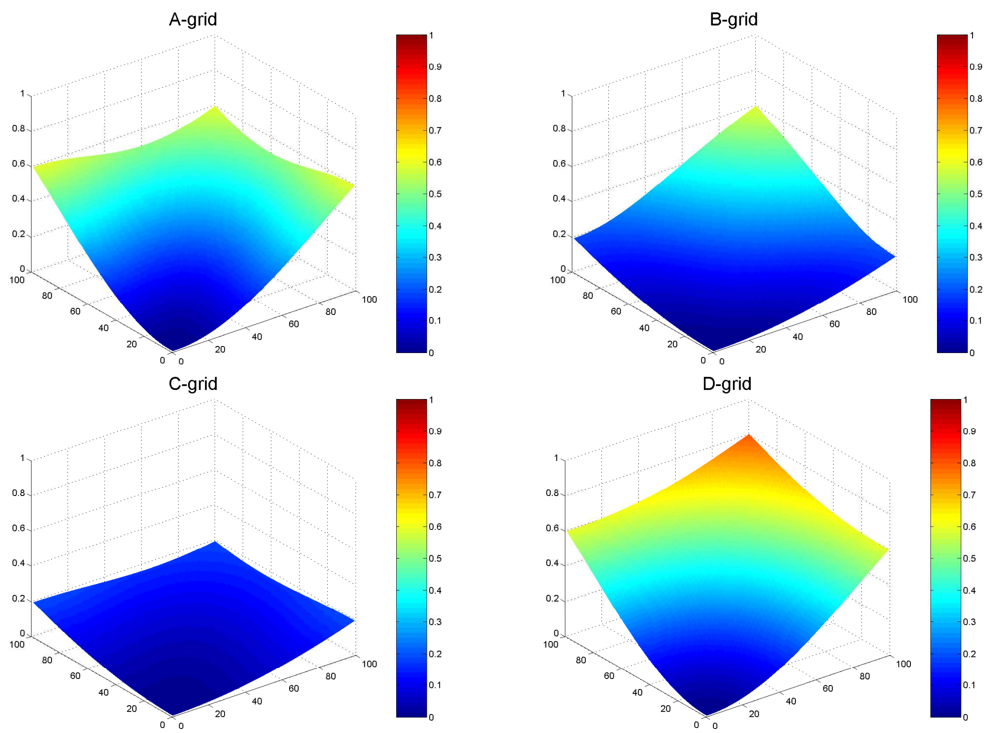

Figure 9-14 For medium resolution compared to the deformation radius ($R/\Delta x = R/\Delta y = 1$), the error (9.67) is depicted as a function of $k_x \Delta x$ and $k_y \Delta y$. Waves with wavenumber higher than $k_x \Delta x = \pi/2$ are not shown, and the x– and y–axes are therefore percents of $\pi/2$. The D–grid clearly exhibits the worst behavior. The B–grid keeps the error low for well resolved waves, while the C–grid creates lower errors for shorter waves.

guaranteed to work uniformly, but it should at least be tried. For example, if tracer advection is of primary interest, the C–grid can be generalized to three-dimensions with vertical velocities defined at the bottom and top of each grid cell. In that case, advection fluxes are readily calculated using one of the advection schemes presented in Section 6.6 without need for velocity interpolations. Similarly, if diffusion in a heterogeneous turbulent environment is the main process at play, the definition of diffusion coefficients between tracer nodes would allow the direct discretization of turbulent fluxes without the need of averaging the diffusion coefficients.

9.8 Numerical simulation of tides and storm surges

The two-dimensional momentum equations (7.12a) and (7.12b) and volume conservation (7.17) describing shallow-water dynamics are the central equations from which storm-surge models of vertically mixed coastal seas have been developed. The prediction of rising sea level (surge) along a coast depends on remotely generated waves that propagate from the stormy area toward the shore. Because shallow-water equations describe well the propagation of such waves, their prediction is indeed feasible, although a few additional processes must be taken into account. Among these other processes are the surface wind stress, through which waves are generated, and bottom friction, which causes attenuation during travel. To include these last two stresses, we can start from the observation that the shallow-water equations used up to now assume that the flow is independent of the vertical coordinate. If this is not the case, we can at least try to predict the evolution of the depth-averaged velocity,

$$\bar{u} = \frac{1}{h}\int_b^{b+h} u\, dz \qquad \bar{v} = \frac{1}{h}\int_b^{b+h} v\, dz \tag{9.72}$$

where $z = b$ is the bottom level and h the total depth. We can derive a governing equation for $\bar{u}$ by integrating vertically the three-dimensional governing equations including the x–momentum equation:

$$\frac{\partial u}{\partial t} \;=\; \frac{\partial}{\partial z}\left(\nu_E \frac{\partial u}{\partial z}\right) \;+\; F(u), \tag{9.73}$$

where the term $F(u)$ gathers all terms other than the time derivative and vertical diffusion. We can then integrate vertically to obtain

$$\frac{1}{h}\int_b^{b+h} \frac{\partial u}{\partial t}\, dz \;=\; \frac{\tau^x}{\rho_0 h} \;-\; \frac{\tau_b^x}{\rho_0 h} \;+\; \overline{F(u)}, \tag{9.74}$$

where boundary conditions similar to (4.34) have been used for the surface wind stress τ and bottom stress τ_b, respectively. Physically, these stresses appear here as body forces applied to the layer h of fluid moving as a slab with the depth-averaged velocity (Figure 9-15).

Two difficulties arise, however, during the integration. The first is that the elevation of the surface is time dependent and does not allow a simple permutation of the integration with the time derivative in the left-hand side of (9.74). The second and more fundamental difficulty is due to the nonlinearities of the equations, which prevent us from equating the average of $F(u)$ with $F(\bar{u})$, *i.e.*,

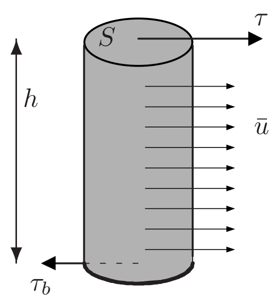

Figure 9-15 For a fluid column of volume hS and moving with the average velocity $\bar{u}$, Newton's second law in the absence of lateral friction and pressure force implicates the forces associated with the surface stress τ and bottom friction: $\rho_0 hS\; d\bar{u}/dt = (\tau - \tau_b)S$.

$$\overline{F(u)} \neq F(\bar{u}) \tag{9.75}$$

so that we cannot express the right-hand side of (9.74) as a function of only the average velocity. The integrated equation then requires some form of parameterization. Hence, shallow-water models include additional parameterization of the horizontal-diffusion type.

For simplicity, the governing equations are written as if depth averaging had not taken place and the overbar ($^-$) operator is ignored. The outcome is that it is sufficient to add the $\tau/(\rho_0 h)$ and $-\tau_b/(\rho_0 h)$ terms to the right-hand side of the two-dimensional momentum equations (7.12a) and (7.12b), and then to include a parameterization of the nonlinear effects. The wind-stress τ appears as an externally imposed source term in the equations while the bottom stress is depending on the flow itself, *i.e.*, $\tau_b = \tau_b(u, v)$. A difficulty arises here because the bottom stress depends on the velocity profile near the bottom whereas the governing equations provide only the vertical average of the velocity. A parameterization is needed here, too. The simplest version is linear bottom friction, in which the frictional term is made linear in, and opposite to, velocity:

$$\tau_b^x \;=\; -\, r\rho_0\, u, \qquad \tau_b^y \;=\; -\, r\rho_0\, v, \tag{9.76}$$

where r is a coefficient with dimensions of velocity (LT^{-1}). The linear formulation is particularly advantageous in analytical studies or with spectral methods. They fail, however, to take into account the turbulent nature of the bottom boundary layer, with stress better expressed as a quadratic function of velocity (see Chapter 14):

$$\tau_b^x \;=\; -\, \rho_0 C_d \sqrt{u^2+v^2}\, u, \qquad \tau_b^y \;=\; -\, \rho_0 C_d \sqrt{u^2+v^2}\, v, \tag{9.77}$$

with a *drag coefficient* C_d either constant or depending on the flow itself.

Finally, the direct driving force associated with a moving disturbance of the atmospheric pressure $p_{atm}(x, y, t)$ can be easily taken into account by including it in the pressure boundary condition at the surface (4.32), $p = \rho_0 g\eta + p_{atm}$.

We can now estimate the wind-induced surge in a shallow sea by considering how the storm piles up water near the coast (Figure 9-16). This accumulation of water creates a surface elevation (surge) and, consequently, an adverse pressure gradient. Eventually, this adverse pressure gradient can grow strong enough to cancel the wind stress. When this balance is reached, the sea-surface slope caused by the wind stress is governed by

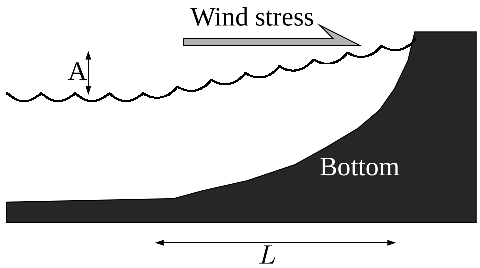

Figure 9-16 The piling up of water by a storm near a coast creates an adverse pressure-gradient force, and an equilibrium can exist if it cancels the wind-stress force.

$$\frac{\partial \eta}{\partial x} \simeq \frac{\tau}{\rho_0 g h} \, . \tag{9.78}$$

This relation provides an estimate of the storm-surge amplitude A as a function of the distance L over which the wind blows:

$$A \simeq \frac{L\tau}{\rho_0 g h} \, . \tag{9.79}$$

Note that the shallower the water, the stronger the effect. In other words, storm surges intensify near the coast where the water is shallower.

Storm surges can become dramatic when superimposed to the tide, and it is therefore important to know how to calculate tidal elevations, too. Tides are forced gravity waves caused by the gravitational attraction of the moon and sun. The following development is also valid for the atmosphere, but the velocities associated with atmospheric tides are much smaller than the wind speed due to atmospheric disturbances. Tides, therefore, are generally negligible in the atmosphere, while tidal currents in the ocean can be an order of magnitude larger than other currents.

To quantify the net effect of the gravitational acceleration of the moon and sun, we have to realize that the whole system is moving. Therefore Newton's law cannot simply be written with respect to axes fixed at the earth center as we did in Chapter 2. Instead, using Newton's law in absolute axes **I**, **J** and **K** of the solar system, we can calculate the absolute acceleration $\mathbf{A}$ of the fluid parcel and of the earth $\mathbf{A}_e$ under the moon's attraction[7]:

$$\rho \mathbf{A} = \rho \boldsymbol{\gamma} + \rho \mathbf{f} \tag{9.80}$$

$$M_e \mathbf{A}_e = M_e \boldsymbol{\gamma}_e . \tag{9.81}$$

We regrouped under the force $\rho\mathbf{f}$ all forces acting on the fluid parcel other than the moon's attraction. The gravitationnal forces $\rho\boldsymbol{\gamma}$ and $M_e\boldsymbol{\gamma}_e$ involve the gravitationnal constant $G = 6.67\times 10^{-11}$ N m^2/kg^2, the earth's mass $M_e = 5.9736\times 10^{24}$ kg, the moon's mass $M_m = 7.349\times 10^{22}$ kg, the distance $D_m \sim 385000$ km between earth and moon, and the actual distance d_m of the point under consideration to the center of the moon (Figure 9-17). The two gravitational accelerations are directed towards the center of the moon and of magnitude

[7] The sun's influence can be studied in an analoguous way.

$$\gamma = \frac{GM_m}{d_m^2}, \qquad \gamma_e = \frac{GM_m}{D_m^2}. \tag{9.82}$$

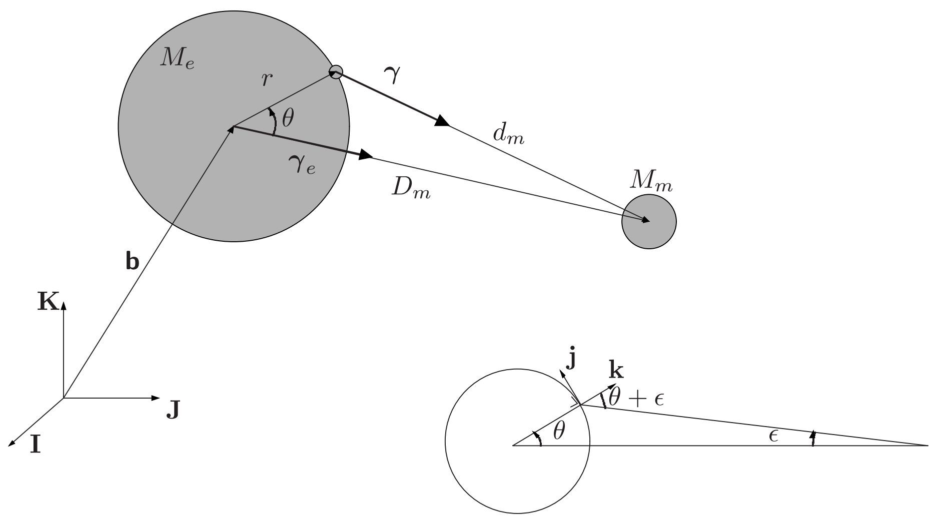

Figure 9-17 A planet acts simultaneously on a fluid parcel lying on the earth's surface as well as on the entire earth. The tidal force results from the respective positions of the celestial bodies and the local gravitational attraction on earth.

We are not so much interested in the movement of earth *per se* and since the absolute acceleration of the fluid parcel is the acceleration of earth plus the relative acceleration of the fluid parcel with respect to earth, $\mathbf{A} = \mathbf{A}_e + d^2\mathbf{r}/dt^2$, the elimination of the earth's acceleration leads to

$$\frac{d^2\mathbf{r}}{dt^2} = \mathbf{f} + (\boldsymbol{\gamma} - \boldsymbol{\gamma}_\mathbf{e}). \tag{9.83}$$

Without the astronomical force, the equation would have been $d^2\mathbf{r}/dt^2 = \mathbf{f}$, and so we note that its effect is the addition of a so-called *tidal force*:

$$\rho\mathbf{f}_t = \rho(\boldsymbol{\gamma} - \boldsymbol{\gamma}_\mathbf{e}). \tag{9.84}$$

We notice that this force is the difference between almost identical forces. Its components in the local coordinate system are, first on its vertical **k**:

$$f_\uparrow = \gamma\cos(\theta+\epsilon) - \gamma_e\cos\theta. \tag{9.85}$$

The expression can be simplified because the angle ϵ is extremely small. By expanding $\cos(\theta+\epsilon)$ and using

$$\cos\epsilon \simeq 1, \qquad D_m\sin\epsilon \simeq r\sin\theta, \tag{9.86}$$

we obtain

$$f_\uparrow \;=\; \frac{GM_m}{D_m^2}\left[\left(\frac{D_m^2}{d_m^2}-1\right)\cos\theta \;-\; \frac{D_m^2}{d_m^2}\,\frac{r\sin\theta}{D_m}\sin\theta\right]. \tag{9.87}$$

The use of d_m in the formulation of the tidal forcing is not very practical (can you tell at any moment the precise distance of your position with respect to the moon?). So, we use the identity $r\cos\theta + d_m\cos\epsilon = D_m$ and the smallness of ϵ to obtain

$$d_m \;\simeq\; D_m\left(1-\frac{r}{D_m}\cos\theta\right). \tag{9.88}$$

For the same reason that ϵ is small, the ratio r/D_m is also considered small[8], and we drop higher-order terms in r/D_m:

$$\frac{D_m^2}{d_m^2} \;\simeq\; 1+2\frac{r}{D_m}\cos\theta, \tag{9.89}$$

so that the vertical component of the tidal force finally is

$$f_\uparrow \;\simeq\; \frac{GM_m}{D_m^3}\, r\,(3\cos^2\theta - 1). \tag{9.90}$$

To compare its magnitude to $g = GM_e/r^2 = 9.8$ m/s^2, the gravitational acceleration of the earth on its surface, we form the ratio $\delta = f_\uparrow/g$ and find it to be on the order of

$$\delta \;\sim\; \frac{r^3 M_m}{D_m^3 M_e} \;\sim\; \mathcal{O}(10^{-7}). \tag{9.91}$$

It appears therefore that the tidal force associated with the moon is completely negligible, not only compared to gravity g but also to any of the typical forces acting along the vertical. So does it mean tidal forces are not responsible for the observed tides? Of course they are, but not through the local vertical attraction as sometimes erroneously thought, but through the horizontal component, which we now proceed to calculate.

The component of the tidal force along the local axis $\mathbf{j}$ is, after several simplifications similar to those used above,

$$f_\leftarrow \;\simeq\; -\frac{GM_m}{D_m^3}\,3r\;\cos\theta\sin\theta. \tag{9.92}$$

The order of magnitude of this force component is the same as that of the vertical one, but since all horizontal forces are much smaller than gravity, the horizontal tidal force is *not* negligible and acts to make the fluid converge or diverge. This is the essential mechanism of tides (Figure 9-18). The spatial distribution of this force along the earth's surface is such that it tends to create a bulge in the region of the earth facing the moon and a second bulge at the diametrically *opposite* place. The explanation is that, for a point closer to the moon than D_m, the gravitational pull of the moon exceeds the centrifugal force associated with the earth-moon co-rotation, while on the opposite side of the earth the inverse is true; the centrifugal force of the earth-moon co-rotation exceeds the gravitational pull of the moon.

[8] In the case of the earth-moon system, its value is about 6400/385000 $\sim$ 0.017.

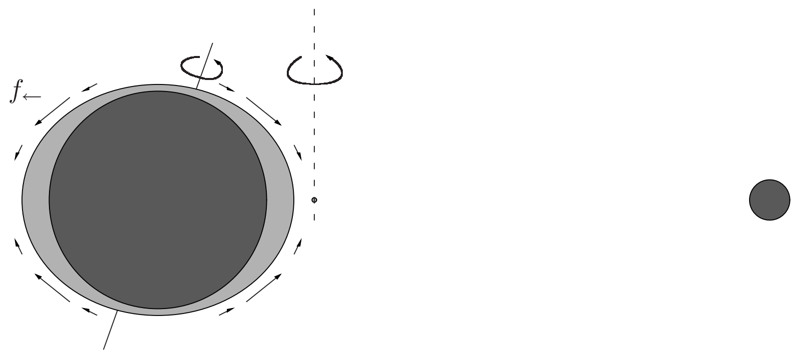

Figure 9-18 The movement of earth and moon around their common center of mass creates a centrifugal force that is weaker than the moon's gravitational attraction for points on earth facing the moon. The resulting horizontal tidal force $f_{\leftarrow}$ has a tendency to create a bulge toward the moon. On the earth's face opposite to the moon, the centrifugal force is larger than the moon's gravitational attraction, and the horizontal force creates a second bulge facing away from the moon. Since the earth rotates around its own South–North axis, the two bulges move with respect to the continents.

The angle θ involved in our formula is constantly changing in time because of the terrestrial rotation and lunar motion, and it must be determined through astronomical calculations (*e.g.*, Doodson, 1921). These calculations also take into account variations in the earth-moon distance D_m, which induce slow modulations of the tidal force. Trigonometric calculations reveal different periods of motion, the most noticeable one being due to the co-rotation of the earth and moon, giving rise to an apparent rotation of the moon over a given point on the earth every 24 h and 50 minutes (24 hours of terrestrial rotation plus the delay due to the fact that the moon rotates around the sun in the same direction). But, because there are two bulges half an earth's circumference apart from each other (mathematically because of the product $\cos\theta\sin\theta$ in (9.92)), the apparent period of the main lunar tide is only half of that, *i.e.*, 12 h 25 minutes.

For practical purposes, it is worth noting that the tidal force derives from the so-called *tidal potential* (see Analytical Problem 9-8). In the local Cartesian coordinate system, the tidal force can be expressed:

$$\mathbf{f}_t = -\left(\frac{\partial V}{\partial x}, \frac{\partial V}{\partial y}, \frac{\partial V}{\partial z}\right) \quad \text{with} \quad V = -\frac{GM_m}{D_m^3}\frac{r^2}{2}(3\cos^2\theta - 1). \tag{9.93}$$

All we have to do then is to calculate the local tidal potential, take its local derivatives and introduce these as tidal forces in the shallow-water equations.

The tidal potential can also be used to estimate tidal amplitudes. Since the tidal force, *i.e.*, the gradient of the potential, has a form similar to the pressure-gradient force associated with the sea surface height, we can ask which distribution of η, denoted η_e, would cancel the tidal force so that no motion would result. Obviously, this is the case when

$$\eta_e = -\frac{V}{g} = \frac{GM_m}{D_m^3}\frac{r^2}{2g}(3\cos^2\theta - 1)$$
$$= \mathcal{O}\left(\frac{GM_m}{D_m^3}\frac{r^2}{g}\right) \sim 0.36\text{m}. \tag{9.94}$$

This defines the so-called *equilibrium tide*, first derived by Isaac Newton. It would be the tidal elevation if the fluid could follow the tidal force in order to remain in equilibrium with the pressure gradient generated by the bulges. In reality, however, continents and topographic features in the ocean do not allow sea water to stay at the equilibrium.

Not only is the equilibrium tide never reached, but the tidal potential is also in need of further adaptation to take into account the solid-earth deformation due to tides and the self-attraction of tides (*e.g.*, Hendershott, 1972). For actual tidal predictions we thus resort to numerical methods. For this, we gather all terms previously mentioned in this chapter and add the components of the tidal force. The governing equations used in a shallow-water model to predict both tides and storm surges are:

$$\frac{\partial u}{\partial t} + u\frac{\partial u}{\partial x} + v\frac{\partial u}{\partial y} - fv = -\frac{1}{\rho_0}\frac{\partial p}{\partial x} + \frac{\tau^x}{\rho_0 h} - \frac{\tau_b^x}{\rho_0 h} - \frac{\partial V}{\partial x} + \frac{1}{h}\frac{\partial}{\partial x}\left(\mathcal{A}\frac{\partial hu}{\partial x}\right) + \frac{1}{h}\frac{\partial}{\partial y}\left(\mathcal{A}\frac{\partial hu}{\partial y}\right) \tag{9.95a}$$

$$\frac{\partial v}{\partial t} + u\frac{\partial v}{\partial x} + v\frac{\partial v}{\partial y} + fu = -\frac{1}{\rho_0}\frac{\partial p}{\partial y} + \frac{\tau^y}{\rho_0 h} - \frac{\tau_b^y}{\rho_0 h} - \frac{\partial V}{\partial y} + \frac{1}{h}\frac{\partial}{\partial x}\left(\mathcal{A}\frac{\partial hv}{\partial x}\right) + \frac{1}{h}\frac{\partial}{\partial y}\left(\mathcal{A}\frac{\partial hv}{\partial y}\right) \tag{9.95b}$$

$$p = \rho_0 g\eta + p_{\text{atm}} \tag{9.95c}$$

together with (7.17) and (9.93). Note that the driving forces of wind and tide act very differently. While the wind-stress acts as a surface force and therefore appears with a factor $1/h$, the tidal force is a body force acting over the whole water column. Consequently, the tidal force is more important in the deeper parts of the ocean. This might surprise us since we are used to observe the highest tides near the coasts, where h is small! In most cases, tides are generated in the deeper parts of the oceans, where the tidal force acts on a thick layer of water, creates a pattern of convergence/divergence and locally modifies the sea surface height. The sea-surface elevation is then propagated as a set of Kelvin and Poincaré waves into shelf seas and coastal regions, where the reduced depth increases their amplitudes (Figure 9-2).

Some shelf models can provide tidal predictions by imposing tidal elevations at distant open boundaries and propagating the waves into the domain while discarding the local tidal force. This is consistent with the idea that, in shallow seas, the wind stress is the dominant local forcing. Indeed, in a 10000m-deep basin the tidal force is equivalent to the surface friction of a 75m/s wind, while in a shallow sea of 100 m, a wind of 7.5 m/s already matches the local tidal force. An example of a tidal calculation in which the tides are imposed along an open boundary is given in Figure 9-19. In this figure, we note in passing the presence of

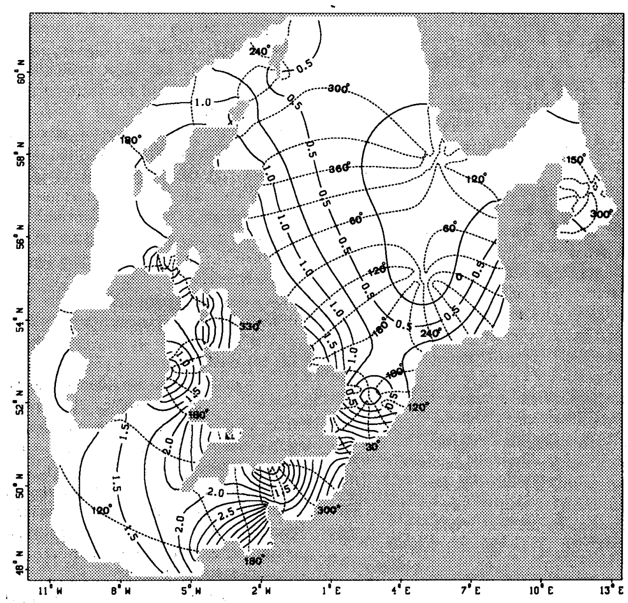

Figure 9-19 Tidal amplitudes (full lines) and phases (dotted lines) over the Northwestern European continental shelf, generated by the moon. (*Eric Delhez*)

nodes where the tidal amplitude is nil and the phase undefined. Each such node, called an *amphidromic point*, is a place where the various wave components cancel each other (destructive interference).

The numerical implementation of the model we have just developed is readily feasible since we have already encountered all its ingredients: time stepping, advection, Coriolis term, pressure gradient, diffusion, which were all treated in detail in previous sections. The only remaining term is that including the bottom stress, and for it we suggest to discretize it with the Patankar technique (to be discussed in Section 14.6) if the nonlinear relationship is selected:

$$\tau_b^x \;=\; -\,\rho_0 C_d \sqrt{(u^n)^2 + (v^n)^2}\; u^{n+1}, \quad \tau_b^y \;=\; -\,\rho_0 C_d \sqrt{(u^n)^2 + (v^n)^2}\; v^{n+1}. \quad (9.96)$$

Since several methods are available for each process, the combination of the various processes at play here leads to a very wide array of possible numerical implementations, all at relatively low cost with two spatial dimensions. This explains the large number of two-dimensional numerical models that were developed relatively early in geophysical fluid modeling (*e.g.*, Nihoul, 1975; Backhaus, 1983; Heaps, 1987).

Analytical Problems

9-1. Prove that Kelvin waves propagate with the coast on their left in the Southern Hemisphere.

9-2. The Yellow Sea between China and Korea (mean latitude: 37°N) has an average depth of 50 m and a coastal perimeter of 2600 km. How long does it take for a Kelvin wave to go around the shores of the Yellow Sea?

9-3. Prove that at extremely large wavelengths, inertia-gravity waves degenerate into a flow field where particles describe circular inertial oscillations.

9-4. An oceanic channel is modeled by a flat-bottom strip of ocean between two vertical walls. Assume that the fluid is homogeneous and inviscid, and that the Coriolis parameter is constant. Describe all waves that can propagate along such channel.

9-5. Consider planetary waves forced by the seasonal variations of the annual cycle. For $f_0 = 8 \times 10^{-5}$ s^{-1}, $\beta_0 = 2 \times 10^{-11}$ m^{-1}s^{-1}, $R = 1000$ km, what is the range of admissible zonal wavelengths?

9-6. Because the Coriolis parameter vanishes along the Equator, it is usual in the study of tropical processes to write

$$f = \beta_0 y,$$

where y is the distance measured from the Equator (positive northward). The linear wave equations then take the form

$$\frac{\partial u}{\partial t} - \beta_0 y v = -g \frac{\partial \eta}{\partial x} \tag{9.97}$$

$$\frac{\partial v}{\partial t} + \beta_0 y u = -g \frac{\partial \eta}{\partial y} \tag{9.98}$$

$$\frac{\partial \eta}{\partial t} + H \left(\frac{\partial u}{\partial x} + \frac{\partial v}{\partial y} \right) = 0, \tag{9.99}$$

where u and v are the zonal and meridional velocity components, η is the surface displacement, g is gravity, and H is the ocean depth at rest. Explore the possibility of a wave traveling zonally with no meridional velocity. At which speed does this wave travel and in which direction? Is it trapped along the Equator? If so, what is the trapping distance? Does this wave bear any resemblance to a mi-latitude wave (f_0 not zero)?

9-7. Seek wave solutions to the nonhydrostatic system of equations with nonstrictly vertical rotation vector:

$$\frac{\partial u}{\partial t} - fv + f_* w = -\frac{1}{\rho_0}\frac{\partial p}{\partial x} \tag{9.100a}$$

$$\frac{\partial v}{\partial t} + fu = -\frac{1}{\rho_0}\frac{\partial p}{\partial y} \tag{9.100b}$$

$$\frac{\partial w}{\partial t} - f_* u = -\frac{1}{\rho_0}\frac{\partial p}{\partial z} \tag{9.100c}$$

$$\frac{\partial u}{\partial x} + \frac{\partial v}{\partial y} + \frac{\partial w}{\partial z} = 0. \tag{9.100d}$$

The fluid is homogeneous ($\rho = 0$), inviscid ($\nu = 0$) and infinitely deep. Consider in particular the equivalent of the Kelvin wave ($u = 0$ at $x = 0$) and Poincaré waves.

9-8. Prove by using a local polar coordinate system that tidal forces derive from the tidal potential (9.93).

9-9. Estimate the average travel time for a gravity wave to circle the earth along the Equator, assuming that there are no continents and that the average depth of the ocean is 3800 m. Compare to the tidal period.

9-10. Based on the mass of the sun and its distance to the earth, how intense do you expect solar tides to be compared to lunar tides? At what period do the combined forces give rise to the strongest tides?

9-11. Knowing that a hurricane approaching Florida has a diameter of 100 km and wind-speeds U of 150 km/h, which storm surge height do you expect in a 10-m deep coastal sea? Use the following wind-stress formula: $\tau = 10^{-6}\rho_0 U^2$.

9-12. Assuming the earthquake near Indonesia's Sumatra Island on 26 December 2004 generated a surface wave (tsunami) by a upward motion of the sea floor during 10 minutes, estimate the wavelength of the wave. For simplicity, assume a uniform depth h = 4 km. Estimate also the time available between the detection of the earthquake and the moment the tsunami reaches another coastline 4000 km away. If instead a unform depth, you use the depth profile $h(x)$ provided in `sumatra.m`, how would you estimate the travel time? Investigate under which conditions you can use the local wave speed of gravity waves over uneven topography. *Hint:* Compare the wavelength to the length scale of topographic variations.

9-13. In order to avoid the problem in Section 9.5 of an infinitely deep layer at large distances, assume now that the flow takes place in a channel of width L. Analyze how the topographic waves are modified by the presence of the lateral boundaries.

9-14. Consider an inertia-gravity wave of wavelength $\lambda = 2\pi/k$ on the f–plane and align the x–axis with the direction of propagation (*i.e.*, $k_x = k$ and $k_y = 0$). Write the partial-differential equations and solve them for u and η proportional to $\cos(kx - \omega t)$

and v proportional to $\sin(kx - \omega t)$. Then calculate the kinetic and potential energies per unit horizontal area, defined as

$$KE = \frac{1}{\lambda} \int_0^\lambda \frac{1}{2} \rho_0 (u^2 + v^2) H \, dx \quad (9.101a)$$

$$PE = \frac{1}{\lambda} \int_0^\lambda \frac{1}{2} \rho_0 g \eta^2 \, dx, \quad (9.101b)$$

each in terms of the amplitude of η and show that the kinetic energy is always greater than the potential energy, except in the case $f = 0$ (pure gravity waves), in which case there is equipartition of energy.

Numerical Exercises

9-1. Establish the numerical stability condition of schemes (9.53) and (9.54). Can you provide an interpretation for the parameter $c\Delta t/\Delta x$? Compare to the CFL criterion.

9-2. Spell out the spatial discretization on the B–, C– and D–grids of Equations (9.4a) through (9.5).

9-3. Implement the C–grid in Matlab for equations (9.4a) through (9.5) with a variable fluid thickness given on a grid at the same location as η. Use a time discretization as in (9.54) and a fractional-step approach for the Coriolis term. Then use your code to simulate a pure Kelvin wave for different values of $\Delta x/R$ and $k_x^2 R^2$ by initializing with the exact solution. *Hint:* Use a periodic domain in the x–direction and a second impermeable boundary in the y–direction, to be justified, at $y = 10R$. Start from `shallow.m`.

9-4. Analyze the way geostrophic equilibrium is represented in discrete Fourier modes on the B– and C–grids.

9-5. Investigate group-velocity errors for the different Arakawa grids using the numerical dispersion relation given in (9.66). Use $\Delta x = \Delta y$ and distinguish two types of waves: $k_x \neq 0$, $k_y = 0$ and $k_x = k_y$. Vary the resolution by taking $R/\Delta x = 0.2, 1, 5$, where R is the deformation radius.

9-6. Design the best staggering strategy for a model in which the eddy viscosity ν_E is chosen proportional to $|\partial u/\partial z| l_m^2$, where l_m is a specified length scale and u is determined numerically from a governing equation that includes vertical turbulent diffusion.

9-7. Assume you need to calculate the vertical component of relative vorticity from a discrete velocity field provided on the two-dimensional C–grid. Where is the most natural node to calculate the relative vorticity? Can you see an advantage to using a D–grid here?

9-8. Can you think of possibilities to include bottom topographic variations as those inducing tsunamis in shallow water?

9-9. Take the variable depth implementation of Numerical Exercise 9-3 and apply it to the following topography

$$h = H_0 + \Delta H \left[1 + \tanh \left(\frac{x - \frac{L}{2}}{D} \right) \right]$$

with $H_0 = 50$ m, $D = L/8$ and $\Delta H = 5H_0$. Use a solid wall at $x = 0$ and $x = L = 100$ km and periodic boundary conditions in the y–direction across a domain of length $5L$. Start with zero velocities and a Gaussian sea surface elevation of width $L/4$ and height of 1 m in the center of the basin. Use linear bottom friction with friction coefficient $r = 10^{-4}$ m/s. Trace the evolution of the sea surface elevation for $f = 10^{-4}$ s^{-1}.

9-10. Perform a storm-surge simulation with the implementation of Numerical Exercise 9-3 by using a uniform wind stress over a square basin with a uniform topography and then with the topography given in Numerical Exercise 9-9. Use the quadratic law (9.77) for bottom friction.

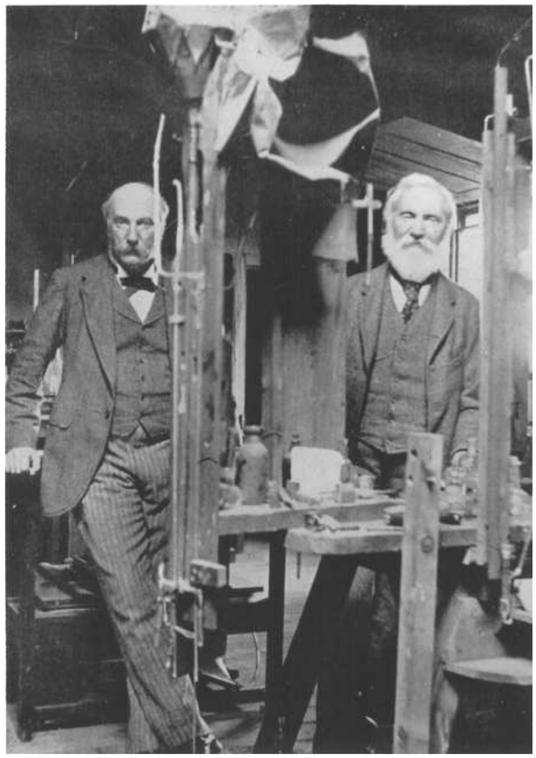

William Thomson, Lord Kelvin
1824 – 1907
(Standing at right, in laboratory of Lord Rayleigh, left)

Named professor of natural philosophy at the University of Glasgow, Scotland, at age 22, William Thomson became quickly regarded as the leading inventor and scientist of his time. In 1892, he was named Baron Kelvin of Largs for his technological and theoretical contributions leading to the successful laying of a transatlantic cable. A friend of *firstname* Joule, he helped establish a firm theory of thermodynamics and first defined the absolute scale of temperature. He also made major contributions to the study of heat engines. With Hermann von Helmholtz, he estimated the ages of the earth and sun, and ventured in fluid mechanics. His theory of the so-called Kelvin wave was published in 1879 (under the name William Thomson). His more than 300 original papers left hardly any aspect of science untouched. He is quoted as saying that he could understand nothing of which he could not make a model. (*Photo by A.G. Webster*)

Akio Arakawa
1920 –

A graduate of the University of Tokyo, Akio Arakawa decided to pursue a career in "practical meteorology" and went to the University of California in Los Angeles (UCLA) for further studies. The atmospheric-circulation computer models of the time (early 1960s) could reproduce weather-like motion but not for long. Beyond a two-week simulation, the computed patterns no longer looked like weather. Arakawa's doctoral thesis demonstrated that the problem lied in the artificial generation of energy by inadequate numerical procedures, and found the remedy. The remedy consisted of enforcing conservation of energy (and also of enstrophy, which is the square of vorticity) at the grid level. The grids, which he proposed and later came to bear his name, were designed to respect numerical conservation of physically conserved quantities. After obtaining his doctorate, Arakawa spent most of his career at UCLA, where is currently a professor emeritus. His legacy to the science of weather prediction by computer modeling is significant and enduring.

Chapter 10

Barotropic Instability

(October 18, 2006) SUMMARY: The waves explored in the previous chapter evolve in a fluid otherwise at rest, propagating without either growth or decay. Here, we investigate waves riding on an existing current and find that, under certain conditions, they may grow at the expense of the energy contained in the mean current while respecting conservation of vorticity. The numerical section exposes the method of contour dynamics, designed specifically for applications in which conservation of vorticity is important.

10.1 What makes a wave grow unstable?

The planetary and topographic waves described in the previous chapter (Sections 9.4 through 9.5) owe their existence to the presence of an ambient potential-vorticity gradient. In the case of planetary waves, the cause is the sphericity of the planet, whereas for topographic waves the gradient results from the bottom slope. We may naturally wonder whether a sheared current that possesses a gradient of relative vorticity, would, too, be able to sustain similar low-frequency waves.

The situation is quite different, however, for several reasons. First, the current would not only create the required ambient potential-vorticity gradient but would also transport the wave pattern; because of the current shear, this translation would be differential, and the wave pattern would be rapidly distorted. Moreover, there is likely to be a place within the current where the speed of the wave matches the velocity of the current; such a location, termed the *critical level*, typically permits a vigorous transfer of energy between the basic current and the wave. As a consequence, the wave may draw energy from the current and grow in time. If this happens, insignificant little wiggles may turn into very large perturbations, and the initial flow can become highly contorted, to the point of becoming unrecognizable. The flow is said to be unstable. To distinguish this situation from other instabilities occurring in baroclinic fluids (*i.e.*, those possessing a stratification; see Chapters 14 and 17), the preceding process is generally known as *barotropic instability*.

The stability theory of homogeneous shear flows is a well developed chapter in fluid mechanics (see, for example, Lindzen, 1988; Kundu, 1990, Section 11-9). Here, we address the problem with the inclusion of the Coriolis force but limit our investigation to establishing general properties and solving one particular case.

10.2 Waves on a shear flow

To investigate the behavior of waves on an existing current in a relatively clear and tractable formalism, it is customary to make the following assumptions: The fluid is homogeneous and inviscid, and the bottom and the surface are flat and horizontal. The Coriolis parameter is, however, allowed to vary (*i.e.*, the beta effect is retained). The governing equations are (Section 4.4)

$$\frac{\partial u}{\partial t} + u\frac{\partial u}{\partial x} + v\frac{\partial u}{\partial y} + w\frac{\partial u}{\partial z} - fv = -\frac{1}{\rho_0}\frac{\partial p}{\partial x} \tag{10.1a}$$

$$\frac{\partial v}{\partial t} + u\frac{\partial v}{\partial x} + v\frac{\partial v}{\partial y} + w\frac{\partial v}{\partial z} + fu = -\frac{1}{\rho_0}\frac{\partial p}{\partial y} \tag{10.1b}$$

$$0 = -\frac{\partial p}{\partial z} \tag{10.1c}$$

$$\frac{\partial u}{\partial x} + \frac{\partial v}{\partial y} + \frac{\partial w}{\partial z} = 0, \tag{10.1d}$$

where the Coriolis parameter $f = f_0 + \beta_0 y$ varies with the northward coordinate y (Section 9.4). As demonstrated in Section 7.3, a horizontal flow that is initially uniform in the vertical will, in the absence of vertical friction, remain so at all times. In GFD parlance, this is what is called a *barotropic flow*, and we consider such a case. Consequently, we drop the terms $w\partial u/\partial z$ and $w\partial v/\partial z$ in equations (10.1a) and (10.1b), respectively. According to (10.1d), $\partial w/\partial z$ must be z-independent, too, which implies that w is linear in z. But, because the vertical velocity vanishes at both top and bottom, it must be zero everywhere ($w = 0$). The continuity equation reduces to

$$\frac{\partial u}{\partial x} + \frac{\partial v}{\partial y} = 0. \tag{10.2}$$

For the basic state, we choose a zonal current with arbitrary meridional profile: $u = \bar{u}(y)$, $v = 0$. This is an exact solution to the nonlinear equations as long as the pressure profile, $p = \bar{p}(y)$, satisfies the geostrophic balance

$$(f_0 + \beta_0 y)\,\bar{u}(y) = -\frac{1}{\rho_0}\frac{d\bar{p}}{dy}\,. \tag{10.3}$$

Next, we add a small perturbation, meant to represent an arbitrary wave of weak amplitude. We write

$$u = \bar{u}(y) + u'(x, y, t) \tag{10.4a}$$
$$v = v'(x, y, t) \tag{10.4b}$$
$$p = \bar{p}(y) + p'(x, y, t), \tag{10.4c}$$

where the perturbations u', v' and p' are taken to be much smaller that the corresponding variables of the basic flow (*i.e.*, u' and v' much less than $\bar{u}$, and p' much less than $\bar{p}$). Substitution in Equations (10.1a), (10.1b), and (10.2) and subsequent linearization to take advantage of the smallness of the perturbation yield:

$$\frac{\partial u'}{\partial t} + \bar{u}\,\frac{\partial u'}{\partial x} + v'\,\frac{d\bar{u}}{dy} - (f_0 + \beta_0 y)v' = -\frac{1}{\rho_0}\,\frac{\partial p'}{\partial x} \tag{10.5a}$$
$$\frac{\partial v'}{\partial t} + \bar{u}\,\frac{\partial v'}{\partial x} + (f_0 + \beta_0 y)u' = -\frac{1}{\rho_0}\,\frac{\partial p'}{\partial y} \tag{10.5b}$$
$$\frac{\partial u'}{\partial x} + \frac{\partial v'}{\partial y} = 0. \tag{10.5c}$$

The last equation admits the streamfunction ψ, defined as

$$u' = -\frac{\partial \psi}{\partial y}, \quad v' = +\frac{\partial \psi}{\partial x}. \tag{10.6}$$

The choice of signs corresponds to a flow along streamlines with the higher streamfunction values on the right.

A cross-differentiation of the momentum equations (10.5a) and (10.5b) and the elimination of the velocity components leads to a single equation for the streamfunction:

$$\left(\frac{\partial}{\partial t} + \bar{u}\,\frac{\partial}{\partial x}\right)\nabla^2 \psi + \left(\beta_0 - \frac{d^2\bar{u}}{dy^2}\right)\frac{\partial \psi}{\partial x} = 0. \tag{10.7}$$

This equation has coefficients that depend on $\bar{u}$ and, therefore, on the meridional coordinate y only. A sinusoidal wave in the zonal direction is then a solution:

$$\psi(x, y, t) = \phi(y)\exp^{\mathrm{i}\,(kx-\omega t)}. \tag{10.8}$$

Substitution provides the following second-order ordinary differential equation for the amplitude $\phi(y)$:

$$\frac{d^2\phi}{dy^2} - k^2\phi + \frac{\beta_0 - d^2\bar{u}/dy^2}{\bar{u}(y) - c}\,\phi = 0, \tag{10.9}$$

where $c = \omega/k$ is the zonal speed of propagation. An equation of this type is called a *Rayleigh equation* (Rayleigh, 1880). Its key features are the non-constant coefficient in the third term and the fact that its denominator may be zero, creating a singularity.

For boundary conditions, let us assume for simplicity that the fluid is contained between two walls, at $y = 0$ and L. We are thus considering waves on a zonal flow in a zonal channel. Obviously, there is no such zonal channel in either the atmosphere or ocean, but wavy zonal flows of limited meridional extent abound. The atmospheric jet stream in the upper troposphere, the Gulf Stream after its seaward turn off Cape Hatteras (36°N), and the Antarctic Circumpolar Current are all good examples. Also, the atmosphere on Jupiter, with the exception of the Great Red Spot and other vortices, consists almost entirely of zonal bands of alternating winds, called *belts* or *stripes* (see Figure 1-5).

If the boundaries prevent fluid from entering and leaving the channel, v' is zero there, and (10.6) implies that the streamfunction must be a constant along each wall. In other words, walls are streamlines. This is possible only if the wave amplitude obeys

$$\phi(y = 0) \ = \ \phi(y = L) \ = \ 0. \tag{10.10}$$

The second-order, homogeneous problem of (10.9) and (10.10) can be viewed as an eigenvalue problem: The solution is trivial ($\phi = 0$), unless the phase velocity assumes a specific value (eigenvalue), in which case a non-zero function ϕ (eigenfunction) can be determined within an arbitrary multiplicative constant.

In general, the eigenvalues c may be complex. If c admits the function ϕ, then the complex conjugate c^* admits the complex conjugate function ϕ^* and is thus another eigenvalue. This can be readily verified by taking the complex conjugate of equation (10.9). Hence, complex eigenvalues come in pairs.

Decomposing the eigenvalue into its real and imaginary components,

$$c = c_r + \mathrm{i}\, c_i, \tag{10.11}$$

we note that the streamfunction ψ has an exponential factor of the form $\exp(kc_i t)$, which grows or decays according to the sign of c_i. Because the eigenvalues come in pairs, to any decaying mode will correspond a growing mode. Therefore, the presence of a non-zero imaginary part in the phase velocity c automatically guarantees the existence of a growing disturbance and thus the instability of the basic flow. The product kc_i is then called the *growth rate*. Conversely, for the basic flow to be stable, it is necessary that the phase speed c be purely real.

Because mathematical difficulties prevent a general determination of the c values for an arbitrary velocity profile $\bar{u}(y)$ (the analysis is difficult even for idealized but nontrivial profiles), we shall not attempt to solve the problem (10.9)–(10.10) exactly but will instead establish some of its integral properties and, in so doing, reach weaker stability criteria.

When we multiply equation (10.9) by ϕ^* and then integrate across the domain, we obtain

$$- \ \int_0^L \ \left(\left| \frac{d\phi}{dy} \right|^2 \ + \ k^2 |\phi|^2 \right) \ dy \ + \ \int_0^L \ \frac{\beta_0 - d^2\bar{u}/dy^2}{\bar{u} - c} \ |\phi|^2 \ dy \ = \ 0, \tag{10.12}$$

after an integration by parts. The imaginary part of this expression is

$$c_i \ \int_0^L \ \left(\beta_0 \ - \ \frac{d^2\bar{u}}{dy^2} \right) \ \frac{|\phi|^2}{|\bar{u} - c|^2} \ dy \ = \ 0. \tag{10.13}$$

Two cases are possible: Either c_i vanishes or the integral does. If c_i is zero, the basic flow admits no growing disturbance and is stable. But, if c_i is not zero, then the integral must vanish, which requires that the quantity

$$\beta_0 \ - \ \frac{d^2\bar{u}}{dy^2} \ = \ \frac{d}{dy}\left(f_0 \ + \ \beta_0 y \ - \ \frac{d\bar{u}}{dy}\right) \tag{10.14}$$

must change sign at least once within the confines of the domain. Summing up, we conclude that a necessary condition for instability is that expression (10.14) vanish somewhere inside the domain. Conversely, a sufficient condition for stability is that expression (10.14) not vanish anywhere within the domain (on the boundaries maybe, but not inside the domain). Physically, the total vorticity of the basic flow, $f_0 + \beta_0 y - d\bar{u}/dy$, must reach an extremum within the domain to cause instabilities. This result was first derived by Kuo (1949).

This first criterion can be strengthened by considering next the real part of (10.12), which takes the form:

$$\int_0^L \ (\bar{u} - c_r)\left(\beta_0 - \frac{d^2\bar{u}}{dy^2}\right) \ \frac{|\phi|^2}{|\bar{u} - c|^2} \ dy \ = \ \int_0^L \ \left(\left|\frac{d\phi}{dy}\right|^2 \ + \ k^2|\phi|^2\right) \ dy. \tag{10.15}$$

In the event of instability, the integral in (10.13) vanishes. Multiplying it by $(c_r - \bar{u}_0)$, where $\bar{u}_0$ is any real constant, adding the result to (10.15), and noting that the right-hand side of (10.15) is always positive for non-zero perturbations, we obtain:

$$\int_0^L \ (\bar{u} - \bar{u}_0)\left(\beta_0 - \frac{d^2\bar{u}}{dy^2}\right) \ \frac{|\phi|^2}{|\bar{u} - c|^2} \ dy \ > \ 0. \tag{10.16}$$

This inequality demands that the expression

$$(\bar{u} - \bar{u}_0)\left(\beta_0 - \frac{d^2\bar{u}}{dy^2}\right) \tag{10.17}$$

be positive in at least some finite portion of the domain. Because this must hold true for any constant $\bar{u}_0$, it must be true in particular if $\bar{u}_0$ is the value of $\bar{u}(y)$ where $\beta_0 - d^2\bar{u}/dy^2$ vanishes. Hence, a stronger criterion is: Necessary conditions for instability are that $\beta_0 - d^2\bar{u}/dy^2$ vanish at least once within the domain *and* that $(\bar{u} - \bar{u}_0)(\beta_0 - d^2\bar{u}/dy^2)$, where $\bar{u}_0$ is the value of $\bar{u}(y)$ at which the first expression vanishes, be positive in at least some finite portion of the domain. Although this stronger criterion still offers no sufficient condition for instability, it is generally quite useful.

10.3 Bounds on wave speeds and growth rates

The preceding analysis taught us that instabilities may occur when certain conditions are met. A question then naturally arises: If the flow is unstable, how fast will perturbations grow? In the general case of an arbitrary shear flow $\bar{u}(y)$, a precise determination of the growth rate of unstable perturbations is not possible. However, an upper bound can be derived relatively easily, and, in the process, we can also determine lower and upper bounds on the phase speed of the perturbations. For simplicity, we will restrict our attention to the f-plane ($\beta_0 = 0$), in which case the derivation is due to Howard (1961). Afterwards, we will cite, without demonstration, the result for the β-plane.

The analysis begins by a change of variable[1]:

$$\phi \;=\; (\bar{u} \;-\; c)\, a, \tag{10.18}$$

which transforms equation (10.9) into

$$\frac{d}{dy}\;\left[(\bar{u}-c)^2\;\frac{da}{dy}\right]\;-\;k^2\;(\bar{u}-c)^2\;a\;=\;0, \tag{10.19}$$

with β_0 set to zero. Because of (10.18), the boundary conditions on a are identical to those on ϕ, namely, $a(0) = a(L) = 0$.

We consider the case of an unstable wave. In this case, c has a non-zero imaginary part, and a is non-zero and complex. Multiplying by the complex conjugate a^* and integrating across the domain, we obtain an expression whose real and imaginary parts are

$$\text{Real part:} \qquad \int_0^L\;[(\bar{u}-c_r)^2\;-\;c_i^2]P\;dy\;=\;0 \tag{10.20}$$

$$\text{Imaginary part:} \qquad \int_0^L\;(\bar{u}-c_r)P\;dy\;=\;0, \tag{10.21}$$

where $P = |da/dy|^2 + k^2|a|^2$ is a non-zero positive quantity. With (10.21), (10.20) can also be recast as

$$\int_0^L\;[\bar{u}^2\;-(c_r^2+c_i^2)]P\,dy = 0 \tag{10.22}$$

It immediately follows from (10.21) that $(\bar{u} - c_r)$ must vanish somewhere in the domain, implying that the phase speed c_r lies between the minimum and maximum values of $\bar{u}(y)$:

$$U_{\min}\;<\;c_r\;<\;U_{\max}. \tag{10.23}$$

Physically, the wavy perturbation, if unstable, must travel with a speed that matches that of the entraining flow, in at least one location. In other words, there will always be a place in the domain where the wave does not drift with respect to the ambient flow and grows in place. It is precisely this local coupling between wave and flow that allows the wave to extract energy from the flow and to grow at its expense. The location where the phase speed is equal to the flow velocity is called a *critical level*.

Armed with bounds for the real part of c, we now seek bounds on its imaginary part. To do so, we introduce the obvious inequality

$$\int_0^L\;(\bar{u}-U_{\min})\;(U_{\max}-\bar{u})P\;dy\;\geq\;0 \tag{10.24}$$

and then expand the expression, replace all linear terms in $\bar{u}$ using (10.21), and replace the quadratic term using using (10.22) to arrive at

[1] It can be shown that the new variable a is the meridional displacement, the material time derivative of which is the v component of velocity

$$\left[\left(c_r - \frac{U_{\min} + U_{\max}}{2}\right)^2 + c_i^2 - \left(\frac{U_{\max} - U_{\min}}{2}\right)^2\right] \int_0^L P \, dy \leq 0. \tag{10.25}$$

Because the integral of P can only be positive, the preceding bracketed quantity must be negative:

$$\left(c_r - \frac{U_{\min} + U_{\max}}{2}\right)^2 + c_i^2 \leq \left(\frac{U_{\max} - U_{\min}}{2}\right)^2. \tag{10.26}$$

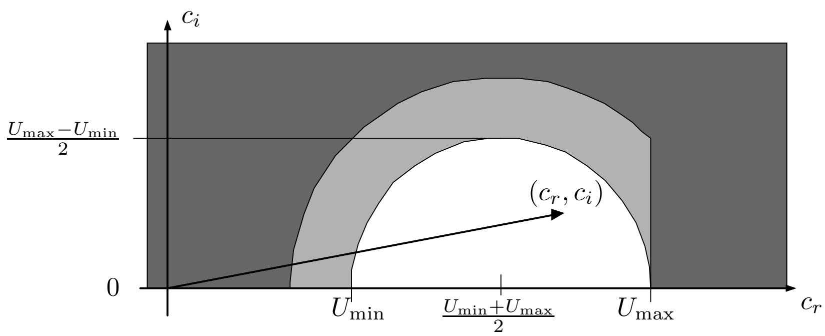

Figure 10-1 The semicircle theorem. Growing perturbations of wavenumber k must have phase speeds c_r and growth rates kc_i such that the tip of the vector (c_r, c_i) falls within the half-circle constructed from the minimum and maximum velocities of the ambient shear flow $\bar{u}(y)$, as depicted in the figure. When the β effect is taken into account the tip of the vector must lie in the slightly enlarged domain that includes the semi-circle and the light gray area.

This inequality implies that, in the complex plane, the number $c_r + ic_i$ must lie within the circle centered at $[(U_{\min} + U_{\max})/2, 0]$ and of radius $(U_{\max} - U_{\min})/2$. Since we are interested in modes that grow in time, c_i is positive, and only the upper half of that circle is relevant (Figure 10-1). This result is called *Howard's semicircle theorem*.

It is readily evident from inequality (10.26) or Figure 10-1 that c_i is bounded above by

$$c_i \leq \frac{U_{\max} - U_{\min}}{2}. \tag{10.27}$$

The perturbation's growth rate kc_i is thus likewise bounded above.

On the beta plane, the treatment of integrals and inequalities is somewhat more elaborate but still feasible. Pedlosky (1987, Section 7.5) showed that the preceding inequalities on c_r and c_i must be modified to

$$U_{\min} - \frac{\beta_0 L^2}{2(\pi^2 + k^2 L^2)} < c_r < U_{\max} \tag{10.28}$$

$$\left(c_r - \frac{U_{\min} + U_{\max}}{2}\right)^2 + c_i^2 \leq \left(\frac{U_{\max} - U_{\min}}{2}\right)^2 + \frac{\beta_0 L^2 (U_{\max} - U_{\min})}{2(\pi^2 + k^2 L^2)}, \tag{10.29}$$

where L is the domain's meridional width and k the zonal wavenumber (Figure 10-1). The westward velocity shift on the left side of (10.28) is related to the existence of planetary waves [see the zonal phase speed, (9.30)]. The last inequality readily leads to an upper bound for the growth rate kc_i. Knowing bounds for the phase speed c_r and growth rate kc_i is useful in the numerical search of stability threshold in specific applications (Proehl, 1996).

10.4 A simple example

The preceding considerations on the existence of instabilities and their properties are rather abstract. So, let us work out an example to illustrate the concepts. For simplicity, we restrict ourselves to the f-plane ($\beta_0 = 0$) and take a shear flow that is piecewise linear (Figure 10-2):

$$y < -L: \quad \bar{u} = -U, \quad \frac{d\bar{u}}{dy} = 0, \quad \frac{d^2\bar{u}}{dy^2} = 0 \tag{10.30}$$

$$-L < y < +L: \quad \bar{u} = \frac{U}{L}\,y, \quad \frac{d\bar{u}}{dy} = \frac{U}{L}, \quad \frac{d^2\bar{u}}{dy^2} = 0 \tag{10.31}$$

$$+L < y: \quad \bar{u} = +U, \quad \frac{d\bar{u}}{dy} = 0, \quad \frac{d^2\bar{u}}{dy^2} = 0, \tag{10.32}$$

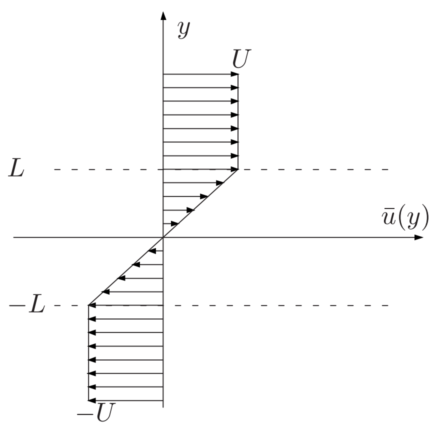

Figure 10-2 An idealized shear-flow profile that lends itself to analytic treatment. This profile meets both necessary conditions for instability and is found to be unstable to long waves.

where U is a positive constant and the domain width is now infinity. Although the second derivative vanishes within each of the three segments of the domain, it is non-zero at their junctions. As y increases, the first derivative $d\bar{u}/dy$ changes from zero to a positive value and back to zero, so it can be said that the second derivative is positive at the first junction ($y = -L$) and negative at the second ($y = +L$). Thus, $d^2\bar{u}/dy^2$ changes sign in the domain, and this satisfies the first condition for the existence of instabilities. The second condition, that expression (10.17), now reduced to

$$- \bar{u} \, \frac{d^2\bar{u}}{dy^2} \; ,$$

be positive in some portion of the domain, is also satisfied because $d^2\bar{u}/dy^2$ has the sign opposite to $\bar{u}$ at each junction of the profile. Thus, the necessary conditions for instability are met, and, although instabilities are not guaranteed to exist, we ought to expect them.

We now proceed with the solution. In each of the three domain segments, governing equation (10.9) reduces to

$$\frac{d^2\phi}{dy^2} \; - \; k^2 \, \phi \; = \; 0, \tag{10.33}$$

and admits solutions of the type $\exp(+ky)$ and $\exp(-ky)$. This introduces two constants of integration per domain segment, for a total of six. Six conditions are then applied. First, ϕ is required to vanish at large distances:

$$\phi(-\infty) \; = \; \phi(+\infty) \; = \; 0.$$

Next, continuity of the meridional displacements at $y = \pm L$ requires, by virtue of (10.19) and by virtue of the continuity of the $\bar{u}(y)$ profile, that ϕ, too, be continuous there:

$$\phi(-L-\epsilon) \; = \; \phi(-L+\epsilon) \quad \text{and} \quad \phi(+L-\epsilon) \; = \; \phi(+L+\epsilon),$$

for arbitrarily small values of ϵ. Finally, the integration of governing equation (10.9) across the lines joining the domain segments

$$\int_{\pm L-\epsilon}^{\pm L+\epsilon} \left[(\bar{u} - c) \, \frac{d^2\phi}{dy^2} \; - \; k^2 \, (\bar{u} - c) \, \phi \; - \; \frac{d^2\bar{u}}{dy^2} \, \phi \right] \, dy \; = \; 0,$$

followed by an integration by parts, implies that

$$(\bar{u} - c) \, \frac{d\phi}{dy} \; - \; \frac{d\bar{u}}{dy} \, \phi$$

must be continuous at both $y = -L$ and $y = +L$. An alternative way of obtaining this result is to integrate Equation (10.19), which is in conservative form, across a discontinuity.

Applying these six conditions leads to a homogeneous system of equations for the six constants of integration. Non-zero perturbations exist when this system admits a nontrivial solution – that is, when its determinant vanishes. Some tedious algebra yields

$$\frac{c^2}{U^2} \; = \; \frac{(1-2kL)^2 - e^{-4kL}}{(2kL)^2} \; . \tag{10.34}$$

Equation (10.34) is the dispersion relation, providing the wave velocity c in terms of the wavenumber k and the flow parameters L and U. It yields a unique and real c^2, either positive or negative. If it is positive, c is real and the perturbation behaves as a non-amplifying wave. But, if c^2 is negative, c is imaginary and one of the two solutions yields an exponentially growing mode [a proportional to $\exp(kc_i t)$]. Obviously, the instability threshold is $c^2 = 0$, in which case the dispersion relation (10.34) yields $kL = 0.639$. There is thus a critical wavenumber $k = 0.639/L$ or critical wavelength $2\pi/k = 9.829L$ separating stable from

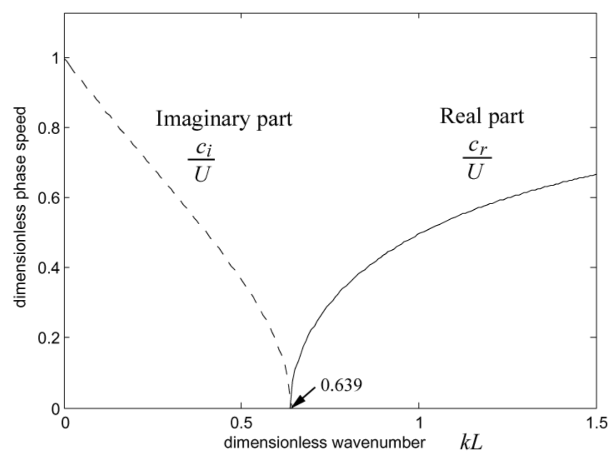

Figure 10-3 Plot of the dispersion relation (10.34) for waves riding on the shear flow depicted in 10-2. The lower wavenumbers k for which c_i is non-zero correspond to growing waves.

unstable waves (Figure 10-3). It can be shown by inspection of the same dispersion relation that shorter waves ($kL > 0.639$) travel without growth (because $c_i = 0$), whereas longer waves ($kL < 0.639$) grow exponentially without propagation (because $c_r = 0$). In sum, the basic shear flow is unstable to long-wave disturbances.

An interesting quest is the search for the fastest growing wave, because this is the dominant wave, at least until finite-amplitude effects become important and the preceding theory loses its validity. For this, we look for the value of kL that maximizes kc_i, where c_i is the positive imaginary root of (10.34). The answer is $kL = 0.398$, from which follows the wavelength of the fastest growing mode:

$$\lambda_{\text{fastest growth}} = \frac{2\pi}{k} = 15.77\,L = 7.89\,(2L). \tag{10.35}$$

This means that the wavelength of the perturbation that dominates the early stage of instability is about 8 times the width of the shear zone. Its growth rate is

$$(kc_i)_{\max} = 0.201\,\frac{U}{L}\,, \tag{10.36}$$

corresponding to $c_i = 0.505U$. It is left to the reader as an exercise to verify the preceding numerical values.

At this point, it is instructive to unravel the physical mechanism responsible for the growth of long-wave disturbances. Figure 10-4 displays the basic flow field, on which is superimposed a wavy disturbance. The phase shift between the two lines of discontinuity is that propitious to wave amplification. As the middle fluid, endowed with clockwise vorticity, intrudes in either neighboring strip where the vorticity is nonexistent, it produces local vorticity anomalies, which can be viewed as vortices. These vortices generate clockwise rotating flows in their vicinity, and, if the wavelength is sufficiently long, the interval between the two lines of discontinuity appears relatively short and the vortices from each side interact with those on the other side. Under a proper phase difference, such as the one depicted in Figure 10-4, the vortices entrain one another further into the regions of no vorticity, thereby amplifying the

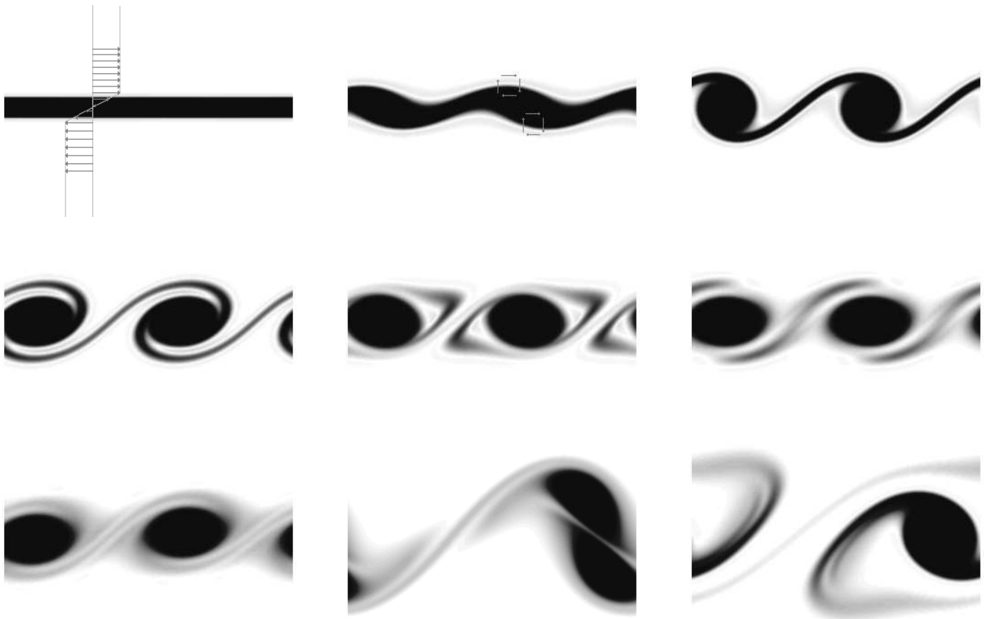

Figure 10-4 Finite-amplitude development of the instability of the shear flow depicted in Figure 10-2. The troughs and crests of the wave induce a vortex field, which, in turn, amplifies those troughs and crests. The wave does not travel but amplifies with time. [The sequence of figures shown here were generated with `shearedflow.m` developped in Chapter 16].

crests and troughs of the wave. The wave amplifies, and the basic shear flow cannot persist. As the wave grows, nonlinear terms are no longer negligible, and some level of saturation is reached. The ultimate state (Figure 10-4) is that of a series of clockwise vortices embedded in a weakened ambient shear flow (Zabusky *et al.*, 1979; Dritschel, 1989).

Lindzen (1988) offers an alternative mechanism for the instability, based on the fact that there are two special locations across the system. The first is the critical level y_c, where the wave speed matches the velocity of the basic flow [$c_r = \bar{u}(y_c)$] and the other is y_0 where the vorticity of the basic flow reaches an extremum [where Expression (10.14) changes sign]. A wave travelling in the direction of y_0 to y_c undergoes overreflection, that is, upon entering the [y_0,y_c] interval, it is being reflected toward its region of origin with a greater amplitude than on arrival. If there is a boundary or other place where the wave can be (simply) reflected, then it returns toward the region of overreflection, and on it goes. The successive overreflections of the echoing wave lead to exponential growth.

10.5 Nonlinearities

From Section 10.2 we note that the nonlinear advection term is responsible for the instability of the basic flow $\bar{u}(y)$. We analyzed the stability by linearizing the equations around the steady-state solution and replaced terms such as $u\partial u/\partial x$ by $\bar{u}\partial u'/\partial x$ and this led to linear equations and wave-like solutions, yet retaining the advection by the basic current $\bar{u}$. When instability occurs, the velocity perturbations grow in time, and, after an initial phase during which linearization holds, they eventually reach such an intensity that $u'\partial u'/\partial x$ may no be neglected. We enter a fully nonlinear regime requiring numerical simulation. In an inviscid problem such as the present one, we then face a serious problem, already mentioned in the Introduction, namely the aliasing of short waves into longer waves.

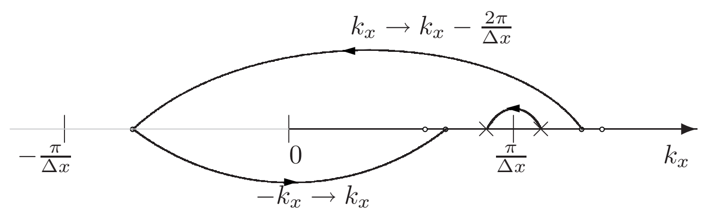

Figure 10-5 Transformation of a unresolved short wave of wavenumber $k_x > \pi/\Delta x$ into a resolved wavenumber $|k_x - 2\pi/\Delta x|$, corresponding to a reflection of wavenumber about the cutoff value $\pi/\Delta x$ as indicated for three particular values of the wavenumber identified by an open circle, a cross and a gray dot to the right of $\pi/\Delta x$ and the wavenumbers into which they are aliased (all to the left of $\pi/\Delta x$).

As shown in Section 1.12 for time series, sampling (read: discretization) sets some limits on the frequencies that can be resolved. In space instead of time, the same analysis applies, and waves of wavenumbers k_x and $k_x + 2\pi/\Delta x$ cannot be distinguished from each other in a discretization with space interval Δx. If a wavenumber k_x larger than $\pi/\Delta x$ exists, it is mistaken by the discretization as being of smaller wavenumber $k_x - 2\pi/\Delta x$ or $2\pi/\Delta x - k_x$. This misinterpretation of too rapidly varying waves can be depicted (Figure 10-5) as a reflection of the wavenumber about the cutoff value $\pi/\Delta x$. Any wave can be decomposed in its spectral components, and let us suppose that the spectrum of a set waves (wave packet) takes the form shown in Figure 10-6. Since waves of higher wavenumbers are reflected around the cutoff wavenumber into the resolved range, the associated spectral energy will also be transferred from the shorter unresolved waves to the longer resolved waves. If the energy level decreases with decreasing wavenumber, the spectrum alteration will be strongest near the cutoff value. In other words, the energy content of marginally resolved waves is the one most influenced by aliasing, and the manifestation is an unwanted excess of energy among barely resolved waves. This is one reason why model results ought generally to viewed as suspect at scales comparable to the grid spacing. But there is more to the problem.

The aliasing problem is particularly irksome when nonlinear advection comes into play, because the quadratic term in the equation creates wave harmonics: If the velocity field is resulting from the superposition of two waves, one of wavenumber k_1 and another of wavenumber k_2 of equal amplitude and phase,

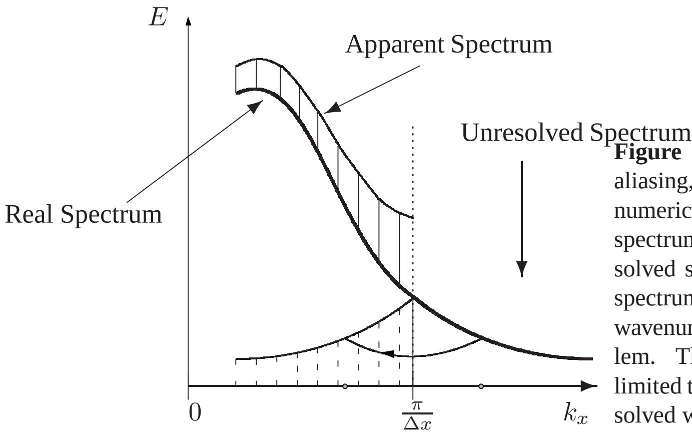

Figure 10-6 Spectrum alteration by aliasing, which effectively folds the numerically unresolved part of the spectrum ($k_x \geq \pi/\Delta x$) into resolved scales. The steeper the energy spectrum decrease around the cutoff wavenumber, the less aliasing is a problem. The spectrum alteration is then limited to the vicinity of the shortest resolved waves.

$$u = u_1 + u_2 \quad \text{with} \quad u_1 = Ae^{\mathrm{i}\,k_1 x} \quad \text{and} \quad u_2 = Ae^{\mathrm{i}\,k_2 x}, \tag{10.37}$$

then the advection term $u\partial u/\partial x$ generates a contribution of the form

$$A^2 \mathrm{i}\,(k_1 + k_2) e^{\mathrm{i}\,(k_1+k_2)x} \tag{10.38}$$

which introduces a new spectral component of higher wavenumber $k_1 + k_2$. Even if the two original waves are resolved by the grid, the newly created and shorter wave may be aliased and mistaken for a longer wave. This happens when $k_1 + k_2 > \pi/\Delta x$. The nonlinear advection thus creates an aliasing problem, which can seriously handicap calculations, especially if the aliasing is such that the newly created waves have a wavenumber identical to one of the original waves, k_1 for example. In this case we have a feedback loop in which component u_1 interacts with another one and, instead of generating a shorter wave as it ought, increases its own amplitude. The process is self-repeating and, before long, the amplitude of the self-amplifying wave will reach an untolerable level. This is known as *numerical instability*, which was first discovered by Phillips (1956).

Such a self-amplification occurs when the interaction of k_1 and k_2 satisfies the aliasing condition and the new wave is aliased back into one of the original wavenumbers (here k_1):

$$(k_1 + k_2) \geq \frac{\pi}{\Delta x} \quad \text{and} \quad \frac{2\pi}{\Delta x} - (k_1 + k_2) = k_1. \tag{10.39}$$

To avoid such a situation for any wavenumber resolved by the grid (*i.e.*, for all admissible values for k_2 varying between 0 and $\pi/\Delta x$), k_1 should not be allowed to take values in the interval $\pi/(2\Delta x)$ to $\pi/\Delta x$. This requirement is a little bit too strong since, if k_1 is not allowed to exceed $\pi/(2\Delta x)$, k_2, too, should not be allowed to do so. The highest permitted value for either k_1 or k_2 is then found by letting $k_1 = k_2$ in (10.39), and this yields $k_{\max} = 2\pi/(3\Delta x)$. In other words, if we are able to avoid all waves of wavelength shorter than $2\pi/k_{\max} = 3\Delta x$, nonlinear instability by aliasing will not occur. Disallowing these waves from the initial condition is not enough, however, because sooner or later, they will be generated by nonlinear interaction among the longer waves. The remedy is to eliminate the shorter waves as they are being generated, and this is accomplished by *filtering*.

Filtering is a form of dissipation that mimics physical dissipation but is designed to remove preferentially the undesirable waves, that is, only those on the shortest scales resolved by the numerical grid. This can be accomplished by the filters discussed in the following section. Other methods to address aliasing and nonlinear numerical instability related to the advection term will be encountered later in Section 16.6. Before concluding this chapter, we will also describe an entirely different approach, which avoids aliasing altogether by not using a grid at all. This method, known as *contour dynamics*, follows fluid parcels along their path of motion thus absorbing the advection terms in the material time derivative.

10.6 Filtering

We saw earlier that the leapfrog method generates spurious modes (flip-flop in time) and we just realized that spatial modes near the $2\Delta x$ cutoff ('saw-tooth' structure in space) are poorly reproduced and prone to aliasing. We further showed how nonlinearities can create aliasing problems around the $2\Delta x$ mode. Naturally, we would now like to remove these unwanted oscillations from the numerical solution. For the spatial saw-tooth structure, we already have at our disposal a method for eliminating shorter waves: physical diffusion. Physical diffusion in the model, however, may not always be sufficient to suppress or even control the $2\Delta x$ mode, and additional dissipation, of a numerical nature, becomes necessary. This is called *filtering*.

In this section, we concentrate on explicitly introduced filtering designed to damp short waves. Let us start with a discrete filter inspired by the physical diffusion operator:

$$\widehat{\tilde{c}}_i^n = \tilde{c}_i^n + \varkappa \underbrace{\left(\tilde{c}_{i+1}^n - 2\tilde{c}_i^n + \tilde{c}_{i-1}^n\right)}_{\simeq \Delta x^2 \frac{\partial^2 c}{\partial x^2}}, \tag{10.40}$$

in which the new (filtered) value $\widehat{\tilde{c}}_i^n$ is henceforth replacing the original (unfiltered) value $\tilde{c}_i^n$. The preceding formulation is equivalent to introducing a diffusion term with diffusivity $\varkappa \Delta x^2/\Delta t$, which enhances physical diffusion, if any.

The behavior of this filter can be analyzed with Fourier modes ($\exp(\mathrm{i}\, k_x i \Delta x)$), thus providing the 'amplification' factor, which in this case is actually a damping factor:

$$\varrho = 1 - 4\varkappa \sin^2\left(\frac{k_x \Delta x}{2}\right). \tag{10.41}$$

For well resolved waves, the amplification factor is close to unity (no change of amplitude), while for the $2\Delta x$ wave ($k_x = 2\pi/2\Delta x$), its value is $1 - 4\varkappa$. The value $\varkappa = 1/4$ therefore eliminates the shortest wave in a single pass of the filter. But intermediate wavelengths, are partially reduced at the same time, and a smaller value of $\varkappa$ is generally used in order not to dampen unnecessarily the intermediate scales of the solution. A compromise, therefore, needs to be reached between our desire to eliminate the $2\Delta x$ component while altering as least as possible the rest of the solution.

To alleviate such compromise, more selective filters can be implemented. These are of the biharmonic type and require a wider stencil (more grid points). For example,

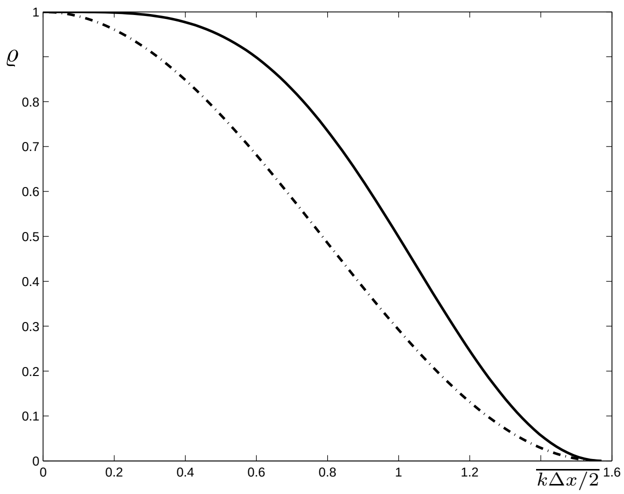

Figure 10-7 Damping factor as a function of wavelength for two different filters: regular diffusion [Eq. 10.40, dashed-dotted line] and biharmonic operator [Eq. 10.42, solid line], both for $\varkappa = 1/4$. Both filters eliminate the $2\Delta x$ mode completely ($\varrho = 0$), but the biharmonic filter is more scale selective in the sense that it damps less the intermediate-scale components (ϱ closer to unity for these).

$$\widetilde{c}_i^n = \tilde{c}_i^n + \frac{\varkappa}{4} \underbrace{\left(-\tilde{c}_{i+2}^n + 4\tilde{c}_{i-1}^n - 6\tilde{c}_i^n + 4\tilde{c}_{i+1}^n - \tilde{c}_{i+2}^n\right)}_{\simeq -\Delta x^4 \frac{\partial^4 \tilde{c}}{\partial x^4}} \tag{10.42}$$

leads to the more scale-selective damping factor

$$\varrho = 1 - \varkappa \left[4 \sin^2\left(\frac{k_x \Delta x}{2}\right) - \sin^2\left(\frac{2k_x \Delta x}{2}\right)\right]. \tag{10.43}$$

The difference in the case $\varkappa = 1/4$ is illustrated in Figure 10-7. Both diffusion-like and biharmonic filters [(10.40) and (10.42), respectively] eliminate the $2\Delta x$ mode with the same value of $\varkappa$. Figure 10-7 also shows that components of intermediate scales are less affected by the biharmonic filter than by the diffusion-like filter. The biharmonic filter, however, may introduce non monotonic behavior because there are negative coefficients in its stencil (10.42).

As for the diffusion-like filter, the biharmonic filter is sometimes written as an additional term of the form $-\mathcal{B}\partial^4\tilde{c}/\partial x^4$ in the undiscretized model equations, with $\mathcal{B} = \varkappa\Delta x^4/(4\Delta t)$. The approach can, of course, be extended to ever larger stencils with increased scale selectivity but at the cost of additional computations.

It should be noted that the coefficients used in the filters are depending on the grid spacing and time step, whereas physical parameters do not, unless they parameterize sub-grid scale effects. In the latter case, the grid size can be involved in the parameterization, as seen in Section 4.2. We should, however, not confuse the different concepts: The physical molecular diffusion, the standard micro-turbulent (eddy) diffusion, sub-grid scale diffusion introduced to parameterize mixing at scales longer than turbulent motions yet shorter than the grid spacing, diffusion associated with explicit filtering (the subject of the present section), and, finally, numerical diffusion caused by the numerical scheme (totally uncoded). It is unfortunately not always clearly stated in model applications which type of diffusion is being referenced when the authors mention their model's diffusion parameters.

For filtering in time, we can adopt the same filtering technique. Because the spatial filter replaces the model values by a filtered version obtained via (10.40), one way of eliminating the flip-flop mode is:

$$\widehat{c}^n = \tilde{c}^n + \varkappa \left(\tilde{c}^{n+1} - 2\tilde{c}^n + \tilde{c}^{n-1} \right). \tag{10.44}$$

This, however, is not very practical since it requires that past values of $\tilde{c}$ be stored for later filtering. Note also how filtering at time level n must wait until values have been computed at time level $n+1$. This does avoid the nonlinear interactions of the spurious mode with the physical modes. It is better, therefore, to blend the filtering with time stepping, by replacing the unfiltered solution by the filtered one as soon as it becomes available. Suppose for example that we have a new value of $\tilde{c}^{n+1}$ obtained with the leapfrog scheme,

$$\tilde{c}^{n+1} = \widehat{c}^{n-1} + 2\Delta t\, Q(t, \tilde{c}^n), \tag{10.45}$$

with the usual source term Q regrouping all spatial operators. We can then filter $\tilde{c}^n$ with

$$\widehat{c}^n = \tilde{c}^n + \varkappa \left(\tilde{c}^{n+1} - 2\tilde{c}^n + \widehat{c}^{n-1} \right), \tag{10.46}$$

and immediately store it in the array holding $\tilde{c}^n$. This is why $\widehat{c}^{n-1}$ appears in the filtering and leapfrog step instead of $\tilde{c}^{n-1}$ because the filtered value has already superseded the original one. This filter, known as *Asselin filter* (Asselin, 1972), is commonly used in models with leapfrog time discretization.

In order not to filter excessively, small values of $\varkappa$ can be used. Alternatively, the filter can be applied only intermittently or with varying intensity $\varkappa$.

More selective filters in time can be inspired by the spatial filter (10.42), but these would require the storage of additional intermediate values of the state vector because the filter involves more time levels (five in the biharmonic case), while the leapfrog scheme itself only requires that only three levels be stored.

Other filters exist, some of them based on intermittent re-initialization of the leapfrog time integration by simple Euler steps, but all of them should be applied with caution because they always filter part of the physical solution or alter the truncation error.

10.7 Contour dynamics

The preceding stability analysis and aliasing problem gives us a nice opportunity to introduce yet another numerical method, the family of so-called *boundary element* methods. This method was first applied to vortex calculations by Norman Zabusky[2] (Zabusky *et al.*, 1979). To illustrate the approach, we start from the simple task of retrieving the velocity field from a known vorticity distribution in two dimensions. The vorticity is related to the velocity

For a localized vortex of vorticity ω, the calculation of the velocity field in an infinite domain without boundary conditions can be obtained from the Stokes theorem:

$$\frac{\partial v}{\partial x} - \frac{\partial u}{\partial y} = \omega \tag{10.47}$$

[2]See his biography at the end of this chapter.

where symmetry considerations directly yield a particular form of the circulation Γ:

$$2\pi r\, dv_\theta = d\Gamma = \omega\, ds, \quad r^2 = (x-x')^2 + (y-y')^2 \tag{10.48}$$

where v_θ is perpendicular to the line joining the vortex to the point under consideration (left part of Figure 10-8). In vectorial notation, the differential velocity associated with a differential surface ds of vorticity ω is

$$d\mathbf{u} = \frac{1}{2\pi}\frac{\omega}{r}\frac{\mathbf{k}\times(\mathbf{x}-\mathbf{x}')}{r}\, ds \tag{10.49}$$

which we can then integrate over a space-dependent collection of vortices $\omega(x,y)$ to obtain

$$\mathbf{u}(x,y) = \frac{1}{2\pi}\int\int \omega(x',y')\,\frac{\mathbf{k}\times(\mathbf{x}-\mathbf{x}')}{r^2}\; dx'dy' \; . \tag{10.50}$$

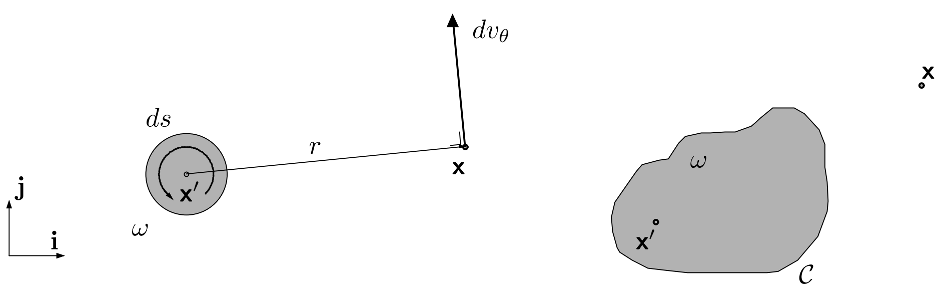

Figure 10-8 An infinitesimal vortex patch allows to calculate the associated velocity field dv_θ. The integration over a surface of constant vorticity limited by the contour $\mathcal{C}$ (right part), allows for the calculation of the velocity field of the vortex patch in an infinite domain.

This provides the velocity field as a function of the vorticity distribution, up to an irrotational velocity field. In an infinite domain and with no boundary condition, the latter is zero. Suppose for now that we have a single patch of constant vorticity so that

$$u(x,y) = \frac{\omega}{2\pi}\int\int \frac{-(y-y')}{(x-x')^2+(y-y')^2}\, dx'\, dy' \tag{10.51a}$$

$$v(x,y) = \frac{\omega}{2\pi}\int\int \frac{(x-x')}{(x-x')^2+(y-y')^2}\, dx'\, dy' \tag{10.51b}$$

where the surface integral is performed over the vorticity patch delimited by its contour $\mathcal{C}$. Noting that integrands are derivatives of

$$\phi = \ln\left[\frac{(x-x')^2+(y-y')^2}{L^2}\right] \tag{10.52}$$

we can reformulate the velocity components as

$$u(x,y) = \frac{\omega}{4\pi}\int\int \frac{\partial\phi}{\partial y'}\, dx'dy' \quad = -\frac{\omega}{4\pi}\oint_{\mathcal{C}} \phi\, dx' \tag{10.53a}$$

$$v(x,y) = \frac{\omega}{4\pi}\int\int -\frac{\partial\phi}{\partial x'}\, dx'dy' = -\frac{\omega}{4\pi}\oint_{\mathcal{C}} \phi\, dy' \; , \tag{10.53b}$$

where we used Green's theorem, the generalization of integration by parts to a closed surface of contour $\mathcal{C}$ (*e.g.*, Riley *et al.* 1997). Finally, the velocity field associated with a patch of uniform vorticity can be calculated at any point as

$$\mathbf{u}(x,y) = -\frac{\omega}{4\pi} \oint_{\mathcal{C}} \ln\left[\frac{(x-x')^2+(y-y')^2}{L^2}\right] d\mathbf{x}' \; . \tag{10.54}$$

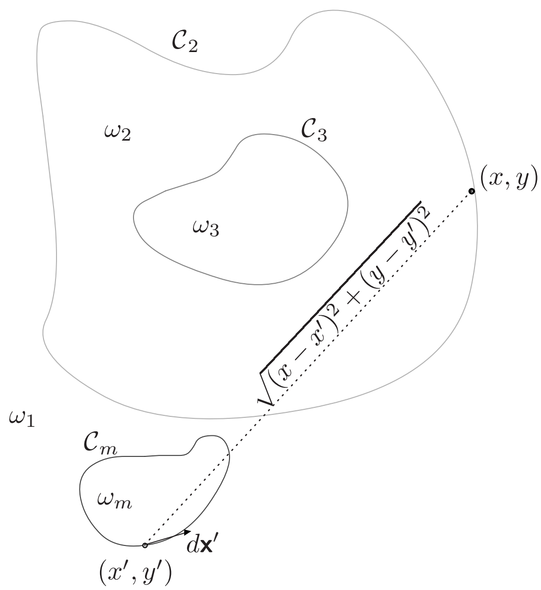

Figure 10-9 When several contours are involved in the velocity determination, contour integrals must be summed up and the relevant quantity to take into account on a contour is the vorticity jump $\delta\omega_k$ across the contour, in the depicted case $\omega_3 - \omega_2$ for contour $\mathcal{C}_3$.

When several vorticity patches are present, all we have to do is to sum up the different contributions of each patch with a slight difficulty if a patch is contained within another one as ω_3 vorticity within the ω_2 vorticity patch of Figure 10-9. For the "outside" patch, the contour integration has two contributions, one on the outside contour $\mathcal{C}_2$ in in the counterclockwise direction with the patch to the left and a second one, also with the patch to the left and hence in clockwise direction in its inner contour $\mathcal{C}_3$. This is the same as an integration in the direction with changed sign of the integral value. Since on the same contour, the inner vorticity patch will we integrated in counterclockwise direction and vorticity ω_3, all we have to do is to integrate once and use the jump of vorticity $\delta\omega_k$ across the contours (from outside to inside) instead of the vorticity inside the contour. Finally in any point (x, y) the velocity field takes the form

$$\mathbf{u}(x,y) \;=\; -\frac{1}{4\pi}\sum_k \delta\omega_k \oint_{\mathcal{C}_k} \ln\left[\frac{(x-x')^2+(y-y')^2}{L^2}\right] d\mathbf{x}' \tag{10.55}$$

where $\delta\omega_k$ is the vorticity jump across the contour $\mathcal{C}_k$ (inside value minus outside value) and where the sum is performed over all K contours.

Up to now we only designed a diagnostic tool to retrieve the velocity field from a given distribution of vorticity patches. To predict the evolution of these patches, we now have to

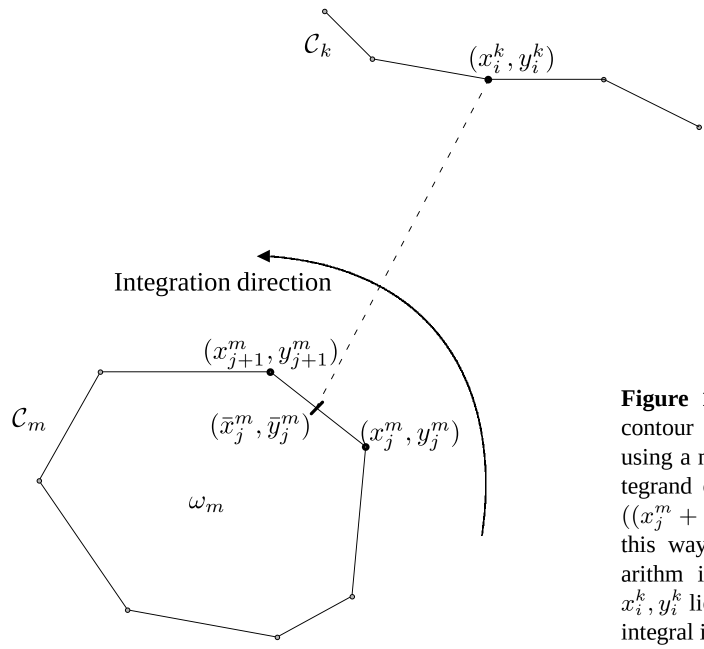

Figure 10-10 The discretization of contour integrals can be achieved by using a mid-point evaluation of the integrand on the contour m at location $((x_j^m + x_{j+1}^m)/2, (y_j^m + y_{j+1}^m)/2)$. In this way, the singularity of the logarithm is avoided even if the point x_i^k, y_i^k lies on the contour on which the integral is calculated.

solve the governing equation for vorticity. In the absence of any friction or vorticity generating processes, vorticity is conserved and simply advected by the current. For points within a given vortex patch, they will remain within this patch and not change their vorticity so that all we have to do is to predict the evolution of the *boundary* of each patch, *i.e.*, the contours. Therefore we simply have to move the contour points with their velocity, *i.e.*, the velocity field on the contour calculated from (10.55), hence the name *contour dynamics*. In practice, integrations can rarely be performed analytically and numerical methods are again called for. The integral discretization has to deal with a singularity if the point (x, y) lies on the contour over which integration takes place. A simple way to avoid numerical problems associated with it, is the use a staggered approach for the integration, or stated differently, the use of a mid-point integration in which the integrand is evaluated at mid-distance between points i and $i+1$ (Figure 10-10): For point i on contour k located in (x_i^k, y_i^k) integrals related to contour $\mathcal{C}_m$ are approximated as

$$I_m(x_i^k, y_i^k) = \sum_{j=1}^{N} \ln \left[\frac{(x_i^k - \bar{x}_j^m)^2 + (y_i^k - \bar{y}_j^m)^2}{L^2} \right] (x_{j+1}^m - x_j^m)$$

$$J_m(x_i^k, y_i^k) = \sum_{j=1}^{N} \ln \left[\frac{(x_i^k - \bar{x}_j^m)^2 + (y_i^k - \bar{y}_j^m)^2}{L^2} \right] (y_{j+1}^m - y_j^m)$$

$$\bar{x}_j^m = \frac{x_{j+1}^m + x_j^m}{2}, \quad \bar{y}_j^m = \frac{y_{j+1}^m + y_j^m}{2}$$

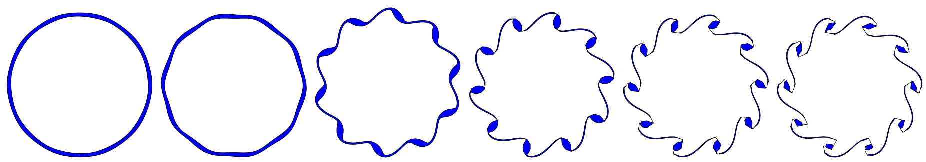

Figure 10-11 Evolution of a thin layer of uniform vorticity simulated with contour dynamics.

where the sum is done over N segments[3] defining each contour and where we defined for convenience $x^m_{N+1} = x_1$ and $y^m_{N+1} = y_1$. Even when m is equal to k (*i.e.*, we integrate over the contour on which lies the point where velocity is to be calculated) the singularity of the logarithm is avoided as long as all contour points (x_j, y_j) are different. Finally, once individual integrals are estimated, the velocity components can be assessed by summing over all contours:

$$u(x_i^k, y_i^k) = -\frac{1}{4\pi}\sum_m \delta\omega_m \, I_m(x_i^k, y_i^k)$$
$$v(x_i^k, y_i^k) = -\frac{1}{4\pi}\sum_m \delta\omega_m \, J_m(x_i^k, y_i^k)$$

Then each point on all contours can be moved with the Lagrangian velocity, deforming the contour:

$$\frac{dx_i^k}{dt} = u(x_i^k, y_i^k) \tag{10.56a}$$
$$\frac{dy_i^k}{dt} = v(x_i^k, y_i^k). \tag{10.56b}$$

The time integration can be performed by any method of chapter 2, leading to Lagrangian displacements of discrete points of the contours (see also Lagrangian approach of Section 12.7).

The simple numerical integration method outlined here is easily implemented (see for example `contourdyn.m`). To check the method, we can apply it to a case akin to the shear layer instability of Section 10.4, and simulate the evolution of thin small layer of uniform vorticity (Figure 10-11). The method can also be used to study the evolution and interaction of inviscid vortex patches in an infinite domain (Figure 10-12) with the distinct advantage that no aliasing is present and that in principle no numerical dissipation needs to be added to stabilize the nonlinear advection. In reality, some dissipation will be needed because the advection, leading to tearing and shearing of the eddies, can lead to the creation of filaments becoming finer and finer when there is no viscosity. Because the discretization uses only a finite number of fluid parcels on the contour, the contours cannot be followed down to the smallest scales and eventually some special treatment is needed when calculation points are getting too close and make other regions of the contour void of calculation points. Then moving or adding new points is required. The techniques to deal with these problems are

[3]the number of segments per contour could of course be chosen different in which case $N = N_m$.

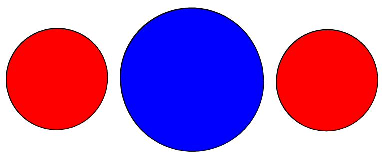

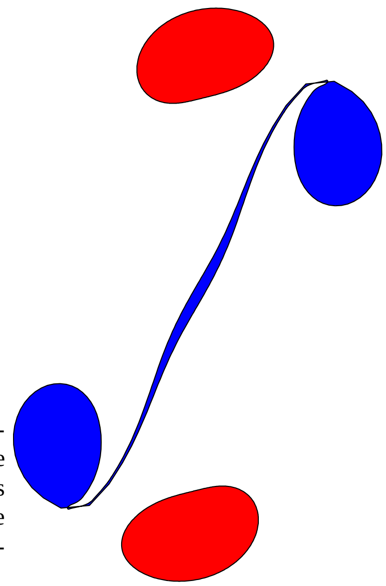

Figure 10-12 Two positive vorticity patches flanking a vortex of opposite vorticity and twice as large in size (left side). Depending on the distances between the initial vortices, several outcomes are possible. One of them is vortex breakup and separation of vortex pairs (right panel).

rightfully called *contour surgery* and where optimized by Dritschel (1988). This eliminates some of the smallest structures and amounts to add some dissipation.

To conclude the section we can observe that we replaced a two-dimensional problem of Eulerian vorticity evolution with the problem of moving contours, which are one-dimensional structures. This reduces the complexity, but we must realize that the numerical cost of the methods still behaves as K^2N^2 for K contours of N segments, since for each of the KN discrete points, an integration/sum over all other points must be performed. This is less than the cost of a two-dimensional Eulerian model in which a Poisson equation must be solved (see Section 16.6), but the reduction of complexity was possible only because we exploited the fact that there were no boundary conditions and that vorticity was constant between contours. For a continuous vorticity distribution without boundaries, we can still apply the approach by discretizing the vorticity levels (see Numerical Exercise 10-5), analogous to what we will do for layered models where density will be discretized (Chapter 12). Also generalizations to stratified systems and more complicated governing equations are possible (*e.g.*, Mohebalhojeh and Dritschel, 2004).

Analytical Problems

10-1. Show that the variable a introduced in (10.18) is the amplitude of the meridional displacement, as claimed in the footnote.

10-2. What can you say of the stability properties of the following flow fields on the f–plane?

$$\bar{u}(y) = U \left(1 - \frac{y^2}{L^2}\right) \qquad (-L \leq y \leq +L) \tag{10.57}$$

$$\bar{u}(y) = U \sin \frac{\pi y}{L} \qquad (0 \leq y \leq L) \tag{10.58}$$

$$\bar{u}(y) = U \cos \frac{\pi y}{L} \qquad (0 \leq y \leq L) \tag{10.59}$$

$$\bar{u}(y) = U \tanh\left(\frac{y}{L}\right) \qquad (-\infty < y < +\infty). \tag{10.60}$$

10-3. A zonal shear flow with velocity profile

$$\bar{u}(y) = U \left(\frac{y}{L} - 3\,\frac{y^3}{L^3}\right)$$

occupies the channel $-L \leq y \leq +L$ on the beta plane. Show that if $|U|$ is less than $\beta_0 L^2/12$, this flow is stable.

10-4. The atmospheric jet stream is a wandering zonal flow of the upper troposphere, which plays a central role in mid-latitude weather. If we ignore the variations in air density, we can model the average jet stream as a purely zonal flow, independent of height and varying meridionally according to

$$\bar{u}(y) = U \exp\left(-\frac{y^2}{2L^2}\right),$$

in which the constants U and L, characteristics of the speed and width, are taken as 40 m/s and 570 km, respectively. The jet center ($y = 0$) is at 45°N where $\beta_0 = 1.61 \times 10^{-11}$ m^{-1}s^{-1}. Is the jet stream unstable to zonally propagating waves?

10-5. Verify the semicircle theorem for the particular shear flow studied in Section 10.4. In other words, prove that $|c_r| < U$ for stable waves and $c_i < U$ for unstable waves. Also, prove that the wavelength leading to the highest growth rate, kc_i, is $15.77L$, as stated in the text.

10-6. Derive the dispersion relation and establish a stability threshold for the jet-like profile of Figure 10-13.

Numerical Exercises

10-1. Redo the analysis of nonlinear aliasing for a cubic term like $du/dt = -u^3$ in the governing equation for u. Why do you think aliasing is less of a concern in this particular case?

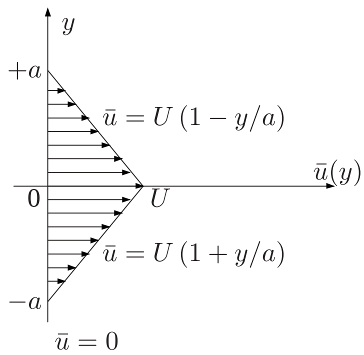

Figure 10-13 A jet-like profile (for Problem 10-6).

10-2. An elliptic vortex patch with uniform vorticity inside and zero vorticity outside is called a *Kirchhoff vortex*. Use `contourdyn.m` with `itest=1` to study the evolution of Kirchhoff vortices of aspect ratios 2:1 and 4:1. What do you observe? Implement another time-integration scheme (among which the explicit Euler scheme) and analyze how it behaves with a circular eddy. *Hint*: Love (1893) provides a stability analysis of the Kirchhoff vortex.

10-3. Experiment with `contourdyn.m` with test case `itest=4` in which two identical eddies are placed at various distances. Start with `dist=1.4` and then try the value `1.1`. What happens? Which numerical parameters would you adapt to improve the numerical simulation? Try it!

10-4. Simulate the eddy separation shown in Figure 10-12 using `contourdyn.m`.

10-5. Discretize a circular eddy with vorticity varying linearly from zero at the rim to a maximum at the center by using K different vorticity values in concentric annuli. Then simulate its evolution with $K = 3$.

10-6. Verify your findings of Analytical Problem 10-6 by adapting `shearedflow.m` to simulate the evolution of the most unstable periodic perturbation.

10-7. Adapt `shearedflow.m` to investigate the so-called *Bickley jet* with profile given by

$$\bar{u}(y) \;=\; U\,\mathrm{sech}^2\left(\frac{y}{L}\right) \qquad (-\infty \;<\; y \;<\; +\infty). \tag{10.61}$$

Louis Norberg Howard
1929 –

Applied mathematician and fluid dynamicist, Louis Norberg Howard has made numerous contributions to hydrodynamic stability and rotating flow. His famous semicircle theorem was published in 1961 as a short note extending some contemporary work by John Miles. Howard is also well known for his theoretical and experimental studies of natural convection. With Willem Malkus, he devised a simple waterwheel model of convection that, like real convection, can exhibit resting, steady, periodic and chaotic behaviors. Howard has been a regular lecturer at the annual Geophysical Fluid Dynamics Summer Institute at the Woods Hole Oceanographic Institution, where his audiences were much impressed by the breadth of his knowledge and the clarity of his explanations. (*Photo credit: L. N. Howard*)

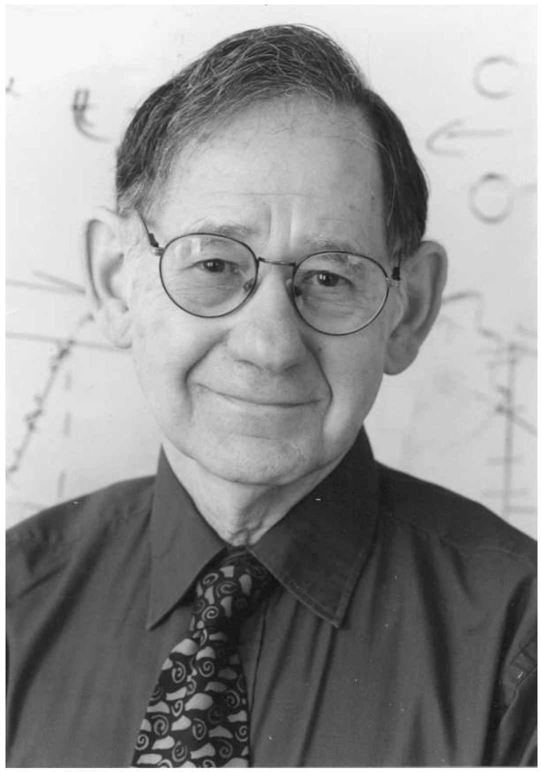

Norman J. Zabusky
19xx –

Invented the method of contour dynamics and made numerous other contributions to computational fluid dynamics. Studied vorticity dynamics in highly turbulent flows. ()

Part III

Stratification Effects

Chapter 11

Stratification

(October 18, 2006) **SUMMARY**: After having studied the effects of rotation in homogeneous fluids, we now turn our attention toward the other distinctive feature of geophysical fluid dynamics, namely, stratification. A basic measure of stratification, the Brunt–Väisälä frequency, is introduced, and the accompanying dimensionless ratio, the Froude number, is defined and given a physical interpretation. The numerical part deals with the handling of unstable stratification in model simulations.

11.1 Introduction

As Chapter 1 stated, problems in geophysical fluid dynamics concern fluid motions with one or both of two attributes, namely, ambient rotation and stratification. In the preceding chapters, attention was devoted exclusively to the effects of rotation, and stratification was avoided by the systematic assumption of a homogeneous fluid. We noted that rotation imparts to the fluid a strong tendency to behave in a columnar fashion — to be vertically rigid.

By contrast, a stratified fluid, consisting of fluid parcels of various densities, will tend under gravity to arrange itself so that the higher densities are found below lower densities. This vertical layering introduces an obvious gradient of properties in the vertical direction, which affects — among other things — the velocity field. Hence, the vertical rigidity induced by the effects of rotation will be attenuated by the presence of stratification. In return, the tendency of denser fluid to lie below lighter fluid imparts a horizontal rigidity to the system.

Because stratification induces a certain degree of decoupling between the various fluid masses (those of different densities), stratified systems typically contain more degrees of freedom than homogeneous systems, and we anticipate that the presence of stratification permits the existence of additional types of motions. When the stratification is mostly vertical (*e.g.*, layers of various densities stacked on top of one another), gravity waves can be sustained internally (Chapter 13). When the stratification also has a horizontal component, additional waves can be permitted, and, if these grow at the expense of the basic potential energy available in the system, instabilities may arise (Chapter 17).

11.2 Static stability

Let us first consider a fluid in static equilibrium. Lack of motion can occur only in the absence of horizontal forces and thus in the presence of horizontal homogeneity. Stratification is then purely vertical (Figure 11-1).

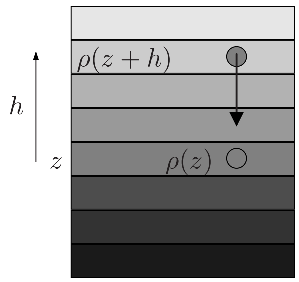

Figure 11-1 When an incompressible fluid parcel of density $\rho(z)$ is vertically displaced from level z to level $z+h$ in a stratified environment, a buoyancy force appears because of the density difference $\rho(z)-\rho(z+h)$ between the particle and the ambient fluid.

It is intuitively obvious that if the heavier fluid parcels are found below the lighter fluid parcels, the fluid is stable, whereas if heavier parcels lie above lighter ones, the system is apt to overturn, and the fluid is unstable. Let us now verify this intuition. Take a fluid parcel at a height z above a certain reference level, where the density is $\rho(z)$, and displace it vertically to the higher level $z+h$, where the ambient density is $\rho(z+h)$ (Figure 11-1). If the fluid is incompressible, our displaced parcel retains its former density despite a slight pressure change, and at that new level feels a buoyancy force equal to

$$g\,[\rho(z+h)\;-\;\rho(z)]\,V,$$

where V is the volume of the parcel. As it is written, this force is positive if it is directed upward. Newton's law (mass times acceleration equals force) yields

$$\rho(z)\,V\,\frac{d^2h}{dt^2}\;=\;g\,[\rho(z+h)\;-\;\rho(z)]\,V. \tag{11.1}$$

Now, geophysical fluids are generally only weakly stratified; the density variations, although sufficient to drive or affect motions, are nonetheless relatively small compared to the average or reference density of the fluid. This remark was the essence of the Boussinesq approximation (Section 3.7). In the present case, this fact allows us to replace $\rho(z)$ on the left-hand side of (11.1) by the reference ρ_0 and to use a Taylor expansion to approximate the density difference on the right by

$$\rho(z+h)\;-\;\rho(z)\;\simeq\;\frac{d\rho}{dz}\,h.$$

After a division by V, equation (11.1) reduces to

$$\frac{d^2h}{dt^2}\;-\;\frac{g}{\rho_0}\,\frac{d\rho}{dz}\,h\;=\;0, \tag{11.2}$$

which shows that two cases can arise. The coefficient $-(g/\rho_0)d\rho/dz$ is either positive or negative. If it is positive ($d\rho/dz\;<\;0$, corresponding to a fluid with the greater densities below the lesser densities), we can define the quantity N^2 as

$$N^2 = -\frac{g}{\rho_0}\frac{d\rho}{dz}, \tag{11.3}$$

and the solution to the equation has an oscillatory character, with frequency N. Physically, this means that, when displaced upward, the parcel is heavier than its surroundings, feels a downward recalling force, falls down, and, in the process, acquires a vertical velocity; upon reaching its original level the particle's inertia causes it to go further downward and to become surrounded by heavier fluid. The parcel, now buoyant, is recalled upward, and oscillations persist about the equilibrium level. The quantity N, defined by the square root of (11.3), provides the frequency of the oscillation and can thus be called the *stratification frequency*. It goes more commonly, however, by the name of Brunt–Väisälä frequency, in recognition of the two scientists who were the first to highlight the importance of this frequency in stratified fluids. (See their biographies at the end of this chapter.)

If the coefficient in equation (11.1) is negative (*i.e.*, $d\rho/dz > 0$, corresponding to a top-heavy fluid configuration), the solution exhibits exponential growth, a sure sign of instability. The parcel displaced upward is surrounded by heavier fluid, finds itself buoyant, and moves farther and farther away from its initial position. Obviously, small perturbations will ensure not only that the single displaced parcel will depart from its initial position, but that all other fluid parcels will likewise participate in a general overturning of the fluid until it is finally stabilized, with the lighter fluid lying above the heavier fluid. If, however, a permanent destabilization is forced onto the fluid, such as by heating from below or cooling from above, the fluid will remain in constant agitation, a process called *convection*.

In this and the following chapters, we will restrict our attention to stably stratified fluids, for which the stratification frequency, N, defined from (11.3), exists.

11.3 A note on atmospheric stratification

In a compressible fluid, such as the air of our planetary atmosphere, density can change in one of two ways: by pressure changes or by internal-energy changes. In the first case, a pressure variation resulting in no heat exchange (*i.e.*, an adiabatic compression or dilation) is accompanied by both density and temperature variations: All three quantities increase (or decrease) simultaneously, though not in equal proportions. If the fluid is made of fluid parcels all having the same heat content, the lower parcels, feeling the weight of those above them, will be more compressed than those in the upper levels, and the system will appear stratified, with the denser and warmer fluid underlying the lighter, colder fluid. But such stratification cannot be dynamically relevant, for if parcels are interchanged adiabatically, they adjust their density and temperature according to the local pressure, and the system is left unchanged.

In contrast, internal-energy changes are dynamically important. In the atmosphere, such variations occur because of a heat flux (such as heating in the tropics and cooling at high latitudes, or according to the diurnal cycle) or because of the variations in air composition (such as water vapor). Such variations among fluid parcels do remain despite adiabatic compression/dilation and cause density differences that drive motions. It is thus imperative to distinguish, in a compressible fluid, the density variations that are dynamically relevant from those that are not. Such separation of density variations leads to the concept of potential density.

First, we consider a neutral (adiabatic) atmosphere – that is, one consisting of all air parcels having the same internal energy. Further, let us assume that the air, a mixture of various gases, behaves as a single perfect gas. Under these assumptions, we can write the equation of state and the adiabatic conservation law:

$$p = R\rho T, \tag{11.4}$$

$$\frac{p}{p_0} = \left(\frac{\rho}{\rho_0}\right)^{\gamma}, \tag{11.5}$$

where p, ρ, and T are, respectively, the pressure, density and absolute temperature (in contrast with the preceding chapters, the variables p and ρ here denote the full pressure and density); $R = C_p - C_v$ and $\gamma = C_p/C_v$ are the constants of a perfect gas. Finally, p_0 and ρ_0 are reference pressure and density characterizing the level of internal energy of the fluid; the corresponding reference temperature T_0 is obtained from (11.4) — that is, $T_0 = p_0/R\rho_0$. Expressing both pressure and density in terms of the temperature, we obtain

$$\frac{p}{p_0} = \left(\frac{T}{T_0}\right)^{\gamma/(\gamma-1)} \tag{11.6}$$

$$\frac{\rho}{\rho_0} = \left(\frac{T}{T_0}\right)^{1/(\gamma-1)}. \tag{11.7}$$

Without motion, the atmosphere is in static equilibrium, which requires hydrostatic balance:

$$\frac{dp}{dz} = -\rho g. \tag{11.8}$$

Elimination of p and ρ by use of (11.6) and (11.7) yields a single equation for the temperature:

$$\begin{aligned} \frac{dT}{dz} &= -\frac{\gamma-1}{\gamma}\,\frac{g}{R} \\ &= -\frac{g}{C_p}\,. \end{aligned} \tag{11.9}$$

In the derivation, it was assumed that p_0, ρ_0, and thus T_0 are not dependent on z, in agreement with our premise that the atmosphere is composed of parcels with identical internal-energy contents. Equation (11.9) states that the temperature in such atmosphere must decrease with increasing height at the uniform rate $g/C_p \simeq 10$ K/km. This gradient is called the *adiabatic lapse rate*. Physically, lower parcels are under greater pressure than higher parcels and thus have higher densities and temperatures. This explains why the air temperature is lower on mountain tops than at in the valleys.

It almost goes without saying that the departures from this adiabatic lapse rate – and not the total temperature gradients — are to be considered in the study of atmospheric motions.

We can demonstrate this clearly by redoing here, with a compressible fluid, the analysis of a vertical displacement performed in the previous section with an incompressible fluid. Consider a vertically stratified gas with pressure, density, and temperature, p, ρ, and T, varying with height z but not necessarily according to (11.9); that is, the heat content in the fluid is not uniform. The fluid is in static equilibrium so that equation (11.8) is satisfied. Consider now a parcel at height z; its properties are $p(z)$, $\rho(z)$, and $T(z)$. Imagine then that this fluid parcel is displaced adiabatically upward over a small distance h. According to the hydrostatic equation, this results in a pressure change $\delta p = -\rho g h$, which causes density and temperature changes given by the adiabatic constraints (11.5) and (11.6): $\delta\rho = -\rho g h/\gamma RT$ and $\delta T = -(\gamma-1)gh/\gamma R$. Thus, the new density is $\rho' = \rho + \delta\rho = \rho - \rho g h/\gamma RT$. But, at that new level, the ambient density is given by the stratification: $\rho(z+h) \simeq \rho(z) + (d\rho/dz)h$. The displaced parcel experiences an upward force equal to the buoyancy force, which per volume is

$$
\begin{aligned}
F &= g\left[\rho_{\text{ambient}} - \rho_{\text{parcel}}\right] \\
&= g\left[\rho(z+h) - \rho'\right] \\
&\simeq g\left(\frac{d\rho}{dz} + \frac{\rho g}{\gamma RT}\right)h.
\end{aligned}
$$

In terms of the temperature, this force is

$$F \simeq -\frac{\rho g}{T}\left(\frac{dT}{dz} + \frac{g}{C_p}\right)h.$$

If

$$
\begin{aligned}
N^2 &= -\frac{g}{\rho}\left(\frac{d\rho}{dz} + \frac{\rho g}{\gamma RT}\right) && (11.10) \\
&= \frac{g}{T}\left(\frac{dT}{dz} + \frac{g}{C_p}\right) && (11.11)
\end{aligned}
$$

is a positive quantity, this force recalls the particle towards its initial level, and the stratification is stable. As we can clearly see, the relevant quantity is not the total temperature gradient but the departure from the adiabatic gradient g/C_p. As in the previous case of a stably stratified incompressible fluid, the quantity N is the frequency of vertical oscillations. It is called the stratification, or Brunt–Väisälä, frequency.

In order to avoid the systematic subtraction of the adiabatic gradient from the temperature gradient, the concept of potential temperature is introduced. The *potential temperature*, denoted by θ, is defined as the temperature that the parcel would have if it were brought adiabatically to a given reference pressure. (In the atmosphere, this reference is usually taken as a nominal ground pressure of 1030 millibars = 1.03×10^5 N/m^2.) From (11.6), we have

$$\frac{p}{p_0} = \left(\frac{T}{\theta}\right)^{\gamma/(\gamma-1)}$$

and hence

$$\theta = T \left(\frac{p}{p_0}\right)^{-(\gamma-1)/\gamma}. \qquad (11.12)$$

The corresponding density is called the *potential density*, denoted σ:

$$\sigma = \rho \left(\frac{p}{p_0}\right)^{-1/\gamma}. \qquad (11.13)$$

The definition of the stratification frequency (11.11) takes the more compact form

$$N^2 = -\frac{g}{\sigma}\frac{d\sigma}{dz}. \qquad (11.14)$$

Comparison with the earlier definition, (11.3), immediately shows that the substitution of potential density for density allows us to treat compressible fluids as incompressible.

During daytime and above land, the lower atmosphere is typically heated from below by the warmer ground and is in a state of turbulent convection. The convective layer not only covers the entire region where the time-averaged gradient of potential temperature is negative, but it also penetrates into the region above where it is positive (Figure 11-2). Consequently, the sign of N^2 at a particular level is not unequivocally indicative of stability at that level. For this reason, Stull (1991) advocates the use of a non-local criterion to determine static stability. Those considerations apply equally well to the upper ocean under surface cooling.

JMB from $\Downarrow$

Benoit This chapter is very short compared to the others. I tried to find some numerics from other chapters that could fit here but was not successful (maybe you have some ideas). On the other hand, we could add a little more on static stability in the atmosphere:

- dry air: lapse rate with C_p of dry air
- humid, unsaturated air: mixture with water vapor (high C_p) hence apparent C_p of mixture is larger and lapse rate smaller
- saturated air: consendation liberates energy hence cooling due to expansion is reduced: even smaller lapse rate

JMB to $\Uparrow$ Hence situation of 11-3.

11.4 Convective adjustment

When static instability is present in the ocean or atmosphere, non-hydrostatic movements very rapidly restore stability through small columns of convection (*e.g.*, Marshall and Schott 1999). Such physical movements are not resolved by most models and parameterizations called *convection schemes* are introduced to remove static instability and to model the vertical motion and mixing associated with convection. Parameterization of the effect can be done trough additional terms in governing equations, typically through a strongly increased eddy viscosity and diffusivity whenever $N^2 \leq 0$ (*e.g.*, Cox, 1984; Marotzke, 1991). Other parameterizations are rather "algorithmical" tools working on rules such as the following

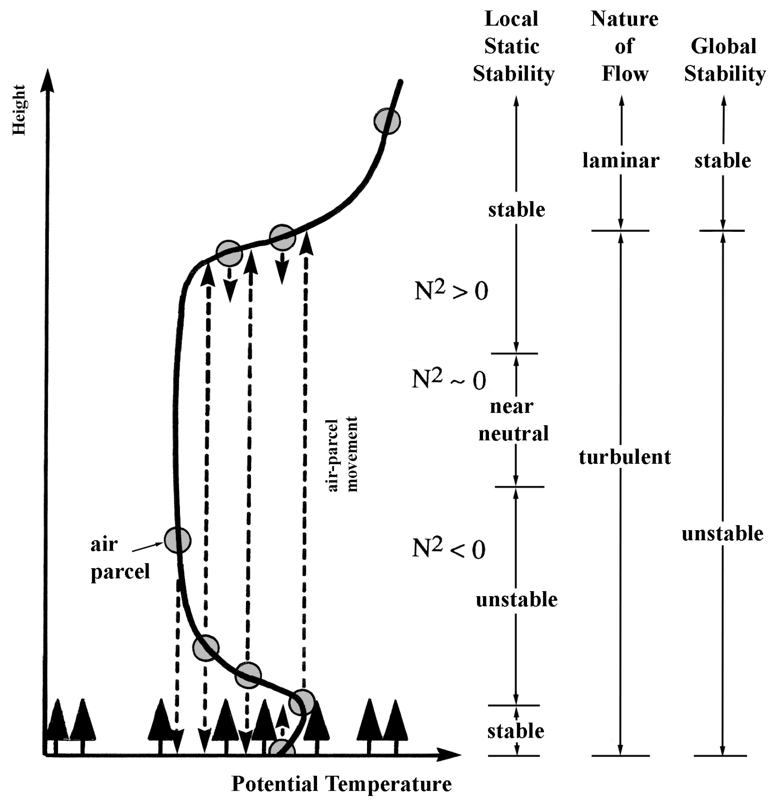

Figure 11-2 Typical profile of potential temperature in the lower atmosphere above warm ground. Heating from below destabilizes the air, generating convection and turbulence. Note how the convective layer extends not only over the region of negative N^2 but also slightly beyond, where N^2 is positive. Such a situation shows that a positive value of N^2 may not always be indicative of local stability. (From Stull, 1991.)

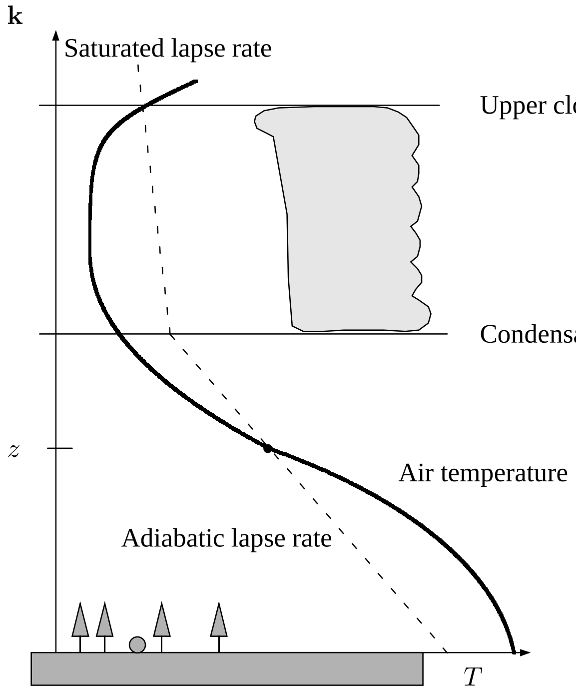

Figure 11-3 A fluid parcel located in z within an ambient temperature (solid line) is in an unstable situation. Parcels that move upward eventually reach their saturation level, condensation takes place and the lapse rate is decreased. If an inversion is present at higher levels, clouds extension is vertically limited.

```
While there is any negative $N^2$
   Loop over all layers
      If pot_density(layer_above) > pot_density(layer_below)
         Mix both layer
      end if
   end loop over all layers
end while
```

The mixing is then a volume-weighted mixing and was used in the first oceanic models (*e.g.*, Bryan, 1969; Cox, 1984) whenever a static instability occurred (Figure 11-4). Such mixing is however too strong in practice, because the model mixes over a complete horizontal grid box of size $\Delta x \Delta y$ while physical convection operates at smaller scales and mixes only part of the physical field contained within a grid box. Therefore, the numerical mixing can be partly replaced by a swapping of water masses, assuming convection carries part of the properties without alteration to their level of equilibrium (*e.g.*, Roussenov *et al.*. 2001). It is clear that some arbitrary choices are done here and require calibrations for real applications. In particular, changing the time step clearly changes the speed at which the column is mixed. For atmospheric conditions, the situation is even more complicated as it involves condensation, latent-heat release and precipitation during convective movements, so that the convection parameterizations involve adjustment of both temperature and moisture vertical structures (*e.g.*, Kuo 1974, Betts 1986).

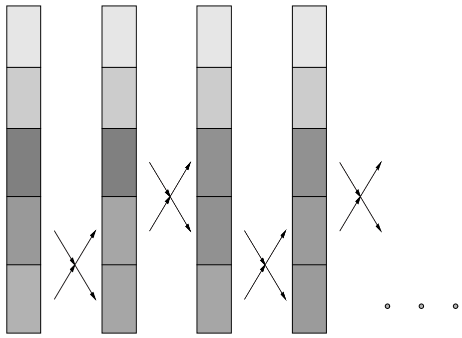

Figure 11-4 Illustration of the convective adjustment with a heating from below, where grid boxes that are statically unstable are mixed until the whole column is stable

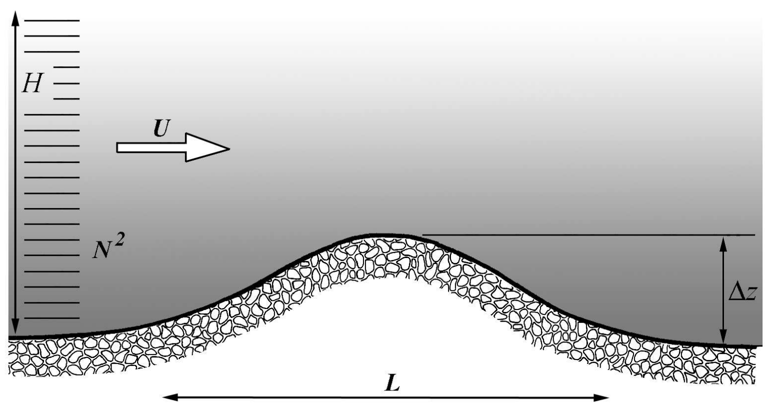

Figure 11-5 Situation in which a stratified flow encounters an obstacle, forcing some fluid parcels to move vertically against a buoyancy force.

11.5 The importance of stratification: The Froude number

It was established in Section 1.5 that rotational effects are dynamically important when the Rossby number is on the order of unity or less. This number compares the distance traveled horizontally by a fluid parcel during one revolution ($\sim U/\Omega$) with the length scale over which the motions take place (L). Rotational effects are important when the former is less than the latter. By analogy, we may ask whether there exists a similar number measuring the importance of the stratification. From the remarks in the preceding sections, we can anticipate that the stratification frequency, N, and the height scale, H, of a stratified fluid will play roles similar to those of Ω and L in rotating fluids.

To illustrate how such a dimensionless number can be derived, let us consider a stratified fluid of thickness H and stratification frequency N flowing horizontally at a speed U over an obstacle of length L and height Δz (Figure 11-5). We can think of a wind in the lower atmosphere blowing over a mountain range. The presence of the obstacle forces some of the fluid to be displaced vertically and, hence, requires some supply of gravitational energy. Stratification will act to restrict or minimize such vertical displacements in some way, forcing the flow to pass around rather than over the obstacle. The greater the restriction, the greater the importance of stratification.

The time passed in the vicinity of the obstacle is approximately the time spent by a fluid parcel to cover the horizontal distance L at the speed U, that is, $T = L/U$. To climb a height of Δz, the fluid needs to acquire a vertical velocity on the order of $W = \Delta z/T = U\Delta z/L$. The vertical displacement is on the order of the height of the obstacle, causes in the presence of stratification $\rho(z)$ a density perturbation on the order of

$$\begin{aligned} \Delta\rho &= \left|\frac{d\bar{\rho}}{dz}\right| \Delta z \\ &= \frac{\rho_0 N^2}{g}\,\Delta z, \end{aligned} \tag{11.15}$$

where $\bar{\rho}(z)$ is the fluid's vertical density profile upstream. In turn, this density variation gives rise to a pressure disturbance that scales, via the hydrostatic balance, as

$$\begin{aligned} \Delta P &= gH\Delta\rho \\ &= \rho_0 N^2 H \Delta z. \end{aligned} \tag{11.16}$$

By virtue of the balance of forces in the horizontal, the pressure-gradient force must be accompanied by a change in fluid velocity [$u\partial u/\partial x + v\partial u/\partial y \sim (1/\rho_0)\partial p/\partial x$]:

$$\begin{aligned} \frac{U^2}{L} &= \frac{\Delta P}{\rho_0 L} \\ U^2 &= N^2 H \Delta z. \end{aligned} \tag{11.17}$$

From this last expression, the ratio of vertical convergence, W/H, to horizontal divergence, U/L, is found to be

$$\frac{W/H}{U/L} = \frac{\Delta z}{H} = \frac{U^2}{N^2H^2}\,. \tag{11.18}$$

We immediately note that if U is less than the product NH, W/H must be less than U/L, implying that convergence in the vertical cannot fully meet horizontal divergence. Consequently, the fluid is forced to be partially deflected horizontally so that the term $\partial u/\partial x$ can be met by $-\partial v/\partial y$ better than by $-\partial w/\partial z$. The stronger the stratification, the smaller is U compared to NH and, thus, W/H compared to U/L.

From this argument, we conclude that the ratio

$$Fr = \frac{U}{NH}\,, \tag{11.19}$$

called the *Froude number*, is a measure of the importance of stratification. The rule is: If $Fr \lesssim 1$, stratification effects are important; the smaller Fr, the more important these effects are.

The analogy with the Rossby number of rotating fluids,

$$Ro = \frac{U}{\Omega L} , \tag{11.20}$$

where Ω is the angular rotation rate and L the horizontal scale, is immediate. Both Froude and Rossby numbers are ratios of the horizontal velocity scale by a product of frequency and length scale; for stratified fluids, the relevant frequency and length are naturally the stratification frequency and the height scale, whereas in rotating fluids they are, respectively, the rotation rate and the horizontal length scale.

The analogy can be pursued a little further. Just as the Froude number is a measure of the vertical velocity in a stratified fluid [via (11.18)], the Rossby number can be shown to be a measure of the vertical velocity in a rotating fluid. We saw (Section 7.2) that strongly rotating fluids (Ro nominally zero) allow no convergence of vertical velocity, even in the presence of topography. This results from the absence of horizontal divergence in geostrophic flows (ruling out here, for the sake of the analogy, an eventual beta effect). In reality, the Rossby number cannot be nil, and the flow cannot be purely geostrophic. The nonlinear terms, of relative importance measured by Ro, yield corrective terms to the geostrophic velocities of the same relative importance. Thus, the horizontal divergence, $\partial u/\partial x + \partial v/\partial y$, is not zero but is on the order of RoU/L. Since the divergence is matched by the vertical divergence, $-\partial w/\partial z$, on the order of W/H, we conclude that

$$\frac{W/H}{U/L} = Ro, \tag{11.21}$$

in rotating fluids. Contrasting (11.18) to (11.21), we note that, with regard to vertical velocities, the square of the Froude number is the analogue of the Rossby number.

In continuation of the analogy, it is tempting to seek the stratified analogue of the Taylor column in rotating fluids. Recall that Taylor columns occur in rapidly rotating fluids ($Ro = U/\Omega L \ll 1$). Let us then ask what happens when a fluid is very stratified ($Fr = U/NH \ll 1$). By virtue of (11.18), the vertical displacements are severely restricted ($\Delta z \ll H$), implying that an obstacle causes the fluid at that level to be deflected almost purely horizontally. (In the absence of rotation, there is no tendency toward vertical rigidity, and parcels at levels above the obstacle can flow straight ahead without much disruption.) If the obstacle occupies the entire width of the domain, such a horizontal detour is not allowed, and the fluid at the level of the obstacle is blocked on both the upstream and downstream sides. This horizontal blocking in stratified fluids is the analogue of the vertical Taylor columns in rotating fluids. Further analogies between homogeneous rotating fluids and stratified nonrotating fluids have been reviewed by Veronis (1967).

11.6 Combination of rotation and stratification

In the light of the previous remarks, we are now in position to ask what happens when, as in actual geophysical fluids, the effects of rotation and stratification are simultaneously present. The preceding analysis remains unchanged, except that we now invoke the geostrophic balance [see (7.7)] in the horizontal momentum equation to obtain the horizontal velocity scale:

$$\Omega U = \frac{\Delta P}{\rho_0 L}$$
$$U = \frac{N^2 H \Delta z}{\Omega L} \,. \tag{11.22}$$

The ratio of the vertical to horizontal convergence then becomes

$$\frac{W/H}{U/L} = \frac{\Delta z}{H} = \frac{\Omega L U}{N^2 H^2}$$
$$= \frac{Fr^2}{Ro} \,. \tag{11.23}$$

As a result, the influence of rotation ($Ro \lesssim 1$) is to increase the scale for the vertical velocity. However, since vertical divergence cannot exist without horizontal convergence ($W/H \lesssim U/L$), the following inequality must hold:

$$Fr^2 \lesssim Ro, \tag{11.24}$$

that is,

$$\frac{U}{NH} \lesssim \frac{NH}{\Omega L} \,. \tag{11.25}$$

This sets an upper bound for the magnitude of the flow field in a fluid under given rotation (Ω) and of given stratification (N) in a domain of given dimensions (L, H). If the velocity is imposed externally (*e.g.*, by an upstream condition), the inequality specifies either the horizontal or the vertical length scales of the possible disturbances. Finally, if the system is such that all quantities are externally imposed and that they do not meet (11.25), then special effects such as Taylor columns or blocking must occur.

Inequality (11.25) brings a new dimensionless number $NH/\Omega L$, namely, the ratio of the Rossby and Froude numbers. For historical reasons and also because it is more convenient in some dimensional analyses, the square of this quantity is usually defined:

$$Bu = \left(\frac{NH}{\Omega L}\right)^2 = \left(\frac{Ro}{Fr}\right)^2 . \tag{11.26}$$

It bears the name of *Burger number*, in honor of Alewyn P. Burger (1927–2003), who contributed to our understanding of geostrophic scales of motions (Burger, 1958). In practice, the Burger number is a useful measure of stratification in the presence of rotation.

In typical geophysical fluids, the height scale is much less than the horizontal length scale ($H \ll L$), but there is also a disparity between the two frequencies Ω and N. Although Ω, the rotation rate of the earth, corresponds to a period of 24 h, the stratification frequency generally corresponds to much shorter periods, on the order of few to tens of minutes in both the ocean and atmosphere. This implies that generally $\Omega \ll N$ and opens the possibility of a Burger number on the order of unity.

This is a particular case of great importance. According to our foregoing scaling analysis, the ratio of vertical convergence to horizontal divergence, $(W/H)/(U/L)$, is given by Fr^2,

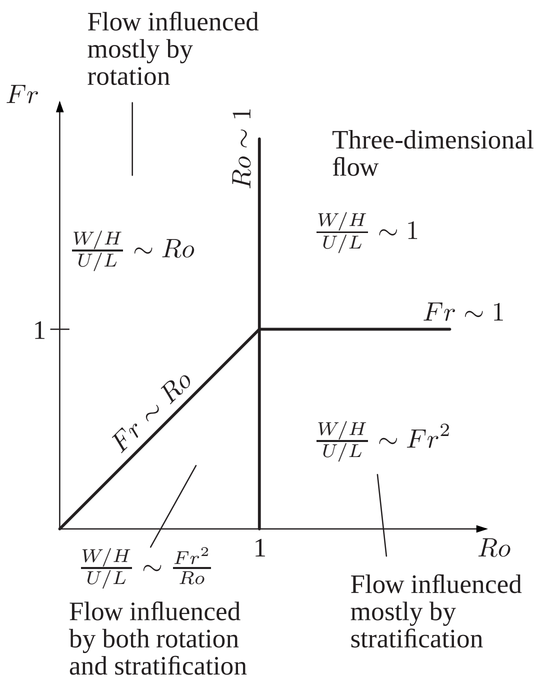

Figure 11-6 Recapitulation of the various scalings of the ratio of the vertical convergence (divergence), W/H, to the horizontal divergence (convergence), U/L, as a function of the Rossby number, $Ro = U/(\Omega L)$, and Froude number, $Fr = U/(NH)$.

Fr^2/Ro, or Ro, depending on whether vertical motions are controlled by stratification or rotation or both (Figure 11-6). Thus, if Fr^2/Ro is less than Ro, stratification restricts vertical motions more than rotation and is the dominant process. The converse is true if Fr^2/Ro is greater than Ro. This relationship implies that stratification and rotation influence the flow field to similar degrees if Fr^2/Ro and Ro are on the same order. Such is the case when the Froude number equals the Rossby number and, consequently, the Burger number is unity. The horizontal length scale then assumes a special value:

$$L = \frac{NH}{\Omega} . \tag{11.27}$$

For the values of Ω and N just cited and a height scale H of 100 m in the ocean and 1 km in the atmosphere, this horizontal length scale is on the order of 50 km and 500 km in the ocean and atmosphere, respectively. At this length scale, stratification and rotation go hand in hand. Later on (Chapter 15), it will be shown that the scale defined above is none other than the so-called *internal radius of deformation*.

Analytical Problems

11-1. The Gulf Stream waters are characterized by surface temperatures around 22°C. At a depth of 800 m below the Gulf Stream, temperature is only 10°C. Using the value 2.1×10^{-4} K^{-1} for the coefficient of thermal expansion, calculate the stratification frequency. What is the horizontal length at which both rotation and stratification play comparable roles? Compare this length scale to the width of the Gulf Stream.

11-2. An atmospheric inversion occurs when the temperature increases with altitude, in contrast to the normal situation when the temperature decays with height. This corresponds to a very stable stratification and, hence, to a lack of ventilation (smog, etc.). What is the stratification frequency when the inversion sets in ($dT/dz = 0$)? Take T = 290 K and C_p = 1005 m^2/s^2.K.

11-3. A meteorological balloon rises through the lower atmosphere, simultaneously measuring temperature and pressure. The reading, transmitted to the ground station where the temperature and pressure are, respectively, 17°C and 1028 millibars, reveals a gradient $\Delta T/\Delta p$ of 6°C per 100 millibars. Estimate the stratification frequency. If the atmosphere were neutral, what would the reading be?

11-4. A wind blowing at a speed of 10 m/s encounters an extinct volcano (of approximately conical shape) 500 m high and 20 km in diameter. The air stratification provides a stratification frequency on the order of 0.02 s^{-1}. How do vertical displacements compare to the height of the volcano? What does this imply about the importance of the stratification? Is the Coriolis force important in this case?

11-5. Redo Problem 11-4 with the same wind speed and stratification but with a mountain range 1000 m high and 500 km wide.

JMB from ⇓

11-6. Vertical soundings of the atmosphere provided temperature profiles of Figure 11-7. Analyze the static stability of each profile.

JMB to ⇑

Numerical Exercises

11-1. Use `medprof.m` to read average Mediterranean temperature and salinity profiles and calculate N^2 for various sizes of averaging boxes. What do you conclude? (*Hint:* use `ies80.m` for the state equation).

11-2. Use the diffusion-equation solver of Exercise 5-4 with a turbulent diffusion coefficient that changes locally from 10^{-4} m^2/s to 10^{-2} m^2/s whenever N^2 is negative. Simulate the evolution of a 50 m heigh water column with an initially stable vertical temperature gradient of 0.3 °C/m. Cool the system at the surface by a heat loss of 100 W/m^2. Salinity is considered constant. Study the effect of changes in Δz and Δt.

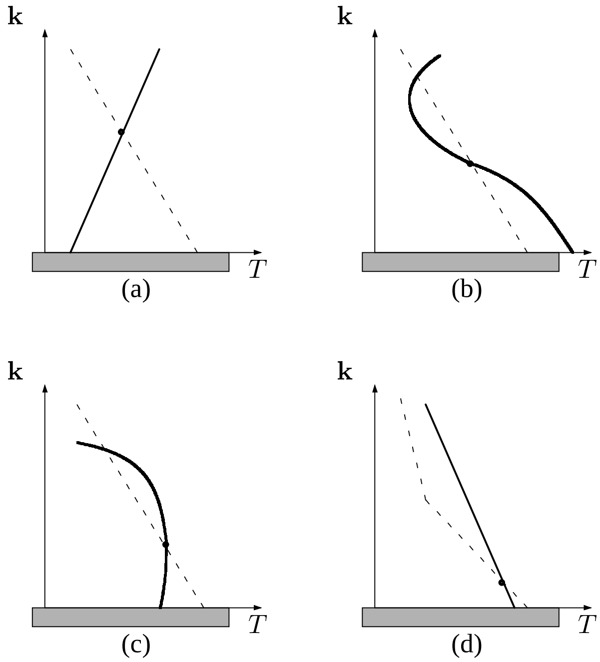

Figure 11-7 Vertical profiles of temperature with lapse rate (dashed line) of fluid parcel (dot) and ambient temperature (solid line).

11-3. Implement the algorithm outlined in Section 11.4, removing any static instability instantaneously. Keep the turbulent diffusion constant at 10^{-4} m^2/s and simulate the same problem as in Exercise 11-2.

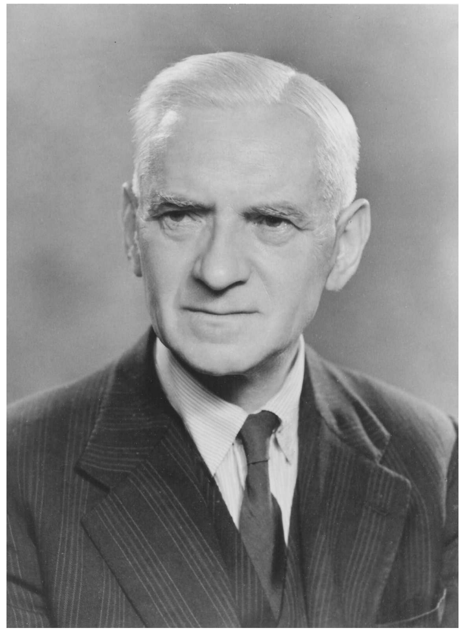

David Brunt
1886 – 1965

As a bright young British mathematician, David Brunt began a career in astronomy, analyzing the statistics of celestial variables. Then, turning to meteorology during World War I, he became fascinated with weather forecasting and started to apply his statistical methods to atmospheric observations in the search for primary periodicities. By 1925, he had concluded that weather forecasting by extrapolation of cyclical behavior was not possible and turned his attention to the dynamic approach, which had been initiated in the late nineteenth century by William Ferrel and given new impetus by Vilhelm Bjerknes in recent years.

In 1926, he delivered a lecture at the Royal Meteorological Society on the vertical oscillations of particles in a stratified atmosphere. Lewis F. Richardson then led him to a paper published the preceding year by Finnish scientist Vilho Väisälä, in which the same oscillatory frequency was derived. This quantity is now jointly known as the Brunt–Väisälä frequency.

Continuing his efforts to explain observed phenomena by physical processes, Brunt contributed significantly to the theories of cyclones and anticyclones and of heat transfer in the atmosphere. His studies culminated in a textbook titled *Physical and Dynamical Meteorology* (1934) and confirmed him as a founder of modern meteorology. (*Photo credit: LaFayette, London*)

Vilho Väisälä
1889 – 1969

Text of second bio (*here*)

Chapter 12

Layered Models

(October 18, 2006) **SUMMARY**: Advantage is taken of the assumption of density conservation by fluid parcels to change the vertical coordinate from depth to density. The new equations allow for a clear discussion of potential-vorticity dynamics and lend themselves to discretization in the vertical. The result is a layered model. Splitting stratification in a series of layers may be interpreted as a vertical discretization in which the vertical grid is a material surface of the flow. This naturally leads to the discussion of general Lagrangian approaches. Note: To avoid problems of terminology, we restrict ourselves here to the ocean. The case of the atmosphere follows with the replacement of depth by height and density by potential density.

12.1 From depth to density

Since a stable stratification requires a monotonic increase of density downward, density can be taken as a surrogate for depth and used as the vertical coordinate. If density is conserved by individual fluid parcels, as it is approximately the case for most geophysical flows, considerable mathematical simplification follows, and the new equations present a definite advantage in a number of situations. It is thus worth expounding on this change of variables at some length.

In the original Cartesian system of coordinates, z is an independent variable and density $\rho(x, y, z, t)$ is a dependent variable, giving the water density at location (x, y), time t, and depth z. In the transformed coordinate system (x, y, ρ, t), density becomes an independent variable, and $z(x, y, \rho, t)$ has become the dependent variable giving the depth at which density ρ is found at location (x, y) and at time t. A surface along which density is constant is called an *isopycnal surface*, or *isopycnic* for short.

From a differentiation of the expression $a = a(x, y, \rho(x, y, z, t), t)$, where a is any variable, the rules for the change of variables follow:

$$
\begin{aligned}
\frac{\partial}{\partial x} &\longrightarrow \left.\frac{\partial a}{\partial x}\right|_z = \left.\frac{\partial a}{\partial x}\right|_\rho + \left.\frac{\partial a}{\partial \rho}\,\frac{\partial \rho}{\partial x}\right|_z \\
\frac{\partial}{\partial y} &\longrightarrow \left.\frac{\partial a}{\partial y}\right|_z = \left.\frac{\partial a}{\partial y}\right|_\rho + \left.\frac{\partial a}{\partial \rho}\,\frac{\partial \rho}{\partial y}\right|_z \\
\frac{\partial}{\partial z} &\longrightarrow \frac{\partial a}{\partial z} = \frac{\partial a}{\partial \rho}\,\frac{\partial \rho}{\partial z} \\
\frac{\partial}{\partial t} &\longrightarrow \left.\frac{\partial a}{\partial t}\right|_z = \left.\frac{\partial a}{\partial t}\right|_\rho + \left.\frac{\partial a}{\partial \rho}\,\frac{\partial \rho}{\partial t}\right|_z .
\end{aligned}
$$

Then, application to $a = z$ gives $0 = z_x + z_\rho \rho_x$, $1 = z_\rho \rho_z$, etc. (where a subscript indicates a derivative). This provides the rule to change the derivative of ρ at z constant to that of z at ρ constant. For a other than z, we can write:

$$
\left.\frac{\partial a}{\partial x}\right|_z = \left.\frac{\partial a}{\partial x}\right|_\rho - \frac{z_x}{z_\rho}\,\frac{\partial a}{\partial \rho}\,, \tag{12.1}
$$

with similar expressions where x is replaced by y or t, and

$$
\frac{\partial a}{\partial z} = \frac{1}{z_\rho}\,\frac{\partial a}{\partial \rho}\,. \tag{12.2}
$$

Here, subscripts denote derivatives. Figure 12-1 depicts a geometrical interpretation of rule (12.1).

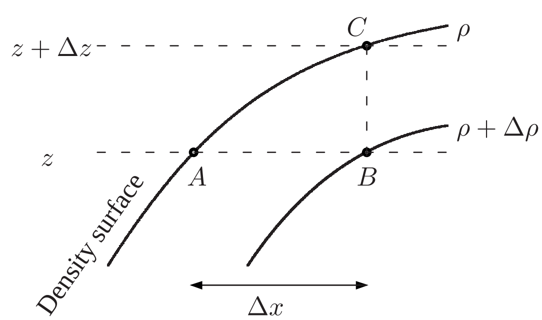

Figure 12-1 Geometrical interpretation of equation (12.1). The x-derivatives of any function a at constant depth z and at constant density ρ are, respectively, $[a(B) - a(A)]/\Delta x$ and $[a(C) - a(A)]/\Delta x$. The difference between the two, $[a(C) - a(B)]/\Delta x$, represents the vertical derivative of a, $[a(C) - a(B)]/\Delta z$, times the slope of the density surface, $\Delta z/\Delta x$. Finally, the vertical derivative can be split as the ratio of the ρ-derivative of a, $[a(C) - a(B)]/\Delta\rho$, by $\Delta z/\Delta\rho$.

The hydrostatic equation (4.19) readily becomes

$$
\frac{\partial p}{\partial \rho} = -\,\rho g\,\frac{\partial z}{\partial \rho} \tag{12.3}
$$

and leads to the following horizontal pressure gradient:

$$
\left.\frac{\partial p}{\partial x}\right|_z = \left.\frac{\partial p}{\partial x}\right|_\rho - \frac{z_x}{z_\rho}\,\frac{\partial p}{\partial \rho} = \left.\frac{\partial p}{\partial x}\right|_\rho + \rho g\,\frac{\partial z}{\partial x} = \left.\frac{\partial P}{\partial x}\right|_\rho .
$$

Similarly, $\partial p/\partial y$ at constant z becomes $\partial P/\partial y$ at constant ρ. The new function P, which plays the role of pressure in the density-coordinate system, is defined as

$$P = p + \rho g z \tag{12.4}$$

and is called the *Montgomery potential*[1]. Later on, when there is no ambiguity, this potential may loosely be called pressure. With P replacing pressure, the hydrostatic balance, (12.3), now takes a more compact form:

$$\frac{\partial P}{\partial \rho} = g z, \tag{12.5}$$

further indicating that P is the natural substitute for pressure when density is the vertical coordinate.

Beyond this point, all derivatives with respect to x, y, and time are meant to be taken at constant density, and the subscript ρ is no longer necessary.

With the use of (12.1)–(12.3) plus the obvious relation $\partial \rho/\partial x|_\rho = 0$, the density-conservation equation, (4.21e) in the absence of diffusion, can be solved for the vertical velocity

$$w = \frac{\partial z}{\partial t} + u\frac{\partial z}{\partial x} + v\frac{\partial z}{\partial y}. \tag{12.6}$$

This last equation simply tells that the vertical velocity is that necessary for the particle to remain at all times on the same density surface, in analogy with surface fluid particles having to remain on the surface [see Equation (7.15)]. Armed with expression (12.6), we can now eliminate the vertical velocity throughout the set of governing equations. First, the material derivative (3.5) assumes a simplified, two-dimensional-like form:

$$\frac{d}{dt} = \frac{\partial}{\partial t} + u\frac{\partial}{\partial x} + v\frac{\partial}{\partial y}, \tag{12.7}$$

where the derivatives are now taken at constant ρ. The absence of an advective term in the third spatial direction results from the absence of motion across density surfaces.

In the absence of friction and in the presence of rotation, the horizontal-momentum equations (4.21a) and (4.21b) become

$$\frac{du}{dt} - fv = -\frac{1}{\rho_0}\frac{\partial P}{\partial x} \tag{12.8a}$$

$$\frac{dv}{dt} + fu = -\frac{1}{\rho_0}\frac{\partial P}{\partial y}. \tag{12.8b}$$

We note that they are almost identical to their original versions. The differences are nonetheless important: The material derivative is now along density surfaces and expressed by (12.7), the pressure p has been replaced by the Montgomery potential P defined in (12.4), and all temporal and horizontal derivatives are taken at constant density. Note, however, that the components u and v are still the true horizontal velocity components and are not measured along sloping density surfaces. This property is important for the proper application of lateral boundary conditions.

[1] In honor of Raymond B. Montgomery who first introduced it in 1937. See his biography at the end of this chapter.

To complete the set of equations, it remains to transform the continuity equation (4.21d) according to rules (12.1) and (12.2). Further elimination of the vertical velocity by using (12.6) leads to

$$\frac{\partial h}{\partial t} + \frac{\partial}{\partial x}(hu) + \frac{\partial}{\partial y}(hv) = 0, \tag{12.9}$$

where the quantity h is introduced for convenience and is proportional to $\partial z/\partial \rho$, the derivative of depth with respect to density. For convenience, we want h to have the dimension of height, and so we introduce an arbitrary but constant density difference, $\Delta\rho$, and define:

$$h = - \Delta\rho \frac{\partial z}{\partial \rho} . \tag{12.10}$$

In this manner, h can be interpreted as the thickness of a fluid layer between the density ρ and $\rho + \Delta\rho$. At this point, the value of $\Delta\rho$ is arbitrary, but later, in the development of layered models, it will be chosen as the density difference between adjacent layers.

The transformation of coordinates is now complete. The new set of governing equations consists of the two horizontal-momentum equations (12.8a) and (12.8b), the hydrostatic balance (12.5), the continuity equation (12.9), and the relation (12.10). It thus forms a closed 5-by-5 system for the dependent variables, u, v, P, z, and h. Once the solution is known, the pressure p and the vertical velocity w can be recovered from (12.4) and (12.6).

Since the aforementioned work of Montgomery (1937), the substitution of density as the vertical variable has been implemented in a number of applications, especially by Robinson (1965) in a study of inertial currents, by Hodnett (1978) in a study of the permanent oceanic thermocline, and by Sutyrin (1989) in a study of isolated eddies. A review in the meteorological context is provided by Hoskins *et al.* (1985).

12.2 Layered models

A *layered model* is an idealization by which a stratified fluid flow is represented as a finite number of moving layers, stacked one upon another and each having a uniform density. Its evolution is governed by a discretized version of the system of equations in which density, taken as the vertical variable, is not varied continuously but in steps: density is restricted to assume a finite number of values. A layered model is the density analogue of a *level model*, which is obtained after discretization of the vertical variable z.

Each layer ($k = 1$ to m, where m is the number of layers) is characterized by its density ρ_k (unchanging), thickness h_k, Montgomery potential P_k, and horizontal velocity components u_k and v_k. The surface marking the boundary between two adjacent layers is called an *interface* and is described by its elevation z_k, measured (negatively downward) from the mean surface level. The displaced surface level is denoted z_0 (Figure 12-2a). The interfacial heights can be obtained recursively from the bottom[2]

[2]Note that contrary to our general approach to use indexes which increase with the Cartesian coordinate directions, we choose to increase the index k downward, in agreement with the traditional notation for isopycnal models and with the fact that our new vertical coordinate is ρ increasing downward, too.

$$z_m = b, \tag{12.11}$$

upward:

$$z_{k-1} = z_k + h_k, \quad k = m \text{ to } 1. \tag{12.12}$$

This geometrical relation can be regarded as the discretized version of (12.10) used to define h.

In a similar manner, the discretization of hydrostatic relation (12.5) provides another recursive relation, which can be used to evaluate the Montgomery potential P from the top,

$$P_1 = p_{\text{atm}} + \rho_0 g z_0, \tag{12.13}$$

downward:

$$P_{k+1} = P_k + \Delta\rho g z_k, \quad k = 1 \text{ to } m-1. \tag{12.14}$$

In writing (12.13), we have selected the uppermost density ρ_1 as the reference density ρ_0. Gradients of the atmospheric pressure p_{atm} rarely play a significant role, and the contribution of p_{atm} to P_1 is usually omitted. If the layered model is for the lower atmosphere, p_{atm} represents a pressure distribution aloft and may, too, be taken as an inactive constant.

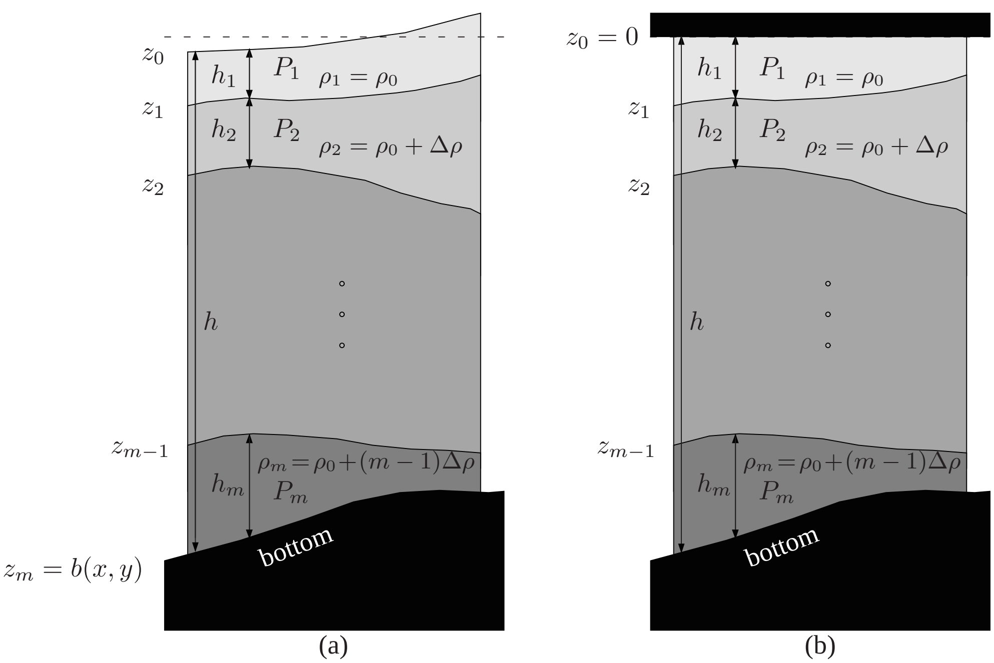

Figure 12-2 A layered model with m active layers: (a) with free surface, (b) with rigid lid.

When the *reduced gravity*,

Table 12.1 LAYERED MODELS.

One layer:

$$z_0 = h_1 + b \qquad P_1 = \rho_0 g(h_1 + b)$$
$$z_1 = b$$

Two layers:

$$z_0 = h_1 + h_2 + b \qquad P_1 = \rho_0 g(h_1 + h_2 + b)$$
$$z_1 = h_2 + b \qquad P_2 = \rho_0 g h_1 + \rho_0 (g + g')(h_2 + b)$$
$$z_2 = b$$

Three layers:

$$z_0 = h_1 + h_2 + h_3 + b \qquad P_1 = \rho_0 g(h_1 + h_2 + h_3 + b)$$
$$z_1 = h_2 + h_3 + b \qquad P_2 = \rho_0 g h_1 + \rho_0 (g + g')(h_2 + h_3 + b)$$
$$z_2 = h_3 + b \qquad P_3 = \rho_0 g h_1 + \rho_0 (g + g') h_2$$
$$z_3 = b. \qquad \qquad + \rho_0 (g + 2g')(h_3 + b)$$

$$g' = \frac{\Delta\rho}{\rho_0}\, g, \tag{12.15}$$

is introduced for convenience, the recursive relations (12.12) and (12.14) lead to simple expressions for the interfacial heights and Montgomery potentials. For up to three layers, these equations are summarized in Table 12.1.

In certain applications, it is helpful to discard surface gravity waves, which travel much faster than internal waves and near-geostrophic disturbances. To do so, we eliminate the flexibility of the surface by imagining that the system is covered by a rigid lid (Figure 12-2b). This is called the *rigid-lid approximation*, which had already been introduced in the study of barotropic motions in section 7.5. In such a case, z_0 is equal to zero, and there are only ($m - 1$) independent layer thicknesses. In return, one of the Montgomery potentials cannot be derived from the hydrostatic relation. If this potential is chosen as the one in the lowest layer, the recursive relations yield the equations of Table 12.2.

In some other instances, mainly in the investigation of upper-ocean processes, the lowest layer may be imagined to be infinitely deep and at rest (Figure 12-3). Keeping m as the number of moving layers, we assign to this lowest (abyssal) layer the index ($m + 1$). The absence of motion there implies a uniform Montgomery potential, the value of which can be set to zero without loss of generality: $P_{m+1} = 0$. For up to three active layers, the recursive relations provide equations of Table 12.3.

In this table, $z_1 = -h_1$ is an approximation that begs for an explanation. The free surface is not at $z = z_0 = 0$ but given by (12.13) when we arrive at the surface integrating upward. For a single layer this yields, in the absence of atmospheric pressure

$$P_2 = 0 \rightarrow \quad P_1 = -\Delta\rho g z_1 = \rho_0 g z_0. \tag{12.16}$$

Table 12.2 RIGID-LID MODELS.

One layer:	
$z_1 = -h_1$	P_1 variable
$h_1 = h$, fixed	
Two layers:	
$z_1 = -h_1$	$P_1 = P_2 + \rho_0 g' h_1$
$z_2 = -h_1 - h_2$	P_2 variable
$h_1 + h_2 = h$, fixed	
Three layers:	
$z_1 = -h_1$	$P_1 = P_3 + \rho_0 g'(2h_1 + h_2)$
$z_2 = -h_1 - h_2$	$P_2 = P_3 + \rho_0 g'(h_1 + h_2)$
$z_3 = -h_1 - h_2 - h_3$	P_3 variable
$h_1 + h_2 + h_3 = h$, fixed.	

Hence $gz_0 = -g'z_1$. Since $h_1 = z_0 - z_1$ we get $(1 - g'/g)z_1 = h_1$ and from there $z_0 = \eta = -g'/gz_1$, leading to a surface lifting in light water lenses for example. This must be the case in order to preserve a constant pressure in the lowest layer: if lighter waters take the place of deep waters, the lost weight must be compensated by an addition of water on top. Because these expressions do not involve the full gravity g but only its reduced value g', this type of model is known as a *reduced-gravity model*.

Generalization to more than three moving layers is straightforward. When a configuration with few but physically relevant layers is desired, the preceding derivations may be extended to non-uniform density differences from layer to layer. Mathematically, this would correspond to a discretization of the vertical density coordinate in unevenly spaced gridpoints.

Once the layer thicknesses, interface depths, and layer pressures (more precisely, the Montgomery potentials) are all related, the system of governing equations is completed by gathering the horizontal-momentum equations (12.8a) and (12.8b) and the continuity equation (12.9), each written for every layer.

In Section 11.6, the length $L = NH/\Omega$ was derived as the horizontal scale at which rotation and stratification play equally important roles. It is noteworthy at this point to formulate the analogue for a layered system. Introducing H as a typical layer thickness in the system (such as the maximum depth of the uppermost layer at some initial time) and $\Delta\rho$ as a density difference between two adjacent layers (such as the top two), an approximate expression of the stratification frequency squared is

$$N^2 = -\frac{g}{\rho_0}\frac{d\rho}{dz} \simeq \frac{g}{\rho_0}\frac{\Delta\rho}{H} = \frac{g'}{H}, \tag{12.17}$$

where $g' = g\,\Delta\rho/\rho_0$ is the reduced gravity defined earlier. Substitution of (12.17) in the

Table 12.3 REDUCED GRAVITY MODELS.

One layer:

$$z_1 = -h_1 \qquad P_1 = \rho_0 g' h_1$$

Two layers:

$$z_1 = -h_1 \qquad P_1 = \rho_0 g'(2h_1 + h_2)$$
$$z_2 = -h_1 - h_2 \qquad P_2 = \rho_0 g\prime(h_1 + h_2)$$

Three layers:

$$z_1 = -h_1 \qquad P_1 = \rho_0 g'(3h_1 + 2h_2 + h_3)$$
$$z_2 = -h_1 - h_2 \qquad P_2 = \rho_0 g'(2h_1 + 2h_2 + h_3)$$
$$z_3 = -h_1 - h_2 - h_3 \qquad P_3 = \rho_0 g'(h_1 + h_2 + h_3).$$

definition of L yields $L \simeq (g'H)^{1/2}/\Omega$. Finally, because the ambient rotation rate Ω enters the dynamics only via the Coriolis parameter f, it is more convenient to introduce the length scale

$$R = \frac{\sqrt{g'H}}{f}, \tag{12.18}$$

called the *radius of deformation*. To distinguish this last scale from its cousin (9.12) derived for free-surface homogeneous rotating fluids (where the full gravitational acceleration g appears), it is customary in situations where ambiguity could arise to use the expressions *internal radius of deformation* and *external radius of deformation* for (12.18) and (9.12), respectively. Because density differences within geophysical fluids are typically a percent or less of the average density, the internal radius is most often less than one-tenth the external radius.

When the model consists of a single moving layer above a motionless abyss, the governing equations reduce to

$$\frac{\partial u}{\partial t} + u\frac{\partial u}{\partial x} + v\frac{\partial u}{\partial y} - fv = -g'\frac{\partial h}{\partial x}, \tag{12.19a}$$

$$\frac{\partial v}{\partial t} + u\frac{\partial v}{\partial x} + v\frac{\partial v}{\partial y} + fu = -g'\frac{\partial h}{\partial y}, \tag{12.19b}$$

$$\frac{\partial h}{\partial t} + \frac{\partial}{\partial x}(hu) + \frac{\partial}{\partial y}(hv) = 0. \tag{12.19c}$$

The subscripts indicating the layer have become superfluous and have been deleted. The coefficient $g' = g(\rho_2 - \rho_1)/\rho_0$ is called the *reduced gravity*. Except for the replacement of the full gravitational acceleration, g, by its reduced fraction, g', this system of equations is identical to that of the shallow-water model over a flat bottom [Equations (7.20)] and is

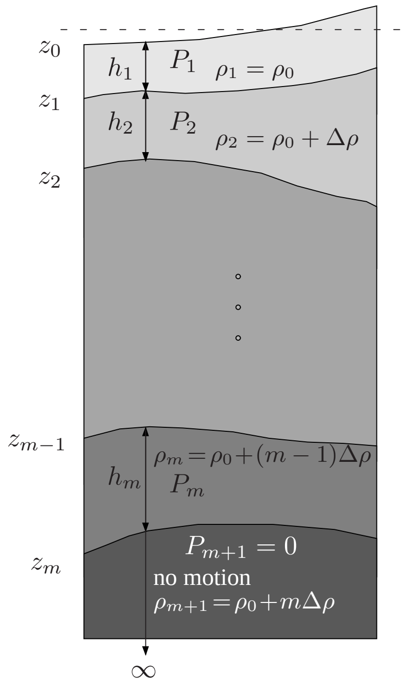

Figure 12-3 A reduced-gravity layered model. The assumption of a very deep ocean at rest can be justified by the need to keep the transport hu_{m+1} and kinetic energy hu_{m+1}^2 bounded so that velocities must vanish as the depth of the last layer increases to infinity. In this case, the pressure in the deeper layer tends towards a constant, which we can choose zero.

thus called the *shallow-water reduced-gravity model*. Because the vertical simplicity of this model permits the investigation of a number of horizontal processes with a minimum of mathematical complication, it will be used in some of the following chapters. Finally, recall that the Coriolis parameter, f, may be taken as either a constant (f-plane) or as a function of latitude ($f = f_0 + \beta_0 y$, beta plane).

12.3 Potential vorticity

The relative vorticity ζ is defined as

$$\zeta = \frac{\partial v}{\partial x} - \frac{\partial u}{\partial y} . \tag{12.20}$$

In layered models, the expression for potential vorticity is

$$\begin{aligned} q &= \frac{f + \zeta}{h} \\ &= \frac{f + \partial v/\partial x - \partial u/\partial y}{h} , \end{aligned} \tag{12.21}$$

which is similar to the expression for a barotropic fluid, except that the denominator is now a differential thickness given by (12.10) rather than the full thickness of the system.

Interpretation (Figure 12-4)

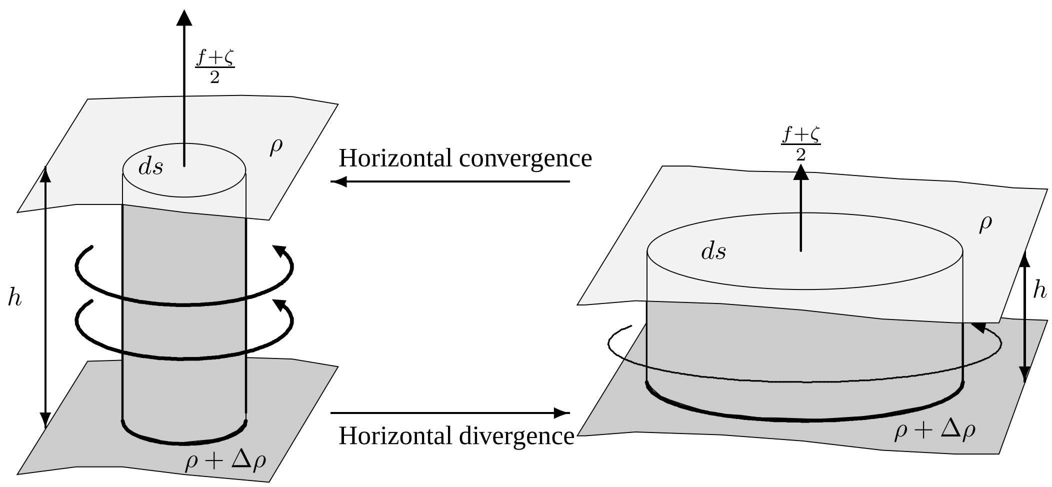

Figure 12-4 Conservation of volume and circulation in a fluid undergoing divergence (squeezing) or convergence (stretching). The products of $h\,ds$ and $(f+\zeta)\,ds$ are conserved during the transformation.

12.4 Two-layer models

Text of section

Expand the equations to show η and amplitude of interface displacement a? Mode decomposition into baroctropic and baroclinic part would be interesting for the numerical mode-splitting interpretation

Energy conservation in a two-layer model? Useful to prepare QG models of two-layer system for baroclinic instability?

12.5 Wind-induced seiches and resonance in lakes

Use 2-layer model with flat bottom, no rotation ($f = 0$) and two lateral boundaries. Conclude by mentioning the Taylor solution in a bay, with amphidromic point.

12.6 Numerical layered models

The development of numerical models based on the governing equations written in isopycnal coordinates is simplified by the fact that we already performed a discretization on the vertical coordinate through the layering illustrated in Section 12.2. Indeed, we arrived at governing equations for a series of m layers, for each of which no vertical coordinate appears anymore. In other words, we replaced a three-dimensional problem by m coupled two-dimensional problems. Since there is no difficulty to generalize the layering and use different $\Delta\rho$ for each layer, we can easily place the layers so as to follow well defined water masses at our will. After choosing the adequate $\Delta\rho$ that define the layers, the only discretization that remains then to be done is related to the two-dimensional "horizontal" structure, an exercise we already performed in the framework of shallow-water equations (Section 9.7 and 9.8). Since the governing equations of each isopycnal layer are very similar to those of the inviscid shallow-water equations, all we have to do is to "repeat" the implementation of the shallow-water equations for each layer, adapting the pressure force calculation. Here we can notice how easily pressure can be calculated in the layered system once the layer heights are known simply integrating (12.14) or its straightforward generalization when density differences vary between layers. To calculate layer heights, the volume-conservation equations are at our disposal and are also similar to those of the shallow-water system. Finally, as for shallow-water equations, additional processes neglected up to now can be reinstated. Bottom stress and wind stress can be taken into account at the lowest and uppermost layer by adding a friction term as for the shallow-water equations. Also friction between layers can be accommodated for and the corresponding momentum exchange then appears as an additional term depending on the velocity difference across the interface. This internal friction terms appears with opposite sign for the two layers on each side of the isopycnal interface. Also any unresolved horizontal sub-grid scale process can be parameterized, typically using a lateral diffusion. Here an important points is to be mentioned because any lateral diffusion formulated in the new coordinate system (remember that $\partial/\partial x$ are derivatives at fixed ρ) leads to an associated mixing which is by construction acting along isopycnals rather than on z levels (see also Section 20.8). This is generally considered advantageous if we consider smaller-scale movements easier to generate in an environment at uniform density and zero buoyancy. The parameterization of sub-grid scale processes as a diffusion along isopycnal is called *isopycnal diffusion* and is thus naturally included in the governing equations of density-layered models by adding a Laplacian term. No diffusion across the layer interfaces is then present in the model. Since velocities act only in the x and y direction of the layer, any numerical diffusion also acts along these coordinate lines and no numerical diffusion across isopycnal surfaces will occur. In other words, no diapycnal diffusion and erosion of stratification will take place so that water masses are conserved. This is at the same time one of the major strength and weaknesses of the formulation. It is an advantage if the physical system presents no mixing, because in that case, the model allows to simulate the movements and oscillations of the system without any artificial destruction of stratification, otherwise a common problem of models. On the other hand, if there is vertical mixing in the physical system, the layered models need to add some "entrainment" of water masses from one layer into another, and more fundamentally, when a columns starts to get well mixed, some of the layers of a given density will not be present anymore because the corresponding isopycnal interface outcrops or intercepts the bottom (Figure 12-5). In other words, for each layer the lateral extend can change in time, a non-trivial problem to deal with. The problem is even worse when static instabilities are present because then the coordinate change is not valid anymore. The problems associated with strong mixing and static instabilities explain why isopycnal models are rarely used for atmospheric models, were static instabilities are much more frequent than in the ocean. Therefore most of our analysis was oriented towards the isopycnal ocean models. Another difficulty of purely isopycnal ocean models is related to the fact that by construction density is constant within a layer so that temperature and salinity cannot vary independently anymore while physical boundary conditions for both are independent. Finally, isopycnal models are not easily applied when both the deep ocean and coastal seas are to be covered because of the very different density structures and hence vertical resolution associated with the layers.

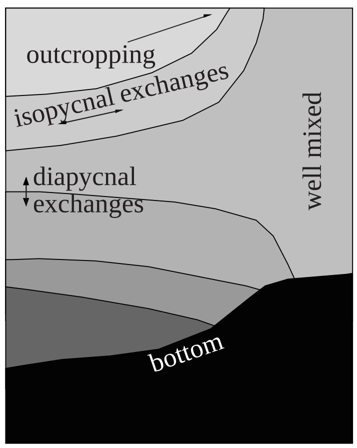

Figure 12-5 The application of a layered model of constant-density layers needs some special care when isopycnals intercept the surface (outcropping) or the bottom. Such situations typically arise near frontal systems or during strong mixing events.

For numerical layered models, we can chose the original model, the rigid-lid approximation or the reduced gravity version. This choice will have some influence on the numerical properties. For example, we can note that the reduced gravity model has replaced gravity g by $g' \ll g$ in all equations. As a consequence, such models will not allow anymore for the propagation of gravity waves which precisely involve the gravity. This can be desirable and has a nice side-effect on numerical stability. Indeed, stability requirements of shallow-water models are typically of the type

$$\frac{\sqrt{gh}\Delta t}{\Delta x} \leq \mathcal{O}(1) \tag{12.22}$$

depending on the particular discretization choses (see Section 9.7). Since gravity is replaced by reduced gravity in the models with infinitely-deep lower layers, the stability constraint related to surface waves disappears and for a reduced-gravity model with a single layer discretized as a shallow-water model, the stability constraint would be

$$\frac{\sqrt{g'h}\Delta t}{\Delta x} \leq \mathcal{O}(1) \tag{12.23}$$

much less stringent than (12.22). Also for rigid-lid models, gravity has disappeared as such and no stability condition as (12.22) applies.

For the original layered model, using neither rigid-lid approximation nor the reduced-gravity approach, surface gravity waves are possible within the system of governing equations and stability condition (12.22) can be very constraining compared to other stability conditions so that some optimization has to be done. A brute force approach would request an implicit treatment of the term responsible for the stability constraint. The velocity field in the governing equation for layer height should therefore be taken implicit as well as the the surface height in the momentum equations. The latter appears in all momentum equations because at the surface $z_0 = \eta$ pressure is $P_1 = p_{\rm atm} + \rho_0 g\eta$ according to (12.13) and the integral (12.14) makes appear η in all layers. Therefore, all equations would have to be solved simultaneously, leading to a rather large, though sparse, linear system to be solved. A more subtle approach is obtained by recalling that surface gravity waves have already been encountered as a solution of the shallow-water two-dimensional equations. Physically, they are created by surface displacements and divergence-convergence of the vertically integrated transports, which we can try to make appear from the equations of a layered model. We take the governing equation (12.9) for the layer thickness and sum over all layers to obtain the equation governing the total height of the column, including η:

$$\frac{\partial h}{\partial t} + \frac{\partial \tilde{\rm U}}{\partial x} + \frac{\partial \tilde{\rm V}}{\partial y} = \tag{12.24}$$

$$\frac{\partial \eta}{\partial t} + \frac{\partial \tilde{\rm U}}{\partial x} + \frac{\partial \tilde{\rm V}}{\partial y} = 0, \tag{12.25}$$

$$h = h_1 + h_2 + h_3 + ... + h_m = H - b + \eta \tag{12.26}$$

$$\tilde{\rm U} = h_1 u_1 + h_2 u_2 + h_3 u_3 + ... + h_m u_m \tag{12.27}$$

$$\tilde{\rm V} = h_1 v_1 + h_2 v_2 + h_3 v_3 + ... + h_m v_m \tag{12.28}$$

We easily recognize the discrete integrals defining transports. A governing equation for transports can now be obtained by multiplying each momentum equation by its corresponding layer depth and summing over the layers. For easier calculation, equations can first be recasted in conservative form by multiplying with the layer thickness and then exploiting (12.9). Concerning the pressure gradient, we can first isolate the surface pressure as follows:

$$P_1 = p_{\rm atm} + \rho_0 g\eta \tag{12.29}$$

$$\begin{aligned} P_k &= P_{k-1} + \Delta\rho z_{k-1} \\ &= P_1 + \underbrace{\Delta\rho\,(z_1 + z_2 + ... + z_{k-1})} \\ &= P_1 + \qquad\quad \mathcal{P}_k \end{aligned} \tag{12.30}$$

Then, summing the pressure gradients multiplied by the layer thickness we get

$$\begin{aligned} h_1\frac{\partial P_1}{\partial x} + h_2\frac{\partial P_2}{\partial x} + h_3\frac{\partial P_3}{\partial x} + ... + h_m\frac{\partial P_m}{\partial x} &= \\ h\frac{\partial P_1}{\partial x} + h_2\frac{\partial \mathcal{P}_2}{\partial x} + h_3\frac{\partial \mathcal{P}_3}{\partial x} + ... + h_m\frac{\partial \mathcal{P}_m}{\partial x} &= h\frac{\partial P_1}{\partial x} + G_x \end{aligned} \tag{12.31}$$

with a straightforward definition of G_x. We see that we performed the numerical equivalent of a double integral, a first one to get $\mathcal{P}_k$ and a second one to calculate G_x, the integrated effect of density variations on the vertically-average pressure gradient. The summing of the advection term in conservative form can be performed in a similar way:

$$\begin{aligned} A_x &= \frac{\partial(h_1 u_1 u_1)}{\partial x} + \frac{\partial(h_2 u_2 u_2)}{\partial x} + ... + \frac{\partial(h_m u_m u_m)}{\partial x} \\ &+ \frac{\partial(h_1 u_1 v_1)}{\partial y} + \frac{\partial(h_2 v_2 u_2)}{\partial y} + ... + \frac{\partial(h_m u_m v_m)}{\partial y} \end{aligned} \tag{12.32}$$

If the velocity components were to be independent of z , then the sum would take the familiar form

$$\frac{\partial(huu)}{\partial x} + \frac{\partial(huv)}{\partial y}. \tag{12.33}$$

Therefore we can define B_x as the difference of A_x and the advection term related to the average velocity $\bar{u} = \tilde{\mathrm{U}}/h$. The vertically integrated advection for x momentum from which the barotropic part is eliminated therefore reads

$$\begin{aligned} B_x &= \frac{\partial(h_1 u_1' u_1')}{\partial x} + \frac{\partial(h_2 u_2' u_2')}{\partial x} + ... + \frac{\partial(h_m u_m' u_m')}{\partial x} \\ &+ \frac{\partial(h_1 u_1' v_1')}{\partial y} + \frac{\partial(h_2 u_2' v_2')}{\partial y} + ... + \frac{\partial(h_m u_m' v_m')}{\partial y} \end{aligned} \tag{12.34}$$

where $u_1' = u_1 - \bar{u}$ and so on. The barotropic part

$$\frac{\partial(h\bar{u}\bar{u})}{\partial x} + \frac{\partial(h\bar{u}\bar{v})}{\partial y} \tag{12.35}$$

is then to be added to the governing equation of the transport we can finally write out:

$$\frac{\partial}{\partial t}(h\bar{u}) + \frac{\partial}{\partial x}(h\bar{u}\bar{u}) + \frac{\partial}{\partial y}(h\bar{u}\bar{v}) - fh\bar{v} = -\frac{h}{\rho_0}\frac{\partial P_1}{\partial x} + G_x + B_x \tag{12.36}$$

and similarly for the $\tilde{\mathrm{V}} = h\bar{v}$ component. This is very similar to the shallow-water equations, with two additional terms. One is related to the density variations (G_x) and the other to the vertical shear (B_x). Because the shallow-water equations were build on the assumption that those processes can be neglected, their appearance here should not be much of a surprise. We can now come back to the problem of time stepping. First, we observe that G_x does not vary much during the passage of a gravity wave, because, according to Section 7.4, the positions of the density interfaces are only changed as a fraction of the changes in η. Since in P_1, changes in η are multiplied by gravity, the changes in G_x, where changes in η are multiplied by reduced gravity, can safely be neglected. In other words, on a short time scale, G_x can be considered constant. Similarly, B_x contains only components from the vertical shear which are unaffected by a frictionless gravity waves, changing only the barotropic part. Therefore, keeping an explicit time-discretization for those two terms is not likely to cause a problem compared to the problem of heaving to deal with the fast gravity waves. In other words, we have isolated the effect of gravity waves into a set of equations similar to shallow-water equations. We could solve these equations in an implicit way (see Exercise 12-4), because there are now only three coupled equations to be solved conjointly instead of $3m$. The time evolution of these equations would therefore allow to calculate η^{n+1} from the older values with a large time step and once this surface elevation known, all layer equations could be calculated with the time-step imposed by the 3D motions. Using a large time-step in the gravity wave propagation deteriorates however the propagation properties of the numerical solution and another approach, called *mode splitting* can be used. The time-step restriction associated with gravity waves is only penalizing insofar all equations are solved with a small time step. But we can use the small time step only with the subset of equations governing the gravity-wave evolution and take a fraction N of the overall time step. Hence, N steps on the shallow-water equations will forward in time elevation η towards the new overall time step (Figure 12-6). In view of the typical values of g and g', the 3D time step is typically an order of magnitude larger than the time step associated with gravity waves, and since the solution of the shallow-water equations with the small time step involves only 3 equations instead of $3m$, an order of magnitude in terms of computational cost can be gained by the mode-splitting approach. At the end of the N shallow-water equation steps and the subsequent 3D step, a problem might occur: The momentum equations of each layer calculated with the new elevation η^{n+1} from the shallow-water equation will lead to velocities at the new time level u_k^{n+1}, v_k^{n+1}. When summing up those velocities, weighted by the layer thickness, we can calculate the transport. Unfortunately, the transport from this calculation will in general be different from the transport that comes out from the shallow-water equations after the N sub-steps, because of nonlinearities in the equations. If nothing is done to correct for this incoherence, instabilities can occur (*e.g.*, Killworth *et al.* 1991). To avoid the problem, we can for example write governing equations for the shear components u'_k, v'_k, with the different terms in the governing equation exactly canceling out when summing over all layers. This is rather complicated and a simpler approach is to correct the velocity fields obtained after solving the layer equations so as to make sure their weighted sum equals the predicted transport from the shallow-water equations. This approach can also be applied to level models or any 3D model dealing with a free surface, the general idea being to integrate vertically the governing equations to make appear the barotropic components solved with a smaller time step than the rest of the equations.

Except for the problems mentioned, we can retain the distinct advantage of aligning coordinate lines (and hence numerical grids) with dynamically significant features. This explains the success of numerical models based on the isopycnal layer approach and several widely used numerical isopycnal models are based among others on the initial implementations of Hulburt and Thompson (1980), Bleck *et al.* (1992) and Hallberg (1995). Today's tendency is to abandon purely isopycnal models in realistic applications in favor of more general vertical coordinate models we will see in Section 20.7.

12.7 Lagrangian approach

In the case of the isopycnal model, we noted that the conservation equation for ρ was simplified because we choose the coordinate surfaces to be material surfaces of the flow. This is a Lagrangian approach (following a flow parcel) rather then an Eulerian one (observing the system from a fixed point) which can be generalized to calculation of individual fluid parcels. In the isopycnal model, the choice of a material surface as vertical coordinate system eliminated vertical velocity from the advection part. A fully Lagrangian approach will therefore

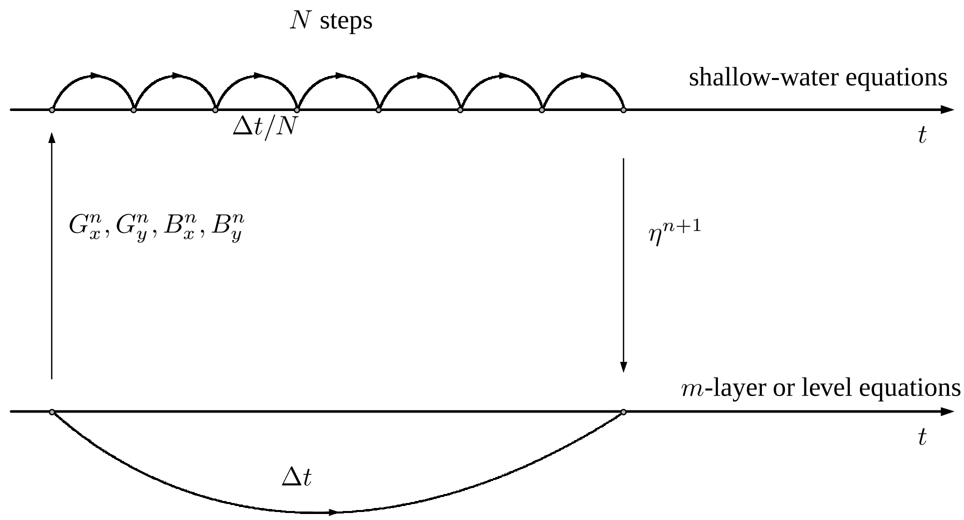

Figure 12-6 At a given time step, information from the layer positions allow to calculate the baroclinic forcing terms of the barotropic equations. The corresponding shallow-water type equations can then be integrated forward in time over several small time-steps, until the overall time step Δt is covered. Then, the surface height η at the new time level can be used in all layers to forward in time the layer structures.

be most interesting in reducing the problems associated with the advection discretization. The astute reader may already have wondered in Section 6.4 why we went through all these complicated Eulerian schemes to find the solution of a pure advection problem, which, when written using a material derivative

$$\frac{dc}{dt} = 0 \tag{12.37}$$

is simply $c = c^0$ for a particle with initial value c^0. First we have to stress that the solution applies to a given, tagged, water parcel which moves with the current along its trajectory. Therefore to have access to the full information, we need not only to know the concentration c^0 of the water mass but also its position at any time. To calculate its position we need to integrate its trajectory by using the definition of velocity of a given water parcel:

$$\frac{dx}{dt} = u(\,x(t), y(t), z(t), t\,), \tag{12.38a}$$

$$\frac{dy}{dt} = v(\,x(t), y(t), z(t), t\,), \tag{12.38b}$$

$$\frac{dz}{dt} = w(\,x(t), y(t), z(t), t\,). \tag{12.38c}$$

The position $x(t), y(t), z(t)$ of a particle starting from an initial position x^0, y^0, z^0 is thus obtained by integrating three ordinary differential equations if the velocity field is known.

A single fluid parcel does however not provide the concentration field at any moment everywhere in the domain but only at the location of the fluid parcel. To assess concentrations everywhere, we can instead of following a single particle calculate the evolution of an ensemble of particles, each of which is launched initially at a different location. The concentration at any point of the domain can be obtained by interpolation from the closest particles or averaging in grid cells (*binning*). In both approaches, in order the method to work, the domain must at any moment be covered by a sufficient amount of particles, distributed as uniformly as possible. If there are regions void of particles, concentrations there cannot be inferred anymore. This is a first problem of the *Lagrangian approach* that follows individual parcels: For an initially relatively uniform distribution of particles, complex flow pattern concentrate water parcels in some regions while other parts a depopulated (Figure 12-7). Therefore complex algorithms eliminating redundant particles in some regions and adding new particles in empty regions are needed. Roughly speaking, if L and H are the horizontal length scale and vertical length scale of the process to resolve in a three-dimensional domain of surface S and depth D we need at least $DS/(L^2H)$ particles, which is roughly the requirement on the number of grid boxes needed in an Eulerian model (1.17). However, because the Lagrangian particles have a tendency to from clusters and leave regions with lower coverage, one to two order of magnitude more particles are needed to resolve the solution.

The time integration itself also imposes some constraints on the method: For accurate time integration of (12.38) we must be able to follow the spatial variations of the velocity field during a time-step which requires

$$U\Delta t \leq L, \tag{12.39}$$

otherwise the trajectory calculation will be inaccurate. For the same reason, we also must follow the time variations of the current $\Delta t \ll T$, if the current varies with a time scale T. Another important aspect is related to the integration of the trajectories. In addition to the above mentioned accuracy requirement, two sources of errors are encountered: the time discretization itself does generally not ensure a reversible calculations. If time or currents are reversed, the numerical integration does not bring the particle back to its initial condition (see Exercise 12-5). Therefore some dispersion can be associated with the integration. The second source of error is related to the knowledge of the velocity field, itself generally calculated by a model and thus available only on a discrete grid. Therefore, assuming the velocity field is given on a regular grid, to calculate the trajectories, the velocity at an arbitrary location $(x(t), y(t), z(t))$ must be retrieved by interpolation of the nearest surrounding velocity information. An error due to this interpolation will then affect the trajectories and induce some additional dispersion of particles.

Except those restrictions, the Lagrangian approach is easily implemented. Also diffusion can be taken into account by simulating the mixing effect as a random displacement of particles, also called *random walk*, according to

$$x^{n+1} = x^n + \int_{t^n}^{t^{n+1}} \left[u(\, x(t), y(t), z(t), t\,) + \frac{\partial \mathcal{A}}{\partial x} \right] dt \;+\; \sqrt{2\Delta t \mathcal{A}}\; \xi \tag{12.40}$$

where ξ is a random variable of Gaussian distribution with zero mean and unit standard deviation (*e.g.*, Gardiner 1997). [3] It can be shown (*e.g.*, Gardiner 1997, Spagnol *et al.* 2002)

[3] It can be noted that in most models the random variable has not a Gaussian distribution but a uniform distribution. This is acceptable as long as time-steps are sufficiently small, because in this case, adding up a large number

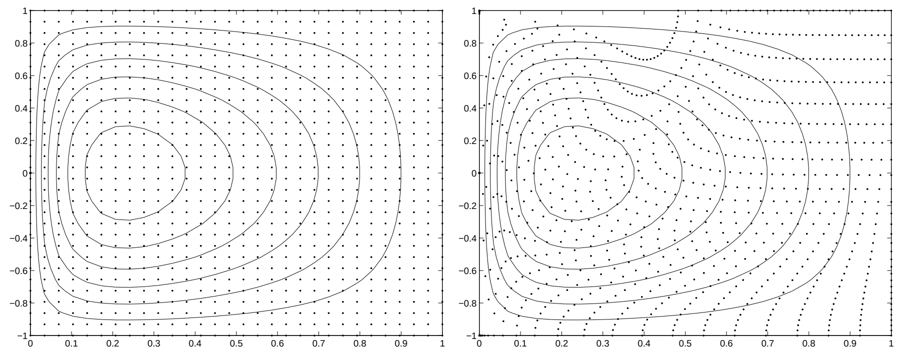

Figure 12-7 Calculation of particle displacement in a current field similar to the one used in Figure 6-18. Use `traj2D.m` for an animation. Particles follow the stationary streamfunction (solid line) and make some regions void of data.

that this stochastic equation leads to particle distributions consistent with

$$\frac{\partial c}{\partial t} + u\frac{\partial c}{\partial x} = \frac{\partial}{\partial x}\left(\mathcal{A}\frac{\partial c}{\partial x}\right) \tag{12.41}$$

A large number of particles moved according to (12.40) then mimic the concentration evolution of (12.41). The role of the term $\partial\mathcal{A}/\partial x$ can easily be understood and illustrated in a situation of a local minimum of $\mathcal{A}$ within the domain of interest, such as near a pycnocline (Exercise 12-8).

Analytical Problems

12-1. Generalize the theory of the coastal Kelvin wave (Section 9.2) to the two-layer system over a flat bottom and under a rigid lid. In particular, what are the wave speed and trapping scale?

12-2. In the case of the shallow-water reduced-gravity model, derive an energy-conservation principle. Then, separate the kinetic and potential energy contributions.

12-3. Show that a steady flow of the shallow-water reduced-gravity system conserves the Bernoulli function $B = g'h + (u^2 + v^2)/2$.

12-4. Establish the equations governing motions in a one-layer model above an uneven bottom and below a thick, motionless layer of slightly lesser density.

of time steps amounts to add up a large number of random process. In this case the *central limit theorem* (*e.g.*, Riley *et al.* 1997) proves that the combined random processes have a Gaussian distribution irrespectively of the individual random process' distributions.

12-5. Seek a solution to the shallow-water reduced-gravity model of the type $h(x,\ t) = A(t)x^2 + 2B(t)x + C(t)$, $u(x,\ t) = U_1(t)x + U_0(t)$, $v(x,\ t) = V_1(t)x + V_0(t)$. To what type of motion does this solution correspond? What can you say of its temporal variability? (Take f = constant.)

12-6. Using the rigid-lid approximation in the shallow-water equations (*i.e.*, a single density layer), analyze the dispersion relation of waves on the β plane. Show that there are no gravity waves and that the only dispersion relation that remains can be compared to the dispersion relation of planetary waves (9.27). How can the difference in dispersion relation be interpreted in terms of the hypotheses used in the rigid-lid approximation? *Hint:* Look again at Section 7.5. JMB from ⇓

12-7. Atlantic waters flow along the Algerian coast, being slightly lighter than the Mediterranean waters. If a typical density difference is 1 kg/m^3 and the thickness of the layer of Atlantic waters 150 m, how large is the sea surface displacement associated with the intrusion of the lighter waters? *Hint:* Assume the lower layers at rest. JMB to ⇑

Numerical Exercises

12-1. Adapt the shallow-water equation model developed in Problem 9-3 to simulate the seiche in a lake where a reduced gravity model can be applied to describe the evolution of the surface layer.

12-2. Discretize in time and horizontal space the linearized two-layer model on an Arakawa grid of your choice. Use a discretization that does not require the solution of a linear system. Provide a stability analysis neglecting Coriolis force.

12-3. Implement the discretization of Exercise 12-2 and calculate the numerical solution of Section 12.5.

12-4. Analyze the implicit treatment of surface elevation in the barotropic components of the layer equations (Equations (12.25), (12.36) and the corresponding equation for $\bar{v}$). Use a C-grid and an implicit treatment of both the divergence term in volume conservation and pressure gradient in the momentum equation. Neglect Coriolis force. Eliminate the yet unknown velocity components from the equations to arrive at an equation for η^{n+1}. Compare the approach with the pressure calculation in the rigid-lid approximation of Section 7.6 and interpret what happens when you take very large time-steps.

12-5. Use different time-integration techniques to calculate trajectories associated with the 2D current field:

$$u \;=\; -\cos(\pi t)\, y, \quad v \;=\; \cos(\pi t)\, x \tag{12.42}$$

from $t = 0$ to $t = 1$ and interpret the results. Prove that the trapezoidal scheme is reversible.

12-6. Implement a random walk into the calculation of the trajectories of Problem 12-5 and verify the dispersive nature of the random walk. *Hint:* Use a large number of particles concentrated at the same initial position.

12-7. Try to use a large number of particles to advect the tracer field of Figure 6-18 by distributing them initially on a regular grid with adequate concentration values. Look at `tvdadv2D.m` to see how the velocity field and initial concentration distribution are defined. Which problem due you face when you need to calculate concentration at an arbitrary position at a later moment?

12-8. Implement (12.40) without advection in a periodic domain between $x = -10L$ and $x = 10L$. Diffusion is given by

$$\mathcal{A} \;=\; \mathcal{A}_0 \tanh^2(x/L) \tag{12.43}$$

Start with a uniform distribution of particles for $x < 0$ and zero particles for $x > 0$. Simulate the evolution with and without the term $\partial \mathcal{A}/\partial x$ and discuss. Take $L = 1000$ km and $\mathcal{A}_0$ = 1000 m^2/s.*Hint:* Periodicity of the domain can be ensured by adequate positioning of particles when crossing $x = -10L$ or $x = 10L$.

Raymond Braislin Montgomery
1910 – 1988

A student of Carl-Gustav Rossby, Raymond Braislin Montgomery earned a reputation as a brilliant descriptive physical oceanographer. Applying dynamic results derived by his mentor and other contemporary theoreticians to observations,he developed precise means of characterizing water masses and currents. By his choice of analyzing observations along density surfaces rather than along level surfaces, an approach that led him to formulate the potential now bearing his name, Montgomery was able to trace the flow of water masses across ocean basins and to arrive at a lucid picture of the general oceanic circulation. Montgomery's lectures and published works, marked by an unusual attention to clarity and accuracy, earned him great respect as a critic and reviewer. (*Photo by Hideo Akamatsu — courtesy of Mrs. R. B. Montgomery*)

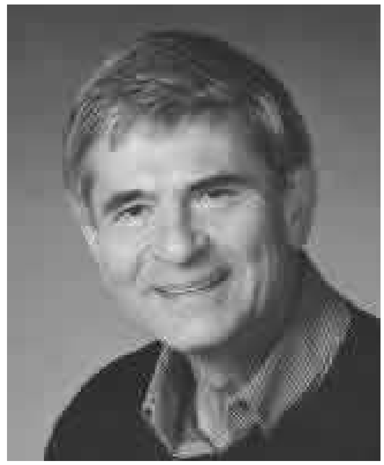

Jörg Imberger
1942 –

Text of second bio (`http://www.cwr.uwa.edu.au/cwr/people/acad/imberger/biog.html`)

Chapter 13

Internal Waves

(October 18, 2006) SUMMARY: This chapter treats internal gravity waves supported by a vertical stratification. After the derivation of the dispersion relation and an examination of wave properties, the chapter also considers mountain waves and nonlinear effects. The vertical-mode analysis of internal waves leads to trapped waves and an eigenvalue problem treated numerically. JMB from ⇓ JMB to ⇑

13.1 From surface to internal waves

Starting at an early age, everyone has seen, experienced, and wondered about surface waves. Sloshing of water in bathtubs and kitchen sinks, ripples on a pond, surf at the beach, and swell further offshore are all manifestations of surface water waves. Sometimes we look at them with disinterest, and sometimes they fascinate us. But, whatever our reaction or interest, their mechanism relies on a simple balance between gravity and inertia. When the surface of the water is displaced upward, gravity pulls it back downward, the fluid develops a vertical velocity (potential energy turns into kinetic energy) and, because of inertia, the surface penetrates below its level of equilibrium. An oscillation results. A change in the phase of the oscillations from place to place causes the wave to travel. Because surface waves carry energy and no volume, they naturally occur wherever there is agitation that causes no overall water displacements, such as the shaking of a half-full bottle, the throwing of a stone in a pond, or a storm at sea.

The gravitational force continuously strives to restore the water surface to a horizontal level, because the water density is greater than that of the air above. It goes almost without saying that the same mechanism is at work whenever two fluid densities differ. This frequently occurs in the atmosphere when warm air overlies cold air; waves may then be manifested by cloud undulations, which may at times be remarkably periodic (Figure 13-1). An oceanic example, known as the phenomenon of dead water (Figure 1-4), is the occurrence of waves at the interface between an upper layer of relatively light water and a denser lower layer. Those waves, although unseen from the surface, can cause a sizable drag on a sailing

Figure 13-1 Evidence of internal waves in the atmosphere. The presence of moisture causes condensation in the rising air (wave crests), thus revealing the internal wave as a periodic succession of cloud bands. (Photo by the authors, February 2005, Tassili N'Ajjer, Algeria)

vessel (Section 1.3).

But the existence of such interfacial waves is not restricted to fluids with two distinct densities and a single interface. With three densities and two interfaces, two internal wave modes are possible; if the middle layer is relatively thin, the vertical excursions of the interfaces interact, letting energy pass from one level to the other. At the limit of a continuously stratified fluid, an infinite number of modes is possible, and wave propagation has both horizontal and vertical components (Figure 13-2). Regardless of the level of apparent complexity in the wave pattern, the mechanism remains the same: There is a continuous interplay between gravity and inertia and a continuous exchange between potential and kinetic energy. (See also Problem 13-6).

JMB from ⇓
JMB to ⇑
JMB from ⇓
JMB to ⇑

13.2 Internal-wave theory

To study internal waves in their purest form, a few assumptions are necessary: There is no ambient rotation, the domain is infinite in all directions, there is no dissipative mechanism of any kind, and, finally, the fluid motions and wave amplitudes are small. This last assumption is made to permit the linearization of the governing equations. However, we reinstate a term previously neglected, namely, the vertical acceleration term $\partial w/\partial t$ in the vertical momentum equation. We do so anticipating that vertical accelerations may play an important role in gravity waves. (Recall the discussion in Section 11.2 on the vertical oscillations of fluid

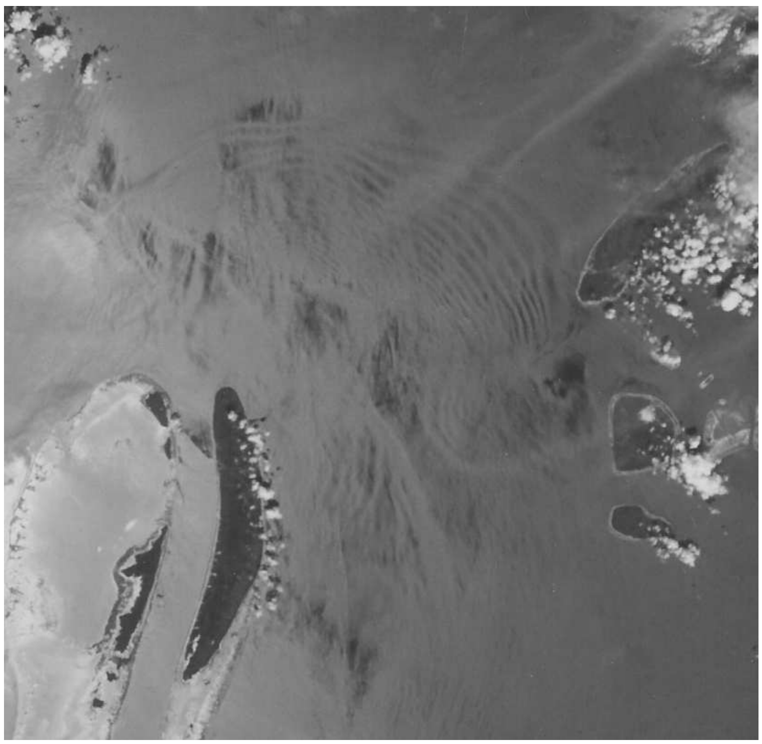

Figure 13-2 Surface manifestation of oceanic internal waves. The upward energy propagation of internal waves modifies the properties of surface waves rendering them visible from space. In this sunglint photograph taken from the space shuttle *Atlantis* on 19 November 1990 over Simbutu Passage in Malyasia (5°N, 119.5°E), a large group of tidally-generated internal waves is seen to propagate northward into the Sulu Sea. (NASA Photo STS-38-084-060)

parcels in a stratified fluid, which included the vertical acceleration.) The inclusion of this term breaks the hydrostatic balance, but so be it! Finally, we decompose the fluid density as follows

$$\text{Actual fluid density} \;=\; \rho_0 \;+\; \bar{\rho}(z) \;+\; \rho'(x,\, y,\, z,\, t), \tag{13.1}$$

where ρ_0 is the reference density (a pure constant), $\bar{\rho}(z)$ is the ambient equilibrium stratification, and $\rho'(x, y, z, t)$ is the density fluctuation induced by the wave (lifting and lowering of the ambient stratification). The inequality $|\ \bar{\rho}\ | \ll \rho_0$ is enforced to justify the Boussinesq approximation (Section 3.7), whereas the further inequality $|\ \rho'\ | \ll |\ \bar{\rho}\ |$ is required to linearize the wave problem. The total pressure field can be decomposed in a similar manner.

With the preceding assumptions, the governing equations become (Section 4.4)

$$\frac{\partial u}{\partial t} \;=\; -\,\frac{1}{\rho_0}\,\frac{\partial p'}{\partial x}, \tag{13.2a}$$

$$\frac{\partial v}{\partial t} \;=\; -\,\frac{1}{\rho_0}\,\frac{\partial p'}{\partial y}, \tag{13.2b}$$

$$\frac{\partial w}{\partial t} \;=\; -\,\frac{1}{\rho_0}\,\frac{\partial p'}{\partial z} \;-\; \frac{1}{\rho_0} g\rho', \tag{13.2c}$$

$$\frac{\partial u}{\partial x} \;+\; \frac{\partial v}{\partial y} \;+\; \frac{\partial w}{\partial z} \;=\; 0, \tag{13.2d}$$

$$\frac{\partial \rho'}{\partial t} \;+\; w\frac{d\bar{\rho}}{dz} \;=\; 0. \tag{13.2e}$$

The factor $d\bar{\rho}/dz$ in the last term can be transformed by introducing the stratification frequency (alias the Brunt–Väisälä frequency) defined earlier in (11.3):

$$N^2 \;=\; -\,\frac{g}{\rho_0}\,\frac{d\bar{\rho}}{dz}. \tag{13.3}$$

For simplicity, we will assume it to be uniform over the extent of the fluid. This corresponds to a linear density variation in the vertical. Because all coefficients in the preceding linear equations are constant, a wave solution of the form

$$e^{\mathrm{i}\,(k_x x + k_y y + k_z z - \omega t)}$$

is sought. Transformation of the derivatives into products (e.g., $\partial/\partial x$ becomes $\mathrm{i}\,k_x$) leads to a 5-by-5 homogeneous algebraic problem. The solution is non-zero if the determinant vanishes, and this requires that the wave frequency ω be given by

$$\omega^2 \;=\; N^2\,\frac{k_x^2 + k_y^2}{k_x^2 + k_y^2 + k_z^2} \tag{13.4}$$

in terms of the wavenumbers, k_x, k_y, and k_z, and the stratification frequency, N. This is the dispersion relation of internal gravity waves.

A number of wave properties can be stated by examination of this relation. First and foremost, it is obvious that the numerator is always smaller than the denominator, meaning the wave frequency will never exceed the stratification frequency; that is,

$$\omega \ \leq \ N \tag{13.5}$$

for positive frequencies. The reason for this upper bound can be traced back to the presence of the vertical acceleration term in (13.2c). Indeed, without that term the denominator in (13.4) reduces from $k_x^2 + k_y^2 + k_z^2$ to only k_z^2, implying that the non-hydrostatic term can be neglected as long as $k_z^2 + k_y^2 \ll k_z^2$. This occurs for waves with horizontal wavelengths much longer than their vertical wavelengths; the frequency of those waves is much less than N. For progressively shorter waves, the correction becomes increasingly important, the frequency rises but saturates at the value N. We may then ask what would happen if we agitate a stratified fluid at a frequency greater than its own stratification frequency. The answer is that, with such short periods, particles do not have the time to oscillate at their natural frequency and instead follow whatever displacements are forced upon them; the disturbance is local, and no energy is carried away by waves.

Another important property derived from the dispersion relation (13.4) is that the frequency does not depend on the wavenumber magnitude (and thus on the wavelength) but only on its angle with respect to the horizontal plane. Indeed, noting that $k_x = k \cos\theta \cos\phi$, $k_y = k \cos\theta \sin\phi$, and $k_z = k \sin\theta$, where $k = (k_x^2 + k_y^2 + k_z^2)^{1/2}$ is the wavenumber magnitude, θ is its angle from the horizontal (positive or negative), and ϕ is the angle of its horizontal projection with the x-axis, we obtain

$$\omega \ = \ \pm \ N \cos\theta, \tag{13.6}$$

proving that the frequency depends only on the pitch of the wavenumber, and, of course, the stratification frequency. The fact that two signs are allowed indicates that the wave can travel in one of two directions, upward or downward along the wavenumber direction. On the other hand, if the frequency is imposed, all waves, regardless of wavelength, propagate at fixed angles from the horizontal. The lower the frequency, the steeper the direction. At the limit of very low frequencies, the phase propagation is purely vertical ($\theta = 90°$).

13.3 Structure of an internal wave

Let us rotate the x and y axes so that the wavenumber vector is contained in the (x, z) vertical plane (*i.e.*, k_y = 0 and there is no variation in the y-direction and no v velocity component). The solutions for the remaining two velocity components and the density fluctuation are

$$u \ = \ -\frac{g\omega k_z}{\rho_0 N^2 k_x} \, A \sin(k_x x + k_z z - \omega t) \tag{13.7a}$$

$$w \ = \ +\frac{g\omega}{\rho_0 N^2} \, A \sin(k_x x + k_z z - \omega t) \tag{13.7b}$$

$$p' \ = \ -\frac{g k_z}{k_x^2 + k_z^2} \, A \sin(k_x x + k_z z - \omega t) \tag{13.7c}$$

$$\rho' \ = \ + A \cos(k_x x + k_z z - \omega t). \tag{13.7d}$$

JMB from ⇓

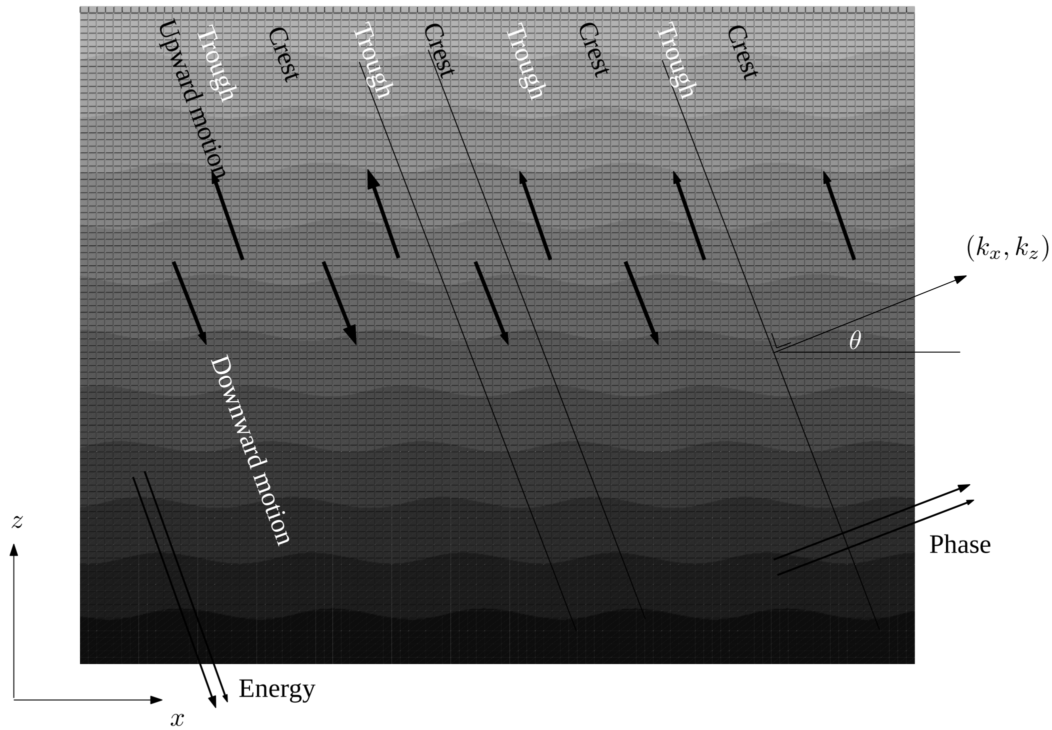

Figure 13-3 Vertical structure of an internal wave.

Benoit why not non -dimensional version:

$$\rho' = + A\rho_0 \cos(k_x x + k_z z - \omega t).$$

JMB to ⤊ and corresponding other components?

For k_x, k_z, and ω all positive, the structure of the wave is depicted on Figure 13-3. The areas of upwelling (crests) and downwelling (troughs) alternate both horizontally and vertically, and lines of constant phase (*e.g.*, following crests) tilt perpendicularly to the wavenumber vector. The trigonometric functions in solution (13.7d) tell us that the phase $k_x x + k_z z - \omega t$ remains constant with time if one translates in the direction (k_x, k_z) of the wavenumber at the speed (see Appendix B):

$$c = \frac{\omega}{\sqrt{k_x^2 + k_z^2}}. \tag{13.8}$$

This is the phase speed, at which lines of crests and troughs translate. Because the velocity components, u and w, are in quadrature with the density fluctuations, the velocity is nil at the crests and troughs but is maximum a quarter of a wavelength away. The signs indicate that when one component is positive, the other is negative, implying downwelling to the right and upwelling to the left, as indicated in Figure 13-3. The ratio of velocities ($-k_x/k_z$)

further indicates that the flow is everywhere perpendicular to the wavenumber vector and thus parallel to the lines connecting crests and troughs. Internal waves are transverse waves. A comparison of the signs in the expressions of w and ρ' reveals that rising motions occur ahead of crests and sinking motions occur ahead of troughs, eventually forming the next crests and troughs, respectively. Thus, the wave moves forward and, because of the inclination of its wavenumber, also upward.

The propagation of the energy is given by the group velocity, which is the gradient of the frequency with respect to the wavenumber (Appendix B):

$$c_{gx} = \frac{\partial \omega}{\partial k_x} = + \frac{\omega k_z^2}{k_x (k_x^2 + k_z^2)} \tag{13.9}$$

$$c_{gz} = \frac{\partial \omega}{\partial k_z} = - \frac{\omega k_z}{(k_x^2 + k_z^2)} . \tag{13.10}$$

The direction is perpendicular to the wavenumber (k_x, k_z) and is downward. Thus, although the crests and troughs appear to move upward, the energy actually sinks. The reader can verify that, irrespective of the signs of the frequency and wavenumber components, the phase and energy always propagate in the same horizontal direction (though not at the same rates) and in opposite vertical directions.

Let us now turn our attention to the extreme cases. The first one is that of a purely horizontal wavenumber ($k_z = 0$, $\theta = 0$). The frequency is then N, and the phase speed is N/k_x. The absence of wavelike behavior in the vertical direction implies that all crests and troughs are vertically aligned. The motion is strictly vertical, and the group velocity vanishes, implying that the energy does not travel. The opposite extreme is that of a purely vertical wavenumber ($k_x = 0$, $\theta = 90°$). The frequency vanishes, implying a steady state. There is then no wave propagation. The velocity is purely horizontal and, of course, laterally uniform. The picture is that of a stack of horizontal sheets each moving, without distortion, with its own speed and in its own direction. If a boundary obstructs the flow at some depth, none of the fluid at that depth, however remote from the obstacle, is allowed to move. This phenomenon, occurring at very low frequencies in highly stratified fluids, is none other than the blocking phenomenon discussed at the end of Section 11.5 and presented as the stratified analogue of the Taylor column in rotating fluids.

In stratified and rotating fluids, the lowest possible internal-wave frequency is not zero but the inertial frequency f (see Problem 13-3). At that limit, the wave motion assumes the form of inertial oscillations, wherein fluid parcels execute horizontal circular trajectories (Section 2.3). Such limiting behavior is an attribute of inertia-gravity waves in homogeneous rotating fluids (Section 9.3) and is not surprising, since internal waves in stratified rotating fluids are the three-dimensional extensions of the inertia-gravity waves of homogeneous rotating fluids.

13.4 Vertical modes and eigenvalue problems

Up to now, we analyzed the internal waves in the rather schematic situation of an unbounded non-rotating domain of uniform stratification. This is tantamount of analyzing waves of wavelength much shorter than the length scales of the ambient fluid (horizontal wavelength much

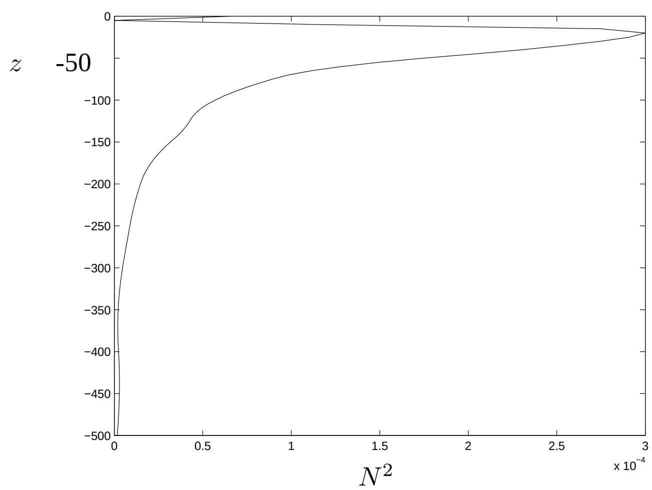

Figure 13-4 Climatological average density profile in the Western Mediterranean was used to calculate the associated profile of squared Brunt-Väisälä frequency N^2 (in s^{-2}). Data from `Medar`©.

smaller than geometric length scales, vertical wavelength much smaller than depth or scales of variations of N^2) and for which the frequency is sufficiently high not to be influenced by earth rotation.

If we look at real vertical profiles of density and associated Brunt-Väisälä frequency (Figure 13-4) it could be questionable that real internal waves can be described for all wavelength by the previous internal-wave theory. To assess to which extend the presence of non-uniform stratification modifies the conclusions from the previous theory, we will now analyze the situation of a vertically varying stratification. To simplify the analysis, we will assume a constant depth and eliminate surface waves by the rigid-lid approximation (Sections 7.5 and 12.2). We take advantage of this additional analysis to reinstate rotation effects by the f-plane approximation, but suppose that stratification is sufficiently strong so that $N^2(z) > f^2$ holds everywhere as it is generally the case in nature.

Within this framework, the governing equations of the perturbations associated with the wave in an ambient stratification $\bar{\rho}(z)$ of Brunt-Väisälä frequency

$$N^2(z) = -\frac{g}{\rho_0}\frac{\partial \bar{\rho}}{\partial z} > f^2 > 0 \tag{13.11}$$

are now

$$\frac{\partial u}{\partial t} = fv - \frac{1}{\rho_0}\frac{\partial p'}{\partial x}, \tag{13.12a}$$

$$\frac{\partial v}{\partial t} = fu - \frac{1}{\rho_0}\frac{\partial p'}{\partial y}, \tag{13.12b}$$

$$\frac{\partial w}{\partial t} = -\frac{1}{\rho_0} g\,\rho' - \frac{1}{\rho_0}\frac{\partial p'}{\partial z}, \tag{13.12c}$$

$$\frac{\partial u}{\partial x} + \frac{\partial v}{\partial y} + \frac{\partial w}{\partial z} = 0, \tag{13.12d}$$

$$\frac{\partial \rho'}{\partial t} + w\frac{\partial \bar{\rho}}{\partial z} = 0. \tag{13.12e}$$

As before, we did not make use of the hydrostatic approximation. For a uniform topography, we can apply the technique of separation of variables and search for solutions of the following type:

$$u = \mathcal{F}(z)\mathcal{U}(x,y)e^{-\mathrm{i}\,\omega t}, \tag{13.13a}$$
$$v = \mathcal{F}(z)\mathcal{V}(x,y)e^{-\mathrm{i}\,\omega t}, \tag{13.13b}$$
$$p' = \rho_o\,\mathcal{F}(z)\mathcal{P}(x,y)e^{-\mathrm{i}\,\omega t}, \tag{13.13c}$$
$$w = \mathrm{i}\,\omega\mathcal{W}(z)\mathcal{P}(x,y)e^{-\mathrm{i}\,\omega t}, \tag{13.13d}$$
$$\rho' = -N^2\,\frac{\rho_0}{g}\mathcal{W}(z)\mathcal{P}(x,y)e^{-\mathrm{i}\,\omega t}. \tag{13.13e}$$

Replacing these expressions into the governing equations (13.12), we realize that (13.12e) is trivially satisfied and that the four remaining equations read after simplifications assuming non-zero solutions

$$-\,\mathrm{i}\,\omega\,\mathcal{U} \;=\; f\mathcal{V} - \frac{\partial \mathcal{P}}{\partial x}, \tag{13.14a}$$
$$-\mathrm{i}\,\omega\,\mathcal{V} \;=\; -f\mathcal{U} - \frac{\partial \mathcal{P}}{\partial y}, \tag{13.14b}$$
$$(\omega^2 - N^2)\,\mathcal{W} \;=\; -\frac{\partial \mathcal{F}}{\partial z}, \tag{13.14c}$$
$$\frac{1}{\mathcal{P}}\left(\frac{\partial \mathcal{U}}{\partial x} + \frac{\partial \mathcal{V}}{\partial y}\right) \;=\; -\mathrm{i}\,\frac{\omega}{\mathcal{F}}\frac{\partial \mathcal{W}}{\partial z}. \tag{13.14d}$$

The first two equation do not depend on z, the third one does not depend on x and y, while in the last one, the left hand side depends only on x, y, whereas the right hand side depends only on z. This can only be true if both terms are constant. For dimensional reasons we call this constant $\mathrm{i}\,\omega/gh^{(i)}$, where $h^{(i)}$ has the dimension of depth and is commonly called *equivalent depth*, the reason for which will become clear rapidly. Substitution of the result of (13.14d)

$$-\mathrm{i}\,\frac{1}{\mathcal{F}}\frac{\partial \mathcal{W}}{\partial z} = \frac{\mathrm{i}}{gh^{(i)}}$$

into the z dependent equation (13.14c) leads to the equation governing the vertical mode $\mathcal{W}$

$$\frac{d^2\mathcal{W}}{dz^2} + \frac{(N^2 - \omega^2)}{gh^{(i)}}\,\mathcal{W} = 0. \tag{13.15}$$

while the horizontal structure $\mathcal{U}, \mathcal{V}, \mathcal{P}$ is solution of (13.14a), (13.14b) completed with the result of (13.14d)

$$\frac{\partial \mathcal{U}}{\partial x} + \frac{\partial \mathcal{V}}{\partial y} = \frac{\mathrm{i}\,\omega}{gh^{(i)}}\mathcal{P}. \tag{13.16}$$

These three equations have in fact the same structure as the wave equations of a shallow-water system of constant depth (Section 9.1). We simply observe that $\mathcal{P}/g$ plays the same role here as does surface elevation η in a shallow-water system of constant depth $h^{(i)}$. Therefore, we can immediately recover the wave solutions of the shallow-water theory and verify that for a horizontal wave-like solution $(\mathcal{U}, \mathcal{V}, \mathcal{P}) = (U, V, P)e^{\mathrm{i}\,(k_x x + k_y y)}$ with constant U, V, P these waves obey the dispersion relation of Poincaré waves:

$$\omega^2 = f^2 + gh^{(i)}(k_x^2 + k_y^2). \tag{13.17}$$

For horizontally finite domains (see Problem 13-10), only discrete sets of k_x, k_y are allowed, but we will not further analyze these possibilities and consider k_x, k_y to be given.

13.4.1 Vertical eigenvalue problem

As we know how to find the horizontal structure of the wave solution, we now have to find its vertical structure, which can be done by substituting the horizontal dispersion relation (13.17) in the vertical mode equation (13.15). This leads to the following eigenvalue problem:

$$\frac{d^2\mathcal{W}}{dz^2} + (k_x^2 + k_y^2)\frac{N^2(z) - \omega^2}{\omega^2 - f^2}\mathcal{W} = 0, \tag{13.18}$$

with the boundary conditions of a rigid-lid system

$$\mathcal{W} = 0 \text{ in } z = 0 \text{ and } z = H. \tag{13.19}$$

We are in the presence of a homogeneous differential equation and homogeneous boundary conditions. The solution of such a system is $\mathcal{W} = 0$ except for some special values of ω. For those values non-zero solution can be found, satisfying both boundary conditions. Those special values of ω are the eigenvalues and the corresponding non-zero solutions $\mathcal{W}$ the eigenfunctions or vertical modes.

13.4.2 Bounds on frequency

We anticipate that there should be some bounds on the frequencies in view of the physical interpretation of the bound $\omega^2 < N^2$ in Section 13.2. In order to find such bounds, we will apply again integral techniques similar to those used to analyze stability of shear flows (Section 10.2).

If we multiply (13.18) by the complex conjugate $\mathcal{W}^*$, integrate vertically across the domain, perform an integration by part on the first term and use boundary conditions (13.19), we get

$$\int_0^H \left|\frac{d\mathcal{W}}{dz}\right|^2 dz = (k_x^2 + k_y^2)\int_0^H \frac{N^2 - \omega^2}{\omega^2 - f^2}\left|\mathcal{W}\right|^2 dz. \tag{13.20}$$

If ω is real, we immediately see that only values within the range

$$f^2 \le \omega^2 \le N_{\max}^2 \tag{13.21}$$

are permitted, since outside this range, the right hand side of (13.20) is always negative (assuming $N^2 \ge f^2$), while the left hand side is always positive.

We could now question ourselves if there could be complex values of ω. A purely imaginary solution is not possible in our case since for $\omega = \mathrm{i}\,\omega_i$, the right hand side of (13.20) is again always negative[1]. To analyze the most general case $\omega = \omega_r + \mathrm{i}\,\omega_i$, it is sufficient to analyze the imaginary part involved in (13.20):

$$\Im\left(\frac{N^2-\omega^2}{\omega^2-f^2}\right) = -2\omega_r\omega_i\,\frac{N^2+f^2}{(\omega_r^2-\omega_i^2-f^2)^2+4\omega_r^2\omega_i^2}. \tag{13.22}$$

We realize that if we assume $\omega_i \neq 0$, the right hand side is different from zero while the left-hand side is zero, which is impossible. Therefore (13.20) allows only real ω.

In conclusion, for $N^2 > f^2$, we find pure wave motions with frequencies that lie within the range (13.21). This is to be compared to the internal wave frequency in an infinite domain without rotation (13.5). We also note that as before, if a wave of frequency ω exists, so does one of frequency $-\omega$, corresponding to a propagation in the opposite direction.

Benoit: Do you have a simple physical explanation why now there is a LOWER bound related to Coriolis force while without stratification, f^2 is an UPPER bound?

13.4.3 Simple example of constant N^2

We can readily analyze the case of uniform stratifiction treated in the unbounded, non-rotating case (Section 13.2). In the rotating bounded domain, the eigenvalue problem has the following simple solution

$$\mathcal{W}(z) = \sin k_z z, \quad k_z = i\frac{\pi}{H}, \quad i = 1, 2, 3, ... \tag{13.23}$$

with the dispersion relation

$$\omega^2 = \frac{(k_x^2+k_y^2)\,N^2 + k_z^2\,f^2}{k_x^2+k_y^2+k_z^2}. \tag{13.24}$$

Due to the finite vertical domain size, the vertical wavenumber k_z now takes discrete values and the corresponding functions $\mathcal{W}$ form a discrete set of eigenfunctions. We can verify that frequencies all fall into the range (13.21) and recognize that the spatial structures of the modes are the same as in the unbounded domain, except that only those wavelengths are permitted that ensure the boundary conditions to be satisfied.

Concerning the separation constant $gh^{(i)}$, we can now calculate the discrete set of values it takes

$$gh^{(i)} = \frac{\omega^2-f^2}{k_x^2+k_y^2} = \frac{N^2-f^2}{k_x^2+k_y^2+\left(i\frac{\pi}{H}\right)^2}. \tag{13.25}$$

Since $gh^{(i)}$ plays the same role for the horizontal structures as gH in a shallow water system, we can calculate the equivalent to the Rossby radius of deformation.

$$R_i = \frac{\sqrt{gh^{(i)}}}{f}. \tag{13.26}$$

The so-called internal radius of deformation plays the same role as the (external) radius of deformation in a shallow-water system and characterizes for example the horizontal scale

[1] We assumed from the beginning $N^2 \geq f^2 \geq 0$; the interested reader could also analyze the case $N^2 < 0$, corresponding to the statically unstable case. In this case he would recover the possibility of complex ω and therefore unstable solutions, as to be expected on physical grounds.

at which both rotation and gravitation, here through stratification, come into play. Also the lateral scale of a Kelvin wave is characterized by this scale (see Problem 13-8). By virtue of $\omega^2/f^2 = 1 + (k_x^2 + k_y^2)\,R_i^2$, waves with a shorter wavelength than the deformation radius are dominantly influenced by stratification, while those with larger scales are dominated by rotation. The Rossby radius of deformation is thus the scale at which both rotation and stratification are at play for the given vertical wave mode. The waves that vary rapidly in the vertical ($i \gg 1$) have a smaller radius of deformation and rotation plays a role for the horizontal structure at smaller scales. On the other hand, waves with large vertical structures also have the largest Rossby radius of deformation and need larger horizontal scales to be influenced by rotation. For small aspect ratios $k_x^2 + k_y^2 \ll k_z^2$ with strong stratification $N^2 \gg f^2$, the expression of the deformation radius simplifies into

$$R_i \sim \frac{NH}{i\pi f}, \quad i = 1, 2, ... \tag{13.27}$$

The simple problem treated up to now has the advantage to show how rotation and a finite domain influence the dispersion relation compared to (13.4), but it is relatively simplistic if we would like to know the eigenfrequencies of a system with a localized pycnocline. Though analytical approximative methods exist to tackle the mathematical eigenvalue problem (for example WKB methods, Bender and Orszag 1978), it is generally easier to resort to numerical methods. This is even more true if the system to be analyzed is a real one, where the density profile was measured or obtained from climatological databases at discrete levels.

13.4.4 Numerical approach for the general case

The discretization chosen here is a straightforward finite-difference technique. For the sake of simplicity, uniform grid spacing Δz is assumed. The first and last grid points are chosen on the rigid bottom and rigid-lid surface (Figure 13-5), since a Dirichlet condition on the unknown is imposed there. The discretized field w of the real solution $\mathcal{W}$ at location z_k is w_k so that the discretization reads

$$\mathsf{w}_{k+1} + \mathsf{w}_{k-1} - 2\,\mathsf{w}_k + \Delta z^2 (k_x^2 + k_y^2) \frac{N^2(z_k) - \omega^2}{\omega^2 - f^2}\,\mathsf{w}_k = 0, \quad k = 2, 3, ..., m-1 \tag{13.28}$$

$$\mathsf{w}_1 = 0, \quad \mathsf{w}_m = 0 \tag{13.29}$$

This problem can be written in a matrix form by collecting all w_k into an array $\mathbf{w}$:

$$\mathbf{A}(\omega^2)\mathbf{w} = 0, \tag{13.30}$$

where the matrix $\mathbf{A}$ is tridiagonal as for the diffusion problem (see Section 5.5), and depends on ω^2. The allowed frequencies are then those which allow a non-zero vertical velocity $\mathbf{w}$, which can only be obtained when the system is singular

$$\det(\mathbf{A}) = 0. \tag{13.31}$$

Basically the problem is then a problem of finding zeros of a given function, here the determinant of the system. For each value of ω^2 for which the determinant is zero, the discretized

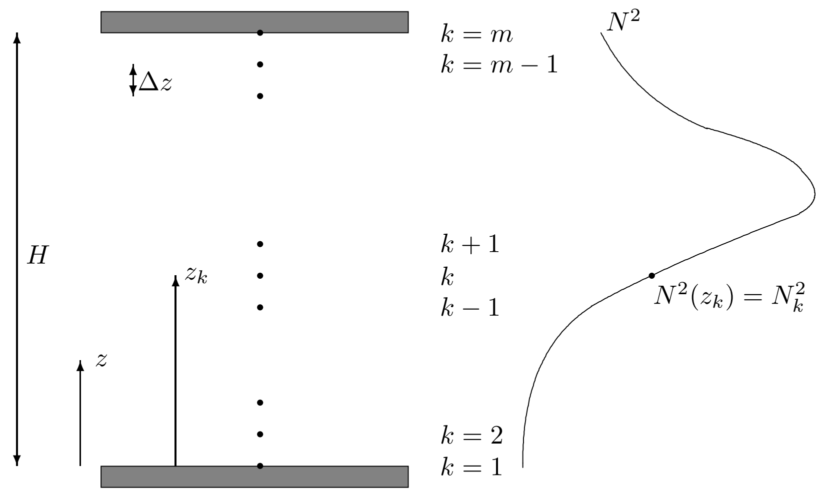

Figure 13-5 Discretization notations for the eigenvalue problem.

spatial eigenmode $\mathbf{w}$ is then the solution of (13.30). In linear algebra, finding this vector for a given singular matrix this is a standard problem and amounts at finding the null-space of the matrix $\mathbf{A}$. The solution of our problem can therefore be obtained by searching those values of ω^2 for which the determinant of $\mathbf{A}$ is zero and then using a linear algebra package to calculate the null-space associated with the now singular matrix to retrieve the discretized vertical structure of the internal wave.

However, finding zeros of a complicated function is not trivial and we are never sure not to miss zeros, even if the theoretical bounds founds (13.21) for ω^2 can guide the searching algorithm. We can neither be sure that numerical solutions of (13.31) also fall into the same range, though those falling outside could certainly be qualified non-physical.

We can illustrate the approach using standard linear algebra routines for this direct approach and `iwnaive.m` creates the matrix $\mathbf{A}$ and calculates its determinant for a large number of values for ω^2 (Figure 13-6).

Even with a logarithmic scale, we see the difficulty to catch the very rapid variations in the function $\det(\mathbf{A})$. For still resolved variations, the precision of the zeros found is obviously deteriorating when ω^2 approaches f^2. This should be no surprise, since those solutions correspond to vertical structures with increasing vertical wavenumber as shown by the analytical solution (13.23)-(13.24). We recover the property that functions with the highest wavenumbers are poorly represented on a numerical grid. In order to find the eigenvalues without the need for "manual" inspection of the function $\det(\mathbf{A})$, we can observe that the problem formulation is not very different from a classic linear eigenvalue problem:

$$\mathbf{A}\mathbf{x} = \lambda\mathbf{x}, \tag{13.32}$$

for which a series of theorems on the number and locations of the eigenvalues λ exist, as well as robust algorithms calculating its solutions numerically.

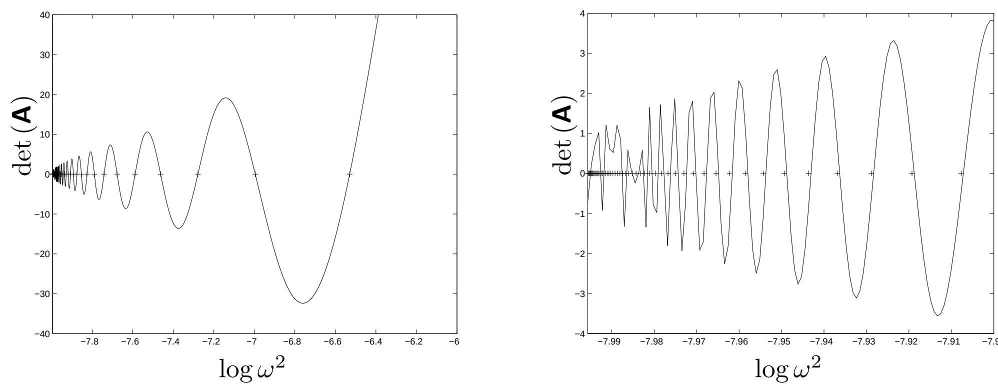

Figure 13-6 Determinant of matrix A for constant N^2 in function of $\log\omega^2$. The points marked with $+$ are the locations of the exact eigenvalues of (13.24). Detail on the right panel.

Eigenvalue problem

We therefore will try to reformulate the problem (13.30) and write it as

$$-\frac{\omega^2}{f^2}\left[-\mathsf{w}_{k+1}-\mathsf{w}_{k-1}+(2+\epsilon)\,\mathsf{w}_k\right]+\left[-\mathsf{w}_{k+1}-\mathsf{w}_{k-1}+\left(2+\epsilon N_k^2 f^{-2}\right)\,\mathsf{w}_k\right]=0 \tag{13.33}$$

with $\epsilon=\Delta z^2(k_x^2+k_y^2)>0$. We limit the unknown vector between $k=2$ and $k=m-1$, since the boundary conditions are readily implemented and (13.33) can be written as a linear problem:

$$\mathbf{Bw}=\lambda\mathbf{Cw},\quad \lambda=\frac{\omega^2}{f^2} \tag{13.34}$$

where matrices $\mathbf{B}$ and $\mathbf{C}$ are tridiagonal matrices independent of ω^2. Both matrices have -1 on the super- and subdiagonal, while on the diagonal, $\mathbf{C}$ is composed of $2+\epsilon$ and $\mathbf{B}$ of $2+\epsilon N_k^2 f^{-2}$.

Both $\mathbf{B}$ and $\mathbf{C}$ are symmetric positive definite since they are diagonally dominant. Luckily (13.34) is already a standard linear algebra problem (called generalized eigenvalue problem) for which solvers and theorems exist (for example a Rayleigh-Ritz criteria given in Exercise 13-2). We can recast it in an even more familiar form by noting that for a positive definite matrix, its inverse exists and therefore, defining $\tilde{\mathbf{w}}=\mathbf{Cw}$ we recover a standard eigenvalue problem

$$\mathbf{A}\tilde{\mathbf{w}}=\lambda\tilde{\mathbf{w}},\quad \mathbf{A}=\mathbf{BC}^{-1}. \tag{13.35}$$

Once the eigenvalues and eigenvectors $\tilde{\mathbf{w}}$ found, the discretized physical mode $\mathbf{w}$ can be recovered by $\mathbf{w}=\mathbf{C}^{-1}\tilde{\mathbf{w}}$.

We can easily demonstrate that the problem has only real solutions. Since both $\mathbf{B}$ and $\mathbf{C}$ are symmetric positive defininite, multiplying (13.34) for a given eigenvalue λ_i and eigenvector $\mathbf{w}^i$ by the transposed complex conjugate $\left(\mathbf{w}^{i*}\right)^T$, we use the fact that both $\left(\mathbf{w}^{i*}\right)^T\mathbf{Bw}^i$ and $\left(\mathbf{w}^{i*}\right)^T\mathbf{Cw}^i$ are real because of the positive definite nature of $\mathbf{B}$ and $\mathbf{C}$ to show that λ_i must also be real.

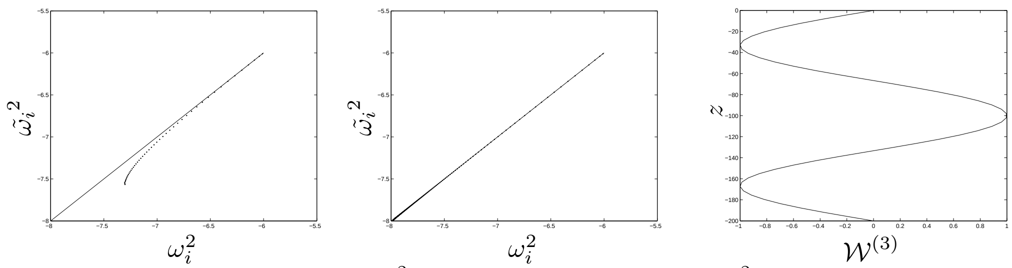

Figure 13-7 Numerical estimation $\tilde{\omega_i}^2$ versus and exact physical value ω_i^2. Left panel for 50 discrete levels, middle panel for 450 modes. Right panel: numerical estimation of the third vertical mode as a function of z. The mode clearly corresponding to $\sin(3\pi z/H)$.

We observe that contrary to the analytical solution, where an infinite number of modes are found, only a finite number $(m-2)$ of eigenvalues and modes are calculated by the discretized version. To verify the numerical method outlined, we can calculate the numerical solution for the case of constant N^2 and compare it with the known analytical solution (13.23)-(13.24). As expected, the largest eigenvalues, corresponding the largest vertical wavelength, are well represented, even for a moderate number of calculation points (Figure 13-7). The frequencies closer to f need however more vertical points to be recovered precisely, because of the short wavelength associated. To represent mode i correctly we would indeed need a spacing $i\Delta z << H$.

13.5 A new physical process: Waves concentrated at a pycnocline

The numerical method developed and partly validated for the uniform stratification can now be used to analyze the pycnocline case. To do so, we take a schematic density profile (Figure 13-8), with a Brunt-Väisälä frequency varying between N_0 and N_1 with $f^2 < N_0^2 < N^2 < N_1^2$.

The first three modes (Figure 13-8) correspond to the highest frequencies represented by the vertical lines on the right panel together with the stratification frequency. We observe that the amplitude of the wave is concentrated at the pycnocline, while outside this region, the amplitude decays rapidly. This can be understood in the light of the sign of $(N^2-\omega^2)/(f^2-\omega^2)$ which appears in (13.18). If this factor is positive, the eigenfunctions are of oscillating nature, whereas if it is negative, they are of exponential nature. Since the term changes sign within the domain if $N_0^2 < \omega^2 < N_1^2$, the solution changes from an oscillating behavior (in regions where $\omega^2 \leq N^2$) to an exponential outside this regions, decreasing towards zero at the boundaries of the domain. The point where $\omega^2 = N^2$ is called a *turning point*. The wave is thus concentrated at the pycnocline for such frequencies, simply because the restoring force there has a frequency near the frequency of the wave.

For higher modes (Figure 13-9), ω^2 decreases and approaches the lower limit of N^2. The turning points move away from the pycnocline until they fall outside the domain of interest. Then $\omega^2 < N^2$ and the solution is of oscillatory behavior everywhere. However we

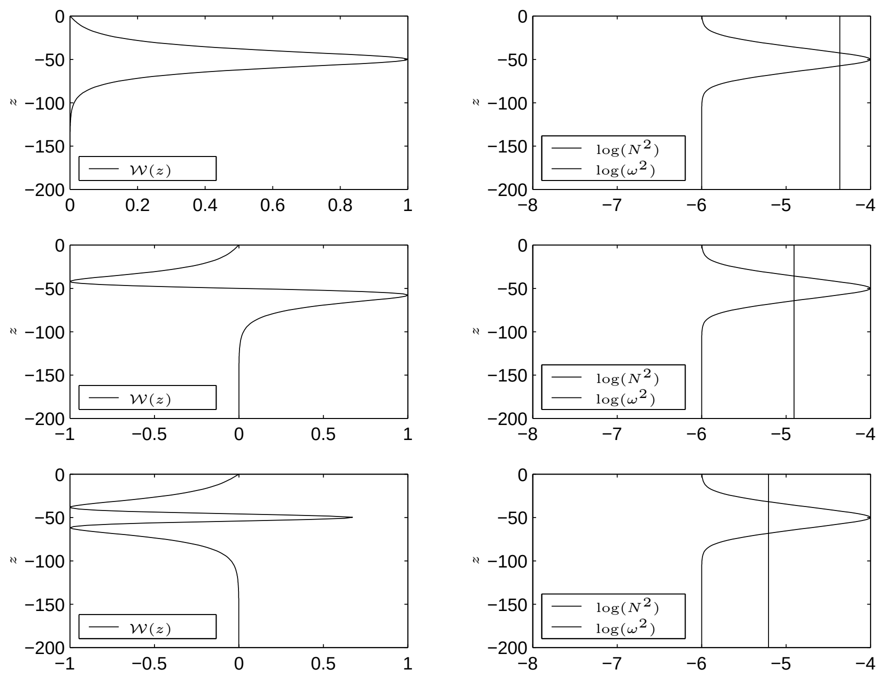

Figure 13-8 Non-uniform stratification and first 3 modes, left panel. Value of ω^2 compared to N^2 on the right panel.

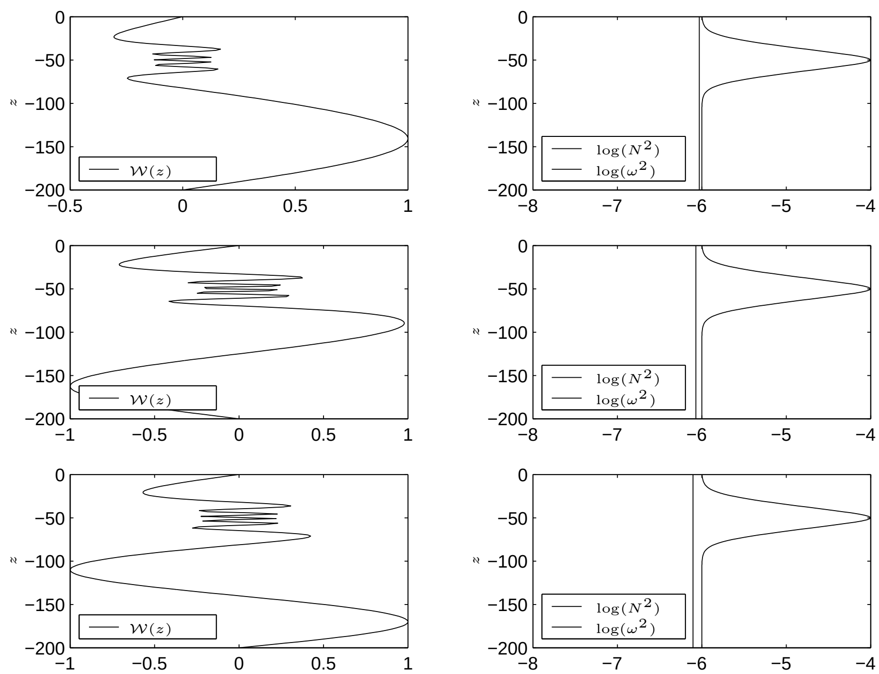

Figure 13-9 Non-uniform stratification and modes 10 to 12, left panel. Value of ω^2 compared to N^2 on the right panel).

now observe lower amplitudes within the pycnocline. This is due to the fact that the eigenfrequency of the restoring force is much further away from ω^2 within the pycnocline than outside. Resonant behavior is thus stronger outside the pycnocline and amplitudes higher.

At even higher modes and frequencies closer to f (Figure 13-10), the regions above and below the pycnocline start to be decoupled. Here the pycnocline acts as a barrier since both regions now have a series of modes oscillating at frequencies near f, which are decoupled from the other layer. This is what can be observed for oscillations near the inertial frequency in a two layer system. **Benoit:** more insight??

Finally the eigenvalue problem with a real profile allows us to estimate the internal radius of deformation for the Western Mediterranean. Based on the climatologically averaged density profile (Figure 13-4), we can use the same eigenvalue calculations for different horizontal wavenumbers $k_x^2 + k_y^2$. For longer waves, we expect the value of the radius of deformation to converge to a constant value associated with the hydrostatic approximation (see also Problem 13-8). Indeed, this has been tested numerically (code `iwavemed.m` and Figure 13-11) and leads to a value of the first internal radius of deformation of $14\,\mathrm{km}$ (to be compared to the external radius of $3000\,\mathrm{km}$).

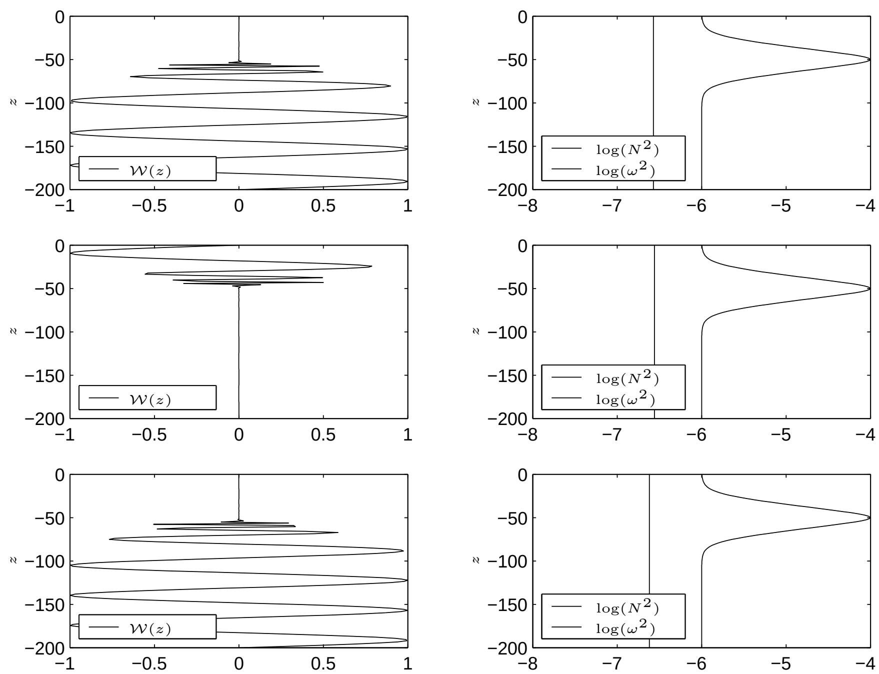

Figure 13-10 Non-uniform stratification and modes 26 to 28 left panel. Value of ω^2 compared to N^2 on the right panel).

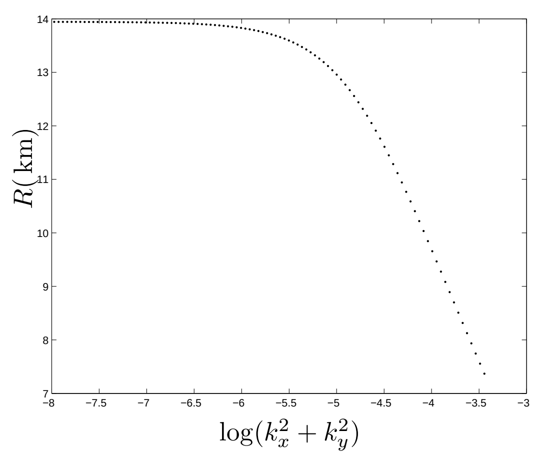

Figure 13-11 First internal radius of deformation R associated to the profile of Figure 13-4 as a function of the horizontal wavenumber.

13.6 Lee waves

Internal waves in the atmosphere and ocean can be generated by a myriad of processes, almost wherever a source of energy has some temporal or spatial variability. Oceanic examples include the ocean tide over a sloping bottom, mixing processes in the upper ocean (such as during a hurricane), instabilities of shear flows, and the passage of a submarine. In the atmosphere, one particularly effective mechanism is the generation of internal waves by a wind blowing over an irregular terrain such as a mountain range or a hilly countryside. We select the latter example to serve as an illustration of internal-wave theory because it has some meteorological importance and lends itself to a simple mathematical treatment.

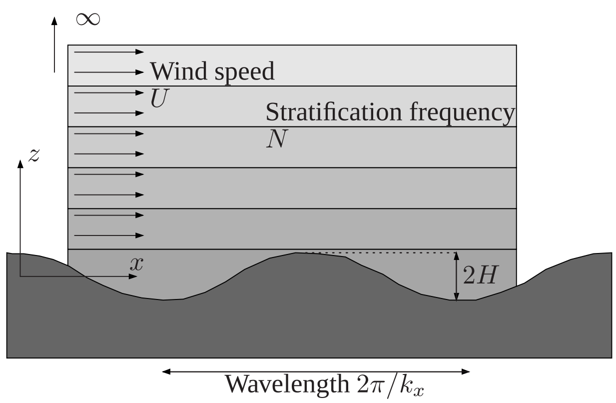

Figure 13-12 Legend

To apply the previous linear-wave theory, we naturally restrict our attention to small-amplitude waves and, consequently, to small topographic irregularities. This restriction also permits us to study a single topographic wavelength, from which the principle of linear superposition would allow us to construct more general solutions. The model (Figure 13-12) consists of a stratified air mass of uniform stratification frequency N flowing at speed U over a slightly wavy terrain. The ground elevation is taken as a sinusoidal function $b = H \cos k_x x$ JMB from ⇓ of amplitude H (the trough-to-crest height difference is then $2H$) and wavenumber k_x (the wavelength is then $2\pi/k_x$). The wind direction (along the x-axis of the model) is chosen to be normal to the troughs and crests, so that the problem is two-dimensional.

Because our theory has been developed for waves in the absence of a main flow, we translate the x-axis with the wind speed. The topography then appears to move at speed U in the negative x-direction:

$$\begin{aligned} z \;=\; b(x+Ut) &= H\;\cos[k_x(x+Ut)] \\ &= H\;\cos(k_x x - \omega t), \end{aligned} \tag{13.36}$$

where the frequency is defined as

$$\omega \;=\; -\,k_x U \tag{13.37}$$

and is a negative quantity. Because a particle initially on the bottom must remain there at all times (no airflow through the ground), a boundary condition is

$$w \;=\; \frac{\partial b}{\partial t} \;+\; u\frac{\partial b}{\partial x} \quad \text{at } z \;=\; b, \tag{13.38}$$

which can be immediately linearized to become

$$\begin{aligned} w \;&=\; \frac{\partial b}{\partial t} \\ &=\; H\omega\,\sin(k_x x - \omega t) \quad \text{at } z \;=\; 0, \end{aligned} \tag{13.39}$$

by virtue of our small-amplitude assumption.

The solution to the problem, which must simultaneously be of type (13.7d) and meet condition (13.39), can be stated immediately:

$$u \;=\; k_z U H\,\sin(k_x x + k_z z - \omega t) \tag{13.40a}$$

$$w \;=\; -k_x U H\,\sin(k_x x + k_z z - \omega t) \tag{13.40b}$$

$$p' \;=\; -\rho_0 k_z U^2 H\,\sin(k_x x + k_z z - \omega t) \tag{13.40c}$$

$$\rho' \;=\; \frac{\rho_0 N^2 H}{g}\,\cos(k_x x + k_z z - \omega t), \tag{13.40d}$$

where the vertical wavenumber k_z is determined by the dispersion relation (13.4):

$$k_z^2 \;=\; \frac{N^2}{U^2} \;-\; k_x^2. \tag{13.41}$$

The mathematical structure of this last expression shows that two cases must be distinguished:
JMB from ⇓ Either $N/U > k_x$ and k_z is real, or $N/U < k_x$ and k_z is imaginary. Note that solutions (13.40) are formulated in the moving reference frame and that when we express it in the fixed
JMB to ⇑ frame, a stationnary solution is obtained, corresponding to $\omega = 0$.

13.6.1 Radiating Waves

Let us first explore the former situation, which arises when the stratification is sufficiently strong ($N > k_x U$) or when the topographic wavelength is sufficiently long ($k_x < N/U$). Physically, the time $2\pi/k_x U$ taken by a particle traveling at the mean wind speed U to go from a trough to the next trough (i.e., up and down once) is longer than the natural oscillatory period $2\pi/N$, and internal waves can be excited. Solving (13.41) for k_z, we have two solutions at our disposal,

$$k_z \;=\; \pm\sqrt{\frac{N^2}{U^2} \;-\; k_x^2}\,, \tag{13.42}$$

but because the source of wave energy is at the bottom of the domain, only the wave with upward group velocity is physically relevant. According to (13.10) and (13.37), we select the positive root.

The wave structure in the framework fixed with the earth (Figure 13-13) is steady and such that all density surfaces undulate like the terrain, with no vertical attenuation but with

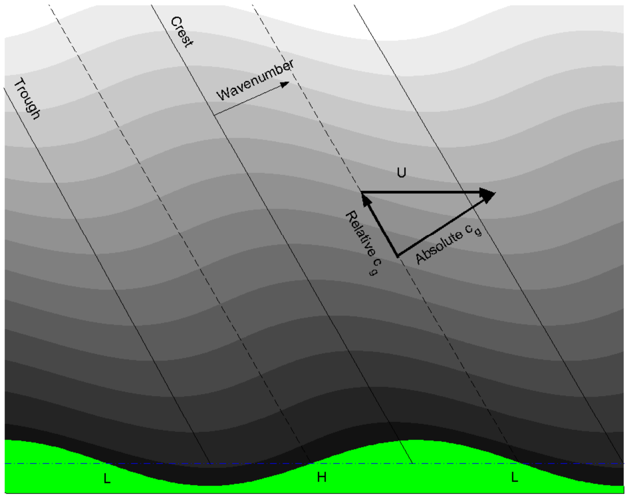

Figure 13-13 Structure.

an upwind phase tilt with height. The tilt angle between the wave fronts (lines joining crests) and the horizontal, ϕ, is given by **Benoit:** Is there a reason you take ϕ now, instead of θ used for the internal wave structure? Also note that (13.42) can be written as $1 = Fr^{-2} - \delta^2$ with Froude number of wave and aspect ratio of wave. Could be interesting when discussing non-linearities? JMB from $\Downarrow$ JMB to $\Uparrow$

$$\sin\,\phi \;=\; \frac{k_x U}{N}\;, \tag{13.43}$$

so that $k_x = k\ \sin\phi$, $k_z = k\ \cos\phi$, with $k = (k_x^2 + k_z^2)^{1/2}$. The group velocity in the fixed frame is equal to the group velocity relative to the moving wind, given by (13.10) with $\omega = -k_x U$, plus the velocity U in the x-direction:

$$c_{gx} \;=\; -U\frac{k_z^2}{k^2} + U \;=\; U\ \sin^2\ \phi \tag{13.44}$$

$$c_{gz} \;=\; U\frac{k_x k_z}{k^2} \;=\; U\ \sin\ \phi\ \cos\ \phi. \tag{13.45}$$

It tilts upward as required, and its direction coincides with that of the wavenumber (Figure 10-5). Energy is thus radiated upward and downwind. We shall not calculate the energy flux and will show only that the terrain exerts a drag force on the flowing air mass. The Reynolds-stress expression for the wave stress is:

$$\text{Drag force} \;=\; -\,\rho_0\overline{uw}\,|_{z=0} \;=\; -\;\frac{1}{2}\,\rho_0 k_x k_z U^2 H^2,$$

where the overbar indicates an average over one wavelength. The minus sign indicates a retarding force. The existence of this force is also related to the fact that the high pressures are situated on the hill flanks facing the wind, and the lows are on the hill flanks in the wind's shadow.

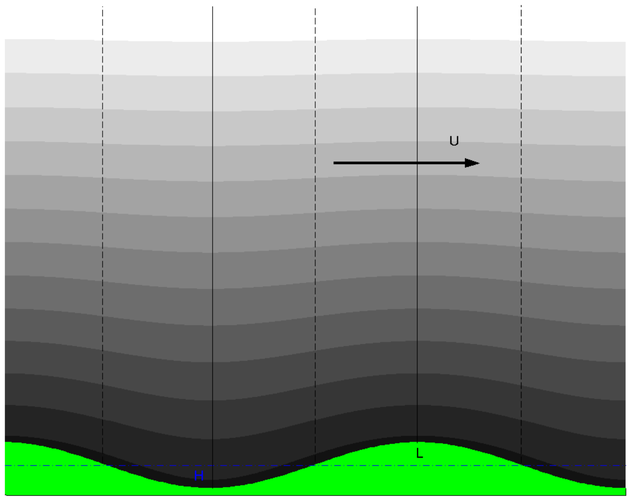

Figure 13-14 Structure.

13.6.2 Trapped Waves

The second case, leading to an imaginary value for k_z, occurs for weak stratifications ($N < k_x U$) or short waves ($k_x > N/U$). To avoid dealing with imaginary numbers we define the quantity a as the positive imaginary part of k_z, that is, $k_z = \pm \mathrm{i}\, a$ with

$$a = \sqrt{k_x^2 - \frac{N^2}{U^2}} \, . \tag{13.46}$$

The solution now contains exponential functions in z, and the physical nature of the problem dictates that we retain only the function that decays away from the ground. In the reference framework translating with the wind speed U, the solution is

$$u = aUH \, e^{-az} \, \cos(k_x x - \omega t) \tag{13.47}$$
$$w = -k_x UH \, e^{-az} \, \sin(k_x x - \omega t) \tag{13.48}$$
$$p' = -\rho_0 a U^2 H \, e^{-az} \, \cos(k_x x - \omega t) \tag{13.49}$$
$$\rho' = \frac{\rho_0 N^2 H}{g} \, e^{-az} \, \cos(k_x x - \omega t). \tag{13.50}$$

The wave structure is depicted in Figure (13-14). Density surfaces undulate at the same wavelength as the terrain, but the amplitude decays with height. There is also no vertical phase shift. Because the waves are contained near the ground, in a boundary layer of thickness on the order of $1/a$, there is no upward energy radiation. The absence of such energy loss is corroborated by the absence of a drag force:

$$\text{Drag force} = - \rho_0 \overline{uw} \, |_{z=0} = 0.$$

The Reynolds stress vanishes because u and w are now in quadrature. Physically, the high pressures are in the valleys, the lows are on the hilltops, and the pressure distribution causes no work against the wind.

13.7 Nonlinear effects

Text of section

13.8 The Garrett-Munk Spectrum

Text of section

Analytical Problems

13-1. In a coastal ocean, the water density varies from 1028 kg/m^3 at the surface to 1030 kg/m^3 at a depth 100 m. What is the maximum internal-wave frequency? What is the corresponding period?

13-2. Internal waves are generated along the coast of Norway by the M_2 surface tide (period of 12.42 h). If the buoyancy frequency N is 2×10^{-3} s^{-1}, at which possible angles can the energy propagate with respect to the horizontal? (*Hint:* Energy propagates in the direction of the group velocity.)

13-3. Derive the dispersion relation of internal gravity waves in the presence of rotation, assuming $f < N$. Show that the frequency of these waves must always be higher than f but lower than N. Compare vertical phase speed to vertical group velocity.

13-4. A 10-m/s wind blows over a rugged terrain, and lee waves are generated. If the stratification frequency is equal to 0.03 s^{-1} and if the topography is approximated to a sinusoidal pattern aligned perpendicularly to the wind, with a 25-km wavelength and a height difference from trough to crest of 500 m, calculate the vertical wavelength, the angle made by the wave fronts (surfaces of constant phase) with the horizontal, and the maximum horizontal velocity at the ground. Also, where is this maximum velocity observed (at crests, at troughs, or at the points of maximum slope)?

13-5. A 75-km/h gale wind blows over a hilly countryside. If the terrain elevation is approximated by a sinusoid of wavelength 4 km and amplitude of 40 m and if the stratification frequency of the air mass is 0.025 s^{-1}, what are the vertical displacements of the air particles at 1000 m and 2000 m above the mean ground level? JMB from ⇓

13-6. Calculate the kinetic and potential energy density of the pure internal-wave field.

13-7. Demonstrate that a single plane internal wave satisfying the dispersion relation is not only solution of the linearized perturbative equations but of the full nonlinear set of equations. What happens if two waves are present in the system?

13-8. Study internal waves in a stratified system of stratification frequency $N(z)$ in a vertically bounded domain using the hydrostratic approximation in (13.12). Show that the separation constant now appears as the eigenvalue to be calculated and that the associated radius of deformation does not depend anymore on the horizontal wavenumbers $k_x^2 + k_y^2$.

13-9. Analyze the possibility of existence of an internal Kelvin wave by using the separation of constants approach. Use the long-wave (or hydrostatic) assumption adapting (13.12). Particularize to the case of uniform N^2.

13-10. A seiche with discrete sets of eigenvalues, unless already treated in layered models? If problem discarded, need to discard reference in text to it.

13-11. Depsite the fact that system (13.2) has four time derivatives, we only analyzed a dispersion relation with two eigenfrequencies. Can you explain?

JMB to ⇑

Numerical Exercises

13-1. Use the dispersion relation of pure internal waves (13.4) and show the superposition of two waves by an animation in the x, z plane of extend L_x, H. Can you see the group velocity when using two waves of equal amplitude and the two wavenumber vectors $(k_x = 35/L_x, k_z = 10/H)$ and $(k_x = 40/L_x, k_z = 12/H)$?

13-2. For the matrices and eigenvalues of problem (13.34), prove

$$\lambda_{\min} \leq \frac{\mathbf{x}^\mathsf{T}\mathbf{B}\mathbf{x}}{\mathbf{x}^\mathsf{T}\mathbf{C}\mathbf{x}} \leq \lambda_{\max}. \tag{13.51}$$

To prove this so-called Rayleigh-Ritz inequality (13.51) for symmetric positive definite matrices $\mathbf{B}$ and $\mathbf{C}$:

- assume that all eigenvalues are different
- demonstrate that $\left(\mathbf{w}^i\right)^\mathsf{T} \mathbf{B}\mathbf{w}^j = \delta_{ij}$ and $\left(\mathbf{w}^i\right)^\mathsf{T} \mathbf{C}\mathbf{w}^j = \delta_{ij}$
- prove that all eigenvectors $\mathbf{w}^i, i = 1, ...$ are linearly independent
- write any vector $\mathbf{x}$ as a weighted sum of those independent vectors and using this expression in the Rayleigh-Ritz quotient prove the Rayleigh-Ritz inequalities.

Adapt then the code `iwnum.m` to provide estimates of the upper and lower bound using a series of random vectors $\mathbf{x}$ to calculate the Rayleigh-Ritz estimator $(\mathbf{x}^\mathsf{T}\mathbf{B}\mathbf{x})/(\mathbf{x}^\mathsf{T}\mathbf{C}\mathbf{x})$ and store the minima and maxima of the quotient found. Look how the bounds are more and more precise the more random vectors you choose.

13-3. By substitution of $\omega^2 = (1+\tilde{\lambda})f^2$ into (13.33) and redefining $\mathbf{B}$, show that all eigenvalues ω_i satisfy $\omega_i^2 \geq f^2$. Incidentally show that you can recast the problem into a standard eigenvalue problem.

By substitution of $\omega^2 = (1-\tilde{\lambda})N_{\max}^2$ into (13.33) and redefining $\mathbf{B}$, show that all eigenvalues ω_i satisfy $\omega_i^2 \leq N_{\max}^2$.

Benoit: I just realized the problem can be recasted in an even simpler version by letting $\lambda = 1 + x$. Then $\mathbf{B}$ is diagonal. see exercise for the demonstration that $x > 0$ (and thus $\omega^2 > f^2$). Should I readapt the text and MATLAB™ codes accordingly? I would suggest not to do so, since for the baroclinic and barotropic stability problem, we would rather obtain a similar structure to the present one. Possibly suggest to find the property in exercise?

13-4. Adapt `iwnummed.m` to read temperature and salinity profiles from other oceanographic data bases, such as the Levitus climatology, and calculate the radius of deformation for the Gulf Stream region. `levitus.m` **to be done**

13-5. Assess numerically the convergence rate for eigenvalues and eigenfunctions in the case of a constant stratification by adapting `iwnum.m`.

13-6. Discretize the eigenvalue problem of the sheared-flow instability (10.9) using the same techniques as in Section 13.4.4. What can you say about the positive-definite nature of the matrices involved? Try to find the numerical eigenvalues and growth rates of profiles you thought probably unstable in Exercise 12-2.

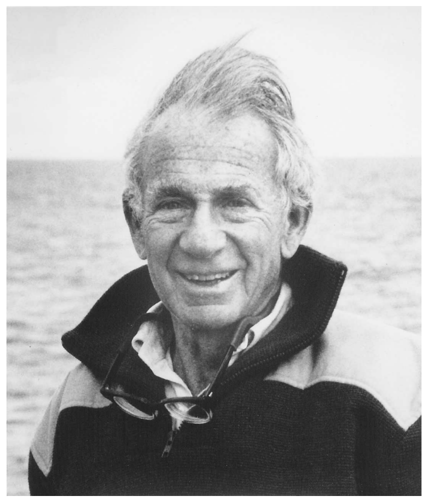

Walter Heinrich Munk
1917 –

Born in Austria and educated in the United States, Walter Heinrich Munk became interested in oceanography during a summer project under Harald Sverdrup at the Scripps Institution of Oceanography and quickly developed a fascination for ocean waves. This interest in waves arose partly because of the wartime need to predict sea and swell and also because Munk found wave research a challenge of intermediate complexity between simple periodic oscillations and hopeless chaos. As years went by, Munk eventually investigated all wavelengths, from the small capillary waves responsible for sun glitter to the ocean-wide tides. His studies of internal waves, in collaboration with Christopher Garrett, led him to propose a universal spectrum for the distribution of internal-wave energy in the deep ocean, now called the Garrett–Munk spectrum. More recently, pursuing an interest in acoustic waves, Munk initiated ocean tomography, a method for determining the large-scale temperature structure in the ocean from the measure of acoustic travel times. (*Photo by Jeff Cordia*.)

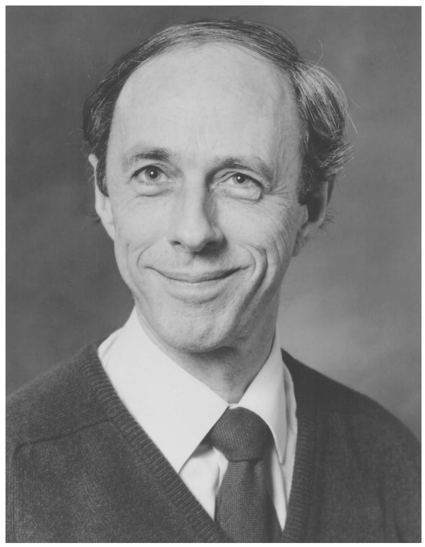

Adrian Edmund Gill
1937 – 1986

Born in Australia, Adrien Edmund Gill pursued his career in Great Britain. His publications spanned a wide range of topics, including wind-forced currents, equatorially trapped ocean waves, tropical atmospheric circulation, and the El Niño–Southern Oscillation phenomenon, and culminated in his treatise *Atmosphere-Ocean Dynamics* (Academic Press, 1982). His greatest contributions relied on the formulation of simple yet illuminating models of geophysical flows. It has been said (only half jokingly) that he could reduce all problems to a simple ordinary differential equation with constant coefficients, with all the essential physics retained. Although he never held a professorship, Gill supervised numerous students at the Universities of Cambridge and Oxford. He is also remembered for his unassuming style and for the generosity with which he shared his ideas with students and colleagues. (*Photo credit:*

Gillman & Soame, Oxford.)

Chapter 14

Turbulence in Stratified Fluids

(October 18, 2006) **SUMMARY**: Whereas the previous chapter treated organized wave flows in stratified fluids, the attention now turns to more complicated motions, such as vertical mixing, flow instability, forced turbulence, and convection. Because the study of such phenomena does not lend itself to detailed analytical solutions, the emphasis is on budgets and scale analysis. The numerical section presents a few schemes by which mixing and turbulence can be represented in numerical models. JMB from ⇓ JMB to ⇑

14.1 Mixing of stratified fluids

Mixing by turbulence generates vertical motions and overturning. In a homogeneous fluid, the energy necessary is only that necessary to overcome mechanical friction (see Sections 5.1 and 8.1) , but in a stratified fluid work must also be performed to raise heavy fluid parcels and lower light parcels. Let us consider, for example, the system pictured in Figure 14-1. Initially, it consists of two layers of equal thicknesses with fluids of different densities and horizontal velocities. After some time, mixing is assumed to have taken place, and the system consists of a single layer of average density flowing with the average velocity[1]. Because the heavier fluid (density ρ_2) lies initially below the lighter fluid (density ρ_1), the center of gravity falls below mid-depth level, whereas in the final state it is exactly at mid-depth. Thus, the center of gravity has been raised in the mixing process, and potential energy must have been provided to the system. Put another way, work has been performed against the buoyancy forces. With identical initial depths $H_1 = H_2 = H/2$, the average density is $\rho = (\rho_1 + \rho_2)/2$, and the potential energy gain is JMB from ⇓ JMB to ⇑

[1] Credit for this illustrative example goes to Prof. William K. Dewar

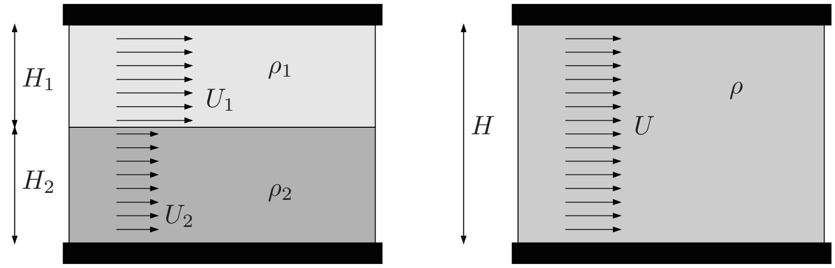

Figure 14-1 Mixing of a two-layer stratified fluid with velocity shear. Rising of dense fluid and lowering of light fluid both require work against buoyancy forces and thus lead to an increase in potential energy. Concomitantly, the kinetic energy of the system decreases during mixing. Only when the kinetic-energy drop exceeds the potential-energy rise can mixing proceed spontaneously.

$$\begin{aligned} PE \text{ gain} &= \int_0^H \rho_{\text{final}}\, gz\, dz - \int_0^H \rho_{\text{initial}}\, gz\, dz \\ &= \frac{1}{2}\,\rho g H^2 - \left[\frac{1}{2}\,\rho_2 g\,\frac{H^2}{4} + \frac{1}{2}\,\rho_1 g\,\frac{3H^2}{4}\right] \\ &= \frac{1}{8}\,(\rho_2 - \rho_1) g H^2. \end{aligned} \tag{14.1}$$

The question arises as to the source of this energy increase. Because human intervention is ruled out in geophysical flows, a natural energy supply must exist or mixing would not take place. In this case, kinetic energy is released in the mixing process, as long as the initial velocity distribution is nonuniform. Conservation of momentum in the absence of external forces and in the context of the Boussinesq approximation ($\rho_1 \simeq \rho_2 \simeq \rho_0$) implies that the final, uniform velocity is the average of the initial velocities: $U = (U_1 + U_2)/2$. This indeed leads to a kinetic-energy loss

$$\begin{aligned} KE \text{ loss} &= \int_0^H \frac{1}{2}\,\rho_0 u_{\text{initial}}^2\, dz - \int_0^H \frac{1}{2}\,\rho_0 u_{\text{final}}^2\, dz \\ &= \frac{1}{2}\,\rho_0 U_2^2\,\frac{H}{2} + \frac{1}{2}\,\rho_0 U_1^2\,\frac{H}{2} - \frac{1}{2}\,\rho_0 U^2 H \\ &= \frac{1}{8}\,\rho_0 (U_1 - U_2)^2 H. \end{aligned} \tag{14.2}$$

Complete vertical mixing is naturally possible only if the kinetic-energy loss exceeds the potential-energy gain; that is,

$$\frac{(\rho_2 - \rho_1) g H}{\rho_0 (U_1 - U_2)^2} < 1. \tag{14.3}$$

Physically, the initial density difference should be sufficiently weak in order not to present an insurmountable gravitational barrier, or alternatively the initial velocity shear should be

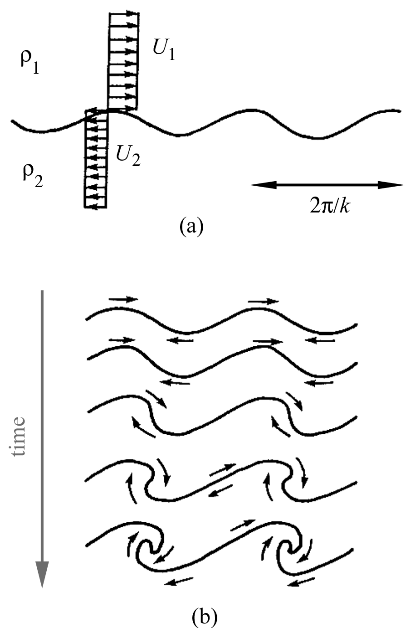

Figure 14-2 Kelvin–Helmholtz instability: (a) initial perturbation of wavenumber k, (b) temporal evolution of an unstable perturbation. The system is always unstable to short waves, which steepen, overturn and ultimately cause mixing. As waves overturn, their vertical and lateral dimensions are comparable.

sufficiently large to supply the necessary amount of energy. When criterion (14.3) is not satisfied, mixing occurs only in the vicinity of the initial interface and cannot extend over the entire system. The determination of the characteristics of such localized mixing calls for a more detailed analysis.

For this purpose, let us now consider a two-fluid system of infinite extent (Figure 14-2), with upper and lower densities and velocities denoted, respectively, by ρ_1, ρ_2 and U_1, U_2, and let us explore interfacial waves of infinitesimal amplitudes. Mathematical derivations, not reproduced here, show that a sinusoidal perturbation of wavenumber k (corresponding to wavelength $2\pi/k$) is unstable if (Kundu, 1990, Section 11-6)

$$(\rho_2^2 \ - \ \rho_1^2)g \ < \ \rho_1\rho_2 k \ (U_1 \ - \ U_2)^2, \tag{14.4}$$

or for a Boussinesq fluid ($\rho_1 \simeq \rho_2 \simeq \rho_0$),

$$2(\rho_2 \ - \ \rho_1)g \ < \ \rho_0 k \ (U_1 \ - \ U_2)^2. \tag{14.5}$$

In a stability analysis, waves of all wavelengths must be considered, and we conclude that there will always be sufficiently short waves to cause instabilities. Therefore, a two-layer shear flow is always unstable. This is known as the *Kelvin–Helmholtz instability*. Among other instances, this instability plays a role in the generation of water waves by surface winds.

The details of the analysis leading to (14.5) reveal that the interfacial waves induce flow perturbations that extend on both sides of the interface across a height on the order of their wavelength. Thus, as unstable waves grow, they form rolls of height comparable to their width (Figures 14-2, 14-3 and 14-4).

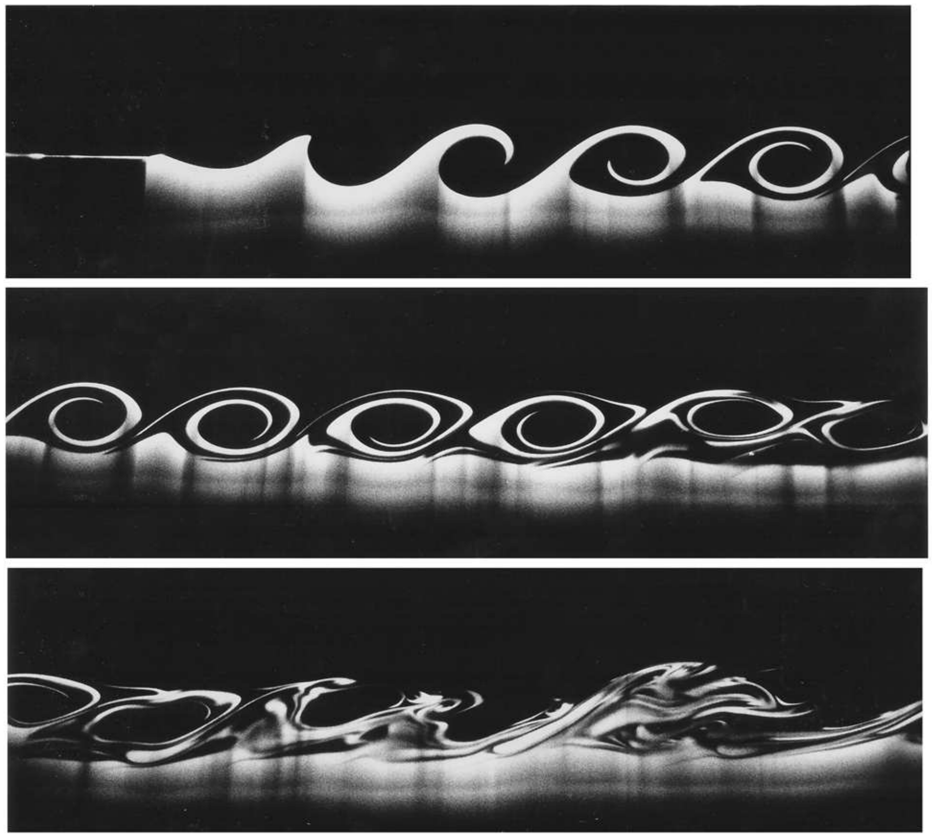

Figure 14-3 Development of a Kelvin–Helmholtz instability in the laboratory. Here, two layers flowing from left to right join downstream of a thin plate (visible on the left of the top photograph). The upper and faster moving layer is slightly less dense than the lower layer. Downstream distance (from left to right on each photograph and from top to bottom panel) plays the role of time. At first, waves form and overturn in a two-dimensional fashion (in the vertical plane of the photo) but, eventually, three-dimensional motions appear that lead to turbulence and complete the mixing. (Courtesy of Greg A. Lawrence. For more details on the laboratory experiment, see Lawrence et al., 1991.)

The rolling and breaking of waves induces turbulent mixing, and it is expected that the vertical extent of the mixing zone, which we denote by ΔH, scales like the wavelength of the longest unstable wave, that for which criterion (14.5) turns into an equality:

$$\Delta H \;\sim\; \frac{1}{k_{\min}} \;=\; \frac{\rho_0 (U_1 - U_2)^2}{2(\rho_2 - \rho_1) g} \,. \tag{14.6}$$

If the fluid system is of finite depth H, the preceding theory is no longer applicable, but we can anticipate, by virtue of dimensional analysis, that the results still hold, within some numerical factors. For a fluid depth H greater than ΔH, mixing must remain localized to a band of thickness ΔH, whereas for a fluid depth H less than ΔH, that is,

$$H \lesssim \frac{\rho_0 (U_1 - U_2)^2}{(\rho_2 - \rho_1) g} \,, \tag{14.7}$$

mixing will engulf the entire system. Note the similarity between this last inequality, derived from a wave theory, and inequality (14.3) obtained from energy considerations.

Figures 14-5 and 14-6 show atmospheric instances when Kelvin–Helmholtz instabilities occurred and were made visible by localized cloud formation. Kelvin–Helmholtz instabilities have also been observed to take place in the ocean (Woods, 1968).

14.2 Instability of a stratified shear flow: The Richardson number

In the preceding section, we restricted our considerations to a discontinuity of the density and horizontal velocity, only to find that such a discontinuous stratification is always unstable. Instability causes mixing, and mixing will proceed until the velocity profile has been made stable. The question then is: For a gradual density stratification, what is the critical velocity shear below which the system is stable and above which mixing occurs? To answer this question, we are led to study the stability of a stratified shear flow.

Let us consider a two-dimensional (x, z) inviscid and nondiffusive fluid with horizontal and vertical velocities (u, w), dynamic pressure p, and density anomaly ρ. In anticipation of the important role played by vertical motions, we reinstate the acceleration term in the vertical momentum equation and write (Section 4.3)

$$\frac{\partial u}{\partial t} + u\,\frac{\partial u}{\partial x} + w\,\frac{\partial u}{\partial z} \;=\; -\,\frac{1}{\rho_0}\,\frac{\partial p}{\partial x} \tag{14.8}$$

$$\frac{\partial w}{\partial t} + u\,\frac{\partial w}{\partial x} + w\,\frac{\partial w}{\partial z} \;=\; -\,\frac{1}{\rho_0}\,\frac{\partial p}{\partial z} - \frac{\rho g}{\rho_0} \tag{14.9}$$

$$\frac{\partial u}{\partial x} + \frac{\partial w}{\partial z} \;=\; 0 \tag{14.10}$$

$$\frac{\partial \rho}{\partial t} + u\,\frac{\partial \rho}{\partial x} + w\,\frac{\partial \rho}{\partial z} \;=\; 0. \tag{14.11}$$

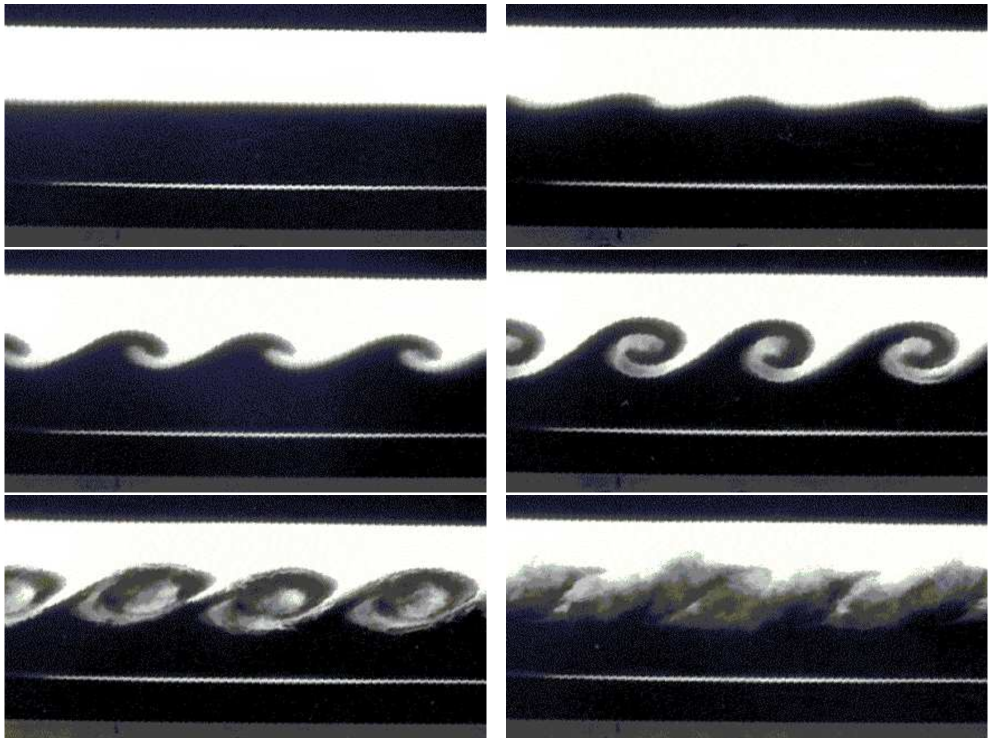

Figure 14-4 Kelvin–Helmholtz instability generated in a laboratory with fluids of two different densities and colours. (*Adapted from GFD-online, Satoshi Sakai, Isawo Iizawa, Eiji Aramaki*) Contact GFD-online@gaia.h.kyoto-u.ac.jp

Figure 14-5 Kelvin–Helmholtz instability in the Algerian sky. **Comment from a meteorologist? Evening cooling hence stratification?** (*Photo by the authors*)

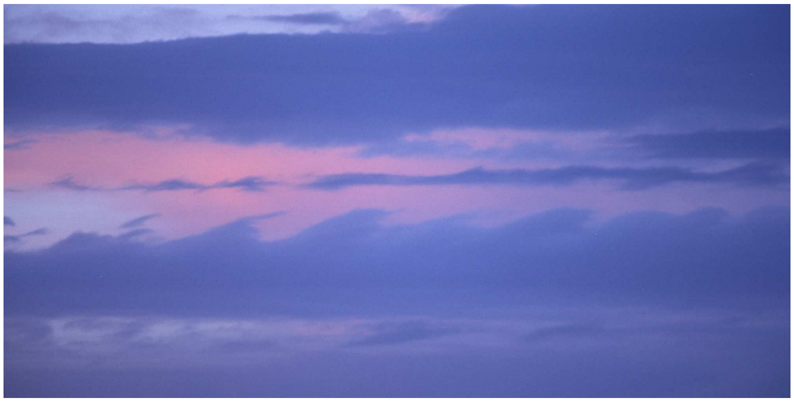

Figure 14-6 Kelvin–Helmholtz instability of the Sahara desert **Comment from a meteorologist?** (*Photo by the authors*)

Our basic state consists of a steady, sheared horizontal flow [$u = \bar{u}(z)$, $w = 0$] in a vertical density stratification [$\rho = \bar{\rho}(z)$]. The accompanying pressure field $\bar{p}(z)$ obeys $d\bar{p}/dz = -g\bar{\rho}(z)$. The addition of an infinitesimally small perturbation ($u = \bar{u} + u'$, $w = w'$, $p = \bar{p} + p'$, $\rho = \bar{\rho} + \rho'$) and a subsequent linearization of the equations yield:

$$\frac{\partial u'}{\partial t} + \bar{u}\,\frac{\partial u'}{\partial x} + w'\,\frac{d\bar{u}}{dz} = -\frac{1}{\rho_0}\,\frac{\partial p'}{\partial x} \tag{14.12}$$

$$\frac{\partial w'}{\partial t} + \bar{u}\,\frac{\partial w'}{\partial x} = -\frac{1}{\rho_0}\,\frac{\partial p'}{\partial z} - \frac{\rho' g}{\rho_0} \tag{14.13}$$

$$\frac{\partial u'}{\partial x} + \frac{\partial w'}{\partial z} = 0 \tag{14.14}$$

$$\frac{\partial \rho'}{\partial t} + \bar{u}\,\frac{\partial \rho'}{\partial x} + w'\,\frac{d\bar{\rho}}{dz} = 0. \tag{14.15}$$

Introducing the perturbation streamfunction ψ via $u' = +\partial\psi/\partial z$, $w' = -\partial\psi/\partial x$, the buoyancy frequency $N^2 = -(g/\rho_0)(d\bar{\rho}/dz)$, assumed to be constant, and a Fourier structure exp[i $k(x - ct)$] in the horizontal, we can reduce the problem to a single equation for ψ in terms of the remaining variable z:

$$(\bar{u} - c)\left(\frac{d^2\psi}{dz^2} - k^2\psi\right) + \left(\frac{N^2}{\bar{u} - c} - \frac{d^2\bar{u}}{dz^2}\right)\psi = 0. \tag{14.16}$$

This is the *Taylor–Goldstein equation* (Taylor, 1931; Goldstein, 1931). It governs the vertical structure of a perturbation in a stratified parallel flow. Note the formal analogy with the Rayleigh equation (10.9) governing the structure of a perturbation on a horizontally sheared flow in the absence of stratification and in the presence of rotation. Therefore, the same analysis can be applied.

First, we state the boundary conditions. For a domain bounded vertically by two horizontal planes, at $z = 0$ and $z = H$, we impose a zero vertical velocity there, or, in terms of the JMB from ⇓

JMB to ⇑

streamfunction:

$$\psi(0) = \psi(H) = 0. \tag{14.17}$$

Then, we recognize that the equation and its accompanying boundary conditions form an eigenvalue problem: Unless the phase velocity c takes on a particular value (eigenvalue), the solution is trivial ($\psi = 0$). In general, the eigenvalues may be complex, but if c admits the function ψ, then its complex conjugate c^* admits the function ψ^* and is thus another eigenvalue. This can be easily verified by taking the complex conjugates of (14.16) and (14.17). Hence, complex eigenvalues come in pairs. In each pair, one of the two eigenvalues will have a positive imaginary part and will correspond to an exponentially growing perturbation. The presence of a non-zero imaginary part to c automatically guarantees the existence of at least one unstable mode. Conversely, the basic flow is stable if and only if all possible phase speeds c are purely real.

Because it is impossible to solve problem (14.16) and (14.17) in the general case of an arbitrary shear flow $\bar{u}(z)$, we will limit ourselves, as in Section 10.2, to deriving integral constraints. A variety of such constraints can be established, but the most powerful one is obtained when the function ϕ, defined by

$$\psi = \sqrt{\bar{u} - c}\, \phi, \tag{14.18}$$

is used to replace ψ. Equation (14.16) and boundary conditions (14.17) become

$$\frac{d}{dz}\left[(\bar{u} - c)\,\frac{d\phi}{dz}\right] - \left[k^2(\bar{u} - c) + \frac{1}{2}\,\frac{d^2\bar{u}}{dz^2} + \frac{1}{\bar{u} - c}\left(\frac{1}{4}\left(\frac{d\bar{u}}{dz}\right)^2 - N^2\right)\right]\phi = 0 \tag{14.19}$$

$$\phi(0) = \phi(H) = 0. \tag{14.20}$$

Multiplying equation (14.19) by the complex conjugate ϕ^*, integrating over the vertical extent of the domain, and utilizing conditions (14.20), we obtain:

$$\int_0^H \left[N^2 - \frac{1}{4}\left(\frac{d\bar{u}}{dz}\right)^2\right] \frac{|\phi|^2}{\bar{u} - c}\, dz = \int_0^H (\bar{u} - c)\left(\left|\frac{d\phi}{dz}\right|^2 + k^2|\phi|^2\right) dz + \frac{1}{2}\int_0^H \frac{d^2\bar{u}}{dz^2}\,|\phi|^2\, dz, \tag{14.21}$$

where vertical bars denote the absolute value of complex quantities. The imaginary part of this expression is

$$c_i \int_0^H \left[N^2 - \frac{1}{4}\left(\frac{d\bar{u}}{dz}\right)^2\right] \frac{|\phi|^2}{|\bar{u} - c|^2}\, dz = -\, c_i \int_0^H \left(\left|\frac{d\phi}{dz}\right|^2 + k^2|\phi|^2\right) dz, \tag{14.22}$$

where c_i is the imaginary part of c. If the flow is such that $N^2 > \frac{1}{4}(d\bar{u}/dz)^2$ everywhere, then the preceding equality requires that c_i times a positive quantity equals c_i times a negative quantity and, consequently, that c_i must be zero. Defining the *Richardson number*

$$Ri = \frac{N^2}{(d\bar{u}/dz)^2} , \tag{14.23}$$

Benoit: Did you define M the Prandtl frequency somewhere? I do not think so. Would be useful later JMB from ⇓

$$M^2 = (d\bar{u}/dz)^2 \tag{14.24}$$

$Ri = N^2/M^2$ JMB to ⇑

we can state that if the inequality

$$Ri > \frac{1}{4} \tag{14.25}$$

holds everywhere in the domain, the stratified shear flow is stable.

Note that the criterion does not imply that c_i must be non-zero if the Richardson number falls below $\frac{1}{4}$ somewhere in the domain. Hence, inequality (14.25) is a sufficient condition for stability, while its converse is a necessary condition for instability. Atmospheric, oceanic, and laboratory data indicate, however, that the converse of (14.25) is generally a reliable predictor of instability.

If the shear flow is characterized by linear variations of velocity and density (note that a linear density variation was already implicitly assumed when we restricted our attention to a constant N^2), with velocities and densities ranging from U_1 to U_2 and ρ_1 to ρ_2 ($\rho_2 > \rho_1$), respectively, over a depth H, then

$$\frac{d\bar{u}}{dz} = \frac{U_1 - U_2}{H} , \quad N^2 = \frac{g}{\rho_0} \frac{\rho_2 - \rho_1}{H}$$

and the Richardson criterion stated as the necessary condition for instability becomes:

$$\frac{(\rho_2 - \rho_1)gH}{\rho_0(U_1 - U_2)^2} < \frac{1}{4}. \tag{14.26}$$

The similarity to (14.3) is not coincidental: Both conditions imply the possibility of large perturbations that could destroy the stratified shear flow. The difference in the numerical coefficients on the right-hand sides can be explained by the difference in the choice of the basic profile [discontinuous for (14.3), linear for (14.26)] and by the fact that the analysis leading to (14.3) did not make provision for a consumption of kinetic energy by vertical motions. The change from 1 in (14.3) to 1/4 in (14.26) is also coherent with the fact that condition (14.3) refers to a complete mixing situation, while (14.26) is a condition on the onset of the instability. JMB from ⇓ JMB to ⇑

More importantly, the similarity between (14.3) and (14.26) imparts a physical meaning to the Richardson number: It is essentially a ratio between potential and kinetic energies, with the numerator being the potential-energy barrier that mixing must overcome if it is to occur and the denominator being the kinetic energy that the shear flow can supply by being smoothed away. In fact, it was precisely by developing such energy considerations that British meteorologist Lewis Fry Richardson first arrived, in 1920, to the dimensionless ratio that now rightfully bears his name. A first formal proof of criterion (14.25), however, did not come until four decades later (Miles, 1961).

In closing this section, it may be worth mentioning that bounds on the real and imaginary parts of the wave velocity c can be derived by the inspection of certain integrals. This analysis, due to Louis N. Horward (see biography at end of Chapter 10), has already been applied to the study of barotropic instability (Section 10.3). Here, we summarize Howard's original derivation in the context of stratified shear flow. To begin, we introduce the vertical displacement a caused by the small wave perturbation

$$\frac{\partial a}{\partial t} \;+\; \bar{u}\frac{\partial a}{\partial x} \;=\; w$$

or

$$(\bar{u} \;-\; c)\, a \;=\; -\, \psi. \tag{14.27}$$

We then eliminate ψ from (14.16) and (14.17) and obtain an equivalent problem for the variable a:

$$\frac{d}{dz}\left[(\bar{u} \;-\; c)^2\, \frac{da}{dz}\right] \;\;+\;\; \left[N^2 \;-\; k^2(\bar{u} \;-\; c)^2\right]\, a \;=\; 0 \tag{14.28}$$

$$a(0) \;\;=\;\; a(H) \;=\; 0. \tag{14.29}$$

A multiplication by the complex conjugate a^* followed by an integration over the domain and use of the boundary conditions yields

$$\int_0^H \;(\bar{u} \;-\; c)^2 P\; dz \;=\; \int_0^H \;N^2 |a|^2\; dz, \tag{14.30}$$

where $P \,=\, |da/dz|^2 + k^2|a|^2$ is a non-zero positive quantity. The imaginary part of this equation implies that if there is instability ($c_i \neq 0$), c_r must lie between the minimum and maximum values of $\bar{u}$, that is,

$$U_{\min} \;<\; c_r \;<\; U_{\max}. \tag{14.31}$$

Physically, the growing perturbation travels with the flow at some intermediate speed, and there exists at least one critical level in the domain where the perturbation is stationary with respect to the local flow. This local coupling between the wave and the flow is precisely what allows the wave to extract energy from the flow and to grow at its expense.

Now, the real part of (14.30),

$$\int_0^H \;\left[(\bar{u} \;-\; c_r)^2 \;-\; c_i^2\right] P\; dz \;=\; \int_0^H \;N^2 |a|^2\; dz \tag{14.32}$$

can be manipulated in a way similar to that used in Section 10.3 to obtain the following inequality:

$$\left(c_r \;-\; \frac{U_{\min} \;+\; U_{\max}}{2}\right)^2 \;+\; c_i^2 \;\leq\; \left(\frac{U_{\max} \;-\; U_{\min}}{2}\right)^2. \tag{14.33}$$

This implies that, in the complex plane, the number $c = c_r + ic_i$ must lie within the circle that has the range $\bar{u}$ as diameter on the real axis. Because instability requires a positive imaginary value c_i, the interest is restricted to the upper half of the circle (Figure 10-1). This result is called the Howard semicircle theorem. In particular, it implies that c_i is bounded by $(U_{\max} - U_{\min})/2$, providing a useful upper bound on the growth rate of unstable perturbations:

$$kc_i \;\leq\; \frac{k}{2}\,(U_{\max}\;-\;U_{\min}). \tag{14.34}$$

14.3 Turbulence closure: k-models

Reynolds averaging (Section 4.1) showed that small-scale processes bear their effect on the mean flow through so-called Reynolds stresses stemming from the nonlinear advection term. Up to now, Reynold stresses were modeled by a diffusion law with an eddy viscosity, a parameter about which we remained rather evasive and imprecise. In particular, how to chose the value of this parameter was not detailed, simply because the parameter is not related to a unique fluid property as molecular viscosity is, but rather to a particular flow configuration. The value of the eddy viscosity is therefore rarely a constant and on the contrary depends on the large-scale fluid movements. Therefore its determination is in fact part of the problem's solution. So we have to come back to the question of estimating the Reynolds stresses appearing in the averaged equations. A naive approach consists in calculating fluctuations such as u' by taking the non-averaged equation (3.21) and subtracting the Reynolds-averaged equations (4.7a) leading to an equation for u' and similarly for the other variables. The solution of those equations then allows to calculate products and Reynolds averages such as $\langle u'u'\rangle$. Formally with a linear operator $\mathcal{L}$ for a very simplified equation of the type

$$\frac{\partial u}{\partial t} + \mathcal{L}\,(\,uu\,) = 0 \tag{14.35}$$

its Reynolds averaged equation is

$$\frac{\partial\,\langle u\rangle}{\partial t} + \mathcal{L}\,(\,\langle u\rangle\,\langle u\rangle\,) = -\mathcal{L}\,(\,\langle u'u'\rangle\,) \tag{14.36}$$

and we obtain the equation governing fluctuations u' by their difference:

$$\frac{\partial u'}{\partial t} + 2\mathcal{L}\,(\,\langle u\rangle\,u'\,) + \mathcal{L}\,(\,u'u'\,) - \mathcal{L}\,(\,\langle u'u'\rangle\,) = 0. \tag{14.37}$$

Solving this equation would provide u' and would allow to calculate the Reynolds stress $\langle u'u'\rangle$ explicitly. This approach is clearly not realistic since we wanted to filter out smaller scales or fluctuations and we are in fact solving the original problem (14.35) as we are calculating both the mean flow and its fluctuations. However the approach suggests a more subtle idea. We are not interested *per se* in the fluctuations but in their average products. Therefore starting from the equations for the fluctuations (and not their solution), let us try to find a governing equation for the Reynolds stresses. To do so, we multiply the governing equations for fluctuations by u' and then take the average to yield an evolution equation for $\langle u'u' \rangle$. Applying this technique to (14.37) we get successively[2]

$$\frac{1}{2}\frac{\partial u'u'}{\partial t} + 2u'\mathcal{L}\left(\langle u \rangle u'\right) + u'\mathcal{L}\left(u'u'\right) - u'\mathcal{L}\left(\langle u'u' \rangle\right) = 0 \tag{14.38}$$

$$\frac{1}{2}\frac{\partial \langle u'u' \rangle}{\partial t} + 2\left\langle u'\mathcal{L}\left(\langle u \rangle u'\right)\right\rangle + \left\langle u'\mathcal{L}\left(u'u'\right)\right\rangle = 0 \tag{14.39}$$

exploiting the fact that $\langle u' \rangle = 0$ because on average, fluctuations are zero. For an operator $\mathcal{L}$ representing the advection terms, it is possible to regroup the variables under the operator and make appear desirable terms as $\langle u \rangle \langle u'u' \rangle$ which can be calculated because we have governing equations for $\langle u \rangle$ and aim at providing one for $\langle u'u' \rangle$, so that the product should be accesible. Unfortunately, the last term of (14.39) makes appear a more annoying product, $\langle u'u'u' \rangle$ which our governing equations does not provide. Should we try to establish a governing equation for this triplet (or third-order term) with the same approach used to write the governing equation for $\langle u'u' \rangle$, it should be no surprise that even more complicated products will appear. We have a so-called *closure problem* and we need at one moment to parameterize the unknown higher-order products in terms of those we decide to calculate by their governing equations. Such parameterizations must be done in coherence with the physical phenomenology of turbulence and keep modeling errors small. Increasing the order of products modeled by governing equations is hoped to reduce the overall modeling errors by assuming that the importance of the higher-order terms also called *moments* decreases with their order and hence any error in modeling higher-order terms is less critical than errors in the parameterization of the lower-order moments. Here we will keep the level of parameterization to eddy viscosity concepts and not provide evolution equations for all second-order Reynolds stresses which are used presently only to simulate laboratory fluid problems (*e.g.*, Gibson and Launder, 1978; Pope, 2000). The latter models are full *second-moment closure* schemes or *second-order closure* schemes that calculate all Reynolds stresses involving products of variables by governing equations, using closure assumptions in triplets. Here we will limit ourself in model complexity at the most to simplified versions of second-order schemes where only some of the second-moment terms will be modelled with their governing equations and the others by algebraic equations. Such models are still called second-order closure schemes and are distinguished by explicitly naming the higher-order moments that are modeled, so as the k *model* we will soon present. To do so, we have now to identify the key features of turbulence that allow for a realizable closure scheme.

Benoit: I wrote this before your wrote turbulence contributions to chapter 5 and 8. Maybe adaptation of notations and elimination of redundant text is needed

The most obvious property of turbulent flows is their tendency to mix efficiently the fluid. This is why we stir our *cafe au lait* rather than to wait for molecular diffusion to distribute milk into the black coffee. The enhanced mixing due to turbulence was the reason to chose a diffusion model for the Reynolds stresses. The rapid fluctuations at the smallest scales seem erratic and isotropic while the largest eddies reflect the anisotropy of the mean flow generating instabilities and turbulence. A link between the two scales must be done, which is achieved

[2] Here we must assume that the average operation can be applied before or after time and space derivatives. Also double averages should be equal to averages. As already mentioned in Section 4.1, this is the case for statistical ensemble averages. For time or space averaging, the properties might be broken, unless scales of the fluctuations are clearly separated of the scales of the movements of interest (*e.g.*, Burchard 2002).

through the so-called *energy cascade* (Kolmogorov 1941, Figure 14-7). For the eddies of velocity scale $\mathring{u}$ and length scale l within the cascade, the Reynolds number is very large so that their evolution is fast compared to the decay time related to viscosity. The dominant nonlinear advection therefore rapidly breaks the eddies up into smaller ones, without any viscous effects. The energy extracted at each moment from the mean flow by instability of the base flow is thus transferred from the larger eddies to the smaller ones without losses. This energy must however be dissipated at some point and is therefore the *dissipation rate* of the cascade. Because of the lack of dissipation during the cascade, the dissipation rate is thus conserved across the cascade. Since viscosity does not influence the dissipation rate within he cascade, the only parameters that can be related to the dissipation rate noted ϵ are the velocity and length scale of the eddies, the time scale being determined by the turn-over scale $l/\mathring{u}$, hence $\epsilon = \epsilon(\mathring{u}, l)$. The dimensionally correct relation is

$$\frac{\epsilon}{(c_\mu^0/4)^{3/4}} = \frac{\mathring{u}^3}{l} \tag{14.40}$$

where we introduced a calibration constant c_μ^0 in a combination that will be useful later. We recover the result of Section 5.1, with notations adapted to current turbulence models. Also the value of ϵ is the one that is extracted from the mean flow at velocity scale u_m and length scale l_m, called *macro scales* and $\epsilon = \epsilon(\mathring{u}, l) = \epsilon(u_m, l_m)$.

Relation (14.40) shows that for a given turbulence cascade, $\mathring{u} \propto l^{1/3}$ and the smaller eddies contain less kinetic energy, so that the bulk of kinetic energy is contained within the largest eddies of size l_m (Figure 14-7). The power spectrum of associated kinetic energy is thus decreasing with increasing wavenumber and dimensional analysis provided relation (5.8) of Section 5.1. The turbulent cascade can also be interpreted in terms of vorticity. In three dimensions, vortex tubes are twisted and stretched by the presence of other vortex tubes (at first sight, this is similar to the the vortex interactions simulated numerically in Section 10.7, see figure 10-12). Because of incompressibility, the stretching of vortex tubes is accompanied by a decrease in cross section and, because of circulation conservation, by an increase in vorticity and decrease in length scales. Therefore vorticity at progressively smaller scales is observed when vortex tubes are stretched. This is only possible in three-dimensions so that the cascade described here does not occur in two dimensions. Turbulence and eddy behavior in two dimensions is indeed a rather special problem we will examine in Section 18.3.

The cascade can of course not continue down to arbitrarily small scales and at one moment, molecular viscosity comes into the play. This is the case when friction is a dominant part of the governing equation. Because the turbulence cascade is governed by the nonlinear advection term, molecular viscosity dominates the dynamics of an eddy when its Reynolds number, measuring advection versus molecular diffusion, is of order one:

$$\frac{u\partial u/\partial x}{\nu \partial^2 u/\partial x^2} \sim \frac{u_v^2/l_v}{\nu u_v/l_v^2} \sim \mathcal{O}(1) \tag{14.41}$$

We are then in a so-called *viscous sink* where the length scale l_v and velocity scale u_v of the eddies, called *micro scales* or *viscous scales* reach

$$\frac{u_v l_v}{\nu} \sim 1. \tag{14.42}$$

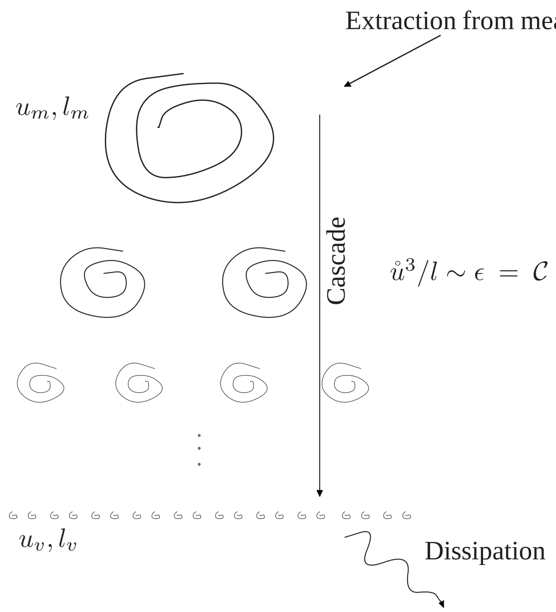

Figure 14-7 The famous quote *the big whirls have little whirls that feed on their velocities, and little whirls have lesser whirls and so on to viscosity - in the molecular sense* from Richardson (in his book of 1922, see also biography at the end of this Chapter) perfectly summarizes the idea used in turbulence modeling according to which the turbulence effect is to transfer energy from the larger unstable flows to the smallest eddies dissipating the excess energy.

Since (14.40) also holds at this scale

$$\epsilon \propto \frac{u_v^3}{l_v} = \frac{u_m^3}{l_m} \tag{14.43}$$

we can determine the range of scales of the cascade by eliminating u_v between (14.43) and (14.42) and by expressing u_m in terms of the Reynolds number $u_m l_m/\nu$ of the macroscales:

$$\frac{l_m}{l_v} \sim Re^{3/4}. \tag{14.44}$$

This relation explains the broad range of eddy scales observed for heigh Reynolds number flows. Alternatively we can express the scales at which dissipation takes places in function of the dissipation rate and molecular viscosity by eliminating u_v from (14.40) and (14.42)

$$l_v \sim \epsilon^{-1/4} \nu^{3/4}. \tag{14.45}$$

The more energy is extracted from the mean flow, the smaller the eddies need to be in order to be able to dissipate the energy. Or stated differently, the more strongly we stir our coffee, the smaller the eddies and the more efficient mixing will be. Here it is worth insisting again that it is molecular viscosity that is *in fine* responsible for the diffusion. The turbulent cascade simply increases the shearing and tearing on fluid parcels, increasing surfaces of contact between two different fluid properties and increasing gradients because of smaller scales, so that molecular diffusion can act more efficiently (Figure 14-8).

Integrating the spectrum (5.8) between the largest eddies and the smallest ones yields the total kinetic energy of the inertial range:

$$\int_{\pi/l_m}^{\pi/l_v} E_k dk = \frac{u_m^2}{2}\left(1 - Re^{-1/2}\right) = \sim \frac{u_m^2}{2} \tag{14.46}$$

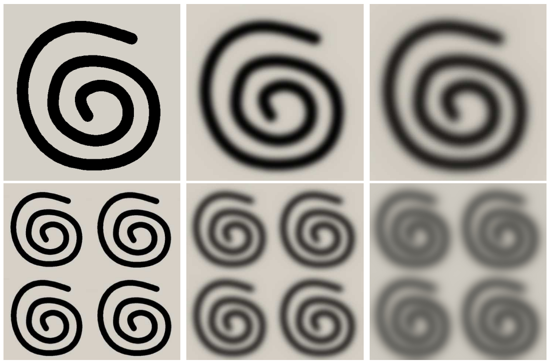

Figure 14-8 Molecular diffusion acts more rapidly when scales are smaller. When eddies have been broken into smaller eddies, for the same molecular diffusion coefficient, mixing is enhanced because the scales involved are reduced and gradients increased. Also surfaces between regions of different flow characteristics are increased, enhancing molecular exchanges. (Figure adapted from a suggestion by H. Burchard)

and hence, the kinetic energy of the eddies is in a good approximation that from the largest eddies.

Having now some ideas on how energy is extracted from the mean flow, we can come back to the question on how to translate the effect of this cascade in a sensible way into a model for the eddy viscosity. We limit our search to a parameterization in which the properties of the turbulent cascade are purely local (so called *one-point closure model*) and do not involve remote parameters. For the mean flow, we suppose that l_m is the scale at which turbulence extracts energy to finally dissipate it at viscous scales. Since we do not model the cascade and associated velocity fluctuations u' explicitly, we have to ensure the dissipation introduced by the eddy-viscosity extracts the energy ϵ. To do so, the Reynolds number based on eddy viscosity must be of order one at the largest eddies in order that turbulent dissipation occurs:

$$\frac{u_m l_m}{\nu_E} \sim 1. \tag{14.47}$$

Interestingly enough this relation is often used as an initial "Ansatz" of turbulent closure schemes by using its analogy with molecular mixing and kinetic-theory of gas, where the root mean square velocity v_{rms} of molecules and their mean free path λ between collisions define the molecular diffusion, while eddy viscosity is given by (14.47):

$$\nu = \frac{v_{rms}\lambda}{3} \quad \longleftrightarrow \quad \nu_E \sim u_m l_m \tag{14.48}$$

The eddy viscosity concept ensures in fact that fluid parcels moving with the eddy velocity u_m over the average distance l_m exchange momentum with other fluids parcels, similarly to the molecular diffusion model where momentum exchange between individual molecules is performed over the mean free path λ. Within this context it is not surprising that the term *mixing length* was coined for l_m.

With (14.47) we ensure that energy is extracted from the mean flow using an eddy viscosity approach. However, another sensible requirement of the closure is that we extract also the correct amount of energy per unit of time. In other words, we must ensure that at the scales l_m we extract energy at a rate which is subsequently dissipated in the viscous part, *i.e.*, ϵ.

Assuming we know this dissipation rate, we hence require

$$\frac{u_m^3}{l_m} = \frac{\epsilon}{(c_\mu^0/4)^{3/4}}. \tag{14.49}$$

In summary: to calculate eddy viscosity we need to know scales u_m and l_m. If we know the dissipation rate ϵ, we can use (14.49) to reduce the number of scales to be prescribed. If in addition, we knew the kinetic energy k at the macroscale, this would add another relation which determines the velocity scale

$$\mathsf{k} = \frac{u_m^2}{2}. \tag{14.50}$$

This can also be used to calculate the dissipation rate (14.49) as follows

$$\epsilon = (c_\mu^0)^{3/4} \frac{\mathsf{k}^{3/2}}{l_m}. \tag{14.51}$$

Knowing k and ϵ would thus allow the calculation of eddy viscosity ν_E and complete our closure scheme. At that point the reader might object that calculating a macro-scale length using micro-scale dissipation rate sounds contradictory, but the paradox is easily explained by the fact the Kolmogorov theory shows that the dissipation rate at micro-scale is the one extracted from the mean flow at the macro-scale, hence the link. This justification and most of the previous reasoning rely on the idea of an equilibrium spectrum, for which at each moment, input at low wavenumber and output at high wavenumber is in equilibrium.

One of the first successful attempts to quantify the eddy viscosity by means of a velocity and length scale was made by Prandtl (see biography at the end of Chapter 8). He analyzed a horizontal flow $\langle u \rangle$ which is vertically sheared and assumed the velocity fluctuations statistically random but with a correlation between velocity components u' and w'. In this case

$$\langle u'w' \rangle = r \sqrt{\langle u'^2 \rangle} \sqrt{\langle w'^2 \rangle} \tag{14.52}$$

where r is nothing else than the correlation coefficient of the two variables u' and w' treated as random fields. Assuming both velocity fluctuations proportional to the velocity scale u_m of the eddies with a constant correlation, he modeled therefore

$$\langle u'w' \rangle = c_1 u_m^2 \tag{14.53}$$

with a calibration constant c_1. Since the eddy viscosity is defined by

$$\langle u'w' \rangle = \nu_E \frac{\partial \langle u \rangle}{\partial z}, \quad \nu_E = u_m l_m \tag{14.54}$$

combining (14.53) and (14.54) we obtain a first turbulence-closure model in which eddy viscosity as calculated by mean flow characteristics:

$$\nu_E = l_m^2 \left| \frac{\partial \langle u \rangle}{\partial z} \right|, \quad u_m = l_m \left| \frac{\partial \langle u \rangle}{\partial z} \right| \tag{14.55}$$

The absolute value was introduced to keep eddy viscosities positive and the only parameter Prandtl still had to prescribe was the mixing length into which all calibration constants have been lumped into. We recognize that for increased shear, turbulent diffusion increases for this model, in accordance with our intuition on the destabilizing effect of shear. The determination of the mixing length depends then on the problem at hand, in particular its geometry. For example, for a flow above a rigid boundary, the size l_m of the largest eddies extracting energy from the flow can be bigger far from a rigid boundary than near a wall. In terms of the Reynolds stresses, because $\langle u'w' \rangle$ must tend towards zero at a rigid boundary and equals $-l_m^2 |\partial \langle u \rangle / \partial z|^2$ with our closure scheme, the mixing length must go to zero there because the shear of the mean current does not. Therefore near a solid boundary it is observed that $l_m = \mathcal{K} z$ where z is the distance from the boundary and $\mathcal{K}$ the so-called Karman constant (*e.g.*, Nezu and Nakagaw, 1993; see also Section 8.1). This algebraic closure scheme with a mixing length l_m can be modified so as to accommodate the stabilizing effect of stratification and generalized to three-dimensional mean flows. These topics will be covered later when we will show that the Prandtl model can be obtained as a simplification of more complex turbulence models. Such more complex turbulence models are necessary in most cases because despite the advantage of the algebraic Prandtl closure schemes of being easily implemented into a model and needing no additional evolution equation. Indeed, we must admit that in this formulation the turbulence level is determined by the sole velocity scale of large-scale flow. Also no memory effects of turbulence are included in the formulation and as soon as the shear has disappeared by mixing, eddy viscosity is zero even if real turbulence is still decaying. This is one of the problems of a so-called *zero-equation turbulence model*.

To design more elaborated models, we will have to establish governing equations with time derivatives, hence memory, for some of the second-moment terms. Here it is interesting to note that the difference of volume conservation of the total flow (3.19) and the mean flow (4.9) provides a constraint on the velocity fluctuations

$$\frac{\partial u'}{\partial x} + \frac{\partial v'}{\partial y} + \frac{\partial w'}{\partial z} = 0 \tag{14.56}$$

we can use during the manipulation of the governing equations for Reynolds stresses. The obvious candidates for a governing equation are of course turbulent kinetic energy k and the dissipation rate, because their knowledge directly determines the scales used in the eddy viscosity approach. Here, we start by developing the so-called turbulent kinetic energy k model[3] where we define

$$\mathsf{k} = \frac{\langle u'^2 \rangle + \langle v'^2 \rangle + \langle w'^2 \rangle}{2}. \tag{14.57}$$

In view of (14.40) and (14.46), the bulk of kinetic energy is contained within the largest eddies so that we can use the velocity scale estimate of the largest eddies as $\sqrt{2\mathsf{k}}$. We will now establish a governing equation for k by applying a closure approach. We can obtain such an equation by taking the difference between (3.21) and (4.7a) to obtain the evolution equation for fluctuations u'. We then multiply the equation by u' and take the average exploiting also (14.56). The same approach is then applied to the momentum equations in y and z directions and we finally make the sum of the three equations to obtain after tedious calculations the following equation

$$\frac{d\mathsf{k}}{dt} = P_s + P_b - \epsilon - \left(\frac{\partial q_x}{\partial x} + \frac{\partial q_y}{\partial y} + \frac{\partial q_z}{\partial z} \right) \tag{14.58}$$

[3] In reality k is rather a kinetic energy per unit of mass. Because of the Boussinesq approximation we do not need to be too purist at this point and use the name energy for k.

where we rearranged terms so as to make appear whenever possible terms in a divergence form. Note that the time derivative is the material derivative based on the mean flow

$$\frac{d}{dt} = \frac{\partial}{\partial t} + \langle u \rangle \frac{\partial}{\partial x} + \langle y \rangle \frac{\partial}{\partial y} + \langle w \rangle \frac{\partial}{\partial z}$$

and that Coriolis terms have disappeared from the equations (remember that the Coriolis force does not provide mechanical work). Up to now, no approximations were invoked and the different terms [4] read

$$\begin{aligned} P_s &= -\langle u'u' \rangle \frac{\partial \langle u \rangle}{\partial x} - \langle u'v' \rangle \frac{\partial \langle u \rangle}{\partial y} - \langle u'w' \rangle \frac{\partial \langle u \rangle}{\partial z} \\ &\quad - \langle v'u' \rangle \frac{\partial \langle v \rangle}{\partial x} - \langle v'v' \rangle \frac{\partial \langle v \rangle}{\partial y} - \langle v'w' \rangle \frac{\partial \langle v \rangle}{\partial z} \\ &\quad - \langle w'u' \rangle \frac{\partial \langle w \rangle}{\partial x} - \langle w'v' \rangle \frac{\partial \langle w \rangle}{\partial y} - \langle w'w' \rangle \frac{\partial \langle w \rangle}{\partial z} \end{aligned} \tag{14.59}$$

$$P_b = -\langle \rho' w' \rangle \frac{g}{\rho_0} \tag{14.60}$$

$$\begin{aligned} \frac{\epsilon}{\nu} &= \left\langle \frac{\partial u'}{\partial x}\frac{\partial u'}{\partial x} \right\rangle + \left\langle \frac{\partial u'}{\partial y}\frac{\partial u'}{\partial y} \right\rangle + \left\langle \frac{\partial u'}{\partial z}\frac{\partial u'}{\partial z} \right\rangle \\ &+ \left\langle \frac{\partial v'}{\partial x}\frac{\partial v'}{\partial x} \right\rangle + \left\langle \frac{\partial v'}{\partial y}\frac{\partial v'}{\partial y} \right\rangle + \left\langle \frac{\partial v'}{\partial z}\frac{\partial v'}{\partial z} \right\rangle \\ &+ \left\langle \frac{\partial w'}{\partial x}\frac{\partial w'}{\partial x} \right\rangle + \left\langle \frac{\partial w'}{\partial y}\frac{\partial w'}{\partial y} \right\rangle + \left\langle \frac{\partial w'}{\partial z}\frac{\partial w'}{\partial z} \right\rangle \end{aligned} \tag{14.61}$$

$$q_x = \frac{1}{\rho} \left\langle \left(p' + \frac{u'^2 + v'^2 + w'^2}{2} \right) u' \right\rangle - \nu \frac{\partial \mathsf{k}}{\partial x} \tag{14.62}$$

and similar expressions for q_y and q_z. All terms involve unknown averages on which we need to make closure assumptions. P_s involves fields from both the mean flow and turbulence and is thus related to the interaction between the two. Since the shear of the large-scale flow appears, this term is called *shear production*. The second term, P_b, clearly involves the work performed by the turbulent buoyancy forces on the vertical stratification and is thus related to the potential energy changes. For obvious reasons we call it *buoyancy production*. The dissipation rate ϵ involves as expected the molecular viscous dissipation by turbulent motions. Finally the last term q_x and its cousins involve only turbulent parameters of pressure and velocity and because of the divergence form of the terms is thus related to the spatial redistrubution of k by turbulence itself. All those terms must now be modeled in terms of the state variables and in the case of the k equation, the closures are directly inspired by the turbulence model we actually use. For example, the Reynolds stresses appearing in the unknown terms are replaced with the eddy viscosity model already in use. By defining the

[4] Strictly speaking, dissipation should read $\epsilon = 2\nu \|\mathbf{D}\|^2$ where the deformation tensor $\mathbf{D}$ of the fluctuations is similar to (14.63). The definition used here is often called pseudo dissipation. Since the numerical values are almost indistinguishable and the mathematical formulation only differs by a vector divergence term that we can lump into the parameterization of vector (q_x, q_y, q_z), we will retain the more compact definition.

deformation tensor (or strain rate tensor)

$$\mathsf{D} = \frac{1}{2}\begin{pmatrix} 2\frac{\partial u}{\partial x} & \left(\frac{\partial u}{\partial y} + \frac{\partial v}{\partial x}\right) & \left(\frac{\partial u}{\partial z} + \frac{\partial w}{\partial x}\right) \\ \left(\frac{\partial u}{\partial y} + \frac{\partial v}{\partial x}\right) & 2\frac{\partial v}{\partial y} & \left(\frac{\partial v}{\partial z} + \frac{\partial w}{\partial y}\right) \\ \left(\frac{\partial u}{\partial z} + \frac{\partial w}{\partial y}\right) & \left(\frac{\partial v}{\partial z} + \frac{\partial w}{\partial x}\right) & 2\frac{\partial w}{\partial z} \end{pmatrix} \tag{14.63}$$

and the Reynolds stress tensor

$$\boldsymbol{\tau} = \begin{pmatrix} \langle u'u' \rangle & \langle u'v' \rangle & \langle u'w' \rangle \\ \langle u'v' \rangle & \langle v'v' \rangle & \langle v'w' \rangle \\ \langle u'w' \rangle & \langle v'w' \rangle & \langle w'w' \rangle \end{pmatrix} \tag{14.64}$$

the eddy-viscosity model reads

$$\boldsymbol{\tau} = -2\nu_E \mathsf{D} + \frac{2\mathsf{k}}{3}\mathsf{I} \tag{14.65}$$

The additional term, with identity matrix I and proportional to k on the right-hand side has been introduced for consistency reasons. Indeed, we make a (probably incorrect) model of the Reynolds stresses but without the last terms, the model is *certainly* incorrect, because the least we can require is that the trace of the matrix on the left-hand side being equal to the trace on the right-hand side. Such a realizability constraint demands the last term to be added on the diagonal of the model matrix. In practice, the term is not very important but is in any case acessible for a k model. Using (14.65) in (14.59) allows then the calculation of the shear production P_s in terms of the mean flow characteristics.

For buoyancy production P_b, the velocity-density correlations are modelled with an eddy diffusivity approach

$$\langle \rho' w' \rangle = -\kappa_E \frac{\partial \langle \rho \rangle}{\partial z} = \kappa_E \frac{\rho_0}{g} N^2 \tag{14.66}$$

and the term P_b does not require further treatment if κ_E is given as part of the closure scheme.

Since the terms q_x, q_y and q_z appear in a flux form, integration over any volume shows that the therm is only responsible of redistributing k in space. Since it involves turbulent quantities, it seems natural to model this term as a turbulent diffusion flux of k, with eddy viscosity ν_E in view of the velocity and pressure correlations involved[5]. The different terms are thus now parameterized as

$$P_s = 2\nu_E \, \| \langle \mathsf{D} \rangle \|, \tag{14.67}$$

$$P_b = -\kappa_E N^2, \tag{14.68}$$

$$q_x = -\nu_E \frac{\partial \mathsf{k}}{\partial x}. \tag{14.69}$$

We notice that the signs of the modeled terms P_s and P_b are coherent with the idea of turbulence extracting energy from the mean flow and transferring it to turbulence, with stratification inhibiting or reducing turbulence intensities because of the required increase of potential

[5] In real models, the eddy diffusivity for turbulent kinetic energy is the eddy diffusivity divided by the so-called *Schmidt number* σ_k.

energy when mixing a stably stratified situation (Section 14.2). We arrive thus finally at the governing equation for turbulent kinetic energy

$$\frac{d\mathsf{k}}{dt} = P_s + P_b - \epsilon + \mathcal{D}(\mathsf{k}) \tag{14.70}$$

$$\mathcal{D}(\mathsf{k}) = \frac{\partial}{\partial z}\left(\nu_E \frac{\partial \mathsf{k}}{\partial z}\right) \tag{14.71}$$

and knowing appropriate boundary conditions, we can predict the evolution of k if we know how to calculate ϵ and the eddy viscosity/diffusivity. We can note that we kept the turbulent diffusion in $\mathcal{D}(\,)$ only in the vertical direction, leaving the horizontal part for subsequent parameterizations of the horizontal subgrid scales. If ϵ is calculated using (14.51) with a prescribed mixing length l_m, the turbulent closure scheme is called a k-model or *one-equation turbulence model*. In view of its mathematical quadratic form, k must be required to be positive in any closure scheme and a realizability condition of the model is that the solution of (14.70) is always positive (Problem 14-8). Subsequent numerical discretization then also should maintain the property (Exercise 14-2).

To summarize, with approximations coherent with our turbulence closure approach, we now have an equation that allows to predict the energy of the turbulent eddies and gives a coherent estimation of their velocity and hence the eddy viscosity

$$\nu_E = \frac{c_\mu}{\left(c_\mu^0\right)^{3/4}} \sqrt{\mathsf{k}}\, l_m \tag{14.72}$$

where the mixing length is to be provided on geometrical considerations of the flow from which ϵ is provided by (14.43) and used in (14.70). In this context c_μ^0 used in (14.72) is the same constant as in (14.43) and c_μ a calibration parameter. Eddy diffusivity κ_E is obtained in a similar way

$$\kappa_E = \frac{c'_\mu}{\left(c_\mu^0\right)^{3/4}} \sqrt{\mathsf{k}}\, l_m \tag{14.73}$$

where the calibration constant c'_μ is different from c_μ. The two parameters will later be defined as functions. The ratio of the two parameters, also equal to the ratio of ν_E and κ_E, is called the turbulent Prandtl number Pr

$$Pr = \frac{c_\mu}{c'_\mu} = \frac{\nu_E}{\kappa_E}. \tag{14.74}$$

We introduced only two different turbulent diffusion coefficients though each state variable could claim its own (*e.g.*, Canuto *et al.*, 2002). We keep a unique κ_E for diffusion of fields related to scalar properties not directly related to pressure and velocity fluctuations but rather to tracer velocity correlations because of the similar physical transport they are subjected to. Hence κ_E is used for the diffusion of density, salinity, temperature, moisture and any tracer concentration. Eddy viscosity ν_E is then generally used for the diffusion of velocities, k and ϵ because of the similar dynamical nature and origin of the variables. If necessary, Schmidt numbers can be introduced to modify the coefficients.

Before further increase the complexity of the closure schemes, we can verify how the model behaves in simple flow structures and look at a sheared flow of uniform density in a

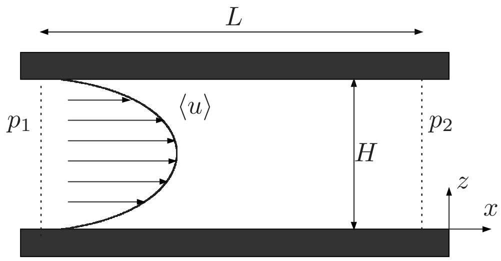

Figure 14-9 Flow in a channel forced by a prescribed pressure gradient.

channel with averaged fields independent of x and y (Figure 14-9). In this case the velocity field is $u = \langle u \rangle + u'$, $w = w'$ and the mean flow only depending in z obeys

$$\frac{\partial \langle u \rangle}{\partial t} = -\frac{1}{\rho_0}\frac{\partial \langle p \rangle}{\partial x} + \frac{\partial}{\partial z}\left(\nu \frac{\partial \langle u \rangle}{\partial z} - \langle u'w' \rangle\right) \tag{14.75}$$

where the pressure gradient is uniform along the channel and over the distance L the pressure difference is $p_2 - p_1$. The total kinetic energy E of the flow is $\left\langle (u^2 + v^2 + w^2) \right\rangle /2$ or

$$E = \frac{\langle u \rangle^2}{2} + \mathsf{k}. \tag{14.76}$$

The first term is the kinetic energy of the mean flow and the second term the turbulent kinetic energy. Multiplying (14.75) by $\langle u \rangle$ we will establish the governing equation for the kinetic energy of the mean flow. For the fluctuation equations we could to the same calculation on the governing equations of u' which would lead to the equations for k simplified to take into account the mean flow structure depends solely on z and we obtain

$$\begin{aligned} \frac{\partial}{\partial t}\left(\frac{\langle u \rangle^2}{2}\right) &= -\frac{1}{\rho_0}\frac{\partial \langle p \rangle \langle u \rangle}{\partial x} + \frac{\partial}{\partial z}\left[\langle u \rangle \left(\nu \frac{\partial \langle u \rangle}{\partial z} - \langle u'w' \rangle\right)\right] \\ &- \nu \left(\frac{\partial \langle u \rangle}{\partial z}\right)^2 + \underline{\langle u'w' \rangle \frac{\partial \langle u \rangle}{\partial z}} \\ \frac{\partial \mathsf{k}}{\partial t} &= -\underline{\langle u'w' \rangle \frac{\partial \langle u \rangle}{\partial z}} - \epsilon + \frac{\partial q_z}{\partial z}. \end{aligned} \tag{14.77}$$

The underlined term of the first equation is nothing else than the shear production of turbulence appearing in the second equation with changed sign. We clearly see how the shear production term is an energy transfer term between kinetic energy of the mean flow and the turbulence. With our eddy viscosity approach the shear production reads

$$P_s = -\langle u'w' \rangle \frac{\partial \langle u \rangle}{\partial z} = \nu_E \left(\frac{\partial \langle u \rangle}{\partial z}\right)^2 \tag{14.78}$$

and energy is extracted from the mean flow to the turbulence for positive eddy viscosity. Note that P_s scales as

$$P_s \sim \nu_E \frac{u_m^2}{l_m^2} \sim \frac{u_m^3}{l_m} \tag{14.79}$$

if we assume that the scales still resolved by the Reynolds averaging are at macroscale. If we integrate the energy equations over a distance L and the channel height, assume stationary solutions, exploit the fact the velocities (both mean and turbulent) are zero in $z = 0$ and $z = H$ and finally use the closure schemes, we obtain

$$\left(\frac{p_1 - p_2}{\rho_0}\right)\frac{UH}{L} = \int_0^H (\tilde{\nu} + \nu)\left(\frac{\partial \langle u \rangle}{\partial z}\right)^2 dz \tag{14.80}$$

where $U = 1/H \int_0^H \langle u \rangle \, dz$ is the average velocity over the inflow and outflow section. For the stationary turbulent kinetic energy equation we have the budget

$$\int_0^H \epsilon \, dz = \int_0^H \tilde{\nu}\left(\frac{\partial \langle u \rangle}{\partial z}\right)^2 dz. \tag{14.81}$$

In the absence of turbulence and eddy viscosity, the first equation shows that for an increased energy input trough higher pressure gradients, the flow must generate increasingly larger shears needed for molecular diffusion to dissipate all energy. Such strong shears lead to instabilities create turbulence and now eddy viscosity can extract energy from the mean flow at much lower values of the shear because of the presence of $\nu_E \gg \nu$. As shown by (14.81), the extracted energy is then dissipated in the viscous sink by ϵ still acting with molecular viscosity but at much smaller scales as indicated by (14.61).

14.4 Other closures: $\mathsf{k} - \epsilon$ or $\mathsf{k} - \mathsf{k}l_m$

The previous one-equation turbulence model still needed a mixing length to be prescribed by an algebraic, *a priori* known function to have a closed system. As indicated before, should we be able to provide the governing equation for either ϵ or l_m, the closure would not need anymore such empirical algebraic closures. Therefore, there have been efforts to establish a governing equation for a combination of k and l_m, or equivalently a combination of k and ϵ so as to have two governing equations for turbulent parameters and an algebraic relationship (14.51) allowing to calculate k, ϵ and l_m and hence eddy viscosity.

Since dissipation rates are now measured by microprofilers (*e.g.*, Osborne, 1974; Lueck *et al.* 2002), ϵ is an attractive candidate for a second equation in turbulence modeling and when trying to establish an equation for ϵ by manipulating the governing equations for velocity fluctuations in a similar way as before, we reach a governing equation of the type

$$\frac{d\epsilon}{dt} = Q \tag{14.82}$$

where, without approximations, the right-hand side contains a series of complicated expressions most of which involving unknown correlations similar to the Reynolds stresses (*e.g.*, Rodi, 1980; Burchard, 2002). Contrary to the k equation however, those terms are not naturally and coherently modeled using the eddy-viscosity approach itself, but require strong additional hypotheses, not to say educated guesses. The most common approach is to use the energy production related terms from the k equation and use a linear combination of them to model the energy dissipation source terms, while terms related to redistribution in space are as usual modeled by a turbulent diffusion. Hence, the modeled governing equation for ϵ reads

$$\frac{d\epsilon}{dt} = \frac{\epsilon}{\mathsf{k}} \left(c_1 P_s + c_3 P_b - c_2 \epsilon \right) + \mathcal{D}(\epsilon) \tag{14.83}$$

where the terms P_s and P_b are those of the k equation and coefficients c_1, c_2 and c_3 calibration constants, $c_1 \approx 1.44$, $c_2 \approx 1.92$, $c_3 \in [-0.6, 0.3]$. Because the two turbulent parameters calculated are k and ϵ, it is useful to express eddy-viscosity in function of these two parameters by eliminating the mixing length l_m between (14.72) and (14.51)

$$\nu_E = c_\mu \frac{\mathsf{k}^2}{\epsilon} \tag{14.84}$$

This a particular *two-equation turbulence model* within a series of possible ones. Instead modeling the governing equation for ϵ an equation for l_m or a combination of l_m and k can be established, with (14.51) allowing to relate the three variables $\mathsf{k}, \epsilon, l_m$. The most famous model in the context of geophysical flows is the so-called $\mathsf{k} - \mathsf{k}l_m$ model of Mellor and Yamada (1982). Their governing equation for $\mathsf{k}l_m$ reads, using notations adapted to our previous models,

$$\frac{d\mathsf{k}l_m}{dt} = \frac{l_m}{2} \left[E_1 P_s + E_3 P_b - \left(1 - E_2 \frac{l_m^2}{l_z^2} \right) \epsilon \right] + \mathcal{D}(\mathsf{k}l_m) \tag{14.85}$$

where E_1, E_2 and E_3 are calibration constants. As for (14.83) the source term is a linear combination P_s, P_b and ϵ, with the appearence of a prescribed length scale l_z that is needed in this formulation to enforce l_m to decrease towards zero near solid boundaries. In the $\mathsf{k} - \epsilon$ model, this is achieved "automatically" if correct boundary conditions are applied (Burchard and Bolding, 2001). Except for this difference, the models are structurally identical since because of (14.51), in the absence of spatial variations, (14.83) and (14.85) are equivalent. The difference between the formulations lies in the quantity that is considered transported by the flow, in the $\mathsf{k}-\epsilon$ model it is dissipation (coherently with the Kolmogorov idea of conserved dissipation rate), while in the Mellor-Yamada model it is $\mathsf{k}l_m$. In fact, it is possible to establish a generic evolution equation for $\mathsf{k}^a \epsilon^b$ whith constants a and b (a=0, b=1 corresponding to the $\mathsf{k} - \epsilon$ model and a=5/2, b=-1 to the $\mathsf{k} - \mathsf{k}l_m$ model) and consider this variable to be transported by the flow (Umlauf and Burchard 2003). Whatever combination is choosen such models are called for obvious reasons *two-equation models* and except for l_z do not need further prescribed spatial functions.

We will not increase complexity of turbulence modeling further but will finish the description of general turbulence modeling with the observation that all closure schemes described here were based on local analysis, never using remote information to model Reynolds stresses. Such models are called *one-point closure* scheme while schemes that use information in remote locations to infer local turbulence are referred to as two-point closure schemes (*e.g.,* Stull 1993). Since we will not look further into turbulence motions, we also come back to the notations without making the distinction between average flow properties and turbulent properties so that from here on, u stands again for the average or mean velocity.

14.5 Mixed-layer modeling

The turbulence models presented in the previous two sections are applicable in three-dimensional flows, but can generally be simplified for geophysical flows by exploiting the small aspect ratio of the mean flows under investigation (*e.g.*, Umlauf and Burchard 2005). In particular, the strain rate is simplified

$$\mathsf{D} = \frac{1}{2}\begin{pmatrix} \sim 0 & \sim 0 & \frac{\partial u}{\partial z} \\ \sim 0 & \sim 0 & \frac{\partial v}{\partial z} \\ \frac{\partial u}{\partial z} & \frac{\partial v}{\partial z} & \sim 0 \end{pmatrix} \tag{14.86}$$

and the shear production reads

$$P_s = \nu_E M^2 \quad M^2 = \left(\frac{\partial u}{\partial z}\right)^2 + \left(\frac{\partial v}{\partial z}\right)^2 \tag{14.87}$$

where the Prandtl frequency M is the direct generalization of (14.24). Also the turbulent diffusion itself is acting essentially in the vertical direction because of the shorter length scales along z. On the other hand, analyzing flows with small aspect ratios inevitably eliminates a series of horizontal subgrid scale processes, whose effects are modeled as before by a horizontal diffusion with diffusion coefficient $\mathcal{A}$

$$\mathcal{D}() = \frac{\partial}{\partial x}\left(\mathcal{A}\frac{\partial}{\partial x}\right) + \frac{\partial}{\partial y}\left(\mathcal{A}\frac{\partial}{\partial y}\right) + \frac{\partial}{\partial z}\left(\nu_E\frac{\partial}{\partial z}\right) \tag{14.88}$$

Is is now quite clear that ν_E is modeling actual turbulence, while $\mathcal{A}$ tries to take into account horizontally unresolved processes at larger scales than l_m but smaller scales than the length scales of the problem or the numerical grid used to solve it. Assuming a cascade in this case a possible closure is

$$\mathcal{A} \sim (\Delta x)^{4/3}\epsilon_H^{(1/3)}, \tag{14.89}$$

directly inspired by $\nu_E \sim l_m^{(4/3)}\epsilon^{1/3}$ obtained by (14.72) and (14.51). For the estimation of $\mathcal{A}$, ϵ_H is then the energy dissipation of the horizontally unresolved processes. According to Okubo (1971), these dissipation rates are relatively uniform and allow to calculate $\mathcal{A}$ depending on the scales under investigation (Figure 14-10) Another subgrid scale parameterization of horizontal movements is directly inspired by the Prandtl model (*e.g.*, Smagorinsky 1964),

$$\mathcal{A} \sim \Delta x \Delta y \left[\left(\frac{\partial u}{\partial x}\right)^2 + \left(\frac{\partial v}{\partial y}\right)^2 + \frac{1}{2}\left(\frac{\partial u}{\partial y} + \frac{\partial v}{\partial x}\right)^2\right]^{1/2} \tag{14.90}$$

where the mixing length is replaced by the average grid spacing, so as to ensure that all scales below the grid size are effectively modeled is have being mixed by eddies. In view of the Δx^2 appearing in the formulation and the $1/\Delta x^2$ stemming from the numerical discretization of the second derivative associated with the lateral diffusion, we can interprete the Smagorinsky formulation as a numerical filter (Section 10.6) acting at grid resolution with and intensity depending on the local shear.

Because later subgrid scale parameterizations are less well established than classical turbulence closure, we come now back to the vertical turbulence modeling and will show that we

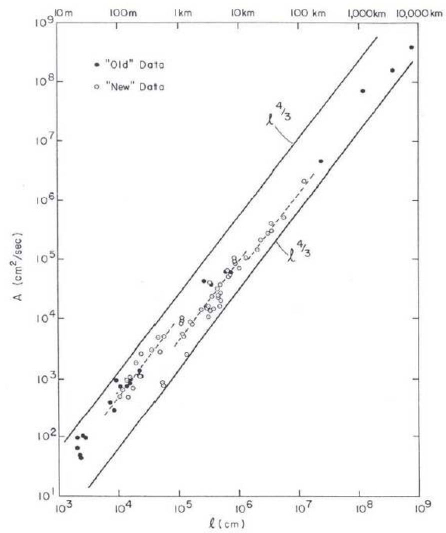

Figure 14-10 Lateral diffusion in function of cut-off scales in the horizontal grids (Okubo 1971).

can recover the Prandtl model if we assume there is not transport of turbulence and an instant adaptation of the energy level to changes in the production. In this case (14.70) reduces to

$$P_s + P_b = \epsilon. \tag{14.91}$$

For the sheared flow $\langle u \rangle$ along z in a stratified fluid of Brunt-Väisälä frequency N, the equilibrium between production and dissipation yields indeed, using (14.72) and (14.51) for a given mixing length l_m and defining the flux Richardson number

$$R_f = \frac{-P_b}{P_s} = \frac{c'_\mu}{c_\mu}\frac{N^2}{M^2} = \frac{c'_\mu}{c_\mu} Ri = Pr\, Ri \tag{14.92}$$

$$\mathsf{k} = \frac{c_\mu}{(c^0_\mu)^{3/2}}\, l_m^2 M^2 (1 - R_f) \tag{14.93}$$

from where the eddy viscosity

$$\nu_E = \left(\frac{c_\mu}{c^0_\mu}\right)^{3/2} l_m^2\, M\, \sqrt{1 - R_f} \tag{14.94}$$

is obtained. We recover the Prandtl closure (14.55) with the eddy viscosity now taking into account the stabilizing effect of the stratification. We see that our simplest models are particular cases of the more complex models.

Further adaptations to the mixed layer flows can be done by introducing so-called *stability functions* into the parameterizations. The derivation of such formulations, starts with the complete second-moment equations for Reynolds stresses. Then simplifying hypotheses on the unknown higher-order moments are used and possibly either neglecting spatial and temporal variations (similar to the equilibrium hypothesis (14.91)) or assuming rather heuristically an advection-diffusion transport proportional to local productions, so-called *algebraic*

Table 14.1 PARAMETERS USED IN THE CLOSURE SCHEME DERIVED FROM CANUTO *et al.* 2001

s_0	s_1	s_2	s_4	s_5	s_6
0.10666	0.01734	-0.00012	0.11204	0.00451	0.00088
d_1	d_2	d_3	d_4	d_5	c_μ^0
0.2554	0.02871	0.00522	0.00867	-0.00003	0.0768

Reynolds-stress models are obtained, generally under the form of a possibly nonlinear algebraic system to be solved. When solved or approximated to provide the Reynolds stresses in function of the mean flow characteristics, formulations as (14.84) appear, where the function c_μ can now be quite complicated.

In all algebraic second order turbulent closure schemes they are formulated in function of two dimensionless stability parameters :

$$\alpha_N = \frac{\mathsf{k}^2}{\epsilon^2} N^2 \qquad \alpha_M = \frac{\mathsf{k}^2}{\epsilon^2} M^2 \tag{14.95}$$

Stability functions widely differ based on the different hypotheses used in the derivation (*e.g.*, Mellor and Yamada, 1982; Galperin *et al.*, 1988; Kantha and Clayson, 1994; Canuto *et al.*, 2001). Here as an example stability functions from Umlauf and Burchard (2005) depicted in figure 14-11 and given by

$$\nu_E = c_\mu \frac{\mathsf{k}^2}{\epsilon}, \tag{14.96}$$

and

$$\kappa_E = c'_\mu \frac{\mathsf{k}^2}{\epsilon}. \tag{14.97}$$

with

$$c_\mu = \frac{s_0 + s_1\alpha_N + s_2\alpha_M}{1 + d_1\alpha_N + d_2\alpha_M + d_3\alpha_N\alpha_M + d_4\alpha_N^2 + d_5\alpha_M^2}, \tag{14.98}$$

$$c'_\mu = \frac{s_4 + s_5\alpha_N + s_6\alpha_M}{1 + d_1\alpha_N + d_2\alpha_M + d_3\alpha_N\alpha_M + d_4\alpha_N^2 + d_5\alpha_M^2}, \tag{14.99}$$

If $P_s + P_b = \epsilon$ is used in some parts of the derivation of stability functions, so-called *quasi-equilibrium versions* are obtained (Galperin *et al.*, 1988); which generally have a more robust behavior than other formulations (see *e.g.*, Burchard and Deleersnijder, 2001 for a discussion).

14.6 Patankar-type discretizations

During the treatment of advection problems (Section 6.4), the reader might have wondered why so much discussion was devoted to monotonic behavior. After all, if we know that the solution must be positive and we find negative values in the numerical solution, we know they are not real and can disregard them. For linear schemes, this is indeed a viable approach. Negative values can however have dramatic effects if nonlinearities are present and the source

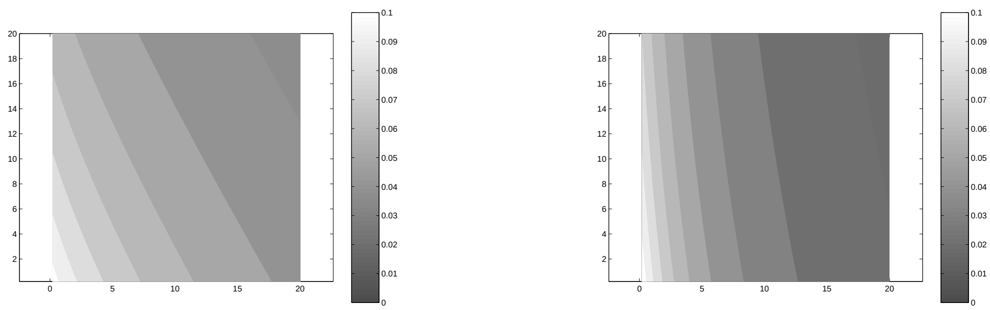

Figure 14-11 Stability functions c_μ and c'_μ as functions of α_N and α_M.

terms appearing in the governing equations for turbulent kinetic energy or the dissipation rate should already give us some hints of the problems, such as taking a square root of turbulent kinetic energy numerically not positive defined. Even for well defined mathematical operations, other problems can appear. Take the example of a quadratic sink for a tracer c without any spatial dependence:

$$\frac{dc}{dt} = -\mu c^2. \tag{14.100}$$

The solution starting from initial condition c^0 is

$$c(t) = \frac{c^0}{1 + \mu t\, c^0}, \tag{14.101}$$

which tends gently to zero for positive initial conditions. Should the value of c^0 be negative, the solution tends however towards negative infinite in a finite time $(-1/\mu c^0)$. If a discretization of such an equation, starting with positive values leads for some reason to a negative value of c, a problem is to be expected since from this moment on, the numerical solution will explode rapidly since after all, it mimics the physical solution, which diverges in a finite time. Problems are even worse if the source term such as $c^{3/2}$ is mathematically not defined for negative arguments. Practically this generates `NaN` (Not a Number) in calculation codes that pollute rapidly all calculation arrays. In view of the above mentioned problems of nonlinear source terms, solutions must be found to avoid occurrence of negative values when the physical solution remains positive.

An implicit treatment of the nonlinear source or sink term would enhance stability and therefore reduce over- or undershooting tendencies, but to be able to calculate numerically the value of $\tilde{c}_i^{n+1}$ we need to invert or solve a nonlinear algebraic equation. This is rarely possible in closed analytical form and we need to resort to numerical techniques. This amounts to find zeros of a function, which can be achieved with standard iterative methods (Picard, Regula Falsi, Newton-Raphson *etc.*, *e.g.*, Dahlquist and Björck, 1974 or Stoer and Burlish 2002). But since we need to solve such such an equation in each grid point and each time step, the approach can become quite time consuming, not to speak about problems of robustness in finding roots that to not converge or converge to unphysical solutions.

Patankar (1960) introduced a method that makes the discretization of a nonlinear source term somehow implicit without actually needing to solve a nonlinear algebraic equation. We start from the semi-discrete version of the governing equations for the model state $\mathbf{x}$:

$$\frac{\partial \mathbf{x}}{\partial t} = \mathsf{Q}(\mathbf{x}) \tag{14.102}$$

where the right-hand side regroups all spatial operators. Such a system can be discretized by one of the many methods we already presented. The algorithm to update the numerical state variable $\mathbf{x}$ is then for example

$$\mathsf{A}\mathbf{x}^{n+1} = \mathsf{B}\mathbf{x}^n + \mathsf{f}, \tag{14.103}$$

where A and B are emerging from the discretization chosen and f may contain forcing terms. If we now add a sink term to the governing equations

$$\frac{\partial \mathbf{x}}{\partial t} = \mathsf{Q}(\mathbf{x}) - \mathsf{K}\mathbf{x} \tag{14.104}$$

where the matrix $\mathsf{K} = \mathsf{diag}(K_i)$ is a diagonal matrix with different K_i if the decay rate is if different for the different components of the state vector. Then an explicit discretization of the sink term would lead to the adapted algorithm

$$\mathsf{A}\mathbf{x}^{n+1} = (\mathsf{B} - \mathsf{b})\,\mathbf{x}^n + \mathsf{f}, \tag{14.105}$$

where $\mathsf{b} = \mathsf{diag}(K_i\,\Delta t)$ is also a diagonal matrix. An implicit treatment of the sink term would lead to

$$(\mathsf{A} + \mathsf{b})\,\mathbf{x}^{n+1} = \mathsf{B}\mathbf{x}^n + \mathsf{f}. \tag{14.106}$$

To use an implicit scheme for the **linear** sink, all we have to do is to modify the matrix to invert, the modified matrix being not more complicated to invert than the original one since only the diagonal is changed. If no system is to be solved initially, $\mathsf{A} = \mathsf{I}$ and the scheme including the implicit source term can locally be inverted simply by multiplying the right-hand side by $\mathsf{diag}(\,1/(1 + K_i\,\Delta t)\,)$.

Patankar's simple yet powerful trick is to assume that the **nonlinear** source Q can be written in a pseudo-linear fashion:

$$Q = -K(c)\,c, \tag{14.107}$$

which is always the case (simply define K by this relationship), as long as Q/c remains bounded for all c. The discretization then uses for each grid point

$$Q_i = -K(\tilde{c}_i^n)\,\tilde{c}_i^{n+1} = Q(\tilde{c}_i^n)\,\frac{\tilde{c}_i^{n+1}}{\tilde{c}_i^n}, \tag{14.108}$$

which is a consistent discretization. All we have to do to calculate $\tilde{c}^{n+1}$ is to modify the system similarly to (14.106) by adding a term $K_i(\tilde{c}_i^n)\,\Delta t$ on the diagonal if a system is to be solved or by dividing the right hand side by $1 + K_i(\tilde{c}_i^n)\,\Delta t$ if all other terms are discretized explicitly.

The method is simple, but how does this trick help to maintain values positive? Consider a sink term where $K(c) > 0$. Then the physical solution, in the absence of spatial operators, must decrease from a positive value towards zero without ever increasing during the adjustment. Also the physical solution remains positive all the time. The explicit discretization applied to a positive value $\tilde{c}^n$ does not ensure such a behavior for arbitrary time steps because

$$\tilde{c}^{n+1} = \tilde{c}^n - K(\tilde{c}^n)\Delta t\, \tilde{c}^n \;=\; (1 - K(\tilde{c}^n)\Delta t)\; \tilde{c}^n$$

is negative whenever $K(\tilde{c}^n)\Delta t > 1$. The Patankar trick replaces the explicit calculation by

$$\tilde{c}^{n+1} = \tilde{c}^n - K(\tilde{c}^n)\Delta t\, \tilde{c}^{n+1} \;=\; \frac{\tilde{c}^n}{1 + K(\tilde{c}^n)\Delta t},$$

which remains positive all the time and makes the solution always decrease in time. The only requirement for the method to work is $K(c)$ to be bounded for $c \to 0$, otherwise, when approaching zero, overflows in the numerical code will occur.

We might wonder why we not just require $K(\tilde{c}^n)\Delta t \leq 1$ when a sink term is present in order to ensure a correct behavior. For so-called *stiff problems*, K may vary over a very large range, in which the largest value of K, and thus the most rapidly disappearing solution, will enforce a very small time step, even if the fast process, by essence, disappears rapidly. In this case, unless adaptive time-stepping is used, it is almost impossible to ensure a sufficiently small time step that keeps $\tilde{c}$ positive all the time without using excessively small time steps in most of the calculations. Specially in coupled nonlinear equations, the stiffness is difficult to apprehend and ecosystem models are prone to non-positive behavior when explicit discretizations are used because of the occasional presence of very fast processes.

We will now slightly generalize the Patankar method taking into account that sinks decrease values but the source terms increase them. For a single equation with a source (production term $P \geq 0$) and a sink (destruction term $D \geq 0$) such that $Q = P - D$

$$\frac{dc}{dt} = P(c) - D(c), \tag{14.109}$$

a discretization *à la* Patankar would read:

$$\tilde{c}^{n+1} = \tilde{c}^n + \Delta t \left\{ \frac{P^n}{\tilde{c}^n}\left(\alpha\tilde{c}^{n+1} + (1-\alpha)\tilde{c}^n\right) - \frac{D^n}{\tilde{c}^n}\left(\beta\tilde{c}^{n+1} + (1-\beta)\tilde{c}^n\right) \right\} \tag{14.110}$$

where α and β are as usual implicitness factors. This equation can directly be solved for $\tilde{c}^{n+1}$ or the linear system matrix $\mathbf{A}$ modified in accordance if implicit spatial operators are added.

For some problems, the solution of (14.109) tends towards an equilibrium solution c^* , $P(c^*) = D(c^*)$ without oscillating around this equilibrium value. It is easy to show that this is the case if

$$P(c) \lesseqqgtr D(c) \quad \text{if} \quad c \gtreqqless c^*. \tag{14.111}$$

It is then possible to show (Exercise 14-8) that in order to have a numerical solution that, as the physical solution, keeps concentrations positive and converges towards the equilibrium value c^* without oscillating around it, we must ensure

$$\frac{1}{\Delta t} \geq \frac{P - D}{c^* - c} + \frac{\alpha P^c - \beta D^c}{c}. \tag{14.112}$$

To obtain the less restrictive time-stepping $\alpha = 0$, $\beta = 1$ would be the best choice. For example with $P = c^r$ and $D = c^{r+1}$, we have an equilibrium position $c^* = 1$ for any $r > 0$.

If $\alpha = 0$, $\beta = 1$, the Patankar scheme then yields a steady convergence towards this value for arbitrary large time steps. The example is not an academic one, because the interested reader might have realized that $r = 1/2$ corresponds to the typical source/sink term of a turbulent closure scheme using a fixed mixing length (Section 14.3), while $r = 1$ refers to the logistic equations of biological components. The method outlined here was recently adapted to a set of coupled equations, ensuring conservation between components and higher-order convergence than the Euler scheme shown here (Burchard *et al.* 2003, 2004), an approach of interest for models transporting ecosystems.

14.7 Penetrative convection

Text of section See also numerical convective adjustment of Section 11.4 This section was alluded to in Section 8.7

Analytical Problems

14-1. A stratified shear flow consists of two layers of depth H_1 and H_2 with respective densities and velocities ρ_1, U_1 and ρ_2, U_2 (left panel of Figure 14-2). If the lower layer is three times as thick as the upper layer and the lower layer is stagnant, what is the minimum value of the upper-layer velocity for which there is sufficient available kinetic energy for complete mixing (right panel of Figure 14-2)?

14-2. In the ocean, a warm current (T = 18°C) flows with a velocity of 10 cm/s above a stagnant colder layer (T = 10°C). Both layers have identical salinities, and the thermal-expansion coefficient is taken as 2.54 $\times$ 10^{-4} K^{-1}. What is the wavelength of the longest unstable wave?

14-3. Formulate the Richardson number for a stratified shear flow with uniform stratification frequency N and linear velocity profile, varying from zero at the bottom to U at a height H. Then, relate the Richardson number to the Froude number and show that instabilities can occur only if the Froude number exceeds the value 2.

14-4. In an oceanic region far away from coasts and strong currents, the upper water column is stably stratified with N = 0.015 s^{-1}. A storm passes by and, during 10 h, exerts an average stress of 0.2 N/m^2. What is the depth of the mixed layer by the end of the storm? (For seawater, take ρ_0 = 1028 kg/m^3.)

14-5. An air mass blows over a cold ocean at a speed of 10 m/s and develops a stable potential-temperature gradient of 8°C per kilometer in the vertical. It then encounters a warm continent and is heated from below at the rate of 200 W/m^2. Assuming that the air mass maintains its speed, what is the height of the convective layer 60 km inshore? What is then a typical vertical velocity of convection? (Take ρ_0 = 1.20 kg/m^3, α = 3.5 $\times$ 10^{-3} K^{-1}, and C_p = 1005 J/kg.K.)

14-6. For the growing atmospheric boundary layer, show that thermals rise faster than the layer grows ($w_* > dh/dt$) and that thermals have a temperature contrast less than the temperature jump at the top of the layer [$T_* < (T - T_0)/2$].

14-7. Why eddy-viscosity is considered positive? What happens in terms of energetics if $\nu_E \leq 0$?

14-8. Consider the a governing equation for k that reads

$$\frac{\partial \mathsf{k}}{\partial t} = \nu_E M^2 - \kappa_E N^2 - \epsilon$$

with (14.72), (14.73) and (14.51) for fixed M^2 , N^2 , l_m and $Pr = 0.7$. Show that the solution is always non-negative if the initial conditions are non-negative.

14-9.

Numerical Exercises

14-1. Assuming the governing equation for k is dominated by the local production and dissipation, how would you define a staggered grid for a one-dimension model of a water column?

14-2. Implement a numerical method that keeps k positive for a decaying turbulence in a homogenous $\mathsf{k} - \epsilon$ model.

14-3. Show that for turbulence in equilibrium, stability functions depend only on the Richardson number

14-4. Revisit our estimate of the computing powers needed to simulate earth fluid dynamics down to the dissipation range, with micro-scale in mind and typical values of $\epsilon = 10^{-7}$ W/kg.

14-5. What to you think should be the a requirement on a vertical grid spacing Δz compared to l_m.

14-6. Implement a complete 1D model including a $\mathsf{k} - \epsilon$ closure scheme. If in trouble look at `kepsmodel.m`, but do not cheat.

14-7. Use the program developed in Exercise 14-6 or `kepsmodel.m` to simulate the wind entrainment case of Problem 14-4. In particular, look at the evolution of the surface velocity as a function of time on a hodograph (u, v axes), with or without Coriolis

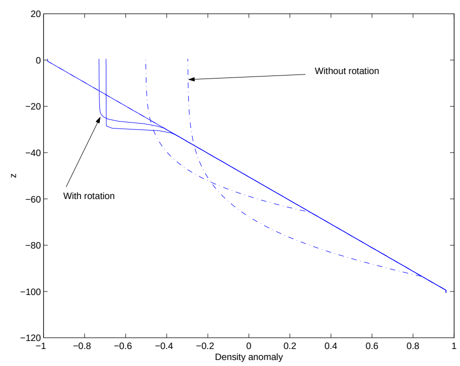

Figure 14-12 A uniform stratification is perturbed by a constant surface wind. In the absence of rotation the mixed layer deepens (two later profiles are shown at regular time-intervals). When rotation is present, the mixed layer stabilizes and the pycnocline is stronger.

force. Then repeat the exercise but do not allow the wind to stop. Again, compare the situations with or without Coriolis force. To do so, observe in both cases the mixed-layer depth evolution as shown in Figure 14-12.

14-8. Prove that (14.112) is the sufficient condition to ensure that the numerical solution obtained with (14.110) converges toward the equilibrium value c^*, remains positive and never crosses the value $c = c^*$.

14-9. Convection case with $N =$. Destabilizing heat loss of 200 w m^{-2} at the surface (equivalent to the atmospheric heating from below). Translate heat flux into density anomaly flux and apply the 1D model without rotation. Start from rest Implement a method to detect the mixed layer depth and show the evolution of this depth as a function of time. Do the same for the wind entrainment in Exercise 14-7. Compare to the theoretical results (???)

14-10. Apply real atmospheric conditions for a density profile ?? PAPA? (Get from GOTM setup?)

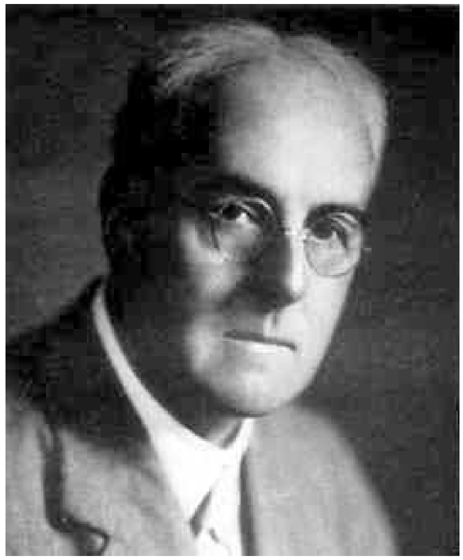

Lewis Fry Richardson
1881 – 1953

Unlike many scientists of his generation and the next, Lewis Fry Richardson did not become interested in meteorology because of a war. On the contrary, he left his secure appointment at the Meteorological Office in England during World War I to serve in a French ambulance convoy and tend the wounded. After the war, he returned to the Meteorological Office (see historical note at the end of Chapter 1), only to leave it again when it was transferred to the Air Ministry, deeply convinced that "science ought to be subordinate to morals".

Richardson's scientific contributions can be broadly classified in three categories: finite-difference solutions of differential equations, meteorology, and mathematical modeling of nations at war and in peace. The marriage of his first two interests led him to conceive of numerical weather forecasting well before computers were available for the task (see Section 1.9). His formulation of the dimensionless ratio that now bears his name is found in a series of landmark publications during 1919–1920 on atmospheric turbulence and diffusion. His mathematical theories of war and peace were developed in search of rational means by which nations could remain in peace.

According to his contemporaries, Richardson was a clear thinker and lecturer, with no enthusiasm for administrative work and a preference for solitude. He confessed to being "a bad listener because I am distracted by thoughts." (*Photo by Bassano and Vandyk, London*)

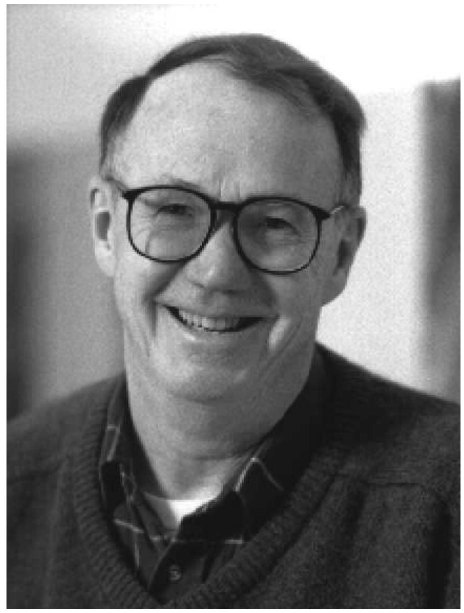

George L. Mellor
19xx –

George Mellor's career has been devoted to fluid turbulence in its many forms. His early interest in aerodynamics of jet engines and turbulent boundary layers soon yielded to a stronger interest in the turbulence of stratified geophysical flows.

Something about numerical modeling and the Princeton Ocean Model, used across the world to simulate ocean dynamics, particularly in coastal regions where dynamics are complex and turbulence is crucial.

In the mid 1970s with Ted Yamada, he developed a closure scheme to model turbulence in stratified flows, which is being used worldwide for atmospheric and oceanographic applications. Their joint 1982 publication in *Reviews of Geophysics and Space Physics* is one of the most widely cited papers in its field.

Include few words about GFDL, Princeton University.

Author of textbook "Introduction to Physical Oceanography" (American Institute of Physics, 1996).

(yet to be approved by George himself) (*credit for source of photo*)

Part IV

Combined Rotation and Stratification Effects

Chapter 15

Dynamics of Stratified Rotating Flows

(October 18, 2006) **SUMMARY**: Geostrophic motions can arise during the adjustment to density inhomogeneities and maintain a stratified fluid away from gravitational equilibrium. The key is a relationship between the horizontal density gradient and the vertical velocity shear, called the thermal-wind relation. Coastal upwelling in the ocean is also considered as it is another example of rotating dynamics of a stratified fluid. Since large gradients and even discontinuities (fronts) can form during geostrophic adjustment, the numerical section shows how to treat large gradients in numerical models. JMB from ⇓ JMB to ⇑

15.1 Thermal wind

Consider a situation where a cold air mass is wedged between the ground and a warm air mass (Figure 15-1). The stratification has then both vertical and horizontal components. Mathematically, the density is a function of both height z and distance x (say, from cold to warm). Now, assume that the flow is steady, geostrophic, and hydrostatic:

$$-\, fv \;=\; -\,\frac{1}{\rho_0}\,\frac{\partial p}{\partial x} \tag{15.1}$$

$$\frac{\partial p}{\partial z} \;=\; -\,\rho g. \tag{15.2}$$

Here, v is the velocity component in the horizontal direction y, and p is the pressure field. Taking the z-derivative of (15.1) and eliminating $\partial p/\partial z$ with (15.2), we obtain

$$\frac{\partial v}{\partial z} \;=\; -\,\frac{g}{\rho_0 f}\,\frac{\partial \rho}{\partial x}\,. \tag{15.3}$$

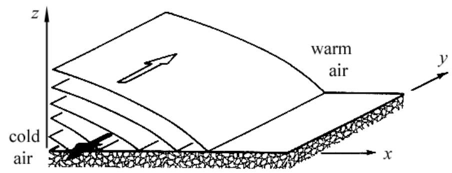

Figure 15-1 Vertical shear of a flow in the presence of a horizontal density gradient. The change of velocity with height is called thermal wind.

Therefore, a horizontal density gradient can persist in steady state if it is accompanied by a vertical shear of horizontal velocity. Where density varies in both horizontal directions, the following also holds:

$$\frac{\partial u}{\partial z} \;=\; + \;\frac{g}{\rho_0 f}\,\frac{\partial \rho}{\partial y}\,. \tag{15.4}$$

These innocent-looking relations have profound meaning. They state that, due to the Coriolis force, the system can be maintained in equilibrium, without tendency toward leveling of the density surfaces. In other words, the rotation of the earth can keep the system away from its state of rest without any continuous supply of energy.

Notice that the velocity field (u, v) is not specified, only its vertical shear, $\partial u/\partial z$ and $\partial v/\partial z$. This implies that the velocity must change with height. (In the case of Figure 15-1, $\partial \rho/\partial x$ is negative and $\partial v/\partial z$ is positive.) For example, the wind speed and direction at some height above the ground may be totally different from those at ground level. The presence of a vertical gradient of velocity also implies that the velocity cannot vanish, except perhaps at some discrete levels. Meteorologists have named such a flow the *thermal wind.*[1]

In the case of pronounced density contrasts, such as across cold and warm fronts, a layered system may be applicable. In this case (Figure 15-2), the system can be represented by two densities (ρ_1 and ρ_2, $\rho_1 < \rho_2$) and two velocities (v_1 and v_2). Relation (15.3) can be discretized into

$$\frac{\Delta v}{\Delta z} \;=\; - \;\frac{g}{\rho_0 f}\,\frac{\Delta \rho}{\Delta x}\,,$$

where we take $\Delta v = v_1 - v_2$ and $\Delta \rho = \rho_2 - \rho_1$ to obtain

[1]Although thermal wind is a meteorological expression, oceanographers use it, too, to indicate a sheared current in geostrophic equilibrium with a horizontal density gradient.

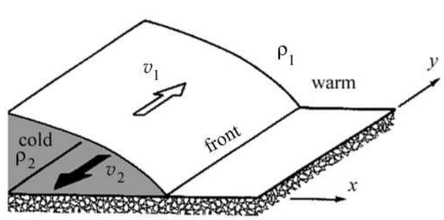

Figure 15-2 The layered version of Figure 15-1, which leads to the Margules relation.

$$v_1 - v_2 = -\frac{g}{\rho_0 f}(\rho_2 - \rho_1)\frac{\Delta z}{\Delta x} . \tag{15.5}$$

The ratio $\Delta z/\Delta x$ is the slope of the interface. We can note that this discrete version is consistent with the continuous version, because in each layer, according to (15.3), a constant density is accompagnied by a vertically uniform velocity. This discrete thermal wind equation is called the *Margules relation* (Margules, 1906), although a more general form of the relation for zonal flows was obtained earlier by Helmholtz (1888). JMB from ⇓ JMB to ⇑

The thermal-wind concept has been enormously useful in analyzing both atmospheric and oceanic data, because observations of the temperature and other variables that influence the density (such as pressure and specific humidity in the air, or salinity in seawater) are typically much more abundant than velocity data. For example, knowledge of temperature and moisture distributions with height and of the surface wind (to start the integration) permits the calculation of wind speed and direction above ground. In the ocean, especially in studies of large-scale oceanic circulation, for which sparse current-meter data may not be representative of the large flow due to local eddy effects, the basinwide distribution may be considered as unknown. For this reason, oceanographers typically assume that the currents vanish at some great depth (e.g., 2000 m) and integrate the "thermal-wind" relations from there upward to estimate the surface currents. Although the method is convenient (the equations are linear and do not require integration in time), we should keep in mind that the thermal-wind relation of (15.3) and (15.4) is rooted in an assumption of strict geostrophic balance. Obviously, this will not be true everywhere and at all times.

15.2 Geostrophic adjustment

We may now ask how situations like the ones depicted in Figures 15-1 and 15-2 can arise. In the atmosphere, the temperature gradient from the warm tropics to the cold polar regions create is a permanent feature of the global atmosphere, although storms do alter the magnitude of this gradient in time and space. Ocean currents can bring in near contact water masses of vastly different origins and thus densities. Finally, coastal processes such as fresh water runoff can create density differences between saltier waters offshore and fresher waters closer to shore. Thus a variety of mechanisms exists by which different fluid masses can be brought in contact.

Oftentimes, the contact between different fluid masses is recent and the flow has not yet had the time to achieve thermal-wind balance. An example is coastal upwelling: Alongshore winds create in the ocean an offshore Ekman drift and the depletion of surface water near the coast brings denser water from below (see later section in this chapter). Such a situation is initially out of equilibrium and gradually seeks adjustment. JMB from ⇓ JMB to ⇑

Let us explore in a very simple way the dynamical adjustment between two fluid masses recently brought into contact. Let us imagine an infinitely deep ocean that is suddenly heated over half of its extent (Figure 15-3a). A warm upper layer develops on that side, while the rest of the ocean, on the other side and below, remains relatively cold (Figure 15-3b). (We could also imagine a vertical gate preventing buoyant water from spilling from one side to the other.) After the upper layer has been created — or, equivalently, when the gate is removed —

the ocean is not in a state of equilibrium, the lighter surface water spills over to the cold side, and an adjustment takes place. In the absence of rotation spilling proceeds, as we can easily imagine, until the light water has spread evenly over the entire domain and the system has come to rest. But, this scenario, as we are about to note, is not what happens when rotational effects are important.

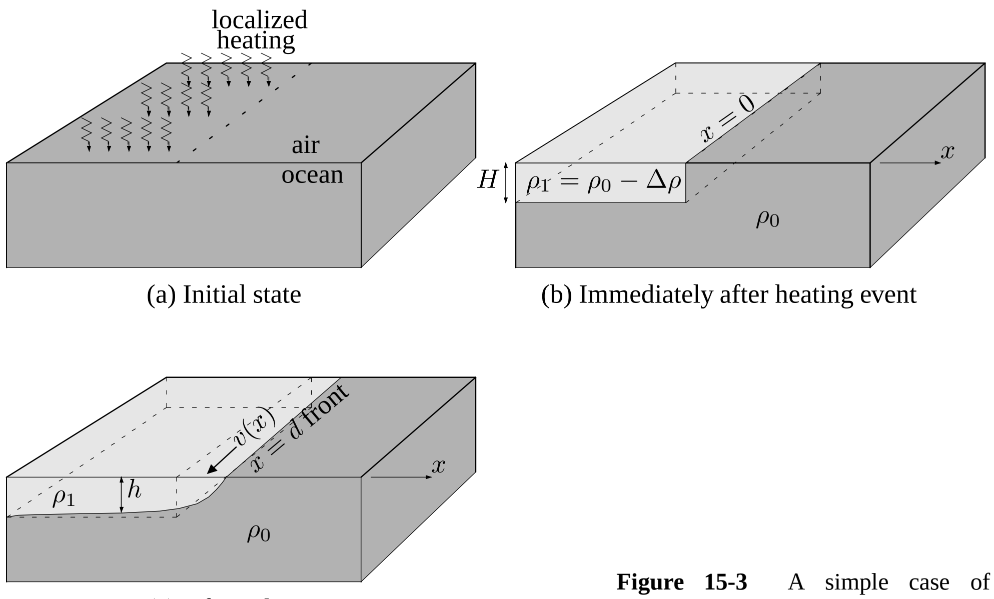

(a) Initial state

(b) Immediately after heating event

(c) After adjustment

Figure 15-3 A simple case of geostrophic adjustment.

Under the influence of the Coriolis force, the forward acceleration induced by the initial spilling creates a current that veers (to the right in the Northern Hemisphere) and can come into geostrophic equilibrium with the pressure difference associated with the density heterogeneity. The result is a limited spill accompanied by a lateral flow (Figure 15-3c).

To model the process mathematically, we use the reduced-gravity model (12.19) on an f-plane and where the reduced-gravity constant is $g' = g(\rho_0 - \rho_1)/\rho_0$ according to the notation of Figure 15-3b. We neglect all variations in the y-direction, although we allow for a velocity, v, in that direction, and write

$$\frac{\partial u}{\partial t} + u\,\frac{\partial u}{\partial x} - fv = -g'\,\frac{\partial h}{\partial x} \tag{15.6}$$

$$\frac{\partial v}{\partial t} + u\,\frac{\partial v}{\partial x} + fu = 0 \tag{15.7}$$

$$\frac{\partial h}{\partial t} + \frac{\partial}{\partial x}(hu) = 0. \tag{15.8}$$

The initial conditions (*i.e.*, immediately after the warming event) are $u = v = 0$, $h = H$ for $x < 0$, and $h = 0$ for $x > 0$. The boundary conditions are $u, v \to 0$ and $h \to H$ as $x \to -\infty$,
JMB from ⇓ whereas velocity component u at the front is given by the material derivative $u = dx/dt$ in

$h = 0$ at $x = d(t)$, the moving point where the interface outcrops. This nonlinear problem cannot be solved analytically, but one property can be stated. The preceding equations conserve the following form of the potential vorticity: JMB to ⇑

$$q = \frac{f + \partial v/\partial x}{h} . \tag{15.9}$$

Initially, all particles have $v = 0$, $h = H$ and share the same potential vorticity: $q = f/H$. Therefore, throughout the layer of light fluid and at all times, the potential vorticity keeps the uniform value f/H:

$$\frac{f + \partial v/\partial x}{h} = \frac{f}{H} . \tag{15.10}$$

This property, it turns out, allows us to relate the initial state to the final state without having to solve for the complex, intermediate evolution.

Once the adjustment is completed, time derivatives vanish. Equation (15.8) then requires that hu be a constant; since $h = 0$ at one point, this constant must be zero, implying that u must be zero everywhere. Equation (15.7) reduces to zero equals zero and tells nothing. Finally, equation (15.6) implies a geostrophic balance,

$$- fv = - g' \frac{dh}{dx} , \tag{15.11}$$

between the velocity and the pressure gradient set by the sloping interface. Alone, equation (15.11) presents one relation between two unknowns, the velocity and the depth profile. The potential-vorticity conservation principle (15.10), which still holds at the final state, provides the second equation, thereby conveying the information about the initial disturbance into the final state.

Despite the nonlinearities of the original governing equations (15.6) through (15.8), the problem at hand, (15.10) and (15.11), is perfectly linear, and the solution is relatively easy to obtain. Elimination of either $v(x)$ or $h(x)$ between the two equations yields a second-order differential equation for the remaining variable, which admits two exponential solutions. Discarding the exponential that grows for $x \to -\infty$ and imposing the boundary condition $h = 0$ at $x = d$ lead to:

$$h = H \left[1 - \exp\left(\frac{x-d}{R}\right)\right] \tag{15.12}$$

$$v = - \sqrt{g'H} \exp\left(\frac{x-d}{R}\right) , \tag{15.13}$$

where R is the deformation radius, defined by

$$R = \frac{\sqrt{g'H}}{f} , \tag{15.14}$$

and d is the unknown position of the outcrop (where h vanishes). To determine this distance, we must again tie the initial and final states, this time by imposing volume conservation. Ruling out a finite displacement at infinity where there is no activity, we require that the depletion of light water on the left of $x = 0$ be exactly compensated by the presence of light water on the right; that is,

$$\int_{-\infty}^{0} (H - h) \, dx \; = \; \int_{0}^{d} h \, dx, \qquad (15.15)$$

JMB from ⇓

which yields a transcendental equation for d, whose solution is surprisingly simple:

JMB to ⇑

$$d \; = \; R \; = \; \frac{\sqrt{g'H}}{f} \; . \qquad (15.16)$$

Thus, the maximum distance over which the light water has spilled is none other than the radius of deformation, hence the name of the latter.

Notice that R has the Coriolis parameter f in its denominator. Therefore, the spreading distance, R, is less than infinity because f differs from zero. In other words, the spreading is confined because of the earth's rotation via the Coriolis effect. In a non-rotating framework, the spreading would, of course, be unlimited.

Lateral heterogeneities are constantly imposed onto the atmosphere and oceans, which then adjust and establish patterns whereby these lateral heterogeneities are somewhat distorted but maintained. Such patterns are at or near geostrophic equilibrium and can thus persist for quite a long time. This explains why discontinuities such as fronts are common occurrences in both the atmosphere and the oceans. As the preceding example suggests, fronts and the accompanying winds or currents take place over distances on the order of the deformation radius. To qualify the activity observed at that length scale, meteorologists refer to the *synoptic scale*, whereas oceanographers prefer to use the adjective *mesoscale*.

We can vary the initial, hypothetical disturbance and generate a variety of geostrophic fronts, all being steady states. A series of examples, taken from published studies, is provided in Figure 15-4. They are, in order: surface-to-bottom front on a flat bottom, which can result from sudden and localized heating (or cooling); surface-to-bottom front at the shelf break resulting from the existence of distinct shelf and deep water masses; double, surface-to-surface front; and three-layer front as the result of localized mixing of an otherwise two-layer stratified fluid. The interested reader is referred to the original articles by C. G. Rossby (1937, 1938), the article by Veronis (1956), the review by Blumen (1972), and other articles on specific situations, by Stommel and Veronis (1980), Hsueh and Cushman-Roisin (1983), and van Heijst (1985). Ou (1984) considered the geostrophic adjustment of a continuously stratified fluid and showed that, if the initial condition is sufficiently away from equilibrium, density discontinuities can arise during the adjustment process. In other words, *fronts* can spontaneously emerge from earlier non-discontinuous conditions.

The preceding applications dealt with situation in which there is no variation in one of the two horizontal directions. The general case (see Hermann et al., 1989) may yield a time-dependent flow that is nearly geostrophic.

15.3 Energetics of geostrophic adjustment

The preceding theory of geostrophic adjustment relied on potential-vorticity and volume conservation principles, but nothing was said of energy, which must also be conserved in

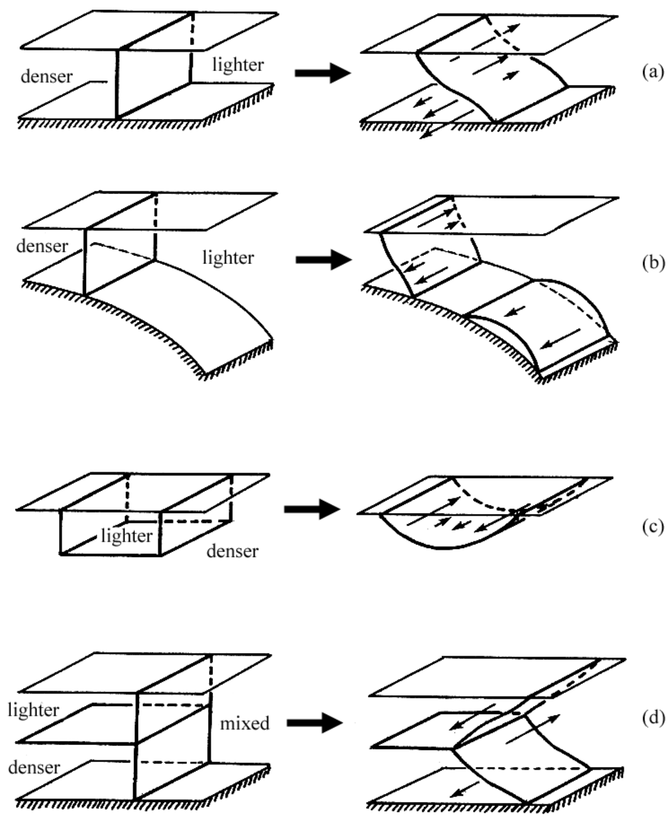

Figure 15-4 Various examples of geostrophic adjustment.

a nondissipative system. All we can do, now that the solution has been obtained, is to check on the budget, where a surprise is awaiting us!

Initially, the system is at rest and there is no kinetic energy ($KE_i = 0$), whereas the initial potential energy (per unit length in the transverse direction) is

$$PE_i \;=\; \frac{1}{2}\,\rho_0\,\int_{-\infty}^{0} g' H^2\,dx. \tag{15.17}$$

Benoit: I do not think we proved that expression of potential energy is given by (15.17). Maybe in Section 12.4 as limiting case for second layer to infinity? Or exercise?
(Although this expression is infinite, only the difference with the final potential energy will interest us. So, there is no problem.) At the final state, the velocity u is zero, leaving the kinetic energy to be

$$KE_f = \frac{1}{2} \rho_0 \int_{-\infty}^{a} hv^2 \, dx, \tag{15.18}$$

and the potential energy is

$$PE_f = \frac{1}{2} \rho_0 \int_{-\infty}^{a} g'h^2 \, dx. \tag{15.19}$$

During the spreading phase, some of the lighter water has been raised and some heavier water has been lowered to take its place. Hence, the center of gravity of the system has been lowered, and we expect a drop in potential energy. Calculations yield

$$\Delta PE = PE_i - PE_f = \frac{1}{4} g'H^2 R. \tag{15.20}$$

Some kinetic energy has been created by setting a transverse current. The amount is

$$\Delta KE = KE_f - KE_i = \frac{1}{12} g'H^2 R. \tag{15.21}$$

Therefore, as we can see, only one-third of the potential-energy drop has been consumed by the production of kinetic energy, and we should ask: What has happened to the other two-thirds of the released potential energy? The answer lies in the presence of transients, which occur during the adjustment: Some of the time-dependent motions are gravity waves (here, internal waves on the interface), which travel to infinity, radiating energy away from the region of adjustment. In reality, such waves dissipate along the way, and there is a net decrease of energy in the system. The ratio of kinetic-energy production to potential-energy JMB from ⇓ release varies from case to case (Ou, 1986) but tends to remain between 1/4 and 1/2. The reason we used a volume-conservation constraint to determine the frontal position and allow for energy to be lost at infinite and not the inverse is rooted in the very different nature of mass and energy propagation. The latter can be transported by waves, without net displacement of JMB to ⇑ fluid parcels, while the former would need a net advection by a flow.

An interesting property of the geostrophically adjusted state is that it corresponds to the greatest energy loss and thus to a level of minimum energy. Let us demonstrate this proposition in the particular case at hand. The energy of the system is at all times

$$E = PE + KE = \frac{\rho_0}{2} \int_{-\infty}^{a} \left[g'h^2 + h\left(u^2 + v^2\right)\right] dx, \tag{15.22}$$

and we know that the evolution is constrained by conservation of potential vorticity:

$$f + \frac{\partial v}{\partial x} = \frac{f}{H} h. \tag{15.23}$$

Let us now search for the state that corresponds to the lowest possible level of energy, (15.22), under constraint (15.23) by forming the variational principle:

$$\mathcal{F}(h,u,v,\lambda) = \frac{\rho_0}{2} \int_{-\infty}^{0} \left[g'h^2 + h(u^2+v^2) - 2\lambda \left(f + \frac{\partial v}{\partial x} - \frac{fh}{H}\right)\right] dx \tag{15.24}$$

$$\delta\mathcal{F} = 0 \quad \text{for any } \delta h,\ \delta u,\ \delta v,\ \text{and } \delta\lambda. \tag{15.25}$$

rom ⇓ Because expression (15.22) is positive definite in the absence of the constraint , the extremum
o ⇑ will be a minimum. The variations with respect to the three state variables h, u, and v and the Lagrange multiplier λ yield, respectively:

$$\delta h: \qquad g'h + \frac{1}{2}(u^2 + v^2) + \frac{f}{H}\lambda = 0 \tag{15.26}$$

$$\delta u: \qquad hu = 0 \tag{15.27}$$

$$\delta v: \qquad hv + \frac{\partial \lambda}{\partial x} = 0 \tag{15.28}$$

$$\delta \lambda: \qquad f + \frac{\partial v}{\partial x} - \frac{f}{H}h = 0. \tag{15.29}$$

Equation (15.27) provides $u = 0$, whereas the elimination of λ between (15.26) and (15.28) leads to

$$\frac{\partial}{\partial x}\left(g'h + \frac{1}{2}v^2\right) + \frac{f}{H}(-hv) = 0,$$

or,

$$g'\frac{\partial h}{\partial x} + v\left(\frac{\partial v}{\partial x} - \frac{f}{H}h\right) = 0.$$

Finally, use of (15.29) reduces this last equation to

$$g'\frac{\partial h}{\partial x} - fv = 0.$$

In conclusion, the state of minimum energy is the state in which u vanishes, and the cross-isobaric velocity is geostrophic — that is, the steady, geostrophic state.

It can be shown that the preceding conclusion remains valid in the general case of arbitrary, multilayer potential-vorticity distributions, as long as the system is uniform in one horizontal direction. Therefore, it is a general rule that geostrophically adjusted states cor- JMB from ⇓
respond to levels of minimum energy. This may explain why geophysical flows commonly JMB to ⇑
adopt a nearly geostrophic balance.

15.4 Coastal upwelling

15.4.1 The upwelling process

Winds blowing over the ocean generate Ekman layers and currents. The depth-averaged currents, called the Ekman drift, forms an angle with the wind, which was found to be 90° (to the right in the Northern Hemisphere) according to a simple theory (Section 8.6). So, when a wind blows along a coast, it generates an Ekman drift directed either onshore or offshore, to which the coast stands as an obstacle. The drift is offshore if the wind blows with the coast on its left (right) in the Northern (Southern) Hemisphere (Figure 15-5). If this is the case, water depletion occurs in the upper layers, and a low pressure sets in, forcing waters from below

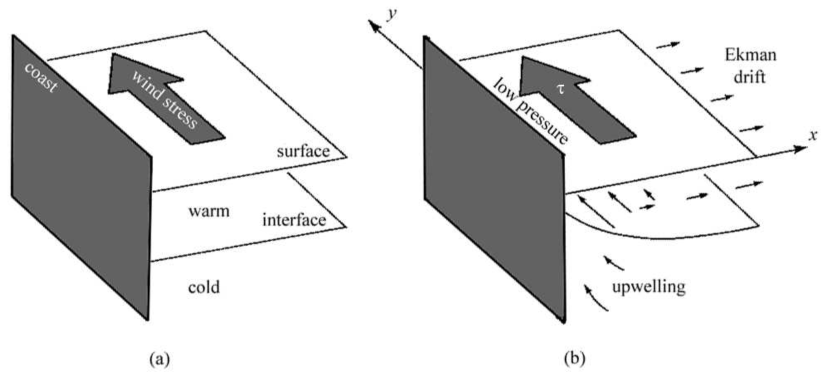

Figure 15-5 Schematic development of coastal upwelling.

to move upward and replenish at least partly the space vacated by the offshore drift. This phenomenon is called *coastal upwelling*. The upward movement calls for a replenishment at the lower levels, which is accomplished by an onshore flow. To recapitulate, a wind blowing along the coast (with the coast on the left or the right in, respectively, the Northern or the Southern Hemisphere) sets an offshore current in the upper levels, an upwelling at the coast, and an onshore current at lower levels. JMB from ⇓ JMB to ⇑

This circulation in the cross-shore vertical plane is not the whole story, however. The low pressure created along the coast also sustains, via geostrophy, a longshore current, while JMB from ⇓ vertical stretching in the lower layer generates relative vorticity and a shear flow. Or, from a different perspective, the vertical displacement create lateral density gradients, which in turn JMB to ⇑ call for a thermal wind, the shear flow. Thus, the flow pattern is rather complex.

At the root of coastal upwelling is a divergent Ekman drift. And, we can easily conceive of other causes besides a coastal boundary for such divergence. Two other upwelling situations are noteworthy: one along the equator and the other at high latitudes. Along the equator, the trade winds blow quite steadily from East to West. On the northern side of the Equator, the Ekman drift is to the right, or away from the Equator, and on the southern side, it is to the left, again away from the Equator (Figure 15-6). Consequently, horizontal divergence occurs along the equator, and mass conservation requires upwelling (Yoshida, 1959; Gill, 1982, Chapter 11).

At high latitudes, upwelling frequently occurs along the ice edge, in the so-called marginal ice zone. A uniform wind exerts different stresses on ice and open water; in its turn, the moving ice exerts a stress on the ocean beneath. The net effect is a complex distribution of stresses and velocities at various angles, with the likely result that the ocean currents at the ice edge do not match (Figure 15-6). For certain angles between wind and ice edge, these currents diverge, and upwelling again takes place to compensate for the divergence of the horizontal flow (Häkkinen, 1990).

The upwelling phenomenon, especially the coastal type, has been the subject of considerable attention, chiefly because of its relation to biological oceanography and, from there, to fisheries. In brief, small organisms in the ocean (phytoplankton) proliferate when two con-

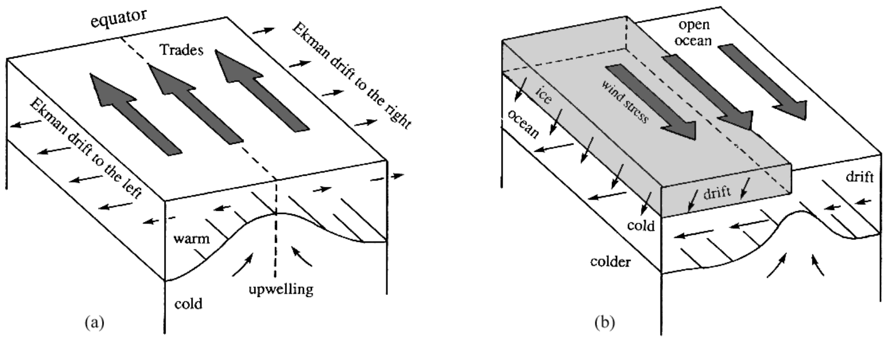

Figure 15-6 Other types of upwelling: (a) equatorial upwelling, (b) upwelling along the ice edge.

ditions are met: sunlight and a supply of nutrients. In general, nutrients lie in the deeper waters, below the reach of sunlight, and so the waters tend to lack either nutrients or sunlight. The major exceptions are the upwelling regions, where deep, nutrient-rich waters rise to the surface, receive sunlight, and stimulate biological activity. Upwelling-favorable winds most generally occur along the west coasts of continents where the prevailing winds blow toward the Equator. For a review of observations and a discussion of the biological implications of coastal upwelling, the interested reader is referred to the volume edited by Richards (1981).

15.4.2 A simple model of coastal upwelling

Consider a reduced-gravity ocean on an f-plane ($f > 0$), bounded by a vertical wall and subjected to a surface stress acting with the wall on its left (Figure 15-5a). The upper moving layer, defined to include the entire vertical extent of the Ekman layer, supports an offshore drift current. The lower layer is, by virtue of the choice of a reduced-gravity model, infinitely deep and motionless. In the absence of longshore variations, the equations of motion are

$$\frac{\partial u}{\partial t} + u\,\frac{\partial u}{\partial x} - fv = -g'\,\frac{\partial h}{\partial x} \tag{15.30a}$$

$$\frac{\partial v}{\partial t} + u\,\frac{\partial v}{\partial x} + fu = \frac{\tau}{\rho_0 h} \tag{15.30b}$$

$$\frac{\partial h}{\partial t} + \frac{\partial}{\partial x}(hu) = 0, \tag{15.30c}$$

where x is the offshore coordinate, τ is the longshore wind stress, and all other symbols are conventional (Figure 15-5b).

Despite its apparent simplicity, the preceding set of equations is nonlinear, and no analytical solution is known. We therefore linearize these equations by assuming that the wind stress τ and, in turn, the ocean's reaction are weak. Noting

$h = H - a$, where H is the depth of the undisturbed upper layer and a the small upward displacement of the interface, we write

$$\frac{\partial u}{\partial t} - fv = g' \frac{\partial a}{\partial x} \tag{15.31}$$

$$\frac{\partial v}{\partial t} + fu = \frac{\tau}{\rho_0 H} \tag{15.32}$$

$$-\frac{\partial a}{\partial t} + H\frac{\partial u}{\partial x} = 0. \tag{15.33}$$

This set of equations contains two independent x-derivatives and thus calls for two boundary conditions. naturally, u vanishes at the coast ($x = 0$) and a vanishes far offshore ($x \to +\infty$).

The solution to the problem depends on the initial conditions, which may be taken to correspond the state of the rest ($u = v = a = 0$). Yoshida (1955) is credited with the first derivation of this solution (extended to two moving layers). However, because of the fluctuating nature of winds, upwelling is rarely an isolated event in time, and we prefer to investigate the periodic solutions to the preceding linear set of equations. Taking $\tau = \tau_0 \sin \omega t$, where τ_0 is a constant in both space and time, we note that the solution must be of the type $u = u_0(x) \sin \omega t$, $v = v_0(x) \cos \omega t$ and $a = a_0(x) \cos \omega t$. Substitution and solution of the remaining ordinary differential equations in x yield

$$u = \frac{f\tau_0}{\rho_0 H\,(f^2 - \omega^2)} \left[1 - \exp\left(-\frac{x}{R_\omega}\right)\right] \sin \omega t \tag{15.34}$$

$$v = \frac{\omega\tau_0}{\rho_0 H\,(f^2 - \omega^2)} \left[1 - \frac{f^2}{\omega^2}\exp\left(-\frac{x}{R_\omega}\right)\right] \cos \omega t \tag{15.35}$$

$$a = \frac{-fR_\omega\tau_0}{\rho_0 g' H\omega} \exp\left(-\frac{x}{R_\omega}\right) \cos \omega t, \tag{15.36}$$

where R_ω is a modified deformation radius defined as

$$R_\omega = \sqrt{\frac{g'H}{f^2 - \omega^2}} \tag{15.37}$$

From the preceding solution, we conclude that the upwelling or downwelling signal is *trapped* along the coast within a distance on the order of R_ω. Far offshore ($x \to \infty$), the interfacial displacement vanishes, and the flow field reduces to the Ekman drift

$$u_{EK} = \frac{\tau_0}{\rho_0 f H} \sin \omega t, \quad v_{EK} = 0, \tag{15.38}$$

on which are superimposed inertial oscillations. At long periods such as weeks and months ($\omega \ll f$), the distance R_ω becomes the radius of deformation, the vertical interfacial displacements become very large (indeed, the wind blows more steadily in one direction before it reverses), and the far-field inertial oscillations become much smaller than the Ekman drift.

At superinertial frequencies ($\omega > f$), the quantity R_ω becomes imaginary, indicating that the solution does not decay away from the coast but instead oscillates. Physically, the ocean's response is not trapped near the coast and inertia-gravity waves (Section 9.3) are excited. These radiate outward, filling the entire basin.

15.4.3 Finite-amplitude upwelling

If the wind is sufficiently strong or is blowing for a sufficiently long time, the density interface can rise to the surface, forming a front. Continued wind action displaces this front offshore and exposes the colder waters to the surface. This mature state is called *full upwelling* (Csanady, 1977). Obviously, the previous linear theory is not applicable in such case.

Because of the added complications arising from the nonlinearities, let us now restrict our investigation to the final state of the ocean after a wind event of finite duration. Equation (15.30b), expressed as

$$\frac{d}{dt}\,(v\;+\;fx)\;=\;\frac{\tau}{\rho_0 h}, \tag{15.39}$$

where $d/dt = \partial/\partial t + u\partial/\partial x$ is the time derivative following a fluid particle in the offshore direction, can be integrated over time to yield:

$$(v\;+\;fx)_{\text{at end of event}}\;-\;(v\;+\;fx)_{\text{initially}}\;=\;I. \tag{15.40}$$

The *wind impulse* I is the integration of the wind-stress term,$\tau/\rho_0 h$, over time and following a fluid particle. Although the wind impulse received by every parcel cannot be precisely determined, it can be estimated by assuming that the wind event is relatively brief. The time integral can then be approximated by using the local stress value and replacing h by H: JMB from ⇓

JMB to ⇑

$$I\;\simeq\;\frac{1}{\rho_0 H}\int_{\text{event}}\tau\;dt. \tag{15.41}$$

If the initial state is one of rest, relation (15.40) implies that a particle initially at distance X from the coast is at distance x immediately after the wind ceases and has a longshore velocity v such that

$$v\;+\;fx\;-\;fX\;=\;I. \tag{15.42}$$

During the oceanic adjustment that follows until equilibrium is reached, Equation (15.39) (with $\tau = 0$) implies that the quantity $v + fx$ is a conserved quantity, and relation (15.42) continues to hold beyond the time when the wind ceased.

If the wind is laterally uniform while it blows, no vorticity is imparted to fluid parcels, **Benoit:** Did we show this? Is physically obvious for us, but have we already proved it somewhere? If so, reference to section or Exercise?? JMB from ⇓

JMB to ⇑

and potential vorticity is conserved during the wind event as well as during the following adjustment:

$$\frac{1}{h}\,\left(f\;+\;\frac{\partial v}{\partial x}\right)\;=\;\frac{f}{H}\;. \tag{15.43}$$

Once a steady state has been achieved, there is no longer any offshore velocity ($u = 0$), according to (15.30c). The remaining equation, (15.30a), reduces to a simple geostrophic balance, which together with (15.43) provides the solution:

$$h = H - A \exp\left(-\frac{x}{R}\right) \tag{15.44}$$

$$v = A\sqrt{\frac{g'}{H}} \exp\left(-\frac{x}{R}\right), \tag{15.45}$$

where R is now the conventional radius of deformation ($\sqrt{g'H}/f$. The constant of integration A represents the amplitude of the upwelled state and is related to the wind impulse via (15.42). Two possible outcomes must be investigated: Either the interface has not risen to the surface (Figure 15-7, case I) or it has outcropped, forming a front and leaving cold waters exposed to the surface near the coast (Figure 15-7, case II).

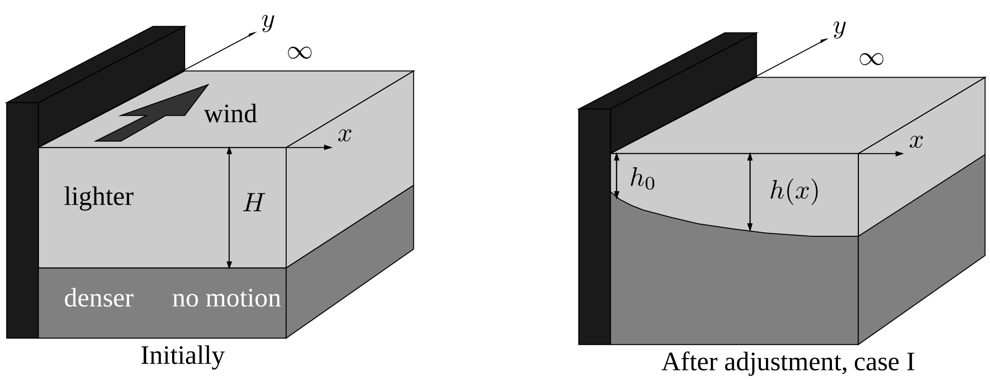

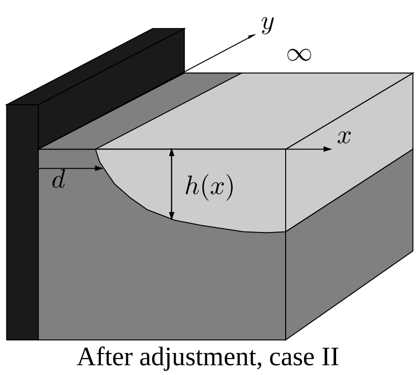

Figure 15-7 The two possible outcomes of coastal upwelling after a longshore wind of finite duration. After a weak or brief wind (case I), the interface has upwelled but not to the point of reaching the surface. A strong or prolonged wind event (case II) causes the interface to reach the surface, where it forms a front; this front is displaced offshore, leaving cold waters from below exposed to the surface. This latter case corresponds to a mature upwelling that favors biological activity.

In case I, the particle initially against the coast ($X = 0$) is still there ($x = 0$), and relation (15.42) yields $v(x = 0) = I$. Solution (15.45) meets this condition if $A = I(H/g')^{1/2}$. The depth along the coast, $h(x = 0) = H - A$, must be positive requiring $A \leq H$; that is, $I \leq (g'H)^{1/2}$. In other words, the no-front situation or partial upwelling of case I occurs if the wind is sufficiently weak or sufficiently brief that its resulting impulse is less than the critical value $(g'H)^{1/2}$.

In the more interesting case II, the front has been formed, and the particle initially against the coast ($X = 0$) is now at some offshore distance ($x = d \geq 0$), marking the position of the front. There the layer depth vanishes, $h(x = d) = 0$, and solution (15.44) yields $A = H \exp(d/R)$. The longshore velocity at the front is, according to (15.45), $v(x = d) = (g'H)^{1/2}$. Finally, relation (15.42) leads to the determination of the offshore displacement d in terms of the wind impulse:

$$d = \frac{I}{f} - R. \tag{15.46}$$

Since this displacement must be a positive quantity, it is required that $I \geq (g'H)^{1/2}$. Physically, if the wind is sufficiently strong or sufficiently prolonged, so that the net impulse is greater than the critical value $(g'H)^{1/2}$, the density interface rises to the surface and forms a front that migrates away from shore, leaving cold waters from below exposed to the surface. Note how the conditions for the realizations of cases I and II complement each other.

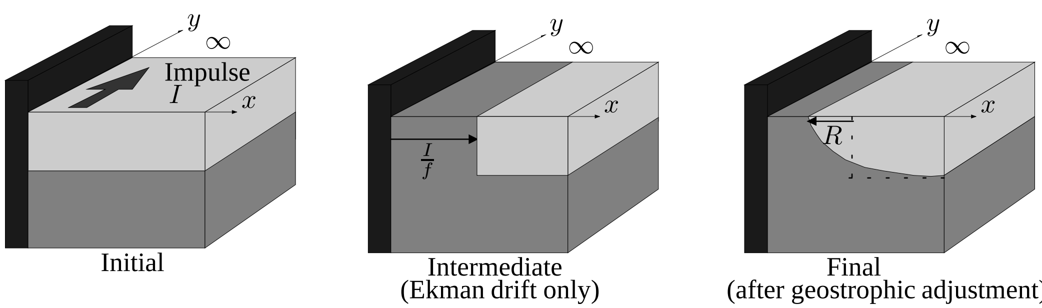

Figure 15-8 Decomposition of the formation of a coastal-upwelling front as a two-stage process: first, an offshore Ekman drift in response to the wind, followed by a backward geostrophic adjustment.

Formula (15.46) has a simple physical interpretation, as sketched in Figure 15-8. The offshore Ekman velocity u_{EK} is the velocity necessary for the Coriolis force to balance the longshore wind stress:

$$u_{EK} = \frac{\tau}{\rho_0 f h}, \tag{15.47}$$

according to (8.34a). Integrated over time, this yields a net offshore displacement proportional to the wind impulse

$$x_{EK} = \frac{I}{f}. \tag{15.48}$$

If we were now to assume that the wind is responsible for an offshore shift of this magnitude, while the surface waters are moving as a solid slab, we would get the intermediate structure of Figure 15-8. But such a situation cannot persist, and an adjustment must follow, causing an onshore spread similar to that considered in Section 15.2 — that is, over a distance equal to the deformation radius. Hence we have the final structure of Figure 15-8 and formula (15.46).

15.4.4 Variability of the upwelling front

Up to this point, we have considered only processes operating in the offshore direction or, equivalently, an upwelling that occurs uniformly along a straight coast. In reality, the wind is often localized, the coastline not straight, and upwelling not at all uniform. A local upwelling sends a wave signal along the coast, taking the form of an internal Kelvin wave, which in the Northern Hemisphere propagates with the coast on its right. This redistribution of information not only decreases the rate of upwelling in the forced region but also generates upwelling in other, unforced areas. As a result, models of upwelling must retain a sizable portion of the coast and both spatial and temporal variations of the wind field (Crépon and Richez, 1982; Brink, 1983).

Adding to this variability are intrinsic instabilities of the upwelling front, because the front is a region of highly sheared currents. In the two-layer formulation presented in the previous section, this shear is manifested by a discontinuity of the current at the front. The warm layer develops anticyclonic vorticity (*i.e.*, counter to the rotation of the earth) under the influence of vertical squeezing and flows alongshore in the direction of the wind. On the other side of the front, the exposed lower layer is vertically stretched, develops cyclonic vorticity (*i.e.*, in the same direction as the rotation of the earth) and flows upwind. The currents on each side of the front thus flow in opposite directions, causing a large shear, which, as we have seen (Chapter 10), is vulnerable to instabilities. In addition to the kinetic-energy supply in the horizontal shear (barotropic instability), potential energy can also be released from the stratification by a spreading of the warm layer (baroclinic instability; see Chapter 17). Offshore jets of cold, upwelled waters have been observed to form near capes; these jets cut through the front, forge their way through the warm layer, and eventually split to form pairs of counterrotating vortices (Flament et al., 1985). This explains why mesoscale turbulence is associated with upwelling fronts (Figure 15-9). The situation is complex and demands careful modeling. Irregularities in the topography and coastline may play influential roles and require adequate spatial resolution, while accurate simulation of the instabilities is only possible if the numerical dissipation of the model is not excessive.

15.5 Atmospheric frontogenesis

Text of section

15.6 Numerical handling of large gradients

A common characteristic of the preceding sections is the appearance and involvement of strong gradients of density. If such a gradient appears in the horizontal plane, we are in the presence of a frontal structure. Should we need to apply numerical techniques on a Eulerian grid to describe the front, we are immediately facing the problem of needing very high resolution in the grid spacing to ensure $\Delta x \ll L$, because the length scale L can become quite small across the front. Such a high resolution covering the whole model domain is generally

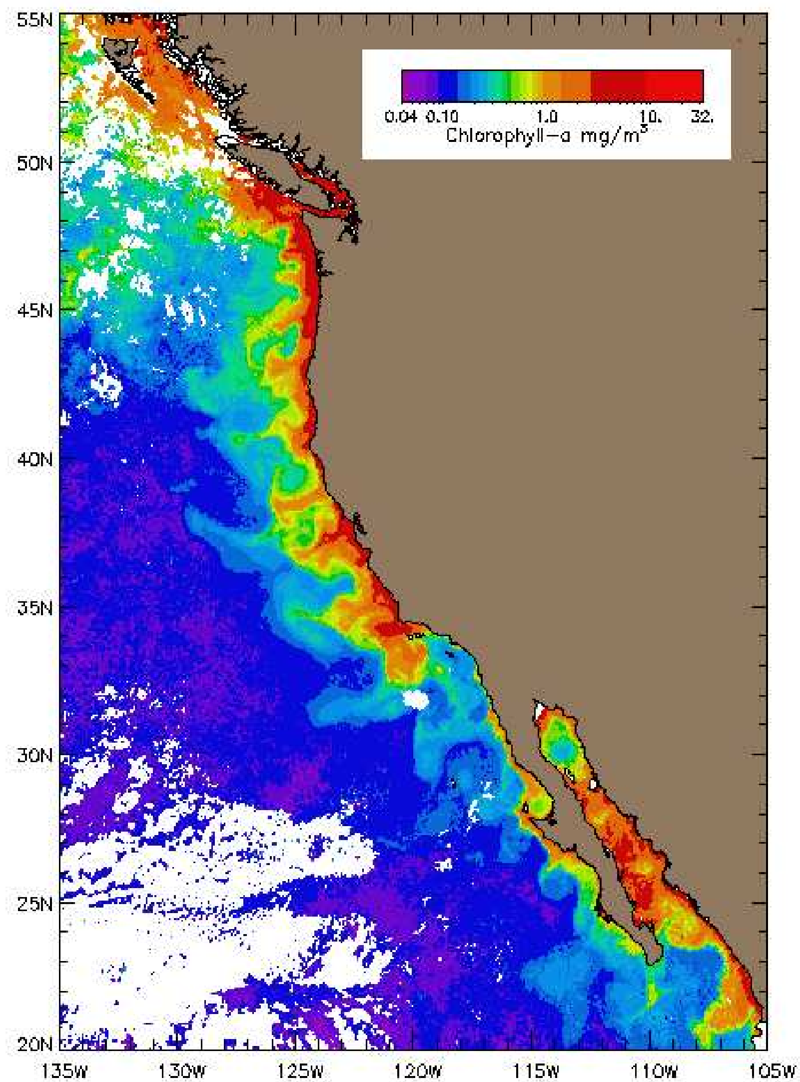

Figure 15-9 SeaWiFS satellite image of the North American Pacific coast showing the occurence of coastal upwelling from Baja California (Mexico) to Vancouver Island (Canada). Colors indicate the amount of chlorophyll concentration in the water, with high values (red and orange colors) in regions of high biological activity and low values (blue and purple colors) in biologically inactive waters. Note how instabilities greatly distort the upwelling front (transition from yellow to light blue color). (*Composite image provided courtesy of Dr. Andrew Thomas, School of Marine Sciences, University of Maine, USA*)

computationally very expensive, and it would be preferable to use the high resolution only near the frontal region. This can be achieved by *nesting* approaches, embedding higher resolution models into coarser resolution models at the location of interest (***e.g.***, Barth ***et al.***, 2005). In this case, an abrupt change in grid size is present at the interface between the two models, which can lead to numerical problems (Exercise 15-9), which require particular care. Here we present therefore a method that allows gradually changing grid spacings. Such a variable resolution was already suggested in the time discretization (see Figure 4-10) when processes are suddenly varying more rapidly. It is now appropriate to formalize a method to place or distribute discrete calculation points in an optimal way. We will first try to distribute a series of discrete points x_i to follow at best a given and known function $f(x)$. The optimality criterion could be to distribute the points so that on average, differences of f between grid points are uniform. In this way, regions with very large variations will be covered with more grid points than regions with weak variations. In other words, it would be advantageous to keep variations constant

$$|f_{i+1} - f_i| \sim \mathcal{C} \tag{15.49}$$

by placing the grid points i adequately. Mathematically we look for a coordinate transformation

$$x = x(\xi, t), \quad \xi_i = i \tag{15.50}$$

where the new coordinate ξ is uniformly discretized in the computational domain, while the discrete points $x_i = x(\xi_i)$ are non-uniformly covering the real domain. In terms of the new coordinate ξ, the variations of f that should be kept uniform are

$$\left|\frac{\partial f}{\partial \xi}\right| \sim \mathcal{C} \tag{15.51}$$

or by taking the derivative with respect to ξ

$$\frac{\partial}{\partial \xi}\left|\frac{\partial f}{\partial \xi}\right| \;=\; 0. \tag{15.52}$$

If we express the variations of f in terms of physical gradients, we therefore should find $x(\xi)$ solution of

$$\frac{\partial}{\partial \xi}\left(\left|\frac{\partial f}{\partial x}\right| \frac{\partial x}{\partial \xi}\right) \;=\; 0. \tag{15.53}$$

Since we are interested in discretizing anyway and can assume without loss of generality $\Delta\xi = 1$, we can directly search for the discrete positions x_i solution of

$$\left|\frac{\partial f}{\partial x}\right|_{i+1/2} (x_{i+1} - x_i) - \left|\frac{\partial f}{\partial x}\right|_{i-1/2} (x_i - x_{i-1}) \;=\; 0. \tag{15.54}$$

This equation is nonlinear since derivatives must be calculated in unknown grid-point positions. To solve the equation, an iterative method or pseudo-time approach can be used (see iterative solvers of Section 5.6):

$$x_i^{(k+1)} = x_i^{(p)} + \Delta t \alpha \left[\left|\frac{\partial f}{\partial x}\right|_{i+1/2} (x_{i+1}^{(k)} - x_i^{(k)}) - \left|\frac{\partial f}{\partial x}\right|_{i-1/2} (x_i^{(k)} - x_{i-1}^{(k)})\right] = 0. \tag{15.55}$$

This can be interpreted as the numerical solution of a pseudo-evolution equation for the grid-nodes.

$$\frac{\partial x}{\partial t} \;=\; \alpha \frac{\partial}{\partial \xi}\left(\left|\frac{\partial f}{\partial x}\right| \frac{\partial x}{\partial \xi}\right), \tag{15.56}$$

where the coefficient α scales with the distance L over with function f changes by its typical value F

$$\alpha = \frac{L}{TF} \tag{15.57}$$

and where the time-scale T determines how fast the stationary solutions should be obtained. If the numerical calculation of gradients is performed in a straightforward approach with the function sampled at $x_i^{(k)}$ denoted by $f_i^{(k)} = f(x_i^{(k)})$, our grid relocation algorithm reads

$$x_i^{(k+1)} \;=\; x_i^{(k)} + \Delta t \alpha \left[\left|f_{i+1}^{(k)} - f_i^{(k)}\right| - \left|f_i^{(k)} - f_{i-1}^{(k)}\right|\right]. \tag{15.58}$$

The algorithm is complemented with prescribed values of x on the known boundary positions. A problem with this formulation appears when the function f is constant in large parts of the domain. By construction, such regions will be void of grid nodes because no variations of f are detected. Therefore a tendency to maintain a uniform background distribution of grid nodes should be required. This can be achieved by the following approach

$$x_i^{(k+1)} = x_i^{(k)} + \Delta t \alpha \left[w_{i+1/2}(x_{i+1}^{(k)} - x_i^{(k)}) - w_{i-1/2}(x_i^{(k)} - x_{i-1}^{(k)})\right] = 0 \tag{15.59}$$

where the weighting function can be calculated as

$$w = \frac{\partial f}{\partial x} + \beta \frac{F}{L}. \tag{15.60}$$

In this approach β controls the tendency to reach a uniform grid distribution. If scales F and L are chosen correctly, $\beta \gg 1$ leads to the stationary equation $\partial^2 x/\partial \xi^2 = 0$ and would lead to a uniform grid, while $\beta \ll 1$ is equivalent to the original version (15.55). The grid positions can thus be obtained by repeated application of the diffusion-like equation (15.59). This is not to be confused with a physical diffusion. Here only positions of the grid nodes are calculated. Later, dynamic equations, possibly without any diffusion, are then to be discretized on this grid. Applying this adapting technique we can then follow strong gradients with some residual grid nodes in the other regions (Figure 15-10). Other techniques to place grid points in regions of interest exist (*e.g.*, Thompson *et al.*, 1985; Liseikin, 1999), the general approach being to reduce some measure of the discretization errors.

The non-uniform grids can be used in a fixed or time-adaptive way. In the frozen version, the grids are created once and the calculation points kept at their initial location. This allows to focus on features whose position is known *a priori*, such as topographic particularities and associated dynamics. Or it simply allows to zoom into a given region of interest. In the adaptive version, the grid is allowed to move in time, following if possible, the dynamically relevant structures (*e.g.*, Beckers and Burchard, 2004). In this case, in addition to the need of using discrete operators on a non-uniform grid, appears the difficulty of a moving grid,

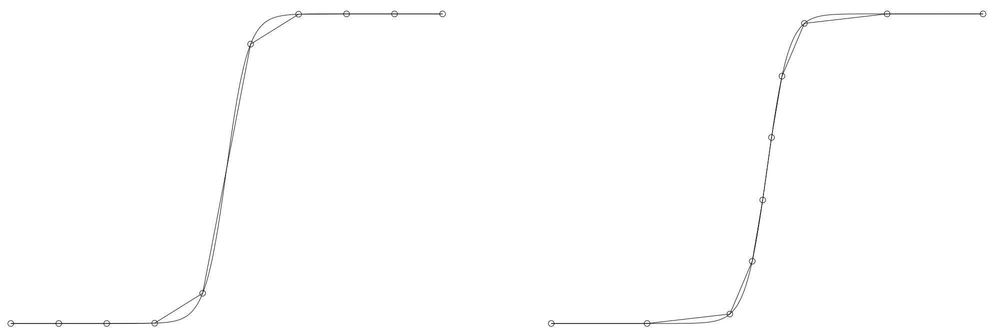

Figure 15-10 Grid nodes sampling a strongly varying function and linear interpolation between nodes. On the left panel the standard uniform grid and on the right panel the adapted grid with higher resolution near the front.

which needs to be reflected in the discretization operators. The modification to the standard methods can be illustrated on the one-dimensional tracer equation in physical space

$$\frac{\partial c}{\partial t} + \frac{\partial (uc)}{\partial x} = \frac{\partial}{\partial x}\left(\mathcal{A}\frac{\partial c}{\partial x}\right). \tag{15.61}$$

The moving grids requires additional treatment which we can introduce mathematically via a coordinate transformation similar to the isopycnal coordinate change. For the one-dimensional problem we will calculate $c(\xi(x,t),t)$. Note that our grid generation provides $x(\xi,t)$ so that we should try to express coordinate-transformation rules in terms of metrics $\partial x/\partial t$ and $\partial x/\partial \xi$ we can calculate numerically when knowing the positions $x(\xi_i, t^n)$. Using the same mathematical approach as in Section 12.1, and exploiting

$$\frac{\partial \xi}{\partial t} = -\frac{\frac{\partial x}{\partial t}}{\frac{\partial x}{\partial \xi}}, \qquad \frac{\partial \xi}{\partial x} = \frac{1}{\frac{\partial x}{\partial \xi}} \tag{15.62}$$

we obtain the governing equation for c in the coordinate system (ξ, t)

$$\frac{\partial x}{\partial \xi}\frac{\partial c}{\partial t} - \frac{\partial x}{\partial t}\frac{\partial c}{\partial \xi} + \frac{\partial (uc)}{\partial \xi} = \frac{\partial}{\partial \xi}\left(\mathcal{A}\left(\frac{\partial x}{\partial \xi}\right)^{-1}\frac{\partial c}{\partial \xi}\right). \tag{15.63}$$

Derivatives are performed in the new coordinate system, in which the numerical grid is now fixed and uniform, so that we can apply our standard discretization techniques. For this, it is advantageous to provide a flux form of the equation exploiting $\partial^2 x/\partial\xi\partial t = \partial^2 x/\partial t\partial\xi$:

$$\frac{\partial}{\partial t}\left(\frac{\partial x}{\partial \xi}c\right) + \frac{\partial}{\partial \xi}\left[\left(u - \frac{\partial x}{\partial t}\right)c\right] = \frac{\partial}{\partial \xi}\left(\mathcal{A}\left(\frac{\partial x}{\partial \xi}\right)^{-1}\frac{\partial c}{\partial \xi}\right). \tag{15.64}$$

$\partial x/\partial \xi$ is readily interpreted as the grid spacing when $\Delta\xi = 1$, whereas the term $u_d = \partial x/\partial t$ is the velocity at which the grid nodes move in physical space. In the numerical space, the advection term involves $(\hat{u} = u - u_d)$ which is the velocity relative to the moving grid and which is needed to advect the information relative to the nodes. Obviously if we move the grid with the current velocity, relative velocity is zero and we are in a Lagrangian framework. But for grid adaptations, the movement of the grid does not need to be related to the flow velocity but can be freely chosen. Care must however be taken to ensure stability of the scheme because of the changed apparent velocity field within the numerical grid.

Instead of the mathematical coordinate change in the governing equations, we can also establish discrete equations on a moving grid by directly applying the space integration in physical space between two moving grid-points $x_a(t)$ and $x_b(t)$. When integrating between two such points, in coherence with the finite volume approach (Section 3.9), we write

$$\int_{x_a(t)}^{x_b(t)} \frac{\partial c}{\partial t} dx \;+\; q_b \;-\; q_a \;=\; 0 \quad q \;=\; uc - \mathcal{A}\frac{\partial c}{\partial x}. \tag{15.65}$$

Here we must take into account that the integration boundaries move and use Leipnitz rule to treat the time derivative so as to make appear the numerical unknown, *i.e.*, the time variation of the grid averaged/integrated concentration

$$\frac{\partial}{\partial t}\int_{x_a(t)}^{x_b(t)} c dx \;+\; c(x_a,t)\,\frac{\partial x_a}{\partial t} \;-\; c(x_b,t)\,\frac{\partial x_b}{\partial t} \;+\; q_b \;-\; q_a = 0. \tag{15.66}$$

Defining the flux

$$\hat{q} = \left(u - \frac{\partial x}{\partial t}\right) c - \mathcal{A}\frac{\partial c}{\partial x} \tag{15.67}$$

the finite volume equation on the moving grid reads

$$\frac{\partial}{\partial t}\int_{x_a(t)}^{x_b(t)} c dx \;+\; \hat{q}_b \;-\; \hat{q}_a = 0, \tag{15.68}$$

where the velocity $u_d = \partial x/\partial t$ of the grid appears again. This is already a discrete formulation in space and we can obtain the same by integrating (15.64) in the fixed numerical-coordinate space where no Leipnitz rule needs to be applied. We therefore obtain for both approaches the semi-discrete equation

$$\frac{\partial}{\partial t}\left[(x_{i+1/2} - x_{i-1/2})\tilde{c}_i\right] \;+\; \hat{q}_b \;-\; \hat{q}_a = 0, \tag{15.69}$$

where the fluxes $\hat{q}$ are discretized as usual in the numerical space. Generalization to three-dimensional equations are obtained by replacing the physical velocity field $\mathbf{u}$ by $\mathbf{u}-\mathbf{u}_d$, where $\mathbf{u}_d$ is the grid velocity that can be calculated at each moment when the grid-node positions are known at each moment. Subtilities in the implementation are then related to the choice of discrete positions that define the grid (interfaces or volume centers in 1D, corners or centers of finite volumes in 2D or 3D, see Exercises 15-4 and 15-5) and the way the changing grid size is discretized in time. As usual, mathematical properties used to obtain the budget equations are not necessarily shared by the numerical operators and in particular, it must be ensure that discretization of (15.69) conserves the volumes $\partial x/\partial \xi$ of the numerical grid in the sense that for constant c, equation (15.69) is identically satisfied. Mathematically this is the case but it also must hold in the discrete case, otherwise an artificial source of c will appear. This is similar to the advection problem in which the divergence operator of the fluxes had to be coherent with the one used in the physical volume conservation (Section 6.6).

The reader might have identified that a particular case of an adaptive grid is the layered model of Section 12, where the vertical positions of discrete levels are moved in a Lagrangien way to follow density interfaces instead of moving them depending on local properties of the solution as in (15.59). Rather than to follow the fronts with moving grids, we also can try to capture the strong gradients in a fixed grid but with appropriate numerical discretizations that preserve fronts such as the TVD advection schemes alluded to in Section 6.4.

15.7 Nonlinear advection schemes

There is intense research going on to design advection schemes in several dimensions that are monotonic but more accurate than the upwind scheme. Several approaches can be mentioned : Flux-Corrected Transport methods (FCT) (Boris and Book, 1973; Zalesak, 1979) make two passes on the numerical grid, the first one with an upwind scheme and then a second pass adding as much antidiffusion as possible without generating new extrema. Flux-limiter methods (presented hereafter in more detail, Sweeby, 1984; Hirsch, 1990) degrade the higher-order flux calculations towards upwind fluxes near problem zones. Finally Essentially Non-Oscillatory methods (ENO, Harten 1982) adapt different interpolation functions near discontinuities.

The common characteristic of these methods (*e.g.*, Thuburn, 1996) is that they allow the scheme to change its functioning depending on the local solution itself. This nonlinearity avoids the consequence of the Godunov theorem (see Section 6.4) by to not adhering to one of its hypotheses. It also means that since consistency is maintained as a basic requirement, we need to look for nonlinear schemes to circumvent the Godunov theorem even if the underlying physical process is linear! The nonlinearity will be activated when over- or undershooting are likely to occur in which case the scheme will be adapted to increase numerical diffusion. In a situation with a very smooth solution, the scheme is however allowed to remain of higher order.

To design such a scheme, we define a measure of the variation of the solution and call it TV, *Total Variation*:

$$\mathrm{TV}^n \equiv \sum_i |\tilde{c}^n_{i+1} - \tilde{c}^n_i|. \tag{15.70}$$

A scheme is said TVD (*Total Variation Diminishing*) if

$$\mathrm{TV}^{n+1} \leq \mathrm{TV}^n. \tag{15.71}$$

The TV value is clearly related to a quantification of the wiggles that appeared in the leapfrog or Lax-Wendroff advection scheme. Suppose now the numerical scheme can be casted into the following form

$$\tilde{c}^{n+1}_i = \tilde{c}^n_i - a_{i-1/2}\left(\tilde{c}^n_i - \tilde{c}^n_{i-1}\right) + b_{i+1/2}\left(\tilde{c}^n_{i+1} - \tilde{c}^n_i\right), \tag{15.72}$$

where the coefficients a and b can depend on $\tilde{c}$. We will prove that the so-defined scheme is TVD when

$$0 \leq a_{i+1/2} \text{ and } 0 \leq b_{i+1/2} \text{ and } a_{i+1/2} + b_{i+1/2} \leq 1. \tag{15.73}$$

Note that $b_{i+1/2}$ appears with $a_{i+1/2}$ in the TVD condition but with $a_{i-1/2}$ in the numerical scheme. The scheme (15.72) can also be written in point $i+1$

$$\tilde{c}_{i+1}^{n+1} = \tilde{c}_{i+1}^{n} - a_{i+1/2}\left(\tilde{c}_{i+1}^{n} - \tilde{c}_{i}^{n}\right) + b_{i+3/2}\left(\tilde{c}_{i+2}^{n} - \tilde{c}_{i+1}^{n}\right),$$

from which we can subtract (15.72) to make appear the variations

$$\begin{aligned}\tilde{c}_{i+1}^{n+1} - \tilde{c}_{i}^{n+1} &= \left(1 - a_{i+1/2} - b_{i+1/2}\right)\left(\tilde{c}_{i+1}^{n} - \tilde{c}_{i}^{n}\right)\\ &+ b_{i+3/2}\left(\tilde{c}_{i+2}^{n} - \tilde{c}_{i+1}^{n}\right) + a_{i-1/2}\left(\tilde{c}_{i}^{n} - \tilde{c}_{i-1}^{n}\right).\end{aligned}$$

Taking the absolute value on each side, assuming the TVD condition (15.73) is satisfied, using the fact that the absolute value of a sum is smaller than the sum of absolute values and summing over the domain we obtain:

$$\begin{aligned}\sum_i \left|\tilde{c}_{i+1}^{n+1} - \tilde{c}_{i}^{n+1}\right| &\leq \sum_i \left(1 - a_{i+1/2} - b_{i+1/2}\right)\left|\tilde{c}_{i+1}^{n} - \tilde{c}_{i}^{n}\right|\\ &+ \sum_i b_{i+3/2}\left|\tilde{c}_{i+2}^{n} - \tilde{c}_{i+1}^{n}\right| + \sum_i a_{i-1/2}\left|\tilde{c}_{i}^{n} - \tilde{c}_{i-1}^{n}\right|.\end{aligned}$$

Neglecting boundary effects or assuming cyclic conditions, the last two terms can be rewritten by shifting the index i, which finally allows to prove (15.72) is TVD if (15.73) is satisfied.

$$\begin{aligned}\sum_i \left|\tilde{c}_{i+1}^{n+1} - \tilde{c}_{i}^{n+1}\right| &\leq \sum_i \left(1 - a_{i+1/2} - b_{i+1/2}\right)\left|\tilde{c}_{i+1}^{n} - \tilde{c}_{i}^{n}\right|\\ + \sum_i b_{i+1/2}\left|\tilde{c}_{i+1}^{n} - \tilde{c}_{i}^{n}\right| &+ \sum_i a_{i+1/2}\left|\tilde{c}_{i+1}^{n} - \tilde{c}_{i}^{n}\right| \leq \sum_i \left|\tilde{c}_{i+1}^{n} - \tilde{c}_{i}^{n}\right|.\end{aligned}$$

Let us now design nonlinear schemes that are TVD in the one-dimensional case with positive velocity u by combining explicit Euler schemes

$$\tilde{c}_{i}^{n+1} = \tilde{c}_{i}^{n} - \frac{\Delta t}{\Delta x}\left(\tilde{q}_{i+1/2} - \tilde{q}_{i-1/2}\right), \tag{15.74}$$

$$\tilde{q}_{i-1/2} = \tilde{q}_{i-1/2}^{L} + \Phi_{i-1/2}(\tilde{q}_{i-1/2}^{H} - \tilde{q}_{i-1/2}^{L}), \tag{15.75}$$

where the lower-order flux is the upwind flux $\tilde{q}_{i-1/2}^{L} = u\tilde{c}_{i-1}^{n}$ which is too diffusive whereas the higher-order flux $\tilde{q}_{i-1/2}^{H} = u\tilde{c}_{i-1}^{n} + u(1-\mathsf{C})/2\left(\tilde{c}_{i}^{n} - \tilde{c}_{i-1}^{n}\right)$ leads to a second-order nonmonotonic scheme (see Section 6.4). We will allow the weighting Φ to vary with the solution by tending towards zero when too many variations are present (exploiting the damping properties of the upwind scheme) but remaining close to one for gentle solutions (maintaining accuracy). Parameter Φ controls the amount of antidiffusion applied to the scheme and is called a *flux limiter*. For the following, we assume Φ to be positive and the Courant number C satisfying the CFL condition. Then the scheme using the weighted flux can be expanded as

$$\begin{aligned}\tilde{c}_{i}^{n+1} = \tilde{c}_{i}^{n} &- \mathsf{C}\left(\tilde{c}_{i}^{n} + \Phi_{i+1/2}\frac{(1-\mathsf{C})}{2}(\tilde{c}_{i+1}^{n} - \tilde{c}_{i}^{n})\right)\\ &+ \mathsf{C}\left(\tilde{c}_{i-1}^{n} + \Phi_{i-1/2}\frac{(1-\mathsf{C})}{2}(\tilde{c}_{i}^{n} - \tilde{c}_{i-1}^{n})\right).\end{aligned} \tag{15.76}$$

It is readily seen that this is not a form that ensures TVD (15.73) because $b_{i-1/2}$ multiplying $\tilde{c}^n_{i+1} - \tilde{c}^n_i$ is always negative. We can however regroup this term with the upwind part as follows:

$$\tilde{c}^{n+1}_i = \tilde{c}^n_i - \mathsf{C}\left[1 - \Phi_{i-1/2}\frac{(1-\mathsf{C})}{2} + \Phi_{i+1/2}\frac{(1-\mathsf{C})}{2}\frac{(\tilde{c}^n_{i+1} - \tilde{c}^n_i)}{(\tilde{c}^n_i - \tilde{c}^n_{i-1})}\right]\left(\tilde{c}^n_i - \tilde{c}^n_{i-1}\right).$$

This is of the much simpler form

$$\tilde{c}^{n+1}_i = \tilde{c}^n_i - a_{i-1/2}\left(\tilde{c}^n_i - \tilde{c}^n_{i-1}\right) \tag{15.77}$$

even if $a_{i-1/2}$ depends on the solution (after all, we design a nonlinear method and this should be no surprise). The scheme can than be enforced to be TVD by imposing $0 \leq a_{i-1/2} \leq 1$ with

$$a_{i-1/2} = \mathsf{C}\left[1 - \Phi_{i-1/2}\frac{(1-\mathsf{C})}{2} + \Phi_{i+1/2}\frac{(1-\mathsf{C})}{2}\frac{(\tilde{c}^n_{i+1} - \tilde{c}^n_i)}{(\tilde{c}^n_i - \tilde{c}^n_{i-1})}\right]. \tag{15.78}$$

The solution appears in this parameter as a ratio of gradients

$$r_{i+1/2} = \frac{(\tilde{c}^n_i - \tilde{c}^n_{i-1})}{(\tilde{c}^n_{i+1} - \tilde{c}^n_i)}, \tag{15.79}$$

which is a measure of the variability: For $r_{i+1/2} = 1$ the solution is linear over the three points involved whereas for $r_{i+1/2} \leq 0$ there is a local extremum. The parameter $r_{i+1/2}$ will thus be involved in deciding the local weighting to be applied and if negative (local extremum), we already require $\Phi_{i+1/2} = 0$ because of the very rapid local variation. The TVD condition requires

$$0 \leq \mathsf{C} + \frac{\mathsf{C}(1-\mathsf{C})}{2}\left[\frac{\Phi_{i+1/2}}{r_{i+1/2}} - \Phi_{i-1/2}\right] \leq 1. \tag{15.80}$$

We would like to chose a value of Φ at in interface independently of the value of Φ at the neighbor interface, otherwise a linear system to solve is likely to appear. Therefore when choosing Φ, the worst case for the other parameter must be assumed in order to get sufficient conditions that ensure the TVD property. For $\Phi_{i-1/2}$ the worst case happens when $\Phi_{i+1/2}$ is zero in which case we need to ensure that $\Phi_{i-1/2}$ is not too large so that $a_{i-1/2}$ remains positive:

$$\Phi_{i-1/2} \leq \frac{2}{(1-\mathsf{C})}. \tag{15.81}$$

For $\Phi_{i+1/2}$ the worst case happens when $\Phi_{i-1/2}$ is zero and we get an upper bound on $\Phi_{i+1/2}$ that ensures $a_{i-1/2} \leq 1$:

$$\frac{\Phi_{i+1/2}}{r_{i+1/2}} \leq \frac{2}{\mathsf{C}}. \tag{15.82}$$

Since those conditions must be satisfied for all i, the following conditions ensure a TVD scheme:

$$\Phi \leq \frac{2}{(1-\mathsf{C})} \quad \text{and} \quad \frac{\Phi}{r} \leq \frac{2}{\mathsf{C}} \tag{15.83}$$

where we do not write the index anymore because we look for a function $\Phi(r)$ that can be applied on every interface. In practise, the parameter C varies and we can use sufficient conditions that encompass the worst cases. Here, they correspond to $\mathsf{C}=0$ and $\mathsf{C}=1$ so that the final sufficient conditions on Φ that ensure the TVD property are

$$\Phi(r) \leq 2 \quad \text{and} \quad \frac{\Phi(r)}{r} \leq 2. \tag{15.84}$$

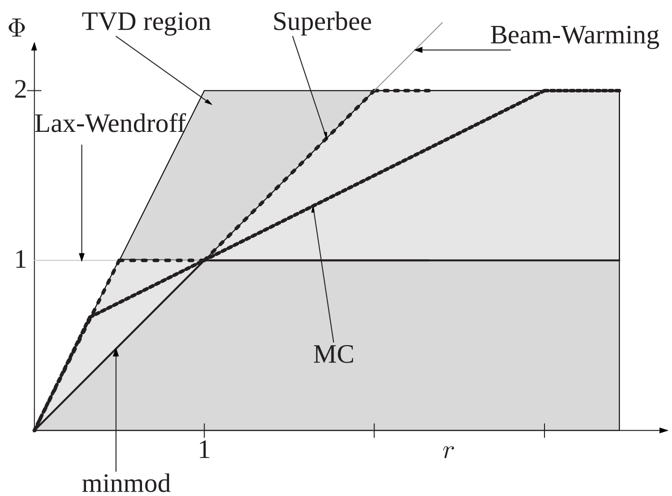

Figure 15-11 TVD domain and some standard limiters. The Lax-Wendroff scheme $\Phi=1$ is not within the TVD region for small r whereas the Beam-Warming is not for large r. The limiters remain in the lighter shaded region in order to interpolate between the two second-order schemes.

We know that $\Phi(r)$ has to obey some rules, but we are relatively free to chose the functional relationship. We take advantage of this degree of freedom by trying to keep the scheme of the highest possible order. The case $\Phi=1$ corresponds to the second-order Lax-Wendroff scheme but falls outside the TVD domain for small r. The case $\Phi=r$ corresponds to the second-order Beam-Warming scheme (see exercise 15-6) but falls outside the TVD domain for larger r. If r is close to 1, the solution is almost linear and a second-order method should be feasible so that we should request $\Phi(1)=1$, which is the case for both the Lax-Wendroff and Beam-Warming scheme. To be close to second order we can thus use $\Phi(r)$ as an interpolation of those two second-order methods, but ensuring Φ lies within the TVD region: Examples of possible combinations are the following limiters

- van Leer: $\Phi = \frac{r+|r|}{1+|r|}$
- minmod: $\Phi = \max(0, \min(1, r))$
- superbee: $\Phi = \max(0, \min(1, 2r), \min(2, r))$
- MC: $\Phi = \max(0, \min(2r, (1+r)/2, 2))$

which are represented on Figure 15-11 together with the TVD region defined by (15.84). Note that flux-limiter calculations depend on the direction of the flow and the ratio r involved in the flux limiter must also be adapted if the velocity changes sign (Exercise 15-8).

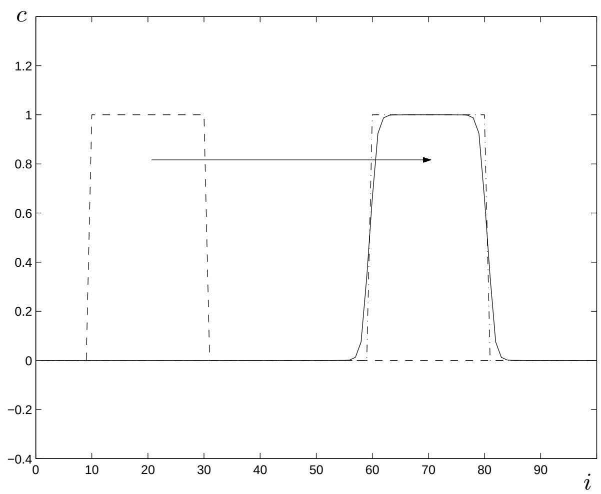

Figure 15-12 Advection scheme with TVD superbee limiter applied to the transport of a "hat" signal with $\mathsf{C} = 0.5$ using 100 times steps. Note that no new extrema are created by the numerical advection and that the diffusion is drastically reduced compared to the upwind scheme.

The question that might rightfully arise after this lengthy design of a TVD scheme is about its relationship with a monotonic scheme. From (15.77) we see that $\tilde{c}_i^{n+1}$ is obtained by a linear interpolation of $\tilde{c}_i^n$ and $\tilde{c}_{i-1}^n$ because $0 \leq a_{i-1/2} \leq 1$. Therefore $\min(\tilde{c}_i^n, \tilde{c}_{i-1}^n) \leq \tilde{c}_i^{n+1} \leq \max(\tilde{c}_i^n, \tilde{c}_{i-1}^n)$ and locally no new extremum is created. Since this is true for all grid points, the scheme does not create over- or undershooting. This can be verified on the standard test case with the superbee limiter (Figure 15-12). The scheme indeed keeps the solution within the initial bounds and results are quite improved compared to previous methods. Specially for GFD applications with large gradients and strong fronts the method is appealing. However, the eventual use of upwind schemes during some parts of the calculations degrades the formal truncation error below second order. Also, when the solution is smooth, fourth-order methods generally perform better in terms of overall accuracy and TVD schemes with fourth order must then be implemented (*e.g.*, Thuburn, 1996). The choice of one scheme or another is thus a question of priorities (conservation, monotonicity, accuracy, ease of implementation, robustness, stability) and expected behavior of solutions (strongly varying, gentle, steady state, nonlinear *etc.*).

Analytical Problems

15-1. In a certain region, at a certain time, the atmospheric temperature along the ground decreases northward at the rate of 1°C every 35 km, and there are good reasons to assume that this gradient does not change much with height. If there is no wind at ground level, what are the wind speed and direction at an altitude of 2 km? To answer, take latitude = 40°N, mean temperature = 290 K, and uniform pressure on the ground.

15-2. A cruise to the Gulf Stream at 38°N provided a cross-section of the current, which was

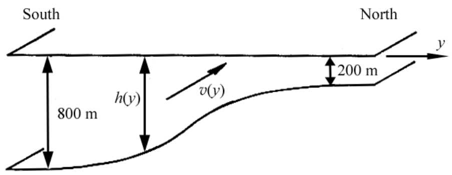

Figure 15-13 Schematic cross-section of the Gulf Stream, represented as a two-layer geostrophic current (Problem 15-2).

then approximated to a two-layer model (Figure 15-13) with a warm layer of density ρ_1 = 1025 kg/m^3 and depth $h(y) = H - \Delta H \tanh(y/L)$, overlying a colder layer of density ρ_2 = 1029 kg/m^3. Taking H = 500 m, ΔH = 300 m, and L = 60 km and assuming that there is no flow in the lower layer and that the upper layer is in geostrophic balance, determine the flow pattern at the surface. What is the maximum velocity of the Gulf Stream? Where does it occur? Also, compare the jet width (L) to the radius of deformation.

15-3. Derive the discrete Margules relation (15.5) from the governing equations written in the density-coordinate system (Chapter 12).

15-4. Through the Strait of Gibraltar, connecting the Mediterranean Sea to the North Atlantic Ocean, there is an inflow of Atlantic waters near the top and an equal outflow of much more saline Mediterranean waters below. At its narrowest point (Tarifa Narrows), the strait is 11 km wide and 650 m deep. The stratification closely resembles a two-layer configuration with a relative density difference of 0.2% and an interface sloping from 175 m along the Spanish coast (North) to 225 m along the African coast (South). Taking f = 8.5 $\times$ 10^{-5} s^{-1}, approximating the cross-section to a rectangle, and assuming that the volumetric transport in one layer is equal and opposite to that in the other layer, estimate this volumetric transport.

15-5. Determine the geostrophically adjusted state of a band of warm water as depicted in Figure 15-4c. The variables are ρ_0 = density of water below, $\rho_0 - \Delta\rho$ = density of warm water, H = initial depth of warm water, $2a$ = initial width of warm-water band, and $2b$ = width of warm-water band after adjustment. In particular, determine the value b, and investigate the limits when the initial half-width a is much less and much greater than the deformation radius R.

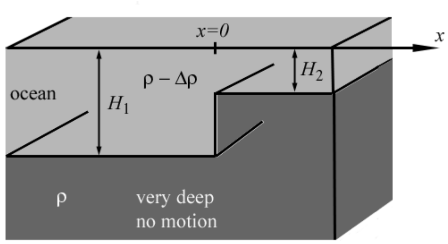

Figure 15-14 State prior to geostrophic adjustment (Problem 15-6).

15-6. Find the solution for the geostrophically adjusted state of the initial configuration shown on Figure 15-14, and calculate the fraction of potential-energy release that has been converted into kinetic energy of the final steady state.

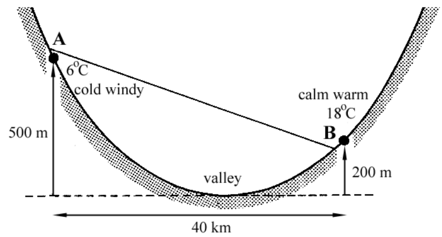

Figure 15-15 Air masses in a valley. What is the wind? (Problem 15-7)

15-7. In a valley of the French Alps ($\simeq 45°$N), one village (**A**) is situated on a flank 500 m above the valley floor and another (**B**) lies on the opposite side 200 m above the valley floor (Figure 15-15). The horizontal distance between the two is 40 km. One day, a shepherd in the upper village, who is also a fine meteorologist, notes a cold wind with temperature 6°C. Upon calling her cousin, a blacksmith in the lower village across the valley, she learns that he is enjoying a calm afternoon with a comfortable 18°C! Assuming that the explanation of this perplexing situation resides in a cold wind blowing along one side of the valley (Figure 15-15), she is able to determine a lower bound for its speed. Can you? Also, in which direction is the wind blowing? (*Hint:* Do not ignore compressibility of air.)

15-8. Using the linearized equations for a two-layer ocean (undisturbed depths H_1 and H_2) over a flat bottom and subject to a spatially uniform wind stress directed along the coast,

$$\frac{\partial u_1}{\partial t} - f v_1 = g' \frac{\partial a}{\partial x} - \frac{1}{\rho_0}\frac{\partial p_2}{\partial x}, \qquad \frac{\partial u_2}{\partial t} - f v_2 = -\frac{1}{\rho_0}\frac{\partial p_2}{\partial x} \tag{15.85a}$$

$$\frac{\partial v_1}{\partial t} + f u_1 = \frac{\tau}{\rho_0 H_1}, \qquad \frac{\partial v_2}{\partial t} + f u_2 = 0 \tag{15.85b}$$

$$-\frac{\partial a}{\partial t} + H_1 \frac{\partial u_1}{\partial x} = 0, \qquad \frac{\partial a}{\partial t} + H_2 \frac{\partial u_2}{\partial x} = 0, \tag{15.85c}$$

study the upwelling response to a wind stress oscillating in time. The boundary conditions are: no flow at the coast ($u_1 = u_2 = 0$ at $x = 0$), no vertical displacements at large distances ($a \to 0$ as $x \to +\infty$). Discuss how the dynamics of the upper layer are affected by the presence of an active lower layer and what happens in the lower layer.

15-9. Demonstrate the assertion made in the text above Equation (15.43) that the potential vorticity is conserved if the wind stress is spatially uniform.

15-10. A coastal ocean at mid-latitude ($f = 10^{-4}$ s^{-1}) has a 50-m thick warm layer capping a much deeper cold layer. The relative density difference between the two layers is $\Delta\rho/\rho_0 = 0.002$. A uniform wind exerting a surface stress of 0.4 N/m^2 lasts for three days. Show that the resulting upwelling includes outcropping of the density interface. What is the offshore distance of the front?

15-11. Generalize to the two-layer ocean the theory for the steady adjusted state following a wind event of given impulse. For simplicity, consider only the case of equal initial layer depths ($H_1 = H_2$).

15-12. Because of the roughness of the ice, the stress communicated to the water is substantially larger in the presence of sea ice than in the open sea. Assuming that the ice drift is at 20° to the wind, that the water drift is at 90° to the wind (in the open) and to the ice drift (under ice), and that the stress on the water surface is twice as large under ice than in the open sea, determine which wind directions with respect to the ice-edge orientation are favorable to upwelling.

Numerical Exercises

15-1. Analyse `upwelling.m` to deduce the governing equations that are discretized. Use the program to simulate a coastal upwelling and see if the outcropping condition (15.46) is realistic. Analyze the algorithm `flooddry.m` used to deal with the outcropping and try what happens when you disactivate it.

15-2. Add a discretization of the momentum advection to `upwelling.m` and redo exercise 15-1. Then diagnose

$$I \simeq \frac{1}{\rho_0} \int_{\text{event}} \frac{\tau}{h}\, dt. \tag{15.86}$$

during the simulation with `upwelling.m` and compare to the estimate (15.86). *Hint:* Remember that I is calculated for a given water parcel.

15-3. Use `adaptive.m` and look at how the linearly interpolated function using a uniform grid and the adapted grid allows to approximate the original function `functiontofollow.m`. Quantify the error by sampling the linear interpolations on a very high resolution grid and calculate the rms error between this interpolation and the original function. Show how this error behaves during the grid-adaptation process.

15-4. Analyze file `adaptiveupwind.m` used to simulate an advection problem with upwind discretization and possibly an adaptive grid (Figure 15-16). Explain how grid size changes and grid velocities must be discretized in a consistent way. Verify your analysis by using a constant value for c. Modify the parameters involved in the grid adaptation. Try to implement a Lagrangian approach by moving the grid nodes with the physical velocity. Which problem does appear in a fixed domain?

15-5. Redo exercise 15-4 but defining and moving the grid nodes at the interface and calculate concentration point positions at the center.

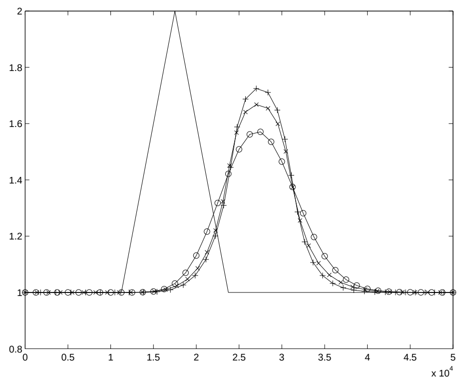

Figure 15-16 Upwind advection of a triangular signal with fixed grid (most diffusive solution) and an adaptive grid with or without added Lagrangian type advection.

15-6. Prove that the Beam-Warming scheme of Section 6.4 can be recovered using a flux-limiter function $\Phi = r$. Implement the scheme and apply it to the standard problem of the top-hat signal advection. How does the solution compare to the Lax-Wendroff solution of Figure 6-9?

15-7. Apply the superbee TVD scheme to the advection of the top-hat signal and then to the advection of a sinusoidal signal. What do you observe? Can you explain the behavior and verify that your explanation is correct by choosing another limiter? Experiment with `tvdadv1D.m`.

15-8. Write out the flux-limiter scheme in the 1D case for $u \leq 0$ by exploiting symmetries of the problem.

15-9. Implement a Leapfrog advection scheme on a non-uniform grid with scalar c defined at the center of the cells of variable with. Use Δx for $x < 0$ and $r\Delta x$ for $x > 0$. **or use an existing code?**. The domain of interest spans $x = -10L$ to $x = 10L$. Advect Gaussian signal of width L, initially located in $x = -5L$. Use $\Delta x = L, L/4, L/8$ and $r = 1, 1/2, 2, 1/10, 10$. **to be tested**

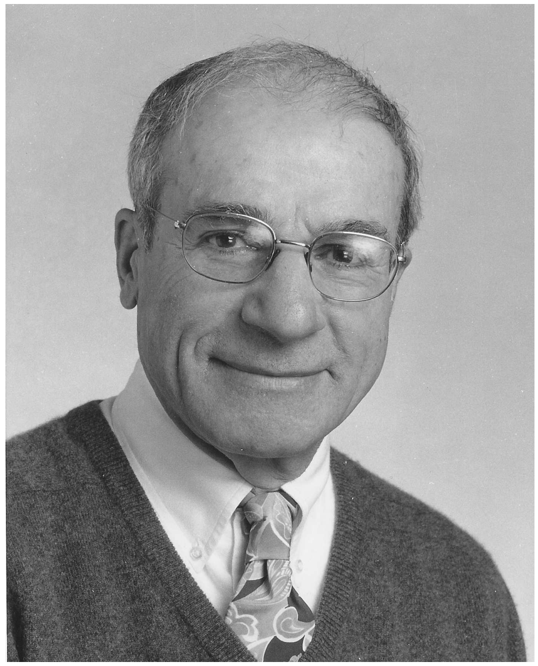

George Veronis
1926 –

An applied mathematician turned oceanographer, George Veronis has been a driving force in geophysical fluid dynamics since its early days. With Willem V. R. Malkus, he cofounded the GFD Summer Program at the Woods Hole Oceanograhic Institution, which continues after more than forty years to bring together oceanographers, meteorologists, physicists and mathematicians to debate problems related to geophysical flows.

Veronis is best known for his theoretical studies on oceanic circulation, rotating and stratified fluids, thermal convection with and without rotation, and double diffusive processes. His model of the circulation of the world ocean was an analytical study based on planetary geostrophic dynamics and the nonlinearity of thermal processes, in which he showed how western boundary currents cross the boundaries of wind gyres and connect all of the world's oceans into a single circulating system.

Veronis has earned a reputation as a superb lecturer, who can explain difficult concepts with amazing ease and clarity. (*Photo credit: G. Veronis*)

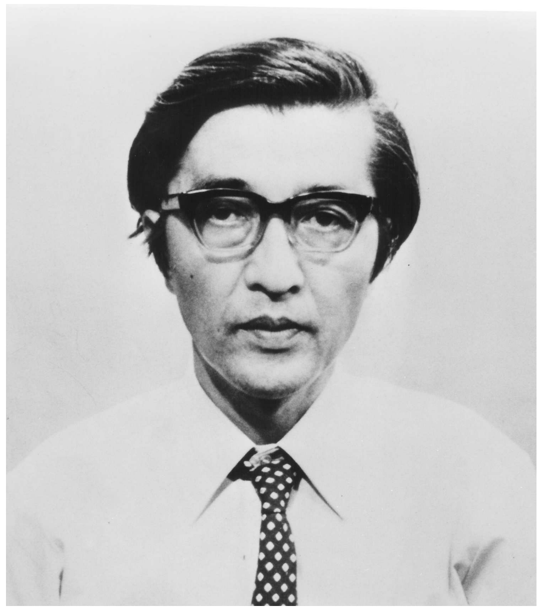

Kozo Yoshida
1922 – 1978

In the early years of his professional career, Kozo Yoshida studied long (tsunami) and short (wind) waves. Later, during a stay at the Scripps Institution of Oceanography, he turned to the investigation of the upwelling phenomenon, which was to become his lifelong interest. His formulations of dynamic theories for both coastal and equatorial upwelling earned him respect and fame. A wind-driven surface eastward current along the equator is called a Yoshida jet. In his later years, he also became interested in the Kuroshio, a major ocean current off the coast of Japan, wrote several books, and promoted oceanography among young scientists.

Known to be very sincere and logical, Yoshida did not shun administrative responsibilities and emphasized the importance of international cooperation in postwar Japan. (*Photo courtesy of Toshio Yamagata*)

Chapter 16

Quasi-Geostrophic Dynamics

(October 18, 2006) **SUMMARY**: At time scales longer than about a day, geophysical flows are ordinarily in a nearly geostrophic state, and it is advantageous to capitalize on this property to obtain a simplified dynamical formalism. Here, we derive the traditional quasi-geostrophic dynamics and present some applications in both linear and nonlinear regimes. The central component of the quasi-geostrophic models, the advection of vorticity, then requires particular attention in the numerical quasi-geostrophic models and the Arakawa Jacobian is presented.

JMB from ⇓

JMB to ⇑

16.1 Simplifying assumption

Rotation effects become important when the Rossby number is on the order of unity or less (Sections 1.5 and 4.5). The smaller the Rossby number, the stronger the rotation effects and the larger the Coriolis force compared to the inertial force. In fact, the majority of atmospheric and oceanic motions are characterized by Rossby numbers sufficiently below unity ($Ro \sim 0.2$ down to 0.01), enabling us to state that, in first approximation, the Coriolis force is dominant. This leads to geostrophic equilibrium (Section 7.1), whereby a balance is struck between the Coriolis force and the pressure-gradient force. In Chapter 7 a theory was developed for perfectly geostrophic flows, whereas in Chapter 9 some near-geostrophic, small-amplitude waves were investigated. In each case, the analysis was restricted to homogeneous flows. Here, we reconsider near-geostrophic motions but in the case of continuously stratified fluids and nonlinear dynamics. Much of the material presented here can be traced to the seminal article by Charney[1] (1948), which laid the foundation of quasi-geostrophic dynamics.

Geostrophic balance, which holds in first approximation, is a linear and diagnostic relationship (there is no product of variables and no time derivative). The resulting mathematical advantages explain why near-geostrophic dynamics are used routinely: The underlying assumption of near-geostrophy may not always be strictly valid, but the formalism is much simpler than otherwise.

[1] See biographical sketch at the end of the chapter.

Mathematically, a state of near-geostrophic balance occurs when the terms representing relative acceleration, nonlinear advection, and friction are all negligible in the horizontal momentum equations. This requires (Section 4.5) that the temporal Rossby number,

$$Ro_T \ = \ \frac{1}{\Omega T} \ , \tag{16.1}$$

the Rossby number,

$$Ro \ = \ \frac{U}{\Omega L} \ , \tag{16.2}$$

and the Ekman number,

$$Ek \ = \ \frac{\nu_E}{\Omega H^2} \ , \tag{16.3}$$

all be small simultaneously. In these expressions, Ω is the angular rotation rate of the earth (or planet or star under consideration), T is the time scale of the motion (*i.e.*, the time span over which the flow field evolves substantially), U is a typical horizontal velocity in the flow, L is the horizontal length over which the flow extends or exhibits variations, ν_E is the eddy vertical viscosity, and H is the vertical extent of the flow.

The smallness of the Ekman number (Section 4.5) indicates that vertical friction is negligible, except perhaps in thin layers on the edges of the fluid domain (Chapter 8). If we exclude small-amplitude waves that can travel much faster than fluid particles in the flow, the temporal Rossby number (16.1) is not greater than the Rossby number (16.2). (For a discussion of this argument, the reader is referred to Section 9.1). By elimination, it remains to require that the Rossby number (16.2) be small. This can be justified in one of two ways: Either velocities are relatively weak (small U) or the flow pattern is laterally extensive (large L). The common approach, and the one that leads to the simplest formulation, is to consider the first possibility; the resulting formalism bears the name of *quasi-geostrophic dynamics*. We ought to keep in mind, however, that some atmospheric and oceanic motions could be nearly geostrophic for the other reason. Such motions would be improperly represented by quasi-geostrophic dynamics.

16.2 Governing equation

To set the stage for the development of quasi-geostrophic equations, it is most convenient to begin with the restriction that vertical displacements of density surfaces be small (Figure 16-1). In the (x, y, z) coordinate system, we write

$$\rho \ = \ \bar{\rho}(z) \ + \ \rho'(x,y,z,t), \quad \text{with} \quad |\rho'| \ \ll \ |\bar{\rho}|. \tag{16.4}$$

In the (x, y, ρ) coordinate system, the equivalent statement is

$$z \ = \ \bar{z}(\rho) \ + \ z'(x,y,\rho,t), \quad \text{with} \quad |z'| \ \ll \ |\bar{z}|. \tag{16.5}$$

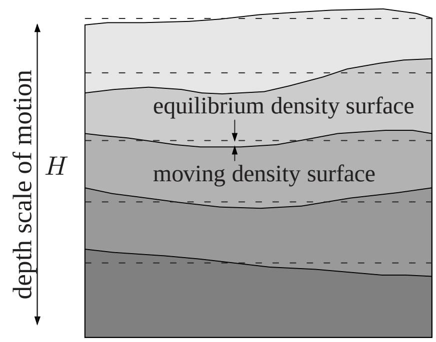

Figure 16-1 A rotating stratified fluid undergoing weak motions, which can then be described by quasi-geostrophic dynamics.

Because the variables ρ and z are, in first approximation, uniquely related [via the function $\bar{\rho}(z)$ or its inverse $\bar{z}(\rho)$], there is no real advantage to be gained by using the density-coordinate system, and we follow the tradition here by formulating the quasi-geostrophic dynamics in the (x, y, z) Cartesian coordinate system.

The density profile $\bar{\rho}(z)$, independent of time and horizontally uniform, forms the basic stratification. Alone, it creates a state of rest in hydrostatic equilibrium. We shall assume that such stratification has somehow been established and that it is maintained in time against the homogenizing action of vertical diffusion. The quasi-geostrophic formalism does not consider the origin and maintenance of this stratification but only the behavior of motions that weakly perturb it.

The following mathematical developments are purposely heuristic, with emphasis on the exploitation of the main idea rather than on a systematic approach. The reader interested in a rigorous derivation of quasi-geostrophic dynamics based on a regular perturbation analysis is referred to Chapter 6 of the book by Pedlosky (1987).

The governing equations of Section 4.4 with $\rho = \bar{\rho}(z) + \rho'(x, y, z, t)$ and, similarly, $p = \bar{p}(z) + p'(x, y, z, t)$ are, on the beta plane and, for simplicity, in the absence of friction and dissipation:

$$\frac{du}{dt} - f_0 v - \beta_0 y v = -\frac{1}{\rho_0}\frac{\partial p'}{\partial x} \tag{16.6a}$$

$$\frac{dv}{dt} + f_0 u + \beta_0 y u = -\frac{1}{\rho_0}\frac{\partial p'}{\partial y} \tag{16.6b}$$

$$0 = -\frac{\partial p'}{\partial z} - \rho' g \tag{16.6c}$$

$$\frac{\partial u}{\partial x} + \frac{\partial v}{\partial y} + \frac{\partial w}{\partial z} = 0 \tag{16.6d}$$

$$\frac{\partial \rho'}{\partial t} + u\frac{\partial \rho'}{\partial x} + v\frac{\partial \rho'}{\partial y} + w\frac{d\bar{\rho}}{dz} = 0, \tag{16.6e}$$

where the advective operator is

$$\frac{d}{dt} = \frac{\partial}{\partial t} + u\frac{\partial}{\partial x} + v\frac{\partial}{\partial y} + w\frac{\partial}{\partial z}\,. \tag{16.7}$$

The basic assumption that $|\rho'|$ is much less than $|\bar{\rho}|$ has been implemented in the density equation (16.6e) by dropping the term $w\partial\rho'/\partial z$. In writing that equation, we have also neglected vertical density diffusion (the right-hand side of the equation) in agreement with
JMB from ⇓ our premise that the basic vertical stratification persists. Because the basic stratification associated with $\bar{\rho}(z)$ is in hydrostatic equilibrium with pressure $\bar{p}(z)$, the corresponding terms
JMB to ⇑ cancel out in the hydrostatic equilibrium and only the perturbed state appears.

If the density perturbations ρ' are small, so are the pressure disturbances p'; by virtue of the horizontal momentum equations, the horizontal velocities are weak. Although the Coriolis terms are small, the nonlinear advective terms, which involve products of velocities, are even smaller. For expediency, we shall use the phrase *very small* for these and all other terms smaller than the small terms. Thus, the ratio of advective to Coriolis terms, the Rossby number, is small. Let us assume now and verify *a posteriori* that the time scale is long compared to the inertial period ($2\pi/f_0$), so the local-acceleration terms are, too, very small. Finally, to guarantee that the beta-plane approximation holds, we further require $|\beta_0 y| \ll f_0$. Having made all these assumptions, we take pleasure in noting that the dominant terms in the momentum equations are, as expected, those of the geostrophic equilibrium:

$$- f_0 v = -\frac{1}{\rho_0}\frac{\partial p'}{\partial x} \tag{16.8a}$$

$$+ f_0 u = -\frac{1}{\rho_0}\frac{\partial p'}{\partial y}\,. \tag{16.8b}$$

As noted repeatedly in Chapter 7, this state is somewhat singular. In particular, it leads to a zero horizontal divergence ($\partial u/\partial x + \partial v/\partial y = 0$), which usually (*e.g.*, over a flat bottom) implies the absence of any vertical velocity. In the case of a stratified fluid, this in turn implies no lifting and lowering of density surfaces and thus no pressure disturbances and no
JMB from ⇓ variations in time. Mathematically we have more unknowns than equations. The dynamics
JMB to ⇑ are degenerate, and the corrections brought by the neglected terms are essential.

We replace u and v by their geostrophic values given by (16.8) in the small terms of equations (16.6a) and (16.6b). The result is

$$-\frac{1}{\rho_0 f_0}\frac{\partial^2 p'}{\partial y \partial t} - \frac{1}{\rho_0^2 f_0^2} J\left(p', \frac{\partial p'}{\partial y}\right) - \frac{1}{\rho_0 f_0} w \frac{\partial^2 p'}{\partial y \partial z} - f_0 v - \frac{\beta_0}{\rho_0 f_0} y \frac{\partial p'}{\partial x} = -\frac{1}{\rho_0}\frac{\partial p'}{\partial x} \tag{16.9a}$$

$$+\frac{1}{\rho_0 f_0}\frac{\partial^2 p'}{\partial x \partial t} + \frac{1}{\rho_0^2 f_0^2} J\left(p', \frac{\partial p'}{\partial x}\right) + \frac{1}{\rho_0 f_0} w \frac{\partial^2 p'}{\partial x \partial z} + f_0 u - \frac{\beta_0}{\rho_0 f_0} y \frac{\partial p'}{\partial y} = -\frac{1}{\rho_0}\frac{\partial p'}{\partial y} \tag{16.9b}$$

The symbol $J(\cdot,\cdot)$ stands the Jacobian operator, defined as $J(a,b) = (\partial a/\partial x)(\partial b/\partial y) - (\partial a/\partial y)(\partial b/\partial x)$.

From these equations, more accurate expressions for u and v can be readily extracted. The improved flow field has a non-zero divergence, which is small because it is caused solely by the weak velocity departures from the otherwise nondivergent geostrophic flow. The vertical velocity is non-zero but very small, and the term of the advection operator (16.7) containing the vertical velocity brings only a correction to corrections. Dropping the corresponding w-terms from equations (16.9a) and (16.9b) and solving for u and v, we obtain

$$\begin{aligned} u &= -\frac{1}{\rho_0 f_0}\frac{\partial p'}{\partial y} - \frac{1}{\rho_0 f_0^2}\frac{\partial^2 p'}{\partial t \partial x} \\ &\quad - \frac{1}{\rho_0^2 f_0^3} J\left(p', \frac{\partial p'}{\partial x}\right) + \frac{\beta_0}{\rho_0 f_0^2}\, y\, \frac{\partial p'}{\partial y} \qquad (16.10a) \\ v &= +\frac{1}{\rho_0 f_0}\frac{\partial p'}{\partial x} - \frac{1}{\rho_0 f_0^2}\frac{\partial^2 p'}{\partial t \partial y} \\ &\quad - \frac{1}{\rho_0^2 f_0^3} J\left(p', \frac{\partial p'}{\partial y}\right) - \frac{\beta_0}{\rho_0 f_0^2}\, y\, \frac{\partial p'}{\partial x} \qquad (16.10b) \end{aligned}$$

which, unlike (16.8), contain both the geostrophic flow and a first series of ageostrophic corrections. Upon substitution of these expressions in continuity equation (16.6d), we obtain

$$\frac{\partial w}{\partial z} = \frac{1}{\rho_0 f_0^2}\left[\frac{\partial}{\partial t}\nabla^2 p' + \frac{1}{\rho_0 f_0} J(p', \nabla^2 p') + \beta_0 \frac{\partial p'}{\partial x}\right], \qquad (16.11)$$

where $\nabla^2 = \partial^2/\partial x^2 + \partial^2/\partial y^2$ is the two-dimensional Laplacian operator.

We now turn our attention to the density-conservation equation (16.6e). The first term is very small because ρ' is small and the time scale is long. Likewise, the last term is very small because, as we concluded before, the vertical velocity arises from the ageostrophic corrections to the already weak horizontal velocity. The middle terms involve the density perturbation, which is small, and the horizontal velocities, which are also small. There is thus no need, in this equation, for the corrections brought by (16.10), and the geostrophic expressions (16.8) suffice, leaving

$$\frac{\partial \rho'}{\partial t} + \frac{1}{\rho_0 f_0} J(p', \rho') - \frac{\rho_0 N^2}{g}\, w = 0, \qquad (16.12)$$

in which the stratification frequency, $N^2(z) = -(g/\rho_0) d\bar{\rho}/dz$, has been introduced. Dividing this last equation by N^2/g, taking its z-derivative, and using the hydrostatic balance (16.6c) to eliminate density, we obtain

$$\frac{\partial}{\partial t}\left[\frac{\partial}{\partial z}\left(\frac{1}{N^2}\frac{\partial p'}{\partial z}\right)\right] + \frac{1}{\rho_0 f_0} J\left[p', \frac{\partial}{\partial z}\left(\frac{1}{N^2}\frac{\partial p'}{\partial z}\right)\right] + \rho_0 \frac{\partial w}{\partial z} = 0. \qquad (16.13)$$

Equations (16.11) and (16.13) form a two-by-two system for the perturbation pressure p' and vertical stretching $\partial w/\partial z$. Elimination of $\partial w/\partial z$ between the two yields a single equation for p':

$$\begin{aligned} &\frac{\partial}{\partial t}\left[\nabla^2 p' + \frac{\partial}{\partial z}\left(\frac{f_0^2}{N^2}\frac{\partial p'}{\partial z}\right)\right] + \frac{1}{\rho_0 f_0} J\left[p', \nabla^2 p' + \frac{\partial}{\partial z}\left(\frac{f_0^2}{N^2}\frac{\partial p'}{\partial z}\right)\right] \\ &\qquad + \beta_0 \frac{\partial p'}{\partial x} = 0. \qquad (16.14) \end{aligned}$$

This is the quasi-geostrophic equation for nonlinear motions in a continuously stratified fluid on a beta plane. Usually, this equation is recast as an equation for the potential vorticity,
JMB from ⇓
and the pressure field is transformed into a streamfunction ψ via $p' = \rho_0 f_0 \psi$. The result is
JMB to ⇑

$$\frac{\partial q}{\partial t} + J(\psi, q) = 0, \tag{16.15}$$

where q is the potential vorticity:

$$q = \nabla^2\psi + \frac{\partial}{\partial z}\left(\frac{f_0^2}{N^2}\frac{\partial \psi}{\partial z}\right) + \beta_0 y. \tag{16.16}$$

Once the solution is obtained for q and ψ, the original variables can be recovered from (16.8a), (16.8b), and (16.12):

$$u = -\frac{\partial \psi}{\partial y} \tag{16.17a}$$

$$v = +\frac{\partial \psi}{\partial x} \tag{16.17b}$$

$$w = -\frac{f_0}{N^2}\left[\frac{\partial^2 \psi}{\partial t \partial z} + J\left(\psi, \frac{\partial \psi}{\partial z}\right)\right] \tag{16.17c}$$

$$p' = \rho_0 f_0 \psi \tag{16.17d}$$

$$\rho' = -\frac{\rho_0 f_0}{g}\frac{\partial \psi}{\partial z}. \tag{16.17e}$$

If turbulent dissipation is retained in the formalism, the equation governing the evolution of potential vorticity becomes complicated, but an approximation suitable for most numerical applications is:

$$\frac{\partial q}{\partial t} + J(\psi, q) = \frac{\partial}{\partial x}\left(\mathcal{A}\frac{\partial q}{\partial x}\right) + \frac{\partial}{\partial y}\left(\mathcal{A}\frac{\partial q}{\partial y}\right) + \frac{\partial}{\partial z}\left(\nu_E\frac{\partial q}{\partial z}\right), \tag{16.18}$$

where q remains defined by (16.16). Among the surprises of the quasi-geostrophic equations is the disappearance of the dynamically dominant component, the Coriolis force. Ironically, earth rotation on the f-plane has disapperead from the governing equation near the
JMB from ⇓
geostrophic equilibrium. **Benoit:** Maybe my comment was too strong f is involved in q, but
JMB to ⇑
only as a relative measure of stratification.

16.3 Length and time scales

Expression (16.16) indicates that q is a potential-vorticity expression. Indeed, the last term represents the planetary contribution to the vorticity, whereas the first term, $\nabla^2\psi = \partial v/\partial x - \partial u/\partial y$, is the relative vorticity. The middle term can be traced to the layer-thickness variations in the denominator of the classical definition of potential vorticity [*e.g.*, (12.21)]. It is thus the contribution of vertical stretching in some linearized form.

It is most interesting to compare the first two terms of the potential-vorticity expression, namely, relative vorticity and vertical stretching. With L and U as the horizontal length and velocity scales, respectively, the streamfunction ψ scales like LU by virtue of (16.17a) and (16.17b). If H is the vertical length scale, the magnitudes of those contributions to potential vorticity are:

$$\text{Relative vorticity} \sim \frac{U}{L}, \quad \text{Vertical stretching} \sim \frac{f_0^2 UL}{N^2 H^2}. \tag{16.19}$$

The ratio of the former to the latter is

$$\frac{\text{Relative vorticity}}{\text{Vertical stretching}} \sim \frac{N^2 H^2}{f_0^2 L^2} = Bu, \tag{16.20}$$

which is the Burger number defined in Section 11.6. For small Burger numbers ($NH \ll f_0 L$), *i.e.*, weak stratification or long length scales, vertical stretching dominates, and the motion is akin to that of homogeneous rotating flows in nearly geostrophic balance (Chapter 7), where topographic variations are capable of exerting great influence. For large Burger numbers ($NH \gg f_0 L$), *i.e.*, strong stratification or short length scales, relative vorticity dominates, stratification reduces coupling in the vertical, and every level tends to behave in a two-dimensional fashion, stirred by its own vorticity pattern, independently of what occurs above and below.

The richest behavior occurs when the stratification and length scale match to make the Burger number of order unity, which occurs when

$$L = \frac{NH}{f_0}. \tag{16.21}$$

As noted in Section 12.2, this particular length scale is the internal radius of deformation. To show this, let us introduce a nominal density difference $\Delta\rho$, typical of the density vertical variations of the ambient stratification. Thus, $|d\bar{\rho}/dz| \sim \Delta\rho/H$ and $N^2 \sim g\Delta\rho/\rho_0 H$. Defining a reduced gravity as $g' = g\Delta\rho/\rho_0$, which is typically much less than the full gravity g, we obtain

$$N \sim \sqrt{\frac{g'}{H}}. \tag{16.22}$$

Definition (16.21) yields

$$L \sim \frac{\sqrt{g'H}}{f_0}. \tag{16.23}$$

Comparing this expression with definition (9.12) for the radius of deformation in homogeneous rotating fluids, we note the replacement of the full gravitational acceleration by a much smaller, reduced acceleration and conclude that motions in stratified fluids tend to take place on shorter scales than dynamically similar motions in homogeneous fluids.

Before concluding this section, it is noteworthy to return to the discussion of the time scale. Very early in the derivation, an assumption was made to restrict the attention to slowly evolving motions, namely, motions with time scale T much longer than the inertial time scale $1/f_0$ (*i.e.*, $T \gg \Omega^{-1}$). This relegated the terms $\partial u/\partial t$ and $\partial v/\partial t$ to the rank of small perturbations to the dominant geostrophic balance. Now, having completed our analysis, we ought to check for consistency.

The time scale of quasi-geostrophic motions can be most easily determined by inspection of the governing equation in its potential-vorticity form. The balance of (16.15) requires that the two terms on its left-hand side be of the same order:

$$\frac{Q}{T} \sim \frac{UL}{L}\,\frac{Q}{L}\,,$$

where Q is the scale of potential vorticity, regardless of whether it is dominated by relative vorticity ($Q \sim U/L$) or vertical stretching ($Q \sim f_0^2 UL/N^2H^2$), and LU is the streamfunction scale. The preceding statement yields

$$T \sim \frac{L}{U}\,, \tag{16.24}$$

in other words, the time scale is advective. The quasi-geostrophic structure evolves on a time T comparable to the time taken by a particle to cover the length scale L at the nominal speed U. For example, a vortex flow (such as an atmospheric cyclone) evolves significantly while particles complete one revolution.

Because the quasi-geostrophic formalism is rooted in the smallness of the Rossby number ($Ro = U/\Omega L \ll 1$), it follows directly that the time scale must be long compared with the rotation period:

$$T \gg \frac{1}{\Omega}\,, \tag{16.25}$$

in agreement with our premise. Note, however, that a lack of contradiction is proof only of consistency in the formalism. It implies that slowly evolving, quasi-geostrophic motions can exist, but the existence of other, non-quasi-geostrophic motions are certainly not precluded. Among the latter, we can distinguish nearly geostrophic motions of other types (Phillips, 1963; Cushman-Roisin, 1986; Cushman-Roisin *et al.*, 1992) and, of course, completely ageostrophic motions (see examples in Chapters 13 and 15). Whereas ageostrophic flows typically evolve on the inertial time scale ($T \sim \Omega^{-1}$), geostrophic motions of type other than quasi-geostrophic usually evolve on much longer time scales ($T \gg L/U \gg \Omega^{-1}$).

16.4 Energetics

Because the quasi-geostrophic formalism is frequently used, it is worth investigating the approximate energy budget that is associated with it. Multiplying the governing equation (16.15) by the streamfunction ψ and integrating over the entire three-dimensional domain, we obtain, after several integrations by parts:

$$\begin{aligned} &\frac{d}{dt}\int\!\!\int\!\!\int \frac{1}{2}\,\rho_0 |\nabla\psi|^2 \; dx\; dy\; dz \quad + \\ &\frac{d}{dt}\int\!\!\int\!\!\int \frac{1}{2}\,\rho_0 \frac{f_0^2}{N^2}\left(\frac{\partial \psi}{\partial z}\right)^2 dx\; dy\; dz \quad = \quad 0. \end{aligned} \tag{16.26}$$

The boundary terms have all been set to zero by assuming rigid bottom and top surfaces, vertical meridional walls, and decay at large distances (or periodicity) in the zonal direction. **Benoit** Why do you distinguish meridional and zonal boundary conditions? closed, periodic or decay leads to zero net effect, be it in meridional or zonal direction? JMB from ⇓ JMB to ⇑

Equation (16.26) can be interpreted as a mechanical-energy statement: The sum of kinetic and potential energies is conserved over time. That the first integral corresponds to kinetic energy is evident once the velocity components have been expressed in terms of the streamfunction ($u^2 + v^2 = \psi_y^2 + \psi_x^2 = |\nabla\psi|^2$). By default, this leaves the second integral to play the role of potential energy, which is not as evident. Basic physical principles would indeed suggest the following definition for potential energy:

$$PE = \int\int\int \rho g z \; dx \; dy \; dz, \qquad (16.27)$$

which by virtue of (16.17e) would yield a linear, rather than a quadratic, expression in ψ.

The discrepancy is resolved by defining the *available potential energy*, a concept first advanced by M. Margules (1903) and developed by E. N. Lorenz (1955). Because the fluid occupies a fixed volume, the rising of fluid in some locations must be accompanied by a descent of fluid elsewhere; therefore, any potential-energy gain somewhere is necessarily compensated, at least partially, by a potential-energy drop elsewhere. What matters then is not the total potential energy of the fluid but only how much could be converted from the instantaneous, perturbed density distribution. We define the available potential energy, APE, as the difference between the existing potential energy, as just defined, and the potential energy that the fluid would have if the basic stratification were unperturbed.

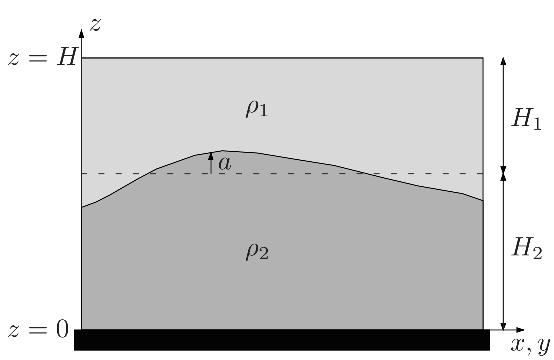

Figure 16-2 A two-layer stratification, for the illustration of the concept of available potential energy.

The situation is best illustrated in the case of a two-layer stratification (Figure 16-2): A lighter fluid of density ρ_1 floats atop of a denser fluid of density ρ_2. In the presence of motion, the interface is at level a above the resting height H_2 of the lower layer. Because of volume conservation, the integral of a over the horizontal domain vanishes identically. The potential energy associated with the perturbed state is

$$
\begin{aligned}
& PE(a) \\
= & \int\int dx\, dy \left[\int_0^{H_2+a} \rho_2 g z\, dz + \int_{H_2+a}^{H} \rho_1 g z\, dz \right] \\
= & \int\int \left[\frac{1}{2}\rho_1 g H^2 + \frac{1}{2}\, \Delta\rho g H_2^2 \right] dx\, dy \\
+ & \int\int \Delta\rho H_2 a\, dx\, dy \;+\; \int\int \frac{1}{2}\, \Delta\rho g a^2\, dx\, dy,
\end{aligned}
$$

where H is the total height and $\Delta\rho = \rho_2 - \rho_1$ is the density difference. The first term represents the potential energy in the unperturbed state, whereas the second term vanishes because a has a zero mean. This leaves the third term as the available potential energy:

$$
\begin{aligned}
APE &= PE(a) \;-\; PE(a=0) \\
&= \int\int \frac{1}{2}\, \Delta\rho g a^2\, dx\, dy.
\end{aligned} \tag{16.28}
$$

Introducing the stratification frequency $N^2 = -(g/\rho_0) d\bar{\rho}/dz = g\Delta\rho/\rho_0 H$ and generalizing to three dimensions, we obtain

$$
APE \;=\; \int\int\int \frac{1}{2}\, \rho_0 N^2 a^2\, dx\, dy\, dz. \tag{16.29}
$$

In continuous stratification, the vertical displacement a of a fluid parcel is directly related to the density perturbation because the density anomaly at one point is created by moving to that point a particle that originates from a different vertical level:

$$
\begin{aligned}
\rho'(x,y,z,t) &= \bar{\rho}[z - a(x,y,z,t)] \;-\; \bar{\rho}(z) \\
&\simeq \; -\, a\, \frac{d\bar{\rho}}{dz} \;=\; \frac{\rho_0 N^2}{g}\, a.
\end{aligned} \tag{16.30}
$$

This Taylor expansion is justified by the underlying assumption of weak vertical displacements. Combining (16.29) and (16.30) and expressing the density perturbation in terms of the streamfunction by (16.17e), we obtain

$$
APE \;=\; \int\int\int \frac{1}{2}\, \rho_0\, \frac{f_0^2}{N^2} \left(\frac{\partial\psi}{\partial z} \right)^2 dx\, dy\, dz. \tag{16.31}
$$

which is the integral that arises in the energy budget, (16.26).

As a final note, we observe that the time rate of change of the available potential energy can be expressed as

$$
\frac{d}{dt}\, APE \;=\; g \int\int\int \rho' w\, dx\, dy\, dz, \tag{16.32}
$$

JMB from ⇓ as can be verified by substitution of (16.17c) and (16.17e) into (16.32) and an integration by parts on the Jacobian part. This shows that potential energy increases when heavy fluid parcels rise (ρ' and w both positive) and light parcels sink (ρ' and w both negative).

16.5 Planetary waves in a stratified fluid

In Chapter 9, it was noted that inertia-gravity waves are superinertial ($\omega \geq f$) and that Kelvin waves require a fundamentally ageostrophic balance in one of the two horizontal directions [see Equation (9.4b) with $u = 0$]. Therefore, the quasi-geostrophic formalism cannot describe these two types of waves. It can, however, describe the slow waves and, in particular, the planetary waves that exist on the beta plane.

It is instructive to explore the three-dimensional behavior of planetary (Rossby) waves in a continuously stratified fluid. The theory proceeds from the linearization of the quasi-geostrophic equation and, for mathematical simplicity only, the assumptions of a constant stratification frequency and no dissipation. Equations (16.15) and (16.16) then yield

$$\frac{\partial}{\partial t}\left(\nabla^2\psi \;+\; \frac{f_0^2}{N^2}\,\frac{\partial^2\psi}{\partial z^2}\right) \;+\; \beta_0\,\frac{\partial\psi}{\partial x} \;=\; 0. \tag{16.33}$$

We seek a wave solution of the form $\psi(x, y, z, t) = \phi(z)\cos(k_x x + k_y y - \omega t)$, with horizontal wavenumbers k_x and k_y, frequency ω, and amplitude $\phi(z)$. The vertical structure of the amplitude is governed by

$$\frac{d^2\phi}{dz^2} \;-\; \frac{N^2}{f_0^2}\left(k_x^2 + k_y^2 + \frac{\beta_0 k_x}{\omega}\right)\phi \;=\; 0, \tag{16.34}$$

which results from the substitution of the wave solution into (16.33). To solve this equation, boundary conditions are necessary in the vertical. For these, let us assume that our fluid is bounded below by a horizontal surface and above by a free surface. In the atmosphere, this situation would correspond to the troposphere above a flat terrain or sea and below the tropopause.

At the bottom (say, $z = 0$), the vertical velocity vanishes, and the linearized form of (16.17c) implies $\partial^2\psi/\partial z\partial t = 0$, or

$$\frac{d\phi}{dz} \;=\; 0 \quad \text{at} \quad z \;=\; 0. \tag{16.35}$$

At the free surface [say, $z = h(x, y, t)$], the pressure is uniform. Because the total pressure consists of the hydrostatic pressures due to the reference density ρ_0 (eliminated when the Boussinesq approximation was made; see Section 3.7) and to the basic stratification $\bar{\rho}(z)$, together with the perturbation pressure caused by the wave, we write:

$$P_0 \;-\; \rho_0 g z \;+\; g\int_z^h \bar{\rho}(z')\,dz' \;+\; p'(x, y, h, t) \;=\; \text{constant}, \tag{16.36}$$

at the free surface $z = h$. Because particles on the free surface remain on the free surface at all times (there is no inflow/outflow), we also state

$$w \;=\; \frac{\partial h}{\partial t} \;+\; u\,\frac{\partial h}{\partial x} \;+\; v\,\frac{\partial h}{\partial y} \quad \text{at} \quad z \;=\; h. \tag{16.37}$$

The preceding two statements are then linearized. Writing $h = H + \eta$, where the free-surface displacement $\eta(x,y,t)$ is small to justify linear wave motions, we expand the variables p' and w in Taylor fashion from the mean surface level $z = H$ and systematically drop all terms involving products of variables of the wave field. The two requirements then reduce to

$$-\;\rho_0 g\eta \;+\; p' \;=\; 0 \quad \text{and} \quad w \;=\; \frac{\partial \eta}{\partial t} \quad \text{at} \quad z \;=\; H. \tag{16.38}$$

JMB from ⇓
JMB to ⇑

Benoit Previous developments can be reduced by referring to sections in boundary conditions 4.6.

Elimination of η yields $\partial p'/\partial t = \rho_0 g w$ and, in terms of the streamfunction,

$$\frac{\partial}{\partial t}\left(\frac{\partial \psi}{\partial z} \;+\; \frac{N^2}{g}\,\psi\right) \;=\; 0 \quad \text{at} \quad z \;=\; H \tag{16.39}$$

or, finally, in terms of the wave amplitude,

$$\frac{d\phi}{dz} \;+\; \frac{N^2}{g}\,\phi \;=\; 0 \quad \text{at} \quad z \;=\; H. \tag{16.40}$$

Together, equation (16.34) and its two boundary conditions, (16.35) and (16.40), define an eigenvalue problem, which admits solutions of the form

$$\phi(z) \;=\; A\,\cos k_z z. \tag{16.41}$$

JMB from ⇓
JMB to ⇑

already satisfying boundary condition (16.35). Substitution of this solution into equation (16.34) yields the dispersion relation linking the wave frequency ω to the wavenumber components, k_x, k_y and k_z:

$$\omega \;=\; -\;\frac{\beta_0 k_x}{k_x^2 + k_y^2 + k_z^2 f_0^2/N^2}\;, \tag{16.42}$$

whereas substitution into boundary condition (16.40) imposes a condition on the wavenumber k_z:

$$\tan\;k_z H \;=\; \frac{N^2 H}{g}\,\frac{1}{k_z H}\;. \tag{16.43}$$

As Figure 16-3 demonstrates graphically, there is an infinite number of discrete solutions. Because negative values of k_z lead to solutions identical to those with positive k_z values [see (16.41) and (16.42)], it is necessary to consider only the latter set of values ($k_z > 0$).

A return to the definition $N^2 = -(g/\rho_0)d\bar{\rho}/dz$ reveals that the ratio N^2H/g, appearing on the right-hand side of (16.43), is equal to $\Delta\rho/\rho_0$, where $\Delta\rho$ is the density difference between top and bottom of the basic stratification $\bar{\rho}(z)$. The factor N^2H/g is thus very small, implying that the first solution of (16.43) falls very near the origin (Figure 16-3). There, $\tan k_z H$ can be approximated to $k_z H$, yielding

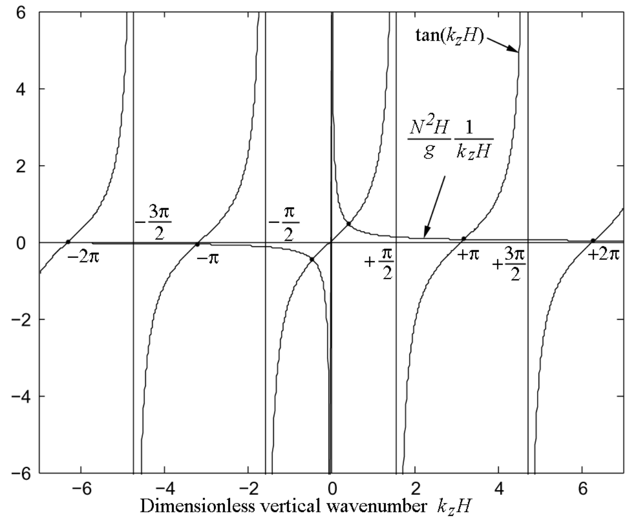

Figure 16-3 Graphical solution of equation (16.43). Every crossing of curves yields an acceptable value for the vertical wavenumber k_z. The pair of values nearest to the origin corresponds to a solution fundamentally different from all others.

$$k_z H \;=\; \frac{NH}{\sqrt{gH}}\;. \tag{16.44}$$

The fraction on the right is the ratio of the internal gravity wave speed to the surface gravity wave speed, which is small. Note also that this mode disappears in the limit $g \to \infty$, which we would have obtained if we had imposed a rigid lid at the top of the domain.

Because $k_z H$ is small, the corresponding wave is nearly uniform in the vertical. Its dispersion relation, obtained from the substitution of the preceding value of k_z into (16.42),

$$\omega \;=\; -\;\frac{\beta_0 k_x}{k_x^2 + k_y^2 + f_0^2/gH}\;, \tag{16.45}$$

is independent of the stratification frequency N and identical to the dispersion relation obtained for planetary waves in homogeneous fluids [see (9.27)]. From this, we conclude that this wave is the barotropic component of the wave set. Because the solution is almost independent of z it deserves this denomer. JMB from ⇓ JMB to ⇑

The other solutions for k_z can also be determined to the same degree of approximation. Because N^2H/g is small, the finite solutions of (16.43) fall very near the zeros of $\tan k_z H$ (Figure 16-3) and are thus given approximately by

$$k_{zn} \;=\; n\,\frac{\pi}{H}\;,\quad n \;=\; 1,\,2,\,3,\,\ldots \tag{16.46}$$

Unlike the barotropic wave, the waves with these wavenumbers exhibit substantial variations in the vertical and can be called *baroclinic*. Their dispersion relation,

$$\omega_n = -\frac{\beta_0 k_x}{k_x^2 + k_y^2 + (n\pi f_0/NH)^2}, \tag{16.47}$$

is morphologically identical to (16.45), implying that they, too, are planetary waves. In summary, the presence of stratification permits the existence of an infinite, discrete set of planetary waves, one barotropic and all other baroclinic.

Comparing the dispersion relations (16.45) and (16.47) of the barotropic and baroclinic waves, we note the replacement in the denominator of the ratio f_0^2/gH by a multiple of $(\pi f_0/NH)^2$, which is much larger, since — again — N^2H/g is very small. Physically, the barotropic component is influenced by the large, external radius of deformation $\sqrt{gH}/f_0$ [see (9.12)], whereas the baroclinic waves feel the much shorter, internal radius of deformation NH/f_0 [see (16.21)].

In the atmosphere, there is not always a great disparity between the two radii of deformation. Take, for example, a midlatitude region (such as 45°N, where $f_0 = 1.03 \times 10^{-4}$ s^{-1}), a tropospheric height $H = 10$ km, and a stratification frequency $N = 0.01$ s^{-1}. This yields $\sqrt{gH}/f_0 = 3050$ km and $NH/f_0 = 972$ km. (The ratio N^2H/g is then 0.102, which is not very small.) In contrast, the difference between the two radii of deformation is much more pronounced in the ocean. Take, for example, $H = 3$ km and $N = 2 \times 10^{-3}$ s^{-1}, which yield $\sqrt{gH}/f_0 = 1670$ km and $NH/f_0 = 58$ km.

In any event, all planetary waves exhibit a zonal phase speed. For the baroclinic members of the family, it is

$$c_n = \frac{\omega_n}{k_x} = -\frac{\beta_0}{k_x^2 + k_y^2 + (n\pi f_0/NH)^2}. \tag{16.48}$$

Because this quantity is always negative, the direction can only be westward[2]. Moreover, the westward speed is confined to the interval

$$-\beta_0 R_n^2 < c_n < 0, \tag{16.49}$$

with the lower bound approached by the longest wave ($k_x^2 + k_y^2 \to \infty$). The lengths R_n, defined as

$$R_n = \frac{1}{n}\frac{NH}{\pi f_0}, \quad n = 1, 2, 3, \ldots \tag{16.50}$$

are identified as internal radii of deformation, one for each baroclinic mode. The greater the value of n, the greater the value of k_{zn}, the more reversals the wave exhibits in the vertical, and the more restricted is its zonal propagation. Therefore, the waves most active in transmitting information and carrying energy from east to west (or from west to east, if the group velocity is positive) are the barotropic and the first few baroclinic components. Indeed, observations reveal that these two modes alone carry generally 80% to 90% of the energy in the ocean.

Let us now turn our attention to the spatial structure of a baroclinic planetary wave. For simplicity, we take the first mode ($n = 1$), which corresponds to a wave with one reversal of the flow in the vertical, and we set k_y to zero to focus on the zonal profile of the wave. The streamfunction, velocity, pressure, and density distributions are as follows

[2] The meridional phase speed, ω_n/k_y, may be either positive or negative, depending on the sign of k_y.

$$\psi = A\ \cos k_z z\ \cos(k_x x - \omega t) \tag{16.51a}$$

$$u = -\frac{\partial \psi}{\partial y} = 0 \tag{16.51b}$$

$$v = +\frac{\partial \psi}{\partial x} = -\ k_x A\ \cos k_z z\ \sin(k_x x - \omega t) \tag{16.51c}$$

$$w = -\frac{f_0}{N^2}\frac{\partial^2 \psi}{\partial t \partial z} = +\ \frac{f_0 \omega k_z}{N^2} A\ \sin k_z z\ \sin(k_x x - \omega t) \tag{16.51d}$$

$$p' = \rho_0 f_0 \psi = \rho_0 f_0\ A\ \cos k_z z\ \cos(k_x x - \omega t) \tag{16.51e}$$

$$\rho' = -\frac{\rho_0 f_0}{g}\frac{\partial \psi}{\partial z} = +\ \frac{\rho_0 f_0 k_z}{g} A\ \sin k_z z\ \cos(k_x x - \omega t). \tag{16.51f}$$

Because the geostrophic zonal velocity, u, is identically zero, it is necessary to consider its leading ageostrophic component. According to (16.10a) and our subsequent restrictions to linear and inviscid dynamics, we find this component to be

$$\begin{aligned} u &= -\frac{1}{\rho_0 f_0^2}\frac{\partial^2 p'}{\partial t \partial x} \\ &= -\frac{k_x \omega}{f_0} A\ \cos k_z z\ \cos(k_x x - \omega t). \end{aligned} \tag{16.52}$$

Its amplitude is only a small fraction ω / f_0 of the meridional component. The corresponding wave structure is displayed in Figure 16-4 and can be interpreted as follows. JMB from ⇓ JMB to ⇑

At the top and bottom, vertical displacements are prohibited **Benoit** Not really, we allowed free surface movement. What happens is that the baroclinic mode has very low amplitude movements of the free surface. Only the barotropic mode has significant surface signature. , and there is no density anomaly. In between, however, vertical displacements do occur and, for the lowest baroclinic mode, they exhibit one maximum at midlevel. Where the middle density surface upwells, heavier (colder) fluid from below is brought upward, forming a cold anomaly. Similarly, a warm anomaly accompanies a subsidence, half a wavelength away. Because colder fluid is heavier and warmer fluid is lighter, the bottom pressure is higher under cold anomalies and lower under warm anomalies. The resulting zonal pressure gradient drives an alternating meridional flow. In the Northern Hemisphere (as depicted in Figure 16-4), the velocity has the higher pressure on its right and therefore assumes a southward direction east of the high pressures and a northward direction east of the low pressures. Due to the baroclinic nature of the wave, there is a reversal in the vertical, and the velocities near the top are counter to those below (Figure 16-4). JMB from ⇓ JMB to ⇑

On the beta plane, the variation in the Coriolis parameter causes this meridional flow to be convergent or divergent. In the Northern Hemisphere, the northward increase of f implies, under a uniform pressure gradient, a decreasing velocity and thus convergence of northward flow and divergence of southward flow. The resulting convergence-divergence pattern calls for transverse velocities, either zonal or vertical or both. According to Figure 16-4, based on (16.51d) and (16.52), both transverse components come into play, each partially relieving the convergence-divergence of the meridional flow. The ensuing vertical velocities at

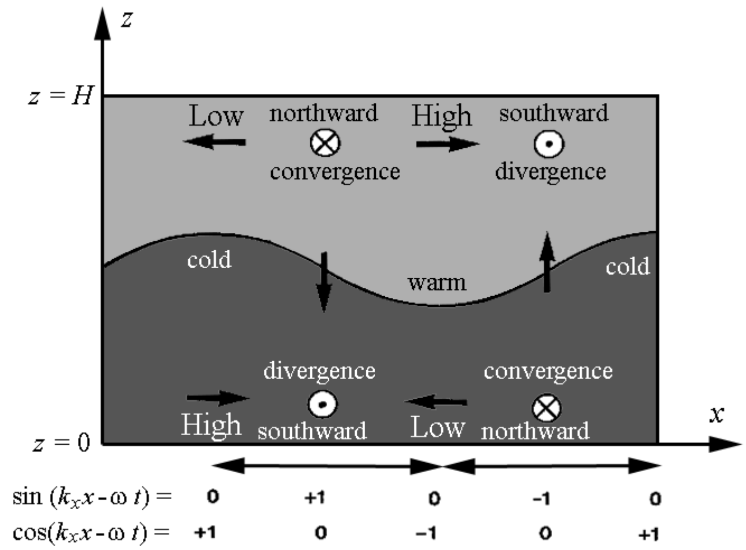

Figure 16-4 Structure of a baroclinic planetary wave. In constructing this diagram, we have taken $f_0 > 0$, $k_x > 0$, $k_y = 0$ and $k_z = \pi/H$, which yield $\omega < 0$ and a wave structure with a single reversal in the vertical.

midlevel cause subsidence below a convergence and above a divergence, feeding the excess of the upper flow into the deficit of that underneath, and create upwelling half a wavelength away, where the situation is vertically reversed. Subsidence generates a warm anomaly, and upwelling generates a cold anomaly. As we can see in Figure 16-4, this takes place a quarter of a wavelength to the west of the existing anomalies, thus inducing a westward shift of the wave pattern over time. The result is a wave pattern steadily translating to the west.

JMB from ⇓

Benoit: May I suggest an adaptation of the text along the following lines?

At the bottom, vertical displacements are prohibited and there is no density anomaly. Also at the surface, density anomalies are nil according to (16.51f), but in between, however, vertical displacements do occur and, for the lowest baroclinic mode, they exhibit one maximum at midlevel. Where the middle density surface has upwelled, heavier (colder) fluid from below is found, forming a cold anomaly. Similarly, a warm anomaly accompanies a subsidence, half a wavelength away. Because colder fluid is heavier and warmer fluid is lighter, the bottom pressure is higher under cold anomalies and lower under warm anomalies. At the lowest order of approximation, the resulting zonal pressure gradient drives an alternating geostrophic meridional flow of intensity v given by (16.51c). In the Northern Hemisphere (as depicted in Figure 16-4), the velocity has the higher pressure on its right and therefore assumes a southward direction east of the high pressures and a northward direction east of the low pressures. Due to the baroclinic nature of the wave, there is a reversal in the vertical, and the velocities near the top are counter to those below (Figure 16-4).

This lowest order approximation is a stationnary solution and the wave propagation must arise from the next order terms of the solution. In particular, the next term to (16.10b) using our restrictions to linear and inviscid dynamics is

$$-\frac{\beta_0}{\rho_0 f_0^2}\, y\, \frac{\partial p'}{\partial x} = \frac{\beta_0 k_x}{f_0}\, y\, A\, \cos k_z z\, \sin(k_x x - \omega t) \tag{16.53}$$

and leads now to a non-zero $\partial v/\partial y$: On the beta plane, the variation in the Coriolis parameter causes this meridional flow to be convergent or divergent. In the Northern Hemisphere, the northward increase of f implies, under a uniform pressure gradient, a decreasing velocity and thus convergence of northward flow and divergence of southward flow. The resulting convergence-divergence pattern calls for transverse ageostrophic velocities, either zonal or vertical or both. According to Figure 16-4, based on (16.51d) and (16.52), both transverse components come into play, each partially relieving the convergence-divergence of the meridional flow. The relative importance of the the vertical convergence to the horizontal one is,

$$\frac{W k_z}{U k_x} = \frac{f_0^2 k_z^2}{N^2 k_x^2} \tag{16.54}$$

and we recover the inverse of the Burger number associated with the scales of the wave. In any case, the ensuing vertical velocities at midlevel cause subsidence below a convergence and above a divergence, feeding the excess of the upper flow into the deficit of that underneath, and create upwelling half a wavelength away, where the situation is vertically reversed. Subsidence generates a warm anomaly, and upwelling generates a cold anomaly. As we can see in Figure 16-4, this takes place a quarter of a wavelength to the west of the existing anomalies, thus inducing a westward shift of the wave pattern over time. The result is a wave pattern steadily translating to the west.

Benoit Also, I would reduce zonal velocity arrows in the figure, because one has the impression of strong velocities. JMB to ⇑

16.6 Quasi-geostrophic ocean modeling

The quasi-geostrophic models were the basis on which the first weather-forecast systems have been build on (see biographies at end of Chapter 5 and the present chapter). The reason for the success of these models were the very simplified mathematics and numerics, yet retaining the most important physical dynamics. The first models implemented were two-dimensional (see Exercise 16-1) on which we will illustrate some numerical ingredients. In two dimensions, the governing equation reduce to

$$\frac{\partial q}{\partial t} \;+\; J(\psi, q) \;=\; 0 \tag{16.55}$$

in the absence of friction and turbulence, completed with the definition of potential vorticity (16.16).

From governing equation (16.55) it is clear that the Jacobian J plays a central role in the

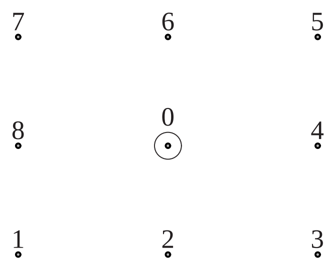

Figure 16-5 Notations for Jacobian $J(\psi, q)$ around the central point called 0. The discretization J^{++} uses ψ and q in points 2,4,6,8, while $J^{+\times}$ evaluates ψ in points 2,4,6,8 and q on 1,3,5,7

evolution and in view of the different mathematical expressions

$$J(\psi, q) = \frac{\partial \psi}{\partial x}\frac{\partial q}{\partial y} - \frac{\partial q}{\partial x}\frac{\partial \psi}{\partial y} \tag{16.56a}$$

$$= \frac{\partial}{\partial x}\left(\psi \frac{\partial q}{\partial y}\right) - \frac{\partial}{\partial y}\left(\psi \frac{\partial q}{\partial x}\right) \tag{16.56b}$$

$$= \frac{\partial}{\partial y}\left(q \frac{\partial \psi}{\partial x}\right) - \frac{\partial}{\partial x}\left(q \frac{\partial \psi}{\partial y}\right) \tag{16.56c}$$

we can readily develop the following corresponding finite-difference forms, all of second order

$$J^{++} = \frac{(\tilde{\psi}_4 - \tilde{\psi}_8)(\tilde{q}_6 - \tilde{q}_2) - (\tilde{q}_4 - \tilde{q}_8)(\tilde{\psi}_6 - \tilde{\psi}_2)}{4\Delta x \Delta y} \tag{16.57a}$$

$$J^{+\times} = \frac{\left[\tilde{\psi}_4(\tilde{q}_5 - \tilde{q}_3) - \tilde{\psi}_8(\tilde{q}_7 - \tilde{q}_1)\right] - \left[\tilde{\psi}_6(\tilde{q}_5 - \tilde{q}_7) - \tilde{\psi}_2(\tilde{q}_3 - \tilde{q}_1)\right]}{4\Delta x \Delta y} \tag{16.57b}$$

$$J^{\times +} = \frac{\left[\tilde{q}_6(\tilde{\psi}_5 - \tilde{\psi}_7) - \tilde{q}_2(\tilde{\psi}_3 - \tilde{\psi}_1)\right] - \left[\tilde{q}_4(\tilde{\psi}_5 - \tilde{\psi}_3) - \tilde{q}_8(\tilde{\psi}_7 - \tilde{\psi}_1)\right]}{4\Delta x \Delta y} \tag{16.57c}$$

The superscrips for the Jacobian clearly indicate where its arguments ψ and q are evaluated with respect to the central point (Figure 16-5). In view of the different discretization, we might question which to chose to obtain the best model. Since all of them are second order, we have to invoke other properties than truncation errors to decide on the optimal discretization. Such properties can be conservation laws derived from the equation to be solved and we can identify the following integral constraints in a domain of surface $\mathcal{S}$ with constant ψ on its boundaries, with periodic boundaries or with decaying solutions in an infinite domain:

$$\int_{\mathcal{S}} J(\psi, q) d\mathcal{S} = 0, \tag{16.58}$$

$$\int_{\mathcal{S}} q J(\psi, q) d\mathcal{S} = 0, \tag{16.59}$$

$$\int_{\mathcal{S}} \psi J(\psi, q) d\mathcal{S} = 0. \tag{16.60}$$

We also have an additional anti-symmetry property

$$J(\psi, q) = -J(q, \psi). \tag{16.61}$$

These mathematical properties of the Jacobian and governing equation (16.55) lead to the following integral properties when $q = \nabla^2\psi$:

$$\frac{d\Gamma}{dt} = \frac{d}{dt}\int_{\mathcal{S}} q\, d\mathcal{S} = 0, \tag{16.62}$$

$$\frac{dZ}{dt} = \frac{d}{dt}\int_{\mathcal{S}} q^2 d\mathcal{S} = 0. \tag{16.63}$$

The first one is an expression of the circulation theorem (see also Section 7.4), while the second one expresses the global conservation of a quadratic form of vorticity called *enstrophy*. Finally (16.60) can be related to kinetic-energy evolution. Numerical discretizations generally do not ensure that the same integral properties are retrieved in the discrete solution. Again Arakawa (see biography end of Chapter 9) had a brilliant idea, combining different versions of the Jacobian discretizations in order to maintain those properties also with the discrete version. The combination

$$J = (1-\alpha-\beta)J^{++} \;+\; \alpha J^{+\times} \;+\; \beta J^{\times+} \tag{16.64}$$

for any α and β leads to a consistent discretization. The two parameters α and β can now be chosen so as to ensure some of the conservation properties.

Integrals (16.60) in their discrete form sum up individual terms involving products $\psi_{i,j} J_{i,j}$ or with shorter notations of Figure 16-5 terms such as

$$\Delta x \Delta y\, \psi_0 J_0. \tag{16.65}$$

For the Jacobian discretized according to (16.57a) this involves

$$4\Delta x \Delta y\, \tilde{\psi}_0 J_0^{++} = \tilde{\psi}_0 \tilde{\psi}_4 (\tilde{q}_6 - \tilde{q}_2) + ... \tag{16.66}$$

From the contribution $\psi_4 J_4$ we find similar terms

$$4\Delta x \Delta y\, \tilde{\psi}_4 J_4^{++} = -\tilde{\psi}_0 \tilde{\psi}_4 (\tilde{q}_5 - \tilde{q}_3) + ... \tag{16.67}$$

For all other terms in the integral, there are no other products of $\tilde{\psi}_0\tilde{\psi}_4$ that appear. Because the only products that appear have different multiplicative factors, their sum has no reason to be zero if only J^{++} is used.

If we look at another discrete Jacobian, $J^{+\times}$, we have similar terms

$$4\Delta x \Delta y\, \tilde{\psi}_0 J_0^{+\times} = \tilde{\psi}_0 \tilde{\psi}_4 (\tilde{q}_5 - \tilde{q}_3) + ... \tag{16.68}$$

and

$$4\Delta x \Delta y\, \tilde{\psi}_4 J_4^{+\times} = -\tilde{\psi}_4 \tilde{\psi}_0 (\tilde{q}_6 - \tilde{q}_2) + ... \tag{16.69}$$

For J^{++} and $J^{+\times}$, no other combinations involving $\psi_0\psi_4$ appear. We immediately see that if we take $(J^{++} + J^{+\times})$ the sum of ψJ over all grid points is conserved for suitable boundary conditions because now all terms in $\tilde{\psi}_0\tilde{\psi}_4$ cancel out. The same reasoning applies to combinations such as those between point 0 and 6 with the same conclusion. Finally for both J^{++} and $J^{+\times}$ there are no products as $\tilde{\psi}_0\tilde{\psi}_5$ that appear. Such products only appear when using $J^{\times+}$

$$4\Delta x\Delta y\,\tilde{\psi}_0 J_0^{\times+} = \tilde{\psi}_0\tilde{\psi}_5(\tilde{q}_6 - \tilde{q}_4) + ... \tag{16.70}$$

$$4\Delta x\Delta y\,\tilde{\psi}_5 J_5^{\times+} = \tilde{\psi}_0\tilde{\psi}_5(\tilde{q}_4 - \tilde{q}_6) + ... \tag{16.71}$$

Because $\psi J^{\times+}$ never makes appear terms as $\tilde{\psi}_0\tilde{\psi}_4$ or $\tilde{\psi}_0\tilde{\psi}_6$, the final conclusion is that the discrete integral of qJ it is conserved if we combine $(J^{++} + J^{+\times})$ and $J^{\times+}$.

Similarly if we take $(J^{++} + J^{\times+})$ the sum of qJ over all grid points is conserved as well if we take $J^{+\times}$ or any linear combination of $(J^{++} + J^{\times+})$ and $J^{+\times}$.

The anti-symmetry condition (16.61) is automatically satisfied for discrete version J^{++} but not for $(J^{+\times}$ or $J^{\times+})$ individually. However the combination $(J^{+\times} + J^{\times+})$ leads to a symmetric version. If view of the above results, the values $\alpha = \beta = 1/3$ seems thus the method of choice for a Jacobian discretization since it allows to satisfy our integral and symmetry constraints. This discretization is called the *Arakawa jacobian*. Of course, time discretization effects can alter the conservation properties such as (16.62)-(16.63) and the same discussion as in Section 6.4 applies.

The second essential ingredient in the quasi-geostrophic evolution is the relation between ψ and q. For a rigid-lid model on the f-plane it reads

$$\frac{\partial^2\psi}{\partial x^2} + \frac{\partial^2\psi}{\partial y^2} = q. \tag{16.72}$$

Since (16.55) provides the tool to advance q in time, (16.72) can be considered the equation to be solved once a new vorticity value is found. Hence we need again to invert a Poisson equation at each time step (see Section 7.8). In the first quasi-geostrophic models this was done by successive overrelaxation method, possibly with a red-black approach on vector computers.

Note that equations (10.1a) and (10.1b) can also be recasted into (16.55) without any approximations and we can therefore use numerical models that can solve the two-dimensional QG equations to analyze the stability of inviscid sheared flows. In reality, to produce Figure **??** in Chapter **??** we used a two-dimensionl QG model to simulate the non-linear evolution beyond the stability threshold.

Analytical Problems

16-1. Derive the one-layer quasi-geostrophic equation

$$\frac{\partial}{\partial t}\left(\nabla^2\psi \;-\; \frac{1}{R^2}\,\psi\right) \;+\; J(\psi, \nabla^2\psi) \;+\; \beta_0\,\frac{\partial\psi}{\partial x} \;=\; 0, \tag{16.73}$$

where $R = (gH)^{1/2}/f_0$, from the shallow-water model (7.20) assuming weak surface displacements. How do the waves permitted by these dynamics compare to the planetary waves exposed in Section 16.5?

16-2. Demonstrate the assertion made at the end of Section 16.4 that the time rate of change of available potential energy is proportional to the integral of the product of density perturbation with vertical velocity.

16-3. Elucidate in a rigorous manner the scaling assumptions justifying simultaneously the quasi-geostrophic approximation and the linearization of the equations for the wave analysis. What is the true restriction on vertical displacements?

16-4. Show that the assumption of a rigid upper surface (combined to the assumption of a flat bottom) effectively replaces the external radius of deformation by infinity. Also show that the approximate solutions for the vertical wavenumber k_z in Section 16.5 then become exact.

16-5. Explore topographic waves using the quasi-geostrophic formalism on an f-plane ($\beta_0 = 0$). Begin by formulating the appropriate bottom-boundary condition. JMB from ⇓

16-6. Establish the so-called *Omega equation* on the f-plane and without friction allowing to diagnose vertical velocity from density observation for horizontally constant N^2 and associated geostrophic current (u_g, v_g).

$$N^2 \frac{\partial^2 w}{\partial x^2} + N^2 \frac{\partial^2 w}{\partial y^2} + f^2 \frac{\partial^2 w}{\partial z^2} = \frac{\partial Q_x}{\partial x} + \frac{\partial Q_y}{\partial y} \tag{16.74}$$

$$Q_x = 2f \left(\frac{\partial u_g}{\partial z} \frac{\partial v_g}{\partial x} + \frac{\partial v_g}{\partial z} \frac{\partial v_g}{\partial y} \right)$$
$$Q_y = -2f \left(\frac{\partial u_g}{\partial y} \frac{\partial v_g}{\partial z} + \frac{\partial u_g}{\partial z} \frac{\partial u_g}{\partial x} \right)$$

JMB to ⇑

Numerical Exercises

16-1. Check numerical conservation (16.58) by adapting `qgmodel.m` in a closed two-dimensional and square domain of width L. Compare a Leapfrog and Euler time-discretization. Initialize with a streamfunction given by

$$\psi = \sin(\pi x/L) \sin(\pi y/L)\ L^2 \omega_0. \tag{16.75}$$

On the solid boundaries $x = 0$n $x = L$, $y = 0$ and $y = L$ streamfunction is kept zero. Use $\omega_0 = 10^{-5}$ s^{-1} and L= 100 km. For simplicity, use also zero vorticity on the boundaries.

16-2. Generalize the vorticity evolution to the β-plane in 2D. Also add superviscosity (biharmonic diffusion) detailed in Section 10.6 to `qgmodel.m`. *Hint:* Keep relative vorticity as dynamic variable and express the beta effect as a forcing term in its governing equation for a subsequent discretization. Redo the simulation of Exercise 16-1, including the beta term with $\beta_0 =$ and using $L = 3000$ km. Observe the evolution of the streamfunction.

16-3. Adapt `qgmodel.m` to simulate the instability of the barotropic flow of Section 10.4. Instead of an infinite domain in y direction, prescribe zero values for the streamfunction in $y = \pm 10L$. Apply a periodicity condition in x direction. What boundary conditions will you use on q? Which problem in prescribing boundary conditions will you encounter if you want to use a biharmonic diffusion? In any case, take a weak diffusion for the simulations. *Hint:* Prepare yourself to take a cup of coffee during the simulations, initialized with the base current perturbed by an unstable wave.

16-4. Try to adapt the overrelaxation parameter to decrease computation time of simulations in Exercise 16-3. Then simulate ..... **another 2D unstable problem with simple vorticity distribution** ?

16-5. Cylindrical symmetric unstable situation

$$\psi = -\,(\tilde{r}+1)e^{-\tilde{r}} \quad \tilde{r} = \frac{\sqrt{x^2+y^2}}{L}\; L^2\omega_0 \tag{16.76}$$

Hint: Use ?? for the calculation of the laplacian in cylindrical coordinates. For the perturbation, multiply r used in the calculation of ψ by ...

Gaussian eddy with

$$\psi = e^{-r^2/L^2}\; L^2\omega_0 \tag{16.77}$$

also works nicely (Figure 16-6).

16-6. Implement a more efficient Poisson-equation solver using MATLAB™ routine `cg` and redo Exercise 16-3. Search the WWW for a multigrid version of the Poisson equation solver to further reduce calculation times.

16-7. A zonal flow unstable without β effect.

16-8. Activate the beta term in an unstable situation to become stable?

7-11. Calculate the amplification factor of Gauss-Seidel iterations including overrelaxation. Can you infer the optimal overrelaxation coefficient for Dirichlet conditions? *Hint:* The optimal parameter will ensure that the slowest damping is done as fast as possible. **TO MOVE into chapter 7**

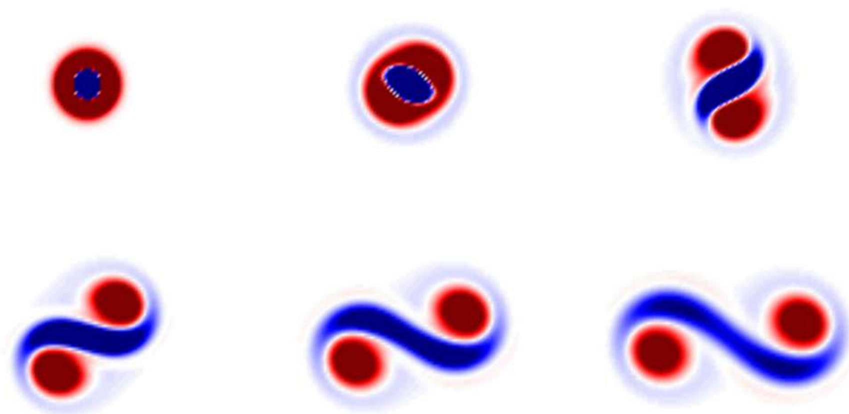

Figure 16-6 Evolution of a perturbed vorticity patch within a quasi-geostrophic framework.

Jule Gregory Charney
1917 – 1981

A strong proponent of the idea that intelligent simplifications of a problem are not only necessary to obtain answers but also essential to understand the underlying physics, Jule Charney was a major contributor to dynamic meteorology. As a student, he studied the instabilities of large-scale atmospheric flows and elucidated the mechanism that is now called baroclinic instability (Chapter 17). His thesis appeared in 1947, and the following year, he published an article outlining quasi-geostrophic dynamics (the material of this chapter). He then turned his attention to numerical weather prediction, an activity envisioned by L. F. Richardson some thirty years earlier. The success of the initial weather simulations in the early 1950s is to be credited not only to J. von Neumann's first electronic computer, but also to Charney's judicious choice of simplified dynamics, the quasi-geostrophic equation. Later on, Charney was instrumental in convincing officials worldwide of the significance of numerical weather predictions, while he also gained much deserved recognition for his work on tropical meteorology, topographic instability, geostrophic turbulence, and the Gulf Stream. Charney applied his powerful intuition to systematic scale analysis. Scaling arguments are now a mainstay in geophysical fluid dynamics. (Photo from archives of the Massachusetts Institute of Technology.) (*http://www.agu.org/inside/awards/charney.html*)

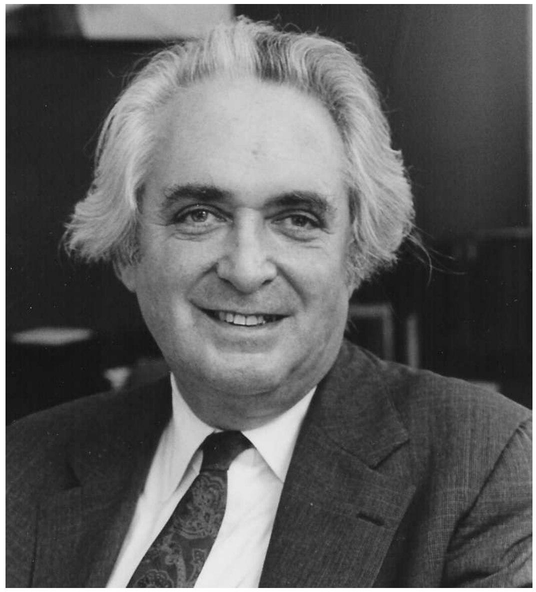

Allan Richard Robinson
1932 –

An avowed "phenomenologist", Allan Robinson is counted among the founding fathers of geophysical fluid dynamics because of his seminal contributions on the dynamics of rotating and stratified fluids, boundary-layer flows, continental shelf waves, and the maintenance of the oceanic thermocline. During the 1970s, he chaired and co-chaired a series of international programs that established the existence and importance of intermediate-scale eddies in the open ocean, the *internal weather of the sea*. His research led him to formulate numerical models for ocean forecasting and to emphasize the role of ocean physics in regulating biological activity. Robinson has also contributed significantly to the development of techniques for the assimilation of data in ocean-forecasting models. Underlying his accomplishments is the firm belief that "curiosity about nature is the primary driving force and rationalization for research". (*A. R. Robinson, Harvard University*)

Chapter 17

Instabilities of Rotating Stratified Flows

(October 18, 2006) **SUMMARY**: In a stratified rotating fluid, not all geostrophic flows are stable, for some are vulnerable to growing perturbations. This chapter presents the two primary mechanisms by which instability may occur: motion of individual particles (called *inertial instability*) and organized motions across the flow (called *baroclinic instability*). In each case, kinetic energy is supplied to the disturbance by release of potential energy from the original flow. Baroclinic instability is at the origin of the midlatitude cyclones and anticyclones that make our weather so variable. Because the evolution of the weather perturbations is essentially non-linear, a two layer quasi-geostrophic model is used to simulate the evolution of the baroclinic instability beyond the linear growth phase. JMB from ⇓ JMB to ⇑

17.1 Two types of instability

There are two broad types of flow instability. One is *local* or *punctual* in the sense that every particle in (at least a portion of) the flow is in an unstable situation. A prime example of this type is gravitational instability, which occurs in the presence of a reverse stratification (top-heavy fluid): if displaced, either upward or downward, a particle is subjected to a buoyancy force that pulls it further away from its original location and, since all other particles are individually subjected to a similar pull, the result is a catastrophic overturn of the fluid followed by mixing In the absence of friction, there is no specific temporal and spatial scales for the event. JMB from ⇓ JMB to ⇑

The second type of instability can exist only if the flow is stable with respect to the first kind. It is more gradual and relies on a collaborative action of many, if not all, particles and for this reason can be called *global* or *organized*. The instability is manifested by the temporal growth of a wave at a preferential wavelength that eventually overturns and forms vortices. An example is the barotropic instability encountered in Chapter 10 (see Section 10.4 in particular).

Table 17.1 CONTRASTING CHARACTERISTICS OF THE TWO TYPES OF INSTABILITY TO WHICH A FLUID FLOW MAY BE SUBJECTED

LOCAL INSTABILITY	**GLOBAL INSTABILITY**
Particles act individually	Particles act in concert
Motion proceeds randomly	Motion proceeds in a wave arrangement
Instability criterion depends only on local properties of the flow	Instability criterion depends on bulk properties of the flow and on wavelength of perturbation
Instability is independent of boundary conditions	Instability is sensitive to boundary conditions
Instability is catastrophic (major overturn, mixing)	Instability is gradual (growing wave and vortex formation)
Example: Overturning of a top-heavy fluid	Example: Kelvin-Helmholtz instability
In rotating stratified flow: Inertial instability	In rotating stratified flow: Mixed barotropic-baroclinic instability

Rotating stratified flows can be subjected to either type of instability. If the instability is local, it is called *inertial instability*, and if it is global, *baroclinic instability*. Table 17.1 summarizes the contrasting properties of the two types of instabilities.

Baroclinic instability is actually an end member of a more general instability, called *mixed barotropic-baroclinic instability*, which occurs when the flow is sheared in both horizontal and vertical directions. Baroclinic instability is the extreme when there is no shear in the horizontal, and barotropic instability (Chapter 10) is the other extreme, when the original flow has a no shear in the vertical.

17.2 Inertial instability

In this section, we consider the possibility of catastrophic instability, namely one in which a fluid particle once displaced from its position of equilibrium keeps moving further away from that position. Such instability is catastrophic because, if one such particle migrates away from its initial position, all others can do so as well and the ensuing situation is overturn, mixing and chaos.

This instability can be characterized also as *inertial* because acceleration is the crux of the growing displacement of the particles in the system. Finally, inertial instability is sometimes called *symmetric instability* because of some symmetry in its formulation, as the following developments will shortly reveal.

Let us consider an inviscid steady flow in thermal-wind balance with variation across the vertical plane (x, z), with sheared velocity $v(x, z)$ in equilibrium with a slanted stratification $\rho(x, z)$. Such flow must be both geostrophic and hydrostatic:

$$-\ fv \ = \ -\frac{1}{\rho_0}\frac{\partial p}{\partial x} \tag{17.1a}$$

$$0 \ = \ -\frac{1}{\rho_0}\frac{\partial p}{\partial z} - \frac{g\rho}{\rho_0}\,. \tag{17.1b}$$

Elimination of pressure p between these two equations yields the thermal-wind balance

$$f\,\frac{\partial v}{\partial z} \ = \ -\ \frac{g}{\rho_0}\frac{\partial \rho}{\partial x}\,. \tag{17.2}$$

From these flow characteristics, let us define the stratification frequency N by

$$N^2 \ = \ -\ \frac{g}{\rho_0}\frac{\partial \rho}{\partial z} \ = \ \frac{1}{\rho_0}\frac{\partial^2 p}{\partial z^2}\,, \tag{17.3}$$

and, similarly, two quantities that will be become useful momentarily:

$$F^2 \ = \ f\left(f + \frac{\partial v}{\partial x}\right) \ = \ f^2 \ + \ \frac{1}{\rho_0}\frac{\partial^2 p}{\partial x^2} \tag{17.4}$$

$$G^2 \ = \ f\,\frac{\partial v}{\partial z} \ = \ -\ \frac{g}{\rho_0}\frac{\partial \rho}{\partial x} \ = \ \frac{1}{\rho_0}\frac{\partial^2 p}{\partial x \partial z}\,. \tag{17.5}$$

Benoit: Why not use instead of G^2 the following $G^2 = fM$ (with M being the Prandtl frequency as before), then in the absence of lateral shear ($F^2 \to f^2$) the condition on stability reduces to $N^2 > M^2$ with a nice recalling of the Richardson number. JMB from ⇓ JMB to ⇑

Note that the three quantities N^2, F^2 and G^2 have all the dimension of a frequency squared. But, although they are defined as squares, we ought to entertain the possibility that they may be negative.

Next, let us perturb such flow by adding time dependency and velocity components u and w within the x–z plane, while assuming still no variation in the perpendicular direction. For clarity of exposition, we further assume inviscid flow and restrict the attention to the f–plane, but we allow for possible non-hydrostaticity in the vertical, in anticipation of large vertical accelerations:

$$\frac{du}{dt} - fv = -\frac{1}{\rho_0}\frac{\partial p}{\partial x} \tag{17.6a}$$

$$\frac{dv}{dt} + fu = 0 \tag{17.6b}$$

$$\frac{dw}{dt} = -\frac{1}{\rho_0}\frac{\partial p}{\partial z} - \frac{g\rho}{\rho_0}, \tag{17.6c}$$

in which d/dt stands for the material derivative (following particle movement).

In this flow, let us track an individual fluid particle with moving coordinates $[x(t), z(t)]$. Its velocity components in the vertical plane are

$$u = \frac{dx}{dt} \quad w = \frac{dz}{dt}, \tag{17.7}$$

which transform equation (17.6b) into

$$\frac{dv}{dt} + f\frac{dx}{dt} = 0. \tag{17.8}$$

Since f is constant in our model, the quantity $v + fx$ is an invariant of the motion[1] and it follows that if the particle is displaced horizontally over a distance Δx it undergoes a change of transverse velocity Δv such that

$$\Delta v + f\Delta x = 0. \tag{17.9}$$

Turning our attention to equations (17.6a) and (17.6c) and eliminating from them u and w by use of (17.7), we obtain:

$$\frac{d^2x}{dt^2} - fv = -\frac{1}{\rho_0}\frac{\partial p}{\partial x} \tag{17.10a}$$

$$\frac{d^2z}{dt^2} = -\frac{1}{\rho_0}\frac{\partial p}{\partial z} - \frac{g\rho}{\rho_0}. \tag{17.10b}$$

Note that in these equations the pressure terms on the right-hand sides are complicated functions of the particle position (x, z).

Let us now imagine that the fluid particle under consideration is only moved from its original position by a small displacement Δx in the horizontal and Δz in the vertical: $x(t) =$
JMB from ⇓ $x_0 + \Delta x(t)$, $z(t) = z_0 + \Delta z(t)$, so that we may linearize the equations. Note that any displacement along y will have no effect on the dynamic balance and can be disregarded.
JMB to ⇑ Neglecting compressibility effects, we assume that the displacement causes no change in density for the particle. At its new position, the particle is out of equilibrium. In the vertical, it is subject to a buoyancy force, while in the horizontal, it is no longer in geostrophic equilibrium. These forces are reflected in the new, local values of the pressure gradient, which for a small displacement can be obtained from the original values by a Taylor expansion:

[1] This is occasionally called the *geostrophic momentum*.

$$\left.\frac{\partial p}{\partial x}\right|_{\text{at } x+\Delta x, z+\Delta z} = \left.\frac{\partial p}{\partial x}\right|_{\text{at } x,z} + \Delta x \left.\frac{\partial^2 p}{\partial x^2}\right|_{\text{at } x,z} + \Delta z \left.\frac{\partial^2 p}{\partial x \partial z}\right|_{\text{at } x,z} \quad (17.11a)$$

$$\left.\frac{\partial p}{\partial z}\right|_{\text{at } x+\Delta x, z+\Delta z} = \left.\frac{\partial p}{\partial z}\right|_{\text{at } x,z} + \Delta x \left.\frac{\partial^2 p}{\partial x \partial z}\right|_{\text{at } x,z} + \Delta z \left.\frac{\partial^2 p}{\partial z^2}\right|_{\text{at } x,z} \quad (17.11b)$$

h After subtraction of the unperturbed state, the equations governing the evolution of the displacement are:

$$\frac{d^2 \Delta x}{dt^2} - f \Delta v = -\frac{1}{\rho_0} \left(\frac{\partial^2 p}{\partial x^2}\right) \Delta x - \frac{1}{\rho_0} \left(\frac{\partial^2 p}{\partial x \partial z}\right) \Delta z \quad (17.12a)$$

$$\frac{d^2 \Delta z}{dt^2} = -\frac{1}{\rho_0} \left(\frac{\partial^2 p}{\partial x \partial z}\right) \Delta x - \frac{1}{\rho_0} \left(\frac{\partial^2 p}{\partial z^2}\right) \Delta z, \quad (17.12b)$$

in which $\Delta v = -f \Delta x$ according to (17.9). The first equation tells that the force imbalance in the x–direction is due in part by the Coriolis force having changed by $f \Delta v$ and in part by immersion in a new pressure gradient. By Newton's second law, this causes a horizontal acceleration $d^2 \Delta x / dt^2$. Likewise, the second equation states that the modified pressure environment causes an imbalance in the vertical. The new neighbors together exert a buoyancy force on our particle and the latter acquires a vertical acceleration $d^2 \Delta z / dt^2$.

Since the equations are now linear, we may seek solutions of the form:

$$\Delta x = X \exp(\mathrm{i}\,\omega t), \qquad \Delta z = Z \exp(\mathrm{i}\,\omega t). \quad (17.13)$$

If the frequency ω is real, the particle oscillates around its original position of equilibrium and the flow can be characterized as stable. On the contrary, should ω be complex and have a negative imaginary part, the solution includes exponential growth, the particle drifts away from its original position, and the flow is deemed to be unstable.

Substitution on the solution type in the governing equations yields a 2-by-2 system for the amplitudes X and Z:

$$(F^2 - \omega^2)\, \Delta x + G^2\, \Delta z = 0 \quad (17.14a)$$

$$G^2\, \Delta x + (N^2 - \omega^2)\, \Delta z = 0, \quad (17.14b)$$

in which we introduced quantities defined in (17.3), (17.4) and (17.5). A non-zero solution exists only if ω obeys

$$(F^2 - \omega^2)\,(N^2 - \omega^2) = G^4, \quad (17.15)$$

of which the ω^2 roots are

$$\omega^2 = \frac{F^2 + N^2 \pm \sqrt{(F^2 - N^2)^2 + 4G^4}}{2}. \quad (17.16)$$

The question is whether one or both ω^2 values can be negative, in which case there is at least one ω root with a negative imaginary part.

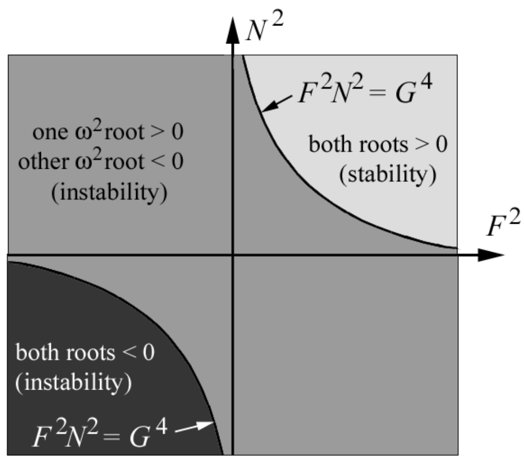

Figure 17-1 Stability diagram in the parameter space (F^2, N^2) for the inertial instability of a thermal-wind flow.

Before proceeding with the general case, it is instructive to consider two extreme cases. First is the case of a pure stratification (v is a constant and ρ is a function of z only; $F^2 = G^2 = 0$ and $N^2 \neq 0$), for which

$$\omega^2 = \frac{N^2 \pm \sqrt{N^4}}{2} = 0 \quad \text{or} \quad N^2. \tag{17.17}$$

All ω values are real if $N^2 \geq 0$, which corresponds to a density increasing downward ($d\rho/dz < 0$). Otherwise the fluid is top heavy and overturns. This is gravitational instability.

The second extreme case is that of a pure shear (v is a function of x only and ρ is a constant: $F^2 \neq 0$ and $G^2 = N^2 = 0$), for which

$$\omega^2 = \frac{F^2 \pm \sqrt{F^4}}{2} = 0 \quad \text{or} \quad F^2. \tag{17.18}$$

All ω values are real is $F^2 \geq 0$, which corresponds to $f(f + \partial v/\partial x) \geq 0$, *i.e.*, $(f + \partial v/\partial x)$ of the same sign as f. Should F^2 be negative, the flow mixes horizontally. This is inertial instability in a pure form.

Returning to the general case, we realize that the switch between stability and instability occurs when $\omega^2 = 0$, which according to (17.16) occurs when

$$F^2N^2 = G^4. \tag{17.19}$$

Around this relation, the signs of the ω^2 roots are as depicted in Figure 17-1. It is clear from this graph that stability demands three conditions[2]:

$$F^2 \geq 0, \quad N^2 \geq 0 \quad \text{and} \quad F^2N^2 \geq G^4 \tag{17.20}$$

The third condition is the most intriguing of the group and deserves some physical interpretation. For this, let us take F^2 and N^2 both positive and define the slope (positive

[2] $F^2N^2 = G^4$ alone is not enough because it could be obtained with F^2 and N^2 both negative.

downward) of the lines in the vertical (x, z) plane along which the geostrophic momentum $v + fx$ and density ρ are constant:

$$\begin{aligned} S_{\text{momentum}} &= \text{slope of line } v + fx = \text{constant} \\ &= \frac{\partial(v+fx)/\partial x}{\partial(v+fx)/\partial z} = \frac{F^2}{G^2} \qquad (17.21) \\ S_{\text{density}} &= \text{slope of line } \rho = \text{constant} \\ &= \frac{\partial\rho/\partial x}{\partial\rho/\partial z} = \frac{G^2}{N^2}\,. \qquad (17.22) \end{aligned}$$

The stability threshold $F^2N^2 = G^4$ then corresponds to equal momentum and density slopes. Normally, the velocity varies strongly in x and weakly in z, whereas density behaves in the opposite way, varying more rapidly in z than in x. Typically, therefore, lines of equal geostrophic momentum are steeper than lines of equal density. This, it turns out, is the stable case $F^2N^2 > G^4$ (left panel of Figure 17-2).

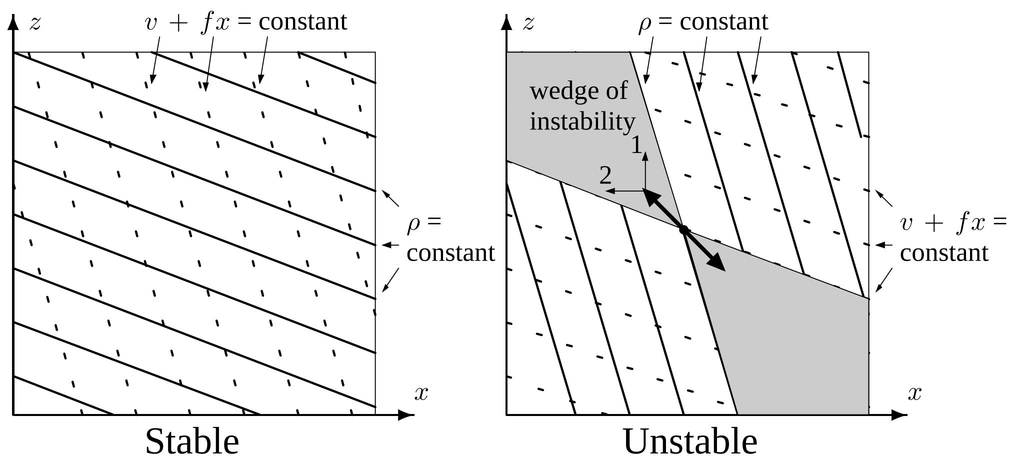

Figure 17-2 Left panel: Stability when lines of constant geostrophic momentum $v + fx$ are steeper than lines of constant density ρ. Right panel: Instability when lines of constant geostrophic momentum are less steep than lines of constant density; a particle displaced within the wedge is pulled further away by a combination of a buoyancy force (1) and a geostrophic imbalance (2).

With increasing thermal wind, momentum lines become less inclined and density lines more steep, until they cross. Beyond this crossing, when the steeper lines are the density lines, $F^2N^2 < G^4$, and the system is unstable (right panel of Figure 17-2). Particles quickly drift away from their initial position and the fluid is vigorously rearranged until it becomes marginally stable, just as a top-heavy fluid ($N^2 < 0$) is gravitationally unstable and becomes mixed until its density is homogenized ($N^2 = 0$). In other words, a situation with density lines steeper than geostrophic lines cannot persist and re-arranges itself quickly until these lines become aligned.

JMB from ⇓
JMB to ⇑

In the unstable regime, it can be shown (see Problem 17-9.) that growing particle displacements lie in the wedge between the momentum and density lines (right panel of Figure 17-2). This justifies yet another name for the process: *wedge instability*.

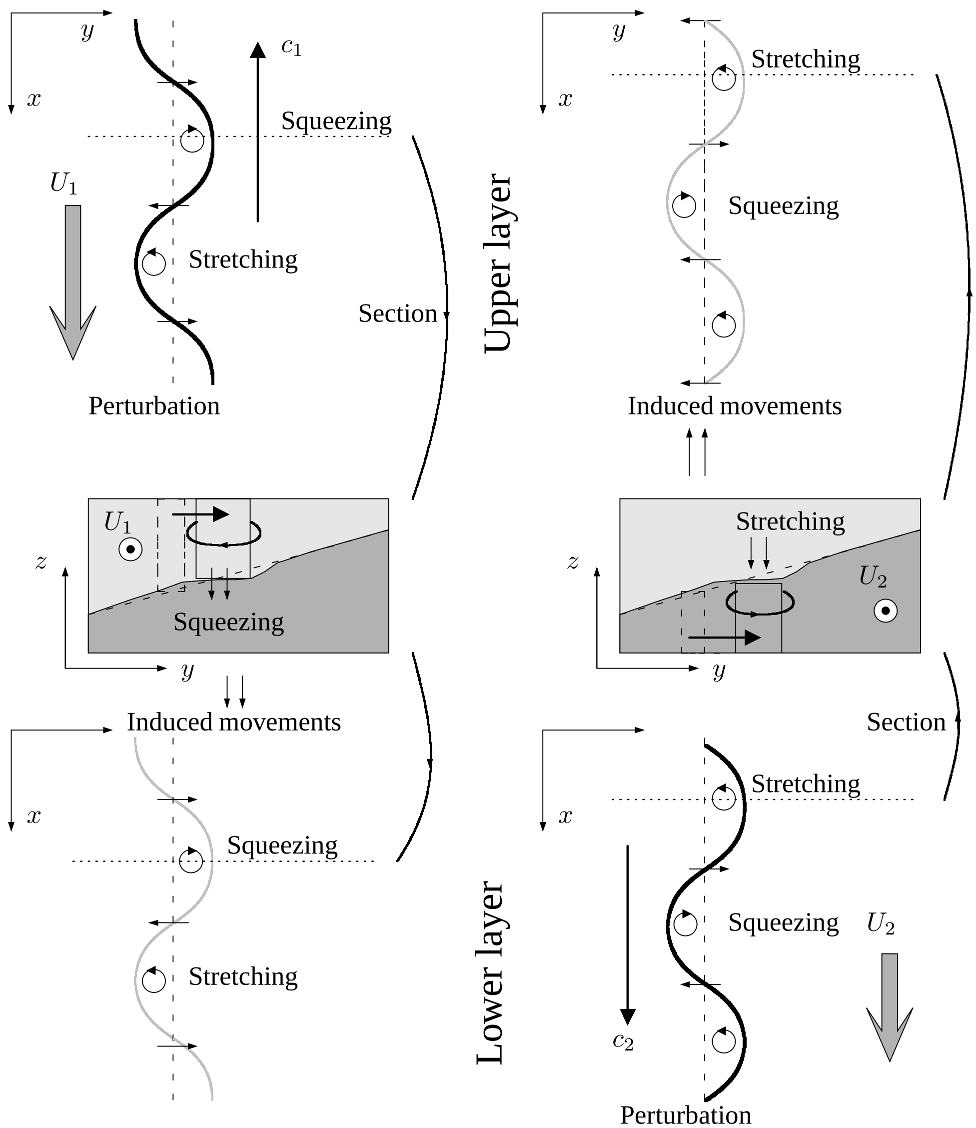

Figure 17-3 Patterns of squeezing and stretching caused by lateral displacements in a two-layer flow in thermal-wind balance. Squeezing generates anticyclonic vorticity (clockwise motion in the Northern Hemisphere), while stretching generates cyclonic vorticity (counterclockwise motion in the Northern Hemisphere). The flexibility of the density interface distributes the squeezing and stretching across both layers, and the result is that a cross-flow displacement in the upper layer (upper-left of figure) causes an accompanying pattern of squeezing and stretching in the lower layer (lower-left of figure). Vice versa, a cross-flow displacement in the lower layer (lower-right of figure) causes a similar pattern of squeezing and stretching in the upper layer (upper-right of figure). Growth occurs when the two sets of patterns mutually reinforce each other.

17.3 Baroclinic instability – The mechanism

In thermal-wind balance, geostrophy and hydrostaticity combine to maintain a flow in equilibrium. Assuming that this flow is stable with respect to inertial instability (previous section), the equilibrium is not that of least energy, because a reduction in slope of density surfaces by spreading of the lighter fluid above the heavier fluid would lower the center of gravity and thus the potential energy. Simultaneously, it would also reduce the pressure gradient, its associated geostrophic flow and the kinetic energy of the system. Evidently, the state of rest is that of least energy (minimum potential energy and null kinetic energy).

In a thermal wind, relaxation of the density distribution and tendency toward the state of rest cannot occur in any direct, spontaneous manner. Such an evolution would require vertical stretching and squeezing of fluid columns, neither of which can occur without alteration of potential vorticity.

Friction is capable of modifying potential vorticity, and under the slow action of friction a state of thermal wind decays, eventually bringing the system to rest. But, there is a more rapid process that operates before the influence of friction becomes noticeable.

Vertical stretching and squeezing of fluid parcels is possible under conservation of potential vorticity if relative vorticity comes into play. As we have seen in Section 12.3, a column of stratified fluid that is stretched vertically develops cyclonic relative vorticity, and one that is squeezed acquires anticyclonic vorticity. In a slightly perturbed thermal-wind system, the vertical stretching and squeezing occurring simultaneously at different places generates a pattern of interacting vortices. Under certain conditions, these interactions can increase the initial perturbation, thus forcing the system to evolve away from its original state.

Physically, a partial relaxation of the density surfaces liberates some potential energy, while the concomitant stretching and squeezing creates new relative vorticity. The kinetic energy of the new motions can naturally be provided by the potential-energy release. If conditions are favorable, these motions can then contribute to further relaxation of the density field and to stronger vortices. With time, large vortices can be formed at the expense of the original thermal wind. Vortices noticeably increase the amount of velocity shear in the system, greatly enhancing the action of friction. The evolution toward a lower energy level is therefore more effective via the transformation from potential into kinetic energy and generation of vortices than by friction acting on the thermal-wind flow.

Let us now investigate how a disturbance of a thermal-wind flow can generate a relative-vorticity distribution favorable to growth. For this purpose, a two-fluid idealization, as depicted in Figure 17-3, is sufficient. For the discussion, let us also ignore the beta effect and align the x–direction with that of the thermal wind ($U_1 - U_2$). The interface then slopes upward in the y–direction (middle panels of Figure 17-3). A perturbation of the upper flow causes some of its parcels to move in the $+y$–direction, into a shallower region (middle-left panel of the figure), and these undergo some vertical squeezing and thus acquire anticyclonic vorticity (clockwise in the figure). But, because the density interface is not a rigid bottom but a flexible surface, it deflects slightly, relieving the upper parcels from some squeezing and creating a complementary squeeze in the lower layer. Thus, lower-layer parcels, too, develop anticyclonic vorticity at the same location. Note in passing that a lowering of the interface on the shallower side is also in the direction of a decrease of available potential energy.

Elsewhere, the disturbance causes upper-layer parcels to move in the opposite direction — that is, toward a deeper region. There, vertical stretching takes place, and, again, because the interface is flexible, this stretching in the upper layer is only partial, the interface rises somewhat, and a complementary stretching occurs in the lower layer. Thus, parcels in both layers develop cyclonic relative vorticity (counterclockwise in the figure). Note that a lifting of the interface on the deeper side is again in the direction of a decrease of available potential energy. If the disturbance has some periodicity, as shown in the figure, alternating positive and negative displacements in the upper layer cause alternating columns of anticyclonic and cyclonic vorticities extending through both layers. Parcels lying between these columns of vortical motion are entrained in the directions marked by the arrows in the figure (upper-left and lower-left panels), creating subsequent displacements. Because these latter displacements occur not at, but between the crests and troughs of the original displacements, they lead not to growth but to a translation of the disturbance[3]. Thus, a pattern of displacement in the upper layer generates a propagating wave. The direction of propagation (c_1 in upper-left panel of Figure 17-3) is opposite to that of the thermal wind ($U_1 - U_2$).

Similarly, cross-flow displacements in the lower layer (right panel of Figure 17-3) generate patterns of stretching and squeezing in both layers. The difference is that, because of the sloping nature of the density interface, displacements in the $+y$–direction (middle-right panel in figure) are accompanied by stretching instead of squeezing. Fluid parcels lying between vortical motions take their turn in being displaced, and the pattern again propagates as a wave (c_2 in lower-right panel of Figure 17-3), this time in the direction of the thermal wind.

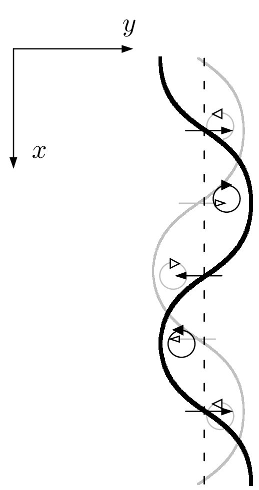

Figure 17-4 Interaction of displacement patterns and vortex tubes in the upper layer of a two-layer thermal-wind flow when displacements occur in both layers. The illustration depicts the case of a mutually reinforcing pair of patterns, when the vortical motions of one pattern act to increase the displacements of the other. A similar figure could be drawn for the lower layer, and it can be shown that, if the combination of patterns is self-reinforcing in one layer, it is self-reinforcing in the other layer, too. This is the essence of baroclinic instability

Each by itself, the displacement pattern in a layer only generates a vorticity wave, but growth or decay of the whole can take place depending on whether the two separately induced patterns reinforce or negate each other. If the vorticity patterns induced by the upper-layer and lower-layer diplacements are in quadrature with each other, the complementary vortical motions (upper-right and upper-left sides of Figure 17-3, respectively) of one set fall at the crests and troughs of the other set, and the ensuing interaction is either favorable or unfavorable to growth. If the spatial phase difference is such that the displacement pattern in one layer is shifted in the direction of the thermal-wind flow in that layer ($U_1 - U_2$ in the upper

[3]The mechanism here is identical to that of planetary and topographic waves, discussed in Section 9.6.

layer — the opposite in the lower layer), as depicted in Figure 17-4, the vortical motions of one pattern act to increase the displacements of the other, and the disturbance in each layer amplifies that in the other. The system evolves away from its initial equilibrium.

The preceding description points to the need of a specific phase arrangement between the displacements in the two layers and emphasizes the role of vorticity generation. A further requirement is necessary for growth: The disturbance must have a wavelength that is neither too short nor too long and must be such that the vertical stretching and squeezing effectively generates relative vorticity. To show this, let us consider the quasi-geostrophic form of the potential vorticity (16.16), on the f-plane:

$$q \;=\; \nabla^2\psi \;+\; \frac{\partial}{\partial z}\left(\frac{f^2}{N^2}\,\frac{\partial\psi}{\partial z}\right), \tag{17.23}$$

where ψ is the streamfunction, f the Coriolis parameter, N is the stratification frequency, and ∇^2 is the two-dimensional Laplacian. For a displacement pattern of wavelength L, the first term representing relative vorticity is on the the order of

$$\nabla^2\psi \;\sim\; \frac{\Psi}{L^2}\,, \tag{17.24}$$

where the streamfunction scale Ψ is proportional to the amplitude of the displacements. If the height of the system is H, the second term (representing vertical stretching) scales as

$$\frac{\partial}{\partial z}\left(\frac{f^2}{N^2}\,\frac{\partial\psi}{\partial z}\right) \;\sim\; \frac{f^2\Psi}{N^2H^2} \;=\; \frac{\Psi}{R^2}\,, \tag{17.25}$$

where we have defined the deformation radius $R = NH/f$.

Now, if L is much larger than R, the relative vorticity cannot match the vertical stretching as scaled. This implies that vertical stretching will be inhibited, and the displacements in the layers will tend to be in phase in order to reduce squeezing and stretching of fluid parcels in each layer. On the other hand, if L is much shorter than R, relative vorticity dominates potential vorticity. The two layers become uncoupled, and there is insufficient potential energy to feed a growing disturbance. In sum, displacement wavelengths on the order of the
JMB from ⇓ deformation radius are the most favorable to growth.

Benoit: From the discussion I somehow miss the place where the quasi-geostrophic nature of the process is justified. PV conservation itself is valid at all scales and you use QG theory to show that $R \sim L$, which is coherent with QG, but not a prove.

Also, maybe a phrase somewhere that the propagating wave pattern not only need the adequate phase shift but also a propagation speed of the wave that is identical in both layers: $U_1 - c_1 = U_2 + c_2$. For identical layer depth and pure "sloping interface wave", by symmetry, the wave speed relative to the fluid (in motion) is identical $c_1 = c_2$ and hence $c_1 = c_2 = \Delta U/2$ and we prove that the instability moves with the average speed $U_1 - c_1 = U_2 + c_2 =$
JMB to ⇑ $(U_1 + U_2)/2$.

Because fluctuations are so ubiquitous in nature, an existing flow in thermal-wind balance will continuously be subjected to perturbations. Most of these will have a benign effect, because they do not have the proper phase arrangement or a suitable wavelength. But, sooner or later, a perturbation with both favorable phase and wavelength will occur, prompting the system to evolve irreversibly from its equilibrium state. We conclude that flows in thermal-wind balance are intrinsically unstable. Because their instability process depends crucially on a phase shift with height, the fatal wave must have a baroclinic structure. To reflect this fact, the process has been termed *baroclinic instability*.

The cyclones and anticyclones of our midlatitude weather are manifestations of the baroclinic instability of the atmospheric jet stream. The person who first analyzed the stability of vertically sheared currents (thermal wind) and who demonstrated the relevance of the instability mechanism to our weather is J. G. Charney[4]. While Charney (1947) performed the stability analysis for a continuously stratified fluid on the beta plane, Eady (1949) did the analysis on the f-plane independently. The comparison between the two theories reveals that the beta effect is a stabilizing influence. Briefly, a change in planetary vorticity (by meridional displacements) is another way to allow vertical stretching and squeezing while preserving potential vorticity. Relative vorticity is then no longer as essential and, in some cases, sufficiently suppressed to render the thermal wind stable to perturbations of all wavelengths.

17.4 Linear theory of baroclinic instability

Numerous stability analyses have been published since those of Charney and Eady, exemplifying one aspect or another. Phillips (1954) idealized the continuous vertical stratification to a two-layer system, a case which Pedlosky (1963, 1964) generalized by allowing arbitrary horizontal shear in the basic flow, and Pedlosky and Thomson (2003) generalized to temporally oscillating basic flow. Barcilon (1964) studied the influence of friction on baroclinic instability by including the effect of Ekman layers, whereas Orlanski (1968; 1969) investigated the importance of non-quasi-geostrophic effects and of a bottom slope. Later, Orlanski and Cox (1973), Gill *et al.* (1974), and Robinson and McWilliams (1974) confirmed that baroclinic instability is the primary cause of the observed oceanic variability at intermediate scales (tens to hundreds of kilometers).

Here, we only present one of the simplest mathematical models, taken from Phillips (1954), because it best exemplifies the mechanism described in the previous section. The fluid consists of two layers with equal thicknesses $H/2$ and unequal densities ρ_1 on top and ρ_2 below, on the beta-plane ($\beta_0 \neq 0$) over a flat bottom (at $z = 0$) and under a rigid lid (at $z = H$, constant). The fluid is further assumed to be inviscid ($\mathcal{A}$ and $\nu_E = 0$). The basic flow is taken as uniform in the horizontal and unidirectional but with distinct velocities in each layer:

$$\bar{u}_1 \;=\; U_1, \quad \bar{v}_1 \;=\; 0 \qquad \text{for} \quad 0 \leq z \leq \frac{H}{2} \tag{17.26a}$$

$$\bar{u}_2 \;=\; U_2, \quad \bar{v}_2 \;=\; 0 \qquad \text{for} \quad \frac{H}{2} \leq z \leq H. \tag{17.26b}$$

As we shall see, it is precisely the velocity difference $\Delta U = U_1 - U_2$ between the two layers, the vertical shear, that causes the instability. For simplicity, the dynamics are chosen to be

[4]For a short biography, see the end of Chapter 16.

quasi-geostrophic, prompting us to introduce a streamfunction ψ and potential vorticity q that obey (16.15) and (16.16):

$$\frac{\partial q}{\partial t} \;+\; J(\psi,\, q) \;=\; 0, \tag{17.27a}$$

$$q \;=\; \nabla^2\psi \;+\; \frac{f_0^2}{N^2}\,\frac{\partial^2\psi}{\partial z^2} \;+\; \beta_0 y. \tag{17.27b}$$

JMB from ⇓

Because of the identical layer thickness, the stratification frequency can be considered constant, coherently with the layered model of Chapter 12.2, where equal layer heights corresponded to a uniform stratification.

JMB to ⇑

The second equation contains derivatives in z, which must be "discretized" to conform with a two-layer representation. For this, we place values ψ_1 and ψ_2 at mid-level in each layer and two additional values ψ_0 and ψ_3 above and below at equal distances (Figure 17-5). These latter values fall beyond the boundaries and are defined for the sole purpose of enforcing boundary conditions in the vertical. The flat bottom and rigid lid require zero vertical velocity at those levels, which by virtue of (16.17c) translate into $\partial\psi/\partial z = 0$. In discretized form, the boundary conditions are $\psi_0 = \psi_1$ and $\psi_3 = \psi_2$. The second derivatives may then be approximated as:

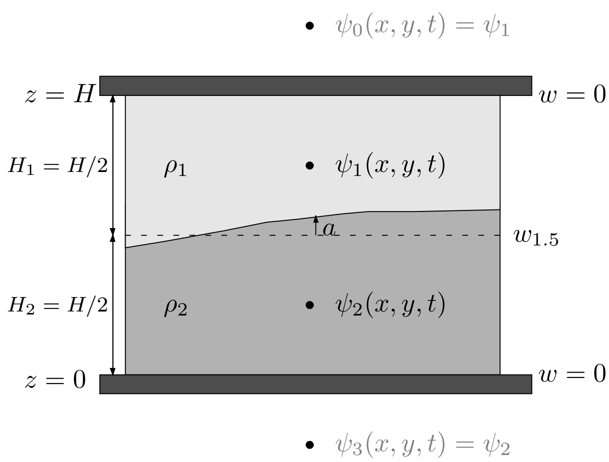

Figure 17-5 Representation of the vertical stratification by two layers of uniform density in a quasi-geostrophic model

$$\left.\frac{\partial^2\psi}{\partial z^2}\right|_1 \;\approx\; \frac{\psi_0 - 2\psi_1 + \psi_2}{\Delta z^2} = \frac{\psi_1 - 2\psi_1 + \psi_2}{(H/2)^2} = \frac{4(\psi_2 - \psi_1)}{H^2}$$

$$\left.\frac{\partial^2\psi}{\partial z^2}\right|_2 \;\approx\; \frac{\psi_1 - 2\psi_2 + \psi_3}{\Delta z^2} = \frac{\psi_1 - 2\psi_2 + \psi_2}{(H/2)^2} = \frac{4(\psi_1 - \psi_2)}{H^2}\,.$$

In a similar vein, we discretize the stratification frequency:

$$N^2 \;=\; -\;\frac{g}{\rho_0}\,\frac{d\rho}{dz}\;\approx\;-\;\frac{g}{\rho_0}\,\frac{\rho_1-\rho_2}{\Delta z}\;=\;+\;\frac{2g(\rho_2-\rho_1)}{\rho_0 H}\;=\;\frac{2g'}{H}\,, \tag{17.28}$$

for which we have defined the reduced gravity $g' = g(\rho_2 - \rho_1)/\rho_0$. It is also convenient to introduce the baroclinc radius of deformation as

$$R \;=\; \frac{1}{f_0}\sqrt{g'\frac{H_1 H_2}{H_1+H_2}} \;=\; \frac{\sqrt{g'H}}{2f_0}\,. \tag{17.29}$$

The set of two governing equations can now be written:

$$\frac{\partial q_1}{\partial t} \;+\; J(\psi_1, q_1) \;=\; 0 \tag{17.30a}$$

$$\frac{\partial q_2}{\partial t} \;+\; J(\psi_2, q_2) \;=\; 0, \tag{17.30b}$$

where the potential vorticities q_1 and q_2 are expressed in terms of the streamfunctions ψ_1 and ψ_2 as

$$q_1 \;=\; \nabla^2\psi_1 \;+\; \frac{1}{2R^2}\,(\psi_2-\psi_1) \;+\; \beta_0 y \tag{17.31a}$$

$$q_2 \;=\; \nabla^2\psi_2 \;-\; \frac{1}{2R^2}\,(\psi_2-\psi_1) \;+\; \beta_0 y. \tag{17.31b}$$

From these quantities, the primary physical variables are derived as follows [see Equations (16.17)]

$$u_i \;=\; -\,\frac{\partial\psi_i}{\partial y}\,,\quad v_i \;=\; +\,\frac{\partial\psi_i}{\partial x} \tag{17.32a}$$

$$w_{1.5} \;=\; \frac{2f_0}{N^2 H}\left[\frac{\partial(\psi_2-\psi_1)}{\partial t} \;+\; J\left(\psi_1,\;\psi_2\right)\right] \tag{17.32b}$$

$$p_i' \;=\; \rho_0 f_0 \psi_i, \tag{17.32c}$$

where $i = 1, 2$. The vertical displacement a of the density interface between the layers can be obtained from the hydrostatic balance $p_2' = p_1' + (\rho_2 - \rho_1)ga$, which in terms of the streamfunctions yields

$$a \;=\; \frac{f_0}{g'}\,(\psi_2 \;-\; \psi_1). \tag{17.33}$$

The same set of equations can be derived from the two-layer model of Section 12.4, in which the quasi-geostrophic approach is applied on each layer, following the technique of Chapter 16. JMB from ⇓ JMB to ⇑

The basic-state values of ψ_i and q_i corresponding to (17.26) are

$$\bar{\psi_1} \;=\; -U_1 y\,, \quad \bar{q_1} \;=\; \left(\beta_0 y \;+\; \frac{\Delta U}{2R^2}\right)\, y \tag{17.34a}$$

$$\bar{\psi_2} \;=\; -U_2 y\,, \quad \bar{q_2} \;=\; \left(\beta_0 y \;-\; \frac{\Delta U}{2R^2}\right)\, y. \tag{17.34b}$$

Adding a perturbation ψ_i' to $\bar{\psi}_i$ with corresponding perturbation q_i' to $\bar{q}_i$, both of infinitesimal amplitudes so that the equations can be linearized, we obtain, from (17.30) and (17.31):

$$\frac{\partial q_i'}{\partial t} \;+\; J(\bar{\psi}_i,\, q_i') \;+\; J(\psi_i',\, \bar{q}_i) \;=\; 0 \tag{17.35a}$$

$$q_1' \;=\; \nabla^2\psi_1' \;+\; \frac{1}{2R^2}\,(\psi_2' - \psi_1') \tag{17.35b}$$

$$q_2' \;=\; \nabla^2\psi_2' \;-\; \frac{1}{2R^2}\,(\psi_2' - \psi_1')\,. \tag{17.35c}$$

Elimination of q' and replacement of the basic-flow quantities with (17.34) yield a pair of coupled equations for ψ_1' and ψ_2':

$$\left(\frac{\partial}{\partial t} + U_1\,\frac{\partial}{\partial x}\right)\left[\nabla^2\psi_1' + \frac{1}{2R^2}\,(\psi_2' - \psi_1')\right] \;+\; \left(\beta_0 + \frac{\Delta U}{2R^2}\right)\,\frac{\partial \psi_1'}{\partial x} \;=\; 0 \tag{17.36a}$$

$$\left(\frac{\partial}{\partial t} + U_2\,\frac{\partial}{\partial x}\right)\left[\nabla^2\psi_2' - \frac{1}{2R^2}\,(\psi_2' - \psi_1')\right] \;+\; \left(\beta_0 - \frac{\Delta U}{2R^2}\right)\,\frac{\partial \psi_2'}{\partial x} \;=\; 0. \tag{17.36b}$$

Because both these equations have coefficients independent of x, y and time, a sinusoidal function in those variables is a solution, and we write:

$$\psi_i' \;=\; \Re[\phi_i\; \mathrm{e}^{\mathrm{i}\,(k_x x + k_y y - \omega t)}], \tag{17.37}$$

where ϕ_1 and ϕ_2 form a pair of unknowns giving the vertical structure of the wave perturbation, k_x and k_y are horizontal wavenumber components (both taken as real), and ω is the angular frequency. Should this frequency be complex with a positive imaginary part, exponential growth occurs in time, and the wave is unstable. Substitution in (17.36) leads to equations for ϕ_1 and ϕ_2:

$$(U_1 - c)\,\left[-k^2\phi_1 + \frac{1}{2R^2}(\phi_2 - \phi_1)\right] \;+\; \left(\beta_0 + \frac{\Delta U}{2R^2}\right)\,\phi_1 \;=\; 0 \tag{17.38a}$$

$$(U_2 - c)\,\left[-k^2\phi_2 - \frac{1}{2R^2}(\phi_2 - \phi_1)\right] \;+\; \left(\beta_0 - \frac{\Delta U}{2R^2}\right)\,\phi_2 \;=\; 0, \tag{17.38b}$$

in which we have defined $c = \omega/k_x$ and $k^2 = k_x^2 + k_y^2$. At this point, it is useful to decompose the ϕ values into barotropic and baroclinic components:

$$\text{Barotropic component:} \qquad A = \frac{\phi_1 + \phi_2}{2} \tag{17.39a}$$

$$\text{Baroclinic component:} \qquad B = \frac{\phi_1 - \phi_2}{2}\,. \tag{17.39b}$$

The sum and difference of the preceding equations then yield:

$$\left[2\beta_0 - k^2(U_1 + U_2 - 2c)\right]\ A - k^2 \Delta U\ B \ = \ 0 \tag{17.40a}$$

$$\left(\frac{1}{R^2} - k^2\right) \Delta U\ A \ + \ \left[2\beta_0 - \left(k^2 + \frac{1}{R^2}\right)(U_1 + U_2 - 2c)\right]\ B \ = \ 0. \tag{17.40b}$$

JMB from ⇓

Note that a purely barotropic solution ($B = 0$, $A \neq 0$) is only possible in the absence of shear ($\Delta U = 0$), and for a wave speed $c = U - \beta_0/k^2$ easily interpreted in terms of planetary waves. **Benoit**: Calculations are more easily presented if we define just before the barotropic/baroclinic decomposition

$$\kappa \ = \ k^2 R^2 \tag{17.41}$$

$$\alpha \ = \ \frac{\beta_0 R^2}{\Delta U} \tag{17.42}$$

$$\gamma \ = \ \frac{U_1 + U_2 - 2c}{\Delta U} \tag{17.43}$$

JMB to ⇑

These two equations form a homogeneous system of coupled linear equations for the constants A and B, the solution of which is trivially $A = B = 0$ unless the determinant of the system vanishes. This occurs when

$$R^2k^2(1 + R^2k^2)\ \left(\frac{U_1 + U_2 - 2c}{\Delta U}\right)^2 \ - \ 2\frac{\beta_0 R^2}{\Delta U}(1 + 2R^2k^2)\ \left(\frac{U_1 + U_2 - 2c}{\Delta U}\right) \\ + \ 4\frac{\beta_0^2 R^4}{\Delta U^2} \ + \ R^2k^2(1 - R^2k^2) \ = \ 0, \tag{17.44}$$

the solution of which is

$$\frac{U_1 + U_2 - 2c}{\Delta U} \ = \ \frac{\beta_0 R^2}{\Delta U}\ \frac{2R^2k^2 + 1}{R^2k^2(R^2k^2 + 1)} \\ \pm \ \frac{1}{R^2k^2(R^2k^2 + 1)} \sqrt{\frac{\beta_0^2 R^4}{\Delta U^2} - R^4k^4(1 - R^4k^4)}\,. \tag{17.45}$$

It is clear from this equation that the phase c of the wave is real as long as the quantity under the square root is positive, that is, as long as the wavenumber k satisfies the condition:

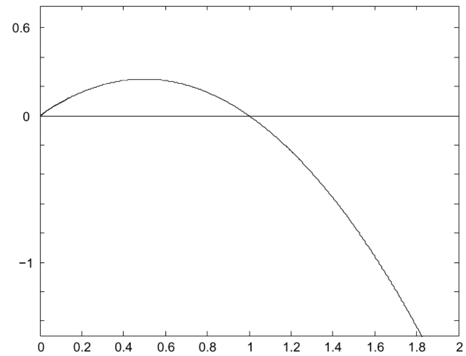

Figure 17-6 Instability interval for two-layer baroclinic instability. Small-amplitude waves with wavenumber k falling in the hatched interval are unstable and grow in time.

$$R^4k^4(1 - R^4k^4) \ \leq \ \left(\frac{\beta_0 R^2}{\Delta U}\right)^2 . \tag{17.46}$$

The function $R^4k^4(1 - R^4k^4)$ reaches a maximum of $1/4$ for $Rk = 1/2^{1/4} = 0.841$ (Figure 17-6), and therefore the condition is met for a perturbation of any wavenumber as long as

$$|\Delta U| \ \leq \ 2\beta_0 R^2 \ = \ \frac{\beta_0 g' H}{2 f_0^2} . \tag{17.47}$$

In other words, the system is stable to all small perturbations when the velocity shear ΔU is sufficiently weak not to exceed $2\beta_0 R^2$. Put another way, shear is destabilizing (because the greater ΔU, the higher the likelihood that the threshold value will be exceeded), whereas the beta effect is stabilizing (because the greater β_0, the more generous the threshold).

When the velocity shear exceeds the threshold value, condition (17.47) is not met, and not all wavenumbers do satisfy condition (17.46). Perturbations of wavenumber $k = \sqrt{k_x^2 + k_y^2}$ within the interval $k_{\min} < k < k_{\max}$ are unstable, where

$$k_{\min} \ = \ \left(\frac{1 - \sqrt{1 - 4\beta_0^2 R^4/\Delta U^2}}{2R^4}\right)^{1/4} \tag{17.48a}$$

$$k_{\max} \ = \ \left(\frac{1 + \sqrt{1 - 4\beta_0^2 R^4/\Delta U^2}}{2R^4}\right)^{1/4} . \tag{17.48b}$$

JMB from ⇓ At smaller scales, when the beta effect may be neglected (f-plane approximation, $f = f_0$), $k_{\max} \to 1/R$

JMB to ⇑ all perturbations of wavenumber k satisfying

$$k \ < \ \frac{1}{R} \ = \ \frac{2f}{\sqrt{g'H}} \tag{17.49}$$

are unstable. The corresponding criterion on the wavelength $\lambda = 2\pi/k$ is

$$\lambda \; > \; 2\pi \, R \; = \; 3.142 \, \frac{\sqrt{g'H}}{f} \; . \tag{17.50}$$

Thus, all perturbations of wavelength exceeding 6.283 times the deformation radius, as defined in (17.29) contribute to take the system away from the initial state.

Until finite-amplitude, nonlinear effects become important, the perturbation that distorts the system most is expected to be the one with the greatest initial growth rate, $\Im(\omega)$. This wave has the wavenumber $k = 1/(2^{1/4}R) = 0.841/R$ and has the wavelength

$$\lambda \; = \; 7.472 \, R. \tag{17.51}$$

JMB from ⇓

Benoit: Are you sure? β appears in the square root but not here?? Maybe again on f-plane, but even there I do not find this solution. For me, the maximum of the growth kc_i is obtained for $k^2R^2 = \sqrt{2}-1$:

On the f-plane, for the unstable case: $c = c_r + \mathrm{i}\, c_i$, $c_r = \frac{U_1+U_2}{2}$

$$c_i = \frac{\Delta U}{2} F(\kappa), \quad F(\kappa) = +\frac{1}{\kappa(1+\kappa)}\sqrt{\kappa^2(1-\kappa^2)} \tag{17.52}$$

(we keep the positive value, corresponding to an unstable mode) and $U_1 - c = \frac{\Delta U}{2}(1 - \mathrm{i}\, F(\kappa))$ and $U_2 - c = -\frac{\Delta U}{2}(1 + \mathrm{i}\, F(\kappa))$

From (17.40a) we also have

$$\frac{B}{A} = \mathrm{i}\, F(\kappa) \tag{17.53}$$

Hence (17.59) and (17.60) read

$$\frac{D_1}{D_2} = -\left(\frac{1+\mathrm{i}\, F}{1-\mathrm{i}\, F}\right)^2 \tag{17.54}$$

$$\frac{\phi_1}{\phi_2} = \frac{1+\mathrm{i}\, F}{1-\mathrm{i}\, F} \tag{17.55}$$

This is true for all unstable modes. For $\kappa = \sqrt{1/2}$, $F = \sqrt{2}-1$ and we obtain + 45 an -90 degrees phase shift. This is the case you consider later. But the most unstable mode is found when kc_i is maximum or equivalently when $\sqrt{\kappa}F(\kappa)$ is maximum. This is the case when $\kappa = \sqrt{2}-1$.

Did I miss something?? Your case of fastest growing wave used later is rater the case maximum instability in the sense that for increasing ΔU (increasing the thermal wind), it is this wave that appears the first on the beta plane. But then the rest of the analysis does not use beta effect any more.

In any case, switching beta on and off too many times can be difficult to follow (just below you switch it on again). I would suggest to move (17.56) with comment just after (17.48) and then look at smaller scales from there on, neglecting beta effect for the rest of the section. JMB to ⇑

Note that unstable waves not only grow but also propagate in time. According to (17.45),

$$\Re(c) \; = \; \frac{U_1+U_2}{2} \; - \; \frac{\beta_0}{2k^2} \, \frac{1+2R^2k^2}{1+R^2k^2} \tag{17.56}$$

when c is complex, and thus the zonal propagation speed is $(U_1 + U_2)/2$, or the average velocity of the basic flow, minus a (westward) planetary wave speed.

It is interesting at this point to return to our initial considerations (Section 17.3) and to confirm them with the preceding solution. First and foremost, the fact that the critical wavelength for instability ($2\pi R$) and the wavelength of the fastest-growing perturbation ($7.472R$) are both proportional to R validates the argument that self-amplification requires a scale on the order of the deformation radius. Physically, it also verifies that the instability process involves a rearrangement of potential vorticity between relative vorticity and vertical stretching. The necessary phase relationship between the transverse displacements of the upper and lower fluids can be checked as follows. We define the transverse displacement d in terms of the meridional velocity by

$$v' \; = \; \frac{\partial d}{\partial t} \; + \; \bar{u} \, \frac{\partial d}{\partial x} \; , \tag{17.57}$$

after linerization. Expressing v' in terms of the streamfunction perturbation ($v' = \partial\psi'/\partial x$) and implementing the wave form $d_i = \Re[D_i \exp \mathrm{i}\,(k_x x + k_y y - \omega t)]$, we then obtain

$$D_i \; = \; \frac{\phi_i}{U_i - c} \; , \tag{17.58}$$

from which we can deduce the ratio of the transverse displacements in the upper and lower layers:

$$\frac{D_1}{D_2} \; = \; \frac{U_2 - c}{U_1 - c} \, \frac{A + B}{A - B} \; . \tag{17.59}$$

For the fastest growing wave on the f-plane in the case $U_1 > U_2$ (*i.e.*, $\Delta U > 0$), the wavenumber is $k = 0.841/R$, the wave speed is $c = (U_1 + U_2)/2 + 0.207\mathrm{i}\,\Delta U$, the two wave amplitudes are related by $B = +0.414\mathrm{i}\,A$, and the ratio of displacements is found to be:

$$\begin{aligned} \frac{D_1}{D_2} \; &= \; -\mathrm{i} \\ &= \; \cos(-90^\circ) + \mathrm{i} \;\; \sin(-90^\circ). \end{aligned} \tag{17.60}$$

Physically, the negative 90° angle corresponds to a quarter-wavelength advance (in the direction of the basic flow) of the top displacement over that in the bottom layer. The quadrature phase shift is the one anticipated from the simple physical argument of the previous section.

From an observational point of view, however, the interest lies in the pressure field, which is proportional to the streamfunction [see (17.32c)]. Within an arbitrary multiplicative constant, which the linear theory is unable to determine, the pressure field associated with the fastest growing perturbation can be expressed in terms of the vertical structure of the streamfunction perturbation:

$$\begin{aligned} \frac{\phi_1}{\phi_2} \; &= \; \frac{A + B}{A - B} \\ &= \; \frac{1 + (\sqrt{2} - 1)\mathrm{i}}{1 - (\sqrt{2} - 1)\mathrm{i}} \; = \; \cos(45^\circ) + \mathrm{i} \;\; \sin(45^\circ). \end{aligned} \tag{17.61}$$

From this, we conclude that the crests and troughs of the pressure pattern at the top lag those of the bottom pattern by an eighth of a wavelength.

17.5 Heat transport

The qualitative arguments developed in Section 17.3 revolved around the idea that if a flow in thermal-wind equilibrium is unstable, it will seek a level of lower energy by relaxation of the density surfaces toward static equilibrium. If we now think of the atmosphere, where the heavier fluid is colder air and the lighter fluid warmer air, relaxation implies a flow of warm air toward the colder side ($+y$–direction in Figure 17-3) and of cold air to the warmer side ($-y$–direction in Figure 17-3). In other words, we expect a net heat flux and, because the atmospheric temperature increases toward the equator, a poleward heat flux. Let us examine what the preceding linear theory predicts.

The heat flux in the y–direction per unit length of the x–direction is defined as

$$q \;=\; \rho_0 C_p \int_0^H \overline{vT}\; dz, \tag{17.62}$$

where C_p is the heat capacity at constant pressure (1005 J/kg°C for air, 4186 J/kg°C for seawater), T is temperature, and an overbar indicates an average over a wavelength in the x–direction. In the two-layer representation of Figure 17-5, the vertical integration is straightforward:

$$\begin{aligned} q &= \rho_0 C_p \left[\overline{v_1 T_1 (H_1 - a)} + \overline{v_2 T_2 (H_2 + a)}\right] \\ &= \rho_0 C_p \left[\overline{v_2 a}\, T_2 - \overline{v_1 a}\, T_1\right]. \end{aligned} \tag{17.63}$$

since the temperature is uniform within each layer and the integral over a wavelength yields $\overline{v_1} = 0$ and $\overline{v_2} = 0$. Using $v_i = v_i' = \partial\psi_i'/\partial x$ and $a = f_0(\psi_2' - \psi_1')/g'$, we have , exploiting $\overline{\partial\psi_2^2/\partial x} = 0$ and $\overline{\partial(\psi_2\psi_1)/\partial x} = 0$ JMB from ⇓ JMB to ⇑ JMB from ⇓ JMB to ⇑

$$\begin{aligned} q &= \frac{\rho_0 C_p f_0}{g'} \left[T_2\, \overline{\frac{\partial\psi_2'}{\partial x}(\psi_2' - \psi_1')} - T_1\, \overline{\frac{\partial\psi_1'}{\partial x}(\psi_2' - \psi_1')}\right] \\ &= \frac{\rho_0 C_p f_0}{g'} \left[-T_2\, \overline{\psi_1' \frac{\partial\psi_2'}{\partial x}} - T_1\, \overline{\psi_2' \frac{\partial\psi_1'}{\partial x}}\right] \\ &= \frac{\rho_0 C_p f_0}{g'}\, (T_1 - T_2)\, \overline{\psi_1' \frac{\partial\psi_2'}{\partial x}}. \end{aligned} \tag{17.64}$$

Some rather lengthy algebra using the periodic structure (17.37) and the modal decomposition (17.39) successively provides:

$$\overline{\psi_1' \frac{\partial \psi_2'}{\partial x}} = \frac{k_x}{2} \left[\Im(\phi_1)\, \Re(\phi_2) - \Re(\phi_1)\, \Im(\phi_2)\right] \mathrm{e}^{2\Im(\omega)t}$$
$$= k_x \left[\Re(A)\, \Im(B) - \Im(A)\, \Re(B)\right] \mathrm{e}^{2\Im(\omega)t}.$$

JMB from ⇓ ??e or e everywhere??

JMB to ⇑ The real and imaginary parts of equation (17.40a) are

$$\left[2\beta_0 - k^2(U_1 + U_2 - 2c_r)\right] \Re(A) - k^2 c_i\, \Im(A) = k^2 \Delta U\, \Re(B)$$
$$\left[2\beta_0 - k^2(U_1 + U_2 - 2c_r)\right] \Im(A) + k^2 c_i\, \Re(A) = k^2 \Delta U\, \Im(B),$$

where c_r and c_i stand respectively for the real and imaginary parts of c. From these relations, it follows that

$$\Re(A)\, \Im(B) - \Im(A)\, \Re(B) = \frac{c_i}{\Delta U}\, |A|^2. \tag{17.65}$$

Putting it altogether we finally obtain the expression of the heat flux

$$q = \frac{\rho_0 C_p f_0 k_x}{g'} \frac{c_i}{\Delta U} (T_1 - T_2)\, |A|^2\, \mathrm{e}^{2\Im(\omega)t}$$
$$= \frac{\rho_0 C_p f_0 k_x}{\alpha g} \frac{c_i}{\Delta U}\, |A|^2\, \mathrm{e}^{2\Im(\omega)t}, \tag{17.66}$$

JMB from ⇓ where α is the thermal expansion coefficient ($\alpha = 1/T_0$ for air). **Benoit:?** I do not understand. For uniform temperature there is no heat flux yet with the last formula there is one???

JMB to ⇑ I would drop the last equation?

It is clear from this expression that the heat flux is nonzero only when the wave is unstable ($c_i \neq 0$) and is positive, as anticipated by the earlier schematic description. In the atmospheric case, this means that the heat flux is poleward.

Because the earth is heated in the tropics and cooled at high latitudes, the global heat budget requires a net poleward heat flux in each hemisphere. The flux is carried by both atmosphere and ocean. In the atmosphere, the higher temperatures in the tropics and lower temperatures at high latitudes maintain an overall thermal wind system, which is baroclinically unstable. Vortices emerge on the scale of the baroclinic radius of deformation ($R \sim$ 1000 km), which carry the heat poleward and tend to relax the thermal-wind structure. The latter, however, is maintained by continuous heating in the tropics and cooling at high latitudes. As a consequence, the cyclones and anticyclones of our weather are the primary agents of meridional heat transfer in the atmosphere. Without baroclinic instability, they would not exist and weather forecasting would be a much simpler task, but the tropical regions would be much hotter and the polar regions, much colder. Also, the dominance of zonal winds would preclude efficient mixing across latitudes, exacerbating certain problems by severely limiting, for example, the spread of volcanic ash. Moreover, less atmospheric variability would imply greatly reduced temperature and moisture contrasts and thus much less precipitation at midlatitudes. All in all, we must concede that baroclinic instability in our atmosphere is highly beneficial.

In the ocean, the situation is quite different. The pressure of meridional boundaries prevents thermal-wind-type currents from encircling the globe, and ocean circulation consists of large-scale gyres (Chapter 20). The meridional branches of these gyres, especially the western boundary currents (Gulf Stream in the North Atlantic, Kuroshio in North Pacific), are the main conveyers of heat toward high latitudes. A Reference ? This greatly reduces the need for poleward heat transfer by eddies. Baroclinic instability is active in regions of strong currents, such as the Gulf Stream and Kuroshio extensions in the deep ocean but the eddies so created transport little net heat across latitudes. JMB from ⇓ JMB to ⇑

17.6 Bulk criteria

The theory exposed in Section 17.4 is admittedly a very simplified version of baroclinic-instability physics. Since it is not our purpose here to review the many advanced analyses that have been published over the years since the pioneering studies of Charney, Eady and Phillips (the interested reader will find a survey in the book of Pedlosky, 1987), we will once again turn to integral relations, from which some necessary but not sufficent criteria for instability can be derived. We already used this approach in the study of horizontally sheared currents in homogeneous fluids (Section 10.2) and of vertically sheared currents in nonrotating stratified fluids (Section 14.2). Although a general presentation that would encompass the preceding two situations as well as baroclinic instability could be formulated, it is most instructive to emphasize the conditions necessary for baroclinic instability by basing the analysis on the quasi-geostrophic equation[5]. The following derivations are based on the work by Charney and Stern (1962).

We start again with equations (17.27) but this time retain continuous variation in the vertical yet uniform stratification frequency. Adding a small perturbation to a basic zonal flow $\bar{u}(y,z)$, possessing both horizontal and vertical shear, we obtain JMB from ⇓ JMB to ⇑

$$\frac{\partial q'}{\partial t} + J(\bar{\psi},\, q') + J(\psi',\, \bar{q}) = 0 \tag{17.67a}$$

$$q' = \nabla^2\psi' + \frac{f_0^2}{N^2}\frac{\partial^2\psi'}{\partial z^2}\,, \tag{17.67b}$$

where $\bar{\psi}(y,z)$ is the streamfunction associated with the basic zonal flow ($\bar{u} = -\partial\bar{\psi}/\partial y$), and the basic potential vorticity is related to it by:

$$\bar{q} = \frac{\partial^2\bar{\psi}}{\partial y^2} + \frac{f_0^2}{N^2}\frac{\partial^2\bar{\psi}}{\partial z^2} + \beta_0 y. \tag{17.68}$$

Substitution of (17.67b) and (17.68) into (17.67a) yields a single equation for the streamfunction perturbation ψ', which includes non-constant coefficients depending on the basic flow structure via $\bar{\psi}$ and $\bar{q}$. Because those coefficients depend only on y and z, a waveform solution in x and time can be sought: $\psi'(x,y,z,t) = \Re[\phi(y,z)\exp(\mathrm{i}\,k_x(x-ct))]$. The amplitude function $\phi(y,z)$ must obey

[5] Actually, this equation eliminates the Kelvin–Helmholtz instability but not the barotropic instability.

$$\frac{\partial^2\phi}{\partial y^2} + \frac{f_0^2}{N^2}\frac{\partial^2\phi}{\partial z^2} + \left(\frac{1}{\bar{u}-c}\frac{\partial\bar{q}}{\partial y} - k_x^2\right)\phi = 0, \tag{17.69}$$

where $\bar{q}$ is defined in (17.68).

The upper and lower boundaries are once again idealized to rigid horizontal surfaces, where the vertical velocity must vanish. According to (16.17c), this implies after splitting between basic flow and perturbation, and linearizing:

$$(\bar{u}-c)\frac{\partial\phi}{\partial z} - \frac{\partial\bar{u}}{\partial z}\phi = 0 \qquad \text{at} \qquad z = 0,\ H. \tag{17.70}$$

In the meridional direction, we idealize the domain to a channel of width L between two vertical walls, where the meridional velocity $v' = \partial\psi'/\partial x$ vanishes. We thus impose

$$\phi = 0 \qquad \text{at} \qquad y = 0,\ L. \tag{17.71}$$

Multiplying (17.69) by the complex conjugate ϕ^* of ϕ, integrating over the meridional and vertical extents of the domain, performing integrations by parts, and using the preceding boundary conditions, we obtain

$$\begin{aligned}\int_0^H\int_0^L \left[\left|\frac{\partial\phi}{\partial y}\right|^2 + \frac{f_0^2}{N^2}\left|\frac{\partial\phi}{\partial z}\right|^2 + k_x^2|\phi|^2\right] dy\,dz \\ = \int_0^H\int_0^L \frac{1}{\bar{u}-c}\frac{\partial\bar{q}}{\partial y}|\phi|^2\,dy\,dz \\ + \int_0^L\left[\frac{f_0^2}{N^2}\frac{1}{\bar{u}-c}\frac{\partial\bar{u}}{\partial z}|\phi|^2\right]_0^H dy.\end{aligned} \tag{17.72}$$

The imaginary part of this equation is

$$c_i\left\{\int_0^H\int_0^L \frac{|\phi|^2}{|\bar{u}-c|^2}\frac{\partial\bar{q}}{\partial y}\,dy\,dz + \int_0^L\left[\frac{f_0^2}{N^2}\frac{|\phi|^2}{|\bar{u}-c|^2}\frac{\partial\bar{u}}{\partial z}\right]_0^H dy\right\} = 0. \tag{17.73}$$

A necessary condition for instability is that c_i not be zero (so that the disturbance grows in time). According to (17.73), this implies that the quantity within braces must vanish, and therefore conditions for instability are

1. $\partial\bar{q}/\partial y$ changes sign in the domain, or
2. the sign of $\partial\bar{q}/\partial y$ is opposite to that of $\partial\bar{u}/\partial z$ at the top, or
3. the sign of $\partial\bar{q}/\partial y$ is the same as that of $\partial\bar{u}/\partial z$ at the bottom.

A sufficient condition for stability is that none of the above three conditions is met.

Before proceeding, it is worth applying this result to the case of a uniform shear flow $\bar{u} = Uz/H$ and in the absence of the beta effect ($\beta_0 = 0$). We then $\bar{q} = 0$ and $\partial\bar{u}/\partial z = U/H$, and (17.73) reduces to

$$c_i \int_0^L \frac{f_0^2 U}{N^2 H} \left[\frac{|\phi(y,H)|^2}{|U-c|^2} - \frac{|\phi(y,0)|^2}{|c|^2} \right] dy = 0, \tag{17.74}$$

in which the integral is obviously not sign definite. Stability cannot be guaranteed, and this flow is unstable (Eady, 1949). Had we instead chosen a weak flow field with no vertical shear at the boundaries [*e.g.*, $\bar{u}(z) = U(3z^2/H^2 - 2z^3/H^3)$] and on the beta plane ($\partial \bar{q}/\partial y \simeq \beta_0$), we would have concluded (after much lengthier mathematics) that this flow is stable to all perturbations. This points to the sensitivity of baroclinic instablity to the type of flow field. Another application of (17.73) is to laterally sheared but vertically uniform flow, $\bar{u}(y)$. Then, the potential-vorticity gradient is $\partial \bar{q}/\partial y = \beta_0 - \partial^2 \bar{u}/\partial y^2$ and (17.73) reduces to

$$c_i \left[H \int_0^L \frac{|\phi|^2}{|\bar{u}-c|^2} \left(\beta_0 - \frac{\partial^2 \bar{u}}{\partial y^2} \right) dy \right] = 0. \tag{17.75}$$

Here, we recover the result of barotropic instability obtained in Section (10.2) [see equation (10.13)]. We conclude that the instability conditions stated previously include both barotropic and baroclinic instability criteria. Put another way, barotropic and baroclinic instabilities are two end members of a more general barotropic-baroclinic mixed instability.

Charney and Stern (1962) explored the case when $\partial \bar{u}/\partial z$ vanishes at both upper and lower boundaries by assuming a vanishing thermal-wind there (*e.g.*, uniform temperature) and/or taking the limits $H \to \infty$, $\bar{u}(H) \to 0$. Of (17.73), only the first integral remains, and the necessary condtion for instability is that $\partial \bar{q}/\partial y$ vanish somewhere in the domain, a statement identical in form to — but differing in content from — the barotropic-instability criterion of Section 10.2.

According to Gill *et al.* (1974), the presence of a bottom slope in the meridional direction modifies the preceding third of the three conditions as follows:

3. The sign of $\partial \bar{q}/\partial y$ is the same as that of $\partial \bar{u}/\partial z - (N^2/f_0) d\bar{b}/dy$ at the bottom $z = \bar{b}(y)$.

Therefore, a bottom slope can act as either a stabilizing or destabilizing influence. It is generally a stabilizing factor if it creates an ambient potential-vorticity gradient in the same direction as the beta effect (*i.e.*, shallower fluid toward higher latitudes; see Figure 9-6) and a destabilizing factor otherwise. However, the theory fails to take into account the zonal topographic gradients that are more common on earth (*e.g.*, the Rocky Mountains in North America for the atmosphere and the Mid-Atlantic Ridge along the North Atlantic for the ocean). JMB from ⇓ JMB to ⇑

There exist a number of other studies in baroclinic instability. The interested reader is referred to Gill (1982, Chapter 13) and Pedlosky (1987, Chapter 7). JMB from ⇓ JMB to ⇑

17.7 Finite-amplitude development

Once instability is triggered, the exponential growth eventually leads to perturbations whose amplitudes are not small anymore compared to the base current. In this case the linear theory ceases to be valid and the fully non-linear equations should be solved. This can be done with numerical models using the QG approximation with definitions (17.31) and solving equations (17.30). These models can be based on the two-dimensional QG model of Section 16.6.

For the study of the baroclinic instability, we can exploit the fact that the base current is stationary to update only perturbations in the governing equations

$$\frac{\partial q_1'}{\partial t} \;+\; J(\psi_1, q_1) \;=\; 0 \tag{17.76}$$

$$\frac{\partial q_2'}{\partial t} \;+\; J(\psi_2, q_2) \;=\; 0 \tag{17.77}$$

where the Jacobian is calculated using the total streamfunction (base current and perturbations) and total potential vorticity.
Once new perturbations q_1' are known at the new time step, we have to invert a Poisson equation. This is more complicated than in the two-dimensional QG model of Chapter 16 because we are now in the presence of two coupled equations. To solve the problem, we may for example use the iterative Gauss-Seidel approach, working conjointly on ψ_1' and ψ_2'. Formally, omitting the $'$, at iteration $(k+1)$, we could update

$$\psi_1^{(k+1)} = \psi_1^{(k)} + \alpha \left[\nabla^2 \psi_1 - q_1 - \frac{(\psi_1^{(k)} - \psi_2^{(k)})}{2R^2} \right]$$

$$\psi_2^{(k+1)} = \psi_2^{(k)} + \alpha \left[\nabla^2 \psi_2 - q_2 + \frac{(\psi_1^{(k+1)} - \psi_2^{(k)})}{2R^2} \right]$$

where the operator ∇^2 is calculated using the most recent values of ψ on the grid. The parameter α contains discretization constants and overrelaxation parameters. This approach is easily implemented and generalized to more than two layers. For the present two-layer model, another option is to decouple the equations for q_1 and q_2 by decomposing them into the barotropic and baroclinic components. The sum and difference of the preceding equations indeed yields two uncoupled equations that can be solved independently, possibly with different pseudo-time steps.

For the numerical simulation of the baroclinic instability of Section 17.3, we have to provide adequate boundary conditions. Along x direction, the length of the domain is dictated by the wavelength whose stability is investigated and periodicity conditions are readily applied for both streamfunction and vorticity. For the y direction, contrary to the theoretical study, we will work in channel configuration, with prescribed streamfunction values on the boundaries, so as to enforce the thermal wind of the base current.

Benoit: I'm not sure here: for linearized perturbations, streamfunction ψ' must be zero on walls (because $\partial\psi/\partial x = 0$ translates for a wave structure into zero amplitude on the wall. But for finite amplitude, the value of the streamfunction could be different, translating the flattening of the interface due to the instability. Do you know how to calculate this elegantly?

Once the perturbations calculated, the total streamfunction and potential vorticity can be evaluated before the calculation of the Jacobian, see `baroclinic.m`. Then the next time step can be integrated. With this approach we can simulate the evolution of the wave (Figure 17-7).

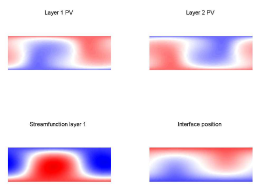

Figure 17-7 Evolution of a perturbed thermal wind **to be replaced**

Some description here

Analytical Problems

17-1. *A question or two on inertial instability.*

17-2. Demonstrate the assertion made at the end of Section 17.6 that the vertically sheared flow

$$\bar{u}(z) \;=\; U \left(3\,\frac{z^2}{H^2} \;-\; 2\,\frac{z^3}{H^3}\right)$$

in $0 \leq z \leq H$ is baroclinically stable on the beta plane if U falls below a critical value. What is that critical value?

17-3. Compare the magnitudes of the potential and kinetic energies of the most unstable wave described in Section 17.4.

17-4. Two-layer stability formulation with general profile of the interface $a(y)$

17-5.

17-6. Prove the assertion that the unstable regime of the wedge instability corresponds to particles moving along surfaces of slopes between geostrophic lines and isopycnals. *Hint:* Analyze the eigenvector $(\Delta x, \Delta z)$ of the system (17.14) with ω^2 corresponding to the unstable case.

17-7.

17-8.

17-9.

Numerical Exercises

17-1. Play with `baroclinic.m`.

17-2. Try adding β_0 and analyze the effect. (Take case from unstable to stable...)

17-3. Include possibility of more general interface profiles. Try with??

17-4. Include diagnostics on energy.

17-5. Program (17.45) and plot, as a function of ΔU, the wavenumber of maximum growth rate and the growth rate itself for different values of β_0 and R.

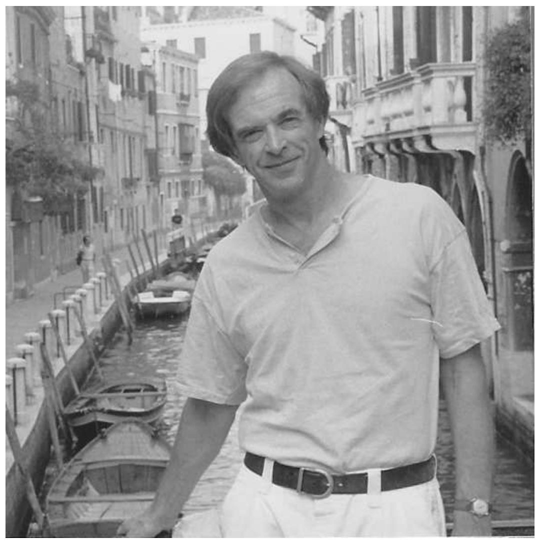

Joseph Pedlosky
1938 –

A student of J. G. Charney, Joseph Pedlosky first followed his mentor's footsteps and developed a fascination for baroclinic instability. He quickly became an authority in the subject, having derived new instability criteria and developed a nonlinear theory for growing baroclinic disturbances in nearly inviscid flow. He also made important contributions to the general theory of rotating stratified fluids, the oceanic thermocline, the Gulf Stream, and the general oceanic circulation. In 1979, Pedlosky published the first treatise on Geophysical Fluid Dynamics, which greatly helped codify the discipline.

Pedlosky's approach to research is first to find a problem that is simple enough to be solved completely, yet physically informative, and then to "worry a great deal about it until I could describe the results to an amateur." This incessant quest for clarity has won him great respect as a scientist and much admiration as a speaker. (*J. Pedlosky*)

Peter Broomell Rhines
19xx –

Text of second bio (*Here*)

Chapter 18

Fronts, Jets and Vortices

(October 18, 2006) **SUMMARY**: When the Rossby number is not small, the dynamics are nonlinear and non-quasigeostrophic. Such regimes exhibit fronts and jets, the latter being related to the former via pressure gradients. Strong jets meander and shed vortices, which also populate this dynamical regime. The chapter ends with a brief discussion of geostrophic turbulence, the state of many interacting vortices under the influence of Coriolis effects. This problem is particularly well suited to introduce spectral methods for nonlinear problems. JMB from ⇓ JMB to ⇑

18.1 Front and jets

18.1.1 Origin and scales

A common occurrence in the atmosphere and ocean is the encounter of two fluid masses that, due to separate origins, have distinct properties. The result is the existence of a local transitional region that is relatively narrow (compared to the dimensions of the main fluid masses) and where properties vary spatially much more rapidly than on either side. Such a region of intensified gradients of fluid properties is called a *front*.

Typically, the adjacent fluid masses have different densities, and the front is accompanied by a relatively large pressure gradient. Under the action of Coriolis forces, the process of geostrophic adjustment is at work, leading to a relatively intense flow aligned with the front. The much weaker density gradients in the main part of each fluid mass confine the motion to the frontal region, and the flow exhibits the form of a jet. The most notable jet in the atmosphere is the so-called polar-front jet stream found around a latitude of 45°N and a few kilometers above sea level (pressure around 300 millibars), at the boundary between subtropical and polar air masses (Figure 18-1). From the thermal-wind relation JMB from ⇓

$$f\frac{\partial u}{\partial z} = \frac{g}{\rho_0}\frac{\partial \rho}{\partial y} \tag{18.1}$$

we can readily understand the intense eastward flow at high altitude assuming velocity is small at sea level. Because of the general north-south gradient of temperature between the

JMB to ⇑

two air masses, the right-hand side is strong and positive and the wind accordingly intensifies with height and is directed eastward. In the ocean, a surface-to-bottom front is often found in the vicinity of the shelf break owing to different water properties above the continental shelf and in the deep ocean; such a front is invariably accompanied by currents along the shelf (Figure 18-2).

According to Section 15.1, the simultaneous presence of a horizontal gradient of density and a vertical gradient of horizontal velocity can yield a thermal-wind balance, which may persist for quite some time. Our earlier discussions of geostrophic adjustment (Section 15.2) demonstrated how such a balance can be achieved following the penetration of one fluid mass into another of different density and indicated that the width of the transitional region is measured by the internal radius of deformation, expressed as

$$R = \frac{NH}{f} \sim \frac{\sqrt{g'H}}{f} \tag{18.2}$$

JMB from ⇓

JMB to ⇑

in the respective cases of continuous stratification and layered configuration. Here f is the Coriolis parameter, H is an appropriate height scale assuming large excursions of isopycnals in frontal systems , N is the stratification frequency, and g' is a suitable reduced gravity. If the density difference between the fluid masses is $\Delta\rho$, the accompanying pressure difference is $\Delta P \sim \Delta\rho\, gH = \rho_0 g'H$, and, via geostrophy, the velocity scale is

$$U = \frac{\Delta P}{\rho_0 f R} \sim \frac{g'H}{fR} = \sqrt{g'H}\,. \tag{18.3}$$

JMB from ⇓

JMB to ⇑

and the internal radius of deformation can also be expressed as $R = U/f$, in which we recognize the inertial radius. Here both coincide because we assumed a frontal structure with $\Delta H = H$.

The Froude and Rossby numbers are, respectively

$$Fr = \frac{U}{NH} \sim \frac{\sqrt{g'H}}{fR} \sim 1, \tag{18.4}$$

$$Ro = \frac{U}{fR} \sim \frac{\sqrt{g'H}}{fR} \sim 1, \tag{18.5}$$

and thus both are on the order of unity, implying that the effects of stratification and rotation are equally important within the jet.

JMB from ⇓

JMB to ⇑

The jet has a velocity maximum, coinciding more or less with the location of the maximum density gradient, on both sides of which the velocity decays. The corresponding shears form a distribution of relative vorticity that is clockwise on the right and counterclockwise on the left (respectively, anticyclonic and cyclonic in the Northern Hemisphere). This shear vorticity scales as $Z = U/R \sim f$ and is thus comparable to the planetary vorticity. so that the total vorticity may change sign compared to the sign of f. Hence use of conservation of potential vorticity requires some care.

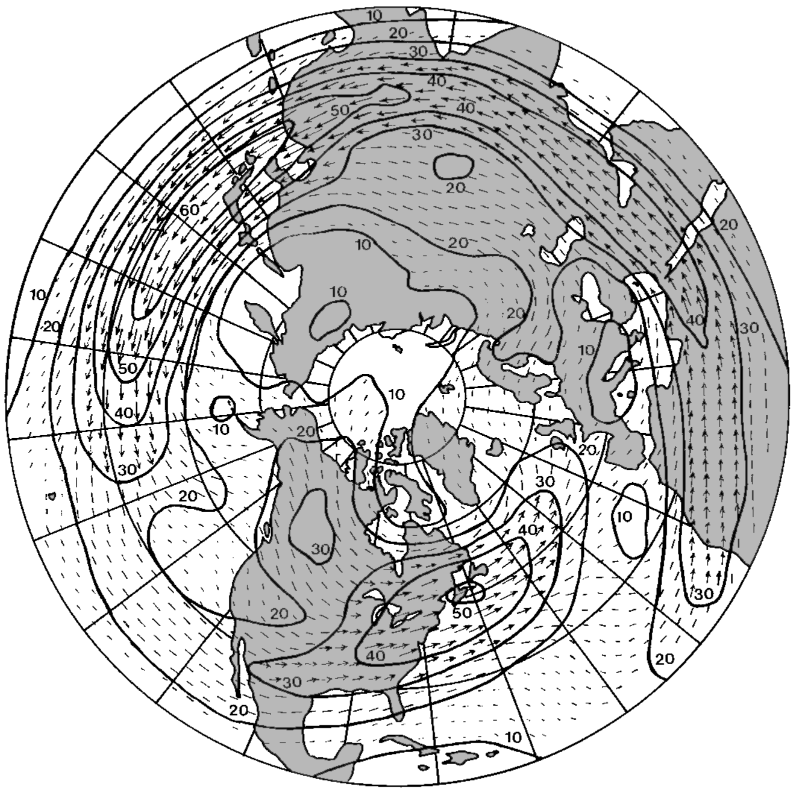

Figure 18-1 Monthly winds (in meters per second) over the Northern Hemisphere for January 1991 at the 300-mb pressure level. Note the jet stream around the 45°N parallel, except over the eastern North Pacific and eastern North Atlantic, where blockings are present. (From National Weather Service, NOAA, Department of Commerce, Washington, D.C.)

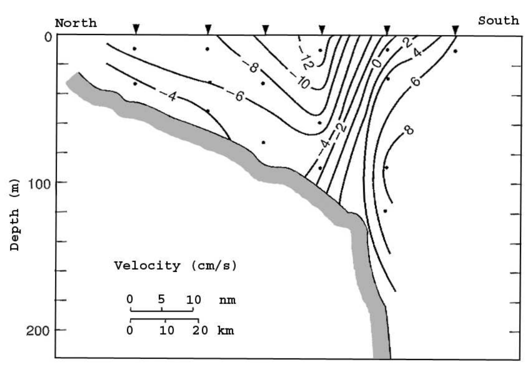

Figure 18-2 Monthly mean alongshelf currents for April 1979 across the shelf break on the southern flank of Georges Bank (41°N, 67°W). The units are centimeters per second, and positive values indicate flow pointing into the page. (From Beardsley *et al.*, 1983, as adapted by Gawarkiewicz and Chapman, 1992.)

18.1.2 Meanders

Observations reveal that all jets meander, unless they are strongly constrained by the local geography. As a fluid parcel flows in a meander, its path curves, subjecting it to a transverse centrifugal force on the order of $\mathcal{K}U^2$, where $\mathcal{K}$ is the local curvature of the trajectory (the inverse of the radius of curvature). This force can be met by a reduction or increase of the Coriolis force if the parcel's velocity adjusts by ΔU, such that $f\Delta U \sim \mathcal{K}U^2$, or

$$\frac{\Delta U}{U} \sim \frac{\mathcal{K}U}{f} \sim \mathcal{K}R. \tag{18.6}$$

JMB from ⇓

Note how the term $\mathcal{K}R$ measures the deformation radius compared to the meandering scale, the inverse of its curvature.

JMB to ⇑

In the Northern Hemisphere ($f > 0$), the Coriolis force acts to the right of the fluid parcel, and thus a rightward turn causing a centrifugal force to the left necessitates a greater Coriolis force and an acceleration ($\Delta U > 0$). Similarly, a leftward turn is accompanied by a jet deceleration ($\Delta U < 0$). The reverse conclusions hold for the Southern Hemisphere, but in each case, the stronger the curvature, the larger the change in velocity, according to (18.6).

JMB from ⇓

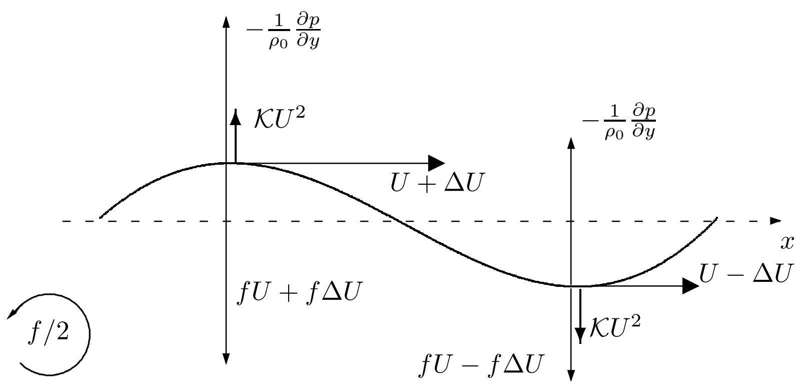

Figure 18-3 For the same pressure gradient, a rightward turn requires a larger velocity enabling Coriolis force to balance pressure and centrifugal force. For a left turn, the inverse applies.

JMB to ⇑

The same result can be obtained by considering the changes in relative vorticity. Neglecting for the moment the beta effect and vertical stretching or squeezing, the relative vorticity is conserved. It can be expressed locally as **Benoit:** Do you think this change of coordinates is familiar to students? Possible as exercise?

JMB from ⇓
JMB to ⇑
JMB from ⇓
JMB to ⇑
JMB from ⇓
JMB to ⇑

$$\zeta = \frac{\partial v}{\partial x} - \frac{\partial u}{\partial y} = \frac{\partial V}{\partial n} - \mathcal{K}V, \tag{18.7}$$

where $V = (u^2 + v^2)^{1/2}$ is the flow speed (scaled by U), n is the cross-jet coordinate (measured positively to the right of the local velocity and scaled by R), and $\mathcal{K}$ is the jet curvature (positive clockwise). The first term, $\partial V/\partial n$, is the contribution of the shear and the second, $-\mathcal{K}V$, represents a vorticity due to the turning of the flow path. We shall call these contributions shear vorticity and orbital vorticity, respectively. In a rightward turn ($\mathcal{K} > 0$), the fluid parcel acquires clockwise orbital vorticity, on the order of $\mathcal{K}U$, which must be at the expense of shear vorticity, $\Delta U/R$. Equating $\mathcal{K}U$ to $\Delta U/R$ again leads to (18.6). JMB from ⇓

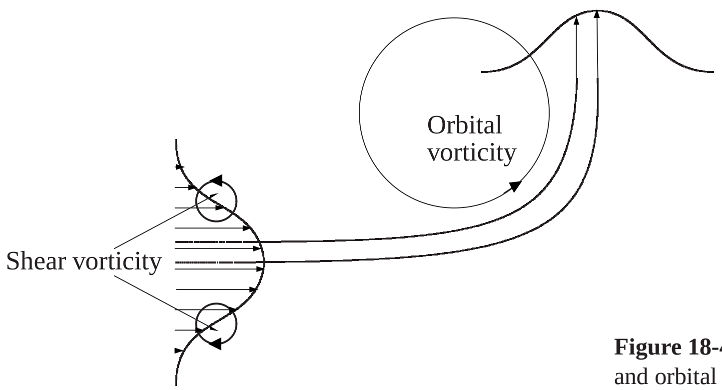

Figure 18-4 Difference between shear and orbital vorticity of a jet.

JMB to ⇑

The change in shear vorticity implies a shift of the parcel with respect to the jet axis. To show this, let us take for example, the fluid parcel that possesses the maximum velocity (*i.e.*, it is on the jet axis) upstream of the meander; there, it has no shear and no orbital vorticity. If this parcel turns to the right in the meander, it acquires clockwise orbital vorticity, which must be compensated by a counterclockwise shear vorticity of the same magnitude. Thus, JMB from ⇓ the parcel must now be on the left flank of the jet. The parcel occupying the jet axis (having JMB to ⇑ maximum velocity and thus no shear vorticity) is one that was on the right flank of the jet upstream and has exchanged its entire clockwise shear vorticity for an equal clockwise orbital vorticity. From this, it is straightforward to conclude that all parcels are displaced leftward with respect to the jet axis in a rightward meander, and vice versa. (This rule is easy to remember: Fluid parcels shift across the jet in the direction of the centrifugal force.)

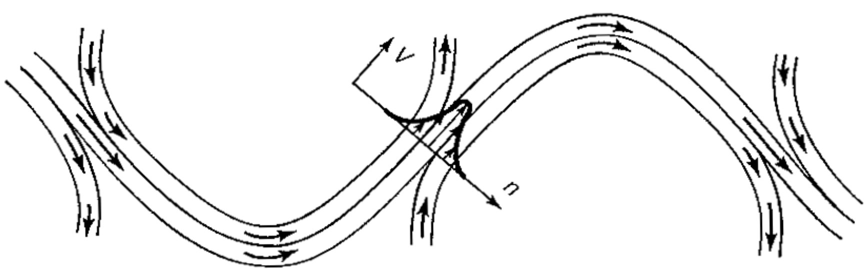

Figure 18-5 Separation and capture of fluid parcels along the sides of a meandering jet. This process occurs because the vorticity adjustment required by the meandering forces marginal parcels to reverse their velocity.

A consequence of these vorticity adjustments created by meandering is that fluid parcels near the edges may separate from the jet or be captured by it. Indeed, a parcel relatively distant from the jet axis may have such low vorticity that it cannot trade shear vorticity for orbital vorticity (Figure 18-5).

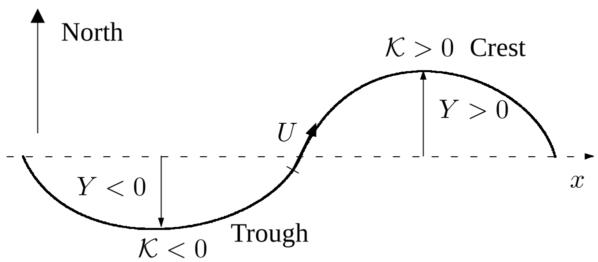

Figure 18-6 Meandering of an eastward jet on the beta plane (Northern Hemisphere). If the meridional displacement Y, curvature $\mathcal{K}$ and jet speed U are related by $\beta_0 Y \simeq \mathcal{K}U$, changes in planetary and orbital vorticity are comparable and opposite in sign, leaving the velocity profile of the jet (shear vorticity) relatively unperturbed.

The preceding considerations ignored the beta effect, by which the Coriolis force is able to vary. Let us limit ourselves here to the case of an eastward (*i.e.*, westerly) jet in the Northern Hemisphere, which is the case of the atmospheric jet stream and the Gulf Stream in the North Atlantic beyond Cape Hatteras. In a northern meander excursion, called a *crest* (because it appears higher on a map), the curvature is rightward or anticyclonic (Figure 18-6). The meridional displacement Y, the meander's amplitude, causes an augmentation to the Coriolis force on the order of $\beta_0 Y U$, acting to the right of the parcel. On the other hand, the centrifugal force on the order of $\mathcal{K}U^2$ acts to its left. Three cases are possible: $\beta_0 Y$ is much less than, on

JMB from ⇓ the order of, or much greater than $\mathcal{K}U$. **Benoit** I added itemize and changed a few phrasing

- If $\beta_0 Y$ is much less than $\mathcal{K}U$, we are in the presence of weak meander amplitudes (small Y) and/or short meander wavelengths (large $\mathcal{K}$). In this case the beta affect mitigates the curvature effect, but the conclusions derived before remain qualitatively unchanged.

- If $\beta_0 Y$ is on the order of $\mathcal{K}U$, then the beta and curvature effects can balance each other, leaving the structure of the jet barely affected. Considering sinusoidal meanders $Y(x) = A \sin k_x x$, where A is the meander amplitude, $\lambda = 2\pi/k_x$ is its wavelength, and x is the eastward coordinate, we deduce that at the meander's peak ($\sin k_x x = +1$), the meridional displacement Y is A and the curvature $\mathcal{K} = -[d^2Y/dx^2]/[1 + (dY/dx)^2]^{3/2}$ is $k_x^2 A$. The balance $\beta_0 Y \sim \mathcal{K}U$ then yields $\beta_0 \sim k_x^2 U$, or

$$\lambda = \frac{2\pi}{k_x} = 2\pi \sqrt{\frac{U}{\beta_0}}. \tag{18.8}$$

From this emerges a particular length scale,

$$L_\beta = \sqrt{\frac{U}{\beta_0}}, \tag{18.9}$$

which we shall call the *critical meander scale*. Cressman (1948) noted its importance in relation to the development of long waves on the atmospheric jet stream, whereas

Moore (1963) obtained a solution to an ocean-circulation model that exhibits meanders at that scale. Later, Rhines (1975) demonstrated how this same scale plays a pivotal role in the evolution of geostrophic turbulence on the beta plane.

- In very large meanders, where meridional displacements are large and curvatures are small ($\beta_0 Y \gg \mathcal{K}U$), the beta effect dwarfs the curvature effect, and the trade-off is almost exclusively between changes in planetary vorticity and shear vorticity. In a meander crest (greater f), the shear vorticity must become less cyclonic or more anticyclonic.

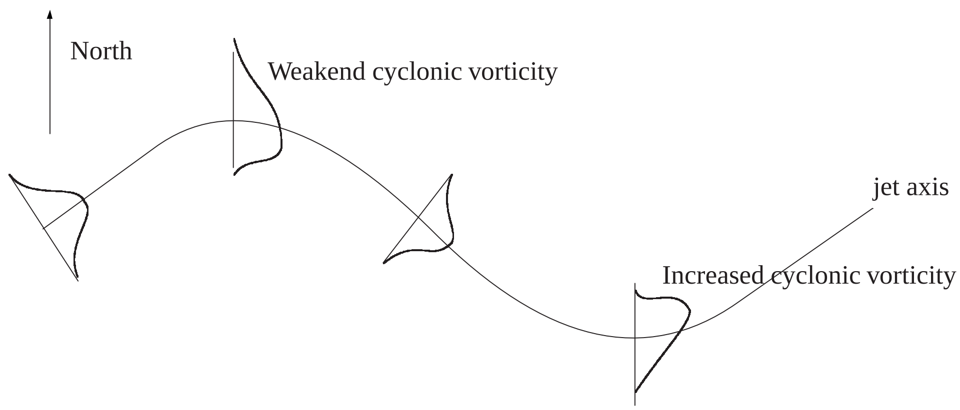

Figure 18-7 Benoit: is this picture correct?: Changes in jet profile induced by south-north displacements.

JMB to ⇑

Meanders on a jet do not remain stationary but propagate, usually downstream and rarely upstream. The direction of propagation can be inferred from vorticity considerations, as outlined previously. In the absence of the beta effect (or $\beta_0 Y \ll \mathcal{K}U$), leftward and rightward turns create, respectively, clockwise and counterclockwise shear vorticity. Picturing these vorticity anomalies as vortices at the meanders' tips (Figure 18-8a), we infer that the entrainment velocities at the inflection points between meanders all have a downstream component and that the meander pattern translates downstream. On a westerly jet, this direction is eastward. At the opposite extreme of a large beta effect and negligible curvature ($\beta_0 Y \gg \mathcal{K}U$), the vorticity anomalies are cyclonic in troughs and anticyclonic in crests (Figure 18-8b). The entrainment velocities at the inflection points all point westward. On a westerly jet, this is upstream. This mechanism is the same as that invoked in Section old6-6 to explain the westward phase propagation of planetary waves. (Compare Figure 18-8b with Figure 9-7)

We note, therefore, that curvature and beta effects induce opposite meander-propagation tendencies on an eastward jet. Comparing $\beta_0 Y$ with $\mathcal{K}U$ — or, equivalently, the wavelength to the critical meander scale — we conclude that if the former is larger than the latter, the meander propagates upstream (westward), and in the opposite direction otherwise. The meander is stationary if the tendencies cancel each other, which occurs if its wavelength is near the critical meander scale. Since this scale is rather long (220 km in the ocean and 1600 km in the atmosphere, with $\beta_0 = 2 \times 10^{-11}$ m^{-1}s^{-1} and U ranging from 1 m/s to 50 m/s), observed meanders are usually of the curvature-type and propagate eastward.

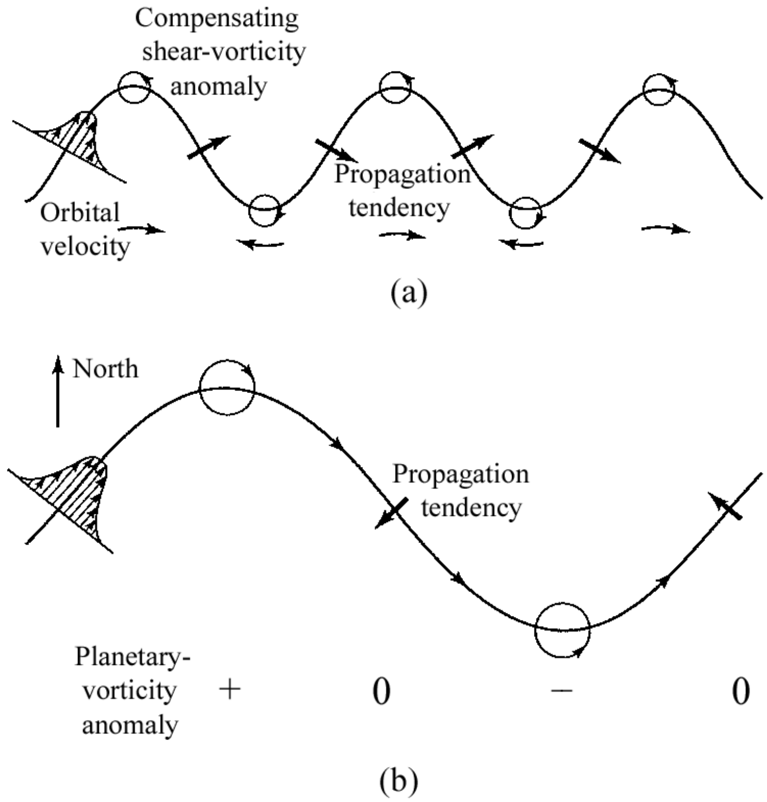

Figure 18-8 Schematic descriptions explaining why (a) curvature and (b) beta effects on an eastward jet induce meander-propagation tendencies that are, respectively, downstream and upstream.

18.1.3 Multiple equilibria

Because the critical meander scale depends on the jet speed U and also because the relation $\beta_0 Y \sim \mathcal{K} U$ depends on the shape of the meander (Y and $\mathcal{K}$ are not simply related if the meander is other than sinusoidal), the critical size for meander stationarity depends on the jet speed and the meander shape. This conclusion is the basis of one explanation for the bimodality of the Kuroshio (Figure 18-9). The geography of coastal Japan and the regional bottom topography force this intense current of the western North Pacific to pass through two channels, south of Yakushima Island (30°N, 134°E) and between Miyake and Hachijo
JMB from ⇓ Islands near the Izu Ridge (34°N, 140°E). **Benoit:** Are you sure about the coordinates? On the figure this does not look rigth. Maybe indicate Yakushima, Miyake and Hachijo Island
JMB to ⇑ on the map?

Between these two points, the current is known to assume one of two preferential states: a relatively straight path or a curved path with a substantial southward excursion. Each pattern persists for several years, whereas the transition from one to the other is relatively brief. The theory (Robinson and Taft, 1972; Masuda, 1982) explains this bimodal character by arguing that a stationary meander with a half-wavelength meeting the geographical specification may or may not exist, depending on the jet velocity. Calculations show that the meander-state occurs if the jet velocity does not exceed a certain threshold value. At any velocity below this value, there exists a stationary-meander shape that meets the geographical constraints. At larger velocities, no stationary meander is possible, and the jet must assume a straight path.

The atmospheric analogue of this oceanic situation is known as *blocking*, a word now used in a sense different from that used in Chapter 11. Here, blocking is a midlatitude phenomenon characterized by the unusual persistence of a nearly stationary meander on an eastward jet over topographic irregularities (Figure 18-1). The theory (Charney and DeVore, 1979; Charney and Flierl, 1981) again invokes multiplicity of equilibrium solutions, including the normal state (no meander) and the anomalous blocking configuration (with large meander).

18.1.4 Stretching and topographic effects

Up to here, our considerations of vorticity adjustments in a jet meander included exchanges among planetary, shear, and orbital vorticity, for an unchanged total. This is correct only for barotropic jets over a flat bottom, whereas in a baroclinic jet, in which vertical stretching can JMB from ⇓
occur, potential vorticity rather than vorticity is the conserved quantity. JMB to ⇑

A complete theory involving all relevant dynamics such as momentum and mass balances is beyond our scope, and we will derive here only the vertical-stretching tendency experienced by a fluid parcel in a meander. Assuming that the trade-off is solely between orbital vorticity due to the meander's curvature and vertical stretching, we reason that a meander crest (with anticyclonic orbital vorticity) lowers the total vorticity and thus calls for a proportional decrease in the column's vertical thickness. If, furthermore, the layer thickness varies like pressure (as for the one-layer reduced-gravity system where the pressure is given by $p = g'h$), vertical squeezing creates a lower pressure and, by geostrophy, a shift toward the JMB from ⇓
cyclonic side of the jet (left in the Northern Hemisphere). In meander troughs, fluid columns are vertically stretched and shifted toward the anticyclonic side of the jet. **Benoit:** Not very clear to me. Maybe a little more text: For a eastward flow, h is lower in the northern part of the jet. If by squeezing in a crest, h decreases, let us say in the middle of the jet, the layer gradient and front is displaced to the south and hence the parcel itself displaced to the northern or anticyclonic side compared to the new jet center. In an oceanic surface jet such as the JMB to ⇑
Gulf Stream, such a modification causes upwelling upon approaching crests and downwelling upon approaching troughs. Observations (Bower and Rossby, 1989) confirm such behavior, which can also be observed in numerical simulations (Figure 18-10). JMB from ⇓

Just as meanders generate vertical stretching or squeezing, vertical stretching or squeez- JMB to ⇑
ing induced by topography can cause meanders. To illustrate this, let us consider the case of a zonal jet (barotropic or baroclinic) on the beta plane that encounters a topographic step (Figure 18-11). If the jet is flowing eastward (the usual situation) and enters a deeper region, the expansion in layer thickness translates first into a cyclonic deflection, away from the equator. As the Coriolis parameter increases away from the equator, this cyclonic vorticity is progressively exchanged downstream by a greater planetary vorticity, and the jet curvature weakens. Further poleward progression reverses the sense of orbital vorticity, and the jet oscillates back

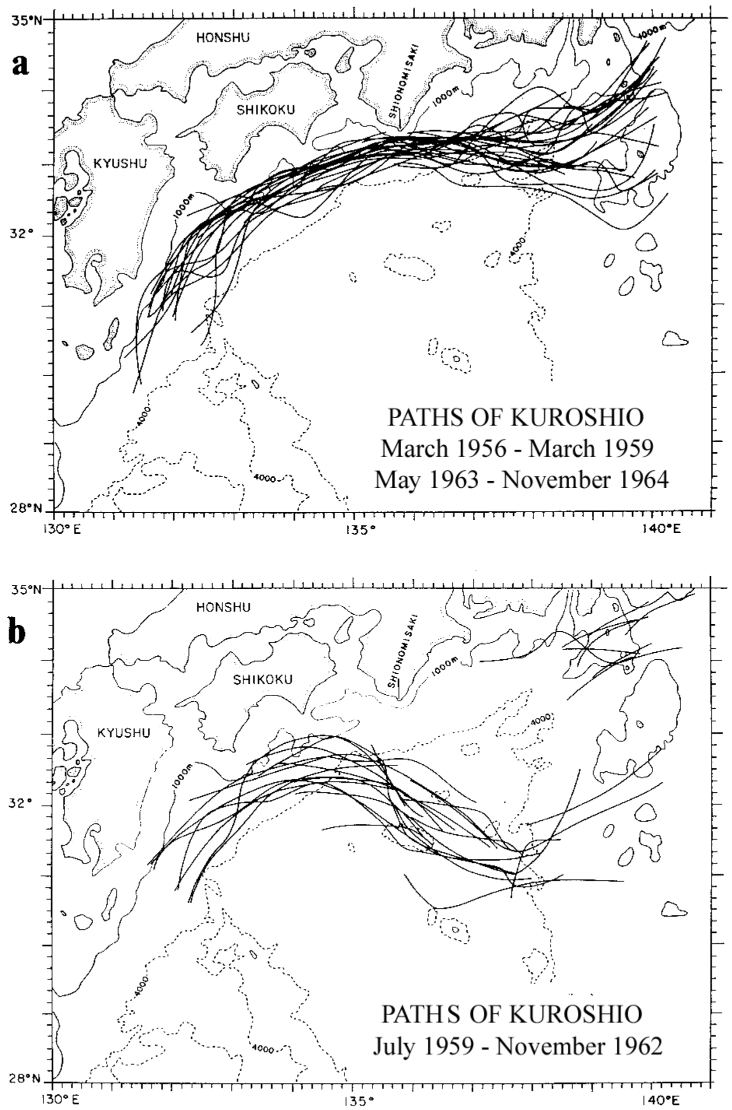

Figure 18-9 Observed Kuroshio paths: (a) straight jet and (b) stationary meander. (From Robinson and Taft, 1972)

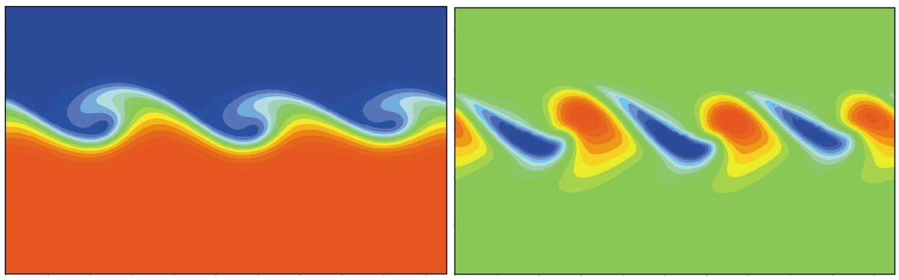

Figure 18-10 Frontal meander on a sea-surface temperature field (left panel) and associated upwelling or downwelling cells (right panel). Note the maximum vertical velocities centered between the meander's crest and troughs (from Rixen *et al.* 2001).

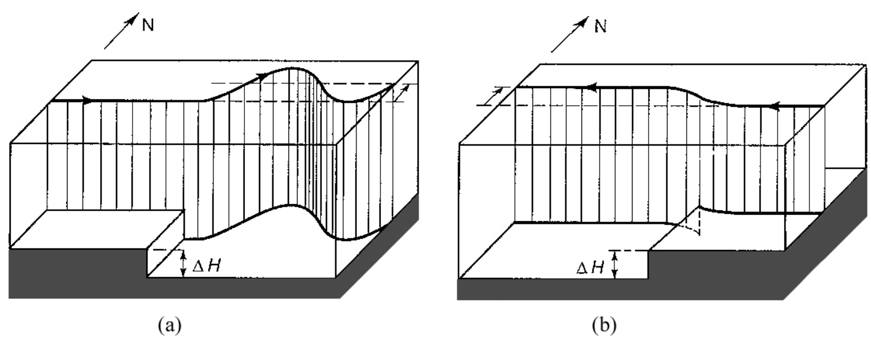

Figure 18-11 Eastward and westward jets passing over a topographic step: (a) the eastward jet develops an oscillatory behavior, whereas (b) the westward jet begins to feel the influence of the step upstream and executes a single meander. Both experience a net meridional shift $Y = f_0 \Delta H / \beta_0 h$, the sign of which depends on whether the step is up or down.

and forth about a new latitude (Figure 18-11a). The average northward shift, Y, of the jet axis corresponds to an exchange between vertical stretching and increased planetary vorticity:

$$\frac{\beta_0 Y}{f_0} \sim \frac{\Delta H}{h}\,, \tag{18.10}$$

where ΔH is the height of the topographic step and h is the upstream thickness of the jet. Because the first meander is rooted at the location of the step, the meander must be stationary,
JMB from ⇓ and therefore the wavelength must be comparable to the critical meander scale.

JMB to ⇑ The same argument can be invoked for an eastward jet entering a shallower region to
JMB from ⇓ conclude that the flow exhibits a stationary oscillation about a net equatorward shift, given
JMB to ⇑ by (18.10) where ΔH is now negative. However, the argument fails for westward jets. Upon entering a deeper region, a fluid parcel acquires cyclonic vorticity and turns equatorward, its planetary vorticity decreases, further increasing the orbital vorticity. Clearly, if this were the case, the jet would be looping onto itself. Instead, the jet begins to be distorted upstream of the topographic step (Figure 18-11b), acquiring a cyclonic curvature in which the increasing
JMB from ⇓ orbital vorticity is compensated by a decrease in planetary vorticity. **Benoit:** Is it not the inverse?? turning northward creates anticyclonic orbital vorticity which is compensated by
JMB to ⇑ increased planetary vorticity??? The jet thus reaches the step at an oblique angle. The nature of the vorticity adjustments past the step progressively restores the jet's original zonal orientation. A remaining meridional shift remains, expressing a balance between changes in planetary vorticity and vertical thickness. The reader can verify that this shift is again given by (18.10).

18.1.5 Instabilities

In addition to their propagation, meanders on a jet also distort and frequently grow, close onto themselves, and form eddies that separate from the rest of the jet. Such a finite change to the jet structure results from an instability, the nature of which is barotropic (Chapter 10), baroclinic (Chapter 17), or mixed. Barotropic instability proceeds with the extraction of kinetic energy from the horizontally sheared flow to feed the growing meander. The greater the shear in the jet, the more likely is this type of instability. Baroclinic instability, on the other hand, is associated with a conversion of available potential energy from the horizontal density distribution in balance with the thermal wind. Although the example treated in Section 10.4 suggests that critical wavelengths associated with barotropic instability scale as the jet width, consideration of baroclinic instability points to the critical role of the internal radius of deformation [see equation (17.51)]. If the two length scales are comparable, as is the case in a baroclinic jet with finite Rossby number, both processes may be equally active, and the instability is most likely of the mixed type (Orlanski, 1968; Griffiths *et al.*, 1982; Killworth *et al.*, 1984). The beta effect further complicates the situation, occasionally facilitating the eddy detachment process: The large meridional displacement of the growing meander induces a westward-propagation tendency, whereas the high-curvature regions where the meander attaches to the rest of the jet induce a downstream propagation tendency. The result is a complex situation in which the outcome sensitively dependent on the relative magnitudes of the different effects (Flierl *et al.*, 1987; Robinson *et al.*, 1988). The meandering and eddy shedding of the Gulf Stream manifest this complexity.

The development of synoptic-scale weather disturbances, a process now called *cyclogenesis*, is thought to be initiated mostly by baroclinic instability, whereas accompanying finer-scale processes, such as cold and warm fronts, are explained by non-geostrophic dynamics. The interested reader is referred to the book by Holton (1992).

18.2 Vortices

A vortex, or eddy, is defined as a closed circulation that is relatively persistent. By persistency , we mean that the turnaround time of a fluid parcel embedded in the structure is shorter than the time during which the structure remains identifiable. A *cyclone* is a vortex where the rotary motion is in the same sense as the earth's rotation, — counterclockwise in the Northern Hemisphere and clockwise in the Southern Hemisphere. An *anticyclone* rotates the other way, clockwise in the Northern Hemisphere and counterclockwise in the Southern Hemisphere. The prototypical vortex is a steady circular motion on the f-plane.

JMB from ⇓

JMB to ⇑

Using cylindrical coordinates, we can express the balance of forces in the radial direction r (measured outward) as follows:

$$- \frac{v^2}{r} - fv = - \frac{1}{\rho_0} \frac{\partial p}{\partial r}, \tag{18.11}$$

where v is the orbital velocity (positive counterclockwise) and p is the pressure (or Montgomery potential). Both v and p may be dependent upon the vertical coordinate, either height z or density ρ. This equation, called the *gradient-wind balance*, represents an equilibrium between three forces, the centrifugal force (first term), the Coriolis force (second term), and the pressure force (third term). Although the centrifugal force is always directed outward, the Coriolis and pressure forces can be directed either inward or outward, depending on the direction of the orbital flow and on the center pressure.

If we introduce the following scales, U for the orbital velocity, L for r (measuring the vortex radius), and ΔP for the pressure difference between the ambient value and that at the vortex center, we note that the terms composing (18.11) scale, respectively, as

$$\frac{U^2}{L}, \quad fU, \quad \frac{\Delta P}{\rho_0 L}. \tag{18.12}$$

At low Rossby numbers ($Ro = U/fL \ll 1$), the first term is negligible relatively to the second (*i.e.*, the centrifugal force is small compared to the Coriolis force), the balance is nearly geostrophic, providing

$$fU = \frac{\Delta P}{\rho_0 L}, \tag{18.13}$$

and thus $U = \Delta P/(\rho_0 f L)$. Since the pressure difference is most likely the result of a density anomaly $\Delta\rho$, the hydrostatic balance provides $\Delta P = \Delta\rho \, gH = \rho_0 g' H$, where H is the appropriate height scale (thickness of vortex) and $g' = g\Delta\rho/\rho_0$ is the reduced gravity. This leads to $U = g'H/fL$ and

$$Ro = \frac{U}{fL} = \frac{g'H}{f^2L^2} = \left(\frac{R}{L}\right)^2, \tag{18.14}$$

in which we recognize the internal deformation radius $R = (g'H)^{1/2}/f$. Thus, a small Rossby number occurs as a consequence of a horizontal scale large compared to the deformation radius. This is typically the case in the largest weather cyclones and anticyclones at midlatitudes and in large-scale oceanic gyres (Figure 18-12-top). Because the Rossby number is identical to the Burger number, its smallness also shows that vorticity of large gyres are mostly constrained by vertical stretching rather then relative vorticity (see...). Also their energy is dominated by potential energy (see...).

JMB from ⇓

JMB to ⇑

JMB from ⇓

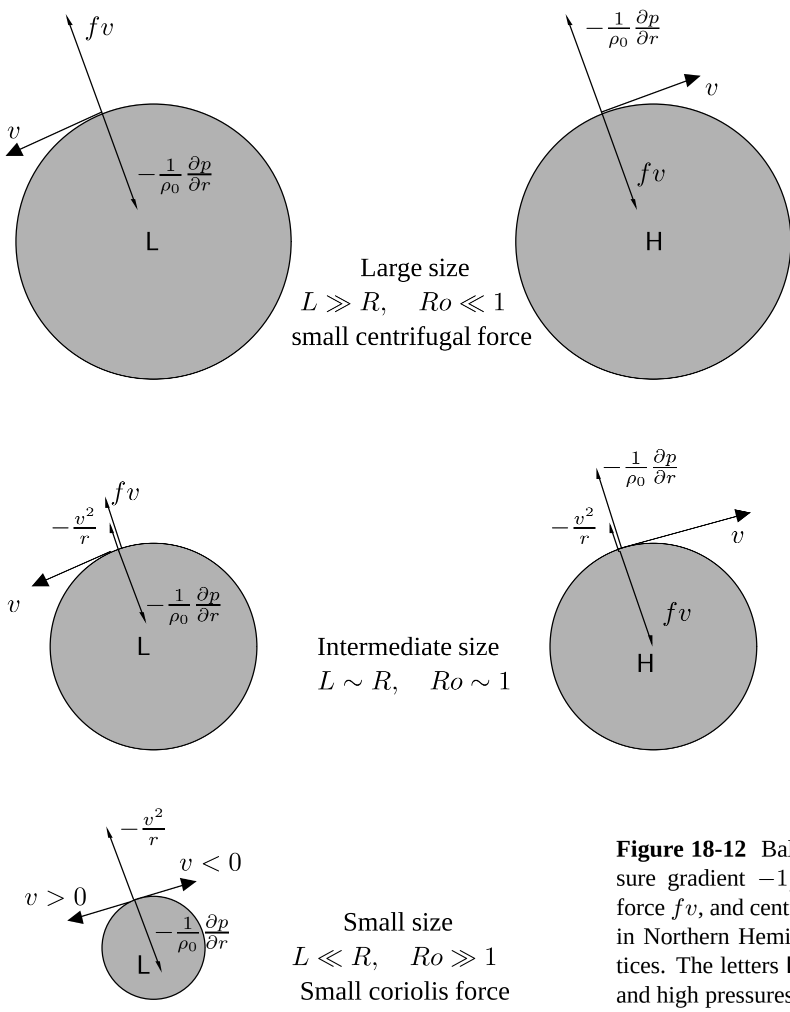

Figure 18-12 Balances between pressure gradient $-1/\rho_0\, \partial p/\partial r$, Coriolis force fv, and centrifugal $-v^2/r$ forces in Northern Hemispheric circular vortices. The letters L and H indicate low and high pressures, respectively.

BenoitI proposed the alternative plot in order to avoid two letter symbols reserved normally for constants as Rossby number etc. Also uses different scale for velocity in cyclone and anticyclone... JMB to ⇑

At scales on the order of the deformation radius, L can be taken equal to R, the Rossby number is on the order of unity, the velocity scale is $U = (g'H)^{1/2}$, and the centrifugal force is comparable to the Coriolis force. Around a low pressure, the outward centrifugal force partially balances the inward pressure force, leaving the Coriolis force to meet only the difference. By contrast, the Coriolis force acting on the flow around a high pressure must balance both the outward pressure force and the outward centrifugal force (Figure 18-12-middle). Consequently, the orbital velocity in an anticyclone is greater than that in a cyclone of identical size and equivalent pressure anomaly. Tropical hurricanes (Anthes, 1982; Emmanuel, 1991) and the so-called rings shed by the Gulf Stream (Flierl, 1987; Olson, 1991) fall in this category. **Benoit:** Hurricanes are synonyme with tropical cyclones and typhoons. JMB from ⇓ The last phrase, should be corrected to refer to cyclones ??? JMB to ⇑

At progressively shorter radii, the centrifugal force becomes increasingly important, and the difference between cyclones and anticyclones amplifies. For $L \ll R$, the Coriolis force becomes negligible. The cyclone-anticyclone nomenclature loses its meaning, and the relevant characteristic is the sign of the pressure anomaly. The inward force around a low pressure is balanced by the outward centrifugal force regardless of the direction of rotation (Figure 18-12-bottom). Such a state is said to be in *cyclostrophic balance*. Examples are tornadoes and bathtub vortices. A vortex with high-pressure center cannot exist, because pressure and centrifugal forces are both directed outward.

It is interesting to determine the minimum size for which an anticyclone of given pressure anomaly can exist. Returning to the gradient-wind balance where we introduce $v = -fr/2 + v'$, we write

$$\frac{f^2 r}{4} + \frac{1}{\rho_0}\frac{\partial p}{\partial r} = \frac{1}{r}\,v'^2 \geq 0. \tag{18.15}$$

Integrating over the radius a of the vortex and defining the pressure anomaly $\Delta p = p(r = 0) - p(r = a)$, we obtain

$$a^2 \geq \frac{8\Delta p}{\rho_0 f^2}\,. \tag{18.16}$$

For a low-pressure center ($\Delta p < 0$), this inequality yields no constraint, whereas for a high-pressure center ($\Delta p > 0$) it specifies a minimum vortex radius. Below this minimum, high-pressure centers simply do not exist as isolated steady structures.

Let us now examine how an existing vortex can move within the fluid that surrounds it. To do this, we consider a vortex contained within a single layer of fluid, be it the lowest, the uppermost, or any intermediate layer in the fluid. If the local thickness of this layer is h and the pressure (actually, Montgomery potential) is p, we write, in density coordinates,

$$\frac{\partial u}{\partial t} + u\frac{\partial u}{\partial x} + v\frac{\partial u}{\partial y} - fv = -\frac{1}{\rho_0}\frac{\partial p}{\partial x}\,, \tag{18.17a}$$

$$\frac{\partial v}{\partial t} + u\frac{\partial v}{\partial x} + v\frac{\partial v}{\partial y} + fu = -\frac{1}{\rho_0}\frac{\partial p}{\partial y}\,, \tag{18.17b}$$

$$\frac{\partial h}{\partial t} + \frac{\partial}{\partial x}(hu) + \frac{\partial}{\partial y}(hv) = 0. \tag{18.17c}$$

We further restrict ourselves to the f-plane. At large distances from the vortex center, in what can be considered the ambient fluid, we assume that there exists a steady uniform flow ($\bar{u}$, $\bar{v}$) and a uniform thickness gradient ($\partial\bar{h}/\partial x$, $\partial\bar{h}/\partial y$). According to (18.17a) and (18.17b), this flow must be geostrophic, and according to (18.17c), it must be aligned with the direction of constant layer thickness:

$$-\,f\bar{v} \;=\; -\,\frac{1}{\rho_0}\,\frac{\partial\bar{p}}{\partial x}\,, \tag{18.18a}$$

$$+\,f\bar{u} \;=\; -\,\frac{1}{\rho_0}\,\frac{\partial\bar{p}}{\partial y}\,, \tag{18.18b}$$

$$\bar{u}\,\frac{\partial\bar{h}}{\partial x} \;+\; \bar{v}\,\frac{\partial\bar{h}}{\partial y} \;=\; 0. \tag{18.18c}$$

A thickness gradient is retained because, in some instances, a thermal wind in layers above or below may be accompanied by such a thickness variation. Also, if the vortex lies in the lowest layer, the thickness gradient may represent a bottom slope. The assumption of uniformity of $\bar{u}$, $\bar{v}$, and of the derivatives of $\bar{p}$ and $\bar{h}$ is justified if the ambient-flow properties vary over horizontal distances much larger than the vortex diameter. Defining the velocity components, pressure, and layer-thickness variations proper to the vortex as $u' = u - \bar{u}$, $v' = v - \bar{v}$,
JMB from ⇓ $p' = p - \bar{p}$, and $h' = h - \bar{h}$, we can transform equations (18.17) as follows: **Benoit** I put the
JMB to ⇑ $\bar{u}$ etc inside derivative to prepare integrations

$$\frac{\partial u'}{\partial t} \;+\; (\bar{u}+u')\,\frac{\partial u'}{\partial x} \;+\; (\bar{v}+v')\,\frac{\partial u'}{\partial y} \;-\; fv' \;=\; -\,\frac{1}{\rho_0}\,\frac{\partial p'}{\partial x} \tag{18.19a}$$

$$\frac{\partial v'}{\partial t} \;+\; (\bar{u}+u')\,\frac{\partial v'}{\partial x} \;+\; (\bar{v}+v')\,\frac{\partial v'}{\partial y} \;+\; fu' \;=\; -\,\frac{1}{\rho_0}\,\frac{\partial p'}{\partial y} \tag{18.19b}$$

$$\frac{\partial h'}{\partial t} \;+\; \frac{\partial(h'\bar{u})}{\partial x} \;+\; \frac{\partial(h'\bar{v})}{\partial y} \;+\; \frac{\partial}{\partial x}\,[(\bar{h}+h')u'] \;+\; \frac{\partial}{\partial y}\,[(\bar{h}+h')v'] \;=\; 0 \tag{18.19c}$$

We then define the anomalous layer volume due to the vortex:

$$V \;=\; \iint h'\,dx\,dy, \tag{18.20}$$

where the integration covers the entire horizontal extent of the layer. The perturbation h' induced by the vortex is assumed to be sufficiently localized to make the preceding integral
JMB from ⇓ finite. The use of continuity equation (18.19c) followed by integration by parts over several
JMB to ⇑ terms shows that the temporal derivative of this volume,

$$\frac{dV}{dt} \;=\; \iint\,\frac{\partial h'}{\partial t}\,dx\,dy \tag{18.21}$$

vanishes, as we expect. Defining the coordinates of the vortex position by the volume-weighted averages

$$X \;=\; \frac{1}{V}\,\iint\,xh'\,dx\,dy\,, \quad Y \;=\; \frac{1}{V}\,\iint\,yh'\,dx\,dy, \tag{18.22}$$

we can track the vortex displacements by calculating their temporal derivatives. For X, we obtain successively

$$\begin{aligned}
\frac{dX}{dt} &= \frac{1}{V} \iint x \frac{\partial h'}{\partial t}\, dx\, dy \\
&= \frac{-1}{V} \iint \left\{ x\bar{u}\frac{\partial h'}{\partial x} + x\bar{v}\frac{\partial h'}{\partial y} + x\frac{\partial}{\partial x}[(\bar{h} + h')u'] + x\frac{\partial}{\partial y}[(\bar{h} + h')v'] \right\} dx\, dy \\
&= \frac{+1}{V} \iint [\bar{u}h' + (\bar{h} + h')\, u']\, dx\, dy \\
&= \bar{u} + \frac{1}{V} \iint hu'\, dx\, dy. \qquad (18.23)
\end{aligned}$$

Similarly, we obtain for the other coordinate

$$\frac{dY}{dt} = \bar{v} + \frac{1}{V} \iint hv'\, dx\, dy. \qquad (18.24)$$

The preceding integrals cannot be evaluated without knowing the precise structure of the vortex. However, a second time derivative will bring forth the acceleration ($\partial u'/\partial t$, $\partial v'/\partial t$), which is provided by the equations of motion, (18.19a) and (**??**). For the X-coordinate, we obtain

$$\begin{aligned}
\frac{d^2X}{dt^2} &= \frac{1}{V} \iint \left[\frac{\partial h'}{\partial t}\, u' + (\bar{h} + h')\, \frac{\partial u'}{\partial t} \right] dx\, dy \\
&= \frac{-1}{V} \iint \left[\frac{\partial}{\partial x}\,(huu') + \frac{\partial}{\partial y}(hvu') \right] dx\, dy \\
&+ \frac{f}{V} \iint hv'\, dx\, dy - \frac{1}{\rho_0 V} \iint h\, \frac{\partial p'}{\partial x}\, dx\, dy. \qquad (18.25)
\end{aligned}$$

The pressure anomaly p' associated with the vortex motions can be related by hydrostatic balance to the layer-thickness anomaly: **Benoit**:Following equation not evident. Maybe as an exercise in chapter of layered models? Not so trivial if the eddy is an intermediate layer with fluid above and below? JMB from ⇓ JMB to ⇑

$$p' = \rho_0 g' h', \qquad (18.26)$$

with a suitable definition of the reduced gravity g'. Note that if the vortex is contained in the lowest layer above an uneven bottom, the bottom elevation does not enter (18.26) but instead enters the corresponding hydrostatic balance for the mean-flow properties.

Noting that the first integral in (18.25) vanishes because u' and v' go to zero at large distances from the vortex, that the second integral can be eliminated by use of (18.24), and that the third integral, integrated by parts, can be simplified with use of (18.26), we obtain JMB from ⇓ JMB to ⇑

$$\frac{d^2X}{dt^2} = f\, \frac{dY}{dt} - f\bar{v} + g'\, \frac{\partial \bar{h}}{\partial x}\, . \qquad (18.27)$$

A similar treatment of the second derivative of Y yields

$$\frac{d^2Y}{dt^2} \;=\; -\; f\,\frac{dX}{dt} \;+\; f\bar{u} \;+\; g'\,\frac{\partial\bar{h}}{\partial y}\,. \tag{18.28}$$

Because the gradient of $\bar{h}$ is assumed uniform and f, $\bar{u}$, and $\bar{v}$ are constants, the preceding two equations can be solved for the velocity of the vortex:

$$\frac{dX}{dt} \;=\; \left(\bar{u} \,+\, \frac{g'}{f}\,\frac{\partial\bar{h}}{\partial y}\right)(1 \,-\, \cos ft) \,-\, \left(\bar{v} \,-\, \frac{g'}{f}\,\frac{\partial\bar{h}}{\partial x}\right)\,\sin ft \tag{18.29a}$$

$$\frac{dY}{dt} \;=\; \left(\bar{v} \,-\, \frac{g'}{f}\,\frac{\partial\bar{h}}{\partial x}\right)(1 \,-\, \cos ft) \,+\, \left(\bar{u} \,+\, \frac{g'}{f}\,\frac{\partial\bar{h}}{\partial y}\right)\,\sin ft, \tag{18.29b}$$

where the constants of integration have been determined under the assumption that the vortex is not translating initially. In the preceding solution, we recognize inertial oscillations superimposed on a mean drift. This mean drift has two components:

$$c_x \;=\; \bar{u} \,+\, \frac{g'}{f}\,\frac{\partial\bar{h}}{\partial y}\,, \quad c_y \;=\; \bar{v} \,-\, \frac{g'}{f}\,\frac{\partial\bar{h}}{\partial x}\,. \tag{18.30}$$

The first contribution ($\bar{u}$, $\bar{v}$) indicates that the vortex is entrained by the ambient motions of its containing layer. Together, this entrainment and the inertial oscillations do not distinguish the vortex from a single fluid parcel. The cause of the second contribution, proportional to the gradient of $\bar{h}$, is less obvious and is what really distinguishes a vortex from a fluid parcel.

The existence of a thickness gradient in the vicinity of the vortex implies a nonuniform distribution of potential vorticity, which the swirling motion of the vortex redistributes; fluid parcels on the edge of the vortex are thus stretched and squeezed and develop vorticity anomalies that, in turn, act to displace the main part of the vortex. As the example in Figure 18-13 illustrates, a northward decrease of layer thickness in the Northern Hemisphere causes squeezing on parcels moved northward and stretching on those moved southward. (The sense of rotation in the vortex is irrelevant here.) This causes the fluid on the northern flank of the vortex to acquire anticyclonic vorticity and that on the southern flank to acquire cyclonic vorticity. Both vorticity anomalies induce a westward displacement of the bulk of the vortex. Equations (18.30) confirm that those conditions ($\partial\bar{h}/\partial x = 0$, $\partial\bar{h}/\partial y < 0$, $f > 0$) imply a negative c_x and a zero c_y. The general rule is that the vortex translates with the thin-layer side on its right in the Northern Hemisphere and on its left in the Southern Hemisphere.

Gradients in the vortex-containing layer can be caused by one of two reasons. If other layers, above or below, flow at speeds different from that of the vortex layer, there exists a thermal wind, which by virtue of the Margules relation [see (15.5)] requires sloping density surfaces and, therefore, varying layer thicknesses. It is left to the reader to show that in such a case the vorticity-induction mechanism described in the preceding paragraph amounts to a drift of the vortex in the same direction as the thermal wind. The other reason for layer-thickness variations is bottom topography. If the vortex is contained in the lower layer, bounded below by a sloping bottom, fluid parcels surrounding the vortex will be moved up or down this slope and undergo vorticity adjustments. The result (see Figure 18-13 again) is a drift of the vortex with the shallower region to its right in the Northern Hemisphere and to its left in the Southern Hemisphere. Nof (1983) discusses this effect for cold eddy lenses on the ocean bottom.

Note that if the vortex starts from a resting position, its migration is not immediately transverse to the thickness gradient but is up-gradient, as solution (18.29) indicates for small values of time. In the case of a sloping bottom, this implies that the vortex first goes downhill, gradually acquiring a velocity in that direction, and under the action of the Coriolis force has its trajectory subsequently deflected in the direction transverse to the topographic gradient. (Compare this situation to that of Problem 2-9.)

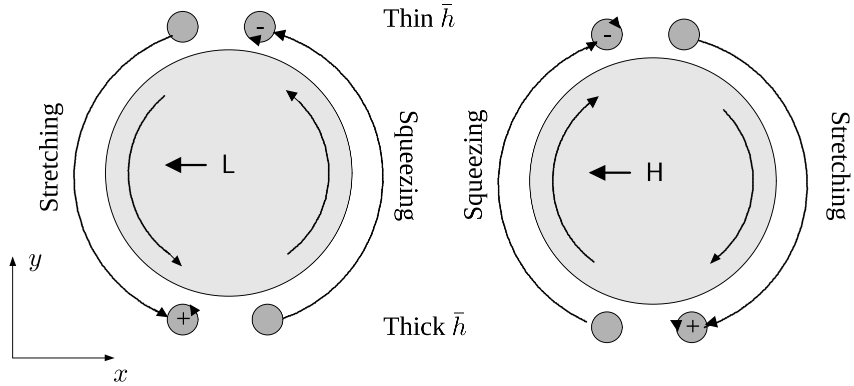

Figure 18-13 Lateral drift of a vortex embedded in layer of varying thickness. The advection of surrounding fluid induces cyclonic and anticyclonic vorticities, which combine to induce a drift of the vortex structure along lines of constant thickness. In the Northern Hemisphere (as drawn in the figure), the vortex moves with the thin-layer side on its right; the direction is opposite in the Southern Hemisphere.

Because of the analogy between a topographic slope and the beta effect (see Section 9.6), the preceding conclusions can be extrapolated to the motion of vortices on the beta-plane. Regardless of their polarity (cyclonic or anticyclonic), vortices have a self-induced westward tendency. Repeating the argument made with Figure 18-13, with the replacement of the thick-to-thin direction by the northward direction, we conclude that surrounding parcels entrained from the southern tip to the northern end acquire planetary vorticity and thus develop anti-cyclonic relative vorticity. Similarly, the surrounding parcels entrained from north to south develop cyclonic relative vorticity. The combined effect at the latitude of the vortex center is a westward drift. Theories (Cushman-Roisin *et al.*, 1990, and references therein) show that the induced speed is on the order of $\beta_0 R^2$, where R is the internal radius of deformation, being slightly larger for anticyclones than cyclones. However, in both atmosphere and oceans this speed is usually too weak to be noticeable compared to the entrainment by the ambient flow. JMB from $\Downarrow$

Rather than to interprete the westward drift in terms of potential vorticity, we can also explain the drift by a a balance of forces. On the northern side of an anticyclonic eddy, geostrophic velocity can be smaller than on the southern side for an identical Coriolis force balancing the pressure gradient (Figure 18-14). The velocity difference yields a divergence / convergence on the western and eastern flanks of the circular trajectories, which in turn deflects the density interface. A westward movement of the eddy is induced. For the cyclone, similar reasoning also yields a westward displacement. JMB to $\Uparrow$

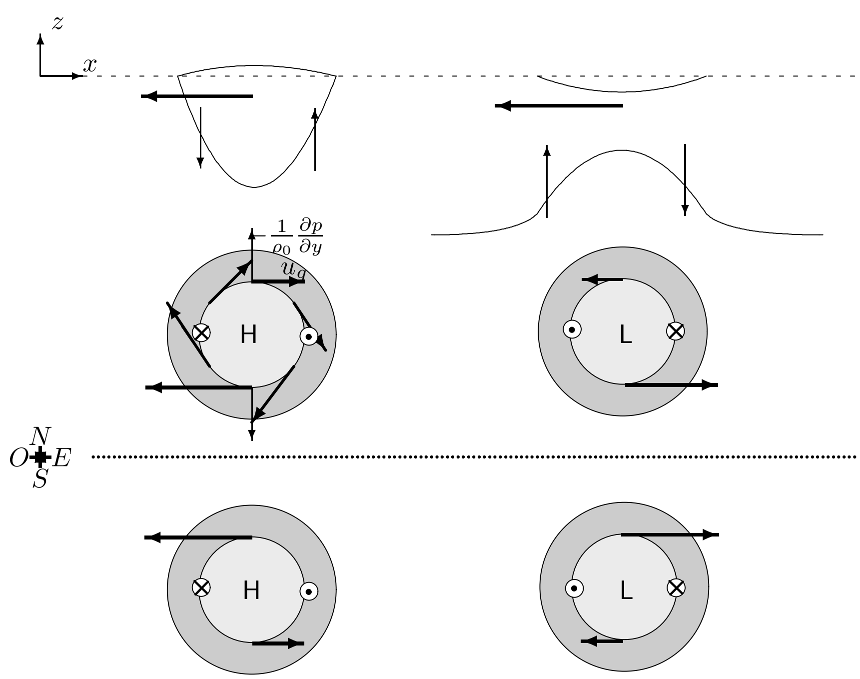

Figure 18-14 Alternative explication of the westward drift. Convergence and divergence associated with velocity differences on the southern and northern side displace the vortex.

Implicit in the preceding derivations was the assumption that all variables related to the vortex decay sufficiently fast away from the vortex core to make all integrals finite. However, in the presence of a potential-vorticity gradient such as one created by a layer-thickness gradient (see the preceding text) or by the beta effect ($\beta_0 = df/dy$), waves are possible (Sections 9.4 and 9.5) and energy can be radiated away to large distances from the vortex, yielding nonnegligible eddy-related motions there. As it turns out, it is possible to predict, at least qualitatively, the effect of such waves by considering the early time evolution of the vortex. Figure **??** depicts the relative-vorticity adjustments brought to surrounding fluid parcels as they are moved by the vortex for the first quarter of their evolution. As for linear waves (Section 9.6), there is a direct analogy between the layer-thickness gradient and the beta effect: The thin-layer side and the poleward direction are dynamically similar, for they both point to an increase in potential vorticity. After a quarter turn, parcels surrounding the vortex acquire relative vorticity by stretching (or squeezing) or a decrease (or increase) in planetary vorticity. As Figure **??** reveals, the cumulative effect in the Northern Hemisphere is a migration of cyclones toward decreasing layer thicknesses or northward; anticyclones migrate in the opposite direction. As vortices move in those directions, their own core fluid undergoes similar stretching or squeezing or planetary-vorticity changes. In all cases, the net result is a decrease in the absolute value of the relative vorticity and thus an overall spin-down of the vortex.

In the study of hurricane motion, Shapiro (1992) distinctly shows how the trajectory of the hurricane center (a low-pressure center and thus a cyclone) can be explained by the mechanisms just summarized. Here, the beta effect is relatively unimportant, but the presence of a westerly wind aloft and its accompanying layer-thickness gradient (thicker southward) combine to make the hurricane progress in the southeastward northwestward???? direction. JMB from ⇓

A discussion of geophysical vortices ought to address additional aspects such as axisymmetrization (assuming a nearly circular shape despite anisotropic birthing conditions), instabilities, secondary motions, frictional spin-down, wave radiation, and so on. Partly, because space does not permit a deeper discussion here but mostly because these aspects tend to be quite different in the atmosphere and ocean, the reader interested in atmospheric vortices is referred to the monograph by Anthes (1982), and the reader interested in oceanic vortices is referred to the book edited by Robinson (1983). Laboratory simulations of geophysical vortices have also been conducted; an interesting article on vortex instabilities is that by Griffiths and Linden (1981). JMB to ⇑

18.3 Geostrophic turbulence

We alluded to this topic, the study of a large number of interacting vortices, at the end of Chapter 16 (**Benoit: this part is not yet included?**) when we introduced nonlinear effects in quasi-geostrophic dynamics. Here, we shall tackle the subject from the vortex point of view, without making the quasi-geostrophic assumption.

When several eddies are present and not too distant from one another, interactions are unavoidable. Vortices shear and peel off the sides of their neighbors and, at times, merge to create larger vortices. The sheared elements either curl onto themselves, forming new, smaller vortices, or dissipate under the action of friction. The net result is a combination of consolidation and destruction. When many vortices are simultaneously present, the situation

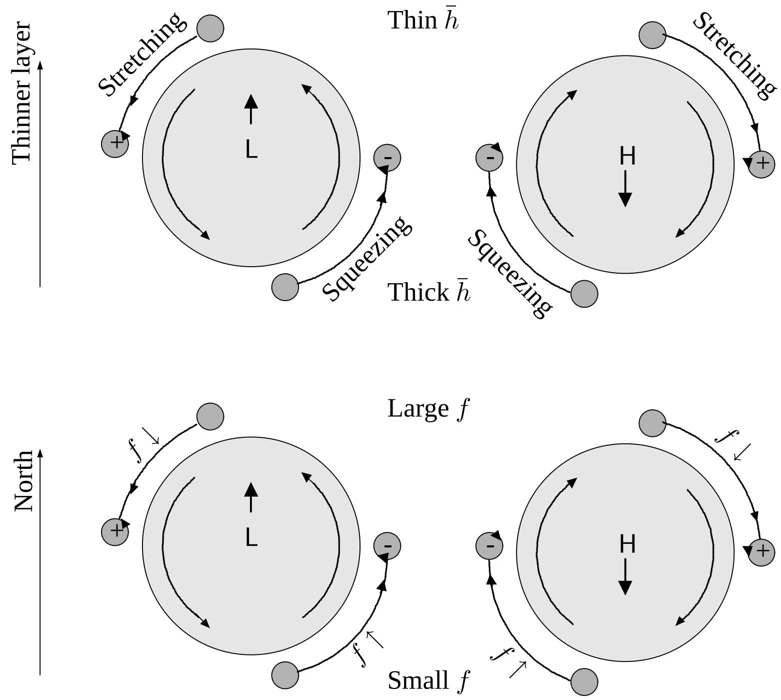

Figure 18-15 Secondary drift of vortices. The advection of surrounding fluids induces cyclonic and anticyclonic vortices on the flanks of the vortex, which combine to cause a drift as indicated. This drift component is perpendicular and in addition to that depicted in Figure 18-13. Again, the figure is drawn for the Northern Hemisphere; in the Southern Hemisphere, cyclones still move in the direction of smaller layer thickness or poleward, and anticylcones move in the direction of greater layer thickness, or equatorward.

is best described in a statistical sense.

A number of important properties can be derived rather simply by considering three integrals of motion, namely, the kinetic energy, the available potential energy, and the *enstrophy*, the latter being the integrated squared vorticity. We thus define the following:

$$\text{Kinetic energy:} \quad KE = \frac{1}{2}\rho_0 \iiint (u^2+v^2)\, dx\, dy\, dz \tag{18.31a}$$

$$\text{Available potential energy:} \quad APE = \frac{1}{2} \iiint N^2 h^2\, dx\, dy\, dz \tag{18.31b}$$

$$\text{Enstrophy:} \quad S = \frac{1}{2} \iiint \left(\frac{\partial v}{\partial x} - \frac{\partial u}{\partial y}\right)^2 dx\, dy\, dz. \tag{18.31c}$$

In the formulation of the kinetic energy, the contribution of vertical velocity is usually insignificant. (It is insignificant whenever hydrostatic balance holds.) If the horizontal velocity scale is U, the domain depth is H, and the horizontal area is A, the size of KE is about $\rho_0 U^2 HA$. The definition of the available potential energy was established in (16.28). If the vertical displacements of the density surfaces scale as ΔH ($\Delta H \leq H$, naturally) and if reduced gravity is introduced via $g' = N^2 H$ [see (18.2)], the available potential energy is on the order of $\rho_0 g' \Delta H^2 A$. For eddies of average size L, vorticity scales as U/L and enstrophy as $(U/L)^2 HA$. Finally, if we invoke geostrophy to set the velocity scale, we state $f_0 U \sim g' \Delta H / L$ (barring a substantial barotropic component) and write

$$KE \sim \rho_0 \left(\frac{g' \Delta H}{f_0 L} \right)^2 HA \tag{18.32a}$$

$$APE \sim \rho_0 g' \Delta H^2 A \tag{18.32b}$$

$$S \sim \left(\frac{g' \Delta H}{f_0 L^2} \right)^2 HA. \tag{18.32c}$$

The ratio of kinetic to potential energy is

$$\frac{KE}{APE} \sim \frac{g' H}{f_0^2 L^2} = \left(\frac{R}{L} \right)^2, \tag{18.33}$$

where R is the internal radius of deformation. Link with Burger number??? Bu. JMB from ⇓

As the interactions among vortices proceed, the shearing and tearing of vortices introduce motions at ever shorter scales, until frictional dissipation becomes important. Because S increases much faster than KE with decreasing length scales, while APE is unaffected, friction removes disproportionally more enstrophy than kinetic energy and, surely, potential energy. In first approximation, we can assume that the total energy is conserved, while enstrophy decays with time. In a fixed domain (HA = constant) and with constant f_0 and g' values (no heating or cooling), a decrease in enstrophy requires, by virtue of (18.31c), a decrease in the ratio $\Delta H / L^2$. JMB to ⇑

At short length scales ($L \ll R$), the energy consists primarily of kinetic energy, via (18.33), and its near conservation requires that $\Delta H / L$ remain approximately constant. The only possibility that satisfies both requirements is a steady increase of the length scale L, with a proportional increase in eddy amplitude ΔH. Thus, the vortices become, on average,larger and stronger. Obviously, to conserve the total space allowed to them, they also become fewer. There is thus a natural tendency toward successive eddy mergers. With every merger, energy is consolidated into larger structures with concomitant enstrophy losses.

As the length scale increases toward the radius of deformation, the relative importance of potential energy increases. Because APE increases like ΔH^2, further increases in mean eddy amplitude ΔH require corresponding decreases in kinetic energy, to preserve the total energy, and $\Delta H^2 / L^2$ must begin to decrease. The result is that ΔH and L continue to increase but no longer proportionally, L increasing faster than ΔH.

As the length scale continues to increase, indicating continued merging activity, it will eventually become much larger than R. Then, the energy is primarily in the form of potential energy, and its conservation requires a saturated value of ΔH. Further enstrophy decrease under frictional action is possible only with a further increase in length scale L (Rhines, 1975; Salmon, 1982). In sum, the interactions of a larger number of vortices without addition of energy lead to an irreversible tendency toward fewer and larger vortices. This implies an emergence of coherent structures from a random initial vorticity field. As for the mean eddy amplitude, it increases only up to a certain point. The maximum possible eddy amplitude is achieved when almost all the energy available is in the form of available potential energy — that is,

$$\Delta H_{\max} \sim \sqrt{\frac{E}{\rho_0 g' A}}\,, \tag{18.34}$$

where E is the total energy present in the system ($E = KE + APE$) and A is the horizontal area of the system. Should this value exceed the depth H of the domain, vortex amplitudes will be limited by the latter and not all the energy can be turned into potential energy; a certain portion of the energy must remain in the form of kinetic energy, implying a limit to the length scale L.

At the time of this writing, geostrophic turbulence is a topic of great interest. New results are published at a rapid pace, and it is not appropriate within the context of the present volume to attempt to summarize them. Pioneering results concerning the emergence of coherent vortices in quasi-geostrophic turbulence can be found in McWilliams (1984; 1989). Let us also note that the tendency toward successive merger is at the basis of the contemporary theories (Williams and Wilson, 1988, and references therein) that explain the persistence of the Great Red Spot in the atmosphere of the planet Jupiter (Figure 1-5). Finally, the question arises as to why no single dominating vortex occurs in our atmosphere as on Jupiter. The answer lies in diabatic and orographic effects constantly acting to form and destroy existing atmospheric vortices. In other words, geostrophic turbulence in the earth's atmosphere is never freely evolving for very long. Similarly, wind forcing over the ocean and dissipation by internal waves and in coastal areas combine to prevent oceanic geostrophic turbulence from following its intrinsic evolution.

JMB from ⇓

JMB to ⇑

Benoit, I think there was a recence paper of Galperin on turbulence on Jupiter, in Geophysical Research Letters that could be interesting to cite

18.4 Simulations of geostrophic turbulence

For statistical analysis of turbulence and understanding of eddy interactions, lateral boundary effects should not perturb the understanding and periodicity in space can be assumed. In this case, a particular *meshless* spectral method can be used. We already used a spectral approach for linear problems (see Sections 8.8) and will now see how to adapt it to a non-linear problem. For the sake of simplicity, we investigate a numerical solution of a single layer quasi-geostrophic system with a scale-selective biharmonic dissipation of vorticity (see Section 10.6 on filtering). The governing equations of the f-plane are thus

$$\frac{\partial q}{\partial t} + J(\psi, q) = -\mathcal{B}\left(\frac{\partial^4 q}{\partial x^4} + 2\frac{\partial^4 q}{\partial x^2 \partial y^x} + \frac{\partial^4 q}{\partial y^4}\right) \tag{18.35a}$$

$$\frac{\partial^2 \psi}{\partial x^2} + \frac{\partial^2 \psi}{\partial y^2} = q \tag{18.35b}$$

where the coefficient $\mathcal{B}$ allows to control the damping. We can make up a solution as a truncated series of sine and cosine functions spanning our periodic domain of interest $0 \leq x \leq L_x$ and $0 \leq y \leq L_y$, for both potential vorticity q and streamfunction ψ. For convenience we use the complex exponentials instead of sine and cosine functions and assume

$$\tilde{\psi}(x,y,t) \;=\; \sum_k \sum_l \; \Psi_{kl}(t)\, e^{\mathrm{i}\,\frac{2\pi k x}{L_x}}\; e^{\mathrm{i}\,\frac{2\pi l y}{L_y}} \;, \tag{18.36a}$$

$$\tilde{q}(x,y,t) \;=\; \sum_k \sum_l \; \mathcal{Q}_{kl}(t)\, e^{\mathrm{i}\,\frac{2\pi k x}{L_x}}\; e^{\mathrm{i}\,\frac{2\pi l y}{L_y}} \;. \tag{18.36b}$$

The time dependent coefficients Ψ_{kl} and $\mathcal{Q}_{kl}$ are the amplitude of the spatial Fourier modes of the solution. These amplitudes are governed by equations we can obain by multiplying the governing equations (18.35) by $e^{-\mathrm{i}\,\frac{2\pi i x}{L_x}}\; e^{-\mathrm{i}\,\frac{2\pi j y}{L_y}}$ and integrating over the domain of interest. The orthogonality of the exponential functions allows to isolate the time evolution of $\mathcal{Q}_{ij}$, which after rechristening i, j back to k, l we can write as

$$\frac{\partial \mathcal{Q}_{kl}}{\partial t} + \frac{1}{L_x L_y} \int_0^{L_x}\!\int_0^{L_y} J(\tilde{\psi},\tilde{q})\, e^{-\mathrm{i}\,\frac{2\pi k x}{L_x}}\; e^{-\mathrm{i}\,\frac{2\pi l y}{L_y}}\; dy dx \;=\; -\,\alpha_{kl}\,\mathcal{Q}_{kl} \tag{18.37}$$

$$\alpha_{kl} \;=\; \mathcal{B}\left[\left(\frac{2\pi k}{L_x}\right)^2 + \left(\frac{2\pi l}{L_y}\right)^2\right]^2 \tag{18.38}$$

$$-\left[\left(\frac{2\pi k}{L_x}\right)^2 + \left(\frac{2\pi l}{L_y}\right)^2\right]\Psi_{kl} \;=\; \mathcal{Q}_{kl} \tag{18.39}$$

Note how nicely the dissipation term has simplified in the spectral space into an algebraic operation and how the associated time attenuation can be interpreted in terms of the properties of the physical damping. Also the solution of the Poisson equation is trivial and reduced to a simple division in spectral space. Note that for the case $k = l = 0$, there is no need for a division by zero because we can always assign any arbitrary constant to Ψ_{00} because the streamfunction is defined up to any constant. All operations seem very easy to perform in the so-called *spectral space*, *i.e.*, in the discrete (k,l) space associated with the wavenumbers $2\pi k/L_x$ and $j2\pi l/L_y$. Also initialization of the fields from a given streamfunction in physical space can be translated without problems into initial conditions on the Fourier amplitudes also called *spectral coefficients*. Because periodic boundary conditions are already taken into account through the wavenumbers of the truncated series, all we have to do is to calculate the evolution of the amplitudes. To obtain the solution in the physical space, series (18.36) can then we calculated at any desired position (x,y). There remains however to calculate the contribution from the nonlinear term. Each derivative in the Jacobian can be evaluated using the derivation of the base functions

$$\frac{\partial \tilde{\psi}}{\partial x} = \sum_k \sum_l a_{kl} e^{\mathrm{i}\,\frac{2\pi k x}{L_x}}\; e^{\mathrm{i}\,\frac{2\pi l y}{L_y}}$$

$$a_{kl} = \mathrm{i}\,\frac{2\pi k}{L_x}\,\Psi_{kl} \tag{18.40}$$

and similarly for other derivatives. Obviously we only have to create a set of spectral coefficients from the original ones by multiplying them with the respective wavenumber to be able to construct the derivative. The Jacobian can then be calculated from the products of the series for these derivatives and reads

$$J(\tilde{\psi}, \tilde{q}) = \frac{4\pi^2}{L_x L_y} \sum_i \sum_j \sum_m \sum_n (jm - in)\, \Psi_{ij} \mathcal{Q}_{mn} e^{\mathrm{i}\, \frac{2\pi(i+m)x}{L_x}}\; e^{\mathrm{i}\, \frac{2\pi(j+n)y}{L_y}} \tag{18.41}$$

Finally, because of the orthogonality, from all those different terms, the projection onto (k, l) component in (18.37) retains only the terms in the sums for which $i + m = k$ and $j + n = l$. Using (18.39) to eliminate streamfunction amplitudes and introducing so-called interaction coefficients c_{mnkl}, we can we arrive at governing equations for the Fourier amplitudes

$$\frac{\partial \mathcal{Q}_{kl}}{\partial t} = -\alpha_{kl} \mathcal{Q}_{kl} - \sum_m \sum_n c_{mnkl}\, \mathcal{Q}_{mn} \mathcal{Q}_{k-m,l-n} \tag{18.42}$$

where α_{kl} depends on the dissipation parameterization retained and is given by (18.38) for the biharmonic version. Clearly the nonlinear term reflects the physical interactions of signals at different scales.

If we retain N Fourier coefficients for each spatial dimension, each sum involves N terms and a double sum requires N^2 operations. Even if the interaction coefficients can be calculated easily, in each of the N^2 equations for Fourier amplitudes we must perform N^2 operations for the sums associated with the nonlinear term. The total cost behaves then as N^4 or M^2 if M is the total number of unknowns actually used. Because the aim of geostrophic turbulence model is avoiding unrealistic sub-grid scale parameterizations, high resolution must be attempted and the cost of the present approach is prohibitive when N increases. On the other hand, we can notice that no aliasing is present because any wavelength appearing from products of Fourier modes (via $(i + m)$ or $(j + n)$) that is not retained in the original series can simply be disregarded and the corresponding interaction coefficient forced to zero.

A major breakthrough in the applicability of the spectral approach was the discovery of the so called Transform method (***e.g.***, Orszag 1970). The idea is to first calculate derivatives in spectral space by creating coefficients as in (18.40). Then the real derivative itself can be calculated in any location from the Fourier series, therefore also on a regular grid spanning the physical domain of interest. Doing the same for all derivatives in the Jacobian, the latter can be calculated from products in each grid node. Then, having the Jacobian on a physical grid, we can assess its spectral amplitudes by a projection into the wavenumber space to finally get access to the time changes in vorticity modes (Figure 18-16). This sounds much more complicated than the calculation in spectral space, but the turnabout in physical space has a distinct advantage: There exists a fast transformation method to swap between the spectral domain and the physical space. Because in physical space, the cost of operations associated with the Jacobian is proportional to the number of grid points only, we can gain from the detour if the transformation cost is lower than M^2.

For a one-dimensional case, the Fourier transformations can be efficiently achieved by so-called Fast Fourier Transforms (FFT, see appendix C) which demands $N \log N$ operations for N retained Fourier modes. In two dimensions, we first perform N FFTs, one for each y grid point along x, each of the N transforms costing $N \log N$ operations. Then we perform N FFTs of the so obtained coefficients in the other direction which requires again $N^2 \log N$

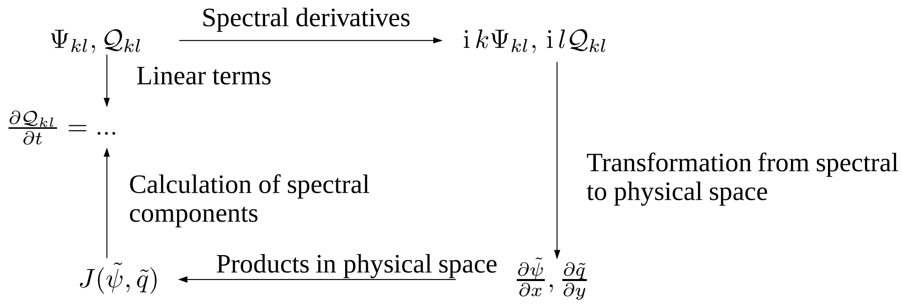

Figure 18-16 Schematic representation of the transform method applied to the evaluation of the Jacobian as the forcing term for spectral components Q_{kl}.

operations. Finally $N^2 \log N^2$ or in terms of the total number M of unknowns $M \log M$ operations are needed. For large M there is thus asymptotically a significant reduction compared to M^2. The transform method can of course be generalized to any term that is not easily calculated from spectral coefficients, as local nonlinear source terms for tracers for example. All we have to do is to calculate those terms on a physical grid and then assess its spectral composition.

Convergence of the truncated spectral series to exact solutions can be shown to be faster than any power of M as long as the solution is smooth for all derivatives. Also note that we actually solve a Poisson equation with $M \log M$ operations so the approach is appealing.

Unfortunately, another problem appears again, the aliasing associated with the products in physical space. As seen in Section 10.5, for a grid spacing of Δx, we can avoid any feedback from aliasing in the quadratic terms if wavelengths between $2\Delta x$ and $3\Delta x$ are removed from the solution. This would permanently downgrade resolution and we can turn the requirement the other way around: For the shortest wavelength λ we actually want to resolve, we just have to create a physical grid such that $\Delta x = \lambda/3$ instead of $\lambda/2$, the strict minimum needed to resolve it. In other words, we simply have to use $3/2N$ grid points instead of N to be sure that the product in physical space is not aliased. In practice, such an interpolation with the Fourier functions into a finer grid can be performed efficiently by padding with zeros the arrays containing Fourier coefficients and is coherent with the interpretation of assigning zero amplitudes to higher wavenumber signals (see appendix C).

We now have a more efficient methods to work with spectral components avoiding aliasing. An additional advantage of working in Fourier space lies in the fact that spectral analysis of the results are trivial and that spectrum of initial conditions are easily controlled in terms of wavelengths. This is particularly useful for statistical analysis of geophysical turbulence in which one looks at a random field's behavior. Generally, the fields are generated as a realization of random streamfunction with Gaussian distribution of zero mean and variance depending on the wavenumber. Initial vorticity is then obtained by space derivations and simulations can be started to see how vortices organize themselves under different dissipation conditions (Figure 18-17)

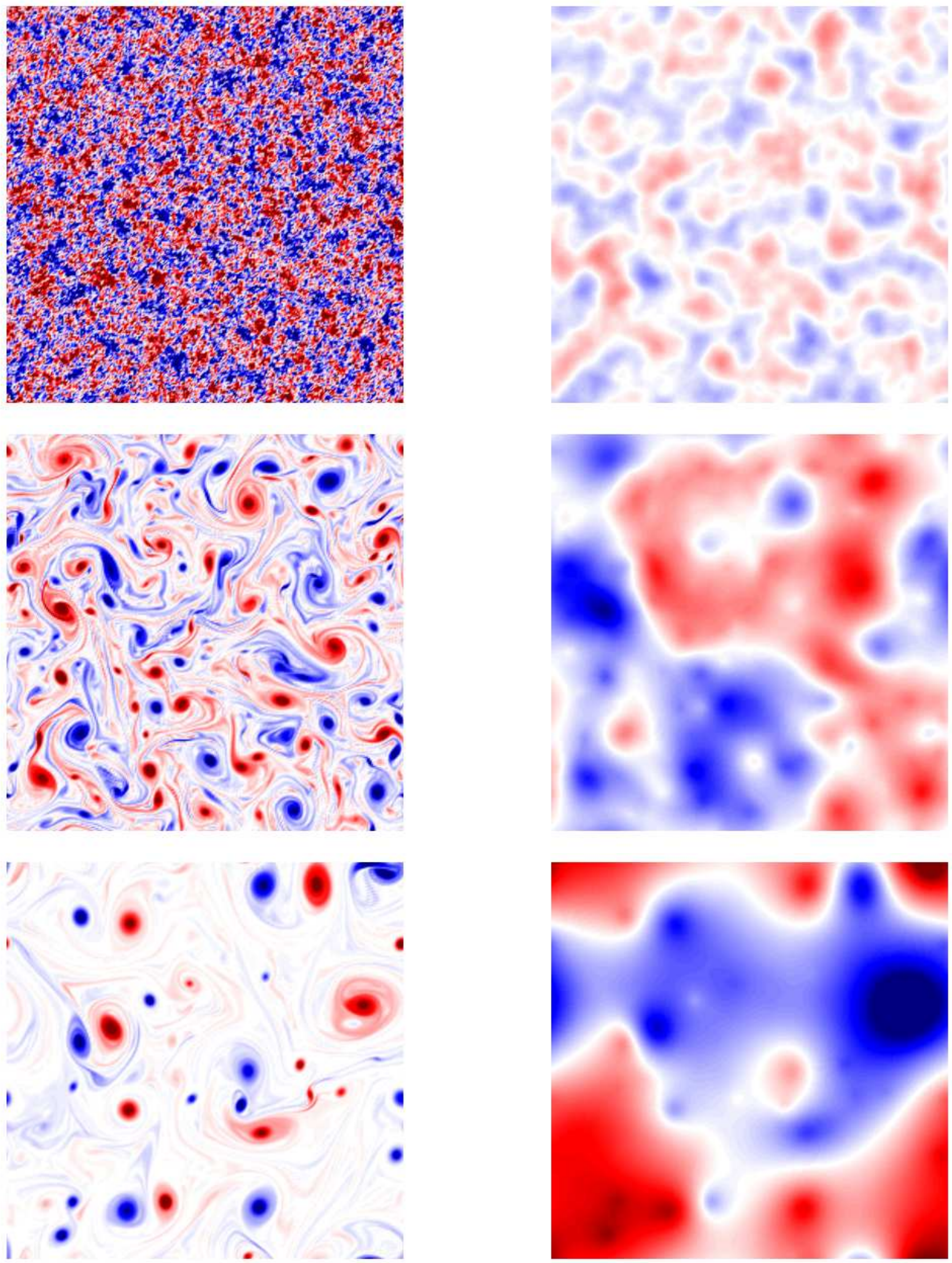

Figure 18-17 Emergence of isolated vortices from a random initial field. Vorticity (left) and streamfunction (right) in a doubly periodic domain simulated with a spectral method `qgspectral.m`.

Analytical Problems

18-1. Consider the center fluid parcel ($y = 0$) of the Gaussian jet $u(y) = U\,\exp(-y^2/2L^2)$ with U = 10 m/s and L = 100 km. On the f-plane, what is the shear vorticity acquired by that parcel in a rightward meander of curvature $\mathcal{K}$ = 1/800 km? On the beta plane, what meridional displacement Y would permit the parcel to conserve its speed and maintain its center position?

18-2. For the one-layer reduced gravity model (12.19), express the gradient-wind balance for steady circular vortices on the f-plane. If the layer thickness is H at the center and the density interface outcrops at radius a [*i.e.*, $h(r = 0) = H$, $h(r = a) = 0$], show that H and a must satisfy the inequality

$$a \;\geq\; \frac{\sqrt{8g'H}}{f}\,. \tag{18.43}$$

18-3. Take a stretch of the jet profile $u(y) = U\,(1\,-\,|y|/a)$ in $|y| \leq a$, $u(y) = 0$ elsewhere (see Figure 10-13), and bend it to create a clockwise vortex. On the f-plane and in the absence of vertical variations, what is the orbital-velocity profile that preserves vorticity? How does the pressure anomaly in the vortex compare to the pressure difference across the jet? Finally, show that the proportion of fluids with each vorticity is the same in the vortex as in the straight jet.

18-4. Determine the behavior of an eastward jet in the Northern Hemisphere flowing over a topographic step-up followed by a step-down of equal height. Is the flow oscillatory beyond the second step? Also discuss the cases where the distance between the two steps is short and long compared to the critical meander scale.

18-5. Redo Problem 18-4 for a westward jet in the Southern Hemisphere.

18-6. Hurricane Hugo (10–22 September 1989 in the western North Atlantic No image anymore) had a maximum wind speed of 62 m/s and a low central pressure of 941.4 millibars during its passage over Guadeloupe on 17 September (Case and Mayfield, 1990). Assuming that the normal pressure outside the hurricane was 1010 millibars, estimate the storm's radius and importance of the centrifugal force relative to the Coriolis force (latitude = 16°N). JMB from ⇓ JMB to ⇑

18-7. Using the gradient-wind balance (18.11) in a reduced-gravity model ($p = g'h$), explore lens-like vortex solutions where the interface exhibits a paraboloical shape between a central maximum depth ($h = H$ at $r = 0$) and a peripheral outcrop ($h = 0$ at $r = R$). Show that the flow is in solid-body rotation. Relate vortex radius R to central depth H and discuss the limiting cases of wide/shallow and narrow/deep vortices. Do you recover an inequality of type (18.16)?

18-8. In first-approximation, the thick atmosphere of Jupiter may be modeled as a reduced-gravity system with g' = 2.64 m/s^2. Knowing that planet radius is 69,000 km and that one Jovian day is only 10 earth-hours long, derive the thickness h of moving fluid for

Figure 18-18 Velocity field on Jupiter in and around the Great Red Spot, obtained after tracking small cloud features in sequential images from *Voyager* spacecraft (Problem 18-8). The origin of each vector is indicated by a dot. (From Dowling and Ingersoll, 1988.)

a few radial sections across the wind-velocity chart provided in Figure 18-18 **Figure missing** JMB from ⇓

18-9. A uniform eastward flow of velocity U over a flat bottom approaches a step in topography at right angle. Topography changes from H_0 to H_1 in $x = 0$. Determine the stationary streamfunction for $x > 0$ assuming rigid-lid approximation holds on the beta plane. Can you identify the critical meander scale in the solution? *Hint:* On a streamline, potential vorticity is conserved. Express that at the step, the relationship between the value of the streamfunction and vorticity is known and is hence valid after the step.

JMB to ⇑ **18-10.** Redo Problem 18-9. for a westward flow.

Numerical Exercises

18-1. Use `qgspectral.m` to experiment with different eddy fields. Then include the beta effect and higher order dissipation such as sixth-order derivatives.

18-2. Include diagnostics on energy, enstrophy and wavelength and simulate with different eddy viscosities. Also include diagnostics on

$$k_e = \frac{\int k \left|k\Psi_k\right|^2 dk}{\int \left|k\Psi_k\right|^2 dk} \tag{18.44}$$

$$k_o = \frac{\int k \left|\mathcal{Q}_k\right|^2 dk}{\int \left|\mathcal{Q}_k\right|^2 dk} \tag{18.45}$$

where integrals are performed over all wavenumbers $k^2 = \sqrt{k_x^2 + k_y^2}$. Look at the time evolution of these quantities.

18-3. Generalize `qgspectral.m` to a two layer system (17.30). In particular, take care of the vertical coupling in (17.31) by solving the coupled problem in spectral space exactly. Now experiment again but with different stratifications.

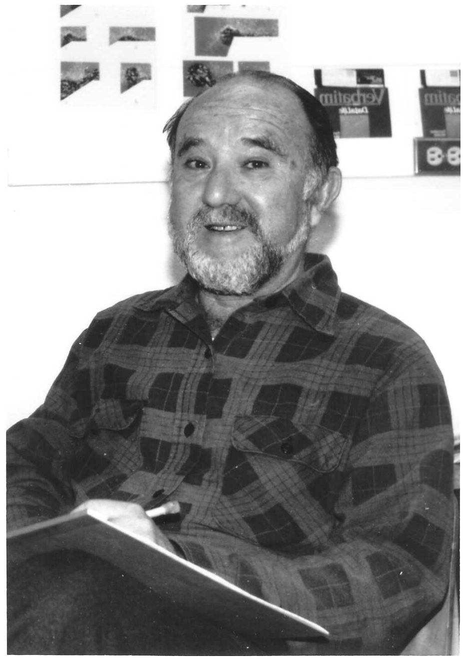

Melvin Ernest Stern
1929 –

Melvin Stern has been an important contributor to the GFD Summer Program at the Woods Hole Oceanographic Institution (see historical note at the end of Chapter 1) and has had a major influence on the evolution of the field ever since the inception of that program. His early work in meteorology was followed by fundamental contributions to our understanding of baroclinic instability (work with J. G. Charney) and of salt fingering (an oceanic small-scale diffusive process). After publishing a book titled *Ocean Circulation Physics* (Academic Press, 1975), Stern dedicated an increasing amount of time and effort to the investigation of vortices. He discovered the *modon* solution - Section 15-6), jets, and jet-vortex interactions, complementing his theoretical studies with original and illuminating laboratory experiments. (*Photo by the authors*)

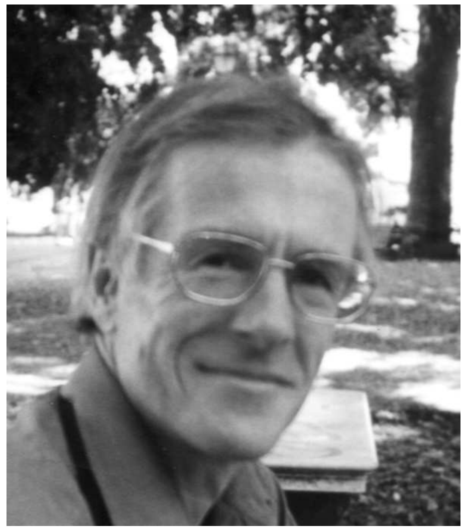

Peter Douglas Killworth
19xx –

Text of second bio
(*Here*)

Part V

Special Topics

Chapter 19

Atmospheric General Circulation

(October 18, 2006) **SUMMARY**: This chapter briefly reviews the principal factors controlling the climate on our planet. We first summarize the global heat budget and then describe the major convective cells and review the major wind systems. The chapter ends with weather forecasting and the particular challenge of simulating cloud dynamics. In this context, ingredients of modern operational weather-forecast models are detailed.

JMB from $\Downarrow$
JMB to $\Uparrow$

19.1 Climate versus weather

Climate is to be distinguished from *weather*. Whereas *weather* includes the detailed behavior of the atmosphere on a time scale of a day to a week, *climate* represents the prevailing or average weather conditions over a period of years. In other words, the climate of the earth can be regarded as the basic state of the atmosphere, subject to variations over years, centuries, millennia, and beyond, while the weather corresponds to its incessant and short-lived instabilities. The engine of climate is a global convection carrying heat from the warmer tropical belt to the much colder polar regions, and its primary manifestation is the distribution of prevailing winds over the globe.

19.2 Planetary heat budget

Because the long-term gradual cooling of the earth's core contributes insignificantly to the heat input near the surface, the incoming solar radiation can be considered as the sole source of heat. From its hot surface ($T \simeq 5750$ K), the sun emits most of its energy in short wavelengths (200 to 4000 nm; 1 nm = 10^{-9} m), of which about 40% is in the visible range (400 to 670 nm). According to the Stefan–Boltzmann law, a so-called *black body* (a perfect emitter and absorber of radiation) emits a radiative flux F depending on its temperature

JMB from $\Downarrow$
JMB to $\Uparrow$

$$F = \sigma T^4, \tag{19.1}$$

where σ is a constant equal to 5.67 $\times$ 10^{-8} W/m^2·K^4 and T is the absolute temperature. Idealizing the sun to a blackbody, we obtain $F_{\rm sun}$ = 6.2 x 10^7 W/m^2 as the outgoing energy flux from the sun's surface. Given the size of the sun, the sun–earth distance, and the earth's area exposed to the sun, the earth receives only a minute fraction of the sun's output: 1376 W/m^2. Averaged over the entire earth's surface (equal to four times the projected area facing the sun), this incident flux amounts to I = 344 W/m^2.

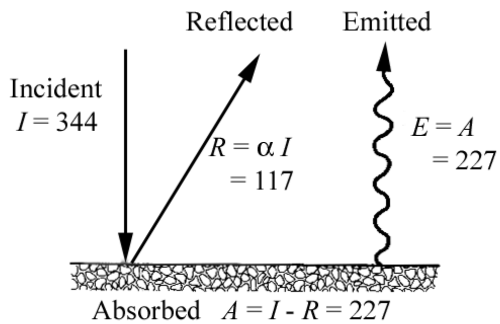

Figure 19-1 Simplest possible model of the earth's budget. Straight lines indicate short-wave radiation whereas the wavy line represents long-wave radiation. (Fluxes are in watts per meter square.) Under this scenario, which does not account for the atmosphere, the earth's average temperature would be a freezing -21°C.

Let us at this point first discard the thickness of the atmosphere and idealize the earth's land and sea surface plus atmosphere as a thin sheet insulated from below. Of the incident radiation, a fraction is reflected out to space by snow, ice, mostly clouds, and everything else that is bright. With α as the reflection coefficient, called the *albedo* ($\alpha \simeq 0.34$), the amount of radiation reflected is $R = \alpha I$ = 117 W/m^2. The difference is the amount absorbed by the earth's surface: $A = I - R = (1-\alpha)I$ = 227 W/m^2 (Figure 119-1). Because the earth is in overall thermal equilibrium[1] (its temperature is not constantly rising), its outgoing radiation matches absorption, and the earth emits a radiative flux E equal to A. This outgoing radiation is in the form of longer wavelengths than the incoming solar radiation and is termed long-wave radiation. Assuming as for the sun that the earth behaves as a blackbody and using the preceding values, we state

$$\sigma T^4 = E = 227\,{\rm W/m^2}, \tag{19.2}$$

and deduce a mean temperature for the earth to be T = 251 K = -21°C. This value is obviously much below the average temperature of the earth as we know it (about 15°C). The failure of this simple model resides in the neglect of the atmospheric layer. The preceding value is more representative of the temperature at the top of the atmosphere than at ground level.

As a next step, we distinguish the atmosphere from the earth's surface (Figure 19-2). The incident short-wave radiation from the sun is unchanged (I = 344 W/m^2); of it, the fraction α_1 (= 0.33) is reflected back to space, primarily by clouds and secondarily by particulate

[1]Some of the heat received by the sun is transformed into mechanical – wind – and chemical – photosynthesis – energies, but these eventually dissipate and turn back into heat.

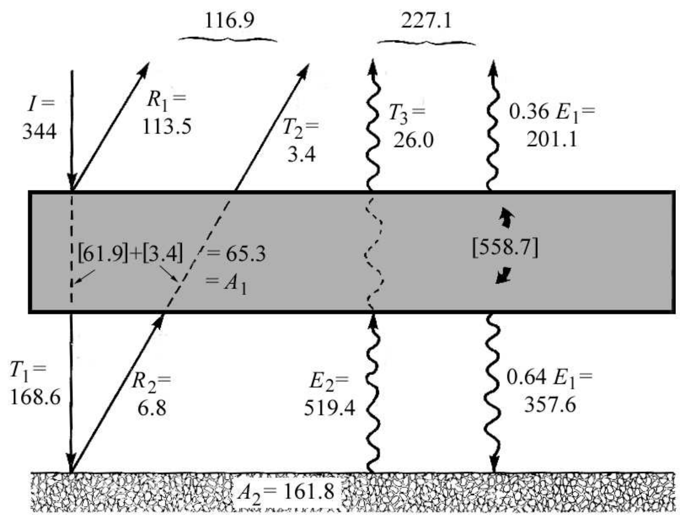

Figure 19-2 A second model of the earth's budget, which distinguishes the atmospheric layer from the earth's surface. All flux values are in watts per meter square. Under this scenario, the earth's average temperature would be a very warm $+36°$C. Here the greenhouse effect (flux loop between the earth's surface and the atmosphere) is present and exaggerated. Note how this effect causes the long-wave radiative fluxes from the earth and atmosphere to exceed the incident short-wave radiative flux from the sun.

matter ($R_1 = \alpha_1 I$ = 113.5 W/m^2), the fraction β_1 (= 0.49) is transmitted to the earth's surface ($T_1 = \beta_1 I$ = 168.6 W/m^2), and the rest is absorbed by the atmosphere. The earth's surface (snow, ice, etc.) reflects a fraction α_2 (= 0.04) of what it receives ($R_2 = \alpha_2 T_1$ = 6.8 W/m^2) and absorbs the rest ($A_2 = T_1 - R_2$ = 161.8 W/m^2). Of the portion R_2 reflected from the earth's surface, the fraction β_1 is transmitted through the atmosphere and out to space ($T_2 = \beta_1 R_2$ = 3.4 W/m^2), whereas the rest is absorbed by the atmosphere. Thus the atmosphere absorbs short-wave radiation directly from the sun ($I - R_1 - T_1$) and indirectly from the earth below ($R_2 - T_2$), and the net is

$$\begin{aligned} A_1 &= (I - R_1 - T_1) + (R_2 - T_2) \\ &= [1 - \alpha_1 - \beta_1 + \beta_1\alpha_2(1 - \beta_1)]I \\ &= 65.3 \text{ W/m}^2. \end{aligned} \tag{19.3}$$

Then both the atmosphere and the earth's surface emit long-wave radiation, in amounts equal to their total intakes of both short- and long-wave radiation. If the atmosphere emits a flux E_1, some of it goes upward into space and the rest goes downward to the earth. Because the top of the atmosphere, where the outgoing radiation originates, is colder than its lower layers, where the earthbound radiation originates, the two amounts are not equal; a representative split is 36% to space and 64% to the earth. Thus, the earth receives $0.64E_1$ of long-wave radiation from the atmosphere in addition to the amount A_2 received in short waves, and its emission E_2 must equal their sum:

$$E_2 \ = \ A_2 \ + \ 0.64 \, E_1. \tag{19.4}$$

At this point, we still do not know either E_1 and E_2, but we can already conclude that the presence of atmospheric radiation toward the earth's surface establishes a loop, whereby the earth's surface emits some radiation, a portion of which returns to the earth. As a consequence, the earth's surface must emit more radiation in the presence of an atmosphere than in its absence and (according to the Stefan–Boltzmann law) must be correspondingly warmer. This is the *greenhouse effect*, so called because of its similarity to the trapping of long-wave infrared radiation by the glass panes of a greenhouse.

Of the amount E_2 radiated by the earth's surface and entering the atmosphere, a fraction β_2 (= 0.05) is transmitted and lost to space ($T_3 = \beta_2 E_2$), with the remainder being absorbed by the atmosphere ($E_2 - T_3$). If the atmosphere absorbs the amounts A_1 and $E_2 - T_3$ in short- and long-wave radiations respectively, its total emission must be equal to their sum; that is,

$$\begin{aligned} E_1 \ &= \ A_1 \ + \ E_2 \ - \ T_3 \\ &= \ A_1 \ + \ (1 - \beta_2) \, E_2. \end{aligned} \tag{19.5}$$

From (19.4) and (19.5), we can derive the emission fluxes E_1 and E_2 to find E_1 = 558.7 W/m^2 and E_2 = 519.4 W/m^2. Note that both are higher than the incident flux I = 344 W/m^2. Then, using the Stefan–Boltzmann law (19.1), we estimate the mean temperature of the earth's surface to be $T = (519.4/\sigma)^{1/4}$ = 309 K = 36°C. This temperature is higher than the first estimate, thanks to the capping effect of the atmosphere (greenhouse effect) but is unrealistically high.

JMB from ⇓

Benoit: $E1 > E2$ might suggest a higher atmospheric layer temperature than earth surface. I suppose in reality upper atmospheric layer temperature would be $((0.36E1 + T)/\sigma)^{1/4} = -21 Celcius$, the previous earth temperature estimate (or $((0.36E1)/\sigma)^{1/4} = -28 Celcius$????) Maybe a note or exercise? I'm not sure here

JMB to ⇑

In reality, the warming influence of the greenhouse effect is partially short-circuited by the hydrological cycle. As water evaporates over the ocean and land, latent heat is extracted from the earth's surface. (Latent heat is the heat required to change the phase of a substance, here to transform liquid water into water vapor. The latent heat of water is 4000 J/kg.) This water vapor rises through the atmosphere, where it condenses in clouds before returning to the earth's surface as rain (liquid phase). Thus, the latent heat extracted from the earth's surface is released in the atmosphere, causing a net heat flux from the earth to the atmosphere that is not in the form of radiation. To this latent-heat flux is added a convective heat transfer. With an estimated total nonradiative heat flux H = 113.6 W/m^2, the earth and atmospheric balances, (19.4) and (19.5), must be amended as (Figure 19-3):

$$E_2 \ = \ A_2 \ + \ 0.64 \, E_1 \ - \ H, \tag{19.6a}$$

$$E_1 \ = \ A_1 \ + \ E_2 \ - \ T_3 \ + \ H, \tag{19.6b}$$

yielding E_1 = 573.2 W/m^2 and E_2 = 415.0 W/m^2. From the radiation law, we deduce a corrected estimate of the mean temperature at the earth's surface: T = (415.0/σ)$^{1/4}$ = 292 K

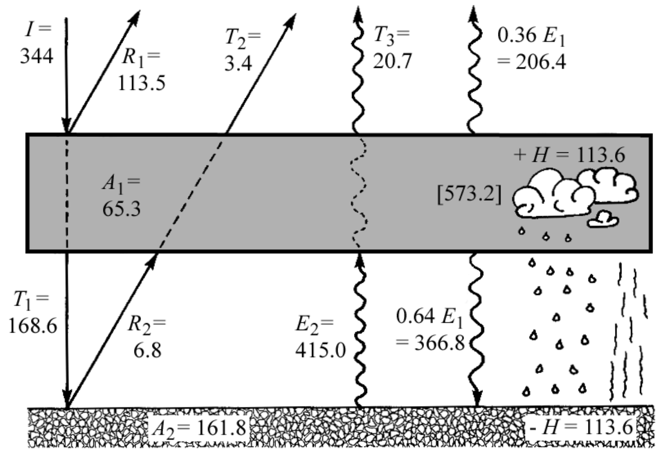

Figure 19-3 A third model of the earth's budget, which atmosphere and hydrological cycle. All flux values are in watts per meter square. This scenario includes the greenhouse effect tempered by the hydrological cycle, resulting in a realistic average temperature at the earth's surface of $+19°$C.

= 19°C. This third estimate is in good agreement with the seasonally and globally averaged temperature on the earth's surface. All in all, we conclude that the greenhouse effect due to the presence of the atmosphere (especially with regard to its near opacity to long-wave radiation) raises the temperature of the earth's surface and that the impact of this effect is partially canceled by the hydrological cycle.

19.3 Direct and indirect convective cells

The preceding considerations exposed the globally averaged heat budget, glossing over all spatial variations. However, that the tropical regions of the globe receive a disproportionate amount of solar radiation, because of their better exposure, is not to be overlooked. Although the earth receives considerably more heat at low latitudes than near the poles, its outgoing radiation is more uniformly spread, decreasing only slightly with latitude (Figure **??**). The resulting heat excess at low latitudes and deficit at high latitudes call for a poleward heat transfer. George Hadley[2] hypothesized that this transfer is accomplished by a giant thermally driven circulation: Warm tropical air rises and flows toward each pole, where it cools and sinks, returning to the tropics along the surface (Hadley, 1735). As it turns out, Hadley was partly correct, insofar as such convective circulations exist on both sides of the equator, and partly incorrect, insofar as these meridional circulations extend only to 30° of latitude. North of 30°N and south of 30°S, opposite circulations are observed, up to 60°, beyond which circulations in the sense predicted by Hadley are again found. Because the convective

[2]British physicist and meteorologist (1685–1768) who first explained the trade winds.

circulations theorized by Hadley follow our intuition, they are generally called *direct cells*. Those direct cells bordering the equator are also called *Hadley cells*. In contrast, the reverse circulations found at midlatitudes bear the name of *indirect cells*. Our purpose here is to explain, in some qualitative manner, why such oppositely directed meridional circulations exist. The story is not simple, invoking the aggregate effect of the transient weather systems

JMB from ⇓ (storms) of the midlatitude regions. **Benoit**: maybe add to the next paragaph something like: To show that a single Hadley cell is unlikely to exist, the conservation of angular momentum can be invoked. A torus of equatorial air mass at rest est with respect to earth conserves the absolute angular momentum when friction is neglected. Hence , when moving northward, we conserve $r^2\Omega = r\cos\varphi(r\cos\varphi + u)$, which would lead to unrealistically high velocities at

JMB to ⇑ midlatidutes, prone to instabilities.

To begin, we note that, although a single direct convective cell could theoretically span an entire hemisphere, such would be unstable. The strong zonal flow in thermal-wind balance with the large meridional temperature gradient would be baroclinically unstable. In fact, the more moderate zonal winds accompanying the alternating circulation structure that exists on the earth are themselves unstable, as the vagaries of the midlatitude weather show so well. According to our discussion of baroclinic instability (Section 17.5), such instabilities develop into coherent vortex systems, called cyclones and anticyclones, that are capable of transferring heat meridionally. At midlatitudes, therefore, the transfer does not take place in a vertical loop, as in a Hadley cell, but via the horizontal circulation of each vortex moving warm air poleward on one side and cold air equatorward on the other. We will now show how the cumulative action of these weather systems at midlatitudes can perform the required poleward transfer of heat so effectively to reverse the meridional circulation in the vertical plane.

The analysis starts with a few modifications of the governing equations. First, the density departure from the reference ρ_0 is expressed in terms of a temperature anomaly T measured from the temperature corresponding to the reference density: $\rho = -\rho_0\alpha T$, where $\alpha = 1/T_0$ is the thermal-expansion coefficient. Then, viscosity and heat diffusivity are neglected, but a heat source or sink term is added in the temperature equation to represent the heat gain in the tropics and the heat loss at high latitudes. From (4.21) we have

$$\frac{\partial u}{\partial t} + u\,\frac{\partial u}{\partial x} + v\,\frac{\partial u}{\partial y} + w\,\frac{\partial u}{\partial z} - fv = -\frac{1}{\rho_0}\frac{\partial p}{\partial x} \tag{19.7a}$$

$$\frac{\partial v}{\partial t} + u\,\frac{\partial v}{\partial x} + v\,\frac{\partial v}{\partial y} + w\,\frac{\partial v}{\partial z} + fu = -\frac{1}{\rho_0}\frac{\partial p}{\partial y} \tag{19.7b}$$

$$\frac{\partial p}{\partial z} = \rho_0\alpha g T \tag{19.7c}$$

$$\frac{\partial u}{\partial x} + \frac{\partial v}{\partial y} + \frac{\partial w}{\partial z} = 0 \tag{19.7d}$$

$$\frac{\partial T}{\partial t} + u\,\frac{\partial T}{\partial x} + v\,\frac{\partial T}{\partial y} + w\,\frac{\partial T}{\partial z} = \frac{Q}{\rho_0 C_p}\,, \tag{19.7e}$$

where Q is the aforementioned thermal forcing (in W/m^3). Focusing exclusively on the Northern Hemisphere, we take Q positive in the tropics (at lower values of y, the northward coordinate) and negative at high latitudes (higher values of y). Thus, the gradient $\partial Q/\partial y$

is negative. The choice of beta-plane equations based on a Cartesian coordinate system over more accurate equations in spherical coordinates is justified in the spirit of a highly simplified analysis aimed at highlighting physical processes in a qualitative way.

We next define the zonal average as the mean over the values of x at any given y and z levels and time t. The zonal averages of the linear equations (19.7c) and (19.7d) are immediate:

$$\frac{\partial \bar{p}}{\partial z} = \rho_0 \alpha g \bar{T} \tag{19.8}$$

$$\frac{\partial \bar{v}}{\partial y} + \frac{\partial \bar{w}}{\partial z} = 0, \tag{19.9}$$

where the overbar denotes this zonal average. With a prime denoting the departure from the average (e.g., $u = \bar{u} + u'$ *etc.*) and with some use of (19.7d), the zonal average of (19.7b) can be expressed as

$$\frac{\partial \bar{v}}{\partial t} + \bar{v}\frac{\partial \bar{v}}{\partial y} + \bar{w}\frac{\partial \bar{v}}{\partial z} + f\bar{u} = -\frac{1}{\rho_0}\frac{\partial \bar{p}}{\partial y} - \frac{\partial}{\partial y}\overline{v'^2} - \frac{\partial}{\partial z}\overline{v'w'}. \tag{19.10}$$

The large meridional pressure gradient ($\partial\bar{p}/\partial y$) associated with the important northward decrease in temperature ($\partial\bar{T}/\partial y < 0$) is balanced by a significant zonal flow ($\bar{u}$). In contrast, the meridional cell ($\bar{v}$, $\bar{w}$) is much weaker, as are the corresponding eddy fluxes ($\overline{v'^2}$, $\overline{v'w'}$). JMB from ⇓
Thus, the preceding may be reduced to JMB to ⇑

$$f\bar{u} = -\frac{1}{\rho_0}\frac{\partial \bar{p}}{\partial y}. \tag{19.11}$$

Together, the hydrostatic balance, (19.8), and the geostrophic relation, (19.11), provide the thermal-wind relation

$$f\frac{\partial \bar{u}}{\partial z} = -\alpha g\frac{\partial \bar{T}}{\partial y}, \tag{19.12}$$

which relates the vertical shear of the average zonal wind to the average meridional temperature gradient. With the temperature decreasing northward in the Northern Hemisphere ($\partial\bar{T}/\partial y < 0$, $f > 0$), the wind shear is positive ($\partial\bar{u}/\partial z > 0$), indicating that the winds must become more westerly (eastward) with altitude.

Finally, we apply the zonal average to the remaining two equations, (19.7a) and (19.7e), to obtain:

$$\frac{\partial \bar{u}}{\partial t} + \bar{v}\frac{\partial \bar{u}}{\partial y} + \bar{w}\frac{\partial \bar{u}}{\partial z} - f\bar{v} = -\frac{\partial}{\partial y}\overline{u'v'} - \frac{\partial}{\partial z}\overline{u'w'} \tag{19.13a}$$

$$\frac{\partial \bar{T}}{\partial t} + \bar{v}\frac{\partial \bar{T}}{\partial y} + \bar{w}\frac{\partial \bar{T}}{\partial z} = \frac{\bar{Q}}{\rho_0 C_p} - \frac{\partial}{\partial y}\overline{v'T'} - \frac{\partial}{\partial z}\overline{w'T'}. \tag{19.13b}$$

According to our previous remarks, the eddy fluxes of momentum and heat associated with the horizontal circulations of the weather systems ($\overline{u'v'}$ and $\overline{v'T'}$) are anticipated to be important, and the corresponding terms are retained. On the other hand, the vertical eddy fluxes ($\overline{u'w'}$ and $\overline{w'T'}$) are neglected. Except for the mean vertical advection of temperature ($\bar{w}\partial\bar{T}/\partial z$) because there is a substantial vertical stratification, mean meridional and vertical advections are unimportant, compared to the meridional eddy transports. In the light of these considerations, the leading terms of the preceding two equations are

$$\frac{\partial \bar{u}}{\partial t} - f\bar{v} = -\frac{\partial}{\partial y}\overline{u'v'} \qquad (19.14)$$

$$\frac{\partial \bar{T}}{\partial t} + \frac{N^2}{\alpha g}\,\bar{w} = \frac{\bar{Q}}{\rho_0 C_p} - \frac{\partial}{\partial y}\overline{v'T'}. \qquad (19.15)$$

Here, we have introduced the stratification frequency N via $N^2 = \alpha g \partial\bar{T}/\partial z$. We shall assume that it does not vary significantly with y.

Forming f times the z-derivative of the first equation plus αg times the y-derivative of the second, to eliminate the time derivatives via (19.12), we obtain

$$\underbrace{\frac{\partial \bar{w}}{\partial y} - \frac{f^2}{N^2}\frac{\partial \bar{v}}{\partial z}}_{=\omega} = \frac{\alpha g}{\rho_0 C_p N^2}\frac{\partial \bar{Q}}{\partial y} - \frac{\alpha g}{N^2}\frac{\partial^2}{\partial y^2}\overline{v'T'} - \frac{f}{N^2}\frac{\partial^2}{\partial y \partial z}\overline{u'v'}. \qquad (19.16)$$

In this last equation, the sign of the left-hand side ω is directly related to the direction of the average circulation in the vertical plane. For simplicity, let us restrict our attention again to the Northern Hemisphere. In a direct cell (Figure 19-4a), $\bar{w}$ decreases northward and $\bar{v}$ increases upward, together yielding a negative ω.On the other hand (Figure 19-4b), an indirect cell corresponds to a positive left-hand side.

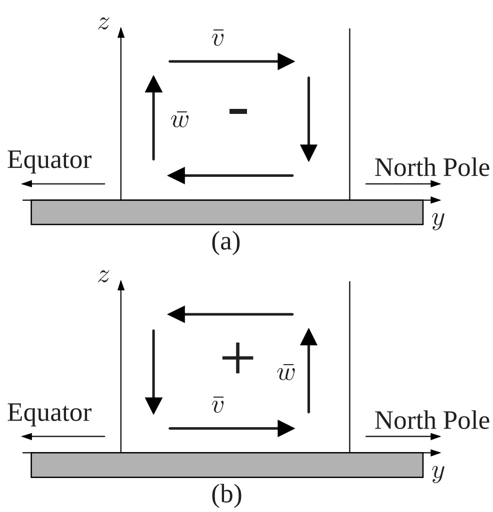

Figure 19-4 Atmospheric circulation in the meridional–vertical plane: (a) direct cell, also called Hadley cell, with $\partial\bar{w}/\partial y < 0$ and $\partial\bar{v}/\partial z > 0$, and (b) indirect cell, also called Ferrel cell, with opposite circulation and positive ω.

According to the right-hand side of (19.16), there are three competing mechanisms influencing the sense of the circulation. In the tropical regions, away from the midlatitude eddy activity, the dominant factor is heating ($\bar{Q}$ term). Because the rate of heating decreases northward ($\partial\bar{Q}/\partial y < 0$), this term is negative, and the circulation in the vertical plane is in the direct sense (as in Figure 19-4a). This occurs up to about 30°N, and the circulation driven by thermal convection is the Hadley cell. The northerly (equatorward) winds along the surface ($\bar{v} < 0$) veer to the right under the action of the Coriolis force, resulting in easterly (westward) zonal winds ($\bar{u} < 0$). These form the *trade winds*.

North of approximately 30°N, where the eddy activity is most intense, the corresponding terms ($\overline{v'T'}$ and $\overline{u'v'}$) dominate the right-hand side of (19.16). Both induce an indirect circulation. This is easy to see with the $\overline{v'T'}$ term and a little harder with the $\overline{u'v'}$ term. The average product $\overline{v'T'}$ is proportional to the meridional heat flux of the eddies. Since this net heat flux must be northward, warm anomalies ($T' > 0$) are preferentially moved northward ($v' > 0$); cold anomalies, on the other hand, are advected southward ($T' < 0$, $v' < 0$), both yielding a net positive $\overline{v'T'}$ correlation. Because the storm activity is most intense at midlatitudes, the term $\overline{v'T'}$ reaches a maximum there. Thus, the second derivative $\partial^2\overline{v'T'}/\partial y^2$ must be negative. Preceded by a minus sign in (19.16), the corresponding term is positive.

The convergence of warm and cold air masses aloft creates a locally intensified gradient of temperature; in thermal-wind balance with this gradient is the polar-front jet stream (Figure **??**old17-1) that flows eastward. The maintenance of this jet in spite of the eddy activity requires a continuous influx of eastward momentum (*i.e.*, positive u' anomalies must be transported to that latitude). This is effected by the eddies, which import positive momentum anomalies from the south ($u' > 0$, $v' > 0$) and from the north ($u' > 0$, $v' < 0$). Thus, the average $\overline{u'v'}$ is positive south of the jet and negative north of it, and the derivative $\partial\overline{u'v'}/\partial y$ must be negative. At the surface, where the jet stream is not found, the correlation $\overline{u'v'}$ is much less important, and we conclude that $\partial\overline{u'v'}/\partial y$ is increasingly negative with altitude, namely, $\partial^2\overline{u'v'}/\partial y\partial z$ is negative. Preceded by a minus sign in (19.16), this term adds to the positive contribution of the other eddy-flux term, and together they overcome the $\bar{Q}$ term. The result is an indirect cell, called the *Ferrel cell*. A corresponding indirect cell is found in the Southern Hemisphere. These Ferrel cells extend to approximately 60°; beyond that, the eddy activity yields to a thermal circulation in the vertical and direct cells exist (Figure 19-5).

The alternation of direct and indirect cells in the meridional direction leads to a similar alternation in surface zonal winds: from the easterly trades to the prevailing westerlies, to the polar easterlies (Figure 19-5). JMB from ⇓

Benoit: Is there a simple explanation (or clear reference) that shows that three cells are the most likely version. Observation tells is that eddy activity is important at mid-latidutes and with previous eddy fluxes this explains the three cell structure. But why the eddy activity is highest at mid-latidute? Other planets other number of cells? JMB to ⇑

19.4 Atmospheric circulation models

Atmospheric circulation models are generally at the forefront of developments in both parameterization of sub-grid scale processes and numerical aspects (see Section 1.9) and still today they are changing permanently in terms of included physics and numerical discretizations. From the first operational models using a single layer quasi-geostrophic approach, we are now arriving at models solving the primitive equations at smaller and smaller scales.

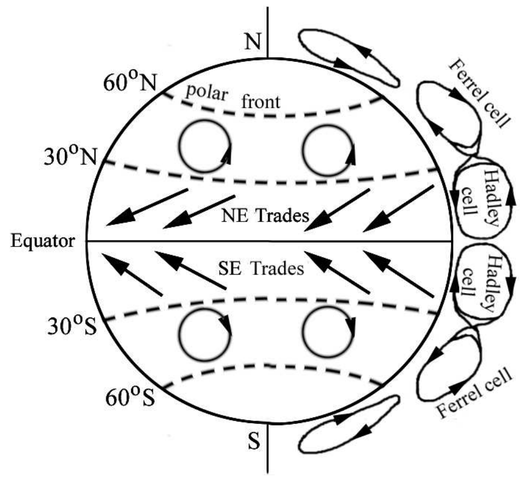

Figure 19-5 Sketch of the general atmospheric circulation, composed of direct (Hadley) and indirect (Ferrel) cells in the meridional direction and alternating winds in the zonal direction.

The equations that are solved are nevertheless still based on the governing equations of section 4.4 to which where added turbulence closures, cloud parameterization, radiation budgets and tracer evolutions. An account of the improvements in atmospheric models during the last decades is out of scope (see Randall, D 2000 for more details), and we now focus on the distinguishing features of atmospheric models compared to ocean models or general geophysical-flow models.

The most widely used models for weather prediction at global scale include those of the European Centre for Medium-Range Weather Forecasts (ECMWF, EU) and the National Centers for Environmental Prediction (NCEP, USA). Both models are adapted to our atmosphere by including a series of physical models or parameterizations, specific to the earth's air behavior. Radiation budgets are more complicated than those of Section 19.2, and in reality, the heat equation should contain a local source term due to radiation, whose behavior depends among others on the orientation of the sun, the wavelength of the radiation, humidity and presence of aerosols, the latter transported with the winds and hence governed by an advection-diffusion equation. Since radiation is behaving differently for each wavelength, different equations for radiative transfers should be included for each wavelength. In practice, they are lumped into spectral bands and at minimum two categories are distinguished: short- and and long-wave radiation as used in our global averages. The models for these radiations include absorption of radiation (and hence local heating) by water vapor, ozone, carbon dioxide and clouds within the atmosphere itself and on the lower boundary, *i.e.,* the earth's surface. Not only absorption must be dealt with in each calculation point, but also the scattering of radiation by aerosols and clouds as well as the reflection by Earth's surface or clouds. Also it must be taken care of the re-emission of longwave radiation by ozone. These processes involve a series of parameterizations which make up the particular radiative transfer equations of the models. The ECMWF model uses for example a radiation scheme based on Orcrette's work (1991): for clear-sky conditions, short-wave radiation is mainly constrained by aerosol scattering and the effects of the absorption by water vapor, ozone, oxygen, carbon monoxide, methane, and nitrous oxide. Clear-sky long-wave radiation is modeled using absorptive properties of water vapor, carbon dioxide, and ozone, which are temperature and pressure dependent. Cloudy skies are dealt with separately and parameterization include absorption and scattering properties of cloud droplets, with clouds being characterized by optical thickness and their scattering properties. The clouds not only constrain the radiative transfer but their prediction is obviously of prime interest for precipitation forecasts. Because of the small scales of clouds compared to grid sizes, parameterizations are again called for and deserve an individual treatment (Section 19.6).

When the weather over the whole planet is calculated, the Atmospheric General Circulation Models (AGCM) have to take into account the spherical nature of the domain and hence governing equations are most naturally written in spherical coordinates (Appendix **??**). This is both a source of complications and simplifications. Complications arise because of the more complex nature of the equations (metric coefficients depend on latidude φ) and the mathematical singularity near the poles (note the presence of $1/\cos\varphi$ in (**??**)). The latter causes numerical stability problems: let us imagine that discretization is performed by using a regular grid in the new "horizontal" longitude-latitude $(\lambda, latitude)$ coordinates with $\Delta\lambda = 2\pi/M$ when M grid points are used in the west-east direction. Then the euclidean distance Δx between two grid points is $\Delta x = r\cos\varphi\,\Delta\lambda$, where r is the distance to the earth center. If follows that this distance Δx approaches zero near the poles. If there are numerical stability conditions of the type $U\Delta t \leq \Delta x$, where U is a physical propagation velocity of similar magnitude at the pole and the equator, the stability condition will be much more stringent near the pole than near the equator, even if the underlying physical process acts similarly in both locations. The overall numerical efficiency is then drastically reduced if the pole imposes its stability condition on the rest of the domain. This is called the problem of *convergence of meridians* and must be addressed. If finite-difference grids in longitude-latitude are used, this requires implicit treatment or filtering close to the poles.

A distinct simplification for AGCM covering the planet is the absence of any lateral boundary, avoiding the application of somehow arbitrary open-boundary conditions (see Section 4.6). Only regional models (so-called *limited area models*, LAMs) need such conditions, generally provided by simulations with an AGCM and nesting techniques. The Aladin model (*Aire Limitée Adaptation dynamique Développement InterNational*[3]) is such a LAM in use for downscaling processes from global scale to regional scale. It predicts smaller-scale processes such as breezes, thunderstrom lines *etc.* using high resolution orography and less parameterizations.

Even if there are no lateral boundaries for AGCMs, they need conditions at the vertical limits of the domain. The upper boundary of atmospheric model is generally taken at a given pressure level (*e.g.*, 0.25 hPa) or at a given height (*e.g.*, 70km) well above the troposphere in which most weather phenomena are confined. The boundary is well above the tropopause to avoid unphysical reflections of waves at the boundary. This is however still an artificial boundary because in reality air rarefies with height instead of changing abruptly its density, which would define a natural boundary. Nevertheless rigid-lid conditions are commonly assumed. At the lower boundary, the atmospheric flow interacts with the cryosphere, oceans and land, which demands proper definition of fluxes.

Depending on the time scale of the processes at hand, those interactions between systems can be simplified (Figure 19-6). If the system coupled to the atmosphere is reacting slowly to atmospheric changes, there is no need to take into account variations in the feed-

[3]Trad: limited area, dynamical adaptation, international development

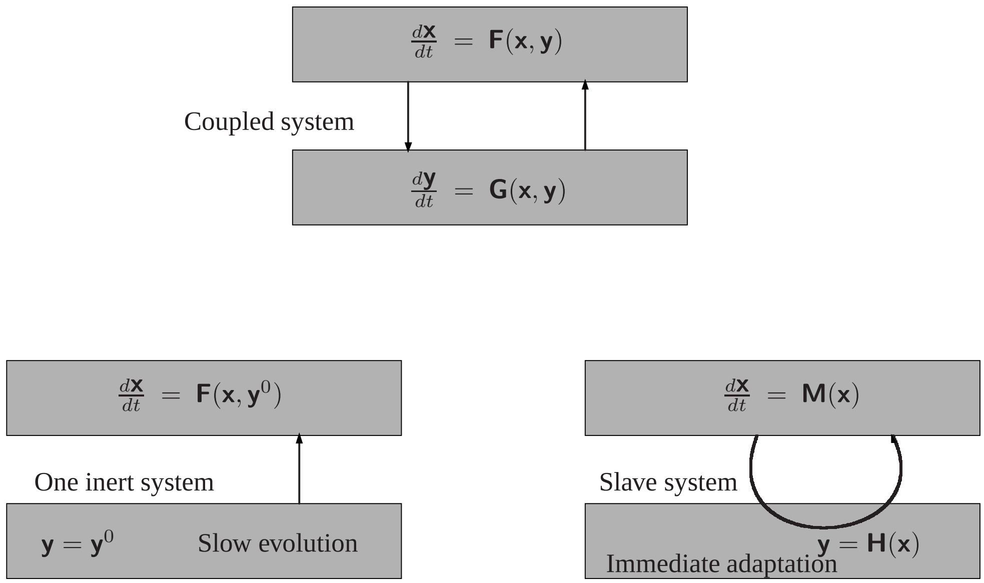

Figure 19-6 Depending on the time scale of the system coupled to the atmosphere, the feedback loop can be simplified into a simple persistence or an immediate adaptation. Only when the time scales of both systems are comparable, the fully coupled version must be retained.

back mechanism: the ice-cover of Antarctica does not change within the few days covered by the weather forecast and hence the observation of the ice-cover at the beginning of the forecast is sufficient to constrain the atmospheric evolution during the forecast. If on the contrary the coupled component reacts extremely fast to changes in the atmospheric conditions, it is often possible to derive quasi-equilibrium laws that allow to predict those fast adaptations directly in terms of atmospheric parameters: the albedo of the land surface changes in time according to changes in land properties and would require a specific land-use model, but if the atmospheric model predicts snow fall, the albedo could immediately be adapted in the atmospheric model so as to take into account the changes in reflection without actually using a dynamic model on land use.

Finally when both coupled components have similar time-scales and interact, they must be modeled in parallel end and forecasts issued simultaneously, including their interactions (see for example the forecast of El Nino events in Section 21.4). Such coupling is however not easy and in the first implementations which coupled AGCM to ocean models for climate calculations, there was a need to correct fluxes between the two systems. Ocean models for example react allergic to errors in wind fields that drive them at the surface and the wind field from atmosperic models must cover the same spectral window as the ocean model is expecting. If fluxes were not adapted, models drifted away. Information on the climate average was then needed in the flux formulations if past climate was to be reconstructed without drifts. This unsatisfactory approach of feeding and relaxing models with part of the solution was for a long time a major reason for objecting that projections into the future are not realistic with such climate models. Now this so-called *flux correction* is not necessary anymore because of improved adequacy between the models that are coupled. Coupled ocean-atmospheric models are now the core of so-called *global climate models* integrating an increasing number of dynamical, biological and chemical components such as ice cover, carbon cycles, land use, hydrological cycles *etc.* The integration allows feedback to be taken into account such as the melting of ice due to heating followed by a change in the albedo itself modifying heat budgets. Other feedback loops are possible through chemical reactions such as the ozone layer that changes under modified climate conditions, itself changing radiative budgets. Such integrated models are called *Earth simulators*. They try to internalize as much processes as possible instead of considering them as forcing functions. Note that because of high computational demands, most of the sub-models are optimized to exploit particular hardware (parallel, distributed or shared) and making them work together is not trivial. It requires information exchange between the models, called message passing on parallel computers, because of the physical coupling. This implementation of exchanges is quite a challenging task both in terms of physical-interaction modeling as well as technical programming. Needless to say that such integrated models are also more and more demanding in terms of understanding the simulation results, particularly when grid resolution increase and more and more physical processes are resolved. After all, in this case, the model should almost react as the real world, which we know is extremely difficult to apprehend. Hence, associated with most models, there is now a suite of statistical and graphical analysis tools to help the modeler ingest the huge amount of information.

When speaking about atmospheric models, it should always be specified if the model is used for weather forecast, seasonal forecast or climate-change scenarios. Indeed, a common argument used to disqualify climate-change studies is the incapacity of predicting weather beyond a few days with current atmospheric models. Since similar numerical models are used to predict climate changes, we should not trust the latter predictions. This argument simply disregards the difference between weather and climate (see Section 19.1). We might well be unable to predict next week weather in New-York but still be able to predict an increase of temperature over the USA in the next years. The situation is similar to the impossibility of predicting the individual behavior of eddies in a turbulent flow but yet being able to predict the average effect of this turbulence on the behavior of transported pollutants, using a same family of governing equations and models. The problem is simply a question of scales we are interested in (look again at Figure 1-7), and which should therefore always be part of the model's definition.

19.5 Weather forecasting

For short-term forecasts, as a weather forecast, most of the feedbacks with systems other than the atmosphere itself can be simplified and rendered non-interactive. In particular, heat fluxes over the ocean depend on the sea surface temperature. In a situation of weather forecast, an atmospheric models uses for example climatological sea surface temperature, observed SST from previous days, a simple mixed-layer model or any of the combination of these approaches instead of a complete ocean model to obtain the required value at the boundary. The general approach of using observations to prescribe forcings adds another explanation why weather forecasts rely on dense observational networks. Enhancement in prediction capabilities are therefore obtained by denser observational networks but also better physical parameterizations, improved numerical methods, increased resolutions and data assimilation (see Chapter 22). Nowadays not only predictions on fields themselves are provided, such as temperature and hours of sunshine for the next 5 days, but also probability of occurrence of events through ensemble predictions (see Chapter 22). In this case forecasters speak about a 60% probability of rain or any other prediction provided by the models, such as temperature, dew point, velocities, pressure, precipitation, cloud cover, snow fall, radiation *etc.*. Though forecast quality has improved significantly in the past, weather remains difficult to predict particularly for rare or extreme events, as well as the absence or presence of precipitations.

19.6 Cloud parameterizations

Problem of precipitation forecasts related to clouds:

Probably most difficult parameterization for atmospheric models is related to clouds. Subgrid scale and complicated physics. Need for parameterization

Insist again on unstable nature of atmosphere because of heating from below.

Feedback: Cloud moving upward, condensation which liberates energy (remember katrina) and hence can accelerate uplift.

Parameterizations still on the base of Arakawa's research (again him).

Also essential role in climate change scenarios (cloud makes shadow at day but greenhouse during night) CO2 changes might modify hydrological cycle hence clouds which further could change climate. IPCC identifies possible changes in cloud cover as one of the major uncertainties in predicting future climate changes

Benoit: Can you provide some text here? I'm not a specialist here and I think I saw some text in your other book on this?

19.7 Spectral methods

Numerical methods employed in atmospheric models have evolved from quasi-geostrophic models using Arakawa Jacobians and inversion of Poisson equations (see Section 16.6) towards more sophisticated spectral models including semi-lagrangien implementations of tracer advections. Most modern global models are based on this approach we will now outline.

The spectral models are based on the same approach as the spectral models presented in the quasi-geostrophic framework. They use a truncated series of orthogonal base functions spanning the domain of interest. For global models, spherical coordinates do not allow a straightforward development of solutions in terms of sine or cosine functions. Assuming vertical dependence be taken care of by standard finite volume of finite-difference techniques, the longitude λ and latitude φ dependence of a field u is expressed as a series of special functions $\mathrm{Y}_{m,n}$ called spherical harmonics:

$$u(\lambda,\varphi,t) \;=\; \sum_m \sum_n a_{m,n} \mathrm{Y}_{m,n}(\lambda, \sin\varphi) \tag{19.17}$$

$$\mathrm{Y}_{m,n}(\lambda,\sin\varphi) = \mathrm{P}_{m,n}(\sin\varphi)\, e^{\mathrm{i}\; m\lambda} \tag{19.18}$$

The so obtained series is of Fourier type in longitude and involves Legendre functions $\mathrm{P}_{m,n}$ on latitude:

$$\mathrm{P}_{m,n}(x) = \sqrt{\frac{(2n+1)(n-m)!}{2(n+m)!}\,(1-x^2)^m}\;\;\frac{d^m}{dx^m}\mathrm{P}_n(x) \tag{19.19}$$

defined in terms of Legendre polynomials of degree n

$$\mathrm{P}_n(x) = \frac{1}{2^n\, n!}\frac{d^n}{dx^n}\left[(x^2-1)^n\right] \tag{19.20}$$

Since P_n is a polynomial of degree n, the Legendre functions are different from zero only when $m \leq n$. Extension towards negative values of m are desirable for the Fourier modes and hence we extend also the definition of Legendre functions by $\mathrm{P}_{-m,n}(x) = (-1)^m \mathrm{P}_{m,n}(x)$. With the scaling of (19.19), Legendre functions are orthonormal:

$$\int_{-1}^{1} \mathrm{P}_{m,n}(x)\mathrm{P}_{m,k}(x)dx = \delta_{n,k} \tag{19.21}$$

On the surface $\mathcal{S}$ of the sphere of radius R, the elementary surface element $R^2\cos\varphi\, d\varphi d\lambda$ can be written in terms if $\xi = \sin\varphi$ as $R^2\, d\xi d\lambda$ so that

$$\frac{1}{R^2}\int_{\mathcal{S}} \mathrm{Y}_{m,n}\mathrm{Y}^*_{p,k}\; d\mathcal{S} = \int_{-1}^{1}\int_{-\pi}^{\pi} \mathrm{Y}_{m,n}\mathrm{Y}^*_{p,k}\, d\lambda d\xi = 2\pi\,\delta_{m,p}\,\delta_{n,k} \tag{19.22}$$

where * stands for the complex conjugate. The horizontal Laplacian of the base functions reads in spherical coordinates :

$$\nabla^2 \mathrm{Y}_{m,n} = -\frac{n(n+1)}{R^2}\mathrm{Y}_{m,n} \tag{19.23}$$

so that inversions of Poisson equations can be performed immediately when working in the transformed space. Note that the pseudo[4] wavenumber $\sqrt{n(n+1)}/R$ is surprisingly independent of m.

Orthogonality of spherical harmonics can be used to isolate governing equations for $a_{m,n}(t)$ by multiplying the governing equations by $\mathrm{Y}_{m,n}{}^*$ and integrating over the globe's surface because the continuous version of the inverse transform is (19.18) and the associated forward transformation reads

$$a_{m,n} = \int_{-1}^{1}\left[\int_0^{2\pi} u(\lambda,\xi,t)\, e^{-\mathrm{i}\, m\lambda} d\lambda\right]\;\mathrm{P}_{m,n}(\xi)\, d\xi \tag{19.24}$$

as can be verified by the orthogonality properties.

[4]In cartesian coordinates we would have $\nabla^2 u = -(k_x^2 + k_y^2)\, u$ with the Fourier spectral approach, hence the analogy.

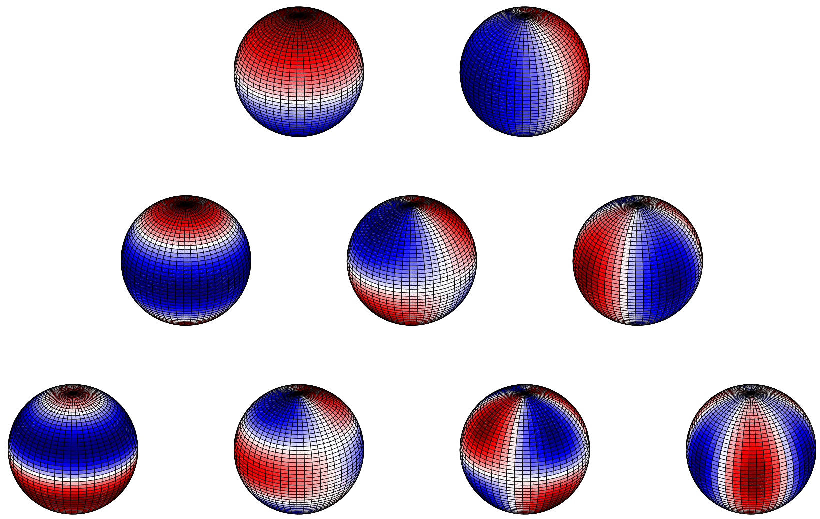

Figure 19-7 Real part of spherical harmonics $\mathrm{Y}_{m,n}$ for (m,n) taking values (0,1),(1,1) on the first line, (0,2),(1,2),(2,2) on the second line and (0,3),(1,3),(2,3),(3,3) on the last line. The white regions separate regions of positive and negative values. The mode (0,0) is constant on the sphere.

Truncation (Figure 19-8) of the sums in numerical schemes can be achieved in several ways, the only constraint being that in all cases $|m| \leq n$ which can be achieved by

$$\tilde{u} = \sum_{m=-M}^{M} \sum_{n=|m|}^{N(m)} a_{m,n} \mathrm{Y}_{m,n} \tag{19.25}$$

The structure of spatial resolution depends on the formulation used for $N(m)$. When $N(m) = M$, called a *triangular truncation*, uniform resolution on the sphere is achieved. Other truncations allow better resolutions in particular regions of the sphere (Figure 19-7 and 19-8). With reference to the chosen truncation, models are nicknamed by terms such as T256L60 for a triangular truncation using $M = 256$ spectral components. The qualifier L60 stands for the vertical grid using 60 discrete levels. For ECMWF, the levels are distributed according to a hybrid vertical coordinate system where the new vertical coordinate s depends on pressure p and surface pressure p_{surf} by $s = s(p, p_{\mathrm{surf}})$, scaled so that $s(0, p_{\mathrm{surf}}) = 0$ and $s(p_{\mathrm{surf}}, p_{\mathrm{surf}}) = 1$. This is a generalization of a pressure coordinate system (called σ coordinates) introduced by Phillips (1957) $s = p/p_{\mathrm{surf}}$, which is used in NCEP. Since more general hybrid vertical coordinates are now used in ocean models, we will postpone the corresponding discussion until Section 20.7. Note that because m takes negative values, the actual wavenumbers resolved are indeed M, contrary to the standard FFT presentation which uses only positive values and hence half of the wavenumbers (see appendix **??**).

For discrete versions of integrals, orthogonality is generally not ensured and hence a direct followed by an inverse transformation not ensured to fall back into the original signal.

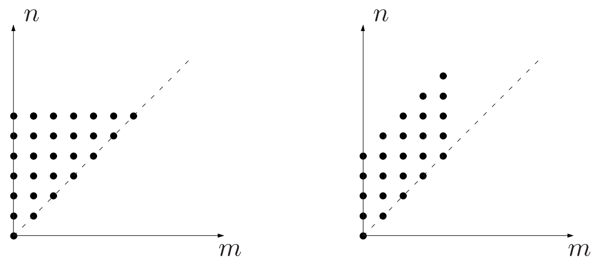

Figure 19-8 Triangular and rhomboidal truncation. Only the part for positive m are shown, the negative part being symmetric. Triangular truncation is now more popular than the originally preferred rhomboidal version.

For discrete Fourier transform orthogonality is maintained (see appendix C and Section 18.4), so that we can evaluate the inner integral of the forward transform through a FFT and the corresponding inverse transform by inverse FFT. There remains thus to ensure that the numerical treatment of the outer integral of (19.24) conserves orthogonality. Unfortunately there is no equivalent numerical tool to the FFT that allows to perform the transforms on the Legendre expansion and we must resort to numerical quadrature of the integrals. First we can performe a FFT at a series of given latitudes φ_j, $j = 1, ..., J$ with $\xi_j = \sin\varphi_j$ to obtain Fourier coefficients

$$b_m(\xi_j, t) = \int_0^{2\pi} u(\lambda, \xi_j, t) e^{-\mathrm{i}\, m\lambda} d\lambda \tag{19.26}$$

defined at locations ξ_j. Then coefficients $a_{m,n}$ can be estimated by a numerical quadrature using the value of the integrand in those locations φ_j:

$$a_{m,n} = \sum_{j=1}^{J} \mathsf{w}_j\, b_m(\xi_j) \mathrm{P}_{m,n}(\xi_j). \tag{19.27}$$

The weights w_j and locations ξ_j can be chose so as to reduce integration errors. Gaussian quadrature can be shown to produce exact results when integrating polynomials of degree $2J-1$ if the J points on which the integrand is evaluated are located at the zeros of $\mathrm{P}_J(\xi_j) = 0$ and weights taken as

$$\mathsf{w}_j = \frac{2}{1-\xi_j^2} \left[\frac{d\mathrm{P}_J}{d\xi}(\xi_j) \right]^2 \tag{19.28}$$

It would appear that the integrands we are dealing with are not polynomials because Legendre functions involve square roots, but what matters is that transforms of the nonlinear physical terms are treated correctly. As those involve products of Legendre functions, it can be shows that they make only appear polynomials and we can integrate exactly. The number of points J must then be taken so as to integrate correctly the highest degree of polynomials that will appear as a consequence of nonlinear terms such as $u\partial u/\partial\theta$. The transform of such a term would require the evaluation of triplet of Legendre functions (one for each appearance of u and then the application of the transform itself involving the third Legendre function). For a highest degree $m = M$ on Legendre functions, a polynomial of degree $3M$ appears and must therefore use $J > (3M+1)/2$ points to integrate it exactly. For the Fourier transform on longitude, the same analysis as in Section 18.4 applies and requires the use of $(3M+1)$ evaluation points in longitude if M Fourier modes are retained. Hence a model with 42 modes, will use typically a 128 $\times$ 64 underlying grid in longitude-latitude for the evaluation of the nonlinear terms (note the rounding towards powers of 2 that allow efficient FFT transforms). This grid is called the *Gaussian grid* or *transform grid*. The calculation of grid spacing based on the number of Gaussian grid points overestimates actual resolution because it is designed to avoid aliasing on nonlinear interactions and the real resolution is provided by the wavenumbers associated with the spectral decomposition.

The transform methods allows thus to calculate some terms in spectral space (linear dynamics) and others in the transformed space (nonlinear terms and physical parameterizations) so as to use the most appropriate technique for each process. In practice it means the model keeps both a spectral and grid representation of the variables. The high convergence rate of spectral methods is inherited with the spherical harmonics, as long as the physical solution is sufficiently regular. On the contrary, when fronts or other fields with jumps are present such as specific humidity fields, Gibb's phenomena appear and local spatial oscillations near the discontinuity emerge when summing up the spectral series. The associated over- or undershooting on the physical grid can the lead to spurious physical reactions. An overshooting of specific humidity leads for example to the poetically named *spectral rain*. Because of the calculation of some terms on the physical grid, the convergence of meridians can also again be a problem. For the advection part, this can be solved by the Semi-Lagrangian approach.

19.8 Semi-Lagrangian methods

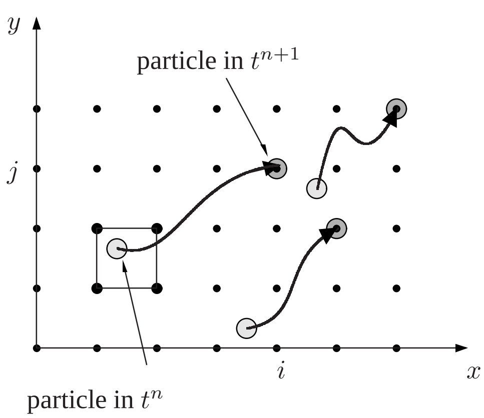

Figure 19-9 Semi-Lagrangian methods integrate backwards trajectories in order to find the location from where originates a particle arriving on a grid node (i, j) at time t^{n+1}. Once this location known, the concentration at that location must be obtained by interpolation of nearby data. The interpolated value is conserved during advection and is thus the concentration in (i, j) at t^{n+1}.

For advection, we again turn attention to passive-tracer concentration c which is conserved along a trajectory of an parcel of fluid when diffusion is negligible. In this case, the Lagrangian approach allows to satisfy the conservation property of a parcel exactly at the price of calculating its trajectory. One of the disadvantage of advection schemes using the pure Lagrangian method is the inhomogeneous distribution of particles after some time. This is because we follow the same set of particles all the time, some of which flow out of the system or are caught in stagnation points. *Semi-Lagrangien* methods use a different set of particles each time step. The set is chosen in t^n so that in t^{n+1} the particles fall on the nodes of an underlying regular numerical grid. This amounts to integrate backward trajectories in order to find the place from where a particle originates that arrives at a given grid location. Once knowing the location of the particle in t^n we need to assess its associated concentration in this location. Since for time t^{n+1} we move particles to a regular grid, we can assume that in t^n we have at our disposal the values of the preceding set of particles on exactly that regular grid. Therefore we need an interpolation using values of the surrounding grid nodes to get the value of the new particle (Figure 19-9).

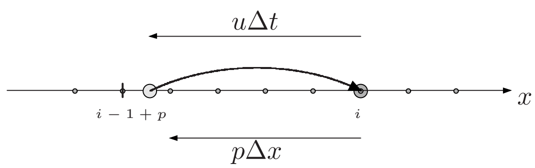

Figure 19-10 Semi-Lagrangian method in 1D. The particle in light gray is displaced during time interval t^n t^{n+1} by a distance $u\Delta t$ to reach a grid node labeled i in t^{n+1}.

Let us consider again the 1D advection case with positive velocity, assuming we have a uniform particle distribution at time t^n (Figure 19-10). The particle arriving in grid node x_i at time t^{n+1} was at a position

$$x = x_i - u\Delta t \tag{19.29}$$

in t^n. In a uniform grid with spacing Δx this position lies within the grid interval

$$x_{i-1+p} \leq x = x_i - u\Delta t \leq x_{i-p}, \quad p = \text{integer part of } u\frac{\Delta t}{\Delta x}. \tag{19.30}$$

and to assess the value of $\tilde{c}_i^{n+1}$ we simply have to know the value of $\tilde{c}^n$ in x, a value we can obtain by interpolation. If the interpolation is linear we get:

$$\tilde{c}_i^{n+1} = \frac{(x_{i+p} - x)}{\Delta x}\tilde{c}_{i-1+p}^n + \frac{(x - x_{i-1+p})}{\Delta x}\tilde{c}_{i+p}^n = \tilde{\mathsf{C}}\tilde{c}_{i-1+p}^n + (1-\tilde{\mathsf{C}})\tilde{c}_{i+p}^n, \quad \tilde{\mathsf{C}} = \left(\frac{u\Delta t}{\Delta x} - p\right).$$

The scheme is monotonic and thus of first order. We can easily see that if $u\Delta t \leq \Delta x$ the scheme is equivalent to the upwind scheme ($p = 0$). However, contrary to the upwind scheme, no stability condition is necessary here, because the method will use the correct grid interval from which to interpolate. The diffusion is however still present, though maybe reduced in the sense that large time steps can be used and the total number of time steps and associated numerical diffusion reduced for a given simulation length. For less diffusive interpolations, parabolic interpolations will be equivalent to the Lax-Wendroff method[5].

In 2D dimensions, the approach is generalized readily with 2D trajectories integrated backward in time and spatial interpolations (bi-linear or bi-parabolic) at the point which arrives on the regular grid at instant t^{n+1}. The trajectory calculation can become quite complicated if $U\Delta t \geq \Delta x$ because if the velocity varies on the grid scale Δx, intermediate time-steps are necessary during the trajectory calculation in order to maintain precision on the trajectory. However, if the velocity is relatively smooth in the numerical grid (which will be the case near the pole), *i.e.*, $\Delta x \ll L$ simple trajectory integrations will suffice. In fact if $\Delta x \ll U\Delta t \ll L$ the Semi-Lagrangian approach will be much more efficient than the Eulerian approach because then during each time step a large number of grids can be

[5]Note the difference: in Eulerian methods we spoke about interpolation for flux calculations to be differenced subsequently, here we speak about interpolations of the solution itself.

"jumped over" by the advection, without need for interpolation (and associated diffusion) there and still resolving correctly the spatial scales of the trajectory. This is the situation with the largest benefit for the Semi-Lagrangian approach. The method should also be considered advantageous if a large number of passive tracers are to be advected since trajectories need to be calculated for one of them, the other tracers being advected by the same flow. If $\Delta x \sim L$ time steps are similar to the Eulerian approach if a reasonable accuracy is required. The major advantage in this case is the stability of the method even for occasionally too large time steps. For accuracy one should however not use larger time steps than $U\Delta t \sim L$.

For source terms or diffusion, fractional step approaches are possible, first using a Semi-Lagrangian advection followed by an Eulerian diffusion on the regular grid or in spectral space for example. Alternatively the evolution of local source terms can be taken into account along the trajectory (REFERENCE). Contrary to the finite-volume approach of Eulerian methods, conservation properties are more difficult to handle but are possible to implement (REFERENCE).

Analytical Problems

19-1. Consider the regular gardening greenhouse and idealize the system as follows: The ground and glass act as black bodies (absorbing all the radiation directed toward them), the air plays no role, the ground absorbs all radiation, and the glass is perfectly transparent to short-wave (visible) radiation and totally opaque to long-wave (heat) radiation. Further, the glass emits its radiation upward and downward in equal parts. Compare the ground temperature inside the greenhouse with that outside. Then, redo the exercise for a greenhouse with two layers of glass separated by a layer of air.

19-2. Consider the crudest heat budget for the earth (without atmosphere and hydrological cycle) and assume the following dependency of the albedo on temperature: At low temperatures, much ice and clouds cover the earth, yielding a high albedo, whereas at high temperatures, the absence of ice and clouds reduce the albedo to zero. Taking the functional dependence as

$$\begin{aligned} \alpha &= 0.5 \quad \text{for} \quad T \le 250\,\mathrm{K} \\ \alpha &= \frac{270 - T}{40} \quad \text{for} \quad 250\,\mathrm{K} \le T \le 270\,\mathrm{K} \\ \alpha &= 0 \quad \text{for} \quad 270\,\mathrm{K} \le T, \end{aligned} \tag{19.31}$$

solve for the earth's average temperature T. Discuss the several solutions.

19-3. Using the global heat budget of the earth model, complete with an atmospheric layer and a hydrological cycle, explore a worst-case scenario whereby elevated concentrations of greenhouse gases completely block the transmission of long-wave radiation from the earth's surface, the intensity of the hydrological cycle is unchanged, and the anticipated global warming has caused the complete melting of all ice sheets, effectively eliminating all reflection by the earth's surface of short-wave solar radiation. What would then be the globally averaged temperature of the earth's surface? (Except for those transmission and reflection coefficients that need to be revised, use the parameter values quoted in the text.)

19-4. In addition to the problem of decreasing grid spacing near the poles, which additional problem can you identify at the poles? *Hint:* Think about boundary conditions for an AGCM on longitude first and then on latitude.

Numerical Exercises

19-1. What is the spatial resolution in km along the Equator for a T256 spectral model? How many grid points has the underlying Gaussian grid that avoids aliasing in the advection terms?

19-2. Use `spherical.m` to look at other base functions $\mathrm{Y}_{m,n}$ than those of figure 19-7

19-3. Estimate the numerical cost of the forward and inverse transform associated with the Legendre functions.

19-4.

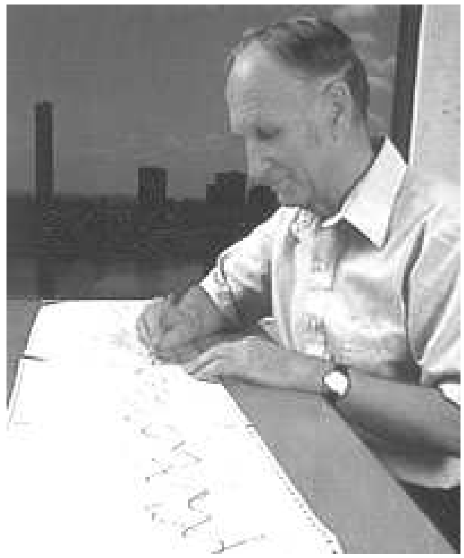

Edward Norton Lorenz
1917 –

Text of first bio (*here*)

Joseph Smagorinsky
1924 – 2005

A native of New York City, Joseph Smagorinsky studied meteorology and began a career with the U.S. Weather Bureau. In 1955, he founded the *Geophysical Fluid Dynamics Laboratory*, which was first established in Washington, D. C., and later relocated at Princeton University. The 1950s were exciting years when the prospect of computers gave great hopes that weather could be predicted by machines. Recognizing this opportunity, Smagorinsky developed numerical methods for predicting weather and climate, and by so doing profoundly influenced the practice of weather forecasting. In particular, he made the first attempt in 1955 to predict precipitation.

Besides numerical methods and models, Smagorinsky also contributed to weather prediction by playing a leading role in the establishment of a global observational network. As director of the Geophysical Fluid Dynamics Institute, Joseph Smagorinsky showed that he was also a very able administrator. (*Photo courtesy of Princeton University*)

Chapter 20

Oceanic General Circulation

(October 18, 2006) SUMMARY: The concepts of geostrophy, hydrostaticity and potential vorticity are merged to study the large-scale baroclinic circulation in the midlatitude oceans. The results lead to the Sverdrup balance, the beta spiral and a number of properties of large-scale oceanic motions. The numerical part of the chapter provides an overview of the issues raised in constructing a model of the 3D circulation at the scale of ocean basins or the planet.

20.1 What drives the oceanic circulation

Ocean motions span a great variety of scales in both time and space. At one extreme, we find microturbulence, not unlike that in hydraulics, and at the other, the large-scale circulation, which spans ocean basins and evolves over climatic time scales. The latter extreme is the objective of this chapter.

There are multiple mechanisms that set oceanic water masses in motion: the gravitational pull exerted by the moon and sun, differences in atmospheric pressure at sea level, wind stress over the sea surface, and convection resulting from atmospheric cooling and evaporation. The moon and sun generate only periodic tides with negligible permanent circulation, whereas differences in atmospheric pressure play no significant role. On the other hand, deep convection at high latitudes generates currents responsible for a very slow movement in the abyss, called the *conveyor belt* (Figure 20-1). This leaves the stress exerted by the winds along the sea surface as the main driving force of basin-wide circulations in the upper part of the water column.

Ocean waters respond to the wind stress because of their low resistance to shear (low viscosity, even after viscosity magnification by turbulence) and because of the relative consistency with which winds blow over the ocean. Good examples are the *trade winds* in the tropics; they are so steady that, shortly after Christopher Columbus and until the advent of steam, ships chartered their courses across the Atlantic according to those winds; hence their name. Further away from the tropics are winds blowing in the opposite direction. While trade winds blow from the east and slightly toward the equator (they are also more aptly

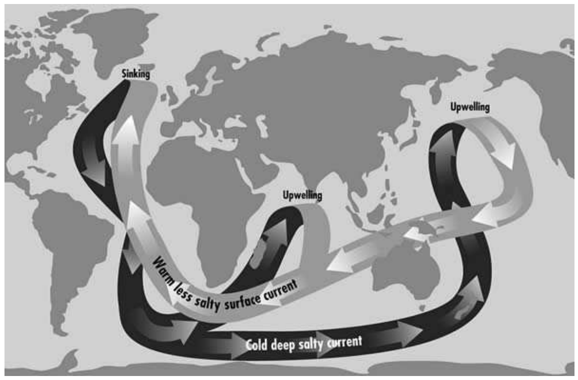

Figure 20-1 Cold and salty waters newly formed by deep convection at high latitudes are carried away by the conveyor belt along the ocean bottom across the ocean basins. These water eventually resurface in warmer climes and are returned towards places of deep convection. The time to complete a loop is on the order of several hundred years. (*Broecker, 1991*)

called northeasterlies and southeasterlies, depending on the hemisphere), midlatitude winds blow from west to east and are called *westerlies* (Figure 20-2). Generally, much more variable than the trades, these westerlies nonetheless possess a substantial average component, and the combination of the two wind systems drives significant circulations in all midlatitude basins: North and South Atlantic, North and South Pacific, and Indian Oceans.

In the ocean, the water column can be broadly divided into four segments. At the top lies the *mixed layer* that is stirred by the surface wind stress. With a depth on the order of 10 m, this layer includes Ekman dynamics and is characterized by $\partial\rho/\partial z \simeq 0$. Below lies a layer called the *seasonal thermocline*, a layer in which the vertical stratification is erased every winter by convection. Its depth is on the order of 100 m. Below the maximum depth of winter convection is the *main thermocline*, which is permanently stratified ($\partial\rho/\partial z \neq 0$). Its thickness is on the order of 500 to 1000 m. The rest of the water column, which comprises most of the ocean water, is the *abyssal layer*. It is very cold, and its movement is very slow.

When considered together, the main thermocline and the abyssal layer form what is called the *oceanic interior*. While mesoscale motions exist in both these layers, under the action of pressure fluctuations in the upper layers, it is believed that, in first approximation, the study of the slow background motion in the oceanic interior can proceed independently of the smaller-scale, higher-frequency processes.

Although mariners have long been aware of the major ocean currents, such as the Gulf Stream[1], ocean circulation theory was long in coming, chiefly for lack of systematic data, especially below surface. The discipline began in earnest with the seminal works of Harald Sverdrup[2], who formulated the equations of large-scale ocean dynamics (Sverdrup, 1947) and Henry Stommel[3], whose major contributions to ocean circulation are many and diverse, beginning with the first correct theory for the Gulf Strean (Stommel, 1948). Today, ocean circulation theory is a significant body of knowledge (Warren and Wunsch, 1981; Pedlosky, 1996).

[1] Benjamin Franklin receives credit for publicizing and mapping the Gulf Stream in 1770.

[2] Harald Ulrik Sverdrup (1888–1957), Norwegian oceanographer who made his greatest contributions while being director of the Scripps Institution of Oceanography in California. A unit of volumetric ocean transport bears his name: 1 sverdrup = 1 Sv = 10^6 m^3/s.

[3] See biography at end of this chapter.

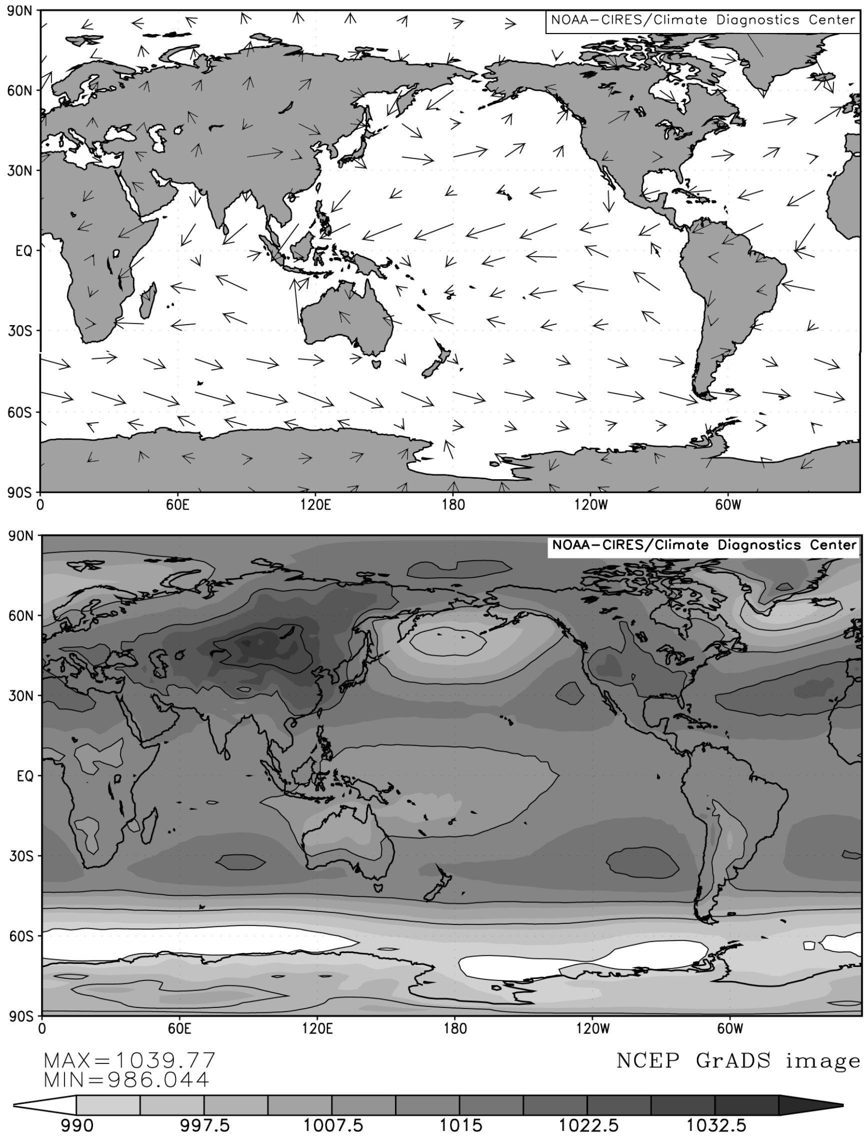

Figure 20-2 The major winds over the world ocean for the month of January averaged over the years 1968–1996 and associated sea surface pressure. (*NCEP*)

20.2 Large-scale ocean dynamics (Sverdrup dynamics)

Because oceanic basins have dimensions comparable to the size of the earth, model accuracy demands the use of spherical coordinates, but because the present book only intends to present an introduction to physical oceanography, clarity of exposition trumps accuracy, and we continue to use Cartesian coordinates, with inclusion nonetheless of the beta effect (see Section 9.4). Spherical coordinates (Pedlosky, 1996, Chapter 1) do not change the qualitative nature of the theoretical results exposed here.

Large-scale flows in the main thermocline and abyss are slow and nearly steady. Their long time scales allows us to ignore all time derivatives, while their low velocities over long distances make their Rossby number very small and allow us to neglect the nonlinear advection terms in the momentum equations. Furthermore, there is a strong indication that dissipation is not an important feature of large-scale dynamics, at least not at the leading order (Pedlosky, 1996, page 6). Without time derivatives, advection and dissipation, the horizontal momentum equations reduce to the geostrophic balance:

$$- fv = -\frac{1}{\rho_0}\frac{\partial p}{\partial x} \tag{20.1a}$$

$$+ fu = -\frac{1}{\rho_0}\frac{\partial p}{\partial y}, \tag{20.1b}$$

in which the Coriolis parameter f includes the so-called beta effect, which is important over the long length scales under consideration:

$$f = f_0 + \beta_0 \, y. \tag{20.2}$$

The y–coordinate is thus directed northward, leaving the x–direction to point eastward. The coefficients (see Equation 9.18) $f_0 = 2\Omega \sin\varphi$ and $\beta_0 = 2(\Omega/a)\cos\varphi$ both depend on the choice of a reference latitude φ, which may be taken as the middle latitude of the basin under consideration.

The geostrophic equations are complemented by the hydrostatic balance

$$\frac{\partial p}{\partial z} = -\rho g, \tag{20.3}$$

the continuity equation (mass conservation for an incompressible fluid)

$$\frac{\partial u}{\partial x} + \frac{\partial v}{\partial y} + \frac{\partial w}{\partial z} = 0, \tag{20.4}$$

JMB from $\Downarrow$ and the energy equation, which states conservation of heat and salt and is expressed as conservation of the density anomaly with the same stationarity approximation as before

JMB to $\Uparrow$

$$u\frac{\partial \rho}{\partial x} + v\frac{\partial \rho}{\partial y} + w\frac{\partial \rho}{\partial z} = 0. \tag{20.5}$$

In the preceding equations, u, v and w are the velocity components in the eastward, northward and upward directions, respectively, ρ_0 is the reference density (a constant), ρ is the density anomaly, the difference between the actual density and ρ_0, p is the hydrostatic pressure induced by the density anomaly ρ, and g is the earth's gravitational acceleration (a constant). This set of five equations for five unknowns (u, v, w, p and ρ) is sometimes referred to as *Sverdrup dynamics*. Note that the problem is nonlinear owing to product of unknowns in the density equation (20.5). We now proceed with the study of some of its most immediate properties.

Elimination of pressure between the two momentum equations, by subtracting the y–derivative of (20.1a) from the x–derivative of (20.1b) yields

$$\frac{\partial}{\partial x}(fu) \;+\; \frac{\partial}{\partial y}(fv) \;=\; 0, \tag{20.6}$$

or, since f is a function of y but not of x,

$$f\left(\frac{\partial u}{\partial x} \;+\; \frac{\partial v}{\partial y}\right) \;+\; \beta_0 v \;=\; 0. \tag{20.7}$$

With the use of continuity equation (20.4), it can be recast as:

$$\beta_0 v \;=\; f\,\frac{\partial w}{\partial z}. \tag{20.8}$$

This most simple equation, called the *Sverdrup relation*, has a clear physical meaning. The factor $\partial w/\partial z$ represents vertical stretching, and any stretching ($\partial w/\partial z > 0$) or squeezing ($\partial w/\partial z < 0$) demands a change in vorticity for the sake of potential-vorticity conservation, which holds in the absence of dissipation. There is no relative vorticity here because of the low Rossby number, and the only way for a parcel of fluid to change its vorticity is to adjust its planetary vorticity (**Benoit:** Relative U/L, planetary as f, and small Rossby number indeed suggests relative vorticity not important. Maybe this is a little bit too fast. What counts is PV as in (16.16)? There planetary part over relative there scales like $\beta L^2/U$... . This requires a meridional displacement, v, to reach the correct f value. JMB from ⇓ JMB to ⇑

This, however, is not the end of the story. We can go further with a vertical integration:

$$\beta_0 \int_0^H v\,dz \;=\; f\,[w(z=H) - w(z=0)], \tag{20.9}$$

where $z = 0$ represents the ocean bottom and $z = H$ the base of the seasonal thermocline. Over a flat bottom, $w(z = 0) = 0$. At the base of the seasonal thermocline, the water column receives Ekman pumping from above due to the wind-stress curl, and thus **Benoit:** I do not think we showed that the pumping is uniform below the Ekman layer and hence can be used to calculate the pumping at the seasonal thermocline?? Some justification needed? JMB from ⇓ JMB to ⇑

$$w(z=H) \;=\; w_{\rm Ek} \;=\; \frac{1}{\rho_0}\left[\frac{\partial}{\partial x}\left(\frac{\tau^y}{f}\right) - \frac{\partial}{\partial y}\left(\frac{\tau^x}{f}\right)\right], \tag{20.10}$$

by virtue of (8.36). If we define the meridional transport as $\mathrm{V} = \int_0^H v\,dz$, we then have:

$$\begin{aligned} \mathrm{V} &= \frac{f}{\beta_0}\, w_{\mathrm{Ek}} \\ &= \frac{f}{\rho_0\beta_0}\left[\frac{\partial}{\partial x}\left(\frac{\tau^y}{f}\right) - \frac{\partial}{\partial y}\left(\frac{\tau^x}{f}\right)\right] \\ &= \frac{1}{\rho_0\beta_0}\left(\frac{\partial \tau^y}{\partial x} - \frac{\partial \tau^x}{\partial y}\right) + \frac{\tau^x}{\rho_0 f}\,. \end{aligned} \tag{20.11}$$

We note this surprising result that the vertically cumulated flow component in the north-south direction is not dependent on the basin shape, size or wind-stress distribution but solely dependent on the local wind stress and its curl. This equation is called the *Sverdrup balance*.

The same cannot be said of the zonal transport $\mathrm{U} = \int_0^H u\, dz$, which can be obtained from the zonal integration of the vertically averaged continuity equation (20.4), still over a flat bottom

JMB from ⇓

JMB to ⇑

$$\frac{\partial \mathrm{U}}{\partial x} + \frac{\partial \mathrm{V}}{\partial y} + w_{\mathrm{Ek}} = 0. \tag{20.12}$$

With (20.11), it becomes

$$\frac{\partial \mathrm{U}}{\partial x} + \frac{\partial}{\partial y}\left(\frac{f}{\beta_0}\, w_{\mathrm{Ek}}\right) + w_{\mathrm{Ek}} = 0, \tag{20.13}$$

JMB from ⇓

JMB to ⇑

which provides after some rearrangements

$$\mathrm{U} = -\frac{1}{\rho_0\beta_0}\int_{x_0}^{x} \frac{\partial}{\partial y}\left(\frac{\partial \tau^y}{\partial x} - \frac{\partial \tau^x}{\partial y}\right) dx - \frac{\tau^y}{\rho_0 f}\,, \tag{20.14}$$

where the starting point of integration ($x = x_0$) is to be selected wisely. We shall address this most important point shortly.

We recognize in expressions (20.11) for V and (20.14) for U that the last terms $+\tau^x/\rho_0 f$ and $-\tau^x/\rho_0 f$ are the opposite of the Ekman drift (see Equations (8.34a)–(8.34b)). Since this Ekman drift exists in the seasonal thermocline above our layer of interest, we can add it to the transport and obtain the total transport of the water column :

JMB from ⇓

JMB to ⇑

$$\mathrm{U}_{\mathrm{Total}} = \mathrm{U} + \mathrm{U}_{\mathrm{Ek}} = -\frac{1}{\rho_0\beta_0}\int_{x_0}^{x} \frac{\partial}{\partial y}\left(\frac{\partial \tau^y}{\partial x} - \frac{\partial \tau^x}{\partial y}\right) dx \tag{20.15a}$$

$$\mathrm{V}_{\mathrm{Total}} = \mathrm{V} + \mathrm{V}_{\mathrm{Ek}} = \frac{1}{\rho_0\beta_0}\left(\frac{\partial \tau^y}{\partial x} - \frac{\partial \tau^x}{\partial y}\right). \tag{20.15b}$$

Ideally, one would wish to impose a boundary condition on the flow at both eastern and western ends of the basin. For example, if we consider a basin limited on both eastern and western sides by north-south coastlines (a fair approximation of the major oceanic basins), the zonal flow and its vertical integral ($\mathrm{U}_{\mathrm{Total}}$) ought to vanish at those ends. This, however, is impossible to require simultaneously because there is only one constant (x_0) to adjust. If we set $x_0 = x_E$, the value of x at the eastern shore of the basin, then we enforce the impermeable-wall condition on the eastern side but make no provision for meeting a boundary condition on the western side, and vice versa if we take $x_0 = x_W$, the value of x at the western shore of the basin. The consequence is that the theory fails at one end of the domain, and, as we will be see in Section 20.4, a boundary layer exists along the western side. JMB from ⇓

Benoit: Alternative derivation: start with:

$$-fv = -\frac{1}{\rho_0}\frac{\partial p}{\partial x} + \frac{\partial}{\partial z}\left(\nu_E \frac{\partial u}{\partial z}\right) \tag{20.16}$$

$$fu = -\frac{1}{\rho_0}\frac{\partial p}{\partial y} + \frac{\partial}{\partial z}\left(\nu_E \frac{\partial v}{\partial z}\right) \tag{20.17}$$

Vertical integration over total, uniform, depth, use of surface stress condition and elimination of pressure immediately leads to (20.15b). Then, volume conservation vertically integrated over full depth and integrated on x immediately yields (20.15a)

Shows necessary ingredients: stationary, linear, beta effect, no lateral friction, arbitrary vertical friction, wind-stress, no bottom stress, arbitrary density (!!density structure disappears from the equation) and most importantly: flat surface and bottom (integral of derivative=derivative of integral). Otherwise appearance of joint effect of baroclinicity and relief (JEBAR): Exercise? Would also allow to add bottom friction easily or laplacian friction. Munk etc.. JMB to ⇑

20.3 Thermohaline circulation

As in Section 20.1, the region below the seasonal thermocline is comprised of two subregions, the main thermocline and the abyssal layer. The dynamics expounded in the previous section are applicable to both these regions. We now turn our attention more specifically to the upper of these two layers, the main thermocline.

In contrast to the abyssal layer, which is fed by deep-water convection at high latitudes, the main thermocline is the region of the ocean in which the circulation is primarily caused by the wind-driven Ekman pumping received from the surface layer and is most pronounced at mid-latitudes. Figure 20-3, compiled by Reid and Lynn (1971), summarizes the meridional distribution of density in the North and South Atlantic, North and South Pacific, and Indian Oceans. They reveal similar patterns in all five oceans, namely: the pycnocline is very strong and shallow (100–200 m) at the Equator, it spreads verticall downward toward the poles, with a tendency to split into two branches, one surfacing around 25° latitude and the other plunging down to 1000 m around 35° before heading upward again and surfacing around 45° latitude.

The process by which water enters the main thermocline is called *subduction* (Stommel, 1979; Cushman-Roisin, 1987).

Equations of Sverdrup dynamics with density as the vertical coordinate. Mention that reasons to work in density coordinates are that density is conserved along the flow, and it makes for simpler equations. We now view vertical position as a function of density, with

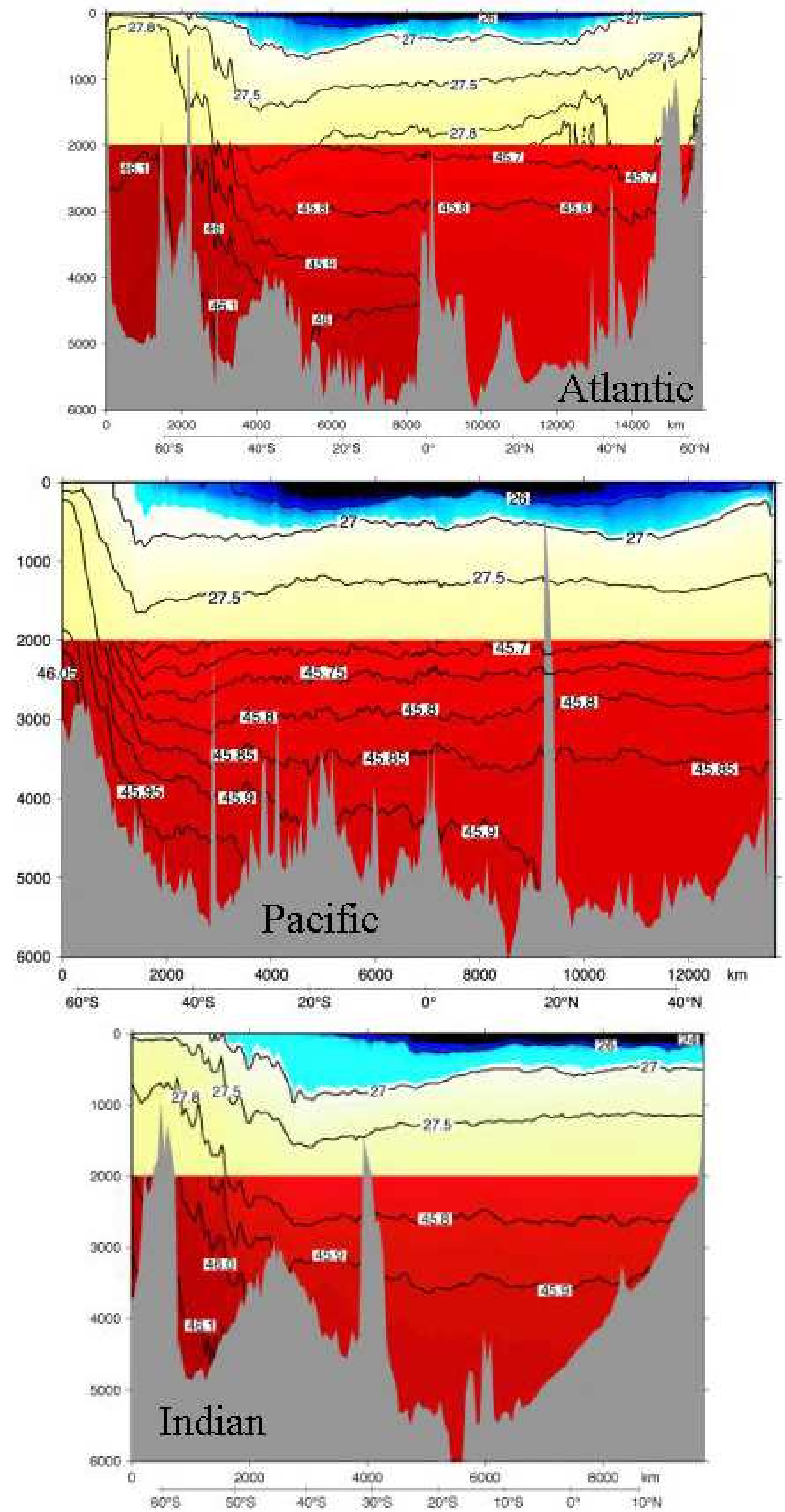

Figure 20-3 Meridional structure of potential density (σ_θ top and σ_4 bottom, in kg/m^{-3}) in the five major ocean basins. Top panel: North and South Atlantic. Middle panel: North and South Pacific. Bottom panel: Indian Ocean. Data were gathered during the World Ocean Circulation Experiment (1990–2002). **Benoit** I to not think we introduced the concept of potential density with respect to 4000m. Maybe use density section with only σ_θ? (*Emery, Talley and Pickard, 2006*)

$z = z(x, y, \rho)$ indicating the vertical position of density surface ρ at location (x, y).

$$- \, fv \;\; = \;\; - \, \frac{1}{\rho_0} \, \frac{\partial P}{\partial x} \tag{20.18a}$$

$$+ \, fu \;\; = \;\; - \, \frac{1}{\rho_0} \, \frac{\partial P}{\partial y}, \tag{20.18b}$$

where $P = p + \rho g z$ is the Montgomery potential (see Section 12.1) and is governed by the hydrostatic balance

$$\frac{\partial P}{\partial \rho} \; = \; gz. \tag{20.19}$$

The remaining equations are the continuity equation:

$$\frac{\partial}{\partial x} \left(u \, \frac{\partial z}{\partial \rho} \right) \; + \; \frac{\partial}{\partial y} \left(v \, \frac{\partial z}{\partial \rho} \right) \; = \; 0, \tag{20.20}$$

and the equation that specifies the vertical velocity w (see (12.6)) : JMB from ⇓

JMB to ⇑

$$w \; = \; u \, \frac{\partial z}{\partial x} \; + \; v \, \frac{\partial z}{\partial y} \; = \; \frac{1}{\rho_0 f} J(P, z) \tag{20.21}$$

where the last expression is obtained using (20.18) and where the Jacobian is calculated on isopycnal surfaces.

Shows that if $P = P(z)$, there is no vertical movement.

Recall 2D advection since no flow across density surfaces (isopycnal surfaces).

20.3.1 Thermal wind and beta spiral

If we take the derivatives of Equations (20.18a) and (20.18b) with respect to density and then eliminate the ρ–derivative of P by use of the hydrostatic Equation (20.19), we obtain the thermal-wind relations in density coordinates:

$$\frac{\partial u}{\partial \rho} \; = \; - \; \frac{g}{\rho_0 f} \, \frac{\partial z}{\partial y} \tag{20.22a}$$

$$\frac{\partial v}{\partial \rho} \; = \; + \; \frac{g}{\rho_0 f} \, \frac{\partial z}{\partial x}. \tag{20.22b}$$

These are powerful relations in analyzing large-scale oceanic data. Because oceanic velocities are almost always fluctuating at the mesoscale, ... but density data are comparatively easy to obtain by dropping a Conductivity-Temperature-Depth (CTD) probe at repeated intervals from a ship cruising across the ocean. After some smoothing over mesoscale wiggles, the data provide the large-scale trends of density across the ocean basin, and we can map the elevations of various isopycnal surfaces (surfaces of constant density), *i.e.*, the function $z(x, y, \rho)$ for selected values of ρ (Figure here as an example). From these, it is straightforward to determine the zonal and meridional slopes. Thus, we can consider $\partial z/\partial x$ and $\partial z/\partial y$

as known quantities and, from them, infer the velocity shear (20.22). Taking $u = v = 0$ at the bottom or, for convenience, at the depth of the lowest density data if these did not extend all the way to the bottom, we can in principle integrate $\partial u/\partial \rho$ and $\partial u/\partial \rho$ upward and determine the horizontal velocity. However, ...

JMB from ⇓

Benoit: Personally I do not like the approach to vertically integrate the thermal wind equation (first we derive with respect to z, to integrate on z immediately afterwards), because it suggests we have two constants of integration (one on each velocity component). This is not the case because we have the constraint that the geostrophic current is divergence free. Working directly with pressure (or Montgomery potential) shows that a single integration constant is available (pressure field at a given level). Using pressure also provides directly dynamic height concept. Level of no motion is then simply a level where pressure is supposed constant. Since now altimeter data are available, also level of no motion assumption replaced by direct use of surface pressure from satellite observation.

JMB to ⇑

Additional information can be obtained by combining the thermal-wind relations (20.22) with Equation (20.21) giving the vertical velocity. For this, we decompose the horizontal velocity (u, v) in its magnitude U and azimuth θ with

$$u = U \cos\theta, \qquad v = U \sin\theta. \tag{20.23}$$

The azimuth angle θ is measured counterclockwise from East and is related to the velocity components by $\theta = \arctan(v/u)$ and

$$\begin{aligned}
\frac{\partial\theta}{\partial\rho} &= \frac{1}{u^2+v^2}\left(u\,\frac{\partial v}{\partial\rho} - v\,\frac{\partial u}{\partial\rho}\right) \\
&= \frac{g}{\rho_0 f(u^2+v^2)}\left(u\,\frac{\partial z}{\partial x} + v\,\frac{\partial z}{\partial y}\right) \\
&= \frac{gw}{\rho_0 f(u^2+v^2)}. \qquad (20.24)
\end{aligned}$$

(20.25)

As we can see, there is a direct relation between the vertical velocity and the veering (twisting) of the horizontal velocity in the vertical. In the Northern Hemisphere ($f > 0$), $\partial\theta/\partial\rho$ has the same sign as w. Thus, in the subtropical gyre of the midlatitudes, where Ekman pumping is downward ($w < 0$), the vector of horizontal velocity turns clockwise with depth (Figure 20-4). refer to (Stommel and Schott, 1977). Give an example from observations.

The veering implies the waters at different levels in the vertical come from different directions, and thus possess different origins. All levels of motion, however, are under the tight constraint of the Sverdrup balance (**??**). The local wind-stress curl appears therefore as a constraint upon, and not the forcing of, the flow.

20.3.2 Potential vorticity

The Montgomery potential P plays the role of a Bernoulli function because it is constant along streamlines:

$$u\partial P/\partial x + v\partial P/\partial y = 0$$

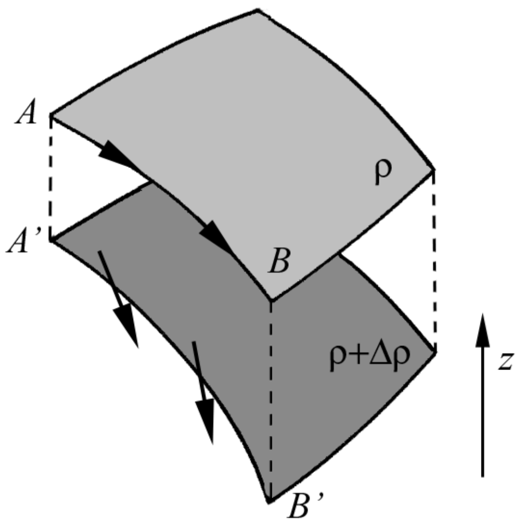

Figure 20-4 Motion on a sloping density surface illustrating the veering of the geopstrophic current vector with depth. For downward motion in the Northern Hemisphere, the veering is to the right with increasing depth.

and there is no 'vertical velocity' in density coordinates, when density conserved along the flow.

Potential vorticity is

$$q \;=\; -f\,\frac{\partial z}{\partial \rho}\,.$$

Relation: PV function of P and ρ only.

Previous equations hold wherever the flow is on a large scale and dissipation is weak, that is, in both main thermocline and abyssal layer.

20.3.3 Flow in the main thermocline

The dynamics of the circulation in the main ocean thermocline are governed by a small number of parameters, namely the constants f_0, β_0, ρ_0 and g that enter the governing equations, and a few external scales that enter through boundary conditions: L_x and L_y, the zonal and meridional lengths of the basin, $W_{\rm Ek}$ a typical magnitude of the Ekman pumping, and $\Delta\rho$ a typical density variation across the thermocline. Following Welander (1975), the thermocline depth H can be derived by balancing the various terms in the equations of Sverdrup dynamics. First, the scale for P is $\Delta P = gH$ from the hydrostatic balance (20.19), from which follow the velocity scales from the geostrophic relations (20.18): $u \sim \Delta P/\rho_0 f_0 L_y = gH\Delta\rho/\rho_0 f_0 L_y$ and $v \sim \Delta P/\rho_0 f_0 L_x = gH\Delta\rho/\rho_0 f_0 L_x$. Then, balancing the two sides of Equation (20.21) for the vertical velocity yields **Benoit:** Maybe a comment or justification why no compensation is found here in the combination of two horizontal terms related to geostrophy. JMB from ⇓ JMB to ⇑

$$W_{\rm Ek} \sim \frac{gH^2\Delta\rho}{\rho_0 f_0 L_x L_y}$$

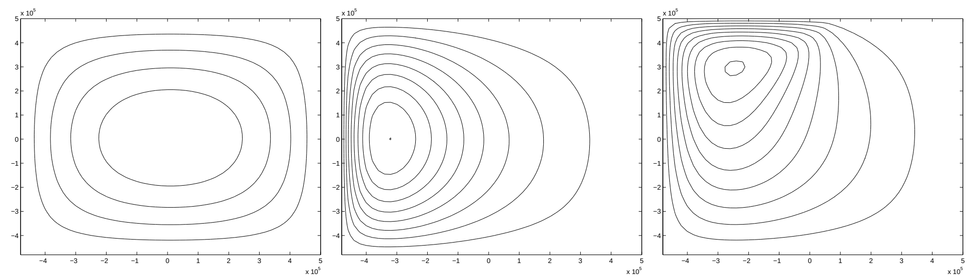

Figure 20-5 Streamfunction with bottom friction and wind effect only (left), adding beta effect (middle) and finally advection. Wind stress is applied by the schematic distribution (20.27).

from which follows the depth scale H of the main thermocline:

$$H = \sqrt{\frac{\rho_0 f_0 L_x L_y W_{\mathrm{Ek}}}{g\Delta\rho}}. \tag{20.26}$$

(Welander, 1975). [Throw some numbers in to show that it is correct.]

Ventilated thermocline theory (Luyten *et al.*, 1983; Huang, 1989a, 1989b). No details.

Closed contours in western sector. Theory of PV homogenization (qualitative description). The Rhines ratio to compare circulation in ventilated and unventilated regions.

20.4 Western boundary currents

Gulf Stream (Stommmel, 1948). A figure. Other oceans.

Scaling of width (inertial only, yielding radius of deformation).

$$\tau^y = \sin(\pi y/(2L)) \tag{20.27}$$

20.5 Abyssal circulation

Key papers by Stommel and Arons (1960a, b).

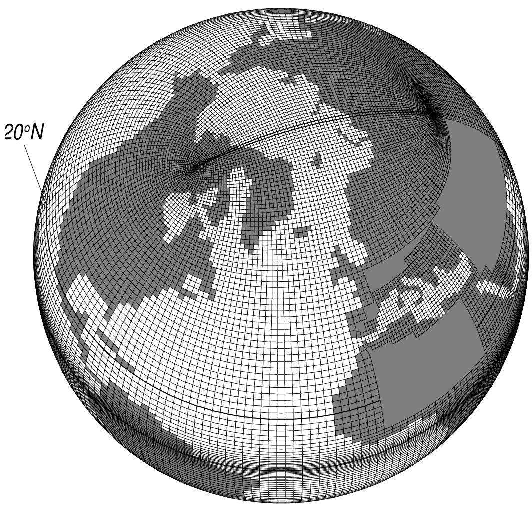

Figure 20-6 Ocean model grid with numerical grid poles over continents. (*LODYC, ORCA configuration, Madec et al.; 1998*)

20.6 Oceanic circulation models

A milestone in numerical ocean modeling was the development of the Ocean general circulation model (OGCM) of the GFDL[4] by Brian (1969). This model, and its successive variants are known under the name Modular Ocean Model (MOM) and the open release of the source code by Mike Cox in 1984 made the model widespread, even or because the numerics were simple for today's standards and were therefore adaptable by modelers. The model was indeed based on a direct finite differencing of the governing equations in longitude-latitude coordinates and a stepwise representation of topography and coastlines (Figure 20-7). This allowed for first general circulation studies with primitive equations, but a series of necessary improvements appeared. The stepwise topography of Figure 20-7 can for example not resolve small slopes and associated potential vorticity constraints, and partially masked cells were introduced (*e.g.*, Adcroft *et al.*, 1997). Also stepwise topography is not adapted for overflow problems typical during deep-water formations (Figure 20-8). For such situations, special algorithms have been developed (*e.g.*, Beckmann and Döscher, 1997). The pole problem and convergence of meridians of spherical coordinates can now be avoided by rotating the spherical coordinate system to place "poles" on continents or more generally by generating curvilinear orthogonal grids that maintain topologically a rectangular grid (Figure 20-6).

In addition to such enhancement, also found in a series of other models similar to MOM, new generations of models are being developed, the most drastic change in terms of numerical implementation being the move from structured to unstructured grids. The presence of lateral continental boundaries in the ocean was indeed an obstacle to the use of spectral models as those employed in the atmosphere and instead, the road towards unstructured grids was opened. Structured grids, natural for models discretized along Cartesian coordinates or longitude-latitude, are topologically similar to a rectangular grid, each grid point having one

[4]Geophysical Fluid Dynamics Laboratory.

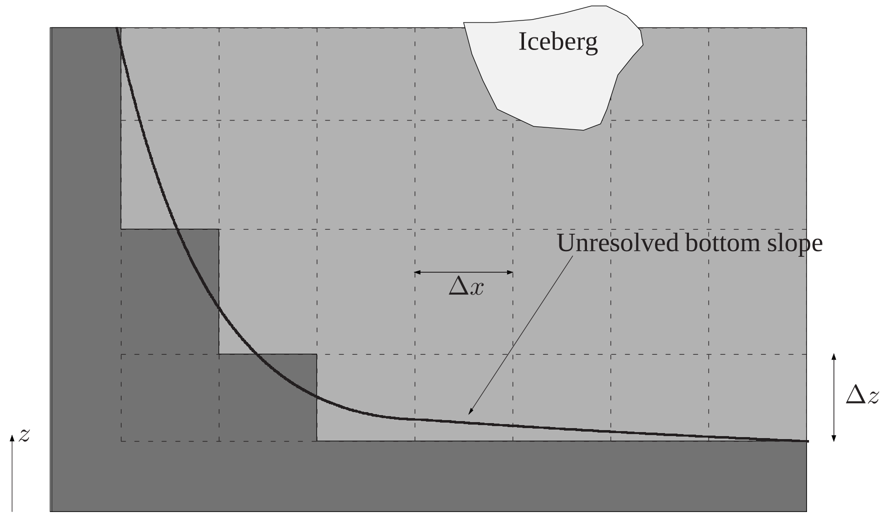

Figure 20-7 Masking of a regular grid allows to discretize topography. For rectangular grid boxes, the small slopes can only be resolved if $\Delta z < \Delta x |\partial b / \partial x|$ when the bottom is given by $z = b$. Otherwise the small slope will be approximated by several grid boxes over a flat bottom followed by a single step. On the contrary, should there be ice coverage, if the grid spacing is too small near the surface, masking should be applied there too.

and only one neighbor to the left, right, below, above, "north" and "south". In unstructured grids, on the contrary, each grid cell as a variable number of neighbors (Figure 20-9), which makes them very flexible in terms of geographical coverage. Coastlines can be followed by adding small elements along the coast, canyons resolved in the same way and open boundaries pushed further away by increasing the elements size in distant regions. Intense model developments are presently going on (See for example Pietrzak *et al.*, 2004)) because the major change in model design does not allow to reuse existing components. An unstructured finite-volume approach is a generalization of the finite-volume approach presented in Section 5.5, where integrations are performed over a each finite volume, the group of which covers the domain of interest. Physical coupling between the finite volumes arises then naturally through the fluxes across the shared interfaces. Finite elements start with another approach based on the Galerkin method (Section 8.8). The solution is expanded in a series of non-orthogonal functions, each governing equation multiplied by these base functions and integrated over the domain of interest. The finite-element methods are using trial functions of a special nature, being only non-zero over a given element. Connection between elements than arise because functions are forced to obey some continuity requirement between elements. The non-orthogonal nature of the base function leads however to large but relatively sparse systems to be solved at each time-step. Beside the very general finite volume or finite-elements approach some special methods have also been implemented for ocean models such as a spherical cube grid (a three-dimensional generalization of the squaring of a circle, with special connectivity of a few nodes, Adcroft *et al.* 2004) or spectral elements (Haidvogel *et al.*, 1991), a method in which a domain is covered by large elements, inside of which spectral

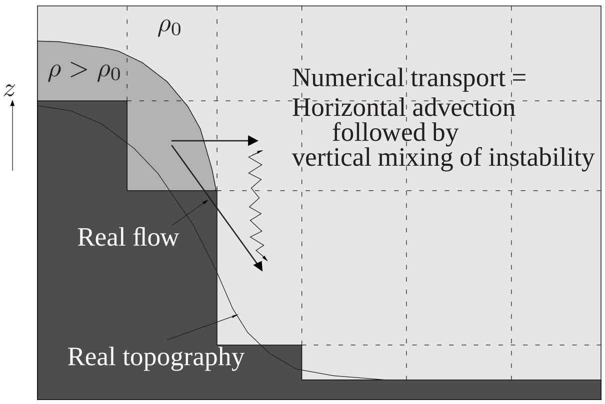

Figure 20-8 Vertical section of a schematic overflow where dense waters cascade down a slope and remain on the bottom. For a step-wise topography approximation, the advection carries the dense water horizontally over a model grid point in which density is lower. The static instability is generally removed by a mixing algorithm and hence instead of a displacement of the water mass, we end up with a mixed plume.

series are used to approximate the solutions.

The advantage of variable resolution of such flexible tools makes again appear the fundamental problems of parameterization. Scales resolved by the grid may change regionally and hence parameterization should change within the same model, blurring the distinction between resolved and unresolved motions. Among the processes that require parameterization, deep-water formation is an example (see Section 11.4). The physical process is dominated by non-hydrostatic effects, hence any hydrostatic model requires a parameterization. Because of the validity of hydrostatic approximation being related to the aspect ratio of the flow (see Section 4.3), non-hydrostatic effects are only relevant for extremely high resolutions. Yet such local refinement are possible with flexible horizontal grids and todays hydrostatic ocean models would then require a non-hydrostatic option such as in the MITgcm (Marshall *et al.* 1998). Other approximations that are currently used in ocean models include the Boussinesq approximation, hence volume conservation instead of mass conservation. The approximation can be relaxed when needed (*e.g.*, Greatbatch *et al.*, 2001), for example when thermal expansion due to a general temperature increase as in climate change scenarios has to be taken into account.

The dynamically relevant density itself is obtained from the solutions of the governing equations for salt and heat and the use of the nonlinear ocean-water equation of state depending on salinity, temperature and pressure. This equation of state is computationally rather time consuming in its original form and several levels of simplifications have been adopted in the different models. For isopycnal models, subtle additional problems appear (*e.g.*, McDougall and Dewar, 1998) notably because salinity and temperature are not independent anymore on isopycnals.

The upper boundary of the ocean model requires special care because this is the location where the atmospheric driving forces are applied to the system. There are the distinctions between rigid-lid model or free-surface models, with a current trend to prefer the latter because of more flexibility and a wider range of applicability, including gravity wave representation[5]. The coupling with the atmosphere (see Section 19.4) remains a difficult problem, since the

[5] If the free surface is treated implicitly or semi-implicitly, a sufficiently large time step can be used to filter out these fast waves if a rigid-lid type of solution is preferred.

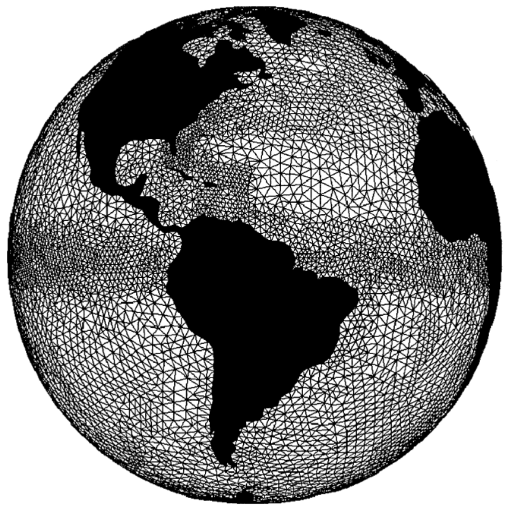

Figure 20-9 Ocean finite element model grid. (*SLIM, Legrand et al. 2000*)

ocean model must simulate both surface temperature and mixed-layer depth correctly. The former is essential for air-sea exchange calculations while the product of temperature and mixed-layer depth is directly related to the heat content and therefore heat budgets. Because the mixed-layer evolution critically depends on turbulence, special care is needed in the specification of the eddy viscosity and diffusivities, particularly if vertical grid spacing is coarse.

20.7 Coordinate systems

The vertical resolution near the surface is essential to capture the air-sea exchanges and most models use smaller vertical grid spacings near the ocean's surface. For the ocean interior, vertical gridding is also considered crucial and we will dedicate a whole section to this problem, separating the vertical-coordinate issue from any horizontal treatment because of the small aspect ratio and different dynamics encountered in the vertical direction and the horizontal plane. We therefore suppose the horizontal discretization is performed using one of the methods outlined before and focus now on the vertical grid. For this, we suppose that a grid point which is topologically above or below another grid point is also physically above or below this point, aligned with the local gravity. Except this requirement, we will allow for the possibility that on each vertical, grid points can be placed freely so as to capture processes of interests, such as a pycnocline. The generation and use of such grids can be achieved in two ways: We can start from the original equations and apply the finite-volume integration technique over the desired vertical cells to write out governing equations for each cell average. Or we can make first a general mathematical coordinate change, after which we integrate (or discretize) in a uniform grid (Figure 20-10; see also Section 15.6). Direct integration in physical space shows that parameterizations are needed because integrals of nonlinear terms are not known in terms of layer averages. Preliminary coordinate transformation and subsequent finite differencing hides this integration in the discretization part. Since the same sub-grid scales are filtered out in both approaches, both need parameterizations. Both approaches lead to similar discrete equations, and so grid stretching equals a coordinate change and only the technical implementations might be easier in one or the other approach.

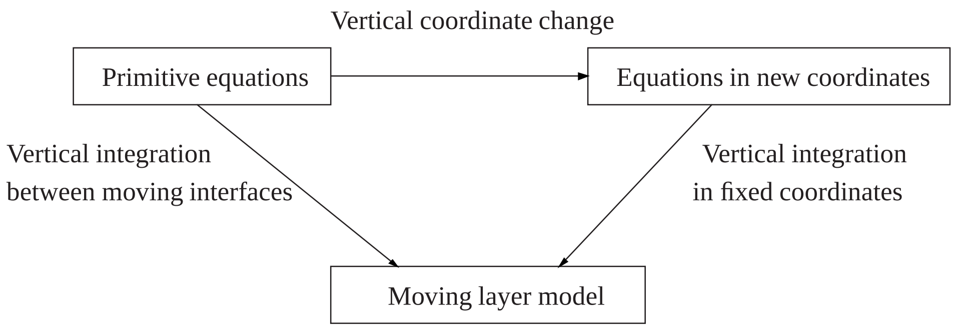

Figure 20-10 Equations for discrete layers can be obtained by directly integrating primitive equations over a moving domain or by a coordinate transformation into a fixed domain in which integration is performed.

Here we present the coordinate transformation approach, in close analogy with the isopycnal coordinate change of Chapter 12. In the original Cartesian system of coordinates, z is an independent variable. In the transformed coordinate system (x, y, s, t), the new coordinate s becomes an independent variable and $z(x, y, \mathsf{s}, t)$ has become the dependent variable[6] giving the depth at which s is found at location (x, y) and at time t. A line along which s is constant is called an *coordinate line* (or surface for the three dimensional case). From a differentiation of the expression $a = a(x, y, \mathsf{s}(x, y, z, t), t)$, where a is any variable, the rules for the change of variables follow

$$\begin{aligned}
\frac{\partial}{\partial x} \quad &\longrightarrow \quad \left.\frac{\partial a}{\partial x}\right|_z = \left.\frac{\partial a}{\partial x}\right|_{\mathsf{s}} + \frac{\partial a}{\partial \mathsf{s}} \left.\frac{\partial \mathsf{s}}{\partial x}\right|_z \\
\frac{\partial}{\partial z} \quad &\longrightarrow \quad \frac{\partial a}{\partial z} = \frac{\partial a}{\partial \mathsf{s}} \frac{\partial \mathsf{s}}{\partial z} \\
\frac{\partial}{\partial t} \quad &\longrightarrow \quad \left.\frac{\partial a}{\partial t}\right|_z = \left.\frac{\partial a}{\partial t}\right|_{\mathsf{s}} + \frac{\partial a}{\partial \mathsf{s}} \left.\frac{\partial \mathsf{s}}{\partial t}\right|_z .
\end{aligned}$$

similar to the isopycnal coordinates used in Chapter 12. We did not repeat the y related terms because they are similar to those for x. A distinct difference with the isopycnal coordinates appears, as now s is not a conserved property of the flow anymore but a prescribed function depending on x, y, z, t. A variable of importance in the coordinate transformation is the Jacobian J

$$\frac{\partial z}{\partial \mathsf{s}} = J \tag{20.28}$$

which is the change of z for a unit change in s and hence a measure of the coordinate layer thickness (analogue to the isopycnal layer thickness). If z increases with s, the Jacobian is

[6] It is the latter relationship that is used in practice, specifying for each grid point of the regularly discretized transformed space the corresponding position of the grid point in the irregularly covered physical domain.

positive. The total derivative

$$daoverdt \;=\; \frac{\partial a}{\partial t} \;+\; u\frac{\partial a}{\partial x} \;+\; v\frac{\partial a}{\partial y} \;+\; w\frac{\partial a}{\partial z} \tag{20.29}$$

where derivatives are taken in the Cartesian coordinate transforms into a similar expression

$$daoverdt \;=\; \frac{\partial a}{\partial t} \;+\; u\frac{\partial a}{\partial x} \;+\; v\frac{\partial a}{\partial y} \;+\; \omega\frac{\partial a}{\partial \mathsf{s}} \tag{20.30}$$

where all derivatives are now taken in the transformed space (*i.e.*, $\partial a/\partial x$ is performed for fixed s) and where a new vertical velocity was defined

$$\omega \;=\; \left.\frac{\partial \mathsf{s}}{\partial t}\right|_z \;+\; u\left.\frac{\partial \mathsf{s}}{\partial x}\right|_z \;+\; v\left.\frac{\partial \mathsf{s}}{\partial y}\right|_z \;+\; w\frac{\partial \mathsf{s}}{\partial z} \tag{20.31}$$

It is clear that ω is nothing else than the material derivative of the coordinate s in z coordinates and $J\omega$ the relative velocity of the flow with respect to the moving s coordinate surface (recall Section 15.6). Clearly, if s is density, transported without mixing, $\omega = 0$ and we recover the isopycnal coordinates. In general $J\omega$ is however not zero. This variable appears indeed as a vertical velocity in the new coordinates and measures therefore the flow across the lines of constant s. It is easy to understand that if the ocean surface or ocean bottom is a coordinate line (with a constant s), the "vertical" velocity ω is zero there.

The transformation of the volume conservation (4.9) using the rules of change of variables and the definition of the vertical velocity leads to

$$\frac{\partial J}{\partial t} \;+\; \frac{\partial}{\partial x}(Ju) \;+\; \frac{\partial}{\partial y}(Jv) \;+\; \frac{\partial}{\partial \mathsf{s}}(J\omega) \;=\; 0 \tag{20.32}$$

with derivatives in s space. In view of the signification of J this is interpreted as the expression of conservation of the quantity "volume" in the transformed space or, alternatively in terms of budgets over a moving volume in z space (Figure 20-11). Interestingly, if we integrated from bottom to surface for coordinate lines that are constant on both the surface and bottom, we obtain

$$\frac{\partial \eta}{\partial t} + \frac{\partial \mathrm{U}}{\partial x} + \frac{\partial \mathrm{V}}{\partial y} = 0 \tag{20.33}$$

because

$$\int_{\text{bottom}}^{\text{surface}} J d\mathsf{s} = z_{\text{surface}} - z_{\text{bottom}} \tag{20.34}$$

which, for a fixed bottom leads, after derivation with respect to time to the variations in sea surface height η. The other two terms involve U and V which are the usual vertically integrated transports

$$\mathrm{U} = \int Ju d\mathsf{s} = \int u dz, \quad \mathrm{V} = \int Jv d\mathsf{s} = \int v dz, \tag{20.35}$$

where the integration is performed from the bottom to the surface. We recover a vertically integrated volume conservation, already used several times. Note that the equation is valid

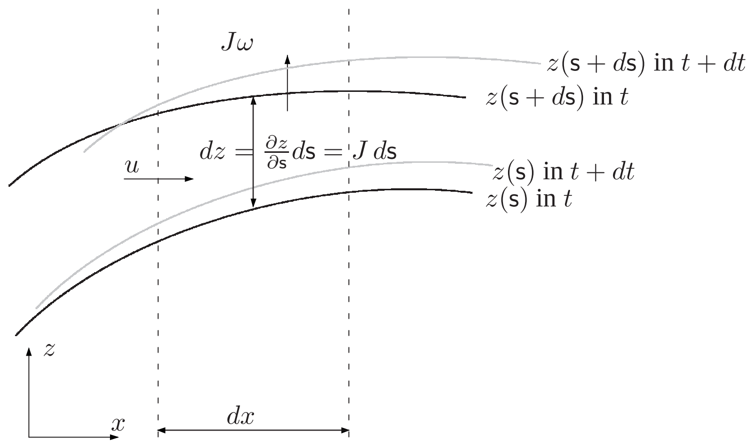

Figure 20-11 Volume conservation over the variable control volume expresses that the change in volume $\partial(Jdxd\mathsf{s})/\partial t$ is due to the lateral volume inflow $Jud\mathsf{s}$ and the flow across the moving interface $J\omega dx$, which leads to (20.32).

irrespectively of whether the density is uniform or not, as long as Boussinesq approximation holds.

The special form of the volume conservation leads to a conservative form of the advection operator

$$J\left(\frac{\partial a}{\partial t} + u\frac{\partial a}{\partial x} + v\frac{\partial a}{\partial y} + \omega\frac{\partial a}{\partial \mathsf{s}}\right)$$
$$= \frac{\partial}{\partial t}(Ja) + \frac{\partial}{\partial x}(Ja\,u) + \frac{\partial}{\partial y}(Ja\,v) + \frac{\partial}{\partial \mathsf{s}}(Ja\,\omega) \qquad (20.36)$$

which we can interpret as the evolution of the content of a within a layer of s. This form is particularly well adapted for integration over a finite volume in the transformed space.

The vertical diffusion term is readily translated into the new coordinate system

$$\frac{\partial}{\partial z}\left(\nu_E\frac{\partial a}{\partial z}\right) = \frac{1}{J}\frac{\partial}{\partial \mathsf{s}}\left(\frac{\nu_E}{J}\frac{\partial a}{\partial \mathsf{s}}\right) \qquad (20.37)$$

so that the governing equation for a vertically diffused tracer c would read

$$\frac{\partial}{\partial t}(Jc) + \frac{\partial}{\partial x}(Jc\,u) + \frac{\partial}{\partial y}(Jc\,v) + \frac{\partial}{\partial \mathsf{s}}(Jc\,\omega) = \frac{\partial}{\partial \mathsf{s}}\left(\frac{\kappa_E}{J}\frac{\partial c}{\partial \mathsf{s}}\right). \qquad (20.38)$$

We could also transform the horizontal diffusion term, but generally we combine this operation with the parameterization of the sub-grid scales not resolved by the vertical grid (see next section).

In view of the isomorphy of (20.38) with a Cartesian-coordinate version, a s-model can thus be implemented in a general way without much additional work, provided the functional relationship between $\mathsf{s}(x,y,z,t)$ is given, or more practically, the positions $z(x,y,\mathsf{s},t)$ of the grid coordinate surfaces in physical space. This must be specified by the modeler and two systems we already encountered are the isopycnal ($\mathsf{s} = -\rho/\Delta\rho$) coordinates[7] and z models ($\mathsf{s} = z$).

Another coordinate change, very popular in coastal modeling, is the so-called σ coordinate system, a particular form of terrain-following coordinates. The coordinate change reads

$$\mathsf{s} = \sigma = \frac{(z-b)}{h}, \quad J = h \tag{20.39}$$

and the new coordinates varies between 0 at the bottom and 1 at the surface, which are both coordinate lines (Figure 20-12). This allows to follow not only any topographic slope but also free surface movements, solving incidentally the problem of discretizing equations in a changing domain. Also calculation points are efficiently used because they all fall into the water column and boundary conditions are topologically simple to implement.

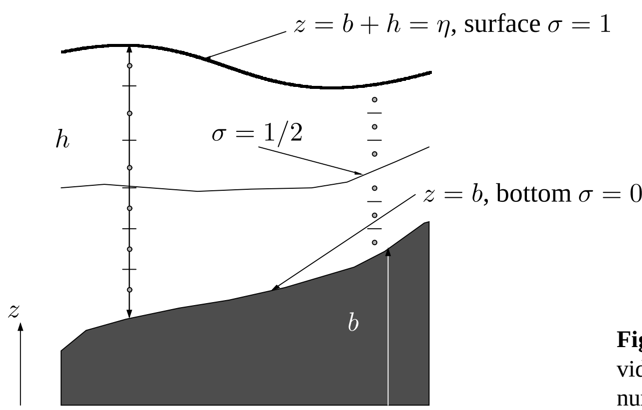

Figure 20-12 Sigma coordinates divide each water column into an equal number of vertical grid cells.

The application of this coordinate change to global-ocean problems raised however some concern about the so-called *pressure-gradient problem* (*e.g.*, Haney, 1991; Deleersnijder and Beckers, 1992). Though the problem was initially identified for the σ coordinates, it is more general and we will present it in the general-coordinate framework. The horizontal pressure gradient, here along x, can be evaluated in the new coordinates by using the transformation rules:

$$\left.\frac{\partial p}{\partial x}\right|_z = \left.\frac{\partial p}{\partial x}\right|_{\mathsf{s}} + \left.\frac{\partial p}{\partial \mathsf{s}}\frac{\partial \mathsf{s}}{\partial x}\right|_z \tag{20.40}$$

while the hydrostatic equilibrium used to calculate pressure reads

$$\frac{\partial p}{\partial z} = \frac{1}{J}\frac{\partial p}{\partial \mathsf{s}} = -\rho g \tag{20.41}$$

Therefore we can derive several, mathematically equivalent expressions of the pressure gra-

[7]Compared to the presentation in Chapter 12, we keep the coordinate in the same direction as z so that the layer thickness is directly given by the Jacobian $h = J = 1/(\partial\mathsf{s}/\partial z) = -\Delta\rho/(\partial\rho/\partial z)$.

dient

$$\frac{1}{\rho_0}\frac{\partial p}{\partial x}\Big|_z = \frac{1}{\rho_0}\frac{\partial p}{\partial x}\Big|_{\mathsf{s}} + \frac{\rho g}{\rho_0}\frac{\partial z}{\partial x}\Big|_{\mathsf{s}} \tag{20.42a}$$

$$= \frac{1}{\rho_0 J} J_{xs}(p, z) \tag{20.42b}$$

$$= \frac{1}{\rho_0}\frac{\partial p}{\partial x}\Big|_{\text{surface}} + \frac{\rho g}{\rho_0}\frac{\partial \eta}{\partial x} - g\int_{\text{surface}}^{\mathsf{s}} J_{xs}(\rho, z)\, d\mathsf{s} \tag{20.42c}$$

$$= \frac{1}{\rho_0}\frac{\partial P}{\partial x}\Big|_{\mathsf{s}} - \frac{gz}{\rho_0}\frac{\partial \rho}{\partial x}\Big|_{\mathsf{s}} \tag{20.42d}$$

where the last expression uses the Montgomery potential $P = p + \rho g z$. For the second and third expression, the Jacobian is $J_{xs}(a,b) = \partial a/\partial x \partial b/\partial s - \partial b/\partial x \partial a/\partial s$ in the transformed space, not to be confused with the Jacobian (20.28) of the transformation. A standard test for terrain-following models is to prescribe a density and pressure field that depends solely on z. In this case, the horizontal pressure field is identically zero and no motion is generated in the absence of any other driving mechanism. The numerical discretization of expressions (20.42a) to (20.42d) or any other equivalent expression in the s coordinates will provide however a non-zero pressure gradient. Mathematically, the two terms on the right hand side cancel each other, but their numerical discretization does not. The reason stems from the different nature of the terms: the first one involves pressure and hence a vertical, numerically, integrated quantity, while the second term is a local one. There is no reason the numerical discretization errors of both terms cancel each other, and as experience shows, a so-called pressure gradient error remains. This error might not be negligible because the pressure field $p(z)$ might become very large: For the mathematical expression, we would simply have a cancellation of two large terms, but for the numerical version, an even small relative error on each large term can lead to severe errors because they do not cancel out. The test in which σ coordinate models are used to simulate a situation at rest with a density field $\rho = \rho(z)$ therefore allows to highlight this error (*e.g.*, Beckmann and Haidvogel, 1993; Exercise 20-5).

We could argue that the problem should disappear with increased resolution, but another problem will appear, the problem of the so-called *hydrostatic consistency*: If we increase vertical resolution more rapidly than the horizontal one, we see (Figure 20-13) that the numerical stencil involved in the calculation of a horizontal pressure gradient involves grid points not at all distributed horizontally around the point of interest. On the contrary, the physically relevant points at similar depth are not taken into account and horizontal gradients evaluated by extrapolations instead of interpolations. Such extrapolations lead to large relative errors (see Exercise 3-5) **Need to add something to chapter 3**: such as JMB from ⇓

For flux calculations, interpolations at the interface are generally used. analyze how a linear interpolation using the two neighbor points behaves compared to a cubic interpolation using four points. To do so, sample the function e^x in $x = -1.5, -0.5, 0.5, 1.5$ and interpolate in $x = 0$. Compare to the exact value. What happens if you calculated the interpolation not at the center but in $x = 3$ or $x = -3$ (extrapolation) ? Redo the exercise but add an alternating error of +0.1 and -0.1 to the four sampled values. and an inconsistency: the vertical gradients JMB to ⇑
in (20.42a)-(20.42d) are not calculated at the same depth than the horizontal gradient to be evaluated from it. For simple finite difference schemes, extrapolations are avoided if slopes

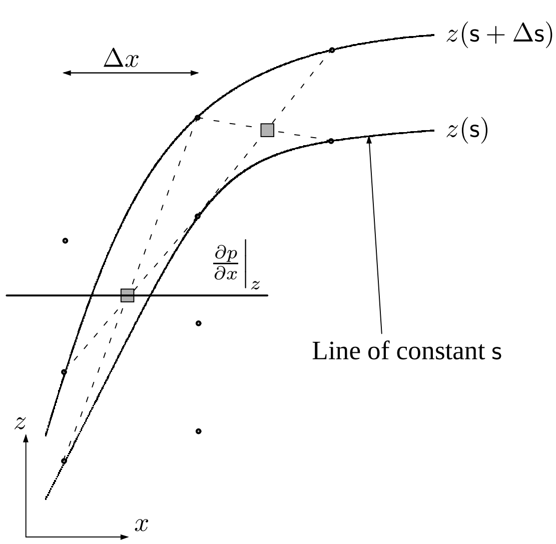

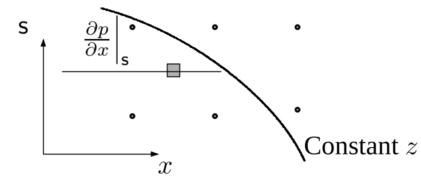

Figure 20-13 In the numerical grid (x,s), a standard finite differencing of the pressure gradient at the location of the squares involves the logical neighbors in the discrete mesh, connected with dashed lines in the physical space (left panel). For upper-right point, the calculation points are physical neighbors but for the lower-left point, the calculation uses far distant points and performs extrapolations.

satisfy

$$\left| \frac{\left.\frac{\partial z}{\partial x}\right|_{\mathsf{s}}}{\frac{\partial z}{\partial \mathsf{s}}} \right| \leq \frac{\Delta s}{\Delta x} \tag{20.43}$$

which provides a constraint on the vertical grid spacing compared to the horizontal one. This constraint is not unlike the constraint on the domain of dependence on the advection schemes (Section 6.4). Contrary to the problem in Figure 20-7, we now have a lower bound for the admissible vertical grid spacing, related to the slope of the coordinate lines. Alternatively, for a fixed vertical grid and given slopes, the requirement imposes a horizontal grid that must be sufficiently fine to resolve the slopes correctly.

For σ-coordinates this translates, neglecting surface gradients, to a constraint in terms of the water column height h

$$\left| \frac{1}{h}\frac{\partial h}{\partial x} \right| \leq \frac{\Delta \sigma}{\Delta x}\frac{1}{(1-\sigma)} \tag{20.44}$$

Hence the most severe problems will be encountered where the topography is steep but not yet deep, *i.e.*, near shelf breaks. This is where the length scale related to topography $\left|\frac{1}{h}\partial h/\partial x\right|^{-1}$ is smallest and must be resolved by the grid spacing. This length scale appears thus as an additional scale to be considered when designing horizontal grids. Since on the shelf break, stratification is also intercepting topography, pressure gradient problems are enhanced: the regions of large variations in ρ coincide with regions of large $\partial z/\partial x|_{\mathsf{s}}$ so that the two contributions to the pressure-gradient expressions will be large so as the associated discretization error. Because the hydrostatic consistency condition may not be satisfied, the relative errors are large for a term which itself is large. Solutions to this problem include higher-order finite differencing (using more grid points and being less prone to extrapolations, *e.g.*, McCalpin, 1994), subtraction of average density profiles $\rho = \rho(z)$ before any pressure calculation (*e.g.*, Mellor *et al.*, 1998), specialized finite differencing (*e.g.*, Song, 1998), partial masking of topography (replacing slopes by vertical sections, *e.g.*, Beckers, 1991; Gerdes, 1993) or filtering of topography.

With the provision of proper treatment of the pressure gradient, such a generalized vertical coordinate is attractive and several models have implemented the approach (*e.g.*, Pietrzak *et al.*, 2002), without actually using them at their full possibilities, generally prescribing *a priori* distribution of coordinate lines. The general rule for the placement of coordinate lines is to match as close as possible the lines on which properties remain smooth (Figure 20-14, see also adaptive grids in Section 15.6). The model grids should therefore adapt themselves so as to be close to isopycnals in the ocean interior, where mixing is extremely weak. Because of the problems of isopycnal models to represent mixed layers, the use of z coordinates should used there. An implementation that is close to achieve this requirement is Hycom (HYbrid Coordinate Ocean Model, *e.g.*, Bleck 2002), which is an extension of an initially isopycnal model, allowing for a mixed layer discretized by several z levels. For further improvements, layers near the bottom should rather behave as σ layers so as to follow topography. Also different isopycnal layers for different regions of the oceans should be made possible.

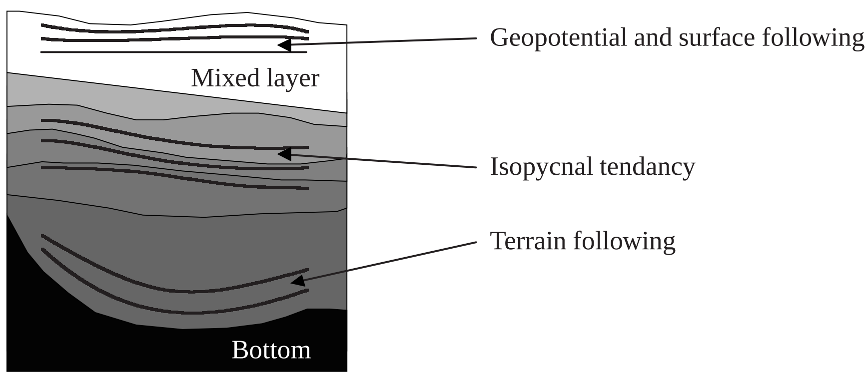

Figure 20-14 Strategies for placing coordinate lines in an ocean model. Near the surface and in the mixed layer coordinate should be flat or at most follow the air-sea interface. In the ocean interior, motions are almost without mixing and isopycnal levels the best choice. Near the bottom, the flow must follow the topography and terrain following coordinates are advocated.

20.8 Parameterization of subgrid-scale processes

Once the grid defined, sub-grid scale processes must again be looked at, in the light of the actual resolution and orientation of the grid volumes. Up to now, sub-grid scale processes other than proper turbulence were modeled by a horizontal diffusion such as

$$\mathcal{D}(c) \;=\; \frac{\partial}{\partial x}\left(\mathcal{A}\frac{\partial c}{\partial x}\right) + \frac{\partial}{\partial y}\left(\mathcal{A}\frac{\partial c}{\partial y}\right) \tag{20.45}$$

for a tracer c. The question that now arises is whether the derivatives should be those of the Cartesian coordinates or of the transformed coordinates. If the Cartesian coordinates are advocated, it means we suppose there is a natural tendency to mix the system into horizontally homogeneous layers. In this case, the Cartesian derivatives must be transformed according to the rules of change of variables.

If on the contrary we suppose the derivatives are taken in the s coordinates, we somehow match our parameterization to the grid scales and see the parameterization rather as a filter, without any further coordinate transformation to be applied in the discretization.

Probably a physically more sound parameterization recognizes that lateral movements are much easier along isopycnals than across them and hence the natural coordinates in which the parameterization would be diffusion like are isopycnal coordinates. From there we could translate the diffusion operator to z coordinates as done in Redi (1992) for inclusion in a z coordinate model, and then make a second transformation into the s coordinate system (should we employ isopycnal coordinates, we would fall back into a Laplacian expression). The resulting operator to discretize is much more complicated than the standard Laplacian and contrary to the mathematical operator, the resulting discretizations are not monotonic anymore (*e.g.*, Beckers *et al.*, 1998). It must also be recognized that if s lines cross isopycnals, mixing[8] along numerical grid lines will result in artificial diapycnal mixing.

The diffusion-like parameterizations are of course based on the analogy of the effect of unresolved eddies with the action of turbulence. However, depending on the scales under consideration some sub-grid scale processes cannot be considered randomly mixing the ocean, specially at larger scales. Near the scales of the internal radius of deformation energetic motions are taking place at these scales, among which baroclinic instability, (see chapter 17). Because the deformation radius in the ocean is an order of magnitude smaller than in the atmosphere, global ocean models rarely resolve baroclinic instability. Hence, unless regional models are used, coarse-resolution ocean models must parameterize the effect of mesoscale motions and in particular baroclinic instability. Baroclinic instability releases potential energy by decreasing the frontal slopes rather than by random mixing. The isopycnal diffusion cannot account for this flattening since by construction it diffuses only along isopycnals, hence not forcing them to flatten out. Instead of a diffusion type parameterization, the so-called Gent-McWilliams parameterization (Gent and McWilliams 1990, Gent *et al.* 1995) adds a velocity field to the large scale currents. The components of this additional velocity field read

$$u^\star = -\frac{\partial Q_x}{\partial z}, \quad v^\star = -\frac{\partial Q_y}{\partial z}, \quad w^\star = \frac{\partial Q_x}{\partial x} + \frac{\partial Q_y}{\partial y} \tag{20.46}$$

where

$$Q_x = -\frac{\kappa}{\rho_z}\frac{\partial \rho}{\partial x} = \kappa \frac{\partial z}{\partial x}\Big|_\rho \tag{20.47}$$

$$Q_y = -\frac{\kappa}{\rho_z}\frac{\partial \rho}{\partial y} = \kappa \frac{\partial z}{\partial y}\Big|_\rho$$

$$\rho_z = \frac{\partial \rho}{\partial z} \tag{20.48}$$

are related to the slope of the isopycnals and include a model parameter κ which has the dimensions of a diffusion coefficient. Here the operators are expressed in the Cartesian co-

[8] be it explicitly formulated or implicitly present because of numerical diffusion.

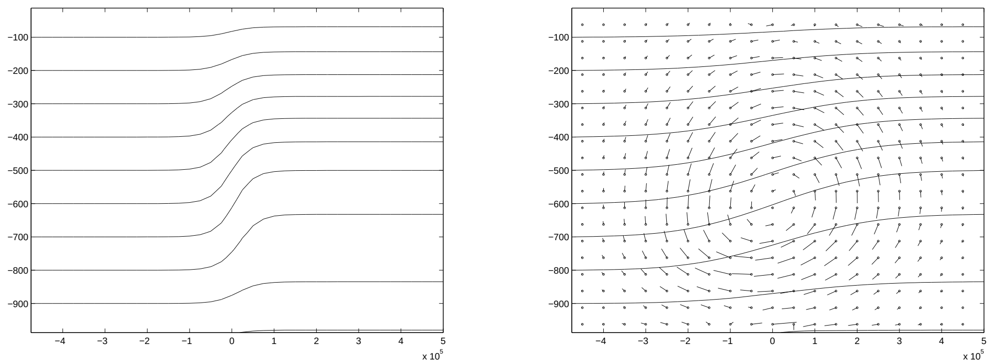

Figure 20-15 Vertical section across a density field exhibiting a frontal structure as shown by the slope of the isopycnals (left panel). Applying the bolus velocity to advect the density field in time, the front flattens (right panel) because of the particular structure of the bolus velocity. Vectors originate from the dots so that the tendency to decrease the frontal slope is evident. Since the bolus velocity itself depends on this slope, the process of flattening slows down after some time.

ordinates and it can be verified that the additional velocity field is divergence free. Also the numerical version of the divergence can be ensured to be zero by proper staggering and expressions translated into the s coordinates if necessary. The additional velocity, called *bolus velocity* has as effect to advect the density field itself and with the chosen signs, indeed leads to a reduction of the frontal slope (Figure 20-15). It is important to note that this advection is performed without any dynamical equations for the bolus velocity, reflecting the fact that we are in the presence of a parameterization of unresolved dynamical motions. The strength of the parameterization can be controlled by the parameter κ and Griffies (1998) shows how to combine the bolus advection parameterization with the isopycnal diffusion into a single operator if the "diffusion" coefficients in advective and diffusive part are identical. For this and a recent review of ocean model developments we refer to a paper by Griffies *et al.* (2000), including additional references.

Analytical Problems

20-1. Sverdrup balance on an uneven bottom.

20-2. Given that the North Pacific Ocean is about twice as wide as the North Atlantic Ocean and that both basins are subjected to equally strong winds, compare their boundary-layer widths and boundary-current speeds.

20-3. Imagine that a single ocean were covering the entire globe, as the atmosphere does.

With no western wall to support a boundary current returning the equatorward Sverdrup flow, what would be the circulation pattern? Relate your results to the existence of the Antarctic Circumpolar Current. [For a succinct description of this major current, see Section 7.2 of the book by Pickard and Emery (1990) or some other oceanography textbook.]

20-4. Some global budget?

20-5. Derive the veering of the horizontal velocity with respect to depth, working with z as the vertical coordinate. Show that at the end one can recover (20.24) by changing to density coordinates.

20-6.

20-7.

20-8.

20-9. Gent and McWilliams. Stationary solution with constant κ and disregarding boundaries in a 2D situation. Isopycnal slope is function of density only. Hence, layer thickness varies linearly and is not diffused anymore in isopycnal models with thickness diffusion.

20-10. When translated into isopycnal coordinates: diffusion of h in the layer thickness equation (12.9).

Numerical Exercises

20-1. Redo Stommel and then add nonlinear term with the QG model developed before on which wind-stress is added. Prepare an illustration for theoretical part.

20-2. Take the density data used in `iwnummed.m` and calculate the geostrophic velocities. To do so, work in z coordinates at the levels of the data. Assume a level of no motion at 500 m . Look at surface currents and currents at 2000m depth. Then repeat with level of no motion at 1500 m.

20-3. Play with `bolus.m` to see flattening. The implement coordinate change and calculate slope by jacobian in vertical plane.

20-4. Get a density section from somewhere and calculate bolus velocity `bolus.m`. Which problems do you expect near boundaries? *Hint:* You might consider κ a calibration parameter variable in space.

20-5. Use `pgerror.m` to explore the pressure-gradient error for a fixed density anomaly profile depending only on z according to

$$\rho = \Delta\rho \tanh((z + D)/W) \tag{20.49}$$

where D and W control the position and width of the pycnocline. Bottom topography is given by

$$h(x) = H_0 + \Delta H \tanh(x/L) \tag{20.50}$$

where L and H controle the slope strength. Calculate the error and associated geostrophic velocity for $f = 10^{-4}$ s^{-1}. Vary the number of vertical grid points, horizontal grid points, the position of the pycnocline, its depth and strength. What happens if you increase solely the number of vertical points? Implement the discretization of another pressure gradient expression of (20.42) in `bcpgr.m` and compare.

20-6. Topography is generally filtered for use in models, by application of a few iterations on a Laplacian-type diffusion. In view of the hydrostatic consistency constraint, which adapted filter technique would you advocate? *Hint:* Remember that a Laplacian filter applied to a function f minimizes the norm of the gradients $\int \left[(\partial f/\partial x)^2 + (\partial f/\partial y)^2\right] d\mathcal{S}$ over the domain $\mathcal{S}$.

Henry Melson Stommel
1920 – 1992

At an early age, Henry Melson Stommel considered a career in astronomy but turned to oceanography as a way to make a peaceful living during World War II. Having been denied admission to graduate school at the Scripps Institution of Oceanography by H. U. Sverdrup, then its director, Stommel never obtained a doctorate. This did not deter him; having soon realized that, in those years, oceanography was largely a descriptive science almost devoid of physical principles, he set out to develop dynamic hypotheses and to test them against observations. To him, we owe the first correct theory of the Gulf Stream (1948), theories of the abyssal circulation (early 1960s), and a great number of significant contributions on virtually all aspects of physical oceanography.

Unassuming and avoiding the limelight, Stommel relied on a keen physical insight and plain common sense to develop simple models that clarify the roles and implications of physical processes. He was generally wary of numerical models. Particularly inspiring to young scientists, Stommel continuously radiated enthusiasm for his chosen field, which, as he was the first to acknowledge, is still in its infancy. (*Photo by George Knapp*)

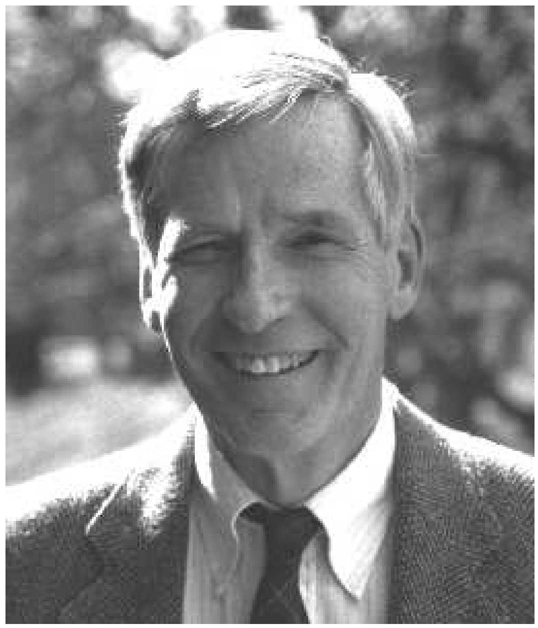

Kirk Bryan
19xx –

Text of second bio (*here*)

Chapter 21

Equatorial Dynamics

(October 18, 2006) **SUMMARY**: Because the Coriolis force vanishes along the equator, tropical regions exhibit particular dynamics. After an overview of linear waves that exist only along the equator, the chapter concludes with a brief presentation of the episodic transfer of warm waters from the western to the eastern tropical Pacific Ocean, a phenomenon called El Niño. The problem of its seasonal forecast then allows to introduce another type of predictive tools, based on empirical relationships. JMB from ⇓ JMB to ⇑

21.1 Equatorial beta plane

Along the equator (latitude $\varphi = 0°$), the Coriolis parameter $f = 2\Omega\ \sin\varphi$ vanishes. Without a Coriolis force, currents cannot be maintained in geostrophic balance, and we expect dramatic dynamical differences between tropical and extratropical regions. The first question is the determination of the meridional extent of the tropical region where these special effects can be expected.

It is most natural here to choose the equator as the origin of the meridional axis. The beta-plane approximation to the Coriolis parameter (see Section 9.4) then yields

$$f \;=\; \beta_0 y, \tag{21.1}$$

where y measures the meridional distance from the equator (positive northward) and $\beta_0 = 2\Omega/a = 2.28 \times 10^{-11}$ m^{-1} s^{-1} with Ω and a being, respectively, the earth's angular rotation rate and radius ($\Omega = 7.29 \times 10^{-5}$ s^{-1}, a = 6371 km). This representation of the Coriolis parameter bears the name of *equatorial beta-plane* approximation.

Our previous considerations of midlatitude processes (see Chapter 16, for example) point to the important role played by the internal deformation radius,

$$R \;=\; \frac{\sqrt{g'H}}{f} \;=\; \frac{c}{f}\,, \tag{21.2}$$

in governing the extent of dynamical structures. Here, g' is a suitable reduced gravity characterizing the stratification and H is a layer thickness. As f varies with y, so does R. If this distance from a given meridional position y includes the equator, equatorial dynamics must supersede midlatitude dynamics. Thus, a criterion to determine the width $R_{\rm eq}$ of the tropical region is (Figure 21-1)

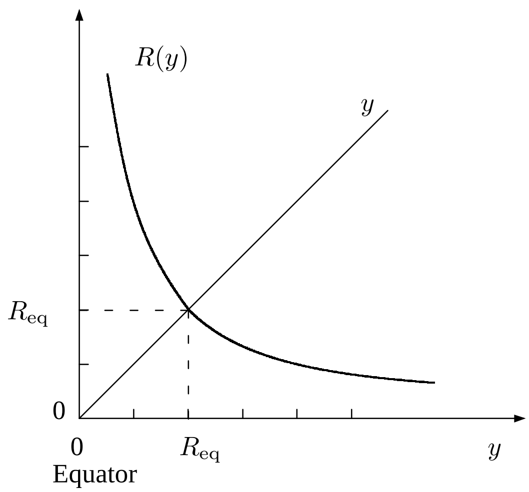

Figure 21-1 Definition of the equatorial radius of deformation.

$$R_{\rm eq} \;=\; R \quad \text{at} \quad y \;=\; R_{\rm eq}. \tag{21.3}$$

Substituting (21.1) into (21.2), the criterion yields

$$R_{\rm eq} \;=\; \sqrt{\frac{c}{\beta_0}}\;, \tag{21.4}$$

which is called the *equatorial radius of deformation*. For the previously quoted value of β_0 and for $c = (g'H)^{1/2}$ = 1.4 m/s, typical of the tropical ocean (Philander, 1990, Chapter 3), we estimate $R_{\rm eq}$ = 248 km, or 2.23° of latitude. Because the stratification of the atmosphere is much stronger than that of the ocean, the equatorial radius of deformation is several times larger in the atmosphere. This implies that connections between tropical and temperate latitudes are different in the atmosphere and oceans.

Since c is a velocity (to be related shortly to a wave speed), we can define an *equatorial inertial time* $T_{\rm eq}$ as the travel time to cover the distance $R_{\rm eq}$ at speed c. Simple algebra yields

$$T_{\rm eq} \;=\; \frac{1}{\sqrt{\beta_0 c}}\;, \tag{21.5}$$

which, for the previous values, is about 2 days.

21.2 Linear wave theory

Because of the important role they play in the so-called El Niño phenomenon, the focus of this section is on oceanic waves. The stratification of the equatorial ocean generally consists of a distinct warm layer separated from the deeper waters by a shallow thermocline (Figure 21-2). Typical values are $\Delta\rho/\rho_0$ = 0.002 and thermocline depth H = 100 m, leading to the previously quoted value of $c = (g'H)^{1/2}$ = 1.4 m/s. This suggests the use of a one-layer reduced-gravity model, which for the purpose of a wave theory is immediately linearized:

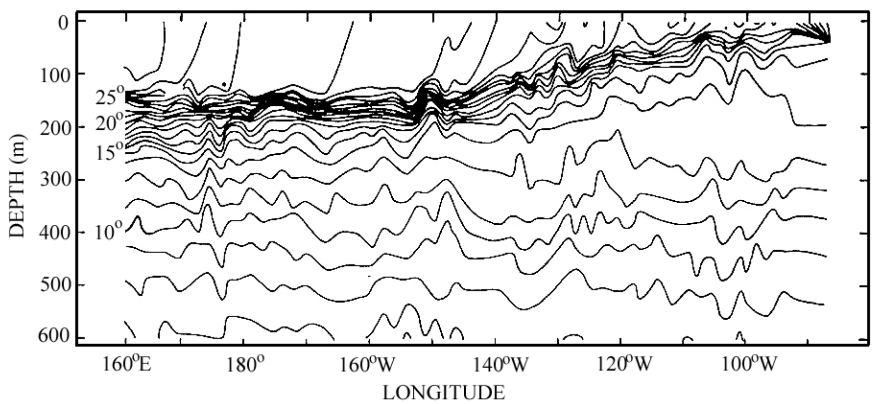

Figure 21-2 Temperature (in °C) as a function of depth and longitude along the equator, as measured in 1963 by Colin *et al.* (1971). Note the strong thermocline between 100 m and 200 m.

$$\frac{\partial u}{\partial t} - \beta_0 y v = -g' \frac{\partial h}{\partial x} \tag{21.6a}$$

$$\frac{\partial v}{\partial t} + \beta_0 y u = -g' \frac{\partial h}{\partial y} \tag{21.6b}$$

$$\frac{\partial h}{\partial t} + H\left(\frac{\partial u}{\partial x} + \frac{\partial v}{\partial y}\right) = 0. \tag{21.6c}$$

Here u and v are, respectively, the zonal and meridional velocity components, g' the reduced gravity $g\Delta\rho/\rho_0$ (= 0.02 m/s^2), and h is the layer-thickness variation (measured positively for an increase in layer thickness). JMB from ⇓ JMB to ⇑

The preceding set of equations admits a solution with zero meridional flow. When $v = 0$, (21.6a) and (21.6c) then reduce to

$$\frac{\partial u}{\partial t} = -g' \frac{\partial h}{\partial x}, \quad \frac{\partial h}{\partial t} + H\frac{\partial u}{\partial x} = 0,$$

having any function of $x \pm ct$ and y as its solution. The remaining equation, (21.6b), sets the meridional structure, which for a signal decaying away from the equator is given by

$$u = c\,F(x - ct)e^{-y^2/2R_{\rm eq}^2} \tag{21.7a}$$
$$v = 0 \tag{21.7b}$$
$$h = HF(x - ct)\,e^{-y^2/2R_{\rm eq}^2}, \tag{21.7c}$$

where $F(\,\cdot)$ is an arbitrary function of its argument and $R_{\rm eq} = (c/\beta_0)^{1/2}$ is the equatorial radius of deformation introduced in the preceding section. This solution describes a wave traveling eastward at speed $c = \sqrt{g'H}$, with maximum amplitude along the equator and decaying symmetrically with latitude over a distance on the order of the equatorial radius of deformation. The analogy with the coastal Kelvin wave exposed in Section 9.2 is immediate (wave speed equal to gravitational wave speed, absence of transverse flow, and decay over a deformation radius); for this reason, it is called the *equatorial Kelvin wave*. Credit for the discovery of this wave, however, does not go to Lord Kelvin but to Wallace and Kousky (1968).

The set of equations (21.6) admits additional wave solutions, more akin to inertia-gravity (Poincaré) and planetary (Rossby) waves. To find these, we seek periodic solutions in time and zonal direction:

$$u = U(y)\,\cos(kx - \omega t) \tag{21.8}$$
$$v = V(y)\,\sin(kx - \omega t) \tag{21.9}$$
$$h = A(y)\,\cos(kx - \omega t). \tag{21.10}$$

Elimination of the $U(y)$ and $A(y)$ amplitude functions yields a single equation governing the meridional structure $V(y)$ of the meridional velocity:

$$\frac{d^2V}{dy^2} + \left(\frac{\omega^2 - \beta_0^2 y^2}{c^2} - \frac{\beta_0 k}{\omega} - k^2\right) V = 0. \tag{21.11}$$

Because the expression between parentheses depends on the variable y, the solutions to this equation are not sinusoidal. In fact, for values of y sufficiently large, this coefficient becomes negative, and we anticipate exponential decay at large distances from the equator. It can be shown that solutions to (21.11) are of the type

$$V(y) = H_n\left(\frac{y}{R_{\rm eq}}\right)\,{\rm e}^{-y^2/2R_{\rm eq}^2}, \tag{21.12}$$

JMB from ⇓

JMB to ⇑

where H_n is a polynomial of degree n, and that these solutions decaying at large distances from the equator, exist only if

$$\frac{\omega^2}{c^2} - k^2 - \frac{\beta_0 k}{\omega} = \frac{2n+1}{R_{\rm eq}^2}\,. \tag{21.13}$$

Thus the waves form a discrete set of modes ($n = 0,\ 1,\ 2,\ \ldots$). Equation (21.13) is the dispersion relation providing frequencies ω as a function of wavenumber k for each mode. As Figure 21-3 shows, three ω roots exist for each n as k varies. (Important note: In this context, the phase speed ω/k of the wave is not necessarily equal to c, the speed of the Kelvin wave encountered previously.)

The largest positive and negative roots for $n \geq 1$ correspond to frequencies greater than the inverse of the equatorial inertial time. The slight asymmetry in these curves is caused by JMB from ⇓ the beta term in (21.13). Without this term, the frequencies can be approximated by JMB to ⇑

$$\omega \;\simeq\; \pm\; \sqrt{\frac{2n+1}{T_{\rm eq}^2} + g'H\,k^2}\,, \qquad n \;\geq\; 1, \tag{21.14}$$

which is analogous to (9.17), the dispersion relation of inertia-gravity waves. These waves are thus the low-latitude extensions of the extratropical inertia-gravity waves (Section 9.3).

The third and much smaller roots for $n \geq 1$ correspond to subinertial frequencies and thus to tropical extensions of the mid-latitude planetary waves (Section 9.4). At long wavelengths (small k values), these waves are nearly nondispersive and propagate westward at speeds

$$c_n \;=\; \frac{\omega_n}{k} \;\simeq\; -\;\frac{\beta_0 R_{\rm eq}^2}{2n+1}\,, \qquad n \;\geq\; 1, \tag{21.15}$$

which are to be compared with (9.30). The case $n = 0$ is peculiar. Its frequency ω_0 is the root of JMB from ⇓

$$(\omega_0 + ck)\left(\omega_0 T_{\rm eq} \;-\; \frac{1}{\omega_0 T_{\rm eq}} \;-\; kR_{\rm eq}\right) \;=\; 0. \tag{21.16}$$

The root $\omega_0 = -ck$ can be shown to be a spurious solution introduced during the elimination of $U(y)$ from the governing equation. This elimination indeed assumed $\omega_0 + ck \neq 0$, which we therefore cannot accept as valid solution anymore. The remaining two roots are readily calculated. JMB to ⇑

As Figure 21-3 shows, this wave exhibits a mixed behavior between planetary and inertia-gravity waves. Finally, the Kelvin-wave solution can formally be included in the set by taking JMB from ⇓ $n = -1$ (Figure 21-3). JMB to ⇑

The polynomials of (21.12) are not arbitrary but must be the so-called Hermite polynomials (Abramowitz and Stegun, 1972, Chapter 22). The first few polynomials of this set are $H_0(\xi) = 1$, $H_1(\xi) = 2\xi$ and $H_2(\xi) = 4\xi^2 - 2$. From the solution $V(y)$, the layer JMB from ⇓ thickness can be retrieved by backward substitution. It is then seen that when V is odd, the layer-thickness anomaly $A(y)$ is even in y and vice-versa. Waves of even order are anti- JMB to ⇑ symmetric about the equator [$h(-y) = -h(y)$], whereas those of odd order are symmetric [$h(-y) = h(y)$]. Thus, the mixed wave is antisymmetric and the Kelvin wave is symmetric.

When the equatorial ocean is perturbed (e.g., by changing winds), its adjustment toward a new state is accomplished by wave propagation. At low frequencies (periods longer than $T_{\rm eq}$, or about 2 days), inertia-gravity waves are not excited, and the ocean's response consists entirely of the Kelvin wave, the mixed wave, and some planetary waves (those of appropriate frequencies). If, moreover, the perturbation is symmetric about the equator (and generally there is a high degree of symmetry about the equator), the mixed wave and all planetary waves of even order are ruled out. The Kelvin wave and odd planetary waves of short wavelengths (if any) carry energy eastward, whereas the odd planetary waves of long wavelengths carry energy westward. Figure 21-4 displays the temporal dispersion of a bell-shaped thermocline displacement imposed on a stretch of equatorial ocean. Clearly visible are the one-bulge

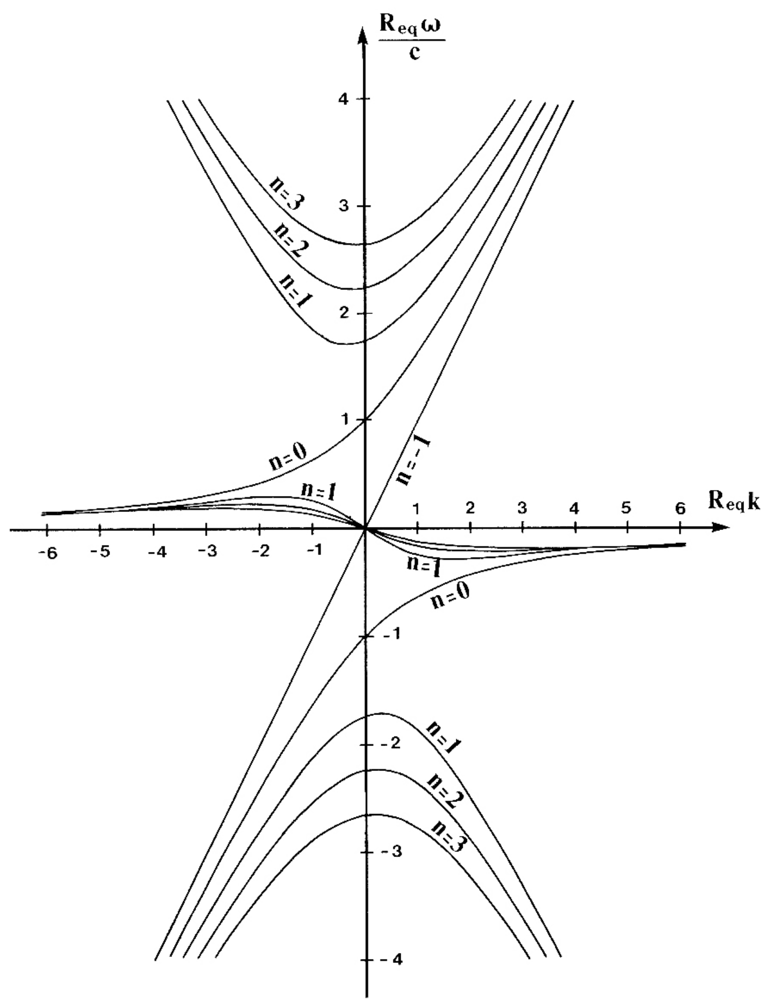

Figure 21-3 Dispersion diagram for equatorially trapped waves.

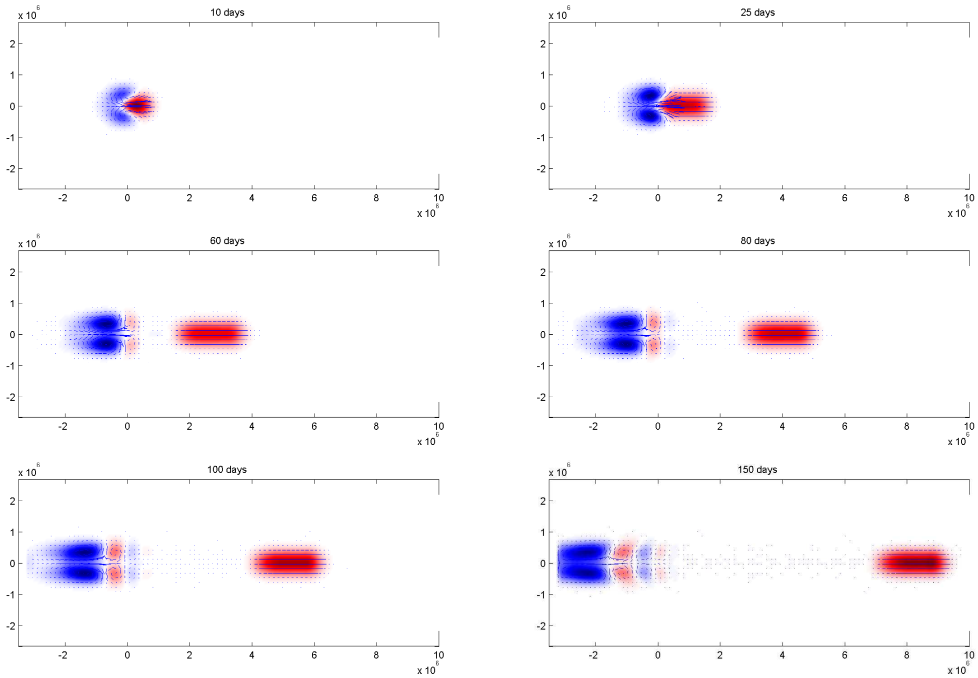

Figure 21-4 The dispersion of an perturbation generated by a ten days wind anomaly imposed on a spot of a stretch of equatorial ocean. Clearly visible are the one-bulge Kelvin wave moving eastward and the double-bulge planetary (Rossby) wave propagating westward at a lower pace.

Kelvin wave progressing eastward and the double-bulge lowest planetary wave ($n = 1$) propagating westward. Although this case is obviously academic, it is believed that Kelvin waves and low-order planetary waves, together with wind-driven currents, are prevalent in the equatorial ocean. JMB from ⇓

At this point, a number of interesting topics can be presented, such as the reflection of a JMB to ⇑ Kelvin wave upon encountering an eastern boundary, waves around islands, and the generation of equatorial currents by time-dependent winds. But, we shall leave these matters for the more specialized literature (Gill, 1982; Philander, 1990; McPhaden and Ripa, 1990; and references therein) and limit ourselves to the presentation of the El Niño phenomenon.

21.3 El Niño – Southern Oscillation (ENSO)

Every year, around the Christmas season, warm waters flow along the western coast of South America from the equator to Peru and beyond. These waters, which are several degrees warmer than usual and are much less saline, perturb the coastal ocean, suppressing — among other things — the semi-permanent coastal upwelling of cold waters. So noticeable is this

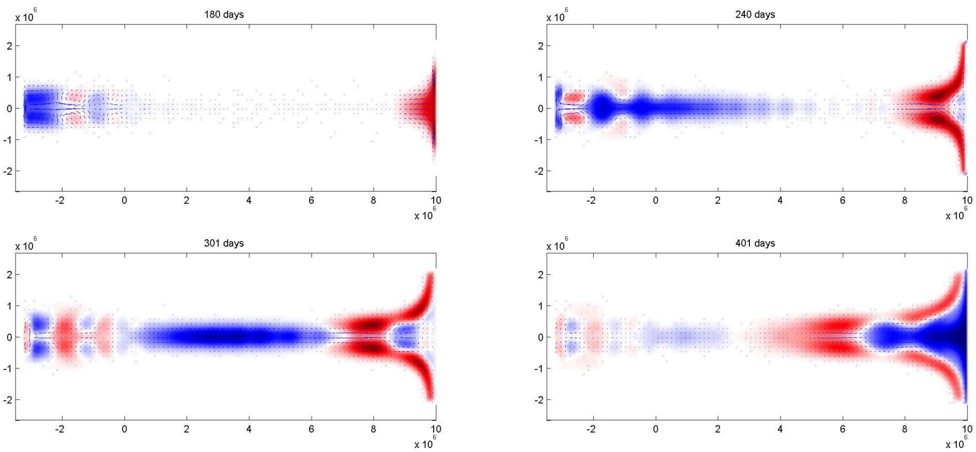

Figure 21-5 Continuation of the wave propagation. Rossby waves are reflected and transformed into Kelvin waves, while the Kelvin wave at the eastern boundary gives birth to a Rossby mode.

phenomenon that early fishermen called it El Niño, which in Spanish means "the child" or more specifically the Christ Child, in relation to the Christmas season.

Regularly but not periodically (every 4 to 7 years), the amount of passing warm waters is substantially greater than in normal years, and life in those regions is greatly perturbed, for better and for worse. Anomalously abundant precipitations, caused by the warm ocean, can in a few weeks turn the otherwise arid coastal region of Peru into a land of plenty. But, suppression of coastal upwelling causes widespread destruction of plankton and fish. The ecological and economic consequences are noticeable. In Peru, the fish harvest is much reduced, sea birds (which prey on fish) die in large numbers, and, to compound the problem, dead fish and birds rotting on the beach create unsanitary atmospheric conditions.

In the scientific community, the name El Niño is being restricted to such anomalous occurrences and, by extension, the name La Niña has been used to signify the opposite situation, when temperatures are abnormally cold in the eastern tropical Pacific. Major El Niño events of the twentieth century occurred in 1904–05, 1913–15, 1925–26, 1940–41, 1957–58, 1972–
JMB from ⇓ 73, 1982–83, 1986–88, 1991–95 1997–98 (the strongest of all), 2002-2003 and 2004-2005
JMB to ⇑ (WMO, 1999; NOAA-WWW 2006). Their cause remained obscure until Wyrtki (1973) discovered a strong correlation with changes in the central and western tropical Pacific Ocean, thousands of kilometers away. It is now well established (Philander, 1990) that El Niño events are caused by changes in the surface winds over the tropical Pacific, which episodically release and drive warm waters, previously piled up by trade winds in the western half of the basin, eastward to the American continent and southward along the coast. The situation is quite complex, and it took oceanographers and meteorologists more than a decade to understand the various oceanic and atmospheric factors.

Under normal conditions, winds over the tropical Pacific Ocean consist of the northeast trade winds (northeasterlies) and the southeast trade winds (southeasterlies) that converge over the *intertropical convergence zone* (ITCZ) and blow westward (Section 19.3). Although it migrates meridionally in the course of the year, the ITCZ sits predominantly in the Northern Hemisphere (around 5° to 10°N). In addition to pushing and accumulating a great amount of warm water in the western tropical Pacific, the trades also generate equatorial upwelling (Section 15.4) over the eastern part of the basin. Thus, in a normal situation, the tropical Pacific Ocean is characterized by a warm-water pool in the west and cold surface waters in the east. This structure is evidenced by the westward deepening of the thermocline, as shown in Figure 21-2.

The origin of an anomalous, El Niño event is associated with a weakening of the trade winds in the western Pacific or with the appearance of a warm sea-surface-temperature (SST) anomaly in the central tropical Pacific. Although one may precede the other, they soon go hand in hand. A slackening of the western trades relaxes the thermocline slope and releases some of the warm waters; this relaxation takes the form of a downwelling Kelvin wave, whose wake is thus a warm SST anomaly. On the other hand, a warm SST anomaly locally heats the atmosphere, creating ascending motions that need to be compensated by horizontal convergence. This horizontal convergence naturally calls for eastward winds on its western side, thus weakening or reversing the trade winds there (Gill, 1980). In sum, a relaxation of the trade winds in the western Pacific creates a warm sea-surface anomaly, and vice versa. Feedback occurs and the perturbation amplifies. On the eastern side of the anomaly, convergence calls for a strengthening of the trades that, in turn, enhances equatorial upwelling. This cooling interferes with the eastward progression of the downwelling Kelvin wave, and it is not clear which should dominate. During an El Niño event, the anomaly does travel eastward while amplifying. Once the warm water arrives at the American continent, it separates into a weaker northward branch and a stronger southward branch, each becoming a coastal Kelvin wave (downwelling). The subsequent events are as described at the beginning of this section.

When an El Niño event occurs, its temporal development is strictly controlled by the annual cycle. The warm waters arrive in Peru around December, and the seasonal variation of the general atmospheric circulation calls for a northward return of the ITCZ and a re-establishment of the southeast trade winds along the equator. The situation returns to normal.

This sequence of events is relatively well understood (Philander, 1990) and has been successfully modeled (Cane *et al.*, 1986). Today, models are routinely used to forecast the next occurrence of an El Niño event and its intensity with a lead time of 9 to 12 months. What remains less clear is the variability of the atmosphere-ocean system on the scales of several years. A strong connection with the *Southern Oscillation* has been made clear, and the broader phenomenon is called ENSO, for El Niño–Southern Oscillation (Rasmusson and Carpenter, 1982). The Southern Oscillation is a quasi-periodic variation of the surface atmospheric pressure and precipitation distributions over large portions of the globe (Troup, 1965; Bromwich *et al.*, 2000).

Much hinges on variations of the so-called *Walker circulation*. This atmospheric circulation (Walker, 1924) consists of westerly trade winds over the tropical Pacific Ocean, low pressure and rising air above the western basin and Indonesia (with associated heavy precipitation) and, at the eastern end of the basin, high pressure, sinking air and relatively dry climate. The strength of this circulation is effectively measured by the sea-level pressure difference $\Delta p_{\rm TD}$ between Tahiti (18°S, 149°W) and Darwin (in northern Australia, at 12°S, 131°E). In practice, the *Southern Oscillation Index* (SOI) is defined as (Troup, 1965):

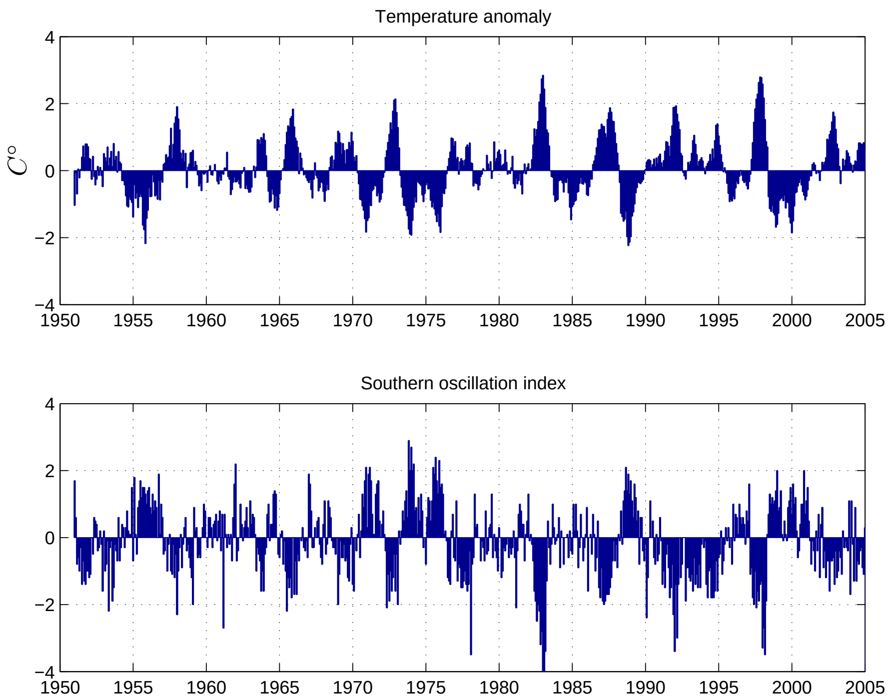

Figure 21-6 Time series of temperature anomalies over the central tropical Pacific Ocean and of the Southern-Oscillation Index.There is a very strong correlation between higher-than-normal temperatures (El Niño events) and negative index values, indicating that El Niño is part of a global climatic variation.

$$SOI \;=\; 10\,\frac{\text{monthly value of}\Delta p_{\rm TD} \;-\; \text{long-term average of}\Delta p_{\rm TD}}{\text{standard deviation of}\Delta p_{\rm TD}}\,, \qquad (21.17)$$

The nearly perfect negative corrolation between these two pressures indicates that both are parts of a larger coherent system. The presence of a higher than normal pressure in Darwin with simultaneous lower pressure in Tahiti (negative SOI value) is intimately connected with an El Niño occurrence (Figure 21-6). In its broad lines, the scenario unfolds as follows. A negative SOI value leads to a weakening of the Walker circulation, reduced strength of the easterly trade winds, especially in the western Pacific. The western warm water pool relaxes and begins to spill as an equatorial Kelvin wave eastward toward the central basin, accompanied by an equal eastward displacement of the low atmospheric pressure above it. Feeding the low pressure from the west are reversed, westerly winds that accelerate the eastward movement of the warm water pool. And so, the situation progresses eastward in an amplifying manner, until the warm water pool reaches the coast of Peru and an El Niño event occurs. Because the atmospheric pressure is then higher than normal on the western side, drought conditions occur over Indonesia and Australia, while South America experiences stronger precipitation than normal. For a more complete description of the many facets and ramifications of the event, the the interested reader is referred to specialized books (Philander, 1990; Diaz and Markgraf, 2000; D'Aleo, 2002).

Benoit: Maybe peak about recharge oscillator of Jin 1997? Easy to present and understand the full cycle

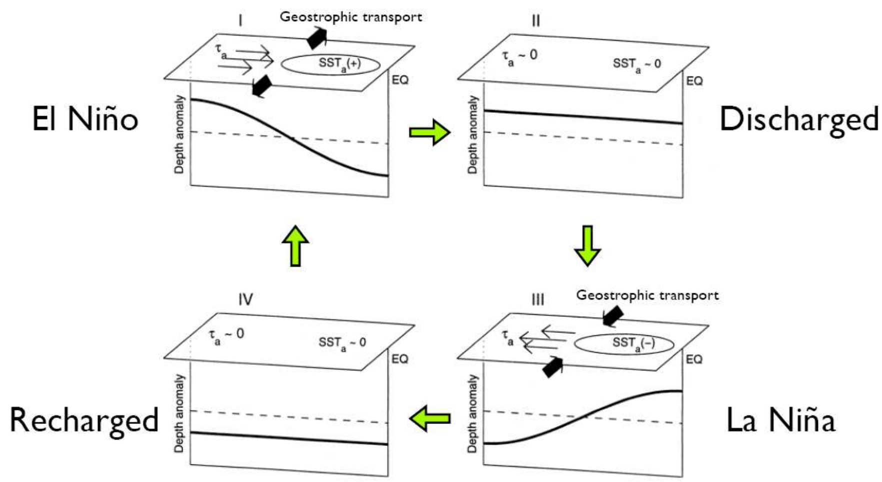

Figure 21-7 Discharge/recharge mechanism of Jin. **Graphic to be redrawn**

Jin FF. 1997a. An equatorial recharge paradigm for ENSO. I. Conceptual model. J. Atmos. Sci. 54:811-29

Jin FF. 1997b. An equatorial recharge paradigm for ENSO. II. A stripped-down coupled model. J. Atmos. Sci. 54:830-47

21.4 ENSO forecasting

Forecasting the El Niño-Southern Oscillation is of prime interest for society, because an impressive number of daily life components are affected, ranging from changes in weather, appearance of droughts or floodings to modifications in crops, fish catchments or population health. Hence it is no surprise that reliable prediction of an El Niño or El Niña event can be of great help preparing to the upcoming modifications. For the forecasting, monthly averaged situations of the weather are of interest because the same month in El-Niõ years is quite different from El Niña years for regions under the influence of the ENSO. But since the forecast has to span several month, if not seasons, coupled atmospheric ocean model are needed, because sea-surface temperature cannot be considered fixed anymore. This was recognized by Zebiak and Cane (1987), who succeeded to build such a coupled model to forecast ENSO. The relevance of the coupling can be nicely shown by the following hindcast experiments:

the use of observed variations in SST during an ENSO event generally allows to model the atmospheric part correctly. Similarly, using observed variations in atmospheric fluxes, the hindcast of ocean variability reveals the oceanic component of ENSO. Hence to forecast, both components are needed.

The ENSO forecast differs from the weather forecast because only average situations are predicted. While weather forecast is mostly constrained by the initial condition on the atmosphere, seasonal forecast benefits from the ocean inertia and its predictability at large scales over several month. Hence seasonal forecast will be constrained rather by initial conditions on the ocean. Therefore observing the tropical ocean is a crucial component of any ENSO forecast system, the most important data being provided by the Tropical Atmosphere Ocean (TAO) moored observation arrays and by satellites measuring sea surface height and temperature.

Seasonal forecast of ENSO is relatively successful because ENSO is known to be the largest single source of predictable internannual variability. Yet, even with a relatively strong signal, models must be able to extract the information out of the overwhelming high frequency signal of atmospheric variability. With the unavoidable model uncertainties, this is a challenging task and one way to reduce uncertainties is to perform model intercomparisons (*e.g.*, Neeling *et al.*, 1992; Mechoso *et al.*, 1995). Such models are also used to identify teleconnections *i.e.*, correlations between distant region's dynamics and the ENSO events. If such teleconnections are identified, predictions of El Niño can be "extrapolated" to other regions. The identification of such teleconnections is generally obtained by statistics on model simulations and observations, leading to as much prediction models as teleconnections found.

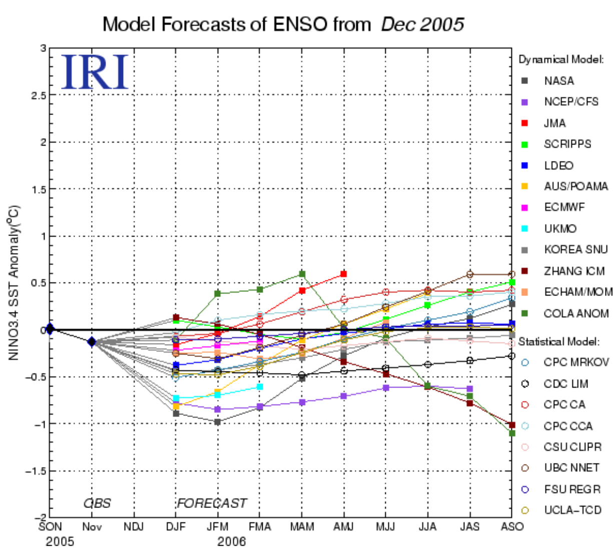

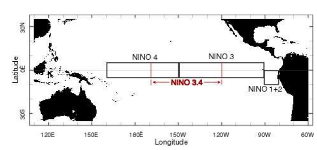

Figure 21-8 Prediction on December 2005 of El Niño by several models, including coupled ocean-atmosphere primitive equation models and statistical models. The probablity of El Niño in 2006 was considered low. Predictions and observations are made for different sub-regions, NINO3.4 referring to a central strip of the basin. (*IRI, International Research Institute for Climate and Society*)

Statistics can also be used to replace the dynamic model's forecasts by an empirical prediction model of El Niño based on past observations of a set of well chosen parameters. This can be done by explicitly searching for correlations and fitting curves of data on a given parametric function such as linear regressions on the SOI. Instead of *a priori* choosing the functional relationship, self-learning approaches such as neural networks (*e.g.*, Tangang *et al.*, 1998) or genetic algorithms (*e.g.*, Alvarez *et al.*, 2001) select themself the "best" functions. To do so, data are separated into two sets, a learning and a validation set. On the learning set, the model is given input data called predictors (such as the SOI of the previous year) and the known output value called predictand (such as the prediction of SOI for the next 6 month). If enough input-output pairs are available, the network or genetic algorithm creates a functional relationship that minimizes the error in the output for this given data set. The danger of such approaches is that overfitting occurs: If the functional relationship contains more adjustable parameters than independent data to be reconstructed, one can always find a "perfect" fit. The latter will however work only on this specific data set. Hence the requirement for a validation data set on which the model must be tested after the learning phase. If the performance in forecasting degrades significantly when switching from the learning set to the validation set, the model is unreliable. However, when the validation is successful, such models offer predictions at extremely small computation costs compared to primitive equation models. To justify their use in operational forecasts, dynamical models, generally much more complex, must therefore show their superiority in prediction quality compared to such empirical models. The simplest models, if they have some skill in prediction, are therefore interesting to define base forecasts to which to compare more complicated versions. For the time being, it seems that dynamical models have better capabilities in predicting early stages of the El Niño phase, but once it is under its way, statistical models work very well. This seems to indicate repeatable patterns of the process, with a triggering effect difficult to catch.

The search for empirical relationships can of course be guided by physical considerations. For El Niño, the wave propagation and reflections on the western and eastern continental boundaries provide a delayed feedback mechanism on the system. This can be translated into a delayed oscillator model (Suarez and Schopf 1988) whose governing equations read

$$\frac{\partial T}{\partial t} = aT(t) - aT^3(t) - bT(t-\delta) \tag{21.18}$$

where T stands for a normalized temperature anomaly associated with El Niño. The term aT models the positive feedback of the initial Kelvin wave with the moving atmospheric perturbation. The cubic terms is associated with a damping and keeps the solution bounded[1]. Finally the last term $-bT(t-\delta)$ models the negative feedback by the initial westward Rossby wave that is reflected as a Kelvin wave of opposite amplitude, responsible for the changed sign. The delay δ is then readily interpreted in terms of the travel time. If the negative feedback is very strong, needing a reflection with some kind of amplification, an opposite event can be triggered and the way paved to swith from El Niño to El Niña. Parameters of this model can then be fitted to observations if a simple model is sought (Exercise 21-7).

Analytical Problems

21-1. How long does an equatorial Kelvin wave take to cross the entire Pacific Ocean?

[1] T can always be scaled so that the cubic term appears with the same coefficient as the linear feedback.

21-2. Generalize the equatorial-Kelvin-wave theory to the uniformly stratified ocean. Assume inviscid and non-hydrostatic motions. Discuss analogies with internal waves.

21-3. Show that equatorial upwelling (mentioned in Section 15.4; see Figure 15-6) must be confined at low frequencies to a width on the order of the equatorial radius of deformation.

21-4. In the Indian Ocean, two current-meter moorings placed at the same longitude and symmetrically about the equator (1.5° of latitude) record velocity oscillations with a dominant period of 12 days. Furthermore, the zonal velocity at the northern mooring leads by a quarter of a period the meridional velocities of both moorings and by half a period the zonal velocity at the southern mooring. The stratification provides $c = 1.2$ m/s. What kind of wave is being observed? What is its zonal wavelength? Can a comparison of the maximum zonal and meridional velocities provide a confirmation of this wavelength?

21-5. Consider geostrophic adjustment in the tropical ocean. What would be the final steady state following the release of buoyant waters with zero potential vorticity along the equator of an infinitely deep and motionless ocean? For simplicity, assume zonal invariance and equatorial symmetry.

JMB from ⇓

21-6. What kind of initial conditions are needed for the delayed oscillator model (21.18)?

22-7. Search for information to check if the forecast provided in December 2005 of a low probability for an El-Niño in 2006 was verified.

22-8. Show that the linearization of the governing equations for a Kelvin wave are valid as long as the function F is small enough $|F| \ll 1$.

JMB to ⇑

Numerical Exercises

21-1. Design a numerical solver for the delayed oscillator equation (21.18). Simulate a solution with $a^{-1} = 50$ days, $\delta = 400$ days and $b^{-1} = 90$ days for different initial conditions. Then change to a^{-1} =100 days and $b^{-1} = 180$ days.

21-2. Design a numerical version of the linear reduced-gravity model (21.6), to which a wind stress is added. Use a finite-difference approach on the C-grid and a time-stepping of your choice. Start with a situation at rest and then apply a zonal wind perturbation acting during 30 days. Take a gaussian wind-stress whose amplitude is

$$\tau = \tau_0 e^{-(x^2+y^2)/L^2} \tag{21.19}$$

and which is directed eastward. Take $\tau_0 = 0.1$ N/m^2 and $L = 300$ km. The reduced-gravity model's parameters are $\Delta\rho/\rho_0$ = 0.002 and a thermocline depth H = 100 m.

For a first simulation, use a closed domain in $x =$ -3000 km and $x =$ 10000 km as well as in $y = \pm$ 2000 km. Simulate over 600 days.

21-3. For Exercise 21-2, the perturbation eventually propagates along the southern and northern boundary when they are supposed to be closed. Which process is responsible for this? Modify the southern and northern boundary conditions by opening the domain and apply $v = \pm\sqrt{g'H}\, h$ there. Choose a physically reasonable sign for each boundary by searching for a physical interpretation of these boundary conditions.

21-4. Change the topology of the domain in Exercise 21-3 by adding land points in the lower left corner and upper right corner to mimic the continents on each side of the Pacific and redo the simulations. Can you identify the modes that are now present compared to the symmetric case?

21-5. Search for a spatial discretization of the Coriolis term on the C-grid that does not create mechanical work in the sense that when multiplying the evolution equation for $u_{i-1/2,j}$ by itself and adding a similar product for $v_{i,j-1/2}$, the Coriolis force contributions cancel out. *Hint:* Analyze which products of u and v appear, similar to the analysis of the Arakawa Jacobien in Section 16.6 and look how to average taking into account variations of y.

21-6. Using the SST anomalies and SOI from 1991 to 2005 retrieved with `soi.m`, perform a linear regression over data windows and look how the extrapolation of these regressions are able or unable to predict the SST or SOI for later moments. First use a data window of 4 month and try to extrapolate for the next month. Plot the prediction error over time when applying the method over all possible data windows. To decide wether your prediction is useful, compare to the prediction error of the simple guess of a persistent anomaly. Then try to change you data window and lead time to improve the prediction capabilities. Instead of a linear regression you also might try other polynomial fits.

21-7. Do the same as in Exercise 21-7, but try to calibrate the delayed oscillator model (21.18) for the temperature anomaly. Use the calibrated model for the extrapolation purposes. Use, if necessary, data windows over several years.

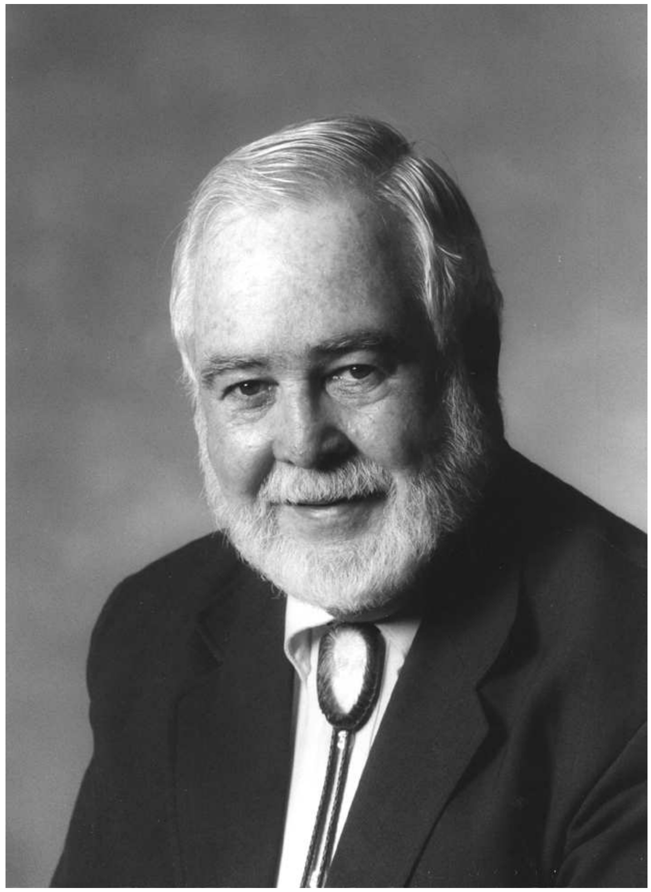

James Jay O'Brien
1937 –

Text of first bio (*here*)

Paola Malanotte Rizzoli
1946 –

Paola Malanotte Rizzoli obtained a doctorate in quantum mechanics and was well on her way to a distinguished career in physics when a massive flood of Venice, where she worked at the time, made her change her mind. She switched to physical oceanography and obtained a second doctorate. Her contributions to this field have been significant and varied, spanning the theory of long-lived geophysical structures, such as eddies and hurricanes, numerical modeling of the Atlantic Ocean and Gulf Stream system, the Black Sea ecosystem, data assimilation, and tropical-subtropical interactions.

Professor Rizzoli teaches at the Massachusetts Institute of Technology and lectures across the world. She is known as a dynamic speaker and an inspiring scientist. In addition to her teaching and research, she has served the oceanographic community in a number of capacities, at both national and international levels.

Never abandoning her love for Venice, Paola Rizzoli was instrumental in developing a system of sea gates to protect the city from future floods and sea level rise. This protection system is currently under construction. (*Photo MIT archives*)

Chapter 22

Data Assimilation

SUMMARY: The chapter outlines methods that blend in some optimal way observations with model computations in order to guide the latter and produce improved simulations of geophysical motions. The methods invoke physical as well as statistical reasoning and rely on certain approximations that facilitate their implementation in operational forecast models.

22.1 Need for data assimilation

Personal experience teaches us that weather forecast is only reliable within a few days from the moment when the forecast is made. The time up to which the prediction is performed is called *lead time* and predictions beyond it are considered so imprecise that very simple prediction methods, such as the use of climatological values or persistence of today's weather, work at least as well as more sophisticated weather forecast system. Before discussing the reasons beyond the forecast errors increasing with lead time, we therefore already realize that any forecast system will need reinitializations if predictions on a regular basis are needed. Such a reinitialization must certainly take into account the recent observations to infer a correct state of the system, an operation called *field estimation* in the forecast jargon. From this better estimate, a forecast can be restarted on better grounds.

For weather forecasts, such field estimates are *sequential* in the sense that they only use already existing data, *i.e.*, from the past up to the day on which the forecast starts. For other applications, the best field estimate of a past situation is thought, in which case data from later moments than the moment of interest can also be taken into account and a non-sequential method used. A typical example in which all available data are used is the so-called *reanalysis*, in which the best fields over a given period are reconstructed using data from the whole period together with physical governing equations to provide the best picture of reality at any moment.

The melding of physical laws and observations, be it in sequential or non-sequential way, is carried out through so-called *data assimilation*, which can be performed intermittently (for example every day using the data from the last day) or continuously (using data whenever

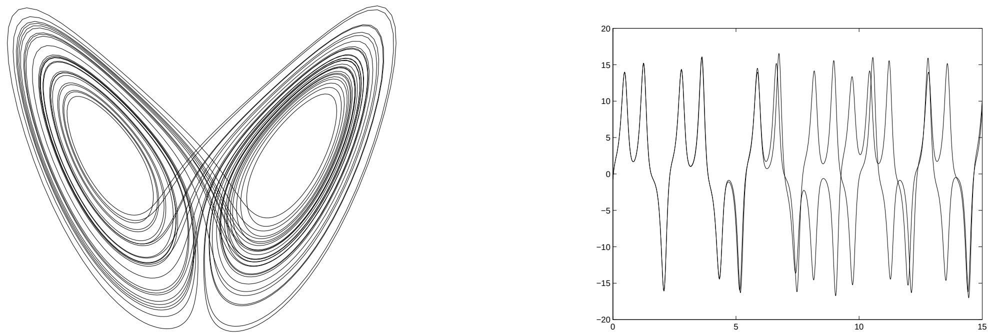

Figure 22-1 Trajectory in (x, z) space (left panel) showing the jumping of the solution between two cycles. For two slightly different initial conditions, two solutions $x(t)$ stay together for some time and then diverge (right panel). Obtained using `chaos.m` with $\sigma = 10$, $r = 28$ and $b = 8/3$.

they arrive).

Since data assimilation heavily exploits observational data, is should also be possible to quantify the forecast errors once new data corresponding to the forecast are delivered. The forecast errors can then be used to assess the skill of the forecast system. Here it is customary to compare the error of the forecast to the error of an elementary forecast. Rudimentary forecasts are persistence (*e.g.*, tomorrow the weather will be as today), climatology (*e.g.*, next week, the weather will be the average weather of the last twenty years) or random forecasts (*e.g.*, one of the two preceding forecasts methods with an added random noise of zero average and prescribed variance). The Brior skill score S, based on an error measure ϵ^f of the forecast system and the same error measure ϵ^b when using a basic forecast system, reads

$$S = \frac{\epsilon^f - \epsilon^b}{\epsilon^p - \epsilon^b} = 1 - \frac{\epsilon^f}{\epsilon^b}, \tag{22.1}$$

where we assume that for a perfect forecast system, the error ϵ^p would be zero. If the forecasts system's skill is less then zero, it means the system is not better than the most basic forecast system, though it might still have some useful information in the forecast. On the other extreme, when the skill is close to one, the forecast system is much better than the baseline versions. Note that such a skill score can also be used to quantify the improvement of a new forecast system over an older version with error ϵ^b.

Clearly the value of the skill will depend on the error norm ϵ (*e.g.*, rms error, error on the maximum temperature, error on the hours of sunshine *etc.*) but more importantly, the skill varies with lead time. The further we try to forecast into the future, the more the skill has a tendency to decrease and we naturally come back to the question why it is so difficult to make accurate long range forecasts. The previous chapters might have biased our perception of the geophysical fluids towards a system that is governed by equations whose solutions are well behaved and whose state is at any moment uniquely defined when adequate initial conditions and boundary conditions are prescribed. This is the case in theory but we can already accept the idea that with imperfect models and inaccurate conditions, errors can have a tendency to accumulate during long forecasts and reduce skill with lead time. But the situation is more dramatic than that. Even if we could control the errors below any arbitrary

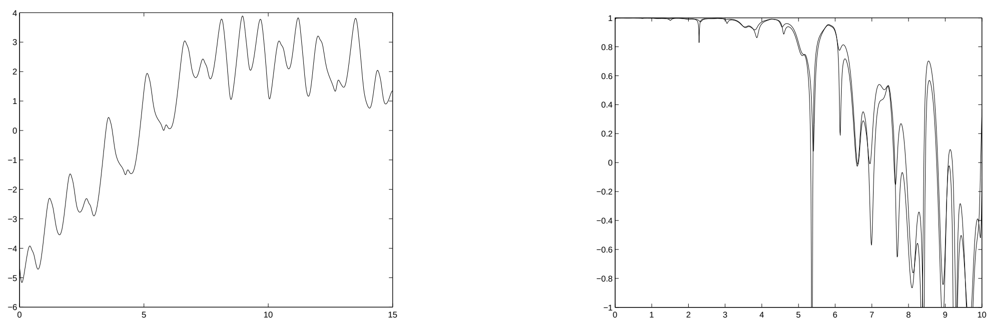

Figure 22-2 Logarithm of a forecast error using incorrect initial conditions as a function of lead time (left panel). Skill score as a function of lead time for two different base forecasts (right panel).

value, which obviously we will never be able to do, some governing equations will lead to solutions that diverge rapidly for even extremely small changes in the conditions. The famous *Lorenz equations* are an archetype of systems of equations that exhibit such a behavior and read

$$\frac{dx}{dt} = \sigma\,(y-x), \tag{22.2a}$$

$$\frac{dy}{dt} = r\,x - y - x\,z, \tag{22.2b}$$

$$\frac{dz}{dt} = x\,y - b\,z, \tag{22.2c}$$

where σ, r and b are parameters. The solution of these innocent looking equations governing a low order truncation of atmospheric motions (Lorenz ????) are known to generate chaotic trajectories such that two very close initial conditions will lead to completely different solutions after some time which we call the *predictability limit* (Figure 22-1).

More generally, the accumulation of errors, even when starting with arbitrarily small errors can result in a predictability limit in strongly nonlinear systems. This limit is estimated to be one to two weeks for the global atmosphere and of the order of a month for mid-latitude ocean eddies. It is then not surprising that forecast skill will decrease with lead time approaching the predictability limit of the system (Figure 22-2). An idea on this time can be obtained by considering the autocorrelation of the solution

$$\rho(\Delta) = \frac{\frac{1}{T}\int_0^T u(t+\Delta)u(t)\,dt}{\sqrt{\frac{1}{T}\int_0^T u(t)^2\,dt}\sqrt{\frac{1}{T}\int_0^T u(t+\Delta)^2\,dt}} \tag{22.3}$$

with $T \rightarrow \infty$. This function measures how well the solution at a given moment is on average related to the solution at a previous moment. In this sense, the delay Δ for which ρ approaches zero defines the delay after which the solution cannot be determined from the knowledge of the past anymore and is "decorellated" with values further apart than Δ. For a purely random signal, the autocorrelation is zero for any $\Delta > 0$, while for the solution of the Lorenz equation, we might indeed expect a limit of predictability (Figure 22-3). Note that the system

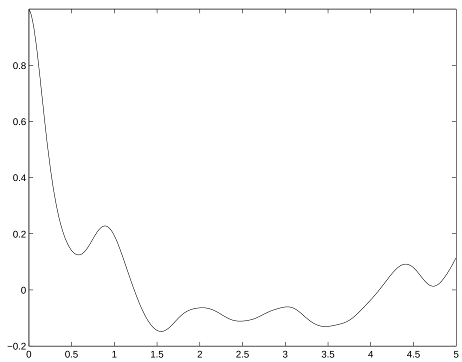

Figure 22-3 Autocorrelation as a function of Δ for the solution $x(t)$ of the Lorenz equations.

can still be deterministic, each initial condition determining a unique trajectory, but the loss of predictability means we are not able anymore to isolate this unique trajectory even with the finest numerical surgery and measurement tools.

For geophysical fluids, solutions are not only controlled by initial conditions but also by boundary conditions, and the predictability limit will depend on the relative importance of boundary conditions versus initial conditions. If boundary conditions are mostly forcing the system, an enclosed shallow sea with strong winds for example, the predictions can be performed for very long times and the skill is essentially constrained by the accuracy of the forcings. Since those forcings and boundary conditions are generally reasonable known, skill remains reasonable for rather long periods. For systems essentially controlled by initial conditions, the global atmosphere for example, initial conditions are generally constructed with care and initial skill is very high. With increasing lead time, predictability limits are reached and skill rapidly drops. Between those two extremes, the skill behavior will thus depend on the relative importance of initial or boundary conditions on the predictability limit (Figure 22-4).

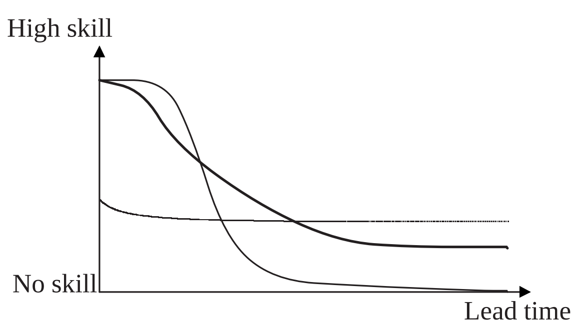

Figure 22-4 Predictability for boundary condition dependent systems (thin line), initial condition dependent systems (medium line) and mixed situations (thick line).

Despite the inherent problem of limitations in predictability, we can increase forecast skills by reducing uncertainties in the model and its initial and boundary conditions, so as to push further away the limits of the forecast system. Some of the errors which we can try to keep under control were already classified for the modeling part (see section 4.8) and in the course of the book we encountered various levels of model simplifications, as hydrostatic approximations, quasi-geostrophic approximations or homogeneous shallow water models for all of which the discretization added further sources of errors. For the initial and boundary conditions based on observed fields, we can also distinguish several kind of errors. The most obvious one is the instrumental error of generally known and relatively low standard deviation. In Section 1.8 we also encountered the representativity error, due to the fact that the measurement (*e.g.*, a temperature measurement in a big city) is not the state variable we actually would like to observe (the temperature at a 100 km scale). Synopticity errors can be a concern when observations are binned into time slots for analysis and assimilation (*e.g.*, assembling into a single snapshot view of the ocean the data gathered during a cruise monitoring a frontal wave propagation can lead to severe Doppler effects, Rixen *et al.* 2002). In general any data treatment before assimilation, such as interpolation, must be taken into account when assessing the errors associated with the "observation". The distinction between modeling and observational errors are not always clear and the discrete sampling induced by the model grid can be considered both a model error (truncation of continuous operators) or an observation error (we do not measure the scales the model is supposed to simulate). In any case, we face the problem that some of the information, both from the model and the observations, are incomplete and corrupted by errors. The objective of data assimilation is the reduction of the influence of those errors by combining model and data information in the best possible way.

22.2 Nudging

Among the first methods used to correct models trajectories by data is the nudging method which starts from the governing equations of the state vector $\mathbf{x}$

$$\frac{d\mathbf{x}}{dt} = \mathcal{Q}(\mathbf{x}, t).$$

Assuming the observations distributed exactly as the state vector (*i.e.*, we observe on the same grid as the numerical model), we group them into a vector $\mathbf{y}$ and the nudging methods adds a linear correction term to the governing equation, proportional to the difference between model results and observations:

$$\frac{d\mathbf{x}}{dt} = \mathcal{Q}(\mathbf{x}, t) \; + \; \mathsf{K}\,(\mathbf{y} - \mathbf{x}) \tag{22.4}$$

The additional term is the product of a matrix with the model-observation misfit. For the nudging method, the matrix is diagonal $\mathsf{K} = \mathsf{diag}(1/\tau_i)$ and is constructed using τ_i, the time scale of the so-called *relaxation*. Since the difference between the model simulation and an observation of the same variable is zero in the case there are no errors, the additional terms only act when a correction is necessary and then pushes the solution towards the observation $\mathbf{y}$. If the time scale τ_i is large compared to the time scales of the system, corrections are small and often qualified as background relaxation. Such background relaxations very often use climatolical values in place of "observations". When no observations are present for some components of the state vector, the corresponding relaxation time is simple set to infinity. When observations are only available at certain moments, the relaxation time scale is kept very large far away from that moment and decreases when approaching the moment t^o at which data is available. In this way, a smooth time-incorporation of data is achieved and an example of time dependent weighting functions is

$$\frac{1}{\tau} = K \exp[-(t - t^o)^2/T^2] \tag{22.5}$$

with T an appropriate time scale over which the observation can leave its footprint on the relaxation. The time relaxation can also be made space dependent when physical reasons allow to identify different dynamical regimes. A particular form of nudging is surface relaxation in ocean models, where the simulated sea surface is relaxed towards observed fields. Such a relaxation is often maintained with a low intensity even when full atmospheric fluxes are applied in order to avoid any drift (REFERENCE). Finally, when relaxation time is very short and comparable to the time stepping, the nudging method basically replaces modeled values by the corresponding observation, a process called *direct insertion* when done in a single time step. Presently nudging is still popular near boundaries, where the relaxation can be interpreted as boundary fluxes corrected by observations. In this case, the time-continous nature of the corrections is beneficial by avoiding sudden shocks in the models.

22.3 Optimal interpolation

The previous method, though robust and quite useful in the past, is rather an *ad hoc* approach and we will now present a method which is based on sound statistical optimizations. In particular relationships between different variables will be exploited enhance corrections. We will use notations slightly different from the discretization notations used up to now. Because sequential assimilation cycles perform an analysis not every time step of the model (Figure 22-5), we use $\mathbf{x}_n$ if we want to refer to a particular cycle of the assimilation[1]. We also should keep in mind that in practical applications, it is advantageous to use a state vector defined by anomalies (*i.e.*, departure from a reference state), normalized so that each element of the state vector should be comparable to the others. The state vector then does not try to compare velocity and temperature but normalized versions of them. But because it contains variables of different types we are heading for so-called *multivariate* approaches. Forecasts will be referenced by index $\quad^f$ and the analyzed parameters, after combining forecast and observations by superscript $\quad^a$.

For the sake of illustration, we start with the very simple problem of having at our disposal at a given moment two pieces of information about a temperature with unknown true state T^t. The information can originate from a measurement and/or a model and include errors ϵ. For the two values T_1 and T_2 we therefore have

$$T_1 = T^t + \epsilon_1, \quad \langle \epsilon_1 \rangle = 0, \quad T_2 = T^t + \epsilon_2, \quad \langle \epsilon_2 \rangle = 0 \tag{22.6}$$

where we assume that on statistical average, denoted by $\langle \quad \rangle$, errors vanish. In other words, we suppose the values to be unbiased. We can estimate the unknown temperature by a linear

[1] It is thus not $\mathbf{x}^n$ we used before to refer to the time-step index.

combination of the two:

$$T = w_1\,T_1 \;+\; w_2\,T_2 \;=\; (w_1 + w_2)T^t \;+\; (w_1\epsilon_1 + w_2\epsilon_2) \tag{22.7}$$

and on average this estimate will take the value

$$\langle T \rangle = (w_1 + w_2)T^t, \tag{22.8}$$

so that we obtain an unbiased estimate of the true state if we take $w_1 + w_2 = 1$. In this case, we perform in fact a weighted average of the two available data, an intuitive approach. An unbiased estimate, or *analysis*, T^a of the true state is therefore

$$T^a = (1 - w_2)T_1 + w_2 T_2 \;=\; T_1 + w_2(T_2 - T_1) \tag{22.9}$$

while in reality there is an error

$$T^a - T^t = (1 - w_2)\epsilon_1 + w_2\epsilon_2, \tag{22.10}$$

which is zero on average but whose variance is not zero:

$$\left\langle (T^a - T^t)^2 \right\rangle = (1 - w_2)^2 \left\langle \epsilon_1^2 \right\rangle + w_2^2 \left\langle \epsilon_2^2 \right\rangle + 2(1 - w_2)w_2 \left\langle \epsilon_1\epsilon_2 \right\rangle \tag{22.11}$$

The actual errors ϵ_1 and ϵ_2 are not known, otherwise we would have access to T^t immediately. However, depending on the origin of the errors, we can specify the so-called *error variance* $\left\langle \epsilon_1^2 \right\rangle$ or, equivalently, the standard deviation of the error $\sqrt{\langle \epsilon_1^2 \rangle}$ generally used to plot error-bars. If the measurements or models leading to T_1 and T_2 are independent, we can reasonably suppose that the errors ϵ_1 and ϵ_2 are uncorrelated, which in statistical terms means $\langle \epsilon_1\epsilon_2 \rangle = 0$. Hence the error variance $\left\langle \epsilon^2 \right\rangle$ of the analysis is

$$\left\langle \epsilon^2 \right\rangle = (1 - w_2)^2 \left\langle \epsilon_1^2 \right\rangle + w_2^2 \left\langle \epsilon_2^2 \right\rangle. \tag{22.12}$$

Naturally, the best estimate is the one with the lowest expected error variance and we will use w_2 that minimizes the right-hand side:

$$w_2 = \frac{\left\langle \epsilon_1^2 \right\rangle}{\langle \epsilon_1^2 \rangle + \langle \epsilon_2^2 \rangle} \tag{22.13}$$

and obtain the minimal error variance that reads

$$\left\langle \epsilon^2 \right\rangle = \frac{\left\langle \epsilon_1^2 \right\rangle \left\langle \epsilon_2^2 \right\rangle}{\langle \epsilon_1^2 \rangle + \langle \epsilon_2^2 \rangle} = \left(1 - \frac{\left\langle \epsilon_1^2 \right\rangle}{\langle \epsilon_1^2 \rangle + \langle \epsilon_2^2 \rangle} \right) \left\langle \epsilon_1^2 \right\rangle, \tag{22.14}$$

while the estimate of the temperature itself reads

$$T^a = T_1 \;+\; \left(\frac{\left\langle \epsilon_1^2 \right\rangle}{\langle \epsilon_1^2 \rangle + \langle \epsilon_2^2 \rangle} \right) (T_2 - T_1)\,. \tag{22.15}$$

We observe that the error variance on the combination of T_1 and T_2 is smaller than both $\left\langle \epsilon_1^2 \right\rangle$ and $\left\langle \epsilon_2^2 \right\rangle$. Using information from two sources, even if one of the sources has a relatively large error, therefore reduces on average the uncertainty. This is the basic idea behind data assimilation combining information with known error statistics from different sources to reduce overall uncertainties. If optimizations as the minimization of (22.12) are used, the process can be quite efficient in decreasing the analysis error.

We can reach the same solution by solving a minimization problem aiming to find T that minimizes a weighted measure of the differences between the analysis and the available information, with weights inversely proportional to the error variance of the information:

$$\min_T J = \frac{(T - T_1)^2}{2\,\langle \epsilon_1^2 \rangle} + \frac{(T - T_2)^2}{2\,\langle \epsilon_2^2 \rangle}. \tag{22.16}$$

In other word, we do not care the analysis to depart from observations that are uncertain but require the analysis to be closer to accurate observations. The minimum of (22.16) is reached when T takes the value T^a of (22.15).

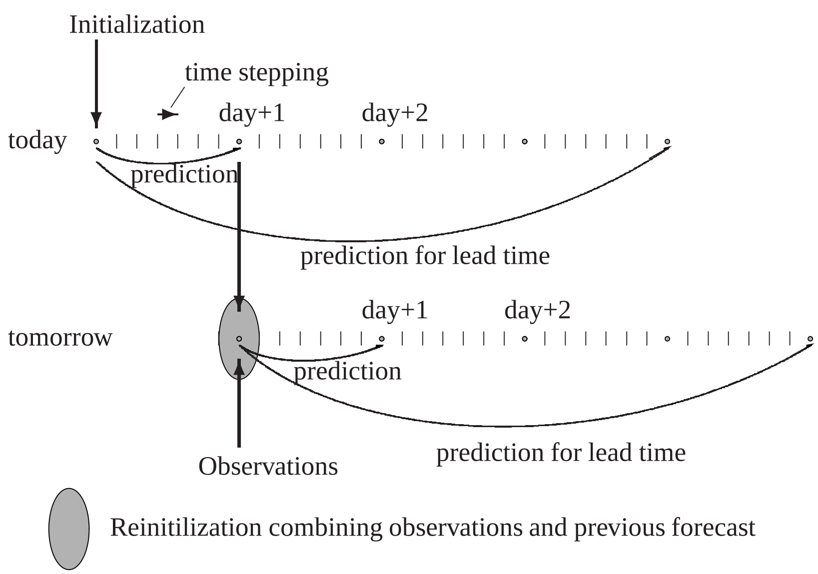

Figure 22-5 Schematic representation of intermittent reinitialization through sequential data assimilation on a daily basis.

The optimal reduction in error can be used to combine model forecasts and observations in the so-called *optimal interpolation*[2]. Generally, there are much more model data than observations [3] so that the size of $\mathbf{x}$ is much larger than that of vector $\mathbf{y}$ containing observations. The state vector $\mathbf{x}$ will thus be considered the reference to be corrected. If we want to reinitialize the model at a given moment, we can construct the analysis $\mathbf{x}^a$ as a linear combination

[2]Sometimes the term *objective analysis* is used as a synonyme, though the latter is in principle just any mathematical interpolation method opposed to the historical subjective drawing by hand of isolines.CHECK

[3]The European Centre for Medium-Range Weather Forecasts, ECMWF, uses M =3 10^7 state variables for its operational ensemble T255 weather forecast model in 2006 and assimilates $P = 3\ 10^6$ observations every cycle of 12 hours; the Mercator ocean model PSY3v1 operates with M =10^8 but “only” $P = 0.25\ 10^6$ data are assimilated once a week in 2005.

of the forecast $\mathbf{x}^f$ and the observations $\mathbf{y}$:

$$\mathbf{x}^a = \mathbf{x}^f + \mathsf{K}\left(\mathbf{y} - \mathsf{H}\mathbf{x}^f\right) \tag{22.17}$$

Here we used a linear *observation operator* H that allows to relate the simulated state variables to the observed ones in order to quantify the model-observation misfits. In the most simple case, H is a matrix that interpolates the model forecast of a variable onto the position on which the corresponding observation is found (*e.g.*, the temperature forecast is interpolated to the position in which a meteorological station measures temperature). In other situations, the matrix can contain mathematical operations that relate some forecasted fields to observed parameters not directly forecasted (*e.g.*,. the gelbstoff measured by satellites are integrated values of matter in the water column, while a dispersion model provides forecasts of the 3D structure of matters so that the observation operator H has to integrate, or sum up, the different layers in each water column). If the relation between model variables and observations is nonlinear, the last term, called *innovation* vector and noted d should be replaced by

$$\mathsf{d} = \mathbf{y} - \boldsymbol{\mathcal{H}}(\mathbf{x}^f) \tag{22.18}$$

where $\boldsymbol{\mathcal{H}}$ is then a nonlinear function. Here we will only consider a matrix H and a linear relation between observed parameters and model parameters. We can also mention that interpretation of observation errors depend on how the data are prepared and the observation operator is constructed. Altimetric data can for example be assimilated along tracks and the observational error is then a combination of instrumental, representativity (mix of spatial scales) , synopticity (time slot binning) and finally interpolation errors when sammpling the model at the track locations using H. If, for convenience, the tracks are beforehand gridded on the same mesh as the model grid, this interpolation, itself performed for example with a spatial optimal interpolation version (Excercise 22-2), has an associated error covariance which must be taken into account in prescribing the previous observational error. Generally, interpolation from the model to data location (through H) introduces less errors when there are more model grid points than observations, the most usual case.

The matrix K of size $M \times P$ is called the Kalman gain matrix and must now be determined so as to lead to the best analysis. The best analysis will depend on the error structures of the forecast and observations since we have both an error on the forecast

$$\boldsymbol{\epsilon} = \mathbf{x} - \mathbf{x}^t \tag{22.19}$$

with respect to the true state $\mathbf{x}^t$. Similarly there is an observational error

$$\boldsymbol{\epsilon}^o = \mathbf{y} - \mathbf{y}^t. \tag{22.20}$$

From such errors, even if we do not know their actual value, we can define statistical averages. Obviously, for unbiased models and observations the first order moment $\langle \boldsymbol{\epsilon}^o \rangle$ is zero. We can also define the error-covariance matrix

$$\mathsf{R} = \left\langle \boldsymbol{\epsilon}^o \boldsymbol{\epsilon}^{o\mathsf{T}} \right\rangle \tag{22.21}$$

which has non-zero elements on the diagonal if observations have some errors associated with them. On the diagonal we find indeed the error variance of each observation. The off-diagonal terms measure how errors of two different observations are correlated. Such correlations can for example arise when satellite observations of turbidity are less precise in a river plume, in which case points close to the estuary will exhibit correlated errors. Note that error covariances are symmetric and that for any vector $\mathbf{z}$, the quadratic form $\mathbf{z}^\mathsf{T}\mathbf{R}\mathbf{z} = \left\langle \left(\mathbf{z}^\mathsf{T}\boldsymbol{\epsilon}^o\right)^2 \right\rangle$ is never negative so that the covariance matrixes are semi-positive defined. This simply means that the error on the model variables as well as variables diagnosed from the model state have positive error variances. If errors are really random and span the whole state vector space, the covariance matrix are strictly positive.

The analysis step (22.17) can be expressed as

$$\mathbf{x}^t + \boldsymbol{\epsilon}^a = \mathbf{x}^t + \boldsymbol{\epsilon}^f + \mathbf{K}\left(\boldsymbol{\epsilon}^o - \mathbf{H}\boldsymbol{\epsilon}^f\right) \;+\; \mathbf{K}\underbrace{\left(\mathbf{y}^t - \mathbf{H}\mathbf{x}^t\right)}_{=0} \tag{22.22}$$

The last term is zero because for a perfect model, the forecast diagnosed through the observation operator $\mathbf{H}$, also called observed part $\mathbf{H}\mathbf{x}$ of the state vector, must correspond to the observed true field. Hence the error of the analysis reads

$$\boldsymbol{\epsilon}^a = \boldsymbol{\epsilon}^f \;+\; \mathbf{K}\left(\boldsymbol{\epsilon}^o - \mathbf{H}\boldsymbol{\epsilon}^f\right) \tag{22.23}$$

We can then construct the error covariance $\left\langle \boldsymbol{\epsilon}^a {\boldsymbol{\epsilon}^a}^\mathsf{T} \right\rangle$ of the analysis by multiplying (22.23) by its transposed and take the statistical average or expectation

$$\begin{aligned}\left\langle \boldsymbol{\epsilon}^a {\boldsymbol{\epsilon}^a}^\mathsf{T} \right\rangle &= \left\langle \boldsymbol{\epsilon}^f {\boldsymbol{\epsilon}^f}^\mathsf{T} \right\rangle + \mathbf{K}\left\langle (\boldsymbol{\epsilon}^o - \mathbf{H}\boldsymbol{\epsilon}^f){\boldsymbol{\epsilon}^f}^\mathsf{T} \right\rangle + \left\langle \boldsymbol{\epsilon}^f ({\boldsymbol{\epsilon}^o}^\mathsf{T} - {\boldsymbol{\epsilon}^f}^\mathsf{T}\mathbf{H}^\mathsf{T}) \right\rangle \mathbf{K}^\mathsf{T} \\ &+ \mathbf{K}\left\langle (\boldsymbol{\epsilon}^o - \mathbf{H}\boldsymbol{\epsilon}^f)({\boldsymbol{\epsilon}^o}^\mathsf{T} - {\boldsymbol{\epsilon}^f}^\mathsf{T}\mathbf{H}^\mathsf{T}) \right\rangle \mathbf{K}^\mathsf{T}\end{aligned} \tag{22.24}$$

defining covariance matrixes

$$\mathbf{P} = \left\langle \boldsymbol{\epsilon}\boldsymbol{\epsilon}^\mathsf{T} \right\rangle \tag{22.25}$$

with $\mathbf{P}^f$ and $\mathbf{P}^a$ forecasted and analyzed version of the error covariance, *i.e.*, where $\boldsymbol{\epsilon}$ is the error of the forecast and the analysis, we can expand the expressions and assume that observational errors and model errors are not correlated, $\left\langle \boldsymbol{\epsilon}^o \boldsymbol{\epsilon}^\mathsf{T} \right\rangle = 0$. Such a decorrelation of observational error and modeling error is justified by the very different origin of the information. The error-covariance matrix after analysis can then be written as

$$\begin{aligned}\mathbf{P}^a &= \mathbf{P}^f - \mathbf{K}\mathbf{H}\mathbf{P}^f - \mathbf{P}^f\mathbf{H}^\mathsf{T}\mathbf{K}^\mathsf{T} + \mathbf{K}\left(\mathbf{R} + \mathbf{H}\mathbf{P}^f\mathbf{H}^\mathsf{T}\right)\mathbf{K}^\mathsf{T} \\ &= \mathbf{P}^f - \mathbf{P}^f\mathbf{H}^\mathsf{T}\mathbf{A}^{-1}\mathbf{H}\mathbf{P}^f \;+\; \left(\mathbf{P}^f\mathbf{H}^\mathsf{T} - \mathbf{K}\mathbf{A}\right)\mathbf{A}^{-1}\left(\mathbf{H}\mathbf{P}^f - \mathbf{A}\mathbf{K}^\mathsf{T}\right)\end{aligned} \tag{22.26}$$

where we define matrix

$$\mathbf{A} = \mathbf{H}\mathbf{P}^f\mathbf{H}^\mathsf{T} + \mathbf{R} \tag{22.27}$$

which is symmetric and we suppose can be inverted [4].

[4]Because $\mathbf{P}$ and $\mathbf{R}$ are semi-positive defined matrixes chances are not bad. In addition, when observations and state variables are covering a spatial domain, the covariances between distant points are generally small compared to pairs of points that are closer, so that the matrixes will have a tendency to be diagonally dominant.

If state variables are properly scaled (to be able to compare errors in temperature with errors in velocity [5]), the overall error ϵ^a of the analysis or the forecast field can be taken as the expected norm of the error vector:

$$\epsilon^a = \left\langle \boldsymbol{\epsilon}^{a\mathsf{T}} \boldsymbol{\epsilon}^a \right\rangle . \tag{22.28}$$

This is however nothing else than the trace of the covariance matrix $\left\langle \boldsymbol{\epsilon}^a \boldsymbol{\epsilon}^{a\mathsf{T}} \right\rangle$ and a global measure of the analysis error is thus

$$\epsilon^a = \mathrm{trace}\left(\mathbf{P}^a\right). \tag{22.29}$$

Since the matrix $\mathbf{K}$, which is an $M \times P$ matrix, is yet unspecified, a clever choice would be to determine the matrix $\mathbf{K}$ that minimizes the global error. We could take the trace of (22.26) and explicitly derive the trace with respect to all components of $\mathbf{K}$ in order to find the stationary value of the global error. Because (22.26) is a quadratic form in terms of $\mathbf{K}$ and because $\mathbf{A}^{-1}$ is positive defined if it exists, the extremum is then a minimum. Alternatively, we can think about the error as being a function $\epsilon^a(\mathbf{K})$ of the gain matrix $\mathbf{K}$ and search an optimal $\mathbf{K}$ for which

$$\epsilon^a(\mathbf{K} + \mathbf{L}) - \epsilon^a(\mathbf{K}) = 0 \tag{22.30}$$

for any small departure matrix $\mathbf{L}$. We require thus

$$\mathrm{trace}\left(-\mathbf{L}\left(\mathbf{H}\mathbf{P}^f - \mathbf{A}\mathbf{K}^\mathsf{T}\right) - \left(\mathbf{P}^f\mathbf{H}^\mathsf{T} - \mathbf{K}\mathbf{A}\right)\mathbf{L}^\mathsf{T}\right) = 0, \tag{22.31}$$

where we neglected quadratic terms in $\mathbf{L}$. The two terms are the transposed of each other and since the trace of the matrix and its transposed are identical, we must request

$$\mathrm{trace}\left(\left(\mathbf{P}^f\mathbf{H}^\mathsf{T} - \mathbf{K}\mathbf{A}\right)\mathbf{L}^\mathsf{T}\right) = 0.$$

Since $\mathbf{L}$ is arbitrary, the optimal solution with minimum error is obtained when

$$\mathbf{K} = \mathbf{P}^f\mathbf{H}^\mathsf{T}\mathbf{A}^{-1} = \mathbf{P}^f\mathbf{H}^\mathsf{T}\left(\mathbf{H}\mathbf{P}^f\mathbf{H}^\mathsf{T} + \mathbf{R}\right)^{-1} \tag{22.32}$$

and we see that in order to find the optimal solution, matrix $\mathbf{A}$ must indeed be invertible. The Kalman gain, which combines linearly model forecasts with data is then the analogue of (22.13). The error covariance of the analysis is obtained by injecting (22.32) into (22.26)

$$\mathbf{P}^a = (\mathbf{I} - \mathbf{K}\mathbf{H})\,\mathbf{P}^f = \left(\mathbf{I} - \mathbf{P}^f\mathbf{H}^\mathsf{T}\left(\mathbf{H}\mathbf{P}^f\mathbf{H}^\mathsf{T} + \mathbf{R}\right)^{-1}\mathbf{H}\right)\mathbf{P}^f \tag{22.33}$$

which is the analogue of (22.14). Note that both the Kalman gain matrix and the error covariance after the analysis do not depend on the *value* of the observations or the forecasted state vector but only their statistical error covariances. The only field that depends on the actual values is of course the state vector itself:

$$\mathbf{x}^a = \mathbf{x}^f + \mathbf{P}^f\mathbf{H}^\mathsf{T}\left(\mathbf{H}\mathbf{P}^f\mathbf{H}^\mathsf{T} + \mathbf{R}\right)^{-1}\left(\mathbf{y} - \mathbf{H}\mathbf{x}^f\right). \tag{22.34}$$

[5] It is interesting to note that the optimal analysis itself is independent of the chosen norm as long as no simplifications are introduced into the procedure (*e.g.,* Kalnay??).

The use of (22.32) in (22.17) to combine the forecast and observation with prescribed error covariance $\mathbf{P}^f$ and $\mathbf{R}$ is known as *optimal interpolation* (OI).

When those covariances are given, an alternative derivation of optimal interpolation can be presented by a variational approach called *3D-Var*, in which we try to find the state vector that minimizes the error measure J given by

$$J(\mathbf{x}) = \frac{1}{2}(\mathbf{x} - \mathbf{x}^f)^{\mathsf{T}} \mathbf{P}^{f\,-1}(\mathbf{x} - \mathbf{x}^f) \; + \; \frac{1}{2}(\mathbf{H}\mathbf{x} - \mathbf{y})^{\mathsf{T}} \mathbf{R}^{-1}(\mathbf{H}\mathbf{x} - \mathbf{y}) \tag{22.35}$$

in other words, we search for the state vector close to the model forecast and the observation, penalizing less the more accurate information, in close analogy with (22.16). Solving this minimization problem, a variational problem, hence the name 3D-Var if the physical problem is three-dimensional, leads to the same analyzed field as in (22.34), the demonstration of which is left as an exercise (22-3). It can also be shown that the error covariance matrix (22.33) can be retrieved by calculating the Hessian matrix, *i.e.*, the second derivatives of J with respect to the state vector components at the minimum of J.

Optimal interpolation can also be introduced in terms of the maximum likelihood estimator of the true field, *i.e.*, the field which has the highest probability to match reality, which is also given by (22.34) if *probability density functions* (pdf) of the errors are Gaussian.

22.4 Kalman filtering

A distinct feature of the optimal interpolation is the fact that except through the forecast-error covariance matrix, the dynamical model properties are never used in the analysis step. In reality, the error covariance is depending on the history of the flow and a local initial error in tracer values is for example transported in preferential directions (along the varying flow) or amplified by unstable modes. We therefore now take into account the fact that between assimilation cycle n and $n+1$ the dynamical model advances the state vector in time according to

$$\mathbf{x}_{n+1} = \boldsymbol{\mathcal{M}}(\mathbf{x}_n) + \mathbf{f}_n \; + \boldsymbol{\eta}_n \tag{22.36}$$

where $\boldsymbol{\eta}_n$ takes into account errors introduced by the model and $\mathbf{f}_n$ includes the external forcings. $\boldsymbol{\mathcal{M}}$ is the model or machinery that allows to step forward in time the state vector between assimilation cycles and includes thus any inversion for implicit models and several time steps when intermittent assimilation is performed. Assuming the simulation cycle between the two analysis was started with the analysis of the previous assimilation and assuming a linearized model we have

$$\mathbf{x}^f_{n+1} = \mathbf{M}\,\mathbf{x}^a_n + \mathbf{f}_n \; + \boldsymbol{\eta}_n \tag{22.37}$$

where we use now a matrix $\mathbf{M}$ instead of the nonlinear operator $\boldsymbol{\mathcal{M}}$ of (22.36). Such a matrix is actually never formed except for didactical purposes but allows to formalize the method more elegantly. The true state evolves without modeling errors and obeys

$$\mathbf{x}^t_{n+1} = \mathbf{M}\,\mathbf{x}^t_n + \mathbf{f}_n \tag{22.38}$$

so that the forecast error $\boldsymbol{\epsilon}^f = \mathbf{x}^f - \mathbf{x}^t$ satisfies

$$\boldsymbol{\epsilon}^f_{n+1} = \mathbf{M}\,\boldsymbol{\epsilon}^a_n + \boldsymbol{\eta}_n. \tag{22.39}$$

Multiplying this equation by its transposed to the right and using the statistical average we get the so-called Lyapunov equation that allow to advance in time the error-covariance matrix:

$$\mathsf{P}^f_{n+1} = \mathsf{M}\mathsf{P}^a_n\mathsf{M}^\mathsf{T} \ + \ \mathsf{Q}_n = \mathsf{M}(\mathsf{M}\mathsf{P}^a_n)^\mathsf{T} \ + \ \mathsf{Q}_n \tag{22.40}$$

in function of the model-error covariance matrix

$$\mathsf{Q}_n = \left\langle \boldsymbol{\eta}_n \boldsymbol{\eta}_n^\mathsf{T} \right\rangle. \tag{22.41}$$

We assumed as usual errors of different origins to be uncorrelated. Since the forcing f disappears from the error evolution, we will not keep it during later developments. Note that the error-covariance matrix can be calculated by using the model evolution on each column c of P^a as shown by the operations Mc involved. To start the calculation of the error evolution we need to know the initial value of P which is related to the error on initial conditions:

$$\mathsf{P}_0 = \left\langle (\mathbf{x}_0 - \mathbf{x}_0^t)(\mathbf{x}_0 - \mathbf{x}_0^t)^\mathsf{T} \right\rangle. \tag{22.42}$$

Now we have a method to calculate the evolution of the error-covariance in time and the Kalman filter assimilation is summarized in Figure 22-6, including an extension towards a nonlinear model with linearized error propagation (Extended Kalman Filter, EKF). The analysis step itself is unchanged compared to optimal interpolation, only the error-covariance is updated.

Two extremes are noteworthy: In the case the time between two assimilations is very short compared to the time scale of evolution of the process being modeled, the state-variable as well as the error fields are almost unchanged and the model can be considered as persistence ($\mathsf{M} \sim \mathsf{I}$). In this case

$$\mathsf{P}^f_{n+1} \sim \mathsf{P}^a_n + \mathsf{Q}_n, \tag{22.43}$$

in other words, the errors of the forecast are the errors of the previous analysis, without any advection or other modification, augmented by the model error introduced by the simulation between the assimilations. The last error will be relatively small for a well constructed model because the time integration is short compared to the time scales of interest.

On the other extreme, when assimilation takes place only after very long periods, nonlinear models may have reached their limit of predictability. In this case, model forecasts are basically random and the forecast is a pure modeling error. Mathematically this amounts to state $\mathsf{M} \sim 0$ and hence

$$\mathsf{P}^f_{n+1} \sim \mathsf{Q}_n, \tag{22.44}$$

meaning that the error field has no trace anymore of the previous error fields (coherent with the trepassing of the limit of predictability) but is purely due to the simulation itself. Obviously, Q_n is in this case much larger than in the other extreme case (22.43) because of the long time integration and error explosions inherent with the predictability limit of the nonlinear system. If the system is almost random after such a too long integration, Q_n will be close to a diagonal matrix, the errors in different locations being not related.

To illustrate the structure of the Kalman filtering in the general case, we first note that for the analysis step the error covariance matrix only appears in the combination $\mathsf{P}^f\mathsf{H}^\mathsf{T}$

$$\mathsf{P}^f\mathsf{H}^\mathsf{T} = \left\langle \boldsymbol{\epsilon}^f {\boldsymbol{\epsilon}^f}^\mathsf{T} \right\rangle \mathsf{H}^\mathsf{T} = \left\langle \left(\mathbf{x}^f - \mathbf{x}^t\right)\left(\mathsf{H}\mathbf{x}^f - \mathsf{H}\mathbf{x}^t\right)^\mathsf{T} \right\rangle \tag{22.45}$$

Initialization:

$$\mathbf{x}_0^a = \mathbf{x}$$
$$\mathbf{P}_0^a = \mathbf{P}$$

Forecast:

$$\mathbf{x}_{n+1}^f = \mathcal{M}(\mathbf{x}_n^a)$$
$$\mathbf{P}_{n+1}^f = \mathbf{M}_n \mathbf{P}_n^a {\mathbf{M}_n}^\mathsf{T} + \mathbf{Q}_n$$

Analysis:

$$\mathbf{x}_{n+1}^a = \mathbf{x}_{n+1}^f + \mathbf{K}_{n+1}\left(\mathbf{y}_{n+1} - \mathbf{H}_{n+1}\mathbf{x}_{n+1}^f\right)$$
$$\mathbf{K}_{n+1} = \mathbf{P}_{n+1}^f \mathbf{H}_{n+1}^\mathsf{T}\left(\mathbf{H}_{n+1}\mathbf{P}_{n+1}^f\mathbf{H}_{n+1}^\mathsf{T} + \mathbf{R}_{n+1}\right)^{-1}$$
$$\mathbf{P}_{n+1}^a = \mathbf{P}_{n+1}^f - \mathbf{K}_{n+1}\mathbf{H}_{n+1}\mathbf{P}_{n+1}^f$$

Figure 22-6 Extended Kalman Filter assimilation scheme with changing observation network (changing $\mathbf{H}$), nonlinear model forecasts ($\mathcal{M}$) and model linearization between assimilation cycles for the error forecast.)

which is the covariance between the observed quantities and all others. Because it is the matrix that finally multiplies a vector of the size of the data, it allows to propagate information from the data locations into the model grid. We also have

$$\begin{aligned} \mathbf{A} &= \mathbf{H}\mathbf{P}^f\mathbf{H}^\mathsf{T} + \mathbf{R} = \left\langle \left(\mathbf{H}\mathbf{x}^f - \mathbf{H}\mathbf{x}^t\right)\left(\mathbf{H}\mathbf{x}^f - \mathbf{H}\mathbf{x}^t\right)^\mathsf{T} \right\rangle + \mathbf{R} \\ &= \left\langle \left(\mathbf{H}\mathbf{x}^f - \mathbf{y}\right)\left(\mathbf{H}\mathbf{x}^f - \mathbf{y}\right)^\mathsf{T} \right\rangle \end{aligned} \tag{22.46}$$

which is easily interpreted in terms of error variance of the forecast in the observed part, combined with the corresponding observational errors, reminiscent of $\langle \epsilon_1^2 \rangle + \langle \epsilon_2^2 \rangle$ in (22.13). Is also shows that $\mathbf{A}^{-1}$ exists depending on the statistics on the innovation vector $\mathbf{H}\mathbf{x}^f - \mathbf{y}$. Should a component of this innvovation vector always be zero, and hence $\mathbf{A}$ be singular, it means the corresponding model part never needs a correction and should be excluded from the analysis procedure. Also note that the Kalman gain matrix is indeed giving weights to the observations the more precise they are and then transmits this signal to other locations.

In particular for the assimilation of a single observation on the k_{th} component of the state vector $\mathbf{x}$:

- $\mathbf{P}^f\mathbf{H}^\mathsf{T}$ is a $M \times 1$ matrix whose components are P^f_{ik} , $i = 1, ..., M$ and is thus responsible for transferring the innovation learned from observation in location k to the other components of the state vector. The covariance matrix appears thus as the matrix allowing to correct fields using remote signals. The structure of the covariance depends on the problem at hand (Figure 22-7).
- $\left(\mathbf{H}\mathbf{P}^f\mathbf{H}^\mathsf{T} + \mathbf{R}\right)^{-1}$ reduces to a scalar value $(P^f_{kk} + \epsilon_0^2)^{-1}$ where ϵ is the variance of the observational error and P^f_{kk} the forecast error covariance at the same location.

The error covariance matrix allows thus the propagation of information from the data location into other parts and on other state variables taking into account the relative error of observations and models. Observation of temperature profiles might well serve to change wind velocity fields in remote locations or sea surface height measurements by altimetry may well be used to correct density fields in deeper layers. Therefore satellite data are very valuable in ocean forecasts because of the difficulty to maintain fixed observing station in the sea or to perform regular cruises to sample the ocean interior, contrary to the atmosphere, with is large network of observing systems and profile sounding with ballons. For the ocean it is then critical to transmit those surface data to correct density fields and currents in the interior of the ocean.

Because of our optimisation of errors, using linear combinations and the hypotheses of zero bias, the full Kalman filter is called a *Best Linear Unbiased Estimation* (BLUE) of the true state. Therefore the other linear methods presented up to now must be suboptimal. It is interesting to note that the Kalman filter approach indeed encompasses the other assimilation methods. If we prescribe *a priori* the forecast error covariance in the Kalman filter instead of calculating it with the model, we downgrade the Kalman filter to an optimal interpolation. If the prescribed error covariance and observational error covariance matrix are furthermore diagonal, it is easy to verify, by introducing a time discretization on (22.4), that we retrieve the nudging scheme in which assimilation is performed during each time-step. Finally, when the nudging time scale is decreased towards zero, the direct insertion method is recover. In

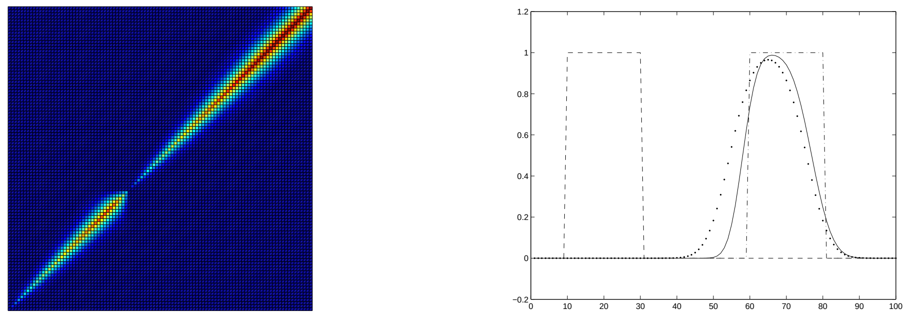

Figure 22-7 Error covariance matrix (left panel) at the end of the simulation and advected signal (right panel) with wrong velocity and upwind diffusion. Data point are provided in $i = 40$ every time step. The assimilation (full curve) corrects some of the model errors (dotted curve for model without assimilation). The covariance matrix is highest on the diagonal and points downwind of the data point have a lower error variance because of the observations with low errors permanently reducing errors. `.m` for details on implementation.

all cases, the term filter method is appropriate because only past data are used to infer the local field estimate.

22.5 Inverse methods

The Kalman filter operation depends only on past information which is sensible for operational purposes. In addition it does not need the assumption the dynamic model to be perfect. The reinitialization cycle optimized with the Kalman filter has however a major drawback in terms of model simulation now analyzed over long time periods: the simulated trajectories are not continuous[6] anymore, but exhibit finite jumps at each assimilation instant (Figure 22-8). In addition, if such jumps are dynamically unbalanced because of inadequate covariance models, unphysical shocks can occur in the model. For some applications, it would be desirable to obtain a state estimation which inherits the continuity properties of the physical system (Figure 22-9).

Since we are concerned by obtaining a continuous model trajectory, we will assume the dynamical model itself to be perfect and only allow errors due to incorrect forcing, initial conditions and possibly incorrect model parameters such as the value of a constant eddy viscosity. Those errors are thus considered responsible for model trajectories not corresponding to reality. The idea we will now follow is to optimize those parameters so that the model trajectory is as close as possible to the observations over a long time period. The state at any moment is then influenced by data prior to this moment but also beyond because all data are taken into account to construct the optimal trajectory. Such a method working with data over an interval is called a *smoother* and useful for reanalysis of past observations.

Mathematically our goal is the minimization of trajectory-data misfit over a time-interval with N data-sets $\mathbf{y}_n$. Here we will search for an optimal initial condition $\mathbf{x}_0$. The name

[6] in the limit of considering the real model time steps sufficiently small.

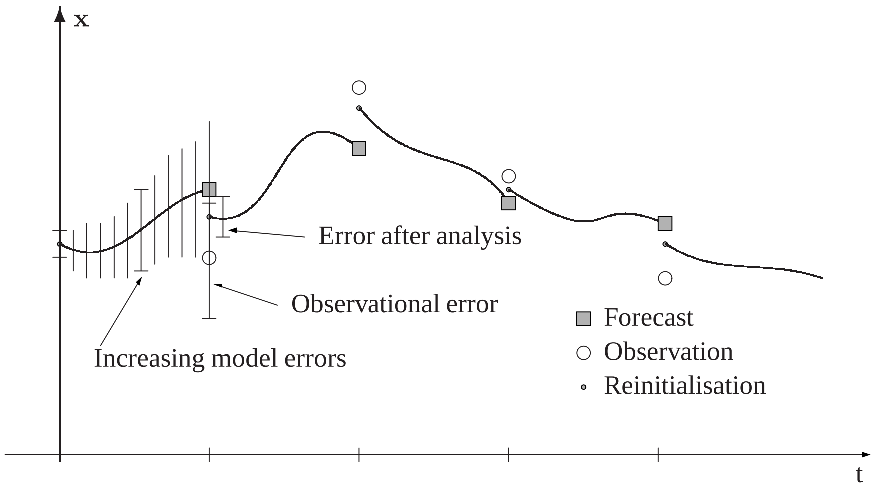

Figure 22-8 The Kalman filter approach leads to a model trajectory that is interrupted at each assimilation cycle but reduces the error during the reinitialization.

inverse model is readily understood in opposition to the standard model which starts from initial conditions and calculates the model evolution in time. Here we try to infer initial conditions from observations of the actual solution by minimizing a so called *cost function*:

$$J = \sum_{n=0}^{N-1} \frac{1}{2} (\mathsf{H}_n \mathbf{x}_n - \mathbf{y}_n)^{\mathsf{T}} \mathsf{R}_n^{-1} (\mathsf{H}_n \mathbf{x}_n - \mathbf{y}_n) + J_b \tag{22.47}$$

We added a term J_b that might be useful if we want to avoid the initial condition $\mathbf{x}_0$ to part too much from a background field $\mathbf{x}_0^b$

$$J_b = \frac{1}{2} (\mathbf{x}_0 - \mathbf{x}_0^b)^{\mathsf{T}} \mathsf{P}_0^{-1} (\mathbf{x}_0 - \mathbf{x}_0^b) \tag{22.48}$$

Such a background state $\mathbf{x}_0^b$ on the initial condition can be provided for example from previous forecasts or climatology. In addition to the minimization of the cost function J, we need to enforce the constraint that the solution $\mathbf{x}$ is a model trajectory and therefore satisfies

$$\mathbf{x}_{n+1} = \boldsymbol{\mathcal{M}}(\mathbf{x}_n) \tag{22.49}$$

For simplicity, we use again the linearized version

$$\mathbf{x}_{n+1} = \mathsf{M}_n \, \mathbf{x}_n \tag{22.50}$$

that our trajectory $\mathbf{x}_n$, $n = 0, ..., N-1$ must satisfy. An elegant way to ensure this constraint is adding so-called Lagrange multipliers $\boldsymbol{\lambda}_n$ to the unknowns of the problem and form the

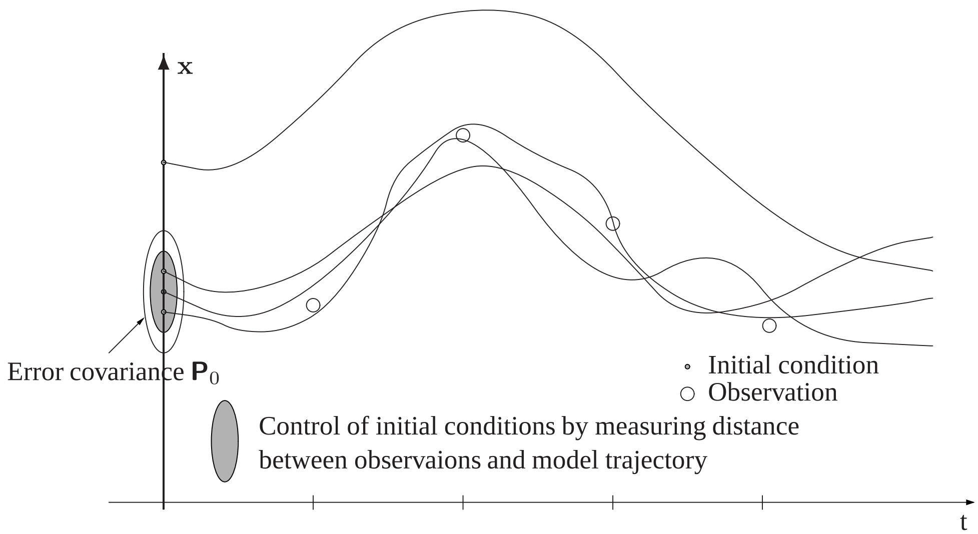

Figure 22-9 The adjoint approach selects the model trajectory that fits best the observations over a given time interval. The initial conditions are drawn with a probability density function centered around a background state $\mathbf{x}_0^b$.

following expression

$$\begin{aligned} J &= \sum_{n=0}^{N-1} \frac{1}{2}(\mathsf{H}_n\mathbf{x}_n - \mathbf{y}_n)^\mathsf{T}\mathsf{R}_n^{-1}(\mathsf{H}_n\mathbf{x}_n - \mathbf{y}_n) \\ &+ \sum_{n=0}^{N-1} \boldsymbol{\lambda}_n^\mathsf{T}\,(\mathbf{x}_{n+1} - \mathsf{M}_n\,\mathbf{x}_n) \\ &+ \frac{1}{2}(\mathbf{x}_0 - \mathbf{x}_0^b)^\mathsf{T}\mathsf{P}_0^{-1}(\mathbf{x}_0 - \mathbf{x}_0^b) \end{aligned} \tag{22.51}$$

The minimum of the original cost function (22.47) with the constraints (22.50) is obtained when (22.51) is stationary, *i.e.*, derivatives with respect to Lagrange multipliers and control parameters are zero. This forms another variational problem, called *4D-Var*. Note that we took the initial observations into account in the cost function but not at the final simulation result $\mathbf{x}_N$, which can thus be regarded as the forecast based on a trajectory that is close to the N previous observation sets

The stationarity condition of (22.51) with respect to changes in Lagrange multipliers $\boldsymbol{\lambda}$ directly provides the model constraint (22.50) for $n = 0..., N-1$.

Variation with respect to the initial state $\mathbf{x}_0$ leads to

$$\nabla_{x_0} J = \mathsf{P}_0^{-1}(\mathbf{x}_0 - \mathbf{x}_0^b) + \mathsf{H}_0^\mathsf{T}\mathsf{R}_0^{-1}(\mathsf{H}_0\mathbf{x}_0 - \mathbf{y}_0) - \mathsf{M}_0^\mathsf{T}\boldsymbol{\lambda}_0 \tag{22.52}$$

which must be zero for the optimal solution.

Variations of (22.51) with respect to any intermediate state $\mathbf{x}_m$ must also be zero. Realizing that $\mathbf{x}_m$ appears in the sum for $n = m$ and $n = m-1$, we obtain the following condition in which we rechristened m back to n:

$$\mathsf{H}_n^\mathsf{T}\mathsf{R}_n^{-1}(\mathsf{H}_n\mathbf{x}_n - \mathbf{y}_n) - \mathsf{M}_n^\mathsf{T}\boldsymbol{\lambda}_n + \boldsymbol{\lambda}_{n-1} = 0 \tag{22.53}$$

for $n = 1, ..., N-1$. Finally, variation with respect to final state $\mathbf{x}_N$ directly provides $\boldsymbol{\lambda}_{N-1} = 0$.

The different conditions can be recasted into the following algorithm. We start with an estimate $\mathbf{x}_0$ of the initial condition and then perform the following operations

$$\mathbf{x}_{n+1} = \mathsf{M}_n\,\mathbf{x}_n, \qquad n = 0, ..., N-1 \tag{22.54a}$$

$$\boldsymbol{\lambda}_{N-1} = 0 \tag{22.54b}$$

$$\boldsymbol{\lambda}_{n-1} = \mathsf{M}_n^\mathsf{T}\boldsymbol{\lambda}_n - \mathsf{H}_n^\mathsf{T}\mathsf{R}_n^{-1}(\mathsf{H}_n\mathbf{x}_n - \mathbf{y}_n), \qquad n = N-1, ..., 1 \tag{22.54c}$$

We note that model-data misfits are basically driving the values of the Lagrange multipliers. All stationary conditions on (22.51) are now satisfied except that $\nabla_{x_0} J$ given by (22.52) is not yet zero. The recurrence (22.54c) on the Lagrange multiplier can formally be extended to $n = 0$ so that $\boldsymbol{\lambda}_{-1}$ takes the value of $-\nabla_{x_0} J$ if no background field is used ($\mathsf{P}_0^{-1} = 0$). But because we have now access to a value of J and its gradient with respect to the variables on which we optimize our solution, the initial condition, we can use any mathematical minimization tool that searches for such minima using gradients. The steepest descent or the more efficient *conjugate gradient* method (REFERENCE) are iterative methods which create a succession of states (here for $\mathbf{x}_0$) that decrease the value of the cost function J depending on the gradient of the function. We therefore have now a relatively simple way to calculate those gradients by performing a forward integration of the model, called direct model, and a backward integration to evaluate the Lagrange multipliers and finally the gradients (Figure 22-10). The apparently simple recipe hides several practical problems. The equation for the Lagrange multipliers is very similar to the direct model equations with the innocent looking difference that instead of matrix M its transposed appears and instead of applying M, we apply its adjoint to $\boldsymbol{\lambda}_n$ to create the time series. Therefore we speak about the *adjoint model* when referring to the backward integration for the Lagrange multipliers. In practise, since a numerical model never explicitly creates the matrix M, it means that a programming of an adjoint model is necessary, whose action on $\boldsymbol{\lambda}$ is equivalent to applying the transposed model matrix. Another practical problem for time-varying models is the need to store or permanently recreate model results over the full simulation interval because of the backward integration. For more details on implementation aspects we refer to REFERENCE, including methods of *preconditionning* ensuring faster convergence of the minimization process.

To present the method, we worked on a discrete model version even if our purpose was to construct continuous trajectories. In fine, a discrete solution is anyway thought and the adjoint method we developed is the adjoint of the discrete direct model, itself continuous in the sense that there are no jumps at the assimilation points. We could have worked with continuous time derivatives instead, but then we need to discretize the associated continuous adjoint model, which will generally not be the adjoint of the discrete direct model, reminiscent of Figure 2-15. The method is readily extended to optimizations of parameter values such as lateral viscosity and boundary conditions. Parameters to be optimized can for example be introduced as an addition state variable into the state vector, with an evolution equation of persistence. In all cases it must however be kept in mind that any inversion is only valid if the direct model itself is able to simulate correct trajectories. In other words, when a

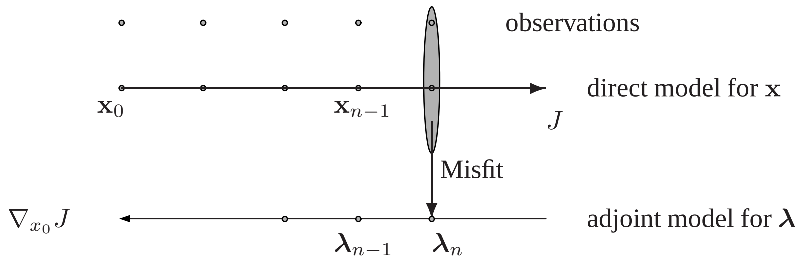

Figure 22-10 The forward integration starts from an initial guess on the control parameters and then provides the state variable over the simulation window. Misfits between observations and model trajectories are stored and error norms in cost function J defined by (22.35) accumulated. Then the adjoint model is integrated backward in time, forced by the misfits. When arriving in $n = 0$ the gradient (22.52) can be calculated. If it is not zero, the optimum is not reached and an improved guess on the control parameters can be calculated by minimization tools using the cost function value J and its gradient with respect to the control parameters.

grossly inadequate model is used with an inverse model to calibrate parameters allowing a reasonable trajectory, parameters obtained by such an inversion have no real physical meaning anymore but are just *ad hoc* values. It might be therefore adequate to relax the hypothesis of a dynamically correct model and allow for errors as in the Kalman filter.

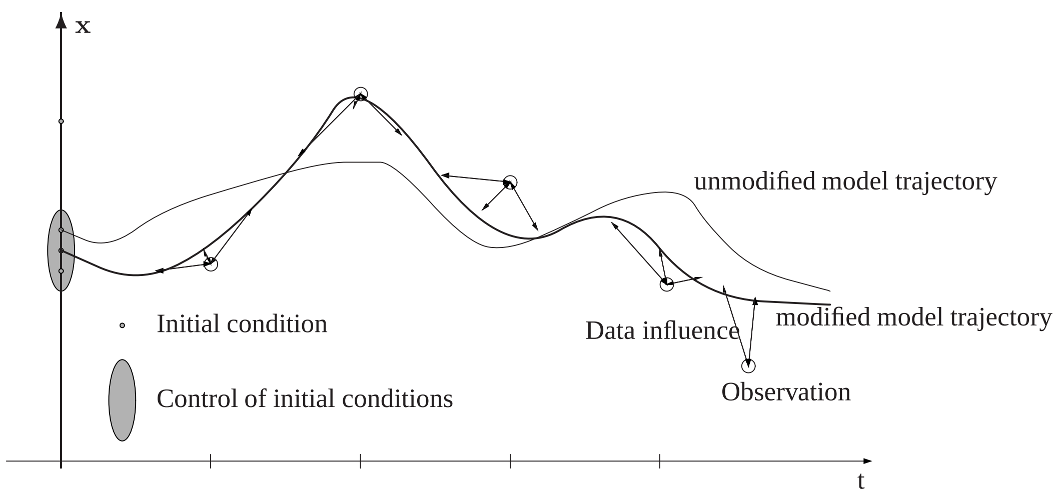

Figure 22-11 Generalized inverse methods allow both to optimize initial conditions and allow the model to depart from a model trajectory to be closer to observations.

Allowing the model solution to part from a model trajectory is achieved by replacing the strong constraint (22.50) by a so-called *weak constraint*, penalizing only too strong departures from (22.50), with penalisation strongest for models which are trustworthy. We can therefore adapt the cost function of the inverse model to form a generalized inverse model by minimizing

$$\begin{aligned} J &= \sum_{n=0}^{N-1} \frac{1}{2}(\mathbf{H}_n \mathbf{x}_n - \mathbf{y}_n)^{\mathsf{T}} \mathbf{R}_n^{-1} (\mathbf{H}_n \mathbf{x}_n - \mathbf{y}_n) \\ &+ \sum_{n=0}^{N-1} \frac{1}{2}(\mathbf{x}_{n+1} - \mathbf{M}_n \mathbf{x}_n)^{\mathsf{T}} \mathbf{Q}_n^{-1} (\mathbf{x}_{n+1} - \mathbf{M}_n \mathbf{x}_n) \\ &+ \frac{1}{2}(\mathbf{x}_0 - \mathbf{x}_0^b)^{\mathsf{T}} \mathbf{P}_0^{-1} (\mathbf{x}_0 - \mathbf{x}_0^b) \end{aligned} \tag{22.55}$$

where $\mathbf{Q}$ is the error-covariance of the model. Derivation with respect to the initial condition provides

$$\nabla_{x_0} J = \mathbf{P}_0^{-1}(\mathbf{x}_0 - \mathbf{x}_0^b) + \mathbf{H}_0^{\mathsf{T}} \mathbf{R}_0^{-1} (\mathbf{H}_0 \mathbf{x}_0 - \mathbf{y}_0) - \mathbf{M}_0^{\mathsf{T}} \mathbf{Q}_0^{-1} (\mathbf{x}_1 - \mathbf{M}_0 \mathbf{x}_0) \tag{22.56}$$

while derivation with respect to intermediate states ($n = 1, .., N-1$) lead to conditions

$$\begin{aligned} \mathbf{H}_n^{\mathsf{T}} \mathbf{R}_n^{-1} (\mathbf{H}_n \mathbf{x}_n - \mathbf{y}_n) &- \\ \mathbf{M}_n^{\mathsf{T}} \mathbf{Q}_n^{-1} (\mathbf{x}_{n+1} - \mathbf{M}_n \mathbf{x}_n) &+ \mathbf{Q}_{n-1}^{-1} (\mathbf{x}_n - \mathbf{M}_{n-1} \mathbf{x}_{n-1}) = 0 \end{aligned} \tag{22.57}$$

and derivation with respect to the final state provides $\mathbf{x}_N = \mathbf{M}_{N-1} \mathbf{x}_{N-1}$. This system of equations can be written in a more familiar way

$$\mathbf{x}_n = \mathbf{M}_{n-1} \mathbf{x}_{n-1} + \mathbf{Q}_{n-1} \boldsymbol{\lambda}_{n-1}, \qquad n = 1, ..., N \tag{22.58a}$$

$$\boldsymbol{\lambda}_{N-1} = 0 \tag{22.58b}$$

$$\boldsymbol{\lambda}_{n-1} = \mathbf{M}_n^{\mathsf{T}} \boldsymbol{\lambda}_n - \mathbf{H}_n^{\mathsf{T}} \mathbf{R}_n^{-1} (\mathbf{H}_n \mathbf{x}_n - \mathbf{y}_n) \qquad n = N-1, ..., 1 \tag{22.58c}$$

with the need for gradient (22.56) to be zero. These equations are very similar to those of the adjoint method (22.54) with the additional term involving $\mathbf{Q}$ in the direct model allowing the propagation of model errors. Though similar, the practical solution is more complicated than for the adjoint method and can be obtained with the so-called *representer method* (Bennett 1992). The generalized inverse method exhibits thus a continuous solution, which is not solution of the direct model but whose distance to observations and a real trajectory is minimal (Figure 22-11).

The variational approaches are attractive since they allow efficient model calibrations, but error-covariances on observations and the model need to be prescribed *a priori*. More importantly, except for the value of the cost function, the analysis is not yet accompanied by error estimates of the final analysis, as those found for the Kalman filter (22.33). It is possible to obtain such estimates also for the variational methods using the second derivative of the cost function with respect to the control parameters to form the Hessian matrix. Intuitively, if the cost function is decreasing sharply and has a deep well, the optimum is much better constrained than for a flat cost function (Figure 22-12). The Hessian matrix allows then the calculation of the error covariance, a property demonstrated in REFERENCE.

Another way to obtain smooth trajectories with error estimates is to generalize the Kalman filter to include not only past values but also future ones. The so-called *Kalman smoother* does so and can be shown to provide identical results to the generalized inverse approach over the whole simulation window for linear systems.

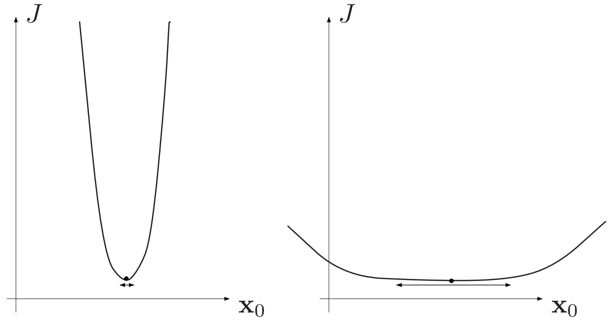

Figure 22-12 When the Hessian matrix of J is large, the minimum is well constrained and errors on the final state small (left panel). Errors on the optimal solution will be larger if the cost function has a wide range over which the initial condition can vary without penalizing the value of J (right panel).

Similarly it can be shown that the standard 4D-Var method and Kalman filter are equivalent for a perfect model with identical data over a given time interval and initial error covariance in the sense that they lead to the same final analysis for linear models and linear observation operators.

Though equivalences are demonstrated in some cases, the methods loose their connections when the underlying hypotheses such as linear models and unbiased information are violated. The methods will then provide different solutions. Also the practical implementations are quite different an can lead to very different algorithmic performances with different levels of additional simplifications.

22.6 Operational models

Practical implementations of the described data assimilation methods are a concern if we look at typical numbers of operations to be performed.

The nudging method barely adds a linear term to existing equations and the overhead cost associated with the assimilation is generally negligible.

For optimal interpolation in its original form, we need at least to invert a matrix whose size is proportional to the number of observations, assuming the covariance matrix P or better HP can be calculated easily. Since matrix H is generally mostly composed by zeros, we neglect costs associated with multiplications by H since the operation consist in extracting some model parameters from the state vector rather than a real matrix multiplication. Nevertheless, for a full matrix $\mathsf{HPH}^\mathsf{T} + \mathsf{R}$, the cost of its inversion is roughly P^3. In addition, we need to store HP of size $M \times P$. This needs already a major effort in computer resources if P is large. If we would like to calculate the error covariance after analysis, the matrix multiplications need PM^2 operations. If only the diagonal of the covariance matrix, *i.e.*, the local error variances are needed, the number of operations reduces to PM.

Things get of course more demanding if we update the error-covariance in time according to the Kalman filter theory. Even if we do not create the matrix M allowing the model transitions, the multiplication of this matrix with a vector is equivalent to a model integration. Hence, if the matrix M multiplies another matrix of size $M \times M$, we can estimate the cost to be equivalent M model integrations, which is therefore the cost to update the forecast error covariance and must be compared to the cost of a single model integration when no assimilation is included.

For the original 3D-Var method, things are not better a because we need M^3 operations to inverse covariance matrixes unless they are provided as inverse already. In this case we need M^2 operations to calculate each cost function, M operations to calculate its gradient and K iterations to find the minimum. To reach the minimum, $K = M$ iterations are needed in theory but good approximations can be found for K being a fraction of M.

For 4D-Var, similar estimates apply with the need to perform a direct model integration and its adjoint integration for each evaluation of the gradient needed during the minimization. For K iterations KM model integrations are performed and each evaluation of the cost function requires M^2 operations unless the error covariances have special forms, as a diagonal one.

In view of the numbers M and P in use for operational models, we clearly see a need for simplifications and yet another reason to keep pressure on computing resources. Indeed, for the sizes of statevectors and observation arrays currently in use, original Kalman filters or 3D-Var are out of question if covariance matrixes are not of a special form.

Reducing the complexity of the assimilation methods to affordable version retaining the advantages is where the "art" of modeling comes to help by identifying unnecessary components or dominant processes to be retained. Also the type and quantity of observation is controlling the design of the simplifications. In the ocean, observations for operational purposes are mostly surface data from satellites (sea level anomaly with respect to an average, possibly dynamical position, sea surface temperature, colour, and soon salinity and sea ice.) or coastal data, with Argo floats (*e.g.*, Poulain) complementing the information with deep profiles. In the atmosphere (TO BE COMPLETED)

The modified assimilation methods generally take into the type of data incorporated. For the ocean, one approach being to perform assimilation in two steps, one incorporating only surface information and the other profile data, with specific simplifications brought to the covariances.

Such a reduction of complexity can be justified in most cases because the system evolution include a series of physically damped modes. For these part of the evolution corrections are not needed because they fade away. Such damped modes occur because of attractors as geostrophic equilibrium. On the other side unstable modes must certainly be followed by the assimilation process. Another justification for the appropriatness of reducing ambitions, is the size of the state vector. The very large number of numerical state variables arises because we request the numerical grid or method to resolve correctly the scales of interest, hence $\Delta x \ll L$ and $\Delta z \ll H$. But this immediately prooves that we use much more calculation points than the real degrees of freedom of the system we actually want to model. Therefore we can try to reduce the dimensions of the data assimilation problem.

One of the most popular approaches to simplify the calculation is the use of a *reduced rank* covariance matrix

$$\mathsf{P} \sim \mathsf{S}\mathsf{S}^\mathsf{T} \tag{22.59}$$

where S is of size $M \times K$, K generally being much smaller than M. It is easily demonstrated that the rank[7] of $\mathsf{S}\mathsf{S}^\mathsf{T}$ is at most K, hence the name reduced rank. Note that we do not need to store P anymore because if we store the much smaller matrix S, we can at any moment

[7] *i.e.*, the number of linearly independent columns.

perform matrix multiplications involving P by a successive matrix multiplication with S and its transposed. In this way a multiplication of P with a square matrix of identical size, instead of requiring M^3 operations, requires only $2KM^2$ operations.

But we also gain in terms of matrixes to be inverted. The effect of a reduced rank can be exemplified most easily if we assume a diagonal matrix R for uncorrelated observational errors with the same error variance μ^2. Defining matrix $\mathsf{U} = \mathsf{HS}$ of dimension $P \times K$ with $K \ll P$, we have

$$\mathsf{PH}^\mathsf{T}\left(\mathsf{HSS}^\mathsf{T}\mathsf{H}^\mathsf{T} + \mathsf{R}\right)^{-1} = \mathsf{SU}^\mathsf{T}\left(\mathsf{UU}^\mathsf{T} + \mu^2\mathsf{I}\right)^{-1} = \mathsf{S}\left(\mathsf{U}^\mathsf{T}\mathsf{U} + \mu^2\mathsf{I}\right)^{-1}\mathsf{U}^\mathsf{T} \tag{22.60}$$

using a special case of the probably most useful matrix identity in data assimilation, the Sherman-Morisson formula (Exercise 22-8). The last operation transformed the matrix to be inverted from a $P \times P$ matrix into a much smaller $K \times K$ one. This is where a major gain in computing as obtained.

The gain in terms of computation is of course at the expense of some optimality of the analysis. This is clearly seen from the analysis step expressed in terms of S

$$\mathbf{x}^a = \mathbf{x}^f + \mathsf{S}\boldsymbol{\alpha}, \quad \boldsymbol{\alpha} = \left(\mathsf{U}^\mathsf{T}\mathsf{U} + \mu^2\mathsf{I}\right)^{-1}\mathsf{U}^\mathsf{T}\left(\mathbf{y} - \mathsf{H}\mathbf{x}^f\right). \tag{22.61}$$

where $\boldsymbol{\alpha}$ is a $K \times 1$ vector. We notice that corrections on $\mathbf{x}^f$ are always a linear combinations of the columns of S. Error corrections are therefore only possible in the space spanned by columns of S and other directions are thus *de facto* considered without errors. If there are errors in reality, they will pass unnoticed as such by the reduced rank approach and interpreted as real signal. A substantial reduction in calculations is however obtained and it can be shown that error covariance updates can benefit from similar reductions in complexity. The essential problem is to assess a relevant reduced form SS^T.

In an ensemble forecast approach, the model is used to create a series of simulations, each being a slightly perturbed version of the others, with perturbations introduced via initial conditions, forcings, parameter values and even topographic perturbations. We then have an ensemble of model results from which statistical parameters can be estimated using the ensemble members $\mathbf{x}^{(j)}$. The average of the ensemble can for example be used as the best estimate for a forecast:

$$\bar{\mathbf{x}} = \frac{1}{K}\sum_{j=1}^{K}\mathbf{x}^{(j)} \tag{22.62}$$

If we accept this as the best estimation of the true state, deviations from this state can be used to estimate the error covariance matrix

$$\mathsf{P} = \frac{1}{K-1}\sum_{j=1}^{K}\left(\mathbf{x}^{(j)} - \bar{\mathbf{x}}\right)\left(\mathbf{x}^{(j)} - \bar{\mathbf{x}}\right)^\mathsf{T} \tag{22.63}$$

The denominator $K - 1$ arises because the K deviations from the mean are not independent anymore and the number of degrees of freedom is reduced to $K-1$. This is the same approach we use when estimating variances from samples. The columns of S are thus directly given by the ensemble members, shifted to have a zero mean and scaled by $1/\sqrt{K-1}$. All we have to do is to perform an ensemble of model simulations and perform statistical calculations on their solutions. In practice, the convergence of variance estimations from K samplings converges only as $1/\sqrt{K}$ and we therefore see the need to use a large ensemble or to create ensemble with optimal distributions of its members (Evensen ????). Combining ensemble approaches and reduced rank approximations lead to a series of assimilation variants with different implementations (Pham, Barth, Brasseur, Lhermusiaux, etc)

The ensemble approach can even be extended to include not only simulation results of a single model with perturbed setups, but also different models, aimed at modelling the same properties (superensemble approach) or even using different physical parameterizations and governing equations (hyperensemble approach). Such combinations can drastically reduce errors, in particular biases (REFERENCE).

Other simplifications are based on the reduction of the size of the state vector on which assimilation works. A possibility is to propagate error covariances with coarser grids or simplified models (to forecast P a quasi-geostrophic model could be used while the state variables are forecasted using primitive equations, Fukumori????). Particular dynamic balances also can directly be taken into account through covariances. But if only one component of such a balance is observed, for example sea surface height in a geostrophically balanced system, velocity does not need to be included in the assimilation step but once a correction of sea surface height and density is found, corrections on velocity can be calculated by using geostrophy on the pressure corrections.

Each time an assimilation method is complementing a model, specific adaptations are therefore implemented, depending on the dynamical regimes, the number and type of available data, the computing resources *etc.* Another aspect requiring attention in operational models is a smooth data flow. In view of the large number of data ingested by the systems, it is out of question to verify manually all data or apply transformations on them because some standards are not followed. Also, even with a strong standardization, transmission errors or instrumental disfunctionning can happen and automated quality controls must verify the likelihood that a given observation is coherent with statistical distributions.

Often forecasts are provided on a large scale and dispatched to regional forecast centers where *downscaling* of the forecasts to the regional scales must be done. This can be achieved by forecasters with knowledge of the regional dynamics, using both knowledge of the local system, statistical tools and possibly regional models to provide accurate forecasts at scales not resolved by the glocal models. In particular rain and cloud related properties require adequate downscaling in weather forecasts.

Operational model are already in use for some applications for quite some time, with weather forecasts based on numerical models initiated in the post-war period and are now widespread with two major centers providing global forecasts (ECMWF, NCEP). Operational tidal models, hurricane predictions and tsunami warning systems in the Pacific are also well established, incorporating data form observational networks in dedicated institutes. Since a few years ocean circulation forecasts are emerging (Mersea, Hycom, Hops...), well before the public demand for tsunami predictions at global scale appeared in December 2004.

A common aspect of operational models is that data assimilation was initially exploited to reduce errors. But it is fair to request that operational model should not only include forecasts but also associated errors or confidence, which assimilation now allows to do. From a scientific point of view, we might argue that the forecast corrections do not provide new insight into physical processes. In reality the analysis of assimilation cycles can help understanding error sources and verify that the model is statistically coherent with observations.

Also verifying the innovations and error estimates are compatible with the statistical models in use allows to identify problem. For example, on average, innovations should be zero, otherwise a bias is probably present in the system and should be corrected. In this sense forecast verifications (Joliffe) can teach us things about the dynamics, model errors and observations and can help to identify the key model or observing system ingredients to improve.

M. Ghil and P. Malanotte-Rizzoli,11 'Data assimilation in meteorology and oceanography', Ad. Geophys., 33, 141 – 266 (1991). A.F. Bennett, Inverse Methods in Physical Oceanography, Cambridge University Press, 1992, 346.

To cite in chapter, Bennet, ghil, rizzoli, robinson, verron, evensen, barth, brasseur, rixen, Carton Kalnay etc Daley 1991, Hollingworth

Pinardi (Navarra) ocean forecasting

Kalnay, E. 2003: *Atmospheric Modeling, Data Assimilation and Predictability*, Cambridge University Press, 341 p.

Fukumori smoothing

(for general kalman theory) Gelb A., 1974 : *Applied optimal estimation*, MIT Press, 374 p.

If speak about EOF, show a nice example (El nino or a decadal oscillation)

Analytical Problems

22-1. Analyze the exact solution of the following equations

$$\frac{du}{dt} = \tilde{f}v - \frac{u - u_o(t)}{\tau} \tag{22.64}$$

$$\frac{dv}{dt} = -\tilde{f}u - \frac{v - v_o(t)}{\tau} \tag{22.65}$$

with $u_o(t) = \cos(ft), v_0 = -\sin(ft)$ and a relaxation time $\tau = 1/(\alpha\tilde{f})$. These equations are modeling a nudging term applied to follow an inertial oscillation of frequency f while the "model" has a tendency to create an inertial oscillation with frequency $\tilde{f}$. Analyze how the nudging corrects an error on the initial condition, distinguishing the effect of an error on amplitude and phase. Then investigate how a difference between $\tilde{f}$ and f affects the solution.

22-2. Estimation of error variances for various fields on a graph. To which variability the errors could be compared?

22-3. Prove that the minimization of (22.35) leads to the same analysis as the optimal interpolation. What is the value of J at the optimum?

22-4. Describe and write out an optimal interpolation method to interpolate in space knowing the spatial covariance of the true field and data errors in given locations.

22-5. Weather forecast is limited to one or two weeks after which forecast skill is nil. Can you justify why climate models, using also the governing equations of geophysical fluid dynamics, can be used to predict tens of years? *Hint:* Think about the signification of state variables and parameterizations.

22-6. Bottom friction is generally parameterized by a quadratic law $\tau_b = \rho_0 C_d u^2$. Show that even for an unbiased estimate of u, the bottomstress itself is biased. What is the error variance?

22-7. Prove

$$\mathbf{L}^{\mathsf{T}}\left(\mathbf{L}\mathbf{L}^{\mathsf{T}} + \mu^2\mathbf{I}\right)^{-1} = \left(\mathbf{L}^{\mathsf{T}}\mathbf{L} + \mu^2\mathbf{I}\right)^{-1}\mathbf{L}^{\mathsf{T}} \tag{22.66}$$

Are there conditions to be satisfied?

22-8. Demonstrate the Sherman-Morrison formula

$$\left(\mathbf{A} + \mathbf{U}\mathbf{V}^{\mathsf{T}}\right)^{-1} = \mathbf{A}^{-1} - \mathbf{A}^{-1}\mathbf{U}\left(\mathbf{I} + \mathbf{V}^{\mathsf{T}}\mathbf{A}^{-1}\mathbf{U}\right)^{-1}\mathbf{V}^{\mathsf{T}}\mathbf{A}^{-1} \tag{22.67}$$

22-9. Assuming the the full state vector $\mathbf{x}$ is observed with zero observational errors, how behaves the Kalman gain matrix?

22-10. Derive the equation that steady state forecast-error covariance assuming the error-covariance matrix $\mathbf{P}$ reaches a stationnary value must satisfy. When do you expect the use of this error covariance obtained from this so-called Ricatti equation to be interesting?

22-11. Why did we distinguish the concept of most likelyhood estimators and the minimum expected error estimators? Can you see the reason for doing so for a system with the schematic probability density function of Figure 22-13? How would you make the link with the trajectories on Figure 22-1 of the Lorenz equations?

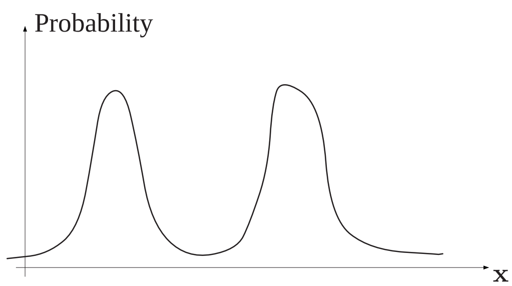

Figure 22-13 A non-gaussian probability density function with two states of high probability.

22-12. Can you see a reason to keep ϵ^p different from zero in the definition (22.1) of the skill-score? *Hint:* Think about what a perfect model is able to predict.

22-13. When do you think the autocorraletion provides usefull information on the predictability limit discussed on Figure 22-4?

22-14. The Lyapunov equation (22.40) can also be used to recover classical results in error estimations: Suppose you use a state equation $\rho(T, S)$ and your measurements on T and S are plagued by errors with known error variance σ_T^2 and σ_S^2. Calculate the extected error-variance on ρ and show that it can be recasted into the form (22.40). Can you interprete $\mathbf{Q}$ in this case?

22-15. Introduce lowering method of Haines?

Numerical Exercises

22-1. Implement a nudging and solve numerically the analytical problem 22-1. When you decrease τ, what specific action to you need to take in the numerical time stepping? Investigate what happens when you add noise to the "observations" u_0 and v_0 and decrease the sampling rate of the "pseudo-data".

22-2. Implementation of OI in a gravity wave problem. Prescribe covariance as ... Which length scale would you suggest if your assimilation cycle is every ?? hour.

22-3. Kalman filter on advection problem to show error propagation? Model error=wrong velocity and numerical diffusion? with observation in a given point at every moment.

22-4. Use the Kalman filter of `kalmangw.m` on the gravity wave problem. Investigate the effect of changing the model and observational noise level.

22-5. Develop an adjoint method for advection problem 22-3. Optimize initial condition. Use $\mathsf{C} = 0.2$ and $\mathsf{C} = 1$ to see the effect of model errors, $\mathsf{C} = 1$ giving the perfect dynamics model. What is the effect of reducing the number of observations and disregarding the background initial conditions? *Hint:* Think about underdetermined and overdetermined problems.

22-6. A more complicated assimilation experiment ? Identification of source of tracers in diffusion problem? Show that unconstrained minimization problems can lead to unphysical results (negative concentrations).

22-7. Estimate the memory needed if we would like to store $\mathbf{P}$ for today's weather forecast systems.

22-8. Lorenz and ensemble (depending on where, short or long predictability)

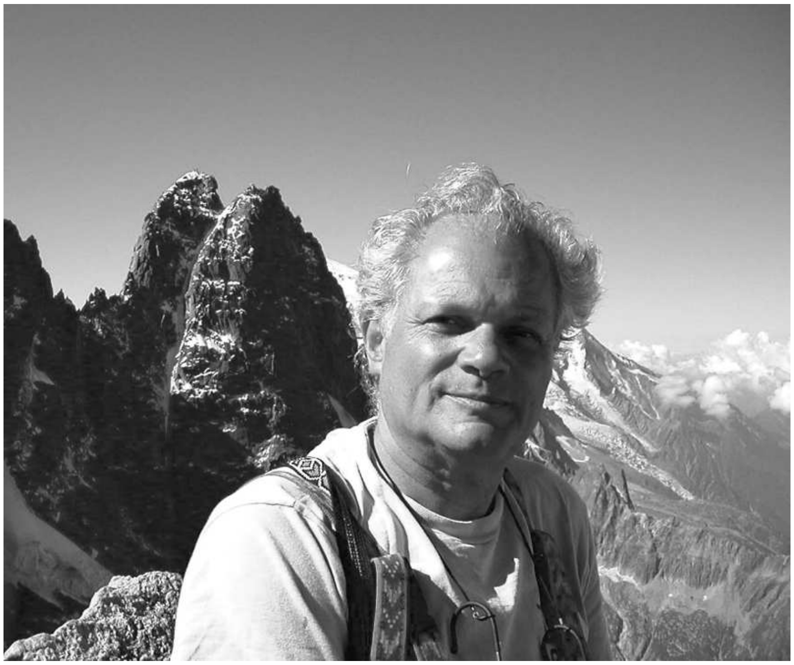

Michael Ghil
1944 –

Born in Budapest, Hungary, Michael Ghil spent his high-school years in Bucharest, Romania, and acquired an engineering education in Israel, where he served as a naval officer. After moving to the United States, he obtained his doctorate at the Courant Institute of Mathematical Sciences at New York University under Professor Peter Lax (see biography at end of Chapter 6).

His scientific work includes seminal contributions to climate system modeling, chaos theory, numerical and statistical methods, data assimilation, and mathematical economics. He provided self-consistent theories of Quaternary glaciation cycles, of the low-frequency variability of extratropical atmospheric flows, and of the mid-latitude oceanic interannual variability. He is a prolific writer, with his name attached to a dozen books and well over two hundred research and review articles.

Professor Ghil takes turns teaching at the École Normale Suprieure in Paris and at the University of California in Los Angeles. He has enjoyed learning from and working with a large number of students and younger colleagues, with whom he often stays in contact. Many of these have attained considerable professional achievements in their own right, on three continents. He speaks six languages fluently. (*Photo by Philippe Bruère, Compagnie des Guides, Chamonix – Mont Blanc*)

Eugenia Kalnay

–

PhD under Charney (See biography end of Chapter ???)

The Reanalysis paper of 1996 is the most cited paper in all geosciences in the last decades.

Eugenia Kalnay was awarded a Ph.D in Meteorology from the Massachusetts Institute of Technology in 1971. Following a position as Associate Professor in the same department, she became Chief of the Global Modeling and Simulation Branch at the NASA Goddard Space Flight Center (1983-1987). From 1987 to 1997 she was Director of the Environmental Modeling Center (US National Weather Service) and in 1998 was awarded the Robert E. Lowry endowed chair at the University of Oklahoma. In 1999 she became the Chair of the Department of Meteorology at the University of Maryland. Professor Kalnay is a member of the US National Academy of Engineering, is the recipient of two gold medals from the US Department of Commerce and the NASA Medal for Exceptional Scientific Achievement, and has received the Jule Charney Award from the American Meteorological Society. The author of more than 100 peer reviewed papers on numerical weather prediction, data assimilation and predictability, Professor Kalnay is a key figure in this field and has pioneered many of the essential techniques.

From 1979 to 1986 Eugenia Kalnay worked at, and later directed, the Global Modeling and Simulation Branch, at NASA/GSFC. She developed the accurate and efficient NASA Fourth Order Global Model which for more than 15 years was the core of many data assimilation and forecasting experiments, as well as stratospheric and climate simulations, and is still being used for climate experiments. From 1987 to 1997, Dr. Kalnay was the Director of the Environmental Modeling Center (EMC, ex Development Division) of the National Centers for Environmental Prediction (NCEP, ex NMC), National Weather Service (NWS). During this decade there were major improvements in the NWS models' forecast skill. Many successful projects such as ensemble forecasting, 3-d and 4-d variational data assimilation, advanced quality control, coastal ocean forecasting, GCIP research with the Eta model, seasonal and interannual dynamical predictions, were started or carried out during those years. She directed the NCEP/NCAR 50- year Reanalysis project and with Zoltan Toth developed the ensemble forecasting method implemented in 1992 at NCEP. Current research interests of Dr. Kalnay are in predictability and ensemble forecasting, numerical weather prediction and data assimilation. With Dr. Ming Cai she is studying the Lyapunov vectors of the coupled ocean-atmosphere system. With her collaborators Dr. Zhao-Xia Pu and Dr. Seon Ki Park, she introduced the method of backward integration of atmospheric models and several novel applications such as Inverse 3D-VAR, and targeted observations. Dr. Zoltan Toth and Dr. Kalnay introduced the breeding method for ensemble forecasting. She is also the author (with Ross Hoffman and Wesley Ebisuzaki) of other widely used ensemble methods known as Lagged Averaged Forecasting (LAF) and Scaled LAF. She has also published papers on atmospheric dynamics and convection, numerical methods, and the atmosphere of Venus. Her book

Her textbook ... Data Assimilatin ...

(*Photo*)

Appendix A: Elements of Fluid Mechanics

A.1 Budgets

Start with a derivation of the 3D compressible continuity equation.

Then, derive momentum equations (3.2)-(3.4), paying close attention to how the pressure force is proportional to the pressure gradient rather than to the pressure itself.

A.2 Equations in spherical coordinates

The preceding equations assume a Cartesian system of coordinates and thus hold only if the dimension of the domain under consideration is much shorter than the earth's radius. Should the domain dimensions be comparable to the size of the planet, the x–, y– and z–axes need to be replaced by spherical coordinates, and curvature terms enter all equations. Equations (3.1) through (3.5) become:

$$\frac{\partial}{\partial t}(\rho\cos\varphi) \;+\; \frac{\partial}{\partial\lambda}\left(\frac{\rho u}{r}\right) \;+\; \frac{\partial}{\partial\varphi}\left(\frac{\rho v\cos\varphi}{r}\right) \;+\; \frac{\partial}{\partial r}(\rho w\cos\varphi) \;=\; 0$$

$$\rho\left(\frac{du}{dt} - \frac{uv\,\tan\varphi}{r} + \frac{uw}{r} + f_* w - f v\right) \;=\; -\frac{1}{r\cos\varphi}\frac{\partial p}{\partial\lambda} + F_\lambda$$

$$\rho\left(\frac{dv}{dt} + \frac{u^2\,\tan\varphi}{r} + \frac{vw}{r} + f u\right) \;=\; -\frac{1}{r}\frac{\partial p}{\partial\varphi} + F_\varphi$$

$$\rho\left(\frac{dw}{dt} - \frac{u^2+v^2}{r} - f_* u\right) \;=\; -\frac{\partial p}{\partial r} - \rho g + F_r$$

where φ is the latitude, λ the longitude and r the distance from the center of the earth (or planet or star). The components F_λ, F_φ, and F_r of the frictional force have complicated expressions and need not be reproduced here. The material derivative becomes

$$\frac{d}{dt} \;=\; \frac{\partial}{\partial t} + \frac{u}{r\cos\varphi}\frac{\partial}{\partial\lambda} + \frac{v}{r}\frac{\partial}{\partial\varphi} + w\frac{\partial}{\partial r}\,.$$

For a detailed development of these equations, the reader is referred to Chapter 4 of the book by Gill (1982).

Appendix B: Wave Kinematics

(October 18, 2006) **SUMMARY**: Because numerous geophysical flow phenomena can be interpreted as waves, some understanding of basic wave properties is required in the study of geophysical fluid dynamics. The concepts of wavenumber, frequency, dispersion relation, phase speed and group velocity are introduced and given physical interpretations.

B.1 Wavenumber and wavelength

For simplicity of presentation and easier graphical representation, we will consider here a two-dimensional plane wave, namely, a physical signal occupying the $(x,\ y)$ plane, evolving with time t and with straight crest lines. The prototypical wave form is the sinusoidal function, and so we assume that a physical variable of the system, denoted by a and being pressure, a velocity component or whatever, evolves according to

$$a \;=\; A\ \cos(k_x x \;+\; k_y y \;-\; \omega t \;+\; \phi). \tag{B.1}$$

The coefficient A is the wave *amplitude* ($-A \leq a \leq +A$), whereas the argument

$$\alpha \;=\; k_x x \;+\; k_y y \;-\; \omega t \;+\; \phi \tag{B.2}$$

is called the *phase*. The latter consists of terms that vary with each independent variable and a constant ϕ, called the reference phase. The coefficients k_x, k_y, and ω of x, y, and t, respectively, bear the names of *wavenumber in* x, *wavenumber in* y and *angular frequency*, most often abbreviated to *frequency*. They indicate how rapidly the wave undulates in space and how fast it oscillates in time.

Equivalent expressions for the wave signal are

$$a \;=\; A_1\ \cos(k_x x \;+\; k_y y \;-\; \omega t) \;+\; A_2\ \sin(k_x x \;+\; k_y y \;-\; \omega t), \tag{B.3}$$

where $A_1 = A\ \cos\phi$ and $A_2 = -A\ \sin\phi$, and

$$a \;=\; \Re\left[A_c\ \mathrm{e}^{i(k_x x + k_y y - \omega t)}\right], \tag{B.4}$$

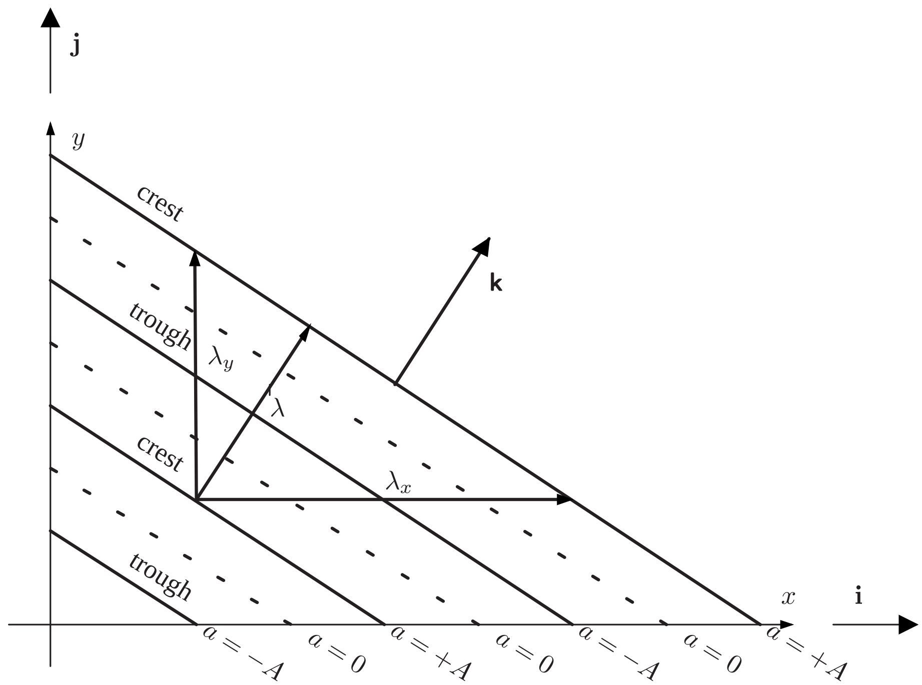

Figure B-1. Instantaneous phase lines of a plane two-dimensional wave signal. The lines are straight and parallel. The distances from crest to nearest crest along the x– and y–axes are λ_x and λ_y, respectively, whereas the wavelength λ is the shortest diagonal distance from crest line to nearest crest line.

where the notation $\Re[\,]$ means "the real part of" and $A_c = A_1 - iA_2 = A\ \mathrm{e}^{i\phi}$ is a complex amplitude coefficient. The choice of mathematical representation is generally dictated by the problem at hand. Formulation (B.3) is helpful in the discussion of problems exhibiting coexisting signals that are either in perfect phase or in quadrature, whereas formulation (B.4) is preferred when a given dynamical system is subjected to a wave analysis. Here, we will use formulation (B.1).

A wave *crest* is defined as the line in the (x, y) plane and at time t along which the signal is maximum ($a = +A$); similarly, a *trough* is a line along which the signal is minimum ($a = -A$). These lines and, in general, all lines along which the signal has a constant value at an instant in time are called *phase lines*. In a plane wave, as the one considered here, all crests, troughs and other phase lines are straight lines. Figure B-1 depicts a few phase lines in the case of positive wavenumbers k_x and k_y.

Because of the oscillatory behavior of the sinusoidal function, crest lines recur at constant intervals, thus giving the wavy aspect to the signal. The distance over which the signal repeats itself in the x–direction is the distance over which the phase portion $k_x x$ increases by 2π, that is,

$$\lambda_x = \frac{2\pi}{k_x}\,. \tag{B.5}$$

Similarly, the distance over which the signal repeats itself in the y–direction is

$$\lambda_y = \frac{2\pi}{k_y} . \tag{B.6}$$

The quantities λ_x and λ_y are called the wavelengths in the x– and y–directions. They are the wavelengths seen by an observer who would detect the signal only through slits aligned with the x and y axes. The actual *wavelength*, λ, of the wave is the shortest distance from the crest to nearest crest (Figure B-1) and is, therefore, smaller than either λ_x and λ_y. Elementary geometric considerations provide

$$\frac{1}{\lambda^2} = \frac{1}{\lambda_x^2} + \frac{1}{\lambda_y^2} = \frac{k_x^2 + k_y^2}{4\pi^2}$$

or

$$\lambda = \frac{2\pi}{k} , \tag{B.7}$$

where k, called the *wavenumber,* is defined as

$$k = \sqrt{k_x^2 + k_y^2} . \tag{B.8}$$

Note that since λ^2 is not the sum of λ_x^2 and λ_y^2, the pair (λ_x, λ_y) does not make a vector. On the other hand, the pair (k_x, k_y) can be used to define the *wavenumber vector*

$$\mathbf{k} = k_x\mathbf{i} + k_y\mathbf{j}, \tag{B.9}$$

where $\mathbf{i}$ and $\mathbf{j}$ are the unit vectors aligned with the axes (Figure B-1). In this fashion, the wavenumber k is the magnitude of the wavenumber vector $\mathbf{k}$.

By definition, phase lines at any given time correspond to lines of constant values of the expression $k_x x + k_y y = \mathbf{k} \cdot \mathbf{r}$, where $\mathbf{r} = x\mathbf{i} + y\mathbf{j}$ is the vector position. Geometrically, this means that a phase line is the locus of points whose vectors from the origin share the same projection onto the wavenumber vector. These points form a straight line perpendicular to $\mathbf{k}$, and therefore the wavenumber vector points perpendicularly to all phase lines (Figure B-1), that is, in the direction of the undulation.

B.2 Frequency, phase speed, and dispersion

Let us now turn our attention to the temporal evolution of the wave signal. At a fixed position (x and y given), an observer sees an oscillatory signal. The interval of time between two consecutive instants at which the signal is maximum is the time taken for the portion ωt of the phase to increase by 2π. It is called the *period*, which is

$$T = \frac{2\pi}{\omega} . \tag{B.10}$$

Let us now follow a particular crest line ($a = A$) from a certain time t_1 to a later time t_2 and note the time interval $\Delta t = t_2 - t_1$. During this time interval, the wave crest has progressed from one position to another (Figure B-2). The intersection with the x–axis has

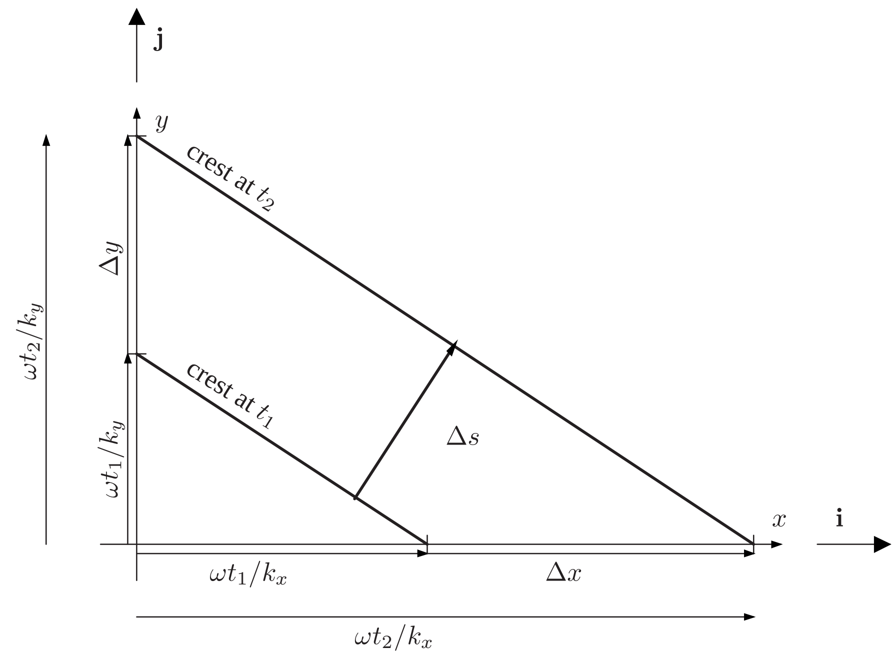

Figure B-2. Progress of a wave crest from time t_1 to time t_2. The ratio of the distance traveled, Δs, to the time interval $\Delta t = t_2 - t_1$ is the phase speed.

translated over the distance $\Delta x = \omega t_2/k_x - \omega t_1/k_x = \omega \Delta t/k_x$ in time Δt. This defines the propagation speed of the wave along the x–direction:

$$c_x = \frac{\Delta x}{\Delta t} = \frac{\omega}{k_x} . \tag{B.11}$$

Similarly, the propagation speed along the y–direction is the distance $\Delta y = \omega t_2/k_y - \omega t_1/k_y$ divided by the time interval Δt, or

$$c_y = \frac{\Delta y}{\Delta t} = \frac{\omega}{k_y} . \tag{B.12}$$

But, these speeds are only speeds in particular directions. The true propagation speed of the wave is the distance Δs, measured perpendicularly to the crest line (Figure B-2), covered by this crest line during the time interval Δt. Again, elementary geometric considerations provide

$$\frac{1}{\Delta s^2} = \frac{1}{\Delta x^2} + \frac{1}{\Delta y^2} ,$$

from which we deduce

$$\Delta s = \frac{\omega \Delta t}{k} ,$$

where k is the wavenumber defined in (B.8). The propagation speed of the crest line is thus

$$c \;=\; \frac{\Delta s}{\Delta t} \;=\; \frac{\omega}{k}\,. \tag{B.13}$$

Because all phase lines propagate at the same speed (so that the wave preserves its sinusoidal form over time), the quantity c is called the *phase speed*. Note that because c^2 is not equal to $c_x^2 + c_y^2$ (in fact, c is less than both c_x and c_y!), the pair (c_x, c_y) does not constitute a physical vector. The direction of phase propagation, as discussed before, is parallel to the wavenumber vector $\mathbf{k}$.

In general, the expression (B.1) of the wave signal appears as the solution to a particular dynamical system. Therefore, it must somehow be constrained by the physics of the problem, and not all its parameters can be varied independently. Let us suppose that the system under consideration is initially unchanging in time (state of rest or steady flow) and that at time $t = 0$, it is perturbed spatially according to a sinusoidal distribution of wavenumbers k_x and k_y in the x– and y–directions, respectively, and of amplitude A for the variable a. Intuition leads us to anticipate that subsequent to this perturbation, the system will react in a time-dependent fashion. If this reaction takes the form of a wave, it will have a frequency ω determined by the system. Therefore, the frequency can be viewed as dependent upon the wavenumber components k_x and k_y and the amplitude A. In most instances, the system's response is a wave because the set of equations representing the physics is linear, and when this is the case, the mathematical analysis yields a frequency that is independent of the amplitude of the perturbation. Therefore, ω is typically a function of k_x and k_y only.

If the frequency is a function of the wavenumber components, so is the phase speed:

$$c \;=\; \frac{\omega(k_x,\; k_y)}{\sqrt{k_x^2\;+\;k_y^2}} \;=\; c(k_x,\; k_y).$$

Physically, this implies that the various waves of a composite signal will all travel at different speeds, causing a distortion of the signal over time. In particular, a localized burst of activity, which by virtue of the Fourier-decomposition theorem contains waves of many different wavelengths, will be progressively less localized as time goes on. This phenomenon is called *dispersion*, and the mathematical function that relates the frequency ω to the wavenumber components k_x and k_y bears the name of *dispersion relation*.

The dispersion relation can be represented, in two dimensions, as a set of curves in the (k_x, k_y) plane along which ω is a constant. Figure B-3 provides an example. At one dimension ($k_x = k$, $k_y = 0$) or at two dimensions when the physical system is isotropic (ω function of k only), a single ω-versus-k curve suffices to represent the dispersion relation.

In some special physical systems, the dispersion relation reduces to a single proportionality between frequency ω and wavenumber k. The phase speed is then the same for all wavenumbers, all waves travel in perfect accord, and the total signal retains its shape as time evolves. Such a wave is called a *nondispersive* wave.

B.3 Group velocity and energy propagation

In general, a wave pattern consists of more than a single wave. A series of waves are superimposed, leading to constructive and destructive interference. In areas where the waves are

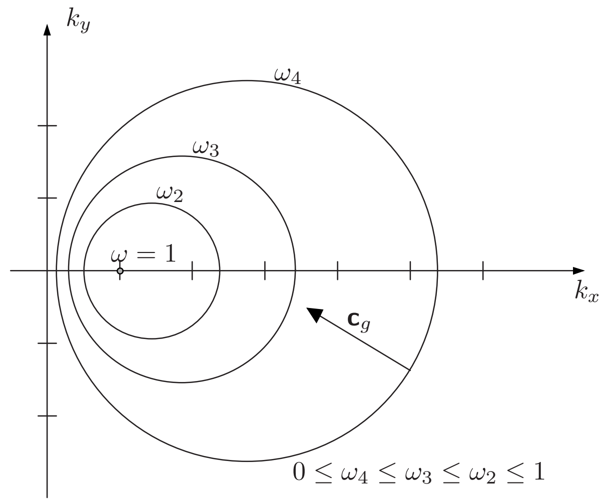

Figure B-3. Graphic representation of the dispersion relation $\omega = 2k_x/(k_x^2 + k_y^2 + 1)$ by curves of constant ω values in the (k_x, k_y) wavenumber plane.

interfering constructively, the wave amplitude is greater and the energy level is higher than in areas where the waves interfere destructively. Therefore, energy distribution is a property of a set of waves rather than of a single wave. (It can be said that a single wave has a uniform energy distribution.) Energy propagation by a set of waves depends on how interference patterns move about and is generally not the average speed of the waves present. To illustrate the principles and determine the speed at which energy propagates, let us restrict our attention to two one-dimensional waves and, more precisely, to two waves of equal amplitude and nearly equal wavenumbers:

$$a = A \cos(k_1 x - \omega_1 t) + A \cos(k_2 x - \omega_2 t), \tag{B.14}$$

where the wavenumbers k_1 and k_2 are close to their average $k = (k_1 + k_2)/2$, and the difference $\Delta k = k_1 - k_2$ is much smaller ($|\Delta k| \ll |k|$). Because both waves obey the single dispersion relation of the dynamical system, $\omega = \omega(k)$, the two frequencies $\omega_1 = \omega(k_1)$ and $\omega_2 = \omega(k_2)$ are close to their average $\omega = (\omega_1 + \omega_2)/2$, which is much larger than their difference $\Delta\omega = \omega_1 - \omega_2$ ($|\Delta\omega| \ll |\omega|$). In expression (B.14), the two reference phases were set to zero, which can always be done under suitable choices of space and time origins.

A trigonometric manipulation transforms expression (B.14) into

$$a = 2A \cos\left(\frac{\Delta k}{2}\, x - \frac{\Delta\omega}{2}\, t\right) \cos(kx - \omega t), \tag{B.15}$$

which now appears as the product of two waves. The second cosine function represents an average wave, of wavenumber and frequency between those of the two individual waves comprising the signal. The first cosine function, on the other hand, involves a much smaller wavenumber (i.e. much longer wavelength) and a much lower frequency. Over the cycle of the shorter (k, ω) wave, the longer wave appears almost unchanging. In other words, the (k,

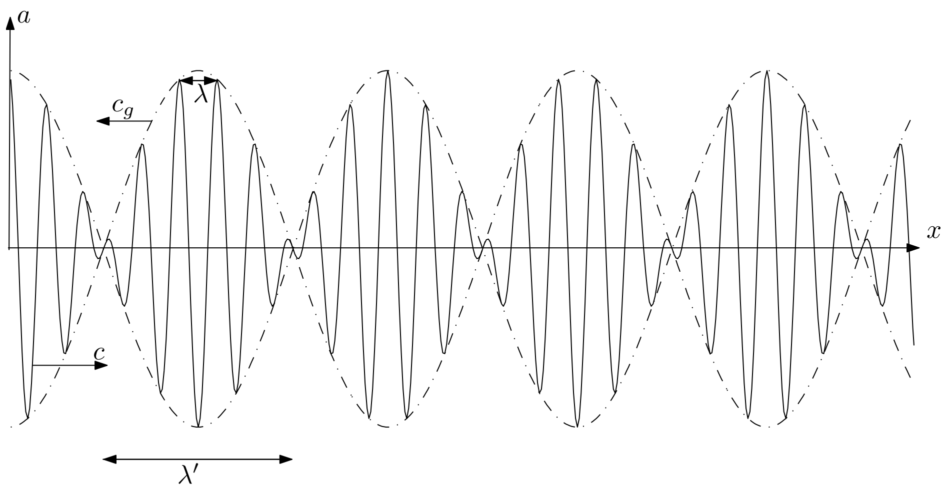

Figure B-4. The interference pattern of two one-dimensional waves with close wavenumbers. While the wave crests and troughs propagate at the speed $c = \omega/k$, the envelope (dashed line) propagates at the group velocity $c_g = d\omega/dk$.

ω) wave appears modulated; its amplitude, $2A\cos[(\Delta kx - \Delta\omega t)/2]$, is slowly varying in space and time, as seen in Figure B-4.

Although the wave signal exhibits a wavelength from crest to trough to the next crest equal to $\lambda = 2\pi/k$, the envelope has a much longer wavelength, $\lambda' = \frac{1}{2}\,[2\pi/(\Delta k/2)] = 2\pi/\Delta k$. The wave pattern is a succession of wave bursts, each of length λ'. Within each burst, the wave propagates at the phase speed $c = \omega/k$, while the burst travels at the speed $c' = \Delta\omega/\Delta k$.

Considering an infinitesimal wavenumber difference, we are led to define

$$c_g \;=\; \frac{d\omega}{dk}. \tag{B.16}$$

Because this is the propagation speed of a burst, or group of similar waves, it is called the *group velocity.* Energy is associated with each group, and so the group velocity is also the velocity at which energy is carried by the waves.

The preceding wave description relies on the existence of two waves of identical amplitudes. When two waves do not have equal amplitude, say A_1 and A_2, destructive interference is nowhere complete (the weak wave cannot completely cancel the strong wave), and there is no clear pinch-off between wave bursts. Rather, the modulating envelope undulates between the values $A_1 + A_2$ and $|A_1 - A_2|$ on the positive side and $-(A_1 + A_2)$ and $-|A_1 - A_2|$ on the negative side. It remains, however, that regions of constructive interference, and thus of higher energy level, propagate at the group velocity.

The theory can easily be extended to multidimensional waves. At two dimensions, for example, we define the group velocities in the x– and y–directions, respectively, as

$$c_{gx} = \frac{\partial \omega}{\partial k_x}, \quad c_{gy} = \frac{\partial \omega}{\partial k_y}, \tag{B.17}$$

given the dispersion relation $\omega(k_x, k_y)$. Because these expressions are the components of the gradient of the function ω in the (k_x, k_y) wavenumber space, they can be interpreted as the components of a physical vector depicting the group velocity

$$\mathbf{c_g} = \nabla_k \omega, \tag{B.18}$$

where ∇_k stands for the gradient operator with respect to the variables k_x and k_y. On the two-dimensional diagram (Figure B-3), this vector group velocity points perpendicularly to the ω curves, toward the higher values of ω. Aligning the k_x– and k_y–axes with the x– and y–axes of the plane provides the direction of energy propagation in space.

Generalization to the three-dimensional space is immediate. An example is the internal wave discussed extensively in Chapter 13.

Analytical Problems

B-1. In waters deeper than half the wavelength, surface gravity waves obey the dispersion relation $\omega = \sqrt{gk}$, where g is the gravitational acceleration (g = 9.81 m/s^2). For these waves, show that the wavelength is proportional to the square of the period. At which speed does a 10 m-long wave travel?

B-2. Show that the group velocity of deep-water waves (see Problem B-1) is always less than the phase speed.

B-3. A former sea captain recounts a stormy night in the middle of the North Atlantic when he observed waves with wavelengths of a few meters passing his 51-m-long ship in less than 3 s. Should you believe him?

B-4. Suppose that you are in the middle of the ocean and off in the distance you see a storm. A little while later, you observe the passage of surface gravity waves of wavelength 5 m. Two hours later, you still observe gravity waves, but now their wavelength is 2 m. How far away was the storm?

B-5. Find the frequency ω of a Kelvin wave of wavenumber k (Section 9.2). Is the Kelvin wave dispersive?

B-6. Show that for inertia-gravity waves [$\omega^2 = f^2 + gH(k_x^2 + k_y^2)$; Section 9.3], the group velocity is always less than the phase speed. In which limit does the group velocity approach the phase speed?

B-7. Demonstrate that when the frequency ω is a function of the ratio k_x/k_y, the energy propagates perpendicularly to the phase.

B-8. Given the dispersion relation of internal waves in a vertical plane (see Section 13.2),

$$\omega \;=\; N\,\frac{k_x}{\sqrt{k_x^2\;+\;k_z^2}}\;,$$

where N is a constant, k_x is the horizontal wavenumber and k_z is the vertical wavenumber, show that phase and energy always propagate in the same horizontal direction but in opposite vertical directions.

Numerical Exercises

B-1. Using animated graphics, display a time sequence (t = 0 to 10π by steps of π/4) of the double wave

$$a\,(x,t) \;=\; A_1\;\cos(k_1x\;-\;\omega_1t)\;+\;A_2\;\cos(k_2x\;-\;\omega_2t)$$

with $A_1 = A_2 = 1$, k_1 = 1.9, k_2 = 2.1, ω_1 = 2.1, ω_2 = 1.9, and for x ranging from 0 to 100. A suggested step in x is 0.25. Notice how the short waves [of wavelength = $4\pi/(k_1+k_2) = \pi$] travel toward increasing x at the speed $c = (\omega_1+\omega_2)/(k_1+k_2) = +1$, while the wave envelope [of wavelength = $2\pi/(k_2 - k_1) = 10\pi$] travels in the opposite direction at speed $c_g = (\omega_1 - \omega_2)/(k_1 - k_2) = -1$. This unequivocally demonstrates the nonintuitive fact that the energy propagation may well propagate in the direction opposite to the advancing crests and troughs. In other words, it is not impossible for energy to be transported up-wave.

Variations of this exercise can include uneven amplitudes (*e.g.*, A_1 = 1 and A_2 = 0.5) and modified values for the wavenumbers and frequencies.

B-2. Using animated graphics, use the same function as in exercise B-1 with k_1 = 0.35, k_2 = 0.5, ω_1 = 0.5, and ω_2 = 0.35 the other values unchanged. Show the evolution of a and then of $a^2/2$. Can you explain the apparently shorter waves?

B-3. Given a dispersion relation

$$\omega = \frac{k}{(k^2+1)}$$

analyze now the signal composed of two waves

$$a\,(x,t) \;=\; A_1\;\cos(k_1x\;-\;\omega(k_1)t)\;+\;A_2\;\cos(k_2x\;-\;\omega(k_2)t),$$

where ω is calculated using the dispersion relation. As before, show the evolution for $A_1 = A_2 = 1$ in the following situations

- k_1 = k_2 = 0.5,

- $k_1 = k_2 = 2$
- $k_1 = 1.95$, $k_2 = 2.05$
- $k_1 = 0.45$, $k_2 = 0.55$

Can you explain the behaviour? *Hint:* Plot the dispersion relation.

B-4. Redo exercise B-1 with $k_1 = 1$, $A_1 = 1$, $A_2 = 0$ and $\omega_1 = 1$. Then change the step in x to $\pi/4$ and $\pi/2$. Finally when using a step of $4\pi/3$, what do you observe?

Appendix C: Recapitulation of Numerical schemes

(October 18, 2006) **SUMMARY**: Certain numerical schemes of general use are regrouped here in order to facilitate implementations of simple models.

C.1 The tridiagonal system solver

An efficient tridiagonal system solver, called *Thomas algorithm*, can be constructed as a special case of the general **LU** decomposition (*e.g.*, Riley *et al.* 1997). We begin by assuming that there exists a decomposition for which the lower (**L**) and upper (**U**) matrices possess the same bandwidth of 2:

$$\begin{pmatrix} a_1 & c_1 & 0 & 0 & \cdots & 0 \\ b_2 & a_2 & c_2 & 0 & \cdots & 0 \\ 0 & b_3 & a_3 & c_3 & \cdots & 0 \\ \vdots & \vdots & \ddots & \ddots & \ddots & \vdots \\ 0 & 0 & \cdots & b_{m-1} & a_{m-1} & c_{m-1} \\ 0 & 0 & \cdots & 0 & b_m & a_m \end{pmatrix} =$$

$$\begin{pmatrix} 1 & 0 & 0 & 0 & \cdots & 0 \\ \beta_2 & 1 & 0 & 0 & \cdots & 0 \\ 0 & \beta_3 & 1 & 0 & \cdots & 0 \\ \vdots & \vdots & \ddots & \ddots & \ddots & \vdots \\ 0 & 0 & \cdots & \beta_{m-1} & 1 & 0 \\ 0 & 0 & \cdots & 0 & \beta_m & 1 \end{pmatrix} \begin{pmatrix} \alpha_1 & \gamma_1 & 0 & 0 & \cdots & 0 \\ 0 & \alpha_2 & \gamma_2 & 0 & \cdots & 0 \\ 0 & 0 & \alpha_3 & \gamma_3 & \cdots & 0 \\ \vdots & \vdots & \ddots & \ddots & \ddots & \vdots \\ 0 & 0 & \cdots & 0 & \alpha_{m-1} & \gamma_{m-1} \\ 0 & 0 & \cdots & 0 & 0 & \alpha_m \end{pmatrix} \quad (22.68)$$

where the first array is the original tridiagonal matrix to be decomposed (*i.e.*, elements a_1 *etc.* are known), the second array is **L** with one line of non-zero elements below the diagonal, and the last array is **U** with one line of non-zero elements above the diagonal.

Performing the product of matrices, we identify elements $(k, k-1)$, (k, k) and $(k, k+1)$ of the product as

$$b_k = \beta_k \alpha_{k-1} \tag{22.69}$$
$$a_k = \beta_k \gamma_{k-1} + \alpha_k \tag{22.70}$$
$$c_k = \gamma_k. \tag{22.71}$$

These relations can be solved for the components of **L** and **U** by observing that $\gamma_k = c_k$, the first row demands $a_1 = \alpha_1$ and subsequent rows provide α_k and β_k recursively from

$$\beta_k = \frac{b_k}{\alpha_{k-1}}, \quad \alpha_k = a_k - \beta_k c_{k-1}, \qquad k = 2, ..., m \tag{22.72}$$

provided that no α_k is zero (otherwise the matrix is singular and cannot be decomposed). Note that there is no β_1.

The tridiagonal matrix **A** has now been decomposed as the product of a lower and upper triangular matrices. The solution of $\mathbf{Ax} = \mathbf{LUx} = \mathbf{f}$ is then obtained by first solving $\mathbf{Ly} = \mathbf{f}$

$$\begin{pmatrix} 1 & 0 & 0 & 0 & \cdots & 0 \\ \beta_2 & 1 & 0 & 0 & \cdots & 0 \\ 0 & \beta_3 & 1 & 0 & \cdots & 0 \\ \vdots & \vdots & \ddots & \ddots & \ddots & \vdots \\ 0 & 0 & \cdots & \beta_{m-1} & 1 & 0 \\ 0 & 0 & \cdots & 0 & \beta_m & 1 \end{pmatrix} \begin{pmatrix} y_1 \\ y_2 \\ y_3 \\ \vdots \\ y_{m-1} \\ y_m \end{pmatrix} = \begin{pmatrix} f_1 \\ f_2 \\ f_3 \\ \vdots \\ f_{m-1} \\ f_m \end{pmatrix} \tag{22.73}$$

by proceeding from the first row downward and then solving $\mathbf{Ux} = \mathbf{y}$

$$\begin{pmatrix} \alpha_1 & \gamma_1 & 0 & 0 & \cdots & 0 \\ 0 & \alpha_2 & \gamma_2 & 0 & \cdots & 0 \\ 0 & 0 & \alpha_3 & \gamma_3 & \cdots & 0 \\ \vdots & \vdots & \ddots & \ddots & \ddots & \vdots \\ 0 & 0 & \cdots & 0 & \alpha_{m-1} & \gamma_{m-1} \\ 0 & 0 & \cdots & 0 & 0 & \alpha_m \end{pmatrix} \begin{pmatrix} x_1 \\ x_2 \\ x_3 \\ \vdots \\ x_{m-1} \\ x_m \end{pmatrix} = \begin{pmatrix} y_1 \\ y_2 \\ y_3 \\ \vdots \\ y_{m-1} \\ y_m \end{pmatrix}, \tag{22.74}$$

by proceeding from the bottom row upward. The solution is

$$y_1 = f_1, \quad y_k = f_k - \beta_k y_{k-1}, \qquad k = 2, ..., m \tag{22.75}$$
$$x_m = \frac{y_m}{\alpha_m}, \quad x_k = \frac{y_k - \gamma_k x_{k+1}}{\alpha_k}, \qquad k = m-1, ..., 1. \tag{22.76}$$

In practice, the α values are stored in a vector **a**, the β values in a vector **b**, the γ values in a vector **c**, and the y and f values can share the same vector **f** as the f_k value is no longer needed once the y_k value has been computed. With the additional vector **x** of the solution, only 5 vectors are required, and the solution is obtained with only three loops over m. This demands approximately $5m$ floating-point operations instead of m^3 that a brutal matrix inversion would have required. The algorithm is implemented in MATLAB™ file `thomas.m`.

Table 22.1 STANDARD FINITE DIFFERENCE OPERATORS FOR UNIFORM GRIDS

FORWARD DIFFERENCE $\mathcal{O}(\Delta t)$

	u^n	u^{n+1}	u^{n+2}	u^{n+3}	u^{n+4}
$\Delta t\ \frac{\partial u}{\partial t}$	-1	1			
$\Delta t^2\frac{\partial^2 u}{\partial t^2}$	1	-2	1		
$\Delta t^3\frac{\partial^3 u}{\partial t^3}$	-1	3	-3	1	
$\Delta t^4\frac{\partial^4 u}{\partial t^4}$	1	-4	6	-4	1

FORWARD DIFFERENCE $\mathcal{O}(\Delta t^2)$

	u^n	u^{n+1}	u^{n+2}	u^{n+3}	u^{n+4}	u^{n+5}
$2\ \Delta t\ \frac{\partial u}{\partial t}$	-3	4	-1			
$\Delta t^2\frac{\partial^2 u}{\partial t^2}$	2	-5	4	-1		
$2\ \Delta t^3\frac{\partial^3 u}{\partial t^3}$	-5	18	-24	14	-3	
$\Delta t^4\frac{\partial^4 u}{\partial t^4}$	3	-14	26	-24	11	-2

BACKWARD DIFFERENCE $\mathcal{O}(\Delta t)$

	u^{n-4}	u^{n-3}	u^{n-2}	u^{n-1}	u^n
$\Delta t\ \frac{\partial u}{\partial t}$				-1	1
$\Delta t^2\frac{\partial^2 u}{\partial t^2}$			1	-2	1
$\Delta t^3\frac{\partial^3 u}{\partial t^3}$		-1	3	-3	1
$\Delta t^4\frac{\partial^4 u}{\partial t^4}$	1	-4	6	-4	1

BACKWARD DIFFERENCE $\mathcal{O}(\Delta t^2)$

	u^{n-5}	u^{n-4}	u^{n-3}	u^{n-2}	u^{n-1}	u^n
$2\ \Delta t\ \frac{\partial u}{\partial t}$				1	-4	3
$\Delta t^2\frac{\partial^2 u}{\partial t^2}$			-1	4	-5	2
$2\ \Delta t^3\frac{\partial^3 u}{\partial t^3}$		3	-14	24	-18	5
$\Delta t^4\frac{\partial^4 u}{\partial t^4}$	-2	11	-24	26	-14	3

CENTRAL DIFFERENCE $\mathcal{O}(\Delta t^2)$

	u^{n-2}	u^{n-1}	u^n	u^{n+1}	u^{n+2}
$2\Delta t\ \frac{\partial u}{\partial t}$		-1	0	1	
$\Delta t^2\frac{\partial^2 u}{\partial t^2}$		1	-2	1	
$2\Delta t^3\frac{\partial^3 u}{\partial t^3}$	-1	2	0	2	1
$\Delta t^4\frac{\partial^4 u}{\partial t^4}$	1	-4	6	-4	1

CENTRAL DIFFERENCE $\mathcal{O}(\Delta t^4)$

	u^{n-3}	u^{n-2}	u^{n-1}	u^n	u^{n+1}	u^{n+2}	u^{n+3}
$12\ \Delta t\ \frac{\partial u}{\partial t}$		1	-8	0	8	-1	
$12\Delta t^2\frac{\partial^2 u}{\partial t^2}$		-1	16	-30	16	-1	
$8\ \Delta t^3\frac{\partial^3 u}{\partial t^3}$	1	-8	13	0	-13	8	-1
$6\ \Delta t^4\frac{\partial^4 u}{\partial t^4}$	-1	12	-39	56	-39	12	-1

C.2 1D finite difference schemes of various orders

C.3 Time stepping algorithms

Table 22.2 STANDARD TIME STEPPING METHODS FOR $du/dt = Q(t, u)$

EULER METHODS

	Scheme	Order
Explicit	$\tilde{u}^{n+1} = \tilde{u}^n \;+\; \Delta t Q^n$	Δt
Implicit	$\tilde{u}^{n+1} = \tilde{u}^n \;+\; \Delta t Q^{n+1}$	Δt
Trapezoidal	$\tilde{u}^{n+1} = \tilde{u}^n \;+\; \frac{\Delta t}{2}\left(Q^n + Q^{n+1}\right)$	Δt^2
General	$\tilde{u}^{n+1} = \tilde{u}^n \;+\; \Delta t\left((1-\alpha)Q^n + \alpha Q^{n+1}\right)$	Δt

MULTI-STAGE METHODS

	Scheme	Order
Runge-Kutta	$\tilde{u}^{n+1/2} = \tilde{u}^n \;+\; \frac{\Delta t}{2} Q(t^n, \tilde{u}^n)$ $\tilde{u}^{n+1} = \tilde{u}^n \;+\; \Delta t Q(t^{n+1/2}, \tilde{u}^{n+1/2})$	Δt^2
Runge-Kutta	$\tilde{u}_a^{n+1/2} = \tilde{u}^n \;+\; \frac{\Delta t}{2}\, Q(t^n, \tilde{u}^n)$ $\tilde{u}_b^{n+1/2} = \tilde{u}^n \;+\; \frac{\Delta t}{2}\, Q(t^{n+1/2}, \tilde{u}_a^{n+1/2})$ $\tilde{u}^\star = \tilde{u}^n \;+\; \Delta t\, Q(t^{n+1/2}, \tilde{u}_b^{n+1/2})$ $\tilde{u}^{n+1} = \tilde{u}^n \;+\; \Delta t\left(\frac{1}{6} Q(t^n, \tilde{u}^n) + \frac{2}{6} Q(t^{n+1/2}, \tilde{u}_a^{n+1/2})\right.$ $\left. + \frac{2}{6} Q(t^{n+1/2}, \tilde{u}_b^{n+1/2}) + \frac{1}{6} Q(t^{n+1}, \tilde{u}^\star)\right)$	Δt^4

MULTI-STEP METHODS

	Scheme	Truncation order
Leapfrog	$\tilde{u}^{n+1} = \tilde{u}^{n-1} \;+\; 2\Delta t Q^n$	Δt^2
Adams-Bashforth	$\tilde{u}^{n+1} = \tilde{u}^n \;+\; \frac{\Delta t}{2}\left(-Q^{n-1} + 3Q^n\right)$	Δt^2
Adams-Moulton	$\tilde{u}^{n+1} = \tilde{u}^n \;+\; \frac{\Delta t}{12}\left(-Q^{n-1} + 8Q^n + 5Q^{n+1}\right)$	Δt^3
Adams-Bashforth	$\tilde{u}^{n+1} = \tilde{u}^n \;+\; \frac{\Delta t}{12}\left(5Q^{n-2} - 16Q^{n-1} + 23Q^{n+1}\right)$	Δt^3

PREDICTOR-CORRECTOR METHODS

	Scheme	Order
Heun	$\tilde{u}^\star = \tilde{u}^n \;+\; \Delta t Q(t^n, \tilde{u}^n)$ $\tilde{u}^{n+1} = \tilde{u}^n \;+\; \frac{\Delta t}{2}\left(Q(t^n, \tilde{u}^n) + Q(t^{n+1}, \tilde{u}^\star)\right)$	Δt^2
Leapfrog-Trapezoidal	$\tilde{u}^\star = \tilde{u}^{n-1} \;+\; 2\Delta t Q^n$ $\tilde{u}^{n+1} = \tilde{u}^n \;+\; \frac{\Delta t}{2}\left(Q^n + 5Q(t^{n+1}, \tilde{u}^\star)\right)$	Δt^2
ABM	$\tilde{u}^\star = \tilde{u}^n \;+\; \frac{\Delta t}{2}\left(-Q^{n-1} + 3Q^n\right)$ $\tilde{u}^{n+1} = \tilde{u}^n \;+\; \frac{\Delta t}{12}\left(-Q^{n-1} + 8Q^n + 5Q(t^{n+1}, \tilde{u}^\star)\right)$	Δt^3

C.4 Partial derivatives finite differences

On a regular grid $x = i\Delta x + x_0$, $y = j\Delta y + y_0$, the following expressions are of second order

- Jacobian $J(a,b) = \frac{\partial a}{\partial x}\frac{\partial b}{\partial y} - \frac{\partial b}{\partial x}\frac{\partial a}{\partial y}$

$$
\begin{aligned}
J_{i,j}^{++} &= \frac{(a_{i+1,j}-a_{i-1,j})(b_{i,j+1}-b_{i,j-1})-(b_{i+1,j}-b_{i-1,j})(a_{i,j+1}-a_{i,j-1})}{4\Delta x\Delta y}\\
J_{i,j}^{+\times} &= \frac{[a_{i+1,j}(b_{i+1,j+1}-b_{i+1,j-1})-a_{i-1,j}(b_{i-1,j+1}-b_{i-1,j-1})]}{4\Delta x\Delta y}\\
&\quad -\frac{[a_{i,j+1}(b_{i+1,j+1}-b_{i-1,j+1})-a_{i,j-1}(b_{i+1,j-1}-b_{i-1,j-1})]}{4\Delta x\Delta y}\\
J_{i,j}^{\times +} &= \frac{[b_{i,j+1}(a_{i+1,j+1}-a_{i-1,j+1})-b_{i,j-1}(a_{i+1,j-1}-a_{i-1,j-1})]}{4\Delta x\Delta y}\\
&\quad -\frac{[b_{i+1,j}(a_{i+1,j+1}-a_{i+1,j-1})-b_{i-1,j}(a_{i-1,j+1}-a_{i-1,j-1})]}{4\Delta x\Delta y}
\end{aligned}
$$

- Cross derivatives

$$
\begin{aligned}
\left.\frac{\partial^2 u}{\partial x\partial y}\right|_{i+1/2,j+1/2} &\sim \frac{u_{i+1,j+1}-u_{i+1,j}+u_{i,j}-u_{i,j+1}}{\Delta x\Delta y}\\
\left.\frac{\partial^2 u}{\partial x\partial y}\right|_{i,j} &\sim \frac{u_{i+1,j+1}-u_{i+1,j-1}+u_{i-1,j-1}-u_{i-1,j+1}}{4\Delta x\Delta y}
\end{aligned}
$$

- Laplacian

$$
\left.\frac{\partial^2 u}{\partial x^2}+\frac{\partial^2 u}{\partial y^2}\right|_{i,j} \sim \frac{u_{i+1,j}+u_{i-1,j}-2u_{i,j}}{\Delta x^2}+\frac{u_{i,j+1}+u_{i,j-1}-2u_{i,j}}{\Delta y^2}
$$

C.5 DFT and FFT

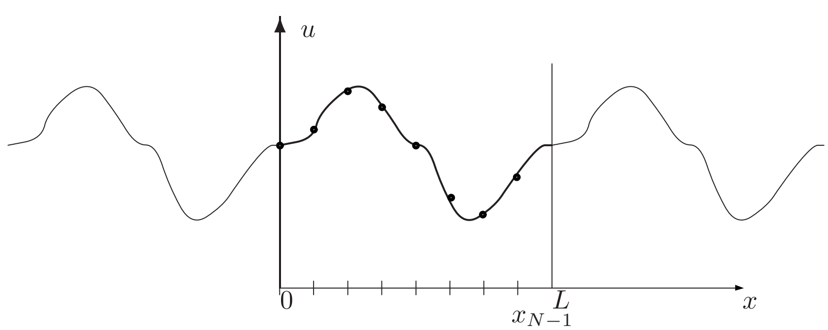

Figure 22-14 Perdiodic signal sampled with N evenly space points x_0 to x_{N-1}.

In a periodic domain in which x varies between 0 and L, a complex function $u(x)$ can be expanded in Fourier modes according to

$$u(x) \ = \ \sum_{n=-\infty}^{+\infty} a_n \, e^{\mathrm{i} \ n \frac{2\pi x}{L}} \tag{22.77}$$

using orthogonality properties of the fourier modes

$$\frac{1}{L} \int_0^L \ e^{\mathrm{i} \ (n-m) \frac{2\pi x}{L}} \, dx \ = \ \delta_{nm} \tag{22.78}$$

the complex coefficients a_n are obtained are readily obtained by multiplying (22.77) by $e^{-\mathrm{i} \ m \frac{2\pi x}{L}}$ and integrating

$$a_m = \frac{1}{L} \int_0^L u(x) \, e^{-\mathrm{i} \ m \frac{2\pi x}{L}} \, dx \tag{22.79}$$

Note that we could have used $a_n = b_n/L$ where b_n would then be calulated using the integral without the normalization $1/L$.

Discrete Fourier Transform (DFT) simply truncates[8] the infinite series to a finite serie

$$\tilde{u}(x) = \sum_{n=0}^{N-1} a_n \, e^{\mathrm{i} \ n \frac{2\pi x}{L}} \tag{22.80}$$

and uses $u(x)$ at a series of sampling points (the discrete values on a numerical grid for example) to determine the coefficients a_n. The points are regularely spaced $x_j \ = \ j \Delta x$, $j = 0, ..., N-1$. Because of periodicity using x_N would amount to use x_0 and is therefore not retained in the sampling. Complex coefficients can be evaluated as

$$\begin{aligned} a_n \quad &= \quad \frac{1}{N} \sum_{j=0}^{N-1} u(x_j) \, e^{-\mathrm{i} \ n \frac{2\pi x_j}{L}} \\ &= \quad \frac{1}{N} \sum_{j=0}^{N-1} u_j \, e^{-\mathrm{i} \ nj \frac{2\pi}{N}} \end{aligned} \tag{22.81}$$

where we write $u(x_j) = u_j$ to highlight the fact that we only use information at the discrete points. Obviously this is a dicrete version of the integral (22.79). The interesting point is that a_m are exact in the sense that if we evaluate $\tilde{u}(x_j)$ with those coefficients, we obtain the values at the grid points $u(x_j)$.

The proof of this not trivial results can be obtained by verifying the if we use coefficients

[8] The truncation from 0 to $N-1$ is somehow arbitrary and sometimes the presentation with a series from $-N/2$ to $N/2$ is preferred.

(22.81) in (22.80) at the grid points, we obtain $\tilde{u}(x_j) = u(x_j)$ We obtain successively

$$\begin{aligned} \tilde{u}(x_j) &= \sum_{n=0}^{N-1} a_n\, e^{\mathrm{i}\; n\frac{2\pi x_j}{L}} && (22.82) \\ &= \sum_{n=0}^{N-1} \frac{1}{N} \sum_{m=0}^{N-1} u_m\, e^{-\mathrm{i}\; nm\frac{2\pi}{N}}\; e^{\mathrm{i}\; nj\frac{2\pi}{N}} \\ &= \frac{1}{N} \sum_{m=0}^{N-1} u_m \left[\sum_{n=0}^{N-1} e^{\mathrm{i}\; (j-m)n\frac{2\pi}{N}} \right] \\ &= \frac{1}{N} \sum_{m=0}^{N-1} u_m \left[\sum_{n=0}^{N-1} \rho^n \right] && (22.83) \end{aligned}$$

where

$$\rho = e^{\mathrm{i}\; (j-m)\frac{2\pi}{N}} \tag{22.84}$$

For $j \neq m$, $\rho \neq 1$ and the geometric sum takes the value

$$\sum_{n=0}^{N-1} \rho^n = \frac{1-\rho^N}{1-\rho} = 0 \tag{22.85}$$

because $j - m$ is an integer so that $\rho^N = 1$.

When $j = m$ the sum is simply N and we arrive at $\tilde{u}(x_j) = u(x_j)$, the desired result. Transformation (22.81) is called the direct transform and (22.82) the inverse transform. As for the Fourier series, scaling can vary and the factor $1/N$ is commonly applied in the inverse transform rather the direct. Note that the inverse and direct transform are almost identical transformations, except for this scaling and more importantly the sign of the exponential.

Now (22.80) can be used for any x in the domain and because the function $\tilde{u}(x)$ takes the values $u(x_j)$ on the discrete points, we now have an interpolation function that can be used to calculate the value of the function at any desired location using N discrete values. Also (22.80) can be used to evaluate derivatives:

$$\frac{d\tilde{u}}{dx} = \sum_{n=0}^{N-1} \mathrm{i}\, k_n a_n\, e^{\mathrm{i}\; k_n x} \quad k_n = \frac{2\pi n}{L} \tag{22.86}$$

and all we have to do to calculate derivatives is to create Fourier coefficients $b_n = \mathrm{i}\, k_n a_n$ for the series on the derivative:

$$u(x) \xrightarrow{\text{sampling}} u(x_j) \xrightarrow{\text{DFT}(u_j)} a_n \xrightarrow{\text{derivation}} b_n = \mathrm{i}\, k_n a_n \xrightarrow{\text{IDFT}(b_n)} \left.\frac{d\tilde{u}}{dx}\right|_{x_j}$$

For a real signal u there is a redundancy in the coefficients a_n: From

$$\begin{aligned} a_{N-m} &= \frac{1}{N}\sum_{j=0}^{N-1} u_j\, e^{-\mathrm{i}\,(N-m)j\frac{2\pi}{N}} \\ &= \frac{1}{N}\sum_{j=0}^{N-1} u_j\, e^{+\mathrm{i}\,mj\frac{2\pi}{N}} \\ &= a_n^*. \end{aligned} \tag{22.87}$$

Also the wave number associated with $N-m$ in the serie (22.80) is equivalent to the one associated with m. In reality, the shortest signal resolved by the series corresponds to $n = N/2$ with wavenumber $k = N\pi/L$ or wavelength $2\Delta x$. Hence coefficient a_0 contains the information on the average value, a_1 on the wavelength L and so on down to $a_{N/2}$ which contains the complex amplitude of the shortest signal. We see why some presentations of the DFT define the series between $-N/2$ and $N/2$. The information content is however the same.

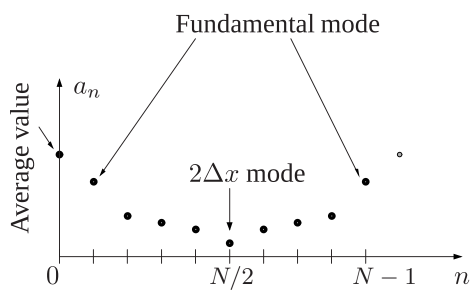

Figure 22-15 Coefficients a_n contain the amplitudes of the different modes. With the summation chosen from 0 to $N-1$, $a_{N/2}$ contains the amplitude of the shortest signal.

For real functions u, the DFT contains this some redundant information and some algorithms exploit this property. Cosine transforms CFT and sine transforms SFT perform in a similar way using only cosine or sine functions. Particularly usefull if the solution of a problem is known to satisfy homogenous boundary conditions. For Neuman conditions in $x = 0$ and $x = L$, CFT is the method of choice while for Dirichlet conditions, the development of the solution in terms of sine functions allows to satisfy these boundary conditions easily.

The problem with the transformation presented up to now is that a straightforward implementation as a sum of factors needs on a data array of length N for each coefficient a_n the calculation of N terms. Therefore N^2 operations in total are necessary for each transform. This is prohibitively expensive when used in large size problems and Cooley and Tukey introduced in 1965 which is probably among the most celebrated numerical algorithm, reducing the cost of the DFT to $N\log_2 N$ operations. Interestingly enough, the original idea of the method, now called Fast Fourier Transform, goes back to Gauss in 1805, long before the advent of calculators able to exploit it.

The Fast Fourier Transform is a practical calculation of the discrete Fourier transform and starts with the observation that we can write the transform by separating even and odd terms in j:

$$\begin{aligned} N a_n &= \sum_{\substack{j=0 \\ j \text{ even}}}^{N-1} u_j \, e^{-\mathrm{i}\, nj \frac{2\pi}{N}} + \sum_{\substack{j=0 \\ j \text{ odd}}}^{N-1} u_j \, e^{-\mathrm{i}\, nj \frac{2\pi}{N}} \\ &= \sum_{m=0}^{N/2-1} u_{2m} \, e^{-\mathrm{i}\, nm \frac{2\pi}{(N/2)}} + e^{-\mathrm{i}\, n \frac{2\pi}{N}} \sum_{m=0}^{N/2-1} u_{2m+1} \, e^{-\mathrm{i}\, nm \frac{2\pi}{(N/2)}} \end{aligned} \quad (22.88)$$

and for simplicity we assume N to be a power of two, which is also the case in which the method performs best. Each of the two sums involved is nothing else than a discrete transform working on $N/2$ data points. But those can in turn again be broken up in two smaller pieces and so on, a technique called *divide and conquer*. When N is a power of two, this recursive division is possible until all series contain only a single term. Such a single data point can transformed in a single operation and the recurrence can be followed back to retrieve the transform of the original series. To estimate the cost $C(N)$ for transformation of N data, we see that it is the cost of two transformations of size $N/2$ and the multiplication by $e^{-\mathrm{i}\, n \frac{2\pi}{N}}$ for each of the N coefficients a_n. Hence

$$C(N) = 2\, C\,(N/2) \, + N \quad (22.89)$$

For a single point one operation so that we can deduce

$$C(N) \sim N \log_2 N \quad (22.90)$$

There is thus a substantial gain compared to brute force approach, which is particularely interesting in spectral methods (Section) where direct and inverse transforms are intensively used.

Interpolation into regular (finer) grid: $x_k = k/ML, k = 0, ..., M-1$ from original data in $x_j = j/NL, j = 0, ..., N-1$ can now also be performed very efficiently. Simply assuming that shorter signal than those initially capture by the N points have zero amplitude. Means adding zeros in the middle of the array a_n and scale. Procedure called *padding*. Care must be taken to add the zeros in correct places, depending on the conventions used in the FFT routines (scale N in direct or inverse transformation and arrangement of coefficients a_n as a function of n or ordered according to their corresponding real wavenumber (from $-pi/L$ to π/L))

$$u(x_j) \xrightarrow{\text{FFT}(u_j)} a_n \xrightarrow{\text{Padding}} b_n = a_n + \text{zeros} \xrightarrow{\text{IFFT}(b_n)} \tilde{u}(x_k)$$

Analytical Problems

C-1. Find the truncation errors of the two Adams-Bashforth schemes by a Taylor expansion.

C-2. Which of the two second-order approximations of the cross-derivative has a lower truncation error?

C-3. Try to establish a finite-difference approximation of a Jacobian at a corner point $i + 1/2, j + 1/2$, using only values from the nearest grid points.

Numerical Exercises

C-1. Compare the behaviour of the second-order Adams-Bashforths method with the Leapfrog-Trapezoidal method on the calculation of an inertial oscillation.

C-2. Discretize a function $u(x, y) = \sin(2pix/L)\cos(2piy/L)$ on a regular grid in (x, y). Calculate the numerical Jacobian between

- $\tilde{u}$ and $\tilde{u}$,
- $\tilde{u}$ and $\tilde{u}^2$,
- $\tilde{u}$ and $\tilde{u}^3$,

and interprete your result.

C-3. Perform a FFT on $f(x) = \sin(2\pi x/L)$ between $x = 0$ and $x = L$, by sampling with 10, 20 or 40 point. Using the spectral coefficients from the FFT, plot the series expansion using a very fine resolution (200 points) and verify that you recover the initial function. Then repeat with the function $f(x) = x$. What do you observe?

C-4. Redo Excercise C-3. using the padding technique instead of a brute force series evaluation to plot the expansion.

REFERENCES

(October 18, 2006)

Backhaus, J. O., 1983: A semi-implicit scheme for the shallow water equations for application to shelf sea modelling. *Continental Shelf Res*, **2**, 243–254.

Bryan, K., 1969: Numerical Method for the Study of the World Ocean Circulation, *J. Comp. Phys.*, *4*, 1687–1712.

Ducet, N., P.-Y. Le Traon, and G. Reverdin, 2000: Global high resolution mapping of ocean circulation from Topex/Poseidon and ERS-1 and -2, *J. Geophys. Res.*, **105** (C8), 19477–19498.

Gardiner, C.W., 1997: *Handbook of Stochastic Methods* Springer Series in Synergetics, 2d ed., Springer, **13**, 442 pp.

Gauss, C. F. 1805: Theoria interpolationis methodo nova tractata, Werke Band **3**n 265–327, Nachlass Königliche Gesellschaft der Wissenschaften, Göttingen 1866)

Golub, and Van Loan, 1990: Matrix Computations

Hackbusch, W., 1985: *Multi-grid methods and applications*. Springer, Berlin, PP.

Heaps, N. S. (Ed.), 1987: Three dimensional Coastal Ocean Models, Vol 4 of Coastal and Estuarine Series, 1–16. American Geophys. Union, Washington, D. C., 208 pp

Killworth, P. D., D. Stainforth, D. J. Webb, and S. M. Paterson, 1991: The development of a free-surface Bryan-Cox-Semtner ocean model. *J. Phys. Oceanogr.*, **21**, 1333–1348.

¡¡¡¡¡¡¡¡¡¡¡¡¡¡¡¡¡¡¡¡¡¡¡¡¡¡¡¡¡¡¡¡¡

Abarbanel, H. D. I., and W. R. Young, eds., 1987: *General Circulation of the Ocean*. Springer-Verlag, New York, 291 pp.

Abbott, P. L., 2004: *Natural Disasters*, 4th ed., McGraw-Hill, 460 pp.

Abel, N. H., 1826: Beweis der Unmöglichkeit, algebraische Gleichungen von höheren Graden als dem vierten allgemein aufzulösen. *J. reine angew. Math.*, **1**, 65.

Abramowitz, M., and I. A. Stegun, eds., 1972: *Handbook of Mathematical Functions.* Dover, New York, 1046 pp.

Adcroft, A., C. Hill, and J. Marshall, 1997: Representation of topography by shaved cells in a height coordinate ocean model. *Mon. Wea. Rev.*, **125**, 2293–2315.

Adcroft, A., J-M Campin, C. Hill, and J. Marshall, 2004: Implementation of an atmosphere-ocean general circulation model on the expanded spherical cube. *Mon. Wea. Rev.*, **132**, 2845–2863.

Akerblom, F., 1908: Recherches sur les courants les plus bas de l'atmosphère au-dessus de Paris. *Nova Acta Reg. Soc. Sci.*, Uppsala, Ser. 4, **2**, 1–45.

Alvarez, A., A. Orfila, and J. Tintore, 2001: DARWIN: An evolutionary program for non-linear modeling of chaotic time series. *Computer Physics Communications*, **136**, 334–349.

Anthes, R. A., 1982: *Tropical Cyclones. Their Evolution, Structure and Effects*. Meteorological Monographs, **19**(41), American Meteorological Society, Boston, 208 pp.

Asselin, R., 1972: Frequency filter for time integrations. *Mon. Wea. Rev.*, **100**, 487–490.

Barcilon, V., 1964: Role of Ekman layers in the stability of the symmetric regime in a rotating annulus. *J. Atmos. Sci.*, **21**, 291–299.

Batchelor, G. K., 1967: *An Introduction to Fluid Dynamics*. Cambridge University Press, London and New York, 615 pp.

Beardsley, R. C., C. A. Mills, J. A. Vermersch, Jr., W. S. Brown, N. Pettigrew, J. Irish, S. Ramp, R. Schlitz, and B. Butman, 1983: *Nantucket Shoals Flux Experiment (NSFE'79). Part 2: Moored array data report.* Woods Hole Oceanographic Institution Tech. Rep. No. WHOI-83-13, 140 pp.

Beckers, J.-M., 1999: On some stability properties of the discretization of the damped propagation of shallow-water inertia-gravity waves on the Arakawa B-grid. *Ocean Modelling*, **1**, 53–69.

Beckers, J.-M., 2002: Selection of a staggered grid for inertia-gravity waves in shallow water. *Int. J. Num. Meth. Fluids*, **38**, 729–746.

Beckers, J.-M., and E. Deleersnijder, 1993: Stability of a FBTCS scheme applied to the propagation of shallow-water inertia-gravity waves on various space grids. *J. Comp. Phys.*, **108**, 95–104.

Beckers, J.-M., H. Burchard, E. Deleersnijder, and P.-P. Mathieu, 2000: Numerical discretisation of rotated diffusion operators in ocean models. *Mon. Wea. Rev.*, **128**, 2711–2733.

Beckers, J.-M., 1999: Application of Miller's theorem to the stability analysis of numerical schemes; some useful tools for rapid inspection of discretisations in ocean modelling. *Ocean Modelling*, **1**, 29–37.

Beckmann A., and D. B. Haidvogel, 1993: Numerical Simulation of Flow around a Tall Isolated Seamount. Part I: Problem Formulation and Model Accuracy. *J. Phys. Oceanogr.*, **23**, 1736–1753.

Beckmann, A., and R. Döscher, 1997: A method for improved representation of dense water spreading over topography in geopotential-coordinate models. *J. Phys. Oceanogr.*, **27**, 581–591.

Bender, C., and S. Orszag, 1978: *Advanced Mathematical Methods for Scientists and Engineers*, International Series in Pure and Applied Mathematics, McGraw-Hill, 593 pp.

Betts, A. K., 1986: A new convective adjustment scheme. Part I: Observational and theoretical basis. *Quart. J. R. Met. Soc.*, **112**, 677–691.

Bjerknes, V., 1904: Das Problem von der Wettervorhersage, betrachtet vom Standpunkte der Mechanik und der Physik (The problem of weather prediction considered from the point of view of Mechanics and Physics). *Meteorologische Zeitschrift*, **21**, 1–7. (English translation by Yale Mintz, 1954, reprinted in *The Life Cycles of Extratropical Cyclones*, M. A. Shapiro and S. Grønås, eds., American Meteorological Society, 1999, pages 1–4.)

Blayo, E., and L. Debreu, 2005: Revisiting open boundary conditions from the point of view of characteristic variables. *Ocean Modelling*, **9**, 231–252.

Bleck, R., C. Rooth, D. Hu, and L.T. Smith, 1992: Ventilation patterns and mode water formation in a wind- and thermodynamically driven isopycnic coordinate model of the North Atlantic, *J. Phys. Oceanogr.*, **22**, 1486–1505.

Bleck, R., 2002: An oceanic general circulation model framed in hybrid isopycnic-cartesian coordinates. *Ocean Modelling*, **4**, 55–88.

Blumen, W., 1972: Geostrophic adjustment. *Rev. Geophys. Space Phys.*, **10**, 485–528.

Booker, J. R., and F. P. Bretherton, 1967: The critical layer for internal gravity waves in a shear flow. *J. Fluid Mech.*, **27**, 513–539.

Boris, J., and D. Book, 1973: Flux-corrected transport. I. SHASTA, a fluid transport algorithm that works. *J. Comp. Phys.*, **11**, 38–69.

Boussinesq, J., 1903: *Théorie Analytique de la Chaleur*, Vol. 2. Gauthier-Villars, Paris.

Bower, A. S., and T. Rossby, 1989: Evidence of cross-frontal exchange processes in the Gulf Stream based on isopycnal RAFOS float data. *J. Phys. Oceanogr.*, **19**, 1177–1190.

Brink, K. H., 1983: The near-surface dynamics of coastal upwelling. *Progr. Oceanogr.*, **12**, 223–257.

Broeker, W. G., 1991: The great ocean conveyor. *Oceanography*, **4**, 79–85.

Brunt, D., 1927: The period of simple vertical oscillations in the atmosphere. *Quart. J. R. Met. Soc.*, **53**, 30–32.

Brunt, D., 1934: *Physical and Dynamical Meteorology*, Cambridge University Press, 411 pp. (Reedited in 1952)

Bryan, K., 1969: A numerical model for the study of the circulation of the world ocean. *J. Comp. Phys.*, **4**, 347–376.

Bryan, K., and M. D. Cox, 1972: The circulation of the world ocean: A numerical study. Part I, A homogeneous model. *J. Phys. Oceanogr.*, **2**, 319–335.

Buchanan, G., 1995: *Schaum's Outline of Finite Element Analysis*, Mc Graw-Hill, 264 pp.

Burchard, H., 2002: *Applied Turbulence Modelling in Marine Waters*, Springer, 229 pp.

Burchard, H., and J.-M. Beckers, 2004: Non-uniform adaptive vertical grids in one-dimensional numerical ocean models. *Ocean Modelling*, **6**, 51–81.

Burchard, H., and K. Bolding, 2001: Comparative analysis of four second-moment turbulence closure models for the oceanic mixed layer. *J. Phys. Oceanogr.*, **31**, 1943–1968.

Burchard, H., and E. D. Deleersnijder, 2001: Stability of algebraic non-equilibrium second-order closure models. *Ocean Modelling*, **3**, 33–50.

Burchard, H., E. Deleersnijder, and A. Meister, 2003: A high-order conservative Patankar-type discretisation for stiff systems of production-destruction equations *Applied Numerical Mathematics*, **47**, 1–30

Burchard, H., E. Deleersnijder, and A. Meister, 2005: Application of modified Patankar schemes to stiff biogeochemical models for the water column, *Ocean Dynamics*, **??**, ???–???.

Burger, A. P., 1958: Scale consideration of planetary motions of the atmosphere. *Tellus*, **10**, 195–205.

Cane, M. A., S. E. Zebiak, and S. C. Dolan, 1986: Experimental forecasts of El Niño. *Nature*, **321**, 827–832.

Canuto, C., M. Y. Hussaini, A. Quarteroni, and T. A. Zang, 1988: *Spectral Methods in Fluid Dynamics*, Springer-Verlag, 558 pp.

Canuto, V. M., A. Howard, Y. Cheng, and M. S. Dubovikov, 2001: Ocean turbulence. Part I: One-point closure model. Momentum and heat vertical diffusivities. *J. Phys. Oceanogr.*, **31**, 1413–1426.

Case, B., and M. Mayfield, 1990: Atlantic Hurricane Season of 1989. *Mon. Wea. Rev.*, **118**, 1165–1177.

Chandrasekhar, S., 1961: *Hydrodynamic and Hydromagnetic Stability.* Oxford University Press, London and New York, 652 pp.

Charney, J. G., 1947: The dynamics of long waves in a baroclinic westerly current. *J. Meteorol.*, **4**, 135–163.

Charney, J. G., 1948: On the scale of atmospheric motions. *Geofys. Publ. Oslo*, **17**(2), 1–17.

Charney, J. G., and J. G. DeVore, 1979: Multiple-flow equilibria in the atmosphere and blocking. *J. Atmos. Sci.*, **36**, 1205–1216.

Charney, J. G., and G. R. Flierl, 1981: Oceanic analogues of large-scale atmospheric motions. In *Evolution of Physical Oceanography*, B. A. Warren and C. Wunsch, eds., Chapter 18 (pp. 504–548) The MIT Press, Cambridge, Massachusetts.

Charney, J. G., and M. E. Stern, 1962: On the stability of internal baroclinic jets in a rotating atmosphere. *J. Atmos. Sci.*, **19**, 159–172.

Chen, D., M. A. Cane, A. Kaplan, S. E. Zebiak, and D. Huang, 2004: Predictability of El Niño over the past 148 years. *Nature*, **428**, 733–736.

Chung, T.J., 2002: *Computational Fluid Dynamics*, Cambridge University Press, 1012 pp.

Colella, P., 1990: Multidimensional upwind methods for hyperbolic conservation laws. *J. Comp. Phys.*, **87**, 171–200.

Colin, C., C. Henin, P. Hisard, and C. Oudot, 1971: Le Courant de Cromwell dans le Pacifique central en février. *Cahiers ORSTOM, Ser. Oceanogr.*, **9**, 167–186.

Conway, E. D., and the Maryland Space Grant Consortium, 1997: *An Introduction to Satellite Image Interpretation*, The Johns Hopkins University Press, 264 pp.

Cooley, J., and J. Tukey, 1965: An algorithm for the machine calculation of complex Fourier series. *Math. Comput*, **9**, 297–301.

Coriolis, G., 1835: Mémoire sur les équations du mouvement relatif des systèmes de corps. *J. Ecole Polytech. (Paris)*, **15**, 142–154.

Courant, R., K.P. Friedrichs, and H. Lewy, 1928: Über die partiellen Differenzengleichungen der mathematischen Physik, *Math. Annalen*, **100**, 32–74.

Courant, R., and D. Hilbert, 1924: *Methoden der mathematischen Physik I*, Springer Verlag Berlin, 470 pp.

Cox, M., 1984: A primitive three-dimensional model of the ocean. Rep. 1, Ocean Group, GFDL, Princeton.

Crank, J., 1987: *Free and moving boundary problems*, The Clarendon Press, Oxford University Press, New York, 424 pp.

Crépon, M., and C. Richez, 1982: Transient upwelling generated by two-dimensional atmospheric forcing and variability in the coastline. *J. Phys. Oceanogr.*, **12**, 1437–1457.

Cressman, G. P., 1948: On the forecasting of long waves in the upper westerlies. *J. Meteorol.*, **5**, 44–57.

Csanady, G. T., 1977: Intermittent 'full' upwelling in Lake Ontario. *J. Geophys. Res.*, **82**, 397–419.

Cushman-Roisin, B., 1984: Analytical, linear stability criteria for the Leap-Frog, Dufort-Frankel method. *J. Comp. Phys.*, **53**, 227–239.

Cushman-Roisin, B., 1986: Frontal geostrophic dynamics. *J. Phys. Oceanogr.*, **16**, 132–143.

Cushman-Roisin, B., 1987: On the role of heat flux in the Gulf Stream–Sargasso Sea–Subtropical Gyre system. *J. Phys. Oceanogr.*, **17**, 2189–2202.

Cushman-Roisin, B., 1987: Subduction. In *Dynamics of the Oceanic Surface Mixed Layer*, Proc. Hawaiian Winter Workshop *'Aha Huliko'a*, P. Müller and D. Henderson, eds., Hawaii Inst. Geophys. Special Pub., 181–196.

Cushman-Roisin, B., E. P. Chassignet, and B. Tang, 1990: Westward motion of mesoscale eddies. *J. Phys. Oceanogr.*, **20**, 758–768.

Cushman-Roisin, B., G. G. Sutyrin, and B. Tang, 1992: Two-layer geostrophic dynamics. Part I: Governing equations. *J. Phys. Oceanogr.*, **22**, 117–127.

Cushman-Roisin, B., and V. Malačič, 1997: Bottom Ekman pumping with stress-dependent eddy viscosity. *J. Phys. Oceanogr.*, **27**, 1967–1975.

Dahlquist, G., and A. Björck, 1974: *Numerical Methods*, Prentice-Hall, Englewood Cliffs, 573 pp.

D'Aleo, J. S., 2002: *The Oryx Guide to El Niño and La Niña*. Oryx Press, 230 pp.

Davies, A., 1987: Spectral models in continental shelf sea oceanography. In *Three-Dimensional Coastal Ocean Models*, N. Heaps, ed., American Geophysical Union, 71–106.

Deleersnijder, E., and J.-M. Beckers, 1992: On the use of the σ-coordinate system in regions of large bathymetric variations. *J. Marine Syst.*, **3** 381–390.

Deleersnijder E., J.-M. Campin, and E. J. M. Delhez, 2001: The concept of age in marine modeling : I. Theory and preliminary model results *J. Marine Syst.*, **28**, 229–267.

Diaz, H. F., and V. Markgraf (eds.), 2000: *El Niño and the Southern Oscillation. Multiscale Variability and Global and Regional Impacts*, Cambridge University Press, 512 pp.

Dongarra, J. J., I. A. Duffy, D. C. Sorensen, and H. A. van der Vorst, 1998: *Numerical Linear Algebra on High-Performance Computers*, SIAM, 342 pp.

Doodson, A. T., 1921: The harmonic development of the tide-generating potential. *Proc. R. Soc. A*, **100**, 304–329.

Dowling, T. E., and A. P. Ingersoll, 1988: Potential vorticity and layer thickness variations in the flow around Jupiter's Great Red Spot and White Oval BC. *J. Atmos. Sci.*, **45**, 1380–1396.

Dowling, T. E., and A. P. Ingersoll, 1989: Jupiter's Great Red Spot as a shallow-water system. *J. Atmos. Sci.*, **46**, 3256–3278.

Dritschel, D. G., 1988: Contour Surgery: A topological reconnection scheme for extended integrations using contour dynamics. *J. Comp. Phys.*, **77**, 240–266.

Dritschel, D. G., 1989: On the stabilization of a two-dimensional vortex strip by adverse shear. *J. Fluid Mech.*, **206**, 193–221.

Dukowicz, J., 1995: Mesh effects for Rossby waves. *J. Comp. Phys.*, **119**, 188–194.

Durran, D., 1999: *Numerical Methods for Wave Equations in Geophysical Fluid Dynamics*, Springer, 465 pp.

Eady, E. T., 1949: Long waves and cyclone waves. *Tellus*, **1**(3), 33–52.

Ekman, V. W., 1904: On dead water. *Sci. Results Norw. Polar Exped. 1893–96*, **5**(15).

Ekman, V. W., 1905: On the influence of the earth's rotation on ocean currents. *Arch. Math. Astron. Phys.*, **2**(11), 1–53.

Ekman, V. W., 1906: Beiträge zur Theorie der Meeresströmungen. *Ann. Hydrogr. Marit. Meteor.*, 1–50.

Ellison, T. H., and J. S. Turner, 1959: Turbulent entrainment in stratified flows. *J. Fluid Mech.*, **6**, 423–448.

Emmanuel, K., 1991: The theory of hurricanes. *Ann. Rev. Fluid Mech.*, **23**, 179–196.

Fernando, H. J. S., 1991: Turbulent mixing in stratified fluids. *Ann. Rev. Fluid Mech.*, **23**, 455–493.

Ferziger, J. M., and M. Perić, 1999: *Computational Methods for Fluid Dynamics*, Springer Verlag, 390 pp.

Flament, P., L. Armi, and L. Washburn, 1985: The evolving structure of an upwelling filament. *J. Geophys. Res.*, **90**, 11765–11778.

Flierl, G. R., 1987: Isolated eddy models in geophysics. *Ann. Rev. Fluid Mech.*, **19**, 493–530.

Flierl, G. R., V. D. Larichev, J. C. McWilliams, and G. M. Reznik, 1980: The dynamics of baroclinic and barotropic solitary eddies. *Dyn. Atmos. Oceans*, **5**, 1–41.

Flierl, G. R., P. Malanotte-Rizzoli, and N. J. Zabusky, 1987: Nonlinear waves and coherent vortex structures in barotropic beta-plane jets. *J. Phys. Oceanogr.*, **17**, 1408–1438.

Fornberg, B., 1998: *A Practical Guide to Pseudospectral Methods*, Cambridge University Press, 242 pp.

Fox, R. W., and A. T. McDonald, 1992: *Introduction to Fluid Mechanics*, 4th ed., John Wiley & Sons, New York, 829 pp.

Galperin, B., A. Rosati, L.H. Kantha, G.L. Mellor, 1989: Modelling rotating stratified turbulent flows with applications to oceanic mixed layers. *J. Phys. Oceanogr.*, **19**, 901–916.

Galperin, B., L.H. Kantha, S. Hassid, and A. Rosati,, 1988: A quasi-equilibrium turbulent energy model for geophysical flows. *J. Atmos. Sci.*, **45**, 55–62.

Garratt, J. R., 1992: *The Atmospheric Boundary Layer*, Cambridge University Press, 316 pp.

Garrett, C., and W. Munk, 1979: Internal waves in the ocean. *Ann. Rev. Fluid Mech.*, **11**, 339–369.

Gawarkiewicz, G., and D. C. Chapman, 1992: The role of stratification in the formation and maintenance of shelf-break fronts. *J. Phys. Oceanogr.*, **22**, 753–772.

Gent, P. R., and J. C . McWilliams, 1990: Isopycnal mixing in ocean circulation models. *J. Phys. Oceanogr.*, **20**, 150–155.

Gent, P. R., J. Willebrand, T. J. McDougall, and J.C. McWilliams, 1995: Parameterizing eddy-induced tracer transports in ocean circulation models. *J. Phys. Oceanogr.*, **25**, 463–474.

Gerdes, R., 1993: A primitive equation model using a general vertical coordinate transformation. Part 1: Description and testing of the model. *J. Geophys. Res.*, **98**, 14683–14701.

Gerschgorin, S., 1931: Über die Abgrenzung der Eigenwerte einer Matrix. *Izv. Akad. Nauk. USSR, Ser. Math.*, **7**, 749–754.

Gill, A. E., 1980: Some simple solutions for heat-induced tropical circulation. *Quart. J. R. Met. Soc.*, **106**, 447–462.

Gill, A. E., 1982: *Atmosphere-Ocean Dynamics*. Academic Press, 662 pp.

Gill, A. E., J. S. A. Green, and A. J. Simmons, 1974: Energy partition in the large-scale ocean circulation and the production of mid-ocean eddies. *Deep-Sea Res.*, **21**, 499–528.

Glantz, M. H., 2001: *Currents of Change: Impacts of El Niño and La Niña on Climate and Society*, 2nd ed., Cambridge University Press, 252 pp.

Goldstein, S., 1931: On the stability of superposed streams of fluids of different densities. *Proc. R. Soc. London A*, **132**, 524–548.

Gottlieb, D., and S. A. Orszag, 1977: *Numerical Analysis of Spectral Methods: Theory and Applications,* SIAM, 170 pp.

Grant, H. L., R. W. Stewart, and A. Moilliet, 1962: Turbulence spectra from a tidal channel. *J. Fluid Mech.*, **12**, 241–268.

Greatbatch, R. J., Y. Lu, and Y. Cai, 2001: Relaxing the Boussinesq approximation in ocean circulation models. *J. Atmos. Oceanic Tech.*, **18**, 1911–1923.

Griffies, S. M., 1998: The Gent-McWilliams skew flux. *J. Phys. Oceanogr.*, **28**, 831–841.

Griffies, S. M., C. Boning, F. O. Bryan, E. P. Chassignet, R. Gerdes, H. Hasumi, A. Hirst, A-M Treguier, and D. Webb. 2000: Developments in ocean climate modelling. *Ocean Modelling*, **2**, 123–192.

Griffiths, R. W., P. D. Killworth, and M. E. Stern, 1982: Ageostrophic instability of ocean currents. *J. Fluid Mech.*, **117**, 343–377.

Griffiths, R. W., and P. F. Linden, 1981: The stability of vortices in a rotating, stratified fluid. *J. Fluid Mech.*, **105**, 283–316.

Gustafson, T., and B. Kullenberg, 1936: Untersuchungen von Trägheitssttrömungen in der Ostsee. *Sven. Hydrogr. — Biol. Komm. Skr., Hydrogr.*, No. 13.

Hack, J. J., 1992: Climate system simulation: Basic numerical & computational concepts. In *Clim. Syst. Modeling*, K. E. Trenberth, ed., Chapter 9 (pp. 283–318), Cambridge University Press.

Hadley, G., 1735: Concerning the cause of the general trade-winds. *Phil. Trans. R. Soc. London*, **39**, 58–62.

Haidvogel, D. B., J. L. Wilkin, and R. Young, 1991: A semi-spectral primitive equation ocean circulation model using vertical sigma and orthogonal curvilinear horizontal coordinates. *J. Comp. Phys.*, **94**, 151–185.

Haidvogel, D., and A. Beckmann, 1999: *Numerical Ocean Circulation Modeling*, Imperial College Press, 318 pp. *Series of environmental science and management*, **2**, 1–318.

Häkkinen, S., 1990: Models and their applications to polar oceanography. In *Polar Oceanography. Part A: Physical Science*, W. O. Smith, Jr., ed., Chapter 7 (pp. 335–384), Academic Press.

Hallberg, R.W., 1995: Some aspects fo the circulation in ocean basins with isopycnals intersecting the sloping boundaries, *Ph.D. thesis, University of Washington, Seattle*, 244 pp.

Hanert, E., V. Legat, and E. Deleernsijder, 2003: A comparison of three finite elements to solve the linear shallow water equations, *Ocean Modelling*, **5**, 17–35.

Haney, R. L., 1991: On the pressure gradient force over steep topography in sigma coordinate ocean models. *J. Phys. Oceanogr.*, **21**, 610–619.

Hansen, J., I. Fung, A. Lacis, D. Rind, S. Lebedeff, R. Ruedy, G. Russell, and P. Stone, 1988: Global climate changes as forecast by the Goddard Institute for Space Studies three-dimensional model. *J. Geophys. Res.*, **93**, 9341–9364.

Harten, A., B. Engquist, S. Osher, and S.R. Chakravarthy, 1982: Uniformly high order accurate essentially non-oscillatory schemes, *J. Comp. Phys.*, **71**, 231–303.

Helmholtz, H. von, 1888: Über atmosphärische Bewegungen I. *Sitzungsberichte Akad. Wissenschaften Berlin*, **3**, 647–663.

Hendershott, M.C., 1972: The effects of solid earth deformation on global ocean tides. *Geophys. J. of the R. Astronomical Soc.*, **29**, 389–402.

Hirsch, C., 1989: *Numerical Computation of Internal and External Flows. Vol.1: Fundamentals of Numerical Discretization*, John Wiley, Chichester, 538 pp.

Hirsch, C., 1990: *Numerical Computation of Internal and External Flows. Vol. 2: Computational Methods for Inviscid and Viscous Flows*, John Wiley, Chichester, 714 pp.

Hodnett, P. F., 1978: On the advective model of the thermocline circulation. *J. Mar. Res.*, **36**, 185–198.

Holton, J. R., 1992: *An Introduction to Dynamic Meteorology*, 3rd ed. Academic Press, 511 pp.

Hoskins, B. J., M. E. McIntyre, and A. W. Robertson, 1985: On the use and significance of isentropic potential vorticity maps. *Quart. J. R. Met. Soc.*, **111**, 877–946.

Howard, L. N., 1961: Note on a paper of John W. Miles. *J. Fluid Mech.*, **10**, 509–512.

Hsueh, Y., and B. Cushman-Roisin, 1983: On the formation of surface to bottom fronts over steep topography. *J. Geophys. Res.*, **88**, 743–750.

Hurlburt, H. E., and J. D. Thompson, 1980: A numerical study of loop current intrusions and eddy-shedding. *J. Phys. Oceanogr.*, **10**, 1611–1651.

Hunkins, K., 1966: Ekman drift currents in the Arctic Ocean. *Deep-Sea Res.*, **13**, 607–620.

Ingersoll, A .P., R. F. Beebe, S. A. Collins, G. E. Hunt, J. L. Mitchell, P. Muller, B. A. Smith, and R. J. Terrile, 1979: Zonal velocity and texture in the Jovian atmosphere inferred from Voyager images. *Nature*, **280**, 773–775.

Intergovernmental Panel on Climate Change (IPCC), 2001: *Climate Change 2001: The Scientific Basis*. Contribution of Working Group I to the Third Report Assessment of the Intergovernmental Panel on Climate Change. J. T. Houghton, Y. Ding, D. J. Griggs, M. Noguer, P. J. van der Linden, X. Dai, K. Maskell and C. A. Johnson (eds.). Cambridge University Press, 892 pp.

Ito, S., 1992: *Diffusion equations*, Translations of mathematical monographs, **114**, American Mathematical Soc., 225 pp.

Jones, W. L., 1967: Propagation of internal gravity waves in fluids with shear flow and rotation. *J. Fluid Mech.*, **30**, 439–448.

Kalnay, E., S. J. Lord, and R. D. McPherson, 1998: Maturity of operational numerical weather prediction: Medium range. *Bull. Am. Met. Soc.*, **79**, 2753–2769.

Kantha, L.H., and C.A. Clayson, 1994: An improved mixed layer model for geophysical applications. *J. Geophys. Res.*, **99**, 25235–25266.

Killworth, P. D., N. Paldor, and M. E. Stern, 1984: Wave propagation and growth on a surface front in a two-layer geostrophic current. *J. Mar. Res.*, **42**, 761–785.

Kolmogorov, A. N., 1941: Dissipation of energy in locally isotropic turbulence. *Dokl. Akad. Nauk SSSR*, **32**, 19–21 (in Russian).

Kraus, E. B., ed., 1977: *Modelling and Prediction of the Upper Layers of the Ocean*. Pergamon, Oxford, 325 pp.

Kreiss, H.-O., 1962: Über die Stabilitätsdefinition für Differenzengleichungen die partielle Differentialgleichungen approximieren. *Nordisk Tidskrift Informationsbehandling (BIT)*, **2**, 153–181.

Kundu, P. K., 1990: *Fluid Mechanics*, Academic Press, 638 pp.

Kuo, H. L., 1949: Dynamic instability of two-dimensional nondivergent flow in a barotropic atmosphere. *J. Meteorol.*, **6**, 105–122.

Kuo, H. L., 1974: Further studies of the parameterization of the influence of cumulus convection on large-scale flow. *J. Atmos. Sci.*, **31**, 1232–1240.

Lawrence, G. A., F. K. Browand, and L. G. Redekopp, 1991: The stability of a sheared density interface. *Phys. Fluids A, Fluid Dyn.*, **3**, 2360–2370.

Lax, P. D., and R. D. Richtmyer, 1956: Survey of the stability of linear finite difference equations. *Comm. Pure Appl. Math.*, **9**, 267–293.

Lax, P. D., and B. Wendroff, 1960: Systems of conservation laws, *Comm. Pure Appl. Math.*, **13**, 217–237.

LeBlond, P. H., and L. A. Mysak, 1978: *Waves in the Ocean*, Elsevier Oceanography Series **20**, 602 pp.

Legrand S., V. Legat, and E. Deleersnijder, 2000: Delaunay mesh generation for an unstructured-grid ocean general circulation model. *Ocean Modelling*, **2**, 17–28

Lindzen, R. S., 1988: Instability of plane parallel shear flow. (Toward a mechanistic picture of how it works.) *Pure and Applied Geophys.*, **126**, 103–121.

Lindzen, R. S., 1990: Some coolness concerning global warming. *Bull. Am. Met. Soc.*, **71**, 288–299.

Liseikin, V., 1999: *Grid Generation Methods*, Springer, Berlin-Heidelberg, 362 pp.

Long, R. R., 1997: Homogeneous isotropic turbulence and its collapse in stratified and rotating fluids. *Dyn. Atmos. Oceans*, **27**, 471–483.

Long, R. R., 2003: Do tidal-channel turbulence measurements support $k^{-5/3}$? *Environmental Fluid Mech.*, **3**, 109–127.

Love, A. E. H., 1893: On the stability of certain vortex motions. *Proc. London Math. Soc. Ser. 1*, **25**, 18–42.

Lorenz, E. N., 1955: Available potential energy and the maintenance of the general circulation. *Tellus*, **7**, 157–167.

Lutgens, F. K., and E. J. Tarbuck, 1986: *The Atmosphere. An Introduction to Meteorology*, 3rd ed., Prentice-Hall, 492 pp.

Luyten, J. R., J. Pedlosky, and H. Stommel, 1983: The ventilated thermocline. *J. Phys. Oceanogr.*, **13**, 292–309.

Madec G., P. Delecluse, M. Imbard, C. Lévy, 1998: *OPA 8.1 Ocean General Circulation Model reference manual. Note du Pôle de modélisation*, Institut Pierre-Simon Laplace, N11, 91, pp

Madsen, O. S., 1977: A realistic model of the wind-induced Ekman boundary layer. *J. Phys. Oceanogr.*, **7**, 248–255.

Manabe, S., 1969: Climate and the ocean circulation. II. The atmospheric circulation and the effect of heat transfer by ocean currents. *Mon. Wea. Rev.*, **97**, 775–805.

Manabe, S., J. Smagorinsky, and R. F. Strickler, 1965: Simulated climatology of a general circulation model with a hydrologic cycle. *Mon. Wea. Rev.*, **93**, 769–798.

Manabe, S., R. J. Stouffer, M. J. Spelman, and K. Bryan, 1991: Transient responses of a coupled ocean-atmosphere model to gradual changes of atmospheric CO_2. Part I: Annual mean response. *J. Climate*, **4**, 785–818.

Margules, M., 1903: Über die Energie der Stürme. *Jahrb. Zentralanst. Meteorol. Wien*, **40**, 1–26. (English translation in Abbe, 1910, *The Mechanics of the Earth's Atmosphere. A Collection of Translations.* Misc. Collect. No. 51, Smithsonian Institution, Washington, D.C.)

Margules, M., 1906: Über Temperaturschitchtung in stationär bewegter und ruhender Luft. *Meteorol. Z.*, **23**, 243–254.

Marotzke, J., 1991: Influence of convective adjustment on the stability of the thermohaline circulation. *J. Phys. Oceanogr.*, **21**, 903–907.

Marshall, J., H. Jones, and C. Hill, 1998: Efficient ocean modeling using non-hydrostatic algorithms. *J. Marine Syst.*, **18**, 115–134.

Marshall, J., and F. Schott, 1999: Open-ocean convection: observations, theory and models. *Rev. Geophys.*, **37**, 1–64.

Marzano, F. S., and G. Visconti, eds., 2002: *Remote Sensing of Atmosphere and Ocean from Space: Models, Instruments and Techniques*. Kluwer Academic Publishers, 246 pp.

Masuda, A., 1982: An interpretation of the bimodal character of the stable Kuroshio path. *Deep-Sea Res.*, **29**, 471–484.

Mathieu, P.-P., E. Deleersnijder, B. Cushman-Roisin, J.-M. Beckers, and K. Bolding, 2002: The role of topography in small well-mixed bays, with application to the lagoon of Mururoa. *Cont. Shelf Res.*, **22**, 1379–1395.

Mathur, M. B., 1991: The National Meteorological Center's quasi-lagrangian model for hurricane prediction. *Mon. Wea. Rev.*, **119**, 1419–1447.

McCalpin, J. D., 1994: A comparison of second-order and fourth-order pressure gradient algorithms in σ-coordinate ocean model. *Int. J. Num. Meth. Fluids*, **128**, 361–383.

McDougall, T. J., and W. K. Dewar, 1998: Vertical mixing and cabbeling in layered models. *J. Phys. Oceanogr.*, **28**, 1458–1480.

McPhaden, M. J., and P. Ripa, 1990: Wave-mean flow interactions in the equatorial ocean. *Ann. Rev. Fluid Mech.*, **22**, 167–205.

McWilliams, J. C., 1984: The emergence of isolated coherent vortices in turbulent flow. *J. Fluid Mech.*, **146**, 21–43.

McWilliams, J. C., 1989: Statistical properties of decaying geostrophic turbulence. *J. Fluid Mech.*, **198**, 199–230.

Mechoso, C. R., A. W. Robertson, N. Barth, M. K. Davey, P. Delecluse, P. R. Gent, S. Ineson, B. Kirtman, M. Latif, H. Letreut, T. Nagai, J. D. Neelin, S. G. H. Philander, J. Polcher, P. S. Schopf, T. Stockdale, M. J. Suarez, L. Terray, O. Thual, and J. J. Tribbia, 1995: The seasonal cycle over the tropical pacific in coupled ocean-atmosphere general-circulation models. *Mon. Wea. Rev.*, **123**, 2825–2838.

Mellor, G. L., and T. Yamada, 1982: Development of a turbulence closure model for geophysical fluid problems. *Rev. Geophys. Space Phys.*, **20**, 851–875.

Mellor, G., L.-Y. Oey, and T. Ezer, 1998: Sigma coordinate pressure gradient errors and the seamount problem. *Atmos. Oceanic Tech.*, **15**, 1112–1131.

Mesinger, F., and A. Arakawa, 1976: Numerical methods used in the atmospheric models. *GARP publications Series*, **1**.

Miles, J. W., 1961: On the stability of heterogeneous shear flows. *J. Fluid Mech.*, **10**, 496–508.

Miller, J. H., 1971: On the Location of Zeros of certain classes of Polynomials with applications to numerical analysis. *J. Inst. Maths. Applics.*, **8**, 397–406.

Mofjeld, H. O., and J. W. Lavelle, 1984: Setting the length scale in a second-order closure model of the unstratified bottom boundary layer. *J. Phys. Oceanogr.*, **14**, 833–839.

Mohebalhojeh, A. R., and D. G. Dritschel, 2004: Contour-advective semi-Lagrangian algorithms for many layer primitive equation models. *Quart. J. R. Met. Soc.*, **130**, 347–364.

Moore, D. W., 1963: Rossby waves in ocean circulation. *Deep-Sea Res.*, **10**, 735–748.

Montgomery, R. B., 1937: A suggested method for representing gradient flow in isentropic surfaces. *Bull. Am. Met. Soc.*, **18**, 210–212.

Munk, W. H., 1981: Internal waves and small-scale processes. In *Evolution of Physical Oceanography*, B. A. Warren and C. Wunsch, eds., Chapter 9 (pp. 264–291) The MIT Press, Cambridge, Massachusetts.

Nebeker, F., 1995: *Calculating the Weather: Meteorology in the 20th Century*. Academic Press, 251 pp.

Neelin, J. D., M. Latif, M. A. F. Allaart, M. A. Cane, U. Cubasch, W. L. Gates, P. R. Gent, M. Ghil, C. Gordon, N. C. Lau, C. R. Mechoso, G. A. Meehl, J.-M. Oberhuber, S. G. H. Philander, P. S. Schopf, K. R. Sperber, A. Sterl, T. Tokioka, J. J. Tribbia, and S. E. Zebiak, 1992: Tropical air-sea interaction in general-circulation models. *Clim. dynamics*, **7**, 73–104.

Nihoul, J. C. J. (ed.), 1975: *Modelling of Marine Systems*, Elsevier Oceanography Series, **10**, Amsterdam, 272 pp.

Nof, D., 1983: The translation of isolated cold eddies on a sloping bottom. *Deep-Sea Res.*, **39**, 171–182.

O'Brien, J. J., 1978: El Niño – An example of ocean/atmosphere interactions. *Oceanus*, **21**(4), 40–46.

Okubo, A., 1971: Oceanic diffusion diagrams. *Deep-Sea Res.*, **18** 789–802.

Okubo, A.,, and S. A. Levin, 2002: *Diffusion and Ecological Problems*, 2nd ed., Springer, 488 pp.

Olson, D. B., 1991: Rings in the ocean. *Ann. Rev. Earth Planet. Sci.*, **19**, 283–311.

Orlanski, I., 1968: Instability of frontal waves. *J. Atmos. Sci.*, **25**, 178–200.

Orlanski, I., 1969: The influence of bottom topography on the stability of jets in a baroclinic fluid. *J. Atmos. Sci.*, **26**, 1216–1232.

Orlanski, I., and M. D. Cox, 1973: Baroclinic instability in ocean currents. *Geophys. Fluid Dyn.*, **4**, 297–332.

Orszag, S. A., 1970: Transform method for calculation of vector-coupled sums: Application to the spectral form of the vorticity equation. *J. Atmos. Sci.*, **27**, 890–895.

Ou, H. W., 1984: Geostrophic adjustment: A mechanism for frontogenesis. *J. Phys. Oceanogr.*, **14**, 994–1000.

Ou, H. W., 1986: On the energy conversion during geostrophic adjustment. *J. Phys. Oceanogr.*, **16**, 2203–2204.

Patankar, S. V., 1980: *Numerical Heat Transfer and Fluid Flow*, McGraw-Hill, New York, 198 pp.

Pedlosky, J., 1963: Baroclinic instability in two-layer systems. *Tellus*, **15**, 20–25.

Pedlosky, J., 1964: The stability of currents in the atmosphere and oceans. Part I. *J. Atmos. Sci.*, **27**, 201–219.

Pedlosky, J., and H. P. Greenspan, 1967: A simple laboratory model for the oceanic circulation. *J. Fluid Mech.*, **27**, 291–304.

Pedlosky, J., 1987: *Geophysical Fluid Dynamics*, 2nd ed., Springer Verlag, 710 pp.

Pedlosky, J., 1996: *Ocean Circulation Theory*. Springer, 453 pp.

Pedlosky, J., 2003: *Waves in the Ocean and Atmosphere: Introduction to Wave Dynamics*. Springer, 260 pp.

Philander, S. G., 1990: *El Niño, La Niña, and the Southern Oscillation*. Academic Press, Orlando, Florida, 289 pp.

Philander, S. G. H., T. Yamagata, and R. C. Pacanowski, 1984: Unstable air-sea interactions in the tropics. *J. Atmos. Sci.*, **41**, 604–613.

Phillips, N. A., 1954: Energy transformations and meridional circulations associated with simple baroclinic waves in a two-level, quasi-geostrophic model. *Tellus*, **6**, 273–286.

Phillips, N. A., 1956: The general circulation of the atmosphere: a numerical experiment. *Quart. J. R. Met. Soc.*, **82**, 123–164.

Phillips, N. A., 1963: Geostrophic motion. *Rev. Geophys.*, **1**, 123–176.

Pickard, G. L., and W. J. Emery, 1990: *Descriptive Physical Oceanography. An Introduction*. 5th ed., Pergamon Press, New York, 320 pp.

Pietrzak, J., 1998: The use of TVD limiters for forward-in-time upstream-biased advection schemes in ocean modeling. *Mon. Wea. Rev.*, **126**, 812–830.

Pietrzak, J. J. Jakobson, H. Burchard, H.-J. Vested, and O. Petersen, 2002: A three-dimensional hydrostatic model for coastal and ocean modelling using a generalised topography following co-ordinate system. *Ocean Modelling*, **4** 173–205.

Pollard, R. T., P. B. Rhines, and R. O. R. Y. Thompson, 1973: The deepening of the wind-mixed layer. *Geophys. Fluid Dyn.*, **4**, 381–404.

Pope, S. B., 2000: *Turbulent Flows*. Cambridge University Press, 771 pp.

Price, J. F., and M. A. Sundermeyer, 1999: Stratified Ekman layers. *J. Geophys. Res.*, **104**, 20467–20494.

Proehl, J. A., 1996: Linear stability of equatorial zonal flows. *J. Phys. Oceanogr.*, **26**, 601–621.

Proudman, J., 1953: *Dynamical Oceanography*. Methuen, London, and John Wiley, New York, 409 pp.

Randall, D., ed., 2000: *General circulation model development. Past, present, and future* 70, International Geophysics Series, Academic Press, pp 807

Rao, P. K., S. J. Holmes, R. K. Anderson, J. S. Winston, and P. E. Lehr, 1990: *Weather Satellites: Systems, Data, and Environmental Applications*. American Meteorological Society, Boston, 503 pp.

Rayleigh, Lord (John William Strutt), 1880: On the stability, or instability, of certain fluid motions. *Proc. London Math. Soc.*, **9**, 57–70. (Reprinted in *Scientific Papers by Lord Rayleigh*, Vol. ?, ???–???).

Rayleigh, Lord (John William Strutt), 1916: On convection currents in a horizontal layer of fluid, when the higher temperature is on the under side. *Phil. Mag.*, **32**, 529–546 (Reprinted in *Scientific Papers by Lord Rayleigh*, Vol. 6, 432–446).

Redi, M. H., 1982: Oceanic isopycnal mixing by coordinate rotation. *J. Phys. Oceanogr.*, **12**, 1154–1158.

Reynolds, O., 1894: On the dynamical theory of incompressible viscous flows and the determination of the criterion. *Phil. Trans. R. Soc. London A*, **186**, 123–161.

Rhines, P. B., 1975: Waves and turbulence on the beta-plane. *J. Fluid Mech.*, **69**, 417–443.

Rhines, P. B., 1977: The dynamics of unsteady currents. In *The Sea*, E.D. Goldberg et al., eds., Vol. 6, Wiley, 189–318.

Richards, F. A., ed., 1981: *Coastal Upwelling*. Coastal and Estuarine Sciences, Vol. 1, American Geophysical Union, Washington, D.C., 529 pp.

Richardson, L. F., 1922: *Weather Prediction by Numerical Process*. Cambridge University press. Reprinted by Dover Publications, 1965, 236 pp.

Richtmyer, R.D., and Morton, K.W., 1967: *Difference methods for initial-value problems (2nd ed.)*. Interscience, John Wiley and Sons, New York, 405pp.

Riley, K. F., M. P. Hobson, and S. J. Bence, 1997: *Mathematical Methods for Physics and Engineering*. Cambridge University Press, 1008 pp.

Ripa, P., 1994: *La Increíble Historia de la Malentendida Fuerza de Coriolis*. La Ciencia/128 desde México, 101 pp.

Rixen, M., J.-M. Beckers, and J. T. Allen, 2001: Diagnosis of vertical velocities with the QG-Omega equation: a relocation method to obtain pseudo-synoptic data sets. *Deep-Sea Res.*, **48**, 1347–1373.

Robinson, A. R., 1965: A three-dimensional model of inertial currents in a variable-density ocean. *J. Fluid Mech.*, **21**, 211–223.

Robinson, A. R., ed., 1983: *Eddies in Marine Science*. Springer-Verlag, 609 pp.

Robinson, A. R., and J. C. McWilliams, 1974: The baroclinic instability of the open ocean. *J. Phys. Oceanogr.*, **4**, 281–294.

Robinson, A. R., M. A. Spall, and N. Pinardi, 1988: Gulf Stream simulations and the dynamics of ring and meander processes. *J. Phys. Oceanogr.*, **18**, 1811–1853.

Robinson, A. R., and B. Taft, 1972: A numerical experiment for the path of the Kuroshio. *J. Mar. Res.*, **30**, 65–101.

Robinson, I., 2004: *Measuring the Oceans from Space. The Principles and Methods of Satellite Oceanography*, Springer-Praxis, 670 pp.

Roll, H. U., 1965: *Physics of the Marine Atmosphere*. Academic Press, 426 pp.

Rossby, C. G., 1937: On the mutual adjustment of pressure and velocity distributions in certain simple current systems. I. *J. Mar. Res.*, **1**, 15–28.

Rossby, C. G., 1938: On the mutual adjustment of pressure and velocity distributions in certain simple current systems. II. *J. Mar. Res.*, **2**, 239–263.

Rossby, C. G., 1940: Planetary flow patterns in the atmosphere. *Quart. J. R. Met. Soc.*, **66**, Suppl., 68–87.

Roussenov, V., R. G. Williams, and W. Roether, 2001: Comparing the overflow of dense water in isopycnic and cartesian models with tracer observations in the eastern Mediterranean. *Deep-Sea Res.*, **48**, 1255–1277.

Saddoughi, S. G., and S. V. Veeravalli, 1994: Local isotropy in turbulent boundary layers at high Reynolds number. *J. Fluid Mech.*, **268**, 333–372.

Saffman, P. G., 1968: Lectures on homogeneous turbulence. In *Topics in Nonlinear Physics*, N. J. Zabusky, ed., Springer Verlag, 485–614.

Salmon, R., 1982: Geostrophic turbulence. In *Topics in Ocean Physics*, Proc. Int. School of Phys. Enrico Fermi LXXX, A. R. Osborne & P. Malanotte-Rizzoli, eds., pp. 30–78, North-Holland Elsevier Sci. Publ.

Schmitz, W. J., Jr., 1980: Weakly depth-dependent segments of the North Atlantic circulation. *J. Mar. Res.*, **38**, 111–133.

Shapiro, L. J., 1992: Hurricane vortex motion and evolution in a three-layer model. *J. Atmos. Sci.*, **49**, 140–153.

Smagorinsky, J. 1963: General circulation experiments with the primitive equations. I. The basic experiment, *Mon. Wea. Rev.*, **91**, 99–164.

Song, T., 1998: A general pressure gradient formulation for ocean models. Part I: scheme design and diagnostic analysis. *Mon. Wea. Rev.*, **126**, 3213–3230.

Sorbjan, Z., 1989: *Structure of the Atmospheric Boundary Layer*. Prentice Hall, Englewood Cliffs, New Jersey, 317 pp.

Spagnol S., E. Wolanski, E. Deleersnijder, R. Brinkman, F. McAllister, B. Cushman-Roisin and E. Hanert, 2002: An error frequently made in the evaluation of advective transport in two-dimensional Lagrangian models of advection-diffusion in coral reef waters, *Marine Ecology Progress Series*, **235**, 299–302.

Spiegel, E. A., and G. Veronis, 1960: On the Boussinesq approximation for a compressible fluid. *Astrophys. J.*, **131**, 442–447.

Stacey, M. W., S. Pond, and P. H. LeBlond, 1986: A wind-forced Ekman spiral as a good statistical fit to low-frequency currents in coastal strait. *Science*, **233**, 470–472.

Stern, A. C., R. W. Boubel, D. B. Turner, and D. L. Fox, 1984: *Fundamentals of Air Pollution*. Academic Press, 530 pp.

Stigebrandt, A., 1985: A model for the seasonal pycnocline in rotating systems with application to the Baltic Proper. *J. Phys. Oceanogr.*, **15**, 1392–1404.

Stoer, J., and R. Bulirsh, 2002: *Introduction to Numerical Analysis*, 3rd ed., Texts in Applied Mathematics, **12**, 744 pp.

Stommel, H. M., 1948: The westward intensification of wind-driven ocean currents. *Trans. Am. Geophys. Union*, **29**, 202–206.

Stommel, H. M., 1965: *The Gulf Stream: A Physical and Dynamical Description*, 2nd ed., University of California Press, Berkeley, 248 pp.

Stommel, H. M., 1979: Determination of water mass properties of water pumped down from the Ekman layer to the geostrophic flow below. *Proc. Nat. Acad. Sci. USA*, **76**, 3051–3055.

Stommel, H. M., and D. W. Moore, 1989: *An Introduction to the Coriolis Force*. Columbia University Press, Irvington, New York, 297 pp.

Stommel, H. M., and F. Schott, 1977: The beta spiral and the determination of the absolute velocity field from hydrographic data. *Deep-Sea Res.*, **24**, 325–329.

Stommel, H., and G. Veronis, 1980: Barotropic response to cooling. *J. Geophys. Res.*, **85**, 6661–6666.

Strang, G., 1968: On the construction and comparison of difference schemes, *SIAM J. Num. Anal.*, **5**, 506–517.

Stull, R. B., 1988: *Boundary-Layer Meteorology*, Kluwer Academic Publishers, 666 pp.

Stull, R. B., 1991: Static stability – An update. *Bull. Am. Met. Soc.*, **72**, 1521–1529 (Corrigendum: *Bull. Am. Met. Soc.*, **72**, 1883).

Stull, R. B., 1993: Review of nonlocal mixing in turbulent atmospheres: Transilient turbulence theory. *Boundary-Layer Meteorol.*, **62**, 21–96.

Sturm , T. W., 2001: *Open Channel Hydraulics*. McGraw-Hill, 493 pp.

Suarez, M., and P. Schopf, 1988: A Delayed Action Oscillator for ENSO. *J. Atmos. Sci.*, **45**, 3283–3287.

Sutyrin, G. G., 1989: The structure of a monopole baroclinic eddy. *Oceanology*, **29**(2), 139–144 (English translation).

Sverdrup, H. U., 1947: Wind-driven currents in a baroclinic ocean, with application to the equatorial currents of the eastern Pacific. *Proc. Nat. Acad. Sci. U.S.A.*, **33**, 318–326.

Sweby, P. K., 1984: High resolution schemes using flux-limiters for hyperbolic conservation laws. *SIAM J. Num. Anal.*, **21**, 995–1011.

Tangang, F. T., B. Tang, A. H. Monahan, and W. W. Hsieh, 1998: Forecasting ENSO events: a neural network - extended EOF approach. *J. Climate*, **11**, 29–41.

Taylor, G. I., 1923: Experiments on the motion of solid bodies in rotating fluids. *Proc. R. Soc. London A*, **104**, 213–218.

Taylor, G. I., 1931: Effect of variation in density on the stability of superposed streams of fluid. *Proc. R. Soc. London A*, **132**, 499–523.

Tennekes, H., and J. L. Lumley, 1972: *A First Course in Turbulence*. The MIT Press, Cambridge, Massachusetts, 300 pp.

Thompson, J. F., Z. U. A. Warsi, and C. W. Mastin, 1985: *Numerical Grid Generation: Foundations and Applications*, North Holland, 483 pp.

Thomson, W. (Lord Kelvin), 1879: On gravitational oscillations of rotating water. *Proc. R. Soc. Edinburgh*, **10**, 92–100. (Reprinted in *Phil. Mag.*, **10**, 109–116, 1880; *Math. Phys. Pap.*, **4**, 141–148, 1910.)

Thuburn, J., 1996: Multidimensional flux-limited advection schemes. *J. Comp. Phys.*, **123**, 74–83.

Turner, J. S., 1973: *Buoyancy Effects in Fluids*, Cambridge University Press, 367 pp.

Umlauf, L., and H. Burchard, 2003: A generic length-scale equation for geophysical turbulence models. *J. Mar. Res.*, **61**, 235–265.

Umlauf, L., and H. Burchard, 2005: Second-order turbulence closure models for geophysical boundary layers. A review of recent work. *Cont. Shelf Res.*, **25**, 795–827.

Väisälä, V., 1925: Über die Wirkung der Windschwankungen auf die Pilotbeobachtungen. *Soc. Sci. Fenn. Commentat. Phys.-Math.*, **219**, 19–37.

Van Dyke, M., 1975: *Perturbation Methods in Fluid Mechanics*, Parabolic Press, 271 pp.

van Heijst, G. J. F., 1985: A geostrophic adjustment model of a tidal mixing front. *J. Phys. Oceanogr.*, **15**, 1182–1190.

Verkley, W. T. M., 1990: On the beta-plane approximation. *J. Atmos. Sci.*, **47**, 2453–2460.

Veronis, G., 1956: Partition of energy between geostrophic and non-geostrophic oceanic motions. *Deep-Sea Res.*, **3**, 157–177.

Veronis, G., 1963: On the approximations involved in transforming the equations of motion from a spherical surface to the β-plane. I. Barotropic systems. *J. Mar. Res.*, **21**, 110–124.

Veronis, G., 1967: Analogous behavior of homogeneous, rotating fluids and stratified, non-rotating fluids. *Tellus*, **19**, 326–336.

Veronis, G., 1981: Dynamics of large-scale ocean circulation. In *Evolution of Physical Oceanography*, B. A. Warren and C. Wunsch, eds., Chapter 5 (pp. 140–183), The MIT Press, Cambridge, Massachusetts.

Vonder Haar, T. H., and A. H. Oort, 1973: New estimate of annual poleward energy transport by northern hemisphere oceans. *J. Phys. Oceanogr.*, **3**, 169–172.

Wallace, J. M., and V. E. Kousky, 1968: Observational evidence of Kelvin waves in the tropical stratosphere. *J. Atmos. Sci.*, **25**, 900–907.

Warren, B. A., and C. Wunsch, 1981: *Evolution of Physical Oceanography: Scientific Surveys in Honor of Henry Stommel*, The MIT Press, Cambridge, Massachusetts, 623 pp.

Weatherly, G. L., and P. J. Martin, 1978: On the structure and dynamics of the ocean bottom boundary layer. *J. Phys. Oceanogr.*, **8**, 557–570.

Williams, G. P., and R. J. Wilson, 1988: The stability and genesis of Rossby vortices. *J. Atmos. Sci.*, **45**, 207–241.

Winston, J. S., A. Gruber, T. I. Gray, Jr., M. S. Varnadore, C. L. Earnest, and L. P. Mannello, 1979: *Earth-atmosphere radiation budget analyses from NOAA satellite data June 1974–February 1978.* National Environmental Satellite Service, NOAA, Dept. of Commerce, Washington, D. C., Volume 2.

WMO, 1999: *WMO Statement on the Status of the Global Climate in 1998.* WMO – No.896, World Meteorological Organization, Geneva, 12 pp.

Woods, J. D., 1968: Wave-induced shear instability in the summer thermocline. *J. Fluid Mech.*, **32**, 791–800 + 5 plates.

Wyrtki, K., 1973: Teleconnections in the equatorial Pacific Ocean. *Science*, **180**, 66–68.

Yoshida, K., 1955: Coastal upwelling off the California coast. *Rec. Oceanogr. Works Japan*, **2**(2), 1–13.

Yoshida, K., 1959: A theory of the Cromwell Current and of the equatorial upwelling – An intepretation in a similarity to a coastal circulation. *J. Oceanogr. Soc. Japan*, **15**, 154–170.

Zabusky, N. J., M. H. Hughes, and K. V. Roberts, 1979: Contour dynamics for the Euler equations in two dimensions. *J. Comp. Phys.*, **30**, 96–106.

Zalesak, S. T., 1979: Fully multidimensional flux-corrected transport algorithms for fluids. *J. Comp. Phys.*, **31**, 335–362.

Zebiak, S. E., and C. A. Cane, 1987: A model El-Niño southern oscillation. *Mon. Wea. Rev.*, **115**, 2262–2278.

Zienkiewicz, O. C., and R. L. Taylor, 2000: *Finite Element Method: Volume 1. The Basis*, 5th ed., Butterworth-Heinemann, 712 pp.

Zienkiewicz, O. C., R. L. Taylor, and P. Nithiarasu, 2005: *The Finite Element Method for Fluid Dynamics*, 6th ed., Butterworth-Heinemann, 400 pp.

Zilitinkevich, S., 1991: *Turbulent Penetrative Convection*. Avebury Technical, Aldershot, 179 pp.

Index

T

U

V

W

Part VI

CD-ROM informations

The CD-ROM contains MATLAB™ scripts.

Some precalculated movies (in Quicktime format).

No optimization in terms of efficient programming was done, and clear identification of numerical schemes preferred.

An OCTAVE clone `http://octave.sourceforge.net`.

To switch between a Matlab or Octave version, edit `matoct.m` for defining which type of graphics to use.

Working tools and rules